To Caroline

Butterworth-Heinemann Ltd
Linacre House, Jordan Hill, Oxford OX2 8DP

A Member of the Reed Elsevier plc group

OXFORD LONDON BOSTON
MUNICH NEW DELHI SINGAPORE SYDNEY
TOKYO TORONTO WELLINGTON

First published 1994

British Library Cataloguing in Publication Data
A catalogue record for this book is available from the British Library

ISBN 0 7506 1143 X

Library of Congress Cataloguing in Publication Data
A catalogue record for this book is available from the Library of Congress

Typeset by Vision Typesetting, Manchester
Printed by Martin's The Printers Ltd., Berwick upon Tweed

Contents

Preface

Although the propeller normally lies well submerged out of sight and therefore, to some extent, also out of mind, it is a deceptively complex component in both the hydrodynamic and the structural sense. The subject of propulsion technology embraces many disciplines: for example, those of mathematics, physics, metallurgy, naval architecture and mechanical and marine engineering. Clearly, the dependence of the subject on such a wide set of basic disciplines introduces the possibility of conflicting requirements within the design process, necessitating some degree of compromise between opposing constraints. It is the attainment of this compromise that typifies good propeller design.

The foundations of the subject were laid during the latter part of the last century and the early years of this century. Since that time much has been written and published in the form of technical papers, but the number of books which attempt to draw together all of these works on the subject from around the world is small. A brief study of the bibliography shows that, with the exception of Gerr's recent book dealing with the practical aspects of the design of small craft propellers, little has been published dealing with the subject as an entity since the early 1960s. Over the last thirty or so years an immense amount of work, both theoretical and empirical, has been undertaken and published, probably more than in any preceding period. The principal aim, therefore, of this book is to collect together the work that has been done in the field of propeller technology up to the present time in each of the areas of hydrodynamics, strength, manufacture and design, so as to present an overall view of the subject and the current levels of knowledge.

The book is mainly directed toward practising marine engineers and naval architects, principally within the marine industry but also in academic and research institutions. In particular when writing this book I have kept in mind the range of questions about propeller technology that are frequently posed by designers, ship operators and surveyors and I have attempted to provide answers to these questions. Furthermore, the book is based on the currently accepted body of knowledge of use to practical design and analysis; current research issues are addressed in a less extensive manner. For example, recent developments in surface panel techniques and Navier–Stokes solutions are dealt with in less detail than the currently more widely used lifting-line, lifting-surface and vortex-lattice techniques of propeller analysis. As a consequence a knowlege of mathematics, fluid mechanics and engineering science is assumed commensurate with these premises. Notwithstanding this, it is to be hoped that students at both undergraduate and postgraduate levels will find the book of value to their studies.

The first two chapters of the book are essentially an introduction to the subject: firstly, a brief history of the early development of propellers and, secondly, an introduction to the different propeller types that are either of topical interest or, alternatively, will not be considered further in the book; for example, paddle wheels or superconducting electric propulsion. Chapter 3 considers propeller geometry and, consequently, this chapter can be viewed as a foundation upon which the rest of the book is built. Without a thorough knowledge of propeller geometry, the subject will not be fully understood. Chapters 4 and 5 concern themselves with the environment in which the propeller operates and the wake field in particular. The wake field and its various methods of prediction and transformation, particularly from nominal to effective, are again fundamental to the understanding of the design and analysis of propellers.

Chapters 6–15 deal with propulsion hydrodynamics, first in the context of model results and theoretical methods relating to propellers fixed to line shafting, then moving on to ship resistance and propulsion, including the important subjects of propeller hull interaction and thrust augmentation devices, and finally to consideration of the specific aspects of fixed and rotable thrusters and waterjets. Chapter 16 addresses the all-important subject of sea trials in terms of the conditions necessary for a valid trial, instrumentation and analysis.

Chapters 17–20 deal with the mechanical aspects of propellers. Materials, manufacture, blade strength and vibration are the principal subjects of these four chapters, and the techniques discussed are generally applicable to all types of propulsors. The final five chapters, 21 through to 25, discuss various practical aspects of propeller technology, starting with design, then continuing to operational problems, service performance and, finally, to propeller inspection, repair and maintenance.

In each of the chapters of the book the attainment of a fair balance between theoretical and practical considerations has been attempted, so that the information presented will be of value to the practitioner in marine science. For more advanced studies, particularly of a theoretical nature, the data presented here will act as a starting point for further research: in the case of the theoretical hydrodynamic aspects of the subject, some of the references contained in the bibliography will be found to be of value.

This book, representing as it does a gathering together of the subject of propulsion technology, is based upon the research of many scientists and engineers throughout the world. Indeed, it must be remembered that without these people, many of whom have devoted considerable portions of their lives to the development of the subject, this book could not have been written and, indeed, the subject of propeller technology could not have developed so far. I hope that I have done justice to their efforts in this book. At the end of each chapter a series of references is given so that, if necessary, the reader may refer to the original work, which will contain full details of the specific research topic under consideration. I am also considerably indebted to my colleagues, both within Lloyd's Register and in the marine industry, for many discussions on various aspects of the subject over the years, all of which have helped to provide a greater insight into, and understanding of, the subject. Particularly, in this respect, thanks are given to Mr C. M. R. Wills, Mr P. A. Fitzsimmons and Mr D. J. Howarth who, as specialists in particular branches of the subject, have also read several of the chapters and made many useful comments concerning their content. I would also like to thank Mr A. W. O. Webb who, as a specialist in propeller materials technology and colleague, has given much helpful advice over the years in solving propeller problems and this together with his many technical papers has influenced much of the text of Chapters 17 and 25. Also, I am particularly grateful to Mr J. Th. Ligtelign of MARIN and to Dr G. Patience of Stone Manganese Marine Ltd, who have supplied me with several photographs for inclusion in the text and with whom many stimulating discussions on the subject have been had over the years. Thanks are also due to the many kind ladies who have so painstakingly typed the text of this book over the years and without whom the book would not have been produced.

J. S. Carlton
London,
May 1993

General nomenclature

Upper case

A	Cross-sectional area
A_C	Admiralty coefficient
A_D	Developed area
A_E	Expanded area
A_M	Mid-ship section area
A_O	Disc area
A_P	Projected area
AR	Aspect ratio
B	Moulded breadth of ship
B_P	Propeller power coefficient
BAR	Blade area ratio
C_A	Correlation factor
	Section area coefficient
C_b	Ship block coefficient
C_D	Drag coefficient
C_F	Frictional resistance coefficient
C_L	Lift coefficient
C_M	Moment coefficient
	Section modulus coefficient
C_P	Pressure coefficient
	Ship prismatic coefficient
	Propeller power coefficient
C_T	Thrust loading coefficient
	Total resistance coefficient
C_W	Wavemaking resistance coefficient
D	Drag force
	Propeller diameter
D_b	Behind diameter
D_o	Diameter of slipstream for upstream
D_s	Shaft diameter
	Force
	Fetch of sea
F_B	Bollard pull
F_n	Froude number
G	Boundary layer unique shape function
	Non-dimensional circulation coefficient
H	Hydraulic head
H_p	Pump head
I	Dry inertia
I_e	Polar entrained inertia
IVR	Inlet velocity ratio
J	Advance coefficient
J_p	Ship polar moment of inertia
K	Prandtl or Goldstein factor
K_a	Knapp's similarity parameter
K_p	Pressure coefficient
K_Q	Propeller torque coefficient
K_{QS}	Spindle torque coefficient
K_T, K_{TP}	Propeller thrust coefficient
K_{TN}, K_{TD}	Duct thrust coefficient
K_Y	Side force coefficient
L	Length of ship or duct
	Lift force
	Section centrifugal bending moment arm
L_P	Sound pressure level
L_{PP}	Length of ship between perpendiculius
L_R	Length of run
L_{WL}	Length of ship along water line
M	Moment of force
M_a	Mach number
N	Rotational speed (RPM)
	Number of cycles
N_S	Specific speed
	Propeller pitch
	Number of fatigue cycles
P_B	Brake power
P_D	Delivered power
P_E	Effective power
P_G	Generator power
P_S	Shaft power

Q	Flow quantity
	Propeller torque
QPC	Quasi propulsive coefficient
Q_s	Total spindle torque
Q_{SC}	Centrifugal spindle torque
Q_{SF}	Frictional spindle torque
Q_{SH}	Hydrodynamic spindle torque
	Radius of propeller, paddle wheel or bubble
	Specific gas constant
R_{AIR}	Air resistance of ship
R_{APP}	Appendage resistance
R_e	Real part
R_F	Frictional resistance
R_n	Reynolds number
R_T	Total resistance
R_V	Viscous resistance
R_W	Wavemaking resistance
S	surface tension
	Ship wetted surface area
S_A	Additional load scale factor
S_a	Apparent slip
SBF	Solid boundary factor
S_C	Camber scale factor
T	Temperature
	Draught of ship
T, T_p	Propeller thrust
T_A	Draught aft
T_F	Draught forward
T_N, T_D	Duct thrust
U_T	Propeller tip speed
V	Volume
	Velocity
V_a	Speed of advance
V_s	Ship speed
x	Distance along coordinate axis
y	Distance along coordinate axis
W	Resultant velocity
	Width of channel
W_e	Weber number
Z	Blade number
	Distance along coordinate axis
Z_m	Section modulus

Lower case

a	Propeller axial inflow factor
a_1	Propeller tangential inflow factor
a_r	Resistance augmentation factor
a_c	Crack length
b	Span of wing
c	Wake contraction factor
	Section chord length
c_d	Section drag coefficient
c_l	Section lift coefficient
c_{li}	Ideal section lift coefficient
c_m	Section moment coefficient
c_{max}	Limiting chord length
f	Frequency
	Function of ...
g	Acceleration due to gravity
	Function of ...
h	Fluid enthalpy
	Height
	Hydraulic head
h_b	Height of bulbous bow centroid from base line in transverse plane
i	Counter
i_G	Section generator line rake
i_p	Propeller rake
i_s	Section skew induced rake
i_T	Total rake of propeller section
j	Counter
k	Counter
k_c	Lifting surface camber correction factor
k_s	Mean apparent amplitude of surface roughness
k_t	Lifting surface thickness correction factor
k_a	Lifting surface ideal angle of attack correction factor
$(1 + k)$	Frictional form factor
l	Counter
	Length
lcb	Longitudinal centre of buoyancy
m	Mass
	Counter
$\dot{m}$	Specific mass flow
n	Rotational speed (rps)
p	Section pitch
	Pressure
p_c	Cavity variation induced pressure
p_H	Propeller induced pressure
p_o	Reference pressure
	Non-cavitating pressure
	Pitch of reference section

p_v	Hull induced vibratory pressure
	Vapour pressure
p^1	Apparent induced pressure
q	Dynamic flow pressure
r	Radius of a propeller section
r_h	Hub or boss radius
s	Length parameter
t	Time
	Thrust deduction factor
	Section thickness
t_F	Thickness fraction
t_{max}	Maximum thickness
t_o	Notional blade thickness at shaft centre-line
u	Local velocity
v	Local velocity
v_a	Axial velocity
v_r	Radial velocity
v_t	Tangential velocity
v_T	Tide speed
w	Downwash velocity
w	Mean wake fraction
w_F	Fraude wake fraction
w_{max}	Maximum value of wake fraction in propeller disc
w_n	Nominal wake fraction
w_p	Potential wake fraction
w_T	Tayler wake fraction
w_v	Viscous wake fraction
w_w	Wave induced wake fraction
x	Distance along a coordinate axis
	Non-dimensional radius (r/R)
x_c	Distance along chord
	Radial position of centroid
x_{cp}	Centre of pressure measured along chord
x_o	Reference section
y	Distance along coordinate axis camber
y_c	Camber ordinate
y_L	Section lower surface ordinate
y_t	Thickness ordinate
y_U	Section upper surface ordinate
z	Distance along coordinate axis

Suffixes

m	Model
s	Ship
U	Upper
L	Lower
b	Bound, behind
F	Free
O	Reference value
x	Reference radius

Greek and other symbols

α	Angle of attack
	Gas content
α_d	Cavitation bucket width
α_i	Ideal angle of attack
α_K	Air content ratio
α_0	Zero lift angle
β	Advance angle
β_t	Hydrodynamic pitch in the ultimate wake
β_i	Hydrodynamic pitch angle
Γ	Circulation
γ	Local vortex strength
	Length parameter
	Ratio of drag to lift coefficient (C_d/C_l)
γ_s	Correction to angle of attack due to cascade effects
Δ	Change in parameter
	Displacement of ships
δ	Boundary layer thickness
	Linear displacement
	Propeller speed coefficient
ε	Thrust eccentricity
	Transformation parameter
ζ	Bendemann static thrust factor
	Damping factor
	Transformation parameter
η_b	Propeller behind hull efficiency
η_h	Hull efficiency
η_i	Ideal efficiency
η_m	Mechanical efficiency
η_o	Propeller open water efficiency
η_p	Pump efficiency
η_r	Relative rotatative efficiency
θ	Pitch angle
	Transformation parameter
	Momentum thickness of boundary layer
θ_{fp}	Face pitch angle
θ_{lp}	Propeller rake angle
θ_{nt}	Nose tail pitch angle
θ_o	Effective pitch angle
θ_s	Section skew angle
θ_{sp}	Propeller skew angle
θ_w	Angular position of transition wake roll-up point
Λ	Frequency reduction ratio
λ	Wave length
	Source–sink strength

	Ship-model scale factor
μ	Coefficient of dynamic viscosity
ϱ	Density of water
ρ_a	Density of air
ϱ_L	Leading edge radius
ϱ_m	Density of blade material
σ	Cavitation number
	Stress on section
σ_a	Alternating stress
σ_F	Corrosion fatigue strength
σ_i	Inception cavitation number
σ_L	Local cavitation number
σ_{MD}	Mean design stress
σ_n	Cavitation number based on rotational speed
	Relative shaft angle
σ_0	Free stream cavitation number
σ_R	Residual stress
σ_s	Blade solidity factor
σ_t	Blade stress at location on blade
τ	Shear stress
τ_C	Thrust loading coefficient
υ	Coefficient of kinematic viscosity
ϕ	Angle of rotation in propeller plane
	Hull form parameter
	Velocity potential
	Angular displacement
	Flow coefficient
	Shaft alignment angle relative to flow
ψ	Transformation parameter
	Gas content number
	Energy transfer coefficient
Ω	Angular velocity
ω	Angular velocity
∇	Volumetric displacement

Abbreviations

A.E.W.	Admiralty Experiment Works, Haslar
AP	After perpendicular
ATTC	American Towing Tank Conference
BHP	Brake Horse Power
BS	British Standard
CAD	Computer aided design
CAM	Computer aided manufacture
cwt	Hundred Weight (1 cwt = 112 lbf = 50.8 kgf)
DES	Design
DHP	Delivered horsepower
DTNSRDC	David Taylor Naval Ship Research and Design Centre
EHP	Effective horsepower
ft	Feet
HMS	Her Majesty's Ship
h.p.	Horsepower
HSVA	Hamburg Ship Model Basin
IMO	International Maritime Organisation
ITTC	International towing tank conference
LE	Leading edge
MARIN	Maritime Research Institute of the Netherlands
MCR	Maximum continuous rating
m.p.h.	Miles per hour
NACA	National Advisory Council for Aeronautics
NC	Numerically controlled
NCR	Normal continuous rating
OD	Oil distribution
PHV	Propulsor hull vortex
qrs	Quarters (4 qrs = 1 cwt)
R.H.	Right handed
RPM	Revolutions per minute
SHP	Shaft horsepower
SM	Simpson's multiplier
SSPA	Statens Skeppsprovningsanstalt, Göteborg
TE	Trailing edge
THP	Thrust horsepower
VTOL	Vertical take-off and landing

Part One

Hydrodynamics

1 The early development of the screw propeller

Both Archimedes (c. 250 BC) and Leonardo da Vinci (c. 1500) can be justly credited with having had the initial thoughts on screw propulsion. In the case of Archimedes, his thinking centred on the application of the screw pump which bears his name and this provided considerable inspiration to the 19th century engineers involved in marine propulsion; unfortunately, however, it also gave rise to several misconceptions about the basis of propeller action. In contrast Leonardo da Vinci, in his sketchbooks which were produced some 1700 years after Archimedes, shows an alternative form of screw propulsion based on the idea of using fan blades having a similar appearance to those used for cooling purposes today.

The development of screw propulsion as we recognize it today, however, can be traced back to the work of Robert Hooke, who is perhaps better remembered for his work on the elasticity of materials. Hooke in his *Philosophical Collections* presented to the Royal Society in 1681, explained the design of a horizontal water-mill which was remarkably similar in its principle of operation to the Kirsten–Boeing vertical axis propeller developed two and a half centuries later. Returning, however, to Hooke's water-mill; it comprised six wooden vanes, geared to a central shaft and pinned vertically to a horizontal circular rotor. The gearing constrained the vanes to rotate through 180° about their own spindle axes for each complete revolution of the rotor.

During his life Hooke was also interested in the subject of metrology and in the course of his work he developed an air flow meter based on the principle of a windmill. He successfully modified this instrument in 1683 to measure water currents and then foresaw the potential of this invention to drive ships through the water if provided with a suitable means of motive power. As seen in Figure 1.1 the instrument comprises

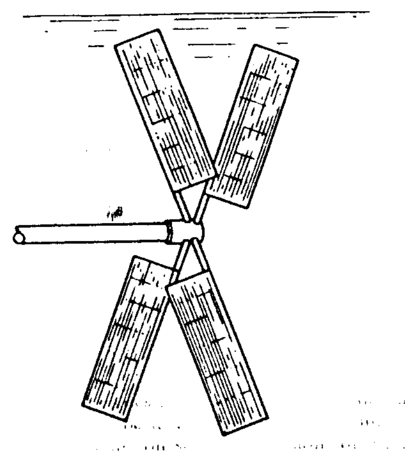

Figure 1.1 Hooke's screw propeller (1683)

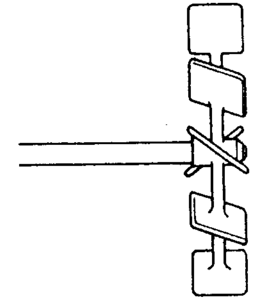

Figure 1.2 Bernoulli's propeller wheel (1752)

four, flat rectangular blades located on radial with the blades inclined to the plane of rotation

Some years later in 1752 the Academie des Sci in Paris offered a series of prizes for research theoretical methods leading to significant developm in naval architecture. As might be expected, famous mathematicians and scientists of Europe attracted by this offer and names such as d'Alem Euler and Bernoulli appear in the contribut Bernoulli's contribution, for which he won a introduced the propeller wheel, shown in Figure which he intended to be driven by a Newc steam-engine. With this arrangement he calcu that a particular ship could be propelled at just $2\frac{1}{2}$ knots by the application of some 20 2 Opinion, however, was still divided as to the suitable propulsor configuration, as indeed it w be for many years to come. For example, the Fr mathematician Paucton, working at about the time as Bernoulli, suggested a different appr illustrated in Figure 1.3 which was based on Archimedean screw.

Thirty-three years after the Paris invitation J. Bramah in England proposed an arrangement screw propeller located at the stern of a vessel w as may be seen from Figure 1.4, contains most features that we associate with screw prop

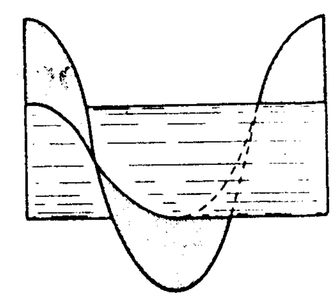

Figure 1.3 Archimedean screw of Paucton

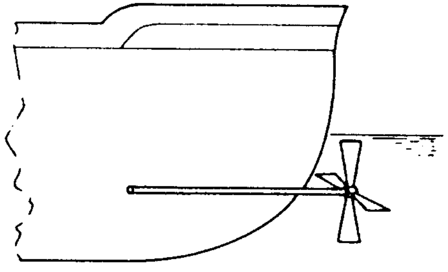

Figure 1.4 Bramah's screw propeller design (1785) (Reproduced from Reference 3, with permission)

today. It comprises a propeller with a small number of blades driven by a horizontal shaft which passes into the hull below the water-line. There appears, however, to be no evidence of any trials of a propeller of this kind being fitted to a ship and driven by a steam engine. Subsequently, in 1803 Edward Shorter used a variation of Bramah's idea to assist sailing vessels that were becalmed to make some headway. In Shorter's proposal, Figure 1.5, the shaft was designed to pass into the vessel's hull above the water-line and consequently eliminated the need for seals; the motive power for this propulsion arrangement was provided by eight men at a capstan. Using this technique, Shorter managed to propel a deeply loaded ship at a speed of 1.5 miles per hour in calm conditions: perhaps understandably, in view of the means of propulsion, no further application of Shorter's propeller was recorded.

Colonel John Stevens, who was a lawyer in the United States of America and a man of substantial financial means, experimented with screw propulsion in the year following Shorter's proposal. As a basis for his work he built a 25 ft long boat into which he installed a rotary steam engine and coupled this directly to a four-bladed propeller. The blades of this propeller were flat iron plates riveted to forgings which formed a 'spider-like' boss attachment to the shaft. Stevens later replaced the rotary engine with a steam-engine of the Watt type and managed to attain a steady cruising speed of 4 m.p.h. with some occasional surges of up to 8 m.p.h. However, he was not impressed with the overall performance of his craft and decided to turn his attention and energies to other means of marine propulsion.

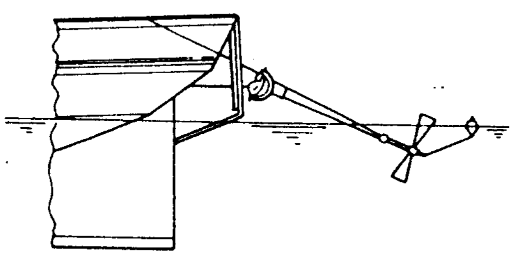

Figure 1.5 Shorter's propulsion system (1803) (Reproduced from Reference 3, with permission)

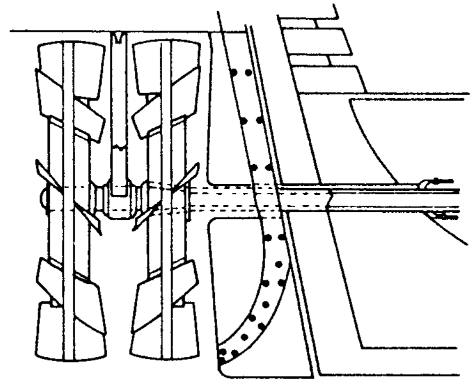

Figure 1.6 Ericsson's contra-rotating screw propeller (1836)

In 1824 contra-rotating propellers made their appearance in France in a design produced by Monsieur Dollman. He used a two-bladed set of windmill type propellers rotating in opposite directions on the same shaft axis to propel a small craft. Following on from this French development the scene turned once again to England, where John Ericsson, a former Swedish army officer residing at that time in London, designed and patented in 1836 a propulsion system comprising two contra-rotating propeller wheels. His design is shown in Figure 1.6, from which it can be seen that the individual wheels were not dissimilar in outline to Bernoulli's earlier proposal. Each wheel comprised eight short, wide blades of a helical configuration mounted on a blade ring with the blades tied at their tips by a peripheral strap. In this arrangement the two wheels were allowed to rotate at different speeds, no doubt to overcome the problem of the different flow configurations induced in the forward and after wheels. Ericsson conducted his early trials on a 3 ft model, and the results proved successful enough to encourage him to construct a 45 ft vessel which he named the *Francis B. Ogden*. This vessel was fitted with his propulsion system having wheels of diameter 5 ft 2 in. Trials were conducted on the Thames in the presence of representatives from the Admiralty and the vessel was observed to be capable of a speed of some 10 m.p.h. However, the members of Admiralty present expressed 'disappointment' with the results of the trial and their response left Ericsson somewhat disillusioned. The precise reasons for the Navy's disappointment at this result, which was good when judged by the standards of the day, is unclear; however, it was said that one reason was their concern over a vessel's ability to steer reliably when propelled from the stern. Following this rebuff Ericsson left England for the United States of America and in 1843 designed the US Navy's first screw propelled vessel, the *Princeton*. It has been suggested that by this time the US merchant marine had some 41 screw propelled vessels in operation.

The British Admiralty modified their view of screw propulsion shortly after Ericsson's trials due to the work of an English farmer, Francis Petit Smith, who was later knighted for his efforts. Smith enjoyed making model boats and testing them on a pond on his farm in Middlesex. From one such model which was propelled by an Archimedean screw he was sufficiently encouraged to build a 6 ton prototype boat powered by a 6 h.p. steam-engine to which he fitted a wooden Archimedean screw of two turns. The vessel underwent trials on the Paddington Canal in 1837; however, by one of those fortunate accidents which sometimes occurs in the history of science and technology, the propeller was damaged during the trials and about half of it broke off, whereupon the vessel immediately increased its speed. Smith recognized the implications of this accident and modified the propeller accordingly. After completing the calm water trials he took the vessel on a voyage down the River Thames from Blackwall in a series of stages to Folkestone and eventually on to Hythe on the Kentish coast: between these last two ports the vessel averaged a speed of some 7 miles per hour. On the return voyage to London, Smith encountered a storm in the Thames Estuary and the reports of the little craft's excellent performance in these adverse conditions reached the Admiralty, who then requested a special trial for their inspection. The Navy's response to these trials was sufficiently encouraging to motivate Smith into constructing a larger ship of 237 tons displacement which he called *Archimedes*. This vessel which was built in 1839, had a length of 125 ft and was rigged as a three-masted schooner. The *Archimedes* was powered by two 45 h.p. engines and fitted with a single turn Archimedean screw which had a diameter 5 ft 9 in and was about 5 ft in length. The propeller is shown in Figure 1.7. After undergoing a series of proving trials the ship arrived at Dover in 1840 to undertake a series of races against the cross-channel packets which at that time were operated by the Royal Navy. The Admiralty was duly impressed with the results of these races and agreed to the adoption of screw propulsion in the Navy. In the meantime, the *Archimedes* was lent to Brunel, who fitted her with a series of propellers having different forms. The result of Brunel's trials with this vessel was that the design of the *Great Britain*, which is now preserved at Bristol in England and was originally intended for paddle propulsion, was adapted for screw propulsion. It is, however, interesting to note that the general form of the propeller adopted by Brunel for the *Great Britain* did not follow the Smith design but was similar to

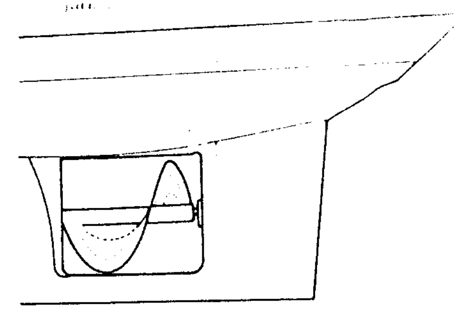

Figure 1.7 Propeller fitted to the *Archimedes* (1839)

that proposed by Ericsson, except that in the case the *Great Britain* the propeller was not of a contra-rotating type.

Concurrent with these developments other invent had introduced novel features into propeller desig Rennie in 1839 had proposed increases in pitch fro forward to aft of the blade, three bladed helices a the use of skewback in the design. Taylor and Nap a year later experimented with tandem propelle some of which were partially submerged. Also by 18 the 'windmill' propeller, as opposed to the Archimede screw, had developed to a fairly advanced state witnessed by Figure 1.8, which depicts the propell fitted to the French mail boat *Napoleon*. This propell is particularly interesting since it was developed to final form from a series of model tests in whic diameter, pitch, blade area and blade number we all varied.

As a direct result of the Royal Navy's commitme to screw propulsion *HMS Rattler* was laid down 1841 at Sheerness Dockyard and underwent initial s trials in the latter part of 1843, when she achieved speed of some $8\frac{3}{4}$ knots. *HMS Rattler* was a sloop approximately 800 tons and was powered by steam-engine of about 200 h.p. Subsequently, she r a race against her paddle half-sister, *HMS Polyphem* A design study was commissioned in an attempt to stu

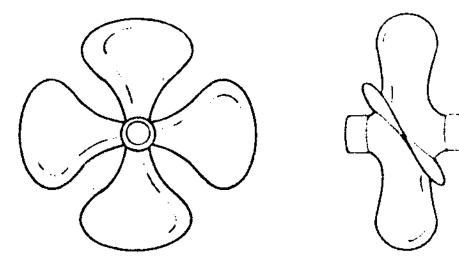

Figure 1.8 Propeller of the *Napoleon* (1842)

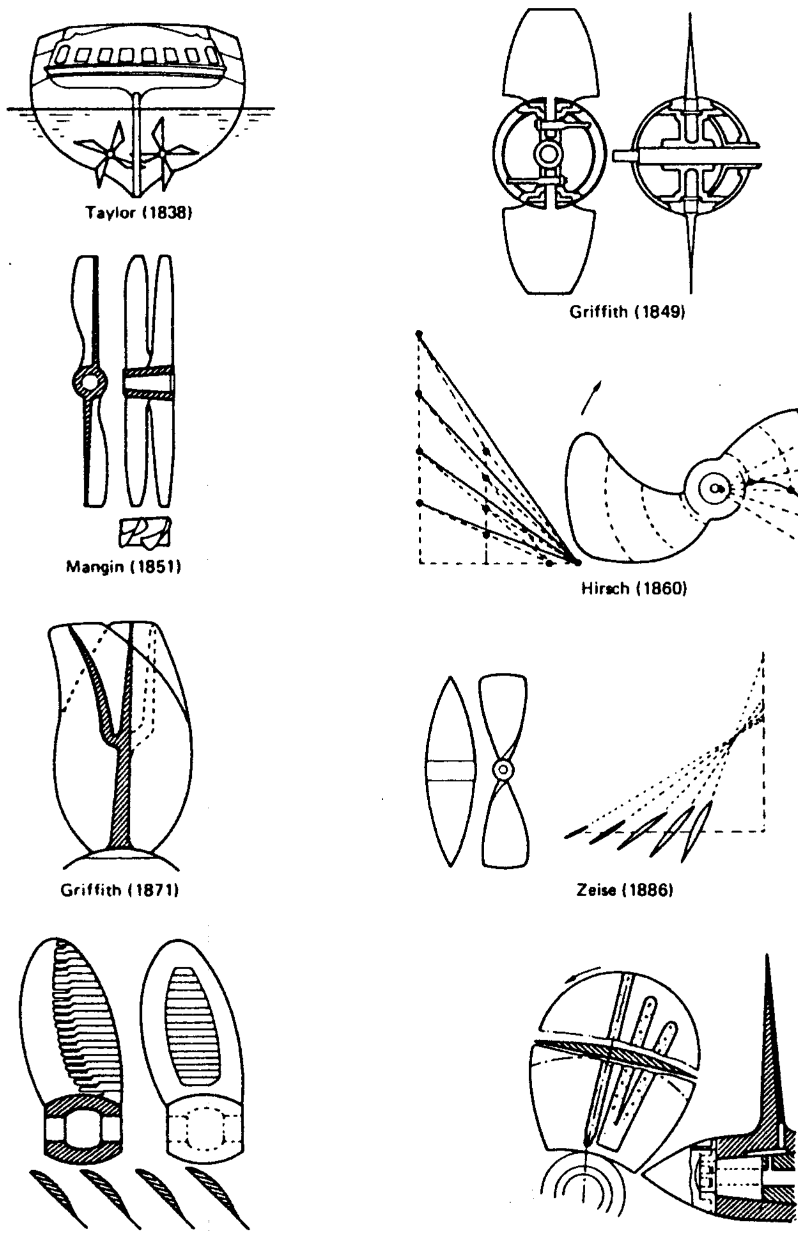

Figure 1.9 Various early propeller developments (Reproduced partly from References 2 and 3, with permission)

the various facets of propeller design and also to optimize a propeller design for *Rattler*; by January 1845 some thirty-two different propeller designs had been tested. The best of these propellers was designed by Smith and propelled the ship at a speed of about 9 knots. This propeller was a two-bladed design, had a diameter of 10 ft 1 in, a pitch of 11 ft and weighed 26 cwt 2 qrs (1.68 tonnes); today it is preserved at the Royal Naval Museum at Portsmouth in England. In the spring of 1845 the *Rattler* ran a series of competitive trials against the paddle steamer *Alecto*. These trials embraced both free running and towing exercises and also a series of separate sail, steam and combined sail and steam propulsion trials. By March 1845 the Admiralty was so convinced of the advantages of screw propulsion that they had ordered seven screw propelled frigates together with a number of lesser ships. In April 1845 the famous 'tug of war' between the *Rattler* and the *Alecto* was held; however, this appears to have been more of a public relations exercise than a scientific trial.

Although accepted by the Navy, screw propulsion had not been universally accepted for seagoing ships in preference to paddle propulsion, as witnessed by the relatively late general introduction of screw propulsion by the North Atlantic Steamship companies. However, the latter part of the 19th century saw a considerable amount of work being undertaken by a great number of people to explore the effects of radial pitch distribution, adjustable blades, blade arrangement and outline and cavitation. For example, in 1860 Hirch patented a propeller having both variable chordal pitch, which we know today as camber, and variable radial pitch; as an additional feature this propeller also possessed a considerable amount of forward skew on the blades. Some 30 years later Hirch also introduced the idea of bolted-on blades, thereby providing an early example of built-up propellers which achieved considerable popularity in the first half of the 20th century. Thornycroft in 1873 designed a propeller with restricted camber in the mid-span regions of the blade and also combined this with a backward curvature of the blades in an attempt to suppress tangential flow. Zeise carried the ideas of the development of the radial pitch distribution a stage further in 1886 when he increased the pitch of the inner sections of the blade in an attempt to make better use of the inner part of the blades.

Other developments worthy of note in the context of this introductory review are those by Mangin, Zeise and Taylor. Mangin in 1851 attempted to increase the thrust of a propeller by dividing the blades radially into two portions. Griffiths also used this idea in 1871 but he used only a partial division of the blades in their centre regions. Zeise in 1901 experimented with the idea of flexible blades, in which the trailing part of the blade was constructed from lamellae, and Taylor some six years later introduced air injection on the blade suction surface in order to control the erosive effects of cavitation. Figure 1.9 shows a collage of some of these propellers together with their novel features during the period 1838 to 1907.

The latter part of the 19th century also saw the introduction of theoretical methods which attempted to explain the action of the screw propeller. Notable among these theoretical treatments were the works of Rankin and Froude; these, together with subsequent developments which occurred during the 20th century, will, however, be introduced in the appropriate later chapters, notably Chapter 8.

These, therefore, were some of the activities and developments in the early years of propeller application which paved the way for the advancement of marine propeller technology during the 20th century, and the subject as we know it and practise it today.

References and further reading

1. Geissler, R. *Der Schraubenpropeller: Eine Darstellung seiner Entwicklung nach dem Inhalt der deutschen, amerikanischen und englischen Patentliteratur*. Berlin, 1918.
2. Taggart, R. *Marine Propulsion: Principles and Evolution*. Gulf Publishing, Texas, 1969.
3. Dirkzwager, J.M. Some aspects on the development of screw-propulsion in the 19th and early 20th century. *4th Lips Propeller Symposium*, October, 1979.
4. Brown, D.K. *A Century of Naval Construction*. Conway, London, 1983.

2 Modern propulsion systems

Contents

The previous chapter gave an outline of the early development of the propeller up to about 1900. In this chapter we move forward to the present day and consider, again in outline, the range of propulsion systems that are either currently in use or under development. The majority of the topical concepts and systems discussed in this chapter are considered, where appropriate, in greater detail in later chapters; it is, however, important to have an overview of the subject prior to discussing the various facets of propulsion technology in more depth. Accordingly, each of the principal propeller types will be briefly reviewed by outlining their major features and characteristics together with their general areas of application.

2.1 Fixed pitch propellers

The fixed pitch propeller has traditionally formed the basis of propeller production over the years in either its monoblock or built-up forms. Whilst the monoblock propeller is commonly used today the built-up propeller, whose blades are cast separately from the boss and then bolted to it after machining, is now rarely used. This was not always the case; in the early years of this century built-up propellers were very common, partly due to the inability to achieve good quality large castings at that time and partly due to the difficulties in defining the correct blade pitch. In both these respects the built-up propeller has obvious advantages.

Monoblock propellers form the major proportion of propellers today and cover a broad spectrum of design types and sizes, ranging from those weighing only a few kilogrammes for use on small power-boats to those destined for large tankers and bulk carriers which can weigh around 80–85 tonnes and perhaps require the simultaneous casting of some 120 tonnes of metal in order to produce the casting. Figure 2.1 illustrates various types of fixed pitch propeller in use today. These range from a large four-bladed propeller fitted to a bulk carrier and is seen in the figure in contrast to the man standing on the dock bottom, through highly skewed propellers for merchant and naval applications, to small high-speed patrol craft and surface piercing propellers.

As might be expected, the materials of manufacture vary considerably over such a wide range of designs and sizes. For the larger propellers, over 300 mm in diameter, the non-ferrous materials predominate: high-tensile brass and the manganese and nickel–aluminium bronzes are the most favoured types of materials; however, stainless steel has also gained a limited use as will be seen in Chapter 17. Cast iron, once a favourite material for the production of spare propellers, has now virtually disappeared from the scene. Alternatively, for small propellers, use is frequently made of materials such as the polymers, aluminium and nylon.

For fixed pitch propellers the choice of blade number, notwithstanding considerations of blade-to-blade clearances at the blade root–boss interface, is largely an independent variable and is normally chosen to give a mismatch to the range of hull, superstructure and machinery vibration frequencies which are considered likely to cause concern. As a consequence blade numbers generally range from two to seven, although in some naval applications, where considerations of radiated noise become important, blade numbers greater than these have been researched and used to solve a variety of propulsion problems. For merchant vessels, however, four, five and six blades are generally favoured, although many tugs and fishing vessels frequently use three-blade designs. In the case of small work or pleasure power-boats two- and three-bladed propellers tend to predominate.

The early propeller design philosophies centred on the optimization of the efficiency from the propeller. Whilst today this aspect is no less important, and, in some respects associated with energy conservation, has assumed a greater importance, other constraints on design have emerged. These additional constraints are in response to calls for reductions of vibration excitation and radiated noise from the propeller. This latter aspect has of course been a prime concern of naval ship and torpedo propeller designers for many years; however, pressure to introduce these constraints, albeit in a generally less stringent form, into merchant ship design practice has grown in recent years. This move has been brought about due to the consequences of the increases in power transmitted per shaft; the use of after deckhouses; the maximization of the cargo carrying capacity, which imposes constraints on the hull lines; ship structural failure and international legislation.

For the greater majority of vessels of over 100 tonnes displacement it is possible to design propellers on whose blades it is possible to control, although not eliminate, the effects of cavitation; in terms of its erosive effect on the material, its ability to impair hydrodynamic performance and it being the source of vibration excitation. In this latter context it must be remembered that there are very few propellers that are free from cavitation: the greater majority experience cavitation at some position in the propeller disc. Submarine propellers when operating at depth, the propellers of towed array frigates and research vessels when operating under part load conditions are a notable exception to this 'rule' since these propellers are normally designed to be subcavitating to meet the very stringent noise emission requirements to minimize either detection or interference with their own instruments.

For some small, high-speed vessels where both the advance and rotational speeds are high and the propeller immersion low, a point is reached where it is not possible to control the effects of cavitation acceptably within the other constraints of the propeller

(a)

(b)

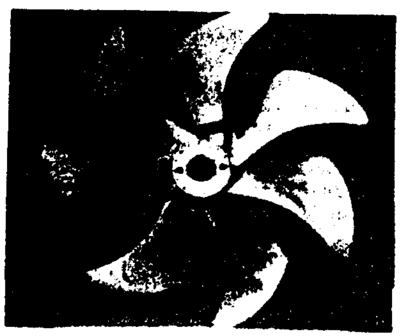

(c)

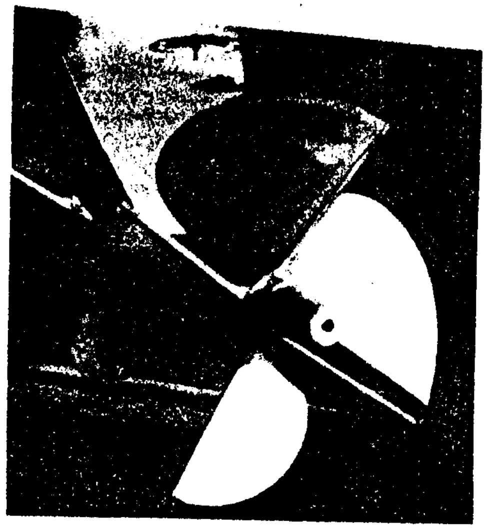

(d)

(e)

Figure 2.1 Typical fixed pitch propellers: (a) large four-bladed propeller for a bulk carrier; (b) high-speed patrol craft propeller; (c) seven-bladed balanced high-screw design; (d) surface piercing propeller; (e) biased high-skew, low-blade-area ratio propeller

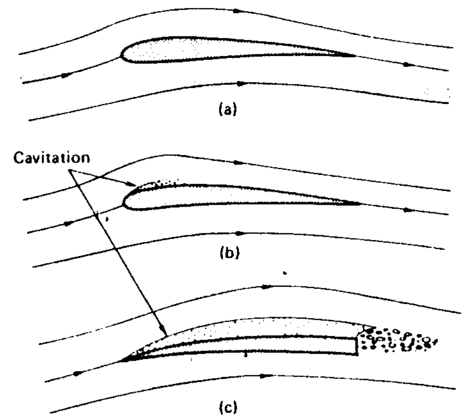

Figure 2.2 Propeller operating regimes: (a) non-cavitating; (b) partially cavitating; (c) supercavitating

design. To overcome this problem the blade sections are permitted to fully cavitate, so that the cavity developed on the back of the blade extends beyond the trailing edge and collapses into the wake of the blades in the slipstream. Such propellers are termed supercavitating propellers and frequently find application on high-speed naval and pleasure craft. Figure 2.2(c) illustrates schematically this design philosophy in contrast to both a non-cavitating and a partially cavitating propeller section, shown in Figures 2.2(a) and (b) respectively.

When the design condition dictates a specific hydrodynamic loading together with a very susceptible cavitation environment, typified by a low cavitation number, there comes a point when even the supercavitating propeller will not perform satisfactorily. For example, when the propeller tip immersion becomes small the propeller tends to draw air from the surface along some convenient path; often along the hull surface or down a shaft bracket. Eventually, if the immersion is reduced sufficiently by either the design or operational constraints, the propeller tips will break surface. Although this condition is well known on cargo vessels when operating in ballast and can, in these cases, lead to certain disadvantages from the point of view of material fatigue and induced vibration, the surface breaking concept can be an effective means of propelling relatively small high-speed craft. Such propellers are termed surface-piercing propellers and their design immersion, measured from the free surface to the static shaft centre line, can be reduced to zero; that is, the propeller operates half in and half out of the water. In these partially immersed conditions the propeller blades are commonly designed to operate such that the pressure face of the blade remains fully wetted and the suction side is fully ventilated or dry. This is an analogous operating regime to the supercavitating propeller, but in this case the blade surface suction pressure is at atmospheric conditions and not the vapour pressure of water.

2.2 Ducted propellers

Ducted propellers, as their name implies, comprise two principal components: the first is an annular duct having an aerofoil cross section which may be either of uniform shape around the duct and symmetric with respect to the shaft centre line, or have certain asymmetric features to accommodate the wake field. The second component, the propeller, is a special case of an open propeller in which the design of the blades has been modified to take account of the flow interactions caused by the presence of the duct in the flow field. The propeller for these units can be either of the fixed or controllable pitch type and in some special applications, such as torpedo propulsion, may be a contra-rotating pair. Ducted propellers, sometimes referred to as Kort nozzles by way of recognition of the Kort Propulsion Company's initial patents and long association with this type of propeller, have found application for many years where high thrust at low speed is required; typically in towing and trawling situations. In such cases, the duct generally contributes some 50% of the propulsor's total thrust at zero ship speed, termed the bollard pull condition; this relative contribution of the duct, however, falls to more modest amounts with increasing ship speed. It is also possible for a duct to give a negative contribution to the propulsor thrust at high advance speed; however, this would be a most unusual condition for the great majority of design situations.

There are two principal types of duct form — the accelerating and decelerating duct — and these are shown in Figures 2.3(a) and (d) respectively. The underlying reason for their designations can be appreciated, in global terms by considering their form in relation to the continuity equation of fluid mechanics. This can be expressed for incompressible flow in a closed conduit between two stations a–a and b–b as

$$\rho A_a v_b = \rho A_b v_b \qquad (2.1)$$

where v_a = velocity at station a–a;
v_b = velocity at station b–b;
A_a = cross-section area at station a–a;
A_b = cross-section area at station b–b;
ρ = density of the fluid.

In this context station b–b can be chosen in way of the propeller disc whilst a–a is some way forward, although not necessarily at the leading edge. In the case of Figure 2.3(a), which shows the accelerating duct, it can be seen that A_a is greater than A_b since the internal diameter of the duct is greater at station

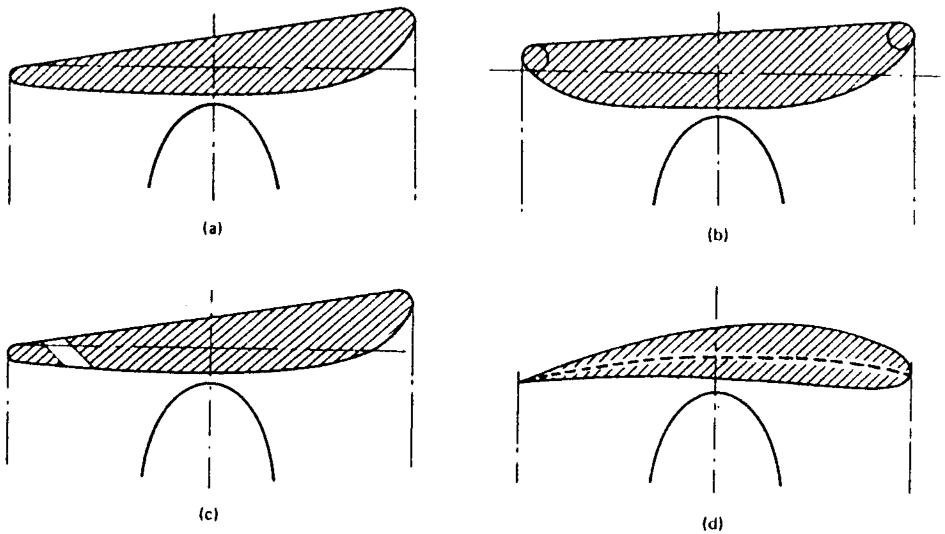

Figure 2.3 Duct types: (a) accelerating duct; (b) 'pull–push' duct; (c) Hannan slotted duct; (d) decelerating duct

a–a. Hence, from equation (2.1) and since the density of water is constant, v_a must be less than v_b, which implies an acceleration of the water between stations a–a and b–b; that is, up to the propeller location. The converse situation is true in the case of the decelerating duct shown in Figure 2.3(d). To determine precisely which form the duct actually is, if indeed this is important, the induced velocities of the propeller also need to be taken into account in the velocities v_a and v_b.

By undertaking detailed hydrodynamic analyses it becomes possible to design complex duct forms intended for specific application and duties. Indeed, attempts at producing non-symmetric duct forms to suit varying wake-field conditions have been made which result in a duct with both varying aerofoil section shape and incidence, relative to the shaft centre line, around its circumference. However, with duct forms it must be appreciated that the hydrodynamic desirability for a particular form must be balanced against the practical manufacturing problem of producing the desired shape if an economic and competitive duct is to result. This tenet is firmly underlined by appreciating that ducts have been produced for a range of propeller diameters from 0.5 m or less through to around 8.0 m. For these larger sizes, fabrication problems can be difficult, not least in maintaining the circularity of the duct and reasonable engineering clearances between the blade tips and the duct.

Many standard duct forms are in use today; those most commonly used are shown in Figure 2.3. Whilst the duct shown in Figure 2.3(a), the Wageningen 19a form, has a good ahead performance its astern performance is less good due to the aerofoil form of the duct having to work in reverse; that is, the trailing edge effectively becomes the leading edge in astern operations. This is of relatively minor importance in, say, a trawler or tanker, since for the majority of their operating lives these are essentially 'unidirectional' ships. However, this is not true for all vessels since some are expected to have broadly equal capabilities in both directions. In cases where a bidirectional capability is required a duct form of the type illustrated in Figure 2.3(b), the Wageningen No. 36 form, might be selected since its trailing edge is a compromise between a conventional trailing and leading edge of, for example, the 19a Form. For this type of duct the astern performance is improved but at the expense of the ahead performance, thereby introducing a measure of compromise in the design process. Several other methods of overcoming the disadvantages of the classical accelerating duct form in astern operations have been patented over the years. One such method is the 'Hannan slot', shown in Figure 2.3(c). This approach, whilst attempting to preserve the aerodynamic form of the duct in the ahead condition allows water when backing to enter the duct both in the conventional manner and also through the slots at the trailing edge in an attempt to improve the astern efficiency of the unit.

When the control of cavitation and more particularly the noise resulting from cavitation is of importance, use can be made of the decelerating duct form. A duct form of this type, Figure 2.3(d), effectively improves the local cavitation conditions by slowing the water before passing through the propeller. Most applications of this duct form are found in naval situations, for example, with submarines and torpedoes. Nevertheless, some specialist research ships also have needs which can be partially satisfied by the use of this type of duct in the appropriate circumstances.

An interesting development of the classical ducted propeller form is found in the pump jet. The pump jet frequently comprises a row of inlet guide vanes, which double as duct support vanes, followed by a row of rotor blades which are finally followed by a row of stator blades. Typically rotor and stator blade numbers might lie between 15 and 20 respectively, each row having a different blade number. Naturally there are variants of this design in which the blade numbers may be reduced or the inlet guide vanes not specified. The pump jet, however, would be largely restricted to military applications, although the principle of operation finds application in commercial water jet propulsion units.

The ducts of ducted propellers, in addition to being fixed structures rigidly attached to the hull, are also frequently found to be steerable. The steerable duct, which obviates the need for a rudder, is mounted on pintles whose axes lie on the vertical diameter of the propeller disc. The duct unit is then able to be rotated about the pintle axes by a steering motor and by this means the thrust of the propeller can be directed to the desired direction for navigation purposes. Clearly, however, the arc through which the thrust can be directed is limited by geometric constraints. Applications of this type can range from small craft, such as harbour tugs, up to comparatively large commercial vessels as shown by Figure 2.4. A further application of the steerable ducted propeller which has gained considerable popularity in recent years, especially in the offshore field, is the azimuthing thruster. In many cases these units can be trained around a full 360° so as to provide a completely directional thrusting capability. To provide this directional capability a mechanical 'Z' or 'L' drive is required for the power transmission line, since the input shaft has of necessity to be concentric with the unit's vertical axis of rotational axis.

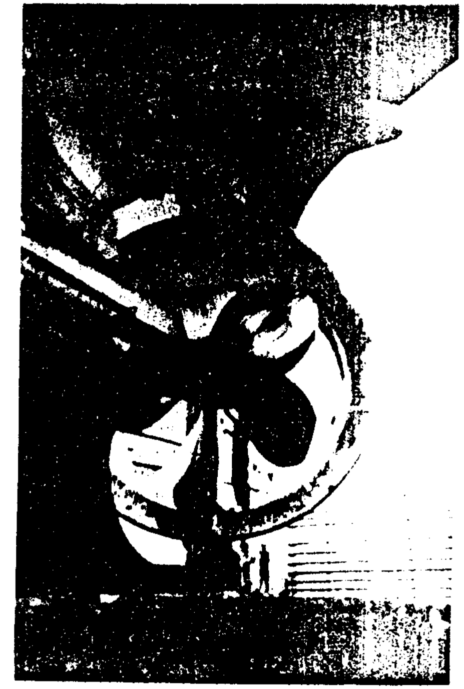

Figure 2.4 Steerable ducted propeller

2.3 Contra-rotating propellers

The contra-rotating propeller principle, comprising two coaxial propellers sited one behind the other and rotating in opposite directions, has been traditionally associated with the propulsion of aircraft, although Ericsson's original proposal of 1836, Figure 1.6, used this method.

Contra-rotating propulsion systems have the hydrodynamic advantage of recovering part of the slipstream rotational energy which would otherwise be lost to a conventional single screw system. Furthermore, because of the two propeller configuration, contra-rotating propellers possess a capability for balancing the torque reaction from the propulsor which is an important matter for torpedo and other similar propulsion problems. In marine applications of contra-rotating propulsion it is also normal to consider the aftermost propeller to have a smaller diameter than the forward propeller, and in this way accommodate for the slipstream contraction effects.

Contra-rotating propeller systems have been the subject of considerable theoretical and experimental research and some practical development exercises. Whilst they have found a significant number of applications, particularly in small outboard units operating at around 1500 to 2000 RPM, the mechanical problems associated with the longer line shafting systems of larger vessels have generally precluded them from use on merchant ships. Interest in the concept has had a cyclic nature with interest growing and then waning; a recent upsurge in interest in 1988, however, has resulted in a system being fitted to a 37 000 dwt bulk carrier, Reference 1, and subsequently to a 258 000 dwt VLCC in 1993.

2.4 Overlapping propellers

This again is a two-propeller concept. In this case the propellers are not mounted coaxially but are each located on separate shaft systems such that the distance between the shaft centre lines is less than the diameter of the propellers. Figure 2.5 shows a typical arrangement of such a system; again this is not a new idea and references can be found dating back over a hundred years; see, for example, Figure 1.9, showing Taylor's design of 1830.

As in the case of the contra-rotating propeller principle, recent work on this concept has been largely confined to research and development, and the system has rarely been used in practice. Research has largely centred on the effects of the shaft spacing to propeller diameter ratio on the overall propulsion efficiency in the context of particular hull forms, References 2 and 3. The prime aim of this type of propulsion arrangement is clearly to gain as much benefit as possible from the low-velocity portion of the wake field and, thereby, increase propulsion efficiency. Consequently, the benefits derived from this propulsion concept are intimately related to the propeller and hull propulsion coefficients.

Despite one propeller working partially in the wake of the other, cavitation problems are not currently thought to pose insurmountable design problems. However, significant increases in the levels of fluctuating thrust and torque have been identified when compared to single-screw applications. In comparison to the twin-screw alternative, research has indicated that the overlapping arrangement may be associated with lower building costs, and this is portrayed as one further advantage for the concept.

When designing this type of propulsion system several additional variables are presented to the designer. These are the direction of propeller rotation, the distance between the shafts, the longitudinal clearance between the propellers and the stern shape. At the present time there are only partial answers to these questions; research work tends to show that the best direction of rotation is outward, relative to the top-dead-centre position, and that the optimum distance between the shaft lies in the region of $0.5D$ to $0.8D$. In addition there are indications that the principal effect of the longitudinal spacing of the propellers is to be found in vibration excitation and that propulsion efficiency is comparatively insensitive to this variable.

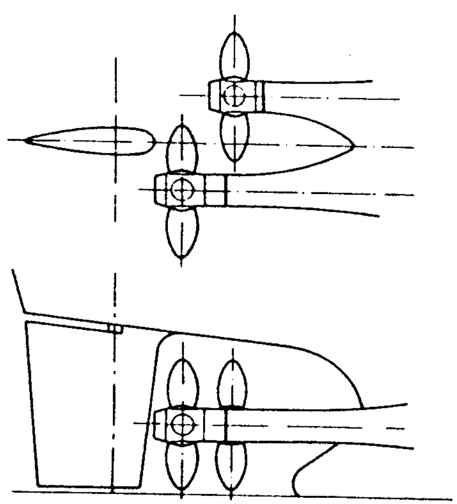

Figure 2.5 Overlapping propellers

2.5 Controllable pitch propellers

Unlike fixed pitch propellers whose only operational variable is rotational speed, the controllable pitch propeller provides an extra degree of freedom in its ability to change blade pitch. However, for some propulsion applications, particularly those involving shaft driven generators, the shaft speed is held constant, thus reducing the number of operating variables again to one.

The controllable pitch propeller has found application in the majority of the propeller types and applications so far discussed in this chapter with the possible exception of the contra-rotating propeller, although even in this extreme example of mechanical complexity some development work has been undertaken for certain specialist propulsion problems. In the last quarter of a century the controllable pitch propeller has grown in popularity from representing a small proportion of propellers produced, to its current position of having a very substantial market share. To illustrate this growth Figure 2.6, taken from Reference 4, shows the proportion of controllable pitch propeller systems when compared to the total number of propulsion systems classed with Lloyd's Register during the period 1960 to 1989, taken at five-year intervals except for the last interval. From this figure it can be seen that currently the controllable pitch propeller has about a 36% market share of propulsion systems, whilst Table 2.1 shows the relative distribution of controllable pitch propellers within certain classes of ship type. From the table, again taken from the same sources, it is seen that the controllable pitch propeller has almost complete dominance in the ferry, tug and trawling markets, noting of course that Table 2.1 relates to vessels with installed powers of greater than 2000 BHP.

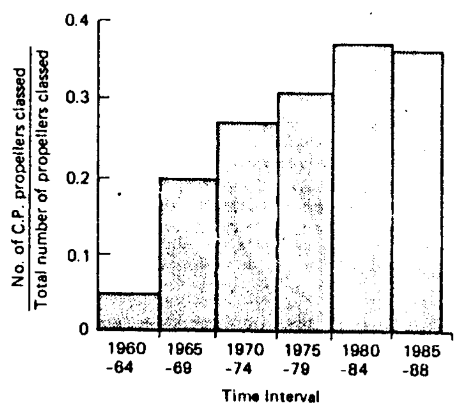

Figure 2.6 Relative increase in popularity of controllable pitch propellers

Table 2.1 Percentage relative distribution of controllable pitch propellers to fixed pitch propellers by ship type classed with Lloyd's Register and having installed powers greater than 2000 BHP

Ship type	*1960–64*	*1965–69*	*1970–74*	*1975–79*	*1980–84*	*1985–89*
Tankers	1	7	15	14	23	1
Bulk carriers	1	9	10	5	5	12
Container ships	0	13	24	3	1	13
General cargo	2	12	20	29	42	43
Passenger vessels and ferries	28	64	82	100	94	100
Tugs and offshore vessels	29	50	44	76	85	100
Fishing vessels	48	54	87	90	93	92

The controllable pitch propeller, although of necessity possessing a greater degree of complexity than the fixed pitch alternative, does possess a number of important advantages. Clearly, manoeuvring is one such advantage in that fine thrust control can be achieved without the need to necessarily accelerate and decelerate the propulsion machinery. Also fine control of thrust is particularly important in certain cases: for example, in dynamic positioning situations or where frequent berthing manoeuvres are required such as in short sea route ferry operations. The controllable pitch propeller permits engine operation at constant shaft speed, which in turn readily facilitates the use of shaft driven generators for shipboard power generation. Furthermore, the basic controllable pitch propeller hub design can in many instances be modified to accommodate the feathering of the propeller blades. The feathering position is the position where the blades are aligned 'roughly' fore and aft and in which they present least resistance to forward motion when not rotating. Such propellers find substantial applications on double-ended ferries or in small warships. In this latter application, the vessel could, for the sake of argument, have three propellers; the two wing screws being used when cruising with centre screw not rotating implying, therefore, that it should be feathered in order to produce minimum resistance to forward motion in this condition. Then when the sprint condition is required all three propellers could be used at their appropriate pitch settings to develop maximum speed.

The details and design of controllable pitch propeller hub mechanisms are outside the scope of this book since this text is primarily concerned with the hydrodynamic aspects of propulsion. It will suffice to say, therefore, that each manufacturer has an individual design of pitch actuating mechanism, but that these designs can be broadly grouped into two principal types; those with inboard and those with outboard hydraulic actuation. Figure 2.7 shows these principal types in schematic form. For further discussion and development of these matters reference can be made to the works of Plumb and Smith, References 5 and 6, which both provide introductions to this subject. Alternatively, propeller manufacturers' catalogues frequently provide a source of detailed information on this aspect of controllable pitch propeller design.

The hub boss, in addition to providing a housing for the blade actuation mechanism, must also be sufficiently strong to withstand the propulsive forces supplied to and transmitted from the propeller blades. In general, therefore, controllable pitch propellers tend to have larger hub diameters than those for equivalent fixed pitch propellers. Typically the controllable pitch propeller hub has a diameter in the range $0.24D$ to $0.32D$, but for some applications this may rise to as high a value as $0.4D$ or $0.5D$. In contrast fixed pitch propeller boss diameters are generally within the range $0.16D$ to $0.25D$. The large boss diameters can clearly give rise to significant hydrodynamic problems, but for the majority of normal applications the larger diameter of the controllable pitch propeller hub does not generally pose a problem that cannot be either directly or indirectly solved by known design practices.

Certain specialist types of controllable pitch propeller have been designed and patented in the past. Two of particular interest at the present time are the self-pitching propeller and the Pinnate propeller, both of which are modern versions of much earlier designs. Self-pitching propellers are a modern development of Griffiths' work in 1849. The blades are sited on an external crank which is pinned to the hub and they are free to

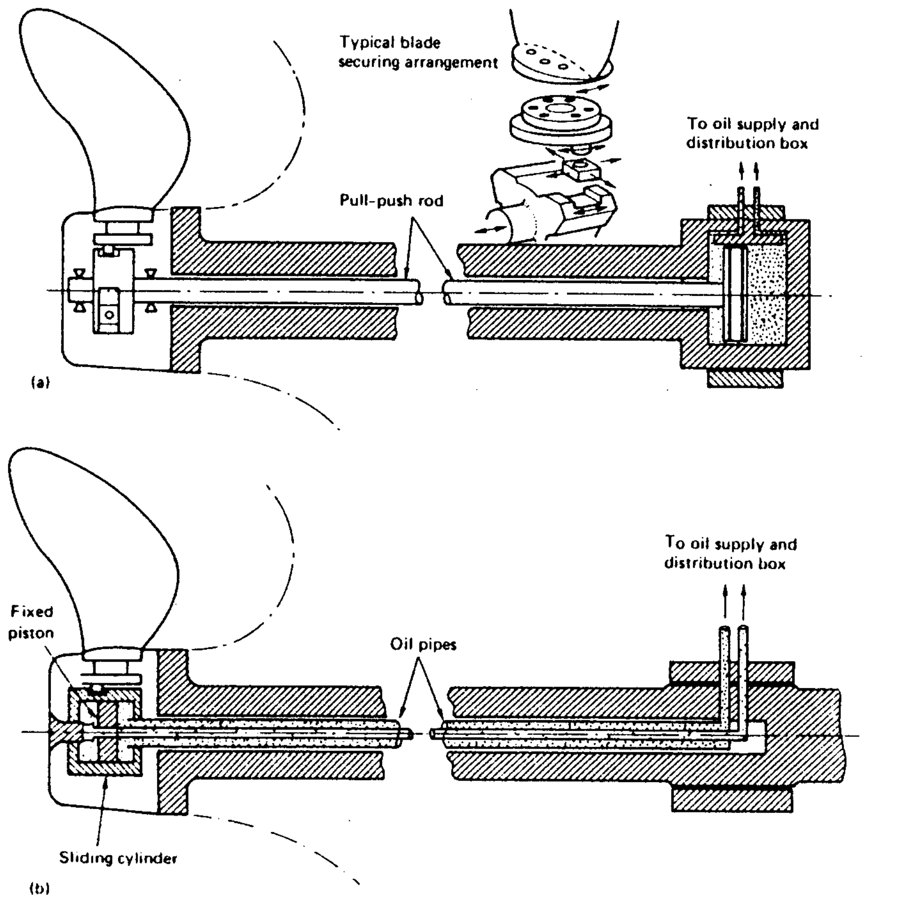

Figure 2.7 Controllable pitch propeller schematic operating systems: (a) pull-push rod system; (b) hub piston system

take up any pitch position. The actual pitch position taken up in service depends on a balance of the blade loading and spindle torque components which are variables depending on, amongst other parameters, rotational speed: at zero shaft speed but with a finite ship speed the blades are designed to feather. At the present time these propellers have only been used on relatively small craft.

The Pinnate design is to some extent a controllable pitch propeller/fixed pitch propeller hybrid. It has a blade activation mechanism which allows the blades to change pitch about mean position by varying angular amounts during one revolution of the propeller. The purpose of the design concept is to reduce both the magnitude of the blade cyclical forces and cavitation by attempting to adjust the blades for the varying inflow velocity conditions around the propeller disc. Trials of these types of propeller have been undertaken on small naval craft and Simonsson describes these applications, Reference 7.

2.6 Waterjet propulsion

Waterjet propulsion has found considerable application in recent years on a wide variety of small high-speed

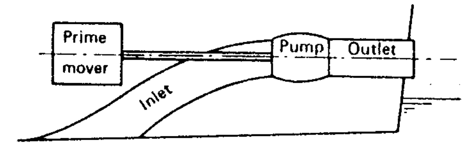

Figure 2.8 Waterjet configuration

craft; however, their application to larger craft is growing rapidly with tunnel diameters of upwards of 2 m being frequently considered at the present time. The original development of the waterjet principle, however, can be traced back to 1661, when Toogood and Hayes produced a description of a ship having a central water channel in which either a plunger or centrifugal pump was installed to provide the motive power. The principle of operation of the present-day waterjet, however, is that in which water is drawn through a ducting system by an internal pump which adds energy whereupon the water is expelled aft at high velocity. The unit's thrust is primarily generated as a result of the momentum increase given in the water. Figure 2.8 shows, in outline form, the main features of the waterjet system and this method of propulsion is further discussed in Chapter 15.

The pump configuration adopted for use with a waterjet system depends on the specific speed of the pump; specific speed N_s being defined in normal hydraulic terms as

$$N_s = \frac{(N)Q^{1/2}}{H^{3/4}} \tag{2.2}$$

where Q is the quantity of fluid discharged and H is the head.

For low values of specific speed centrifugal pumps are usually adopted, whereas for the intermediate and high values of N_s axial pumps and inducers are used respectively. The prime movers usually associated with the driving of these various pumps are either gas turbines or high-speed diesel engines.

Waterjet propulsion units offer a further dimension to the range of propulsion alternatives and tend to be used where other propulsion forms are rejected for some reason: typically for reasons of efficiency, cavitation extent, noise or immersion and draught. For example, in the case of a small vessel travelling at say 45 knots one might expect that a conventional propeller would be fully cavitating, whereas in the corresponding waterjet unit the pump should not cavitate. Consequently, it can be seen that the potential for waterjet application, neglecting any small special purpose craft with particular requirements, is where conventional, transcavitating and supercavitating propeller performance is beginning to fall off. Indeed surface piercing propellers and waterjet systems tend to some extent to be competitors for similar applications. Waterjets, however, tend to be heavier than conventional propeller based systems and, therefore, might be expected to find favour with larger craft, for example, large wave-piercing ferries.

In terms of manoeuvrability the waterjet system is potentially very good, since deflector units are normally fitted to the jet outlet pipe which then direct the water flow and hence introduce turning forces by changing the direction of the jet momentum. Similarly for stopping manoeuvres flaps or a 'bucket' can be introduced over the jet outlet to redirect the flow forward and hence apply a very effective reactive retarding force to the vessel.

2.7 Cycloidal propellers

Cycloidal propeller development started in the 1920s, initially with the Kirsten-Boeing and subsequently the Voith-Schneider designs. As observed in Chapter 1, it is interesting to note that the Kirsten-Boeing design was very similar in its hydrodynamic action to the horizontal waterwheel developed by Robert Hooke some two and half centuries earlier in 1661.

The cycloidal, or vertical axis propellers, basically comprise a set of vertically mounted vanes, six or eight in number, which rotate on a disc mounted in a horizontal or near horizontal plane. The vanes are constrained to move about their spindle axis relative to the rotating disc in a predetermined way by a governing mechanical linkage. Figure 2.9(a) illustrates schematically the Kirsten-Boeing principal. It can be seen from the figure that the propulsion unit comprises a set of vanes whose relative attitude to the circumference

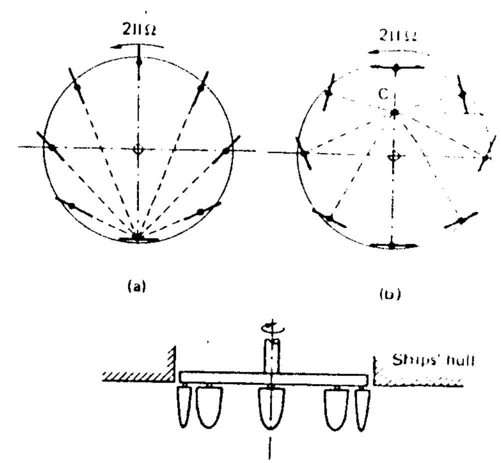

Figure 2.9 Vertical axis propeller principle: (a) Kirsten-Boeing propeller; (b) Voith-Schneider propeller

of the circle, which governs their tracking path, is determined by referring the motion of the vanes to a particular point on that circumference. It can be deduced that each vane makes half a revolution about its own pintle axis during one revolution of the entire propeller disc. The thrust magnitude developed by this propeller design is governed by rotational speed alone and the direction of the resulting thrust by the position of the reference point on the circumference of the vane-tracking circle.

The design of the Voith–Schneider propeller is considerably more complex than that of the Kirsten–Boeing, since it comprises a series of linkages which enable the individual vane motions to be controlled from points other than on the circumference of the vane-tracking circle. Figure 2.9(b) demonstrates this for a particular value of the eccentricity (*e*) of the vane-control centre point from the centre of the disc. By controlling the eccentricity, which in turn governs the vane pitch angles, both the thrust magnitude and direction can be controlled independently of rotational speed. In the case of the Voith–Schneider design, and in contrast to the Kirsten–Boeing propeller, the individual vanes make one complete revolution about their pintle axes for each complete revolution of the propeller disc.

Vertical axis propellers do have considerable advantages when manoeuvrability or station keeping is an important factor in the ship design, since their resultant thrust can be readily directed along any navigational bearing and have a variable magnitude. Indeed, this type of propeller avoids the necessity for a separate rudder installation on the vessel. These propellers have shown themselves to be reliable in operation over many years of service, and in many cases are provided with guards to help protect the propulsor from damage from external sources.

2.8 Paddle wheels

Paddle propulsion, as is well known, predates screw propulsion; however, this form of propulsion has almost completely disappeared except for a very few specialized cases. These are to be found largely on lakes and river services either as tourist or nostalgic attractions, or alternatively, where limited draughts are encountered. The Royal Navy, until a few years ago, also favoured their use on certain classes of harbour tug, where they were found to be exceptionally manoeuvrable.

The principal reason for the demise of the paddle wheel was its intolerance of large changes of draught and the complementary problem of variable immersion in seaways. Once having been superseded by screw propulsion for ocean-going vessels their use was largely confined through the first half of this century to river steamers and tugs. Paddle wheels, however,

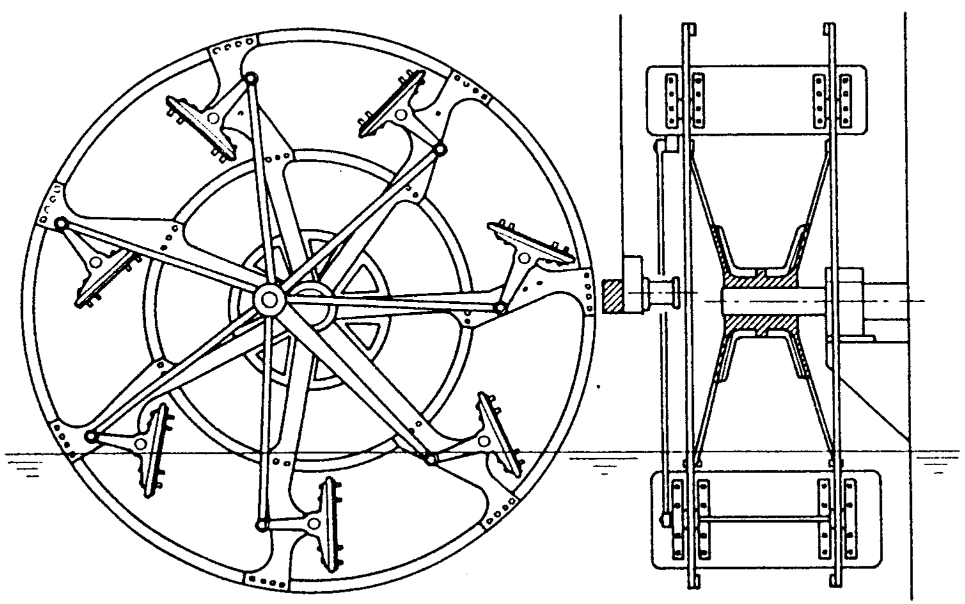

Figure 2.10 Paddle wheel (Reproduced from Reference 8)

also suffered from damage caused by flotsam in rivers and were relatively expensive to produce when compared to the equivalent fixed pitch propeller.

Paddle design progressed over the years from the simple fixed float designs which were originally used to the feathering float system which featured throughout much of its life. Figure 2.10 shows a typical feathering float design of paddle wheel from which can be seen that the float attitude is governed from a point just slightly off-centre of the wheel axis. Feathering floats are essential to good efficiency on the relatively small diameter and deeply immersed wheels; however, on the larger wheels, which are not so deeply immersed, feathering floats are not essential and fixed float designs were normally adopted. This led to the normal practice of adopting feathered wheels in side-mounted wheel applications, such as were found on the Clyde or Thames excursion steamers, because of the consequent diameter restriction imposed by the draught of the vessel. However, on the stern wheelers, such as those designed for the Mississippi services, the use of fixed floats were preferred since the wheel diameter restriction did not apply.

The design of paddles is considerably more empirical than that of screw propellers today; however, high propulsion efficiencies, of similar orders to equivalent screw-propelled steamers, were achieved. Ideally, each float of the paddle wheel should enter the water 'edgeways' and without shock: that is, the floats should be normal to the water on entry, having taken due account of the relative velocity of the float to the water. The relative velocity in this sense in still water has two components: the angular speed due to the rotation of the wheel and the speed of the vessel V_a. From Figure 2.11 it can be seen that at the point of entry A, a resultant vector $\bar{a}$ is produced from the combination of advance speed V_a and the rotational vector ωR. The resultant vector represents the absolute velocity at the point of entry and consequently to

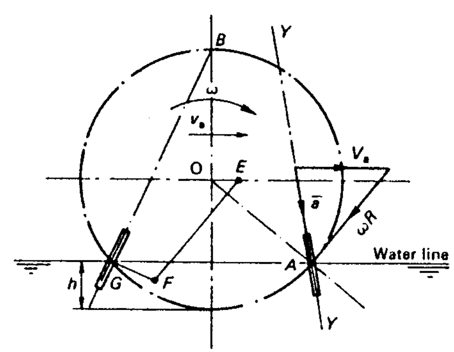

Figure 2.11 Paddle wheel float relative velocities

avoid shock at entry, that is a vertical thrusting action of the float, the float should be aligned parallel to this vector along the line YY. However, this is not possible practically and the best that can be achieved is to align the floats to the point B and to achieve this a linkage EFG is introduced into the system. Also from Figure 2.11 it is obvious that the less the immersion of the wheel (h), the less is the advantage to be gained from adopting a feathering float system: this illustrates why the fixed float principal is adopted for large, lightly immersed wheels.

With regard to the overall design parameters it was generally found, based on experience, that the number of fixed floats on a wheel should be about one for every foot of diameter of the wheel: for feathering designs this number was reduced to around 60% or 70% of the fixed float 'rule'. The width of the floats used in a particular design was of the order of 25–40% of the float length for feathering designs, but this figure was reduced for the fixed float paddle wheel to between 20 and 25%. The constraint on the immersion of the floats was that the peripheral speed at the top of the float should not exceed the ship speed and in general feathering floats were immersed in the water up to about half a float width whilst with sternwheelers, the tops of the floats were never far from the water surface.

The empirical nature of paddle design was recognized as being unsatisfactory and in the mid-1950s Volpich and Bridge (References 9–11) conducted systematic experiments on paddle wheel performance at the Denny tank in Dumbarton. Unfortunately this work came at the end of the time when paddle wheels were in use as a common form of propulsion and, therefore, never achieved its full potential.

2.9 Superconducting electric propulsion

Superconducting electric propulsion potentially provides a ship propulsion without the aid of either propellers or paddles.

The idea of electromagnetic thrusters was first patented in the United States of America by Rice during 1961, Reference 12. Following this patent the USA took a leading role in both theoretical and experimental studies culminating in a report from the Westinghouse Research Laboratory in 1966. This report showed that greater magnetic field densities were required before the idea could become practicable in terms of providing a realistic alternative for ship propulsion. In the 1970s supeconducting coils enabled further progress to be made with this concept and from this time the leading role was taken by Japan in all aspects of the study: theoretical, model testing and full-scale trials.

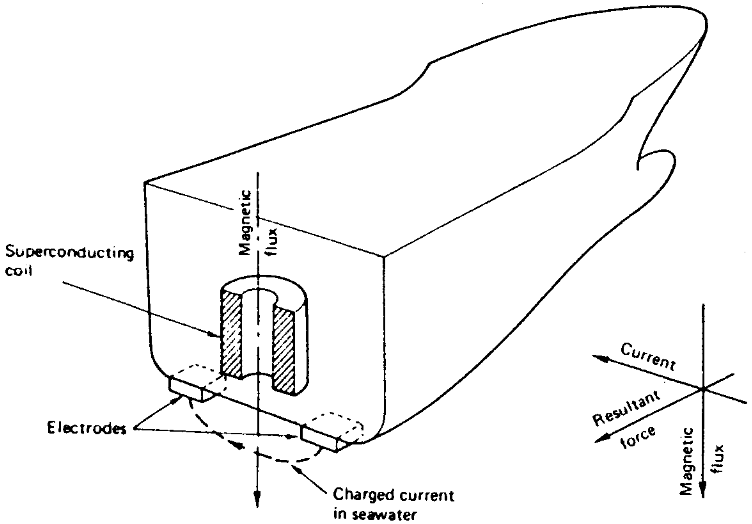

Figure 2.12 Principle of electromagnetic propulsion using an external field

The fundamental principal of electromagnetic propulsion is that of the interaction between a fixed coil placed inside the ship and an electric current passed through the sea-water from electrodes in the bottom of the ship, as shown diagrammatically in Figure 2.12. Since the magnetic field and the current are in mutually orthogonal directions, then by Fleming's left-hand rule, a force is produced in the third orthogonal direction as seen in Figure 2.12. Iwata *et al.*, in Reference 13 and subsequently in Reference 14, presents an interesting description of the state of the art of superconducting propulsion.

Figure 2.12 essentially typifies an electromagnetic propulsion system having an external magnetic field. An alternative to this is to use an arrangement which creates an internal magnetic field. The principle of this type of system is shown in Figure 2.13(a) in which a duct, through which sea-water flows, is surrounded by superconducting magnetic coils which are immersed in a cryostat. Inside the duct are placed two electrodes, which create the electric field necessary to interact with the magnetic field in order to create the Lorentz forces of propulsion. Model tests, concluded in Japan, have indicated that the internal magnetic field system enhances efficiency over the external alternative. In addition the environmental impact of the system is considerably reduced due to the containment of the electromagnetic fields. The efficiency of a unit is low due to the losses caused by the low conductivity of sea-water; however, efficiency is proportional to the square of the magnetic flux intensity and to the flow speed, which clearly is a function of ship speed. Consequently, in order to arrive at a reasonable efficiency it is necessary to create a strong magnetic flux intensity by the use of powerful magnets. In order to investigate the full potential of these systems at prototype scale a small craft, *Yamato 1* has been built for trial purposes by the Japanese at this time. Figure 2.13(b) shows a cross section through one of the prototype propulsion units, indicating the arrangement of the six dipole propulsion ducts within the unit.

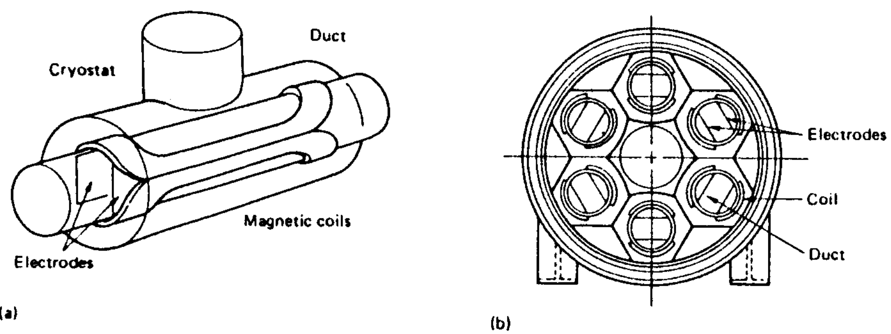

Figure 2.13 Internal magnetic field electromagnetic propulsion unit: (a) the dipole propulsion unit with internal magnetic field, (b) a cross-section through a prototype propulsion unit

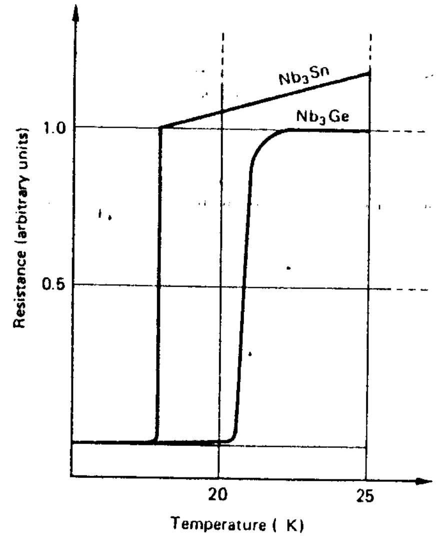

Figure 2.14 Superconducting effect

Electromagnetic propulsion does have certain potential advantages in terms of providing a basis for noise- and vibration-free hydrodynamic propulsion. However, a major obstacle to the development of electromagnetic propulsion until recently was that the superconducting coil, in order to maintain its zero-resistance property, required to be kept at the temperature of liquid helium, 4.2 K (−268 °C). This clearly requires the use of thermally well-insulated vessels in which the superconducting coil could be placed in order to maintain these conditions. The criticality of this thermal condition can be seen from Figure 2.14 which indicates how the resistance of a superconductor behaves with temperature and eventually reaches a critical temperature when the resistance falls rapidly to zero. Superconductors are also sensitive to current and magnetic fields; if either become too high then the superconductor will fail in the manner shown in Figure 2.15.

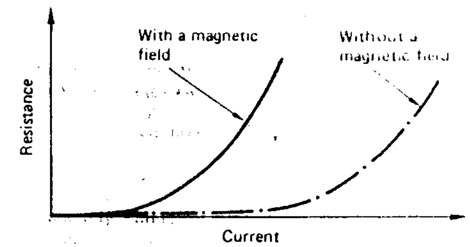

Figure 2.15 Effect of a magnetic field on a superconductor

Superconductivity began with the work of Kamerlingh Onnes at Leiden University in 1911 when he established the superconducting property for mercury in liquid helium; for this work he won a Nobel Prize. Work continued on supercónductivity, however, progress was slow in finding metals which would perform at temperatures as high as that of liquid nitrogen, −196 C. By 1973 the best achievable temperature was 23 K. In 1986 Muller and Bednorz in Zurich turned their attention to ceramic oxides which had hitherto been considered as insulators. The result of this shift of emphasis was to immediately increase the critical temperature to 35 K by the use of a lanthanum, barium, copper oxide compound: this discovery led to Muller and Bednorz also being awarded a Nobel Prize for their work. Consequent on this discovery, work in the United States of America, China, India and Japan intensified, leading to the series of rapid developments depicted in Table 2.2.

Table 2.2 Development of superconducting ceramic oxides

Date	*Ceramic oxide*	*Superconducting temperatures (K)*
September 1986	La Ba Cu O	35
January 1987	Y Ba Cu O	93
January 1988	Bi Sr Ca Cu O	118
February 1988	Tl Ba Ca Cu O	125

Whilst these advances are clearly encouraging since they make the use of superconducting coils easier from the thermal insulation viewpoint, ceramic oxides are at present comparatively difficult to produce. Firstly, the process by which the superconductor is made is very important if the correct molecular structure is to be obtained and secondly, ceramics are brittle. Consequently, whilst this form of propulsion clearly has potential and significant advances have been made, both in the basic research and application, much work still has to be done before this type of propulsion can become a reality on a commercial scale or even the concept fully tested.

References and further reading

1. *IHI CRP System for Large Merchant Ships*, Ship Technology International '93, SPG, 1993.
2. Kerlen, H., Esveldt, J., Wereldsman, R. *Propulsion, Cavitation and Vibration Characteristics of Overlapping Propellers for a Container Ship.* Schiffbautechnische Gesellschaft, Berlin. November, 1970.
3. Restad, K., Volcy, G.G., Garnier, H., Masson, J. C. Investigation on free and forced vibrations of an LNG tanker with overlapping propeller arrangement. *Trans. SNAME*, 1973.
4. Carlton, J.S. Propeller service experience, *7th Lips Propeller Symposium*, September, 1989.
5. Plumb, C.M. Warship propulsion system selection, *I. Mar. E.*, 1987.
6. Smith, D.W. *Marine Auxiliary Machinery* (6th edn). Butterworths, 1983.
7. Simonsson, P. *The Pinnate Propeller*, Dept. of Mechanics, Royal Inst. of Tech., Stockholm, 1983.
8. Hamilton, F.C. *Famous Paddle Steamers*, Marshall, London, 1948.
9. Volpich, Bridge. Preliminary model experiments, *Trans. IESS*, **98**, 1954–55.
10. Volpich, Bridge. Systemic model experiments, *Trans. IESS*, **99**, 1955–56.
11. Volpich, Bridge, Further model experiments and ship model correlation, *Trans. IESS*, **100**, 1956 57.
12. Rice, W.A. US Patent 2997013. August 22, 1961.
13. Iwata, A., Tada, E., Saji, Y. Experimental and theoretical study of superconducting electromagnetic ship propulsion. Paper No. 2, *5th Lips Propeller Symposium*, May 1983.
14. Iwata, A. Superconducting electromagnetic propulsion system. *Bulletin of Mar. Eng. Soc.*, Japan, 18(1), 1990.

3 Propeller geometry

Contents

To appreciate fully propeller hydrodynamic action from either the empirical or theoretical standpoint it is essential to have a thorough understanding of basic propeller geometry and the corresponding definitions used. Whilst each propeller manufacturer, consultant or test tank has proprietary ways of presenting propeller geometric data on drawings or in dimension books produced either by hand or with the aid of a computer, these differences are most commonly in matters of detail rather than in fundamental changes of definition. Consequently, this chapter will not generally concern itelf with a detailed account of each of the different ways of representing propeller geometric information. Instead it will present a general account of propeller geometry which will act as an adequate basis for any particular applications with which the reader will be concerned.

3.1 Frames of reference

A prerequisite for the discussion of the geometric features of any object or concept is the definition of a suitable reference frame. In the case of propeller geometry and hydrodynamic analysis many reference frames are encountered in the literature, each, no doubt, chosen for some particular advantage or preference of the author concerned. However, at the 10th International Towing Tank Conference (ITTC) in 1963 the preparation of a dictionary and nomenclature of ship hydrodynamic terms was initiated; this work was completed in 1975 and the compiled version presented in 1978, Reference 1. The global reference frame proposed by the ITTC is that shown in Figure 3.1(a) which is a right-handed, rectangular Cartesian system. The X-axis is positive, forward and coincident with the shaft axis; the Y-axis is positive to starboard and the Z-axis is positive in the vertically downward direction. This system is adopted as the global reference frame for this book since no other general agreement exists in the field of propeller technology. For propeller geometry, however, it is convenient to define a local reference frame having a common axis such that OX and Ox are coincident, but allowing the mutually perpendicular axes Oy and Oz to rotate relative to the OY and OZ fixed global frame as shown in Figure 3.1(b).

3.2 Propeller reference lines

The propeller blade is defined about a line normal to the shaft axis called either the 'propeller reference line' or the 'directrix': the word 'directrix' being the older term used for this line. In the case of the controllable pitch propeller the term 'spindle axis' is frequently synonymous with the reference line or directrix. However, in a few special design cases the spindle axis has been defined to lie normally to the surface of a

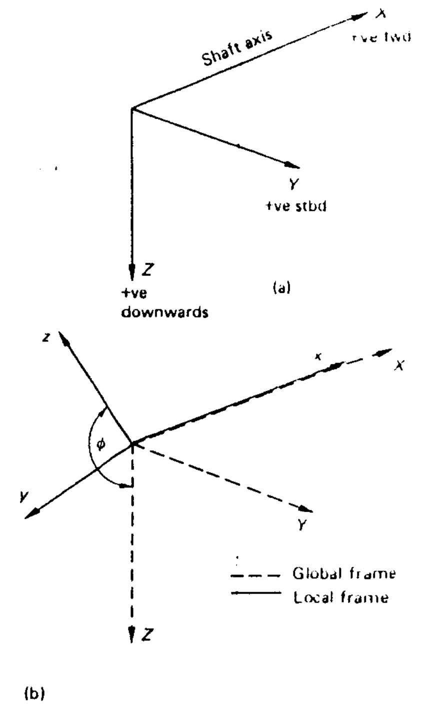

Figure 3.1 Reference frames: (a) global reference frame (b) local reference frame

shallow cone whose axis is coincident with the shaft axis and tapers towards the aft direction. In these cases the spindle axis is inclined to the reference line by a few degrees; such applications are, however, comparatively rare. For the greater majority of cases, therefore, the terms spindle axis, directrix and reference line relate to the same line, as can be seen in Figure 3.2. These lines are frequently, but not necessarily, defined at the origin of the Cartesian reference frame discussed in the previous section.

The aerofoil sections which together comprise the blade of a propeller are defined on the surface of cylinders whose axes are concentric with the shaft axis, hence the term 'cylindrical sections' which is frequently encountered in propeller technology. Figure 3.3 shows this cylindrical definition of the section, from which it will be seen that the section lies obliquely over the surface of the cylinder and thus its nose tail line, connecting the leading and trailing edges of the section, form a helix over the cylinder. The point A shown in Figure 3.2 where this helix intersects the plane defined by the directrix and the x-axis is of particular interest since it forms one point, at the

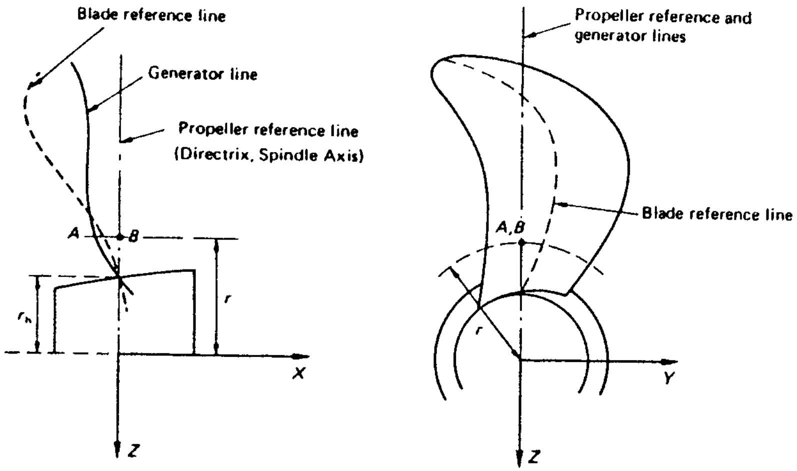

Figure 3.2 Blade reference lines

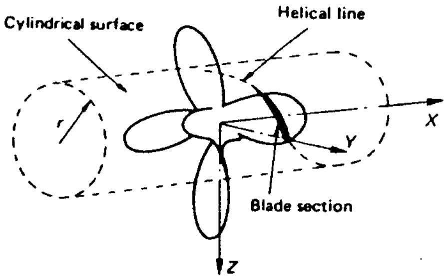

Figure 3.3 Cylindrical blade section definition

radius r of the section considered, on the 'generator line'. The generator line is thus the locus of all such points between the tip and root of the blade as seen in Figure 3.2. Occasionally the term 'stacking line' is encountered, this is most frequently used as a synonym for the generator line; however, there have been instances when the term has been used by designers to mean the directrix: consequently care is needed for all cases except the special case when the generator line is the same as the directrix.

3.3 Pitch

Consider a point P lying on the surface of a cylinder of radius r which is at some initial point P_0 and moves so as to form a helix over the surface of a cylinder. The equations governing the motion of the point P over the surface of the cylinder (points $P_0, P_1, P_2, \ldots, P_n$) in Figure 3.4(a) are as follows:

$$\left.\begin{aligned} x &= f(\phi) \\ y &= r\sin(\phi) \\ z &= r\cos(\phi) \end{aligned}\right\} \qquad (3.1)$$

where ϕ is the angle of rotation in the Y–Z-plane of radius arm r relative to the OZ-axis in the global reference frame. When the angle $\phi = 360°$ or 2π radians then the helix, defined by the locus of the points P_n, has completed one complete revolution of the cylinder it again intersects the X–Z-plane but at a distance p measured along the OX-axis from the origin. If the cylinder is now 'opened out' as shown in Figure 3.4(b) we see that the locus of the point P, as it was rotated through 2π radians on the surface of the cylinder, lies on a straight line. In the projection one revolution of the helix around the cylinder, measured normal to the OX direction, is equal to a distance $2\pi r$. The distance moved forward by the helical line during this revolution is p and hence the helix angle (θ) is given by

$$\theta = \tan^{-1}\left(\frac{p}{2\pi r}\right) \qquad (3.2)$$

The angle θ is termed the pitch angle and the distance p is the pitch. Hence equation (3.1), which defines a point on a helix, can be written as follows:

$$\left.\begin{aligned} x &= r\phi\tan\theta \\ y &= r\sin(\phi) \\ z &= r\cos(\phi) \end{aligned}\right\} \qquad (3.1a)$$

There are several pitch definitions that are of importance in propeller analysis and the distinction between them

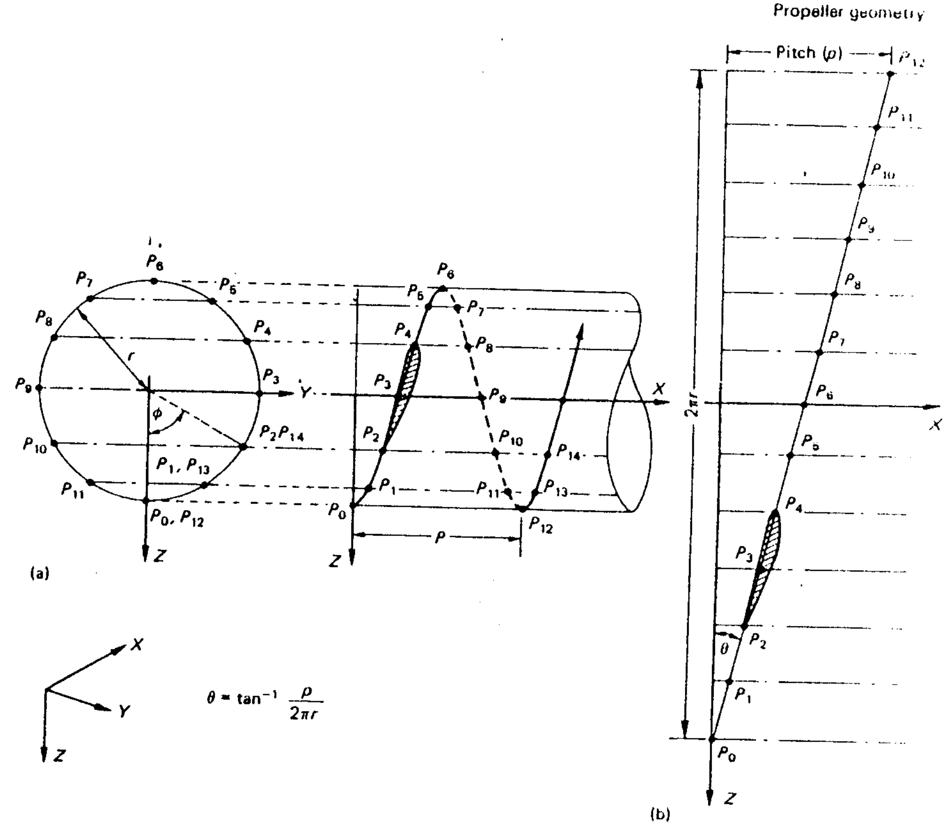

Figure 3.4 Definition of pitch: (a) helix definition on a cylinder of radius r; (b) development of helix on the cylinder

is of considerable importance if serious analytical mistakes are to be avoided. In all cases, however, the term pitch in propeller technology refers to the helical progress along a cylindrical surface rather than, for example, in gear design where pitch refers to the distance between teeth. The important pitch terms with which the analyst needs to be thoroughly conversant are as follows:

1. nose–tail pitch;
2. face pitch;
3. effective or 'no-lift' pitch;
4. hydrodynamic pitch.

Figure 3.5 shows these pitch lines in association with an arbitrary aerofoil section profile. The nose–tail pitch line is today the most commonly used reference line by the principal propeller manufacturers in order to define blade sections, and it is normally defined at a pitch angle θ_{nt} to the thwart-ship direction. This line also has a hydrodynamic significance too, since the section angles of attack are defined relative to it in the conventional aerodynamic sense.

Face pitch is now rarely used by the large propeller manufacturers, but it will frequently be seen on older drawings and is still used by many smaller manufacturers. Indeed many of the older model test series, for example the Wageningen B Series, use this pitch reference as a standard to present the open water characteristics. Face pitch has no hydrodynamic significance at all, but was a device invented by the manufacturers to simplify the propeller production process by obviating the need to 'hollow out' the surface of the propeller mould to accommodate that part of the section between the nose–tail and face pitch lines. The face pitch line is basically a tangent to section's pressure side surface, and therefore has a degree of arbitrariness about its definition since many tangents can be drawn to the aerofoil pressure surface

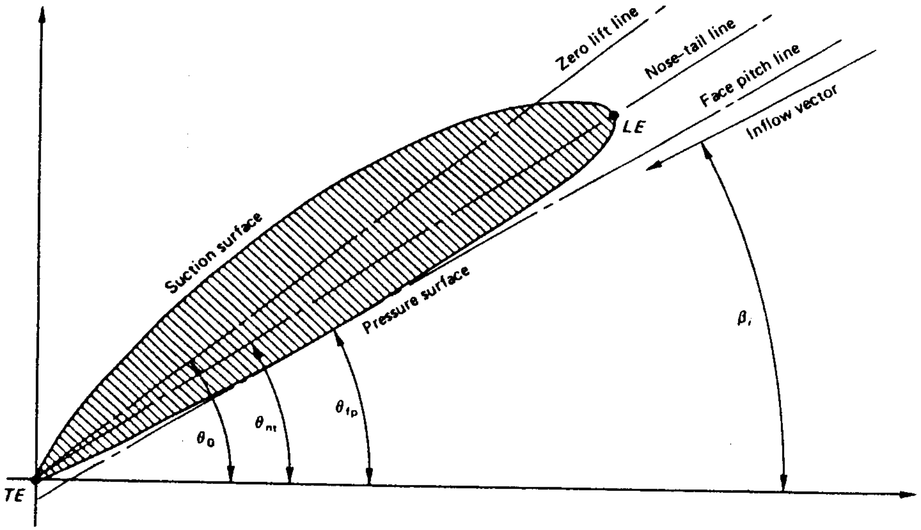

Figure 3.5 Pitch lines

The effective pitch line of the section corresponds to the conventional aerodynamic no-lift line and is the line that if the incident water flowed along, zero lift would result from the aerofoil section. The effective pitch angle (θ_0) is greater than the nose–tail pitch angle by an amount corresponding to the three-dimensional zero lift angle of the section. As such this is a fundamental pitch angle as it is the basis about which the hydrodynamic forces associated with the propeller section are calculated. Finally the hydrodynamic pitch angle (β_i) is the angle at which the incident flow encounters the blade section and is a hydrodynamic inflow rather than a geometric property of the propeller: neither this angle nor the effective pitch angle would, however, be expected to be found on the propeller drawing in normal circumstances.

From the above discussion it can be seen that the three pitch angles, effective, nose–tail and hydrodynamic pitch, are all related by the equations

effective pitch angle = nose–tail pitch angle
+ 3D zero lift angle
= hydrodynamic pitch angle
+ angle of attack of section
+ 3D zero lift angle.

The fuller discussion of the effective pitch, hydrodynamic pitch and zero lift angles will be left until Chapters 7 and 8; they have only been included here to underline the differences between them and thereby prevent confusion and serious analytical mistakes.

The mean pitch of a propeller blade is calculated using a moment mean principle. As such it is defined by

$$\bar{p} = \frac{\int_{x=x_h}^{1.0} px\,dx}{\int_{x=x_h}^{1.0} x\,dx} \tag{3.3}$$

The reason for adopting a moment mean is a practical expedient, which has been confirmed both experimentally and by calculation. As a consequence it can be used, in the context of effective pitch, to compare propellers, which may have different radial pitch distributions, from the viewpoint of power absorption. For continuous and fair distributions of pitch from the root to the tip it will be frequently found that the moment mean pitch corresponds in magnitude to the local pitch in the region of $0.6R$–$0.7R$.

For practical calculation purposes of equation (3.3), because the radial pitch distribution is normally represented by a well-behaved curve without great changes in gradient (Figure 3.6), it is possible to use a lower-order numerical integration procedure. Indeed the trapezoidal rule provides a satisfactory procedure if the span of the blade is split into ten intervals giving 11 ordinates. Then the mid-point of these intervals x_j ($j = 1, 2, 3, \ldots, 10$) are defined as follows, where x is the non-dimensional radius $x = r/R$:

$$x_j = \frac{x_i + x_{i+1}}{2} \qquad i, j = 1, 2, 3, \ldots, 10$$

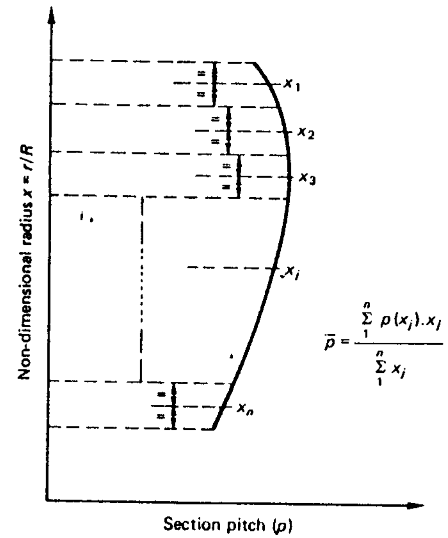

Figure 3.6 Mean pitch definition

Since the integral

$$\int_{x=x_h}^{1.0} p(x)x\,dx = \sum_{j=1}^{10} p(x_j)x_j\left(\frac{x_{TIP} - x_{HUB}}{10}\right)$$

and similarly,

$$\int_{x=x_h}^{1.0} x\,dx = \sum_{j=1}^{10} x_j\left(\frac{x_{TIP} - x_{ROOT}}{10}\right)$$

Hence,

$$\bar{p} = \frac{\sum_{j=1}^{10} p(x_j)x_j}{\sum_{j=1}^{10} x_j} \tag{3.4}$$

where

$$x_j = \frac{x_i + x_{i+1}}{2} \qquad i, j = 1, 2, 3, \ldots, 10$$

and

$$x_{i=1.0} = 1.0, \qquad x_{i=11} = \text{root radius}$$

3.4 Rake and skew

The terms rake and skew, although defining the propeller geometry in different planes, have a cross-coupling component due to the helical nature of blade sections. As with the Cartesian reference frame, many practitioners have adopted different definitions of skew. The author prefers the following definition, since as well as following the ITTC code it has also been adopted by several other authorities in Europe, the USA and the Far East. The skew angle $\theta_s(x)$ of a particular section, Figure 3.7, is the angle between the directrix and a line drawn through the shaft centre line and the mid-chord point of a section at its non-dimensional radius (x) in the projected propeller outline; that is, looking normally, along the shaft centre line, into the y–z-plane of Figure 3.1. Angles forward of the directrix, that is in the direction of rotation, in the projected outline are considered to be negative. The propeller skew angle (θ_{sp}) is defined as the greatest angle, measured at the shaft centre line, in the projected plane, which can be drawn between lines passing from the shaft centre line through the mid-chord position of any two sections. Propeller skew also tends to be classified into two types: balanced and biased skew designs. The balanced skew design is one where the locus of the mid-chord line generally intersects with the directrix at least twice in the inner regions of the blade. In contrast, in the biased skew design the mid-chord locus crosses the directrix not more than once; normally only in the inner sections.

Propeller rake is divided into two components: generator line rake (i_G) and skew induced rake (i_s). The total rake of the section with respect to directrix (i_T) is given by

$$i_T(r) = i_s(r) + i_G(r) \tag{3.5}$$

The generator line rake is measured in the x–z-plane of Figure 3.1 and is simply the distance AB shown in Figure 3.2. That is, it is the distance, parallel to the x-axis, from the directrix to the point where the helix of the section at radius r cuts the x–z-plane. To understand skew induced rake consider Figure 3.8, which shows an 'unwrapping' of two cylindrical sections, one at the root of the propeller and the other at some radius r between the tip and root of the blade. It will be seen that skew induced rake is the component, measured in the x-direction, of the helical distance around the cylinder from the mid-chord point of the section to the projection of the directrix when viewed normally to the y–z-plane. That is,

$$i_s = r\theta_s \tan(\theta_{nt}) \tag{3.6}$$

Consequently, it is possible then to define the locus of the mid-chord points of the propeller blade in space as follows for a rotating right-handed blade initially defined, $\phi = 0$, about the OZ-axis of the global reference frame (Figure 3.9):

$$\left.\begin{aligned} X_{c/2} &= -[i_G + r\theta_s \tan(\theta_{nt})] \\ Y_{c/2} &= -r\sin(\phi - \theta_s) \\ Z_{c/2} &= r\cos(\phi - \theta_s) \end{aligned}\right\} \tag{3.7}$$

And for the leading and trailing edges of the blade equation (3.7) can be extended to give:

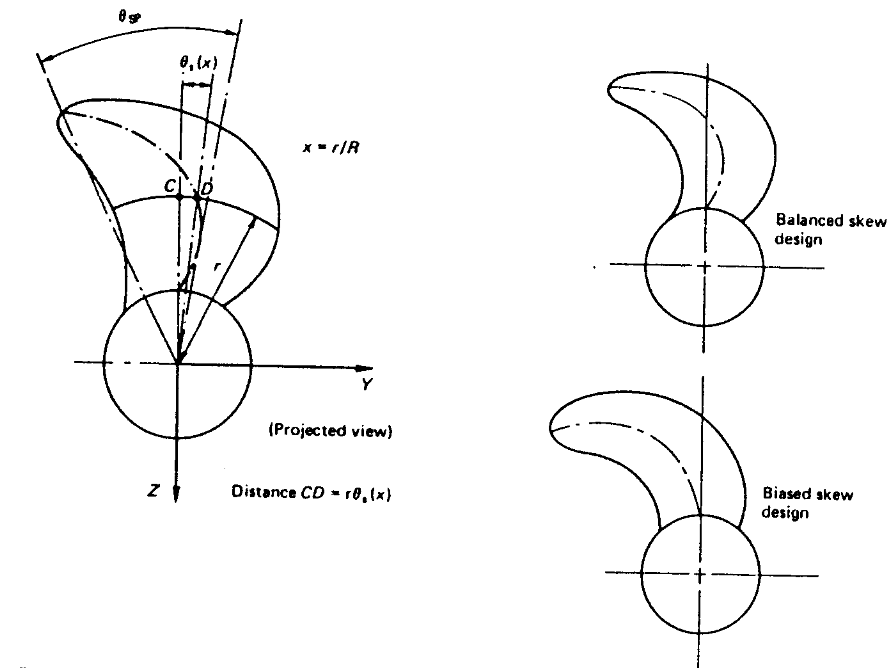

Figure 3.7 Skew definition

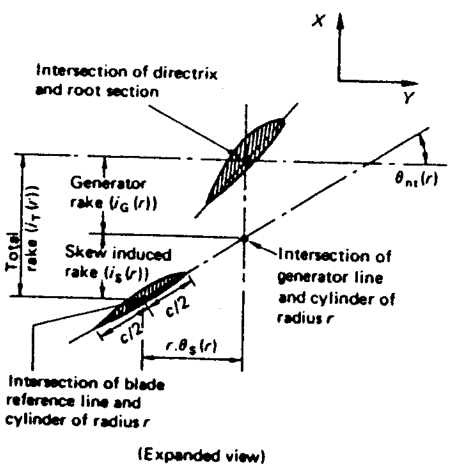

Figure 3.8 Definition of total rake

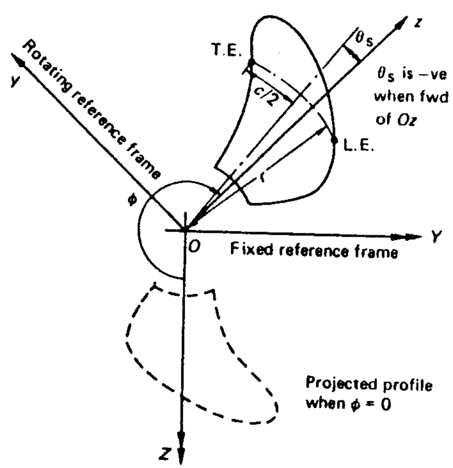

Figure 3.9 Blade coordinate definition

for the leading edge:

$$X_{LE} = -[i_G + r\theta_s \tan(\theta_{nt}) + \frac{c}{2}\sin(\theta_{nt})$$

$$Y_{LE} = -r\sin\left[\phi - \theta_s + \frac{90c\cos(\theta_{nt})}{\pi r}\right]$$

$$Z_{LE} = r\cos\left[\phi - \theta_s + \frac{90c\cos(\theta_{nt})}{\pi r}\right]$$

and for the trailing edge: (3.8)

$$X_{TE} = -[i_G + r\theta_s \tan(\theta_{nt})] - \frac{c}{2}\sin(\theta_{nt})$$

$$Y_{TE} = -r\sin\left[\phi - \theta_s - \frac{90c\cos(\theta_{nt})}{\pi r}\right]$$

$$Z_{TE} = r\cos\left[\phi - \theta_s - \frac{90c\cos(\theta_{nt})}{\pi r}\right]$$

where c is the chord length of the section at radius x and ϕ and θ_s are expressed in degrees.

In cases when the generator line is a linear function of radius it is meaningful to talk in terms of either a propeller rake (i_p) or a propeller rake angle (θ_{ip}). These are measured at the propeller tip as shown in Figure 3.10, where the propeller rake is given by

$$i_p = i_G(r/R = 1.0)$$

and

$$\theta_{ip} = \tan^{-1}\left[\frac{i_G(r/R = 1.0)}{R}\right] \quad (3.9)$$

In equation (3.9), i_p is taken as positive when the generator line at the tip is astern of the directrix, and similarly with θ_{ip}. In applying equation (3.9) it should be noted that some manufacturers adopt the alternative notation of specifying the rake angle from the root section:

$$\theta'_{ip} = \tan^{-1}\left[\frac{i_G(r/R = 1.0)}{(R - r_h)}\right]$$

where r_h is the radius of the root section. Consequently some care is needed in interpreting specific propeller applications.

3.5 Propeller outlines and area

The calculation of the blade width distribution is always made with reference to the cavitation criteria to which the propeller blade will be subjected. However, having once calculated the blade section widths based on these criteria it is necessary to fair them into a blade outline. This can either be done by conventional draughting techniques or by the fitting of a suitable mathematical expression. One such expression which gives good results is

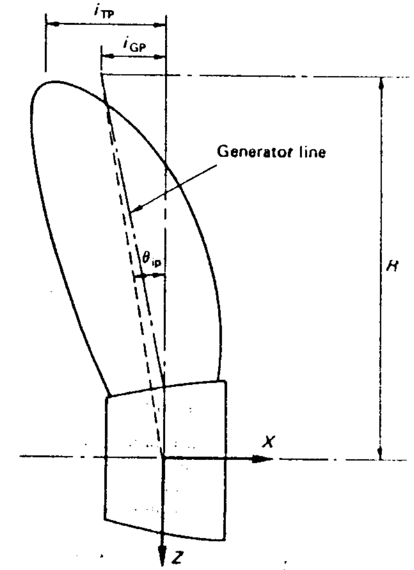

Figure 3.10 Tip rake definition

$$\frac{c}{D} = K_0(1 - x)^{1/2} + K_1 + K_2(1 - x) + K_3(1 - x)^2 + K_4(1 - x)^3 + K_5(1 - x)^4$$

where x is the non-dimensional radius and K_n, ($n = 0, 1, .., 5$) are coefficients. There are four basic outlines in general use currently which describe the propeller blade shape:

1. the projected outline;
2. the developed outline;
3. the expanded outline;
4. the swept outline.

The projected outline is the view of the propeller blade that is actually seen when the propeller is viewed along the shaft centre line, that is normal to the y–z-plane. Convention dictates that this is the view seen when looking forward. In this view the helical sections are defined in their appropriate pitch angles and the sections are seen to lie along circular arcs whose centre is the shaft axis; Figure 3.11 shows this view together with the developed and expanded views. The projected area of the propeller is the area seen when looking forward along the shaft axis. From Figure 3.11 it is clear that the projected area A_p is given by

$$A_p = Z\int_{r_h}^{R} (\theta_{TE} - \theta_{LE})r\,dr \quad (3.10)$$

where the same sign convention applies for θ as in the case of the skew angle and Z is the number of blades.

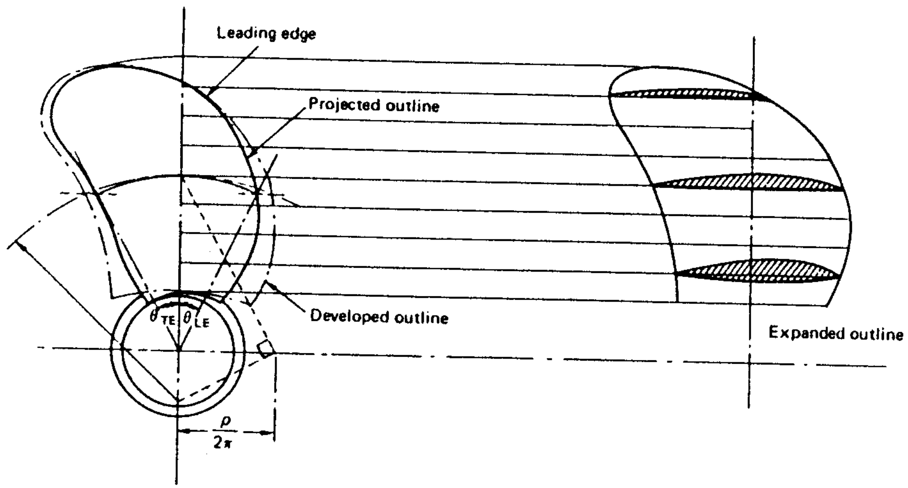

Figure 3.11 Outline definition

Projected area is of little interest today. However, in the early years of propeller technology the projected area was used extensively on a thrust loading per unit projected area basis for determining the required blade area to avoid the harmful effects of cavitation. It will be noted that the projected area is the area in the plane normal to the thrust vector.

The developed outline is related to the projected outline in so far as it is a helically based view, but the pitch of each section has been reduced to zero; that is the sections all lie in the thwart-ship plane. This view is used to give an appreciation of the true form of the blade and the distribution of chord lengths. The developed and projected views are the most commonly seen representations on propeller drawings; Figure 3.11 shows this view in relation to the projected outline.

To calculate the developed area it is necessary to integrate the area under the developed profile curve numerically if a precise value is required. For most purposes, however, it is sufficient to use the approximation for the developed area A_D as being

$$A_D \simeq A_E$$

where A_E is the expanded area of the blade.

In the past several researchers have developed empirical relationships for the estimation of the developed area; one such relationship, proposed by Burrill for non-skewed forms, is

$$A_D \simeq \frac{A_p}{(1.067 - 0.229P/D)} \tag{3.11}$$

In general, however, the developed area is greater than the projected area and slightly less than the expanded area.

The expanded outline is not really an outline in any true geometric sense at all. It could more correctly be termed a plotting of the chord lengths at their correct radial stations about the directrix; no attempt in this outline is made to represent the helical nature of the blades and the pitch angle of each section is reduced to zero. This view is, however, useful in that it is sometimes used to give an idea of the blade section forms used, as these are frequently plotted on the chord lengths, as seen in Figure 3.11.

The expanded area is the most simple of the areas that can be calculated, and for this reason is the area most normally quoted, and is given by the relationship:

$$A_E = Z\int_{r_h}^{R} c\,dr \tag{3.12}$$

In order to calculate this area it is sufficient for most purposes to use a Simpson's procedure with 11 ordinates, as shown in Figure 3.12.

Blade area ratio is simply the blade area, either the projected, developed or expanded depending on the context, divided by the propeller disc area A_o:

$$\left.\begin{aligned} \frac{A_P}{A_o} &= \frac{4A_P}{\pi D^2} \\ \frac{A_D}{A_o} &= \frac{4A_D}{\pi D^2} \\ \frac{A_E}{A_o} &= \frac{4A_D}{\pi D^2} \end{aligned}\right\} \tag{3.13}$$

By way of example, the difference in the value of the projected, developed and expanded area ratio for the propeller shown in Figure 3.11 can be seen from Table 3.1. The propeller was assumed to have four blades and a constant pitch ratio for this example.

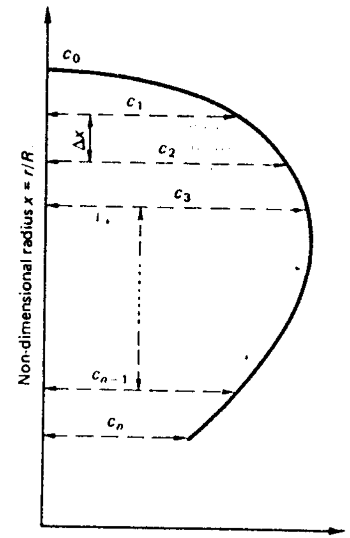

x	c	SM	c.SM
1.00	c_0	1/2	$c_0/2$
$1-\Delta x$	c_1	2	$2c_1$
$1-2\Delta x$	c_2	1	c_2
$1-3\Delta x$	c_3	2	$2c_3$
.	.	.	.
.	.	.	.
.	.	.	.
$1-(n-1)\Delta x$	c_{n-1}	2	$2c_{n-1}$
$1-n\Delta x$	c_n	1/2	$c_n/2$
			$\Sigma(c.\text{SM})$

$$A_E \simeq 0.667z\,\Delta x\,\Sigma(c.\text{SM})$$

Figure 3.12 Evaluation of expanded area

Table 3.1 Example of comparative blade area ratios

	Projected area	*Developed area*	*Expanded area*
Area ratio (A/A_o)	0.480	0.574	0.582

In each of the areas discussed so far the blade has been represented by a lamina of zero thickness. The true surface area of the blade will need to take account of the blade thickness and the surface profile on the suction and pressure faces; which will be different in all cases except for the so-called 'flat plate' blades found in applications like controllable pitch transverse propulsion units. To calculate the true surface area of one of the blade surfaces the algorithm of Figure 3.13 needs to be adopted.

This algorithm is based on a linear distance – that between the successive points on the surface. This is sufficient for most calculation purposes, but higher-order methods can be used at the expense of a considerable increase in computational complexity.

The swept outline of a propeller is precisely what is conventionally meant by a swept outline in normal engineering terms. It is normally used only to represent stern frame clearances. For the case of the highly skewed propeller a representation of the swept outline

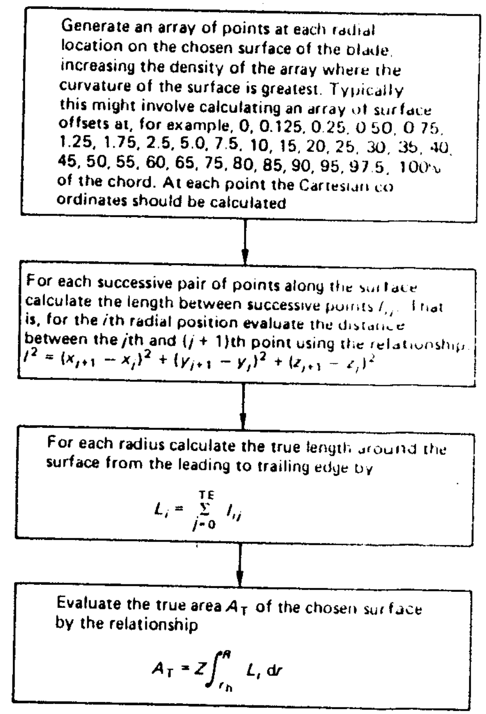

Figure 3.13 Algorithm for calculating surface area

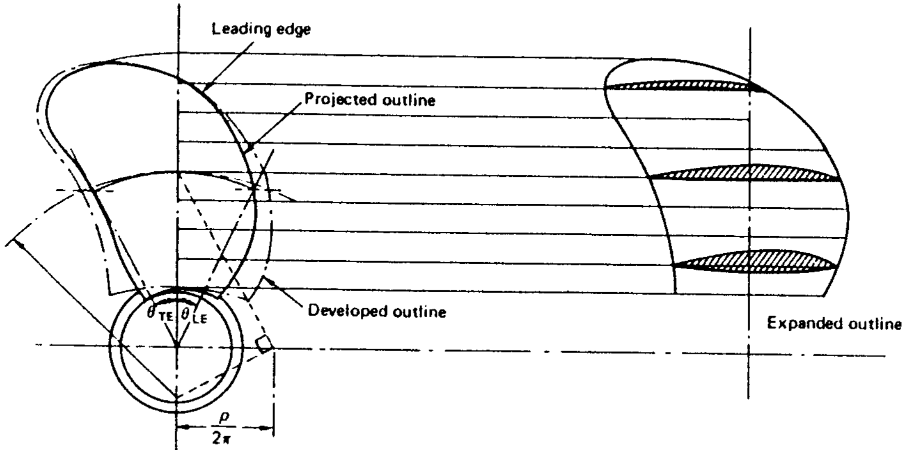

Figure 3.11 Outline definition

Projected area is of little interest today. However, in the early years of propeller technology the projected area was used extensively on a thrust loading per unit projected area basis for determining the required blade area to avoid the harmful effects of cavitation. It will be noted that the projected area is the area in the plane normal to the thrust vector.

The developed outline is related to the projected outline in so far as it is a helically based view, but the pitch of each section has been reduced to zero; that is the sections all lie in the thwart-ship plane. This view is used to give an appreciation of the true form of the blade and the distribution of chord lengths. The developed and projected views are the most commonly seen representations on propeller drawings; Figure 3.11 shows this view in relation to the projected outline.

To calculate the developed area it is necessary to integrate the area under the developed profile curve numerically if a precise value is required. For most purposes, however, it is sufficient to use the approximation for the developed area A_D as being

$$A_D \simeq A_E$$

where A_E is the expanded area of the blade.

In the past several researchers have developed empirical relationships for the estimation of the developed area; one such relationship, proposed by Burrill for non-skewed forms, is

$$A_D \simeq \frac{A_P}{(1.067 - 0.229P/D)} \tag{3.11}$$

In general, however, the developed area is greater than the projected area and slightly less than the expanded area.

The expanded outline is not really an outline in any true geometric sense at all. It could more correctly be termed a plotting of the chord lengths at their correct radial stations about the directrix; no attempt in this outline is made to represent the helical nature of the blades and the pitch angle of each section is reduced to zero. This view is, however, useful in that it is sometimes used to give an idea of the blade section forms used, as these are frequently plotted on the chord lengths, as seen in Figure 3.11.

The expanded area is the most simple of the areas that can be calculated, and for this reason is the area most normally quoted, and is given by the relationship:

$$A_E = Z\int_{r_h}^{R} c\,dr \tag{3.12}$$

In order to calculate this area it is sufficient for most purposes to use a Simpson's procedure with 11 ordinates, as shown in Figure 3.12.

Blade area ratio is simply the blade area, either the projected, developed or expanded depending on the context, divided by the propeller disc area A_o:

$$\left.\begin{aligned} \frac{A_P}{A_o} &= \frac{4A_P}{\pi D^2} \\ \frac{A_D}{A_o} &= \frac{4A_D}{\pi D^2} \\ \frac{A_E}{A_o} &= \frac{4A_D}{\pi D^2} \end{aligned}\right\} \tag{3.13}$$

By way of example, the difference in the value of the projected, developed and expanded area ratio for the

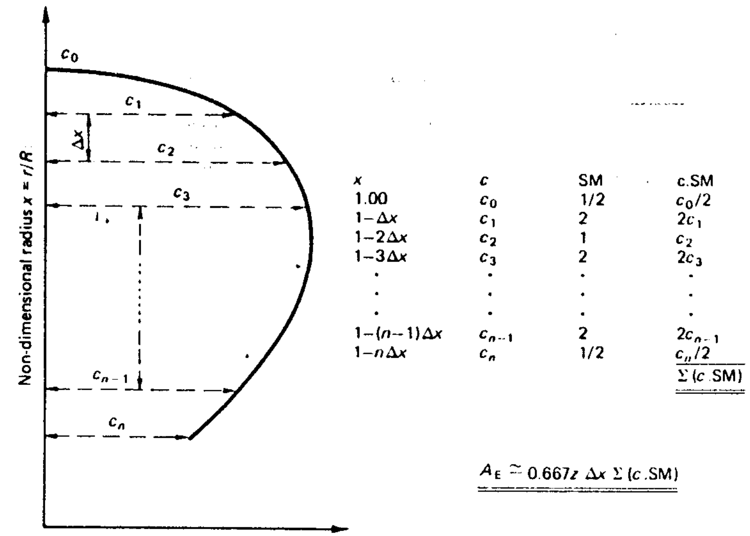

Figure 3.12 Evaluation of expanded area

propeller shown in Figure 3.11 can be seen from Table 3.1. The propeller was assumed to have four blades and a constant pitch ratio for this example.

Table 3.1 Example of comparative blade area ratios

	Projected area	*Developed area*	*Expanded area*
Area ratio (A/A_o)	0.480	0.574	0.582

In each of the areas discussed so far the blade has been represented by a lamina of zero thickness. The true surface area of the blade will need to take account of the blade thickness and the surface profile on the suction and pressure faces; which will be different in all cases except for the so-called 'flat plate' blades found in applications like controllable pitch transverse propulsion units. To calculate the true surface area of one of the blade surfaces the algorithm of Figure 3.13 needs to be adopted.

This algorithm is based on a linear distance – that between the successive points on the surface. This is sufficient for most calculation purposes, but higher-order methods can be used at the expense of a considerable increase in computational complexity.

The swept outline of a propeller is precisely what is conventionally meant by a swept outline in normal engineering terms. It is normally used only to represent stern frame clearances. For the case of the highly skewed propeller a representation of the swept outline

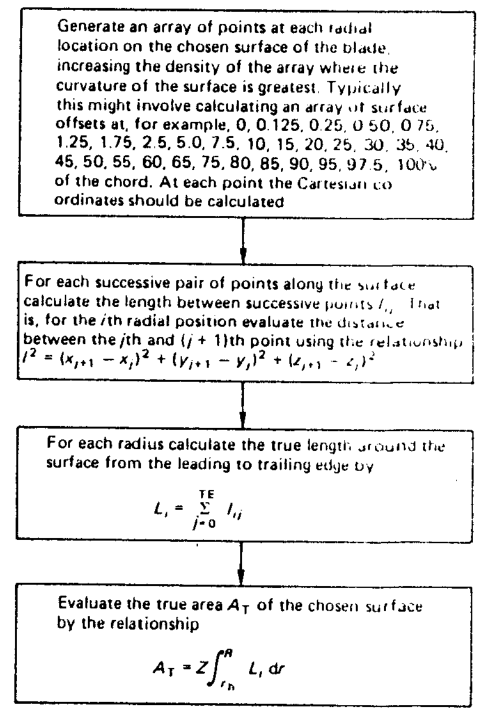

Figure 3.13 Algorithm for calculating surface area

is important since the skew induced rake term, if not carefully controlled in design, can lead to considerable 'overhang' of the blade which, in turn, can lead to mechanical interference with the stern frame. The swept outline is derived by plotting the rotation of each of the leading and trailing edge about the shaft axis.

3.6 Propeller drawing methods

The most commonly used method for drawing a propeller is that developed by Holst, Reference 2. This method relies on being able to adequately represent the helical arcs along which the propeller sections are defined by circular arcs, of some radius which is greater than the section radius, when the helical arcs have been swung about the directrix into the zero pitch or developed view (see Figure 3.11). This drawing method is an approximation but does not lead to significant errors unless used for very wide bladed or highly skewed propellers; in these cases errors can be significant and the alternative and more rigorous method of Rosingh (Reference 3) would then be used to represent the blade drawings.

The basis of Holst's construction is as shown in Figure 3.14. This Figure, however, shows the construction for only one particular radius in the interests of clarity; other radii are treated identically. A series of arcs with centre on the shaft axis at O are constructed at each of the radial stations on the directrix where the blade is to be defined. A length $p/2\pi$ is then struck off along the horizontal axis for each section and the lines AB are joined for each of the sections under consideration. A right angle ABC is then constructed, which in turn defines a point C on the extension of the directrix below the shaft centre line. An arc AC is then drawn with the centre C and radius r'. The distances from the directrix to the leading edge AA_L and the directrix to the trailing edge AA_T are measured around the circumference of the arc. Projections, normal to the directrix, through A_L and A_T meet the arc of radius r, about the shaft centre line, at P_L and P_T respectively. These latter two points form two points on the leading and trailing edges of the projected outline, whilst A_L and A_T lie on the developed outline. Consequently, it can be seen that distances measured around the arcs on the developed outline represent 'true lengths' that can be formed on the actual propeller.

The Holst drawing method was a common procedure used in propeller drawing offices years ago. However, the advent of the computer and its associated graphics capabilities have permitted the designer to plot automatically blade outlines using points calculated by analytical geometry, for example equation (3.8), together with curve-fitting routines, typically cubic splines.

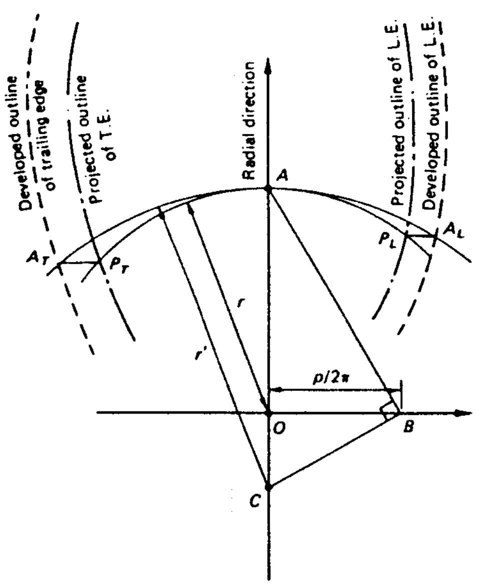

Figure 3.14 Holst's propeller drawing method

3.7 Section geometry and definition

The discussion so far has, with the exception of that relating to the true surface area, assumed the blade to be a thin lamina. This section redresses this assumption by discussing the blade section geometry.

In the early 1930s the National Advisory Committee for Aeronautics (NACA) in the United States of America – now known as NASA – embarked on a series of aerofoil experiments which were based on aerofoil geometry developed in a both rational and systematic way. Some of these aerofoil shapes have been adopted for the design of marine propellers, and as such have become widely used by manufacturers all over the world. Consequently, this discussion of aerofoil geometry will take as its basis the NACA definitions whilst, at the same time recognizing that with the advent of prescribed velocity distribution capabilities some designers are starting to generate their own section forms to meet specific surface pressure requirements.

Figure 3.15 shows the general definition of the aerofoil. The mean line or camber line is the locus of the mid-points between the upper and lower surfaces when measured perpendicular to the camber line. The extremities of the camber line are termed the leading and trailing edges of the aerofoil and the straight line joining these two points is termed the chord line. The distance between the leading and trailing edges when measured along the chord line is termed the chord length (c) of the section. The camber of the section is the maximum distance between the mean camber line and the chord line, measured perpendicular to the chord line. The aerofoil thickness is the distance between the upper and lower surfaces of the section, also measured perpendicularly to the chord line. The leading edges are usually circular, having a leading edge radius defined about a point on the camber line. However, for marine propellers, leading edge definition practices vary widely from manufacturer to manufacturer and care should be taken in establishing the practice actually used for the propeller in question.

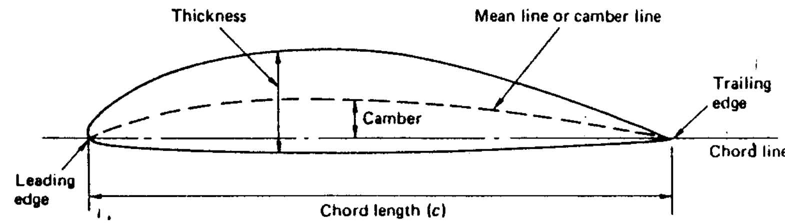

Figure 3.15 General definition of an aerofoil section

The process of combining a chosen camber line with a thickness line in order to obtain the desired section form is shown in Figure 3.16 for a given chord length c. In the figure only the leading edge is shown for the sake of clarity; however, the trailing edge situation is identical. The mean line is defined from the offsets (y_c) relating to the chosen line and these are 'laid off' perpendicularly to the chord line. The upper and lower surfaces are defined from the ordinates y_t of the chosen symmetrical thickness distribution, and these are then laid off perpendicularly to the camber line. Hence, a point P_u on the upper surface of the aerofoil is defined by

$$\left.\begin{aligned} x_u &= x_c - y_t \sin\psi \\ y_u &= y_c + y_t \cos\psi \end{aligned}\right\} \quad (3.14a)$$

where ψ is the slope of the camber line at the non-dimensional chordal position x_c.

Similarly for a point P_L on the lower surface of the aerofoil we have

$$\left.\begin{aligned} x_L &= x_c + y_t \sin\psi \\ y_L &= y_c - y_t \cos\psi \end{aligned}\right\} \quad (3.14b)$$

Although equations (3.14a, b) give the true definition of the points on the section surface, since y_c/c is usually of the order of 0.02–0.06 for marine propellers, the value of ψ is small. This implies $\sin\psi \to 0$ and $\cos\psi \to 1$. Hence, it is valid to make the approximation

$$\left.\begin{aligned} x_u &= x_c \\ y_u &= y_c + y_t \\ x_L &= x_c \\ y_L &= y_c - y_t \end{aligned}\right\} \quad (3.15)$$

where $y_t = \frac{t(x_c)}{2}$ (i.e. the local section semi-thickness) and the approximation defined by equation (3.15) is

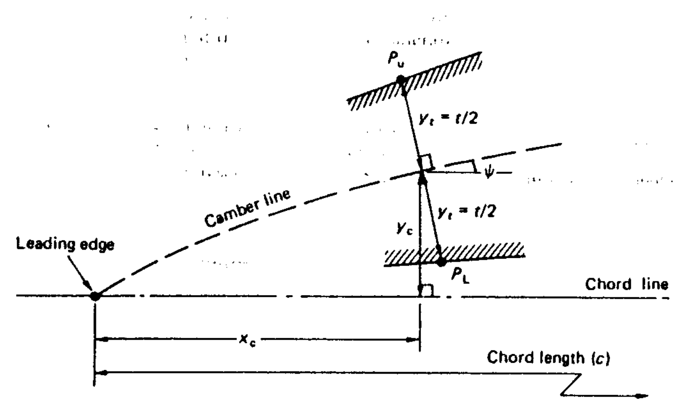

Figure 3.16 Aerofoil section definition

Table 3.2 NACA series camber or mean lines

x_c (per cent c)	64 mean line y_c (per cent c)	dy_c/dx_c	65 mean line y_c (per cent c)	dy_c/dx_c	66 mean line y_c (per cent c)	dy_c/dx_c
0	0	0.30000	0	0.24000	0	0.20000
1.25	0.369	0.29062	0.296	0.23400	0.247	0.19583
2.5	0.726	0.28125	0.585	0.22800	0.490	0.19167
5.0	1.406	0.26250	1.140	0.21600	0.958	0.18333
7.5	2.039	0.24375	1.665	0.20400	1.406	0.17500
10	2.625	0.22500	2.160	0.19200	1.833	0.16667
15	3.656	0.18750	3.060	0.16800	2.625	0.15000
20	4.500	0.15000	3.840	0.14400	3.333	0.13333
25	5.156	0.11250	4.500	0.12000	3.958	0.11667
30	5.625	0.07500	5.040	0.09600	4.500	0.10000
40	6.000	0	5.760	0.04800	5.333	0.06667
50	5.833	−0.03333	6.000	0	5.833	0.03333
60	5.333	−0.06667	5.760	−0.04800	6.000	0
70	4.500	−0.10000	5.040	−0.09600	5.625	−0.07500
80	3.333	−0.13333	3.840	−0.14400	4.500	−0.15000
90	1.833	−0.16667	2.160	−0.19200	2.625	−0.22500
95	0.958	−0.18333	1.140	−0.21600	1.406	−0.26250
100	0	−0.20000	0	−0.24000	0	−0.30000

x_c (per cent c)	a = 0.8 mean line y_c (per cent c)	dy_c/dx_c	a = 0.8 (mod) mean line y_c (per cent c)	dy_c/dx_c	a = 1.0 mean line y_c (per cent c)	dy_c/dx_c
0	0		0		0	
0.5	0.287	0.48535	0.281	0.47539	0.250	0.42120
0.75	0.404	0.44925	0.396	0.44004	0.350	0.38875
1.25	0.616	0.40359	0.603	0.39531	0.535	0.34770
2.5	1.077	0.34104	1.055	0.33404	0.930	0.29155
5.0	1.841	0.27718	1.803	0.27149	1.580	0.23430
7.5	2.483	0.23868	2.432	0.23378	2.120	0.19995
10	3.043	0.21050	2.981	0.20618	2.585	0.17485
15	3.985	0.16892	3.903	0.16546	3.365	0.13805
20	4.748	0.13734	4.651	0.13452	3.980	0.11030
25	5.367	0.11101	5.257	0.10873	4.475	0.08745
30	5.863	0.08775	5.742	0.08595	4.860	0.06745
35	6.248	0.06634	6.120	0.06498	5.150	0.04925
40	6.528	0.04601	6.394	0.04507	5.355	0.03225
45	6.709	0.02613	6.571	0.02559	5.475	0.01595
50	6.790	0.00620	6.651	0.00607	5.515	0
55	6.770	−0.01433	6.631	−0.01404	5.475	−0.01595
60	6.644	−0.03611	6.508	−0.03537	5.355	−0.03225
65	6.405	−0.06010	6.274	−0.05887	5.150	−0.04925
70	6.037	−0.08790	5.913	−0.08610	4.860	−0.06745
75	5.514	−0.12311	5.401	−0.12058	4.475	−0.08745
80	4.771	−0.18412	4.673	−0.18034	3.980	−0.11030
85	3.683	−0.23921	3.607	−0.23430	3.365	−0.13805
90	2.435	−0.25583	2.452	−0.24521	2.585	−0.17485
95	1.163	−0.24904	1.226	−0.24521	1.580	−0.23430
100	0	−0.20385	0	−0.24521	0	

generally used in propeller definition. The errors involved in this approximation are normally small – usually less than 0.5 mm and certainly within most manufacturing tolerances.

The centre for the leading edge radius is found from the NACA definition as follows. A line is drawn through the forward end of the chord at the leading edge with a slope equal to the slope of the mean line close to the leading edge. Frequently the slope at a point $x_c = 0.005$ is taken, since the slope at the leading edge is theoretically infinite. This approximation is justified by the manner in which the slope approaches infinity close to the leading edge. A distance is then laid off along this line equal to the leading edge radius and this forms the centre of the leading edge radius.

Details of all of the NACA series section forms can be found in Reference 4; however, for convenience the more common section forms used in propeller practice are reproduced here in Tables 3.2 and 3.3. In Table 3.3 the NACA 66 (Mod) section has been taken from Brockett (Reference 5) who thickened the edge region of the parent NACA 66 section for marine use. The basic NACA 65 and 66 section forms cannot be represented in the same y/t_{max} form for all section t_{max}/c ratios, as with the NACA 16 section, and Reference 4 needs to be consulted for the ordinates for each section thickness to chord ratio. In practice, for marine propeller purposes all of the basic NACA sections need thickening at the edges, otherwise they would frequently incur damage. Typical section edge thicknesses are shown in Table 3.4 as a proportion of the maximum section thickness for conventional free-running, non-highly skewed propellers. In the case of a highly skewed propeller, defined by the Rules of Lloyd's Register as one having a propeller skew angle in excess of 25°, the trailing edge thicknesses would be expected to be increased from those of Table 3.4 by amounts depending on the type and extent of the skew. The implication of Table 3.4 is that the leading and trailing edges have 'square' ends. This clearly is not the case: these are the thicknesses that would exist at the edges if the section thicknesses were extrapolated to the edges without rounding.

It is frequently necessary to interpolate the camber and thickness ordinates at locations away from those defined by Tables 3.2 and 3.3. For normal types of

Table 3.3 Typical aerofoil section thickness distributions

	x/c	NACA 16 y/t_{max}	NACA 66 (Mod) y/t_{max}
L.E.	0	0	0
	0.005	—	0.0665
	0.0075	—	0.0812
	0.0125	0.1077	0.1044
	0.0250	0.1504	0.1466
	0.0500	0.2091	0.2066
	0.0750	0.2527	0.2525
	0.1000	0.2881	0.2907
	0.1500	0.3445	0.3521
	0.2000	0.3887	0.4000
	0.2500	—	0.4363
	0.3000	0.4514	0.4637
	0.3500	—	0.4832
	0.4000	0.4879	0.4952
	0.4500	—	0.5000
	0.5000	0.5000	0.4962
	0.5500	—	0.4846
	0.6000	0.4862	0.4653
	0.6500	—	0.4383
	0.7000	0.4391	0.4035
	0.7500	—	0.3612
	0.8000	0.3499	0.3110
	0.8500	—	0.2532
	0.9000	0.2098	0.1877
	0.9500	0.1179	0.1143
T.E.	1.0000	0.0100	0.0333

Section t_{max}/c	0.06	0.09	0.12	0.15	0.18	0.21	
L.E. radius/c (%)	0.176	0.396	0.703	1.100	1.584	2.156	$\rho_L = 0.448c\left(\frac{t_{max}}{c}\right)^2$

Table 3.4 Typical section edge thickness ratio for conventional free running, non-highly skewed propellers

r/R	*Edge thickness ratios* $\frac{t(x_c/x = 0 \text{ or } 1.0)}{t_{max}}$	
	Leading edge	*Trailing edge*
0.9	0.245	0.245
0.8	0.170	0.152
0.7	0.143	0.120
0.6	0.134	0.100
0.5	0.130	0.085
0.4	0.127	0.075
0.3	0.124	0.068
0.2	0.120	0.057

camber lines standard interpolation procedures can be used, provided they are based on either second- or third-order polynomials. This is also the case with the thickness distribution away from the rapid changes of curvature that occur close to the leading edge. To overcome this difficulty van Oossanen (Reference 6) proposed a method based on defining an equivalent ellipse having a thickness to chord ratio equal to that of the section under consideration. Figure 3.17 demonstrates the method in which a thickness ratio T_R is formed between the actual section and the equivalent elliptical section:

$$T_R = \frac{y_t}{y_{t_{max}} \sin[\cos^{-1}(1 - 2x_c/c)]}$$

This provides a smooth well-behaved function between the leading and trailing edges and having a value of unity at these points. This function can then be interpolated at any required point x'_c and the required thickness at this point derived from the relationship

$$y'_t = T'_R y_{t_{max}} \sin[\cos^{-1}(1 - 2x_c/c)] \qquad (3.16)$$

This method can be used over the entire section in order to provide a smooth interpolation procedure; however, a difficulty is incurred right at the leading edge where the thickness distribution gives way to the leading edge radius. For points between this transition point, denoted by P in Figure 3.17, and the leading edge, the value of the thickness ratio T_R is given by

$$T_R = \frac{\rho_L^2 - (x_c - \rho_L)^2}{y_{t_{max}} \sin[\cos^{-1}(1 - 2x_c/c)]}$$

At the point P it should be noted that the tangent to both the leading edge radius and the thickness form are equal.

Having, therefore, defined the basis of section geometry, it is possible to revert to equations (3.8) and define the coordinates for any point P on the surface of the aerofoil section. Figure 3.18 shows this definition, and the equations defining the point P about the local reference frame (Ox, Oy, Oz) are given by

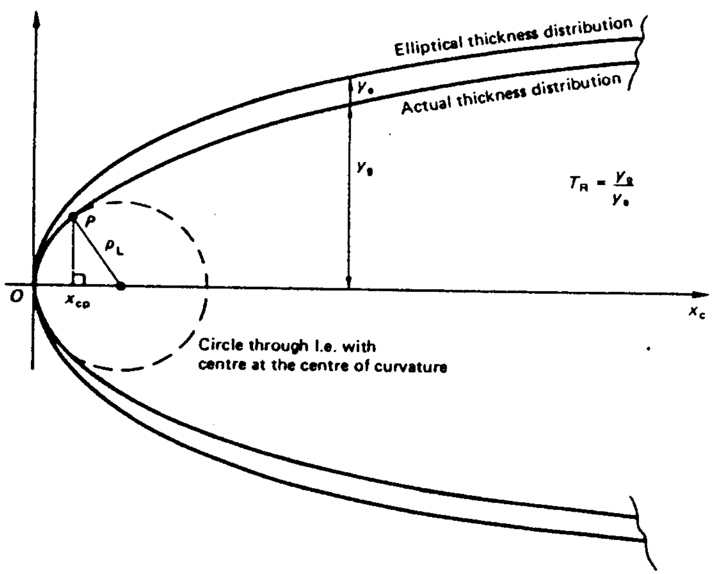

Figure 3.17 Van Oossanen's section thickness interpolation procedure

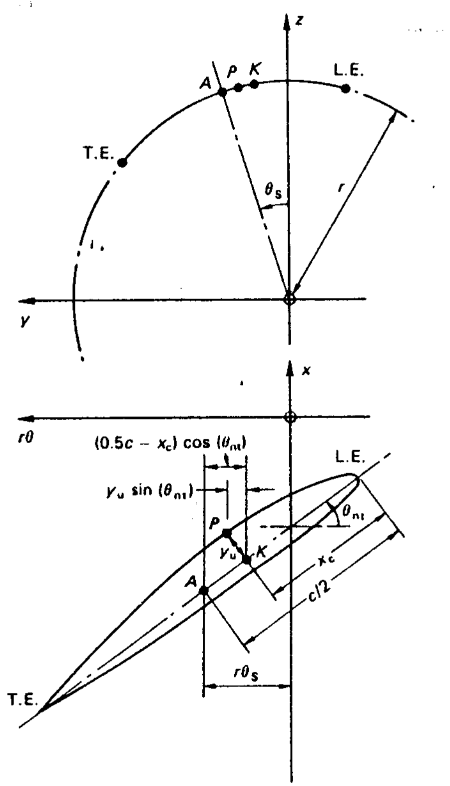

Figure 3.18 Definition of an arbitrary point p on a propeller blade surface

$$\left.\begin{aligned} x_p &= -[i_G + r\theta_s \tan(\theta_{nt})] + (0.5c - x_c)\sin(\theta_{nt}) + y_{u,L}\cos(\theta_{nt}) \\ y_p &= r\sin\left[\theta_s - \frac{180[(0.5c - x_c)\cos(\theta_{nt}) - y_{u,L}\sin(\theta_{nt})]}{\pi r}\right] \\ z_p &= r\cos\left[\theta_s - \frac{180[(0.5c - x_c)\cos(\theta_{nt}) - y_{u,L}\sin(\theta_{nt})]}{\pi r}\right] \end{aligned}\right\} \qquad (3.17)$$

where $y_u = y_c \pm y_t \cos\psi$ as per equations (3.14).

To convert these to the global reference frame (OX, OY, OZ), we simply write the transformation

$$\begin{bmatrix} X_p \\ Y_p \\ Z_p \end{bmatrix} = \begin{bmatrix} 1 & 0 & 0 \\ 0 & \cos\phi & -\sin\phi \\ 0 & \sin\phi & \cos\phi \end{bmatrix} \begin{bmatrix} x_p \\ y_p \\ z_p \end{bmatrix} \qquad (3.18)$$

where ϕ is the angle between the reference frames as shown in Figure 3.9. By combining equations (3.17) and (3.18) and inserting the appropriate values for x_c

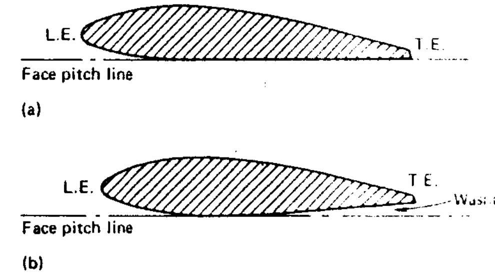

Figure 3.19 Section 'washback': (a) section without washback; (b) section with washback

and $y_{u,L}$, the expressions for the leading, trailing edges and mid-chord points, equations (3.8) and (3.7) respectively, can be derived.

The term 'washback' is sometimes seen in older papers dealing with propeller technology and in classification society rules. It relates to the definition of the after part of the face of the section and its relation to the face pitch line as shown in Figure 3.19. From this figure it is seen that for a section to have no 'washback', the face of the blade astern of the maximum thickness position is coincident with the face pitch line. When there is a 'wash back', the blade section lifts above the face pitch line.

Section edge geometry is a complex matter, since cavitation properties can be influenced greatly by the choice of the geometric configuration. In the case of the leading edge it is becoming increasingly popular to use a NACA type definition; however, some quite complex edge definitions will be found. For example, the choice of a radius defined about some arbitrary but well-defined point relative to the section chord line. These types of definition have largely been introduced from empiricism and experience of avoiding one type of cavitation or another prior to the advent of adequate flow computational procedures. Consequently, great care must be exercised in interpreting drawings from different manufacturers. With regard to the trailing edge, this generally receives less detailed consideration. In the absence of an anti-singing edge, see Figure 20.9, it is usual to specify either a half or quarter round trailing edge.

3.8 Blade thickness distribution and thickness fraction

Blade maximum thickness distributions are normally selected on the basis of stress analysis calculations. Sometimes this involves a calculation of the stress at some radial location, for example at the $0.25R$ radius, with the use of a standard thickness line found by the designer to give satisfactory service experience. More

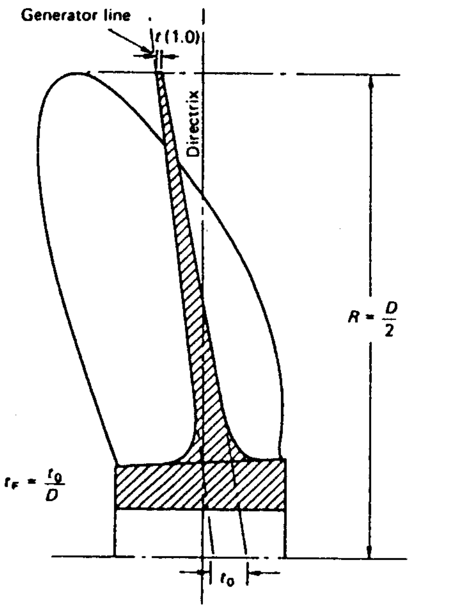

Figure 3.20 Typical representation of propeller maximum thickness distribution and notional thickness at shaft centre line

frequently today the maximum thickness distribution is the subject of detailed stress calculations over the entire blade using finite element techniques.

The resulting thickness distributions for large propellers are normally non-linear in form and vary considerably from one manufacturer to another. In the case of smaller propellers a linear thickness distribution is sometimes selected, and although this gives a conservative reserve of strength to the blade, it also causes an additional weight and drag penality to the propeller. On propeller drawings it is customary to show the maximum thickness distribution of the blade in an elevation as shown in Figure 3.20. In this elevation the maximum thicknesses are shown relative to the blade generator line. The blade thickness fraction is the ratio

$$t_F = \left(\frac{t_0}{D}\right) \tag{3.19}$$

where t_0 is the notional blade thickness defined at the shaft centre line as shown in Figure 3.20. In the case of a linear thickness distribution the value of t_0 is easy to calculate since it is simply a linear extrapolation of the maximum thickness distribution to the shaft centre line:

$$t_0 = t(1.0) + \frac{t(x) - t(1.0)}{(1.0 - x)}$$

where $t(x)$ is the blade maximum thickness at the non-dimensional radius x and $t(1.0)$ is the blade maximum thickness at the tip before any edge treatment. In the case of a non-linear thickness distribution the thickness fraction is calculated by a moment mean approximation as follows:

$$t_F = \frac{1}{D}\left[\frac{\sum t(x)x/(1-x)}{\sum x} + \left[t(1.0) - \frac{t(1.0)\sum x/(1-x)}{\sum x}\right]\right]$$

where x can take a range of nine or ten values over the blade span. For example,

;000 $x = 0.9, 0.8, 0.7, 0.6, 0.5, 0.4, 0.3, 0.2; (x \neq 1.0)$

or

$x = 0.9375, 0.875, 0.75, 0.625, 0.5, 0.375, 0.25; (x \neq 1.0)$.

3.9 Blade interference limits for controllable pitch propellers

In order that a controllable pitch propeller controllable pitch propeller can be fully reversible in the sense that its blades can pass through the zero pitch condition, care has to be taken that the blades will not interfere with each other. To establish the limiting conditions for full reversibility, either use can be made of equation (3.8), together with an interpolation procedure, or alternatively, the limits can be approximated using Holt's drawing method.

The latter method, as shown by Hawdon *et al.* (Reference 7), gives rise to the following set of relationships for the interference limits of three-, four-, and five-bladed controllable pitch propellers:

$$\left.\begin{array}{l}\text{Three-bladed propeller}\\ c_{max}/D = [1.01x + 0.050(P/D - 1) + 0.055]\\ \text{Four-bladed propeller}\\ c_{max}/D = [0.771x + 0.025(P/D - 1) + 0.023]\\ \text{Five-bladed propeller}\\ c_{max}/D = [0.632x + 0.0125(P/D - 1) + 0.010]\end{array}\right\} \tag{3.20}$$

3.10 Controllable pitch propeller off-design section geometry

A controllable pitch propeller presents further complications in blade section geometry if rotated about its spindle axis from the design pitch conditions for which the original helical section geometry was designed. Under these conditions it is found that helical sections at any given radii are subjected to a distortion when compared to the original designed section profile. To

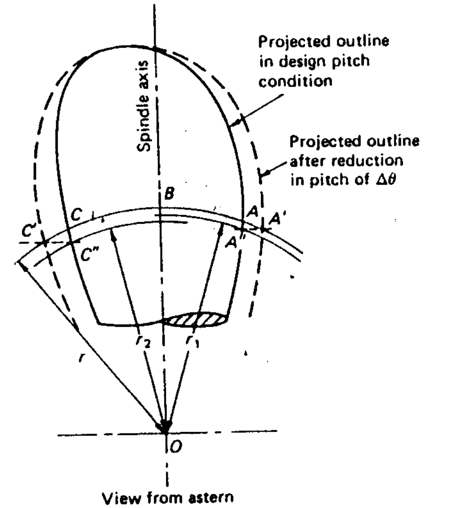

Figure 3.21 Geometric effects on blade section resulting from changes in pitch angle

illustrate this point further, consider a blade in the designed pitch setting together with a section denoted by a projection of the arc ABC at some given radius r (Figure 3.21). When the blade is rotated about its spindle axis, through an angle $\Delta\theta$, such that the new pitch angle attained is less than the designed angle, then the blade will take up a position illustrated by the hatched line in the diagram. Therefore, at the particular radius r chosen, the helical section is now to be found as a projection of the arc $A'BC'$. However, the point A' has been derived from the point A'', which with the blade in the design setting was at a radius r_1 ($r_1 < r$). Similarly with the point C', since this originated from the point C'' at a radius r_2 ($r_2 < r$). Consequently, the helical section $A'BC'$ at radius r becomes a composite section containing elements of all the original design sections at radii within the range r to r_2 assuming $r_1 > r_2$. These distortions are further accentuated by the radially varying pitch angle distribution of the blade, causing an effective twisting of the leading and trailing edges of the section. A similar argument applies to the case when the pitch angle is increased from that of the design value. This latter case, however, is normally of a fairly trivial nature from the section of definition viewpoint, since the pitch changes in this direction are seldom in excess of 4–5°.

The calculation of this 'distorted' section geometry at off-design pitch can be done either by draughting techniques, which is extremely laborious, or by using computer based surface geometry software packages. The resulting section distortion can be quite significant, as seen in Figure 3.22, which shows the distortion found in the section definition of a North Sea ferry propeller blade at the 0.5R and 0.8R sections for pitch change angles of 20° and 40°.

Rusetskiy (Reference 8) has also addressed this problem of section distortion at off-design conditions from the point of view of mean line distortion. He developed a series of construction curves to calculate the distortion of the mean line for a given pitch change angle from design geometrical data. This technique is suitable for hand calculation purposes.

An analogous problem to the one just described also exists in the definition of planar or 'straight-cut' sections through a blade. Such data are often required as input to N.C. machinery and other quality control operations. Klein (Reference 9) provides a treatment of this and other geometric problems.

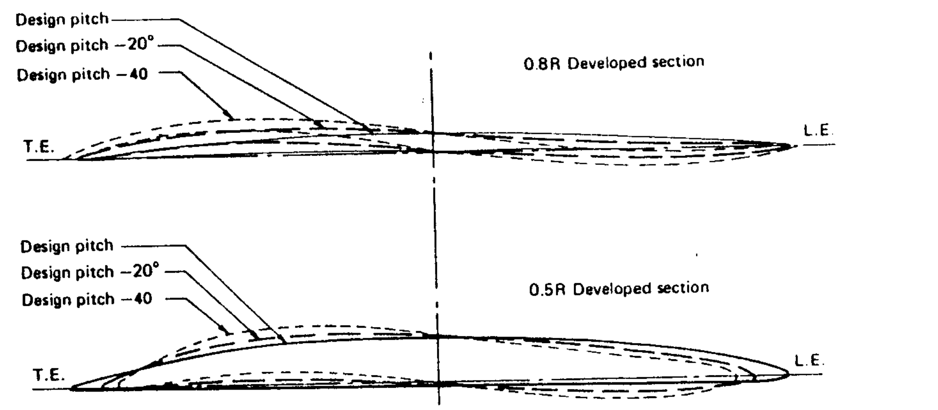

Figure 3.22 Section distortion due to changes of pitch angle

3.11 Miscellaneous conventional propeller terminology

In keeping with many aspects of marine engineering and naval architecture use is made in propeller technology of several terms which need further clarification.

The terms 'right-' and 'left-handed propellers' refer to the direction of rotation. In the case of a right-handed propeller, this type of propeller rotates in a clockwise direction, when viewed from astern, and thus describes a right-handed helical path. Similarly, the left-handed propeller rotates in an anticlockwise direction describing a left-handed helix.

The face and back of propellers are commonly applied terms both to the propeller in its entirety and also to the section geometry. The face of the propeller is that part of the propeller seen when viewed from astern and along the shaft axis. Hence the 'faces' of the blade sections are those located on the pressure face of the propeller when operating in its ahead design condition. Conversely, the backs of the propeller blades are those parts of the propeller seen when viewed from ahead in the same way. The backs of the helical sections, located on the backs of the propeller blades, are the same as the suction surfaces of the aerofoil in the normal design conditions.

References and further reading

1. Maritime Technology Monograph No. 6, *ITTC Dictionary of Ship Hydrodynamics*, RINA, 1978.
2. Holst, C.P. *The Geometry of the Screw Propeller*. Leiden, 1924.
3. Rosingh, W.H.C.E. Over de constructie en sterkteberekening van hoogbelaste scheepsschroeven. *Schip en Werf*, pp. 103–121, 1937.
4. Abbott, I.H., Doenhoff, A.E. von. *Theory of Wing Sections*. Dover, 1959.
5. Brockett, T. Minimum Pressure Envelopes for Modified NACA 66 Sections with NACA $a = 0.8$ Camber and BUships Type I and Type II Sections. DT NSRDC Report No. 1780, February 1966.
6. Oossanen, P. van. Calculation of Performance and Cavitation Characteristics of Propellers, Including Effects of Non-Uniform Flow and Viscosity. NSMB Publication 457, 1974.
7. Hawdon, L., Carlton, J.S., Leathard, F.I. The analysis of controllable pitch propeller characteristics at off-design conditions. *Trans. I.Mar.E.*, 1975.
8. Rusetskiy, A.A. *Hydrodynamics of Controllable Pitch Propellers*. Shipbuilding Publishing House, Leningrad, 1968.
9. Klein, J.L. A rational approach to propeller geometry. *Propellers '75 Symposium, Trans SNAME*, 1975.

4 The propeller environment

Contents

Sea water is a complex natural environment and it is the principal environment in which propellers operate. It is, however, not the only environment, since many vessels, some of considerable size, are designed to operate on inland lakes and waterways. Consequently, the properties of both fresh and sea water are of interest to the propulsion engineer.

This chapter considers the nature and physical properties of both fresh and sea water. The treatment of water properties is brief, however, since although much of the information is considered to be a prerequisite for propeller design, the subject of water properties is adequately covered by other standard texts on fluid mechanics (References 1, 2) and oceanography (References 3, 4). As a consequence, the information presented in this chapter is intended to be both an *aide-memoire* to the reader and also a condensed source of reference material for the practising designer and engineer.

4.1 Density of water

The density of sea water is a variable. It increases with either increase in salinity or pressure, and with decrease in temperature. Figure 4.1 shows the relationship between density, temperature and salinity. From the Figure it can be seen that temperature has a greater influence on density at a given salinity in the higher-temperature than in the lower-temperature regions. Conversely, at lower temperatures it is the salinity which has the greater effect on density since the isopleths run more nearly parallel to the temperature axis in these lower-temperature regions.

Density can normally be expected to increase with depth below the free surface. In tropical regions of the Earth a thin layer of low-density surface water is separated from the higher-density deep water by a zone of rapid density change, as seen in Figure 4.2.

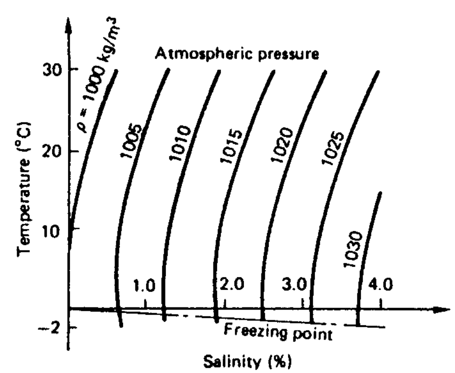

Figure 4.1 Variation of density with salinity and temperature at atmospheric pressure

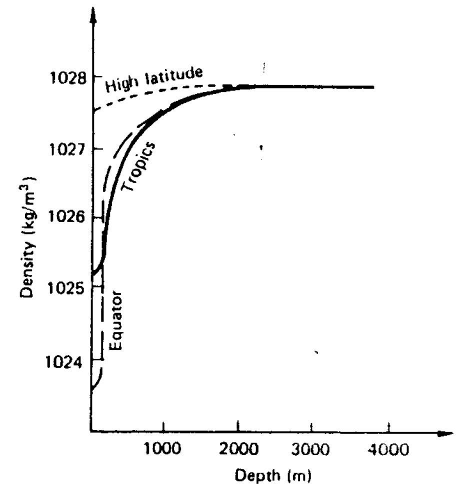

Figure 4.2 Typical variation of depth versus density for different global latitudes. (Reprinted from Reference 3 with kind permission from Pergamon Press)

In the higher latitudes this change is considerably less marked. Furthermore, it will be noted that the density deep in the ocean, below a depth of about 2000 m, is more or less uniform at 1027.9 kg/m³ for all latitudes. At the surface, however, the average density varies over a range between about 1022 kg/m³ near the equator to 1027.5 kg/m³ in the southern latitudes, as seen in Figure 4.3. Also shown in this diagram are the average relationships of temperature and salinity for differing latitudes, from which an idea of the global variations can be deduced.

When designing propellers for surface ships that are intended as ocean-going vessels it is usual to consider a standard salinity value of 3.5%. For these cases the associated density changes with temperature are given in Table 4.1.

The corresponding density versus temperature relationship for fresh water is shown in Table 4.2.

4.2 Salinity

With the exception of those areas of the world where fresh water enters the sea, the salinity of the oceans remains relatively constant and lies between 3.4 and 3.5% with an average value of 3.47% by weight. Figure 4.3 indicates the average variation over the world. From this figure it can be seen that salinity is lowest near the poles, due to the influence of the polar caps, and reaches a double maximum in the region of the tropics.

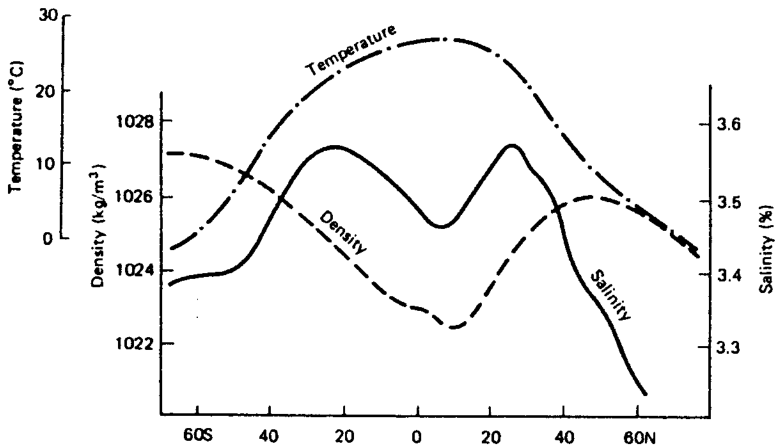

Figure 4.3 Variation of surface temperature, salinity and density with latitude—average for all oceans (Reprinted from Reference 3 with kind permission from Pergamon Press)

Table 4.1 Density variations with temperature (salinity 3.5%)

Temperature (°C)	0	5	10	15	20	25	30
Density (kg m³)	1028.1	1027.7	1026.8	1025.9	1024.7	1023.3	1021.7

It will be found that slightly higher than average values of salinity are found where evaporation rates are high, for example in the Mediterranean Sea or in the extreme case of the Dead Sea. Conversely, lower values will be found where melting ice is present or abnormally high levels of precipitation occur.

Salinity is again a variable with depth. In deep water the salinity is comparatively uniform and varies only between about 3.46 and 3.49%. Near the surface, above say 2000 m, the salinity varies to a greater extent as seen in Figure 4.3.

Six principal elements account for just over 99% of the dissolved solids in sea water

Chlorine	Cl^-	55.04%
Sodium	Na^+	30.61%
Sulphate	SO_4^{-2}	7.68%
Magnesium	Mg^{+2}	3.69%
Calcium	Ca^{+2}	1.16%
Potassium	K^+	1.10%
		99.28%

The relation between salinity and chlorinity was assessed in the 1960s and is taken as

$$\text{Salinity} = 1.80655 \times \text{Chlorinity} \quad (4.1)$$

Table 4.2 Density variations with temperature (fresh water)

Temperature (°C)	0	5	10	15	20	25	30
Density (kg/m³)	999.8	999.9	999.6	999.0	998.1	996.9	995.6

By measuring the concentration of the chlorine ion, which accounts for 55% of the dissolved solids as seen above, the total salinity can be deduced from equation (4.1). The average chlorinity of the oceans is 1.92% which then, from equation (4.1), gives an average salinity of 3.47%.

The definition given in equation (4.1) is termed the 'absolute salinity'; however, this has been superseded by the term 'practical salinity', which is based on the electrical conductivity of sea water, since most measurements of salinity are based on this property.

4.3 Water temperature

The distribution of surface temperature of the ocean is zonal with lines of constant temperature running nearly parallel to the equator in the open sea. Near the coast, of course, these isotherms deflect due to the action of currents. The open sea surface temperature

varies from values as high as 28°C just north of the equator down to around −2°C near the ice in the high latitudes (Figure 4.3).

The principal exchange of heat energy occurs at the air–water boundary. Surface heating is not a particularly efficient process, since convection plays little or no part in the mixing process, with the result that heating and cooling effects rarely extend below about two or three hundred metres below the surface of the sea. Consequently, below the surface the ocean can be divided broadly into three separate zones which describe its temperature distribution. Firstly, there is an upper layer, at between 50 and 200 m below the surface, where the temperatures correspond to those at the surface. Secondly, there is a transition layer where the temperature drops rapidly; this layer extends down to perhaps 1000 m and then finally there is the deep ocean region where temperature changes very slowly with depth. A typical temperature profile for low latitudes might be: 20°C at the surface; 8°C at 500 m; 5°C at 1000 m and 2°C at 4000 m.

Pickard and Emery (Reference 3) publish statistics relating to the ocean water temperatures and salinities. These are reproduced here since they are useful for guidance purposes:

1. 75% of the total volume of the ocean water has properties within the range from 0 to 6°C in temperature and 3.4 to 3.5% in salinity.
2. 50% of the total volume of the oceans has properties between 1.3 and 3.8°C and between 3.46 and 3.47%.
3. the mean temperature of the world's oceans is 3.5°C and the mean salinity is 3.47%.

4.4 Viscosity

The resistance to the motion of one layer of fluid relative to an adjacent layer is termed the viscosity of the fluid. Consequently, relative motion between different layers in a fluid requires the presence of shear forces between the layers, which themselves must be parallel to the layers in the fluid.

Consider the velocity gradient shown in Figure 4.4, in which two adjacent layers in the fluid are moving with velocities u and $u + \delta u$. In this case the velocity gradient between these two layers, distant δy apart, is $\delta u/\delta y$; or $\partial u/\partial y$ in the limit. Because the layers are moving with different velocities, there will be shear forces between the layers giving rise to a shear stress τ_{yx}. Newton postulated that the tangential stress between the layers is proportioned to the velocity gradient:

$$\tau_{yx} = \mu \frac{\partial u}{\partial y} \quad (4.2)$$

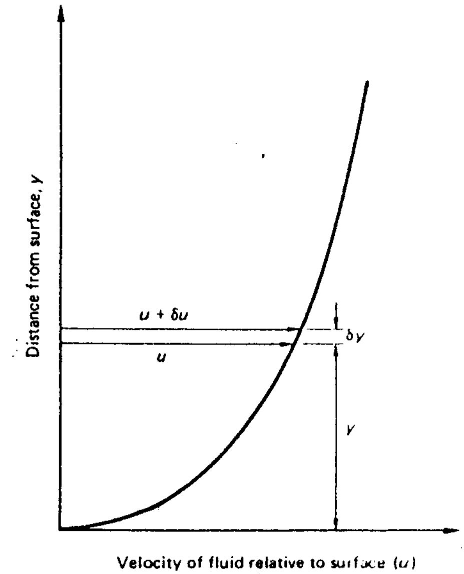

Figure 4.4 Typical viscous velocity gradient

where μ is a constant of proportionality known as the dynamic coefficient of viscosity of the fluid. Fluids which behave with a constant coefficient of viscosity, that is independent of the velocity gradient, are termed Newtonian fluids: both fresh water and sea water behave in this way, although some drag reduction fluid additives such long chain polymers have far from constant coefficients of viscosity and are thus termed non-Newtonian fluids.

In the majority of problems concerning propeller technology we are concerned with the relationship of the fluid viscous to inertia forces as expressed by the flow Reynolds number. To assist in these studies, use is made of the term kinematic viscosity (ν) which is the ratio μ/ρ, since the viscous forces are proportional to the viscosity μ and the inertia forces to the density ρ.

For the purposes of propeller design and analysis, the values of the kinematic viscosity for sea and fresh water are given by Tables 4.3 and 4.4 respectively.

4.5 Vapour pressure

At the free surface of the water there is a movement of water molecules both in and out of the fluid. Just above the surface, the returning molecules create a pressure which is known as the partial pressure of the vapour. This partial pressure, together with the partial pressures of the other gases above the liquid, make

Table 4.3 Viscosity of sea water with temperature salinity 3.5%

Temperature (°C)	0	5	10	15	20	25	30
Kinematic viscosity 10^6 (m²/s)	1.8284	1.5614	1.3538	1.1883	1.0537	0.9425	0.8493

Table 4.4 Viscosity of fresh water with temperature

Temperature (°C)	0	5	10	15	20	25	30
Kinematic viscosity 10^6 (m²/s)	1.7867	1.5170	1.3064	1.1390	1.0037	0.8929	0.8009

up the total pressure just above the surface of the water. The molecules leaving the water generate the vapour pressure whose magnitude is determined by the rate at which molecules escape from the surface. When the rates of release and return of the molecules from the water are the same, the air above the water is said to be saturated and the vapour pressure equals the partial pressure of the vapour: at this condition the value of the vapour pressure is the saturation pressure. Furthermore, the vapour pressure varies with temperature since temperature influences the energy of the molecules and hence their ability to escape from the surface. If the saturation pressure increases above the total pressure acting on the fluid surface then molecules escape from the water very rapidly and the phenomenon known as boiling occurs. In this condition bubbles of vapour are formed in the liquid itself and then rise to the surface.

A similar effect to boiling occurs if the water contains dissolved gases, since when the pressure is reduced the dissolved gases are released in the form of bubbles. The reduction in pressure required for the release of bubbles is, however, less than that which will cause the liquid to boil at the ambient temperature. Within a fluid the pressure cannot generally fall below the vapour pressure at the temperature concerned since the liquid will then boil and small bubbles of vapour form in large numbers.

Table 4.5 gives the values of the saturation vapour pressure of both sea and fresh water for a range of temperatures relevant to propeller technology.

Table 4.5 Saturation vapour pressure p_v for fresh and sea water

Temperature (°C)	0.01	5	10	15	20	25	30
Fresh water p_v (Pa)	611	872	1228	1704	2377	3166	4241
Sea water p_v (Pa)	590	842	1186	1646	2296	3058	4097

4.6 Dissolved gases in sea water

The most abundant dissolved gases which are found throughout the whole mass of the ocean are nitrogen, oxygen and argon. Additionally, there are traces of many other inert gases.

The quantities of these gases which are dissolved in the ocean are a function of salinity and temperature, with the greatest amounts being found in the cooler, less saline regions. At depth all gases with the exception of oxygen tend to be retained in the saturated state by the water as it sinks from the ocean surface. In these cases it is found that the gas concentrations change little with geographic location. At the surface, the oxygen concentration is normally of the order of 0.1–0.6% with values on occasion rising as high as 1%. Furthermore, at the surface the water is usually very close to being saturated and consequently is sometimes found to be supersaturated in the upper 15 m or so due to photosynthesis by marine plants. Below this level oxygen tends to get consumed by living organisms and the oxidation of detritus.

When undertaking cavitation studies, particularly at model scale, it is pertinent to ask what is the correct nuclei content of the tunnel water in order to achieve realistic sea conditions. Much work has been done on this subject and Figure 4.5 shows a range of measured nuclei distributions from different sources for ocean and tunnel conditions. Weitendorf and Keller also conducted a series of nuclei distribution measurements using laser techniques on board the *Sydney Express* in 1978 as part of a much wider cavitation study. They found that the number of nuclei per unit volume having radii greater than 1 μm was broadly in agreement with the levels established by oceanographers; however, they recorded little in the way of smaller particles on these trials. In general terms, however, nuclei distribution measurements must be considered in the context of

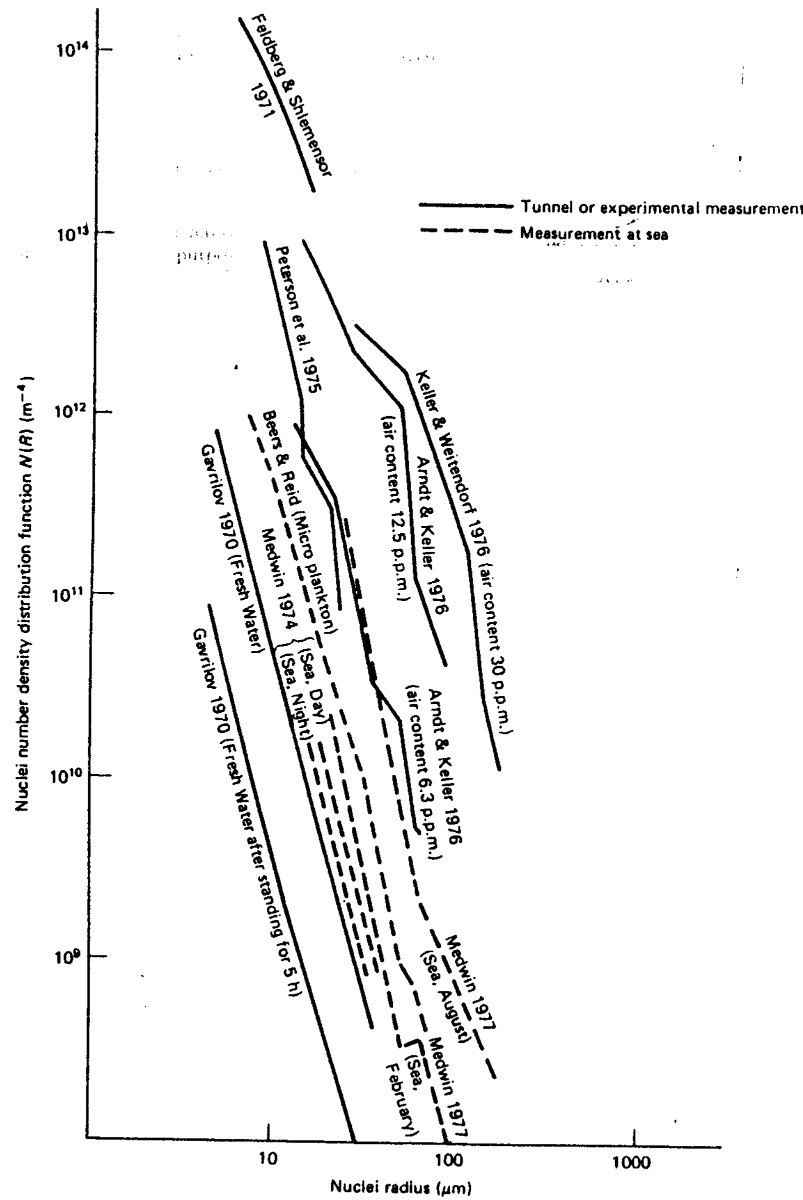

Figure 4.5 Nuclei density distribution

both weather and seaway and also of shallow or deep water.

4.7 Surface tension

Although the subject of surface tension is normally considered to be more in the province of physicists, it does have relevance when considering the bubble dynamics associated with cavitation.

A molecule has associated with it a 'sphere of influence' within which it attracts other molecules; this attraction is known as molecular attraction and is distinct from the gravitational attraction found between any two objects. The molecular attraction forces do not extend further than three or four times the average distance between molecules. To appreciate how surface tension forces arise consider the two molecules A and B shown in Figure 4.6. Molecule A, which is in the body of the fluid, exerts and receives a uniform attraction from all directions. However, molecule B, which is at the surface, receives its major attraction from within the fluid and so experiences a net inward force F: it is assumed here that we are considering a boundary between water and air or a vapour. This net inward force on the surface molecules increases the pressure on the main bulk of the liquid and hence needs to be balanced in order to keep the molecules in equilibrium. If the area of liquid surface increases, the number of molecules constituting that surface must also increase, and the molecules will arrive at the surface against the action of the inward force. Mechanical work is, therefore, expended in increasing the liquid surface area, which implies the existence of a tensile force in the surface.

Table 4.6 gives an indication of the values of surface tension for both fresh and sea water. However, in applying these values, it must be remembered that they can be considerably influenced by small quantities of additives, for example, detergent. In practice they can change by as much as 22 dynes/cm because of contamination with oily matter.

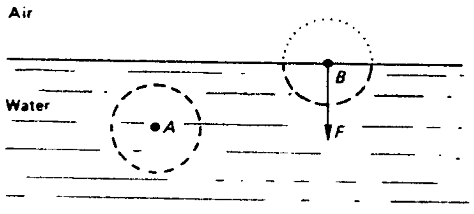

Figure 4.6 Molecular explanation of surface tension

Table 4.6 Typical values of surface tension for sea and fresh water with temperature

Temperature (°C)	0	5	10	15	20	25	30
Sea water (dynes/cm)	76.41	75.69	74.97	74.25	73.55	72.81	72.09
Fresh water (dynes/cm)	75.64	74.92	74.20	73.48	72.76	72.04	71.32

(1 dyne = 10^{-5} N)

4.8 Weather

The weather, or more fundamentally the air motion, caused by the dynamics of the Earth's atmosphere, influences marine propulsion technology by giving rise to additional resistance caused by both the wind and resulting disturbances to the sea surface.

The principal physical properties of air of concern are density and viscosity. The density at sea level for dry air is given by the relationship:

$$\rho = 0.4647\left[\frac{p}{T}\right]\text{kg/m}^3 \qquad (4.3)$$

where p is the barometric pressure (mm Hg) and T is the local temperature (K).

For the viscosity of the air use can be made of the following relationship for dry air:

$$\mu = 170.9 \times 10^{-6}\left[\frac{393}{120 + T}\right]\left(\frac{T}{273}\right)^{3/2} \text{poise} \qquad (4.4)$$

where T is the temperature (K).

When the wind blows over a surface the air in contact with the surface has no relative velocity to that surface. Consequently, a velocity gradient exists close to the solid boundary in which the relative velocity of successive layers of the wind increases until the actual wind speed in the free stream is reached (Figure 4.7). Indeed the flow pattern is analogous to the boundary layer velocity distribution measured over a flat plate. To overcome problems of definition in wind speed due to surface perturbations it is normal practice to measure wind speed at a height of 10 m above the surface of either the land or the sea: this speed is often referred to as the '10 metre wind' (Figure 4.7).

As well as recording wind velocities, wind conditions are often related to the Beaufort Scale, which was initially proposed by Admiral Beaufort in 1806. This scale has also been extended to give an indication of sea conditions for fully developed seas. The scale is not accurate enough for very detailed studies, since it was primarily intended as a guide to illustrate roughly what might be expected in the open sea. Indeed the scale is sufficient for many purposes, both technical and descriptive; however, great care should be exercised if it is used in the reverse way, that is for logging or

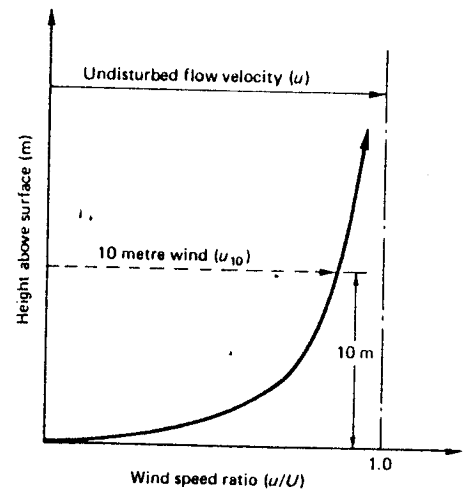

Figure 4.7 Wind speed definition

reporting the state of the sea, since significant errors can be introduced into the analysis. This is particularly true in confined and restricted sea areas, such as the North Sea or English Channel, since the sea generally has two components: a surface perturbation and an underlying swell component, both of which may have differing directional bearings. Table 4.7 defines the Beaufort scale up to Force 12. Above Force 12 there are further levels defined: 13, 14, 15, 16 and 17, with associated wind-speed bands of 72–80, 81–89, 90–99, 100–108 and 109–118 knots, respectively. For these higher states descriptions generally fail except to note that conditions become progressively worse.

Until comparatively recently the only tools available to describe the sea conditions were, for example, the Beaufort Scale, which as discussed relates overall sea state to observed wind, and formulae such as Stevens' formula:

$$Z = 1.5\sqrt{F} \qquad (4.5)$$

where Z is the maximum wave height in feet and F is the fetch in miles.

However, from wave records it is possible to statistically represent the sea. Using these techniques an energy spectrum indicating the relative importance of the large number of different component waves can be produced for a given sea state. Figure 4.8 shows one such example, for illustration purposes, based on the Neumann spectrum for different wind speeds and for fully developed seas. From Figure 4.8 it will be seen that as the wind speed increases, the frequency about which the maximum spectra energy is concentrated, termed the modal frequency f_0, is reduced.

Many spectra have been advanced by different authorities and these will give differing results; partly because of the dependence of wave energy on the wind duration and fetch which leads to the problem of defining a fully developed sea. When the wind begins to blow short, low amplitude waves are initially formed. These develop into larger and longer waves if the wind continues to blow for a longer period of time. This leads to a time-dependent set of spectra for different wind duration, as seen in Figure 4.9. An analogous, but opposite, situation is seen when the wind dies down as the longer waves, due to their greater velocity, move out of the area, leaving only the smaller shorter waves. For continuous spectra the area under the spectrum can be shown to be equal to the mean square of the surface elevation of the water surface.

In order to study the effects of waves the energy spectrum concept provides the most convenient and rigorous of approaches. However, for many applications, the simpler approach of appealing directly to wave data will suffice. Typical of such data is that given by Darbyshire (Reference 5) or more recently that produced by Hogben *et al.* (Reference 6) which provides a wave atlas based on some 55 million visual observations from ships during the period 1854 to 1984. Furthermore the World Meteorological Organisation (WMO) produced a standard sea state code in 1970; this is reproduced in Table 4.8. In the context of this table, the significant wave height is the mean value of the highest third of a large number of peak to trough wave heights. It should, however, be noted that wave period does not feaure in this well-established sea state definition.

4.9 Silt and marine organisms

The sea, and indeed fresh water, contains a quantity of matter in suspension. This matter is of the form of small particles of sand, detritus and marine animal and vegetable life.

Particulate matter such as sand will eventually separate out and fall to the sea bottom; however, depending on its size this separation process may be measured in either hours or months. Therefore, the presence of abrasive particles must always be considered, especially in areas, such as the North Sea, which have shallow sandy bottom seas.

Marine animal and vegetable life covers a wide, indeed almost boundless, variety of organisms. Of particular interest to the propulsion engineer are algae, barnacles, limpets, tubeworms and weed, since these all act as fouling agents for both the hull and propeller. Christie (Reference 7) distinguishes between two principal forms of fouling: algae and animal fouling. The latter form of fouling requires the development and establishment of larvae over a period of several days, whereas algae fouling results in a slime

Table 4.7 The Beaufort Wind Scale

Number	*Wind speed at 10 m (knots)*	*Wind description*	*Probable mean wave height (m)*	*Noticeable effect of wind on land*	*At sea*
0	Less than 1	calm	none	smoke vertical; flags still	Sea like a mirror.
1	1–3	light air	<0.1	smoke drifts; vanes static	Ripples with the appearance of scales are formed, but without foam crests.
2	4–6	light breeze	0.2	wind felt on face; leaves, flags rustle; vanes move	Small wavelets, still short but more pronounced; crests have a glassy appearance and do not break.
3	7–10	gentle breeze	0.6	leaves and twigs in motion; light flags extended	Large wavelets. Crests begin to break. Foam of glassy appearance Perhaps scattered white horses.
4	11–16	moderate breeze	1.0	raises dust; moves small branches	Small waves, becoming longer; fairly frequent white horses.
5	17–21	fresh breeze	1.9	small trees sway	Moderate waves, taking a more pronounced long form, many white horses formed (chance of some spray).
6	22–27	strong breeze	2.9	large branches move; telephone wire 'sing'	Large waves begin to form; the white foam crests are more extensive everywhere (probably some spray).
7	28–33	moderate gale	4.1	whole trees in motion	Sea heaps up and white foam from breaking waves begins to be blown in streaks along the direction of the wind (spindrift begins to be seen).
8	34–40	fresh gale	5.5	twigs break off; progress impeded	Moderately high waves of greater length; edge of crests break into spindrift. The foam is blown in well-marked streaks along the direction of the wind.
9	41–47	strong gale	7.0	chimney pots removed	High waves. Dense streaks of foam along the direction of the wind. Sea begins to roll. Spray may effect visibility.
10	48–55	whole gale	8.8	trees uprooted; structural damage	Very high waves with long, overhanging crests. The resulting foam in great patches is blown in dense white streaks along the direction of the wind. On the whole, the surface of the sea takes a white appearance. The rolling of the sea becomes heavy and shocklike. Visibility is affected.
11	56–64	storm	11.0	widespread damage	Exceptionally high waves. (Small and medium-sized ships might, for a long time, be lost to view behind the waves). The sea is completely covered with long white patches of foam lying along the direction of the wind. Everywhere the edges of the wave crests are blown into froth. Visibility is affected.
12	65–71	hurricane	over 13.0	countryside devastated	The air is filled with foam and spray. Sea completely white with driving spray; visibility very seriously affected.

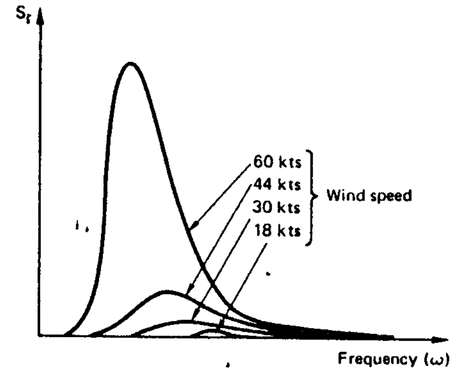

Figure 4.8 Typical wave spectra for varying wind speed

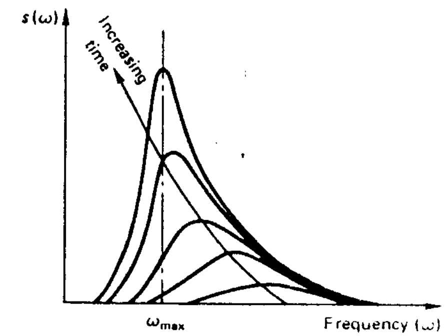

Figure 4.9 Growth of a wave spectra with wind duration

Table 4.8 World Meteorological Organisation (WMO) sea state code

Sea state code	*Significant wave height (m)*		*Description*
	Range	*Mean*	
0	0	0	Calm (glassy
1	0–0.1	0.05	Calm (rippled)
2	0.1–0.5	0.30	Smooth (wavelets)
3	0.5–1.25	0.875	Slight
4	1.25–2.5	1.875	Moderate
5	2.5–4.0	3.250	Rough
6	4.0–6.0	5.000	Very rough
7	6.0–9.0	7.500	High
8	9.0–14.0	11.500	Very high
9	Over 14.0	Over 14.00	Phenomenal

Table 4.9 Port classification for fouling according to Reference 7

Clean ports	*Fouling ports*		*Cleaning ports*	
	Light	*Heavy*	*Non-scouring*	*Scouring*
Most UK Ports	Alexandria	Freetown	Bremen	Calcutta
Auckland	Bombay	Macassar	Brisbane	Shanghai
Cape Town	Colombo	Mauritius	Buenos Aires	Yangtze Ports
Chittagong	Madras	Rio de Janeiro	E. London	
Halifax	Mombasa	Sourabaya	Hamburg	
Melbourne	Negapatam	Lagos	Hudson Ports	
Valparaiso	Karadii		La Plata	
Wellington	Pernambuco		St Lawrence Ports	
Sydney*	Santos		Manchester	
	Singapore			
	Suez			
	Tuticorin			
	Yokohama			

*Variable conditions

which can take only a matter of hours to form. These growths are of course dependent on temperature, salinity and concentrations of marine bacteria in the water. Whilst no direct estimates of fouling rates are available, Evans and Svensen (Reference 8) conducted a survey which showed those areas of the world which are more prone to the fouling of hulls and propellers. Table 4.9 summarizes their findings.

References and further reading

1. Massey, B.A. *Mechanics of Fluids.* Van Nostrand Reinhold, London.
2. Anderson, J.D. *Fundamentals of Aerodynamics.* McGraw-Hill, 1985.
3. Pickard, G.L. and Emergy, W. J. *Descriptive Physical Oceanography, An Introduction*, Pergamon Press, Oxford, 1982.
4. Thurman, V. *Introductory Oceanography*, Charles E. Merrill, Columbus, 1975.
5. Darbyshire, J. Wave statistics in the North Atlantic Ocean and on the coast of Cornwall. *The Marine Observer*, **25**, April 1955.
6. Hogben, Dacuna and Olliver. *Global Wave Statistics*, BMT, 1986.
7. Christie, A.O. *IMAEM*, 1981.
8. Evans, J.P. and Svensen, T.E. Voyage simulation model and its application to the design and operation of ships. *Trans. RINA*, November 1987.

5 The wake field

Contents

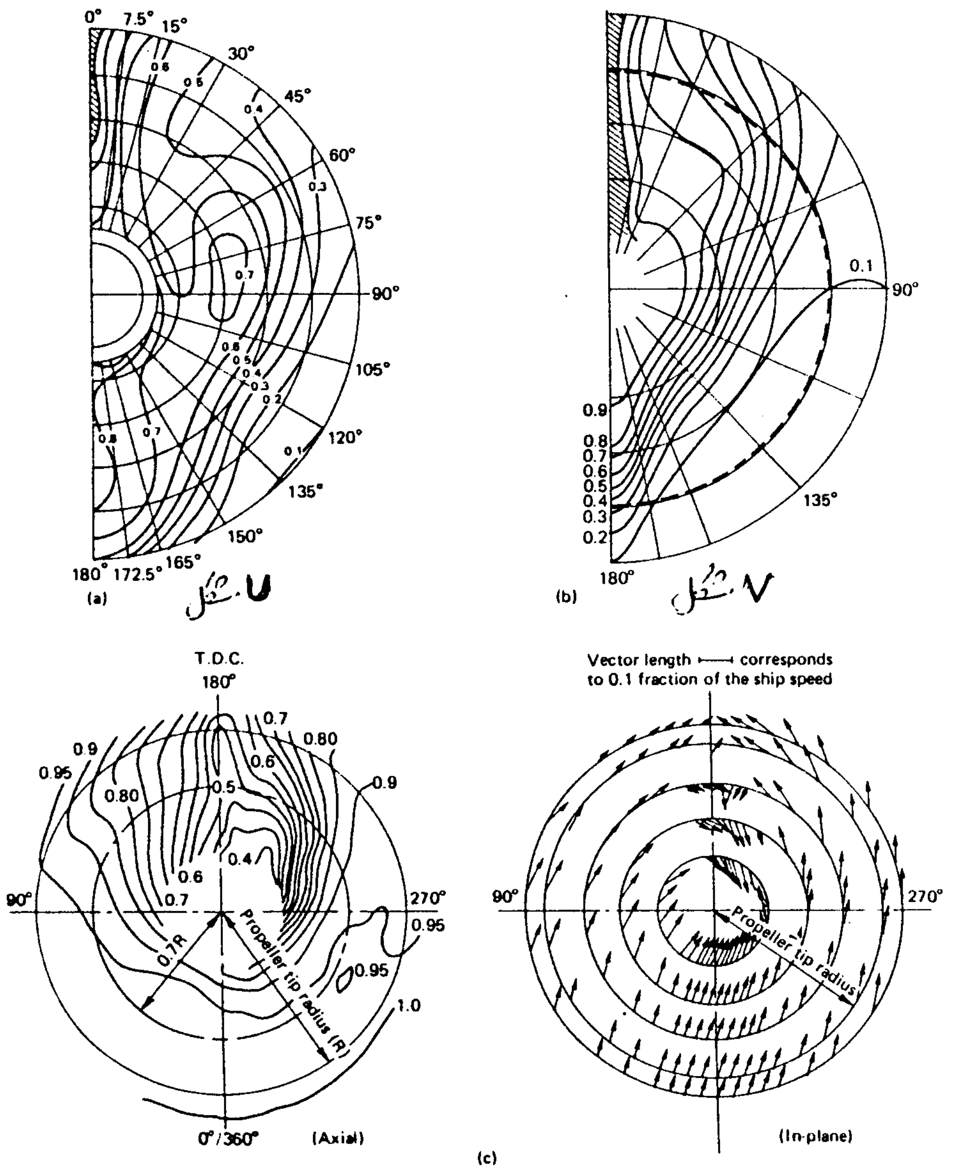

Figure 5.1 Typical wake field distributions: (a) axial wake field—U form hull; (b) axial wake field—V form hull; (c) axial and in-plane wake field—twin-screw hull. (Parts (a) and (b) reproduced from Reference 1, with permission)

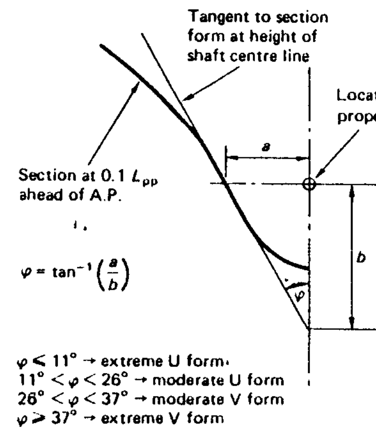

Figure 5.2 Definition of U and V form hulls

principal methods; the velocity ratio, Taylor and Froude methods, although today the method based on Froude's wake a fraction is rarely, if ever, used. The definitions of these methods are as follows.

Velocity ratio method. Here the iso-velocity contours are expressed as a proportion of the ship speed (V_s) relative to the far-field water speed. Accordingly, water velocity at a point in the propeller disc is expressed in terms of its axial, tangential and radial components, v_a, v_t and v_r respectively:

$$\frac{v_a}{V_s}, \quad \frac{v_t}{V_s} \quad \text{and} \quad \frac{v_r}{V_s}$$

Figure 5.1(c) is expressed using above velocity component definitions. The velocity ratio method has today become perhaps the most commonly used method of wake field representation, due firstly to the relative conceptual complexities the other, and older, representations have in dealing with the in-plane propeller components, and secondly, the velocity ratios are more convenient for data input into analytical procedures.

Taylor's method. In this characterization the concept of 'wake fraction' is used. For axial velocities the Taylor wake fraction is defined as

$$w_T = \frac{V_s - v_A}{V_s} = 1 - \left(\frac{v_A}{V_s}\right) \tag{5.1}$$

that is, one minus the axial velocity ratio or, alternatively, it can be considered as the loss of axial velocity at the point of interest when compared to the ship speed and expressed as a proportion of the ship speed. For the other in-plane velocity components we have the following relationships:

$$w_{T_t} = 1 - \left(\frac{v_t}{V_s}\right) \quad \text{and} \quad w_{T_r} = 1 - \left(\frac{v_r}{V_s}\right)$$

However, these forms are rarely used today, and preference is generally given to expressing the tangential and radial components in terms of their velocity ratios v_t/V_s and v_r/V_s.

Notice that in the case of the axial components the subscript 'a' is omitted from w_T.

Froude method. This is similar to the Taylor characterization, but instead of using the vehicle speed as the reference velocity the Froude notation uses the local velocity at the point of interest. For example, in the axial direction we have

$$w_F = \frac{V_s - v_a}{v_a} = \left(\frac{V_s}{v_a}\right) - 1$$

For the sake of completeness it is worth noting that the Froude and Taylor wake fractions can be transformed as follows:

$$w_F = \frac{w_T}{1 - w_T} \quad \text{and} \quad w_T = \frac{w_F}{1 + w_F}$$

Mean velocity or wake fraction. The mean axial velocity within the propeller disc is found by integrating the wake field on a volumetric basis of the form

$$\left.\begin{aligned} \bar{w}_T &= \frac{\int_{r_h}^{R} (w_T r)\,dr}{\int_{r_h}^{R} r\,dr} \\ \left(\frac{\bar{v}_a}{V_s}\right) &= \frac{\int_{r_h}^{R} \left(\frac{v_a}{V_s}\right) r\,dr}{\int_{r_h}^{R} r\,dr} \end{aligned}\right\} \tag{5.2}$$

Much debate has centred on the use of the volumetric or impulsive integral form for the determination of mean wake fraction, for example References 3 and 4; however, modern analysis techniques generally use the volumetric basis as a standard.

Fourier analysis of wake field. Current propeller analysis techniques rely on being able to describe the wake field encountered by the propeller at each radial location in a reasonably precise mathematical way. Figure 5.3 shows a typical transformation of the wake field velocities at a particular radial location of a polar wake field plot, similar to those shown in Figure 5.1, into a mean and fluctuating component. Figure 5.3 then shows diagrammatically how the total fluctuating component can then be decomposed into an infinite set of sinusoidal components of various harmonic orders. This follows from Fourier's theorem, which states that any periodic function can be represented by an infinite set of sinusoidal functions. In practice,

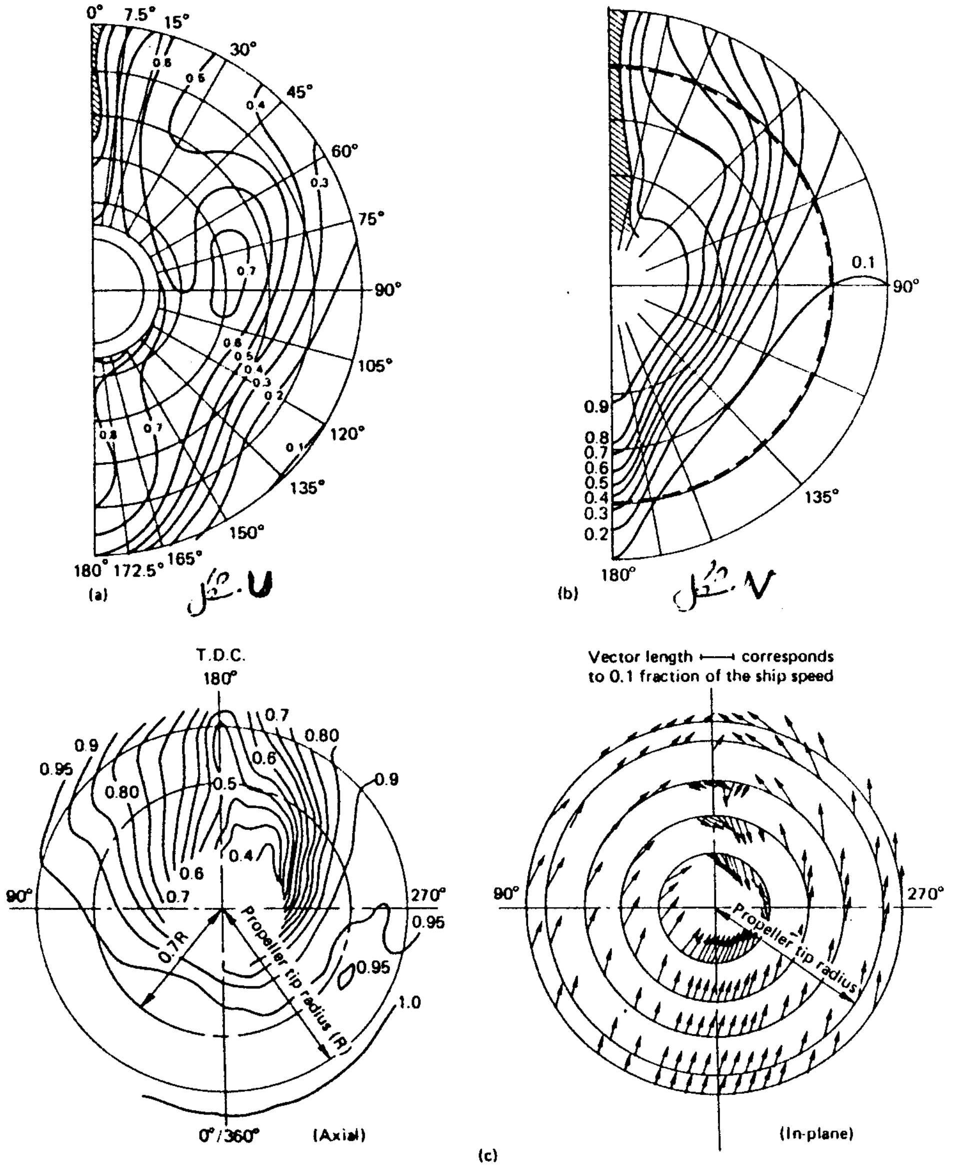

Figure 5.1 Typical wake field distributions: (a) axial wake field—U form hull; (b) axial wake field—V form hull; (c) axial and in-plane wake field—twin-screw hull. (Parts (a) and (b) reproduced from Reference 1, with permission)

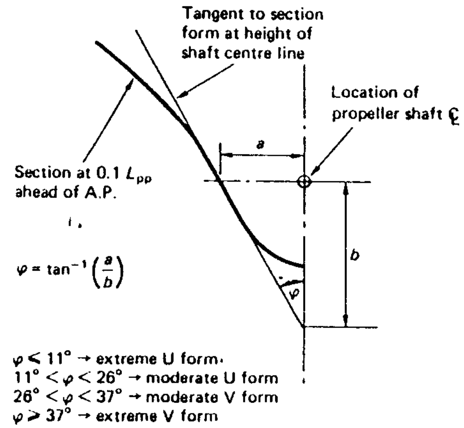

Figure 5.2 Definition of U and V form hulls

principal methods; the velocity ratio, Taylor and Froude methods, although today the method based on Froude's wake a fraction is rarely, if ever, used. The definitions of these methods are as follows.

Velocity ratio method. Here the iso-velocity contours are expresed as a proportion of the ship speed (V_s) relative to the far-field water speed. Accordingly, water velocity at a point in the propeller disc is expressed in terms of its axial, tangential and radial components, v_a, v_t and v_r respectively:

$$\frac{v_a}{V_s}, \quad \frac{v_t}{V_s} \quad \text{and} \quad \frac{v_r}{V_s}$$

Figure 5.1(c) is expressed using above velocity component definitions. The velocity ratio method has today become perhaps the most commonly used method of wake field representation, due firstly to the relative conceptual complexities the other, and older, representations have in dealing with the in-plane propeller components, and secondly, the velocity ratios are more convenient for data input into analytical procedures.

Taylor's method. In this characterization the concept of 'wake fraction' is used. For axial velocities the Taylor wake fraction is defined as

$$w_T = \frac{V_s - v_A}{V_s} = 1 - \left(\frac{v_A}{V_s}\right) \tag{5.1}$$

that is, one minus the axial velocity ratio or, alternatively, it can be considered as the loss of axial velocity at the point of interest when compared to the ship speed and expressed as a proportion of the ship speed. For the other in-plane velocity components we have the following relationships:

$$w_{T_t} = 1 - \left(\frac{v_t}{V_s}\right) \quad \text{and} \quad w_{T_r} = 1 - \left(\frac{v_r}{V_s}\right)$$

However, these forms are rarely used today, and preference is generally given to expressing the tangential and radial components in terms of their velocity ratios v_t/V_s and v_r/V_s.

Notice that in the case of the axial components the subscript 'a' is omitted from w_t.

Froude method. This is similar to the Taylor characterization, but instead of using the vehicle speed as the reference velocity the Froude notation uses the local velocity at the point of interest. For example, in the axial direction we have

$$w_F = \frac{V_s - v_a}{v_a} = \left(\frac{V_s}{v_a}\right) - 1$$

For the sake of completeness it is worth noting that the Froude and Taylor wake fractions can be transformed as follows:

$$w_F = \frac{w_T}{1 - w_T} \quad \text{and} \quad w_T = \frac{w_F}{1 + w_F}$$

Mean velocity or wake fraction. The mean axial velocity within the propeller disc is found by integrating the wake field on a volumetric basis of the form

$$\left.\begin{aligned} \bar{w}_T &= \frac{\int_{r_h}^{R} (w_T r)\,dr}{\int_{r_h}^{R} r\,dr} \\ \left(\frac{\bar{v}_a}{V_s}\right) &= \frac{\int_{r_h}^{R} \left(\frac{v_a}{V_s}\right) r\,dr}{\int_{r_h}^{R} r\,dr} \end{aligned}\right\} \tag{5.2}$$

Much debate has centred on the use of the volumetric or impulsive integral form for the determination of mean wake fraction, for example References 3 and 4; however, modern analysis techniques generally use the volumetric basis as a standard.

Fourier analysis of wake field. Current propeller analysis techniques rely on being able to describe the wake field encountered by the propeller at each radial location in a reasonably precise mathematical way. Figure 5.3 shows a typical transformation of the wake field velocities at a particular radial location of a polar wake field plot, similar to those shown in Figure 5.1, into a mean and fluctuating component. Figure 5.3 then shows diagrammatically how the total fluctuating component can then be decomposed into an infinite set of sinusoidal components of various harmonic orders. This follows from Fourier's theorem, which states that any periodic function can be represented by an infinite set of sinusoidal functions. In practice

A body, by virtue of its motion through the water, causes a wake field in the sense of an uneven flow velocity distribution to occur behind it; this is true whether the body is a ship, a submarine, a remotely operated vehicle or a torpedo. The wake field at the propulsor plane arises from three principal causes; the streamline flow around the body, the growth of the boundary layer over the body and the influence of any wave-making components. The latter effect naturally is dependent upon the depth of immersion of the body below the water surface. Additionally, and equally important, is the effect that the propulsor has on modifying the wake produced by the propelled body.

5.1 General wake field characteristics

The wake field is strongly dependent on ship type and so each vessel can be considered to have a unique wake field. Figure 5.1 shows three wake fields for different ships. Figure 5.1(a) relates to a single-screw bulk carrier form in which a bilge vortex can be seen to be present and dominates the flow in the thwart-ship plane of the propeller disc. The flow field demonstrated by Figure 5.1(b) relates again to a single screw vessel, but in this case to a fairly fast and fine lined vessel having a 'V' formed afterbody unlike the 'U' form of the bulk carrier shown in Figure 5.1(a). In Figure 5.1(b) it is seen, in contrast to the wake field produced by the 'U' form hull, that a high-speed axial flow field exists for much of the propeller disc except for the sector embracing the top dead centre location, where the flow is relatively slow and in some cases may even reverse in direction. Definitions of 'U' and 'V' form hulls are shown in Figure 5.2; however, there is no 'clear-cut' transition from one form to another and Figures 5.1(a) and (b) represent extremes of the hull form type. Both of the flow fields discussed so far relate to single-screw hull forms and, therefore, might be expected to exhibit a reflective symmetry about the vertical centre plane of the vessel. For a twin-screw vessel, however, no such symmetry naturally exists, as seen by Figure 5.1(c), which shows the wake field for a twin-screw ferry. In this figure the location of the shaft supports, in this case 'A' brackets, is clearly seen, but due to the position of the shaft lines relative to the hull form, symmetry of the wake field across the 'A' bracket centre line cannot be maintained. Indeed, considerable attention needs to be paid to the design of the shaft supports, whether these are 'A' brackets, bossings or gondolas, in order that the flow does not become too disturbed or retarded in these locations, otherwise vibration and noise may arise and become difficult problems to solve satisfactorily. This is also of equal importance for single-, twin- or triple-screw ships.

It is of interest to note how the parameter ϕ tends to influence the resulting wake field at the propeller disc of a single-screw ship. For the V-form hull (Figure 5.1(b)), one immediately notes the very high wake peak at the top dead centre position of the propeller disc and the comparatively rapid transition from the 'dead-water' region to the near free-stream condition in the lower part of the disc. This is caused by the water coming from under the bottom of the ship and flowing gently around the curvature of the hull, so that the fluid elements which were close to the hull and thus within its boundary layer, also remain close to the hull around the bilge and flow into the propeller close to the centre plane. Consequently, a high wake peak is formed in the centre plane of the propeller disc.

The alternative case of a wake field associated with an extreme U-form hull is shown in Figure 5.1(a): here the flow pattern is completely different. The water flowing from under the hull is in this case unable to follow the rapid change of curvature around the bilge and, therefore, separates from the hull surface. These fluid elements then flow upwards into the outer part of the propeller disc, and the region above the separated zone is then filled with water flowing from above: this creates a downward flow close to the hull surface. The resultant downward flow close to the hull and upward flow distant from the hull give rise to a rotational motion of the flow into the propeller disc which is termed the bilge vortex. The bilge vortex, therefore, is a motion which allows water particles in the boundary layer to be transported away from the hull and replaced with water from outside the boundary layer; the effect of this is to reduce the wake peak at the centre plane of the propeller disc.

Over the years, in order to help designers produce acceptable wake fields for single-screw ships, several hull form criteria have been proposed, as outlined, for example, in References 1 and 2. Criteria of these types basically reduce to a series of guide lines such as:

1. The angle of run of the water lines should be kept to below 27–30° over the entire length of run. Clearly it is useless to reduce the angle of run toward the stern post if further forward the angles increase to an extent which induces flow separation.
2. The stern post width should not exceed 3% of the propeller diameter in the ranges $0.2R$ to $0.6R$ above the shaft centre-line.
3. The angle of the tangent to the hull surface in the plane of the shaft centre line (see Figure 5.2) should lie within the range 11° to 37°.

The detailed flow velocity fields of the type shown in Figure 5.1 and used in propeller design are almost without exception derived from model tests. Analytical methods of wake field determination at this time are not reliable for general ship forms.

5.2 Wake field definition

In order to make use of the wake field data it needs to be defined in a suitable form. There are three

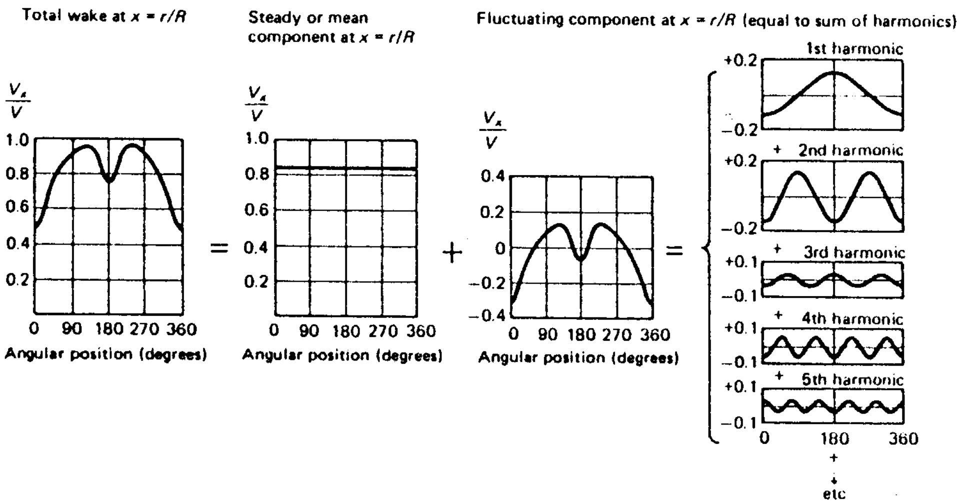

(N.B. 0/360° indicates T.D.C. position in propeller disc)

Figure 5.3 Decomposition of wake field into mean and fluctuating components

however, only a limited set of harmonic components are used, since these are sufficient to define the wake field within both the bounds of calculation and experimental accuracy: typically the first eight to ten harmonics are those which might be used, the exact number depending on the propeller blade number. A convenient way, therefore, of describing the velocity variations at a particular radius in the propeller disc is to use Fourier analysis techniques and to define the problem using the global reference frame discussed in Chapter 3. Using this basis the general approximation of the velocity distribution at a particular radius becomes

$$\frac{v_a}{V_s} = \sum_{k=0}^{\infty} a_k \cos\left(\frac{k\phi}{2\pi}\right) + b_k \sin\left(\frac{k\phi}{2\pi}\right) \qquad (5.3)$$

Equation (5.3) relates to the axial velocity ratio; similar equations can be defined for the tangential and radial components of velocity.

5.3 The nominal wake field

The nominal wake field is the wake field that would be measured at the propeller plane without the presence or influence of the propeller modifying the flow at the stern of the ship. The nominal wake field $\{w_n\}$ of a ship can be considered to effectively comprise three components; the potential wake, the frictional wake and the wave-induced wake, so that the total nominal wake field $\{w_n\}$ is given by

$$\{w_n\} = \{w_p\} + \{w_v\} + \{w_w\} + \{\Delta w\} \qquad (5.4)$$

where the suffixes denote the above components respectively and the curly brackets denote the total wake field rather than values at a particular point. The component $\{\Delta w\}$ is the correlation or relative interaction component representing the non-linear part of the wake field composition.

The potential wake field $\{w_p\}$ is the wake field that would arise if the vessel were working in an ideal fluid, that is one without viscous effects. As such the potential wake field at a particular transverse plane on the body is directly calculable using analytical methods, and it matters not whether the body is moving ahead or astern. Clearly, for underwater bodies, and particularly for bodies of revolution, the calculation procedures are comparatively simpler to use than for surface ship forms. For calculations on ship forms use is made of panel methods which today form the basis of three-dimensional, inviscid, incompressible flow calculations. The general idea behind these methods is to cover the surface with three-dimensional body panels over which there is an unknown distribution of singularities: for example, point sources, doublets or vortices. The unknowns are then solved through a system of simultaneous linear algebraic equations generated by calculating the induced velocity at control points on the panels and applying the flow tangency condition. In recent years many such programs have been developed by various institutes and software houses around the world. For axisymmetric bodies in axial flow a distribution of sources and sinks along the axis will prove sufficient for the calculation of the potential wake.

In contrast to calculation methods an approximation to the potential wake at the propeller plane can be found by making a model of the vehicle and towing it backwards in a towing tank, since in this case the viscous effects at the propeller plane are minimal.

In general, the potential wake field can be expected to be a small component of the total wake field, as shown by Harvald (Reference 5). Furthermore, since the effects of viscosity do not have any influence on the potential wake, the shape of the forebody does not have any influence on this wake component at the stern.

The frictional wake field $\{w_v\}$ arises from the viscous nature of the water passing over the hull surface. This wake field component derives from the growth of the boundary layer over the hull surface, which, for all practical purposes, can be considered as being predominantly turbulent in nature at full scale. To define the velocity distribution within the boundary layer it is normal, in the absence of separation, to use a power law relationship of the form

$$\frac{v}{V} = \left(\frac{y}{\delta}\right)^n$$

where v is the local velocity at a distance y from the boundary surface, V is the free stream velocity and δ is the boundary layer thickness, which is normally defined as the distance from the surface to where the local velocity attains a value of 99% of the free stream velocity. The exponent n for turbulent boundary layers normally lies within the range 1/5 to 1/9.

A further complication within the ship boundary layer problem is the onset of separation which will occur if the correct conditions prevail in an adverse pressure gradient; that is a pressure field in which the pressure increases in the direction of flow. Consider, for example, Figure 5.4(a), which shows the flow around some part of the hull. At station 1 the normal viscous boundary layer has developed; further along the hull at station 2 the velocity of fluid elements close to the surface is less than at station 1, due to the steadily increasing pressure gradient. As the elements continue further downstream they may come to a stop under the action of the adverse pressure gradient, and actually reverse in direction and start moving back upstream as seen at station 3. The point of separation occurs when the velocity gradient $\partial v/\partial n = 0$ at the surface, and the consequence of this is that the flow separates from the surface leaving a region of reversed flow on the surface of the body. Re-attachment of the flow to the surface can subsequently occur if the body geometry and the pressure gradient become favourable.

The full prediction by analytical means of the viscous boundary layer for a ship form is a very complex procedure, and at the present time only partial success has been achieved using large computational codes. A typical calculation procedure for a ship form divides the hull into three primary areas for computation: the potential flow zone, the boundary layer zone and the stern flow and wake zone (Figure 5.4(b)). Whilst much effort is being devoted to the enhancement of these Navier–Stokes computational codes to give accurate predictions for all ship forms, at present the most reliable practical and cost-effective procedure for determining the total wake field is by model tests in a towing tank.

The wake component due to wave action $\{w_w\}$ is due to the movement of water particles in the system of gravity waves set up by the ship on the surface of the water. Such conditions can also be induced by a vehicle operating just below the surface of water. Consequently, the wave wake field depends largely on Froude number, and is generally presumed to be of a small order. Harvald, in Reference 6, has undertaken experiments from which it would appear that the magnitudes of $\{w_w\}$ are generally less than about 0.02

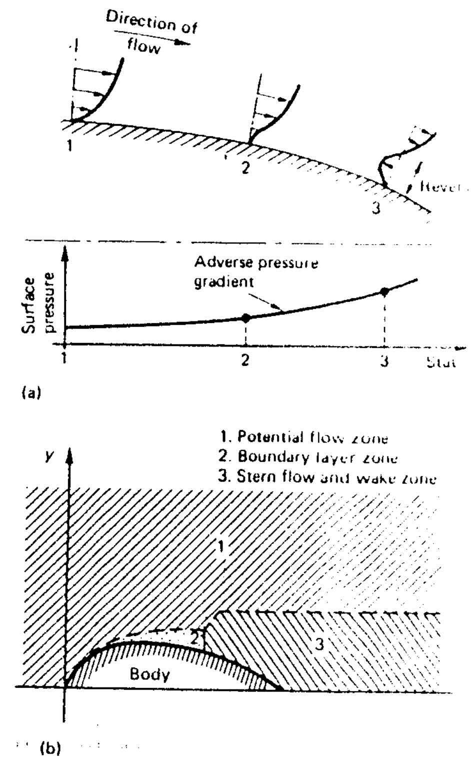

Figure 5.4 Flow boundary layer considerations (a) origin of separated flow; (b) typical flow computational zones

5.4 Estimation of wake field parameters

From the propeller design viewpoint the determination of the wake field in which the propeller operates is of fundamental importance. The mean wake field determines, along with other parameters of power, revolutions and ship speed, the overall design dimensions of the propeller, and the variability of the wake field about the mean wake influences the propeller blade section design and local pitch. Clearly, the most effective way of determining the detailed characteristics of the wake field is from model tests; this, however, is not without problems in the areas of wake scaling and propeller interaction. In the absence of model wake field data the designer must resort to other methods of prediction; these can be in the form of regression equations, the plotting of historical analysis data derived from model or full-scale trials, or from his own intuition and experience, which in the case of an experienced designer must never be underestimated. In the early stages of design the methods cited above are likely to be the ones used.

The determination of the mean wake has received much attention over the years. Harvald (Reference 6) discusses the merits of some two dozen methods developed in the period from 1896 through to the late 1940s for single-screw vessels. From this analysis he concluded that the most reliable, on the basis of calculated value versus value from model experiment, was due to Schoenherr (Reference 7):

$$\bar{w}_a = 0.10 + 4.5\frac{C_{pv}C_{ph}(B/L)}{(7 - C_{pv})(2.8 - 1.8C_{ph})} + \tfrac{1}{2}(E/T - D/B - k\eta)$$

where
- L = length of the ship
- B = breadth of the ship
- T = draught of the ship
- D = propeller diameter
- E = height of the propeller shaft above the keel
- C_{pv} = vertical prismatic coefficient of the vessel = $\nabla/A_w T$
- C_p = C_{ph} = horizontal prismatic coefficient of the vessel = $\nabla/A_x L$
- η = angle of rake of the propeller in radians
- k = coefficient (0.3 for normal sterns and 0.5–0.6 for sterns having the deadwood cut way.

In contrast, the more simple formula of Taylor (Reference 8) was also found to give acceptable values as a first approximation; this was

$$\bar{w}_a = 0.5C_b - 0.05$$

where C_b = block coefficient of the vessel.

The danger with using formulae of this type and vintage today is that hull form design has progressed to a considerable extent in the intervening years. Consequently, whilst they may be adequate for some simple hull forms their use should be undertaken with great caution and is, therefore, not to be recommended as a general design tool.

Amongst the more modern methods the method proposed by Harvald (Reference 9) and illustrated in Figure 5.5 is useful. This method approximates the mean axial wake fraction and thrust deduction by the following relationships:

$$\left.\begin{aligned}\bar{w}_a &= w_1 + w_2 + w_3\\ t &= t_1 + t_2 + t_3\end{aligned}\right\} \qquad (5.5)$$

where

t_1, w_1 is a function of B/L and block coefficient

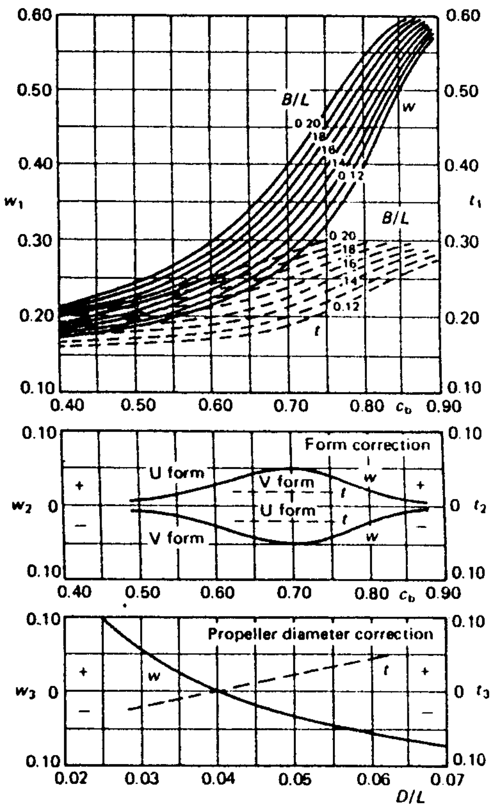

Figure 5.5 The wake and thrust deduction coefficient for single-screw ships. (Reproduced from Reference 9, with permission)

t_2, w_2 is a function of the hull forms
t_3, w_3 is a propeller diameter correction.

Alternatively, the later work by Holtrop and Manen and developed over a series of papers, resulted in the following regression formulae for single- and twin-screw vessels (Reference 10):

Single screw:

$$\bar{w}_a = C_9(1 + 0.015C_{stern})[(1 + k)C_F + C_A]\frac{L}{T_A} \times \left(0.050776 + 0.93405C_{11} \times \frac{[(1 + k)C_F + C_A]}{(1.315 - 1.45C_p + 0.0225\text{lcb})}\right) + 0.27915(1 + 0.015C_{stern}) \times \sqrt{\frac{B}{L(1.315 - 1.45C_p + 0.0225\text{lcb})}} + C_{19}(1 + 0.015C_{stern})$$

Twin screw:

$$\bar{w}_a = 0.3095C_b + 10C_b[(1 + k)C_F + C_A] - 0.23\frac{D}{\sqrt{BT}} \qquad (5.6)$$

where:

$$C_9 = C_8 \qquad (C_8 < 28)$$
$$= 32 - 16/(C_8 - 24) \qquad (C_8 > 28)$$

and

$$C_8 = BS/(LDT_A) \qquad (B/T_A < 5)$$
$$= S(7B/T_A - 25)/(LD(B/T_A - 3)) \qquad (B/T_A > 5)$$
$$C_{11} = T_A/D \qquad (T_A/D < 2)$$
$$= 0.0833333(T_A/D)^3 + 1.33333 \qquad (T_A/D > 2)$$
$$C_{19} = 0.12997/(0.95 - C_B) - 0.11056/(0.95 - C_p) \qquad (C_p < 0.7)$$
$$= 0.18567/(1.3571 - C_M) - 0.71276 + 0.38648C_p \qquad (C_p > 0.7)$$

and

Single-screw afterbody form	C_{stern}
Pram with gondola	−25
V-shaped sections	−10
Normal section shape	0
U-shaped sections with Hogner stern	10

These latter formulae were developed from the results of single- and twin-screw model tests over a comparatively wide range of hull forms. The limits of applicability are referred to in the papers and should be carefully studied before the use of the formulae.

In the absence of model tests the radial distribution of the mean wake field, that is the average wake value at each radial location, is difficult to assess. Traditionally this has been approximated by the use of van Lammeren's diagrams (Reference 11), which are reproduced in Figure 5.6. Van Lammeren's data is based on the single parameter of vertical prismatic coefficient, and is therefore unlikely to be truly representative for all but first approximations to the radial distribution of mean wake. Harvald (Reference 6) re-evaluated the data in which he corrected all the data to a common value of D/L of 0.004 and then arranged the data according to block coefficient and breadth-to-length ratio as shown in Figure 5.7 for single-screw models together with a correction for frame shape. In this study Harvald drew attention to the considerable scale effects that occurred between model and full scale. He extended his work to twin-screw vessels, shown in Figure 5.8, for a diameter-to-length ratio of 0.03, in which certain corrections were made to the model test data partly to correct for the boundary layer of the shaft supports. The twin-screw data shown in the diagram refers to the use of bossings to support the shaft lines rather than the modern practice of 'A' and 'P' brackets.

It must be emphasized that all of these methods for the estimation of the wake field and its various parameters are at best approximations to the real situation and not a substitute for properly conducted model tests.

5.5 Effective wake field

Propeller theories assume the flow field to be irrotational and unbounded; however, because the propeller normally operates behind the body which is being propelled these assumptions are rarely satisfied. When the propeller is operating behind a ship the flow field in which the propeller is operating at the stern of the ship is not simply the sum of the flow field in the absence of the propeller together with the propeller induced velocities calculated on the basis of the nominal wake. In practice a very complicated interaction takes place which gives rise to noticeable effects on propeller performance. Figure 5.9 shows the composition of the velocities that make up the total velocity at any point in the propeller disc. From the propeller design viewpoint it is the effective velocity field that should be input into propeller design and analysis procedures. The effective velocity field can be seen from the figure to be defined in one of two ways:

effective velocity = nominal velocity + interaction velocity

or

effective velocity = total velocity − propeller induced velocity (5.7)

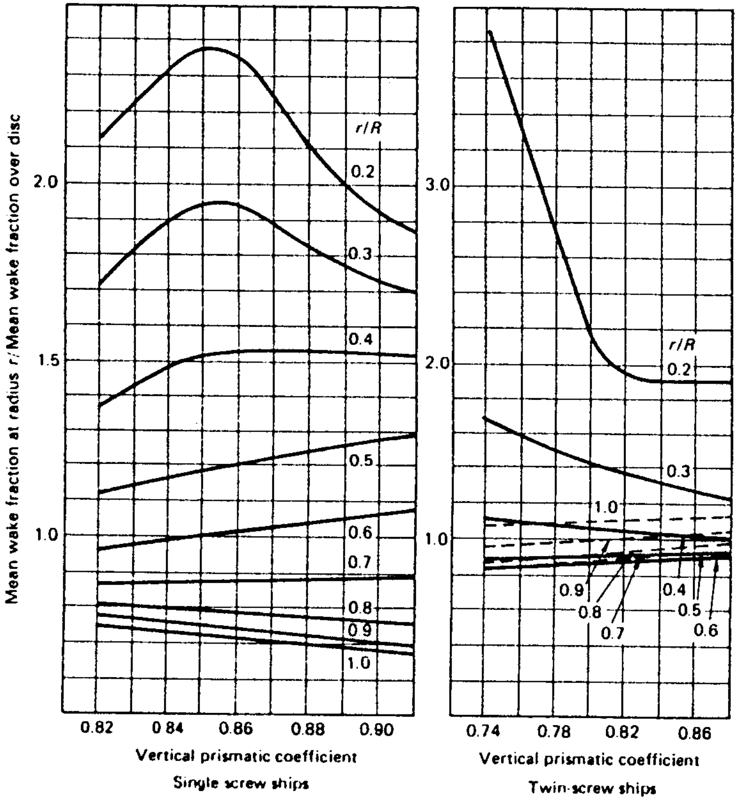

Figure 5.6 Van Lammeren's curves for determining the radial wake distribution (Reproduced from Reference 6, with permission)

If the latter of the two relationships is used, an iterative procedure can be employed to determine the effective wake field if the total velocity field is known from measurements just ahead of the propeller. Thè procedure used for this estimation is shown in Figure 5.10 and has been shown to converge. However, this procedure has the disadvantage of including within it all the shortcomings of the particular propeller theory used for the calculation of the induced velocities. As a consequence this may lead to an incorrect assessment of the interaction effects arising, for example, from the differences in the theoretical treatment of the trailing vortex system of the propeller.

An alternative procedure is to use the former of the two formulations of effective velocity defined in equations (5.7). This approach makes use of the nominal wake field measured in the towing tank, this being a considerably easier measurement than that of measuring the total velocity, since for the nominal velocity measurement the propeller is absent. Several appoaches to this problem have been proposed, including those known as the V-shaped segment and force field approaches. The V-shaped segment method finds its origins in the work of Huang and Groves (Reference 12), which was based on investigations of propeller–wake interaction for axisymmetric bodies. This approach is perhaps the simplest of all effective wake estimation procedures since it uses only the nominal wake field and principal propeller dimensions as input without undertaking detailed hydrodynamic computations. In the general case of a ship wake field, which contrasts with the axisymmetric basis upon which the method was first derived by being essentially non-uniform, the velocity field is divided into a number of V-shaped segments over which the general non-uniformity is replaced with an equivalent uniform

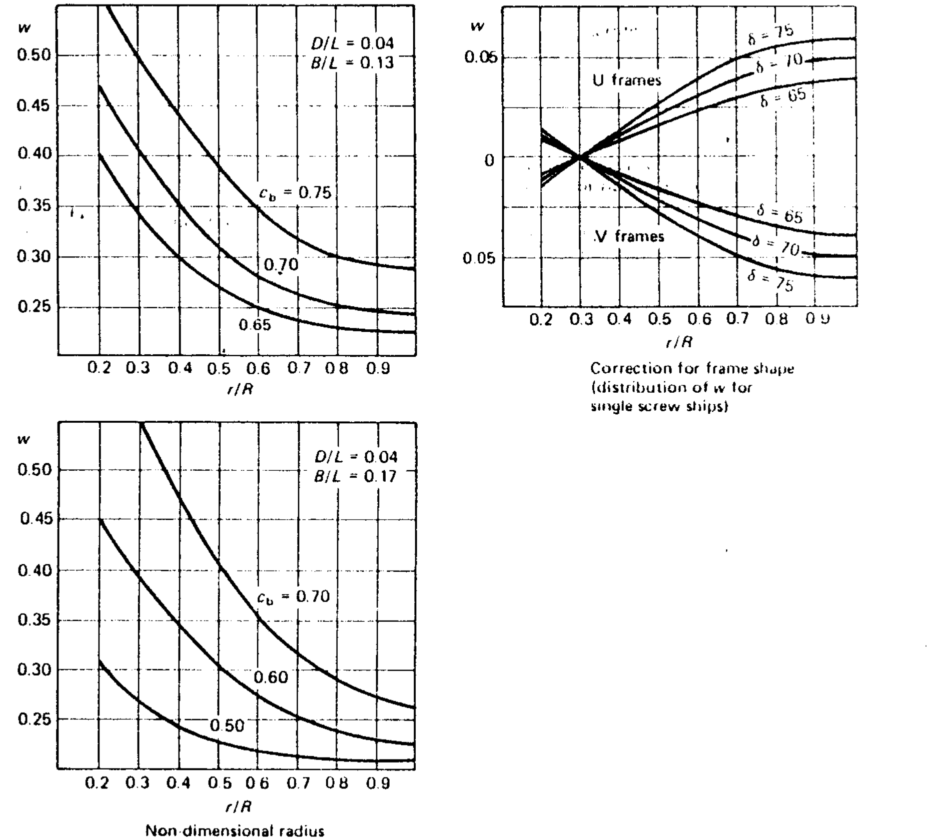

Figure 5.7 The radial variation of the wake coefficient of single screw ships ($D/L = 0.04$) (Reproduced from Reference 6 with permission)

flow. The basis of a V-shaped segment procedure is actuator disc theory, and the computations normally commence with an estimate of the average thrust loading coefficient based on a mean effective wake fraction; typically such an estimate comes from standard series open water data. From this estimate an iterative algorithm commences in which an induced velocity distribution is calculated, which then allows the associated effective velocities and their radial locations to be computed. Procedures of this type do not take into account any changes of flow structure caused by the operating propeller since they are based on the approximate interaction between a propeller and a thick stern boundary layer.

An alternative, and somewhat more complex, effective wake estimation procedure is the force-field method. Such approaches usually rely for input on the nominal wake field and the propeller thrust together with an estimate of the thrust deduction factor. These methods calculate the total velocity field by solving the Euler and continuity equations describing the flow in the vicinity of the propeller. The propeller action is modelled by an actuator disc having only an axial force component and a radial thrust distribution which is assumed constant circumferentially at each radial station. The induced velocities, which are identified within the Euler equations, can then, upon convergence, be subtracted from the total velocity estimates at each point of interest to give the effective wake distribution.

Clearly methods of effective wake field estimation such as the V-shaped segment, force-field and the (T–I) approaches are an essential part of the propeller design and analysis procedure. However, all of these

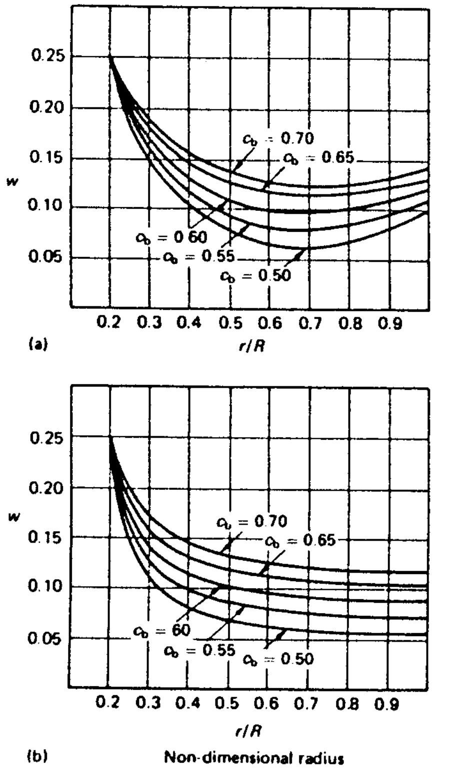

Figure 5.8 (a) The radial variation of the wake coefficient for models having twin screws ($D/L = 0.03$); (b) the radial variation of the wake coefficient for twin-screw ships ($D/L = 0.03$) (Reproduced from Reference 6, with permission)

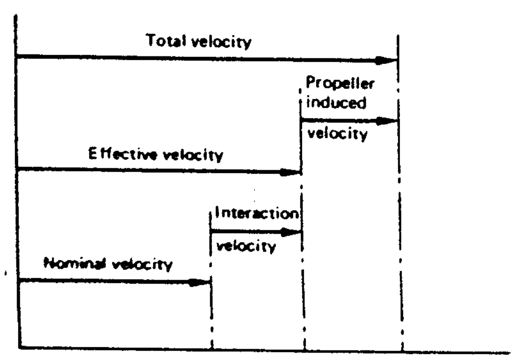

Figure 5.9 Composition of the wake field

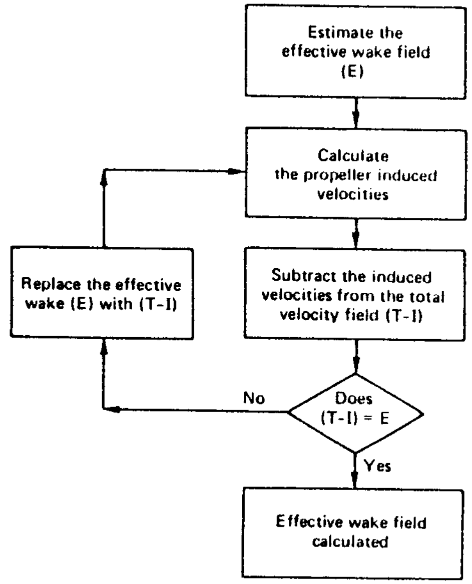

Figure 5.10 (T–I) approach to effective wake field estimation

methods lack the wider justification from being subjected to correlation, in open literature, between model and full-scale measurements. Indeed the number of vessels upon which appropriate wake field measurements have been undertaken is minimal for a variety of reasons; typically cost, availability and difficulty of measurement. The latter reason has at least been partially removed with the advent of laser-Doppler techniques which allow effective wake field measurement; nevertheless, this is still a complex procedure.

5.6 Wake field scaling

Since the model of the ship which is run in the towing tank is tested at Froude identity, that is equal Froude numbers between the ship and model, a disparity in Reynolds number exists which leads to a relative difference in the boundary layer thickness between the model and the full-scale ship; the model having the relatively thicker boundary layer. Consequently, for the purposes of propeller design it is necessary to scale, or contract as it is frequently termed, the wake measured on the model so that it becomes representative of that on the full-size vessel. Figure 5.11 illustrates the changes that can typically occur between the wake fields measured at model and full scale and with and without a propeller. The results shown in Figure 5.11

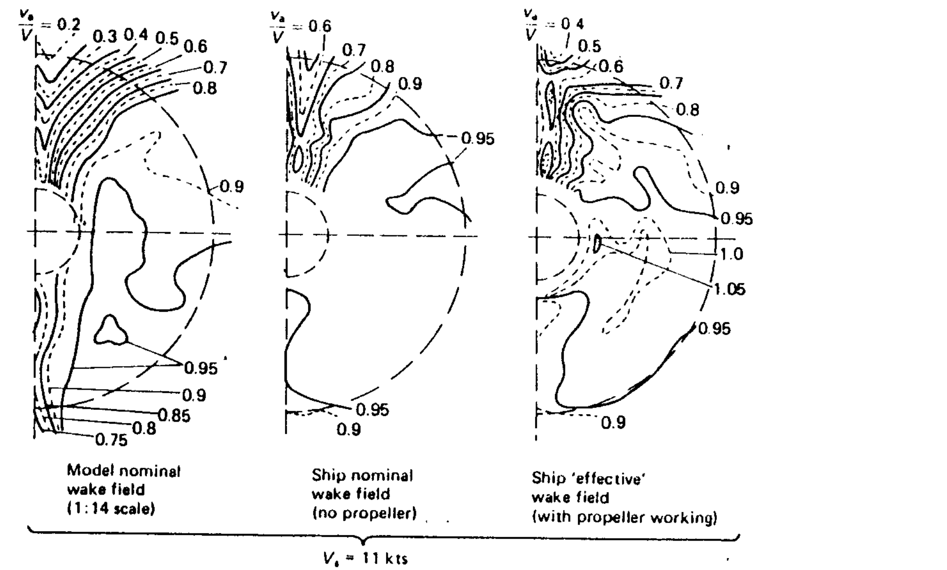

Figure 5.11 Comparison of model and full-scale wake fields—meteor trials (1967)

relate to trials conducted on the research vessel *Meteor* in 1967 and show respectively pitot measurements made with a 1/14th scale model; the full-scale vessel being towed without a propeller and measurements, again at full scale, made in the presence of the working propeller.

In order to contract nominal wake fields in order to estimate full-scale characteristics two principal methods have been proposed in the literature and are in comparatively wide use. The first method is due to Sasajima *et al.* (Reference 13) and is applicable to single-screw ships. In this method it is assumed that the displacement wake is purely potential in origin and as such is independent of scale effects, and the frictional wake varies linearly with the skin friction coefficient. Consequently, the total wake at a point is considered to comprise the sum of the frictional and potential components. The total contraction of the wake field is given by

$$c = \frac{C_{f_s} + \Delta C_{f_s}}{C_{f_m}}$$

where C_{f_s} and C_{f_m} are the ship and model ITTC 1957 friction coefficients expressed by

$$C_f = \frac{0.075}{(\log_{10} R_n - 2)^2}$$

and ΔC_{f_s} is the ship correlation allowance.

The contraction in Sasajima's method is applied with respect to the centre plane in the absence of any potential wake data, this being the normal case. However, for the general case the contraction procedure is shown in Figure 5.12 in which the ship frictional wake (w_{f_s}) is given by

$$w_{f_s} = w_{f_m}\frac{(1 - w_{p_s})}{(1 - w_{p_m})}$$

The method was originally intended for full form ships having block coefficients in the order of 0.8 and L/B values of around 5.7. Numerous attempts by a number of researchers have been made to generalize and improve the method. The basic idea behind Sasajima's method is to some extent based on the flat plate wake idealization; however, to account for the full range of ship forms encountered in practice, that is those with bulbous sterns, flat afterbodies above the propeller and so on, a more complete three-dimensional contraction process needs to be adopted. Hoekstra (Reference 14) developed such a procedure in the mid-1970s in which he introduced, in addition to the centre-plane contraction, a concentric contraction and a contraction to a horizontal plane above the propeller.

In this procedure the overall contraction factor (c) is the same as that used in the Sasajima approach. However, this total contraction is split into three component parts:

$$c = ic + jc + kc \qquad (i + j + |k| = 1)$$

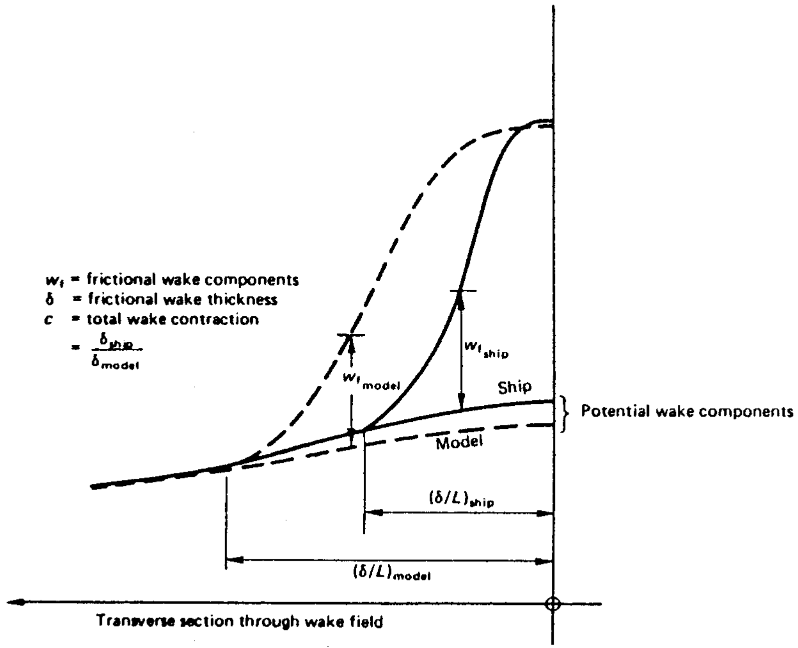

Figure 5.12 Basic of Sasajima wake scaling method

where i is the concentric contraction, j is the centre-plane contraction and k is the contraction to a horizontal surface above the propeller.

In Hoekstra's method the component contractions are determined from the harmonic content of the wake field; as such the method makes use of the first six Fourier coefficients of the circumferential wake field at each radius. The contraction factors are determined from the following relationships:

$$i = \frac{F_i}{|F_i| + |F_j| + |F_k|} \qquad j = \frac{F_j}{|F_i| + |F_j| + |F_k|}$$

$$\text{and} \quad k = \frac{F_k}{|F_i| + |F_j| + |F_k|}$$

in which

$$F_i = \int_{r_{hub}}^{2R} S_i(r)\,dr, \qquad F_j = \int_{r_{hub}}^{2R} S_j(r)\,dr$$

$$\text{and} \quad F_k = \int_{r_{hub}}^{2R} S_k(r)\,dr$$

with

$$S_i = 1 - A_0 + \begin{cases} A_2 + A_4 + A_6 - \frac{1}{2}S_k & \text{if } S_k \geqslant S_j \\ -S_j + (A_2 + A_4 + A_6) & \text{if } S_k < S_j \end{cases}$$

$$S_j = -[A_2 + A_4 + A_6 + |\max(A_2 \cos 2\phi + A_4 \cos 4\phi + A_6 \cos \phi|] \qquad (\phi \neq 0, \pi, 2\pi)$$

$$S_k = 2(A_1 + A_3 + A_5)$$

where A_n $(n = 0, 1, \ldots, 6)$ are the Fourier coefficients and at the hub S_i is taken as unity with $S_j = S_k = 0$.

The method as proposed by Hoekstra also makes an estimation of the scale effect on the wake peak velocity in the centre plane and for the scale effect on any bilge vortices that may be present. The method has been shown to give reasonable agreement in a limited number of cases of full scale to model correlation. However, there have been very few sets of trail results available upon which to base any firm conclusions of this or any other wake field scaling procedure.

Figure 5.13 essentially draws the discussions of effective wake and wake scaling together. In most design or analysis situations the engineer is in possession of the model nominal wake field and wishes to derive the ship or full-scale effective wake field

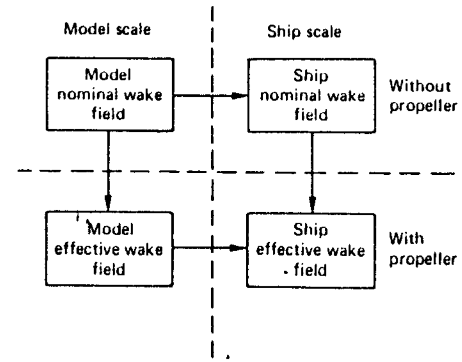

Figure 5.13 Relationship between model and ship wake field

characteristics. There are essentially two routes to achieve this. The most common is to scale the derived nominal wake field from model to full scale and then to derive the effective wake field at ship scale from the derived nominal full-scale wake.

5.7 Wake quality assessment

The assessment of wake quality is of considerable importance throughout the ship design process. Available methods generally divide themselves into two distinct categories: analytical methods and heuristic methods. Analytical methods generally use a combination of all the available wake field data (axial, tangential and radial components) to assess the flow quality, whereas heuristic methods normally confine themselves to the axial component only. Unfortunately the use of analytical methods such as those proposed by Truesdell (Reference 15), who introduced a vorticity measure, Mockros (Reference 16), who attempted to include the effects of turbulence into the vorticity measurement and Oswatitsch (Reference 17), who attempted a vorticity measure for perturbed unidirectional flows, tend to be limited by commercial wake measurement practices. As a consequence heuristic assessment procedures are the ones most commonly used at the present time.

Of the many methods proposed three have tended to become reasonably widely used as an assessment basis. In 1973 van Gunsteren and Pronk (Reference 18) proposed a method based on the diagrams shown in Figure 5.14 in which the basis of the criterion is the entrance speed cavitation number and the propeller design thrust loading coefficient C_T for various values of $\Delta J/J$, that is the ratio of the fluctuation in advance coefficient to the design advance coefficient. The value ΔJ is directly related to the variation in the wake field at $0.7R$, consequently, the diagram may be used as both a propeller design and wake quality assessment criteria. In using this diagram it must, however, be remembered that it only takes into account the broad parameters of propeller design and the wake field characteristics and, therefore, must be used in role commensurate with that caveat.

Huse (Reference 1) developed a set of criteria based on the characteristics of the axial velocity field. In particular his criteria address the very important area of the wake peak in the upper part of the propeller disc. His criteria are expressed as follows:

1. For large tankers and other ships with high block coefficients w_{max}, the maximum wake measured at the centre plane in the range of $0.4R$ to $1.15R$ above the shaft centre line, should preferably be less than 0.75:

$$w_{max} < 0.75$$

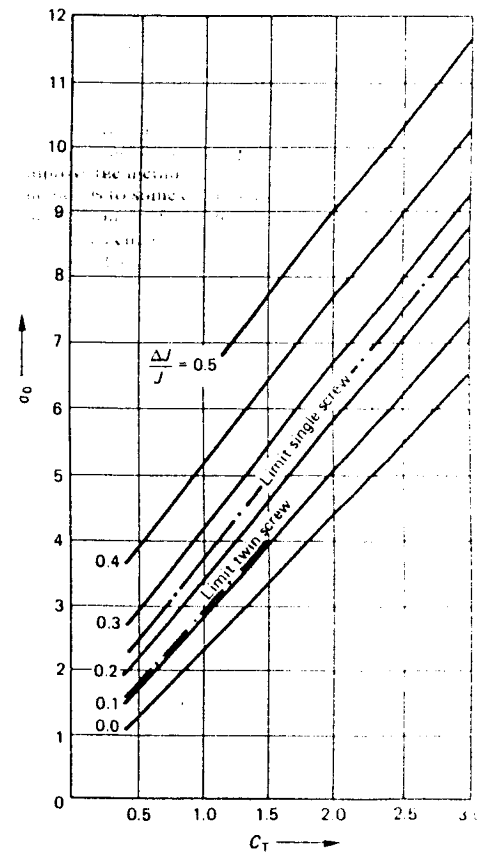

Figure 5.14 Van Gunsteren and Pronk assessment basis (Reproduced from Reference 18, with permission)

2. For fine ships (block coefficients below 0.60) the w_{max} value should preferably be below 0.55:

$$w_{max} < 0.55 \quad \text{for} \quad C_b < 0.60$$

3. The maximum acceptable wake peak should satisfy the following relationship with respect to the mean wake at $0.7R$, $\bar{w}_{0.7}$:

$$w_{max} < 1.7\bar{w}_{0.7}$$

4. The width of the wake peak should also be taken into account. If the width is slightly smaller than the distance between propeller blades, pressures on the hull due to cavitation will be maximum.

From the above it is clear that Huse's criteria addresses the quality of wake, largely in the absence of the propeller. In practice, however, it is the propeller–wake combination that gives rise to potential propulsion and vibration problems. Odabasi and Fitzsimmons (Reference 19) have extended Huse's work in an attempt to advance wake quality assessment in this area. The criteria proposed in this latter work are as follows:

1. The maximum wake measured inside the angular interval $\theta_B = 10 + 360/Z$ degrees and in the range $0.4R$ to $1.15R$ around the top dead centre position of the propeller disc should satisfy the following:

$$w_{max} < 0.75 \quad \text{or} \quad w_{max} < C_b$$

whichever is smaller.

2. The maximum acceptable wake peak should satisfy the following relationship with respect to the mean wake at $0.7R$:

$$w_{max} < 1.7\bar{w}_{0.7}$$

3. The width of the wake peak should not be less than θ_B. The definition of the wake peak for various wake distributions is shown diagrammatically in Figure 5.15.
4. The cavitation number for the propeller tip, defined as

$$\sigma_n = \frac{9.903 - D/2 - Z_p + T_A}{0.051(\pi n D)^2}$$

and the averaged non-dimensional wake gradient at a characteristic radius, defined as

$$[\Delta w/(1-\bar{w})]|_{x=1.0}$$

should lie above the dividing line of Figure 5.16. In these relationships,

D is the propeller diameter (m);
z_p is the distance betwen the propeller shaft axis and the base line (m);

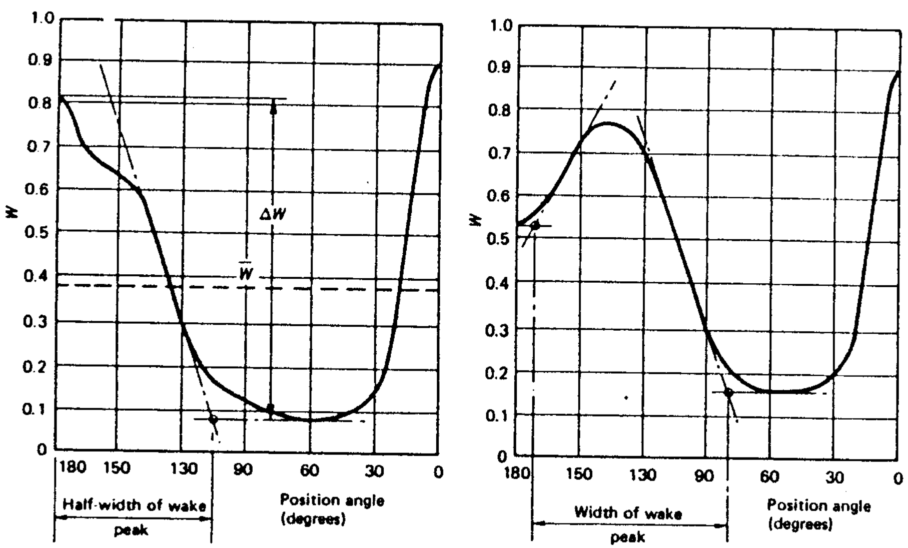

(a) (b)

Figure 5.15 Definition of the width of the wake peak: (a) single wake peak; (b) double wake peak (Reproduced from Reference 19, with permission)

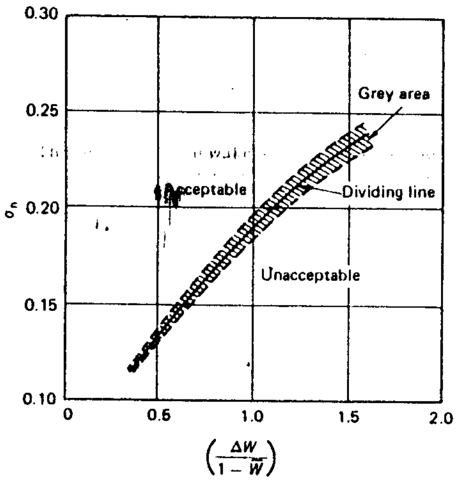

Figure 5.16 Wake non-uniformity criterion (Reproduced from Reference 19, with permission)

T_A is the ship's draught at the aft-perpendicular (m);
n is the propeller rotations speed (rev/s);
Δw is the wake variation defined in Figure 5.14.

5. For the propellers susceptible to cavitation, that is near the grey area of Figure 5.16, the local wake gradient per unit axial velocity for radii inside the angular interval θ_B in the range of $0.7R$ to $1.15R$ should be less than unity; that is,

$$\frac{1}{(r/R)}\left|\frac{(dw/d\theta)}{(1-w)}\right| < 1.0$$

where θ is in radians.

The underlying reasoning behind the formulation of these criteria has been the desire to avoid high vibratory hull surface pressures, and Figure 5.16 was developed in the basis of results obtained from existing ships.

5.8 Wake field measurement

Measurements of the wake field are required chiefly for the purposes of propeller design and for research where the various aspects of wake field scaling are being explored. Until comparatively recently methods of measurement have been intrusive; for example, pitot tubes, hot wire anemometry, tufts and so on. With these methods the influence on the flow field of locating the measurement apparatus in the flow has always been the subject of much debate. In recent years, however, the use of laser-Doppler techniques have become available for both model and full-scale studies and these require only that beams of laser light are passed into the fluid.

In the case of model scale measurements detailed measurements of the wake field have largely been accomplished by using pitot rakes, which have in some cases been placed on the shaft in place of the model propeller, Figure 5.17(a). In these cases the rakes have been rotated to different angular positions to define the wake field characteristics. Alternatively, some experimental facilities have favoured the use of a fixed pitot rake, Figure 5.17(b), in which the ends of the pitot rake are placed in the propeller plane. Such measurements provide quantitative data defining the nominal wake field and are based on the theory of pitot tubes which in turn is based on Bernoulli's equation. For a general point in any fluid flow the following relationship applies:

total head (h_t) = static head (h_s) + dynamic head (h_d)

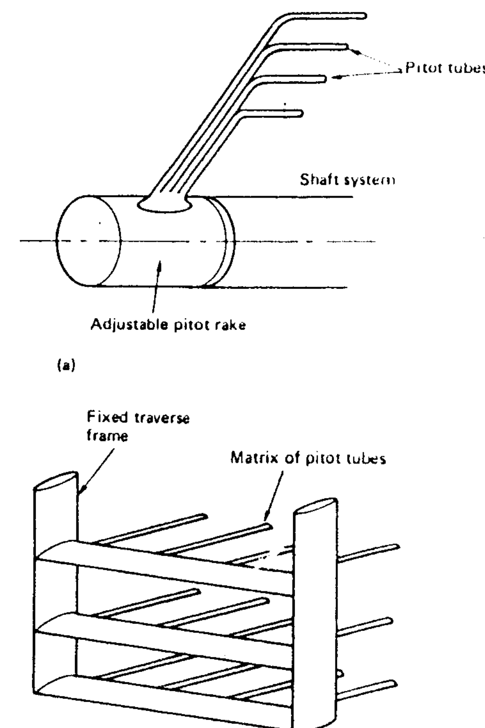

Figure 5.17 Types of wake field traversing methods using pitot, total and static head tubes: (a) rotating pitot rake located on shaft; (b) schematic fixed pitot rake

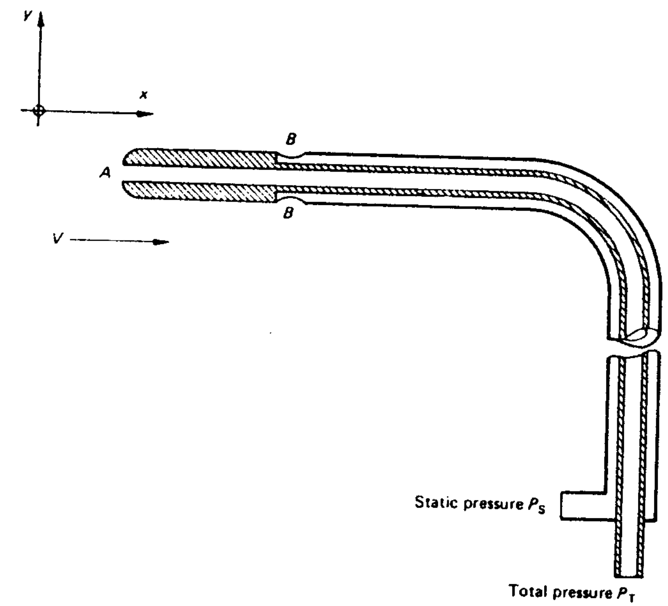

Figure 5.18 Pitot-static probe layout

The pitot-static tube shown in Figure 5.18 essentially comprises two tubes; a total head tube and a static head tube. The opening A measures the total head in the dirction Ox whilst the ports B, aligned in the Oy direction, measure the static head of the fluid. As a consequence from the above relationship, expressed in terms of the corresponding pressures, we have

$$p_d = p_T - p_s \qquad (5.8)$$

from which

$$v = \sqrt{\frac{2(p_T - p_s)}{\rho}} \qquad (5.9)$$

Depending on the type of flow problem that requires measurement, the probe is selected based on the information required and the physical space available. As such total head, static head or pitot static tubes may be used. Clearly the former two probes only measure one pressure component, whereas the latter measures both values simultaneously. Rakes comprising combinations of total head and static head tubes are sometimes constructed to enable complete measurement to be made, or alternatively, when space is very limited, total head and static head tubes can be inserted into the flow sequentially.

When directionality of the flow is important, since the foregoing tubes are all unidirectional, special measurement tubes can be used. These normally comprise either three- or five-hole total head tubes; an example of the latter is shown in Figure 5.19. From the figure it will be seen that the outer ring of tubes are chamfered and this allows the system to become directional, since opposite pairs of tubes measure different pressures and, from previous calibration, the differential pressures can be related to the angle of incidence of flow relative to the probe axis. References 20 and 21 should be consulted for further detailed discussion of flow measurement by total head and static head tubes, which is a specialist subject in itself.

In the case of full-scale ship wake field measurement the pitot tube principle has provided much of the data

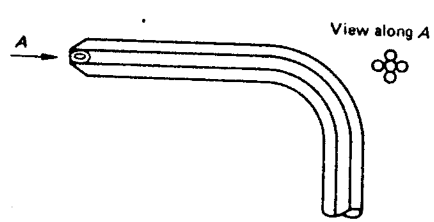

Figure 5.19 Typical five-hole total head tube

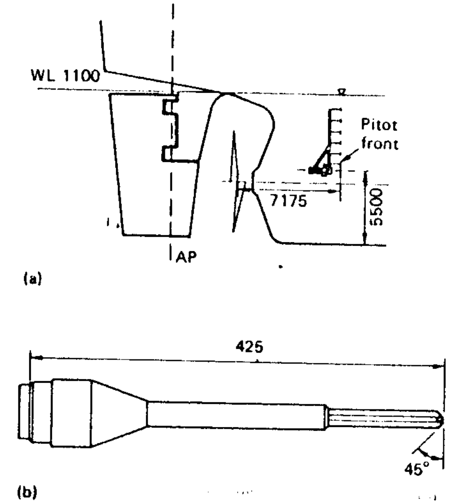

Figure 5.20 Full-scale wake pitot probe: (a) the mounting place of the test equipment; (b) example of one of the six, five hole pitot tubes (Reproduced from Reference 24, with permission)

that we have at our disposal at this time. Pitot rakes have either been placed on the shaft in place of the propeller, see for example Canham (Reference 22), to measure full-scale nominal wake or, alternatively, fitted to the hull just in front of the propeller to measure the inflow into the propeller (References 23 and 24); Figure 5.20 shows this type of layout together with the five-hole tube used in this latter case. Clearly in the former case of nominal wake measurement, the ship has to be towed by another vessel, whilst in the latter case it is self-propelled. The pitot rakes, whether they be shaft or hull mounted, are made adjustable in the angular sense so that they can provide as comprehensive a picture as possible of the wake field.

An alternative to the measurement of flow velocity by pitot tube is to use hot-wire or hot-film anemometry techniques. Such probes rely on the cooling effect of the fluid passing over either the heated wires or hot film to determine the flow velocities. In their most basic form the current passing through the wire is maintained constant and the flow velocity is determined by the voltage applied across the wire, since the wire resistance is dependent upon the temperature of the wire. A more complex, but widely used, mode of operation is to employ a feed-back circuit which maintains the wire at constant resistance and as a consequence at constant temperature: the current required to do this is a function of the fluid velocity. Hot-wire anemometers, like pitot tubes, require calibration.

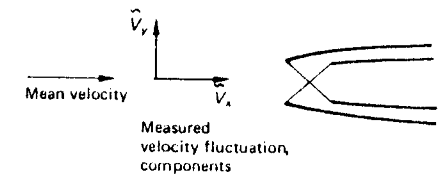

Figure 5.21 Hot 'X' wire anemometer

A typical hot-wire anemometer is shown in Figure 5.21, where two wires are arranged in an X configuration. If such an 'X' wire is located such that the mean velocity is in the plane of the 'X' wire it can be used to measure both components of velocity fluctuation in that plane. The more robust hot-film anemometer comprises a heated element of a thin metallic film placed on a wedge-shaped base which is both a thermal and electric insulator. When used in water, to which it is ideally suited due to its greater robustness, the hot film is covered with a thin layer of insulation to prevent electrical shorting problems.

In many ways the hot-film or -wire anemometer extends the range of fluid measurement scenarios into areas where pitot tubes tend to fail. In particular, since they are small and rapidly responding, they are ideal for measuring fluctuating flows; in particular the phenomena of transition and the structure of turbulent flows. In aerodynamic work hot-wire and film techniques have been used widely and very successfully for one-, two- and three-dimensional flow studies. Lomas (Reference 25) and Perry (Reference 26) discuss hot-wire anemometry in considerable detail whilst Scragg and Sandell (Reference 27) present an interesting comparison between hot-wire and pitot techniques. For full-scale wake field measurements no application of hot-film techniques is known to the author.

Laser-Doppler methods are advanced measurement techniques which can be applied to fluid velocity measurement problems at either model or full scale. The laser-Doppler anemometer measures flow velocity by measuring the Doppler shift of light scattered within the moving fluid, and hence it is a non-intrusive measurement technique. The light scatter is caused by the passage of tiny particles suspended in the fluid, typically dust or fine sand grains, such that they effectively trace the streamline paths of the fluid flow. In general there are usually sufficient particles within the fluid and in many instances, at full scale, problems of over-seeding can occur.

The operating principle of a laser-Doppler system is essentially described in Figure 5.22. In the case of a single laser beam, Figure 5.22(a), the Doppler shift is dependent upon the velocity of the object and the relative angles between the incident and scattered light. If f_i and f_s are the frequencies of the incident and scattered beams, then the Doppler shift is given by $(f_s - f_i)$:

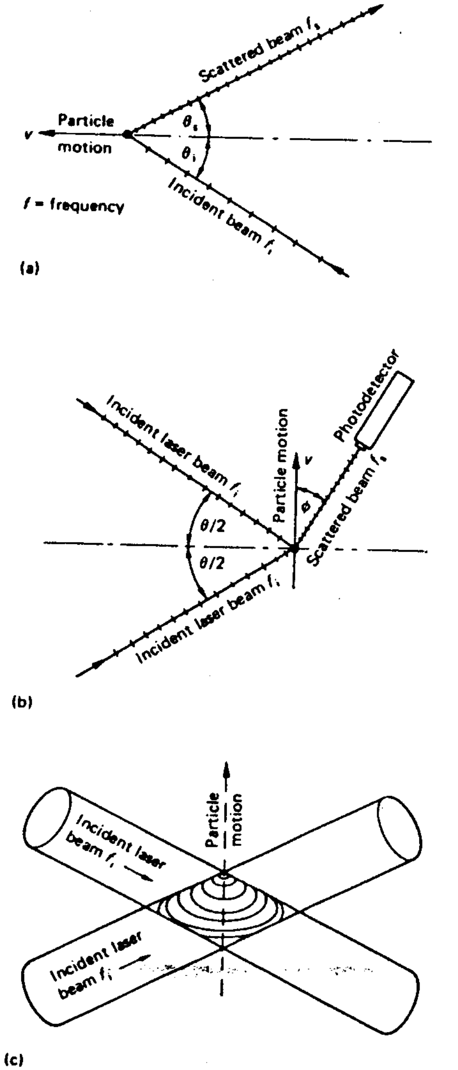

Figure 5.22 Laser-Doppler principle: (a) Doppler shift of a single incident laser beam; (b) intersecting laser beam arrangement; (c) fringe pattern from two intersecting laser beams

$$f_s - f_i = \frac{V}{\lambda}[\cos\theta_i + \cos\theta_s]$$

where λ is the wavelength of the laser.

This expression can be made independent of the position of the receiver, that is the angle θ_s, by using two laser beams of the same frequency as shown in Figure 5.22(b). This configuration leads to differential Doppler shift seen by the receiver, at some angle ϕ, as follows:

$$\text{differential Doppler shift} = \frac{2V}{\lambda}\sin\left(\frac{\theta}{2}\right) \qquad (5.10)$$

The use, as in this case, of two intersection laser beams of the same frequency leads to the introduction of beam splitting optical arrangements obtaining light from a single laser.

Equation (5.10) can be considered in the context of the physically equivalent model of the interference fringes that are formed when two laser beams intersect. If the two beams, Figure 5.22(c) are of equal intensity and wavelength, the fringe pattern will appear as a series of flat elliptical discs of light separated by regions of darkness. If a particle moves through these fringes it will scatter light each time it passes through a light band at a frequency proportional to its speed. Since the separation of the fringes d is given by the expression $\lambda/(2\sin\theta/2)$ and if the particle moves with a velocity V, it will move from one interference band to another with a frequency

$$f = \frac{2V\sin(\theta/2)}{\lambda}$$

The scattered light will, therefore, be modulated at this frequency, which is the same as the differential Doppler frequency above. Since the angle θ and the wavelength λ can be precisely defined, a measurement of the modulation frequency gives a direct measure of the velocity of the particle crossing through the intersection of the laser beams.

In terms of practical measurement capabilities several modes of operation exist. These, however, chiefly divide themselves into forward and back scatter techniques. Forward scatter methods essentially place the laser and photodetector on opposite sides of the measurement point, whilst in the back scatter mode both the laser and photodetector are on the same side. For discussion purposes four methods are of interest in order to illustrate the basic principles of the measurement procedure; these are:

1. reference beam method;
2. differential Doppler – forward scatter;
3. differential Doppler – backward scatter;
4. multi-colour differential Doppler.

In the case of the reference beam method (Figure 5.23(a)), the photodetector is mounted coaxially with the reference laser beam in order to measure the

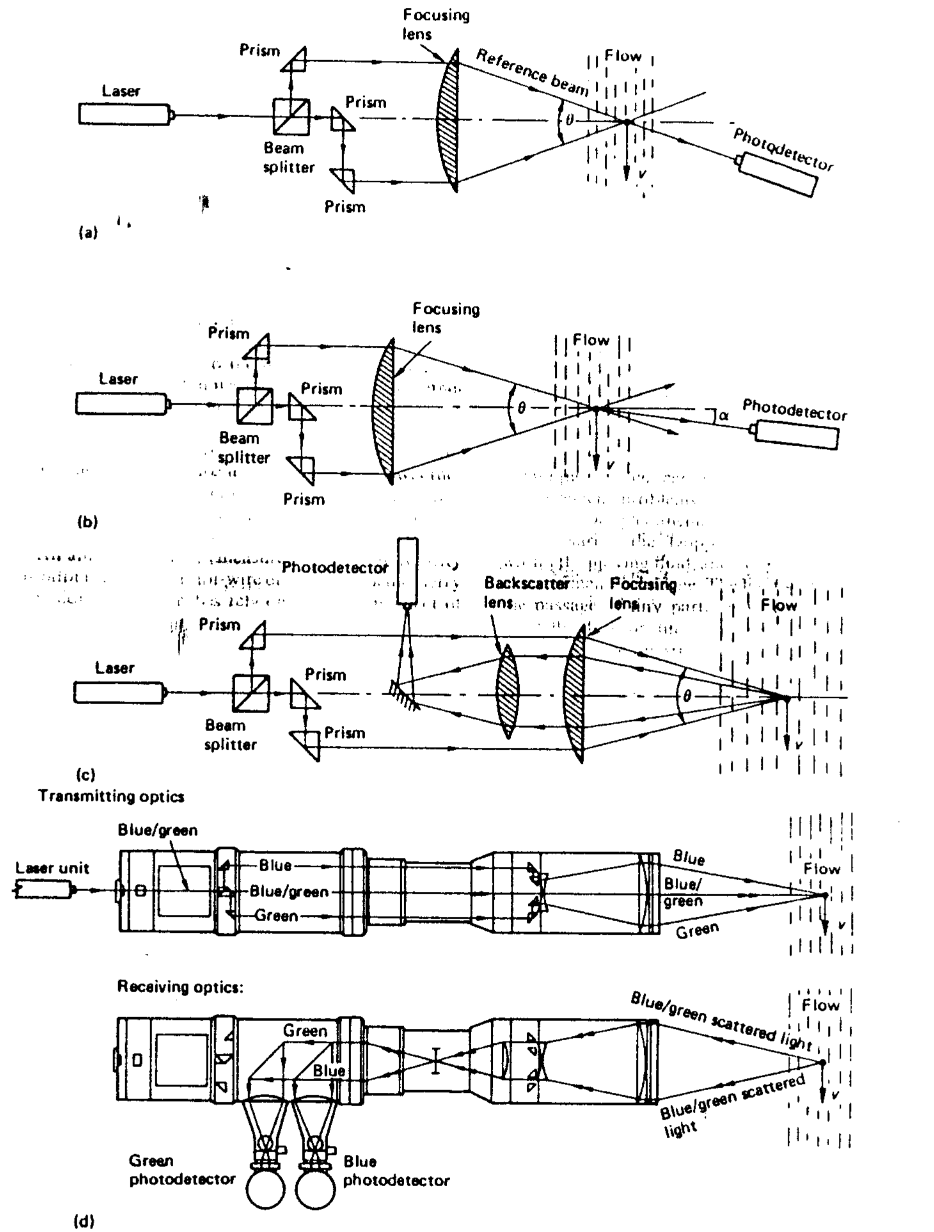

Figure 5.23 Laser-Doppler modes of operation: (a) reference beam method; (b) differential Doppler—forward scatter; (c) differential Doppler—back scatter; (d) multi-colour differential Doppler mode

velocity within the fluid normal to the optical axis of the instrument. In order to optimize the Doppler signal quality an adjustable neutral density filter is normally used to reduce the intensity of the reference beam.

The differential Doppler, forward scatter mode of measurement employs two laser beams of equal intensity which are focused at a point of interest in the fluid (Figure 5.23(b)). The scattered light can then be picked up by the photodetector, which is inclined at a suitable angle α to the optical axis of the instrument: the angle α is not critical, since the detected Doppler frequency is independent of the direction of detection. This method is often employed when the intensity of the scattered light is low. Furthermore, the method has obvious advantages over the preceding one since the photodetector does not have to be located on the reference beam.

The backward scatter differential Doppler mode (Figure 5.23(c)) permits the laser optics and the measurement optics to lie on the same side of the flow measurement point – an essential feature if full-scale ship wake measurements are contemplated. The disadvantage of this type of system is that the intensity of the back-scattered light is usually much lower than that of the forward scattered light. This normally requires either a higher concentration of scattering particles or a higher laser power to be used to overcome this problem.

The three foregoing systems only measure velocities in one component direction. To extend this into two or more velocity components a multi-colour system must be used. Figure 5.23(d) outlines a two-colour back-scatter differential Doppler mode. In such a system the transmitting optics splits a dual-colour laser beam into converging single-colour beams with a combined dual-colour central beam; that is, three beams in total. The beams are then focused at the point where the measurement is required and the scattered light is returned through the receiving optics, mounted coaxially with the transmitting optics, and then diverted to photodetectors – one for each colour light. The two views shown in Figure 5.23(d) are in reality a single unit containing both sets of optics. The ability of such systems to detect two velocity components can be visualized from Figure 5.24, in which the two pairs of fringe patterns are made to intersect in orthogonal planes and give a resultant fringe pattern of the type shown in the measurement volume. In this way the particles passing through this measurement volume will scatter light from both orthogonal fringe patterns.

For shipboard measurements a laser system of considerable power is required, and this requires both a carefully designed mounting system to avoid vibration problems and the provision of adequate cooling arrangements. At model scale less powerful systems are required and these can be of the forward scatter type since the limitation of approaching the measurement from one side of the flow does not normally apply. Reference 28 provides a very good introduction to the subject of laser Doppler anemometry.

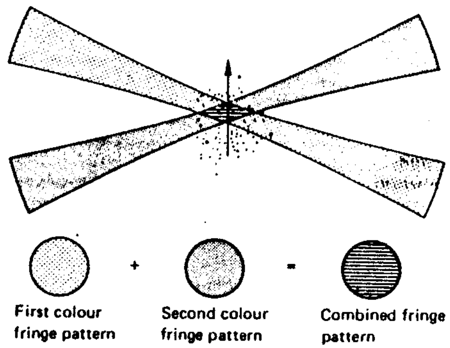

Figure 5.24 Two-colour fringe model (Courtesy: DANTEC Electronics Ltd)

References and further reading

1. Huse, E. Effect of Afterbody Forms and Afterbody Fins on the Wake Distribution of Single Screw Ships. NSFI Report R31-74, 1974.
2. Carlton, J.S., Bantham, I. Full scale experience relating to the propeller and its environment. *Propellers 78 Symposium, Trans. SNAME*, 1978.
3. Prohaski, C.W., Lammeren, W.P.A. van. *Mitstrommessung on Schiffsmodellen*, Heft 16, S.257, Schiffban 1937.
4. Lammeren, W.P.A. van. 'Analysis der voortstuwingscomponenten in verband met het schaleffect bij scheepsmodelproven', blz.58, 1938.
5. Harvald, Sv.Aa. Potential and frictional wake of ships. *Trans. RINA*, 1972.
6. Harvald, Sv.Aa. *Wake of Merchant Ships*. Danish Technical Press, 1950.
7. Schoenherr, K.E. Propulsion and propellers. *Principles of Naval Architecture*, Vol. 2, p. 149, 1939.
8. Taylor, D.W. *Speed and Power of Ships*, 1933.
9. Harvald, Sv.Aa. *Estimation of Power of Ships*, ISP, 1977.
10. Holtrop, J. A statistical re-analysis of resistance and propulsion data. ISP, 31, November 1988.
11. Lammeren, W.P.A. van, Troost, L., Koning, J.G. *Weerstand en Voortsluwing van Schepen*, 1942.
12. Huang, T.T., Groves, N.C. Effective wake: theory and experiment. *13th ONR Symposium*, 1980.
13. Sasajima, H., Tanaka, I., Suzuki, T. Wake distribution of full ships. *J. Soc. Nav. Arch.*, Japan, **120**, 1966.
14. Hoekstra, M. Prediction of full scale wake characteristics based on model wake survey. *Int. Shipbuilding*, Prog. No. 250, June 1975.
15. Truesdell, C. Two measures of vorticity. *Rational Mech. Anal.* **2**, 1953.
16. Mockros, F.L. The Significance of Vorticity, Vortex Motion and Dissipation in Turbulent Fluid Flows. Dissertation, Univ. of California, Berkeley, 1962.
17. Oswatitsch, K. Über Wirbelkennzahlen und Wirbelmusse. *Z. angew. Math. Phys.*, **20**, 1969.
18. Gunsteren, L.A. van, Pronk, C. Propeller design concepts. *Int. Shipbuilding Prog.*, **20**(227), 1973.
19. Odabasi, A.Y., Fitzsimmons, P.A. Alternative methods for wake quality assessment. *Int. Shipbuilding Prog.*, **25**(282), February 1978.
20. Pankhurst, R.C., Holder, D.W. *Wind Tunnel Technique*, Pitman, London, 1952.
21. Piercy, N.A. *Aerodynamics*, English Universities Press, London, 1937.
22. Canham, H.J.S. Resistance, propulsion and wake tests with HMS Penelope, *Trans. RINA*, Spring Meeting, 1974.
23. Naminatsu, M., Muraoka, K. Wake distribution measurements an actual tanker and its large scale model, *Proc.1 14th ITTC*.
24. Fagerjord, O. *Experience from Stern Wake Measurements during Sea Trial*, Norwegian Maritime Research, No. 2, 1978.
25. Lomas, C.G. *Fundamentals of Hot-wire Anemometry*. Cambridge University Press, Cambridge, 1986.
26. Perry, A.E. *Hot Wire Anemometry*. Clarendon Press, Oxford, 1982.
27. Scragg, C.A., Sandell, D.A. A statistical evaluation of wake survey techniques. *Int. Symp. on Ship Viscous Resistance*, SSPA, Göteborg, 1978.
28. Durst, F., Melling, A., Whitelaw, J.H. *Principles and Practice of Laser-Doppler Anemometry*. Academic Press, 1976.

6

Propeller performance characteristics

Contents

For discussion purposes the performance characteristics of a propeller can conveniently be divided into open water and behind hull properties. In the case of open water characteristics, these relate to the description of the forces and moments acting on the propeller when operating in a uniform fluid stream; hence the open water characteristics, with the exception of inclined flow problems, are steady loadings by definition. The behind hull characteristics are those generated by the propeller when operating in a mixed wake field behind a body. Clearly these latter characteristics have both a steady and unsteady component by the very nature of the environment in which the propeller operates. In this chapter both types of characteristics will be treated separately: the discussion will initially centre on the open water characteristics since these essentially form the basic performance parameters about which the behind hull characteristics are generated when the propeller is working behind a body.

6.1 General open water characteristics

The forces and moments produced by the propeller are expressed in their most fundamental form in terms of a series of non-dimensional characteristics: these are completely general for a specific geometric configuration. The non-dimensional terms used to express the general performance characteristics are as follows:

$$
\begin{aligned}
&\text{thrust coefficient} && K_T = \frac{T}{\rho n^2 D^4} \\
&\text{torque coefficient} && K_Q = \frac{Q}{\rho n^2 D^5} \\
&\text{advance coeffficient} && J = \frac{V_a}{nD} \\
&\text{cavitation number} && \sigma = \frac{p_0 - e}{\frac{1}{2}\rho V^2}
\end{aligned}
\qquad (6.1)
$$

where in the definition of cavitation number, V is a representative velocity which can either be based on free stream advance velocity or propeller rotational speed. Whilst for generalized open water studies the former is more likely to be encountered there are exceptions when this is not the case, notably at the bollard pull condition when $V_a = 0$ and hence $\sigma_0 \to \infty$. Consequently, care should be exercised when using design charts or propeller characteristics for analysis purposes.

To establish the non-dimensional groups involved in the above expressions (equations (6.1)), the principle of dimensional similarity can be applied to geometrically similar propellers. The thrust of a marine propeller when working sufficiently far away from the free surface so as not to cause surface waves may be expected to depend upon the following parameters:

(a) the diameter (D);
(b) the speed of advance (V_a);
(c) the rotational speed (n);
(d) the density of the fluid (ρ);
(e) the viscosity of the fluid (μ);
(f) the static pressure of the fluid at the propeller station ($p_0 - e$).

Hence the thrust (T) can be assumed to be proportional to ρ, D, V_a, n, η and $(p_0 - e)$:

$$T \propto \rho^a D^b V_a^c n^d \eta^f (p_0 - e)^g$$

Since the above equation must be dimensionally correct it follows that

$$\mathrm{MLT^{-2}} = (\mathrm{ML^{-3}})^a \mathrm{L}^b (\mathrm{LT^{-1}})^c (\mathrm{T^{-1}})^d \times (\mathrm{ML^{-1}T^{-1}})^f (\mathrm{ML^{-1}T^{-2}})^g$$

and by equating indices for M, L and T we have

$$
\begin{aligned}
&\text{For mass M:} & 1 &= a + f + g \\
&\text{For length L:} & 1 &= -3a + b + c - f - g \\
&\text{For time T:} & -2 &= -c - d - f - 2g
\end{aligned}
$$

from which it can be shown that

$$
\begin{aligned}
a &= 1 - f - g \\
b &= 4 - c - 2f - g \\
d &= 2 - c - f - 2g
\end{aligned}
$$

Hence from the above we have

$$T \propto \rho^{(1-f-g)} D^{(4-c-2f-g)} V_a^c n^{(2-c-f-2g)} \eta^f (p_0 - e)^g$$

from which

$$T = \rho n^2 D^4 \left(\frac{V_a}{nD}\right)^c \cdot \left(\frac{\eta}{\rho n D^2}\right)^f \cdot \left(\frac{p_0 - e}{\rho n^2 D^2}\right)^g$$

These non-dimensional groups are known by the following:

$$
\begin{aligned}
&\text{Thrust coefficient} && K_T = \frac{T}{\rho n^2 D^4} \\
&\text{Advance coefficient} && J = \frac{V_a}{nD} \\
&\text{Reynolds number} && R_n = \frac{\rho n D^2}{\eta} \\
&\text{Cavitation number} && \sigma_0 = \frac{p_0 - e}{\frac{1}{2}\rho n^2 D^2}
\end{aligned}
$$

$$\therefore \; K_T \propto \{J, R_n, \sigma_0\}$$

that is

$$K_T = f(J, R_n, \sigma_0) \qquad (6.2)$$

The derivation for propeller torque K_Q is an analogous problem to that of the thrust coefficient just discussed. The same dependencies in this case can be considered to apply, and hence the torque (Q) of the propeller can be considered by writing it as a function of the following terms:

$$Q = \rho^a D^b V_a^c n^d \eta^f (p_0 - e)^g$$

and hence by equating indices we arrive at

$$Q = \rho n^2 D^5 \left(\frac{V_a}{nD}\right)^c \left(\frac{\eta}{\rho n D^2}\right)^f \cdot \left(\frac{p_0 - e}{\rho n^2 D^2}\right)^e$$

which reduces to

$$K_Q = g(J, R_n, \sigma_0) \qquad (6.3)$$

where the torque coefficient

$$K_Q = \frac{Q}{\rho n^2 D^5}$$

With the form of the analysis chosen the cavitation number and Reynold's number have been non-dimensionalized by the rotational speed. These numbers could equally well be based on advance velocity, so that

$$\sigma_0 = \frac{p_0 - e}{\frac{1}{2}\rho V^2} \quad \text{and} \quad R_n = \frac{\rho V D}{\eta}$$

Furthermore, by selecting different groupings of indices in the dimensional analysis it would be possible to arrive at an alternative form for the thrust loading:

$$T = \rho V_a^2 D^2 \phi(J, R_n, \sigma_0)$$

which gives rise to the alternative form of thrust coefficient C_T defined as

$$C_T = \frac{T}{\frac{1}{2}\rho V_a^2 (\pi D^2/4)} = \frac{8T}{\pi \rho V_a^2 D^2}$$

$$C_T = \Phi(J, R_n, \sigma_0) \qquad (6.4)$$

Similarly it can be shown that the power coefficient C_P can also be given by

$$C_P = \phi(J, R_n, \sigma_0) \qquad (6.5)$$

In cases where the propeller is sufficiently close to the surface, so as to disturb the free surface or to draw air, other dimensionless groups will apply. These will principally be the Froude and Weber numbers, and these can readily be shown to apply by introducing gravity and surface tension into the foregoing dimensional analysis equations for thrust and torque.

A typical open water diagram for a set of fixed pitch propeller working in a non-cavitating environment at forward, or positive, advance coefficient is shown in Figure 6.1. This figure defines, for the particular propeller, the complete set of operating conditions at positive advance and rotational speed, since the propeller under steady conditions can only operate along the characteristic line defined by its pitch ratio P/D. The diagram is general in the sense that, subject to scale effects, it is applicable to any propeller having the same geometric form as the one for which the characteristic curves were derived, but the subject

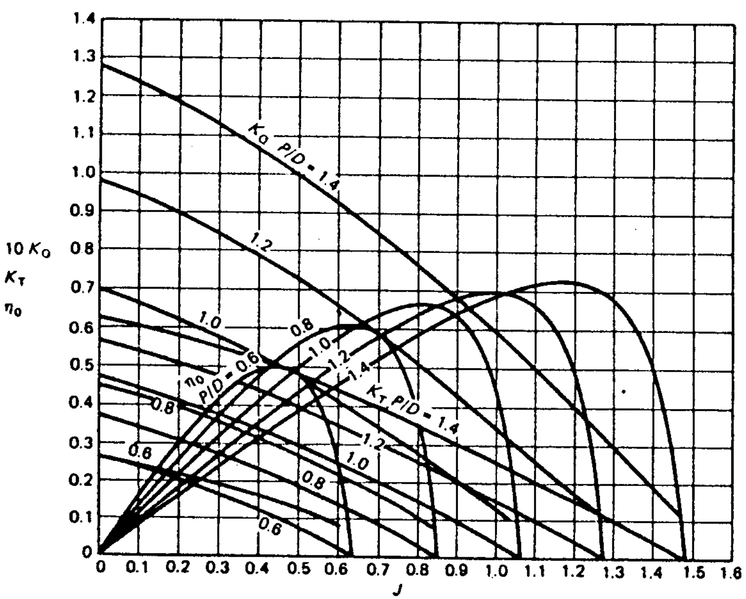

Figure 6.1 Open water diagram for Wageningen B5-75 screw series (Courtesy MARIN)

propeller may have a different diameter or scale ratio and can work in any other fluid, subject to certain Reynolds number effects. When, however, the K_T, K_Q versus J diagram is used for a particular propeller of a given geometric size and working in a particular fluid medium, the diagram, since the density of the fluid and the diameter then become constants, effectively reduces from general definitions of K_T, K_Q and J to a particular set of relationships defining torque, thrust, revolutions and speed of advance as follows:

$$\left\{\frac{Q}{n^2}, \frac{T}{n^2}\right\} v \left(\frac{V_a}{n}\right)$$

The alternative form of the thrust and torque coefficient which stems from equations (6.4) and (6.5), and which is based on the advance velocity rather than the rotational speed, is defined as follows:

$$C_T = \frac{T}{\frac{1}{2}\rho A_0 V_a^2}$$

$$C_P = \frac{P_D}{\frac{1}{2}\rho A_0 V_a^3} \qquad (6.6)$$

From equation (6.6) it can be readily deduced that these thrust loading and power loading coefficients can be expressed in terms of the conventional thrust and torque coefficient as follows:

$$C_T = \frac{8}{\pi}\frac{K_T}{J^2}$$

and

$$C_P = \frac{8}{\pi}\frac{K_Q}{J^3} \qquad (6.7)$$

The open water efficiency of a propeller (η_o) is defined as the ratio of the thrust horsepower to delivered horsepower:

$$\eta_o = \frac{\text{THP}}{\text{DHP}}$$

Now since THP $= TV_a$
and DHP $= 2\pi n Q$

where T is the propeller thrust, V_a, the speed of advance, n the rotational speed of the propeller and Q the torque. Consequently, we may write

$$\eta_o = \frac{TV_a}{2\pi n Q}$$

i.e.

$$\eta_o = \frac{K_T}{K_Q} \cdot \frac{J}{2\pi} \qquad (6.8)$$

The K_Q, K_T versus J characteristic curves contain all of the information necessary to define the propeller performance at a particular operating condition. Indeed, the curves can be used for design purposes for a particular basic geometry when the model characteristics are known for a series of pitch ratios. This, however, is a cumbersome process and to overcome these problems Admiral Taylor derived a set of design coefficients termed B_p and δ; these coefficients, unlike the K_T, K_Q and J characteristics, are dimensional parameters and so considerable care needs to be exercised in their use. The terms B_p and δ are defined as follows:

$$B_p = \frac{(\text{DHP})^{1/2} N}{V_a^{2.5}}$$

$$\delta = \frac{ND}{V_a} \qquad (6.9)$$

where DHP = the delivered horsepower in British or metric units depending on the data used;
N = the propeller RPM;
V_a = the speed of advance (knots);
D = the propeller diameter (ft).

From Figure 6.2, which shows a typical propeller design diagram, it can be seen that it essentially comprises a plotting of B_p, as abscissa, against pitch ratio as ordinate with lines of constant δ and open water efficiency superimposed. This diagram is the basis of many design procedures for marine propellers, since the term B_p is usually known from the engine and ship characteristics. From the Figure a line of optimum propeller open water efficiency can be seen as being the locus of the points on the diagram which have the highest efficiency for a given value of B_p. Consequently, it is possible with this diagram to select values of δ and P/D to maximize the open water efficiency η_o for a given powering condition as defined by the B_p parameter. Hence a basic propeller geometry can be derived in terms of diameter D, since $D = \delta V_a/N$, and P/D. Additionally this diagram can be used for a variety of other design purposes, such as, for example, RPM selection; however, these aspects of the design process will be discussed later in Chapter 21.

It will be seen that the B_p versus δ diagram is limited to the representation of forward speeds of advance only, that is, where $V_a > 0$, since $B_p \to \infty$ when $V_a = 0$. This limitation is of particular importance when considering the design of tugs and other similar craft, which can be expected to spend an important part of their service duty at zero ship speed, termed bollard pull, whilst at the same time developing full power. To overcome this problem, a different sort of design diagram was developed from the fundamental K_T, K_Q versus J characteristics, so that design and analysis problems at or close to zero speed of advance can be considered. This diagram is termed the $\mu - \sigma$ diagram, and a typical example of one is shown in Figure 6.3. In this diagram the following relationships apply:

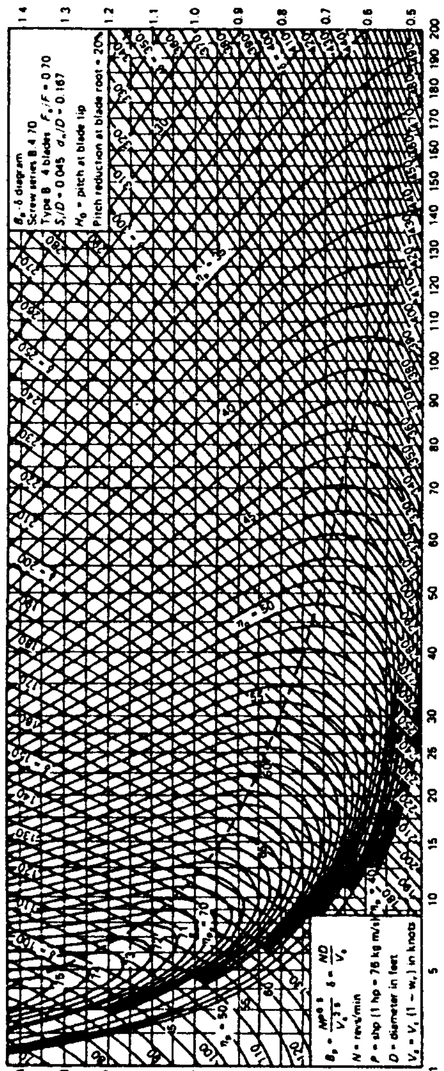

Figure 6.2 Original B4·70 B_p–δ diagram (Courtesy: MARIN)

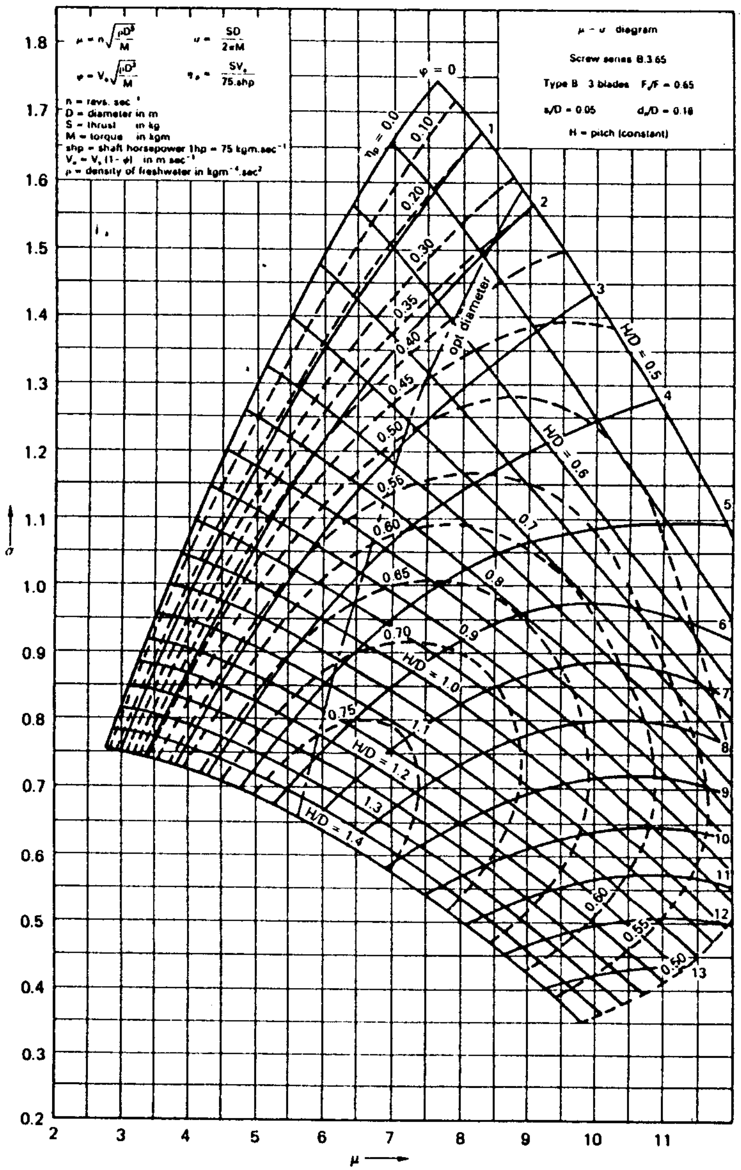

Figure 6.3 Original B3.65 μ–σ diagram (Courtesy: MARIN)

$$\mu = n\sqrt{\frac{\rho D^5}{Q}}$$

$$\phi = V_a\sqrt{\frac{\rho D^3}{Q}} \qquad (6.10)$$

$$\sigma = \frac{TD}{2\pi Q}$$

where D = propeller diameter (m);
Q = delivered torque (kgf m);
ρ = mass density of water (kg m^{-4} s^2);
T = propeller thrust (kgf);
n = propeller rotational speed (rev/s);
V_a = ship speed of advance (m/s).

Diagrams of the type shown in Figure 6.3 are non-dimensional in the same sense as those of the fundamental K_T, K_Q characteristics and it will be seen that the problem of zero ship speed, that is when $V_a = 0$, has been removed, since the function $\phi \to 0$ as $V_a \to 0$. Consequently, the line on the diagram defined by $\phi = 0$ represents the bollard pull condition for the propeller. It is important, however, not to confuse propeller thrust with bollard pull, as these terms are quite distinct and mean different things. Propeller thrust and bollard pull are exactly what the terms imply; the former relates to the hydrodynamic thrust produced by the propeller, whereas the latter is the pull the vessel can exert through a towline on some other stationary object. Bollard pull is always less than the propeller thrust by a complex ratio, which is dependent on the underwater hull form of the vessel, the depth of water, the distance of the vessel from other objects, and so on.

In the design process it is frequently necessary to change between coefficients, and to facilitate this process. Tables 6.1 and 6.2 are produced in order to show some of the more common relationships between the parameters.

Note the term σ in Tables 6.1 and 6.2 and in equations (6.10) should not be confused with cavitation number, which is an entirely different concept. The term σ in the above Tables and equation (6.10) relates to the μ–σ diagram, which is a non-cavitating diagram.

6.2 The effect of cavitation on open water characteristics

Cavitation, which is a two-phase flow phenomenon, is discussed more fully in Chapter 9; however, it is pertinent here to recognize the effect that cavitation development can have on the propeller open water characteristics.

Cavitation for the purposes of generalized analysis is defined by a free stream cavitation number σ_0 which is the ratio of the static to dynamic head of the flow. For our purposes in this chapter we will consider a cavitation number based on the static pressure at the shaft centre line and the dynamic head of the free stream flow ahead of the propeller:

$$\sigma_0 = \frac{\text{static head}}{\text{dynamic head}} = \frac{p_0 - e}{\frac{1}{2}\rho V_a^2}$$

where p_0 is the absolute static pressure at the shaft centre line and e is the vapour pressure at ambient temperature. Consequently, a non-cavitating flow is one where $(p_0 - e) \gg \frac{1}{2}\rho V_a$, that is one where σ_0 is large. As σ_0 decreases in value cavitation takes more effect as demonstrated in Figure 6.4. This figure illustrates the effect that cavitation has on the K_T and K_Q curves and, for guidance purposes only, shows a typical percentage of cavitation on the blades experienced at various cavitation numbers in uniform flow. It is immediately apparent from the figure that moderate levels of cavitation do not affect the propulsion performance of the propeller and significant cavitation activity is necessary in order to get thrust and torque breakdown. Furthermore, it will frequently be noted that the K_T and K_Q curves rise marginally above the non-cavitating line just prior to their rapid decline after thrust or torque breakdown.

It is, however, important not necessarily to associate the other problems of cavitation, for example hull induced vibration and erosion of the blade material, with the extent of cavitation necessary to cause thrust and torque performance breakdown. Relatively small levels, in terms of the extent, of cavitation, given the correct conditions, are sufficient to give rise to these problems.

Table 6.1 Common functional relationships (British units)

$$K_Q = 9.5013 \times 10^6\left(\frac{P_D}{N^3D^5}\right) \text{ (salt water)}$$

$$B_p = 23.77\sqrt{\frac{\rho K_Q}{J^5}}$$

$$J = \frac{101.33V_a}{ND} = \frac{101.33}{\delta}$$

$$\mu = \frac{1}{\sqrt{K_Q}} = 3.2442 \times 10^{-4}\sqrt{\frac{N^3D^5}{P_D}} \text{ (salt water)}$$

$$\phi = \frac{J}{\sqrt{K_Q}} = J\mu$$

$$\sigma = \frac{\eta_o}{J} = \frac{\eta_o\mu}{\phi} = \frac{K_T}{2\pi K_Q}$$

where:

P_D = delivered horsepower in Imperial units;
Q = delivered torque at propeller in (lbf ft);
T = propeller thrust (lbf);
N = propeller rotational speed in (rpm);
n = propeller rotational speed in (rev/s);
D = propeller diameter in (ft);
V_a = propeller speed of advance in (knots);
v_a = propeller speed of advance in (ft/s);
ρ = mass density of water (1.99 slug/ft^3 sea water; 1.94 slug/ft^3 for fresh water)

Table 6.2 Common functional relationships (Metric units)

$$K_Q = 2.4669 \times 10^4\left(\frac{P_D}{N^3D^5}\right) \text{ (salt water)}$$

$$B_p = 23.77\sqrt{\frac{\rho K_Q}{J^5}}$$

$$J = \frac{30.896V_a}{ND} = \frac{101.33}{\delta}$$

$$\mu = \frac{1}{\sqrt{K_Q}} = 6.3668 \times 10^{-3}\sqrt{\frac{N^3D^5}{P_D}} \text{ (salt water)}$$

$$\phi = \frac{J}{\sqrt{K_Q}} = J\mu$$

$$\sigma = \frac{\eta_o}{J} = \frac{\eta_o\mu}{\phi} = \frac{K_T}{2\pi K_Q}$$

where:

P_D = delivered horse power (metric units);
Q = delivered propeller torque (kp m);
T = propeller thrust (kp);
N = propeller rotational speed (RPM);
n = propeller rotational speed (rev/s);
D = propeller diameter (m);
V_a = propeller speed of advance (knots);
v_a = propeller speed of advance (m/s);
ρ = mass density of water (104.48 sea water) (101.94 fresh water)

6.3 Propeller scale effects

Open water characteristics are frequently determined from model experiments on propellers run at high speed and having diameters of the order of 200–300 mm. It is, therefore, reasonable to pose the question of how the reduction in propeller speed and increase in diameter at full scale will affect the propeller performance characteristics. Figure 6.5 shows the principal features of scale effect, from which it can be seen that whilst the thrust characteristic is largely unaffected the torque coefficient is somewhat reduced for a given advance coefficient.

The scale effects affecting performance characteristics are essentially viscous in nature, and as such are primarily due to boundary layer phenomena dependent on Reynolds number. Due to the methods of testing model propellers and the consequent changes in Reynolds number between model and full scale, or indeed a smaller model and a larger model, there can arise a different boundary layer structure to the flow over the blades. Whilst it is generally recognized that most full-scale propellers will have a primarily turbulent flow over the blade surface this need not be the case for the model where characteristics related to laminar flow can prevail over significant parts of the blade.

In order to quantify the effect of scale on the performance characteristics of a propeller an analytical procedure is clearly required. There is, however, no common agreement as to which is the best procedure. In survey conducted by the 1987 ITTC it was shown that from a sample of 22 organizations, 41% used the ITTC 1978 procedure; 23% made corrections based on correlation factors developed from experience; 13%, who dealt with vessels having open shafts and struts, made no correction at all; a further 13% endeavoured to scale each propulsion coefficient whilst the final 10% scaled the open water test data and then used the estimated full-scale advance coefficient. It is clear, therefore, that research is needed in this area in order to bring a measure of unification between organizations.

At present the principal analytical tool available is the 1978 ITTC performance prediction method, which is based on a simplification of Lerbs' equivalent profile procedure. Lerbs showed that a propeller can be represented by the characteristics of an equivalent section at a non-dimensional radius of around $0.70R$ or $0.75R$, these being the two sections normally chosen. The method calculates the change in propeller performance characteristics as follows.

The revised thrust and torque characteristics are given by

$$\left.\begin{aligned} K_{T_s} &= K_{T_m} - \Delta K_T \\ K_{Q_s} &= K_{Q_m} - \Delta K_Q \end{aligned}\right\} \qquad (6.11)$$

where the scale corrections ΔK_T and ΔK_Q are given by

$$\Delta K_T = -0.3\Delta C_D\left(\frac{P}{D}\right)\left(\frac{cZ}{D}\right)$$

$$\Delta K_Q = 0.25\Delta C_D\left(\frac{cZ}{D}\right)$$

and in equations (6.11) the suffixes s and m denote the full-scale ship and model test values respectively. The term ΔC_D relates to the change in drag coefficient introduced by the differing flow regimes at model and full scale, and is formally written as

$$\Delta C_D = C_{DM} - C_{DS}$$

where

$$C_{DM} = 2\left(1 + \frac{2t}{C}\right)\left[\frac{0.044}{(R_{nx})^{1/6}} - \frac{5}{(R_{nx})^{2/3}}\right]$$

and

$$C_{DS} = 2\left(1 + \frac{2t}{c}\right)\left(1.89 + 1.62\log_{10}\left(\frac{c}{K_p}\right)\right)^{-2.5}$$

In these relationships t/c is the section thickness to chord ratio; P/D is the pitch ratio; c is the section chord length and R_{nx} is the local Reynolds number, all relating to the section located $0.75R$. The blade roughness K_p is taken as 30×10^{-6} m.

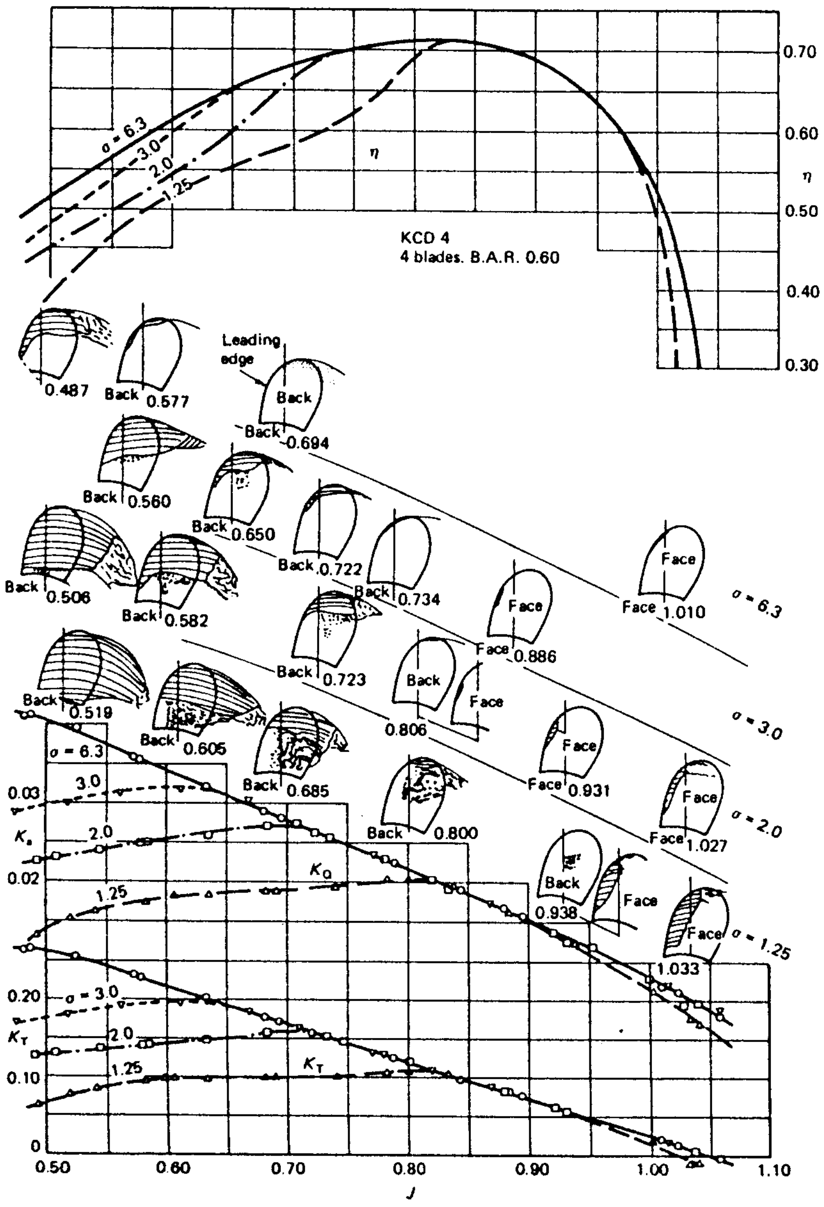

Figure 6.4 Curves of K_T, K_Q and η and cavitation sketches for KCD 4 (Reproduced from Reference 15)

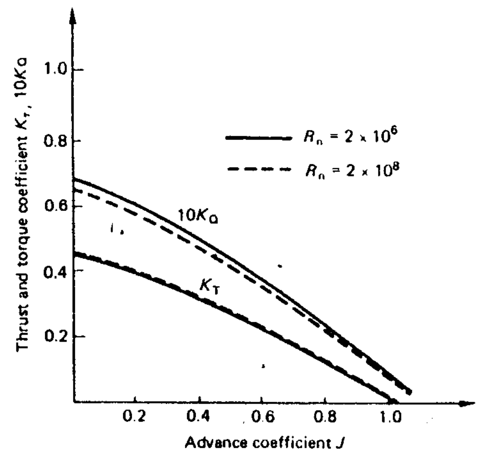

Figure 6.5 Principal features of scale effect

In this method it is assumed that the full-scale propeller blade surface is hydrodynamically rough and the scaling procedure considers only the effect of Reynolds number on the drag coefficient.

An alternative approach to the use of equation (6.11) has been proposed by Varsarmov (Reference 1) in which the correction for the Reynolds effect on propeller open water efficiency is given by

$$\eta_{os} = \eta_{om} - F(J)\left[\left(\frac{1}{R_{nm}}\right)^{0.2} - \left(\frac{1}{R_{ns}}\right)^{0.2}\right] \qquad (6.12)$$

where

$$F(J) = \left(\frac{J}{J_0}\right)^{a}$$

From the analysis of the function $F(J)$ from open water propeller data, it has been shown that J_0 can be taken as the zero thrust advance coefficient for the propeller. Consequently, if model tests are undertaken at two Reynolds numbers and the results analysed according to equation (6.12); then the function $F(J)$ can be uniquely determined.

Yet another approach has recently been proposed (Reference 2) in which the scale effect is estimated using open water performance calculations for propellers having similar geometric characteristics to the Wageningen B series.

The results of the analysis are presented in such a way as

$$\left.\begin{aligned} 1 - \frac{K_T}{K_{T_I}} &= f(R_n, K_T) \\ 1 - \frac{\eta_0}{\eta_{0_I}} &= g(R_n, K_T) \end{aligned}\right\} \qquad (6.13)$$

where the suffix I represents the values of K_T and η_0 for an ideal fluid. Consequently, if model values of the thrust and torque at the appropriate advance coefficient are known, that is K_{T_m}, K_{Q_m}, together with the model Reynolds number, then from equation (6.13) we have

$$\frac{K_{T_m}}{K_{T_I}} = 1 - f(R_{n_m}, K_{T_m})$$

$$\Rightarrow K_{T_I} = \frac{K_{T_m}}{(1 - f(R_{n_m}, K_{T_m}))} = \frac{K_{T_m}}{1 - \left(1 - \frac{K_{T_m}}{K_{T_I}}\right)}\Bigg|_{R_{n_m}}$$

Similarly

$$\eta_{0_I} = \frac{\eta_{0_m}}{1 - \left(1 - \frac{\eta_{0_m}}{\eta_{0_I}}\right)}\Bigg|_{R_{n_m}}$$

From which the ideal values of K_{T_I} and η_{0_I} can be determined for the propeller in the ideal fluid. Since the effect of scale on the thrust coefficient is usually small and the full-scale thrust coefficient will lie between the model and ideal values the assumption is made that

$$K_{T_s} \simeq \left(\frac{K_{T_M} + K_{T_I}}{2}\right)$$

that is the mean value, and since the full-scale Reynolds number R_{n_s} is known, the functions

$$f(R_{n_s}, K_{T_s}) \quad \text{and} \quad g(R_{n_s}, K_{T_s})$$

can be determined from which the full-scale values of K_{T_s} and η_{0_s} can be determined from equation (6.13):

$$K_{T_s} = K_{T_I}[1 - f(R_{n_s}, K_{T_s})]$$
$$\eta_{0_s} = \eta_{0_I}[1 - g(R_{n_s}, K_{T_s})]$$

from which the full-scale torque coefficient can be derived as follows:

$$K_{Q_s} = \frac{J}{2\pi}\frac{K_{T_s}}{\eta_{0_s}}$$

The essential difference between these latter two approaches is that the scale effect is assumed to be a function of both Reynolds number and propeller loading rather than just Reynolds number alone as in the case of the present ITTC procedure. It has been shown that significant differences can arise between the results of the various procedures. Scale effect correction of model propeller characteristics is not a simple procedure and much attention needs to be paid to the effects of the flow structure in the boundary layer and the variations of the lift and drag characteristics within the flow regime. With regard to the general question of scaling, the above methods were primarily intended for non-ducted propellers operating on their own. Clearly compound propellers such as contra-rotating screws and ducted propellers will present particular problems in scaling. In the case of the ducted propeller the interactions between the propeller, the duct and the hull are of particular concern and importance. In addition there is also some evidence to suggest that vane wheels are particularly sensitive to Reynolds number effects since both the section chord lengths and the wheel rotational speed are low, which can cause difficulty in interpreting model test data.

6.4 Specific propeller open water characteristics

Before proceeding to outline the various standard series available to the propeller designer or analyst, it is helpful to briefly consider the types of characteristic associated with each of the principal propeller types, since there are important variants between, say, fixed pitch and controllable pitch propellers or non-ducted and ducted propellers.

6.4.1 Fixed pitch propellers

The preceding discussions in this chapter have used as examples the characteristics relating to fixed pitch propellers since these are the simplest form of propeller characteristic. Figure 6.1 is typical of this type of propeller in that the propeller, in the absence of significant amounts of cavitation, as already discussed, is constrained to operate along a single set of characteristic thrust and torque lines.

6.4.2 Controllable pitch propellers

With the controllable pitch propeller the additional variable of pitch angle introduces a three-dimensional nature to the propeller characteristics, since the total characteristics comprise sets of K_T and K_Q versus J curves for each pitch angle as seen in Figure 6.6. Indeed, for analysis purposes the performance characteristics can be considered as forming a surface, in contrast to the single line for the fixed pitch propeller.

When analysing the performance of a controllable pitch propeller at off-design conditions use should not be made of fixed pitch characteristics beyond say 5° or 10° from design pitch since the effects of section distortion, discussed in Chapter 3, can affect the performance characteristics considerably.

A further set of parameters arises with controllable pitch propellers and these are the blade spindle torques, a knowledge of which is of considerable importance when designing the blade actuating mechanism. The total spindle torque, which is the torque acting about the spindle axis of the blade and which requires either to be balanced by the hub mechanism in order to hold the blades in the required pitch setting or, alternatively, to be overcome when a pitch change is required, comprises three components as follows:

$$Q_S(J,\Delta\theta) = Q_{SH}(J,\Delta\theta) + Q_{SC}(n,\Delta\theta) + Q_{SF}(J,\Delta\theta) \quad (6.14)$$

where Q_S is the total spindle torque at a given value of J and $\Delta\theta$;
Q_{SH} is the hydrodynamic component of spindle torque due to the pressure field acting on the blade surfaces;
Q_{SC} is the centrifugal component resulting from the blade mass distribution;
Q_{SF} is the frictional component of spindle torque resulting from the relative motion of the surfaces within the blade hub.

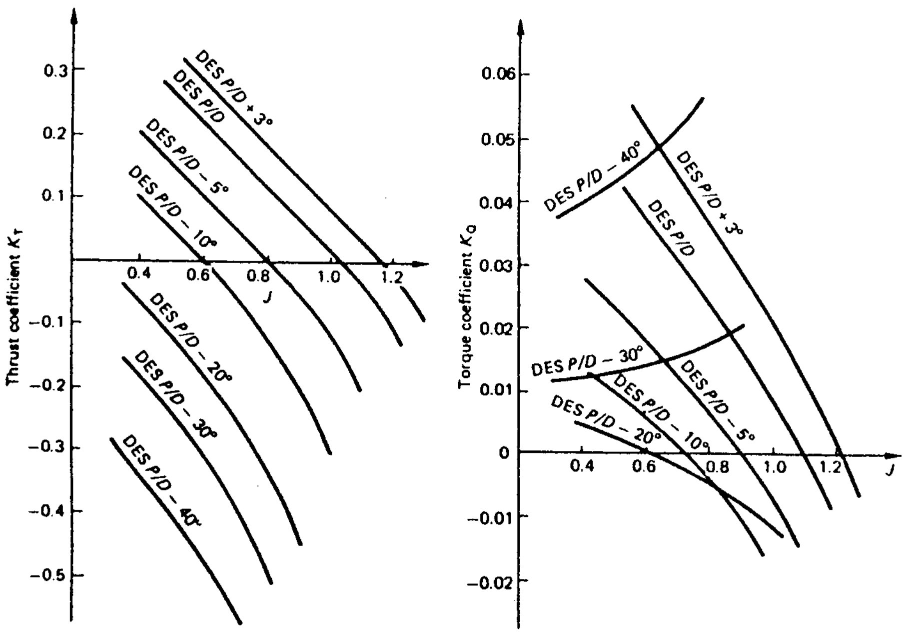

Figure 6.6 Typical controllable pitch propeller characteristic curves

The latter component due to friction is only partly in the domain of the hydrodynamicist, since it depends both on the geometry of the hub mechanism and the system of forces and moments generated by the blade pressure field and mass distribution acting on the blade palm.

Figure 6.7 shows typical hydrodynamic and centrifugal blade spindle torque characteristics for a controllable pitch propeller. In Figure 6.7 the spindle torques are expressed in the coefficient form of K_{QSH} and K_{QSC}. These coefficients are similar in form to the conventional propeller torque coefficient in so far as they relate to the respective spindle torques as follows:

$$K_{QSH} = \frac{Q_{SH}}{\rho n^2 D^5}$$
$$K_{QSC} = \frac{Q_{SC}}{\rho_m n^2 D^5} \quad (6.15)$$

where ρ is the mass density of water and ρ_m is the mass density of the blade material. Clearly, since the centrifugal component is a mechanical property of the blade only, it is independent of advance coefficient. Hence K_{QSC} is a function of $\Delta\theta$ only.

6.4.3 Ducted propellers

Whilst the general aspects of the discussion relating to non-ducted, fixed and controllable pitch propellers apply to ducted propellers, the total ducted propulsor thrust is split into two components: the algebraic sum of the propeller and duct thrusts and any second-order interaction effects. To a first approximation, therefore, the total propulsor thrust T can be written as

$$T = T_p + T_n$$

where T_p is the propeller thrust
and T_n is the duct thrust.

In non-dimensional form this becomes

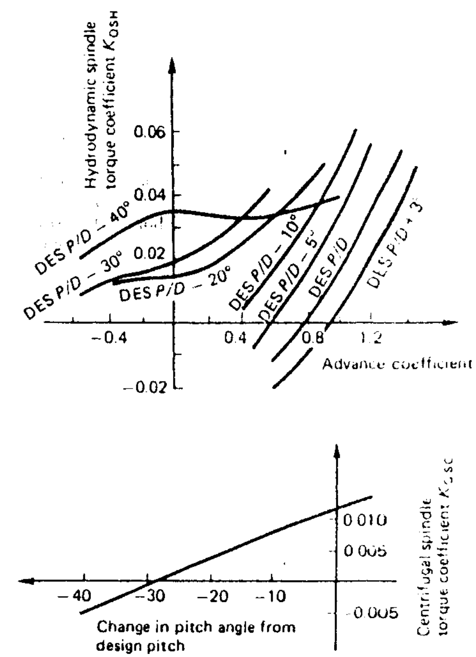

Figure 6.7 Typical controllable pitch propeller spindle torque characteristic curves

$$K_T = K_{TP} + K_{TN} \quad (6.16)$$

where the non-dimensionalization factor is $\rho n^2 D^4$ as before.

The results of model tests normally present values of K_T and K_{TN} plotted as a function of advance coefficient J as shown in Figure 6.8 for a fixed pitch ducted propulsor. The torque characteristic is, of course, not split into components since the propeller itself absorbs all of the torque of the engine. In general the proportion of thrust generated by the duct to that of the total propulsor thrust is a variable over the range of advance coefficient. In merchant practice by far the greater majority of ducted propellers are designed with accelerating ducts, as discussed previously in Chapter 2. For these duct forms the ratio of K_{TN}/K_T is of the order of 0.5 at the bollard pull, or zero advance coefficient, condition, but this usually falls to around 0.05 or 0.10 at the design free-running condition. Indeed, if the advance coefficient is increased to a sufficiently high level, then the duct thrust will change sign, as seen in Figure 6.8, and act as a drag; however, this situation is unlikely to arise in normal practice. When decelerating ducts are used, analogous conditions

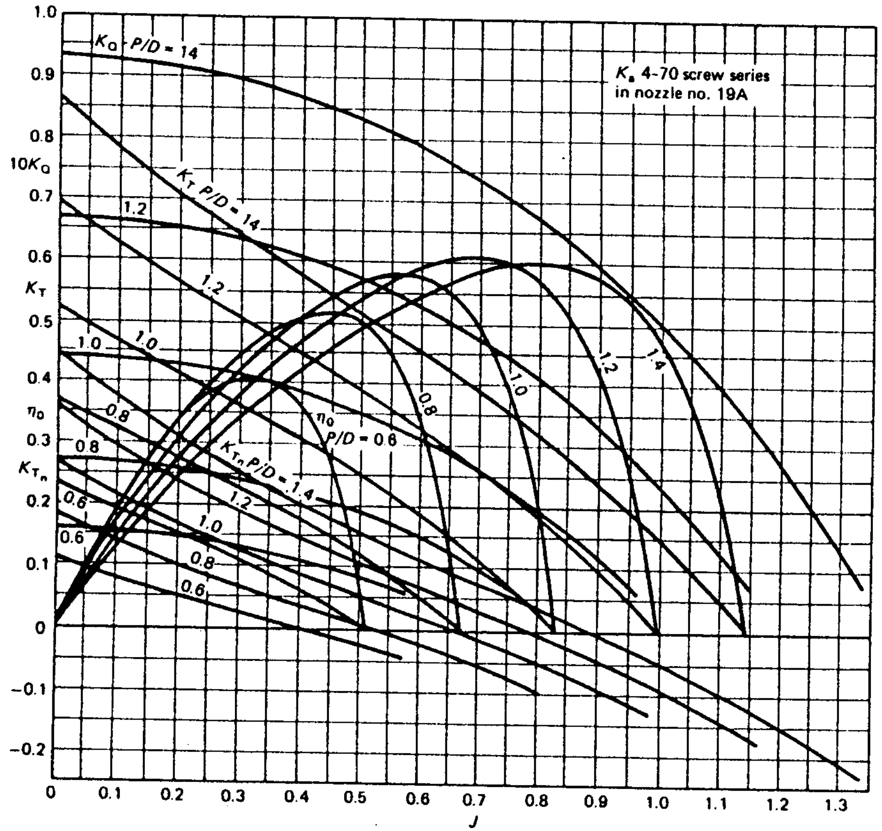

Figure 6.8 Open-water test results of K_a 4-70 screw series with nozzle no. 19A (Courtesy: MARIN)

arise, but the use of these ducts is confined to certain specialist cases, normally those having a low radiated noise requirement.

6.4.4 High-speed propellers

With high-speed propellers much of what has been said previously will apply depending upon the application. However, the high-speed propeller will be susceptible to two other factors. The first is that cavitation is more likely to occur, and consequently the propeller type and section blade form must be carefully considered in so far as any supercavitating blade section requirements need to be met. The second factor is that many high-speed propellers are fitted to shafts with considerable rake angles. This rake angle, when combined with the flow directions, gives rise to two flow components acting at the propeller plane as seen in Figure 6.9. The first of these is parallel to the shaft and has a magnitude $V_a \cos(\lambda)$ and the second is perpendicular to the shaft with a magnitude $V_a \sin(\lambda)$ where λ is the relative shaft angle as shown in the figure. It will be appreciated that the second, or perpendicular, component immediately presents an asymmetry when viewed in terms of propeller relative velocities, since on one side of the propeller disc the perpendicular velocity component is additive to the propeller rotational velocity whilst on the other side it is subtractive (see Figure 6.9). This gives rise to a differential loading of the blades as they rotate around the propeller disc, which causes a thrust eccentricity and side force components. Figure 6.10 demonstrates

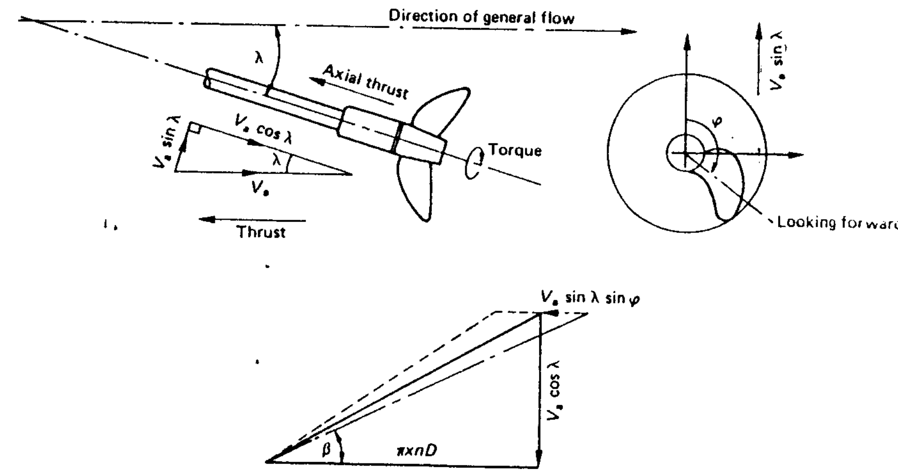

Figure 6.9 Inclined flow velocity diagram

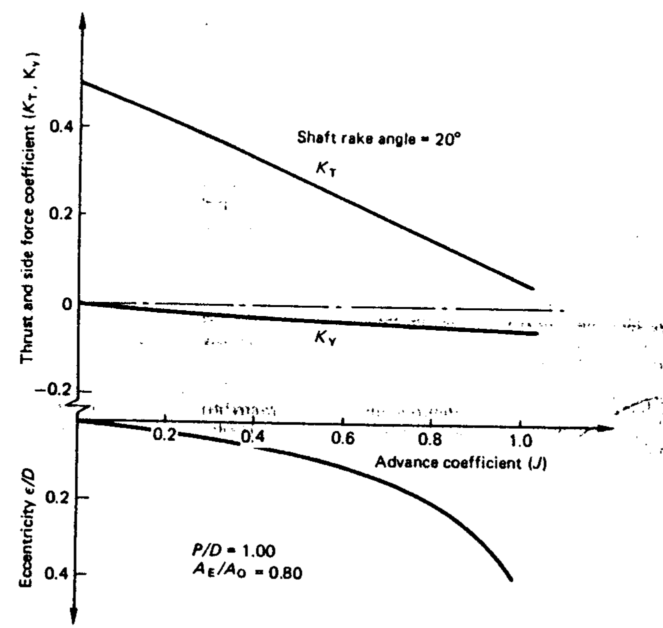

Figure 6.10 Thrust eccentricity and side forces on a raked propeller

these features which of course will apply generally to all propellers working in non-uniform flow but are more noticeable with high-speed propellers due to the speeds and inclinations involved. The magnitude of these eccentricities can be quite large; for example, in the case of unity pitch ratio with a shaft rake of 20°, the transverse thrust eccentricity indicated by Figure 6.10 may well reach 0.40*R*. Naturally due to the non-uniform tangential wake field the resulting cavitation pattern will also be anti-symmetric.

6.5 Standard series data

Over the years there have been a considerable number of standard series propellers tested in many different establishments around the world. To discuss them all in any detail would clearly be a large undertaking requiring considerable space; consequently, those most commonly used today by propeller designers and analysts are referenced here.

The principal aim in carrying out systematic propeller tests is to provide a data base to help the designer understand the factors which influence propeller performance and the inception and form of cavitation on the blades under various operating conditions. A secondary purpose is to provide design diagrams, or charts, which will assist in selecting the most appropriate dimensions of actual propellers to suit full-size ship applications.

The purpose of this section is not to provide the reader with an exhaustive catalogue of results but to introduce the various model series in terms of their nature and extent and provide suitable references from which the full details can be found. Table 6.3 summarizes the fixed pitch, non-ducted propeller series referenced here to enable rapid selection of the appropriate series for a particular set of circumstances.

6.5.1 Wageningen B-screw series

This is perhaps the most extensive and widely used propeller series. The series was originally presented in a set of papers presented by Troost (References 3–5) in the late 1940s and, amongst many practitioners, is still referred to as the 'Troost series'. Over the years the model series has been added to so as to provide a comprehensive fixed pitch, non-ducted propeller series. From analysis of the early results it was appreciated that a certain unfairness between the various design diagrams existed and this was considered to result from the scale effects resulting from the different model tests. This led to a complete re-appraisal of the series in which the differences in test

Table 6.3 Fixed pitch, non-ducted propeller series summary

Series	*No. of propellers in series*	*Range of parameters*			D (*mm*)	r_h/R	*Cavitation data available*	*Notes*
		Z	A_E/A_O	P/D				
Wageningen B series	≃120	2–7	0.3–1.05	0.6–1.4	250	0.169	No	Four bladed propeller has non-constant pitch dist.
Au series	34	4–7	0.4–0.758	0.5–1.2	250	0.180	No	
Gawn series	37	3	0.2–1.1	0.4–2.0	508	0.200	No	
KCA series	≃30	3	0.5–1.25	0.6–2.0	406	0.200	Yes	
Ma series	32	3 and 5	0.75–1.20	1.0–1.45	250	0.190	Yes	
Newton Radar series	12	3	0.5–1.0	1.05–2.08	254	0.167	Yes	
KCD series	24	3–6 (mainly 4)	0.587 Princ. 0.44–0.8	0.6–1.6	406	0.200	Yes	Propellers not geosyms
Meridian series	20	6	0.45–1.05	0.4–1.2	305	0.185	Yes	Propellers not geosyms

Table 6.4 Extent of the Wageningen B-screw series (taken from Reference 6)

Blade number (Z)	*Blade area ratio* A_E/A_O													
2	0.30													
3		0.35			0.50			0.65			0.80			
4			0.40			0.55			0.70			0.85	1.00	
5				0.45			0.60			0.75				1.05
6					0.50			0.65			0.80			
7						0.55			0.70			0.85		

Table 6.5 Geometry of the Wageningen B-screw series (taken from Reference 7)

Dimensions of four, five, six and seven bladed propellers

r/R	$\frac{c}{D} \cdot \frac{Z}{A_E/A_O}$	a/c	b/c	$t/D = A_r - B_r Z$	
				A_r	B_r
0.2	1.662	0.617	0.350	0.0526	0.0040
0.3	1.882	0.613	0.350	0.0464	0.0035
0.4	2.050	0.601	0.351	0.0402	0.0030
0.5	2.152	0.586	0.355	0.0340	0.0025
0.6	2.187	0.561	0.389	0.0278	0.0020
0.7	2.144	0.524	0.443	0.0216	0.0015
0.8	1.970	0.463	0.479	0.0154	0.0010
0.9	1.582	0.351	0.500	0.0092	0.0005
1.0	0.000	0.000	0.000	0.0030	0.0000

Dimensions for three bladed propellers

r/R	$\frac{c}{D} \cdot \frac{Z}{A_E/A_O}$	a/c	b/c	$t/D = A_r - B_r Z$	
				A_r	B_r
0.2	1.633	0.616	0.350	0.0526	0.0040
0.3	1.832	0.611	0.350	0.0464	0.0035
0.4	2.000	0.599	0.350	0.0402	0.0030
0.5	2.120	0.583	0.355	0.0340	0.0025
0.6	2.186	0.558	0.389	0.0278	0.0020
0.7	2.168	0.526	0.442	0.0216	0.0015
0.8	2.127	0.481	0.478	0.0154	0.0010
0.9	1.657	0.400	0.500	0.0092	0.0005
1.0	0.000	0.000	0.000	0.0030	0.0000

A_r, B_r = constants in equation for t/D
a = distance between leading edge and generator line at r
b = distance between leading edge and location of maximum thickness
c = chord length of blade section at radius r
t = maximum blade section thickness at radius r

Position of generator line

Position of maximum thickness

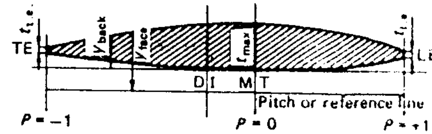

LE = leading edge
TE = trailing edge
MT = location of maximum thickness
DI = location of directrix

$$\left.\begin{aligned} y_{face} &= V_1 (t_{max} - t_{t.e.}) \\ y_{back} &= (V_1 + V_2)(t_{max} - t_{t.e.}) + t_{t.e.} \end{aligned}\right\} \text{for } P \leq 0$$

and

$$\left.\begin{aligned} y_{face} &= V_1 (t_{max} - t_{l.e.}) \\ y_{back} &= (V_1 + V_2)(t_{max} - t_{l.e.}) + t_{l.e.} \end{aligned}\right\} \text{for } P \geq 0$$

Referring to the diagram, note the following:

y_{face}, y_{back} = vertical ordinate of a point on a blade section on the face and on the back with respect to the pitch line.
t_{max} = maximum thickness of blade section.
$t_{t.e.}, t_{l.e.}$ = extrapolated blade section thickness at the trailing and leading edges.
V_1, V_2 = tabulated functions dependent on r/R and P.
P = non-dimensional coordinate along pitch line from position of maximum thickness to leading edge (where $P = 1$), and from position of maximum thickness to trailing edge (where $P = -1$).

Values of V_1 for use in the equations

r/R \ P	−1.0	−0.95	−0.9	−0.8	−0.7	−0.6	−0.5	−0.4	−0.2	0
0.7–1.0	0	0	0	0	0	0	0	0	0	0
0.6	0	0	0	0	0	0	0	0	0	0
0.5	0.0522	0.0420	0.0330	0.0190	0.0100	0.0040	0.0012	0	0	0
0.4	0.1467	0.1200	0.0972	0.0630	0.0395	0.0214	0.0116	0.0044	0	0
0.3	0.2306	0.2040	0.1790	0.1333	0.0943	0.0623	0.0376	0.0202	0.0033	0
0.25	0.2598	0.2372	0.2115	0.1651	0.1246	0.0899	0.0579	0.0350	0.0084	0
0.2	0.2826	0.2630	0.2400	0.1967	0.1570	0.1207	0.0880	0.0592	0.0172	0
0.15	0.3000	0.2824	0.2650	0.2300	0.1950	0.1610	0.1280	0.0955	0.0365	0

r/R \ P	+1.0	+0.95	+0.9	+0.85	+0.8	+0.7	+0.6	+0.5	+0.4	+0.2	0
0.7–1.0	0	0	0	0	0	0	0	0	0	0	0
0.6	0.0382	0.0169	0.0067	0.0022	0.0006	0	0	0	0	0	0
0.5	0.1278	0.0778	0.0500	0.0328	0.0211	0.0085	0.0034	0.0008	0	0	0
0.4	0.2181	0.1467	0.1088	0.0833	0.0637	0.0357	0.0189	0.0090	0.0033	0	0
0.3	0.2923	0.2186	0.1760	0.1445	0.1191	0.0790	0.0503	0.0300	0.0148	0.0027	0
0.25	0.3256	0.2513	0.2068	0.1747	0.1465	0.1008	0.0669	0.0417	0.0224	0.0031	0
0.2	0.3560	0.2821	0.2353	0.2000	0.1685	0.1180	0.0804	0.0520	0.0304	0.0049	0
0.15	0.3860	0.3150	0.2642	0.2230	0.1870	0.1320	0.0920	0.0615	0.0384	0.0096	0

Table 6.5 (Cont.)

Values of V_2 for use in the equations

r/R \ P	−1.0	−0.95	−0.9	−0.8	−0.7	−0.6	−0.5	−0.4	−0.2	0
0.9–1.0	0	0.0975	0.19	0.36	0.51	0.64	0.75	0.84	0.96	1
0.85	0	0.0975	0.19	0.36	0.51	0.64	0.75	0.84	0.96	1
0.8	0	0.0975	0.19	0.36	0.51	0.64	0.75	0.84	0.96	1
0.7	0	0.0975	0.19	0.36	0.51	0.64	0.75	0.84	0.96	1
0.6	0	0.0965	0.1885	0.3585	0.5110	0.6415	0.7530	0.8426	0.9613	1
0.5	0	0.0950	0.1865	0.3569	0.5140	0.6439	0.7580	0.8456	0.9639	1
0.4	0	0.0905	0.1810	0.3500	0.5040	0.6353	0.7525	0.8415	0.9645	1
0.3	0	0.0800	0.1670	0.3360	0.4885	0.6195	0.7335	0.8265	0.9583	1
0.25	0	0.0725	0.1567	0.3228	0.4740	0.6050	0.7184	0.8139	0.9519	1
0.2	0	0.0640	0.1455	0.3060	0.4535	0.5842	0.6995	0.7984	0.9446	1
0.15	0	0.0540	0.1325	0.2870	0.4280	0.5585	0.6770	0.7805	0.9360	1

r/R \ P	+1.0	+0.95	+0.9	+0.85	+0.8	+0.7	+0.6	+0.5	+0.4	+0.2	0
0.9–1.0	0	0.0975	0.1900	0.2775	0.3600	0.51	0.6400	0.75	0.8400	0.9600	1
0.85	0	0.1000	0.1950	0.2830	0.3660	0.5160	0.6455	0.7550	0.8450	0.9615	1
0.8	0	0.1050	0.2028	0.2925	0.3765	0.5265	0.6545	0.7635	0.8520	0.9635	1
0.7	0	0.1240	0.2337	0.3300	0.4140	0.5615	0.6840	0.7850	0.8660	0.9675	1
0.6	0	0.1485	0.2720	0.3775	0.4620	0.6060	0.7200	0.8090	0.8790	0.9690	1
0.5	0	0.1750	0.3056	0.4135	0.5039	0.6430	0.7478	0.8275	0.8880	0.9710	1
0.4	0	0.1935	0.3235	0.4335	0.5220	0.6590	0.7593	0.8345	0.8933	0.9725	1
0.3	0	0.1890	0.3197	0.4265	0.5130	0.6505	0.7520	0.8315	0.8020	0.9750	1
0.25	0	0.1758	0.3042	0.4108	0.4982	0.6359	0.7415	0.8259	0.8899	0.9751	1
0.2	0	0.1560	0.2840	0.3905	0.4777	0.6190	0.7277	0.8170	0.8875	0.9750	1
0.15	0	0.1300	0.2600	0.3665	0.4520	0.5995	0.7105	0.8055	0.8825	0.9760	1

procedures were taken into account and the results of this work were presented by van Lammeren *et al.* (Reference 6).

The extent of the series in terms of a blade number versus blade area ratio matrix is shown in Table 6.4 from which it may be seen that the series numbers some 20 blade area–blade number configurations. The geometry of the series is shown in Table 6.5, from which it can be seen that a reasonably consistent geometry is maintained between the members of the series with only a few anomalies; notably the non-constant nature of the face pitch near the root of the four-blade series and the blade outline of the three-bladed propellers. For completeness purposes Figure 6.11 shows the geometric outline of the B5 propeller set. Note that the propellers of this series are generally referred to by the notation B $Z \cdot y$, where the B denotes the 'B' series, Z is the blade number and y is the blade expanded area. The face pitch ratio for the series is in the range 0.6–1.4.

The results of the fairing exercise reported by Oosterveld paved the way for detailed regression studies on the performance characteristics given by this model series. Oosterveld and van Oossanen (Reference 7) reported the findings of this work in which the open water characteristics of the series are

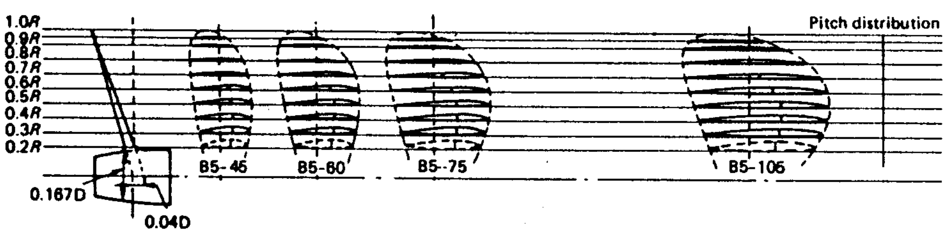

Figure 6.11 General plan of B 5 screw series (Reproduced from Reference 6, with permission)

Table 6.6 Coefficients for the K_T and K_Q polynomials representing the Wageningen B-screen series for a Reynolds number of 2×10^6 (taken from Reference 7)

Thrust (K_T)						Torque (K_Q)					
n	$C_{s,t,u,v}$	s (J)	t (P/D)	u (A_E/A_O)	v (Z)	n	$C_{s,t,u,v}$	s (J)	t (P/D)	u (A_E/A_O)	v (Z)
1	+0.00880496	0	0	0	0	1	+0.00379368	0	0	0	0
2	−0.204554	1	0	0	0	2	+0.00886523	2	0	0	0
3	+0.166351	0	1	0	0	3	−0.032241	1	1	0	0
4	+0.158114	0	2	0	0	4	+0.00344778	0	2	0	0
5	−0.147581	2	0	1	0	5	−0.0408811	0	1	1	0
6	−0.481497	1	1	1	0	6	−0.108009	1	1	1	0
7	+0.415437	0	2	1	0	7	−0.0885381	2	1	1	0
8	+0.0144043	0	0	0	1	8	+0.188561	0	2	1	0
9	−0.0530054	2	0	0	1	9	−0.00370871	1	0	0	1
10	+0.0143481	0	1	0	1	10	+0.00513696	0	1	0	1
11	+0.0606826	1	1	0	1	11	+0.0209449	1	1	0	1
12	−0.0125894	0	0	1	1	12	+0.00474319	2	1	0	1
13	+0.0109689	1	0	1	1	13	−0.00723408	2	0	1	1
14	−0.133698	0	3	0	0	14	+0.00438388	1	1	1	1
15	+0.00638407	0	6	0	0	15	−0.0269403	0	2	1	1
16	−0.00132718	2	6	0	0	16	+0.0558082	3	0	1	0
17	+0.168496	3	0	1	0	17	+0.0161886	0	3	1	0
18	−0.0507214	0	0	2	0	18	+0.00318086	1	3	1	0
19	+0.0854559	2	0	2	0	19	+0.015896	0	0	2	0
20	−0.0504475	3	0	2	0	20	+0.0471729	1	0	2	0
21	+0.010465	1	6	2	0	21	+0.0196283	3	0	2	0
22	−0.00648272	2	6	2	0	22	−0.0502782	0	1	2	0
23	−0.00841728	0	3	0	1	23	−0.030055	3	1	2	0
24	+0.0168424	1	3	0	1	24	+0.0417122	2	2	2	0
25	−0.00102296	3	3	0	1	25	−0.0397722	0	3	2	0
26	−0.0317791	0	3	1	1	26	−0.00350024	0	6	2	0
27	+0.018604	1	0	2	1	27	−0.0106854	3	0	0	1
28	−0.00410798	0	2	2	1	28	+0.00110903	3	3	0	1
29	−0.000606848	0	0	0	2	29	−0.000313912	0	6	0	1
30	−0.0049819	1	0	0	2	30	+0.0035985	3	0	1	1
31	+0.0025983	2	0	0	2	31	−0.00142121	0	6	1	1
32	−0.000560528	3	0	0	2	32	−0.00383637	1	0	2	1
33	−0.00163652	1	2	0	2	33	+0.0126803	0	2	2	1
34	−0.000328787	1	6	0	2	34	−0.00318278	2	3	2	1
35	+0.000116502	2	6	0	2	35	+0.00334268	0	6	2	1
36	+0.000690904	0	0	1	2	36	−0.00183491	1	1	0	2
37	+0.00421749	0	3	1	2	37	+0.000112451	3	2	0	2
38	+0.0000565229	3	6	1	2	38	−0.0000297228	3	6	0	2
39	−0.00146564	0	3	2	2	39	+0.000269551	1	0	1	2
						40	+0.00083265	2	0	1	2
						41	+0.00155334	0	2	1	2
						42	+0.000302683	0	6	1	2
						43	−0.0001843	0	0	2	2
						44	−0.000425399	0	3	2	2
						45	+0.0000869243	3	3	2	2
						46	−0.0004659	0	6	2	2
						47	+0.0000554194	1	6	2	2

represented at a Reynolds number 2×10^6 by an equation of the following form:

$$\left.\begin{aligned} K_Q &= \sum_{n=1}^{47} C_n (J)^{x_n} (P/D)^{y_n} (A_E/A_O)^{u_n} (Z)^{v_n} \\ K_T &= \sum_{n=1}^{39} C_n (J)^{x_n} (P/D)^{y_n} (A_E/A_O)^{u_n} (Z)^{v_n} \end{aligned}\right\} \qquad (6.17)$$

where the coefficients are reproduced in Table 6.6.

To extend this work further so that propeller characteristics can be predicted for other Reynolds numbers within the range 2×10^6 to 2×10^9 a set of corrections of the following form was derived:

$$\begin{Bmatrix} K_T(R_n) \\ K_Q(R_n) \end{Bmatrix} = \begin{Bmatrix} K_T(R_n = 2 \times 10^6) \\ K_Q(R_n = 2 \times 10^6) \end{Bmatrix} + \begin{Bmatrix} \Delta K_T(R_n) \\ \Delta K_Q(R_n) \end{Bmatrix} \qquad (6.18)$$

where

$$\begin{aligned} \Delta K_T = {} & 0.000353485 \\ & -0.00333758(A_E/A_O)J^2 \\ & -0.00478125(A_E/A_O)(P/D)J \\ & +0.000257792(\log R_n - 0.301)^2 \cdot (A_E/A_O)J^2 \\ & +0.0000643192(\log R_n - 0.301)(P/D)^6 J^2 \\ & -0.0000110636(\log R_n - 0.301)^2 (P/D)^6 J^2 \\ & -0.0000276305(\log R_n - 0.301)^2 Z(A_E/A_O)J^2 \\ & +0.0000954(\log R_n - 0.301)Z(A_E/A_O)(P/D)J \\ & +0.0000032049(\log R_n - 0.301)Z^2(A_E/A_O) \\ & \quad \times (P/D)^3 J \end{aligned}$$

$$\begin{aligned} \Delta K_Q = {} & -0.000591412 \\ & +0.00696898(P/D) \\ & -0.0000666654Z(P/D)^6 \\ & +0.0160818(A_E/A_O)^2 \\ & -0.000938091(\log R_n - 0.301)(P/D) \\ & -0.00059593(\log R_n - 0.301)(P/D)^2 \\ & +0.0000782099(\log R_n - 0.301)^2 (P/D)^2 \\ & +0.0000052199(\log R_n - 0.301)Z(A_E/A_O)J^2 \\ & -0.00000088528(\log R_n - 0.301)^2 Z(A_E/A_O) \\ & \quad \times (P/D)J \\ & +0.0000230171(\log R_n - 0.301)Z(P/D)^6 \\ & -0.00000184341(\log R_n - 0.301)^2 Z(P/D)^6 \\ & -0.00400252(\log R_n - 0.301)(A_E/A_O)^2 \\ & +0.000220915(\log R_n - 0.301)^2 (A_E/A_O)^2 \end{aligned}$$

The Wageningen series is a general purpose, fixed pitch, non-ducted propeller series which is used extensively for design and analysis purposes. A variant of the series, designated the BB-series, was introduced, since it was felt that the B-series had tip chord lengths that were not entirely representative of modern practice. Accordingly the BB-series had a re-defined blade outline with wider tips than the parent form. However, the BB-series, of which only a few members exist, has not been widely used.

6.5.2 Japanese AU series

This propeller series is in many ways a complementary series to the Wageningen B series; however, outside of Japan it has not gained the widespread popularity of the B-series. The series reported by Reference 8 comprises some propellers having a range of blade numbers from four to seven and blade area ratios in the range 0.40 to 0.758. Table 6.7 details the members of the series and Table 6.8 the blade geometry. The propeller series, as its name implies, has AU type aerofoil sections and was developed from an earlier series having Unken-type sections.

6.5.3 Gawn series

This series of propellers whose results were presented by Gawn (Reference 9) comprised a set of 37 three-bladed propellers covering a range of pitch ratios from 0.4 to 2.0 and blade area ratios from 0.2 to 1.1.

The propellers of this series each had a diameter of 503 mm (20 in), and by this means many of the scale effects associated with smaller diameter propeller series have been avoided. Each of the propellers has a uniform face pitch; segmental blade sections; constant blade thickness ratio, namely 0.060, and a boss diameter of 0.20. The developed blade outline was of elliptical form with the inner and outer vertices at $0.1R$ and the blade tip respectively. Figure 6.12 shows the outline of the propellers in this series. The entire

Table 6.7 Members of the AU series (taken from Reference 8)

No. blades	*4*		*5*		*6*			*7*	
Model prop No.	1305–1309	1310–1314	1128–1132	1133–1137	1189–1192	1193–1196	1197–1200	1144	1147
Pitch ratio	0.5, 0.6, 0.8, 1.0, 1.2		0.4, 0.6, 0.8, 1.0, 1.2		0.5, 0.7, 0.9, 1.1			0.8	
Blade section	AU		AU		AU	AU_w	AU_w	AU	
Diameter (m)	0.250		0.250		0.250			0.250	
Exp. area ratio	0.40	0.55	0.50	0.65	0.70	0.70	0.55	0.65	0.758
Boss ratio	0.180		0.180		0.180			0.180	
Blade thickness ratio	0.050		0.050		0.050			0.050	
Rake angle	10°	0°	10°	0°	10°	0°		10°	0°

Table 6.8 Blade geometry of the AU series (taken from Reference 8)

Dimensions of AU-4 series propeller

	r/R	0.2	0.3	0.4	0.5	0.6	0.66	0.7	0.8	0.9	0.95	1.0	
Width of blade as % of max. blade width	From generator line to trailing	27.96	33.45	38.76	43.54	47.96	49.74	51.33	52.39	48.49	42.07	17.29	Max. blade width at 0.66 r/R 0.226D for $A_E/A = 0.40$
	From generator line to leading edge	38.58	14.25	48.32	50.80	51.15	50.26	48.31	40.53	25.13	13.55		
	Total blade width	66.54	77.70	87.08	94.34	99.11	100.00	96.64	92.92	73.62	55.62		
Blade thickness as % of D		4.06	3.59	3.12	2.65	2.18	1.90	1.71	1.24	0.77	0.54	0.30	Max blade thickness at prop. axis 0.050D
Distance of the point of max. thickness from the leading edge as % of blade width		32.0	32.0	32.0	32.5	34.9	37.9	40.2	45.4	48.9	50.0		

Offsets of AU-type propeller

(1) Ordinates of X-value are given as % of blade width (2) Ordinates of Y-value are given as % of Y_{max}

r/R																		
0.20	X	0	2.00	4.00	6.00	10.00	15.00	20.00	30.00	32.00	40.00	50.00	60.00	70.00	80.00	90.00	95.00	100.00
	Y_o	35.00	51.85	59.75	66.15	76.05	85.25	92.20	89.80	100.00	97.75	89.95	78.15	63.15	45.25	25.30	15.00	4.50
	Y_U		24.25	19.05	15.00	10.00	5.40	2.35										
0.30	X	0	2.00	4.00	6.00	10.00	15.00	20.00	30.00	32.00	40.00	50.00	60.00	70.00	80.00	90.00	93.00	100.00
	Y_o	35.00	51.85	59.75	66.15	76.05	85.25	92.20	99.80	100.00	97.75	89.95	78.15	63.15	45.25	25.30	15.00	4.50
	Y_U		24.25	19.05	15.00	10.00	5.40	2.35										
0.40	X	0	2.00	4.00	6.00	10.00	15.00	20.00	30.00	32.00	40.00	50.00	60.00	70.00	80.00	90.00	95.00	100.00
	Y_o	35.00	51.85	59.75	66.15	76.05	85.25	92.20	99.80	100.00	97.75	89.95	78.15	63.15	45.25	25.30	15.00	4.50
	Y_U		24.25	19.05	15.00	10.00	5.40	2.35										
0.50	X	0	2.03	4.06	6.09	10.16	15.23	20.31	30.47	32.50	40.44	50.37	60.29	70.22	80.15	90.07	95.04	100.00
	Y_o	35.00	51.85	59.75	66.15	76.05	85.25	92.20	99.80	100.00	97.75	89.95	78.15	63.15	45.25	25.30	15.00	4.50
	Y_U		24.25	19.05	15.00	10.00	5.40	2.35										
0.60	X	0	2.18	4.36	6.54	10.91	16.36	21.81	32.72	34.90	42.56	52.13	61.70	71.28	80.85	90.43	95.21	100.00
	Y_o	34.00	49.60	58.00	64.75	75.20	84.80	91.80	99.80	100.00	97.75	89.95	78.15	63.15	45.25	25.30	15.00	4.50
	Y_U		23.60	18.10	14.25	9.45	5.00	2.25										
0.70	X	0	2.51	5.03	7.54	12.56	18.84	25.12	37.69	40.20	47.23	56.03	64.82	73.62	82.41	91.21	95.60	100.00
	Y_o	30.00	42.90	52.20	59.90	71.65	82.35	90.60	99.80	100.00	97.75	89.95	78.15	63.15	45.25	25.30	15.00	4.50
	Y_U		20.50	15.45	11.95	7.70	4.10	1.75										
0.80	X	0	2.84	5.68	8.51	14.19	21.28	28.38	42.56	45.40	51.82	59.85	67.88	75.91	83.94	91.97	95.99	100.00
	Y_o	21.00	32.45	41.70	50.10	64.60	78.45	88.90	99.80	100.00	97.75	89.95	78.15	63.15	45.25	25.30	15.00	4.50
	Y_U		14.00	10.45	8.05	5.05	2.70	1.15										
0.90	X	0	3.06	6.11	9.17	15.28	22.92	30.56	45.85	48.90	54.91	62.42	69.94	77.46	84.97	92.49	96.24	100.00
	Y_o	8.30	21.10	31.50	40.90	57.45	74.70	87.45	99.70	100.00	98.65	92.75	83.00	69.35	51.85	30.80	19.40	6.85
	Y_U		4.00	2.70	2.05	1.20	0.70	0.30										
0.95	X	0	3.13	6.25	9.38	15.63	23.44	31.25	46.87	50.00	55.88	63.23	70.59	77.94	85.30	92.65	96.32	100.00
	Y_o	6.00	19.65	30.00	39.60	56.75	74.30	87.30	99.65	100.00	99.00	93.85	84.65	71.65	54.30	33.50	21.50	8.00
	Y_U																	

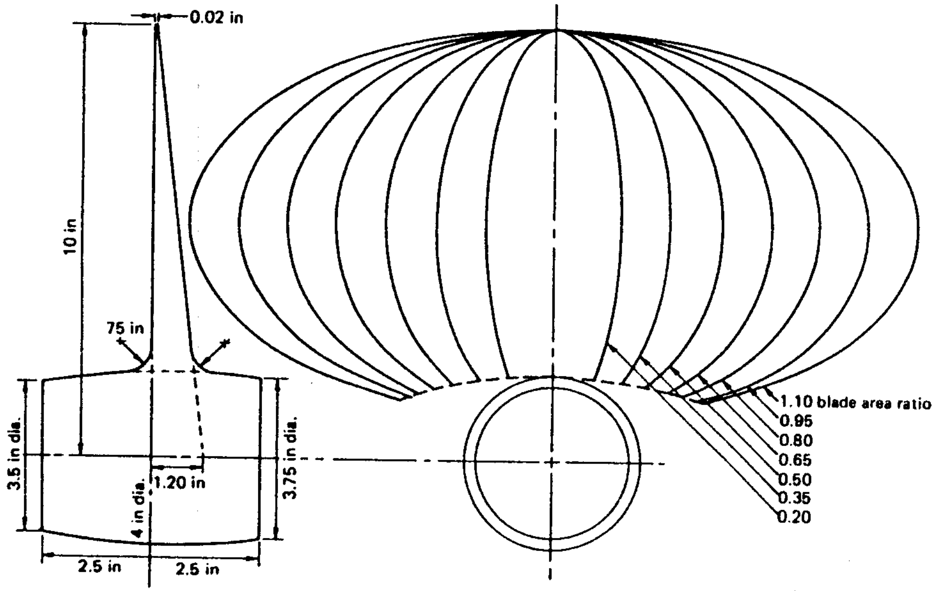

Figure 6.12 Blade outline of the Gawn series (Reproduced from Reference 9, with permission)

series were tested in the No. 2 towing rank at A.E.W. Haslar within range of slip from zero to 100%: to achieve this the propeller rotational speed was in the range 250–500 RPM. No cavitation characteristics are given for the series.

The propeller series represents a valubale data set, despite the somewhat dated propeller geometry, for undertaking preliminary design studies for warships and other high-performance craft due to the wide range of P/D and A_E/A_O values covered. Blount and Hubble (Reference 10) in considering methods for the sizing of small craft propellers developed a set of regression coefficients of the form of equation (6.17) to represent the Gawn series. The coefficients for this series are given in Table 6.9 and it is suggested that the range of applicability of the regression study should be for pitch ratio values from 0.8 to 1.4, although the study was based on the wider range of 0.6 to 1.6. Inevitably, however, some regression formulations of model test data tend to deteriorate towards the outer limits of the data set, and this is the cause of the above restriction.

6.5.4 KCA series

The KCA series, or as it is sometimes known, the Gawn–Burrill series (Reference 11) is in many ways a complementary series to the Gawn series introduced above. The KCA series comprise 30 three-bladed, 406 mm (16 in) models embracing a range of pitch ratios from 0.6 to 2.0 and blade area ratios from 0.5 to 1.1. Thus the propellers can be seen to cover a similar range of parameters to the Gawn series in that they have the same upper limits for P/D and A_E/A_O, but slightly curtailed lower limits. The propellers of the KCA series all had uniform face pitch, segmental sections over the outer half of the blade, and in the inner half, the flat faces of the segmental sections were lifted at the leading and trailing edges. The blade thickness fraction of the parent screw, shown in Figure 6.13, was 0.045 and the blade outline was elliptical. The boss diameter of the series was $0.2D$.

This propeller series was tested in the cavitation tunnel at The University of Newcastle upon Tyne, England and consequently, since the cavitation tunnel was used rather than the towing tank, the propeller series was tested at a range of different cavitation numbers. The range used gave a series of six cavitation numbers, based on the free stream advance velocity, as follows: 5.3, 2.0, 1.5, 0.75 and 0.50. As a consequence using this series it is possible to study the effects of the global cavitation performance of a proposed propeller design.

In order to assist in design studies using the KCA series, Emerson and Sinclair (Reference 12) have presented B_p–δ diagrams for the series both at non-cavitating and cavitating conditions, together with

Table 6.9 Blount and Hubble coefficients for Gawn propeller series – equation (6.17) (taken from Reference 10)

Thrust (K_T)						*Torque* (K_Q)					
n	C_n	s (J)	t (P/D)	u (EAR)	v (Z)	n	C_n	s (J)	t (P/n)	u (EAR)	v (Z)
1	−0.0558636300	0	0	0	0	1	0.0051589800	0	0	0	0
2	−0.2173010900	1	0	0	0	2	0.0160666800	2	0	0	0
3	0.2605314000	0	1	0	0	3	−0.0441153000	1	1	0	0
4	0.1581140000	0	2	0	0	4	0.0068222300	0	2	0	0
5	−0.1475810000	2	0	1	0	5	−0.0408811000	0	1	1	0
6	−0.4814970000	1	1	1	0	6	−0.0773296700	1	1	1	0
7	0.3781227800	0	2	1	0	7	−0.0885381000	2	1	1	0
8	0.0144043000	0	0	0	1	8	0.1693750200	0	2	1	0
9	−0.0530054000	2	0	0	1	9	−0.0037087100	1	0	0	1
10	0.0143481000	0	1	0	1	10	0.0051369600	0	1	0	1
11	0.0606826000	1	1	0	1	11	0.0209449000	1	1	0	1
12	−0.0125894000	0	0	1	1	12	0.0047431900	2	1	0	1
13	0.0109689000	1	0	1	1	13	−0.0072340800	2	0	1	1
14	−0.1336980000	0	3	0	0	14	0.0043838800	1	1	1	1
15	0.0024115700	0	6	0	0	15	−0.0269403000	0	2	1	1
16	−0.0005300200	2	6	0	0	16	0.0558082000	3	0	1	0
17	0.1684960000	3	0	1	0	17	0.0161886000	0	3	1	0
18	0.0263454200	0	0	2	0	18	0.0031808600	1	3	1	0
19	0.0436013600	2	0	2	0	19	0.0129043500	0	0	2	0
20	−0.0311849300	3	0	2	0	20	0.0244508400	1	0	2	0
21	0.0124921500	1	6	2	0	21	0.0070064300	3	0	2	0
22	−0.0064827200	2	6	2	0	22	−0.0271904600	0	1	2	0
23	−0.0084172800	0	3	0	1	23	−0.0166458600	3	1	2	0
24	0.0168424000	1	3	0	1	24	0.0300449000	2	2	2	0
25	−0.0010229600	3	3	0	1	25	−0.0336974900	0	3	2	0
26	−0.0317791000	0	3	1	1	26	−0.0035002400	0	6	2	0
27	0.0186040000	1	0	2	1	27	−0.0106854000	3	0	0	1
28	−0.0041079800	0	2	2	1	28	0.0011090300	3	3	0	1
29	−0.0006068480	0	0	0	2	29	−0.0003139120	0	6	0	1
30	−0.0049819000	1	0	0	2	30	0.0035895000	3	0	1	1
31	0.0025963000	2	0	0	2	31	−0.0014212100	0	6	1	1
32	−0.0005605280	3	0	0	2	32	−0.0038363700	1	0	2	1
33	−0.0016365200	1	2	0	2	33	0.0126803000	0	2	2	1
34	−0.0003287870	1	6	0	2	34	−0.0031827800	2	3	2	1
35	0.0001165020	2	6	0	2	35	0.0033426800	0	6	2	1
36	0.0006909040	0	0	1	2	36	−0.0018349100	1	1	0	2
37	0.0042174900	0	3	1	2	37	0.0001124510	3	2	0	2
38	0.0000565229	3	6	1	2	38	−0.0000297228	3	6	0	2
39	−0.0014656400	0	3	2	2	39	0.0002695510	1	0	1	2
						40	0.0008326500	2	0	1	2
						41	0.0015533400	0	2	1	2
						42	0.0003026830	0	6	1	2
						43	−0.0001843000	0	0	2	2
						44	−0.0004253990	0	3	2	2
						45	0.0000869243	3	3	2	2
						46	−0.0004659000	0	6	2	2
						47	0.0000554194	1	6	2	2

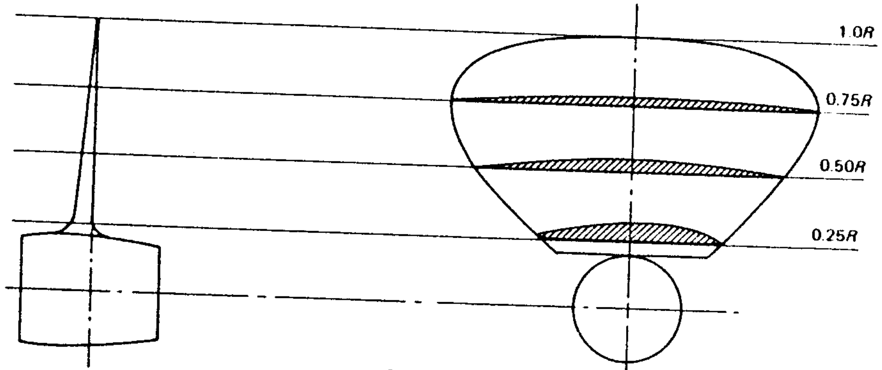

Parent	Propeller
Diameter	16.0 in
Blade thickness fraction	0.045
Boss diameter ratio	0.20
Number of blades	3
Direction of rotation	RH
Blade area ratio	0.80

Table of chord lengths							
	Non-dimensional radius						
	0.25	0.375	0.50	0.625	0.750	0.875	0.9375
$C/C_{0.50}$	0.604	0.819	1.00	1.140	1.212	1.139	0.946
	Sections symmetrical about directrix						

Figure 6.13 KCA Blade outline

additional thrust and torque data for a BAR of 1.25 and P/D of unity.

Despite a lack of data at very low advance coefficients due to the experimental limitation of the cavitation of the cavitation tunnel, the KCA series of propellers, when used in conjunction with the Gawn series, provides an immensely valuable set of data upon which to base design studies of high-speed or naval craft.

Table 6.10 Propellers of the Ma-series

Three-bladed propellers				
P/D A_E/A_O	0.75	0.90	1.05	1.20
1.000	•	•	•	•
1.150	•	•	•	•
1.300	•	•	•	•
1.450	•	•	•	•
Five-bladed propellers				
P/D A_E/A_O	0.75	0.90	1.05	1.20
1.000	•	•	•	•
1.152	•	•	•	•
1.309	•	•	•	•
1.454	•	•	•	•

6.5.5 Lindgren series (Ma-series)

Lindgren, working at SSPA in the 1950s, tested a series of three- and five-bladed propellers embracing a range of P/D ratios from 1.00 to 1.45 and developed area ratios from 0.75 to 1.20 (Reference 13). The series, designated the Ma-series, is shown in Table 6.10 from which it is seen that a total of 32 propellers were tested.

The propellers are all constant pitch with modified elliptical blade forms and sections of approximately circular black profiles. The diameter of the propellers is 250 mm, which is smaller than either of the two previous series and the boss diameter of the series is $0.19D$. The thickness fraction of this propeller series varies between the members of the series, and is shown in Table 6.11.

Table 6.11 Newton-Rader series

A_D/A_O	Blade thickness fraction	
	$Z = 3$	$Z = 5$
0.75	0.063	0.054
0.90	0.058	0.050
1.05	0.053	0.046
1.20	0.053	0.042

The propellers of this series were tested in both a towing tank and cavitation tunnel and, consequently, provide a reasonably comprehensive set of data for preliminary study purposes. The data is presented in both K_T, K_Q versus J form and also in design diagram form. Although the basic design of the Ma-series propellers can be considered to be somewhat dated, it does provide a further complementary set of data to the Gawn and Gawn–Burrill results for the design of high-performance and naval craft.

6.5.6 Newton–Rader series

The Newton–Rader series embraces a relatively limited set of twelve, three-bladed propellers intended for high-speed craft. The series (Reference 14) was designed to cover pitch ratios in the range 1.0–2.0 and blade area ratios from about 0.5 to 1.0.

The parent model of the series, based on a design for a particular vessel, had a diameter of 254 mm (10 in). The principal features of the parent design were a constant face pitch ratio of 1.2 and a blade area ratio of 0.750, together with a non-linear blade thickness distribution having a blade thickness fraction of 0.06. The blade section form was based on the NACA $a = 1.0$ mean line with a quasi-elliptic thickness form superimposed. The series was designed in such a way that the propellers in the series should have the same camber ratio distribution as the parent propeller. Since previous data and experience was limited with this type of propeller it was fully expected that the section form would need to be modified during the tests. This expectation proved correct and the section form was modified twice on the parent screw to avoid the onset of face cavitation; the modification essentially involved the cutting back and 'lifting' of the leading edge. These modifications were carried over onto the other propellers of the series, which resulted in the series having the characteristics shown in Table 6.12 and the blade form shown in Figure 6.14.

Table 6.12 Extent of the Newton–Rader series

BAR	*Face pitch ratio*			
0.48	1.05	1.26	1.67	2.08
0.71	1.05	[1.25]	1.66	2.06
0.95	1.04	1.24	1.65	2.04

Note: Box indicates resultant parent form.

Each of the propellers of the series was tested in a cavitation tunnel at nine different cavitation numbers; 0.25, 0.30, 0.40, 0.50, 0.60, 0.75, 1.00, 2.50 and 5.5. For the tests the Reynolds number ranged from about 7.1×10^5 for the narrow-bladed propeller through to 4.5×10^6 for the wide-bladed design at $0.7R$. The results of the series are presented largely in tabular form by the authors.

This series is of considerable importance for the design of propellers, usually for relatively small craft, where significant cavitation is likely to be encountered.

6.5.7 Other fixed pitch series and data

Apart from the major fixed pitch propeller series there have been numerous smaller studies which provide useful data, either for design purposes or for research or correlation studies. Amongst these other works, the KCD propeller series (References 15, 16), the Meridian series (Reference 12), the contra rotating series of MARIN and SSPA (References 17, 18) and the DTMB research skewed propeller series (Reference 19) are worthy of specific mention.

The KCD series originally comprised a series of models for which 'interesting' full-scale results were available, and the purpose of the series was to try and correlate the observed phenomena in the tunnel with the results of particular experience on ships. All the model propellers in this series had diameters of 406.4 mm (16 in) and the first three members of the series KCD 3, 4 and 5 had a blade area ratio of 0.6 in association with three, four and five blades respectively. These propellers were tested at a range of cavitation numbers in the Newcastle University tunnel in order to study the open water performance of the propellers under cavitating conditions. The results shown in Figure 6.4 relate to the KCD4 propellers of this series. After a further nine years of testing various designs (Reference 16) the series had grown to encompass some 17 members. Of these members six, including the parent KCD4R, had a common blade area ratio and blade number of 0.587 and four respectively, and a range of pitch ratios from 0.6 to 1.6. These propellers were used to define a set of K_T, K_Q versus J diagrams and B_p versus δ charts for a series of cavitation numbers of 8.0, 6.0, 4.0 and 2.0. The remaining propellers of the series were used to explore the effects of geometric changes such as moderate amounts of skew, radial pitch variations and blade outline changes on cavitation performance. Hence the series presents an interesting collection of cavitation data for merchant ship propeller designs.

The Meridian series (Reference 12), so called since it was derived from the proprietary design of Stone Manganese Marine Ltd, comprised four parent models having BARs of 0.45, 0.65, 0.85 and 1.05. For each parent model five mean pitch ratios 0.4, 0.6, 0.8, 1.0 and 1.2 were tested so as to cover the useful range of pitch ratios for each blade area ratio. All the propellers had a diameter of 304.8 mm (12 in) and six blades with a boss diameter of $0.185R$. The parent propellers are not geosims of each other and consequently interpolation between propellers of different blade area ratios for general use becomes rather more complicated than for a completely geometrically similar series. As with the KCD series this series was tested at a range of cavitation numbers resulting in the presentation of open water data in the form of K_T, K_Q diagrams and B_p-δ charts under cavitating conditions.

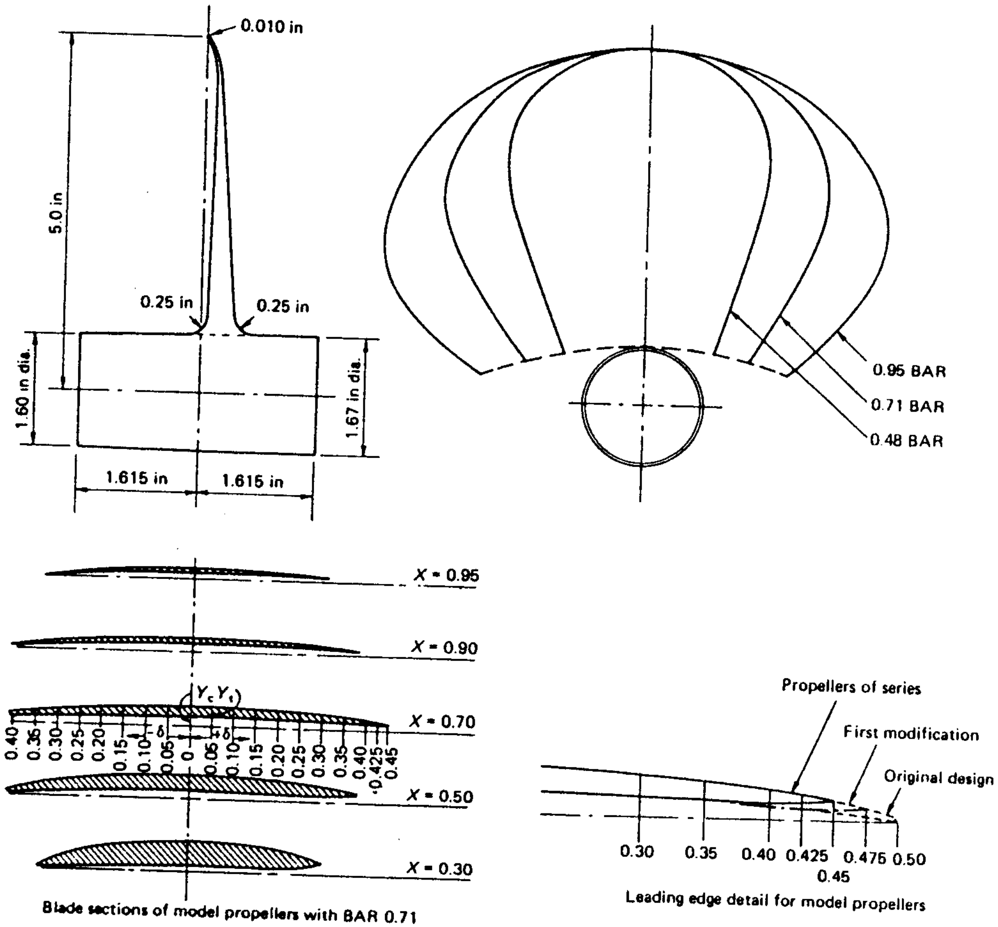

Figure 6.14 Newton–Rader series blade form (Reproduced from Reference 14, with permission)

Over the years interest has fluctuated in contra-rotating propellers as a means of ship propulsion. This has led to model tests being undertaken at variety of establishments around the world. Two examples of this are the MARIN series (Reference 17) and the SSPA series (Reference 18). The MARIN series comprised five sets of propulsors with a four-bladed forward propeller and a five-bladed aft propeller. The after propeller was designed with smaller diameter than the forward screw, the diameter reduction being consistent with the expected slip stream contraction at the design condition. The range of pitch ratios of the forward propeller at 0.7*R* spanned the range 0.627–1.235 with a constant expanded area ratio of 0.432, and clearly the after-propeller dimensions varied with respect to the flow conditions leaving the forward screw. Non-cavitating open water characteristics were presented for the series.

The SSPA series (Reference 18) comprised a family of contra-rotating propellers having a forward propeller of four blades with a developed area ratio of 0.40 and an aft propeller of five blades with a developed area ratio of 0.5. The forward propellers all had diameters of 250 mm and used section forms constructed from NACA 16 profiles and $a = 0.8$ mean lines. The pitch ratios of the leading propeller ranged from 0.8 to 1.4 and the tests were conducted in the SSPA No. 1 cavitation tunnel. Consequently, open water data is presented along with design diagrams, together with some cavitation data in homogeneous flow.

Boswell (Reference 19) presented cavitation tunnel and open water results for a series of skewed propellers. The series comprised four propellers having maximum projected skew angles of 0°, 36°, 72° and 108° at the propeller tip. The propellers each had a diameter of 304.8 mm (12 in), five blades, an A_E/A_O of 0.725, and NACA $a = 0.8$ mean lines with 66 modified profiles, similar chordal and thickness distributions and the same design conditions; they were given the NSRDC designation of propellers 4381 (0° skew), 4382 (36° skew), 4383 (72° skew) and 4384 (108° skew). The geometry of this series of propellers, in view of their importance in propeller research, is given in Table 6.13. For each of these propellers open water K_T, K_Q versus J results are presented together with cavitation inception speed. These propellers, although giving certain useful information about the effects of skew, find their greatest use as research propellers for comparing the results of theoretical methods and studies. Indeed these propellers have found widespread application in many areas of propeller technology.

Table 6.13 Blade geometry of DTNSRDC propellers 4381, 4382, 4383 and 4384 (taken from Reference 43, Chapter 8)

Characteristics of DTNSRDC propeller 4381

Number of blades, Z: 5
Hub diameter ratio: 0.2
Expanded area ratio: 0.725
Section mean line: NACA $a = 0.8$
Section thickness distribution: NACA 66 (modified)
Design advance coefficient, J_A: 0.889

r/R	c/D	P/D	θ_s (deg)	X_s/D	t_0/D	f_0/c
0.2	0.174	1.332	0	0	0.0434	0.0351
0.25	0.202	1.338	0	0	0.0396	0.0369
0.3	0.229	1.345	0	0	0.0358	0.0368
0.4	0.275	1.358	0	0	0.0294	0.0348
0.5	0.312	1.336	0	0	0.0240	0.0307
0.6	0.337	1.280	0	0	0.0191	0.0245
0.7	0.347	1.210	0	0	0.0146	0.0191
0.8	0.334	1.137	0	0	0.0105	0.0148
0.9	0.280	1.066	0	0	0.0067	0.0123
0.95	0.210	1.031	0	0	0.0048	0.0128
1.0	0	0.995	0	0	0.0029	–

Characteristics of DTNSRDC propeller 4382

Number of blades, Z: 5
Hub diameter ratio: 0.2
Expanded area ratio: 0.725
Section mean line: NACA $a = 0.8$
Section thickness distribution: NACA 66 (modified)
Design advance coefficient, J_A: 0.889

r/R	c/D	P/D	θ_s (deg)	X_s/D	t_0/D	f_0/c
0.2	0.174	1.455	0	0	0.0434	0.0430
0.25	0.202	1.444	2.328	0.0093	0.0396	0.0395
0.3	0.229	1.433	4.655	0.0185	0.0358	0.0370
0.4	0.275	1.412	9.363	0.0367	0.0294	0.0344
0.5	0.312	1.361	13.948	0.0527	0.0240	0.0305
0.6	0.337	1.285	18.378	0.0656	0.0191	0.0247
0.7	0.347	1.200	22.747	0.0758	0.0146	0.0199
0.8	0.334	1.112	27.145	0.0838	0.0105	0.0161
0.9	0.280	1.027	31.575	0.0901	0.0067	0.0134
0.95	0.210	0.985	33.788	0.0924	0.0048	0.0140
1.0	0	0.942	36.000	0.0942	0.0029	

Characteristics of DTNSRDC propeller 4383

Number of blades, Z: 5
Hub diameter ratio: 0.2
Expanded area ratio: 0.725
Section mean line: NACA $a = 0.8$
Section thickness distribution: NACA 66 (modified)
Design advance coefficient, J_A: 0.889

r/R	c/D	P/D	θ_s (deg)	X_s/D	t_0/D	f_0/c
0.2	0.174	1.566	0	0	0.0434	0.0402
0.25	0.202	1.539	4.647	0.0199	0.0396	0.0408
0.3	0.229	1.512	9.293	0.0390	0.0358	0.0407
0.4	0.275	1.459	18.816	0.0763	0.0294	0.0385
0.5	0.312	1.386	27.991	0.1078	0.0240	0.0342
0.6	0.337	1.296	36.770	0.1324	0.0191	0.0281
0.7	0.347	1.198	45.453	0.1512	0.0146	0.0230
0.8	0.334	1.096	54.245	0.1651	0.0105	0.0189
0.9	0.280	0.996	63.102	0.1745	0.0067	0.0159
0.95	0.210	0.945	67.531	0.1773	0.0048	0.0168
1.0	0	0.895	72.000	0.1790	0.0029	

Characteristics of DTNSRDC propeller 4384

Number of blades, Z: 5
Hub diameter ratio: 0.2
Expanded area ratio: 0.725
Section mean line: NACA $a = 0.8$
Section thickness distribution: NACA 66 (modified)
Design advance coefficient, J_A: 0.889

r/R	c/D	P/D	θ_s (deg)	X_s/D	t_0/D	f_0/c
0.2	0.174	1.675	0	0	0.0434	0.0545
0.25	0.202	1.629	6.961	0.0315	0.0396	0.0506
0.3	0.229	1.584	13.921	0.0612	0.0358	0.0479
0.4	0.275	1.496	28.426	0.1181	0.0294	0.0453
0.5	0.312	1.406	42.152	0.1646	0.0240	0.0401
0.6	0.337	1.305	55.199	0.2001	0.0191	0.0334
0.7	0.347	1.199	68.098	0.2269	0.0146	0.0278
0.8	0.334	1.086	81.283	0.2453	0.0105	0.0232
0.9	0.280	0.973	94.624	0.2557	0.0067	0.0193
0.95	0.210	0.916	101.300	0.2578	0.0048	0.0201
1.0	0	0.859	108.000	0.2578	0.0029	

6.5.8 Tests with propellers having significant shaft incidence

As discussed earlier in this chapter, the effects of operating a propeller at an oblique angle to the incident flow introduce significant side forces and thrust eccentricity. Several experimental studies into this effect have been undertaken, and notable in this respect are those by Gutsche (Reference 20), Taniguchi *et al.*

(Reference 21), Bednarzik (Reference 22), Meyne and Nolte (Reference 23) and Peck and Moore (Reference 24).

Gutsche worked with a series of six three-bladed propellers: three having developed area ratios of 0.35 and the others 0.80 each in association with three pitch ratios: 0.5, 1.0 and 1.5. The propellers, all having a diameter of 200 mm, were tested at shaft angle inclinations of 0°, 10°, 20° and 30° over a range of approximately 0–100% slip in the non-inclined shaft angle position.

Taniguchi *et al.* (Reference 21) used a series of five three-bladed propellers having a diameter of 230 mm. Three of the propellers had a pitch ratio of 1.286 whilst the remaining two had pitch ratios at 0.7*R* of 1.000 and 1.600. For the three propellers embracing the range of pitch ratios the expanded area ratio was held constant at 0.619, whilst for the three propellers having the same pitch ratio the expanded area ratio was varied as follows: 0.619, 0.514 and 0.411. All of the propellers had Tulin supercavitating sections. Results of K_Q and K_T are presented for six cavitation numbers, each at three angles of incidence: 0°, 4° and 8°. No side force or eccentricity data is given.

Bednarzik (Reference 22) uses a similar test series arrangement to Taniguchi in that three of his propel-

Table 6.14 Ducted propeller configurations tested at MARIN forming the ducted propeller series (taken from Reference 26)

Nozzle no.	*L/D*	*S/L*	*Open water test*	*Multi-quadrant* 2Q meas.	*Multi-quadrant* 4Q meas.	*Azimuth* ⊙
2	0.67	0.15	B 4-55			
3	0.50	0.15	B 4-55			
4	0.83	0.15	B 4-55			
5	0.50	0.15	B 4-55			
6	0.50	0.15	B 4-55			
7	0.50	0.15	B 4-55			
7	0.50	0.15	B 4-40			
7	0.50	0.15	B 4-70			
7	0.50	0.15	B 2-30			
7	0.50	0.15	B 3-50			
7	0.50	0.15	B 5-60			
8	0.50	0.15	B 4-55			
10	0.40	0.15	B 4-55			
11	0.30	0.15	B 4-55			
18	0.50	0.15	K 4-55			
19	0.50	0.15	K 4-55			
20	0.50	0.15	K 4-55			
19A	0.50	0.15	Ka 3-50*			
19A	0.50	0.15	Ka 3-65*			
19A	0.50	0.15	Ka 4-55*			
19A	0.50	0.15	Ka 4-70*	Ka 4-70*	Ka 4-70*	Ka 4-70
19A	0.50	0.15	Ka 5-75*			
19A	0.50	0.15	B 4-70*			
21	0.70	0.15	Ka 4-70*			
22	0.80	0.15	Ka 4-70*			
23	0.90	0.15	Ka 4-70*			
24	1.00	0.15	Ka 4-70*			
37	0.50	0.15	Ka 4-70*	Ka 4-70*	Ka 4-70*	
30	0.60	0.15	Kd 5-100			
31	0.60	0.15	Kd 5-100			
32	0.60	0.15	Kd 5-100			
33	0.60	0.15	Kd 5-100			
34	0.60	0.09	Kd 5-100			
35	0.9	0.1125	Kd 5-100			
36	1.2	0.0750	Kd 5-100			

* Mathematical representation of test data available.
Tests at different incidence angles.

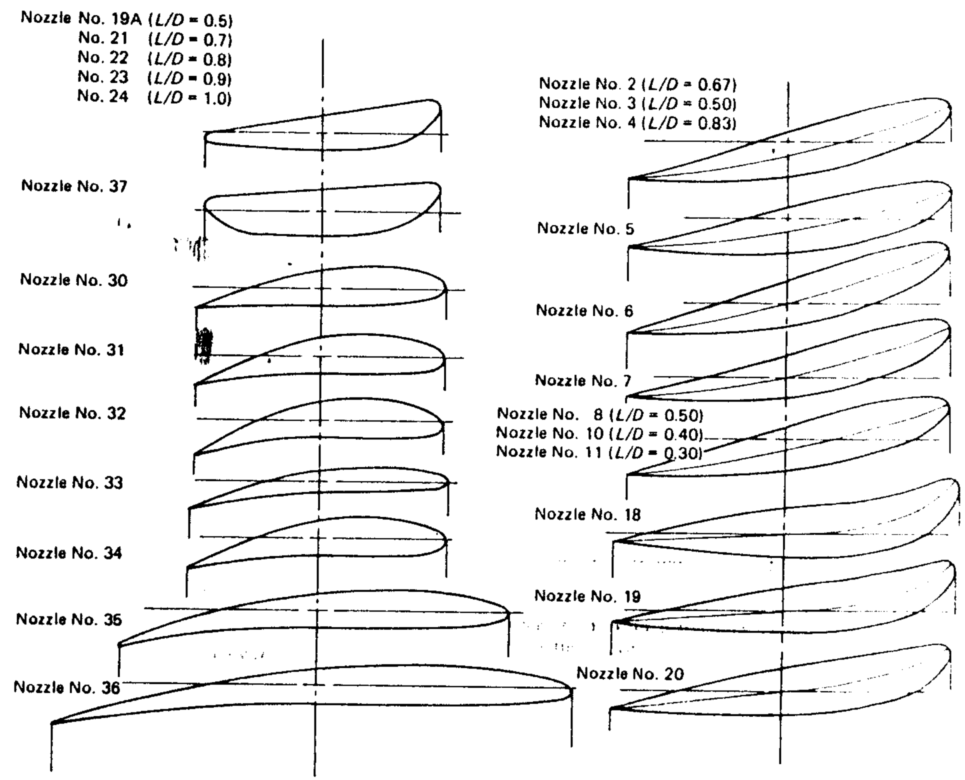

Figure 6.15 Duct outlines described in Table 6.14 (Reproduced from Reference 26, with permission)

ler series have the same pitch ratio of 0.60 with varying developed area ratios of 0.35, 0.55 and 0.75. Each of the remaining two propellers has a developed area ratio of 0.55, but pitch ratios of 1.00 and 1.40 respectively. The propeller diameters are all 260 mm and each has three blades with a hub-to-tip diameter ratio of 0.3. The propellers are tested over a range of shaft inclinations of 0°, 5°, 15° and 25° with side force and eccentricity data being presented in addition to conventional K_Q and K_T coefficients.

Meyne and Nolte (Reference 23) considered a 355.46 mm diameter, four-bladed propeller having a hub ratio of 0.328*R* and an expanded blade area ratio of 0.566. The pitch ratio of the propeller was varied from 1.0 to 1.6 in a single step and tests were made with shaft inclination of 0°, 6°, 9° and 12°. Results of K_Q, K_T, side force and eccentricity are given by the authors.

Peck and Moore (Reference 24) used four 254 mm (10 in) diameter, four-bladed propellers having nominal pitch ratios of 0.8, 1.0, 1.2 and 1.4 respectively. Measurements were made over a range of cavitation numbers at 0°, 7.5° and 15° shaft inclinations and side force data is presented in addition to the other performance data.

6.5.9 Wageningen ducted propeller series

A very extensive set of ducted propeller standard series tests has been conducted at MARIN in the Netherlands over the years and these have been reported in several publications. The best source material for this series can be found in References 25 and 26.

The extent of the series can be judged from Table 6.14 which itemizes the tests conducted within this series, whilst Figure 6.15 shows the profiles of the various duct forms tested. In general it can be considered that ducts No. 2 through No. 24 and No. 37 represent accelerating ducts whilst those numbered

Table 6.15 Duct ordinates for 19A and 37 duct forms

Duct profile No. 19A

	L.E.																	T.E.
x/L	0	0.0125	0.025	0.050	0.075	0.100	0.150	0.200	0.25	0.30	0.40	0.50	0.60	0.70	0.80	0.90	0.95	1.00
y_i/L	0.1825	0.1466	0.1280	0.1087	0.0800	0.0634	0.0387	0.0217	0.0110	0.0048	0	0	0	0.0029	0.0082	0.0145	0.0186	0.0236
y_u/L		0.2072	0.2107	0.2080	Straight line													0.0636

Duct profile No. 37

	L.E.																	T.E.
x/L	0	0.0125	0.025	0.050	0.075	0.100	0.150	0.200	0.25	0.30	0.40	0.50	0.60	0.70	0.80	0.90	0.95	1.00
y_i/L	0.1833	0.1500	0.1310	0.1000	0.0790	0.0611	0.0360	0.0200	0.0100	0.0040	0	0	0	0.0020	0.0110	0.0380	0.0660	0.1242
y_u/L	0.1833	0.2130	0.2170	0.2160	Straight line												0.1600	0.1242

Duct upper ordinate = propeller radius + clearance + y_u.
Duct inner ordinate = propeller radius + tip clearance + y_i.

Table 6.16 Details of the K_a series propellers (taken from Reference 26)

Dimensions of the K_a-screw series

	r/R	0.2	0.3	0.4	0.5	0.6	0.7	0.8	0.9	1.0	
Length of the blade sections in percentages of the maximum length of the blade section at 0.6R	from centre line to trailing edge	30.21	36.17	41.45	45.99	49.87	52.93	55.04	56.33	56.44	Length of blade section at 0.6R $= 1.969 \frac{1}{Z} \frac{A_E}{A_0}$
	from centre line to leading edge	36.94	40.42	43.74	47.02	50.13	52.93	55.04	56.33	56.44	
	total length	67.15	76.59	85.19	93.01	100.00	105.86	110.08	112.66	122.88	
Max. blade thickness in percentages of the diam.		4.00	3.52	3.00	2.45	1.90	1.38	0.92	0.61	0.50	Maximum thickness at centre of shaft = 0.049D
Distance of maximum thickness from leading edge in percentages of the length of the sections		34.98	39.76	46.02	49.13	49.98	—	—	—	—	

Ordinates of the K_a-screw series

	Distance of the ordinates from the maximum thickness											
	From maximum thickness to trailing edge					*From maximum thickness to leading edge*						
r/R	100%	80%	60%	40%	20%	20%	40%	60%	80%	90%	95%	100%
	Ordinates for the back											
0.2	—	38.23	63.65	82.40	95.00	97.92	90.83	77.19	55.00	38.75	27.40	—
0.3	—	39.05	66.63	84.14	95.86	97.63	90.06	75.62	53.02	37.87	27.57	—
0.4	—	40.56	66.94	85.69	96.25	97.22	88.89	73.61	50.00	34.72	25.83	—
0.5	—	41.77	68.59	86.42	96.60	96.77	87.10	70.46	45.84	30.22	22.24	—
0.6	—	43.58	68.26	85.89	96.47	96.47	85.89	68.26	43.58	28.59	20.44	—
0.7	—	45.31	69.24	86.33	96.58	96.58	86.33	69.24	45.31	30.79	22.88	—
0.8	—	48.16	70.84	87.04	96.76	96.76	87.04	70.84	48.16	34.39	26.90	—
0.9	—	51.75	72.94	88.09	97.17	97.17	88.09	72.94	51.75	38.87	31.87	—
1.0	—	52.00	73.00	88.00	97.00	97.00	88.00	73.00	52.00	39.25	32.31	—
	Ordinates for the face											
0.2	20.21	7.29	1.77	0.1	—	0.21	1.46	4.37	10.52	16.04	20.62	33.33
0.3	13.85	4.62	1.07	—	—	0.12	0.83	2.72	6.15	8.28	10.30	21.18
0.4	9.17	2.36	0.56	—	—	—	0.42	1.39	2.92	3.89	4.44	13.47
0.5	6.62	0.68	0.17	—	—	—	0.17	0.51	1.02	1.36	1.53	7.81

Note: The percentages of the ordinates relate to the maximum thickness of the corresponding section.

30–36 represent decelerating duct forms. In merchant practice the ducts most commonly encountered are the 19A and 37 since they are both relatively easy to fabricate and have many desirable hydrodynamic features. Ease of fabrication of the duct is essential; the feature which helps this significantly is the use of straight lines, wherever possible, in the profiles shown in Figure 6.15. The profile ordinates of Ducts No. 19A and No. 37 are given in Table 6.15. Three principal propeller types have been used; the B series propeller in ducts Nos. 2–11, the K_a series propellers in ducts Nos. 1–24 and No. 37 with limited work using the B series propeller for duct 19A, and the K_d series propeller for ducts Nos. 30–36. The details of the K_a series propellers are reproduced in Table 6.16, and Figure 6.16 shows the general forms of the propellers for this series. These propellers have a diameter of 240 mm.

Typical of the results derived from this series are the characteristics shown in Figure 6.8. However, regression polynomials have been developed to express K_T, K_{TN} and K_Q as functions of P/D and J. The form of the polynomials is as follows:

$$
\begin{aligned}
K_T = A_{0,0} &+ A_{0,1} J + \cdots + A_{0,6} J^6 \\
&+ A_{1,0}\left(\frac{P}{D}\right) + A_{1,1}\left(\frac{P}{D}\right) J + \cdots + A_{1,6}\left(\frac{P}{D}\right) J^6 \\
&+ A_{2,0}\left(\frac{P}{D}\right)^2 + A_{2,1}\left(\frac{P}{D}\right)^2 J + \cdots + A_{2,6}\left(\frac{P}{D}\right)^2 J^6 \\
&\cdots\cdots\cdots\cdots\cdots\cdots \\
&+ A_{6,0}\left(\frac{P}{D}\right)^6 + A_{6,1}\left(\frac{P}{D}\right)^6 J + \cdots + A_{6,6}\left(\frac{P}{D}\right)^6 J^6 \\
K_{TN} = B_{0,0} &+ B_{0,1} J + \cdots \\
&+ B_{6,6}\left(\frac{P}{D}\right)^6 J^6 \\
K_Q = C_{0,0} &+ C_{0,1} J + \cdots \\
&+ C_{6,6}\left(\frac{P}{D}\right)^6 J^6
\end{aligned}
\tag{6.19}
$$

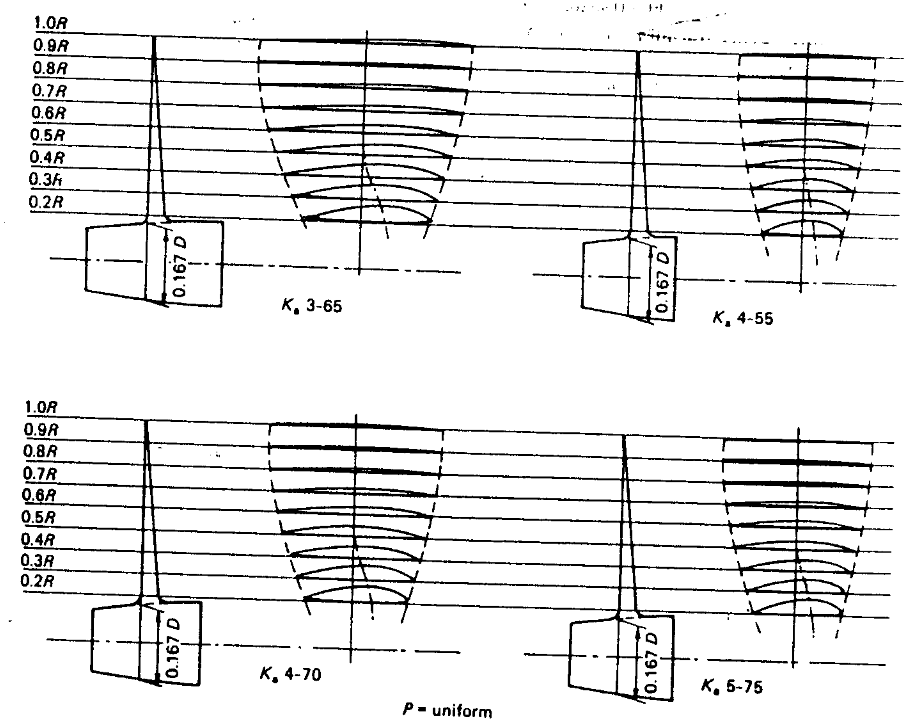

Figure 6.16 General outline of the K_a series propeller (Reproduced from Reference 26, with permission)

Table 6.17 Coefficients for duct nos. 19A and 37 for equation (6.19) – K_a propeller 4-70 (taken from Reference 26)

	x	y	Nozzle no. 19A			Nozzle no. 37		
			Axy	Bxy	Cxy	Axy	Bxy	Cxy
0	0	0	+0.030550	+0.076594	+0.006735	−0.0162557	−0.016806	+0.016729
1		1	−0.148687	+0.075223				
2		2		−0.061881	−0.016306			
3		3	−0.391137	−0.138094				
4		4			−0.007244			
5		5		−0.370620				
6		6		+0.323447			−0.099544	+0.030559
7	1	0		−0.271337		−0.598107		0.048424
8		1	−0.432612	−0.687921		−1.009030	−0.548253	−0.011118
9		2		+0.225189	−0.024012		+0.230675	−0.056199
10		3						
11		4						
12		5						
13		6		−0.081101				
14	2	0	+0.667657	+0.666028		+0.085087	+0.460206	+0.083476
15		1				+0.425585		
16		2	+0.285100	+0.734285	+0.005193			+0.045637
17		3						−0.042003
18		4						
19		5						
20		6						
21	3	0	−0.172529	−0.202467	+0.046605		−0.216246	−0.008652
22		1						
23		2		−0.542490				
24		3						
25		4						
26		5				−0.021044		
27		6		−0.016149				
28	4	0			−0.007366		+0.042997	
29		1						
30		2						
31		3		+0.099819				
32		4						
33		5						
34		6						
35	5	0						
36		1		+0.030084		−0.038383		
37		2						
38		3						
39		4						
40		5						
41		6						
42	6	0			−0.001730			
43		1	−0.017283		−0.000337			−0.001176
44		2		−0.001876	+0.000861	+0.014992		+0.002441
45		3						
46		4						
47		5						
48		6						
49	0	7				+0.036998	+0.051753	−0.012160

where the coefficients A, B and C are given in Table 6.17 for the 19A and 37 duct profiles with the K_a 4-70 propeller.

6.5.10 Gutsche and Schroeder controllable pitch propeller series

The Gutsche and Schröeder propeller series (Reference 27) comprises a set of five three-bladed controllable pitch propellers. The propellers were designed according to the Gawn series (Reference 9) with certain modifications; these were that the blade thickness fraction was reduced to 0.05 and the inner blade chord lengths were restricted to allow the blades to be fully reversing. Additionally the boss radius was increased to $0.25D$ in order to accommodate the boss actuating mechanism.

The propeller series was designed to have a diameter of 200 mm and three of the propellers were produced with a design P/D of 0.7 and having varying developed area ratios of 0.48, 0.62 and 0.77. The remaining two propellers of the series had blade area ratios of 0.62 with design pitch ratios of 0.5 and 0.9. The three propellers with a design P/D of 0.7 were tested for both positive and negative advance speed over a range of pitch ratios at $0.7R$ of 1.5, 1.25, 1.0, 0.75, 0.5, 0, −0.5, −0.75 and −1.00. The remaining two propellers of the series were tested at the limited P/D range of 1.00, 0.50, −0.50 and −1.00.

6.5.11 The JD–CPP series

The JD-CPP series is also a three-bladed controllable pitch series comprising 15 model propellers each having a diameter of 267.9 mm. The propellers are split into three groups of five having expanded area ratios of 0.35, 0.50 and 0.65. The propellers all have a boss diameter of $0.28D$ and each of the members of the expanded area groups have design pitch ratios of 0.4, 0.5, 0.8, 1.0 and 1.2 respectively. As in the case of the Gutsche series the blade thickness fraction is 0.05. The blade design pitch distribution is constant from the tip to $0.6R$ but is reduced in the inner region of the blade near the root.

The propeller series, presented by Chu *et al.* (Reference 28), was tested at the Shanghai Jiao Tong University and measurements were made over a range of 50° of pitch change distributed about the design pitch setting. Results are presented for thrust, torque and hydrodynamic spindle torque coefficient for the series in non-cavitating conditions. The range of conditions tested extend to both positive and negative advance coefficients. Hence, by including spindle torque data this series is one of the most complete for controllable pitch propeller hydrodynamic study purposes and to aid studies polynomial regression coefficients have also been given by the authors.

6.5.12 Other controllable pitch propeller series tests

In general the open water characteristics of controllable pitch propeller series have been very largely neglected in the open literature. This is particularly true of the spindle torque characteristics. Apart from the two series mentioned above which form the greatest open literature data source for controllable pitch propellers in off-design conditions, there have been other limited amounts of test data presented. Amongst these are Yazaki (Reference 29), Hansen (Reference 30) and Miller (Reference 31). Model tests with controllable pitch propellers in the Wageningen duct forms 19A, 22, 24, 37 and 38 are presented in Reference 40.

6.6 Multi-quadrant series data

So far in this chapter discussion has centred on the first quadrant performance of propellers. That is for propellers working with positive rotational speed and forward or zero advance velocity. This clearly is the conventional way of operating a propeller, but for studying manoeuvering situations or astern performance of vessels other data is required.

In the case of the fixed pitch propeller it is possible to define four quadrants based on an advance angle

$$\beta = \tan^{-1}\left(\frac{V_a}{0.7\pi n D}\right) \tag{6.20}$$

as follows:

1st quadrant: Advance speed —ahead
Rotational speed—ahead
This implies that the advance angle β varies within the range $0 \leqslant \beta \leqslant 90°$

2nd quadrant: Advance speed —ahead
Rotational speed—astern
In this case β lies in the range $90° < \beta \leqslant 180°$

3rd quadrant: Advance speed —astern
Rotational speed—astern
Here β lies in the range of $180° < \beta \leqslant 270°$

4th quadrant: Advance speed —astern
Rotational speed—ahead
Where β is within the range $270° < \beta \leqslant 360°$

Provided sufficient experimental data is available it becomes possible to define a periodic function based on the advance angle β to define the thrust and torque characteristics of the propeller in each of the quadrants. In this context it should be noted that when $\beta = 0$

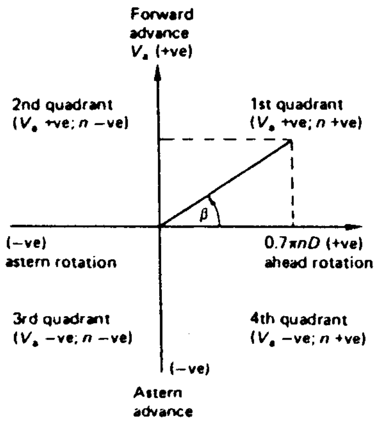

Figure 6.17 Four-quadrant notation

or 360° then this defines the ahead bollard pull condition and when $\beta = 180°$ this corresponds to the astern bollard pull situation. For $\beta = 90°$ and 270°, these positions relate to the condition when the propeller is not rotating and is being dragged ahead or astern through the water respectively. Figure 6.17 assists in clarifying this notation for fixed pitch propellers.

For multi-quadrant studies the advance angle notation offers a considerably more flexible representation than the conventional advance coefficient J; since when the propeller RPM is 0, such as when $\beta = 90°$ or 270°, then $J \to \infty$. Similarly, the thrust and torque coefficients need to be modified in order to prevent similar problems from occurring and the following are derived:

$$C_T^* = \frac{T}{\frac{1}{2}\rho V_r^2 A_O}$$

and

$$C_Q^* = \frac{Q}{\frac{1}{2}\rho V_r^2 A_O D}$$

where V_r is the relative advance velocity at the 0.7R blade section. Consequently, the above equations can be written explicitly as

$$\left.\begin{aligned} C_T^* &= \frac{T}{(\pi/8)\rho[V_a^2 + (0.7\pi nD)^2]D^2} \\ \text{and} \\ C_Q^* &= \frac{Q}{(\pi/8)\rho[V_a^2 + (0.7\pi nD)^2]D^3} \end{aligned}\right\} \quad (6.21)$$

Note the asterisks in equations (6.21) are used to avoid confusion with the free stream velocity based thrust and torque coefficients C_T and C_Q defined in equations (6.4)–(6.6).

Results plotted using these coefficients take the form shown in Figures 6.18–6.20 for the Wageningen B4-70 screw propeller series. These curves, as can be seen, are periodic over the range $0° \leqslant \beta \leqslant 360°$ and, therefore, lend themselves readily to a Fourier type representation. Van Lammeren *et al.* (Reference 6) suggests a form:

$$\left.\begin{aligned} C_T^* &= \sum_{k=0}^{20} [A_k \cos(k\beta) + B_k \sin(k\beta)] \\ C_Q^* &= \sum_{k=0}^{20} [A_k \cos(k\beta) + B_k \sin(k\beta)] \end{aligned}\right\} \quad (6.22)$$

When evaluating the off-design characteristics by open water data it is important to endeavour to find data from a model which is close to the design under consideration. From the Wageningen data it will be seen that blade area ratio has an important influence on the magnitude of C_T^* and C_Q^* in the two regions $40° < \beta < 140°$ and $230° < \beta < 340°$. In these regions the magnitude of C_Q^* can vary by as much as a factor of 3, at model scale, for a blade area ratio change from 0.40 to 1.00. Similarly, the effect of pitch ratio will have a considerable influence on C_Q^* over almost the entire range of β as seen in Figure 6.18. Blade number does not appear to have such pronounced effects as pitch ratio or expanded area ratio and, therefore, can be treated as a less significant variable.

Apart from the Wageningen B screw series there have over the years been other studies, undertaken on propellers operating in off-design conditions. Notable amongst these are Conn (Reference 32) and Nordstrom (Reference 33); these latter works, however, are considerably less extensive than the Wageningen data cited above.

With regard to ducted propellers a twenty-term Fourier representation has been undertaken (Reference 25) for the 19A and 37 ducted systems when using the K_a 4.70 propeller and has been shown to give a satisfactory correlation with the model test data. Consequently, as with the case of the non-ducted propellers the coefficients C_T^*, C_Q^* and C_{TN}^* are defined as follows:

$$\left\{\begin{matrix} C_T^* \\ C_Q^* \\ C_{TN}^* \end{matrix}\right\} = \sum_{k=0}^{20} [A_k \cos(k\beta) + B_k \sin(k\beta)] \quad (6.23)$$

The corresponding tables of coefficients are reproduced from (Reference 25) in Tables 6.18 and 6.19 for the 19A and 37 ducts respectively.

As might be expected the propeller, in this case the $K_a = 4$–70, still shows the same level of sensitivity to P/D, and almost certainly to $A_E A_O$, with β as did the non-ducted propellers; however, the duct is comparatively insensitive to variations in P/D except in the region $-20° \leqslant \beta \leqslant 20°$.

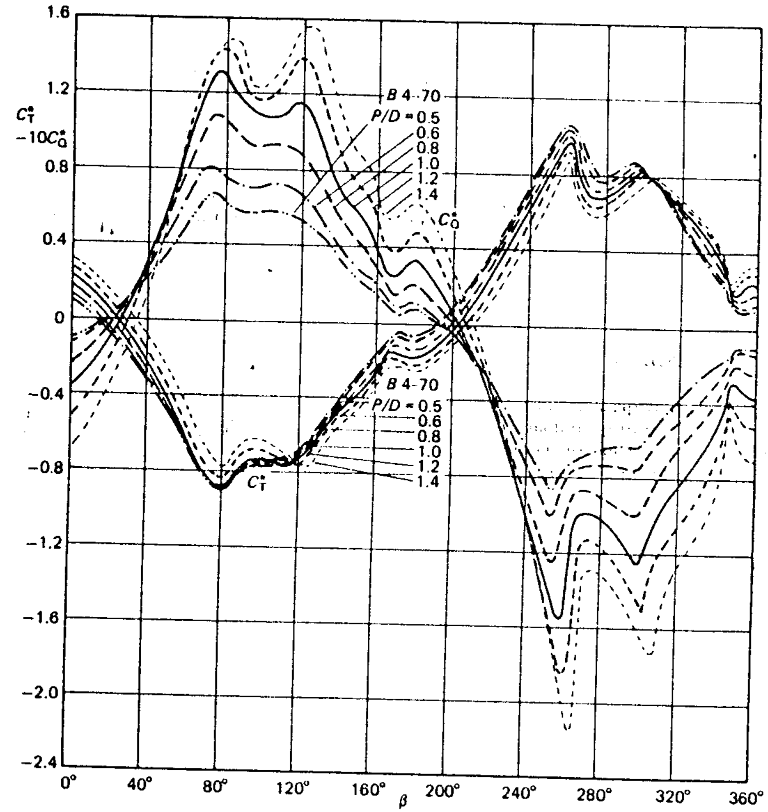

Figure 6.18 Open water test results with B 4-70 screw series in four quadrants (Reproduced from Reference 6)

Full details of the Wageningen propeller series can be found in Reference 40 which includes a diskette containing the data and computer programs to perform calculations based on the various propeller series.

In the case of the controllable pitch propeller the number of quadrants reduces to two since this type of propeller is unidirectional in terms of rotational speed. Using the fixed pitch definition of quadrants the two of interest for controllable pitch propeller work are the first and fourth, since the advance angle lies in the range $90° \leqslant \beta \leqslant -90°$. As discussed earlier, the amount of standard series data for controllable pitch propellers in the public domain is comparatively small; the work of Gutsche and Schroeder (Reference 27), Yazaki (Reference 29) being perhaps the most prominent. Strom-Tejsen and Porter (Reference 34) undertook an analysis of the Gutsche Schroeder three-bladed c.p.p. series, and by applying regression methods to the data derived equations of the form:

$$\left.\begin{matrix} C_T^* \\ C_Q^* \end{matrix}\right\} = \sum_{l=0}^{L} R_{l,2}(z) \sum_{m=0}^{M} P_{m,10}(y) \sum_{n=0}^{N} \times \{a_{l,m,n}\cos(n\beta) + b_{l,m,n}\sin(n\beta)\} \quad (6.24)$$

where $y = \{[P_{0.7}/D]_{set} + 1.0\}/0.25$

and $z = (A_D/A_O - 0.50)/0.15$

and $R_{l,2}(z)$ and $P_{m,10}(y)$ are orthogonal polynomials defined by

$$P_{m,n}(x) = \sum_{k=0}^{m} (-1)^k \binom{m}{k}\binom{m+k}{k} \frac{x^{(k)}}{n^{(k)}}$$

The coefficients a and b of equation (6.24) are defined in Table 6.20 for use in the equations; however,

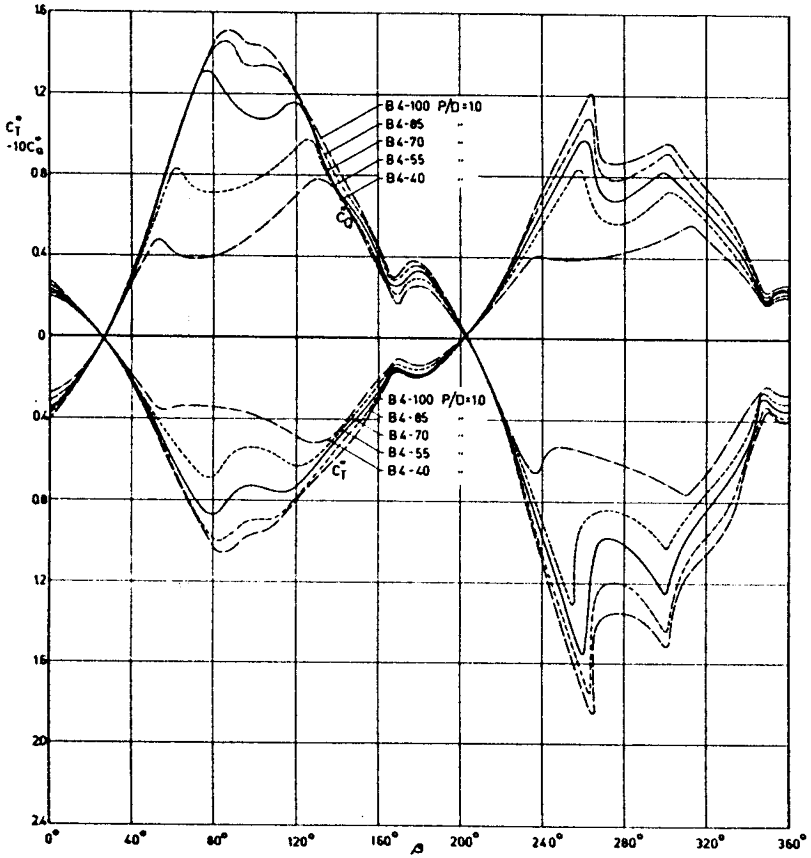

Figure 6.19 Open water test results with B4 screw series and $P/D = 1.0$ in four quadrants (Reproduced from Reference 6)

it has been found that it is unnecessary for most purposes to use the entire table of coefficients and that fairing based on $L = 2$, $M = 4$ and $N = 14$ provides sufficient accuracy.

6.7 Slipstream contraction and flow velocities in the wake

When a propeller is operating in open water the slipstream will contract uniformly as shown in Figure 6.21(a). This contraction is due to the acceleration of the fluid by the propeller and, consequently, is dependent upon the thrust exerted by the propeller. The greater the thrust produced by the propeller for a given speed of advance, the more the slipstream will contract.

Nagamatsu and Sasajima studied the effect of contraction through the propeller disc (Reference 35) and concluded that the contraction could be represented to a first approximation by the simple momentum theory relationship:

$$\frac{D_o}{D} = [0.5(1 + (1 + C_T)^{1/2})]^{1/2} \qquad (6.25)$$

where D_o is diameter of the slipstream far upstream
D is diameter of the propeller disc
C_T is the propeller thrust coefficient.

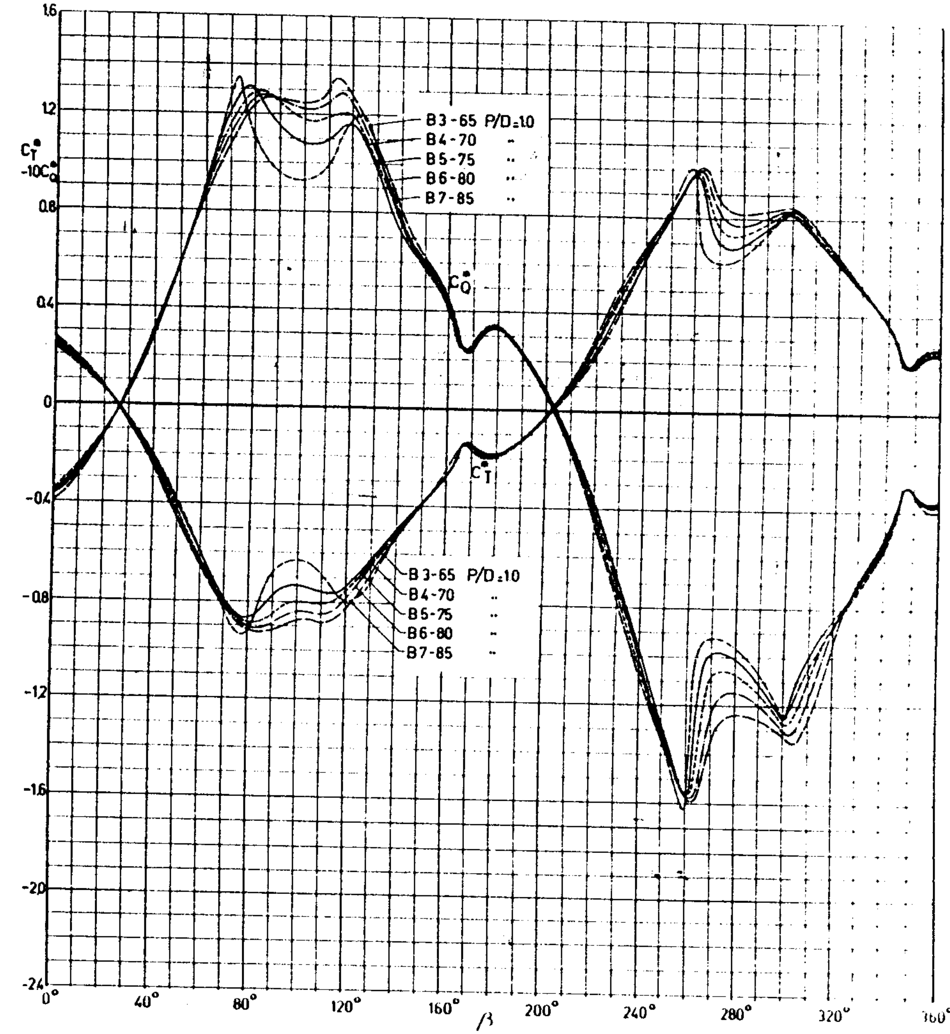

Figure 6.20 Open water test results with B series propellers of variable blade number, approximately similar blade area ratio and $P/D = 1.0$ (Reproduced from Reference 6)

Table 6.18 Fourier coefficients for K_s 4-70 propeller in 19A duct (Oosterveld [25])

	K	P/D = 0.6 A(K)	P/D = 0.6 B(K)	P/D = 0.8 A(K)	P/D = 0.8 B(K)	P/D = 1.0 A(K)	P/D = 1.0 B(K)	P/D = 1.2 A(K)	P/D = 1.2 B(K)	P/D = 1.4 A(K)	P/D = 1.4 B(K)
	0	−0.14825E 0	+0.00000E+0	−0.13080F 0	+0.00000E+0	−0.10985F 0	+0.00000F+0	−0.90888F −1	+0.00000F+0	−0.73487E−1	+0.00000E+0
	1	+0.84697E−1	−0.10838E+1	+0.10985E 0	−0.10708E+1	+0.14064E 0	−0.10583E+1	+0.17959E 0	−0.11026E+1	+0.22861E 0	−0.98101E 0
	2	+0.16700E 0	−0.18023E−1	+0.15810E 0	+0.24163E−1	+0.15785E 0	+0.47284E−1	+0.14956E 0	+0.61459E−1	+0.14853E 0	+0.71510E−1
	3	+0.96610E−3	+0.11825E 0	+0.18367E−1	+0.12784E 0	+0.45544E−1	+0.13126E 0	+0.65675E−1	+0.13715E 0	+0.75328E−1	+0.14217E 0
	4	+0.14754E−1	−0.70713E−2	+0.16168E−1	−0.14064E−2	+0.51639E−2	−0.77539E−2	+0.52107E−2	−0.17280E−1	+0.34084E−2	−0.22675E−1
	5	−0.11806E−1	+0.62894E−1	−0.37402E−2	+0.76213E−1	−0.25560E−2	+0.93507E−1	−0.68232E−2	+0.96379E−1	−0.11643E−2	+0.91082E−1
	6	−0.14888E−1	+0.11519E−1	−0.11736E−1	+0.13259E−1	−0.60502E−2	+0.92520E−2	−0.62896E−2	+0.58809E−2	+0.18576E−3	−0.40283E−2
	7	+0.73311E−2	+0.17070E−2	+0.25483E−2	−0.42300E−2	+0.67368E−2	−0.14828E−1	+0.18178E−1	−0.22587E−1	+0.26970E−1	−0.22759E−1
	8	+0.75022E−2	+0.22990E−2	+0.12350E−2	−0.26246E−2	+0.68571E−2	−0.96554 −2	+0.60694E−2	−0.14819E−1	+0.20616E−2	−0.16727E−1
	9	−0.15128E−1	+0.13458E−1	−0.20772E−2	+0.16328E−1	+0.47245E−2	+0.96216E−2	+0.61942E−2	−0.10398E−1	+0.78666E−2	+0.86970E−2
C_T^*	10	+0.33002E−2	+0.54810E−3	+0.69749E−2	−0.33979E−3	+0.23591E−2	−0.75453E−3	+0.26482E−2	−0.29324E−2	+0.46912E−2	−0.47515E−2
	11	+0.31416E−2	+0.42076E−2	+0.59838E−2	+0.23506E−2	+0.87912E−2	+0.24453E−2	+0.12137E−1	+0.40913E−2	+0.14771E−1	+0.22828E−2
	12	−0.21144E−2	−0.57232E−2	−0.14599E−2	−0.69497E−2	+0.11968E−2	−0.87981E−2	−0.35705E−2	−0.44436E−2	−0.75056E−2	−0.49383E−2
	13	+0.29438E−2	+0.74689E−2	+0.83533E−2	+0.61925E−2	+0.83808E−2	+0.18184E−2	+0.32985E−2	−0.12190E−2	+0.14983E−2	−0.25924E−2
	14	+0.33857E−3	−0.84815E−4	+0.11093E−2	+0.35046E−3	−0.82098E−3	+0.20077 −2	−0.88652E−3	−0.22551E−2	+0.24058E−2	−0.25143E−2
	15	+0.41236E−2	−0.13374E−2	+0.41885E−2	−0.11571E−2	+0.27371E−2	−0.33070E−2	+0.69807E−2	−0.32272E−2	+0.55647E−2	−0.33659E−2
	16	+0.16259E−2	−0.91934E−3	−0.12438E−3	−0.32566E−3	−0.26121E−3	−0.79201E−3	−0.17560E−3	+0.17553E−2	−0.38178E−2	+0.28153E−2
	17	+0.12759E−2	+0.27412E−2	+0.38034E−2	+0.63420E−3	+0.19133E−2	−0.36311E−3	+0.21643E−2	+0.14875E−2	+0.26704E−2	−0.22162E−3
	18	+0.20647E−2	−0.10198E−2	+0.90073E−3	−0.22749E−2	+0.32290E−3	−0.19377E−2	+0.35362E−3	+0.45353E−4	+0.15745E−2	−0.53749E−3
	19	+0.34157E−2	+0.19845E−2	+0.31147E−2	−0.36805E−3	+0.15223E−2	−0.12135E−2	+0.25772E−2	−0.88702E−3	+0.24500E−3	−0.35190E−2
	20	−0.58703E−3	−0.13980E−2	−0.10633E−3	−0.12350E−2	−0.10151E−2	−0.31678E−3	−0.18279E−2	−0.94609E−3	−0.42370E−4	−0.42846E−3
	0	−0.14276E 0	+0.00000E+0	−0.12764E 0	+0.00000E+0	−0.11257E 0	+0.00000E+0	−0.10166E 0	+0.00000E+0	−0.86955E−1	+0.00000E+0
	1	−0.55946E−2	−0.21875E 0	+0.68679E−3	−0.24100E 0	+0.93340E−2	−0.26265E 0	+0.18593E−1	−0.27769E 0	+0.30046E−1	−0.29799E+0
	2	+0.15519E 0	+0.10114E−1	+0.14639E 0	+0.18919E−1	+0.13788E 0	+0.27587E−1	+0.13408E 0	+0.35459E−1	+0.12651E 0	+0.43403E−1
	3	+0.15915E−1	+0.47120E−1	+0.23195E−1	+0.55513E−1	+0.33223E−1	+0.65262E−1	+0.43767E−1	+0.72317E−1	+0.55034E−1	+0.83309E−1
	4	+0.66633E−2	−0.58914E−3	+0.10292E−1	−0.12453E−2	+0.12672E−1	−0.40234E−2	+0.13604E−1	−0.83408E−2	+0.19376E−1	−0.14571E−1
	5	+0.89343E−3	−0.12958E−2	+0.86651E−2	−0.14748E−2	+0.14250E−1	+0.10255E−2	+0.18658E−1	+0.44854E−2	+0.22082E−1	+0.43398E−2
	6	−0.38876E−2	−0.20824E−2	−0.39124E−2	−0.21899E−2	−0.30407E−3	−0.32045E−2	+0.26598E−2	−0.37642E−2	+0.76282E−2	−0.39256E−2
	7	+0.10976E−1	+0.52475E−2	+0.15984E−1	+0.56694E−2	+0.19888E−1	−0.21752E−2	+0.24097E−1	+0.75727E−3	+0.31821E−1	−0.23504E−2
	8	+0.31959E−2	−0.15428E−2	+0.46295E−2	−0.49911E−2	+0.48334E−2	−0.59535E−2	+0.47924E−2	−0.88802E−2	+0.51835E−2	−0.13633E−1
	9	+0.14201E−2	+0.23580E−2	+0.68371E−3	+0.13631E−2	+0.28427E−2	+0.90664E−3	+0.36556E−2	+0.40541E−3	+0.38898E−2	−0.14000E−2
C_{TN}^*	10	+0.13507E−2	+0.23491E−3	+0.16740E−2	+0.12877E−2	+0.32326E−2	−0.10222E−2	+0.39850E−2	−0.12811E−2	+0.49300E−2	−0.28212E−2
	11	+0.50526E−2	−0.26868E−2	+0.83495E−2	−0.35176E−2	+0.97693E−2	−0.48133E−2	+0.10643E−1	−0.55230E−2	+0.10731E−1	−0.77360E−2
	12	−0.90855E−3	−0.45635E−2	−0.77063E−3	−0.55571E−2	−0.28378E−3	−0.56355E−2	+0.25495E−3	−0.63566E−2	+0.11388E−2	−0.68665E−2
	13	+0.42758E−4	−0.44554E−4	+0.14936E−2	+0.31438E−3	+0.29395E−2	−0.18248E−2	+0.29347E−2	−0.25338E−2	+0.31378E−2	−0.42392E−2
	14	+0.42084E−3	−0.18564E−4	+0.11017E−2	−0.11179E−2	+0.53177E−3	−0.20263E−2	+0.36599E−3	−0.20504E−2	−0.82607E−3	−0.33252E−2
	15	+0.20269E−2	−0.80547E−3	+0.16804E−2	−0.24577E−2	+0.16229E−2	−0.30382E−2	+0.13115E−2	−0.38485E−2	−0.17537E−4	−0.45496E−2
	16	−0.79748E−3	−0.10170E−2	−0.10338E−2	−0.55484E−3	−0.27265E−3	−0.11128E−2	−0.13511E−2	−0.63908E−3	−0.36227E−2	−0.12282E−2
	17	+0.97452E−3	−0.46721E−4	+0.22409E−2	+0.10968E−3	+0.20276E−2	−0.15327E−2	+0.17101E−2	−0.10819E−2	−0.22400E−3	−0.15759E−2
	18	+0.48897E−3	−0.17088E−3	+0.11000E−2	−0.73945E−3	+0.35477E−3	−0.12433E−2	+0.33765E−3	−0.96321E−3	−0.58416E−3	−0.77655E−6
	19	+0.84347E−3	−0.60673E−3	+0.48406E−3	−0.15400E−2	+0.39082E−3	−0.20069E−2	−0.39681E−3	−0.20969E−2	−0.12806E−2	−0.17787E−2
	20	−0.39298E−3	−0.36317E−3	−0.33008E−3	+0.22408E−3	−0.92513E−3	−0.45842E−3	−0.11814E−2	−0.19298E−3	−0.19870E−2	+0.49570E−3

Table 6.18 (cont)

	K	P/D = 0.6 A(K)	P/D = 0.6 B(K)	P/D = 0.8 A(K)	P/D = 0.8 B(K)	P/D = 1.0 A(K)	P/D = 1.0 B(K)	P/D = 1.2 A(K)	P/D = 1.2 B(K)	P/D = 1.4 A(K)	P/D = 1.4 B(K)
	0	+0.17084E−1	+0.00000E+0	+0.19368E−1	+0.00000E+0	+0.35189E−1	+0.00000E+0	+0.43800E−1	+0.00000E+0	+0.73202E−1	+0.00000E+0
	1	+0.10550E 0	−0.78070E 0	+0.17050E 0	−0.99912E 0	+0.24406E 0	−0.11717E+1	+0.35299E 0	−0.12949E+1	+0.47301E 0	−0.14062E+1
	2	−0.27380E−1	+0.38134E−1	−0.11901E−1	+0.31924E−1	−0.73880E−2	+0.51155E−1	−0.10917E−1	+0.59030E−1	−0.33300E−1	+0.71683E−1
	3	−0.11827E−1	+0.74292E−1	−0.25601E−2	+0.81384E−1	+0.28260E−1	+0.89069 −1	+0.47062E−1	+0.93540E−1	+0.62786E−1	+0.11449E 0
	4	+0.28671E−1	−0.13568E−1	+0.17763E−1	−0.35096E−3	−0.55959E−2	−0.65670E−2	−0.10779E−1	−0.61148E−2	−0.19511E−1	−0.13400E−1
	5	+0.42504E−2	+0.66595E−1	+0.82085E−2	+0.10631E 0	+0.26558E−3	+0.14204E 0	−0.10193E−1	+0.16121E 0	−0.27569E−1	+0.17547E 0
	6	−0.78835E−2	+0.10330E−1	−0.34336E−2	+0.15116E−1	+0.11368E−1	+0.77052E−2	−0.88824E−3	+0.14624E−1	−0.38296E−2	+0.25715E−1
	7	−0.70981E−2	−0.17885E−1	−0.24534E−1	−0.27045E−1	−0.47401E−1	−0.36091E−1	−0.37893E−1	−0.53549E−1	−0.23310E−1	−0.54967E−1
	8	+0.76691E−2	−0.36187E−2	−0.10289E−2	−0.59389E−2	−0.65686E−2	+0.42036E−2	−0.70346E−2	−0.31589E−2	−0.84525E−2	−0.12576E−1
	9	−0.12506E−1	+0.10015E−1	−0.74938E−2	+0.11085E−1	−0.74990E−2	+0.21139E−2	−0.81030E−2	+0.14382E−1	−0.48956E−2	+0.13084E−1
C_Q^*	10	−0.70343E−2	+0.55926E−2	+0.15444E−2	+0.83787E−2	+0.12873E−2	+0.13095E−1	+0.72622E−2	+0.99836E−2	+0.48544E−2	+0.10733E−1
	11	−0.10254E−1	+0.69688E−2	−0.14173E−1	+0.15192E−1	+0.46502E−2	+0.30961E−1	−0.54390E−2	+0.38781E−1	−0.71945E−2	+0.44142E−1
	12	+0.25186E−2	−0.47676E−2	−0.28034E−2	−0.51507E−2	−0.46676E−2	−0.99459E−2	−0.20060E−2	−0.46749E−2	−0.53185E−2	−0.10945E−2
	13	+0.96613E−2	+0.88889E−2	+0.14246E−1	+0.14836E−1	+0.33438 −2	+0.17921E−1	+0.39281E−2	+0.14944E−1	+0.13281E−2	+0.12209E−1
	14	+0.14934E−2	+0.49081E−2	+0.34663E−2	+0.25041E−2	+0.22046E−2	−0.81917E−2	−0.65256E−3	−0.63253E−2	+0.68695E−2	−0.14074E−2
	15	−0.28323E−2	−0.58150E−4	+0.20764E−2	−0.78615E−3	+0.70034E−2	−0.78428E−3	+0.15414E−1	+0.22275E−2	+0.18071E−1	+0.17837E−2
	16	−0.30360E−2	+0.52044E−2	−0.29424E−2	−0.24526E−2	+0.39147E−1	+0.72661E−2	+0.30356E−2	+0.71826E−2	−0.15725E−2	+0.37948E−2
	17	+0.20889E−2	+0.12522E−2	+0.30149E−2	−0.32187E−3	+0.73719E−2	−0.47316E−2	+0.59073E−2	+0.10229E−2	+0.11527E−1	+0.49971E−2
	18	+0.31929E−2	+0.33109E−2	+0.27714E−2	−0.48551E−3	−0.94083E−3	−0.25731E−2	+0.41433E−2	−0.59201E−2	+0.10168E−1	−0.42398E−2
	19	−0.91635E−3	+0.52446E−2	+0.18423E−3	+0.35455E−2	+0.60560E−2	+0.11136E−2	+0.46102E−2	−0.14814E−2	+0.81504E−3	−0.77298E−2
	20	−0.23922E−2	−0.20591E−2	−0.81634E−4	−0.34936E−3	−0.42390E−3	−0.15470E−2	−0.57423E−3	−0.43092E−2	+0.14051E−2	−0.34485E−2

Table 6.19 Fourier coefficients of K_s 4-70 propeller in No. 37 duct (Oosterveld [25])

	K	P/D = 0.6 A(K)	P/D = 0.6 B(K)	P/D = 0.8 A(K)	P/D = 0.8 B(K)	P/D = 1.0 A(K)	P/D = 1.0 B(K)	P/D = 1.2 A(K)	P/D = 1.2 B(K)	P/D = 1.4 A(K)	P/D = 1.4 B(K)
	0	−0.78522E−1	+0.00000E+0	−0.81169E−1	+0.00000E+0	−0.78681E−1	+0.00000E+0	−0.60256E−1	+0.00000E+0	−0.47437E−1	+0.00000E+0
	1	+0.91962E−1	−0.12241E+1	+0.12849E 0	−0.11842E+1	+0.17005E 0	−0.11152E+1	+0.22360E 0	−0.10687E+1	+0.26393E 0	−0.10004E+1
	2	+0.96733E−1	−0.10805E−1	+0.11331E 0	+0.58341E−3	+0.12604E 0	+0.20371E−1	+0.12353E 0	+0.29643E−1	+0.11478E 0	+0.46145E−1
	3	−0.14657E−2	+0.16207E 0	+0.15131E−1	+0.16441E 0	+0.24444E−1	+0.15275E 0	+0.24086E−1	+0.14275E 0	+0.47309E−1	+0.14074E 0
	4	+0.10810E−1	+0.10642E−2	+0.41567E−2	+0.62103E−2	−0.69987E−2	+0.28881E−2	−0.14518E−1	−0.14016E−1	−0.11061E−1	−0.21940F−1
	5	−0.20708E−1	+0.78648E−1	−0.16220E−1	+0.76506E−1	−0.52998E−2	+0.78299E−1	−0.62461E−2	+0.73413E−1	+0.11308E−1	+0.67294E−1
	6	−0.80316E−2	+0.14098E−1	−0.11305E−1	+0.96359E−2	−0.77500E−2	+0.18665E−2	−0.43441E−2	+0.70950E−3	−0.83647E−3	−0.44987E−2
	7	+0.11052E−1	−0.11329E−1	+0.93452E−2	−0.18036E−1	+0.67088E−2	−0.24665E−1	+0.17726E−1	−0.26735E−1	+0.24933E−1	−0.25518E−1
	8	+0.21070E−2	−0.52596E−2	+0.17779E−2	−0.12146E−1	+0.78818E−2	−0.82956E−2	+0.10820E−1	−0.10309E−1	+0.19552E−2	−0.12518E−1
	9	−0.16466E−1	+0.11815E−1	−0.62214E−2	+0.92879E−2	+0.83058E−2	+0.15085E−1	+0.89902F−2	+0.15399E−1	+0.60531E−2	+0.14151E−1
C_T^*	10	+0.85238E−3	−0.23771E−2	+0.46290E−2	+0.40488E−2	+0.20833E−2	+0.15879E−2	−0.24474E−2	−0.72466E−2	−0.28748E−2	+0.12588E−2
	11	+0.39384E−2	+0.64113E−2	+0.69293E−2	+0.73891E−2	+0.72262E−2	−0.95129E−2	+0.51620E−2	+0.93292E−2	+0.64118E−2	+0.55618E−2
	12	−0.32905E−2	+0.50027E−2	−0.20445E−2	−0.40761E−2	−0.58329F−3	−0.73249E−2	−0.48962F−2	−0.39241F−2	−0.48164E−2	−0.53289E−2
	13	+0.25672E−2	+0.60467E−2	+0.59366F−2	+0.59367E−2	+0.88467F−2	+0.34931E−2	+0.80184F−2	+0.55616F−2	+0.64267E−2	+0.44079F−2
	14	+0.24770E−2	−0.26242E−2	0.44055F−3	0.22663F−2	−0.29559F−2	−0.63570F−2	0.25019F−2	0.31513E−3	0.40358E−2	+0.49467E−3
	15	−0.62208F−2	−0.20499E−2	+0.72301E−2	0.15145F−2	+0.11530E−1	0.22474E−2	+0.14983E−3	0.17566E−2	[illegible]	[illegible]
	16	+0.34143E−3	+0.31069E−3	0.53198E−3	0.13262F−3	0.83077E−3	+0.25069E−2	0.26220E−3	+0.18460E−2	[illegible]	[illegible]
	17	+0.19780E−2	−0.63925F−3	+0.26800F−2	+0.40006E−2	+0.31339E−2	0.12990E−2	+0.23533E−2	+0.29180F−2	[illegible]	[illegible]
	18	+0.60762E−3	0.22062F−2	0.55582E−3	0.11431F−2	0.13290E−2	0.41965E−3	0.64457E−3	[illegible]	[illegible]	[illegible]
	19	+0.34488E−2	+0.30421E−2	+0.32728F−2	0.25883F−2	[illegible]	0.26298E−2	+0.12248E−2	[illegible]	[illegible]	[illegible]
	20	0.17166E−2	0.52072E−3	0.11347E−2	0.91296E−4	[illegible]	[illegible]	[illegible]	[illegible]	[illegible]	[illegible]

	K	P/D = 0.6 A(K)	P/D = 0.6 B(K)	P/D = 0.8 A(K)	P/D = 0.8 B(K)	P/D = 1.0 A(K)	P/D = 1.0 B(K)	P/D = 1.2 A(K)	P/D = 1.2 B(K)	P/D = 1.4 A(K)	P/D = 1.4 B(K)
C^*_T	0	−0.75854E−1	+0.00000E+0	−0.85104E−1	+0.00000E−1	−0.80432E−1	+0.00000E+0	−0.72310E−1	+0.0000E+0	−0.63893E−1	+0.00000E+0
	1	+0.91152E−2	−0.34397E−0	+0.15122E−1	−0.33237E−0	+0.29904E−1	−0.32774E 0	+0.47220E−1	−0.32899E 0	+0.60260E−1	−0.33060E 0
	2	+0.85316E−1	−0.60863E−2	+0.10325E 0	+0.24803E−2	+0.10546E 0	+0.81952E−2	+0.10455E 0	+0.17983E−1	+0.10016E 0	+0.28880E−1
	3	+0.47203E−2	+0.82506E−1	+0.15649E−1	+0.89761E−1	+0.21277E−1	+0.93073E−1	+0.23912E−1	+0.93061E−1	+0.33369E−1	+0.99036E−1
	4	+0.31838E−2	+0.51816E−2	+0.75680E−3	+0.45883E−2	−0.14818E−2	+0.38289E−2	−0.32961E−2	−0.63572E−2	−0.17785E−2	−0.10075E−1
	5	+0.45464E−2	+0.99282E−2	+0.92408E−2	+0.26548E−2	+0.15667E−1	+0.21950E−3	+0.24863E−1	+0.74431E−3	−0.38604E−1	+0.71186E−1
	6	+0.31828E−2	+0.59292E−3	−0.25160E−8	−0.42819E−2	−0.17592E−2	−0.63045E−2	+0.17700E−3	−0.30252E−2	+0.43713E−2	−0.48584E−1
	7	+0.95481E−2	−0.19148E−2	+0.18041E−1	−0.24385E−2	+0.25671E−1	−0.23125E−2	+0.30933E−1	−0.26122E−2	+0.35035E−1	−0.18671E−1
	8	−0.19432E−2	−0.17686E−2	−0.14737E−2	−0.45051E−2	−0.90447E−3	−0.36290E−2	+0.15955E−2	−0.64419E−2	+0.50841E−3	−0.10093 −1
	9	+0.58607E−2	−0.78198E−3	+0.48237E−2	−0.15233E−2	+0.88204E−2	−0.90853E−3	+0.12406E−1	+0.33704E−3	+0.12764E−1	+0.24435E−4
	10	−0.15047E−2	−0.30445E−2	−0.99338E−3	−0.15358E−2	−0.18008E−2	−0.18997E−2	−0.13918E−2	−0.29805E−2	−0.24911E−3	−0.22708E−2
	11	+0.38003E−2	−0.27783E−2	+0.48625E−2	−0.32041E−2	+0.81643E−2	−0.40480E−2	+0.10216E−1	−0.50133E−2	+0.13320E−1	−0.77347E−2
	12	−0.63250E−3	+0.17514E−3	−0.11657E−2	+0.17286E−4	−0.97356E−3	−0.34197E−3	+0.16203E−4	−0.28858E−2	−0.18539E−2	−0.40802E−2
	13	+0.10102E−2	−0.60004E−3	+0.43615E−2	−0.80871E−3	+0.69039E−2	−0.13522E−2	+0.72150E−2	−0.28057E−2	+0.77057E−2	−0.20523E−2
	14	−0.28923E−3	−0.32771E−3	−0.38004E−3	−0.21661E−2	−0.56244E−3	−0.22322E−2	−0.39249E−3	−0.11737E−2	+0.22148E−3	−0.21040E−2
	15	+0.26588E−2	+0.16418E−3	+0.32422E−2	−0.21791E−3	+0.45475E−2	−0.14808E−2	+0.48746E−2	−0.34043E−2	+0.51024E−2	−0.47028E−2
	16	−0.11302E−3	−0.14323E−2	−0.37155E−3	−0.72641E−3	−0.38196E−3	−0.11481E−2	−0.21174E−2	−0.20546E−2	−0.26606E−2	−0.19265E−2
	17	+0.19966E−2	−0.11456E−2	+0.22704E−2	−0.13466E−2	+0.31160E−2	−0.28678E−2	+0.31669E−2	−0.31834E−2	+0.24555E−2	−0.39615E−2
	18	−0.56644E−3	−0.74530E−3	−0.11253E−2	−0.23762E−3	−0.11878E−2	−0.25410E−3	−0.13671E−2	−0.11222E−2	−0.26363E−2	−0.60252E−3
	19	+0.95964E−3	−0.83559E−3	+0.19759E−2	−0.10735E−2	+0.19158E−2	−0.25631E−2	+0.16721E−2	−0.26716E−2	+0.10883E−2	−0.27663E−2
	20	−0.58527E−3	−0.54179E−4	−0.96980E−3	−0.57005E−5	−0.13129E−2	+0.22029E−4	−0.19020E−2	−0.49627E−3	−0.28978E−2	+0.10214E−3
C^*_Q	0	+0.14884E−1	+0.00000E+0	+0.20089E−1	+0.00000E+0	−0.30767E−1	+0.00000E+0	+0.44351E−1	+0.00000E+0	+0.64033E−1	+0.00000E+0
	1	+0.10044E 0	−0.79096E 0	+0.16636E 0	−0.99219E 0	+0.24472E 0	−0.11315E+1	+0.34230E 0	−0.12562E+1	+0.45620E 0	−0.13383E+1
	2	−0.25182E−1	+0.12206E−1	−0.18383E−1	+0.12892E−1	−0.11316E−1	+0.33712E−1	−0.18087E−1	+0.55298E−1	−0.26747E−1	+0.57075E−1
	3	−0.10918E−1	+0.90718E−1	−0.19051E−1	+0.95272E−1	−0.81658E−2	+0.90343E−1	+0.35568E−2	+0.92837E−1	+0.16152E−1	+0.89051E−1
	4	+0.27502E−1	+0.72669E−2	+0.16808E−1	+0.16045E+1	+0.16208E−2	+0.12113E−1	−0.63786E−2	−0.49373E−2	−0.15846E−1	−0.97724E−2
	5	−0.26072E−2	+0.57653E−1	+0.52434E−2	+0.94354E−1	+0.86632E−2	+0.12138E 0	−0.13513E−1	+0.14129E 0	−0.19336E−1	+0.15575E 0
	6	−0.11409E−1	+0.11032E−3	−0.11019E−1	−0.36169E−2	−0.34936E−2	−0.54322E−2	+0.94572E−3	−0.31662E−2	+0.55030E−2	+0.25599E−2
	7	+0.93808E+3	−0.99388E−2	−0.26942E−1	−0.22539E−1	−0.46075E−1	−0.35712E−1	−0.35793E−1	−0.45159E−1	−0.28670E−1	−0.42572E−1
	8	+0.82783E−2	−0.22892E−2	+0.94780E−2	−0.30457E−4	+0.66651E−2	+0.63862E−2	+0.10295E−1	+0.56348E−2	+0.28700E−3	+0.29638E−2
	9	−0.17756E−1	+0.53796E−2	−0.19689E−2	+0.21436E−2	+0.61510E−2	+0.14021E−1	+0.22438E−2	+0.28053E−1	−0.49652E−2	+0.24850E−1
	10	−0.42598E−2	+0.36876E−2	+0.16447E−2	+0.37463E 2	+0.51947E−2	+0.28095E−2	−0.26275E−2	+0.23267E−2	+0.23913E−2	+0.30607E−2
	11	−0.46664E−2	+0.96603E−2	−0.14766E−1	+0.21398E−1	−0.13702E−1	+0.32828E−1	−0.17427E−1	+0.38309E−1	−0.20976E−1	+0.41837E−1
	12	+0.10278E−2	+0.41719E−3	−0.22670E−2	+0.19168E−2	+0.12766E−3	−0.19195E−2	−0.21233E−2	−0.69986E−2	+0.14416E−2	−0.32116E−2
	13	+0.20667E−2	+0.72900E−2	+0.93023E−2	+0.76358E−2	+0.61680E−2	+0.88817E−2	+0.98031E−2	+0.14268E−1	+0.39953E−2	+0.17848E−1
	14	+0.18501E−2	+0.96970E−3	+0.41823E−2	−0.33249E−2	+0.12713E−2	−0.71309E−2	+0.38115E−2	−0.77495E−3	−0.13605E−2	+0.30114E−2
	15	+0.26112E−2	+0.87227E−3	+0.77675E−2	+0.24934E−2	+0.14570E−1	+0.30977E−2	+0.22608E−1	+0.32200E−2	+0.28437E−1	+0.75977E−2
	16	−0.32505E−2	+0.21002E−3	−0.13283E−2	+0.39206E−3	+0.44360E−2	+0.64517E−3	−0.37227E−3	+0.69956E−2	+0.19337E−2	+0.27087E−2
	17	−0.77389E−3	+0.28832E−2	−0.92032E−3	−0.83670E−3	+0.18140E−2	−0.22876E−2	+0.14353E−3	−0.21184E−3	+0.75472E−2	−0.13255E−2
	18	+0.13220E−2	+0.70445E−3	+0.25952E−3	−0.31653E−2	−0.43127E−2	−0.98748E−4	+0.16375E−2	−0.84958E−3	+0.29007E−2	+0.30258E−3
	19	+0.16856E−2	+0.39547E−2	+0.23462E−2	+0.41032E−2	+0.38794E−2	+0.10718E−2	+0.51490E−2	−0.14700E−2	+0.32369E−2	−0.37368E−2
	20	−0.48127E−3	+0.17791E−2	+0.69823E−3	+0.20375E−2	+0.14728E−3	−0.23283E−2	+0.26719E−2	−0.27758E−2	+0.32247E−2	−0.23794E−2

Table 6.20 Coefficients for Strom-Tejsen polynomials defining the Gutsche–Schroeder series – thrust (taken from Reference 34)

N	A coefficients $A(L, M, N) \times 10^6$ M = 0	1	2	3	4	5	B coefficients $B(L, M, N) \times 10^6$ M = 0	1	2	3	4	5
L = 0												
0	3055	−8255	−2412	3344	−531	−468	0	0	0	0	0	0
1	21920	−325109	2702	4081	344	646	−781450	−58146	94995	−3948	9	4189
2	3788	4004	1217	2091	−1045	−266	−10445	11179	6492	−10669	1714	1954
3	33766	55497	6639	−13267	−7191	852	65631	19985	−53191	−14561	4949	4129
4	−4176	−2115	−2876	−1533	1651	97	7884	−7946	−4414	6304	138	1549
5	−19955	38365	−6849	−2351	758	−160	75207	−9133	−6045	11322	714	−2566
6	492	6657	3006	−2619	411	−101	−2706	1972	2150	−2104	−806	814
7	8923	−18381	5533	−1756	−2055	391	−25357	−13015	18690	−4754	3027	1404
8	5	−5883	−3671	3389	−176	−40	1551	−1903	−95	1112	135	−99
9	7832	5642	6948	−1283	−276	−75	29992	5151	2897	1913	−209	106
10	482	4105	2507	−1989	−580	373	931	−585	−679	19	88	−322
11	626	−9723	−1720	−431	−1745	−444	3172	−3470	10337	6767	−1973	−585
12	226	−4453	−909	1458	538	−275	−1335	242	1977	−1158	158	478
13	5755	−13923	−1571	−1958	−2669	348	5390	3640	396	−2450	−510	137
14	365	2814	−321	−593	−190	−24	1196	−64	−1544	565	122	−504
15	1559	−7313	−45	−701	−314	−284	137	3618	−3589	810	−883	820
16	−334	−1561	47	414	522	−266	−712	−111	731	−147	113	137
17	1274	−6396	−3567	930	−132	−153	−1327	4113	−3339	−1200	−368	149
18	916	40	−473	120	−158	−81	553	−250	−94	24	−304	76
19	−225	−1818	−1704	1930	213	10	−1357	2334	−4036	−1506	183	−329
20	−348	−207	275	145	131	36	−565	576	−254	233	6	29
21	−601	719	−1132	1511	903	−257	−1833	2294	−1620	−1176	256	−106
22	515	−262	−680	407	−74	−158	−228	233	282	−415	−54	130
23	−932	1075	−1922	1391	608	−99	−514	468	−610	−798	76	97
24	−291	267	146	−17	55	86	−143	176	132	−107	−36	103
L = 1												
0	930	−457	2417	627	−1599	268	0	0	0	0	0	0
1	5560	35199	−2215	−5043	−1334	−1448	87660	−3013	−2277	−4736	−4304	2672
2	−278	−4286	1106	−2442	1082	786	2340	−1514	−5003	3866	336	−1044
3	−16436	−7937	4940	3197	890	2011	−39708	−14817	2086	−447	−2085	807
4	3837	−1713	1185	1923	−300	−1020	−2190	1872	5151	−3950	76	311
5	16902	−1515	1015	758	10	−159	22508	11572	2165	5732	−1117	−390
6	−1803	778	−3364	50	372	195	−82	−437	−2086	530	340	291
7	−7349	−7633	−6192	1604	246	−566	−2373	−497	−4279	−210	763	−743
8	55	688	4577	−2291	382	63	−1426	3428	207	−199	−205	−202
9	2745	6168	1898	326	−635	36	−14199	1281	−4762	−4345	1906	1196
10	−149	−1956	−417	−261	−473	365	1878	−3528	−597	371	523	−182
11	−3305	4518	−1406	397	1630	−0	8888	995	1792	1752	−1344	−657
12	56	1434	931	157	−163	114	−431	1907	−848	1352	−770	−16
13	−1063	2444	822	904	455	123	−4444	−5828	−419	−1940	284	267
14	804	−2297	−1016	907	−225	−202	−1275	1578	−1128	−512	624	−253
15	2553	3274	3444	−354	59	−2	2303	1520	1760	567	165	255
16	−490	2436	−737	259	−66	36	941	−516	−214	245	186	−63
17	−1944	−752	−441	−724	110	100	1462	−644	2032	2322	−439	−103
18	−199	−628	−170	18	167	−96	−878	700	365	−360	−11	−27
19	1837	−1653	129	−232	−585	118	−161	−1086	−460	−595	41	177
20	201	753	−578	151	−53	−34	373	−395	160	−514	320	−29
21	−375	−433	803	27	−5	117	542	912	−3	853	−84	−134
22	−744	572	270	−444	270	−59	51	−221	484	149	−167	11
23	51	−1265	−864	−367	−178	5	−675	163	−507	327	39	251
24	564	−488	−41	−56	−49	16	233	−836	657	−414	−117	143

Table 6.20 (cont)

N	A coefficients A(L, M, N) × 10⁶ M = 0	1	2	3	4	5	B coefficients B(L, M, N) × 10⁶ M = 0	1	2	3	4	5
L = 2												
0	1858	−2160	−339	1565	−716	−262	0	0	0	0	0	0
1	−5491	4872	575	−2650	641	196	4845	−9037	−4263	5372	1176	−256
2	1235	−1831	−1031	1248	323	−59	−4966	5145	2923	−4738	852	819
3	3549	−17	1598	1886	261	951	−355	−961	873	701	345	967
4	−1689	2875	202	−1366	151	17	3842	−3410	−1954	2584	126	−777
5	−2078	−4121	2644	1146	−527	−696	−1541	5925	1516	−1287	−731	−993
6	119	−491	−58	−337	659	−75	−1526	744	626	−539	−203	218
7	1389	2406	−5103	−2698	814	−85	1449	−3291	−2144	1010	−135	156
8	504	115	−1102	1228	−362	−305	1370	−793	−354	582	42	−333
9	−720	938	4174	1982	−624	−0	−1523	297	1073	−1157	−413	493
10	−238	−142	371	−409	101	132	−226	−366	25	−55	102	113
11	66	−1373	−570	−295	230	576	701	2248	858	1258	151	−410
12	640	−755	174	264	−91	−58	−293	523	847	−932	102	67
13	−751	1405	−431	−707	518	−248	260	−508	−904	71	−255	321
14	−146	391	−716	256	158	−154	253	−352	−594	591	41	−92
15	−326	−47	287	569	−707	129	−801	−365	371	159	387	17
16	103	−338	592	−287	−55	138	−91	27	538	−448	−120	177
17	145	−298	−676	−545	−129	216	569	61	408	68	63	−156
18	174	−98	−318	196	39	−39	135	−93	−323	358	68	−153
19	−517	141	439	−204	180	−235	114	−1331	−412	127	−100	−81
20	17	−102	14	56	59	−102	−281	369	−37	−125	−71	36
21	596	−591	117	32	−144	169	49	42	341	−80	−156	−10
22	108	43	−202	107	−40	34	−19	60	128	−86	−10	102
23	11	−202	96	96	16	10	87	−71	−266	259	13	−61
24	−107	−11	32	20	27	−5	−144	50	−16	9	−20	−42

Coefficients for Strom-Tejsen polynomials defining the Gutsche–Schrouder series – torque

N	A M = 0	1	2	3	4	5	B M = 0	1	2	3	4	5
L = 0												
0	−5224	7097	−3358	−4473	3041	−860	0	0	0	0	0	0
1	−283498	105460	−391193	−7431	−400	−2300	241457	−1211300	−80321	65830	13946	−5256
2	−2361	5401	4755	−1329	339	305	1447	−3138	−308	5690	−4903	1186
3	4626	30645	31836	2313	−764	−328	−28541	57594	4960	−28659	−9074	44
4	6544	−13318	−2369	5157	−3336	126	−304	−1966	4951	−3924	558	956
5	30438	−21864	21469	−6644	−4951	−2600	−21066	127800	14368	−4137	−415	2594
6	1011	−142	7201	−2119	346	661	−643	3704	−3358	−1047	2824	−1403
7	−20754	3236	−28269	1160	1133	1634	−2371	−45356	−23439	17969	3844	487
8	−4584	3992	−4253	−2827	1937	−840	−906	960	−2239	3190	−1860	273
9	3803	24969	1468	5987	−1828	−1517	−6720	78975	9414	2656	−2003	−1103
10	4882	−4494	3950	2282	−1158	199	1005	−1106	1313	−577	−124	65
11	−13344	60	−21041	−2939	21	2	−3240	−3368	−5230	4811	4211	−156
12	−4039	3206	−3752	−613	236	116	−962	1337	−2601	1732	−172	−96
13	−10403	14236	−11831	−4367	94	−644	1834	13753	7111	−5097	−1390	−594
14	2500	−890	1653	1003	−246	−145	400	440	197	2	−246	36
15	−5294	3369	−9874	−1982	331	−427	1856	−5692	3713	−3019	−305	−234
16	−1246	−579	−1381	474	−352	199	−525	−151	−521	−8	358	−21
17	−6537	−1127	−5471	−3833	696	578	3379	−9884	2963	−3672	−770	230
18	245	1555	75	−72	139	−57	−168	1014	422	−381	−145	112
19	−650	35	2755	−1385	1061	206	1634	−6289	1642	−2826	−1180	87
20	−216	−798	−392	601	−164	20	151	−1090	152	−264	485	−127
21	−489	−4630	2405	−1581	1048	511	2020	−7368	312	−311	−706	96
22	−244	794	−171	−308	96	−12	389	−146	393	−16	−228	39
23	1430	−1749	5017	−943	638	256	60	−2317	−1202	328	−593	423
24	461	−827	700	67	−20	85	−11	−425	25	81	131	71

Table 6.20 (cont)

N	A coefficients A(L, M, N) × 10⁶ M = 0	1	2	3	4	5	B coefficients B(L, M, N) × 10⁶ M = 0	1	2	3	4	5
L = 1												
0	9424	−13356	−731	3382	−1996	116	0	0	0	0	0	0
1	55888	14526	49411	−3400	−7754	−1769	−55003	119608	7412	5292	5423	6134
2	−14831	23859	−5164	832	1620	−7	−4005	9943	−6587	−1536	4015	1675
3	−19531	−23447	−11081	7816	9892	1883	10736	−28008	−21466	−7133	−1292	4745
4	1132	−2698	1536	−6920	1830	−852	−1316	−3353	8037	−3160	−2432	1771
5	−1976	34238	4648	−2054	−4018	−94	1676	29233	10863	894	894	527
6	4286	−5416	−1003	8609	−2272	528	3025	−155	−6340	4801	284	501
7	222	−18644	−7190	−735	455	−378	−648	−21742	7485	−3452	1759	1824
8	−8048	13227	−5046	−2936	−742	593	1337	−4706	4231	−1606	128	186
9	−1191	3493	4079	−3133	2881	474	4855	−11699	−6139	−2186	−1211	1549
10	6779	−11303	3004	2760	672	−422	−952	1091	1858	−1658	−167	840
11	8417	−2428	9459	3462	−2476	348	−1140	1265	2616	2964	−292	1888
12	−3001	6360	−1543	−1351	−486	−6	735	−1188	−285	18	5961	−442
13	382	−7205	−626	2438	440	306	−3191	−2228	−6197	−639	886	−560
14	−1161	−636	20	−199	602	283	697	−1836	2483	−1214	79	305
15	2804	8763	5562	2238	230	−104	316	5018	1043	−439	65	87
16	2436	−1925	2635	−624	−481	−6	659	−1328	278	775	−650	213
17	102	−3301	−2018	830	−1060	−8	−1287	2977	1019	2547	1139	530
18	−957	−1255	−318	79	−52	353	267	−294	−130	313	−153	59
19	−2432	3712	−2846	−615	653	−57	−447	1497	−1377	−2460	6	−449
20	1417	−408	1703	−403	−104	−169	−424	894	−522	−179	357	−197
21	659	1995	672	202	−124	−292	797	−371	3233	713	192	166
22	−202	−1418	−66	−14	100	112	53	301	−919	982	−321	38
23	−1253	−1514	−1940	−1300	−25	−142	41	−1084	211	−209	43	−285
24	373	484	98	165	−211	−17	−818	1674	−1168	45	205	−80
L = 2												
0	−667	2038	637	−1161	1244	−298	0	0	0	0	0	0
1	554	−7720	−1326	−4857	453	−706	−558	−4300	−2556	3381	−2542	1485
2	−3194	2831	−1895	−1012	−677	574	−774	344	895	810	−1930	862
3	2703	−1389	6164	12655	1152	1605	−403	1131	−78	5553	1034	−576
4	4377	−5899	4002	1540	−964	260	106	−1226	1498	−1122	515	−22
5	−3174	990	−8664	−7321	−2829	−1039	1598	−313	3787	−4531	2320	−30
6	−1162	−89	−842	−810	−122	119	697	819	−1737	264	916	673
7	−1301	3368	3117	454	1490	54	−2252	630	−2404	−3766	−3161	59
8	4	1418	1358	−890	848	−340	−1226	714	−245	908	−1073	−794
9	2261	−2467	713	2376	1003	−25	2195	−3687	679	2615	1205	−33
10	705	−2529	−568	899	−748	336	1219	−1191	507	117	−335	−61
11	−87	1335	992	−2572	−1117	134	1840	2341	4119	967	−82	130
12	−553	2154	193	−288	106	−123	−1260	1486	−939	263	178	100
13	−345	−2443	−715	878	1046	61	−1409	−2660	−3194	−954	−610	−23
14	−145	−776	−551	230	82	78	618	−325	−148	277	−274	−75
15	1407	−360	−174	−499	−18	−517	1964	241	2290	936	−163	51
16	226	618	104	110	−212	−177	−368	169	132	−131	109	175
17	−292	−1007	95	−500	−171	51	−1376	−95	−1849	−961	−361	176
18	−368	−65	−404	165	119	130	58	−30	−55	38	−157	32
19	−26	−181	−775	678	191	1	−94	713	−357	361	−307	113
20	293	63	70	155	−307	23	235	−334	379	−180	138	6
21	89	1069	−54	−271	−466	−11	−62	−128	230	−324	10	12
22	−95	−189	5	70	2	87	−71	−169	−31	−55	7	−27
23	−418	−341	−235	254	133	148	−425	−41	−302	−432	−53	87
24	180	−157	112	−57	9	−25	148	128	71	−33	112	−87

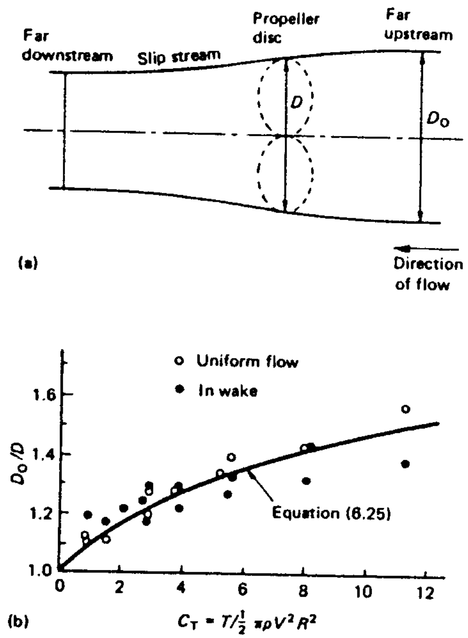

Figure 6.21 Slipstream contraction: (a) contraction of slipstream; (b) relation between contraction flow and propeller thrust

Figure 6.20(b) shows the correlation found by Nagamatsu and Sasajima for both uniform and wake flow conditions. Whilst the uniform flow results fit the curve well, as might be expected, and the wake flow results show broad agreement, it must be remembered that our understanding of the full interaction effects is far from complete at this time.

The flow in the slipstrream of the propeller is complex and a great deal has yet to be understood. Leathard (Reference 36) shows measurements of field point velocity studies conducted on the KCD 19 model propeller which formed a member of the KCD series discussed in Section 6.5.7 and tested at the University of Newcastle upon Tyne. The measurements were made using an assembly of rotating pitot tubes and the results are shown in terms of the axial distribution of hydrodynamic pitch angle over a range of plus or minus seven propeller diameters, as shown in Figure 6.22 for an advance coefficient of 0.80 which corresponds to the optimum efficiency condition. Studies by Keh-Sik (Reference 37) using non-intrusive laser-Doppler anemometry techniques on a series of NSRDC research propellers show similar patterns. Figure 6.23 shows the changes in slipstream radius, hydrodynamic pitch angle of the tip vortex and the field point velocities close to the trailing edge of the NSRDC 4383 propeller working at its design J of 0.889. The propeller has a skew of 72° which accounts for the slipstream non-dimensional radius starting at unity at a distance of some 0.35R behind the propeller. This propeller is one of the series, referred to in Section 6.5.7, and tested originally by Boswell (Reference 19).

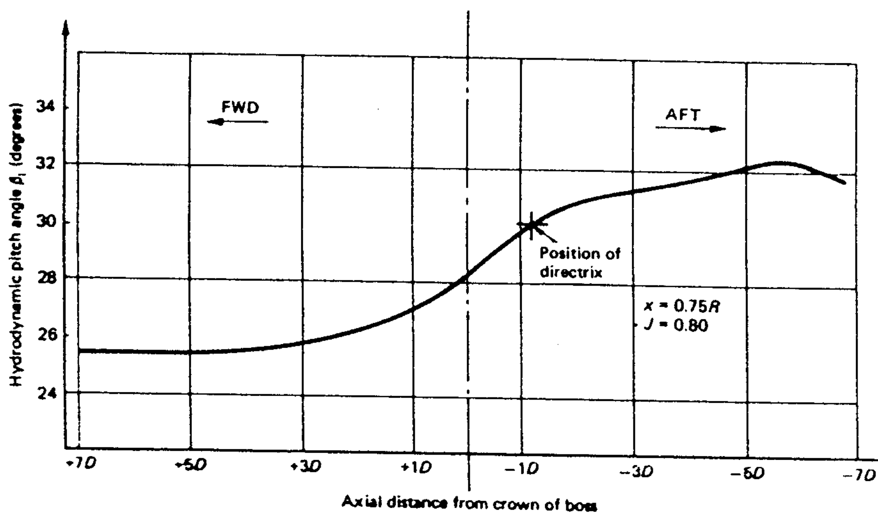

Figure 6.22 Axial distribution of hyrodynamic pitch for KCD19 propeller

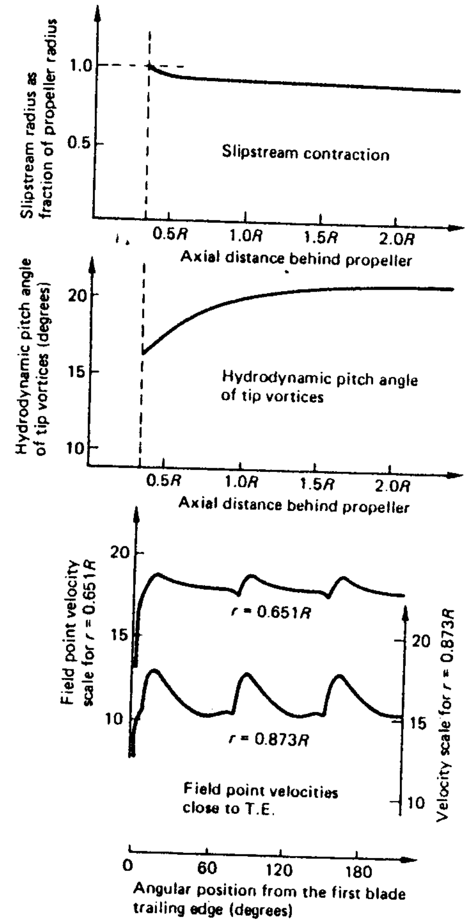

Figure 6.23 Slipstream properties of NSRDC propeller 4383 at design advance

6.8 Behind-hull propeller characteristics

The behind-hull propeller characteristics, so far as powering is concerned, have been traditionally accounted for by use of the term relative rotative efficiency η_r. This term, which was introduced by Froude, accounted for the difference in power absorbed by the propeller when working in a uniform flow field at a given speed and that absorbed when working in a mixed wake field having the same mean velocity

$$\eta_r = \frac{\text{power absorbed in open water of speed } V_a}{\text{power absorbed in mixed wake field of mean velocity } V_a} \tag{6.26}$$

Normally the correction defined by this efficiency parameter is very small since η_r is usually close to unity unless there is some particularly abnormal characteristic of the wake field. Typically, one would expect to find η_r in the range $0.96 < \eta_r < 1.04$.

As a consequence of this relationship the behind-hull efficiency (η_b), that is the efficiency of the propeller when working behind a body, is defined as

$$\eta_b = \eta_o \cdot \eta_r$$

$$\eta_b = \frac{\eta_r K_T J}{2\pi K_Q} \tag{6.27}$$

Such considerations as relative rotative efficiency are clearly at the global level of ship propulsion. At the more detailed level there is much still to be understood about the nature of the interactions between the propeller, its induced and interaction velocities and the wake field in which it operates.

As might be expected the effect of the mixed wake field induces on the propeller a series of fluctuating load components due to the changing nature of the flow incidence angles on the blade sections. Figure 11.4 shows a typical example of the variation in thrust acting on the blade of a single-screw container ship due to the operation of the propeller in the wake field. The asymmetry is caused by the tangential velocity components of the wake field, which act in opposite senses in each half of the propeller disc. Clearly such considerations also apply to the torque forces on the blade and also the hydrodynamic spindle torque in the case of a controllable pitch propeller. Figure 6.24 shows the resulting bearing forces, that is those reacted by the bearings of the vessel, which are the sum of the individual blade components at each shaft angular position. From the Figure it is seen that not only is there a thrust and torque fluctuation as derived from individual blade loads, similar to that shown in Figure 11.4, but also loads in the vertical and horizontal directions, F_Y and F_Z, and also moments M_Z and M_Y. In Figure 11.5 the orbit of the thrust eccentricity relative to the shaft centre line is shown for a merchant ship. These orbits define the position of thrust vector in the propeller disc at a given instant; it should, however, be noted that the thrust vector marches around the orbit at blade rate frequency.

In addition to the blade loadings the varying incidence angles around the propeller disc introduce a fluctuating cavitation pattern over the blades. Typical of such a pattern is that shown in Figure 6.25, from which it is seen that the wake induced assymetry also manifests itself here in the growth and decay of the cavity volume.

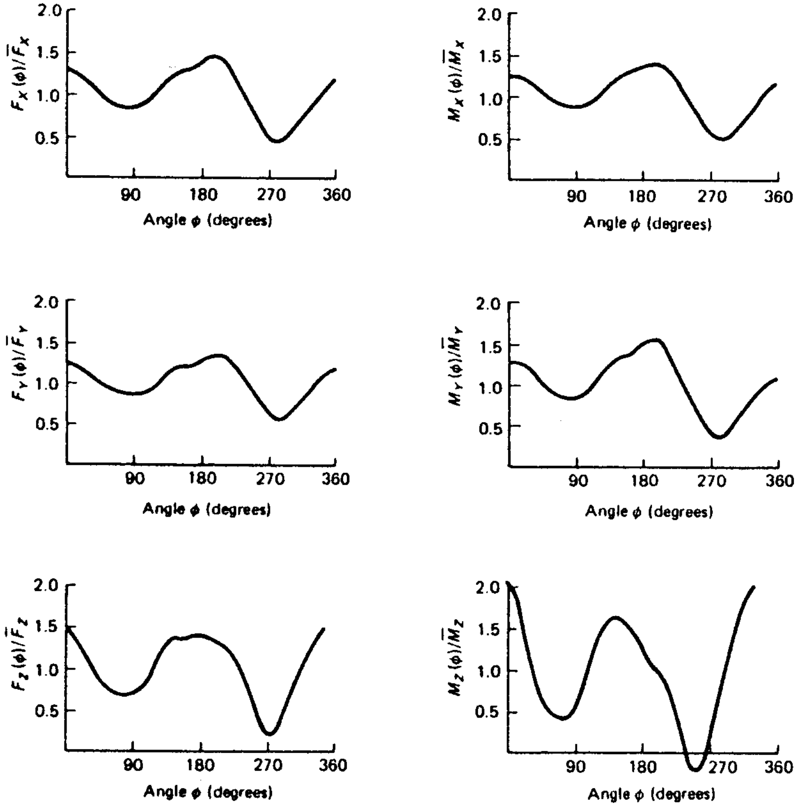

Figure 6.24 Typical fluctuation in bearing forces and moments for a propeller working in a wake field

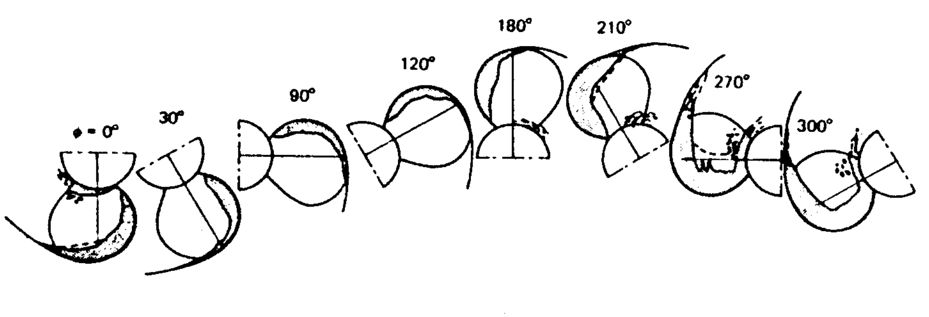

Figure 6.25 Cavitation pattern on the blades of a model propeller operating in a wake field (Reproduced partly from Reference 6)

References and further reading

1. Vasamarov, K.G., Minchev, A.D. A propeller hydrodynamic scale effect. BSHC Rep. No. PD-83-108, 1983.
2. Voitkounski, Y.I. (ed.) *Ship Theory Handbook*. Vol. 1, Sudostroeme, Leningrad, 1985.
3. Troost, L., Open water test series with modern propeller forms. *Trans. NECIES*, **54**, 1938.
4. Troost, L., Open water test series with modern propeller forms. Part 2 – three bladed propellers. *Trans. NECIES*.
5. Troost, L., Open water test series with modern propeller forms. Part 3 – two bladed and five bladed propellers – extension of the three and four bladed B-series. *Trans. NECIES*, **67**, 1951.
6. Lammeren, W.P.A. van, Manen, J. D. van, Oosterveld, M.W.C. The Wageningen B-screw series. *Trans. SNAME*, 1969.
7. Oosterveld, M.W.C., Ossannen, P. van. Further computer-analysed data of the Wageningen B-screw series. *ISP*, **22**, July 1975.
8. Yazaki, A. Design diagrams of modern four, five, six and seven-bladed propellers developed in Japan. *4th Naval Hydrodynamics Symposium*, National Academy of Sciences, Washington, 1962.
9. Gawn, R.W.L. Effect of pitch and blade width on propeller performance. *Trans. RINA*, 1952.
10. Blount, D.L., Hubble, E.N. Sizing for segmental section commercially available propellers for small craft. *Propellers 1981 Conference, Trans. SNAME*, 1981.
11. Gawn, R.W.L., Burrill, L.C. Effect of cavitation on the performance of a series of 16 in model propellers. *Trans. RINA*, 1957.
12. Emerson, A., Sinclair, L. Propeller design and model experiments. *Trans. NECIES*, 1978.
13. Lingren, H. Model tests with a family of three and five bladed propellers. *SSPA* Paper No. 47, Göteborg, 1961.
14. Newton, R.N., Rader, H.P. Performance data of propellers for high speed craft. *Trans. RINA*, Vol. 103, 1961.
15. Burrill, L.C., Emerson, A. Propeller cavitation: some observations from the 16 in propeller tests in the New King's College cavitation tunnel. *Trans. NECIES*, **79**, 1963.
16. Burrill, L.C., Emerson A. Propeller cavitation: further tests on 16 in propeller models in the King's College cavitation tunnel. *Trans. NECIES*, 1978.
17. Manen, J.E. van, Oosterveld, M.W.C. Model Tests on Contra-Rotating Propellers. Publ. No. 317, NSMB Wageningen, 1969.
18. Bjarne, E. Systematic studies of control-rotating propellers for merchant ships, *IMAS Conference, Trans. I.Mar.E.*, 1973.
19. Boswell, R.J. Design, Cavitation Performance, and Open Water Performance of a Series of Research Skewed Propellers. NSRDC Rep. No. 3339, March 1971.
20. Gutsche, F. Untersuchung von Schiffsschrauben in Schräger Anstromung. *Schiffbauforschung*, 3, 1964.
21. Taniguchi, K., Tanibayashi, H., Chiba, N. Investigation into the Propeller Cavitation in Oblique Flow. Mitsubishi Technical Bulletin No. 45, March, 1969.
22. Bednarzik, R. Untersuchungen über die Belaslungsschwankungen am Einzelflügel schräg angeströmter Propeller. *Schiffbauforschung*, 8, 1969.
23. Meyne, K., Nolte, A. Experimentalle Untersuchungen der hydrodynamischen Kräfte und Momente an einem Flügel eines Schiffspropellers bei schräger Anströmung. *Schiff und Hafen*, 5, 1969.
24. Peck, J.G., Moore, D. H. Inclined-shaft propeller performance characteristics. *Trans. IESS*.
25. Oosterveld, M.W.C. Wake Adapted Ducted Propellers. NSMB Wageningen Publ. No. 345, June, 1970.
26. Oosterveld, M.W.C. Ducted propeller characteristics. *RINA Symposium on Ducted Propellers*, London, 1973.
27. Gutsche, F.A., Schroeder, G. Freifahruersuche an Propellern mit festen und verstellbaren Flugeln 'voraus' und 'zuruck'. *Schiffbauforschung*, 2(4), 1963.
28. Chu, C., Chan, Z.L., She, Y.S., Yuan, V.Z. The 3-bladed JD-CPP series. *4th Lips Propeller Symposium*, October, 1979.
29. Yazaki, A. Model Tests on Four Bladed Controllable Pitch Propellers. *Ship Research Inst.*, Tokyo, Paper 1. March, 1964.
30. Hansen, E.O. Thrust and Blade Spindle Torque Measurements of Five Controllable Pitch Propeller Designs for MS0421. NSRDC Report 2325 April, 1967.
31. Miller, M.L. Spindle Torque Tests on Four CPP Propeller Blade Designs for MS0421 DTMB Report 1837. July, 1964.
32. Conn, J.F.C. Backing of propellers. *Trans. IESS*.
33. Nordstrom, H.F. Screw Propeller Characteristics. SSPA Publ. No. 9, 1948, Göteborg.
34. Strom-Tejsen, J., Porter, R.R. Prediction of controllable-pitch propeller performance in off-design conditions. *Third Ship Control System Symp.*, Bath, UK. Paper VII B-1.
35. Nagamatsu, T., Sasajima, T. Effect of Propeller Suction on Wake. *J. Soc. Nav. Arch. of Japan*, **137**, 1975.
36. Leathard, F.I. Analysis of the Performance of Marine Propellers, with Particular Reference to Controllable Pitch Propellers. M.Sc Thesis, Newcastle University, 1974.
37. Keh-Sik, Min. Numerical and Experimental Methods for the Prediction of Field Point Velocities around Propeller Blades. MIT, Dept. Ocean Eng. Rep. No. 78-12, June, 1978.

38. Kerwin, J.E., Chang-Sup Lee. Prediction of steady and unsteady marine propeller performance by numerical lifting-surface theory. *Trans. SNAME*, Paper No. 8, Annual Meeting, 1978.
39. Oossanen, P. van. *Calculation of Performance and Cavitation Characteristics of Propellers Including Effects of Non-Uniform Flow and Viscosity*. MARIN Publ. 457.
40. Kuiper, *The Wageningen Propeller Series*, MARIN, May 1992.

7 Theoretical methods – basic concepts

Contents

Theoretical methods to predict the action of propellers began to develop in the latter part of the 19th century. Perhaps the most notable of these early works was that of Rankine, with his momentum theory, which was closely followed by the blade element theories of Froude. The modern theories of propeller action, however, had to await the more fundamental works in aerodynamics of Lanchester, Kutta, Joukowski, Munk and Prandtl in the early years of this century before they could commence their development.

Lanchester, an English automobile engineer and self-styled aerodynamicist was the first to relate the idea of circulation with lift and he presented his ideas to the Birmingham Natural History and Philosophical Society in 1894. He subsequently wrote a paper to the Physical Society, who declined to publish these ideas. Nevertheless, he published two books, *Aerodynamics* and *Aerodonetics*, in 1907 and 1908 respectively. In these books, which were subsequently translated into German and French, we find the first mention of vortices that trail downstream of the wing tips and the proposition that these trailing vortices must be connected by a vortex that crosses the wing: the first indication of the 'horse-shoe' vortex model.

It appears that quite independently of Lanchester's work in the field of aerodynamics, Kutta developed the idea that lift and circulation were related; however, he did not give the quantitative relation between these two parameters. It was left to Joukowski, working in Russia in 1906, to propose the relation

$$L = \varrho V\Gamma \qquad (7.1)$$

This has since been known as the Kutta–Joukowski theorem. History shows that Joukowski was completely unaware of Kutta's note on the subject, but in recognition of both their contributions the theorem has generally been known by their joint names.

Prandtl, generally acclaimed as the father of modern aerodynamics, extended the work of aerodynamics into finite wing theory by developing a classical lifting line theory. This theory evolved to the concept of a lifting line comprising an infinite number of horse-shoe vortices as sketched in Figure 7.1. Munk, a colleague of Prandtl at Gottingen, first introduced the term 'induced drag' and also developed the aerofoil theory which has produced such exceptionally good results in a wide variety of subsonic applications.

From these beginnings the development of propeller theories started, slowly at first but then gathering pace through the 1950s and 1960s. These theoretical methods, whether aimed at the design or analysis problem, have all had the common aim of predicting propeller

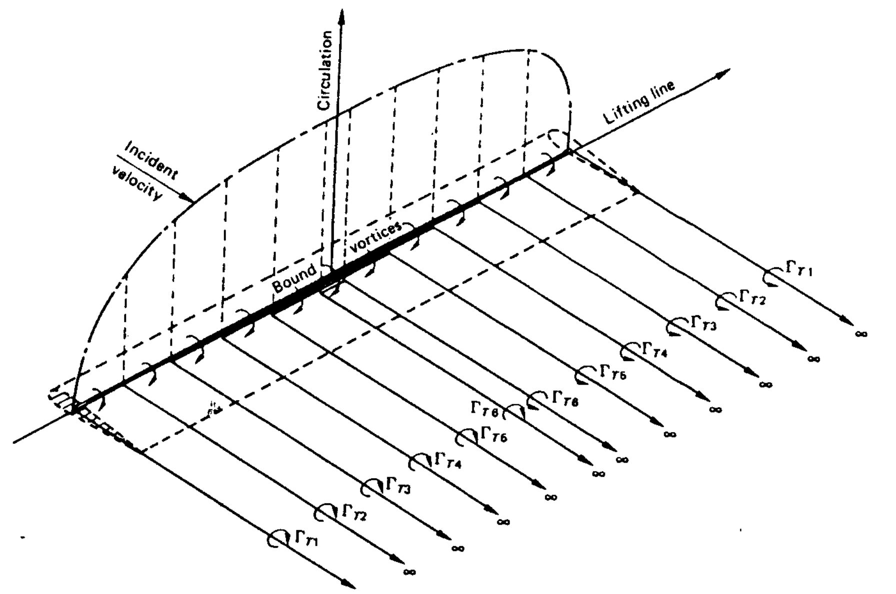

Figure 7.1 Prandtl's classical lifting line theory

performance by means of a mathematical model which has inherent assumptions built into it. Consequently, these mathematical models of propeller action rely on the same theoretical basis as that of aerodynamic wing design, and therefore appeal to the same fundamental theorems of aerodynamics or hydrodynamics. Although aerodynamics is perhaps the wider ranging subject in terms of its dealing with a more extensive range of flow speeds, for example subsonic, supersonic and hypersonic flows, both non-cavitating hydrodynamics and aerodynamics can be considered the same subject provided the Mach number does not exceed a value of around 0.4 to 0.5, which is where the effects of compressibility in air start to become appreciable.

This book is not a treatise on fluid mechanics in general, and therefore it will not deal in detail with the more fundamental and abstract ideas of fluid dynamics. For these matters the reader is referred to References 1-4. In both this chapter and Chapter 8 we are concerned with introducing the various theoretical methods of propeller analysis, so as to provide a basis for further reading or work. However, in order to do this certain prerequisite theoretical ideas are needed, some of which can be useful analytical tools in their own right. To meet these requirements the subject is structured into two parts; this chapter deals with the basic theoretical concepts necessary to evolve and understand the theories of propeller action which are then discussed in more detail in Chapter 8: Table 7.1 shows this structure. The review of the basic concepts will of necessity be in overview terms consistent with this being a book concerned with the application of fluid mechanics to the marine propeller problem. Furthermore, the discussion of the propeller theories, if conducted in a detailed and mathematically rigorous way, would not be consistent with the primary aim of this book and would also require many books of this size to do justice to them. Accordingly the important methods will be discussed sufficiently for the reader to understand their essential features, uses and limitations, and references will be given for further detailed study. Also, where several complementary methods exist within a certain class of theoretical methods, only one will be discussed and references given to the others.

Table 7.1 Outline of Chapters 7 and 8

Chapter 7 Basic concepts and theoretical methods	Chapter 8 Propeller theories
General Introduction	Momentum Theory
Experimental Single and Cascade Aerofoil Characteristics	Blade Element Theory Burrill Analysis Method Lerbs Method
Vortext Filaments and Sheets	Early Design Methods - Burill and Eckhardt and Morgan
Field Point Velocities	
Kutta Condition	Heavily Loaded Propellers (Glover)
Kelvin's Theorem	
Thin Aerofoil Theory	Lifting Surface Models (Morgan et al., van-Gent, Breslin)
Pressure Distribution Calculations	
NACA Pressure Distribution Approximation	Advanced Lifting Line Lifting Surface Hybrid Models
Boundary Layer Growth over Aerofoil	Votex Lattice Models (Kerwin) Boundary Element Methods
Finite Wing and Downwash	Special Propeller Types Controllable Pitch
Hydrodynamic Models of Propeller Action	Ducted Propellers Contra-Rotating
Vortex and Source Panel Methods	Supercavitating

7.1 Basic aerofoil section characteristics

Before discussing the theoretical basis for propeller analysis it is perhaps worth spending some time considering the experimental characteristics of wing sections, since these are in essence what the analytical methods are attempting to predict.

Figure 7.2 shows the experimental results for a two-dimensional aerofoil having an NACA 65 thickness form superimposed on an $a = 1.0$ mean line. The figure shows the lift, drag and pitching moment characteristics of the section as a function of angle of attack and for different Reynold numbers. In this instance the moment coefficient is taken about the quarter chord point; this point is frequently chosen since it is the aerodynamic centre under the assumptions of thin aerofoil theory, and in practice lies reasonably close to it. The aerodynamic centre is the point where the resultant lift and drag forces are assumed to act and hence do not influence the moment, which is camber profile and magnitude related. The lift, drag and moment coefficients are given by the relationships

$$C_L = \frac{L}{\frac{1}{2}\varrho A V^2}$$

$$C_D = \frac{D}{\frac{1}{2}\varrho A V^2} \qquad (7.2)$$

and

$$C_M = \frac{M}{\frac{1}{2}\varrho A l V^2}$$

in which A is the wing area, l is a reference length, V is the free stream incident velocity, ϱ the density of the fluid, L and D are the lift and drag forces, perpendicular and parallel respectively to the incident flow, and M is the pitching moment defined about a convenient point.

These coefficients relate to the whole wing section and as such can relate to average values for a finite wing section.

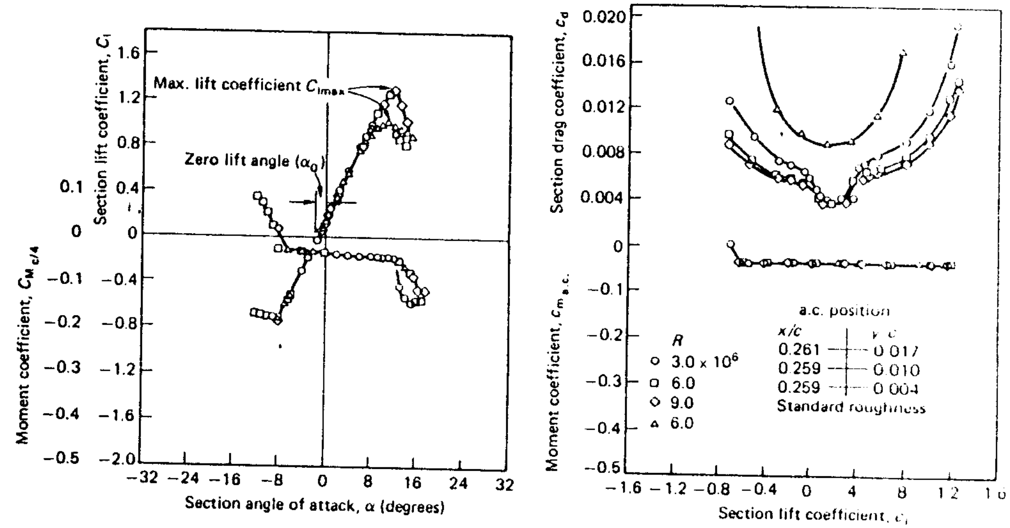

Figure 7.2 Experimental single aerofoil characteristics (NACA 65-209) (Reproduced from Reference 11, with permission)

For analysis purposes, however, it is of importance to deal with the elemental values of the aerodynamic coefficients, and these are denoted by the lower case letters c_l, c_d, c_m, given by

$$c_l = \frac{L'}{\frac{1}{2}\varrho c V^2}$$

$$c_d = \frac{D'}{\frac{1}{2}\varrho c V^2} \qquad (7.3)$$

and

$$c_m = \frac{M'}{\frac{1}{2}\varrho c^2 V^2}$$

in which c is the section chord length and L', D' and M' are the forces and moments per unit span.

Returning now to Figure 7.2, it will be seen that whilst the lift slope is not influenced by Reynolds number, the maximum lift coefficient $C_{L_{max}}$ is dependent upon R_n. The quarter chord pitching moment is also largely unaffected by Reynolds numbers over the range of non-stalled performance and the almost constant nature of the quarter-chord pitching moment over the range is typical. There is, by general agreement, a sign convention for the aerodynamic moments which states that moments which tend to increase the incidence angle are considered positive, whilst those which decrease the incidence angle are negative. Moments acting on the aerofoil can also be readily transferred to other points on the blade section, most commonly the leading edge or, in the case of a controllable pitch propeller, the spindle axis. With reference to the simplified case shown in Figure 7.3 it can be seen that

$$M'_{LE} = \frac{-cL'}{4} + M'_{c/4} = -x_{cp}L' \qquad (7.4)$$

Clearly, in the general case of Figure 7.3 both the lift and drag would need to be resolved with respect to the angle of incidence to obtain a valid transfer of moment.

In equation (7.4) the term x_{cp} is defined as the centre of pressure of the aerofoil and is the location of the point where the resultant of the distributed load over the section effectively acts. Consequently, if moments were taken about the centre of pressure the integrated effect of the distributed loads would be zero. The centre of pressure is an extremely variable quantity; for example, if the lift is zero, then by equation (7.4) it will be seen that $x_{cp} \rightarrow \infty$, and this tends to reduce its usefulness as a measurement parameter.

The drag of the aerofoil as might be expected from its viscous origin is strongly dependent on Reynolds number, this effect is seen in Figure 7.2. The drag coefficient c_d shown in this figure is known as the profile drag of the section and it comprises both a skin friction drag c_{df} and a pressure drag c_{dp}, both of which are due to viscous effects. However, in the case of a three-dimensional propeller blade or wing there is a third drag component, termed the induced drag,

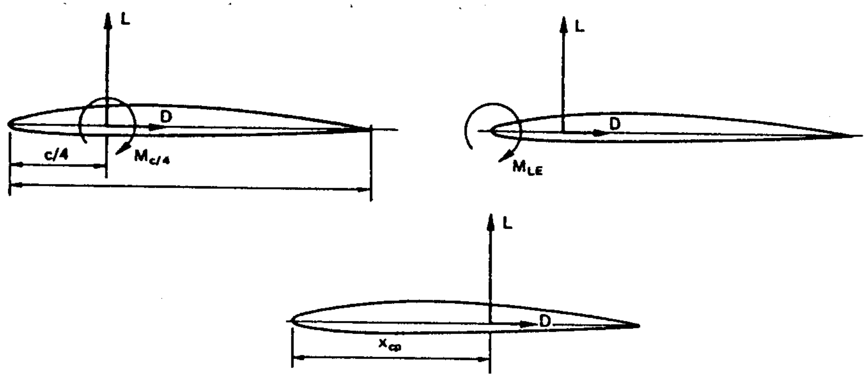

Figure 7.3 Moment and force definitions for aerofoils

c_{di}, which arises from the free vortex system. Hence the total drag on the section is given by equation (7.5):

$$c_d = c_{df} + c_{dp} + c_{di} \tag{7.5}$$

The results shown in Figure 7.2 also show the zero lift angle for the section which is the intersection of the lift curve with the abscissa; as such, it is the angle at which the aerofoil should be set relative to the incident flow in order to give zero lift. The propeller problem, however, rather than dealing with the single aerofoil in isolation is concerned with the performance of aerofoils in cascades. By this we mean a series of aerofoils, the blades in the case of the propeller, working in sufficient proximity to each other so that they mutually affect each other's characteristics. The effect of cascades on single aerofoil performance characteristics is shown in Figure 7.4. From the figure it is seen that both the lift slope and the zero lift angle are altered. In the case of the lift slope this is reduced from the single aerofoil case, as is the magnitude of the zero lift angle. As might be expected, the section drag coefficient is also influenced by the proximity of the other blades; however, this results in an increase in drag.

7.2 Vortex filament and sheets

The concept of the vortex filament and the vortex sheet is central to the understanding of many mathematical models of propeller action. The idea of a vortex flow, Figure 7.5(a), is well known and is considered in great detail by many standard fluid mechanics textbooks. It is, however, worth recalling the sign convention for these flow regimes, which state that a positive circulation induces a clockwise flow. For the purposes of developing propeller models, this two-dimensional vortex flow has to be extended into

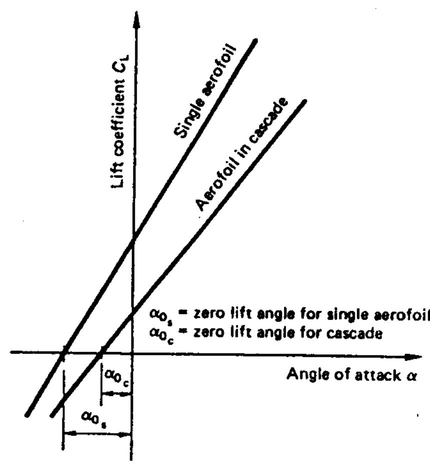

Figure 7.4 Effect of cascade on single aerofoil properties

the concept of a line vortex or vortex filament as shown in Figure 7.5(b).

The line vortex is a vortex of constant strength Γ acting along the entire length of the line describing its path through space; in the case of propeller technology this space will be three dimensional. With regard to vortex filaments Helmholtz, the German mathematician, physicist and physician, established some basic principles of vortex behaviour which have generally become known as Helmholtz' vortex theorems:

1. The strength of a vortex filament is constant along its length.

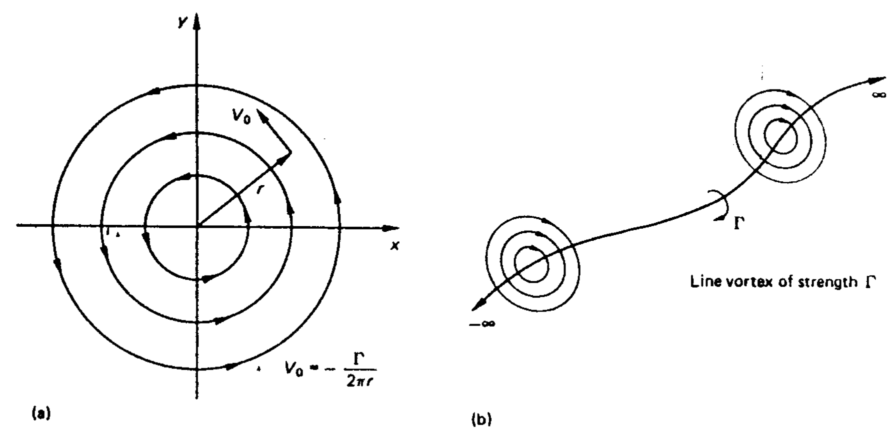

Figure 7.5 Vortex flows: (a) two-dimensional vortex; (b) line vortex

2. A vortex filament cannot end in a fluid. As a consequence the vortex must extend to the boundaries of the fluid which could be at ±∞ or, alternatively, the vortex filament must form a closed path within the fluid.

These theorems are particularly important since they govern the formation and structure of vortex models.

The idea of the line vortex or vortex filament can be extended to that of a vortex sheet. For simplicity at this stage we will consider a vortex sheet comprising an infinite number of straight line vortex filaments side by side as shown in Figure 7.6. Although we are here considering straight line vortex filaments the concept is readily extended to curved vortex filaments such as might form a helical surface, as shown in Figure 7.7. Returning, however, to Figure 7.6, let us consider the sheet 'end-on' looking in the

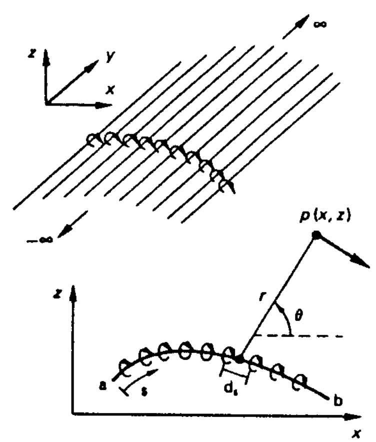

Figure 7.6 Vortex sheet

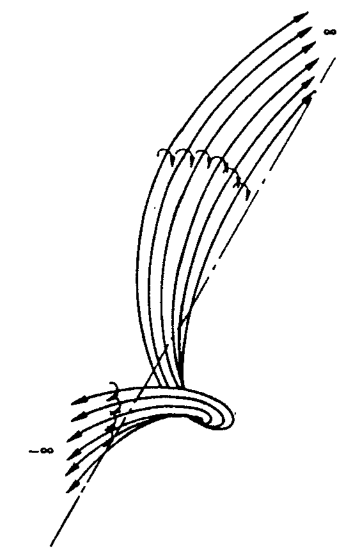

Figure 7.7 Helical vortex sheet

direction Oy. If we define the strength of the vortex sheet, per unit length, over the sheet as $\gamma(s)$, where s is the distance measured along the vortex sheet in the edge view, we can then write for an infinitesimal portion of the sheet, ds, the strength as being equal to $\gamma\, ds$. This small portion of the sheet can then be treated as a distinct vortex strength which can be used to calculate the velocity at some point P in the neighbourhood of the sheet. For the point $P(x, z)$ shown in Figure 7.6 the elemental velocity dV, perpendicular to the direction r, is given by

$$dV = \frac{-\gamma\, ds}{2\pi r} \tag{7.6}$$

Consequently, the total velocity at the point P is the summation of the elemental velocities at that point arising from all the infinitesimal sections from a to b.

The circulation Γ around the vortex sheet is equal to the sum of the strengths of all the elemental vortices located between a and b, and is given by

$$\Gamma = \int_a^b \gamma\, ds \tag{7.7}$$

In the case of a vortex sheet there is a discontinuity in the tangential component of velocity across the sheet. This change in velocity can readily be related to the local sheet strength such that if we denote upper and lower velocities immediately above and below the vortex sheet, by u_1 and u_2 respectively, then the local jump in tangential velocity across the vortex sheet is equal to the local sheet strength:

$$\gamma = u_1 - u_2$$

The concept of the vortex sheet is instrumental in analysing the properties of aerofoil sections and finds many applications in propeller theory. For example, one such theory of aerofoil action might be to replace the aerofoil with a vortex sheet of variable strength, as shown in Figure 7.8. The problem then becomes to calculate the distribution of $\gamma(s)$ so as to make the aerofoil surface become a streamline to the flow.

These analytical philosophies were known at the time of Prandtl in the early 1920s; however, they had to await the advent of high-speed digital computers some 40 years later before solutions could be attempted.

In addition to being a convenient mathematical device for modelling aerofoil action, the idea of replacing the aerofoil surface with a vortex sheet also has a physical significance. The thin boundary layer which is formed over the aerofoil surface is a highly viscous region in which the large velocity gradients produce substantial amounts of vorticity. Consequently, there is a distribution of vorticity along the aerofoil surface due to viscosity and the philosophy of replacing the aerofoil surface with a vortex sheet can be construed as a way of modelling the viscous effects in an inviscid flow.

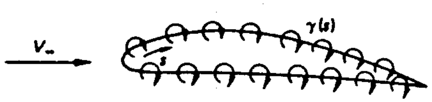

Figure 7.8 Simulation of an aerofoil section by a vortex sheet

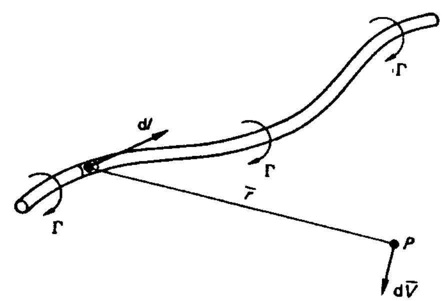

Figure 7.9 Application of the Biot–Savart law to a general vortex filament

7.3 Field point velocities

The field point velocities are those fluid velocities that may be in either close proximity to or remote from the body of interest. In the case of a propeller the field point velocities are those that surround the propeller both upstream and downstream of it.

The mathematical models of propeller action are today based on systems of vortices combined in a variety of ways in order to give the desired physical representation. As a consequence of this the principal tool for calculating field point velocities is the Biot–Savart law. This law is a general result of potential theory and describes both electromagnetic fields and inviscid, incompressible flows. In general terms the law can be stated (see Figure 7.9) as the velocity $d\bar{V}$ induced at a point P of radius r from a segment $d\bar{s}$ of a vortex filament of strength Γ given by

$$d\bar{V} = \frac{\Gamma}{4\pi}\frac{d\bar{l} \times \bar{r}}{|\bar{r}|^3} \tag{7.8}$$

To illustrate the application of the Biot–Savart law, two common examples of direct application to propeller theory are cited here; the first is a semi-infinite line vortex and the second is a semi-infinite regular helical vortex. Both of these examples commonly represent systems of free vortices emanating from the propeller.

First, the semi-infinite line vortex. Consider the system shown in Figure 7.10, which shows a segment $d\bar{s}$ of a straight line vortex originating at O and extending to infinity in the positive x-direction. Note that in practice, according to Helmholtz' theorem, the vortex could not end at the point O but must be joined to some other system of vortices. However, for our purposes here it is sufficient to consider this part of the system in isolation. Now the velocity induced at the point P distant r from $d\bar{s}$ is given by equation (7.8) as

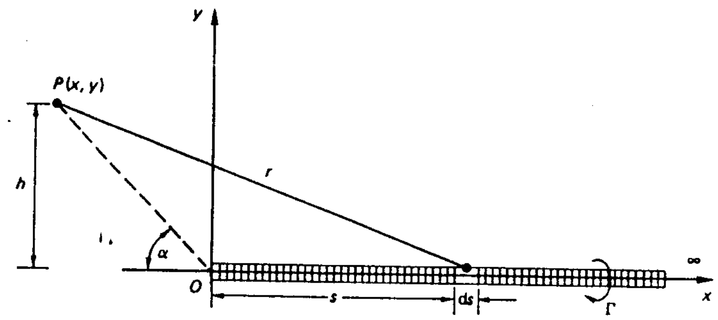

Figure 7.10 Application of the Biot–Savart law to a semi-infinite line vortex filament

$$d\bar{V} = \frac{\Gamma}{4\pi}\frac{\sin\theta\, d\bar{s}}{r^2}$$

from which the velocity at P is written as

$$V_P = \frac{\Gamma}{4\pi}\int_{\theta=\alpha}^{\theta=0} \frac{\sin\theta\, ds}{r^2}$$

which since $s = h\,(\cot\theta - \cot\alpha)$ we have

$$V_P = -\frac{\Gamma}{4\pi h}\int_{\theta=\alpha}^{0} \sin\theta\, d\theta$$

i.e.

$$V_P = \frac{\Gamma}{4\pi h}(1 - \cos\alpha) \tag{7.9}$$

The direction of V_P is normal to the plane of the paper, by the definition of a vector cross product.

In the second case of a regular helical vortex the analysis becomes a little more complex, although the concept is the same. Consider the case where a helical vortex filament starts at the propeller disc and extends to infinity having a constant radius and pitch angle, as shown in Figure 7.11. From equation (7.8) the velocity at the point P due to the segment $d\bar{s}$ is given by

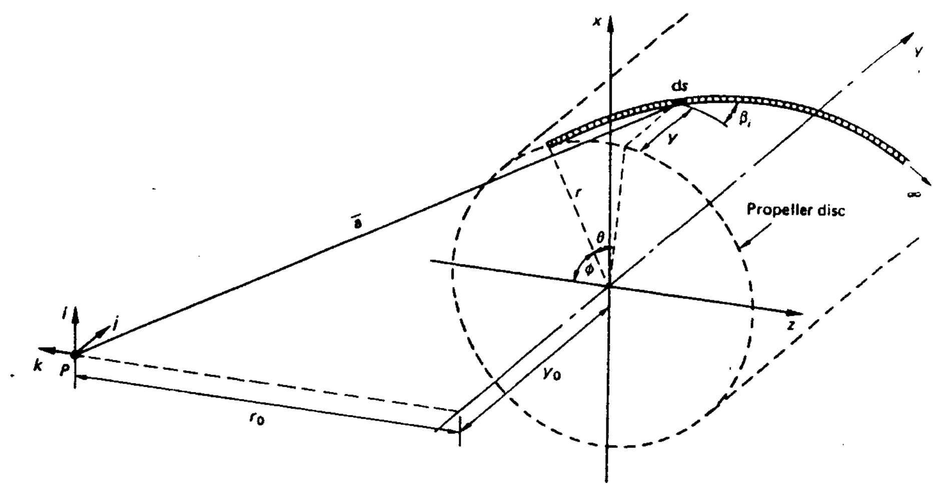

Figure 7.11 Application of Biot–Savart law to a semi-infinite regular helical vortex filament

$$d\bar{u} = \frac{\Gamma}{4\pi|a|^3}(d\bar{s} \times \bar{a})$$

and from the geometry of the problem we can derive from

$$\bar{a} = a_x\bar{i} + a_y\bar{j} + a_z\bar{k}$$

that

$$\bar{a} = -r\sin(\theta + \phi)\bar{i} - (y + y_0)\bar{j} + (r_0 - r\cos(\theta + \phi))\bar{k}$$

Similarly,

$$\bar{s}(\theta) = r\sin(\theta + \phi)\bar{i} + r\theta\tan\beta_i\bar{j} + r\cos(\theta + \phi)\bar{k}$$

from which we can derive

$$d\bar{u} = \frac{\Gamma}{4\pi|a|^3} \times \begin{vmatrix} i & j & k \\ r\cos(\theta + \phi) & r\theta\tan\beta_i & -r\sin(\theta + \phi) \\ -r\sin(\theta + \phi) & -(y + y_0) & r_0 - r\cos(\theta + \phi) \end{vmatrix}$$

where the scalar a is given by

$$[(y + y_0)^2 + r^2 + r_0^2 - 2r_0 r\cos(\theta + \phi)]^{3/2}$$

Hence the component velocities u_x, u_y and u_z are given by the relations

$$u_x = \frac{r\Gamma}{4\pi} \times \int_0^\infty \frac{\tan\beta_i(r\cos(\theta + \phi)) - (y + y_0)\sin(\theta + \phi)}{[(y + y_0)^2 + r^2 + r_0^2 - 2rr_0\cos(\theta + \phi)]^{3/2}}\,d\theta$$

$$u_y = \frac{r\Gamma}{4\pi} \times \int_0^\infty \frac{r - r_0\cos(\theta + \phi)}{[(y + y_0)^2 + r^2 + r_0^2 - 2rr_0\cos(\theta + \phi)]^{3/2}}\,d\theta$$

$$u_z = \frac{r\Gamma}{4\pi} \times \int_0^\infty \frac{r\tan\beta_i\sin(\theta + \phi) - (y + y_0)\cos(\theta + \phi)}{[(y + y_0)^2 + r^2 + r_0^2 + 2rr_0\cos(\theta + \phi)]^{3/2}}\,d\theta \qquad (7.10)$$

These two examples are sufficient to illustrate the procedure behind the calculation of the field point velocities in inviscid flow. Clearly these principles can be extended to include horseshoe vortex systems, irregular helical vortices (that is ones where the pitch and radius vary) and other more complex systems as required by the modelling techniques employed.

It is, however, important to keep in mind, when applying these vortex filament techniques to calculate the velocities at various field points, that they are simply conceptual hydrodynamic tools for synthesizing more complex flows of an inviscid nature. As such they are a convenient means of solving Laplace's equation, the equation governing these types of flow, and are not by themselves of any great significance. However, when a number of vortex filaments are used in conjunction with a free stream flow function it becomes possible to synthesize a flow which has a practical propeller application.

7.4 The Kutta condition

From work with potential flow over a cylinder we know that, depending on the strength of the circulation, a number of possible solutions are attainable. A similar situation applies to the theoretical solution for an aerofoil in potential flow; however, nature selects just one of these solutions.

In 1902, Kutta made the observation that the flow leaves the top and bottom surfaces of an aerofoil smoothly at the trailing edge. This, in general terms, is the Kutta condition. More specifically, however, this condition can be expressed as follows:

1. The value of the circulation Γ for a given aerofoil at a particular angle of attack is such that the flow leaves the trailing edge smoothly.
2. If the angle made by the upper and lower surfaces of the aerofoil is finite, that is non-zero, then the trailing edge is a stagnation point at which the velocity is zero.
3. If the trailing edge is 'cusped', that is the angle between the surfaces is zero, the velocities are non-zero and equal in magnitude and direction.

By returning to the concept discussed in Section 7.2, in which the aerofoil surface was replaced with a system of vortex sheets and where it was noted that the strength of the vortex sheet $\gamma(s)$ was variable along its length, then according to the Kutta condition the velocities on the upper and lower surfaces of the aerofoil are equal at the trailing edge. Then from equation (7.7) we have

$$\gamma_{(TE)} = u_1 - u_2$$

which implies in order to satisfy the Kutta condition

$$\gamma_{(TE)} = 0 \qquad (7.11)$$

7.5 The starting vortex

Kelvin's circulation theorem states that the rate of change of circulation with time around a closed curve comprising the same fluid element is zero. In mathematical form this is expressed as

$$\frac{D\Gamma}{Dt} = 0 \qquad (7.12)$$

This theorem is important since it helps explain the generation of circulation about an aerofoil. Consider an aerofoil at rest as shown by Figure 7.12(a); clearly in this case the circulation Γ about the aerofoil is zero.

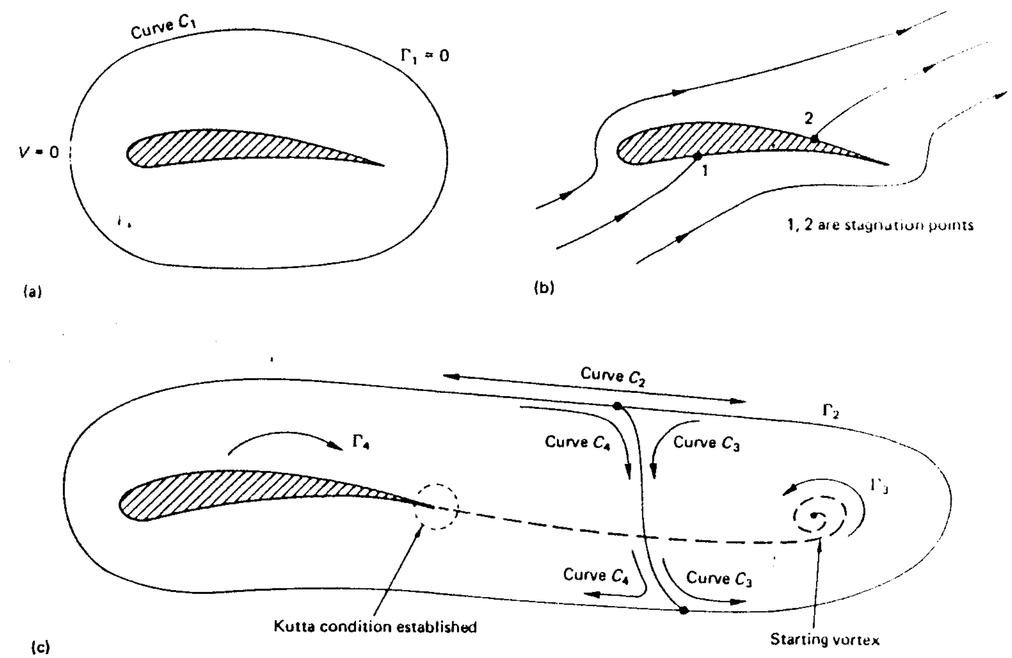

Figure 7.12 Establishment of the starting vortex: (a) aerofoil at rest; (b) streamlines on starting prior to Kutta condition being established; (c) conditions at some time after starting

Now as the aerofoil begins to move the streamline pattern in this initial transient state looks similar to that shown in Figure 7.12(b). From the Figure we observe that high-velocity gradients are formed at the trailing edge and these will lead to high levels of vorticity. This high vorticity is attached to a set of fluid elements which will then move downstream as they move away from the trailing edge. As they move away this thin sheet of intense vorticity is unstable and consequently tends to roll up to give a point vortex which is called the starting vortex; Figure 7.12(c). After a short period of time the flow stabilizes around the aerofoil, the flow leaves the trailing edge smoothly and the vorticity tends to decrease and disappear as the Kutta condition establishes itself. The starting vortex has, however, been formed during the starting process, and then continues to move steadily downstream away from the aerofoil.

If we consider for a moment the same contour comprising the same fluid elements both when the aerofoil is at rest and also after some time interval when the aerofoil is in steady motion, Kelvin's theorem tells us that the circulation remains constant. In Figures 7.12(a) and 7.12(c) this implies that

$$\Gamma_1 = \Gamma_2 = 0$$

for the curves C_1 and C_2 which embrace the same fluid elements at different times, since $\Gamma_1 = 0$ when the aerofoil was at rest. Let us now consider C_2 split into two regions, C_3 enclosing the aerofoil and C_4 the starting vortex. Then the circulation around these contours Γ_3 and Γ_4 are given by

$$\Gamma_3 + \Gamma_4 = \Gamma_2$$

but since $\Gamma_2 = 0$, then

$$\Gamma_4 = -\Gamma_3 \qquad (7.13)$$

which implies that the circulation around the aerofoil is equal and opposite to that of the starting vortex.

In summary, therefore, we see than when the aerofoil is started large velocity gradients at the trailing edge are formed leading to intense vorticity in this region which rolls up downstream of the aerofoil to form the starting vortex. Since this vortex has associated with it an anticlockwise circulation it induces a clockwise circulation around the aerofoil. This system of vortices builds up during the starting process until the vortex around the aerofoil gains the correct strength to satisfy the Kutta condition, at which point the shed vorticity ceases and steady conditions prevail around the aerofoil. The starting vortex then trails away downstream of the aerofoil.

These conditions have been verified experimentally by flow visualization studies on many occasions; the classic pictures taken by Prandtl and Tietjens (Reference 5) are typical and well worth studying.

7.6 Thin aerofoil theory

Figure 7.8 showed the simulation of an aerofoil by a vortex sheet of variable strength $\gamma(s)$. If one imagines a thin aerofoil such that both surfaces come closer together, it becomes possible, without significant error, to consider the aerofoil to be represented by its camber line with a distribution of vorticity placed along its length. When this is the case the resulting analysis is known as thin aerofoil theory, and is applicable to a wide class of aerofoils, many of which find application in propeller technology.

Consider Figure 7.13, which shows a distribution of vorticity along the camber line of an aerofoil. For the camber line to be a stream line in the flow field the component of velocity normal to the camber line must be zero along its entire length. This implies that

$$V_n + \omega_n(s) = 0 \qquad (7.14)$$

when v_n is the component of free stream velocity normal to the camber line, see inset in Figure 7.13; and $\omega_n(s)$ is the normal velocity induced by the vortex sheet at some distance s around the camber line from the leading edge.

If we now consider the components of equation (7.14) separately. From Figure 7.13 it is apparent, again from the inset, that for any point Q along the camber line,

$$V_n = V \sin\left[\alpha + \tan^{-1}\left(-\frac{dz}{dx}\right)\right]$$

For small values of α and dz/dx, which are conditions of thin aerofoil theory and are almost always met in steady propeller theory, the general condition that $\sin\theta \simeq \tan\theta \simeq \theta$ holds and, consequently, we may write for the above equation

$$V_n = V\left[\alpha - \left(\frac{dz}{dx}\right)\right] \qquad (7.15)$$

where α, the angle of incidence, is measured in radians.

Now consider the second term in equation (7.14), the normal velocity induced by the vortex sheet. We have previously stated that dz/dx is small for thin aerofoil theory, hence we can assume that the camber–chord ratio will also be small. This enables us to further assume that normal velocity at the chord line will be approximately that at the corresponding point on the camber line and to consider the distribution of vorticity along the camber line to be represented by an identical distribution along the chord without

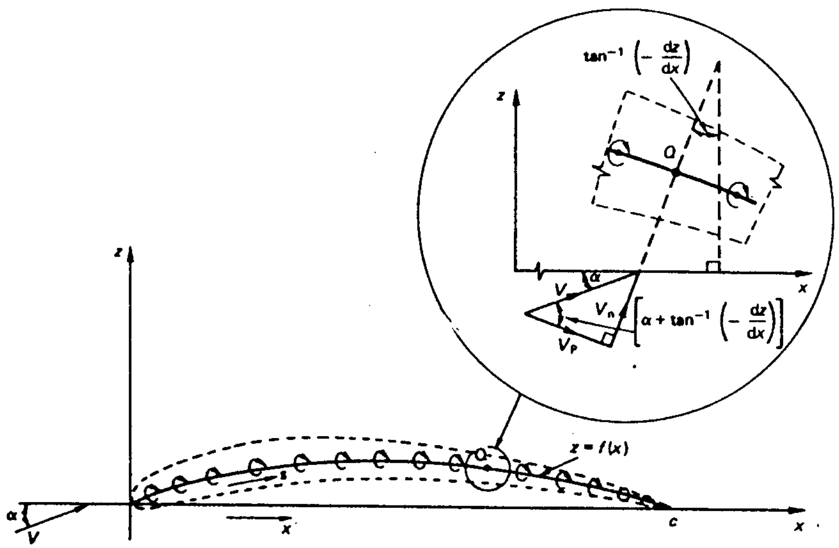

Figure 7.13 Thin aerofoil representation of an aerofoil

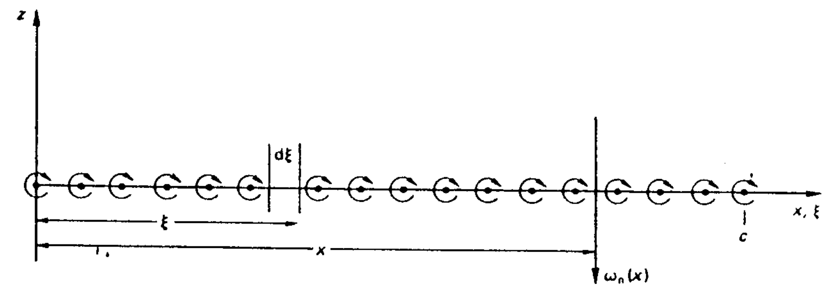

Figure 7.14 Calculation of induced velocity at the chord line

incurring any significant error. Furthermore, implicit in this assumption is that the distance s around the camber line approximates the distance x along the section chord. Now to develop an expression for $\omega_n(s)$ consider Figure 7.14, which incorporates these assumptions.

From equation (7.6) we can write the following expression for the component of velocity $d\omega_n(x)$ normal to the chord line resulting from the vorticity element $d\xi$ whose strength is $\gamma(\xi)$:

$$d\omega_n(x) = -\frac{\gamma(\xi)\,d\xi}{2\pi(x-\xi)}$$

Hence the total velocity $\omega_n(x)$ resulting from all the contributions of vorticity along the chord of the aerofoil is given by

$$\omega_n(x) = -\int_0^c \frac{\gamma(\xi)\,d\xi}{2\pi(x-\xi)}$$

Consequently, by substituting this equation together with equation (7.15) back into equation (7.14), we derive the fundamental equation of thin aerofoil theory

$$\frac{1}{2\pi}\int_0^c \frac{\gamma(\xi)\,d\xi}{(x-\xi)} = V\left[\alpha - \left(\frac{dz}{dx}\right)\right] \qquad (7.16)$$

This equation is an integral equation whose unknown is the distribution of vortex strength $\gamma(\xi)$ for a given incidence angle α and camber profile. In this equation ξ, as in all of the previous discussion, is simply a dummy variable along the Ox axis or chord line.

In order to find a solution to the general problem of a cambered aerofoil, and the one of most practical importance to the propeller analyst, it is necessary to use the substitutions

$$\xi = \frac{c}{2}(1 - \cos\theta)$$

which implies $d\xi = (c/2)\sin\theta\,d\theta$ and

$$x = \frac{c}{2}(1 - \cos\theta_0)$$

which then transforms equation (7.16) into

$$\frac{1}{2\pi}\int_0^\pi \frac{\gamma(\theta)\sin\theta\,d\theta}{(\cos\theta - \cos\theta_0)} = V\left[\alpha - \left(\frac{dz}{dx}\right)\right] \qquad (7.17)$$

In this equation the limits of integration $\theta = \pi$ corresponds to $\xi = c$ and $\theta = 0$ to $\xi = 0$, as can be deduced from the above substitutions.

Now the solution of equation (7.17), which obeys the Kutta condition at the trailing edge, that is $\gamma(\pi) = 0$, and makes the camber line a streamline to the flow, is found to be

$$\gamma(\theta) = 2V\left[A_0\left(\frac{1+\cos\theta}{\sin\theta}\right) + \sum_{n=1}^{\infty} A_n \sin(n\theta)\right] \qquad (7.18)$$

in which the Fourier coefficients A_0 and A_n can be shown, as stated below, to relate to the shape of the camber line and the angle of the incidence flow by the substitution of equation (7.18) into (7.17) followed by some algebraic manipulation:

$$\left.\begin{aligned} A_0 &= \alpha - \frac{1}{\pi}\int_0^\pi \left(\frac{dz}{dx}\right) d\theta_0 \\ A_n &= \frac{2}{\pi}\int_0^\pi \left(\frac{dz}{dx}\right)\cos(n\theta_0)\,d\theta_0 \end{aligned}\right\} \qquad (7.18a)$$

For the details of this manipulation the reader is referred to any standard textbook on aerodynamics.

In summary, therefore, equations (7.18) and (7.18a) define the strength of the vortex sheet distributed over a camber line of a given shape and at a particular incidence angle so as to obey the Kutta condition at the trailing edge. The restrictions to this theoretical treatment are that

1. the aerofoils are two-dimensional and operating as isolated aerofoils;
2. the thickness and camber chord ratios are small;
3. the incidence angle is also small.

Conditions (2) and (3) are normally met in propeller technology, certainly in the outer blade sections. However, because the aspect ratio of a propeller blade is small and all propeller blades operate in a cascade, Condition (1) is never satisfied and corrections have to be introduced for this type of analysis, as will be seen later.

With these reservations in mind, equation (7.18) can be developed further, so as to obtain relationships for the normal aerodynamic properties of an aerofoil.

From equation (7.7) the circulation around the camber line is given by

$$\Gamma = \int_0^c \gamma(\xi)\,d\xi$$

which, by using the earlier substitution of $\xi = (c/2)(1 - \cos\theta)$, takes the form

$$\Gamma = \frac{c}{2}\int_0^c \gamma(\theta)\sin\theta\,d\theta \qquad (7.19)$$

from which equation (7.18) can be written as

$$\Gamma = cV\left[A_0\int_0^\pi (1 + \cos\theta)\,d\theta + \sum_{n=1}^{\infty} A_n\int_0^\pi \sin\theta\sin(n\theta)\,d\theta\right]$$

which, by reference to any table of standard integrals, reduces to

$$\Gamma = cV\left[\pi A_0 + \frac{\pi}{2}A_1\right] \qquad (7.20)$$

Now by combining equations (7.1) and (7.3), one can derive an equation for the lift coefficient per unit span as

$$c_l = \frac{2\Gamma}{Vc}$$

from which we derive from equation (7.20)

$$c_l = \pi[2A_0 + A_1] \qquad (7.21)$$

Consequently, by substituting equations (7.18a) into (7.21) we derive the general thin aerofoil relation for the lift coefficient per unit span as

$$c_l = 2\pi\left[\alpha + \frac{1}{\pi}\int_0^\pi \left(\frac{dz}{dx}\right)(\cos\theta_0 - 1)\,d\theta_0\right] \qquad (7.22)$$

Equation (7.22) can be seen as a linear equation between c and α for a given camber geometry by splitting the terms in the following way:

$$c_l = 2\pi\alpha + 2\int_0^\pi \left(\frac{dz}{dx}\right)(\cos\theta_0 - 1)\,d\theta_0$$

Lift slope   Lift at zero incidence

in which the theoretical lift slope

$$\frac{dc_l}{d\alpha} = 2\pi/\text{rad} \qquad (7.23)$$

Figure 7.15 shows the thin aerofoil characteristics schematically plotted against experimental single and cascaded aerofoil results. From the figure it is seen that the actual lift slope curve is generally less than 2π.

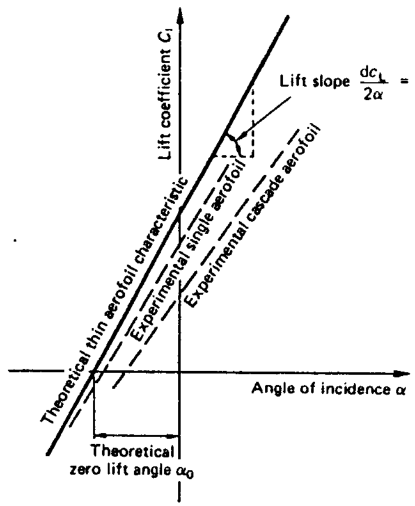

Figure 7.15 Thin aerofoil and experimental aerofoil characteristics

The theoretical zero lift angle α_0 is the angle for which equation (7.22) yields a value of $c_l = 0$. As such it is seen that

$$\alpha_0 = -\frac{1}{\pi}\int_0^\pi \left(\frac{dz}{dx}\right)(\cos\theta_0 - 1)\,d\theta_0 \qquad (7.24)$$

Again from Figure 7.15 it is seen that the experimental results for zero lift angle for single and cascaded aerofoils are less than these predicted by thin aerofoil theory.

Thin aerofoil theory also predicts the pitching moment of the aerofoil. Consider Figure 7.16 which shows a more detailed view of the element of the vortex sheet shown in Figure 7.14. From Figure 7.16 we see

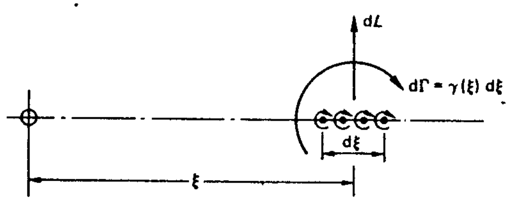

Figure 7.16 Calculation of moments about the leading edge

that the moment per unit span of the aerofoil is given by

$$M'_{LE} = -\int_0^c \xi(dL) = -\varrho V\int_0^c \xi\gamma(\xi)\,d\xi$$

Which by substituting in the distribution of vorticity given by equation (7.18) and again using the transformation $\xi = (c/2)(1 - \cos\theta)$ gives

$$M'_{LE} = -\frac{\varrho V^2c^2}{2}\left[\int_0^\pi A_0(1 - \cos^2\theta)\,d\theta + \int_0^\pi \sum_{n=1}^{\infty} A_n\sin\theta\sin(n\theta)\,d\theta - \int_0^\pi \sum_{n=1}^{\infty} A_n\sin\theta\cos\theta\sin(n\theta)\,d\theta\right]$$

which, by solving in an analogous way to that for c_l and using the definition of the moment coefficient given in equation (7.3) gives an expression for the pitching moment coefficient about the leading edge of the aerofoil as

$$c_{m_{LE}} = -\frac{\pi}{2}\left[A_0 + A_1 - \frac{A_2}{2}\right]$$

or by appeal to equation (7.21)

$$c_{m_{LE}} = -\left[\frac{c_l}{4} + \frac{\pi}{4}(A_1 - A_2)\right] \qquad (7.25)$$

and since from equation (7.4)

$$c_{m_{LE}} = -\frac{c_l}{4} + c_{m_{c/4}}$$

we may deduce that

$$c_{m_{c/4}} = \frac{\pi}{4}[A_2 - A_1] \qquad (7.26)$$

Equation (7.26) demonstrates that, according to thin aerofoil theory, the aerodynamic centre is at the quarter chord point, since the pitching moment at this point is dependent only on the camber profile (see equation (7.18a) for the basis of the coefficients A_1 and A_2) and independent of the lift coefficient.

Equations (7.23)–(7.26) are important results in thin aerofoil theory and also in many branches of propeller analysis. It is therefore important to be able to calculate these parameters readily for an arbitrary aerofoil. The theoretical lift slope curve presents no problem, since it is a general result independent of aerofoil geometry. However, this is not the case with the other equations, since the integrals behave badly in the region of the leading and trailing edges. To overcome these problems various numerical procedures have been developed over the years. In the case of the aero lift angle, Burrill (Reference 6) and Hawdon *et al.* (Reference 7) developed a tabular method based on the relationship

$$\alpha_0 = \frac{1}{c}\sum_{n=1}^{19} f_n(x)y_n(x)\ \text{degrees} \qquad (7.27)$$

Table 7.2 Zero lift angle multipliers for use with equation (7.27)

n	x_c	$f_n(x)$ Burrill	$f_n(x)$ Hawdon et al.
	L.E.		
1	0.15	5.04	5.04
2	0.10	3.38	3.38
3	0.15	3.01	3.00
4	0.20	2.87	2.85
5	0.25	2.81	2.81
6	0.30	2.84	2.84
7	0.35	2.92	2.94
8	0.40	3.09	3.10
9	0.45	3.32	3.33
10	0.50	3.64	3.65
11	0.55	4.07	4.07
12	0.60	4.64	4.65
13	0.65	5.44	5.46
14	0.70	6.65	6.63
15	0.75	8.59	8.43
16	0.80	11.40	11.40
17	0.85	17.05	17.02
18	0.90	35.40	−22.82
19	0.95	186.20	310.72
	T.E.		

where the chordal spacing is given by

$$x_n = \frac{cn}{20} \qquad (n = 1, 2, 3, 4, \ldots, 20)$$

The multipliers $f_n(x)$ are given in Table 7.2 for both sets of references. The Burrill data is sufficient for most conventional aerofoil shapes; however, it does lead to inaccuracies when dealing with 'S' shaped sections, such as might be encountered when analysing controllable pitch propellers in off-design pitch settings. This is due to its being based on a trapezoidal rule formulation. The Hawdon relationship was designed to overcome this problem by using a second-order relationship and systematic tests with camber lines ranging from a parabolic form to a symmetrical 'S'

Table 7.3 Pitching moment coefficient multipliers for equation (7.28) (taken from Reference 11)

n	x_n	B_n
1	0 (L.E.)	−0.119
2	0.025	−0.156
3	0.05	−0.104
4	0.10	−0.124
5	0.20	−0.074
6	0.30	−0.009
7	0.40	0.045
8	0.50	0.101
9	0.60	0.170
10	0.70	0.273
11	0.80	0.477
12	0.90	0.786
13	0.95	3.026
14	1.00 (T.E.)	−4.289

shape showed this latter relationship to agree to within 0.5% of the thin aerofoil results.

With regard to the pitching moment coefficient a similar approximation method was developed by Pankhurst (Reference 8). In this procedure the pitching moment coefficient is given by the relationship

$$c_{m_{c/4}} = \frac{1}{c} \sum_{n=1}^{14} B_n(y_b(x_n) + y_f(x_n)) \tag{7.28}$$

where y_b and y_f are the back and face ordinates of the aerofoil at each of the x_n chordal spacings. The coefficients B_n are given in Table 7.3.

7.7 Pressure distribution calculations

The calculation of the pressure distribution about an aerofoil section having a finite thickness has traditionally been undertaken by making use of conformal transformation methods. Theodorsen (References 9, 10) recognized that most wing forms have a general resemblance to each other, and since a transformation of the type

$$\zeta = z + \frac{a^2}{z}$$

transforms a circle in the z-plane (complex plane) into a curve resembling a wing section in the ζ plane (also a complex plane), most wing forms can be transformed into nearly circular forms. He derived a procedure that evaluated the flow about a nearly circular curve from that around a circular form and showed this process to be a rapidly converging procedure. The derivation of Theodorsen's relationship for the velocity distribution about an arbitrary wing form is divided into three stages as follows:

1. The establishment of relations between the flow in the plane of the wing section (ζ-plane) and that of the 'near circle' plane (z'-plane).
2. The derivation of the relationship between the flow in z'-plane and the flow in the true circle plane (z-plane).
3. The combining of the two previous stages into the final expression for the velocity distribution in the ζ-plane in terms of the ordinates of the wing section.

The derivation of the final equation for the velocity distribution, equation (7.29), can be found in Abbott and van Doenhoff (Reference 11) for the reader who is interested in the details of the derivation. For our purposes here, however, we merely state the results as

$$v = \frac{V[\sin(\alpha_0 + \phi) + \sin(\alpha_0 + \varepsilon_T)][1 + (d\varepsilon/d\theta)]e^{\psi_0}}{\sqrt{\{(\sinh^2\psi + \sin^2\theta)[1 + (d\psi/d\theta)^2]\}}} \tag{7.29}$$

where v is the local velocity on any point on the surface of the wing section and V is the free streams velocity.

In order to make use of equation (7.29) to calculate the velocity at some point on the wing section it is necessary to define the coordinates of the wing section with respect to a line joining a point which is located midway between the nose of the section and its centre of curvature to the trailing edge. The coordinates of these leading and trailing points are taken to be $(-2a, 0$ and $2a, 0)$ respectively with $a = 1$ for convenience. Next the values of θ and ψ are found from the coordinates (x, y) of the wing section as follows:

$$2\sin^2\theta = p + \sqrt{\left[p^2 + \left(\frac{y}{a}\right)^2\right]} \tag{7.30}$$

with

$$p = 1 - \left(\frac{x}{2a}\right)^2 - \left(\frac{y}{2a}\right)^2$$

and

$$\left.\begin{aligned} y &= 2a\sinh\psi\sin\theta \\ x &= 2a\sinh\psi\cos\theta \end{aligned}\right\} \tag{7.31}$$

The function $\psi_0 = (1/2\pi)\int_0^{2\pi}\psi\,d\theta$ has then to be determined from the relationship between ψ and θ. A first approximation to the parameter ε can be found by conjugating the curve of ψ against θ using the relationship

$$\varepsilon(\phi) = \frac{1}{n}\sum_{k=1}^{n}(\psi_{-k} - \psi_k)\cot\left(\frac{k\pi}{2n}\right) \tag{7.32}$$

with

$$\psi_k = \psi\left(\phi + \frac{k\pi}{n}\right)$$

where the coordinates in the z-plane are defined by $z = a\,e^{(\lambda + i\phi)}$.

For most purposes a value of $n = 40$ will give sufficiently accurate results.

Finally the values of $(d\varepsilon/d\theta)$ and $(d\psi/d\theta)$ are determined from the curves of ε and ψ against θ and hence equation (7.29) can be evaluated, usually in terms of v/V.

For many purposes the first approximation to ε is sufficiently accurate, however, if this is not the case then a second approximation can be made by plotting ψ against $\theta + \varepsilon$ and re-working the calculation from the determination of the function ψ_0.

This procedure is exact for computations in ideal fluids, however, the presence of viscosity to a real fluid leads to discrepancies between experiment and calculation. The growth of the boundary layer over the section effectively changes the shape of the section, and one result of this is that the theoretical rate of changes of lift with angle of incidence is not realized. Pinkerton (Reference 12) found that fair agreement with experiment for the NACA4412 aerofoil could be obtained by effectively distorting the shape of the section. The amount of the distortion is determined

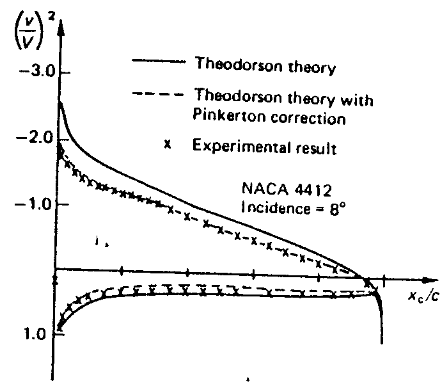

Figure 7.17 Comparison of theoretical and experimental pressure distributions around an aerofoil

by calculating the increment $\Delta\varepsilon_T$ required to avoid infinite velocities at the trailing edge after the circulation has been adjusted to give the experimentally observed lift coefficient. This gives rise to a modified function:

$$\varepsilon_a = \varepsilon + \frac{\Delta\varepsilon_T}{2}(1 - \cos\theta) \tag{7.33}$$

where ε is the original inviscid function
and ε_a is the modified value of the section.

Figure 7.17 shows the agreement obtained from the NACA4412 pressure distribution using the Theodorsen and Theodorsen with Pinkerton correction methods.

The Theodorsen method is clearly not the only method of calculating the pressure distribution around an aerofoil section. It is one of a class of inviscid methods; other methods commonly used are those by Riegels and Wittich (Reference 13) and Weber (Reference 14). The Weber method was based originally on the earlier work of Riegels and Wittich, which in itself was closely related to the works of Goldstein, Thwaites and Watson, and provides a readily calculable procedure at either 8, 16 or 32 points around the aerofoil. The location of the calculation points is defined by a cosine function, so that a much greater distribution of calculation points is achieved at the leading and trailing edges of the section. Comparison of the methods, those based on Theodorsen, Riegels–Wittich and Weber, show little variation for the range of aerofoils of interest to propeller designers so the choice of method reduces to one of personal preference for the user. The inviscid approach was extended to the cascade problem by Wilkinson (Reference 15). In addition to the solutions to the aerofoil pressure distribution problem discussed here, the use of numerical methods based on vortex panel methods have been shown to give useful and reliable results. These will be introduced later in the chapter.

The calculation of the viscous pressure distribution around an aerofoil is a particularly complex procedure, and rigorous methods such as those by Firmin (Reference 16) need to be employed. Indeed the complexity of these methods has generally precluded them from propeller analysis and design programs at the present time in favour of more approximate methods, as will be seen later.

If the section thickness distribution and camber line are of standard forms for which velocity distributions are known, such as the NACA forms, then the resulting velocity distribution can be readily approximated. The basis of the approximation is that the load distribution over a thin section may be considered to comprise two components:

1. a basic load distribution at the ideal angle of attack;
2. an additional distribution of load which is proportional to the angle of attack as measured from the ideal angle of attack.

The basic load distribution is a function only of the shape of the thin aerofoil section, and if the section is considered only to be the mean line, then it is a function only of the mean line geometry. Hence, if the parent camber line is modified by multiplying all of the ordinates by a constant factor, then the ideal design of attack α_i and the design lift coefficient c_{li} of the modified camber line are similarly derived by multiplying the parent values by the same factor.

The second distribution cited above results from the angle of attack of the section and is termed the additional load distribution; theoretically this does not contribute to any additional moment about the quarter chord point of the aerofoil. In practice there is a small effect since the aerodynamic centre in viscous flow is usually just astern of the quarter chord point. This additional load distribution is dependent to an extent on aerofoil shape and is also non-linear with incidence angle but can be calculated for a given aerofoil shape using the methods cited earlier in this chapter. The non-linearity with incidence angle, however, is small and for most marine engineering purposes can be assumed linear. As a consequence, additional load distributions are normally calculated only for a series of profile forms at a representative incidence angle and assumed to be linear for other values.

In addition to these two components of load, the actual thickness form at zero incidence has a velocity distribution over the surface associated with it, but this does not contribute to the external load produced by the aerofoil. Accordingly, the resultant velocity distribution over the aerofoil surface can be considered to comprise three separate and, to a first approximation, independent components, which can be added to give the resultant velocity distribution at a particular incidence angle. These components are

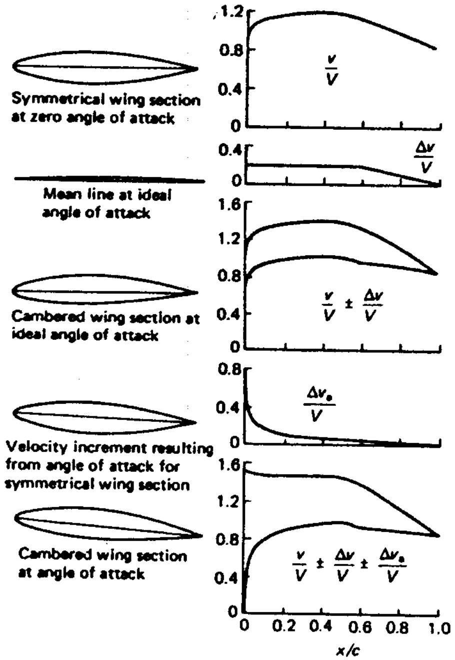

Figure 7.18 Synthesis of pressure distribution (Reproduced from Reference 11, with permission)

1. a velocity distribution over the basic thickness form at zero incidence;
2. a velocity distribution over the mean line corresponding to the load distribution at its ideal angle of incidence;
3. a velocity distribution corresponding to the additional load distribution associated with the angle of incidence of the aerofoil.

Figure 7.18 demonstrates the procedure and the velocity distributions for standard NACA aerofoil forms can be obtained from Reference 11. By way of example of this data, Table 7.4 shows the relevant data for a NACA 16-006 basic thickness form and a NACA $a = 0.8$ modified mean line. It will be seen that this data can be used basically in two ways: firstly, given a section form at incidence, to determine the resulting pressure distribution and secondly, given the section form and lift coefficient, to determine the appropriate design incidence and associated pressure distribution.

In the first case for a given maximum camber of the subject aerofoil the value of c_{l_i}, α_i, $c_{m_{c/4}}$ and the $\Delta v/V$ distribution are scaled by the ratio of the maximum camber–chord ratio, taking into account any flow curvature effects from that shown in Table 7.4.

In the case of the $a = 0.8$ (modified) mean line:

$$\text{Camber scale factor } (S_c) \simeq \frac{y/c \text{ of actual aerofoil}}{0.06651} \tag{7.34}$$

The values of v/V relating to the basic section thickness velocity distribution at zero incidence can be used directly from the appropriate table relating to the thickness form. However, the additional load velocity distribution requires modification since that given in Table 7.4 relates to a specific lift coefficient c_l: in many cases this lift coefficient has a value of unity, but this needs to be checked (Reference 11) for each particular application in order to avoid serious error. Since the data given in Reference 11 relates to potential flow, the associated angle of incidence for the distribution can be calculated as

$$\alpha_* = \frac{C_{L*}}{2\pi} \tag{7.35}$$

Hence the $\Delta v_a/V$ distribution has to be scaled by a factor of

$$\text{additional load scale factor } (S_A) = \left(\frac{\alpha - \alpha_i}{\alpha_*}\right) \tag{7.36}$$

The resultant velocity distribution over the surface of the aerofoil is then given by

$$\begin{aligned} (u/V)_U &= \frac{v}{V} + S_c\left(\frac{\Delta v}{V}\right) + S_A\left(\frac{\Delta v_a}{V}\right) \\ (u/V)_L &= \frac{v}{V} - S_c\left(\frac{\Delta v}{V}\right) - S_A\left(\frac{\Delta v_a}{V}\right) \end{aligned} \tag{7.37}$$

where the suffices U and L relate to the upper and lower aerofoil surfaces respectively.

In the second case, cited above, of a given section form and desired lift coefficient an analogous procedure is adopted in which the camber scale factor, equation (7.34), is applied to the $\Delta v/V$ distribution. However, in this case equation (7.36) is modified to take the form

$$S_A = \left(\frac{C_L - C_{L_i}}{C_{L_*}}\right) \tag{7.36a}$$

The resultant surface velocity distribution is then calculated using equations (7.37).

The pressure distribution around the aerofoil is related to the velocity distribution by Bernoulli's equation:

$$p_\infty + \tfrac{1}{2}\varrho V^2 = p_L + \tfrac{1}{2}\varrho u^2 \tag{7.38}$$

where p_∞ and p_L are the static pressures remote from the aerofoil and at a point on the surface where the

Table 7.4 Typical NACA data for propeller type sections

x (per cent c)	y (per cent c)	$(v/V)^2$	v/V	$\Delta v_a/V$
0	0	0	0	5.471
1.25	0.646	1.050	1.029	1.376
2.5	0.903	1.085	1.042	0.980
5.0	1.255	1.097	1.047	0.689
7.5	1.516	1.105	1.051	0.557
10	1.729	1.108	1.053	0.476
15	2.067	1.112	1.055	0.379
20	2.332	1.116	1.057	0.319
30	2.709	1.123	1.060	0.244
40	2.927	1.132	1.064	0.196
50	3.000	1.137	1.066	0.160
60	2.917	1.141	1.068	0.130
70	2.635	1.132	1.064	0.104
80	2.099	1.104	1.051	0.077
90	1.259	1.035	1.017	0.049
95	0.707	0.962	0.981	0.032
100	0.060	0	0	0

L.E. radius: 0.176 per cent c

NACA 16-006 basic thickness form

$c_{l_i} = 1.0 \quad \alpha_i = 1.40° \quad c_{m_{c/4}} = -0.219$

x (per cent c)	y (per cent c)	dy_c/dx	P_R	$\Delta v/V = P_R/4$
0	0			
0.5	0.281	0.47539		
0.75	0.396	0.44004		
1.25	0.603	0.39531		
2.5	1.055	0.33404	1.092 (0.5–10)	0.273
5.0	1.803	0.27149		
7.5	2.432	0.23378		
10	2.981	0.20618		
15	3.903	0.16546		
20	4.651	0.13452		
25	5.257	0.10873	1.096 (15–30)	0.274
30	5.742	0.08595		
35	6.120	0.06498		
40	6.394	0.04507	1.100 (35–45)	0.275
45	6.571	0.02559		
50	6.651	0.00607		
55	6.631	−0.01404	1.104 (50–60)	0.276
60	6.508	−0.03537		
65	6.274	−0.05887	1.108	0.277
70	5.913	−0.08610	1.108	0.277
75	5.401	−0.12058	1.112	0.278
80	4.673	−0.18034	1.112	0.278
85	3.607	−0.23430	0.840	0.210
90	2.452	−0.24521	0.588	0.147
95	1.226	−0.24521	0.368	0.092
100	0	−0.24521	0	0

Data for NACA mean line $a = 0.8$ (modified)

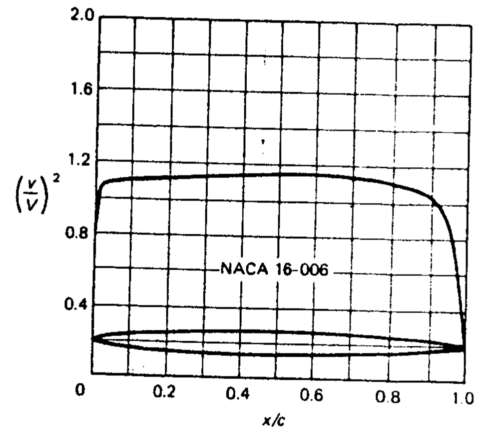

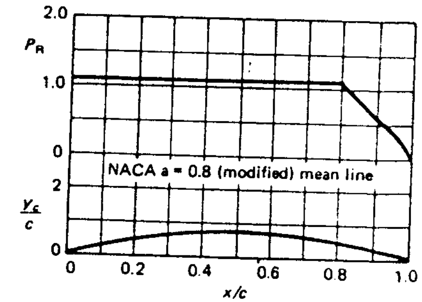

local velocity is u respectively. Then by rearranging equation (7.38), we obtain

$$p_L - p_\infty = \tfrac{1}{2}\varrho(V^2 - u^2)$$

and dividing by the free stream dynamic pressure $\frac{1}{2}\varrho V^2$, where V is the free stream velocity far from the aerofoil, we have

$$\frac{p_L - p_\infty}{\frac{1}{2}\varrho V^2} = \left[1 - \left(\frac{u}{V}\right)^2\right] \qquad (7.39)$$

The term $[(p_L - p_\infty)/\frac{1}{2}\varrho V^2]$ is termed the pressure coefficient (C_p) for a point on the surface of the aerofoil; hence in terms of this coefficient equation (7.39) becomes

$$C_p = \left[1 - \left(\frac{u}{V}\right)^2\right] \qquad (7.40)$$

7.8 Boundary layer growth over an aerofoil

Classical theoretical methods of the type outlined in this chapter very largely ignore the viscous nature of water by introducing the inviscid assumption early in their development. The viscous behavour of water, however, provides a generally small but, nevertheless, significant force on the propeller blade sections, and as such needs to be taken into account in calculation methods.

Traditionally viscous effects have been taken into account in a global sense by considering the results of model tests on standard aerofoil forms and then plotting faired trends. Typical in this respect are the drag characteristics derived by Burrill (Reference 6) which were based on the NACA and other data available at that time. For many propeller sections, typically in the tip region, where the thickness to chord values are low, and also for non-conventional propulsors, it becomes necessary either to extrapolate data, develop new data or establish reliable calculation procedures. Of these options the first can clearly lead to errors, the second can be expensive, which leaves the third as an alternative course of action.

Boundary layer theory in the general sense of its application to the aerofoil problem and the complete solution of the Navier–Stokes equations is a complex and lengthy matter. As such, it has not been attempted for propeller design and analysis procedures, outside of research exercises, and approximate methods have largely been applied in the various propeller theories. Schlichting (Reference 17) gives a very rigorous and thorough discussion of the boundary layer and its analysis and for a detailed account of this branch of the subject the reader is referred to this work, since all that can be provided within the confines of this chapter is an introduction to the subject in the context of propeller performance.

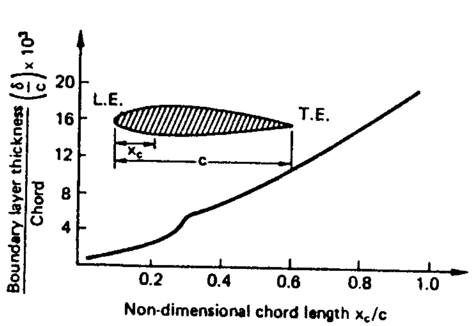

Figure 7.19 Typical growth of boundary layer thickness over an aerofoil section

For the general case of an aerofoil the boundary layer development commences from the leading edge, or more specifically, the forward stagnation point. In these early stages of development the flow around the section is normally laminar; however, after a period of time the flow undergoes a transition to a fully turbulent state. The time, or alternatively the distance around the section, at which the transition takes place is a variable dependent upon the flow velocities involved and the blade surface texture; in the case of a full-size propeller these times and distances are very short, but in the case of model this need not be the case. When transition takes place between the laminar and turbulent flow it takes place over a finite distance, and the position of the transition is of considerable importance to the growth of the boundary layer. Figure 7.19 shows the typical growth of a boundary layer over a symmetrical aerofoil, as found from experiment. It will be seen that in this case the boundary layer thickens rapidly between 0.27c and 0.30c, which is a common feature in the presence of an adverse pressure gradient, and is also associated with the transition from laminar to turbulent flow.

Separation is a phenomenon which occurs in either the laminar or tubulent flow regimes. In the case of laminar flow the curvature of the upper surface of the aerofoil may be sufficient to initiate laminar separation, and under certain conditions the separated laminar layer may undergo the transition to turbulent flow with the characteristic rapid thickening of the layer. The increase in thickness may be sufficient to make the lower edge of the shear layer contact the aerofoil surface and reattach as a turbulent boundary layer, as seen in Figure 7.20. This has the effect of forming a separation bubble which, depending on its size will have a greater or lesser influence on the pressure distribution over the aerofoil. Owen and Klanfer (Reference 18) suggested a criterion that if the Reynolds number based on the displacement thickness (R_{δ_1}) of the boundary layer is greater than 550, then a short bubble, of the order of 1% of the chord, forms, and

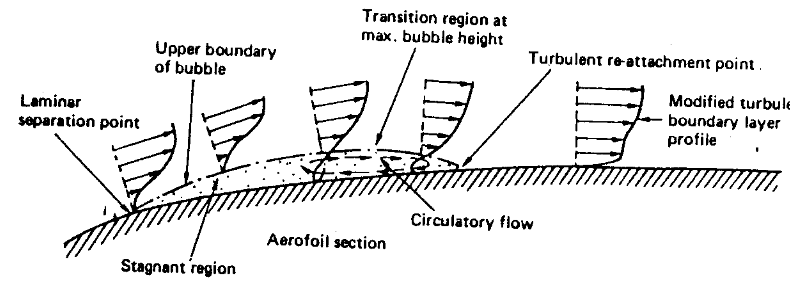

Figure 7.20 Laminar separation bubble

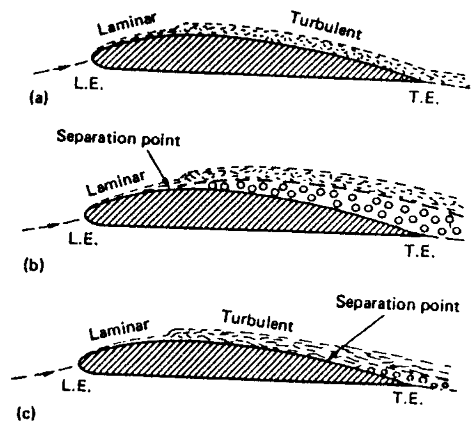

Figure 7.21 Schematic flow regimes over the suction surface of an aerofoil: (a) fully attached laminar followed by turbulent boundary layer flow over suction surface; (b) laminar, leading edge separation without reattachment of flow over suction surface; (c) laminar followed by turbulent boundary layer with separation near the trailing edge

has a negligible effect on the pressure distribution. If $R_{\delta_1} < 400$, then a long bubble, ranging from a few per cent of the chord up to almost the entire chord length, forms. In the case of the turbulent flow regime the flow will separate from the surface of the aerofoil in the presence of an adverse pressure gradient, this being one where the pressure increases in magnitude in the direction of travel of the flow. Here, as the fluid close to the surface, which is travelling at a lower speed than fluid further away from the surface due to the action of the viscous forces, travels downstream it gets slowed up to a point where it changes direction and becomes reversed flow. The point where this velocity first becomes zero, apart from the fluid layer immediately in contact with the surface whose velocity is zero by definition, is termed the stagnation point. Figure 7.21 shows three possible flow regimes about an aerofoil; the first is of a fully attached flow comprising a laminar and turbulent part whilst the second, Figure 7.21(b), illustrates a laminar separation condition without reattachment and the final flow system, Figure 7.21(c), shows a similar case to Figure 7.21(a) but having turbulent separation near the trailing edge. Figure 7.22 shows in some detail the structure and definitions used in the analysis of boundary layers.

Whilst detailed boundary layer calculation procedures are beyond the scope of this book and the reader is

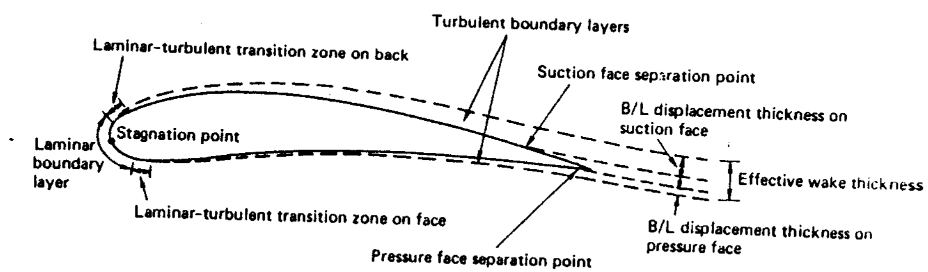

Figure 7.22 Boundary layer structure

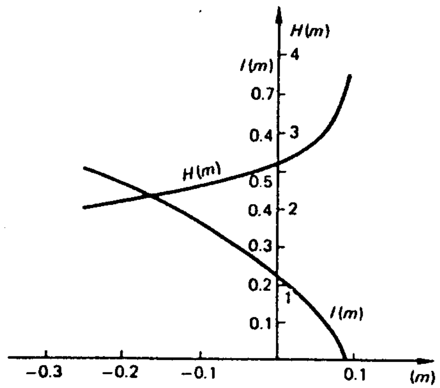

Figure 7.23 Laminar boundary layer parameter

referred to other literature, it is possible to make estimates of the boundary layer behaviour. Van Oossanen (Reference 19) establishes a useful boundary layer approximation for aerofoil forms commonly met in propeller technology. The laminar part of the boundary layer is dealt with using Thwaites' approximation, which results from the analysis of a number of exact laminar flow solutions:

$$\frac{V_s \theta^2}{\nu} = \frac{0.45}{V_s^5} \int_0^s V_s^5 \, ds \qquad (7.41)$$

in which V_s is the velocity at the edge of the boundary layer at a point s around the profile from the stagnation point and θ is the momentum thickness.

From the momentum thickness calculated by equation (7.41) a parameter m can be evaluated as follows:

$$m = -\frac{dV_s}{ds}\left(\frac{\theta^2}{\nu}\right) \qquad (7.42)$$

where ν is the kinematic viscosity of water.

Curl and Skan (Reference 20) defined a relationship between the form parameter H and m together with a further shear stress parameter l; these values are shown in Figure 7.23. Consequently, the boundary layer displacement thickness δ^* and wall shear stress τ_w can be calculated from

$$\left.\begin{aligned} \delta^* &= \theta H(m) \\ \frac{\tau_w}{\varrho V_s^2} &= \frac{l(m)\nu}{V_s \theta} \end{aligned}\right\} \qquad (7.43)$$

Separation of the laminar boundary layer is predicted to occur when $m = 0.09$.

To determine when the laminar to turbulent transition takes place the method developed by Michel, and extended by Smith (Reference 21), appears to work reasonably well for profile having a peaked minimum in the pressure distribution. For flat pressure distribution profiles, however, the method is less accurate. According to the correlation upon which the Michel–Smith method is based, laminar to turbulent transition is predicted to occur when the Reynolds number based on momentum thickness R_θ reaches the critical value given by

$$R_\theta = 1.174 R_s^{0.46} \qquad (7.44)$$

in which

$$R_s = \frac{sv}{\nu} \quad \text{and} \quad R_\theta = \frac{\theta V_s}{\nu}$$

and V and V_s are the free stream and local velocities respectively, S is the distance of the point under consideration around the surface of the foil from the stagnation point and θ is the momentum thickness.

Van Oossanen suggests that the validity of this criterion can be considered to be the range $10^5 \leqslant R_s \leqslant 10^8$.

For the turbulent part of the boundary layer, which is principally confined to the region of increasing pressure for most aerofoils, the method proposed by Nash and Macdonald (Reference 22) provides a useful assessment procedure. In this method the turbulent boundary layer is characterized by a constant value pressure gradient parameter Π and a corresponding constant value shape factor G along the body. These parameters are defined by

$$\left.\begin{aligned} \Pi &= \frac{\delta^*}{\tau_w}\left(\frac{dp}{ds}\right) \\ &\text{and} \\ G &= \sqrt{\left(\frac{\varrho V_s^2}{\tau_w}\right)}\left[1 - \frac{1}{H}\right] \end{aligned}\right\} \qquad (7.45)$$

where dp/ds is the pressure gradient at the edge of the boundary layer and $H = \delta^*/\theta$.

Nash showed that a good empirical fit to experimental data gave rise to a unique function G (Π) defined as

$$G = 6.1\sqrt{(\Pi - 1.81)} - 1.7 \qquad (7.46)$$

To establish the growth of the turbulent boundary layer over the aerofoil surface in two dimensions it is necessary to integrate the momentum-integral equation

$$\frac{d}{ds}(\varrho V_s^2 \theta) = \tau_w(1 + \Pi) \qquad (7.47)$$

This equation, which can be written as

$$\frac{d\theta}{dx_s} = -(H + 2)\frac{\theta}{V_s}\left(\frac{dV_s}{ds}\right) + \frac{\tau_w}{\varrho V_s^2} \qquad (7.47a)$$

if used in association with Nash's skin friction law for incompressible flow,

$$\frac{\tau_w}{\varrho V_s^2} = \left[2.4711 \ln\left(\frac{V_s \theta}{\nu}\right) + 475 + 1.5G + \frac{1724}{(G^2 + 200)} - 16.87\right]^{-2} \qquad (7.48)$$

can be used to calculate the growth of the turbulent boundary layer from the point of transition. At the transition point, given by equation (7.44), the continuity of momentum thickness is assumed to give a Reynolds number based on momentum thickness greater than 320: if this is not the case, then the momentum thickness is increased so as to give a value of 320. In order to start the calculation procedure at the transition point, which is an iteration involving θ, Π, G, τ_w and H in equations (7.45) and (7.46), an initial value of $G = 6.5$ can be assumed.

Turbulent separation is predicted to occur when

$$\frac{\tau_w}{\varrho V_s} < 0.0001 \qquad (7.49)$$

Van Oossanen (Reference 19) has shown that the resulting magnitude of the effective wake thickness (Figure 7.22) of the aerofoil has a significant effect on the lift slope curve and the zero lift angle correlation factor. As such, a formulation of lift slope and zero lift angle correlation factors based on the effective boundary layer thickness was derived using the above analytical basis and represented the results of wind tunnel test well. These relationships are

$$\left.\begin{aligned} \frac{dc_l}{d\alpha_2} &= 7.462 - \sqrt{\left[135.2\left(\frac{t_s}{c}\right) - 2.899\right]} \\ \frac{\alpha_{02}}{\alpha_{02p}} &= 6.0 - 5.0\left[\frac{y_{ss} + \delta^*_{ss}}{y_{sp} + \delta^*_{sp}}\right] \\ &\text{for } (y_{ss} + \delta^*_{ss}) < (y_{sp} + \delta^*_{sp}) \\ &\text{and} \\ \frac{\alpha_{02}}{\alpha_{02p}} &= 1.2 - 0.2\left[\frac{y_{ss} + \delta^*_{ss}}{y_{sp} + \delta^*_{sp}}\right] \\ &\text{for } (y_{ss} + \delta^*_{ss}) > (y_{sp} + \delta^*_{sp}) \end{aligned}\right\} \qquad (7.50)$$

where α_2 is the two-dimensional angle of attack
α_{02} is the two-dimensional zero lift angle
α_{02p} is the two-dimensional zero lift angle from thin aerofoil theory

Equations (7.50) are in contrast to the simpler formulations used by Burrill (Reference 6), which are based on the geometric thickness to chord ratio of the section. Therefore, these earlier relationships should be used with some caution, since the lift slope and zero lift angle correction factors are governed by the growth of the boundary layer over the aerofoil to a significant degree.

The boundary layer contributes two distinct components to the aerofoil drag. These are the pressure drag (D_p) and the skin friction drag (D_f). The pressure drag, sometimes referred to as the form drag, is the component of force, measured in the drag direction, due to the integral of the pressure distribution over the aerofoil. If the aerofoil were working in an inviscid fluid, then this integral would be zero – this is d'Alembert's well-known paradox. However, in the case of a real fluid the pressure distribution decreases from the inviscid prediction in the regions of separated flow and consequently gives rise to non-zero values of the integral. The skin friction drag, in contrast, is the component of the integral of the shear stresses τ_w over the aerofoil surfaces, again measured in the drag direction. Hence the viscous drag of a two-dimensional aerofoil is given by

2D viscous drag = skin friction drag + pressure drag

that is,

$$D_v = D_f + D_p \qquad (7.51)$$

7.9 The finite wing

Up to the present time discussion has largely been based on two-dimensional, infinite aspect ratio, aerofoils. Aspect ratio is taken in the sense defined in the classical aerodynamic way:

$$AR = \frac{b^2}{A} \qquad (7.52)$$

where b is the span of the wing and A is the plan form area. Marine propellers and all wing forms clearly do not possess the infinite aspect ratio attribute; indeed marine propellers generally have quite low aspect ratios. The consequence of this is that for finite aspect ratio wings and blades the flow is not two-dimensional but has a spanwise component. This can be appreciated by studying Figure 7.24 and by considering the mechanism by which lift is produced. On the pressure surface of the blade the pressure is higher than for the suction surface. This clearly leads to a tendency for the flow on the pressure surface to 'spill' around onto the suction surface at the blade tips. Therefore, there is a tendency for the streamlines on the pressure surface of the blade to deflect outwards and inwards on the suction surface; (Figure 7.24a, b). Hence the flow moves from a regime which is two-dimensional in the case of the infinite aspect ratio wing case to become a three-dimensional problem in the finite blade. The tendency for the flow to 'spill' around the tip establishes a circulatory motion at the tips as seen in Figure 7.24(b), and this creates the trailing vortex which is seen at each wing or blade tip, and is sketched in Figure 7.24(c). These tip vortices trail away downstream and their strength is clearly dependent upon the pressure differential, or load distribution, over the blade.

One consequence of the generation of trailing vortices is to produce an additional component of velocity at the blade section called downwash. For

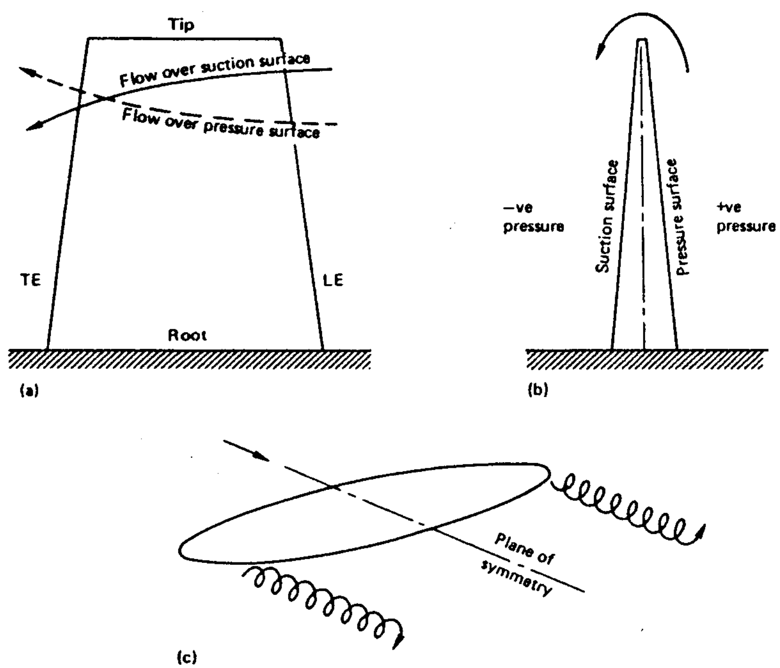

Figure 7.24 Flow over a finite aspect ratio wing: (a) plan view of blade; (b) flow at blade tip; (c) schematic view of wing tip vortices

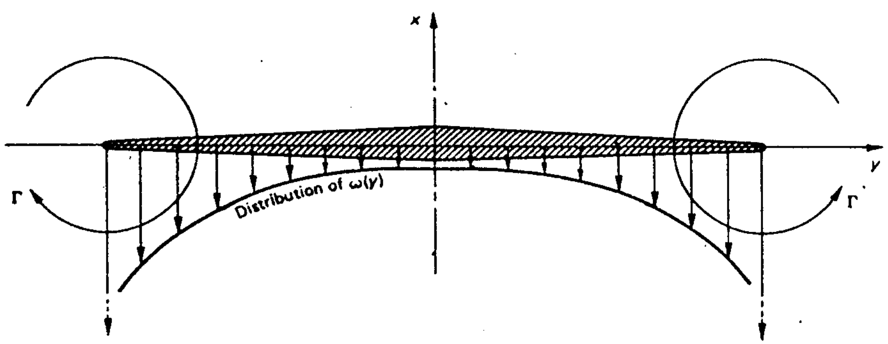

Figure 7.25 Downwash distribution for a pair of tip vortices on a finite wing

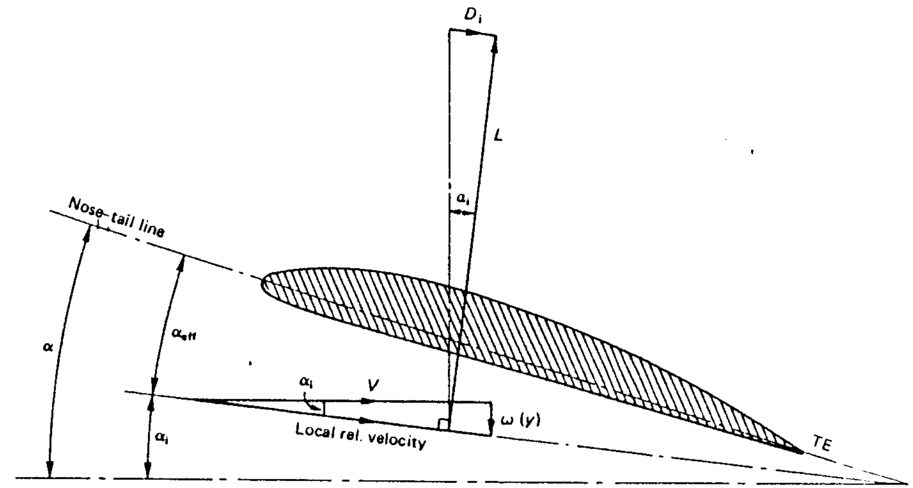

Figure 7.26 Derivation of induced drag

the case of the two wing tip vortices shown in Figure 7.24(c), the distribution of downwash $\omega(y)$ along the chord is shown in Figure 7.25. This distribution derives from the relationship

downwash at any point y = contribution from the left-hand vortex + contribution from the right-hand vortex

that is,

$$\omega(y) = -\frac{\Gamma}{4\pi}\left[\frac{1}{(b/2+y)} + \frac{1}{(b/2-y)}\right]$$
$$\omega(y) = -\frac{\Gamma}{4\pi}\left[\frac{b}{(b/2)^2 - y^2}\right] \qquad (7.53)$$

where the span of the aerofoil is b. The downwash velocity $\omega(y)$ combines with the incident free stream velocity V to produce a local velocity which is inclined to the free stream velocity at the blade section, as shown in Figure 7.26, by an angle α_i.

Consequently, although the aerofoil is inclined at a geometric angle of attack α to the free stream flow, the section is experiencing a smaller angle of attack α_{eff} such that

$$\alpha_{eff} = \alpha - \alpha_i \qquad (7.54)$$

Since the local lift force is by definition perpendicular to the incident flow, it is inclined at an angle α_i to the direction of the incident flow. Therefore, there is a component of this lift force D_i which acts parallel to the free stream's flow, and this is termed the 'induced drag' of the section. This component is directly related to the lift force and not to the viscous behaviour of the fluid.

As a consequence, we can note that the total drag on the section of an aerofoil of finite span comprises three distinct components, as opposed to the two components of equation (7.51) for the two-dimensional aerofoil, as follows:

total 3D drag = skin friction drag + pressure drag + induced drag

that is,

$$D = D_v + D_f + D_i \qquad (7.55)$$

where the skin friction drag D_f and the pressure drag and D_p are viscous contributions to the drag force.

In Figure 7.24 it was seen that a divergence of the flow on pressure and suction surfaces took place. At the trailing edge, where these streams combine, the difference in spanwise velocity will cause the fluid at this point to roll up into a number of small streamwise vortices which are distributed along the entire span of the wing, as indicated by Figure 7.27. From this figure it is seen that the velocities on the upper and lower surfaces can be resolved into a spanwise component (v) and an axial component (u). It is the difference in spanwise components on the upper and lower surfaces, v_U and v_L respectively, that give rise to the shed vorticity as sketched in the inset to the diagram. Although vorticity is shed along the entire length of the blade these small vortices roll-up into two large vortices just inboard of the wings or blade tips and at some distance from the trailing edge as shown in Figure 7.28. The strength of these two

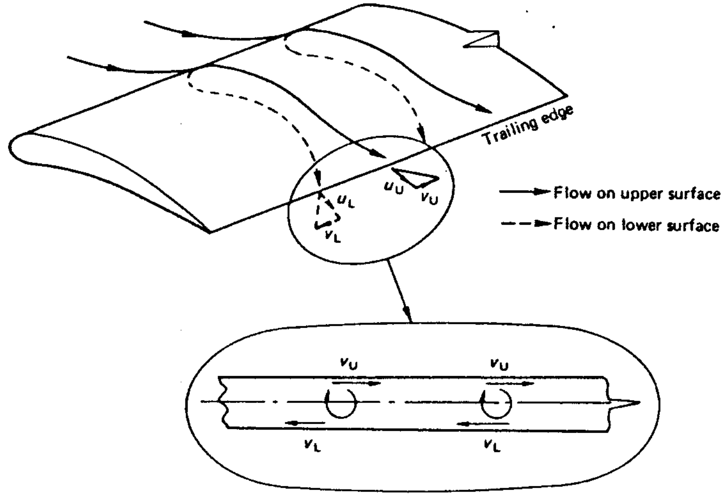

Figure 7.27 Formation of trailing vortices

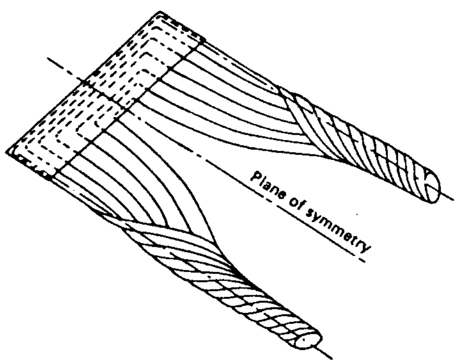

Figure 7.28 Schematic roll-up of trailing vortices

vortices will of course, by Helmholtz's theorem, be equal to the strength of the vortex replacing the wing itself and will trail downstream to join the starting vortex, Figure 7.12; again in order to satisfy Helmholtz's theorems. Furthermore, it is of interest to compare the trailing vortex pattern of Figure 7.28 with that of Prandtl's classical model, shown in Figure 7.1, where roll-up of the free vortices was not considered. Although Figure 7.28 relates to a wing section, it is clear that the same hydrodynamic mechanism applies to a propeller blade form.

7.10 Models of propeller action

Models aimed at describing the action of the marine propeller tend in general to solve the potential flow problem, subject to viscous constraints, defined by the propeller operating at a particular advance and rotational speed. In one case, the design problem, the aim is to define the required blade geometry for a given set of operating conditions; and in the other, the analysis problem, which is the inverse of the design problem, the geometry is defined and the resulting load and flow condition calculated.

The propeller analysis problem, for example, is formulated by considering the propeller to function in an unbounded incompressible fluid and to have an inflow which is defined as the effective flow field. This effective flow field, which was discussed in Chapter 5, is defined in terms of a fixed Cartesian reference frame, and the propeller, whose shaft axis is coincident with one of the axes of the effective flow field reference frame, is defined with respect to a rotating reference frame (Chapter 3). For the purposes of analysis the propeller is considered to comprise a number of identical blades, symmetrically arranged around a boss which is assumed to rotate with constant speed. The boss is either idealized as an axisymmetric body or, alternatively, ignored: this latter option was normally the case with many of the earlier theoretical models.

The definition of the blade geometry within the analytical model is normally based on the locus of the mid-chord line of each of the sections. This locus is defined with respect to one axis of the rotating reference frame by its radial distribution of rake and skew. Having defined this locus, the leading and trailing edges of the blade can then be defined by laying off the appropriate half chord lengths along each of the helix lines at the defined radii. These helix lines are defined by the radial distribution of the section nose–tail pitch. This process effectively defines the section nose–tail lines in space, whereupon the blade section geometry can be defined in terms of the radial and chordwise distribution of camber and section thickness.

The solution of the hydrodynamic problem of defining the velocity potential at a point on the surface of the blades can be expressed, in the same way as any other incompressible flow problem around a lifting body, as a surface integral over the blade surfaces and the wake by employing Green's formula. For analysis purposes this generalized formulation of the propeller analysis problem can be defined as a distribution of vorticity and sources over the blades together with a distribution of free vorticity in the wake of the propeller defining the vortex sheets emanating from the blades. The distribution of sources, and by implication sinks, is to represent in hydrodynamic terms the flow boundaries defined by the blade surface geometry. In some propeller analysis formulations the distributions of vorticity are replaced by an equivalent distribution of normal dipoles in such a way that the vortex strength is defined by the derivative of the strength of the dipoles. The completion of the definition of the analysis problem is then made by the imposition of the Kutta condition at the trailing edge, thereby effectively defining the location in space of the vortex sheets, and the introduction of a boundary layer approximation.

In order to solve the analysis problem it is frequently the case that the longitudinal and time-dependent properties of the effective inflow field are ignored. When this assumption is made the flow can be considered to be cyclic, and as a consequence the effective inflow defined in terms of the normal Fourier analysis techniques.

The foregoing description of the analysis problem, the design problem being essentially the inverse of the analysis situation but conducted under a mean inflow condition, defines a complex mathematical formulation, the solution of which has been generally attempted only in comparatively recent times, as dictated by introduction of enhanced computational capabilities. Having said this, there were early examples of solutions based on these types of approach, notably those by Strescheletzky, who achieved solutions using an 'army' of technical assistants armed with hand calculators. As previously discussed, the solution of the propeller problem is essentially similar to any other incompressible flow problem about a three-dimensional body and, in particular, there is a close connection between subsonic aeroplane wing and marine propeller technologies. Indeed the latter, although perhaps older, relied for much of its development on aerodynamic theory. Notwithstanding the similarities there are significant differences, the principal ones being the helical nature of marine propeller flow and the significantly lower aspect ratio of the blades.

For discussion purposes, however, the models of propeller action normally fall into one of four categories as follows:

1. momentum or blade element models;
2. lifting line models;
3. lifting surface models;
4. boundary element models.

With regard to these four models, the momentum and blade element approaches will be introduced and discussed in the next chapter. However, the remaining three models will be briefly introduced here in the

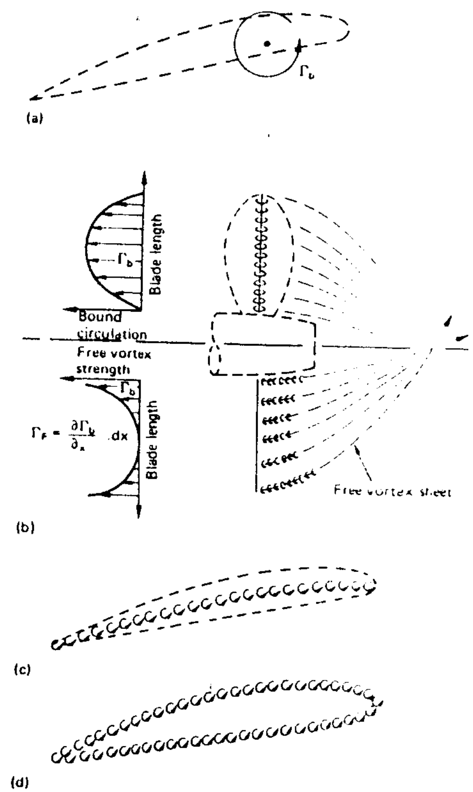

Figure 7.29 Hydrodynamic models of propeller action (a) lifting line; (b) lifting line model of propeller action; (c) lifting surface; (d) surface vorticity

context of basic principles prior to discussion of particular approaches or combinations of approaches in Chapter 8.

The lifting line model is perhaps the simplest mathematical model of propeller action in that it assumes the aerofoil blade sections to be replaced by a single line vortex whose strength varies from section to section. The line, which is a continuous line in the radial direction about which vortices act, is termed the lifting line, and is normally considered to pass through the aerodynamic centres of the sections; this, however, is not always the case, especially with the earlier theories, where the directix was frequently used as the location for the lifting line. Figure 7.29(a) demonstrates for a particular section the lifting line concept in which the aerofoil and its associated geometry is replaced by a single point. The lifting line concept is ideal for aeroplane propellers on account of their high aspect ratio, but for the marine propeller, with low aspect ratios and consequent strong three-dimensional effects over the wide blades, this approach, although simple, does have significant disadvantages. Since the strength of the bound vortices vary in the radial direction, then to satisfy Helmholtz's theorem, free vortices are shed from bound vortices along the lifting line whose strengths are given by

$$\Gamma_F = \left(\frac{d\Gamma_b}{dr}\right)\Delta r \qquad (7.56)$$

where Γ_b is the bound vortex strength and r is the radial position on the propeller. Figure 7.29(b) also outlines this concept and the similarity with Prandtl's classical lifting line theory for wings, shown in Figure 7.1, can be appreciated.

A higher level of blade representation is given by the lifting surface model. Rather than replacing the aerofoil section with single bound vortex, as in the lifting line case, here the aerofoil is represented by an infinitely thin, bound vortex sheet. This bound vortex sheet is used to represent the lifting properties of the blade, in a manner analogous to thin aerofoil theory, and in the later theories the section thickness geometry is represented by source–sink distribution in order to estimate more correctly the section surface pressure distributions for cavitation prediction purposes. Such a model, normally referred to as a lifting surface model, is shown schematically in Figure 7.29(c). Models of this type present an order of numerical complexity greater than those for the lifting line concept; however, they too provide an attractive compromise between the simpler models and a full surface vorticity model. In this latter class of models the distribution of vorticity is placed around the section as seen in Figure 7.29(d), and thereby takes into account the effects of section thickness more fully than otherwise would be the case. Clearly, in both the lifting surface and surface vorticity models the strengths of the component vortices must be such that they generate the required circulation at each radial station.

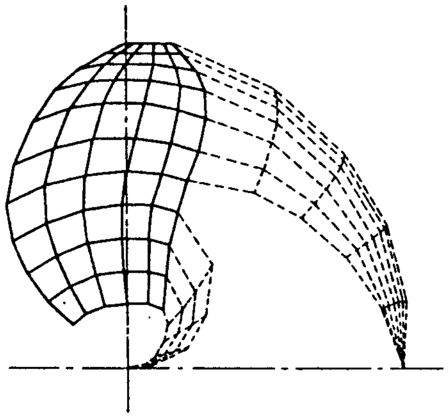

Figure 7.30 Vortex lattice model of propeller

Vortex lattice models, Figure 7.30, represent one of the more recent developments in propeller theoretical models. In this figure the solid lines represent the blade model and the hatched line the model of the propeller wake in terms of the roll-up of the vortices from the tip and root sections. Vortex lattice models make use of the concept of straight line segments of vortices joined together to cover the propeller blade with a system of vortex panels. The velocities at the control points, defined in each panel, over the blade are expressed in terms of the unknown strengths of the vortices, and by applying a flow tangency condition at each control point the vortex strengths over the blade can be calculated and the flow problem solved. Hence vortex lattice models are a subclass of lifting surface models, and consider the flow problem using a discrete rather than continuous system of singularities over the blade, which makes the computations somewhat less onerous.

In order to move toward the full surface vorticity concept idealized in Figure 7.29(d), much interest has been generated in the use of panel methods to provide a solution to the propeller design and analysis problems. The next section in this chapter considers the underlying principles of panel methods.

7.11 Source and vortex panel methods

Classical hydrodynamic theory shows that flow about a body can be generated by using the appropriate distributions of sources, sinks, vortices and dipoles distributed both within and about itself. Increased computational power has led to the development of panel methods, and these have now become common-

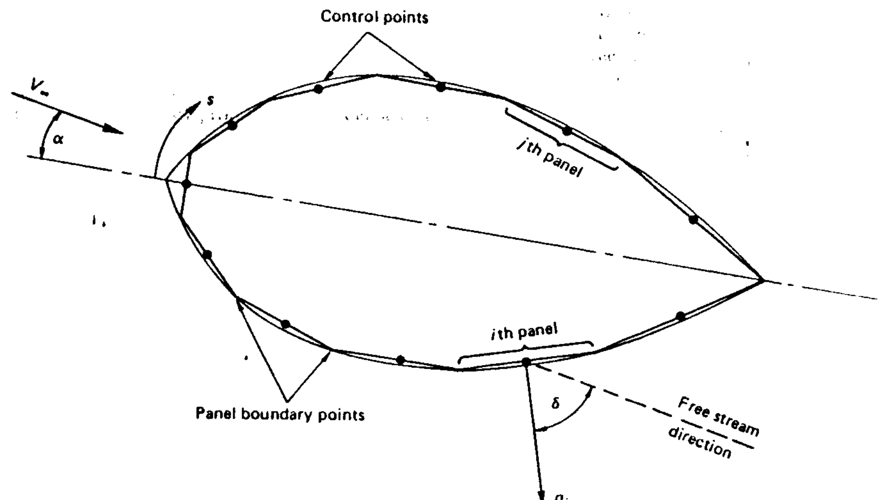

Figure 7.31 Source panel solution method

place for the solution of potential flow problems about arbitrary bodies.

In the case where the body generates no lift the flow field can be computed by replacing the surface of the body with an appropriate distribution of source panels (Figure 7.31). These source panels effectively form a source sheet whose strength varies over the body surface in such a way that the velocity normal to the body surface just balances the normal component of the free stream velocity. This condition ensures that no flow passes through the body and its surface becomes a streamline of the flow field. For practical computation purposes, the source strength λ_j, is assumed to be constant over the length of the jth panel but allowed to vary from one panel to another. The mid-point of the panel is taken as the control point at which the resultant flow is required to be a tangent to the panel surfaces, thereby satisfying the flow normality condition defined above. The end points of each panel, termed the boundary points, are coincident with those of the neighbouring panels and consequently form a continuous surface.

From an analysis of this configuration of n panels as shown in Figure 7.31, the total velocity at the surface at the ith control point, located at the mid-point of the ith panel, is given by the sum of the contributions of free stream velocity V and those of the source panels:

$$V_i = V_\infty \sin\delta + \sum_{j=1}^{n} \frac{\lambda_j}{2\pi}\int_j \frac{\partial}{\partial s}(\ln r_{ij})\,ds_j \qquad (7.57)$$

from which the associated pressure coefficient is given by

$$C_{P_i} = 1 - \left(\frac{V_i}{V_\infty}\right)^2 \qquad (7.57a)$$

In equation (7.57) r is the distance from any point on

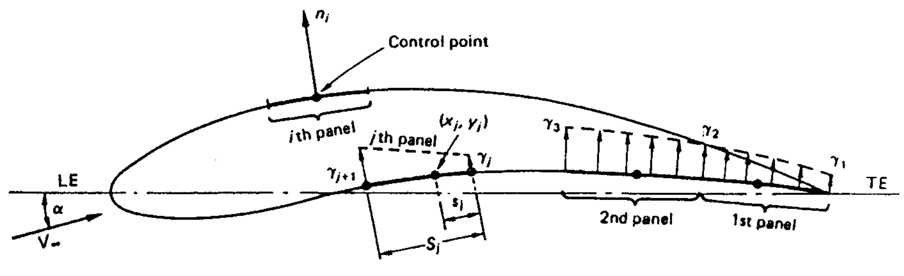

Figure 7.32 Vortex panel solution method

the jth panel to the mid-point on the ith panel and s is the distance around the source sheet.

When the body for analysis is classified as a lifting body, the alternative concept of a vortex panel must be used since the source panel does not possess the circulation property which is essential to the concept of lift generation. The modelling procedure for the vortex panel is analogous to that for the source panel in that the body is replaced by a finite number of vortex panels as seen in Figure 7.32. On each of the panels the circulation density is varied from one boundary point to the other and is continuous over the boundary point. In these techniques the Kutta condition is easily introduced and is generally stable unless large numbers of panels are chosen on an aerofoil with a cusped trailing edge.

As in the case of the source panels the boundary points and control points are located on the surface of the body; again with control points at the mid-panel position. At these control points the velocity normal to the body is specified so as to prevent flow through the aerofoil. Using this approach the velocity potential at the ith control point (x_i, y_i) is given by

$$\phi(x_i, y_i) = V_\infty(x_i \cos\alpha + y_i \sin\alpha) - \sum_{j=1}^{m} \int \frac{\gamma(s_j)}{2\pi} \tan^{-1}\left(\frac{y_i - y_j}{x_i - x_j}\right) ds_j \quad (7.58)$$

for a system of m vortex panels, with

$$\gamma(s_j) = \gamma_j + (\gamma_{j+1} - \gamma_j)\frac{s_j}{S_j} \quad (7.58a)$$

Methods of this type – and the outline discussed here is but one example – can be used in place of the classical methods, for example Theodorsen or Weber, to calculate the flow around aerofoils. Typically for such a calculation one might use 50 or so panels to obtain the required accuracy, which presents a fairly extensive numerical task as compared to the classical approach. However, the absolute number of panels used for a particular application is dependent upon the section thickness to chord ratio in order to preserve the stability of the numerical solution. Nevertheless, methods of this type do have considerable advantages when considering cascades or aerofoils with flaps, for which exact methods are not available.

In a similar manner to the classical two-dimensional methods, source and vortex panel methods can be extended to three-dimensional problems. However, for the panel methods the computations become rather more complex but no new concepts are involved.

References and further reading

1. Milne-Thomson, L.M. *Theoretical Aerodynamics*, Dover, 1973.
2. Milne-Thomson, L.M. *Theoretical Hydrodynamics*, Macmillan, 1968.
3. Lighthill, J. *An Informal Introduction to Theoretical Fluid Mechanics*, Oxford, 1986.
4. Anderson, J.D. *Fundamentals of Aerodynamics*, McGraw-Hill, 1985.
5. Prandtl, L., Tietjens, O.G. Applied Hydro- and Aeromechanics, United Engineering Trustees, 1934; also Dover, 1957.
6. Burrill, L.C. Calculation of marine propeller performance characteristics. *Trans NECIES*, 1944.
7. Hawdon, L., Carlton, J.S., Leathard, F.I. The analysis of controllable pitch propellers characteristics at off-design conditions. *Trans. I.Mar.E.*, 1976.
8. Pankhurst, R.C. A Method for the Rapid Evaluation of Glauert's Expressions for the Angle of Zero Lift and the Moment at Zero Lift. R. & M. No. 1914, March, 1944.
9. Theodorsen, T. Theory of Wing Sections of Arbitrary Shape. NACA Report No. 411, 1931.
10. Theodorsen, T., Garrick, I.E. General Potential Theory of Arbitrary Wing Sections. NACA Report No. 452, 1933.
11. Abbott, H., Doenhoff, A.E. van. *Theory of Wing Sections*. Dover, 1959.
12. Pinkerton, R.M. Calculated and Measured Pressure Distributions over the Mid-Span Sections of the NACA 4412 Airfoil. NACA Rept. No. 563, 1936.
13. Riegels, F., Wittich, H. *Zur Bereschnung der Druckverteilung von Profiles*. Jahrbuch der Deutschen Luftfahrtforschung, 1942.
14. Weber, J. The Calculation of the Pressure Distribution on the Surface of Thick Cambered Wings and the Design of Wings with Given Pressure Distributions. R. & M. No. 3026 June, 1955, HMSO.
15. Wilkinson, D.H. A Numerical Solution of the Analysis and Design Problems for the Flow Past one or more Aerofoils in Cascades. R. & M. No. 3545, 1968, HMSO.
16. Firmin, M.C.P. Calculation of the Pressure Distribution, Lift and Drag on Aerofoils at Subcritical Conditions. RAE Tech. Rep. 72235, 1972.
17. Schlichting, H. *Boundary Layer Theory*. McGraw-Hill, 1979.
18. Owen, R.R., Klanfer, L. RAE Report Aero, 2508, 1953.
19. Oossanen, P. van. Calculation of Performance and Cavitation Characteristics of Propellers Including Effects of Non-Uniform Flow and Viscosity. NSMB Publication 457.
20. Curle, N., Skau, S.W. Approximation methods for predictory separation properties of laminar boundary layers. *Aeronautical Quarterly*, No. 3, 1957.
21. Smith, A.M.O. Transition, pressure gradient, and stability theory. *Proc. 9th Int. Congress of App. Mech.*, Brussels, 4, 1956.
22. Nash, J.F., Macdonald, A.G.J. The Calculation of Momentum Thickness in a Turbulent Boundary Layer at Mach Numbers up to Unity. ARC Paper C.P. No. 963, 1967.

8 Theoretical methods – propeller theories

Contents

The proceeding chapter introduced and discussed the basic building blocks upon which the theory of propeller action has been based. This chapter, as outlined in Table 7.1, will now build upon that foundation and outline the important theories. However, as only a cursory glance at the propeller literature will reveal, this is a vast subject, and therefore in this chapter we will discuss classes of propeller theory and use one method from the class as being representative of that class for discussion purposes. The choice of method for this purpose will perhaps say more about the author's own usage and preferences rather than represent any general consensus about the superiority of the method. In each case, however, references will be given to other methods in the class under discussion.

The theoretical methods have, as far as possible, been introduced in their chronological order so as to underline the thread of development of the subject through time. Consequently, it is logical to start with the earliest attempt by Rankine (Reference 1) at producing a basis for propeller action.

8.1 Momentum theory – Rankine (1865); R.E. Froude (1887)

Rankine proposed a simple theory of propeller action based on the axial motion of the water passing through the propeller disc. Hence his theory did not concern itself with the geometry of the propeller which was producing the thrust, and consequently, his work is not very useful for blade design purposes. It does, however, lead to some general conclusions about propeller action which have subsequently been validated by more recent propeller theoretical methods and experiment.

The assumptions upon which Rankine based his original theory are as follows:

1. The propeller works in an ideal fluid and, therefore, does not experience energy losses due to frictional drag.
2. The propeller can be replaced by an actuator disc, and this is equivalent to saying that the propeller has an infinite number of blades.
3. The propeller can produce thrust without causing rotation in the slipstream.

The actuator disc concept is very common in earlier propeller theories and can be considered to be a notional disc having the same diameter as the propeller but of infinitesimal thickness. This disc, which is located at the propeller plane, is considered to absorb all of the power of the engine and dissipate this power by causing a pressure jump, and hence an increase of total head of the fluid, across the two faces of the disc.

Rankine's original theory, which is based on the above three assumptions, is generally known as the 'axial momentum theory'. R.E. Froude in his subsequent work (Reference 2) removed the third assumption and allowed the propeller to impart a rotational velocity to the slipstream, and thereby to become a more realistic model of propeller action. The subsequent theory is known either as the Rankine Froude momentum theory or the general momentum theory of propellers. Here we shall follow the more general case of momentum theory, which is based on the first two assumptions only.

Figure 8.1 shows the general case of a propeller which has been replaced by an actuator disc and is working inside a stream tube; in the Figure the flow is proceeding from left to right. Stations A and C are assumed to be far upstream and downstream respectively of the propeller, and the actuator disc is located at station B. The static pressure in the slipstream at stations A and C will be the local static pressure p_o, and the increase in pressure immediately behind the actuator disc is Δp, as also shown in Figure 8.1. Now the power P_D absorbed by the propeller and the thrust T generated are equal to the increase in kinetic energy of the slipstream per unit time and the increase in axial momentum of the slipstream respectively:

$$\left.\begin{aligned} P_D &= (\dot{m}/2)[V_C^2 - V_A^2] \\ T &= \dot{m}[V_C - V_A] \end{aligned}\right\} \tag{8.1}$$

where $\dot{m}$ is the mass flow per unit time through the disc, from which it can be shown that

$$P_D = \tfrac{1}{2}T[V_C + V_A] \tag{8.2}$$

However, the delivered power P_D is also equal to the work done by the thrust force of the propeller:

$$P_D = TV_B \tag{8.3}$$

Then, by equating equations (8.2) and (8.3), we find that the velocity at the propeller disc is equal to the mean of the velocities far upstream and downstream of the propeller:

$$V_B = \tfrac{1}{2}[V_C + V_A] \tag{8.4}$$

If V_B and V_C are expressed in terms of the velocity V_A far upstream as follows:

$$\left.\begin{aligned} V_B &= V_A + aV_A \\ V_C &= V_A + a_1 V_A \end{aligned}\right\} \tag{8.5}$$

where a and a_1 are known as the axial inflow factors at the propeller disc and in the ultimate wake (far upstream), then by combining equation (8.4) with equation (8.5) we derive that

$$a_1 = 2a \tag{8.6}$$

Equations (8.4)–(8.6) lead to the important result that half the acceleration of the flow takes place before the propeller disc and the remaining half after the propeller disc. As a consequence of this result it follows that the slipstream must contract between the conditions existing far upstream and those existing downstream in order to satisfy the continuity equation of fluid mechanics.

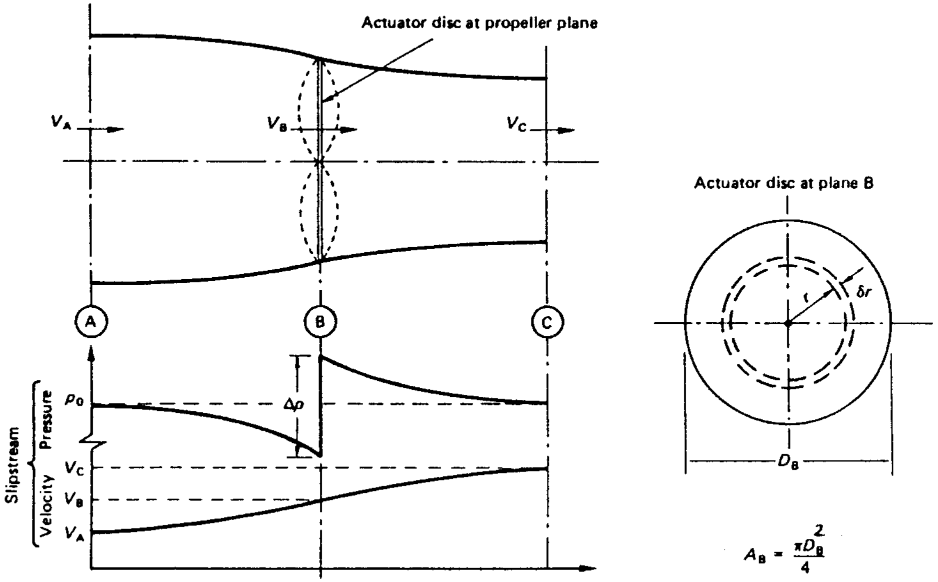

Figure 8.1 Basis of momentum theory

From equation (8.1) the thrust is given by

$$T = \dot{m}[V_C - V_A]$$

and by combining this equation with (8.4) and the continuity equation

$$\varrho V_B A_B = \varrho V_A A_A \tag{8.7}$$

we can derive that

$$C_T = \frac{T}{\varrho A_B V_A^2} = 2\left(\frac{D_A}{D_B}\right)^2\left[\left(\frac{D_A}{D_B}\right)^2 - 1\right]$$

from which it can be shown that the contraction at the propeller plane D_B/D_A is given in terms of the propeller thrust coefficient C_T as

$$\left(\frac{D_B}{D_A}\right) = \frac{1}{\sqrt{[\frac{1}{2}(1 + \sqrt{(1 + 2C_T)}]}} \tag{8.8}$$

A similar, although slightly more complex, result can be derived for the contraction of the slipstream after the propeller. Figure 6.21 showed some experimental correlation by Nagamatsu and Sasajima with this formula which, as can be seen, is derived purely from axial momentum consideration.

If it is conjectured that the increase in pressure Δp is due to the presence of an angular velocity ω in the slipstream immediately behind the propeller disc, then the angular velocity of the water relative to the propeller blades, immediately ahead and astern of the propeller, is respectively Ω, and $\Omega - \omega$. Then from Bernoulli's theorem the increase in pressure Δp at a particular radius r is given by

$$\Delta p = \varrho(\Omega - \tfrac{1}{2}\omega)\omega r^2$$

Also the elemental thrust dT acting at some radius r is

$$dT = 2\pi r \Delta p\, dr$$

which, by writing $\omega = 2a'\Omega$, where a' is a rotational inflow factor, reduces to

$$dT = 4\pi\varrho r^3\Omega^2(1 - a')a' \tag{8.9}$$

Now the elemental torque dQ at the same radius r is equal to the angular momentum imparted to the slipstream per unit time within the annulus of thickness dr, namely

$$\begin{aligned} dQ &= \dot{m}\omega r^2 = 2\pi\varrho r^3\omega\, dr \\ &= 4\pi\varrho r^3 V_A\Omega(1 + a)a'\, dr \end{aligned} \tag{8.10}$$

The ideal efficiency of the blade element (η_i) is given by

$$\eta_i = \frac{\text{thrust horsepower}}{\text{delivered horsepower}} = \frac{V_A\, dT}{\Omega\, dQ} \tag{8.11}$$

hence, by substituting equations (8.9) and (8.10) into equation (8.11), we have

$$\eta_i = \frac{(1 - a')}{(1 + a)} \tag{8.12}$$

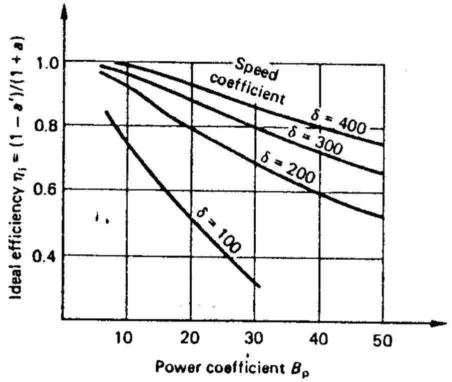

Figure 8.2 Ideal propeller efficiency from general momentum theory

It can further be shown from this theory that for maximum efficiency the value of η_i should be the same for all radii. Equation (8.12) leads to the second important result of momentum theory, which is that there is an upper bound on the efficiency of an ideal, frictionless propeller. The ideal efficiency is a measure of the losses incurred by the propeller because the changes in momentum necessary to generate the required forces are accompanied by changes in kinetic energy. Figure 8.2 shows the relationships obtained from general momentum theory between η_i and the normal propulsion coefficients of B_p and δ for comparison purposes with actual experimental propeller results, remembering of course that the curves of η_i represent an upper bound for the efficiency value.

If the rotational assumption had not been removed in the derivation for η_i, then the ideal efficiency would have been found to be

$$\eta_i = \frac{1}{(1 + a)} \tag{8.13}$$

8.2 Blade element theory – W. Froude (1878)

In contrast to the work of Rankine, W. Froude (Reference 3) developed a quite different model of propeller action, which took account of the geometry of the propeller blade. In its original form the theory did not take account of the acceleration of the inflowing water from its far upstream value relative to the propeller disc. This is somewhat surprising, since this could have been deduced from the earlier work of Rankine; nevertheless, this omission was rectified in subsequent developments of the work.

Blade element theory is based on dividing the blade

up into a large number of elementary strips, as seen in Figure 8.3. Each of these elementary strips can then be regarded as an aerofoil subject to a resultant incident velocity W.

The resultant incident velocity was considered to comprise an axial velocity V together with a rotational velocity Ωr, which clearly varies linearly up the blade. In the normal working condition the advance angle β is less than the blade pitch angle θ at the section, and hence gives rise to the section having an angle of incidence α. The section will, therefore, experience lift and drag forces from the combination of this incidence angle and the section zero lift angle, from which one can deduce that, for a given section geometry, the elemental thrust and torques are given by

$$\left.\begin{aligned} dT &= \tfrac{1}{2}\varrho ZcW^2(c_l\cos\beta - c_d\sin\beta)\,dr \\ dQ &= \tfrac{1}{2}\varrho ZcW^2(c_l\sin\beta + c_d\cos\beta)\,dr \end{aligned}\right\} \tag{8.14}$$

where Z and c are the number of blades and the chord length of the section respectively.

Now since the efficiency of the section η is given by

$$\eta = \frac{V\,dT}{\Omega\,dQ}$$

then by writing $c_d/c_l = \gamma$ and substituting equation (8.14) into this expression for efficiency, we derive that

$$\eta = \frac{\tan\beta}{\tan(\beta + \gamma)} \tag{8.15}$$

Consequently, this propeller-theoretical model allows the thrust and torque to be calculated provided that the appropriate values of lift and drag are known. This, however, presented another problem since the values of c_l and c_d could not be readily calculated for the section due to the difficulty in establishing the effective aspect ratio for the section.

The basic Froude model can, as mentioned previously, be modified to incorporate the induced velocities at the propeller plane. To do this the advance angle β is modified to the hydrodynamic pitch angle β_i, and the velocity diagram shown in Figure 8.3 is amended accordingly to incorporate the two induced velocities, as shown in the inset to the figure.

Although Froude's work of 1878 failed in some respects to predict propeller performance accurately, it was in reality a great advance, since it contained the basic idea upon which all modern theory is founded. It was, however, to be just over half a century later before all of the major problems in applying these early methods had been overcome.

8.3 Propeller-theoretical development (1900–1930)

Immediately prior to this period propeller theory was seen to have been developing along two quite separate paths, namely the momentum and blade element

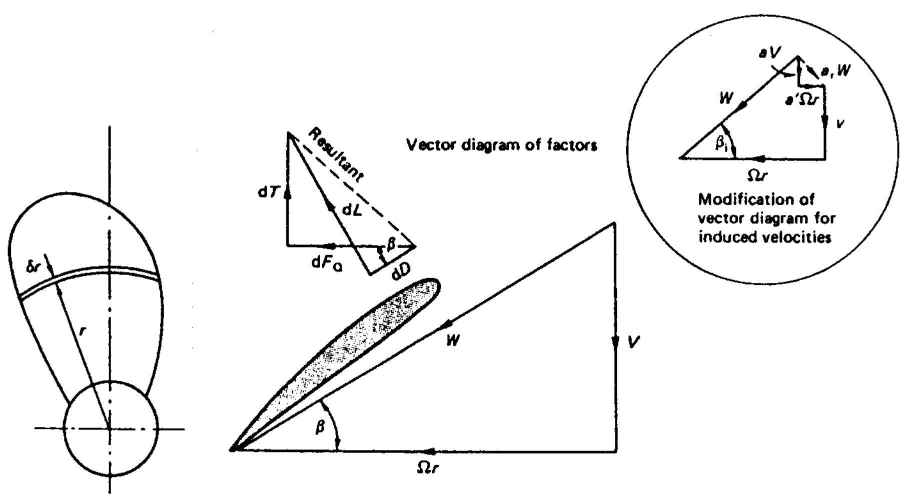

Figure 8.3 Blade element theory

theories. This led to some very inconsistent results; for example, blade element theory suggests that propeller efficiency will tend towards 100% if the viscous forces are reduced to zero, whereas momentum theory, which is an inviscid approach, defines a specific limit on efficiency which is dependent upon speed of advance and thrust coefficient; Figure 8.2. This and other discrepancies led to a combination of the two theories by some engineers in which the induced velocities are determined by momentum theory and the analysis then conducted by the blade element theory. Although this was successful in many respects, none of these combined theories were entirely satisfactory.

In Chapter 7 we have seen how Lanchester and Prandtl put forward the concept that the lift of a wing was due to the development of circulation around the section and that a system of trailing vortices emanated from the blade and its tips. However, it was not until 1919 that Prandtl had the necessary experimental confirmation of this new vortex theory. The application of this method to the propeller problem led to the conclusion that free vortices must spring from the tips of the propeller when operating, and that if due allowance is made for the induced velocities caused by these free vortices, which have a helical form, the forces at the blade elements will be the same as in two-dimensional flow. Consequently, the lift and drag coefficients for the section could be obtained from two-dimensional wind tunnel test data provided the results were corrected for aspect ratio according to Prandtl's formula. As this is standard wind tunnel technique, this then opened up a fund of aeronautical data for propeller design purposes.

The total energy loss experienced by the propeller comprises the losses caused by the creation of kinetic energy in the slipstream due to the effects of induced drag and the losses resulting from the motion of sections in a viscous fluid; that is, their profile drag. This latter component can be minimized by proper attention to the design of the blade sections; however, this is not the case with the losses resulting from the induced drag. The induced drag is a function of the design conditions, and in order to maximize the efficiency of a propeller it is necessary to introduce a further parameter which will ensure that the induced drag is minimized. Betz (References 4, 5) established the basic minimum energy loss condition by analysing the vortex system in the slipstream of a lightly loaded propeller having an infinite number of blades and working in a uniform stream. He established that the induced drag is minimized when the vortex sheets far behind the propeller are of constant pitch radially; in formal terms this leads to the condition for each radius:

$$x\pi D \tan \beta_\varepsilon = \text{constant} \qquad (8.16)$$

where β_ε is the pitch angle of the vortex sheet at each radius far behind the propeller in the ultimate wake.

It follows from the Betz condition that for a uniform stream propeller the vortex sheets will leave the lifting line at constant pitch and undergo a deformation downstream of the propeller until they finally assume a larger constant pitch in the ultimate wake. Furthermore, for the propeller working in the uniform stream condition the direction of the resultant induced velocity $a_t W$, in the inset of Figure 8.3, is normal to the direction of the inflow velocity W at the lifting line.

This result is known as the 'condition of normality' for a propeller working in an ideal fluid. In an appendix to Betz's paper Prandtl established a simple method for correcting the results for propellers having a small number of blades. This was based on the results of a model which replaced a system of vortex sheets by a series of parallel lines with a regular gap between them.

The total circulation at any radius on a propeller blade derived from the Betz condition relates to the infinitely bladed propeller. For such a propeller it can be shown (Reference 6) that the induced velocities at the propeller disc are the same as those derived from simple axial momentum theory. In the case of the 'infinite' blade number the helical vortex sheets emanating from each blade are 'very close' together; however, for the real case of a propeller with a small number of blades, the trailing vortices are separated from each other. Hence, the mean induced velocity in the latter case, when considered about a circumferential line at some radius in the propeller disc, is less than the local induced velocity at the blades. Prandtl's earlier relationship for the mean velocity at a particular radius, when compared to the velocity of the lifting line, was

$$K = \frac{2}{\pi}\cos^{-1}\left[\exp\left\{-\frac{Z}{2\tan\beta_i}(1-x)\sqrt{(1+\tan^2\beta_i)}\right\}\right] \qquad (8.17)$$

This important effect was studied later by Goldstein (Reference 7) who considered the flow past a series of true helicoidal surfaces of infinite length. He obtained

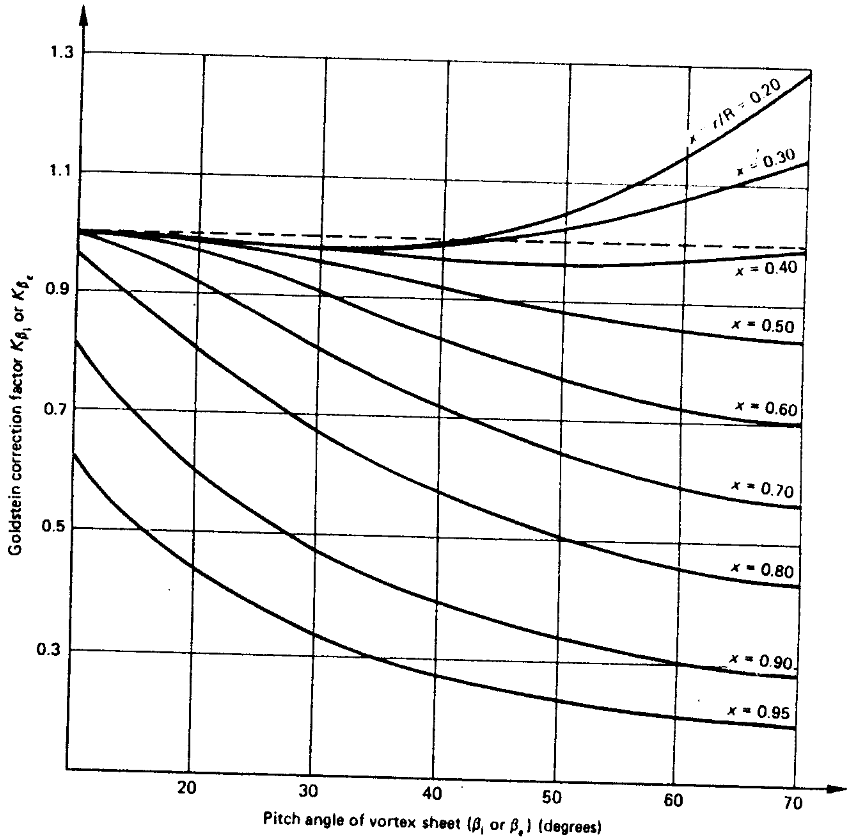

Figure 8.4 Goldstein correction factors for a four-bladed propeller

an expression for the ratio between the mean circulation taken around an annulus at a particular radius and the circulation at the helicoidal surfaces. These values take the form of a correction factor K and an example is shown in Figure 8.4 for a four-bladed propeller. From this Figure it is readily seen that the corrections have more effect the greater the non-dimensional radius of the propeller. This is to be expected, since the distance between the blade sections is greater for the outer radii, and since the induced velocity at the lifting line would normally be a maximum it follows that the mean induced velocity through an annulus at a particular radius will be less than the value at the lifting line, the ratio being given by the Goldstein factor. At zero pitch angle the value of the correction factor is clearly unity.

Goldstein's work was based on the model of a propeller which has zero boss radius. In practice this is clearly not the case and Tachmindji and Milam (Reference 8) subsequently made a detailed set of calculations for propellers with blade numbers ranging from 3 to 6 and having a finite hub radius of $0.167R$. Table 8.1 defines these values, from which it is seen that values at the outer radii are broadly comparable, as might be expected, whereas those at the inner radii change considerably.

With the work of Goldstein, Betz, Prandtl and Lanchester, the basic building blocks for a rational propeller theory were in place by about 1930. Although Perring (Reference 9) and Lockwood Taylor (Reference 10) established theories of propeller action, it was left to Burrill (Reference 11) to establish an analytical method which gained comparatively wide acceptance within the propeller community. Indeed the analysis procedure that Burrill published in 1944 is still used quite widely today for general non-specialist, moderately loaded propellers; largely because it lends itself to rapid hand calculation.

Table 8.1 Goldstein–Tachminji correction factors for $x_n = 0.167$ (compiled from Reference 8)

Blade number = 3

	r/R 0.950	0.900	0.800	0.700	0.600	0.500	0.400	0.300
0	1.000	1.000	1.000	1.000	1.000	1.000	1.000	1.000
5	0.729	0.902	0.990	0.999	1.000	1.000	1.000	1.000
10	0.543	0.732	0.916	0.979	0.995	0.997	0.996	0.988
15	0.443	0.612	0.818	0.925	0.971	0.985	0.982	0.963
20	0.372	0.523	0.725	0.854	0.928	0.961	0.963	0.934
25	0.320	0.454	0.645	0.782	0.876	0.929	0.943	0.911
30	0.280	0.401	0.578	0.716	0.822	0.893	0.923	0.896
35	0.249	0.358	0.523	0.658	0.771	0.857	0.904	0.888
40	0.225	0.325	0.479	0.609	0.726	0.823	0.888	0.886
45	0.206	0.298	0.442	0.569	0.686	0.793	0.874	0.891
50	0.191	0.277	0.413	0.536	0.654	0.767	0.863	0.902
55	0.179	0.260	0.390	0.509	0.627	0.745	0.855	0.916
60	0.170	0.247	0.372	0.488	0.605	0.728	0.850	0.935
65	0.162	0.236	0.357	0.471	0.589	0.715	0.849	0.957
70	0.157	0.228	0.347	0.459	0.577	0.707	0.850	0.982

Blade number = 5

	r/R	0.900	0.800	0.700	0.600	0.500	0.400	0.300
0	1.000	1.000	1.000	1.000	1.000	1.000	1.000	1.000
5	0.858	0.973	0.992	1.000	1.000	1.000	1.001	1.002
10	0.681	0.864	0.980	0.998	0.999	0.999	0.999	1.000
15	0.572	0.759	0.932	0.984	0.995	0.997	0.996	0.992
20	0.496	0.675	0.872	0.957	0.985	0.991	0.990	0.980
25	0.438	0.606	0.811	0.919	0.968	0.982	0.982	0.966
30	0.393	0.549	0.753	0.876	0.944	0.971	0.975	0.956
35	0.356	0.502	0.701	0.834	0.918	0.960	0.970	0.949
40	0.326	0.462	0.656	0.794	0.891	0.948	0.969	0.949
45	0.302	0.430	0.617	0.758	0.865	0.937	0.971	0.957
50	0.282	0.403	0.584	0.727	0.842	0.928	0.977	0.972
55	0.266	0.382	0.557	0.700	0.822	0.920	0.986	0.994
60	0.258	0.364	0.535	0.678	0.805	0.914	0.997	1.023
65	0.243	0.351	0.517	0.660	0.791	0.911	1.011	1.058
70	0.235	0.331	0.503	0.646	0.781	0.909	1.025	1.095

Blade number = 4

	r/R 0.950	0.900	0.800	0.700	0.600	0.500	0.400	0.300
0	1.000	1.000	1.000	1.000	1.000	1.000	1.000	1.000
5	0.804	0.949	0.997	0.999	1.000	1.000	1.000	1.001
10	0.620	0.810	0.959	0.993	0.998	0.999	0.999	0.997
15	0.514	0.696	0.890	0.966	0.989	0.994	0.992	0.983
20	0.440	0.609	0.813	0.921	0.969	0.983	0.982	0.964
25	0.385	0.539	0.742	0.868	0.938	0.967	0.970	0.946
30	0.341	0.483	0.679	0.814	0.902	0.948	0.959	0.933
35	0.307	0.437	0.624	0.763	0.864	0.927	0.950	0.926
40	0.279	0.400	0.578	0.717	0.828	0.906	0.944	0.927
45	0.257	0.369	0.539	0.678	0.795	0.886	0.941	0.935
50	0.240	0.345	0.507	0.644	0.766	0.869	0.941	0.951
55	0.225	0.325	0.481	0.617	0.741	0.854	0.944	0.973
60	0.214	0.309	0.460	0.594	0.721	0.843	0.949	1.000
65	0.205	0.297	0.440	0.576	0.705	0.834	0.956	1.033
70	0.198	0.288	0.431	0.562	0.694	0.829	0.965	1.068

Blade number = 6

	r/R 0.950	0.900	0.800	0.700	0.600	0.500	0.400	0.300
0	1.000	1.000	1.000	1.000	1.000	1.000	1.000	1.000
5	0.897	0.986	1.000	1.000	1.000	1.000	1.001	1.002
10	0.730	0.902	0.990	0.999	1.000	1.000	1.000	1.001
15	0.620	0.808	0.958	0.992	0.998	0.998	0998	0.997
20	0.543	0.728	0.912	0.976	0.992	0.994	0.993	0.989
25	0.484	0.661	0.859	0.949	0.982	0.989	0.988	0.979
30	0.437	0.604	0.808	0.917	0.967	0.983	0.983	0.970
35	0.398	0.556	0.761	0.883	0.949	0.976	0.980	0.964
40	0.367	0.516	0.718	0.849	0.930	0.970	0.980	0.964
45	0.341	0.483	0.680	0.818	0.911	0.965	0.985	0.970
50	0.320	0.455	0.647	0.789	0.893	0.961	0.993	0.982
55	0.303	0.432	0.620	0.765	0.878	0.959	1.004	1.002
60	0.289	0.413	0.598	0.744	0.864	0.958	1.019	1.029
65	0.278	0.398	0.579	0.727	0.854	0.959	1.036	1.061
70	0.269	0.386	0.565	0.714	0.845	0.961	1.053	1.098

8.4 Burrill's analysis procedure (1944)

Burrill's procedure is essentially a strip theory method of analysis which combines the basic principles of the momentum and blade element theories with certain aspects of the vortex analysis method. As such the method works quite well for moderately loaded propellers working at or near their design condition; however, for heavily and lightly loaded propellers the correlation with experimental results is not so good, although over the years several attempts have been made to improve its performance in these areas; for example, Sontvedt (Reference 12).

In developing his theory, Burrill considered the flow through an annulus of the propeller, as shown in Figure 8.5. From considerations of continuity through the three stations identified (far upstream, propeller disc and far downstream) one can write, for the flow through the annulus in one revolution of the propeller,

$$2\pi\varrho r_0 \frac{V_a}{n}\delta r_0 = 2\pi\varrho r_1 \frac{V_a(1 + K_{\beta_1}a)}{n}\delta r_1$$
$$= 2\pi\varrho r_2 \frac{V_a(1 + 2K_e a)}{n}\delta r_2$$

where K_{β_1} and K_e are the Goldstein factors at the propeller disc and in the ultimate wake respectively. Also V_a is the speed of advance of the uniform stream and a is the axial induction factor.

From this relation, by assuming that the inflow is constant at each radius, that is a = constant, it can be shown that the relationship between the radii of the slipstream is given by

$$r_0 = r_1(1 + K_{\beta_1}a)^{1/2} = r_2(1 + K_e a)^{1/2} \qquad (8.18)$$

Furthermore, it is also possible, by considering the momentum of the fluid in relation to the quantity flowing through the annular region, to define a relation for the thrust acting on the fluid:

$$dT = V\,dQ$$

for which the thrust at the propeller disc can be shown to be

$$dT = 4\pi r_1 K_e a V_A^2[1 + K_{\beta_1}a]\varrho\,dr_1 \qquad (8.19)$$

However, by appealing to the blade element concept, an alternative expression for the elemental thrust at a particular radius r_1 can be derived as follows:

$$dT = \frac{\rho}{2}Zc(1 + a)^2$$
$$\times \frac{V_A^2}{\sin^2\beta_i}[c_l\cos\beta_i - c_d\sin\beta_i]\,dr_1 \qquad (8.20)$$

and then by equating these two expressions, equations (8.19) and (8.20), and in a similar manner deriving two further expressions for the elemental torque acting at the particular radius, one can derive the following pair of expressions for the axial and tangential inflow factors a and a' respectively:

$$\left.\begin{aligned} \frac{a}{1+a}\left(\frac{1 + K_{\beta_1}a}{1+a}\right) &= \left(\frac{c_l\sigma_s}{2K_e}\right)\frac{\cos(\beta_i + \gamma)}{2\sin^2\beta_i\cos\gamma} \\ \frac{a'}{1-a'}\left(\frac{1 - K_{\beta_1}a}{1+a}\right) &= \left(\frac{c_l\sigma_s}{2K_e}\right)\frac{\sin(\beta_i + \gamma)}{\sin 2\beta_i\cos\gamma} \end{aligned}\right\} \qquad (8.21)$$

in which σ_s is the cascade solidity factor defined by $Zc/(2\pi r)$ and γ is the ratio of drag to lift coefficient c_d/c_l.

In equations (8.21) the lift coefficient c_l is estimated from the empirical relationships derived from wind tunnel tests on aerofoil sections and applied to the results of thin aerofoil theory as discussed in the preceding chapter. Thus the lift coefficient is given by

$$c_l = 2\pi k_s \cdot k_{gs}(\alpha + \alpha_0) \qquad (8.22)$$

where k_s and k_{gs} are the thin aerofoil to single aerofoil and single aerofoil to cascade correction factors for lift slope derived from wind tunnel test results and α_0 is the experimental zero lift angle shown in Figure 8.5(b). The term α is the geometric angle of attack relative to the nose–tail line of the section as seen in Figure 8.5(c). From equation (8;22) it can be seen that the lift slope curve reduces from 2π in the theoretical thin aerofoil case to $2\pi k_s k_{gs}$ in the experimental cascade situation; that is, the line CC in Figure 8.5(b). Burrill chooses to express k_s as a simple function of thickness to chord ratio, and k_{gs} as a function of hydrodynamic pitch angle β_i and cascade solidity σ_s. Subsequently work by van Oossanen, discussed in Chapter 7, has shown that these parameters, in particular k_s and k_{gs}, are more reliably expressed as functions of the section boundary layer thicknesses at the trailing edge of the sections.

With regard to the effective angle of attack of the section, this is the angle represented by the line CD measured along the abscissa of Figure 8.5(b) and the angle $(\alpha + \alpha_0)$ on Figure 8.5(c). This angle α_e is again calculated by appeal to empirically derived coefficients as follows:

$$\alpha_e = \alpha + \alpha_0 = \alpha + \alpha_{0_{TH}}(K_{a0} - K_{ga0}) \qquad (8.23)$$

where $\alpha_{0_{TH}}$ is the two-dimensional theoretical zero lift angle derived from equation (7.27) and K_{a0} and K_{ga0} are the single aerofoil to theoretical zero lift angle correlation factor and cascade allowance respectively. The former, as expressed by Burrill, is a function of thickness to chord ratio and position of maximum camber whilst the latter is a function of hydrodynamic pitch angle β_i and solidity of the cascade σ_s.

Now by combining equations (8.21) and (8.22) and noting that the term $(1 + K_{\beta_1}a)/(1 + a)$ can be expressed as

$$1 - [(1 - K_{\beta_1})\tan(\beta_i - \beta)/\tan\beta_i]$$

it can be shown that the effective angle of attack an expression for the ratio between the mean circulation taken around an annulus at a particular radius and the circulation at the helicoidal surfaces. These values take the form of a correction factor K and an example is shown in Figure 8.4 for a four-bladed propeller. From this Figure it is readily seen that the corrections have more effect the greater the non-dimensional radius of the propeller. This is to be expected, since the distance between the blade sections is greater for the outer radii, and since the induced velocity at the lifting line would normally be a maximum it follows that the mean induced velocity through an annulus at a particular radius will be less than the value at the lifting line, the ratio being given by the Goldstein factor. At zero pitch angle the value of the correction factor is clearly unity.

Goldstein's work was based on the model of a propeller which has zero boss radius. In practice this is clearly not the case and Tachmindji and Milam (Reference 8) subsequently made a detailed set of calculations for propellers with blade numbers ranging from 3 to 6 and having a finite hub radius of 0.167R. Table 8.1 defines these values, from which it is seen that values at the outer radii are broadly comparable, as might be expected, whereas those at the inner radii change considerably.

With the work of Goldstein, Betz, Prandtl and Lanchester, the basic building blocks for a rational propeller theory were in place by about 1930. Although Perring (Reference 9) and Lockwood Taylor (Reference 10) established theories of propeller action, it was left to Burrill (Reference 11) to establish an analytical method which gained comparatively wide acceptance within the propeller community. Indeed the analysis procedure that Burrill published in 1944 is still used quite widely today for general non-specialist, moderately loaded propellers; largely because it lends itself to rapid hand calculation.

Table 8.1 Goldstein–Tachminji correction factors for $x_n = 0.167$ (compiled from Reference 8)

Blade number = 3

	r/R							
	0.950	0.900	0.800	0.700	0.600	0.500	0.400	0.300
0	1.000	1.000	1.000	1.000	1.000	1.000	1.000	1.000
5	0.729	0.902	0.990	0.999	1.000	1.000	1.000	1.000
10	0.543	0.732	0.916	0.979	0.995	0.997	0.996	0.988
15	0.443	0.612	0.818	0.925	0.971	0.985	0.982	0.963
20	0.372	0.523	0.725	0.854	0.928	0.961	0.963	0.934
25	0.320	0.454	0.645	0.782	0.876	0.929	0.943	0.911
30	0.280	0.401	0.578	0.716	0.822	0.893	0.923	0.896
35	0.249	0.358	0.523	0.658	0.771	0.857	0.904	0.888
40	0.225	0.325	0.479	0.609	0.726	0.823	0.888	0.886
45	0.206	0.298	0.442	0.569	0.686	0.793	0.874	0.891
50	0.191	0.277	0.413	0.536	0.654	0.767	0.863	0.902
55	0.179	0.260	0.390	0.509	0.627	0.745	0.855	0.916
60	0.170	0.247	0.372	0.488	0.605	0.728	0.850	0.935
65	0.162	0.236	0.357	0.471	0.589	0.715	0.849	0.957
70	0.157	0.228	0.347	0.459	0.577	0.707	0.850	0.982

Blade number = 5

	r/R							
		0.900	0.800	0.700	0.600	0.500	0.400	0.300
0	1.000	1.000	1.000	1.000	1.000	1.000	1.000	1.000
5	0.858	0.973	0.992	1.000	1.000	1.000	1.001	1.002
10	0.681	0.864	0.980	0.998	0.999	0.999	0.999	1.000
15	0.572	0.759	0.932	0.984	0.995	0.997	0.996	0.992
20	0.496	0.675	0.872	0.957	0.985	0.991	0.990	0.980
25	0.438	0.606	0.811	0.919	0.968	0.982	0.982	0.966
30	0.393	0.549	0.753	0.876	0.944	0.971	0.975	0.956
35	0.356	0.502	0.701	0.834	0.918	0.960	0.970	0.949
40	0.326	0.462	0.656	0.794	0.891	0.948	0.969	0.949
45	0.302	0.430	0.617	0.758	0.865	0.937	0.971	0.957
50	0.282	0.403	0.584	0.727	0.842	0.928	0.977	0.972
55	0.266	0.382	0.557	0.700	0.822	0.920	0.986	0.994
60	0.258	0.364	0.535	0.678	0.805	0.914	0.997	1.023
65	0.243	0.351	0.517	0.660	0.791	0.911	1.011	1.058
70	0.235	0.331	0.503	0.646	0.781	0.909	1.025	1.095

Blade number = 4

	r/R							
	0.950	0.900	0.800	0.700	0.600	0.500	0.400	0.300
0	1.000	1.000	1.000	1.000	1.000	1.000	1.000	1.000
5	0.804	0.949	0.997	0.999	1.000	1.000	1.000	1.001
10	0.620	0.810	0.959	0.993	0.998	0.999	0.999	0.997
15	0.514	0.696	0.890	0.966	0.989	0.994	0.992	0.983
20	0.440	0.609	0.813	0.921	0.969	0.983	0.982	0.964
25	0.385	0.539	0.742	0.868	0.938	0.967	0.970	0.946
30	0.341	0.483	0.679	0.814	0.902	0.948	0.959	0.933
35	0.307	0.437	0.624	0.763	0.864	0.927	0.950	0.926
40	0.279	0.400	0.578	0.717	0.828	0.906	0.944	0.927
45	0.257	0.369	0.539	0.678	0.795	0.886	0.941	0.935
50	0.240	0.345	0.507	0.644	0.766	0.869	0.941	0.951
55	0.225	0.325	0.481	0.617	0.741	0.854	0.944	0.973
60	0.214	0.309	0.460	0.594	0.721	0.843	0.949	1.000
65	0.205	0.297	0.440	0.576	0.705	0.834	0.956	1.033
70	0.198	0.288	0.431	0.562	0.694	0.829	0.965	1.068

Blade number = 6

	r/R							
	0.950	0.900	0.800	0.700	0.600	0.500	0.400	0.300
0	1.000	1.000	1.000	1.000	1.000	1.000	1.000	1.000
5	0.897	0.986	1.000	1.000	1.000	1.000	1.001	1.002
10	0.730	0.902	0.990	0.999	1.000	1.000	1.000	1.001
15	0.620	0.808	0.958	0.992	0.998	0.998	0998	0.997
20	0.543	0.728	0.912	0.976	0.992	0.994	0.993	0.989
25	0.484	0.661	0.859	0.949	0.982	0.989	0.988	0.979
30	0.437	0.604	0.808	0.917	0.967	0.983	0.983	0.970
35	0.398	0.556	0.761	0.883	0.949	0.976	0.980	0.964
40	0.367	0.516	0.718	0.849	0.930	0.970	0.980	0.964
45	0.341	0.483	0.680	0.818	0.911	0.965	0.985	0.970
50	0.320	0.455	0.647	0.789	0.893	0.961	0.993	0.982
55	0.303	0.432	0.620	0.765	0.878	0.959	1.004	1.002
60	0.289	0.413	0.598	0.744	0.864	0.958	1.019	1.029
65	0.278	0.398	0.579	0.727	0.854	0.959	1.036	1.061
70	0.269	0.386	0.565	0.714	0.845	0.961	1.053	1.098

8.4 Burrill's analysis procedure (1944)

Burrill's procedure is essentially a strip theory method of analysis which combines the basic principles of the momentum and blade element theories with certain aspects of the vortex analysis method. As such the method works quite well for moderately loaded propellers working at or near their design condition; however, for heavily and lightly loaded propellers the correlation with experimental results is not so good, although over the years several attempts have been made to improve its performance in these areas; for example, Sontvedt (Reference 12).

In developing his theory, Burrill considered the flow through an annulus of the propeller, as shown in Figure 8.5. From considerations of continuity through the three stations identified (far upstream, propeller disc and far downstream) one can write, for the flow through the annulus in one revolution of the propeller,

$$2\pi \varrho r_0 \frac{V_a}{n}\delta r_0 = 2\pi \varrho r_1 \frac{V_a(1 + K_{\beta_i}a)}{n}\delta r_1$$

$$= 2\pi \varrho r_2 \frac{V_a(1 + 2K_\varepsilon a)}{n}\delta r_2$$

where K_{β_i} and K_ε are the Goldstein factors at the propeller disc and in the ultimate wake respectively. Also V_a is the speed of advance of the uniform stream and a is the axial induction factor.

From this relation, by assuming that the inflow is constant at each radius, that is $a =$ constant, it can be shown that the relationship between the radii of the slipstream is given by

$$r_0 = r_1(1 + K_{\beta_i}a)^{1/2} = r_2(1 + K_\varepsilon a)^{1/2} \qquad (8.18)$$

Furthermore, it is also possible, by considering the momentum of the fluid in relation to the quantity flowing through the annular region, to define a relation for the thrust acting on the fluid:

$$\mathrm{d}T = V\,\mathrm{d}Q$$

for which the thrust at the propeller disc can be shown to be

$$\mathrm{d}T = 4\pi r_1 K_\varepsilon a V_A^2[1 + K_{\beta_i}a]\varrho\,\mathrm{d}r_1 \qquad (8.19)$$

However, by appealing to the blade element concept, an alternative expression for the elemental thrust at a particular radius r_1 can be derived as follows:

$$\mathrm{d}T = \frac{\rho}{2}Zc(1 + a)^2 \times \frac{V_A^2}{\sin^2\beta_i}[c_l\cos\beta_i - c_d\sin\beta_i]\,\mathrm{d}r_1 \qquad (8.20)$$

and then by equating these two expressions, equations (8.19) and (8.20), and in a similar manner deriving two further expressions for the elemental torque acting at the particular radius, one can derive the following pair of expressions for the axial and tangential inflow factors a and a' respectively:

$$\left.\begin{aligned} \frac{a}{1+a}\left(\frac{1 + K_{\beta_i}a}{1 + a}\right) &= \left(\frac{c_l\sigma_s}{2K_\varepsilon}\right)\frac{\cos(\beta_i + \gamma)}{2\sin^2\beta_i\cos\gamma} \\ \frac{a'}{1-a'}\left(\frac{1 - K_{\beta_i}a}{1 + a}\right) &= \left(\frac{c_l\sigma_s}{2K_\varepsilon}\right)\frac{\sin(\beta_i + \gamma)}{\sin 2\beta_i\cos\gamma} \end{aligned}\right\} \qquad (8.21)$$

in which σ_s is the cascade solidity factor defined by $Zc/(2\pi r)$ and γ is the ratio of drag to lift coefficient c_d/c_l.

In equations (8.21) the lift coefficient c_l is estimated from the empirical relationships derived from wind tunnel tests on aerofoil sections and applied to the results of thin aerofoil theory as discussed in the preceding chapter. Thus the lift coefficient is given by

$$c_l = 2\pi k_s \cdot k_{gs}(\alpha + \alpha_0) \qquad (8.22)$$

where k_s and k_{gs} are the thin aerofoil to single aerofoil and single aerofoil to cascade correction factors for lift slope derived from wind tunnel test results and α_0 is the experimental zero lift angle shown in Figure 8.5(b). The term α is the geometric angle of attack relative to the nose–tail line of the section as seen in Figure 8.5(c). From equation (8;22) it can be seen that the lift slope curve reduces from 2π in the theoretical thin aerofoil case to $2\pi k_s k_{gs}$ in the experimental cascade situation; that is, the line CC in Figure 8.5(b). Burrill chooses to express k_s as a simple function of thickness to chord ratio, and k_{gs} as a function of hydrodynamic pitch angle β_i and cascade solidity σ_s. Subsequently work by van Oossanen, discussed in Chapter 7, has shown that these parameters, in particular k_s and k_{gs}, are more reliably expressed as functions of the section boundary layer thicknesses at the trailing edge of the sections.

With regard to the effective angle of attack of the section, this is the angle represented by the line CD measured along the abscissa of Figure 8.5(b) and the angle $(\alpha + \alpha_0)$ on Figure 8.5(c). This angle α_e is again calculated by appeal to empirically derived coefficients as follows:

$$\alpha_e = \alpha + \alpha_0 = \alpha + \alpha_{0_{TH}}(K_{a0} - K_{ga0}) \qquad (8.23)$$

where $\alpha_{0_{TH}}$ is the two-dimensional theoretical zero lift angle derived from equation (7.27) and K_{a0} and K_{ga0} are the single aerofoil to theoretical zero lift angle correlation factor and cascade allowance respectively. The former, as expressed by Burrill, is a function of thickness to chord ratio and position of maximum camber whilst the latter is a function of hydrodynamic pitch angle β_i and solidity of the cascade σ_s.

Now by combining equations (8.21) and (8.22) and noting that the term $(1 + K_{\beta_i}a)/(1 + a)$ can be expressed as

$$1 - [(1 - K_{\beta_i})\tan(\beta_i - \beta)/\tan\beta_i]$$

it can be shown that the effective angle of attack

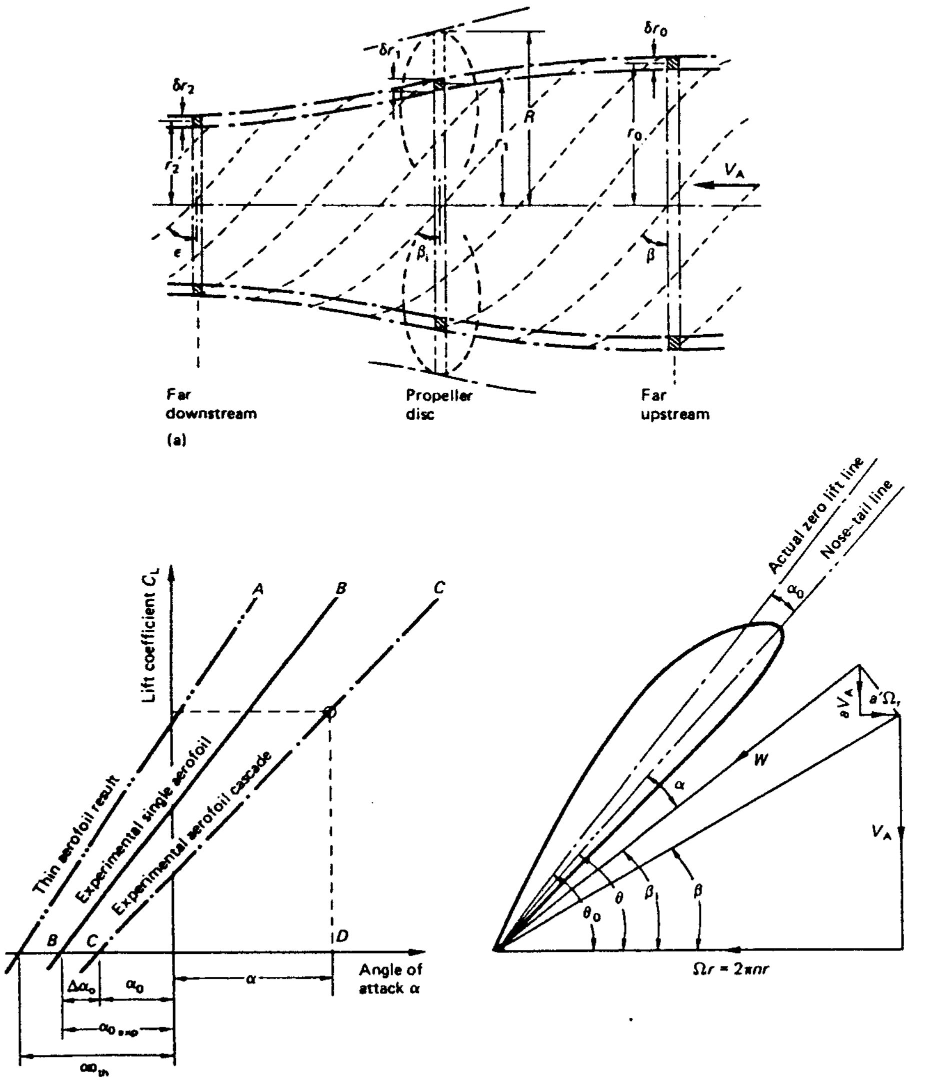

Figure 8.6 The Burrill analysis procedure: (a) slipstream contraction model; (b) lift evaluation; (c) flow vectors and angles

$(\alpha + \alpha_0)$ is given by

$$\alpha + \alpha_0 = \frac{2}{K_s K_\mu \pi \sigma_s} K_s \sin\beta_i \tan(\beta_i - \beta) \times \left[1 - \frac{\tan(\beta_i - \beta)}{\tan\beta_i}(1 - K_{\beta_i})\right] \quad (8.24)$$

This equation enables, by assuming an initial value, the value of the effective angle of attack to be calculated for any given value of $(\beta_i - \beta)$, by means of an iterative process. Once convergence has been achieved the lift can be calculated from equation (8.22). The drag coefficient again is estimated from empirical data based on wind tunnel test results and this permits the calculation of the elemental thrust and torque loading coefficients:

$$\left.\begin{aligned} dK_Q &= \frac{\pi^3 x^4 \sigma_s}{8}(1 - a')^2(1 + \tan^2\beta_i)c_i \frac{\sin(\beta_i + \gamma)}{\cos\gamma}dx \\ dK_T &= \left(\frac{dK_Q}{dx}\right)\frac{2}{x\tan(\beta_i + \gamma)}dx \end{aligned}\right\} \quad (8.25)$$

where the rotational induced velocity coefficient a' can most conveniently be calculated from

$$a' = \frac{(\tan\beta_i - \tan\beta)\tan(\beta_i + \gamma)}{1 + \tan\beta_i \tan(\beta_i + \gamma)} \quad (8.26)$$

Figure 8.6 shows the algorithm adopted by Burrill to calculate the radial distribution of loading on the propeller blade, together with certain modifications, such as the incorporation of the drag coefficients from his later paper on propeller design (Reference 13).

Burrill's analysis procedure represents the first coherent step in establishing a propeller calculation procedure. It works quite well for the moderately loaded propeller working at or near its design condition; however, at either low or high advance the procedure does not behave as well. In the low advance ratios the constant radial axial inflow factor, consistent with a lightly loaded propeller, must contribute to the underprediction of thrust and torque coefficient for these advance ratios. Furthermore, the Goldstein factors rely on the conditions of constant hydrodynamic pitch and consequently any significant slipstream distortion must affect the validity of applying these factors. Alternatively, in the lightly loaded case it is known that the theory breaks down when the propeller conditions tend toward the production of ring vortices.

Clearly since the Goldstein factors are based on the concept of zero hub radius, the theory will benefit from the use of the Tachminji factors, which incorporate a boss of radius 0.167R. Additionally, the use of the particular cascade corrections used in the method were criticized at the time of the method's publication; however, no real alternative for use with a method of this type has presented itself to this day.

The Burrill method represents the final stage in the development of a combined momentum–blade element approach to propeller theory. Methods published subsequent to this generally made greater use of the lifting line, and subsequently lifting surface concepts of aerodynamic theory. The first of these was perhaps due to Hill (Reference 14) and was followed by Strscheletsky (Reference 15); however, the next significant development was that due to Lerbs (Reference 16), who laid the basis for moderately loaded lifting line theory. Strscheletsky's work, although not generally accepted at the time its introduction due to the numerical complexity of his solution, has subsequently formed a basis for lifting line heavily loaded propeller analysis.

8.5 Lerbs analysis method (1952)

Lerbs followed the sequence of lifting line development by proposing a method of analysis for the moderately loaded propeller working in an inviscid fluid. The moderately loaded assumption requires that the influence of the induced velocities are taken into account, and as such the vortex sheets emanating from each blade differ slightly from the true helical form, this latter form only being true for the lightly loaded propeller.

The development of the model, which has to some extent become regarded as a classic representation of lifting line models, followed the work of Kawada. Kawada considered the problem of a propeller whose blades were represented by a line of constant bound vorticity from the root to the tip with a system of free helical tip vortices, one from each blade, and an axial hub vortex whose strength is equal to the sum of the tip vortex strengths. Lerbs considered the more advanced case of the blades being represented by a line of radially varying bound vorticity $\Gamma(x)$. In this case, in order to satisfy Stokes' theorem, this must give rise to the production of a vortex sheet whose strength is a variable depending upon the radius. The strength of a particular element of the vortex sheet is given by

$$\Gamma_F(x) = \left(\frac{\partial \Gamma}{\partial r}\right)dr \quad (8.27)$$

Figure 8.7 outlines in schematic form the basis of Lerbs' model. Within the model centrifugal and slipstream contraction effects are ignored, and so the sheets comprise cylindrical vortex lines of constant diameter and pitch in the axial direction.

Unlike some previous work, within the model, prior assumptions with respect to the pitch of the vortex sheets are avoided, and consequently it is necessary to evaluate both the axial and induced velocity components, since no unique relation between them exists when the sheet form differs from the truly helical. In his approach Lerbs also considered the presence of a propeller hub in the calculation procedure, but assumed the circulation at the hub to be zero. This

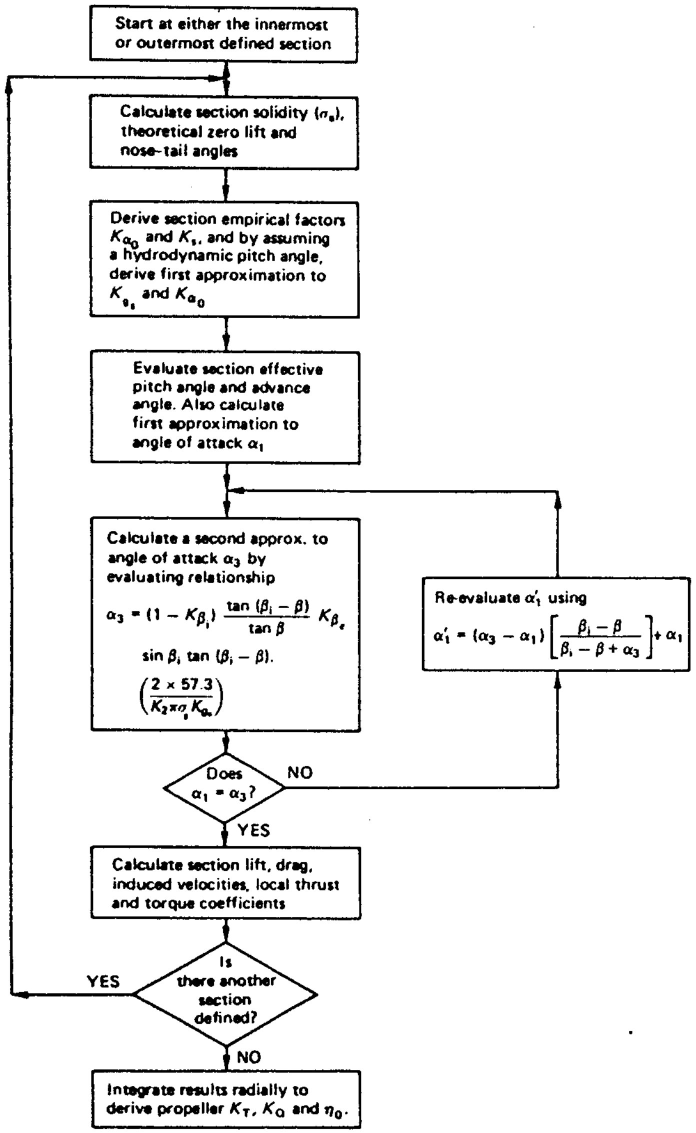

Figure 8.6 Burrill calculation algorithm

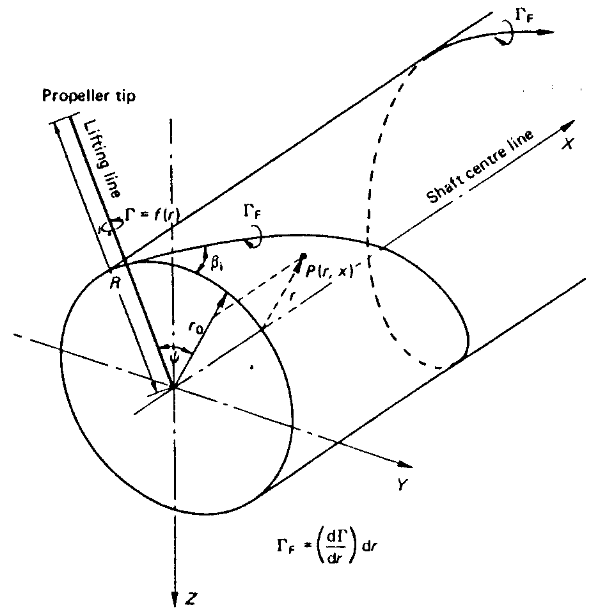

Figure 8.7 Basis of the Lerbs model

latter assumption clearly does not represent actual conditions on a propeller but is a computational convenience.

Lerbs showed, by appealing to the Biot–Savart law, that Kawada's expressions for induced velocity, based on infinite vortices extending from $-\infty$ in one direction to $+\infty$ in the other, are valid for the calculation of the induced velocities at the propeller disc ($X = 0$) provided that the resultant induced axial and tangential velocities are divided by two. For points in the slipstream that are not in the plane of the propeller disc, the relations governing the induced velocity is less simple. Lerbs gives the following set of equations for the axial and tangential induced velocities at a radius r in the propeller disc induced by a single free helical vortex line emanating from a radius r_0 in the propeller disc (Figure 8.7):

Axial induced velocities:

Internal points ($r < r_0$)

$$\bar{w}_{ai} = \frac{Z\Gamma_F}{4\pi k_0}\left\{1 - 2Z\frac{r_0}{k_0}\sum_{n=1}^{\infty} nI_{nz}\left(\frac{nZ}{k_0}r\right)K'_{nz}\left(\frac{nZ}{k_0}r_0\right)\right\}$$

External points ($r > r_0$)

$$\bar{w}_{ae} = -\frac{Z^2\Gamma_F r_0}{2\pi k_0^2}\sum_{n=1}^{\infty} nK_{nz}\left(\frac{nZ}{k_0}r\right)I'_{nz}\left(\frac{nZ}{k_0}r_0\right)$$

Tangential induced velocities:

Internal points ($r < r_0$)

$$\bar{w}_{ti} = \frac{Z^2\Gamma_F r_0}{2\pi k_0 r}\sum_{n=1}^{\infty} nI_{nz}\left(\frac{nZ}{k_0}r\right)K'_{nz}\left(\frac{nZ}{k_0}r_0\right)$$

External points ($r < r_0$)

$$\bar{w}_{te} = \frac{Z\Gamma_F}{4\pi r}\left\{1 + 2Z\frac{r_0}{k_0}\sum_{n=1}^{\infty} nK_{nz}\left(\frac{nZ}{k_0}r\right)I'_{nz}\left(\frac{nZ}{k_0}r_0\right)\right\}$$

where $k_0 = r_0 \tan\beta_{i0}$ and I_{nz} and K_{nz} are the modified Bessel functions of the first and second kind respectively. In order to evaluate these expressions, use is made of Nicholson's asymptotic formulae to replace the Bessel functions, from which it is then possible to derive the following set of expressions after a little manipulation of the algebra involved:

$$(r < r_0)\bar{w}_{ai} = \frac{Z\Gamma_F}{2\pi k_0}(1 + B_2); \qquad \bar{w}_{ti} = -\frac{Z\Gamma_F}{4\pi r}B_2$$

$$(r > r_0)\bar{w}_{ae} = \frac{-Z\Gamma_F}{4\pi k_0}B_1; \qquad \bar{w}_{te} = \frac{Z\Gamma_F}{4\pi r}(1 + B_1)$$

where

$$B_{1,2} = \left(\frac{1 + y_0^2}{1 + y^2}\right)^{0.25}\left[\frac{1}{e^{ZA_{1,2}} - 1} \mp \frac{1}{2Z}\frac{y_0^2}{(1 + y_0^2)^{1.5}} \times \log_e\left(1 + \frac{1}{e^{ZA_{1,2}} - 1}\right)\right]$$

and

$$A_{1,2} = \pm(\sqrt{(1 + y^2)} - \sqrt{(1 + y_0^2)}) \mp \tfrac{1}{2}\log_e\frac{(\sqrt{(1 + y_0^2)} - 1)(\sqrt{(1 + y^2)} + 1)}{(\sqrt{(1 + y_0^2)} + 1)(\sqrt{(1 + y^2)} - 1)}$$

in which

$$y_0 = \frac{1}{\tan\beta_{i0}} \quad \text{and} \quad y = \frac{x}{x_0\tan\beta_{i0}} \tag{8.28}$$

The distinction between the two conditions of $(r < r_0)$ and $(r > r_0)$ is made since when the point of interest coincides with the radius at which free vortex emanates, that is when $r = r_0$, the velocity components tend to an infinite magnitude. To avoid this problem Lerbs introduces the concept of an induction factor, which is a non-dimensional parameter and is the ratio of the velocity induced by a helical vortex line to that produced by a semi-infinite straight line vortex parallel to the shaft axis at radius r_0. A semi-infinite vortex is, in this context, one that ranges from $z = 0$ to $+\infty$, and the velocity induced by such a straight line vortex at a radius r in the propeller disc is given by $\Gamma_F/[4\pi(r - r_0)]$. The induction factors in the axial and tangential directions are formally defined as

$$\bar{w}_a = \frac{\Gamma_F}{4\pi(r - r_0)}i_a; \quad \bar{w}_t = \frac{\Gamma_F}{4\pi(r - r_0)}i_t \tag{8.29}$$

It will readily be seen from equation (8.29) that the velocity induced by a straight line vortex also tends to an infinite magnitude when $r = r_0$. However, when $r \to r_0$, both the velocities induced by the straight line and helical vortices are of the same order, consequently, the ratio of the velocities and hence the induction factors remain finite. When interpreted in the context of the expressions for the axial and tangential induced velocities given in equation (8.28), we have

$$\left.\begin{aligned} i_{ai} &= \frac{Zx}{x_0\tan\beta_{i0}}\left(\frac{x_0}{x} - 1\right)(1 + B_2) \\ i_{ae} &= -\frac{Zx}{x_0\tan\beta_{i0}}\left(\frac{x_0}{x} - 1\right)B_1 \\ i_{ti} &= Z\left(\frac{x_0}{x} - 1\right)B_2 \\ i_{te} &= -Z\left(\frac{x_0}{x} - 1\right)(1 + \beta_1) \end{aligned}\right. \tag{8.30}$$

in which the suffices i and e refer to internal and external radii relative to the nominal value x_0.

From these equations it is apparent that the induction factors do not depend upon the circulation but are simply a function of the geometry of the flow. The induction factors defined by equation (8.30) describe the induction of Z free helical vortices of non-dimensional radius x_0 at a point in the propeller plane at a non-dimensional radius x. There are, however, other induced velocities acting in this plane. These come from the bound vortices on the lifting lines, but in the case of uniform flow these cancel out provided the blades are symmetrically arranged.

In introducing the concept of a propeller hub into the analysis procedure, Lerbs used as a representation an infinitely long cylinder of radius r_h. This leads to two effects, firstly the definition of the circulation at the root of the blades, and secondly the effect on the induced flow. With respect to the problem of the circulation at the root it is argued that for any two adjacent blades, the pressure on the face of one will tend to equalize with the suction on the back of the other. Consequently, it follows that for the purposes of this theory the circulation at the root of the blade can be written to zero. For the induced flow effect this clearly leads to the condition that the radial component of flow at the hub must be zero, since no flow can pass through the hub. Lerbs had some difficulty in incorporating this last effect; however, he derived a tentative solution by appealing to Kawada's equation for the radial component of flow, and treated the problem as though the boss were located in the ultimate wake.

Equations (8.30) relate to the effects of a single vortex emanating from each blade of a propeller at a given radius. In order to generalize these relations so as to incorporate the effect of all the free vortices emanating from the propeller, it is necessary to sum the contributions of all of the free vortices at the point of interest. For example, in the case of the tangential component,

$$w_t(r) = \int_{r_h}^{R}\bar{w}_t(\bar{r}_0)\,dr_0$$

which, when expanded in association with equations (8.27) and (8.29), gives

$$\frac{w_t}{V} = \frac{1}{2}\int_{x_h}^{1.0}\left(\frac{dG}{dx_0}\right)\frac{i_t}{(x - x_0)}dx_0 \tag{8.31}$$

where G is the non-dimensional circulation coefficient given by $\Gamma/(\pi DV)$. The improper integrals representing the values of w_t and in the analogous expression for w_a, are similar to those encountered in aerofoil theory, the difference being that in the propeller case the induction factors allow for the curvature of the vortex sheets. To establish a solution for the propeller problem Lerbs extended the work of Glauert and introduced a variable (ϕ) defined by equation (8.32), which allows a circular representation of the radial location on the lifting line:

$$x = 0.5[(1 + x_h) - (1 - x_h)\cos\phi] \tag{8.32}$$

The distribution of circulation $G(x)$ is continuous for all but very few propellers, which must be treated separately, and the boundary values at the tip and root are known. As a consequence of this the circulation distribution can be represented by an odd Fourier series:

$$G = \sum_{m=1}^{\infty}{}'G_m\sin(m,\phi)$$

in addition, the induction factors depends upon ϕ and ϕ_0, equation (8.32), and can be represented by an even Fourier series:

$$i(\phi,\phi_0) = \sum_{n=0}^{\infty}I_n(\phi)\cos(n\phi_0)$$

Now by combining these expressions with equation (8.31), one is able to write expressions for the tangential and, analogously, the axial induced velocities at a radial location ϕ as follows:

$$\left.\begin{aligned} \frac{w_a}{V} &= \frac{1}{1 - x_h}\sum_{m=1}^{\infty}mG_m h_m^a(\phi) \\ \frac{w_t}{V} &= \frac{1}{1 - x_h}\sum_{m=1}^{\infty}mG_m h_m^t(\phi) \end{aligned}\right\} \tag{8.33}$$

where

$$h_m^a(\phi) = \frac{\pi}{\sin\phi}\left[\sin(m\phi)\sum_{n=0}^{m}I_n^t(\phi)\cos(n\phi) + \cos(m\phi)\sum_{n=m+1}^{\infty}I_n^t(\phi)\sin(n\phi)\right]$$

and

$$h_m^t(\phi) = \frac{\pi}{\sin\phi}\left[\sin(m\phi)\sum_{n=0}^{m}I_n^t(\phi)\cos(n\phi) + \cos(m\phi)\sum_{n=m+1}^{\infty}I_n^t(\phi)\sin(n\phi)\right]$$

It should be noted that at the hub and root the functions become indefinite, that is when $\phi = 0°$ or 180°. From l'Hôpital's rule the limits for the function become

$$h_m^{a,t}(0) = \pi\left[m\sum_{n=0}^{m}I_n^{a,t}(0) + \sum_{n=m+1}^{\infty}nI_n^{a,t}(0)\right]$$

$$h^{a,t}(180°) = -\pi\cos(m\pi)\left[m\sum_{n=0}^{m}I_n^{a,t}\cos(n\pi) + \sum_{n=m+1}^{\infty}nI_n^{a,t}\cos(n\pi)\right]$$

These equations enable the induced velocity components to be related to the circulation distribution and also to the induction factors.

More recently Morgan and Wrench (Reference 99) made a significant contribution to the calculation of Lerbs' induction factors, and their method is used by many modern lifting line procedures.

Lerbs, having proposed the foregoing general theoretical model, then proceeded to apply it to two cases in Reference 16. The first was the moderately loaded, free-running propeller, whilst the second application was for wake adapted propellers.

In the first case, it is deduced from a consideration of the energy balance over the propeller and its slipstream that the pitch of the vortex sheets coincides with the hydrodynamic pitch angle of the section. Furthermore, it is shown that the Betz condition holds at the lifting line as well as in the ultimate wake, which implies the regularity of the vortex sheets in terms of their helical shape, so that the condition of normality holds. That is, that the induced velocities are normal to the incident flow on to the section. Lerbs then applied this basis to the solution of optimum and non-optimum propellers, and in this respect a strong agreement was shown to exist between this work and the earlier studies of Goldstein.

For the case of the wake adapted propeller, the propeller is considered to operate in a wake field which varies radially, but is constant circumferentially; that is, the normal design condition. For this case the optimum and non-optimum loading cases were considered which led, in the former case, to the condition

$$\frac{\tan\beta}{\tan\beta_i} = c\sqrt{\frac{1 - w_T(x)}{1 - t(x)}} \tag{8.34}$$

where $w_T(x)$ and $t(x)$ are the Taylor wake fraction and thrust deduction respectively and c is a constant which requires to be determined in each case. An approximation to c can be calculated according to

$$c = \eta_i\sqrt{\frac{1 - t}{1 - w_0}} \tag{8.35}$$

where η_i is the ideal propeller efficiency and w_0 and t_0 are the effective wake and thrust deduction factors respectively. In the case of the non-optimum propeller, in which the problem is that of determining the induced velocity components when the powering conditions, wake field and the character of the circulation distribution are known, the induced velocity components become

$$\frac{w_{a,t}}{V} = \frac{k}{1 - x_h}\sum_{m=1}^{\infty}mF_m h_m^{a,t} \tag{8.36}$$

in which the constant k, defined by equation (8.37), is determined from the given powering conditions characterized by the power coefficient C_p:

$$k^2 + k(1-x_b)\frac{\int_{x_b}^{1} F_x[1-w(x)]\,\mathrm{d}x}{\int_{x_b}^{1} F_x\left(\sum_{m=1}^{\infty} mF_m h_m^*\right)\mathrm{d}x} - C_{pi}\left(\frac{1-x_b}{4z}\right)\frac{J_s}{\int_{x_b}^{1} F_x\left(\sum_{m=1}^{\infty} mF_m h_m^*\right)\mathrm{d}x} = 0$$

and in order to determine the functions h_m^* the hydrodynamic pitch angle β_i is derived from

$$\tan\beta_i = \frac{[1-w(x)] + \dfrac{k}{(1-x_b)}\sum_{m=1}^{\infty} mF_m h_m^*}{\dfrac{x}{J_s} - \dfrac{k}{(1-x_b)}\sum_{m=1}^{\infty} mF_m h_m^*}$$

The values of k and h_m are in this procedure determined from an iterative procedure. In the above equation the circulation characterizing function F is used since the exact distribution is unknown. The characterizing function is related to the circulation distribution by a constant term k such that

$$G(x) = kF(x) \tag{8.37}$$

Clearly in the case of the open water propeller the terms $t(x)$ and $w(x)$ are zero for all values of the non-dimensional radius x. Hence equation (8.34) reduces to the simpler expression $\tan\beta/\tan\beta_i$ = constant, and equation (8.36) also reduces accordingly.

8.6 Eckhardt and Morgan's design method (1955)

The mid-1950s saw the introduction of several new design methods for propellers. This activity was largely driven by the increases in propulsive power being transmitted at that time coupled with the new capabilities in terms of the mathematical analysis of propeller action. Among these new methods were those by Burrill (Reference 13), which to a large extent was an extension to his earlier analysis procedure, van Manen and van Lammeren (Reference 17) and Eckhardt and Morgan (Reference 18). This latter procedure found considerable favour, as did the other methods in their countries of origin, at the time of its introduction, and is today a method that is still widely used in design, either in its original form or as a basic vehicle to which other more recent developments have been appended.

Eckhardt and Morgan's method is an approximate design method which relies on two basic assumptions of propeller action. The first is that the slipsteam does not contract under the action of the propeller, whilst the second is that the condition of normality of the induced velocity applies. Both of these assumptions, therefore, confine the method to the design of light and moderately loaded propellers.

The design algorithm is outlined in Figure 8.8. In their paper the authors put forward two basic procedures for propeller design; one for open water propellers and the other for a wake adapted propeller. In either case the design commences by choosing the most appropriate diameter, obtained perhaps from standard open water series data such as the Troost series, and also the blade number which will have been selected, amongst other considerations on the basis of the ship and machinery natural vibration frequencies; see the discussion in Chapter 21. Additionally, at this preliminary stage in the design the hub or boss diameter will have been chosen, as will also the initial ideas on the radial distributions of rake and skew. At the time that this work was first proposed the full hydrodynamic implications of rake, but more particularly skew, were very much less well understood than they are today.

In outlining the Eckhardt and Morgan procedure, the wake adapted version of the procedure will be followed, since the open water case is a particular solution of the more general wake adapted problem. For wake adapted design purposes the circumferential average wake fraction $\bar{w}_x$ at each radius is used as an input to the design procedure. Hence the radial distribution of advance angle β can readily be calculated using equation (6.20), as can the propeller thrust loading coefficient C_{TS}, equation (6.6), but based on ship speed V_s rather than advance speed V_a. Lerbs derived a relationship for the non-viscous flow case which can be deduced from equations (8.34) and (8.35) for the hydrodynamic pitch angle based on the ideal efficiency:

$$\tan\beta_i \simeq \frac{\tan\beta}{\eta_i}\sqrt{\frac{1-\bar{w}}{1-\bar{w}_x}} \tag{8.38}$$

The ideal efficiency η_i is estimated from Kramer's diagrams, assuming a non-viscous thrust coefficient C_{TSi}, which is some 2% to 6% greater than that based on the ship speed and calculated above. Kramer's diagrams are based on an extension of Goldstein's approach, and whilst some reservations have been expressed concerning their accuracy, especially at high blade numbers, they are suitable for a first approximation purpose. Following on from this initial estimate of the radial hydrodynamic pitch distribution, the elemental ideal thrust loading coefficients for each section are computed and the ideal propeller thrust coefficient C_{TSi} evaluated from

$$C_{TSi} = 8\int_{x_b}^{1.0} Kx\frac{u_t}{2V_s}\left(\frac{x\pi}{J_s} - \frac{u_t}{2V_s}\right)\mathrm{d}x$$

where (8.39)

$$\frac{u_t}{2V_s} = \frac{(1-w_x)\sin\beta_i\sin(\beta_i-\beta)}{\sin\beta}$$

and K is the Goldstein Function. The latter equation follows from the implied condition of normality.

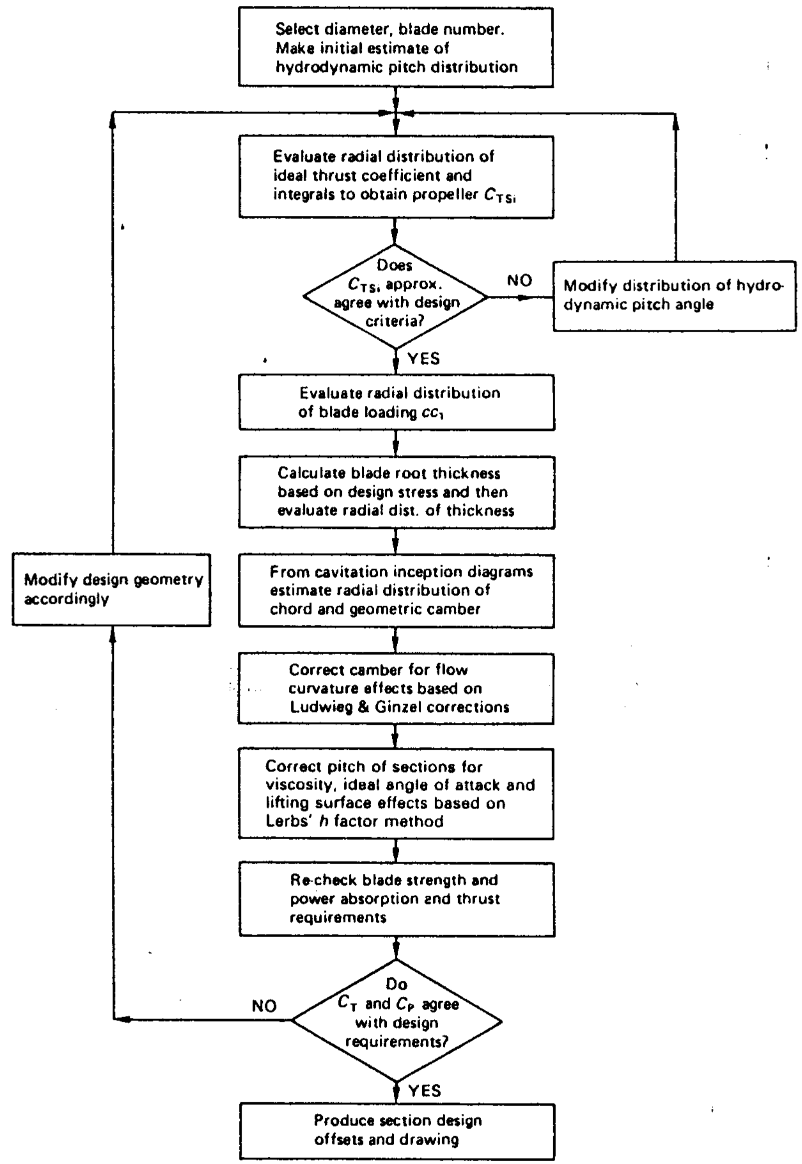

Figure 8.8 Edhardt–Morgan design algorithm

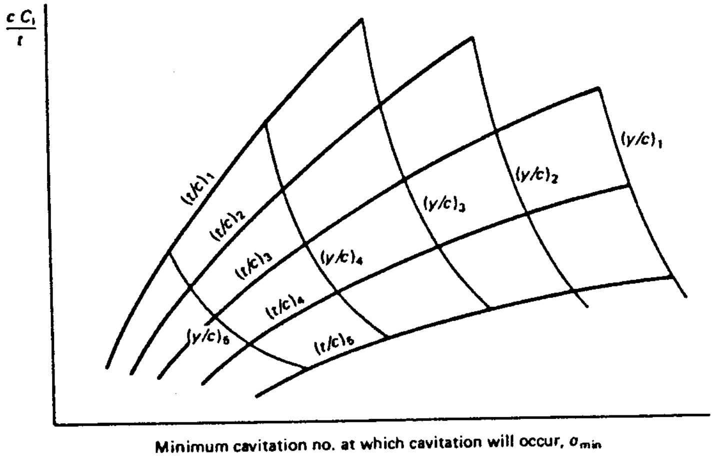

Figure 8.9 Cavitation inception diagram

The value of C_{TSi} can then be compared to the original design assumption of being within the range of 2% to 6% greater than C_{TS}, and if there is a significant difference a new value of the hydrodynamic pitch angle β_i at $0.7R$ can be estimated from the relationship

$$(\tan \beta_i)_{j+1} \simeq (\tan \beta_i)_j \left[1 - \frac{(C_{Ti})_{desired} - (C_{Ti})_{calc}}{5(C_{Ti})_{desired}} \right] \tag{8.40}$$

Hence, upon convergence of the values of the ideal ship thrust coefficient, the product cc_l, which effectively represents the load of the section under a given inflow condition, see equation (7.3), can be evaluated from

$$cc_l = \frac{4\pi D}{Z} \left[\frac{Kx(u_t/2V_s)}{x\pi/J_s - u_t/2V_s} \right] \cos \beta_i \tag{8.41}$$

Now in order to derive the propeller blade chord lengths from equation (8.41) it is necessary to ensure compatibility with the cavitation criteria relating to the design. Eckhardt and Morgan did this by making use of incipient cavitation charts which had been derived from theoretical pressure distribution calculations for a series of standard sections forms. The forms presented in their paper relate to the NACA 16 section with either an $a = 0.8$ or $a = 1.0$ mean line and the NACA 66 section with an $a = 0.8$ mean line. Figure 8.9 shows the essential features of the diagram in which the minimum cavitation number at which cavitation will occur, σ_{min}, is plotted as abscissa and the function cc_l/t forms the ordinate. The thickness to chord and camber chord ratios act as parameters in the manner shown in Figure 8.9. As far as the propeller blade section cavitation criteria are concerned these are calculated at the top dead centre position in the propeller disc. Consequently, the blade section cavitation numbers, based on the velocities at the lifting line, are calculated for this location in the propeller disc since these will represent a combination of the worst static head position coupled with a mean dynamic head.

With regard to section thickness, Eckhardt and Morgan base this on the calculation of the root thickness using Taylor's approach, from which they derive the radial distribution of thickness. Chapters 18 and 21 discuss these concepts in more detail. Consequently, since the section thicknesses and their cavitation numbers are known the values of (t/c) and (y/c) can be deduced from inception diagrams of the type shown in Figure 8.9, and hence the radial distribution of chord length can be determined by a process of direct calculation followed by fairing.

The values of camber chord ratio derived from the inception diagram are in fact two-dimensional values operating in rectilinear flow, and therefore need to be corrected for flow curvature effects. This is done by introducing a relationship of the form

$$\frac{y}{c} = k_1 k_2 \left(\frac{y}{c} \right)' \tag{8.42}$$

in which (y/c) is the actual section camber chord ratio, $(y/c)'$ is the two-dimensional value and k_1 and k_2 are correction factors derived from the work of Ludwieg and Ginzel (Reference 19). The factor $k_1 = f(J_i, A_E/A_O)$ whilst $k_2 = g(x, A_E/A_O)$. Ludwieg and Ginzel addressed themselves to the relative effectiveness of a camber line in curved and straight flows; in a curved flow the camber is less effective than in a straight or rectilinear flow. Their analysis was based on the effectiveness of circular arc camber lines operating at their shock-free entry conditions by evaluating the streamline curvature, or the change in downwash in the direction of the flow.

In addition to the camber correction factor, the pitch of the sections needs corrections for viscosity, for the ideal angle of attack of the camber line, and for the change in curvature over the chord, for which the Ludwieg and Ginzel corrections are insufficient. The first two corrections are dealt with by the authors by the use of a single correction factor to determine a pitch correction:

$$\alpha_1 = k_3 c_l \tag{8.43}$$

where k_3 depends upon the shape of the mean line. With regard to the latter effect, Lerbs, using Weissinger's simplified lifting surface theory, defined the further pitch correction angle α_2.

This correction is necessary since the Ludwieg and Ginzel correction was made upon considerations of the flow curvature at the mid-point of the section, and experiments with propellers showed that they were underpitched with this correction: Lerbs used Weissinger's theory in reverse since the bound circulation is known from lifting line theory. Lerbs satisfied the boundary condition at the 0.75c position on the chord by an additional angle of attack, assuming that the bound vortex was sited at the 0.25c point. This correction is made in two parts; one due to the effects of the bound vortices and the other due to the free vortex system, such that

$$\alpha_2 = \alpha_b + \alpha_f - (\alpha_i - \alpha_o) \tag{8.44}$$

The bound vortex contribution α_b is defined by the equation

$$\alpha_b = \frac{\sin \beta_i}{2} \sum_1^Z \left[\left(\frac{c}{D} \sin \theta_z - 0.7 \cos \beta_i \cos \theta_z \right) \times \int_{x_h}^{1.0} \frac{c\,dx}{(P/R)^3} \right] \tag{8.45}$$

in which θ_z is the angular position of the blade and

$$\left(\frac{P}{R} \right)^3 = \left[x^2 + \left(\frac{c}{D} \right)^2 + 0.49 - 2 \times \left(\frac{c}{D} \cos \theta_z \cos \beta_i + 0.7 \sin \theta_z \right) x \right]^{3/2}$$

In evaluating equation (8.45) the calculation is made for the blade in the 90°, or athwart ship position, and the effects of the other blades on the bound vortex of this blade are determined.

For the free vortex contribution α_f this is determined from the approximation

$$\alpha_f \simeq (\beta_i - \beta) \frac{2}{1 + \cos^2 \beta_i \left(\frac{2}{h} - 1 \right)} \text{ rad} \tag{8.46}$$

in which the parameter h is a function of θ_β, and θ_β

is defined as

$$\theta_\beta = \tan^{-1} \left(\frac{0.7}{\sin \beta_i} \frac{D}{c} \right)$$

Given these two correction factors α_b and α_f, equation (8.44) can be evaluated to give a total pitch correction factor $\Delta P/D$. This factor is applied at $0.7R$, and the same percentage correction applied to the other blade radii. The correction is defined as

$$1 + \frac{\Delta P/D}{P/D} = \frac{\tan(\beta_i + \alpha_2)_{0.7}}{(\tan \beta_i)_{0.7}} \tag{8.47}$$

Using this and incorporating the correction α_1 for viscosity and ideal angle of attack the final pitch can be computed as

$$P/D = \pi x \tan(\beta_i + \alpha_1) \left(1 + \frac{\Delta P/D}{P/D} \right) \tag{8.48}$$

With equation (8.48) the design is essentially complete; however, it is indeed essential to ensure that the final values of thrust and power coefficients agree with the initial design parameters. If this is the case, then the blade section geometry can be calculated; if not, then another iteration of the design is required.

A design method of this type produces an answer to a particular design problem; it does not, however, produce a unique solution relative to other methods. To illustrate this problem McCarthy (Reference 20) compared four contemporary design methods and the solutions they produced for two particular design problems – a single-screw tanker and a twin-screw liner. The methods compared were those of Burrill (Reference 13), Eckhardt and Morgan, van Manen and van Lammeren (Reference 17) and the earlier work of Hill (Reference 14). Each of the methods used contemporary calculation procedures; however, they differed in their initial minimum energy loss assumptions and also in the correction factors applied to the camber line and the section pitch angle. In this latter respect Burrill uses the Gutsche data, Eckhardt and Morgan as we have seen use both the Ludwieg and Ginzel camber correction and the Lerbs lifting surface correction, van Manen uses Ludwieg and Ginzel and Hill uses empirically derived factors. With regard to the minimum energy loss assumptions these are shown in Table 8.2.

The Burrill condition is essentially the Betz condition, whilst the methods of Eckhardt and Morgan and van Manen use the Betz condition for uniform wake. Hill initially uses the Betz conditions; however, the thrust distribution is then altered so as to reduce tip loading, which then moves away from the initial assumption. For the variable wake case Burrill and also Eckhardt and Morgan assume the local thrust deduction factor to be constant over the disc, whereas, in contrast to this, the van Manen method assumes a distribution

$$\frac{1 - t_x}{1 - \bar{t}} = \left(\frac{1 - w_x}{1 - \bar{w}} \right)^{1/4} \tag{8.49}$$

Table 8.2 Minimum energy loss assumptions

	Variable wake	*Uniform wake*
Burrill	$x\pi \tan \varepsilon$ = constant	$x\pi \tan \varepsilon$ = constant
Eckhardt and Morgan	$\dfrac{\tan \beta}{\tan \beta_i} = \eta_i \sqrt{\dfrac{1-\bar{w}_x}{1-w}}$	$\dfrac{\tan \beta}{\tan \beta_i} = \eta_i$ = constant
Hill	$\dfrac{\tan \beta}{\tan \beta_i} = \eta_i$ = constant	$\dfrac{\tan \beta}{\tan \beta_i} = \eta_i$ = constant
van Manen *et al.*	$\dfrac{\tan \beta}{\tan \beta_i} = \eta_i$ = constant	$\dfrac{\tan \beta}{\tan \beta_i} = \eta_i$ = constant

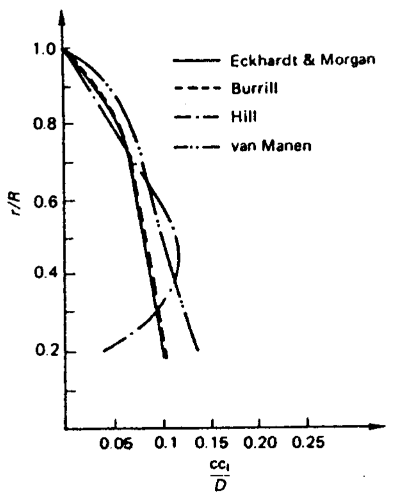

Figure 8.10 Comparison of propeller design methods (Reference 20)

The changes caused by these various assumptions and corrections can be seen, for example, in Figure 8.10, which shows the radial distribution of $cc_{L/D}$ for the liner example of McCarthy. In this example all the propellers had the same blade number and diameter and were all designed for the same powering condition assuming a van Lammeren radial distribution of mean wake fraction. Whilst Figure 8.10 is instructive in showing the non-convergence of the methods to a single solution the relative trends will tend to change from one design example to another, consequently, when using design methods of this type the experience of the designer is an important input to the procedure, as is the analysis of the design, either by advanced mathematical models in the various positions around the propeller disc or by model test.

8.7 Lifting surface correction factors – Morgan *et al.*

Figure 8.10 showed a divergence between design methods in the calculation of the radial loading parameter cc_l/D. If this is carried a stage further the divergence becomes increasingly larger in the determination of camber and angle of attack and hence section pitch. This is in part due to the variety of correction procedures adopted for the lifting line model: for example, those by Gutsche, Ludwieg and Ginzel, Lerbs etc.

To help in rationalizing these various methods of correcting lifting line results Morgan *et al.* (Reference 21) derived a set of correction factors, based on the results of lifting surface theory, for camber, ideal angle due to loading and ideal angle due to thickness.

In general terms the lifting surface approach to propeller analysis can be seen from Figure 8.11, which shows the salient features of the more recent models. Earlier models adopted a fan lattice approach and distributed singularities along the camber line, which clearly was not as satisfactory as the more recent theoretical formulations.

The mathematical model that Morgan *et al.* used was based on the work of Cheng (Reference 22) and Kerwin and Leopold (Reference 23) and comprised two distinct components. The blade loading model assumed a distribution of bound vortices to cover the blades and a system of free vortices to be shed from these bound vortices downstream along helical paths. The second part of the model, relating to the effects of blade thickness, assumed a network of sources and sinks to be distributed over the blades. In addition to the normal inviscid and incompressible assumptions of most propeller theories, the free stream inflow velocity was assumed to be axisymmetric and steady, that is, the propeller is assumed to be proceeding at a uniform velocity. Furthermore, in the model each of the blades is replaced by a distribution of bound vortices such that the circulation distribution varied both radially and chordally over the blades. The restriction on these bound vortices is, therefore, that

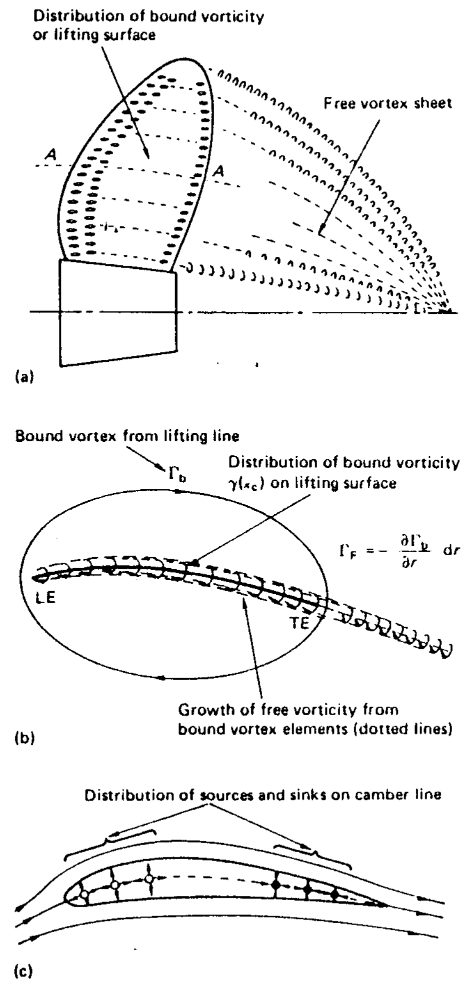

Figure 8.11 Lifting surface concept: (a) lifting surface model for a propeller blade; (b) lifting surface concept at section A–A to simulate blade loading; (c) source-sink distribution to simulate section thickness

the integral of the local circulation at a particular radial location between the leading and trailing edges is equal to the value $G(r)$ required by the lifting line design requirement:

$$\int_{TE}^{LE} G_b(r, c)\,dc = G(r) \qquad (8.50)$$

This is analogous to the thin aerofoil theory requirement discussed in the previous chapter. In their work the authors used the NACA $a = 0.8$ mean line distribution, since this line has the benefit of developing approximately all of its theoretical lift in viscous flow whereas the $a = 1.0$ mean line, for example, develops only about 74% of its theoretical lift, which would, therefore, introduce viscous flow considerations, leading to considerably more complicated numerical computations. Since the bound vorticity varies at each point on the blade surface, by Helmholtz's vortex theorems a free vortex must be shed at each point on the blade. Hence, at any given radius the strength of the free vorticity builds up at that radius until it reaches the trailing edge, where its strength is equal to the rate of change of bound circulation at that radius

$$G_f(r) = -\frac{dG(r)}{dr}dr \qquad (8.51)$$

which is analogous to equation (8.27).

With regard to the free vortex system at each radius they are considered to lie on a helical path defined by a constant diameter and pitch; the pitch, however, is allowed to vary in the radial direction. Therefore, since the slipstream contraction and the centrifugal effects on the shape of the free vortex system are ignored, their analysis is consistent with moderately loaded propeller theory. In their model, as with many others of this type, the boundary conditions on the blade are linearized and this implies that only small deviations exist betwen the lifting surface representing the blade and the hydrodynamic pitch angle. This is an analogous situation to that discussed for this aerofoil theory in Chapter 7, where the conditions are satisfied on the profile chord and not on the profile. Finally the hub is assumed to be small in this approach and is, consequently, ignored; also the propeller rake is not considered. With respect to blade pitch angles it is assumed that the pitch of the blades and of the free trailing vortex sheets is the hydrodynamic pitch angle obtained from lifting line considerations.

The method of analysis essentially uses the basis of equations (8.50) and (8.51) to define the circulation acting on the system from which the velocities at points on the lifting surface, representing the blade, can be calculated by applications of the Biot–Savart law to each of the vortex systems emanating from each blade. In this analysis the radial components of velocity are neglected. The analysis, in a not dissimilar way to that outlined previously for the thin aerofoil theory, derives from lifting surface theory the relevant flow velocities and compares them to the resulting induced velocity derived from lifting line theory. From this comparison it develops two geometric correction factors, one for the maximum camber ordinate and the other for the ideal angle of attack for use when these have been derived from purely lifting line studies. This is done using the boundary condition at each section:

$$\alpha_i(r) + \frac{\partial y_p(r, x_c)}{\partial x_c} = \frac{u_n}{V_r}(r, x_c) - \frac{u}{V_r}(r) \tag{8.52}$$

where α_i is the ideal angle of attack, y_p is the chordwhise camber ordinate at a position x_c along the chord. V_r is the resultant inflow velocity to the blade section and u_n and u are resultant induced velocities normal to the section chord and induced velocities from lifting line theory; Figure 8.12 demonstrates these parameters for the sake of clarity. It is of interest to compare equation (8.52) with equation (7.15) so as to appreciate the similarities in the two computational procedures.

The camber correction $k_c(r)$ derived from this procedure is defined by

$$k_c(r) = \frac{\text{maximum camber ordinate}}{\text{maximum 2D camber ordinate}} \tag{8.53}$$

in which the maximum two-dimensional camber ordinate is that derived from a consideration of the section lift coefficient in relation to the aerofoil data given in, say, Reference 24. At other positions along the chord the camber ordinates are scaled on a pro rata basis.

The second correction for the ideal angle of attack $k_a(r)$, to give shock free entry, is defined as follows:

$$k_a(r) = \frac{\text{section ideal angle of attack}}{\text{section 2D ideal angle of attack for } c_l = 1.0} \tag{8.54}$$

In keeping with the mathematical model the denominator of equation (8.54) relates to the NACA $a = 0.8$ mean line at an ideal angle of attack for $c_l = 1.0$.

For the final correction of the three developed by Morgan *et al.*, that relating to blade thickness effects, this was determined by introducing a source–sink system distributed after the manner developed by Kewin and Leopold (Reference 23) and demonstrated by Figure 8.11(c). In this case the induced velocities were again calculated at a point on the lifting surface since the source strength distribution is known from the normal linearized aerofoil theory approximation. As with the previous two corrections the radial component of velocity is ignored. The effects of blade thickness over the thin aerofoil case can then be studied by defining a further linear boundary condition, which is analogous to equation (8.52):

$$\alpha_t(r) + \frac{\partial y_{pt}}{\partial x_c}(r, x_c) = \frac{u_{nt}}{V_r}(r, x_c) \tag{8.55}$$

where α_t is the ideal angle induced by thickness, y_{pt} is the change in camber along the chord x_c due to thickness effects and u_{nt} is the induced velocity normal to the section chord.

Calculations show that introducing a finite blade section thickness causes an increase in the inflow angle to maintain the same loading together with a change in the camber: this latter effect is, however, small for all cases except for small values of pitch ratio. The thickness correction factor $k_t(r)$ is made independent of the magnitude of the thickness by dividing it by blade thickness fraction (t_F):

$$k_t(r) = \frac{1}{t_F}\int_0^1 \frac{u_{nt}}{V_r}(r, x_c)\,dx_c \tag{8.56}$$

From equation (8.56) the required correction to the ideal angle of attack, which is added to the sum of the hydrodynamic pitch and ideal angles, is calculated by

$$\alpha_{it} = k_t(r)t_F \tag{8.57}$$

It will be seen that $k_t(r)$ is a function of propeller loading, since V_r is also a function of loading; however, this is small and can be ignored.

To provide data for design purposes Morgan *et al.* applied the Cheng and Kerwin and Leopold procedures to a series of open water propellers of constant hydrodynamic pitch having a non-dimensional hub diameter of 0.2R. The lifting line calculations were based on the induction factor method of Lerbs, and then the lifting surface calculations were made on the basis of the loading and pitch distributions derived from Lerbs' method.

The lifting surface corrections were calculated for propellers having four, five and six blades, expanded area ratios from 0.35 to 1.15, hydrodynamic pitch ratios of 0.4 to 2.0, and for symmetrical and skewed blades, the latter having skew angles of 7°, 14° and 21°. The design of the propellers was based on the NACA $a = 0.8$ mean line together with the NACA 66 (modified) thickness distribution. The radial thickness distribution was taken to be linear and the blade outlines were chosen to be slightly wider toward the tip than the Wageningen B series, as can be seen by comparing Table 8.3 with the appropriate data in Table 6.5.

The radial distribution of skew was chosen for this series such that the blade section mid-chord line followed a circular arc in the expanded plane. Figure 8.13 shows a typical example of the correction factors for a five-bladed propeller at 0.7R and having a propeller skew angle of 21°.

Table 8.3 Blade chord coefficient for Morgan *et al.* series

r/R	$C(r)$
1.0	0
0.95	1.5362
0.90	1.8931
0.80	2.1719
0.70	2.2320
0.60	2.1926
0.50	2.0967
0.40	1.9648
0.30	1.8082
0.20	1.6338

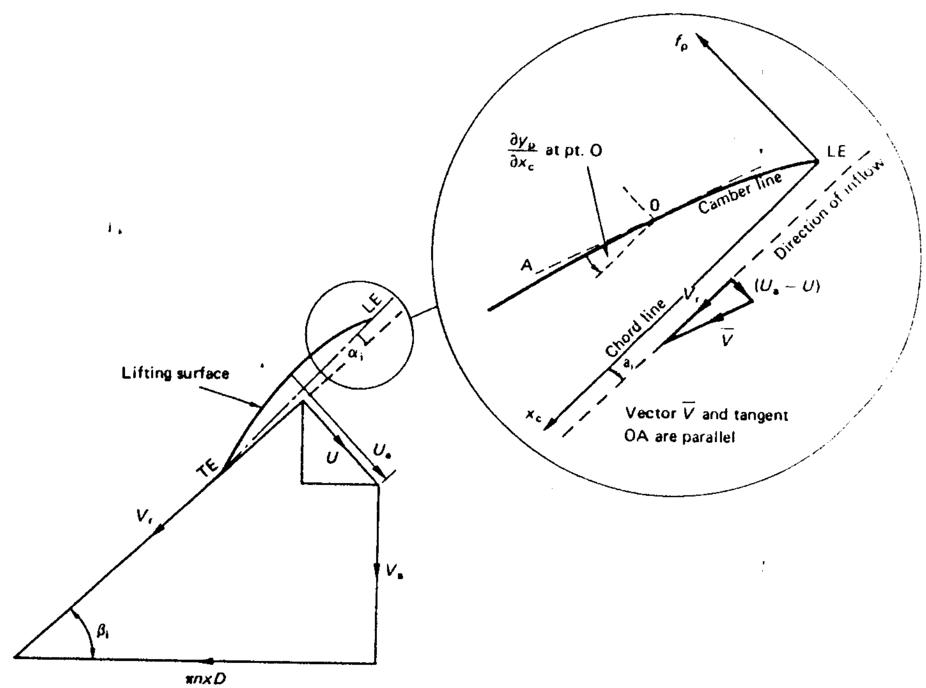

Figure 8.12 Boundary condition for determination of camber line

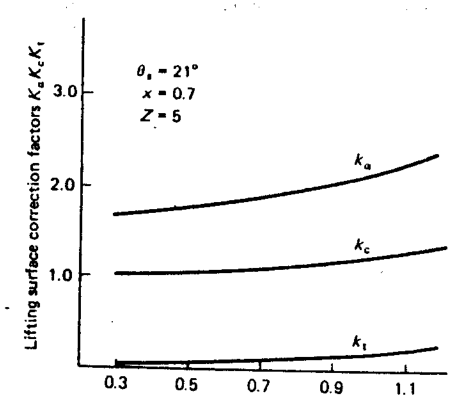

Figure 8.13 Lifting surface correction factors derived by Morgan *et al.*

In general terms the three-dimensional camber and ideal angles are usually larger than the two-dimensional values when developing the same lift coefficient. The correction factors tend to increase with expanded area ratio and k_c and k_a decrease with increasing blade number. Blade thickness, in general, tends to induce a positive angle to the flow. This addition to the ideal angle is largest near the blade root and decreases to negligible values toward the blade tip: the correction increases with increasing blade number. Skew induces an inflow angle which necessitates a pitch change which is positive toward the blade root and negative toward the tip.

A polynomial representation of these corrections factor offers many advantages for design purposes. van Oossanen (Reference 25) derived by means of multiple regression analysis a polynomial representation of the correction factors calculated both by Morgan *et al.* (Reference 21) and Minsaas and Slattelid (Reference 26), resulting in an expression of the form

$$k_c, k_a, k_t = \sum_{i=1} C_i Z^{S_i}(\tan\theta_{sx})^{t_i}(A_E/A_O)^{u_i}(\lambda_i)^{v_i} \tag{8.58}$$

van Oossanen found that although no data was given for a blade number of 7, because of the regularity of the curves extrapolation to a blade number of 7 was possible. Hence, the limits for equation (8.58) are suggested by Oossanen as being

$$3 \leqslant Z \leqslant 7$$
$$0.35 \leqslant A_E/A_O \leqslant 1.15$$
$$0.4 \leqslant \pi\lambda_i \leqslant 2.0$$
$$0 \leqslant \tan\theta_{sx} \leqslant 1.0256 - [1.0518 - (x - 0.2)^2]$$

where θ_{sx} is the blade section skew angle and λ_i is the hydrodynamic advance coefficient $x \tan\beta_i$.

These polynomials are limited to moderate skew propellers. Cummings *et al.* (Reference 27) extended the range of these corrections into the highly skewed propeller range. Unfortunately, however, the range of applicability is not so great as in the previous works: blade numbers for 4 to 6, the parameter $\pi\lambda_i = 0.8$ and 1.2 and a single expanded area ratio of 0.75. van Oossanen using similar techniques developed polynomials for each of the cases $\pi\lambda_i = 0.8$ and 1.2, of the form

$$k_c, k_a, k_t = \sum_{i=1} c_i x_i^{a_i} z^{b_i} (\theta_{sx})^{d_i} \qquad (8.59)$$

The original factors published by Cummings, Morgan and Boswell are given in Table 8.4.

8.8 Lifting surface models

Figure 8.11 showed in a conceptual way the basis of the lifting surface model. Essentially the blade is replaced by an infinitely thin surface which takes the form of the blade camber line and upon which a distribution of vorticity is placed in both the spanwise and chordal directions. Early models of this type used this basis for their formulations and the solution of the flow problem was in many ways analogous to the thin aerofoil approach discussed in Chapter 7. Later lifting surface models then introduced a distribution of sources and sinks in the chordal directions so that, in conjunction with the incident flow field, the section thickness distribution could be simulated and hence the associated blade surface pressure field approximated. The use of lifting surface models, as indeed for other models of propeller action, is for both the solution of the design and analysis problems. In the design problem the geometry of the blade is only partially known in so far as the radial distributions of chord, rake skew and section thickness distributions are known. The radial distribution of pitch and the chordwise and radial distribution of camber remain to be determined. In order to solve the design problem the source and vortex distributions representing the blades and their wake need to be placed on suitable reference surfaces to enable the induced velocity field to be calculated. Linear theories assume that the perturbation velocities due to the propeller are small compared with the inflow velocities. In this way the blades and their wake can simply be projected onto stream surfaces formed by the undisturbed flow. However, in the majority of practical design cases the resulting blade geometry deviates substantially from this assumption, and as a consequence the linear theory is generally not sufficiently accurate.

The alternative problem, the analysis problem, differs from the design solution in that the propeller geometry is completely known and we are required to determine the flow field generated under known conditions of advance and rotational speed. The analysis exercise divides into two comparatively well-defined types: the steady flow and the unsteady flow solutions. In the former case the governing equations are the same as in the design problem, with the exception that the unknowns are reversed. The circulation distribution over the blades is now the unknown. As a consequence, the singular integral which gives the velocity induced by a known distribution of circulation in the design problem becomes an integral equation in the analysis problem, which is solved numerically by replacing it with a system of linear algebraic equations. In the case of unsteady propeller flows their solution is complicated by the presence of shed vorticity in the blade wake that depends on the past history of the circulation around the blades. Accordingly, in unsteady theory the propeller blades are assumed to generate lift in gusts, for which an extensive literature exists for the general problem, for example McCroskey (Reference 28), Crighton (Reference 29) and the widely used Sear's function. The unsteadiness of the incident flow is characterized by the non-dimensional parameter k, termed the reduced frequency parameter. This parameter is defined as the product of the local semichord, and the frequency of encounter divided by the relative inflow speed. For the purposes of unsteady flow calculations the wake or inflow velocity field is characterized at each radial station by the harmonic components of the circumferential velocity distribution (Figure 5.3), and with the assumption that the propeller responds linearly to changes in inflow, the unsteady flow problem reduces to one of estimating the response of the propeller to each harmonic. In the case of a typical marine propeller the reduced frequency k corresponding to the first harmonic is of the order of 0.5, whilst the value corresponding to the blade rate harmonic will be around 2 or 3. From classical two-dimensional theory of an aerofoil encountering sinusoidal gusts, it is known that the effects of flow unsteadiness become significant for values of k greater than 0.1. As a consequence the response of a propeller to all circumferential harmonics of the wake field is unsteady in the sense that the lift generated from the sections is considerably smaller than that predicted from the equivalent quasi-steady value and is shifted in phase relative to the inflow.

Table 8.4 k_c, k_a and k_t factors derived by Cummings for highly skewed propellers (taken from Reference 27)

Correction factors for highly skewed propellers, $\pi\lambda_i = 0.8$, $EAR = 0.75$

Skew θ_s (%)	r	Z = 4 k_c	Z = 4 k_a	Z = 4 k_t	Z = 5 k_c	Z = 5 k_a	Z = 5 k_t	Z = 6 k_c	Z = 6 k_a	Z = 6 k_t
0	0.3	1.540	1.961	0.521	1.490	1.795	0.783	1.469	1.699	1.080
	0.4	1.237	1.711	0.370	1.169	1.549	0.540	1.129	1.452	0.732
	0.5	1.259	1.591	0.253	1.143	1.430	0.357	1.076	1.311	0.474
	0.6	1.338	1.589	0.166	1.185	1.396	0.225	1.090	1.285	0.291
	0.7	1.498	1.682	0.105	1.307	1.468	0.137	1.190	1.318	0.172
	0.8	1.778	1.844	0.067	1.534	1.623	0.084	1.376	1.449	0.103
	0.9	2.389	2.356	0.046	2.062	2.057	0.058	1.842	1.832	0.070
50	0.3	1.588	7.227	0.491	1.517	5.985	0.719	1.476	5.148	0.971
	0.4	1.310	4.737	0.350	1.219	3.909	0.499	1.165	3.383	0.660
	0.5	1.310	4.182	0.237	1.186	3.504	0.328	1.110	3.050	0.425
	0.6	1.422	3.257	0.151	1.249	2.789	0.204	1.145	2.432	0.257
	0.7	1.602	1.948	0.091	1.389	1.778	0.119	1.240	1.636	0.147
	0.8	1.881	0.613	0.057	1.619	0.808	0.071	1.435	0.884	0.086
	0.9	2.557	−5.100	0.045	2.188	−3.607	0.056	1.935	−2.718	0.064
100	0.3	1.838	11.914	0.477	1.683	9.804	0.683	1.585	8.396	0.912
	0.4	1.562	7.580	0.354	1.396	6.166	0.499	1.286	5.235	0.657
	0.5	1.608	6.625	0.247	1.398	5.481	0.345	1.266	4.700	0.448
	0.6	1.747	4.969	0.161	1.493	4.179	0.221	1.333	3.697	0.284
	0.7	1.949	2.427	0.097	1.648	2.258	0.432	1.154	2.039	0.167
	0.8	2.219	−0.105	0.059	1.867	0.281	0.079	1.640	0.547	0.097
	0.9	2.944	−11.674	0.050	2.446	−8.766	0.064	2.164	−6.923	0.076

Correction factors for highly skewed propellers, $\pi\lambda_i = 1.2$, $EAR = 0.75$

Skew θ_s (%)	r	Z = 4 k_c	Z = 4 k_a	Z = 4 k_t	Z = 5 k_c	Z = 5 k_a	Z = 5 k_t	Z = 6 k_c	Z = 6 k_a	Z = 6 k_t
0	0.3	1.640	1.815	0.382	1.565	1.687	0.580	1.532	1.607	0.827
	0.4	1.330	1.691	0.308	1.257	1.556	0.459	1.223	1.469	0.631
	0.5	1.354	1.636	0.237	1.242	1.483	0.341	1.176	1.394	0.458
	0.6	1.431	1.674	0.174	1.285	1.493	0.241	1.196	1.390	0.315
	0.7	1.573	1.749	0.122	1.392	1.556	0.161	1.277	1.416	0.205
	0.8	1.803	1.886	0.083	1.580	1.661	0.106	1.430	1.530	0.131
	0.9	2.360	2.320	0.063	2.030	2.029	0.080	1.818	1.817	0.098
50	0.3	1.714	7.726	0.345	1.605	6.187	0.517	1.552	5.610	0.733
	0.4	1.427	5.124	0.277	1.318	4.131	0.404	1.270	3.402	0.572
	0.5	1.434	4.439	0.211	1.319	3.960	0.298	1.217	3.133	0.419
	0.6	1.538	3.433	0.150	1.365	2.884	0.206	1.253	3.104	0.285
	0.7	1.703	2.078	0.101	1.485	1.889	0.134	1.361	1.596	0.179
	0.8	1.930	0.486	0.067	1.684	0.778	0.087	1.509	0.802	0.111
	0.9	2.560	−5.527	0.053	2.169	−4.112	0.069	1.918	−2.549	0.090
100	0.3	2.028	12.649	0.340	1.826	10.337	0.510	1.737	8.784	0.701
	0.4	1.733	8.241	0.274	1.548	6.645	0.401	1.347	5.612	0.540
	0.5	1.779	7.034	0.203	1.551	5.826	0.293	1.350	5.036	0.389
	0.6	1.913	5.206	0.136	1.646	4.496	0.195	1.433	3.933	0.256
	0.7	2.090	2.555	0.082	1.781	2.343	0.117	1.554	2.241	0.155
	0.8	2.337	−0.212	0.047	1.981	0.241	0.068	1.719	0.641	0.090
	0.9	2.998	−12.356	0.040	2.488	−5.222	0.057	2.006	−7.293	0.073

In the early 1960s many lifting surface procedures made their appearance due mainly to the various computational capabilities that became available generally at that time. Prior to this, the work of Strschelelzky (Reference 15), Guilloton (Reference 30) and Sparenberg (Reference 31) laid the foundations for the development of the method. Pien (Reference 32) is generally credited with producing the first of the lifting surface theories subsequent to 1960. The basis of this method is that the bound circulation can be assumed to be distributed over the chord of the mean line, the direction of the chord being given by the hydrodynamic pitch angle derived from a separate lifting line calculation. This lifting line calculation was also used to establish the radial distribution of bound circulation. In Pien's method the free vortices are considered to start at the leading edge of the surface and are then continued into the slipstream in the form of helical vortex sheets. Using this theoretical model the required distortion of the chord into the required mean line can be determined by solving the system of integral equations defining the velocities along the chord induced by the system of bound and free vortices. The theory is linearized in the sense that a second approximation is not made using the vortex distribution along the induced mean line.

Pien's work was followed by that of Kerwin (Reference 33), van Manen and Bakker (Reference 34), Yamazakji (Reference 35), English (Reference 36), Cheng (Reference 22), Murray (Reference 37), Hanaoka (Reference 38), van Gent (References 39, 40) and a succession of papers by Breslin, Tsakonas and Jacobs spanning something over thirty years' continuous development of the method. Typical of modern lifting surface theories is that by Brockett (Reference 41). In this method the solid boundary effects of the hub are ignored; this is consistent with the generally small magnitude of the forces being produced by the inner regions of the blade. Furthermore, in Brockett's approach it is assumed that the blades are thin, which then permits the singularities which are distributed on both sides of the blades to collapse into a single sheet. The source strengths, located on this single sheet, are directly proportional to the derivative of the thickness function in the direction of flow, conversely the vortex strengths are defined. In the method a helicoidal blade reference surface is defined together with an arbitrary specified radial distribution of pitch. The trailing vortex sheet comprises a set of constant radius helical lines whose pitch is to be chosen to correspond either to that of the undisturbed inflow or to the pitch of the blade reference surface. Brockett uses a direct numerical integration procedure for evaluating the induced velocities. However, due to the non-singular nature of the integrals over the other blades and the trailing vortex sheets the integrands are approximated over prescribed sets of chordwise and radial intervals by trigonometric polynomials. The integrations necessary for both the induced velocities and the camber line form are undertaken using predetermined weight functions. Unfortunately the integral for the induced velocity at a point on the reference blade contains a Cauchy principle-value singularity. This is solved by initially carrying out the integration in the radial direction and then factoring the singularity out in the chordwise integrand. A cosine series is then fitted to the real part of the integrand, the Cauchy principal value of which was derived by Glauert in 1948.

8.9 Lifting line–lifting surface hybrid models

The use of lifting surface procedures for propeller design purposes clearly requires the use of computers having a reasonably large capacity. Such capabilities are not always available to designers and as a consequence there has developed a generation of hybrid models essentially based on lifting line procedures and incorporating lifting surface corrections together with various cavitation prediction methods.

It could be argued that the very early methods of analysis fell, to some extent, into this category by relying on empirical section and cascade data to correct basic high aspect ratio calculations. However, the real evolution of these methods can be considered to have commenced subsequent to the development of the correction factors by Morgan *et al.* (Reference 21). The model of propeller action proposed by van Oossanen (Reference 25) typifies an advanced method of this type by providing a very practical approach to the problem of propeller analysis. The method is based on the Lerbs induction factor approach (Reference 16), but because this was a design procedure the Lerbs method has to be used in the inverse sense, which is notoriously unstable. To overcome this instability in order to determine the induced velocities and circulation distribution for a given propeller geometry, van Oossanen introduced an additional iteration for the hydrodynamic pitch angle. In order to account for the effects of non-uniform flow, the average of the undisturbed inflow velocities over the blade sections is used to determine the advance angle at each blade position in the propeller disc, and the effect of the variation of the undisturbed inflow velocities is accounted for by effectively distorting the geometric camber distribution. The effect of the bound vortices is also included because of their non-zero contribution to the induced velocity in a non-uniform flow. The calculation of the pressure distribution over the blades at each position in the propeller disc is conducted using the Theodorsen approach after first distorting the blade section camber and by defining an effective angle of attack such that a three-dimensional approximation is derived by use of a two-dimensional method.

So as to predict propeller performance correctly, particularly in off-design conditions, van Oossanen

calculates the effect of viscosity on the lift and drag properties of the blade sections. The viscous effects on lift are accounted for by boundary layer theory, in which the lift curve slope is expressed in terms of the boundary layer separation and the zero lift angle is calculated as a function of the relative wake thickness on the suction and pressure sides. In contrast, the section drag coefficient is based on an equivalent profile analysis of the experimental characteristics of the Wageningen B-series propellers.

The cavitation assessment is calculated from a boundary layer analysis and is based on the observation that cavitation inception occurs in the laminar-turbulent transition region of the boundary layer. The extent of the cavitation is derived by calculating the value of Knapp's dynamic similarity parameter for spherical cavities for growth and decline, based on the results of cavitation measurements on profiles.

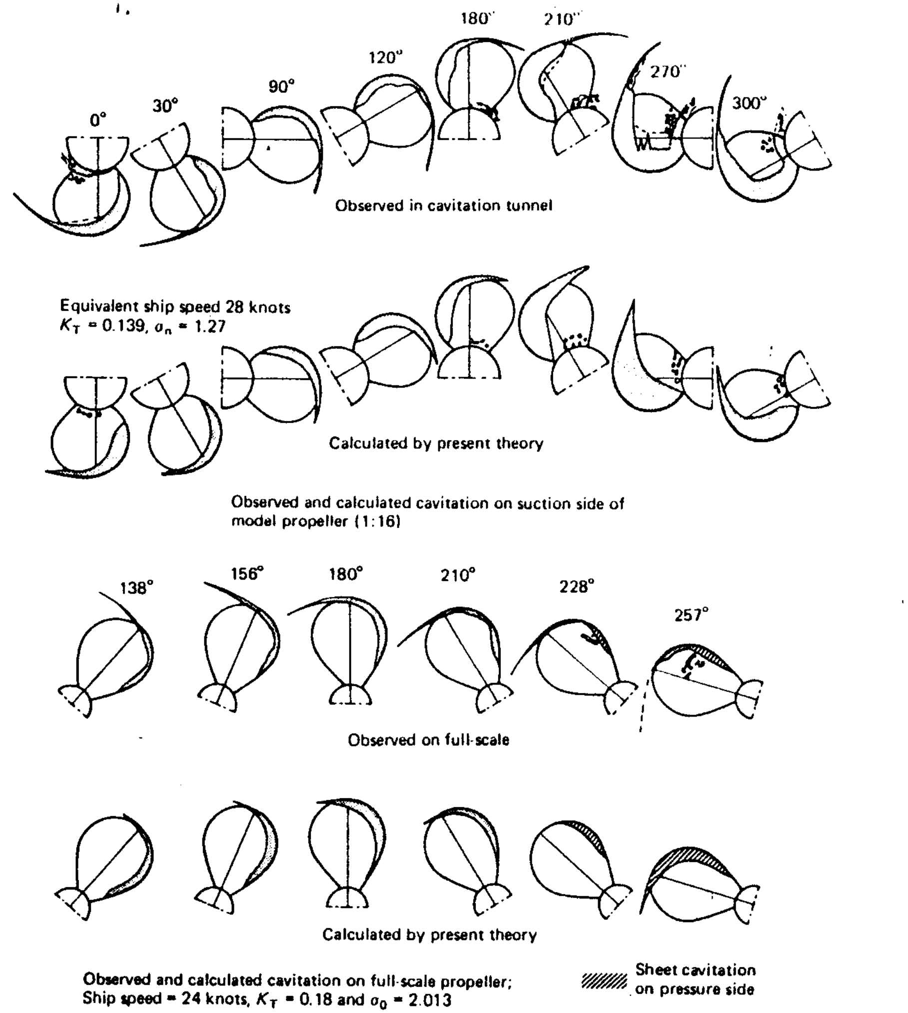

Figure 8.14 Comparison of observed and predicted cavitation by van Oossanen's hybrid method of propeller analysis (Courtesy MARIN)

This method has proved a particularly effective analysis tool for general design purposes and Figure 8.14 underlines the value of the method in estimating the extent of cavitation and its comparison with observations.

8.10 Vortex lattice methods

The vortex lattice method of analysis is in effect a subclass of the lifting surface method. In the case of propeller design and analysis it owes its origins largely to Kerwin, working at the Massachussetts Institute of Technology, although in recent years others have taken up the development of the method: for example, Szantyr (Reference 42).

In the vortex lattice approach the continuous distributions of vortices and sources are replaced by a finite set of straight line elements of constant strength whose end points lie on the blade camber surface (Figure 7.31). From this system of line vortices the velocities are computed at a number of suitably located control points between the elements. In the analysis problem the vortex distributions (Figure 8.15) are unknown functions of time and space and as a consequence have to be determined from the boundary conditions of the flow condition being analysed. The source distributions, however, can be considered to be independent of time, and their distribution over the blade is established using a stripwise application of thin aerofoil theory at each of the radial positions. As such, the source distribution is effectively known, leaving the vortex distribution as the principal unknown. Kerwin and Lee (Reference 43) consider the vortex strength at any point as a vector lying in the blade or vortex sheet which can be resolved into spanwise and chordwise components on the blades, with the corresponding components termed shed and trailing vorticity in the vortex sheets emanating from the blades (Figure 8.15). Based on this approach the

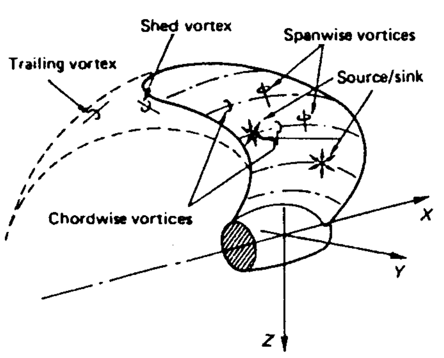

Figure 8.15 Basic components of lifting surface models

various components of the vortex system can be defined with respect to time and position by applying Kelvin's theorem in association with the pressure continuity condition over the vortex wake. Hence the distributed spanwise vorticity can be determined from the boundary conditions of the problem.

In essence there are four principal characteristics of the vortex lattice model which need careful consideration in order to define a valid model. These are as follows:

1. the element's orientation;
2. the spanwise distribution of elements and control points;
3. chordwise distribution of elements and control points;
4. the definition of the Kutta condition in numerical terms.

With regard to element distribution Greeley and Kerwin (Reference 44) proposed for steady flow analysis that the radial interval from the hub r_h to the tip R be divided into M equal intervals with the extremities of the lattice inset one-quarter interval from the ends of the blade. The end points of the discrete vortices are located at radii r_m given by

$$r_m = \frac{(R - r_h)(4m - 3)}{4M + 2} + r_h \quad (m = 1, 2, 3, \ldots, M + 1) \qquad (8.60)$$

In the case of the chordwise distribution of singularities they chose a cosine distribution in which the vortices and control points are located at equal intervals of $\bar{s}$, where the chordwise variable s is given by:

$$S = 0.5(1 - \cos\bar{s}) \qquad (0 \leqslant \bar{s} \leqslant \pi)$$

If there are N vortices over the chord, the positions of the vortices, $S_v(n)$, and the control points, $S_c(i)$, are given by

$$S_v(n) = 0.5\left\{1 - \cos\left[\frac{(n - \frac{1}{2})\pi}{N}\right]\right\} \quad n = 1, 2, \ldots, N$$

and

$$S_c(i) = 0.5\left\{1 - \cos\left[\frac{i\pi}{N}\right]\right\} \quad i = 1, 2, \ldots, N \qquad (8.61)$$

With this arrangement the last control point is at the trailing edge and two-dimensional calculations show that this forces the distribution of vorticity over the chord to have the proper behaviour near the trailing edge; that is, conformity with the Kutta condition. In the earlier work (Reference 43) Kerwin and Lee showed that for the solution of both steady and unsteady problems the best compromise was to use a uniform chordwise distribution of singularities together with an explicit Kutta condition:

$$S_s(n) = \frac{n - 0.75}{N} \qquad (n = 1, 2, \ldots, N) \qquad (8.62)$$

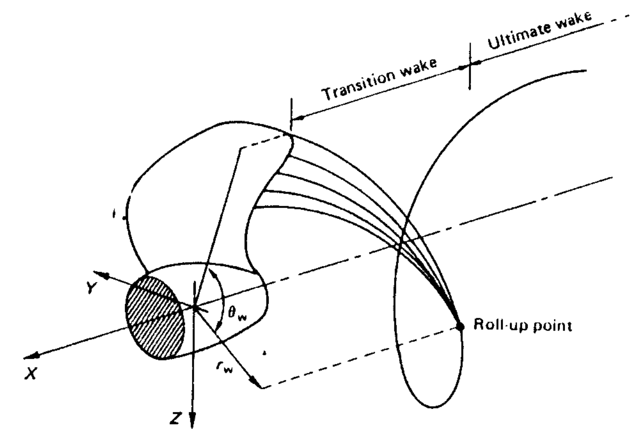

Figure 8.16 Deformation of wake model

Lan (Reference 45) showed that chordwise spacing of singularity and control points proposed by equation (8.61) gave exact results for the total lift of a flat plate or parabolic camber line and was more accurate than the constant spacing arrangement equation (8.62), in determining the local pressure near the leading edge. This choice, as defined by equation (8.61), commonly referred to as cosine spacing, can be seen as being related to the conformal transformation of a circle into a flat or parabolically cambered plate by a Joukowski transformation.

The geometry of the trailing vortex system has an important influence on the accuracy of the calculation of induced velocities on the blade. The normal approach in lifting surface theories is to represent the vortex sheet emanating from each blade as a pure helical surface with a prescribed pitch angle. Cummings (Reference 46), Loukakis (Reference 47) and Kerwin (Reference 48) developed conceptually more advanced wake models in which the roll up of the vortex sheet and the contraction of the slipstream were taken into account. Current practice with these methods is to consider the slipstream to comprise two distinct portions: a transition zone and an ultimate zone as shown in Figure 8.16. The transition zone of the slipstream is the one where the roll-up of the trailing vortex sheet and the contraction of the slipstream are considered to occur and the ultimate zone comprises a set of Z helical tip vortices together with either a single rolled-up hub vortex or Z helical hub vortices. Hence the slipstream model is defined by some five parameters as follows (see Figure 8.16):

1. radius of the rolled-up tip vortices (r_w)
2. angle between the trailing edge of the blade tip and the roll-up point (θ_w);
3. pitch angle of the outer extremity of the transition slipstream (β_T);
4. pitch angle of the ultimate zone tip vortex helix (β_w);
5. radius of the rolled up hub vortices (r_{wh}) in the ultimate zone if this is not considered to be zero.

In using vortex lattice approaches it has been found that whilst a carefully designed lattice arrangement should be employed for the particular blade which is being analysed, the other $Z - 1$ blades can be

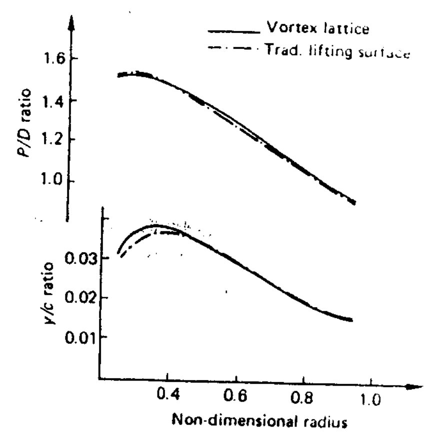

Figure 8.17 Comparison of results obtained between traditional lifting surface and vortex lattice methods (Kerwin)

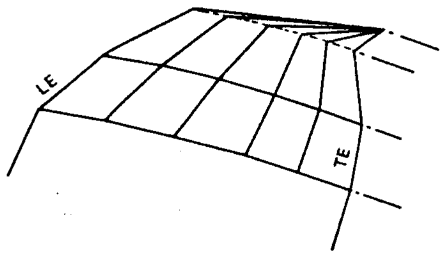

Figure 8.18 Simplified leading-edge vortex separation model (Kerwin and Lee)

represented by significantly coarser lattices without causing any important changes in the computed results. This, therefore, permits economies of computing time to be made without loss of accuracy. Kerwin (Reference 49) shows a comparison of the radial distributions of pitch and camber obtained by the vortex lattice approach and by traditional lifting surface methods (Reference 41) (Figure 8.17). Although the results are very similar, some small differences are seen to occur particularly with respect to the camber at the inner radii.

The problem of vortex sheet separation and the theoretical prediction of its effects at off-design conditions are currently occupying the attention of many hydrodynamicists around the world. At these conditions the vortex sheet tends to form from the leading edge at some radius inboard from the tip rather than at the tip. Kerwin and Lee (Reference 43) developed a somewhat simplified representation of the problem which led to a substantial improvement in the correlation of theoretical predictions with experimental results. In essence their approach is shown in Figure 8.18, in which for a conventional vortex lattice arrangement the actual blade tip is replaced by a vortex lattice having a finite tip chord. The modification is to extend the spanwise vortex lines in the tip panel as free vortex lines which join at a 'collection point', this then becomes the origin of the outermost element of the discretized vortex sheet. The position of the collection point is established by setting the pitch angle of the leading-edge free vortex equal to the mean of the undisturbed inflow angle and the pitch angle of the tip vortex as it leaves the collection point. Greeley and Kerwin (Reference 44) developed the approach further by establishing a semi-empirical method for predicting the point of leading-edge separation. The basis of this method was the collapsing of data for swept wings in a non-dimensional plotting of critical leading-edge suction force, as determined from inviscid theory as a function of a local leading-edge Reynolds number, as shown in Figure 8.19. This then allowed the development of an approximate model in which

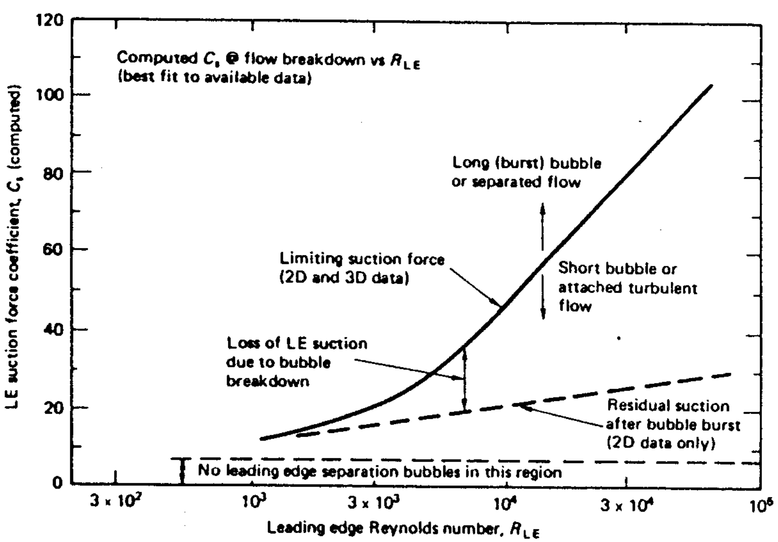

Figure 8.19 Empirical relationship between the value of the leading-edge suction force coefficient at the point of flow breakdown as a function of leading-edge Reynolds number (Reproduced from Reference 44, with permission)

the free vortex sheet was placed at a height equal to 16-blade boundary-layer thickness and the resulting change in the calculated chordwise pressure distribution found.

8.11 Boundary element methods

Boundary element methods for propeller analysis have been developed in recent years in an attempt to overcome two difficulties of lifting surface analyses. The first is the occurrence of local errors near the leading edge and the second in the more widespread errors which occur near the hub where the blades are closely spaced and relatively thick. Although the first problem can to some extent be overcome by introducing a local correction derived by Lighthill (Reference 49), in which the flow around the leading edge of a two-dimensional, parabolic half-body is matched to the three-dimensional flow near the leading edge derived from lifting surface theory, the second problem remains.

Boundary element methods are essentially panel methods, which were introduced in Chapter 7, and their application to propeller technology began in the 1980s. Prior to this the methods were pioneered in the aircraft industry, notably by Hess and Smith, Maskew and Belotserkovski. Hess and Valarezo (Reference 50) introduced a method of analysis based on the earlier work of Hess and Smith (Reference 51) in 1985. Subsequently, Hoshino (Reference 52) has produced a surface panel method for the hydrodynamic analysis of propellers operating in steady flow. In this method the surfaces of the propeller blades and hub are approximated by a number of small hyperboloidal quadrilateral panels having constant source and doublet distributions. The trailing vortex sheet is also represented by similar quadrilateral panels having constant doublet distributions. Figure 8.20, taken from Reference 52, shows a typical representation of the propeller and vortex sheet combination using this approach. The strengths of the source and doublet distributions are determined by solving the boundary value problems at

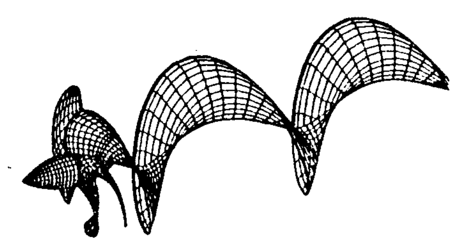

Figure 8.20 Panel arrangement on propeller and trailing vortex wake for boundary element representation (Reproduced from Reference 52, with permission)

each of the control points which are located on each panel. Within this solution the Kutta condition is obviously obeyed at the trailing edge.

Using methods of this type good agreement between theoretical and expeimental results for blade pressure distributions and open water characteristics has been achieved. Indeed a better agreement of the surface pressure distributions near the blade–hub interface has been found to exist than was the case with conventional lifting surface methods.

8.12 Methods for specialist propulsors

The discussion in this chapter has so far concentrated on methods of design and analysis for conventional propellers. It is pertinent to comment briefly on the application of these methods to specialist propulsor types: particularly controllable pitch propellers, ducted propellers, contra-rotating propellers and supercavitating propellers.

The controllable pitch propeller, in its design pitch condition, is in most respects identical to the conventional fixed pitch propeller. It is in its off-design conditions that special analysis procedures are required to determine the blade loads, particularly the blade spindle torque and hence the magnitude of the actuating forces required. Klaassen and Arnoldus (Reference 53) made an early attempt at describing the character of these forces and the methods of translating these into actuating forces. This work was followed by that of Gutsche (Reference 54) in which he considered the philosophical aspects of loading assumptions for controllable pitch propellers Rusetskiy (Reference 55), however, developed hydrodynamic models based on lifting line principles to calculate the forces acting on the blades during the braking, ring vortex and contra-flow stages of controlled pitch propeller off-design performance. This procedure whilst taking into account section distortion by means of the effect on the mean line, is a straightforward procedure which lends itself to hand calculation. The fundamental problem with the calculation of a controllable pitch propeller at off-design conditions is not that of resolving the loadings acting on the blades into their respective actuating force components, but of the calculating the blade loadings on surface pressure distributions under various, and in some cases extreme, flow regimes and with the effects of blade section distortion; see Chapter 3. The basic principles of Rusetskiy's method were considered and various features enhanced by Hawdon *et al.* (Reference 56), particularly in terms of section deformation and the flow over these deformed sections. Lifting line based procedures continued to be the main method of approaching the calculation of the hydrodynamic loading components until the 1980s: the centrifugal spindle torque is a matter of propeller geometry and the frictional spindle torque, dependent on mechanics and the magnitude of the resultant hydrodynamic and centrifugal components. Pronk (Reference 57) considered the calculation of the hydrodynamic loading by the use of a vortex lattice approach based on the general principles of Kerwin's work. In this way the computation of the blade hydrodynamics lost many of the restrictions that the earlier methods required to be placed on the calculation procedure.

As early as 1879 Parsons fitted and tested a screw propeller having a complete fixed shrouding and guide vanes. However, the theoretical development of the ducted propeller essentially started with the work of Kort (Reference 58). In its early form the duct took the form of a long channel through the hull of the ship but soon gave way to the forerunners of the ducted propellers we know today, comprising an annular aerofoil placed around the outside of a fixed or controllable pitch propeller.

Following Kort's original work, Steiss (Reference 59) produced a one-dimensional actuator disc theory for ducted propeller action; however, development of ducted propeller theory did not really start until the 1950s. Horn and Amtsberg (Reference 60) developed an earlier approach by Horn, in which the duct was replaced by a distribution of vortex rings of varying circulation along the length of the duct, and in 1955 Dickmann and Weissinger (Reference 61) considered the duct and propeller to be a single unit replaced by a vortex system. In this system the propeller is assumed to have an infinite number of blades and constant bound vortex along the span of the blade. The slipstream is assumed to be a cylinder of constant radius and no tangential induced velocities are present in the slipstream. Despite the theoretical work the early design methods, several of which are used today, were essentially pseudo-empirical methods. Typical of these are those presented by van Manen and co-workers (References 62–64) and they represent a continuous development of the subject which was based on the development of theoretical ideas supported by the results of model tests, chiefly the K_a ducted propeller series. Theoretical development, however, continued with contributions by Morgan (Reference 65), Dyne (Reference 66) and Oosterveld (Reference 66) for ducted propellers working in uniform and wake adapted flow conditions.

Chaplin developed a non-linear approach to the ducted propeller problem and subsequently Ryan and Glover (Reference 68) presented a theoretical design method which avoided the use of a linearized theory for the duct by using surface vorticity distribution techniques to represent both the duct and the propeller boss. The representation of the propeller was by means of an extension of the Strscheletsky approach and developed by Glover in earlier studies on heavily loaded propellers with slipstream contraction (Reference 69). The treatment of the induced velocities, however, was modified in order to take proper account of the induced velocities of the duct to achieve good correlation with experimental results. In this way the local hydrodynamic pitch angle at the lifting line was defined as

$$\beta_i = \tan^{-1}\left[\frac{V_a + u_{ap} + u_{ad}}{\omega r - u_{tp}}\right]$$

where u_{ap} is the axial induced velocity of the propeller
u_{ad} is the axial induced velocity of the duct
u_{tp} is the tangential induced velocity of the propeller.

Subsequently, Caracostas (Reference 70) extended the Ryan and Glover work to off-design operation conditions using some of the much earlier Burrill (Reference 11) philosophies of propeller analysis.

Tsakonas and Jacobs (Reference 71) extended the theoretical approach to ducted propeller operation by utilizing unsteady lifting surface theory to examine the interaction of the propeller and duct when operating in a non-uniform wake field. In this work they modelled the duct and propeller geometry in the context of their camber and thickness distributions. In addition to the problem of the interactions bewteen the duct and propeller there is also the problem of the interaction between the ducted propulsor and the body which is being propelled. Falcao de Campos (Reference 72) has recently studied this problem in the context of axisymmetric flows. The basic approach pursued in this study assumes the interaction flow between the ducted propulsor and the hull, which ultimately determines the performance of the duct and propeller, is inviscid in nature and can, therefore, be treated using Euler's equations of motions. Whilst this approach is valid for the global aspects of the flow, viscous effects in the boundary layers on the various components of the ducted propulsor system can be of primary importance in determining the overall forces acting on the system. As a consequence Falcao de Campos considers these aspects in some detail and then moves on to consider the operation of a ducted propeller in axisymmetric shear flow. The results of his studies led to the conclusion that inviscid flow models can give saisfactory predictions of the flow field and duct performance over a wide range of propeller loadings, provided that the circulation around the duct profile can be accurately determined and a detailed account of the viscous effects on the duct can be made in the establishment of the criteria for the determination of the duct circulation.

The main thrust of ducted propeller research has been in the context of the conventional accelerating or decelerating duct forms, including azimuthing systems, although this latter aspect has been treated largely empirically. The pumpjet is a closely related member of the ducted propeller family and has received close attention for naval applications. Clearly, as a result much of the research is classified but certain aspects of the work are published in open literature. Two particularly good treatments of the subject are to be found in References 73 and 74, and a more recent exposition of the subject is given by Wald (Reference 75). In this latter work equations have been derived to describe the operation of a pumpjet which is closely integrated into the hull design and ingests a portion of the hull boundary layer. From this work it is shown that maximum advantage of this system is attained only if full advantage is taken of the separation inhibiting effect of the propulsor on the boundary layer of the afterbody, a fact not to be underestimated in other propulsor configurations. Another closely related member of the ducted propeller family is the ring propeller, which comprises a fixed pitch propeller with an integrally mounted or cast annular aerofoil, with low length to diameter ratio, at the blade tips. In addition to the tip-mounted annular aerofoil designs, some of which can be found in small tugs or coasters, there have been designs proposed where the ring has been sited at some intermediate radial location on the propeller: one such example was the English Channel packet steamer *Cote d'Azur*, built in 1950. Work on ring propellers has mainly been confined to model test studies and reported by van Gunsteren (Reference 76) and Keller (Reference 77). From these studies the ring propeller is shown to have advantages when operating in off-design conditions, with restricted diameter, or by giving added protection to the blades in ice, but has the disadvantage of giving a relatively low efficiency.

Contra-rotating propellers, as discussed in Chapter 2, have been the subject of interest which has waxed and waned periodically over the years. The establishment of theoretical methods to support contra-rotating propeller development has a long history starting with the work of Greenhill (Reference 78) who produced an analysis method for the Whitehead torpedo; however, the first major advances in the study was made by Rota (Reference 79) who carried out comparative tests with single and contra-rotating propellers on a steam launch. In a subsequent paper (Reference 80) he further developed this work by comparing and contrasting the results of the work contained in his earlier paper with some propulsion experiments conducted by Luke (Reference 81). Little more appears to have been published on the subject until Lerbs introduced a theoretical treatment of the problem in 1955 (Reference 82), and a year later van Maneñ and Sentic (Reference 83) produced a method based on vortex theory supported by empirical factors derived from open water experiments. Morgan (Reference 84) subsequently produced a step-by-step design method based on Lerbs' theory, and in addition he showed that the optimum diameter can be obtained in the usual way for a single-screw propeller but assuming the absorption of half the required thrust or power and that the effect on efficiency of axial spacing between the propellers was negligible. Whilst Lerbs' work was based on lifting line principles, Murray

(Reference 37) considered the application of lifting surface to the theory of contra-rotating propellers.

Van Gunsteren (Reference 85) developed a method for the design of contra-rotating propellers in which the interaction effects of the two propellers are largely determined with the aid of momentum theory. Such an approach allows the slipstream contraction effects and an allowance for the mutually induced pressures in the cavitation calculation to be taken into account in a relatively simple manner. The radial distributions of the mutually induced velocities are calculated by lifting line theory; however, the mutually induced effects are separated from self-induced effects in such a way that each propeller of the pair can be designed using a procedure for simple propellers. Agreement between this method and experimental results indicated a reasonable level of correlation.

Tsakonas *et al.* (Reference 86) has extended the development of lifting surface theory to the contra-rotating propeller problem by applying linearized unsteady lifting surface theory to propeller systems operating in uniform or non-uniform wake fields. In this latter approach the propeller blades lie on helicoidal surfaces of varying pitch, and have finite thickness distributions, together with arbitrary definitions of blade outline, camber and skew. Furthermore, the inflow field of the after propeller is modified by accounting for the influence of the forward propeller so that the potential and viscous effects of the forward propeller are incorporated in the flow field of the after propeller. It has been shown that these latter effects play an important role in determining the unsteady loading on the after propeller and as a consequence cannot be ignored. Subsequently, work at the Massachussetts Institute of Technology has extended panel methods to rotor–stator combinations.

High speed and more particularly supercavitating propellers have been the subject of considerable research effort. Two problems present themselves: the first is the propeller inflow and the second is the blade design problem. In the first case of the oblique flow characteritics these have to some extent been dealt with empirically, as discussed in Chapter 6. In the case of calculating the performance characteristics, the oblique flow characteristics manifest themselves as an in-plane flow over the propeller disc, whose effect needs to be taken into account. Theoretical work on what was eventually to become a design method started in the 1950s with the work of Tulin on steady two-dimensional flows over slender symmetrical bodies (Reference 87), although supercavitating propellers had been introduced by Posdunine as early as 1943. This work was followed by other studies on the linearized theory for supercavitating flow past lifting foils and struts at zero cavitation number (References 88, 89), in which Tulin used the two-term Fourier series for the basic section vorticity distribution. Subsequently Johnson (Reference 90) in developing a theoretical analysis for low drag supercavitating sections used three- and five-term expressions. Tachmindji and Morgan (Reference 91) developed a practical design method based on a good deal of preceding research work which was extended with additional design information (Reference 92). The general outline of the method essentially followed a similar form to the earlier design procedure set down by Eckhardt and Morgan in Reference 18.

A series of theoretical design charts for two-, three- and four-bladed supercavitating propellers was developed by Caster (References 93, 94). This work was based on the two-term blade sections and was aimed at providing a method for the determination of optimum diameter and revolutions. Anderson (Reference 95) developed a lifting line theory which made use of induction factors and was applicable to normal supercavitating geometry and for non-zero cavitation numbers. However, it was stressed that there was a need to develop correction factors in order to get satisfactory agreement between the lifting line theory and experimental results.

Supercavitating propeller design generally requires an appeal to theoretical and experimental results – not unlike many other branches of propeller technology. However, in the case of supercavitating propellers the theoretical methods are not so extensively researched. This may change with the current upsurge in requirements for high-speed craft for commercial and pleasure purposes. With regard to the experimental data to support the design of supercavitating propellers the designer can make appeal to the works of Newton and Radar (Reference 96), van de Voorde and Esveldt (Reference 97) and Taniguchi and Tanibayashi (Reference 98).

References and further reading

1. Rankine, W.J. On the mechanical principles of the action of propellers. *Trans. RINA*, **6**, 1865.
2. Froude, R.E. On the part played in the operation of propulsion differences in fluid pressure. *Trans. RINA*, **30**, 1889.
3. Froude, W. On the elementary relation between pitch, slip and propulsive efficiency. *Trans. RINA*, **19**, 1878.
4. Betz, A. Ergebn. aerodyn. Vers Anst Gottingen 1919.
5. Betz, A. Eine Erweiterung der Schrauben Theorie. *Zreits. Flugtech*, 1920.
6. Burrill, L.C. On propeller theory. *Trans. IESS*, 1947.
7. Goldstein, S. On the vortex theory of screw propellers. *Proc. Royal Soc.*, Ser. A, **123**, 1929.
8. Tachmindji, A.J., Milam, A.B. The Calculation of the Circulation for Propellers with Finite Hub having 3, 4, 5 and 6 Blades. D.T.M.B. Report No. 1141, 1957.
9. Perring, W.G.A. The Vortex Theory of Propellers, and its Application to the Wake Conditions Existing Behind a Ship. *Trans. RINA*, 1920.
10. Lockwood Taylor, J. Screw propeller theory. *Trans. NECIES*, 1942.
11. Burrill, L.C. Calculation of marine propeller performance characteristics. *Trans. NECIES*, 1944.
12. Sontvedt, T. Open water performance of propellers. *Shipping World and Shipbuilder*, January, 1973.
13. Burrill, L.C. The optimum diameter of marine propellers: a new design approach. *Trans. NECIES*, 1956.
14. Hill, J.G. The design of propellers. *Trans. SNAME*, 1949.
15. Strscheletsky, M. *Hydrodynamische Grundlagen zur Berechnung der Schiffschranben*. G. Braun, Karlsruhe, 1950.
16. Lerbs, H.W. Moderately loaded propellers with a finite number of blades and an arbitrary distribution of circulation. *Trans. SNAME*, **60**, 1952.
17. Manen, J.D. van, Lammeren, W.P.A. van. The design of wake-adapted screws and their behaviour behind the ship. *Trans. IESS*, 1955.
18. Eckhardt, M.K., Morgan, W.B. A propeller design method. *Trans. SNAME*, **63**, 1955.
19. Ludwieg, H., Ginzel, J. *Zur Theorie der Breitblattschranbe*, Aerodyn. Versuchsanst., Göttingen, 1944.
20. McCarthy, J.H. Comparing four methods of marine propeller design. *ASNE J.*, August, 1960.
21. Morgan, W.B., Silovic, V., Denny, S.B. Propeller lifting-surface corrections. *Trans. SNAME*, **76**, 1968.
22. Cheng, H.M. Hydrodynamic Aspect of Propeller Design Based on Lifting Surface Theory Parts I and II. DTMB Rep. 1802, 1964; 1803, 1965.
23. Kerwin, J.E., Leopold, R. A design theory for subcavitating propellers. *Trans. SNAME*, **72**, 1964.
24. Abbott, I.H., Doenhoff, A.E. von. *Theory of Wing Sections*, Dover, 1958.
25. Oossanen, P. van. Calculation of Performance and Cavitation Characteristics of Propellers Including Effects of Non-Uniform Flow and Viscosity. NSMB Publ. No. 457, 1974.
26. Minsaas, K., Slattelid, O.H. Lifting Surface Correction for 3 Bladed Optimum Propellers. *ISP*, **18**, 1971.
27. Cummings, R.A., Morgan, W.B., Boswell, R.J. Highly skewed propellers. *Trans. SNAME*, **20**, 1972.
28. McCrosky, W.J. Unsteady aerofoils. *Ann. Rev. Fluid Mech.*, **14**, 1982.
29. Crighton, D.G. The Kutta conditions in unsteady flows. *Ann. Rev. Fluid Mech.*, **17**, 1985.
30. Guilloton, R. Calcul des vitesses induites en vue du trace des helices. *Schiffstechnik*, 4, 1957.
31. Sparenberg, J.A. Application of lifting surface theory to ship screws. *Proc. K. Ned. Akad. Wet.*, Ser B., **62(S)**, 1959.
32. Pien, P.C. The calculation of marine propellers based on lifting surface theory. *J. Ship Res.*, **5**(2), 1961.
33. Kerwin, J.E. The solution of Propeller Lifting Surface Problems by Vortex Lattice Methods. Rep. Dept. of Ocean Eng., MIT, 1961.
34. Manen, J.D. van, Bakker, A.R. Numerical results of Sparenberg's lifting surface theory for ship screws. *Proc. 4th Symp. Nav. Hydro.*, Washington, 1962.
35. Yamazaki, R. On the theory of screw propellers. Proc. 4th Symp. Nav. Hydro., Washington, 1962.
36. English, J.W. The Application of a Simplified Lifting Surface Technique to the Design of Marine Propellers. Ships Div. Rep. SH R30/62 NPL, 1962.
37. Murray, M.T. *Propeller Design and Analysis by Lifting Surface Theory. ARL*, 1967.
38. Hanaoka, T. Numerical Lifting Surface Theory of a Screw Propeller in Non-Uniform Flow (Part 1 – Fundamental Theory). Rep. Ship Res. Inst., Tokyo, **6(5)**, 1969.
39. Gent, W. van. Unsteady lifting surface theory of ship screws: derivation and numerical treatment of integral equation. *J. Ship Res.*, **19**(4), 1975.
40. Gent, W. van. On the Use of Lifting Surface Theory for Moderately and Heavily Loaded Ship Propellers. NSMB Rep. No. 536.
41. Brockett, T.E. Lifting surface hydrodynamics for design of rotating blades. *Propellers '81 Symp. SNAME*, 1981.
42. Szantyr, J.A. A new method for the analysis of unsteady propeller cavitation and hull surface pressures. *Trans. RINA*, Spring Meeting, 1984.
43. Kerwin, J.E., Chang-Sup Lee. Prediction of steady and unsteady marine propeller performance by numercial lifting-surface theory. *Trans. SNAME*, Paper No. 8, Annual Meeting, 1978.
44. Greeley, D.A., Kerwin, J.E. Numerical methods for propeller design and analysis in steady flow. *Trans. SNAME*, **90**, 1982.
45. Lan, C.E. A quasi-vortex lattice method in thin wing theory. *J. Airer*, **11**, 1974.
46. Cummings, D.E. Vortex Interaction in a Propeller Wake. Dept. Nav. Arch. Rep. 68-12, MIT, 1968.
47. Loukakis, T.A. A New Theory for the Wake of Marine Propellers. Dept. Nav. Arch. Rep. 71-7, MIT, 1971.
48. Kerwin, J.E. A Deformed Wake Model for Marine Propellers. Dept. Ocean Eng. Rep. 76-6, MIT, 1976.
49. Lighthill, M.J. A new approach to thin aerofoil theory. *Aeronautical Quart.*, No. 3, 1951.
50. Hess, J.L., Valarezo, W.O. Calculation of Steady Flow about Propellers by Means of a Surface Panel Method. *AIAA*, Paper No. 85, 1985.
51. Hess, J.L., Smith, A.M.O. Calculation of potential flow about arbitrary bodies. *Prog. Aeronaut. Sci.*, **8**, 1967.
52. Hoshino, T. Hydrodynamic analysis of propellers in steady flow using a surface panel method. *Trans. Soc. Nav. Arch of Japan*, 1989.
53. Klassen, H., Arnoldus, W. Actuating forces in controllable pitch propellers. *Trans. I.Mar.E.*, 1964.
54. Gutsche, F. Loading assumptions for controllable pitch propellers. *Schiffbanforschung*, 4, 1965

55. Rusetskiy, A.A. *Hydrodynamics of Controllable Pitch Propellers*. Idatelstvo Sudostroyeniye, Leningrad, 1968.
56. Hawdon, L., Carlton, J.S., Leathard, F.I. The analysis of controllable pitch propeller characteristics at off design conditions. *Trans. I.Mar.E.*, 1978
57. Pronk, C. *Blade Spindle Torque and Off Design Behaviour of Controllable Pitch Propellers*. Delft, 1980.
58. Kort, L. Der neue Dusen schraubenartrieb. *Werft Reederei and Hafen*, 15, 1934.
59. Stiess, W. Erweiterte Stahltheorie für Dusenschraubon mit und ne Leitapparat. *Werft Reederei und Hafen*, 17, 1936.
60. Horn, F., Amtsberg, H. *Entwurf von Schiffdusensystemen* (*Kortdusen*). *Jahrbuch der Schiffbautechnishen*, Gesellschaft, Vol. 44, 1950, 1961.
61. Dickmann, H.E., Weissinger, J. Beitrag zur Theories Optimaler Dusenschrauben (Kortdusen). *Jahrbuch der Schiffbautechnischon Gessellschaft*, Vol. 49, 1955.
62. Manen, J.D. van, Superina, A. The design of screw propellers in nozzles. *ISP*, **6**, March, 1959.
63. Manen, J.D. van. Effect of radial load distribution on the performance of shrouded propellers. *Trans. RINA*, 1962.
64. Manen, J.D. van, Oosterveld, M.W.C. Analysis of ducted-propeller design. *Trans. SNAME*, 1966.
65. Morgan, W.B. Theory of Ducted Propeller with Finite Number of Blades. University of California, Inst. of Eng. Res., May, 1961.
66. Dyne, G. A Method for the Design of Ducted Propellers in a Uniform Flow. SSPA Rep. No. 62, 1967.
67. Oosterveld, M.W.C. Wake Adapted Ducted Propellers. NSMB Rep. No. 345, 1970.
68. Ryan, P.G., Glover, E.J. A ducted propeller design method: a new approach using surface vorticity distribution techniques and lifting line theory. *Trans. RINA*, 1972.
69. Glover, E.J. Slipstream Deformation and its Influence on Marine Propeller Design. Ph.D. Thesis, Newcastle upon Tyne, 1970.
70. Caracostas, N. Off-design performance analysis of ducted propellers. *Propellers '78 Symp., Trans. SNAME*, 1978.
71. Tsakonas, S., Jacobs, W.R. Propeller-duct interaction due to loading and thickness effects. *Propellers '78 Symp., Trans. SNAME*, 1978.
72. Falcao de Campos, J.A.C. On the Calculation of Ducted Propeller Performance in Axisymmetric Flows. NSMB Rep. No. 696, 1983.
73. McCormick, B.W., Eisenhuth, J.J. The design and performance of propellers and pumpjets for underwater propulsion. *American Rocket Soc. 17th Ann. Mtg*, 1962.
74. Henderson, R.E., McMahon, J.F., Wislicenus, G.F. A Method for the Design of Pumpjets. Ord. Res. Lab., Pennsylvania State Univ., 1964.

75. Wald, Q.E. Analysis of the integral pumpjet. *J. Ship Res.*, December, 1970.
76. Gunsteren, L.A. van. Ringpropellers. *SNAME & I. Mar.E. Mtg*, Canada, 1969.
77. Keller, W.H. auf'm. Comparative Tests with B-Series Screws and Ringpropellers. NSMB Rep. No. 66-047, DWT, 1966.
78. Greenhill, A.G. A theory of the screw propeller. *Trans. RINA*, 1988.
79. Rota, G. The propulsion of ships by means of contrary turning screws on a common axis. *Trans. RINA*, 1909.
80. Rota, G. Further experiments on contrary turning co-axial screw propellers. *Trans. RINA*, 1992.
81. Luke, W.J. Further experiments upon wake and thrust deduction. *Trans. RINA*, 1914.
82. Lerbs, H.W. Contra-Rotating Optimum Propellers Operating in a Radially Non-Uniform Wake. DTMB Rep. 941, 1955.
83. Manen, J.D. van, Sentic, A. Contra-rotating propellers. *ISP*, 3, 1956.
84. Morgan, W.B. The design of contra-rotating propellers using Lerbs' theory. *Trans. SNAME*, 1960.
85. Gunsteren, L.A. van. Application of momentum theory in counter-rotating propeller design. *ISP*, 1970.
86. Tsakonas, S., Jacobs, W.R., Liao, P. Prediction of steady and unsteady loads and hydrodynamic forces on counter-rotating propellers. *J. Ship Res.*, 27, 1983.
87. Tulin, M.P. Steady Two Dimensional Cavity Flow about Slender Bodies. DTMB Rep. No. 834, 1953.
88. Tulin, M.P., Burkart, MF. Linearized Theory for Flows about Lifting Foils at Zero Cavitation Number. DTMB Rep. 638, 1955.
89. Tulin, M.P. Supercavitating flow past foils and struts. *Proc. Symp. on Cavitation in Hydrodynamics*, NPL, 1956.
90. Johnson, V.E. Theoretical Determination of Low-Drag Supercavitating Hydrofoils and their Two-Dimensional Characteristics at Zero Cavitation Number. NACA Rep., 1957.
91. Tachmindji, A.J., Morgan, W.B. The Design and Performance of Supercavitating Propellers. DTMB Rep. 807, 1957.
92. Tachmindji, A.J., Morgan, W.B. The design and estimated performance of a series of supercavitating propellers. *Proc. 2nd Symp. on Nov. Hydro.*, 1969.
93. Caster, E.B. TMB 3-Bladed Supercavitating Propeller Series. DTMB Rep. 1245, 1959.
94. Caster, E.B. TMB 2, 3 and 4 Bladed Supercavitating Propeller Series. DTMB Rep. 1637.
95. Anderson, P. Lifting-line theory and calculations for supercavitating propellers, *ISP*, 1974.
96. Newton, R.N., Radar H.P. Performance data for propellers for high speed craft. *Trans. RINA*, 103, 1961.
97. Voorde, C.B. van de, Esveldt, J. Tunnel tests on supercavitating propellers. *ISP*, 9, 1962.
98. Taniguchi, K., Tanibayashi, H. Cavitation tests on a series of supercavitating propellers. *IAHR Symp. on Cav. and Hydraulich Mach.*, Japan, 1962.
99. Morgan, W.B., Wrench, J.W. Some computational aspects of propeller design. *Meth. in Comp. Phys.*, 4, 1965.

9 Cavitation

Contents

Cavitation is a general fluid mechanics phenomenon which can occur whenever a liquid is used in a machine which induces pressure and velocity fluctuations in the fluid. Consequently, pumps, turbines, propellers, bearings and even the human body, in for example the heart and knee-joints, are all examples of machines where the destructive consequences of cavitation may occur.

The history of cavitation has been traced back to the middle of the 18th century, when some attention was paid to the subject by the Swiss mathematician Euler (Reference 1) in a paper read to the Berlin Academy of Science and Arts in 1754. In that paper Euler discussed the possibility that a phenomenon that we would today call cavitation occurs on a particular design of water wheel and the influence this might have on its performance.

However, little reference to cavitation pertaining directly to the marine industry has been found until the mid-19th century, when Reynolds wrote a series of papers (Reference 2) concerned with the causes of engine-racing in screw propelled steamers. These papers introduced cavitation as we know it today by discussing the effect it had on the performance of the propeller: when extreme cases of cavitation occur, the shaft rotational speed is found to increase considerably from that expected from the normal power absorption relationships.

The trial reports of *HMS Daring* in 1894 noted this overspeeding characteristic, as did Sir Charles Parsons, shortly afterwards, during the trials of his experimental steam turbine ship *Turbinia*. The results of the various full-scale experiments carried out in these early investigations showed that an improvement in propeller performance could be brought about by the increase in blade surface area. In the case of the *Turbinia*, which originally had a single propeller on each shaft and initially only achieved just under 20 knots on trials, Parsons found that to absorb the full power required on each shaft it was necessary to adopt a triple propeller arrangement to increase the surface area to the required proportions. Consequently, he used three propellers mounted in tandem on each shaft, thereby deploying a total of nine propellers distributed about the three propeller shafts. This arrangement not only allowed the vessel to absorb the full power at the correct shaft speeds, but also permitted the quite remarkable trial speed of 32.75 knots to be attained.

In an attempt to appreciate fully the reasons for the success of these decisions, Parsons embarked on a series of model experiments designed to investigate the nature of cavitation. To accomplish this task, Parsons constructed in 1895 an enclosed circulating channel. This apparatus allowed the testing of 2-inch diameter propellers and was a forerunner of cavitation tunnels as we know them today. However, recognizing the limitations of this tunnel, Parsons constructed a much larger tunnel 15 years later in which he could test 12-inch diameter propeller models. Subsequently other larger tunnels were constructed in Europe and America during the 1920s and 1930s, each incorporating the lessons learned from its predecessors.

9.1 The basic physics of cavitation

The underlying physical process which governs the action of cavitation can, at a generalized level, be considered as an extension of the well-known situation in which a kettle of water will boil at a lower temperature when taken to the top of a high mountain. In the case of cavitation the pressure is allowed to fall to a low level while the ambient temperature, which in the case of a propeller is that of the surrounding sea water, is kept constant. Parsons had an early appreciation of this concept and he, therefore, allowed the atmospheric pressure above the water level in his tunnels to be reduced by means of a vacuum pump, which enabled cavitation to appear at much lower shaft speeds, making its observation easier.

The explanation of cavitation as being simply a water boiling phenomenon, although true, is an oversimplification of the actual physics that occur. To initially appreciate this, consider first the phase diagram for water shown in Figure 9.1. If it is assumed that the temperature is sufficiently high for the water not to enter its solid phase, then at either point B or C one would expect the water to be both in its liquid state and have an enthalpy equivalent to that state. For example, in the case of fresh water at standard pressure and at a temperature of 10°C this would be of the order of 42 kJ/kg. However, at point A, which lies in the vapour phase, the fluid would be expected to have an enthalpy equivalent to a superheated vapour, which in the example quoted above, when the pressure was dropped to say 1.52 kPa, would be in excess of 2510 kJ/kg. The differences in these figures is primarily because the fluid gains a latent enthalpy change as the liquid–vapour line is crossed, so that

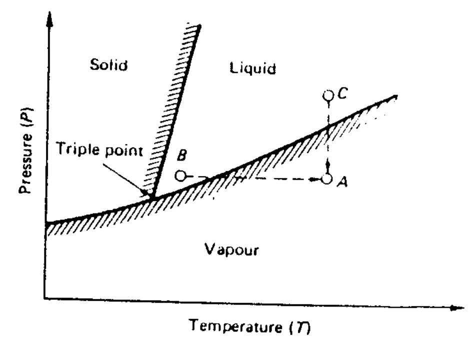

Figure 9.1 Phase diagram for water

at points B and C the enthalpies are

$$h_{B,C} = h_{fluid}(p, t)$$

and at the point A the fluid enthalpy becomes

$$h_A = h_{fluid} + h_{latent} + h_{superheat}$$

Typically for fresh water the liquid–vapour line is defined by Table 9.1.

Table 9.1 Saturation temperatures of fresh water

Pressure (kPa)	0.689	6.894	13.79	27.58	55.15	101.3	110.3
Saturation temperature (°C)	1.6	38.72	52.58	67.22	83.83	100.0	102.4

Secondly, it is important to distinguish between two types of vaporization. The first is the well-known process of vaporization across a flat surface separating the liquid and its vapour. The corresponding variation in vapour pressure varies with temperature as shown in Table 9.1, and along this curve the vapour can coexist with its liquid in equilibrium. The second way in which vaporization can occur is by cavitation, which requires the creation of cavities within the liquid itself. In this case the process of creating a cavity within the liquid requires work to be done in order to form the new interface. Consequently, the liquid can be subjected to pressures below the normal vapour pressure, as defined by the liquid–vapour line in Figure 9.1, or Table 9.1, without vaporization taking place. As such, it is possible to start at a point such as C, shown in Figure 9.1, which is in the liquid phase, and reduce the pressure slowly to a value well below the vapour pressure, to reach the point A with the fluid still in the liquid phase. Indeed, in cases of very pure water, this can be extended further, so that the pressure becomes negative; when a liquid is in these over-expanded states it is said to be in a metastable phase. Alternatively it is possible to bring about the same effect at constant pressure by starting at a point B and gradually heating the fluid to a metastable phase at the point A. If either of these paths, constant pressure or temperature, or indeed some intermediate path, is followed, then eventually the liquid reaches a limiting condition at some point below the liquid–vapour line in Figure 9.1, and either cavitates or vaporizes.

The extent to which a liquid can be induced metastably to a lower pressure than the vapour pressure depends on the purity of the water. If water contains a significant amount of dissolved air, then as the pressure decreases the air comes out of the solution and forms cavities in which the pressure will be greater than the vapour pressure. This effect applies also when there are no visible bubbles; submicroscopic gas bubbles can provide suitable nuclei for cavitation purposes. Hence cavitation can either be vaporous or gaseous or, perhaps, a combination of both. Consequently, the point at which cavitation occurs can be either above or below the vapour pressure corresponding to the ambient temperatures.

In the absence of nuclei a liquid can withstand considerable negative tensions without undergoing cavitation. For example, in the case of a fluid, such as water, which obeys van der Waals' equation:

$$\left(p + \frac{a}{V^2}\right)(V - b) = RT \tag{9.1}$$

a typical isotherm is shown in Figure 9.2, together with the phase boundary for the particular temperature. In addition, the definition of the tensile strength of the liquid is also shown on this figure. The resulting limiting values of the tensions that can be withstood form a wide band; for example, at room temperature, by using suitable values for a and b in equation (9.1), the tensile strength can be shown to be about 500 bars. However, some researchers have suggested that the tensile strength of the liquid is the same as the intrinsic pressure a/V^2 in equation (9.1); this yields a value of around 10 000 bars. In practice, water subjected to rigorous filtration and pre-pressurization seems to rupture at tensions of the order of 300 bars. However, when solid, non-wetted nuclei having a diameter of about 10^{-6} cm are present in the water it will withstand tensions of only the order of tens of bars. Even when local pressure conditions are known accurately it is far from easy to predict when cavitation will occur because of the necessity to estimate the size and distribution of the nuclei present.

Despite the extensive literature on the subject, both the understanding and predictability of bubble nucleations is a major problem for cavitation studies. There are in general two principal models of nucleation; these are the stationary crevice model and the entrained nuclei models. Nuclei in this sense refers to clusters

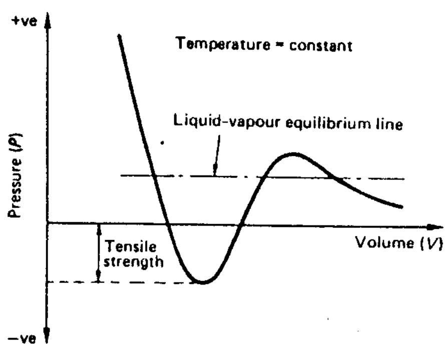

Figure 9.2 Van der Waals' isotherm and definition of tensile strength of liquid

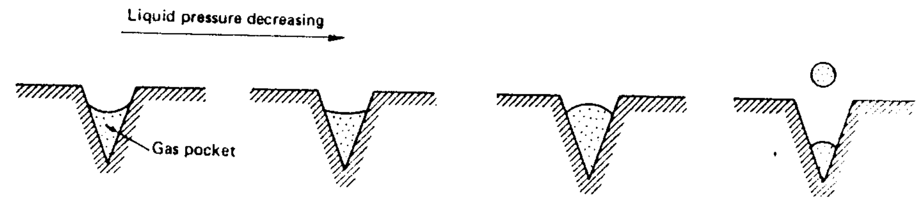

Figure 9.3 Nucleation model for a crevice in an entrained microparticle (Harvey)

of gas or vapour molecules of sufficient size to allow subsequent growth in the presence of reduced pressure. The stationary nuclei are normally assumed to be harboured in small crevices of adjacent walls whilst, in contrast, the travelling nuclei are assumed to be entrained within the mainstream of the fluid. Consequently, entrained nuclei are considered the primary source of cavitation, although of course cavitation can also be initiated from stationary nuclei located in the blade surface at the minimum pressure region. Of the nucleation models proposed those of Harvey *et al.* (References 3–6) and subsequently by others (References 7–10) are probably the most important. These models propose that entrained microparticles in the liquid, containing in themselves unwetted acute angled microcrevices, are a source of nucleation. This suggests that if a pocket of gas is trapped in a crevice then, if the conditions are correct, it can exist in stable equilibrium rather than dissolve into the fluid. Consider first a small spherical gas bubble of radius R in water. For equilibrium, the pressure difference between the inside and outside of the bubble must balance the surface tension force:

$$p_v - p_l = \frac{2S}{R} \tag{9.2}$$

where p_v = vapour and/or gas pressure (internal pressure)
p_l = pressure of the liquid (external pressure)
and S = surface tension.

Now the smaller the bubble becomes, according to equation (9.2), the greater must be the pressure difference across the bubble. Since, according to Henry's law, the solubility of a gas in a liquid is proportional to gas pressure, it is reasonable to assume that in a small bubble the gas should dissolve quickly into the liquid. Harvey *et al.*, however, showed that within a crevice, provided the surface is hydrophobic, or imperfectly wetted, then a gas pocket can continue to exist. Figure 9.3 shows in schematic form the various stages in the nucleation process on a microparticle. In this Figure the pressure reduces from left to right, from which it is seen that the liquid–gas interface changes from a convex to concave form and eventually the bubble in the crevice of the microparticle grows to a sufficient size so that a part breaks away to form a bubble entrained in the body of the fluid.

Other models of nucleation have been proposed for example those of Fox and Herzfeld (Reference 11) and Plesset (Reference 14) – and no doubt these also play a part in the overall nucleation process, which is still far from well understood. Fox and Herzfeld suggested that a skin of organic impurity, for example fatty acids, accumulates on the surface of a spherical gas bubble in order to inhibit the dissolving of the gas into the fluid as the bubble decreases in size; this reduction in size causes the pressure differential to increase, as seen by equation (9.2). In this way it is postulated that the nuclei can stabilize against the time when the bubble passes through a low-pressure region, at which point the skin would be torn apart and a cavity initiated. The 'skin' model has in latter years been refined and improved by Yount (References 12, 13). Plesset's unwetted mote model suggested that such motes can provide bubble-nucleation without the presence of gases other than the inevitably present vapour of the liquid. The motes, it is suggested, would provide weak spots in the fluid about which tensile failure of the liquid would occur at pressures much less than the theoretical strength of the pure liquid.

Cavitation gives rise to a series of other physical effects which, although of minor importance to ship propulsion, are interesting from the physical viewpoint and deserve passing mention especially with regard to material erosion. The first is sonoluminescence, which is a weak emission of light from the cavitation bubble in the final stage of its collapse. This is generally ascribed to the very high temperatures resulting from the essentially adiabatic compression of the permanent gas trapped within the collapsing cavitation bubbles. Schlieren and interferometric pictures have succeeded in showing the strong density gradients or shock waves in the liquid around collapsing bubbles. When bubbles collapse surrounding fluid temperatures as high as 100 000 K have been suggested and Wheeler (Reference 15) has concluded that temperature rises of the order of 500–800°C can occur in the material adjacent to the collapsing bubble. The collapse of the bubbles is completed in a very short space of time (milli- or even microseconds) and it has been shown that the resulting shock waves radiated through the liquid adjacent to the bubble may have a pressure difference as high as 4000 atmospheres.

The earliest attempt to analyse the growth and collapse of a vapour or gas bubble in a continuous liquid medium from a theoretical viewpoint appears to have been made by Besant (Reference 16). This work was to some extent ahead of its time, since bubble dynamics was not an important engineering problem in the mid-1800s and it was not until 1917 that Lord Rayleigh laid the foundations for much of the analytical work that continues to the present time (Reference 17). His model considered the problem of a vapour-filled cavity collapsing under the influence of a steady external pressure in the liquid, and although based on an oversimplified set of assumptions, Rayleigh's work provides a good model of bubble collapse and despite the existence of more modern and advanced theories is worthy of discussion in outline form.

In the Rayleigh model the pressure p_v within the cavity and the pressure at infinity p_0 are both considered to be constant. The bubble is defined using a spherical coordinate system whose origin is at the centre of the bubble whose initial steady state radius is R_0 at time $t = 0$. At some later time t, under the influence of the external pressure p_0 which is introduced at time $t = 0$, the motion of the bubble wall is given by

$$\frac{d^2R}{dt^2} + \frac{3}{2R}\left(\frac{dR}{dt}\right)^2 = \frac{1}{\varrho R}(p_v - p_0) \qquad (9.3)$$

where ϱ is the density of the fluid. By direct integration of equation (9.3), assuming that both p_v and p_0 are constant, Rayleigh described the collapse of the cavity in terms of its radius R at a time t as being

$$\left(\frac{dR}{dt}\right)^2 = \frac{2}{3}\frac{(p_0 - p_v)}{\varrho}\left(\left(\frac{R_0}{R}\right)^3 - 1\right) \qquad (9.4)$$

By integrating equation (9.4) numerically it is found that the time to collapse of the cavity t_0, known as the 'Rayleigh collapse time', is

$$t_0 = 0.91468 R_0\left(\frac{\varrho}{p_0 - p_v}\right)^{1/2} \qquad (9.5)$$

This time t presupposes that at the time $t = 0$ the bubble is in static equilibrium with a radius R_0. The relationship between bubble radius and time in non-dimensional terms is derived from the above as being

$$\frac{t}{t_0} = 1.34\int_{R/R_0}^{1}\frac{dx}{(1/x^2 - 1)^{1/2}} \qquad (9.6)$$

and the results of this equation, shown in Figure 9.4, have been shown to agree well with experimental observations of a collapsing cavity.

The Rayleigh model of bubble collapse leads to a series of very significant results from the viewpoint of cavitation damage; however, because of the simplifications involved it cannot reveal the detailed mechanism

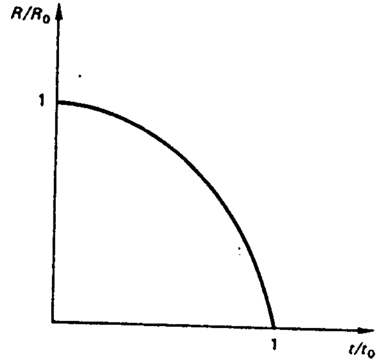

Figure 9.4 Collapse of a Rayleigh cavity

of cavitation erosion. The model shows that infinite velocities and pressures occur at the point when the bubble vanishes and in this way points toward the basis of the erosion mechanism. The search for the detail of this mechanism has led to considerable effort on the part of many researchers in recent years. Such work has introduced not only the effects surface tension, internal gas properties and viscosity effects, but also those of bubble asymmetries which predominate during the collapse process. Typical of these advanced studies is the work of Mitchell and Hammitt (Reference 18) who also included the effects pressure gradient and relative velocity as well as wall proximity. An alternative approach by Plesset and Chapman (Reference 19) used potential flow assumptions which precluded the effects of viscosity, which in the case of water is unlikely to be of major importance. Plesset and Chapman focused on the bubble collapse mechanism under the influence of wall proximity, which is of major significance in the study of cavitation damage, as will be seen in Section 9.5. Their approach was based on the use of cylindrical coordinates as distinct from Mitchell's spherical coordinate approach, and this allowed them to study the microjet formation during collapse to a much deeper level because the spherical coordinates required the numerical analysis to be terminated as the microjet approaches the initial bubble centre. Figure 9.5 shows the results of a computation of an initially spherical bubble collapsing close to a solid boundary, together with the formation of the microjet directed toward the wall.

Subsequently, Chahine has studied cloud cavity dynamics by modelling the interaction between bubbles. In his model he was able to predict the occurrence of high pressures during collapse principally by considering the coupling between bubbles in an idealized way through symmetric distributions of identically sized bubbles.

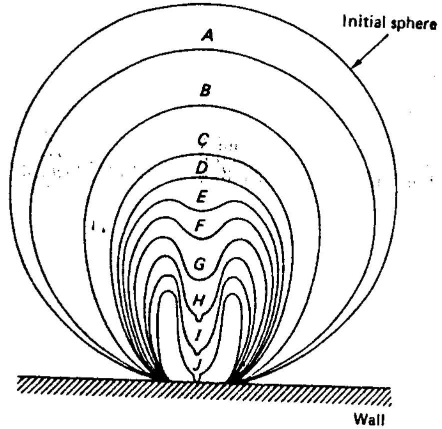

Figure 9.5 Computed bubble collapse (Plesset–Chapman)

9.2 Types of cavitation experienced by propellers

Cavitating flows are by definition multi-phase flow regions. The two phases that are most important are the water and its own vapour; however, in almost all cases there is a quantity of gas, such as air, which has significant effects in both bubble collapse and inception – most importantly in the inception mechanism. As a consequence cavitation is generally considered to be a two-phase, three-component flow regime. Knapp *et al.* (Reference 20) classified cavitation into fixed, travelling or vibratory forms, the first two being of greatest interest in the context of propeller technology.

A fixed cavity is one in which the flow detaches from the solid boundary of the immersed object to form a cavity or envelope which is fixed relative to the object upon which it forms, and in general such cavities have a smooth glassy appearance. In contrast, as their name implies, travelling cavities move with the fluid flowing past the body of interest. Travelling cavities originate either by breaking away from the surface of a fixed cavity, from which they can then enter the flow stream, or from nuclei entrained within the fluid medium. Figure 9.6 differentiates between these two basic types of cavitation.

The cavitation patterns which occur on marine propellers are usually referred to as comprising one or more of the following types: sheet, bubble, cloud, tip vortex or hub vortex cavitation.

Sheet cavitation initially becomes apparent at the leading edges of the propeller blades on the back or suction surface of the blades if the sections are working at positive incidence angles. Conversely, if the sections are operating at negative incidence this type of cavitation may initially appear on the face of the blades. Sheet cavitation appears because when the sections are working at non-shock-free angles of incidence, large suction pressures build up near the leading edge of the blades of the 'flat plate' type of distribution shown in Figure 7.18. If the angles of incidence increase in magnitude, or the cavitation number decreases, then the extent of the cavitation over the blade will grow both chordally and radially. As a consequence the cavitation forms a sheet over the blade surface whose

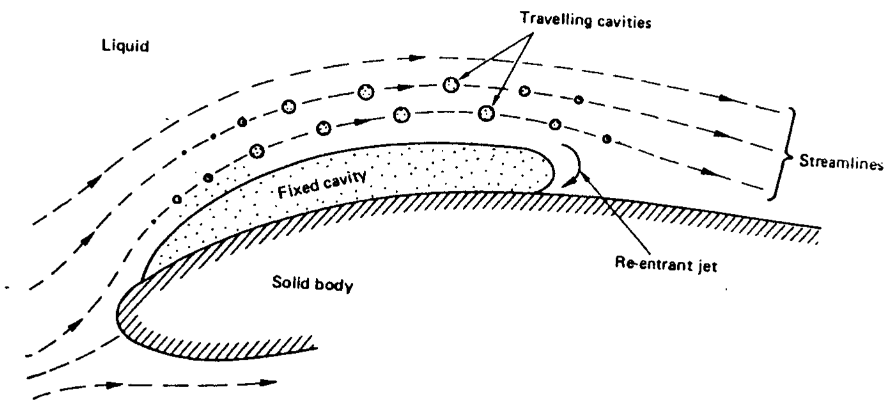

Figure 9.6 Fixed and travelling cavities

(a)

(b)

(c)

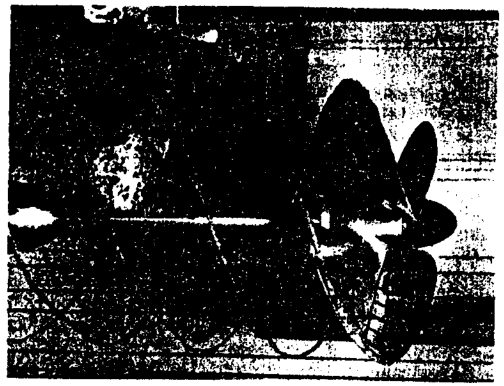

(d)

Figure 9.7 Types of cavitation on propellers (MARIN): (a) sheet and cloud cavitation together with a tip vortex; (b) mid-chord bubble cavitation together with a tip vortex and some leading edge streak cavitation; (c) hub vortex cavitation with traces of LE and tip-vortex in top of propeller disc (Courtesy: MARIN); (d) tip vortex cavitation

extent depends upon the design and ambient conditions. Figure 9.7(a) shows an example of sheet cavitation on a model propeller, albeit with tip vortex cavitation also visable. Sheet cavitation is generally stable in character, although there are cases in which a measure of instability can be observed. In these cases the reason for the instability should be sought, and if it is considered that the instability will translate to full scale, then a cure should be sought, as this may lead to blade erosion or unwanted pressure fluctuations.

Bubble cavitation (Figure 9.7(b)), is primarily influenced by those components of the pressure distribution which cause high suction pressures in the mid-chord region of the blade sections. Thus the combination of camber line and section thickness pressure distributions identified in Figure 7.18 have a considerable influence on the susceptibility of a propeller toward bubble cavitation. Since bubble cavitation normally occurs first in the mid-chord region of the blade, it tends to occur in non-separated flows. This type of cavitation, as its name implies, appears as individual bubbles growing, sometimes quite large in character, and contracting rapidly over the blade surface.

Cloud cavitation is frequently to be found behind strongly developed stable sheet cavities and generally in moderately separated flow in which small vortices form the origins for small cavities. This type of cavitation (Figure 9.7(a) with traces on Figure 9.7(b)) appears as a mist or 'cloud' of very small bubbles and its presence should always be taken seriously.

The vortex types of cavitation, with few exceptions, occur at the blade tips and hub of the propeller and they are generated from the low-pressure core of the shed vortices at the ends of the blades. The hub vortex is formed by the combination of the individual vortices shed from each blade root, and although individually these vortices are unlikely to cavitate, under the influence of a converging propeller cone the combination of the blade root vortices has a high susceptibility to cavitate. When this occurs the resulting cavitation is normally very stable and appears to the observer as a rope with strands corresponding to the number of blades of the propeller. Tip vortex cavitation is normally first observed some distance behind the tips of the propeller blades. At this time the tip vortex is said to be 'unattached', but as the vortex becomes stronger, either through higher blade loading or decreasing cavitation number, it moves toward the blade tip and ultimately becomes attached. Figures 9.7(c) and (d) shows typical examples of the hub and tip vortices respectively.

In addition to the principal classes of cavitation, there is also a type of cavitation that is sometimes referred to in model test reports as 'streak' cavitation. This type of cavitation, again as its name implies, forms relatively thin streaks extending from the leading edge region of the blade chordally across the blades.

Propulsor–hull vortex (PHV) cavitation was reported by Huse (Reference 21) in the early 1970s. This type of cavitation may loosely be described as the 'arcing' of a cavitating vortex between a propeller tip and the ship's hull. Experimental work with flat, horizontal plates above the propeller in a cavitation tunnel shows that PHV cavitation is most pronounced for small tip clearances. In addition, it has been observed that the advance coefficient also has a significant influence on its occurrence; the lower the advance coefficient the more likely PHV cavitation is to occur. Figure 9.8 shows a probable mechanism for PHV cavitation formation. In the figure it is postulated that at high loading the propeller becomes starved of water due to the presence of the hull surface above and possibly the hull in the upper part of the apperture ahead of the propeller. To overcome this water starvation the propeller endeavours to draw water from astern, which leads to the formation of a stagnation streamline from the hull to the propeller disc, as shown. The PHV vortex is considered to form due to turbulence and other flow disturbances close to the hull, causing a rotation about the stagnation point, which is accentuated away from the hull by the small radius of the control volume forming the vortex. This theory of PHV action is known as the 'pirouette effect' and is considered to be the most likely of all the theories proposed. Thus the factors leading to the likelihood of the formation of PHV cavitation are thought to be:

1. low advance coefficients;
2. low tip clearance;
3. flat hull surfaces above the propeller.

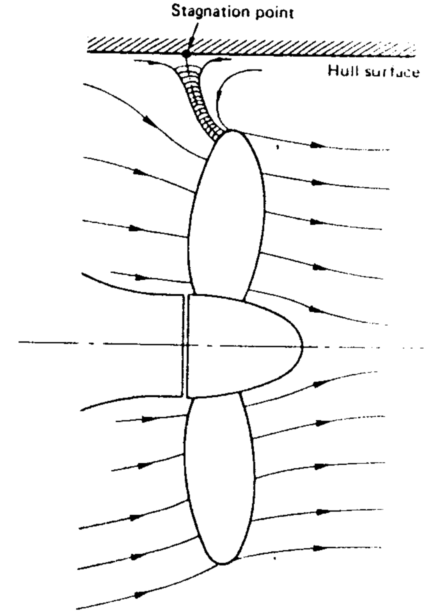

Figure 9.8 Basis for PHV cavitation

Van der Kooij and co-workers (References 53, 54) studied the problem of propeller hull vortex cavitation for the ducted propeller case and concluded that the occurrence of PHV cavitation depended strongly on hull–duct clearance and propeller blade position.

Methods of overcoming the effects of PHV cavitation are discussed in Chapter 22.

9.3 Cavitation considerations in design

The basic cavitation parameter used in propeller design is the cavitation number which was introduced in Chapter 6. In its most fundamental form the cavitation number is defined as

$$\text{cavitation number} = \frac{\text{static pressure head}}{\text{dynamic pressure head}} \quad (9.7)$$

The relationship has, however, many forms in which the static head may relate to the shaft centre line immersion to give a mean value over the propeller disc, or may relate to a local section immersion either at the top dead centre position or some other

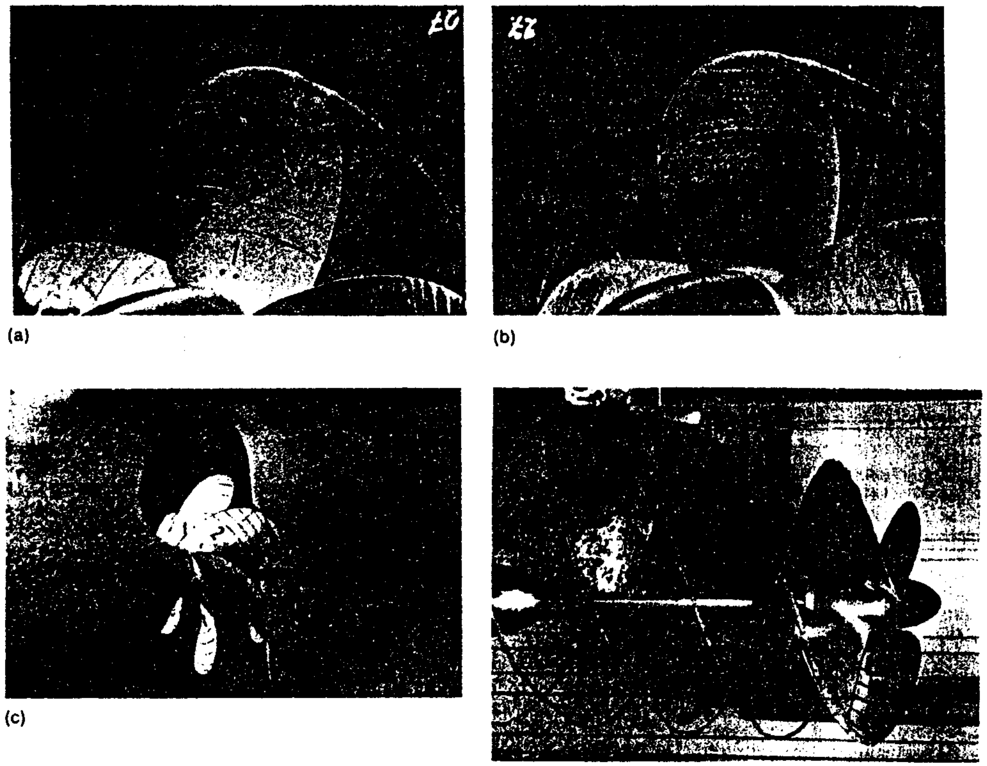

(a) (b) (c) (d)

Figure 9.7 Types of cavitation on propellers (MARIN): (a) sheet and cloud cavitation together with a tip vortex; (b) mid-chord bubble cavitation together with a tip vortex and some leading edge streak cavitation; (c) hub vortex cavitation with traces of LE and tip-vortex in top of propeller disc (Courtesy: MARIN); (d) tip vortex cavitation

extent depends upon the design and ambient conditions. Figure 9.7(a) shows an example of sheet cavitation on a model propeller, albeit with tip vortex cavitation also visable. Sheet cavitation is generally stable in character, although there are cases in which a measure of instability can be observed. In these cases the reason for the instability should be sought, and if it is considered that the instability will translate to full scale, then a cure should be sought, as this may lead to blade erosion or unwanted pressure fluctuations.

Bubble cavitation (Figure 9.7(b)), is primarily influenced by those components of the pressure distribution which cause high suction pressures in the mid-chord region of the blade sections. Thus the combination of camber line and section thickness pressure distributions identified in Figure 7.18 have a considerable influence on the susceptibility of a propeller toward bubble cavitation. Since bubble cavitation normally occurs first in the mid-chord region of the blade, it tends to occur in non-separated flows. This type of cavitation, as its name implies, appears as individual bubbles growing, sometimes quite large in character, and contracting rapidly over the blade surface.

Cloud cavitation is frequently to be found behind strongly developed stable sheet cavities and generally in moderately separated flow in which small vortices form the origins for small cavities. This type of cavitation (Figure 9.7(a) with traces on Figure 9.7(b)) appears as a mist or 'cloud' of very small bubbles and its presence should always be taken seriously.

The vortex types of cavitation, with few exceptions, occur at the blade tips and hub of the propeller and they are generated from the low-pressure core of the shed vortices at the ends of the blades. The hub vortex is formed by the combination of the individual vortices shed from each blade root, and although individually these vortices are unlikely to cavitate, under the influence of a converging propeller cone the combination of the blade root vortices has a high susceptibility to cavitate. When this occurs the resulting cavitation is normally very stable and appears to the observer as a rope with strands corresponding to the number of blades of the propeller. Tip vortex cavitation is normally first observed some distance behind the tips of the propeller blades. At this time the tip vortex is said to be 'unattached', but as the vortex becomes stronger, either through higher blade loading or decreasing cavitation number, it moves toward the blade tip and ultimately becomes attached. Figures 9.7(c) and (d) shows typical examples of the hub and tip vortices respectively.

In addition to the principal classes of cavitation, there is also a type of cavitation that is sometimes referred to in model test reports as 'streak' cavitation. This type of cavitation, again as its name implies, forms relatively thin streaks extending from the leading edge region of the blade chordally across the blades.

Propulsor–hull vortex (PHV) cavitation was reported by Huse (Reference 21) in the early 1970s. This type of cavitation may loosely be described as the 'arcing' of a cavitating vortex between a propeller tip and the ship's hull. Experimental work with flat, horizontal plates above the propeller in a cavitation tunnel shows that PHV cavitation is most pronounced for small tip clearances. In addition, it has been observed that the advance coefficient also has a significant influence on its occurrence; the lower the advance coefficient the more likely PHV cavitation is to occur. Figure 9.8 shows a probable mechanism for PHV cavitation formation. In the figure it is postulated that at high loading the propeller becomes starved of water due to the presence of the hull surface above and possibly the hull in the upper part of the apperture ahead of the propeller. To overcome this water starvation the propeller endeavours to draw water from astern, which leads to the formation of a stagnation streamline from the hull to the propeller disc, as shown. The PHV vortex is considered to form due to turbulence and other flow disturbances close to the hull, causing a rotation about the stagnation point, which is accentuated away from the hull by the small radius of the control volume forming the vortex. This theory of PHV action is known as the 'pirouette effect' and is considered to be the most likely of all the theories proposed. Thus the factors leading to the likelihood of the formation of PHV cavitation are thought to be:

1. low advance coefficients;
2. low tip clearance;
3. flat hull surfaces above the propeller.

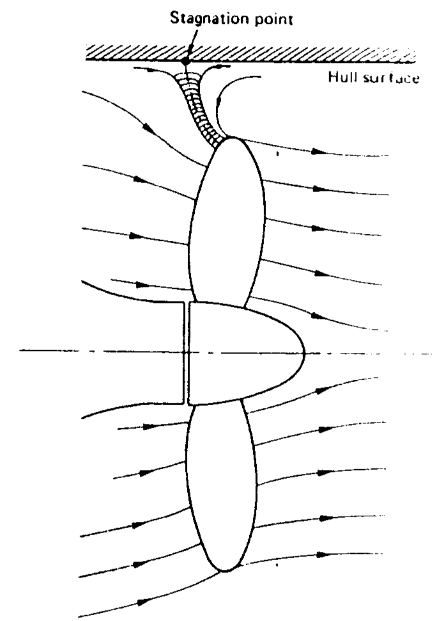

Figure 9.8 Basis for PHV cavitation

Van der Kooij and co-workers (References 53, 54) studied the problem of propeller hull vortex cavitation for the ducted propeller case and concluded that the occurrence of PHV cavitation depended strongly on hull–duct clearance and propeller blade position.

Methods of overcoming the effects of PHV cavitation are discussed in Chapter 22.

9.3 Cavitation considerations in design

The basic cavitation parameter used in propeller design is the cavitation number which was introduced in Chapter 6. In its most fundamental form the cavitation number is defined as

$$\text{cavitation number} = \frac{\text{static pressure head}}{\text{dynamic pressure head}} \quad (9.7)$$

The relationship has, however, many forms in which the static head may relate to the shaft centre line immersion to give a mean value over the propeller disc, or may relate to a local section immersion either at the top dead centre position or some other

Table 9.2 Common formulations of cavitation numbers

Definition	*Symbol*	*Formulation*
Free stream based cavitation no.	σ_0	$\frac{p_0 - p_v}{\frac{1}{2}\rho v_A^2}$
Rotational speed based cavitation no.	σ_n	$\frac{p_0 - p_v}{\frac{1}{2}\rho(\pi x n D)^2}$
Mean cavitation no.	σ	$\frac{p_0 - p_v}{\frac{1}{2}\rho[v_A^2 + (\pi x n D)^2]}$
Local cavitation no.*	σ_L	$\frac{p_0 - p_v + xRg\cos\theta}{\frac{1}{2}\rho[\{v_A(x,\theta) + u_A(x,\theta)\}^2 + \{\pi x n D - v_T(x,\theta) - u_T(x,\theta)\}^2]}$ u_A and u_T are the propeller induced velocities v_A and v_T are the axial and tangential wake velocities

* Sometimes the local cavitation number is calculated without the influence of u_A and u_T, and also v_T when this is not known.

instantaneous position in the disc. Alternatively, the dynamic head may be based upon either single velocity components such as the undisturbed free stream advance velocity and the propeller rotational speed or the vectorial combination of these velocities in either the mean or local sense. Table 9.2 defines some of the more common cavitation number formulations used in propeller technology: the precise one chosen depends upon the information known or the intended purpose of the data.

The cavitating environment in which a propeller operates has a very large influence not only on the detail of the propeller design but also upon the type of propeller that is used. For example, whether it is better to use for a given application a conventional, supercavitating or surface piercing propller. A useful initial guide to determining the type of propeller most suited to a particular application is afforded by the diagram shown in Figure 9.9, which was derived from the work of Tachmindji and Morgan. The diagram is essentially concerned with the influence of inflow velocities, propeller geometric size and static head and attempts from these parameters, grouped into advance coefficient and cavitation number, to give guidance on the best regions in which to adopt conventional and supercavitating propellers. Clearly the 'grey' area

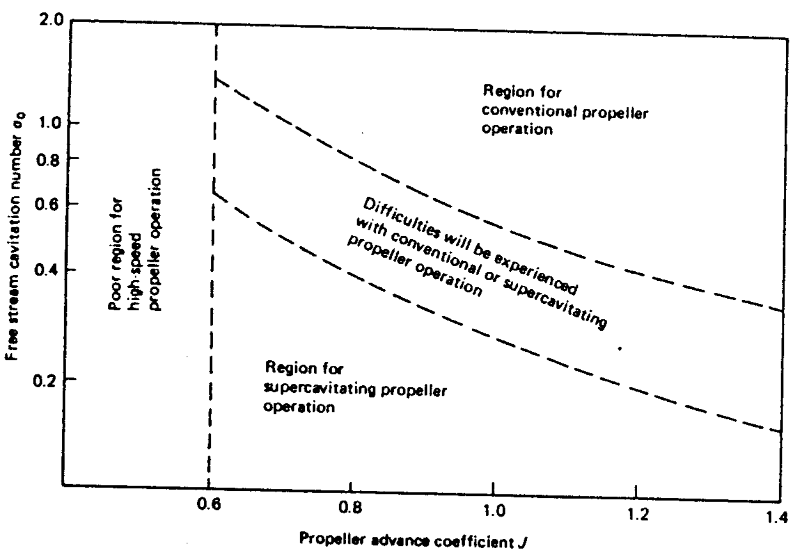

Figure 9.9 Zones of operation for propellers

in the middle of the diagram is dependent amongst other variables on both the wake field fluctuations and also shaft inclination angle. Should neither the conventional nor supercavitating propeller option give a reasonable answer to the particular design problem, then the further options of waterjet or surface piercing propulsors need to be explored, since these extend the range of propulsion alternatives.

From the early works of Parsons and Barnaby and Thornycroft on both models and at full scale it was correctly concluded that extreme back or suction side cavitation of the type causing thrust breakdown could be avoided by increasing the blade surface area. Criteria were subsequently developed by relating the mean thrust to the required blade surface area in the form of a limiting thrust loading coefficient. The first such criterion of 77.57 kPa (11.25 lbf/in²) was derived in the latter part of the last century. Much development work was undertaken in the first half of the century in deriving refined forms of these thrust loading criteria for design purposes; two of the best known are those derived by Burrill (Reference 22) and Keller (Reference 23).

Burrill's method, which was proposed for fixed pitch, conventional propellers, centres around the use of the diagram shown in Figure 9.10. The mean cavitation number is calculated based on the static head relative to the shaft centre line, and the dynamic head is referred to the 0.7R blade section. Using this cavitation number $\sigma_{0.7R}$, the thrust loading coefficient τ_c is read off from Figure 9.10 corresponding to the permissible level of back cavitation. It should, however, be remembered that the percentage back cavitation allowances shown in the figure are based on cavitation tunnel estimates in uniform axial flow. From the value of τ_c read off from the diagram the projected area for the propeller can be calculated from the following:

$$A_P = \frac{T}{\frac{1}{2}\tau_c \rho[V_A^2 + (0.7\pi n D)^2]} \quad (9.8)$$

To derive the expanded area from the projected area, Burrill provides the empirical relationship which is valid for conventional propeller forms only:

$$A_E \simeq \frac{A_P}{(1.067 - 0.229P/D)} \quad (9.9)$$

The alternative blade area estimate is due to Keller and is based on the relationship for the expanded area ratio:

$$\frac{A_E}{A_O} = \frac{(1.3 + 0.3Z)T}{(p_0 - p_v)D^2} + K \quad (9.10)$$

where p_0 is the static pressure at the shaft centre line (kgf/m²)
p_v is the vapour pressure (kgf/m²)
T is the propeller thrust (kgf)
Z is the blade number
and D is the propeller diameter (m)

The value of K in equation (9.10) varies with the number of propellers and ship type as follows: for single screw ships $K = 0.20$, but for twin-screw ships it varies within the range $K = 0$ for fast vessels through to $K = 0.1$ for the slower twin-screw ships.

Both the Burrill and Keller methods have been used with considerable success by propeller designers as a means of estimating the basic blade area ratio associated with a propeller design. In many cases, particularly for small ships and boats, these methods and even more approximate ones perhaps form the major part of the cavitation analysis; however, for larger vessels and those for which measured model wake field data is available, the cavitation analysis should proceed considerably further to the evaluation of the pressure distributions around the sections and their tendency towards cavitation inception and extent.

In Chapter 7 various methods were discussed for the calculation of the pressure distribution around an aerofoil section. The nature of the pressure distribution around an aerofoil is highly dependent on the angle of attack of the section. Figure 9.11 shows typical velocity distributions for an aerofoil in a non-cavitating flow at positive, ideal and negative angles of incidence. This figure clearly shows how the areas of suction on the blade surface change to promote back, mid-chord or face cavitation in the positive, ideal or negative incidence conditions respectively. When cavitation occurs on the blade section the non-cavitating pressure distribution is modified with increasing significance as the cavitation number decreases. Balhan (Reference 24) showed, by means of a set of two-dimensional aerofoil experiments in a cavitation tunnel, how the pressure distribution changes. Figure 9.12 shows a typical set of results at an incidence of 5° for a Karman–Trefftz profile with thickness and camber chord ratios of 0.0294 and 0.0220 respectively. From the figure the change in form of the pressure distribution for cavitation numbers ranging from 4.0 down to 0.3 can be compared with the results from potential theory; the Reynolds number for these tests was within the range 3×10^6 to 4×10^6. The influence that these pressure distribution changes have on the lift coefficient can be deduced from Figure 9.13, which is also taken from Balhan and shows how the lift coefficient varies with cavitation number and incidence angle of the aerofoil. From this figure it is seen that at moderate to low incidence the effects are limited to the extreme low cavitation numbers, but as incidence increases to high values, 5° in propeller terms, this influence spreads across the cavitation number range significantly.

For propeller blade section design purposes the use of 'cavitation bucket diagrams' is valuable, since they capture in a two-dimensional sense the cavitation behaviour of a blade section. Figure 9.14(a) outlines the basic features of a cavitation bucket diagram. This diagram is plotted as a function of the section angle of attack against the section cavitation number, however, several versions of the diagrams have been produced:

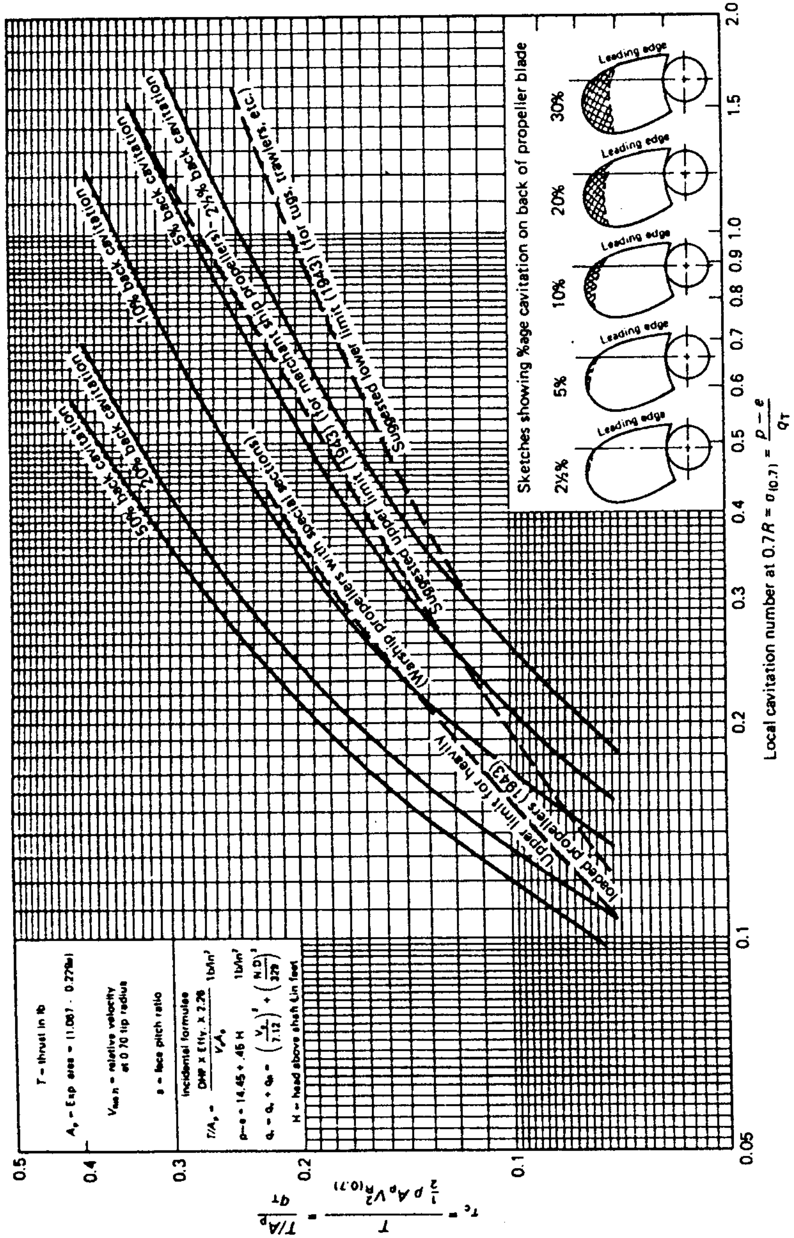

Figure 9.10 Burrill cavitation diagram for uniform flow (Reproduced from Reference 22)

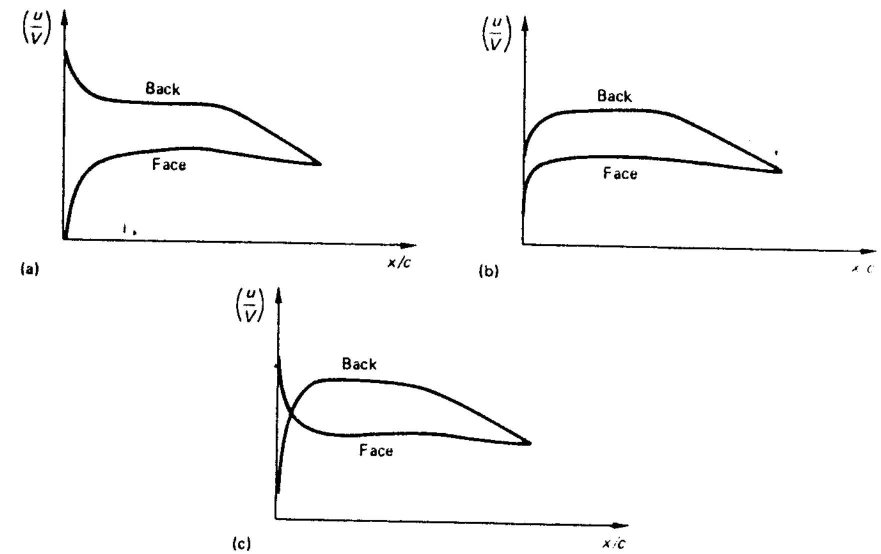

Figure 9.11 Typical section velocity distributions: (a) positive incidence; (b) ideal incidence; (c) negative incidence

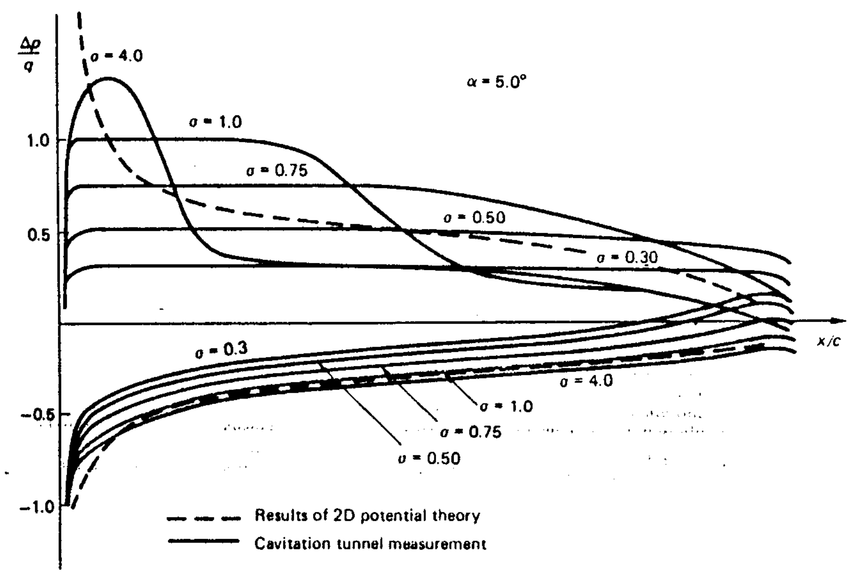

Figure 9.12 The effect of cavitation on an aerofoil section pressure distribution (Reference 24)

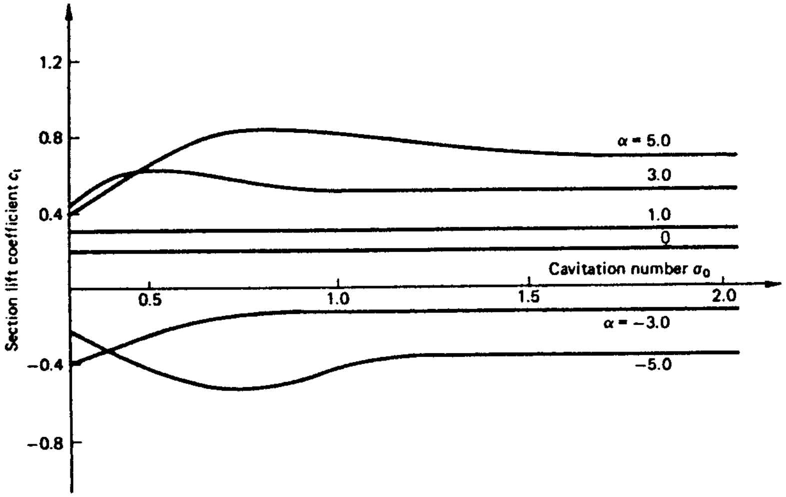

Figure 9.13 The effect of cavitation on the section lift coefficient (Reference 24)

typically, angle of attack may be replaced by lift coefficient and cavitation number by minimum pressure coefficient. From the diagram, no matter what its basis, four primary areas are identified: the cavitation-free area and the areas where back sheet, bubble and face cavitation can be expected. Such diagrams are produced from systemic calculations on a parent section form and several cases are supported by experimental measurement; see for example Reference 25. The width of the bucket defined by the parameter α_d is a measure of the tolerance of the section to cavitation-free operation. Figure 9.14(b) shows an example of a cavitation bucket diagram based on experimental results using flat faced sections. This work, conducted by Walchner and published in 1947, clearly shows the effect of the leading edge form on the section cavitation inception characteristics. Furthermore, the correlation with the theoretical limiting line can be seen for shockless entry conditions.

Whilst useful for design purposes the bucket diagram is based on two-dimensional flow characteristics, and can therefore give misleading results in areas of strong three-dimensional flow; for example, near the blade tip and root.

Propeller design is based on the mean inflow conditions that have either been measured at model scale or estimated empirically using procedures as discussed in Chapter 5. When the actual wake field is known, the cavitation analysis needs to be considered as the propeller passes around the propeller disc. This can be done either in a quasi-steady sense using procedures based on lifting line methods with lifting surface corrections, or by means of unsteady lifting surface methods. The choice of method depends in essence on the facilities available to the analyst and both approaches are commonly used. Figure 8.14 shows the results of a typical analysis carried out for a twin-screw vessel (Reference 26). Figure 8.14 also gives an appreciation of the variability that exists in cavitation extent and type on a typical propeller when operating in its design condition.

The calculation of the cavitation characteristics can be done either using the pseudo-two-dimensional aerofoil pressure distribution approach in association with cavitation criteria or using a cavitation modelling technique; the latter method is particularly important in translating propeller cavitation growth and decay into hull-induced pressures. The use of the section pressure distributions calculated from either a Theodoressen or Weber basis to determine the cavitation inception and extent has been traditionally carried out by equating the cavitation number to the section suction pressure contour as seen in Figure 9.15(a). Such analysis, however, does not take account of the time taken for a nucleus to grow from its size in the free stream to a visible cavity and also for its subsequent decline. Although these parameters of growth and decline are far from fully understood, attempts have been made to derive engineering approximations for calculation purposes. Typical of these is that by van Oossanen (Reference 26) in which the growth and decay is based on Knapp's similarity parameter

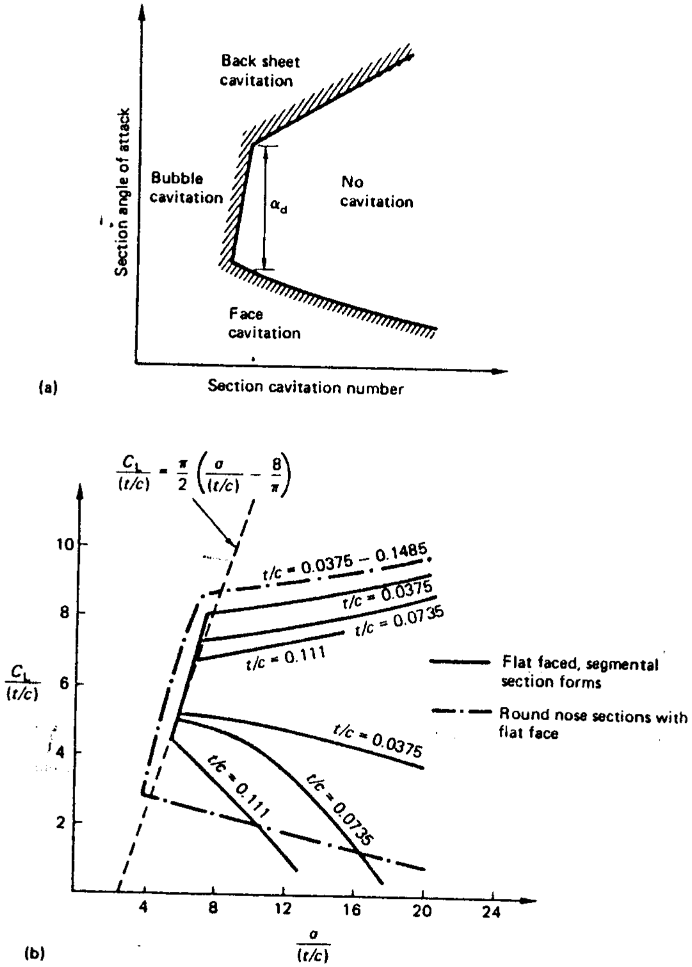

Figure 9.14 Cavitation 'bucket' diagrams: (a) basic features of a cavitation bucket diagram; (b) Walchner's foil experiments with flat-faced sections

(Reference 27). In van Oossanen's approach (Figure 9.15(b)), at a given value of cavitation number σ the nuclei are expected to grow at a position x_{c1}/C on the aerofoil and reach a maximum size at x_{c2}/C, whence the cavity starts to decline in size until it vanishes at a position x_{c3}/C. Knapp's similarity parameter, which is based on Rayleigh's equation for bubble growth and collapse, defines a ratio K_a as follows:

$$K_a = \frac{t_D\sqrt{(\Delta p)_D}}{t_G\sqrt{(\Delta p)_G}} \qquad (9.11)$$

where t and Δp are the total change times and effective liquid tension producing a change in size respectively and the suffixes D and G refer to decline and growth. Van Oossanen undertook a correlation exercise on the coefficient K_a for the NACA 4412 profile, which

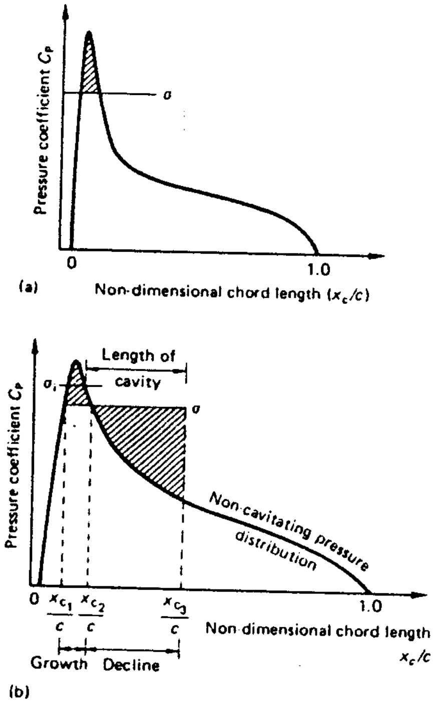

Figure 9.15 Determination of cavitation extent: (a) traditional approach to cavitation inception; (b) modern approach to cavitation inception

resulted in a multiple regression based formula for K_n as follows:

$$\log_{10} K_n = 9.407 - 84.88(\sigma/\sigma_i)^2 + 75.99(\sigma/\sigma_i)^3 - \frac{0.5607}{(\sigma/\sigma_i)} + \log_{10}(\theta_{inc}/c) \times \left[1.671 + 4.565(\sigma/\sigma_i) - 32(\sigma/\sigma_i)^2 + 25.87(\sigma/\sigma_i)^3 - \frac{0.1384}{(\sigma/\sigma_i)}\right] \quad (9.12)$$

in which θ_{inc} is the momentum thickness of the laminar boundary layer at the cavitation inception location. For calculation purposes it is suggested that if the ratio (θ_{inc}/c) is greater than 0.0003 bubble cavitation occurs and for smaller values sheet cavitation results. As a consequence of equation (9.12) it becomes possible to solve equation (9.11) iteratively in order to determine the value of x_{c_3} since equation (9.11) can be rewritten as

$$K_n = \frac{\int_{x_{c_2}/c}^{x_{c_3}/c} \frac{d(x_c/c)}{V_{x_c}(x_c/c)} \sqrt{\int_{x_c/c}^{x_{c_3}/c} [\sigma + C_p(x_c/c)]\, d(x_c/c)}}{\int_{x_{c_1}/c}^{x_{c_2}/c} \frac{d(x_c/c)}{V_{x_c}(x_c/c)} \sqrt{\int_{x_{c_1}/c}^{x_c/c} -[\sigma + C_p(x_c/c)]\, d(x_c/c)}}$$

where V_{x_c} is the local velocity at x_c.

The starting point x_{c_1} for the cavity can, for high Reynolds numbers in the range $1 \times 10^5 < Rx_{tr} < 6 \times 10^7$, be determined from the relationship derived by Cebeci (Reference 28) as follows:

$$R_{\theta_{tr}} = 1.174\left[1 + \frac{22\,400}{R_{x_{tr}}}\right] R_{x_{tr}}^{0.46} \quad (9.13)$$

where $R_{\theta_{tr}}$ is the Reynolds number based on momentum thickness and local velocity at the position of transition and Rx_{tr} is the Reynolds number based on free stream velocity and the distance of the point of transition from the leading edge. For values of Rx_{tr} below this range, the relationship

$$R_{\theta_{ci}} = 4.048 R_{x_{ci}}^{0.368} \quad (9.14)$$

holds in the region $1 \times 10^4 < Rx_{ci} < 7 \times 10^5$. In this case $R_{\theta_{ci}}$ is the Reynolds number based on local velocity and momentum thickness at the point of cavitation inception and Rx_{ci} is the Reynolds number based on distance along the surface from the leading edge and free stream velocity at the position of cavitation inception.

Having determined the length of the cavity, van Oossanen extended this approach to try and approximate the form of the pressure distribution on a cavitating section, and for these purposes assumed that the cavity length is less than half the chord length of the section. From work on the pressure distribution

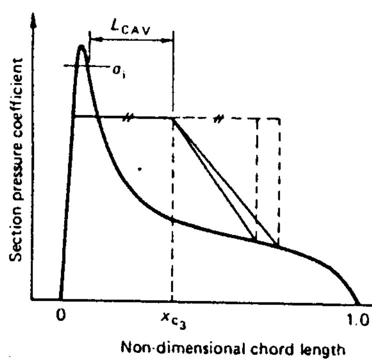

Figure 9.16 Van Oossanen's approximate construction of a cavitation pressure distribution on an aerofoil section

over cavitating sections it is known that the flat part of the pressure distribution, Figure 9.12 for example, corresponds to the location of the actual cavity. Outside this region, together with a suitable transition zone, the pressure returns approximately to that of a non-cavitating flow over the aerofoil. Van Oossanen conjectured that the length of the transition zone is approximately equal to the length of the cavity and the resulting pressure distribution approximation is shown in Figure 9.16.

Ligtelijn and Kuiper (Reference 29) conducted a study to investigate the importance of the higher harmonics in the wake distribution on the type and extent of cavitation, and as a consequence give guidance on how accurately the wake should be modelled. Their study compared the results of lifting surface calculations with the results of model tests in a cavitation tunnel where the main feature of the wake field was a sharp wake peak. If was concluded that the lower harmonics of the wake field principally influence the cavity length prediction and that the difference between two separate calculations based on 4 and 10 harmonics was negligible.

Considerable work has in the past been done in attempting to model cavitation mathematically. The problem is essentially a free streamline problem, since there is a flow boundary whose location requires determination as an integral part of the solution. Helmholtz and Kirchoff in the latter part of the 19th century attempted a solution of the flow past a supercavitating flat plate at zero cavitation number using complex variable theory. Subsequently, Levi-Civita extended this work to include the flow past curved bodies. The zero cavitation number essentially implied an infinite cavity, and the next step in the solution process was to introduce finite cavitation numbers which, as a consequence, introduce finite sized cavities. The finite cavity, however, requires the cavity to be terminated in an acceptable mathematical and physical manner. Several models have been proposed, amongst which the Riabouchinsky cavity termination model, which employs a 'wall' to provide closure of the cavity (Figure 9.17), and the more physically realistic re-entrant jet model (Figure 9.6), are examples. These models, most of which were developed in the late 1940s, are non-linear models which satisfy the precise kinematic and dynamic boundary conditions over the cavity surface. As a

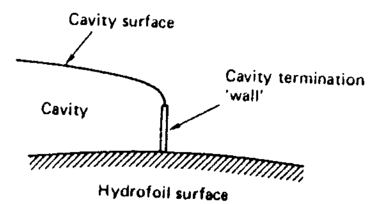

Figure 9.17 Riabouchinsky-type cavity termination 'wall'

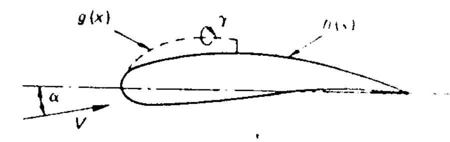

Figure 9.18 Uhlman's non-linear model of a two-dimensional partially cavitating flow

consequence considerable analytical complexity is met in their use. Tulin (Reference 30) developed a linearized theory for zero cavitation number and this was extensively applied and extended such that Geurst (Reference 31) and Geurst and Verbrugh (Reference 32) introduced the linearized theory for partially cavitating hydrofoils operating at finite cavitation numbers, and extended this work with a corresponding theory for supercavitating hydrofoils (Reference 33).

Three-dimensional aspects of the problem were considered by Leehey (Reference 34) who proposed a theory for supercavitating hydrofoils of finite span. This procedure was analogous to the earlier work of Geurst on two-dimensional cavitation problems in that it uses the method of matched asymptotic expansions from which a comparison can be made with the earlier work. Uhlman, using a similar procedure (Reference 35), developed a method of analysis for partially cavitating hydrofoils of finite span. With the advent of large computational facilities significantly more complex solutions could be attempted. Typical of these is the work of Jiany (Reference 36) who examined the three-dimensional problem using an unsteady numerical lifting surface theory for supercavitating hydrofoils of finite span using a vortex source lattice technique.

Much of the recent work is based on analytical models which incorporate some form of linearizing assumptions. However, techniques now exist, such as boundary-integral or surface singularity methods, which permit the solution of a Neumann, Dirichlet or mixed boundary conditions to be expressed as an integral of appropriate singularities distributed over the boundary of the flow field. Uhlman (Reference 37), taking advantage of these facilities, has presented an exact non-linear numerical model for the partially cavitating flow about a two-dimensional hydrofoil (Figure 9.18). His approach uses a surface vorticity technique in conjunction with an iterative procedure to generate the cavity shape and a modified Riabouchinsky cavity termination wall to close the cavity. Comparison with Tulin and Hsu's earlier thin cavity theory (Reference 38) shows some significant deviations between the calculated results of the non-linear and linear approaches to the problem.

Stern and Vorus (Reference 39) developed a non-linear method for predicting unsteady sheet cavitation on propeller blades by using a method which separates the velocity potential boundary value problem into a static and dynamic part. A sequential solution technique is adopted in which the static potential problem relates to the cavity fixed instantaneously relative to the blade whilst the dynamic potential solution addresses the instantaneous reaction of the cavity to the static potential and predicts the cavity deformation and motion relative to the blades. In this approach, because the non-linear character of the unsteady cavitation is preserved, the predictions from the method contain many of the observed characteristics of both steady and unsteady cavitation behaviour. Based on this work two modes of cavity collapse were identified, one being a high-frequency mode where the cavity collapsed towards the trailing edge whilst the second was a low-frequency mode where the collapse was toward the leading edge.

Isay (Reference 40), in association with earlier work by Chao, produced a simplified bubble grid model in order to account for the compressibility of the fluid, surrounding a single bubble. From this work the Rayleigh–Plesset equation (9.3) was corrected to take account of the compressibility effects of the ambient fluid as follows:

$$\frac{d^2R}{dt^2}+\frac{3}{2R}\left(\frac{dR}{dt}\right)^2 = \frac{1}{\varrho R}\left(p_G-\frac{2S}{R}-p_\infty e^{-\alpha\alpha_{**}}+p_v e^{-\alpha\alpha_{**}}\right) \quad (9.15)$$

where p_v and p_∞ are vapour pressure and local pressure in the absence of bubbles, α is the local gas volume ratio during bubble growth, α_{**} is an empirical parameter and S is the surface tension. Furthermore, Isay showed that bubbles growing in an unstable regime reach the same diameter in a time-dependent pressure field after a short distance. This allows an expression to be derived for the bubble radius just prior to collapse. Mills (Reference 41) extended the above theory, which was based on homogeneous flow, to inhomogeneous flow conditions met within propeller technology and where local pressure is a function of time and position on the blade. Following this theoretical approach equation (9.3) then becomes

$$\frac{3\omega^2}{2}\left(\frac{\partial R_{\phi_0}}{\partial\chi}\right)^2+R_{\phi_0}\omega^2\left(\frac{\partial^2R_{\phi_0}}{\partial\chi^2}\right) = \frac{1}{\varrho}[p(R_{\phi_0})-p(\chi,\phi_0-\chi)] \quad (9.16)$$

from which computation for each class of bubble radii can be undertaken.

In equation (9.16) χ is the chordwise coordinate, ω is the rate of revolution and ϕ_0 is the instantaneous blade position.

For computation purposes the gas volume α_{ϕ_0} at a position on the section channel can be derived from

$$\frac{\alpha_{\phi_0}(\chi)}{1+\alpha_{\phi_0}(\chi)}=\frac{4\pi}{3}\sum_{j=1}^{J}\zeta_{0j}\cdot R_{0j}^3(\chi,\phi_0-\chi) \quad (9.17)$$

in which ζ_{0j} is the bubble density for each class and R_0 is the initial bubble size. Using equations (9.16) and (9.17) in association with a blade undisturbed pressure distribution calculation procedure, Chapter 8, the cavity extent can be estimated over the blade surface.

9.4 Cavitation inception

Cavitation inception is defined as taking place when nuclei, due to being subjected to reduced pressure, reach a critical size and grow explosively.

The mechanisms underlying cavitation inception are important for a number of reasons; for example, in predicting the onset of cavitation from calculations and interpreting the results of model experiments to make full-scale predictions.

Cavitation inception is a complex subject which is far from completely understood at the present time. It is dependent on a range of characteristics embracing the nuclei content of the water, see Chapter 4, the growth of the boundary layer over the propeller sections and the type of cavitation experienced by the propeller. Thus it is not only related to the environment in which the propeller is working but also to intimate details of the propeller geometry and the wake field.

The nuclei content of the water has been shown to be important in determining the cavitation extent over the blades of a propeller in a cavitation tunnel. In particular, the free air content as a proportion of the nuclei content, rather than oxygen or total air content, should be measured during cavitation experiments. Figure 22.4 demonstrates this somewhat indirectly in terms of the cavitation erosion rate and its variability with air content of the water. This Figure implies that the structure and perhaps extent of the cavity changes with air or gas content. Kuiper (Reference 42) explored the effect of artificially introducing nuclei into the water by electrolysis techniques. When electrolysis is used the water is decomposed into its hydrogen and oxygen components, the amount of gas produced being dependent only on the current applied. The governing equations for this are

$$4H_2O + 4e \rightarrow 2H_2\uparrow + 4OH^- \quad \text{(at the cathode)}$$

$$4OH^- + 4e \rightarrow 2H_2O + O_2\uparrow \quad \text{(at the anode)}$$

Since the electrolysis method produces twice the amount of hydrogen when compared to the amount of oxygen, the cathode is generally used for the production of the bubbles. This method is also known under the name of the 'hydrogen bubble technique' for flow visualization. Kuiper has shown that this technique, when introduced into the flow, can have a significant effect on the observed cavitation over the blades; the extent clearly depends on the amount of nuclei present in the water initially. Figure 9.19 demonstrates this effect for sheet cavitation observed

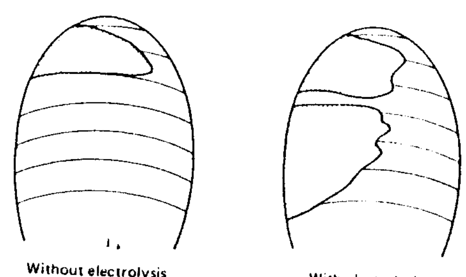

Figure 9.19 Effect of electrolysis (nuclei content) on cavitation inception

on a propeller; similar effects can be observed with bubble cavitation – to the extent of its not being present with low nuclei concentrations and returns with an enhanced nuclei content. Care, however, needs to be taken in model tests not to overseed the flow with nuclei such that the true cavitation pattern is masked.

In the case of a full-scale propeller the boundary layer is considered to be fully turbulent except for a very small region close to the leading edge of the blade. This is not always the case on a model propeller, also shown by Kuiper (Reference 42) using paint pattern techniques on models. The character of the boundary layer on the suction side of a propeller blade is shown in Figure 9.20. In the region where the loading is generally highest, in the outer radii of the blade, a short laminar separation bubble *AB* can exist near the leading edge, causing the boundary layer over the remainder of the blade at the tip to be turbulent. A separation radius *BC*, whose position is dependent on the propeller loading, may also be found, as shown

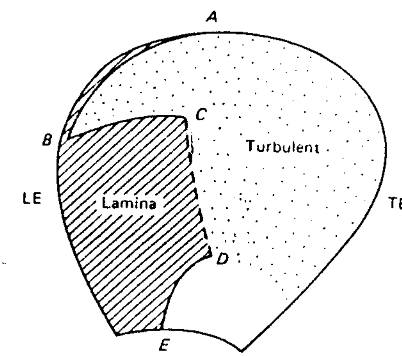

Figure 9.20 Schematic representation of the boundary layer on the suction side of a model propeller in open water

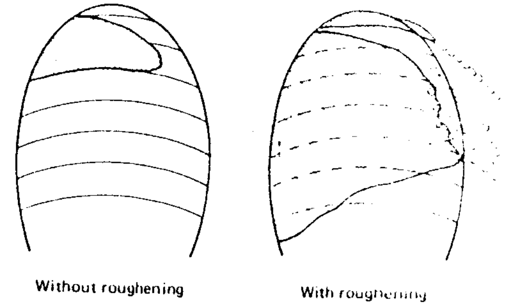

Figure 9.21 Effect of LE roughening (turbulence stimulation) on cavitation inception

in the figure, below which the flow over the blade is laminar. The region *CD* is then a transition region whose chordwise location is dependent on Reynolds number but is generally located at some distance from the leading edge. The region aft of the line *DE* is a region of laminar separation at mid-chord due to the very low sectional Reynolds numbers at those radii in combination with thick propeller sections. The locations of the points *B*, *C* and *D* in specific cases are strongly dependent on the propeller geometric form, the propeller loading and flow Reynolds number. The boundary layer on the pressure face of the blades is generally considerably less complex: under normal operating conditions no laminar separation occurs and a significant laminar region may exist near the leading edge. Transition frequently occurs more gradually than on the suction surface due to the more favourable pressure gradient.

Because the boundary layer can be laminar over a considerable region of the blade and an increase in Reynolds number does not generally move the transition region to the leading edge of the blade, some testing establishments have been undertaking experiments using artificial stimulation of the boundary layer to induce turbulent flow close to the leading edge. Such stimulation is normally implemented by gluing a small band of carborundum grains of the order of 60 μm at the leading edge of the blades. Figure 9.21 shows the effect of stimulating a fully turbulent boundary layer over the blades for the same propeller conditions as shown in Figure 9.19; in this case the introduction of electrolysis in addition to the leading edge roughening had little further significant effect. The use of leading edge roughening is, however, not a universally accepted technique of cavitation testing among institutes. Consequently, the interpretive experience of the institute in relation to its testing procedure is an important factor in estimating full-scale cavitation behaviour.

It is frequently difficult to separate out the effects due to nuclei changes and Reynolds effects since the parameters involved change simultaneously if the

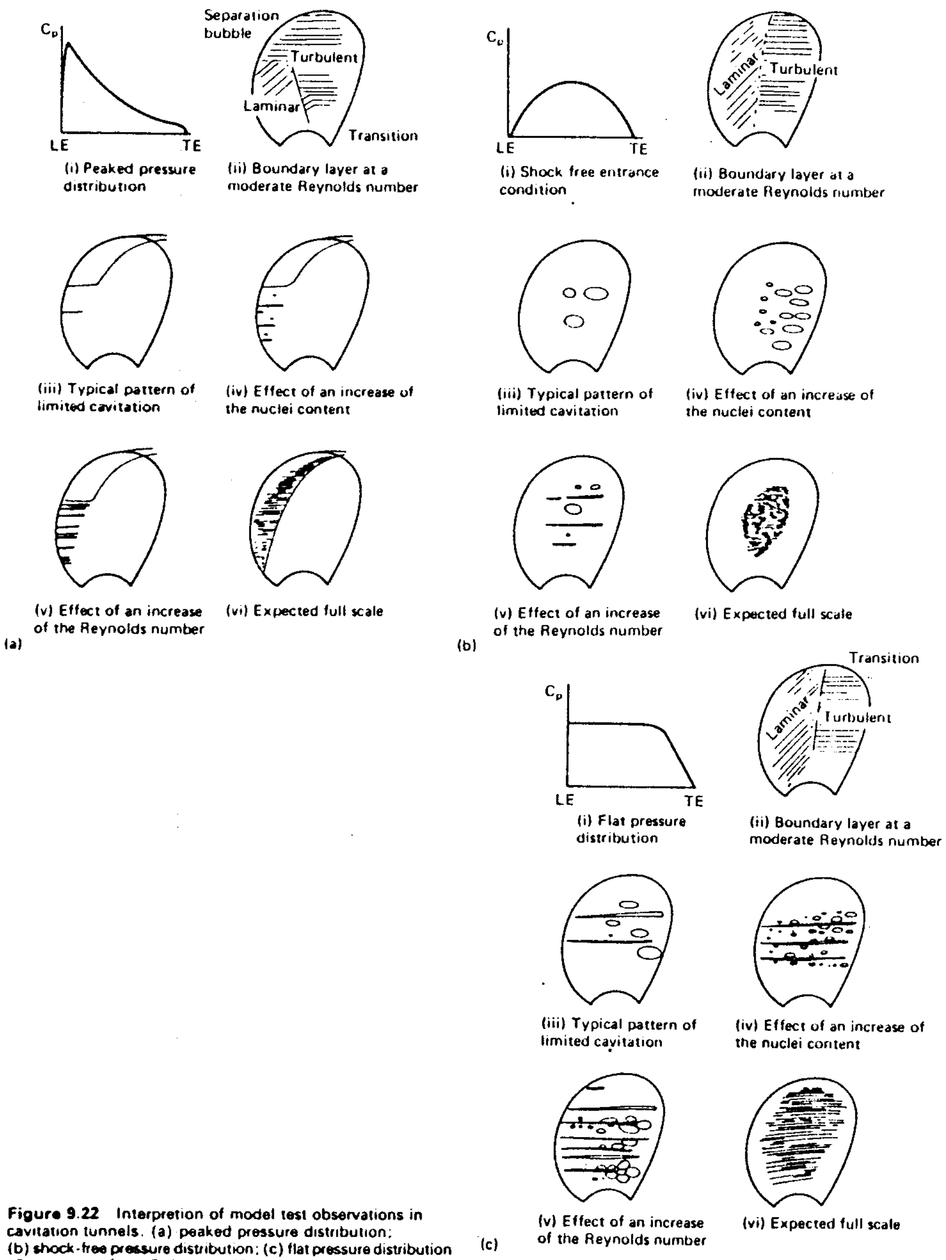

Figure 9.22 Interpretion of model test observations in cavitation tunnels. (a) peaked pressure distribution; (b) shock-free pressure distribution; (c) flat pressure distribution (Reproduced from Reference 43)

tunnel velocity is altered. Furthermore, the cavitation patterns expected at full scale are normally estimated from model test results, and consequently it is necessary to interpret the model test results. The ITTC Proceedings (Reference 43) give a distillation of the current knowledge on this subject, detailed below, and in so doing considered the cases of a peaked pressure distribution, a shock-free entrance condition and a 'flat' pressure distribution. Figure 9.22, taken from Reference 43, shows these three cases, and for each case considers the following: (i) a typical boundary layer distribution over the suction surface; (ii) a typical cavitation pattern with few nuclei at moderate Reynolds numbers, of the order of 2×10^5; (iii) the effect of increasing nuclei; (iv) the effect of increasing Reynolds number, and (v) the expected full-scale extrapolation.

For a peaked pressure distribution, Figure 9.22(a), if the flow is separated a smooth glassy sheet will be observed, whereas if the flow is attached no cavitation inception may occur, although the minimum pressure may be below the vapour pressure. In the latter case the flow is sensitive to surface irregularities and these can cause some streaks of cavitation as seen in the Figure. With the water speed held constant the effect of increasing the nuclei content on the sheet cavitation in a region with a laminar separation bubble is negligible. In this case only a few nuclei enter the cavity, and therefore the increase of the partial pressure of the gas is small and cavitation inception is hardly affected. In the case of an attached laminar boundary layer in association with a peaked pressure distribution, the effect of increasing nuclei content is also small, although the number of streaks may increase. Furthermore, if the pressure peak is not too narrow some bubble cavitation may also be noticed. The effect of Reynolds number on sheet cavitation in a separated region is small; however, the appearance of the cavity becomes rather more 'foamy' at higher Reynolds numbers. In the alternative case of a region of attached laminar flow the effect of Reynolds number is indirect, as the boundary layer becomes thinner and, as a consequence, the surface irregularities become more pronounced. This has the effect of increasing the number of streaks, which at very high Reynolds numbers or speeds will tend to merge into a 'foamy' sheet. In these cases the character of the cavity at the leading edge remains streaky, with perhaps open spaces between the streaks. When extrapolating the observations of cavitation resulting from a peaked pressure distribution in the case of a smooth sheet cavity the boundary layer at model scale normally has a laminar separation bubble. As a consequence scale effects on inception and developed cavitation are likely to be small in most cases. When regions of attached laminar flow occur, then scale effects tend to be large. In such cases the application of leading edge roughness may be necessary or, alternatively, the tests should be conducted at high Reynolds numbers. The cavitation streaks found in attached laminar flow regions indicate the presence of a sheet cavity at full scale, as seen in Figure 9.22(a).

In the case of a shock-free entry pressure distribution, that shown in Figure 9.22(b), the boundary layer over the model propeller for Reynolds numbers of the order of 2×10^5 at $0.7R$ changes from that seen from the peaked pressure distribution in Figure 9.22(a). For this type of pressure distribution bubble cavitation can be expected, and its extent is strongly dependent on the nuclei content of the water, as seen in Figure 9.22(b). In contrast the effect of Reynolds number is small for this kind of pressure distribution. Nevertheless, it must be remembered that the nuclei content may change with speed, as does the critical pressure of the nuclei, and this can result in an increase in bubble cavitation. Also due to the thinner boundary layer at the higher Reynolds number, surface irregularities may generate nuclei more readily, which can result in streak-like rows of bubble or spot-like cavitation. The scale effects for this type of pressure distribution often occur at both inception and with developed cavitation. Clearly the nuclei content at model scale should be as high as possible, as should the Reynolds number. Furthermore, the application of leading edge roughness can assist in reducing scale effect. When bubble cavitation occurs at model scale, the full-scale cavity is expected to take the form of a 'frothy' cloud which can have consequences for the erosion performance of the blades, as will be seen in Section 9.5.

In the case of a flat pressure distribution (Figure 9.22(c)), bubble cavitation can also be expected to occur. The bubbles reach their maximum size at or beyond the constant pressure region and long streaks of cavitation, which originate at the leading edge, may also occur. These streaks may give the appearance of merging bubble rows, so that they have a cloudy appearance, and the cavities are found to be very unstable. The effect of increasing the nuclei content has a similar effect to that for bubble cavitation in that the bubbles become smaller and more extensive. In addition, the number of streaks may increase and the cavities remain unstable. If roughness is applied, a sheet cavity is formed, and this has a somewhat cloudy appearance at its trailing edge. The influence of Reynolds number on a flat pressure distribution is particularly pronounced: the number of streaks increases, which frequently results in the formation of a sheet cavity instead of bubble cavitation. The extrapolation to full scale results in a cloudy sheet cavitation, as seen in Figure 9.22(c).

In the foregoing discussion of cavitation inception, no mention has been made of tip vortex cavitation. Cavitation of the vortices which emanate from propeller blade tips is a rather poorly understood phenomenon at this time, and this is partly due to a general lack of understanding of the complex flow regime which exists at the propeller tip. Tip vortex cavitation is very often one of the first forms of cavitation to be observed in model tests, and the prediction of the onset of this type of cavitation is particularly important in the design of 'silent' propellers, as a cavitating vortex represents a significant source of noise. Tip vortex cavitation occurs in the low-pressure core of the tip vortex; in a recent experimental study Arakeri *et al.* found a strong coupling effect between velocity and the dissolved gas content in a cavitation tunnel on the tip vortex cavitation inception. Observations in a cavitational tunnel show that the radius of the cavitating core of a tip vortex near inception is relatively constant with the distance from the blade tip. However, the strength of the tip vortex increases with distance behind the tip of the propeller due to the roll-up of the vortex sheets: this increase in strength occurs rapidly with distance in the initial stages. This explains why cavitation of the tip vortex is sometimes noticed to commence some distance from the propeller tip; however, this depends on the nature of the boundary layer over the blade in the tip region. If the boundary layer separates near the tip, then an attached tip vortex results, whereas if the boundary layer is laminar near the tip then the tip vortex is detached. Kuiper (Reference 42) suggests that the radius of the cavitating core of a tip vortex is independent of Reynolds number and nuclei content, and consequently this can be used as a basis for the determination of cavitation inception, both on the model and on the full-scale propeller. Based on data from Chandrashekhara (Reference 44) and also tests on a propeller especially designed to study tip vortex phenomena, Kuiper suggests the following relationship to give an approximation to the inception index for a tip vortex:

$$\sigma_{ni} = 0.12(P/D - J)_{0.9R}^{1.4} \cdot R_n^{0.35} \qquad (9.18)$$

It is also suggested that this relationship gives a good initial estimate for both conventional and strongly tip unloaded propellers at model scale.

Within the general field of fluid mechanics and aerodynamics the phenomenon of vortex bursting has been extensively researched. This effect manifests itself as a sudden enlargement of the vortex, which then gives rise to a particularly confused flow regime. English (Reference 45) discusses this phenomenon in relation to the cavitating tip vortices of a series of container ship propellers.

9.5 Cavitation induced damage

There have been very few propellers designed which do not induce cavitation at some point in the propeller disc; not all propellers, however, exhibit cavitation erosion and, therefore, it is wrong to simply equate the presence of cavitation on the blades with the erosion of the material. Cavitation erosion in the greater majority of cases is thought to derive from the action of travelling bubbles which either pass around the aerofoil, pass around a fixed cavity or break off from a fixed cavity. Figure 9.23(a) shows a schematic

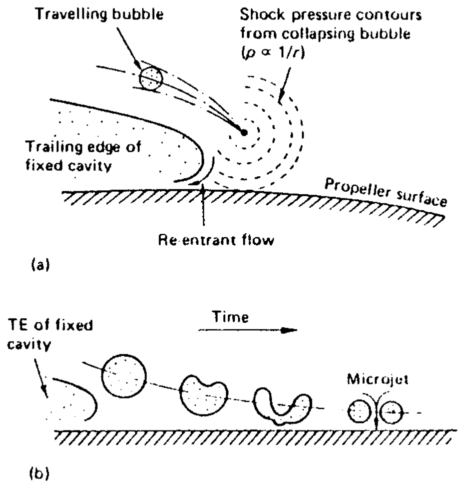

Figure 9.23 Erosive mechanisms formed during bubble collapse: (a) pressure waves from bubble collapse, (b) micro-jet formation close to surface

drawing of the collapse of a bubble which in this case has passed around the outside of a fixed cavity located on the surface of an aerofoil section. As the pressure recovers the bubble reaches the collapse point in the stagnation region behind the downstream end of the fixed cavity. The collapse mechanism generates a set of shock pressure contours, the magnitude of the pressure on each contour being inversely proportional to the radius from the point of collapse. In addition to the pressures generated by bubble collapse, if the collapse mechanism takes place close to a solid boundary surface a microjet is formed which is directed towards the surface (Figure 9.23(b)). The formation of a microjet in the proximity of a wall can be explained as follows, albeit in somewhat oversimplified terms, by assuming a spherical bubble close to a rigid wall starting to collapse. If the spherical form of the bubble were to be maintained during collapse the radial motion of the water would need to be uniform at âll points around the bubble during collapse. However, the presence of the wall restricts the water flow to the collapsing bubble in the regions of the bubble adjacent to the wall. As a consequence the upper part of the bubble, that remote from the wall, tends to collapse faster, leading to a progessive asymmetry of the bubble as shown in Figures 9.5 and 9.23(b), which induces a movement of the bubble centroid toward the wall and creates a linear momentum of the bubble centroid toward the wall. This leads to an acceleration of the virtual mass of the bubble toward the wall as the collapse progresses, resulting eventually in the formation of a high-velocity microjet. The formation of the microjet, with velocities thought to be up to the order of 1000 m/s (Reference 46), is normally considered to be one of the more important causes of cavitation erosion damage. However, in addition to the microjet, the final event of bubble collapse, that of 'rebound', is also considered to be of importance. Rebound is the regrowth of the vapour and gaseous mass of the cavity; this is probably due to the entrapped gas and non-condensing vapour in the short time available for the primary collapse. The rebound process is considered important, since it is known that the strength of the pressure pulses in the liquid due to a growing bubble are considerably greater than those due to collapse. This mechanism, therefore, is thought to provide important assistance to the damaging process originating from the microjet impact.

Erosion damage on a propeller blade normally starts with a surface deterioration or roughening, and this is followed by a plastic deformation of the blade surface so as to give the surface the appearance of orange peel: hence this stage is known generally within the marine industry as 'orange peeling' of the surface. This deformation of the surface is essentially caused by a large-scale and essentially random bombardment of the surface by microjet impact and pressure waves from collapsing cavities. This deformation continues until large-scale fatigue failure eventually occurs over the surface and the material starts to erode. The calculation of the stresses applied to a propeller blade surface during cavitation is, however, not possible within the present state of the art.

Cavitation erosion damage occurs in many forms and at many different rates. The erosion damage first occurs at the collapse point of the cavities and not generally at the inception point of the cavity. Thus it is the travelling cavities that are generally responsible for erosion, and as a consequence, bubble and cloud cavitation, rather than stable sheet cavitation, is considered most responsible for material erosion attack. The speed with which erosion can take place is variable: in some extreme cases significant material damage can occur as rapidly as in a few hours, whereas

Figure 9.24 Trailing edge curl

in other instances the erosion develops slowly over a period of months or years. In some cases the erosion starts and then the rate of erosion falls off, so as to stabilize with no further erosion occurring. This stabilization takes place when a certain critical depth is reached and the profile of the cavity is such as to cause and promote favourable flow conditions with the material boundary out of reach of the destructive effects of the microjet and pressure waves from the cavity collapse. In other instances the formation of a primary erosion cavity will cause a flow disturbance sufficient to re-introduce cavitation further downstream, and this may give rise to secondary erosion upon the collapse of this additional cavitation. Much further research work is required into the field of propeller erosion before prediction can be achieved with confidence.

Cavitation can lead to the phenomenon of 'trailing edge curl'. This type of cavitation damage, shown in Figure 9.24, is, as its name implies, a physical bending of the trailing edge of the blade. This bending of the blade is caused by the 'peening' action of cavitation collapse in the vicinity of the thinner sections of blade in the region of the trailing edge. Van Manen (Reference 47) discusses this effect in some detail.

9.6 Cavitation testing of propellers

In order to study cavitation and its effects using propeller models it is necessary to ensure both geometric and flow similarity, as any deviation from these similarity requirements causes a scale effect to occur. Geometric similarity requires that the model is a geosim of its full-scale counterpart and that considerable care has been taken in the model manufacture to ensure that the tolerances on design dimensions are satisfactory for model testing purposes. If the tolerances are not satisfactory, then a false cavitation patterns and inception behaviour will result from the model tests.

Flow or dynamic similarity is fully obtained when the effects of gravitation, viscosity, surface tension, vaporization characteristics, static pressure, velocity, fluid density, gas diffusion and so on are properly accounted for. Unfortunately, in a real flow situation using a model to represent a full-scale propeller, it is impossible to satisfy all of these parameters simultaneously. In Chapter 6 the main propeller non-dimensional groupings were derived from dimensional analysis and for the purposes of cavitation testing the primary groupings are:

Froude number $$F_n = \frac{V_a}{\sqrt{(gD)}}$$

Reynolds number $$R_n = \frac{\varrho V_a D}{\eta}$$

Weber number $$W_n = \frac{\varrho V_a^2 D}{S}$$

Advance ratio $J = \frac{V_a}{nD}$

Cavitation number $\sigma_0 = \frac{p - p_v}{\frac{1}{2}\varrho V_a^2}$

By making the assumption that the properties of sea water and the water in the cavitation facility are identical, this being a false assumption but a close enough approximation for these present discussion purposes, it can be seen that simultaneous identity can be obtained only for the following non-dimensional groups:

1. F_n, σ_0 and J when the pressure and propeller rotational speed can be freely chosen;
2. R_n, σ_0, J and ψ (where ψ is the gas content number $d/(VD)$) where again the pressure and rotational speed can be freely chosen and the high flow speeds required for R_n present no problem.
3. W_n, σ_0, J and ϕ (where ϕ is the gas content number $cD/(\varrho V_a^2)$) where once again the pressure and rotational speed can be chosen freely.

In a cavitation tunnel model testing with marine propellers is normally undertaken using a K_T identity basis. This essentially requires that the cavitation number and advance coefficient are set. As the simultaneous satisfaction of the Reynolds and Froude identity is not possible, water speeds are normally chosen as high as possible to minimize the differences between model- and full-scale Reynolds number. However, running at the correct full-scale Reynolds number is generally not possible in most laboratories. Nevertheless, cavitation testing frequently attempts to follow the second group of non-dimensional coefficients identified above.

The implications of ignoring the Froude identity is that for a given radial position on the blade and angular position in the disc the local cavitation number will not be the same for model and ship. Indeed, the cavitation number identity for model and ship under these conditions is obtained at only one point, normally taken as the shaft centre line. Although this secures a mean cavitation number, it does not model the cavitation conditions correctly since the conditions for cavitation inception are not the same as those required once cavitation has been formed. Newton (Reference 48) discusses the influence of the effect of Froude number on the onset of tip vortex cavitation, from which it is seen that this is significant. As a consequence, when undertaking cavitation inception studies for propellers, the correct Froude number should be modelled. In order to improve the simulation of the pressure field over the propeller disc Newton suggests using a nominal cavitation number based on the 0.7R position in the top-dead-centre position.

The walls of a cavitation tunnel have an effect on the flow conditions in the test section. If the propeller is considered to be an actuator disc, that is having an infinite number of blades, then the corrections for the effect of the tunnel walls can be calculated for a non-cavitating propeller using the Wood and Harris method (Reference 49). Van Manen has shown that, if a finite number of blades is considered, this influence is negligible for the normal ratios of propeller disc area to tunnel cross section. Equivalent and validated corrections for cavitating propellers have, however, yet to be derived. The cavitation experienced by a propeller at the various positions in the propeller disc is fundamentally influenced by the inflow velocities and hence, by implication, the simulation of the wake field. Many methods of simulating the wake field of the vessel are used. The simplest of these is through the use of a wire gauge arrangement, termed a wake screen, located upstream of the propeller. The design of the wake screen is done on a trial and error basis in attempting to simulate the required wake fields. A more favoured approach is to use a dummy model comprising a forebody and afterbody with a shortened parallel mid-body section. This produces the general character of the wake field and the 'fine tuning' is accomplished with a simplified wake screen attached to the dummy hull body. In several institutes a full model hull form can now be used in the cavitation facility.

However, by representing the measured nominal wake field of the model only part of the inflow problem is solved, since there are both scale effects on ship wake and propeller induction effects to be considered, as discussed in Chapter 5. As a consequence these other effects need to be accounted for if a proper representation of the inflow velocity field is to be correctly simulated: the methods for doing this, however, can still only be regarded as being tentative.

The nuclei content of the water is an important aspect, as already discussed. Various means exist by which the nuclei content can be measured, and these can be divided into two main types. The first type is where a sample of the water is taken from the main flow and forced to cavitate, thereby providing information on the susceptibility of the liquid to cavitate. The second type consists of those employing holographic and light-scattering methods and giving information on the nuclei distribution itself. An example of the first type of method is where the tunnel water is passed through a glass venturi tube whose pressure has been adjusted in such a way that a limited number of bubbles explode in the throat of the venturi, the bubble explosions being limited to the order of 20 per second. The detection of the bubbles passing through the venturi tube is by optical means. With regard to the second group of methods, the holographic method discriminates between particulates and bubbles, and can therefore be regarded as an absolute method, and is extremely useful for calibration purposes. However, the analysis of holograms is tedious, and therefore makes the method less useful for routine work. In the case of light scattering techniques, these have improved considerably since the mid-1920s and their reliability for routine measurements is now adequate for practical purposes.

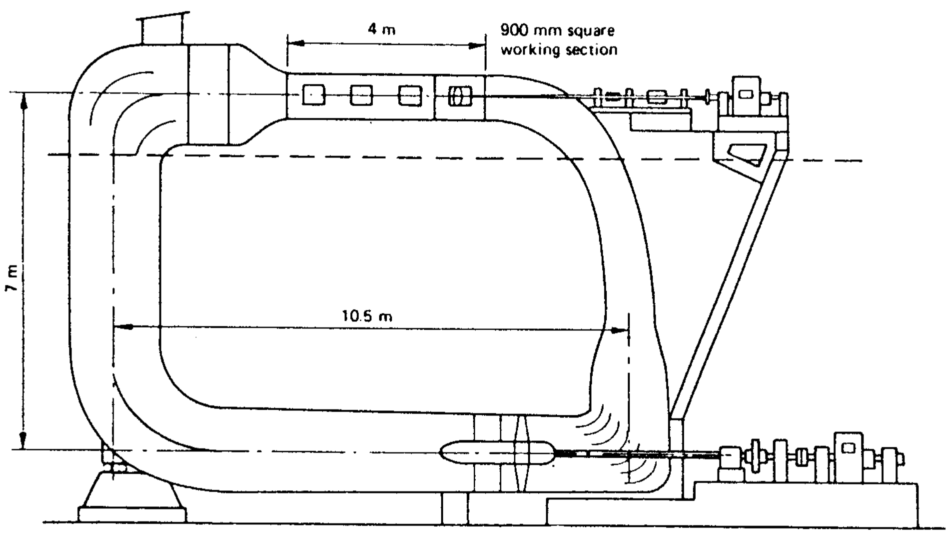

Figure 9.25 Typical modern cavitation tunnel (Reproduced from Reference 42, with permission)

The science, or art, of cavitation testing of model propellers was initiated by Sir Charles Parsons in his attempts to solve the cavitation problems of his steam turbine proptype vessel *Turbinia*. He constructed the first cavitation tunnel from a copper rectangular conduit of uniform section. This conduit was formed into an 'oval' so as to form a closed circuit having a major axis of the order of one metre. The screw shaft was inserted horizontally through a gland in the upper limb and driven externally, initially by a small vertical steam engine and later by an electric motor. Within the tunnel Parsons installed windows on either side of the tunnel and a plane mirror was fixed to an extension of the shaft, which reflected light from an arc lamp in order to illuminate the model propeller for a fixed period each revolution. The propeller diameter was 2 inches and cavitation commenced at about 1200 RPM. In constructing the tunnel Parsons recognized the importance of static pressure and made provision for the reduction of the atmospheric pressure by an air pump in order to allow cavitation to be observed at lower rotational speeds. This forerunner of the modern cavitation tunnel, constructed in 1895, is today preserved in working order in the Department of Marine Technology at the University of Newcastle upon Tyne. It is frequently cited alongside the current facility of the University, and in this way provides an interesting contrast in the developments that have taken place over the intervening years. In 1910 Parsons constructed a larger facility at Wallsend, England, in which he was able to test propeller models of up to 12 inches in diameter. The tunnel, which was a closed conduit, had a working section of cross section 0.7 m × 0.76 m, and the flow rate in the test section was controlled by a circulating pump of variable speed. The propeller model was mounted on a dynamometer which was capable of measuring thrust, torque and rotational speed. Unlike its predecessor, this tunnel has not survived to the present day.

In the years that followed, several cavitation facilities were constructed in Europe and the United States of America. In 1929 a tunnel capable of testing 12-inch diameter propellers was built at the David Taylor Model Basin. This was followed by the building of facilities in Hamburg, Wageningen, Massachussetts Institute of Technology, Haslar (UK) and so on.

Today there are both what might be termed traditional cavitation tunnels and the new breed of large tunnels that are being constructed around the world. Typical of the traditional tunnels, traditional in the sense of their size, is that shown in Figure 9.25. The tunnel is usually mounted in the vertical plane and is formed from a closed recirculating conduit having a variable speed and pressure capability. Typical of the speed and pressure ranges of this kind of tunnel are speeds of up to 10–11 m/s and pressure ranges of 10–180 kPa.

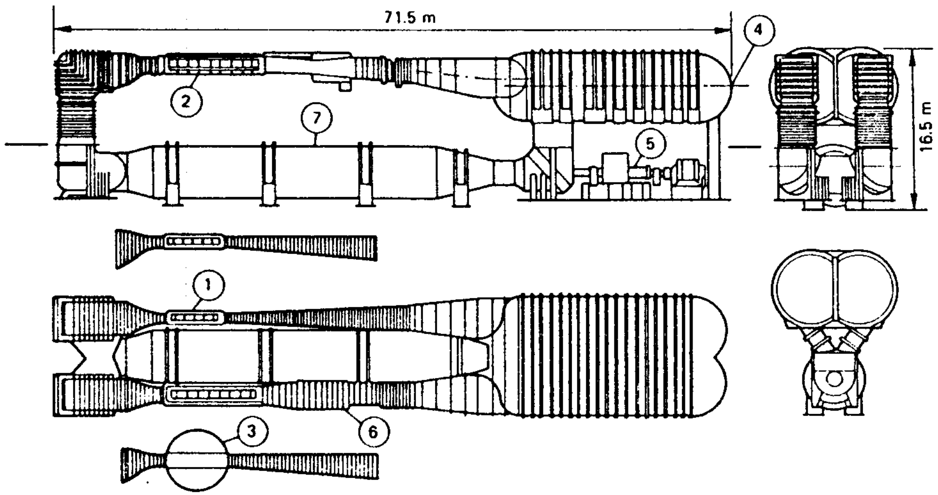

1 Small test section (STS): 1.14 x 1.14 x 6 m
2 Large test section (LTS): 2 x 1.35 x 10 m
3 Hydroacoustic chamber
4 Downstream tank for bubbles separations
5 Pump station
6 Large test section skimmer
7 Resorber

Tunnel performance characteristics:

	STS	LTS
Flow velocity (m/s)	20	12
σ_{min}	0.065	0.125

Figure 9.26 Grand tunnel hydrodynamique (GTH) (Courtesy: DCN)

giving cavitation number capabilities in the range 0.2 to 6.0.

Some modern cavitation facilities also have variable test sections, thereby allowing the one of the appropriate dimensions to be installed into the tunnel body so as to meet the particular requirements of a measurement assignment. One such facility is that owned by SSPA, in which the test section can be varied from 2.5 m to 9.6 m, thereby allowing hull models to be inserted into the facility. Clearly, in such cavitation tunnels the maximum velocity attainable in the working section is dependent on the test section body deployed for the measurement.

To meet the increasingly stringent demands of naval hydrodynamic research a new breed of large cavitation tunnel is making its appearance; facilities have been constructed in the United States of America, Germany and France. Figure 9.26 shows the Grand Tunnel Hydrodynamique located at Le Val de Reuil, France and owned by Bassin d'Essais des Carenes de Paris. This tunnel has two parallel test sections; the larger of the two has a cross section of 2.0 m × 1.35 m and is 10 m long, whilst the smaller section has a 1.14 m square section and is 6 m long. The larger and smaller sections can give maximum flow velocities of 12 and 20 m/s respectively, and the larger limb can be used as either a free surface or fully immersed test section. In Figure 9.26 the large downstream tank is used to remove the air produced in, or injected into, the test section. This tank has a total volume of 1600 m^3 and can remove the air from dispersions with void fractions of up to 10%. No bubbles larger than 100 μm can pass through the tank at its maximum flow rate. In this facility cavitation nuclei concentrations are automatically controlled by nuclei generators and measurement systems. In addition to the larger downstream tank a resorber, 5 m in diameter, ensures that no nuclei return to the test section after one revolution, and in order to reduce flow noise, the water velocities are kept below 2.5 m/s except in the test section. A second large European facility built in Germany at HSVA and called the HYKAT has been commissioned and has working section dimensions of 2.8 m × 1.6 m × 11.0 m with a maximum flow velocity of 12.6 m/s. Apart from being able to insert complete hull models of towing tank size into the tunnel, one of the major benefits of these larger tunnel facilities is their quiet operation, thereby allowing greater opportunities for noise measurement and research. Figure 9.27, from data supplied by Wietendorf and

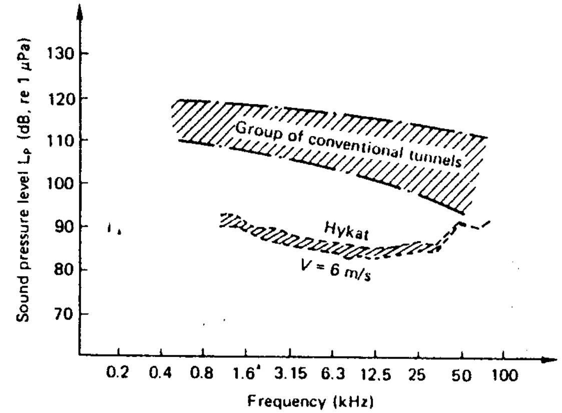

Figure 9.27 Comparison of background noise levels of the HYKAT facility with other tunnels

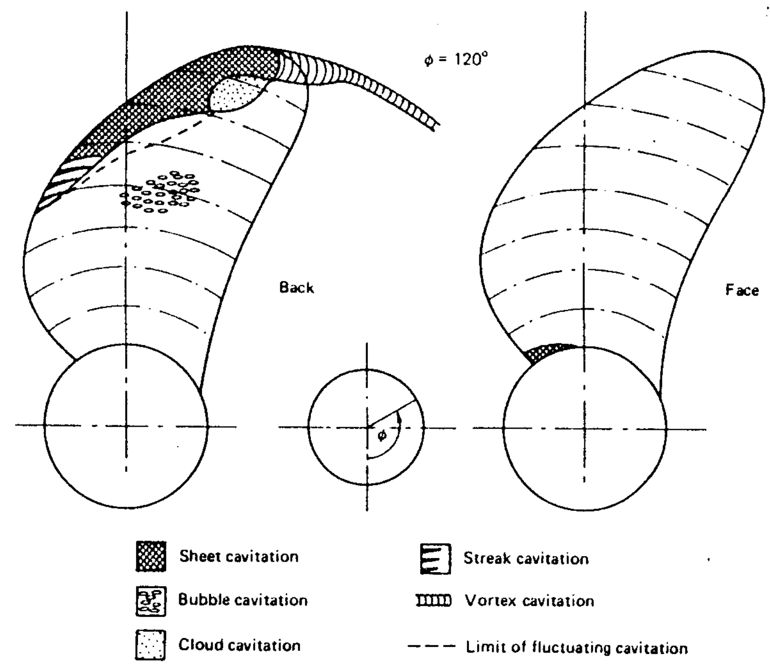

Figure 9.28 Typical cavitation sketch

Friesel for different water gas contents, shows the measured background noise levels of the HYKAT in relation to conventional tunnels.

The recently built facility in the United States of America, known as the Large Cavitation Channel (LCC) and operated by DTRC, is currently the largest facility in the world. It has a working section having a cross section of the order of 3 m square.

Apart from cavitation tunnels, there is also the depressurized towing tank facility which, in essence, is a conventional towing tank contained within a concrete pressure vessel which can be evacuated in order to reduce the internal air pressure. This depressurization capability naturally complicates both the initial construction and subsequent operation of the facility, since a series of air locks is required in order to allow personnel to travel with the carriage to make observations. This facility, owned by MARIN, has a tank dimension of 240 m × 18 m × 8 m and was designed to be evacuated to a pressure of 0.04 atmospheres in around eight hours: it exists on a separate site at Ede in the Netherlands. The depressurized towing tank allows testing at the correct Froude number, cavitation number and advance coefficient. In addition, as is the case with the large and variable test section cavitation facilities, the flow around the complete model hull helps considerably in modelling the inflow into the propeller, although the scale effects on wake are still present. In the depressurized facility the free surface effects are readily modelled and the tank boundaries are comparatively remote from the model.

In cavitation facilities around the world, of which the above are a few European examples for illustration purposes, several measurement and visualization capabilities exist for a variety of cavitation related measurements. The basic method of viewing cavitation is by the use of stroboscopic lighting. The stroboscopic lighting circuitry is triggered from the model propeller shaft rotational speed together with a multiplier and phase adjustment to account for differences in blade number and position around the disc. The traditional method of recording cavitation is to use the cavitation sketch, Figure 9.28, which is the experimenter's interpretation of the cavitation type and extent observed at various positions of the blade around the propeller disc. In many cases this method has been replaced or supplemented with the use of photographs taken under stroboscopic lighting or by video cameras, the latter being particularly useful. Laser methods have increased in recent years for measuring flow velocities around the propeller and have very largely taken over from the intrusive measurements of pitot tubes and pitot rakes; although these latter methods are still generally retained for reference and special purpose measurements.

Over the years several attempts have been made to predict cavitation erosion qualitatively using 'soft surface' techniques which are applied to the blade surface: typical of this work is that of Kadoi and Sasajima (Reference 50), Emerson (Reference 51) and Lindgren and Bjarne (Reference 52). The techniques used have been based on the application of marine paint, soft aluminium and stencil ink. The ITTC have proposed the use of the latter. Care has, however, to be exercised in interpreting the results, in terms of both the surface used and the cavitation formation at model scale due to the various scale effects.

At the present time research is being undertaken on the use of sonoluminescence in the use of cavitation studies. Sonoluminescence is generally ascribed to the high internal temperatures resulting from the essentially adiabatic compression of the permanent gas and vapour which is trapped within a collapsing cavitation bubble.

In recent years several full-scale observations of cavitation have been made. These require the placing of observation windows in the hull, usually in several locations. Stroboscopic lighting is directed at the propeller through one of the observation windows and video-camera, pencil sketches and direct observation is made as appropriate through the other windows. To obtain good results night-time viewing is required to minimize ambient light and clear, good quality water is essential. This latter requirement places severe restrictions on the locations where such measurements can be undertaken satisfactorily.

References and further reading

1. Euler, M. Théorie plus complète des machines qui sont mises en movement par la réaction de l'eau. L'Académie Royale des Sciences et Belles Lettres, Berlin, 1756.
2. Reynolds, O. The causes of the racing of the engines of screw steamers investigated theoretically and by experiment. *Trans. INA*, 1873.
3. Harvey, E.N. *et al.* Bubble formulation in animals – I. Physical factors. *J. Cellular and Comp. Physiol.*, **24**(1), 1944.
4. Harvey, E.N. *et al.* Bubble formation in animals – II. Gas nuclei and their distribution in blood and tissues. *J. Cellular and Comp. Physiol.*, **24**(1), 1944.
5. Harvey, E.N. *et al.* Removal of gas nuclei from liquids and surfaces. *J. Amer. Chem. Soc.*, **67**, 1945.
6. Harvey, E.N. *et al.* On cavity formation in water. *J. Appl. Phys.*, **18**(2), 1947.
7. Strasberg, M.J. *Acoust. Soc. Am.*, **31**, 1959.
8. Flynn, H.G. *Physical Acoustics*, Vol. 1. Academic Press, New York.
9. Winterton, R.H.S. *J. Phys. D: Appl. Phys.*, **10**, 1977.
10. Cram, L.A. *Cavitation and Inhomogeneities in Underwater Acoustics*. Springer, Berlin, 1980.
11. Fox, F.E., Herzfeld, K.F. Gas bubbles with organic skin as cavitation nuclei. *J. Acoustic. Soc. Amer.*, **26**, 1954.
12. Yount, D.E. *J. Acoust. Soc. Am.*, **65**, 1979.
13. Yount, D.E. *J. Acoust. Soc. Am.*, **71**, 1982.
14. Plesset, M.S. Bubble Dynamics. CIT Rep. 5.23. Calif. Inst. of Tech., February, 1963.
15. Wheeler, W.H. Indentation of metals by cavitation. *ASME Trans.*, Series D, **82**, 1960.
16. Besant, W.H. *Hydrostatics and Hydrodynamics*. Art ISE, Cambridge University Press, Cambridge, 1859.
17. Rayleigh, Lord. On the pressure developed in a liquid during the collapse of a spherical cavity. *Phil. Mag.*, **34**, 1917.
18. Mitchell, T.M., Hammitt, F.G. Asymmetric cavitation bubble collapse. *Trans. ASME J., Fluids Engineering*, **95**(1), 1973.
19. Plesset, M.S., Chapman, R.B. Collapse of an initially spherical vapour cavity in neighbourhood of a solid boundary. *J. Fluid Mech.*, **47**(2), 1971.
20. Knapp, R.T., Daily, J.W., Hammitt, F.G. *Cavitation*. McGraw-Hill, New York, 1970.
21. Huse, E. Propeller–Hull Vortex Cavitation. Norw. Ship Model Exp. Tank Publ. No. 106, May, 1971.'
22. Burrill, L.C., Emerson, A. Propeller cavitation: further tests on 16 in propeller models in the King's College Cavitation Tunnel. *Trans. NECIES*, 195, 1978.
23. Keller, J. auf'm. Enige Aspecten bij het Ontwerpen van Scheepsschroeven. *Schip en Werf*, No. 24, 1966.
24. Balhan, J. Metingen aan Enige bij Scheepsschroeven Gebruikelijke Profielen in Vlakke Stroming met en Zonder Cavitatie. NSMB Publ. No. 99, 1951.
25. Shan, Y.T. Wing section for hydrofoils – Part 3: experimental verifications. *J. Ship Res.*, **29**, 1985.
26. Oossanen, P. van. Calculation of Performance and Cavitation Characteristics of Propellers Including Effects of Non-Uniform Flow and Viscosity. NSMB Publ. No. 457, 1974.
27. Knapp, R.T. Cavitation Mechanics and its Relation to the Design of Hydraulic Equipment. *Proc. I.Mech.E. Pt*, No. 166, 1952.
28. Cebeci, T., Mosinskis, G.J., Smith, A.M.O. Calculation of Viscous Drag on Two-Dimensional and Axi-Symmetric Bodies in Incompressible Flows. Amer. Inst of Aero. and Astronautics. Paper No. 72-1, 1972.
29. Ligtelign, J.Th., Kuiper, G. Intentional cavitation as a design parameter. 2^{nd} *PRADS Symp.*, 1983.
30. Tulin, M.P. Steady Two Dimensional Cavity Flows about Slender Bodies. DJMB Report 834, May, 1953.
31. Geurst, J.A. Linearised theory for partially cavitated hydrofoils. ISP, **6**, 1959.
32. Geurst, J.A., Verbrugh, P.J. A note on cambered effects of a partially cavitated hydrofoil. ISP, **6**, 1959.
33. Geurst, J.A. Linearised theory for fully cavitated hydrofoils. ISP, **7**, 1960.
34. Leehey, P. Supercavitating hydrofoil of finite span. *Proc. IUTAM Symp. on Non-Steady Flow of Water at High Speeds*, Leningrad, 1971.
35. Uhlman, J.S. A partially cavitated hydrofoil of finite span. *J.F.E.*, **100**, 1978.
36. Jiang, C.W. Experimental and Theoretical Investigations of Unsteady Supercavitating Hydrofoils of Finite Span. Ph.D. Thesis, MIT, 1977
37. Uhlman, J.S. The surface singularity method applied to partially cavitating hydrofoils. *5th Lips Symp.*, May, 1983.
38. Tulin, M.P., Hsu, C.C. The theory of leading-edge cavitation on lifting surfaces with thickness. *Symp on Hydro. of Ship and Offshore Prop. Syst.*, March, 1977.
39. Stern, F., Vorus, W.G. A non-linear method for predicting unsteady sheet cavitation on marine propellers. *J. Ship. Res.*, 17, 1983.
40. Isay, W.H. *Kavitation*. 1981.
41. Mills, L. Die Anwendung der Blasendynamik auf die theoretische mit experimentellen Daten. Ph.D. Thesis, Hamburg, 1991.
42. Kuiper, G. Cavitation Inception on Ship Propeller Models. Publ. No. 655, NSMB, 1981.
43. Report of Cavitation Committee. Proc. of 18th ITTC, Kobe, 1987.
44. Chandrashekhara, N. Analysis of the tip vortex cavitation inception at hydrofoils and propellers. *Schiffstechnik*, **112**.
45. English, J. Caviation induced hull surface pressures – measurements in a water tunnel. *RINA Symp. on Propeller Induced Vibration*, London, 1979.
46. Brunton, J.H. Cavitation damage. *Proc. Third Int. Cong. on Rain Erosion*, August, 1970.
47. Manen, J.D. van. Bent trailing edges of propeller blades of high powered single screw ships. ISP, **10**, 1963.
48. Newton, R. N. Influence of cavitation on propeller performance. *Int. Ship. Prog.*, **8**, Aug., 1961
49. Wood, R.McK., Harris, R.G. Some Notes on the Theory of an Airscrew Working in a Wind Channel A.R.C., R&M No. 662, 1920.
50. Kadoi, H., Sasajima, T. Cavitation Erosion Production using a 'Soft Surface'. ISP, **25**, June, 1978.
51. Emerson, A. Cavitation Patterns and Erosion – Model–Full Scale Comparison. Appl. 6, Rep. of Cav. Comm. 14th ITTC, 1975.
52. Lindgren, H.B., Bjarne, E. Studies of Propeller Cavitation Erosion. Conf. on Cavitation, I Mech.E., Edinburgh, 1976.
53. Gent, W. van, Kooij, Juander. Influence of Hull Inclination and Hull–Duct Clearance on Performance, Cavitation and Hull Excitation of a Ducted Propeller: Part I. NSMB.
54. Kooij, J. van der, Berg, W. van den. Influence of Hull Inclination and Hull–Duct Clearance on Performance, Cavitation and Hull Excitation of a Ducted Propeller: Part II. NSMB.

10 Propeller noise

Contents

The noise produced by a propeller, in terms of both its intensity and its spectral content, has been of considerable importance to warship designers and military strategists for many years. However, in recent years the subject has assumed a growing importance in the merchant shipping sector, and is likely to maintain and perhaps increase this importance in the future.

Before considering the noise characteristics generated by marine propellers it is first useful to briefly remind ourselves of the basic nature and physics of underwater sound and its propagation.

10.1 Physics of underwater sound

The speed of sound in water is some 4.3–4.4 times greater than that in air, as shown by Table 10.1. The speeds shown in this Table are approximate values, since some variations occur with ambient conditions, and relate to locations close to sea level. For a more precise determination of the speed of sound in sea water use can be made of an equation based on the work of Lovett (Reference 1), which relates the speed of sound to the temperature, salinity, latitude and the depth at which the speed is required. This relationship has the following form:

$$\begin{aligned} C(z, S, T, \phi) &= 1449.05 + 4.57T - 0.0521T^2 \\ &+ 0.00023T^2 + (1.333 - 0.0126T + 0.00009T^2) \\ &\times (S - 35) + (16.23 + 0.0253T)(1 - 0.0026\cos\phi)z \\ &+ (0.213 - 0.01T)(1 - 0.0026\cos\phi)^2 z^2 \\ &+ [0.016 + 0.0002(S - 35)](S - 35) \\ &\times (0.1 - 0.00026\cos\phi)Tz \end{aligned} \qquad (10.1)$$

where T = the ambient temperature (deg C)
S = the salinity in parts per thousand
z = the depth (km)
ϕ = the latitude (degrees)

This regression equation is essentially valid for all oceanic waters down to a depth of around 4 km with a standard deviation of 0.02 m/s.

Table 10.1 Speed of sound in air and water close to sea level

Medium	*Speed (m/s)*
Air at 21°C	344
Fresh water	1480
Salt water at 21°C and 3.5% salinity	1520

As a direct consequence of the speed increase in water over that in air, the acoustic wavelengths in water will be greater than in air by the same factor, since:

$$\text{wavelength } (\lambda) = \frac{\text{speed of sound}}{\text{frequency}} \qquad (10.2)$$

It is found that the transmissibility of sound in water is considerably affected by the frequency of the noise source. In general, high frequencies in water are strongly attentuated with increasing distance from the source, whilst the lower frequencies tend to travel further, and are therefore considerably more serious from the ship radiated noise viewpoint. This is demonstrated in Figure 10.1, which shows the variation in absorption factor, measured in dB per 1000 m, over the range of frequencies 10^2 to 10^7 Hz.

Noise levels are measured using the decibal scale. Whilst the original definition of the decibel was based on power ratios:

$$\text{dB} = 10\log_{10}(W/W_0)\,\text{dB} \qquad (10.3)$$

where W_0 is a reference power, the use of the scale has widened from its original transmission line theory application to become a basis for many measurements of different quantities having a dynamic range of more than one or two decades. In the context of noise assessment, the sound pressure level (L_p) is the fundamental measure of sound pressure, and it is defined in terms of a pressure ratio as follows:

$$L_p = 20\log_{10}(P/P_0)\,\text{dB} \qquad (10.4)$$

where P is the pressure measured at a point of interest and P_0 is a reference pressure set normally to 20 μPa in air and 1 μPa in other media. Table 10.2 shows a conversion of the decibel scale into pressure ratios, this can be used when two sound pressure levels L_{p1} and L_{p2} are given and their difference (ΔL_p) can be expressed independently of the reference pressure P_0 as follows:

$$\begin{aligned} \Delta L_p &= L_{p2} - L_{p1} \\ &= 20[\log_{10}(P_2/P_0) - \log_{10}(P_1/P_0)] \end{aligned}$$

that is

$$\Delta L_p = 20[\log_{10}(P_1/P_2)] \qquad (10.5)$$

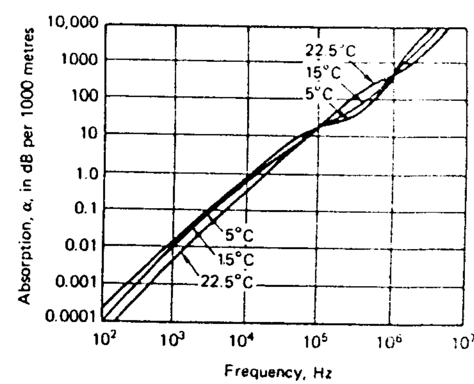

Figure 10.1 Sound absorption in sea water (Reproduced from Reference 22, with permission)

Table 10.2 Decibel to power ratio conversion

Pressure ratio	*− dB +*	*Pressure ratio*
1.000	0.0	1.000
0.989	0.1	1.012
0.977	0.2	1.023
0.966	0.3	1.035
0.955	0.4	1.047
0.933	0.6	1.072
0.912	0.8	1.096
0.891	1.0	1.122
0.841	1.5	1.189
0.794	2.0	1.259
0.708	3.0	1.413
0.631	4.0	1.585
0.562	5.0	1.778
0.501	6.0	1.995
0.447	7.0	2.239
0.398	8.0	2.512
0.355	9.0	2.818
0.316	10.0	3.162
0.251	12.0	3.981
0.200	14.0	5.012
0.158	16.0	6.310
0.126	18.0	7.943
0.100	20.0	10.000
0.0316	30.0	31.62
0.0100	40.0	100.0
0.0032	50.0	316.2
10^{-3}	60.0	10^3
10^{-4}	80.0	10^4
10^{-5}	100.0	10^5

Table 10.3 Third octave and octave passbands

Band number	*Nominal centre frequency*	*Third-octave passband*	*Octave passband*
1	1.25 Hz	1.12–1.41 Hz	
2	1.6	1.41–1.78	
3	2	1.78–2.24	1.41–2.82 Hz
4	2.5	2.24–2.82	
5	3.15	2.82–3.55	
6	4	3.55–4.47	2.82–5.62
7	5	4.47–5.62	
8	6.3	5.62–7.08	
9	8	7.08–8.91	5.62–11.2
10	10	8.91–11.2	
11	12.5	11.2–14.1	
12	16	14.1–17.8	11.2–22.4
13	20	17.8–22.4	
14	25	22.4–28.2	
15	31.5	28.2–35.5	22.4–44.7
16	40	35.5–44.7	
17	50	44.7–56.2	
18	63	56.2–70.8	44.7–89.1
19	80	70.8–89.1	
20	100	89.1–112	
21	125	112–141	89.1–178
22	160	141–178	
23	200	178–224	
24	250	224–282	178–355
25	315	282–355	
26	400	355–447	
27	500	447–562	355–708
28	630	562–708	
29	800	708–891	
30	1000	891–1120	708–1410
31	1250	1120–1410	
32	1600	1410–1780	
33	2000	1780–2240	1410–2820
34	2500	2240–2820	
35	3150	2820–3550	
36	4000	3550–4470	2820–5620
37	5000	4470–5620	
38	6300	5620–7080	
39	8000	7080–8910	5620–11 200
40	10 kHz	8910–11 200	
41	12.5 kHz	11.2–14.1 kHz	
42	16 kHz	14.1–17.8 kHz	11.2–22.4 kHz
43	20 kHz	17.8–22.4 kHz	

From Table 10.2 it is seen that a change of, say, 6 dB causes either a doubling or halving of the sound pressures experienced. Similarly, a change of 12 dB effectively either quadruples or quarters the pressure levels.

Because the human ear does not respond equally to all frequencies within the audible noise range a weighting scale was devised by the industry to correct the actual physical pressure levels to those interpreted by the ear. This weighted scale is generally known as the A-weighting scale and its effect is shown by Figure 10.2 for the audible sound range of about 20 Hz to 20 kHz. From this figure a marked fall-out in response can be seen for frequencies less than about 1000 Hz.

In general acoustic measurements make use of third-octave and octave filters in order to study and define noise spectra. A third-octave filter is one in which the ratio of the upper to the lower passband limits, that is the range of frequencies the filter will allow to pass through it, is $2^{1/3}$ (i.e. 1.2599). In the case of the octave filter, this ratio between the upper and lower passband limits is 2 and it is normally centred, as are the third-octave filters, on one of the preferred centre frequencies in the ISO R266. These centre frequencies are calculated from $10^{n/10}$, where n is the band number; in practice nominal values are used to identify the centre frequencies and Table 10.3 lists the set of third-octave and octave passbands relating to the audible range for convenience of reference.

Whilst the subject of propeller noise is important to both the merchant and naval worlds the reasons for this importance derive from different origins. The exception to this statement is in the case of oceanographic and research vessels, which have similar noise requirements to naval vessels, in that they require to use instrumentation with ranges of the order of up to 10 kHz. In the merchant service the increasing awareness of the health hazards caused by the long-term exposure to high noise levels has led to the formulation of recommended levels of noise in different areas of a merchant vessel by the International Maritime Organisation (IMO). The 1981 IMO Code on noise levels (Reference 2) define maximum levels of noise as shown in Table 10.4.

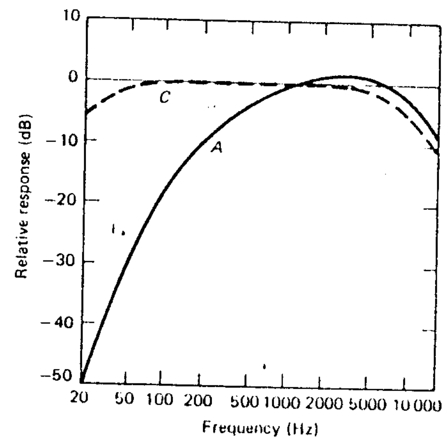

Figure 10.2 Filter characteristics for *A*- and *C* weighted sound levels

Table 10.4 Maximum noise levels permitted on a ship according to the 1981 IMO Code

Location	*Level (dBA)*
Engine room	110
Workshops	85
Machinery control room	75
Navigating bridge	65
Mess room	65
Recreation room	65
Cabins and hospital	60

In addition to defined levels of noise of this type there are further considerations of passenger comfort and annoyance in, for example, cruise liners and ferries. In order to appreciate the magnitude of the propeller noise problem it is instructive to compare the results of full-scale measurements on a variety of ships, recorded inside the hull but close to the propeller with the levels quoted in Table 10.4. The measurements reported by Flising (Reference 3) are shown in Figure 10.3 for a variety of ship types ranging from larger tankers to Rhine push boats, and it can be seen that levels of the order of a 100–110 dBA are frequently noted at the lower frequency bands. These measurements have been recorded in locations close to the propeller, such as in the aft peak tank and near the aft peak bulkhead. By considering this Figure, which shows noise levels of the order of 100 dB at the aft peak region of the vessel, it can be seen by reference to Table 10.2 that these sound pressure levels have to be considerably reduced by the time they reach a hospital or cabin location in the vessel according to the IMO code.

The origins of the naval interest in the subject of noise stem from a set of rather different design constraints. These are largely twofold; firstly, there is interference from the noise generated by the vessel on its own sensors and weapons systems, and secondly, there is the radiated noise, which is transmitted from the ship to the far field, and by which the ship can be detected by an enemy. In this latter context a ship noise signature of a few tens of watts could be sufficient to give an enemy valuable information at a considerable range. Indeed by undertaking noise signature analysis at remote locations, it is possible not only to determine which class of vessel has been located, but if sufficient is known about the character of each signature, to identify the particular ship. Clearly the ultimate goal of a warship designer must be to make the ship's signature vanish into the background noise of the sea which comprises contributions from the weather, marine life and also other shipping from a wide geographical area.

This leads to an important distinction in the types of noise that are generated by the various components of ship. These are termed self- and radiated noise and it is convenient to define these as follows:

Self-noise	The noise, from all shipboard sources, generated by the subject vessel, considered in terms of effect it has on the vessel's own personnel and equipment.
Radiated noise	The noise generated by the ship and experienced at some point distant from the ship, by which its detection or recognition could be initiated

Clearly, most merchant ship considerations, with the exception of certain specialist vessels, such as research or hydrographic ships, lie in the field of self-noise, whilst naval interest spans both categories.

When considering the noise generated by ships it is useful to place it in the context of the ambient noise level in deep water. Wenz (Reference 4) and Perrone (Reference 5) considered the ambient noise levels in deep water and the results of their work is shown in Figure 10.4, measured from omnidirectional receivers. From this figure it is seen that below about 20 Hz ocean turbulence and seismic noise predominate, whereas in the range 20 Hz to around 200 Hz the major contributions are from distant shipping and biological noise. Above 500 Hz to around 20 kHz the agitation of the local sea surface is the strongest source of ambient noise and above 50 kHz thermal agitation of the water molecules becomes an important noise source, where the noise spectrum level increases at

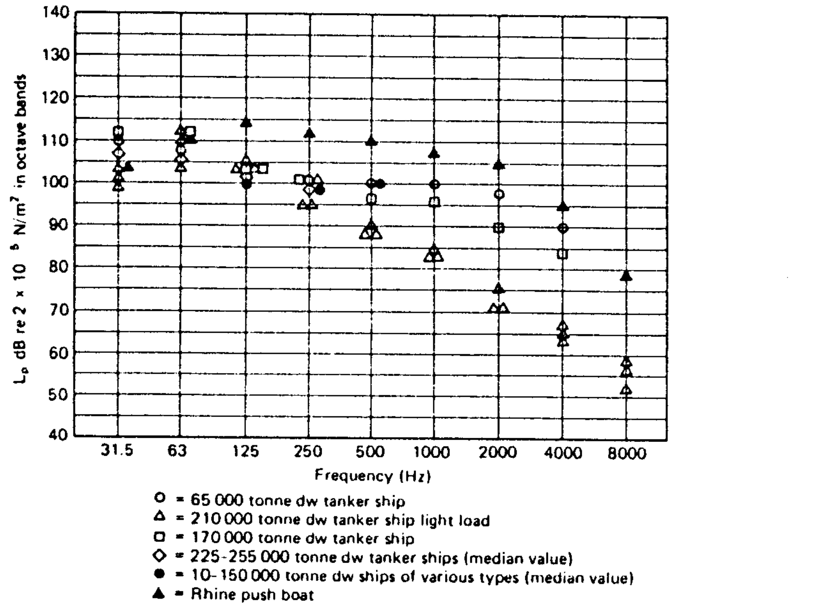

Figure 10.3 Sound pressure levels in hull close to propeller (Reproduced from Reference 3, with permission)

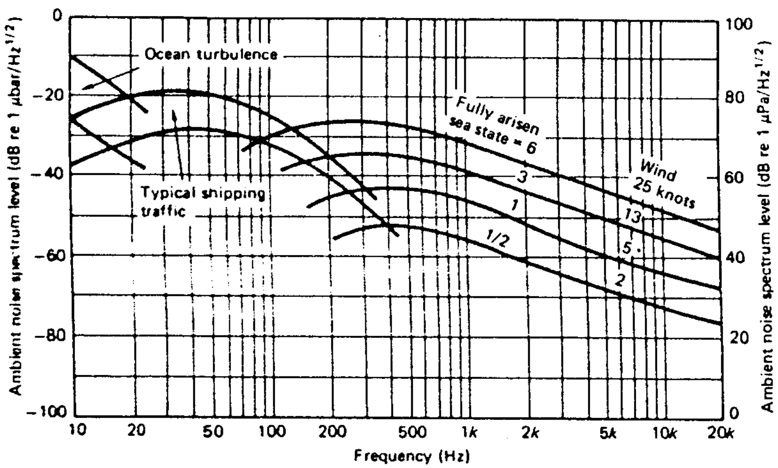

Figure 10.4 Deep-water ambient noise

around 6 dB/octave. In the case of shallow water the noise levels can be considerably higher due to heavier shipping, nearby surf and waves breaking, higher biological noise, shore-based noises, and so on.

10.2 Nature of propeller noise

There are four principal mechanisms by which a propeller can generate pressure waves in water and hence give rise to a noise signature. These are:

1. the displacement of the water by the propeller blade profile;
2. the pressure difference between the suction and pressure surfaces of the propeller blade when they are rotating;
3. the periodic fluctuation of the cavity volumes caused by operation of the blades in the variable wake field behind the vessel;
4. the sudden collapse process associated with the life of a cavitation bubble or vortex.

Clearly, the first two causes are associated with the propeller in either its cavitating or non-cavitating state, but are non-cavitating effects only. The latter two causes are cavitation dependent phenomena, and therefore occur only when the propeller is experiencing cavitation.

Propeller noise can, therefore, be considered as comprising two principal constituents: a non-cavitating and a cavitating component. In terms of the noise signature of a vessel, prior to cavitation inception, all components of noise arising from the machinery, hull and propeller are important. Subsequent to cavitation inception, whilst the hull and machinery sources need consideration, the propeller noise usually becomes the dominant factor. Figure 10.5 typifies this latter condition, in which the self-noise generated at the sonar dome of a warship is seen. This figure shows the comparative noise levels at this position of the hull boundary layer, the machinery, electrical and the propeller. When studying this Figure it should be remembered that the propeller, in this case, is at the opposite end of the vessel to the sonar dome, and hence the importance of the propeller as a noise source can be appreciated and is seen to dominate at speeds above 25 knots.

Propeller noise comprises a series of periodic components, or tones, at blade rate and its multiples, together with a spectrum of high-frequency noise due to cavitation and blade boundary layer effects. Figure 10.6 shows a radiated cavitation noise spectrum based on a 1/3 octave band analysis; the sound pressure levels are referred to 1 μPa level in keeping with the normal practice. Within this noise spectrum the blade rate noise is commonly below the audible threshold, although not below sensor detection limits: typically in the case of a four-bladed propeller operating at say 250 RPM this gives a blade rate frequency of 16.7 Hz,

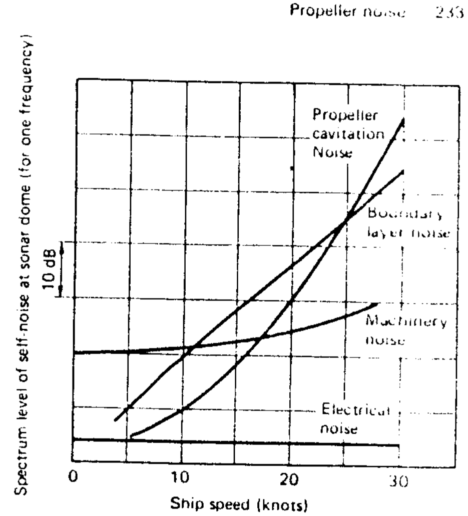

Figure 10.5 Example of the variations in self noise as a function of ship speed due to propeller, boundary layer machinery (Reproduced from Reference 25, with permission)

which is just below the human audible range of about 20–20 000 Hz.

To consider the generation of noise further, it is convenient to consider separately the issues of non-cavitating and cavitating noise. The former, although not practical for most merchant ships, is of considerable interest in the case of research ships and naval vessels, such as anti-submarine frigates, who rely on being able to operate quietly in order to detect potential threats. For these latter cases, a designer endeavours to extend the non-cavitating range of operation of the vessel as far as possible.

Blake (Reference 20) gives a particularly detailed treatment of the analysis of both non-cavitating and cavitating noise for marine applications. The reader, if pursuing the subject in detail, is recommended to consult this work.

10.2.1 Non-cavitating propeller noise

The marine propeller in its non-cavitating state, in keeping with other forms of turbo-machinery, produces a noise signature of the type sketched in Figure 10.7. It is seen from this Figure that there are distinct tones associated with the blade frequencies together with a broad-band noise at higher frequencies. The broad-band noise comprises components derived from inflow turbulence into the propeller and various edge effects such as vortex shedding and trailing edge noise.

For analysis purposes there are certain distinct similarities between the marine propeller as a noise

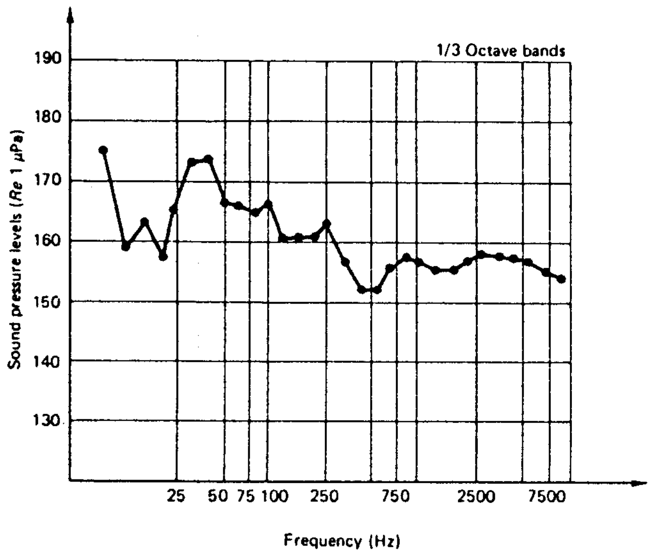

Figure 10.6 Radiated cavitation noise spectra measured outside hull at full scale

source and both air propellers and helicopter rotors. A marine propeller can, for the purposes of noise prediction, be considered as a compact noise source, since the product of the wave number times the radius is much less than unity, the wave number being defined as the frequency divided by the speed of sound. This considerably simplifies the analytical assessment of the noise characteristics from that of, say, a helicopter rotor. However, this simplification is perhaps balanced by the greater density of water, since this increases the entrained mass of the blades relative to their mass in air, such that their flexibility becomes a significant consideration in terms of the radiation efficiency.

With regard to the blade rate noise, the propeller is normally operating behind a vessel or underwater vehicle, and so works in a circumferentially varying wake field. This causes a fluctuating angle of incidence to occur on the blade sections, which can be represented as gust normal to the blade when considered relative to the propeller blade. From this gust model an expression can be generated for the far-field radiated source pressure.

The analysis of the broad-band components is different. In the blade rate problem, the unsteadiness is caused by the circumferential variation in the wake field; however, in the inlet turbulence case we need to consider the level of turbulence in the incident flow. This implies that the wake harmonics associated with this feature become a function of time and not necessarily just the analysis position in the propeller disc. To accommodate this feature, the turbulence velocity spectrum has to be incorporated into the analysis procedure to describe the flow and derive an expression for the radiated pressure due to this component.

Trailing edge noise is perhaps the least well understood of the broad-band noise mechanisms, since it involves a detailed knowledge of the flow around the trailing edge of the sections. The role of viscosity within the boundary layer is a crucial parameter in estimating the levels of radiated noise produced, and is an effect which is at present the subject of much research. Blake, however, in his extensive study of the

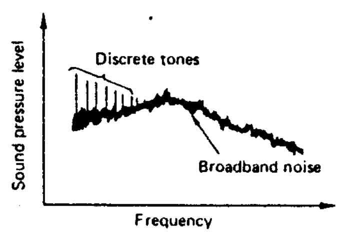

Figure 10.7 Idealized non-cavitating noise spectrum

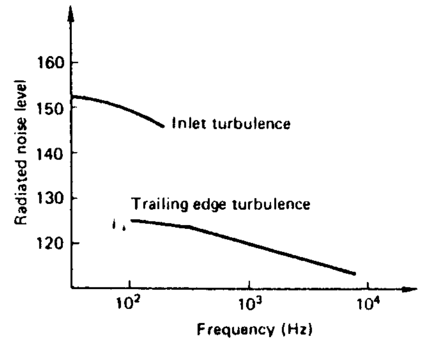

Figure 10.8 Typical radiated noise levels from a rigid hydrofoil moving in disturbed water. (Reproduced from Reference 20)

subject, gives an appreciation of the relative levels of trailing edge and inlet turbulence noise. Figure 10.8 is taken from his work for illustration purposes.

The problem of optimizing marine propellers for noise in sub-cavitating conditions by theory is still in its infancy since the complete solution requires both a detailed viscous flow calculation over the propeller blades together with an inlet turbulence spectrum in addition to the normal wake field data. Jenkins (Reference 6) discusses this problem further in the context of the non-cavitating marine propeller.

In addition to the foregoing effects, there are also hydro-elastic and fouling effects which need consideration in non-cavitating noise terms.

10.2.2 Cavitation noise

The collapse of cavitation bubbles creates shock waves and hence noise. This is essentially 'white noise' covering a frequency band up to around 1 MHz. From the theoretical viewpoint, the problem of noise radiation by cavitation was approached until recently from the behaviour of a single cavitation bubble such that the bubble dynamics were considered in a variable pressure field (Reference 7); for example, along the surface of a propeller blade section. Under these conditions the bubble will undergo volume fluctuations and as a consequence radiate acoustic energy. Using this approach the spectral power density of a set of bubbles becomes the product of the number of bubbles per unit time and the spectral energy density due to the growth and collapse of a single bubble, assuming that the bubbles occur as random events. Such models, however, only partially predict the real behaviour of cavitating propeller blades, and tend to fail in their prediction capability at very high bubble densities. Work by van der Kooij (Reference 8) and Arakeri and Shonmuganathan (Reference 9) support this conclusion. Van der Kooij shows by means of model tests on smooth and roughened blades that the noise generated by bubble cavitation initially increases with increasing number of bubbles and then falls off very markedly when a large number of bubbles are present. Figure 10.9, taken from Reference 8, shows this effect. In the case of the smooth blade different bubble densities were induced by a varying electrolysis current ranging from zero to 2.4 A, and in the case of the roughened blade a large number of bubbles were generated from the application of artificial leading edge roughness in association with an electrolysis current of 2.4 A.

Figure 10.10, based on Reference 21, shows in a schematic way the relative contribution of different cavitation types to the sound power spectrum. Hence an appreciation can be gained of the influence a particular cavitation type has on either the continuous or discrete spectrum.

The prediction of noise from cavitation by theoretical

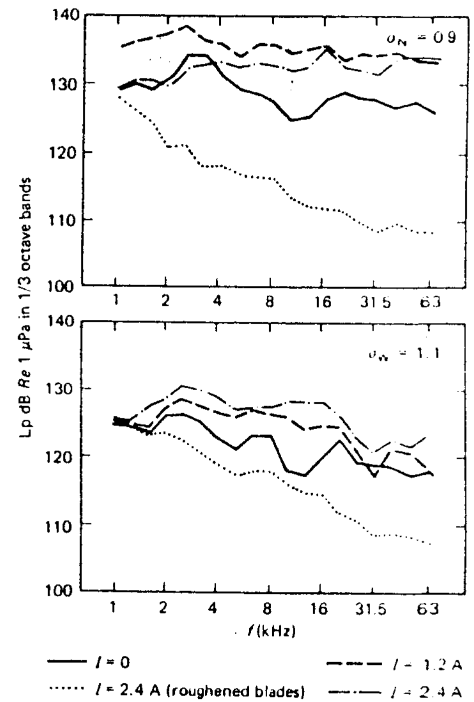

Figure 10.9 Measured sound pressure spectra, results with smooth blades, comparison with results with roughened blades (I = electrolysis current (Reproduced with modification from Reference 8, with permission from ASME)

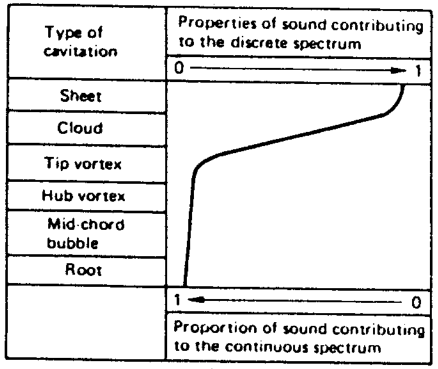

Figure 10.10 Relative contribution of different cavitation types to the sound power spectrum (Reproduced with modification from Reference 21, with permission)

means is even more complex than for the non-cavitating propeller, and as a consequence most prediction is done using model propellers operating in a cavitation tunnel. At present the inability of theoretical methods to take account of the detailed boundary layer and cavitation dynamics tend to preclude them from use, notwithstanding their requirement for large computational facilities.

The noise emitted by a cavitating propeller depends on the type of cavitation present at the particular operating condition. For example, back, face, hub and tip vortex cavitation types all have different noise signatures, as seen in Figure 10.11, which is taken from Sunnersjö (Reference 10). From this Figure the wide range of noise spectra derived from the same propeller for four particular load conditions can be noted.

Noise measurements are now a regular feature of many cavitation tunnel test programmes. The purpose of these tests can be to compare the noise spectra derived from different load conditions for the same propeller or comparisons between different propellers, or the full-scale prediction of the noise spectra under different characteristic load conditions for any particular design. However, when a noise study is undertaken in a cavitation tunnel the presence of the walls of the tunnel influence the results to an extent that the results are not, without correction, representative of the free field conditions. As a consequence of this a correction factor has to be developed by substituting a calibrated noise source in place of the propeller, so that a comparison can be made as to what the noise level would have been in the free field without the tunnel walls. This leads to the definition of a transfer function for the particular configuration of the form

$$P_{ff} = \phi P_t \qquad (10.6)$$

where P_{ff} is the required free field noise spectrum, P_t is the measured noise spectrum in the tunnel and ϕ is the transfer function between the tunnel and free field.

10.3 Noise scaling relationships

The basic requirement for deriving the full-scale noise prediction from model measurement is that the cavitation dynamics between model and full scale are identical. Scaling laws and their relation to bubble dynamics are discussed by many researchers, and for a full study of these see References 11 and 12. The scaling laws are based on the production of the pressure waves produced by a pulsating spherical bubble and immersed in an infinite volume of water, from which the pressure at some point remote from the cavity, or bubble, can be expressed as follows:

$$p(r,t) = \frac{\varrho}{3r}\frac{d^2R^3}{dt^2} \qquad (10.7)$$

in which R is the cavity radius, t is the time, r is distance from the centre of the cavity and ϱ is the water density.

The relevant scaling laws are then derived from the transformation of the variables in equation (10.7) and a relationship can be derived, consistent with the approximation of a first-order model for the scaling of the continuous part of the power spectrum:

$$\frac{G_s(f_s)}{G_m(f_m)} = \left(\frac{r_m D_s}{r_s D_m}\right)^2 \left(\frac{\varrho_s}{\varrho_m}\right)^{1/2} \left(\frac{\Delta P_s}{\Delta P_m}\right)^{3/2} \lambda \qquad (10.8)$$

where the suffixes m and s refer to model and ship scale respectively.

If this equation is applied to the measured sound pressure p in a frequency band Δf about a centre frequency f and, furthermore, if the analysis bandwidth Δf is a constant percentage of the centre frequency f (i.e. $\Delta f = af$, where a = constant as in Table 10.3) then equation (10.8) reduces to

$$\left[\frac{p_s(f_s, af_s)}{p_m(f_m, af_m)}\right]^2 = \left(\frac{r_m D_s}{r_s D_m}\right)^2 \left(\frac{\Delta P_s}{\Delta P_m}\right)^2 \qquad (10.9)$$

Equation (10.9) can be shown to be valid for both spectral lines and for the continuous part of the spectrum, which reinforces the need to use a constant percentage bandwidth for the analysis of propeller noise. Equation (10.9) can be transformed from its dependence on the pressure difference Δp which drives cavity collapse to a dependence on propeller shaft speed n by assuming that the cavitation extents are idential between model and full scale at equal cavitation numbers.

$$\left[\frac{p_s(f_s, af_s)}{p_m(f_m, af_m)}\right]^2 = \left(\frac{r_m D_s}{r_s D_m}\right)^2 \left(\frac{\varrho_s}{\varrho_m}\right)^2 \left(\frac{n_s D_s}{n_m D_m}\right)^4 \qquad (10.10)$$

With regard to frequency scaling, in relation to the first two sources of noise mentioned earlier, that is

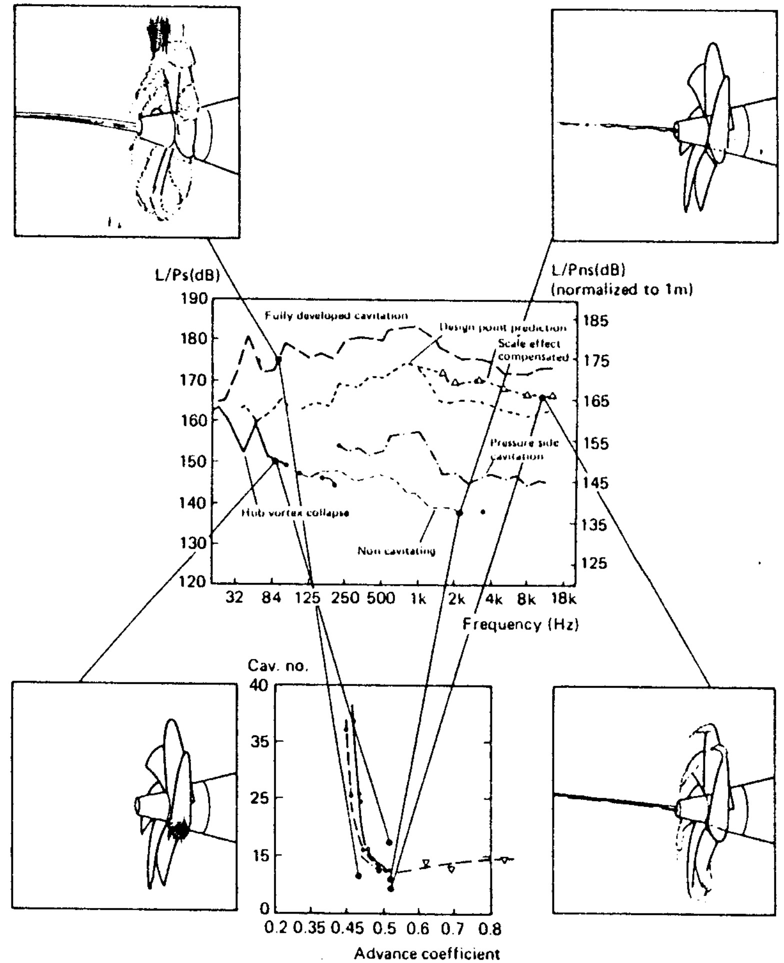

Figure 10.11 Effect of cavitation type of noise spectra (Reproduced from Reference 10, with permission)

the displacement of the water by the blade profile and the pressure difference across the blade, it is clear that these are linked by the blade rate frequency. As a consequence of this inverse shaft speed provides a suitable reference. However, in the case of a cavitating blade the collapse process cannot be directly linked to blade frequency. To overcome this problem a suitable time reference can be derived from the Rayleigh formula for the collapse time of a vapour-filled cavity:

$$T_c = 0.915 R_{max}\left(\frac{\varrho}{\Delta p}\right)^{1/2} \qquad (10.11)$$

in which R_{max} is the cavity radius, Δp is the pressure difference and ϱ is the density. If this equation is then made non-dimensional, the frequency scaling law becomes

$$\frac{f_s}{f_m} = \frac{n_s}{n_m}\left(\frac{\sigma_s}{\sigma_m}\right)^{1/2} \qquad (10.12)$$

This is in contrast to the frequency scaling law for the non-cavitating or indeed the slowly fluctuating cavitating process:

$$\frac{f_s}{f_m} = \frac{n_s}{n_m} \quad (10.13)$$

However, it can be seen that provided σ_s and σ_m are the same, which is a prerequisite for cavitation similarity, together with the implied assumption concerning the extents and dynamics, then equations (10.12) and (10.13) become identical and equation (10.13) suffices, and then becomes the counterpart of equation (10.10) for propeller noise scaling.

The assumptions concerning cavity extents at equal cavitation numbers is reasonable under well-developed cavitation conditions. However, close to incipient cavitation this is not always the case, since many model tests suffer from scale effects, which require that $\sigma_s > \sigma_m$ for equivalent cavitation extents. Under such conditions equations (10.10) and (10.13) do not apply and appeal should be made to References 12 and 13.

The scaling relationships (10.10) and (10.13) are entirely applicable for fully developed cavitation states at multiples of blade frequency below about one-fifth blade rate. However, above this value, due to simplifications made in their deviation, they should be considered as a first approximation only.

10.4 Noise prediction and control

If a definitive prediction of the noise spectra emission from a particular propeller–ship combination is required, then model test studies are at the present time the only realistic means of achieving this. Bark (Reference 14) discusses the correlation achievable and the reasons likely for any disparity of correlation between model and full scale. Figure 10.12, taken from Reference 14, demonstrates a good correlation of the non-dimensional noise in 1/3 octave bands using mean RMS levels. The diagram shows results for several speed conditions and a single gas content $\alpha/\alpha_s = 0.4$. In the Figure the non-dimensional noise $L(K_p)$ is given by

$$L(K_p) = 20 \log 10^6 \qquad K_p = 20 \log \left[\frac{p_{rms} \times 10^6}{\varrho n^2 D^2} \right] \quad (10.14)$$

In his study, Bark suggests that the best correlation was found with the highest water velocities and that the influence of gas content in the range $0.4 < \alpha/\alpha_s < 0.7$ was not particularly great. Clearly, however, if this were to be extended to too high a value, then the high-frequency noise would be damped by the gas bubbles. This type of effect was demonstrated by van der Kooij (Reference 8). From Figure 10.12 it is seen that the spectrum shape is similar in both model and full scale, although certain deviations will be noted in the frequency scaling, which can be attributed to wave reflection at the hull or to differences in the cavitation scaling assumptions.

If model tests cannot be undertaken or contemplated, for whatever reason, it is still possible to make estimates of the propeller noise based on previous measurements. This type of prediction is, however, not as accurate as that based on model tests, and it needs to be used with great care as the values derived are based on historical data, sometimes quite old, and therefore may not be strictly applicable. Typical of this type of method is data on surface ship radiated noise spectra made during the Second World War and reported in a compendium issue by the US Office of Scientific Research and Development in 1945. These measurements were based on results from American, British and Canadian ranges and the results converted into source levels at 1 m relative to 1 μPa using a process with an error bound of the order of 3 dB. This resulted in an expression for the noise level L_S at a given frequency being defined by the relationship

$$L_S = L'_S + 20(1 - \log f) \qquad 100\,\text{Hz} < f < 10\,\text{kHz} \quad (10.15)$$

where L'_S is the overall level measured in the band from 100 Hz to 10 kHz and f is the frequency in Hz.

Subsequent measurements made after the war on a variety of cargo vessels and tankers showed that deviations in the overall level L'_S occurred throughout much of the spectrum of the order of 1–3 dB. Reanalysis of the original measurements by Ross (Reference 15), together with further more modern data, showed that the term L'_S could be expressed as a function of the propeller tip speed and blade number, and the use of the following expression for ships over 100 m in length was proposed:

$$L'_S \simeq 175 + 60 \log \frac{U_T}{25} + \log \frac{Z}{4} \quad (10.16)$$

where U_T is the tip speed in the range 15–50 m/s and Z is the number of cavitating blades. As a consequence equations (10.15) and (10.16) can be used to obtain an approximation for the noise spectrum referred to a source level at 1 m.

The control of the noise emitted from a propeller can be done either by attempting a measure of control by redesign at the propeller blade surfaces or, assuming no further design improvement is possible, by attempting acoustic suppression through the vessel. Either of the methods are applicable to the merchant service because they are concerned with self-noise in the majority of cases. In the naval applications the concern with radiated noise frequently dictates that the source of the noise is suppressed.

The suppression of the noise within the vessel is a matter of calculating the noise paths through the vessel and designing an appropriate suppression system: as such this aspect lies outside the scope of this text and

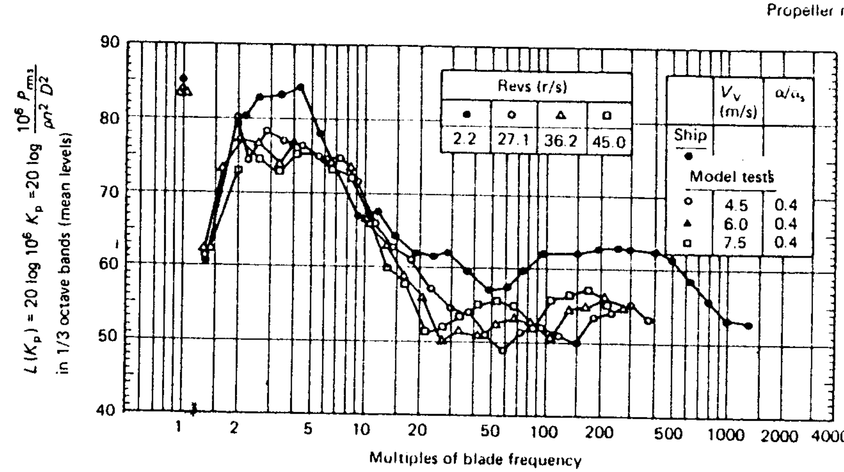

Figure 10.12 Non-dimensional noise presented as $L(K_p)$ in 1/3-octave bands (mean RMS levels). Comparison of full-scale data (filled symbols) with model data at three water velocities (open symbols) (Reproduced from Reference 14, with permission)

reference should be made to documents such as References 16 and 17. Where it is required that the noise be suppressed at source, this can be achieved by the consideration of any one or a combination of the following changes:

1. re-design of the hull form to improve the wake field;
2. change in radial distribution of skew;
3. change in radial pitch distribution;
4. adjustment of the general section profiles;
5. changes to the leading edge and/or trailing edge geometry;
6. changes to the section chord lengths.

10.5 Transverse propulsion unit noise

Transverse propulsion units are recognized as a major source of noise when they are in use for docking manoeuvres. A unit of this type, as a source of noise, is integrated into the hull structure rather than having a fluid medium between it and the hull surface as in the case of the propeller. In Chapter 14 the design of transverse propulsion units is discussed in some detail; however, the prediction of the likely levels of noise from these units is considered here.

A noise prediction method for controllable pitch units developed by the Institute of Applied Physics, Delft (Reference 18) is based on a large number of measurements on board different types of ships. In essence the noise emitted by the transverse propulsion unit is defined as

$$L_p(P_B, \Delta\theta, L/D, \mathscr{L}) = L_{p0}(P_B, \mathscr{L}_0) - L_{p\Delta}(\Delta\theta, L/D, \Delta\mathscr{L}) \quad (10.17)$$

where L_p = level of noise predicted at the point of interest (dBA);
L_{p0} = base level of noise at full power (P_B) in a standard cabin located near the thruster on the tanktop ($\mathscr{L}_0$);
$L_{p\Delta}$ = is the change of noise level due to part load or pitch ($\Delta\theta$), tunnel length diameter ratio (L/D) and position in ship ($\Delta\mathscr{L}$) as defined by deck (D_K) or frame number (F_r).

From a regression analysis based on the results of Reference 18 it was found that the base level of noise in equation (10.17) can be defined by the following relationship:

$$L_{p0}(P_B, \mathscr{L}_0) = 108.013 - 7.074K + 10.029K^2 + (24.058 - 4.689K + 0.615K^2) \times \log_{10}(P_B) \quad (10.17a)$$

where K is the tunnel centre line immersion ratio I/D with K in the range $1 < K < 3$.
P_B is the maximum continuous rating of the unit.

With regard to the change in noise level, $L_{p\Delta}$ can thus be defined as

$$L_{p\Delta}(\Delta\theta, L/D, \Delta\mathscr{L}) = L_p(\Delta\theta) + L_p(L/D) + L_p(\Delta\mathscr{L}) \quad (10.17b)$$

in which

$$L_p(\Delta\theta) = 26.775 - 13.387\log_{10}(\Delta P_B)$$
$$L_p(L/D) = -4.393 + 14.593\log_{10}(L/D)$$

and

$$L_p(\Delta\mathscr{S}) = 10\exp[0.904827 + 0.968977\log_{10}(D_K) - 0.348142(\log_{10}(D_K))^2] + 10\exp[-0.222330 - 0.126009(D_K) + 0.007657(D_K)^2]F_r$$

where ΔP_B = percentage MCR at which the unit is working
L/D is in the range $1 < L/D < 10$
D_K is in the range $1 < D_K < 5$ ($D_K = 0$ = tank-top)
Fr is in the range $1 < Fr < 50$.

Clearly in using a formula of the type described by equation (10.17), care needs to be exercised, particularly in respect of the absolute accuracy; however, the relationship does provide guidance as to the noise levels that can be expected.

10.6 Measurement of radiated noise

The measurement of the radiated noise is an important aspect of the trials of surface warships and submarines in the context of sonar detection and torpedo navigation systems. Furthermore, such trials form an important stage in the development of future designs of vessels. In addition to warships, certain specialist vessels such as research ships also have a radiated noise control requirement, and so benefit from noise emission trials.

Radiated noise measurements are conducted on noise ranges especially constructed for the purpose. For the purposes of the measurement two hydrophones should be used: one directly under the track of the vessel and another a distance to one side of the track – not less than 100 m from the track. Water depth is important and the hydrophone located on the vessel's track should not be at a depth of less than 20 m, and if the water depth lies between 20 m and 60 m then it should be planted on the bottom. For regions where the depth is greater than 60 m, the hydrophone should be located at a depth from the surface of one-third of the water depth. Furthermore, the trial noise ranges must be selected so that the acoustic background levels are well below the likely levels of the quietest machinery to be evaluated and the level of bottom reflection is insignificant.

The purpose of the two hydrophones is different. The one residing on the track of the vessel is primarily intended for the detailed study of the noise spectra over the frequency range 10–1200 Hz, whereas the beam hydrophone looks at the wider frequency range of 10–80 000 Hz in connection with sonar detection and torpedo acquisition risk. The performance characteristics of the hydrophones are particularly important and reference should be made to agreed codes of practice: Reference 19 details the standardization agreement of NATO for these purposes and also for the conduct of the trials.

For the purposes of these trials, as in the case of normal power absorption trials – Chapter 16, the vessel needs to be maintained at steady conditions with the minimum use of helm. Records of nominal speed, actual speed, main engine and propeller shaft speeds, propeller pitch, vibration characteristics and so on, need to be maintained during and prior to the trials to establish cavitation inception speeds of the propulsors. Accurate shaft rotational speeds and vibration spectra of the more important main and auxiliary items of machinery are also important measurements to be recorded. Where large changes in operating draught occur the vessel should also be ranged in at least the extreme operating conditions. Additionally it is also useful to measure, by means of over-side measurements, the noise spectra from the vessel when the ship is moored between buoys.

References and further reading

1. Lovett, J. *Acoust. Soc. Am.* **63**, 1978.
2. *Code on Noise Levels on Board Ships*. International Maritime Organisation, 1981.
3. Flising, A. Noise reduction in ships. *Trans. I.Mar.E.*, 1978.
4. Wenz, J. *Acoust. Soc. Am.* **34**, 1962.
5. Perrone, I. *Acoust. Soc. Am.* **46**, 1969.
6. Jenkins, C.J. Optimising propellers for noise. *Adv. in Underwater Tech., Ocean Science and Offshore Eng.*, **15**, Tech. Common to Aero and Marine Engineering 1988.
7. Fitzpatrick, H.M., Strasberg, M. Hydrodynamic sources of sound. *Proc. 1st Symposium on Naval Hydrodynamics*, Washington DC, September, 1956.
8. Kooij, J. van der, Sound generation by bubble cavitation on ship model propellers; the effects of leading edge roughness. *Proc. 2nd Int. Symposium on Cavitation and Multiphase Flow Noise*, ASME, December, 1986.
9. Arakeri, V.H., Shanmuganthan, V. On the evidence for the effect of bubble interference on cavitation noise. *J. Flutd Mechanics*, **159**, 1985.
10. Sunnersjö, S. Propeller noise prediction, *SSPA Highlights* 2, 1986.
11. Baiter, H.J. Aspects of cavitation noise, *High Powered Propulsion of Large Ships Symposium*, NSMB, Wageningen, 1974.
12. Strasberg, M. Propeller cavitation noise after 35 years of study. *Symposium of Noise and Fluids Eng, Proc ASME*, Atlanta.
13. Blake, W.K., Sevik, M.M. Recent developments in cavitation noise research. *Int. Symp. on Cavitation Noise*, ASME, November, 1982.

14. Bark, G. Prediction of Propeller Cavitation Noise from Model Tests and its Comparison with Full Scale Data. SSPA Report No. 103, 1986.
15. Ross, D. *Mechanics of Underwater Noise*, Pergamon Press, Oxford, 1976.
16. *Ship Design Manual – Noise*, BSRA, 1982.
17. Morrow, R.T. Noise Design Methods for Ships, *Trans R.I.N.A.*, Paper No 7, Spring Meeting, 1988.
18. Dekker, N. *Lips Newsletters*, March, 1987.
19. Standards for Use When Measuring and Reporting Radiated Noise Characteristics of Surface Ships, Submarines, Helicopters, etc. in Relation to Sonar Detection and Torpedo Acquisition Risk. NATO, STANAG No. 1136, November, 1984.
20. Blake, W.K. *Aero-Hydroacoustics for Ships*, Vols I and II. DTNSRDC. Rep. No. 84/010. June, 1984.
21. Baiter, H.J. Advanced views of cavitation noise. *Int. Symp. on Propulsors and Cavitation*, Hamburg, 1992.
22. Brüel, Kjaer. *Noise Pocket Handbook*.
23. Oossanen, P. van. Calculation of Performance and Cavitation Characteristics of Propellers Including Effects of Non-uniform Flow and Viscosity. Publ. No. 457, 1974.

11 Propeller–ship interaction

Contents

The propeller and ship interact in a variety of ways. This interaction is effected either through the coupling between the shafting system and the vessel or via pressure pulses transmitted through the water from the propeller to the hull surface. The interaction forces and moments can be considered to comprise both a constant and a fluctuating component. The constant components of the interaction originate from attributes like propeller weight, inertia and the mean wake field, whilst the fluctuating interactions derives principally from the variations in the wake field generated by the ship and within which the propeller has to operate. The main exception to the wake field being the source of the fluctuating interaction is where significant propeller out-of-balance forces and moments are present.

For the convenience of discussion the propeller–ship interaction can be considered in two separate categories. The first consists of the forces and moments transmitted through the shafting system, frequently termed, somewhat loosely, 'bearing forces', and the second consists of the forces experienced by the ship that are transmitted through the water in the form of pressure pulses; these being termed 'hydrodynamic forces'. These two classes of interaction will, therefore, be considered separately as follows.

11.1 Bearing forces

The loadings experienced by the vessel which come under the heading of bearing forces are listed under generalized headings in Table 11.1. It will be seen that they form a series of mechanical and hydrodynamically based forces and moments, all of which are either reacted at the bearings of the shafting system or change the vibratory properties of the shafting system in some way: for example, by altering the inertia or mass of the system. In the case of bearing reactions, the propeller generated forces and moments are supported by the lubrication film in the bearings, which itself is supported by the mechanical structure of the bearings and their seatings. As a consequence, in the analysis of marine shafting systems it is important also to recognize that, in addition to the influence of the propeller, the stiffness and damping of the lubrication film in the bearings can have important effects in terms of shafting response (Reference 1).

11.1.1 Propeller weight

The weight of a propeller requires to be calculated for each marine installation and is usually presented by manufacturers in terms of its dry weight. The dry weight, as its name implies, is the weight of the propeller in air, whilst the weight reacted by the shafting when the vessel is afloat is somewhat less, due to the Archemedean upthrust resulting from the displacement of the water by the volume of the propeller. Hence the effective weight of the propeller experienced by the ship's tail shaft is

Table 11.1 Propeller bearing forces

Propeller weight and centre of gravity
Dry propeller inertia
Added mass, inertia and damping
Propeller forces and moments
Out-of-balance forces and moments

$$W_E = W_D - U \tag{11.1}$$

where W_E is the effective propeller weight
W_D is the weight of the propeller in air
U is the Archemedean upthrust.

The dry weight of the propeller W_D, which represents a constant downward force by its nature unless any out of balance occurs, is calculated from the propeller detailed geometry. This calculation is carried out in two parts; first the blade weight including an allowance for fillets, and in the case of a controllable pitch propeller the blade palm also, and secondly the calculation of the weight of the propeller boss or hub.

The blade weight calculation is essentially performed by means of a double integration over the blade form. The first integration evaluates the area of each helicoidal section by integration of the section thickness distribution over the chord length. Hence for each helical section the area of the section is given by

$$A_x = c \int_0^1 t(x_c)\, dx_c \tag{11.2}$$

where x_c is the non-dimensional chordal length
$t(x_c)$ is the section thickness at each chordal location
c is the section chord length
A_x is the section area at the radial position $x = r/R$.

This integration can most conveniently be accomplished in practice by a Simpson's numerical integration over about 11 ordinates, as shown in Figure 11.1. Whilst this procedure will give an adequate estimate of the section areas for most detailed purposes, it is often useful to be able to bypass this stage of the calculation for quick estimates. This can be done by defining an area coefficient C_A which derives from equation (11.2) as follows:

$$C_A = \frac{A_x}{c t_{max}} \tag{11.3}$$

where t_{max} is the section maximum thickness.

The area coefficient is the ratio of the section area to the rectangle defined by the chord length and section maximum thickness. Table 11.2 gives a typical set of C_A values for fixed and controllable pitch propellers which may be used for estimates of the section area A_x using equation (11.3).

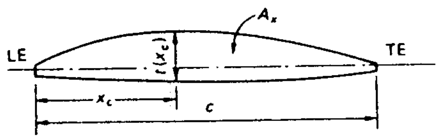

x_c	$t(x_c)$	Simp. mult. (SM)	SM × $t(x_c)$
0.0	t_{LE}	1/2	$t_{LE}/2$
0.1	$t_{0.1c}$	2	$2t_{0.1c}$
0.2	$t_{0.2c}$	1	$t_{0.2c}$
0.3	$t_{0.3c}$	2	$2t_{0.3c}$
.	.	.	.
.	.	.	.
0.9	$t_{0.9c}$	2	$2t_{0.9c}$
1.0	t_{TE}	1/2	$t_{TE/2}$
		Σ_0	

$$A_x = \frac{0.2c\,\Sigma_0}{3}$$

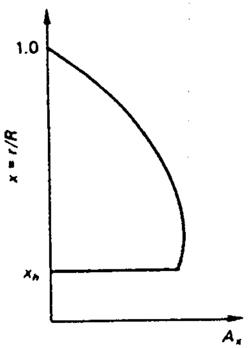

x	A_x	SM	SM × A_x	1st moment arm	SM × A_x × 1st. Mt. A
1.0	$A_{1.0}$	1/2	$A_{1.0}/2$	0	0
x_2	A_{x2}	2	$2A_{x2}$	1	$2A_{x2}$
x_3	A_{x3}	1	A_{x3}	2	$2A_{x3}$
x_4	A_{x4}	2	$2A_{x4}$	3	$6A_{x4}$
.	.	.	.	.	.
.	.	.	.	.	.
.	.	.	.	.	.
x_{10}	A_{x10}	2	$2A_{x10}$	9	$18A_{x10}$
x_h	A_{xh}	1/2	$A_{xh}/2$	10	$5A_{xh}$
		Σ_1		Σ_2	

Blade volume $V' = \dfrac{(R - r_h)\,\Sigma_1}{15}$

Posn of centroid from tip $= \dfrac{\Sigma_2 (R - r_h)}{10\Sigma_1} = x_{g_t}$

Posn of centroid from shaft $C_L = R - x_{g_t} = x_{g_o}$

Figure 11.1 Calculation of blade volume and centroid

Table 11.2 Approximate section area coefficient values

Non-dimensional radius $x = r/R$	*Area coefficient* C_A	
	Fixed pitch	*Controllable pitch*
0.95	0.78	0.78
0.90	0.74	0.74
0.80	0.72	0.72
0.70	0.71	0.71
0.60	0.71	0.71
0.50	0.71	0.71
0.40	0.70	Fair to 0.8 at hub radius
0.30	0.70	
0.20	0.69	

The second integration to be performed is the radial quadrature of the section areas A_x between the boss, or hub radius, and the propeller tip. This integration gives the blade volume for conventional blade forms as follows:

$$V' = \int_{r_h}^{R} A_x \, dr \qquad (11.4)$$

Again this integration can best be performed numerically using a Simpson's procedure as shown in Figure 11.1. Additionally the radial location of the centre of gravity of the blade can also be estimated for conventional blades by the incorporation of a series of moment arms, also shown in Figure 11.1.

For non-conventional blade forms it is advisable to evaluate these parameters by means of higher-order geometric definition and interpolation coupled with numerical integration procedures.

The blade volume V' calculated from equation (11.4) needs to be corrected for the additional volume of the blade fillets and a factor of the order of 2–5% would be reasonable for most cases. The weight of the blades can then be determined from

$$W_b = \varrho_m Z V \qquad (11.5)$$

where Z is the number of blades;
ϱ_m is the material density;
V is the volume of one blade corrected for the fillets.

For the controllable pitch propeller the blade weight W_b is further corrected for the weight of the blade palm, the evaluation of which is dependent upon the specific geometry of the palm. The dry propeller weight W_D is the sum of the blade weights and the boss or hub weight. In the case of the fixed pitch propeller the boss weight can normally be best calculated from approximating the boss form by a series of concentric annular cylinders or by the first theorem of Guldemus (i.e. volume = area times the distance travelled by its centroid). For the controllable pitch propeller the calculation of the hub weight is a far more complex matter since it involves the computation of the weights of the various internal and external components of the hub and the oil present in the hub: thus each hub has to be treated on its own particular merits.

The resulting dry weight of the propeller W_D is then given by

$$W_D = W_b + W_H \qquad (11.6)$$

where W_H is the boss or hub weight.

The Archimedean upthrust U is readily calculated for the blades and the boss of a fixed pitch propeller as

$$U = \frac{\varrho}{\varrho_m} W_D$$

where ϱ is the density of the water and it is assumed that the boss is a homogeneous solid mass, such as might be experienced with an oil injection fitted propeller, in contrast to a conventional key fitted boss with a lightning chamber. Hence from equation (11.1) the effective weight W_E of the propeller is given by

$$W_e = W_D\left[1 - \frac{\varrho}{\varrho_m}\right] \qquad (11.7)$$

Since for sea water and nickel aluminium bronze the ratio ϱ/ϱ_m is about 0.137, it can be seen that the upthrust is about one-seventh of the dry propeller weight.

In the case of the controllable pitch propeller equation (11.7) does not apply since the hub weight W_H in equation (11.6) is the sum of the internal weights and not derived from a homogeneous mass; similarly for the fixed pitch propeller with the non-homogeneous boss. As a consequence the upthrust derives from the following rewrite of the upthrust equation:

$$U = \frac{\varrho}{\varrho_m} W_B + \varrho V_H$$

where V_H is the external volume of the propeller hub.

11.1.2 Dry propeller inertia

The evaluation of the dry propeller inertia is in effect an extension of the calculation procedure outlined in Figure 11.1. At its most fundamental the mechanical inertia is the sum of all of the elemental masses in the propeller multiplied by the square of their radii of gyration. This, however, is not a particularly helpful definition in calculating the inertia of a propeller.

For many practical purposes it is sufficient for conventional propellers to extend the table shown by Figure 11.1 to that shown by Table 11.3. From this Table the moment of inertia of a blade can be estimated about the blade tip from the following equation:

$$I_{tip} = \frac{2}{3}\Sigma_3\left(\frac{R - r_h}{10}\right)^3$$

and by using the parallel axes theorem of applied

Table 11.3 Calculation of moment of inertia of a blade

x	A_x	*SM*	A_x × *SM*	*1st moment arm*	A_x × *SM* × *1st M.A.*	*2nd M.A.*	A_x × *SM* × *2nd M.A.*
1.0	$A_{1.0}$	1/2	$A_{1.0/0.5}$	0	0	0	0
x_2	A_{x_2}	2	$2A_{x_2}$	1	$2A_{x_2}$	1	$2A_{x_2}$
x_3	A_{x_3}	1	A_{x_3}	2	$2A_{x_3}$	2	$4A_{x_3}$
x_4	A_{x_4}	2	$2A_{x_4}$	3	$6A_{x_4}$	3	$18A_{x_4}$
x_5	A_{x_5}	1	A_{x_5}	4	$4A_{x_5}$	4	$16A_{x_5}$
x_6	A_{x_6}	2	$2A_{x_6}$	5	$10A_{x_6}$	5	$50A_{x_6}$
x_7	A_{x_7}	1	A_{x_7}	6	$6A_{x_7}$	6	$36A_{x_7}$
x_8	A_{x_8}	2	$2A_{x_8}$	7	$14A_{x_8}$	7	$98A_{x_8}$
x_9	A_{x_9}	1	A_{x_9}	8	$8A_{x_9}$	8	$64A_{x_9}$
x_{10}	$A_{x_{10}}$	2	$2A_{x_{10}}$	9	$18A_{x_{10}}$	9	$162A_{x_{10}}$
x_h	A_{x_h}	1/2	$A_{x_h/0.5}$	10	$5A_{x_h}$	10	$50A_{x_h}$
		Σ_1 =		Σ_2 =		Σ_3 =	

mechanics the moment of inertia of the blade can be deduced about the shaft centre line as

$$I_{OX} = \varrho_m k \left[I_{Tip} - \frac{2}{3} \sum_1 (R - r_h)\{l_{gt}^2 - l_{go}^2\} \right] \quad (11.8)$$

where ϱ_m is the density of the material
l_{gt} is the distance of the centroid from the blade tip
l_{go} is the distance of the centroid from the shaft centre line
k is the allowance for the fillets.

For a fixed pitch propeller, the estimation of the boss inertia is relatively straightforward, since it can be approximated by a series of concentric cylinders to derive the inertia I_H about the shaft centre line. In the case of the controllable pitch propeller hub, the contribution of each component of I_H has to be estimated separately. When this has been done the dry moment of inertia of the propeller can be found as follows:

$$I_O = I_H + ZI_{OX} \quad (11.9)$$

11.1.3 Added mass, inertia and damping

When a propeller is immersed in water the effective mass and inertia characteristics of the propeller when vibrating as part of a shafting system change due to the presence of water around the blades. In addition, there is also a damping term to consider deriving from the propeller's vibration in water. This mode of vibration considers the global properties of the propeller as a component of the line shafting, and so is a vibratory behaviour distinct from the individual vibration of the blades which is discussed separately in Chapter 20.

The global vibrational characteristics of a propeller are governed by two hydrodynamic effects. The first is that the propeller is excited by variations of hydrodynamic loading due to its operation in a non-uniform wake field. The second is a reaction loading caused by the vibrational behaviour of the propeller, which introduces a variation in the section angle of attack, which in turn produces the hydrodynamic reaction load. Now provided the variations in angle of attack are small, the vibratory loading can be considered to vary linearly, and the principle of superposition applied, which means that independent evaluations of the excitation load and reaction load are possible. As a consequence, to derive the excitation load caused by a propeller working in a wake field in the absence of any vibrational motion, only the steady state rotation of the propeller is considered. To derive the reaction loading the propeller is considered to be a rigid body vibrating in a homogeneous steady flow. Since the forces and moments generated by a vibrating propeller are assumed to vary linearly with the magnitude of the vibratory motion the forces and moments can be determined per unit motion, and so are termed propeller coefficients, whose magnitude can be determined either by calculation from lifting surface or vortex lattice methods or by experiment.

In general terms a propeller vibrates in the six rigid body modes defined in Figure 11.2, where δ_i and ϕ_i refer to the displacements and rotations respectively. Assuming that the propeller vibrates as a rigid body and operates in a non-homogeneous wake field the consequent vibratory component of lift gives rise to forces F_i and moments Q_i about the Cartesian reference frame. Now as the propeller is vibrating in water, it experiences the additional hydrodynamic force and moment loadings f_i and q_i due to its oscillating motion: these additional terms give rise to the added mass and damping coefficients. Because of the linearizing assumption, these forces and moments can be considered as deriving from the propeller's vibratory motion in a uniform wake field, and the equation of motion for the vibrating propeller can be written as

$$M\ddot{\mathbf{x}} = \mathbf{f}_e + \mathbf{f}_H + \mathbf{f}_S \quad (11.10)$$

where $\mathbf{x}$, $\mathbf{f}_e$, $\mathbf{f}_H$ and $\mathbf{f}_S$ are the displacement, excitation, additional hydrodynamic force and the external excitation (e.g. shaft forces and moments from the engine and transmission) vectors respectively given by

$$\mathbf{x} = [\delta_x, \delta_y, \delta_z, \phi_x, \phi_y, \phi_z]^T$$
$$\mathbf{f}_e = [F_x, F_y, F_z, Q_x, Q_y, Q_z]^T$$
$$\mathbf{f}_H = [f_x, f_y, f_z, q_x, q_y, q_z]^T$$

and the propeller mass matrix M is the diagonal matrix

$$M = \begin{bmatrix} m & 0 & 0 & 0 & 0 & 0 \\ 0 & m & 0 & 0 & 0 & 0 \\ 0 & 0 & m & 0 & 0 & 0 \\ 0 & 0 & 0 & I_{xx} & 0 & 0 \\ 0 & 0 & 0 & 0 & I_{yy} & 0 \\ 0 & 0 & 0 & 0 & 0 & I_{zz} \end{bmatrix}$$

in which $I_{yy} = I_{zz}$ since they are the diametral mass moments of inertia, I_{xx} is the polar moment about the shaft axis and m the mass of the propeller.

Now the additional hydrodynamic force vector $\mathbf{f}_H$ depends upon the displacements, velocities and accelerations of the propeller, and so can be represented by the relationship from classical vibration theory as

$$\mathbf{f}_H = -M_a\ddot{\mathbf{x}} - C_p\dot{\mathbf{x}} - K_p\mathbf{x} \quad (11.11)$$

in which the matrices M_a and C_p are the added mass and damping matrices respectively and K_p is a stiffness matrix depending upon the immersion of the propeller. If the propeller is fully immersed, then the matrix $K_p = 0$ and need not be considered further: this would

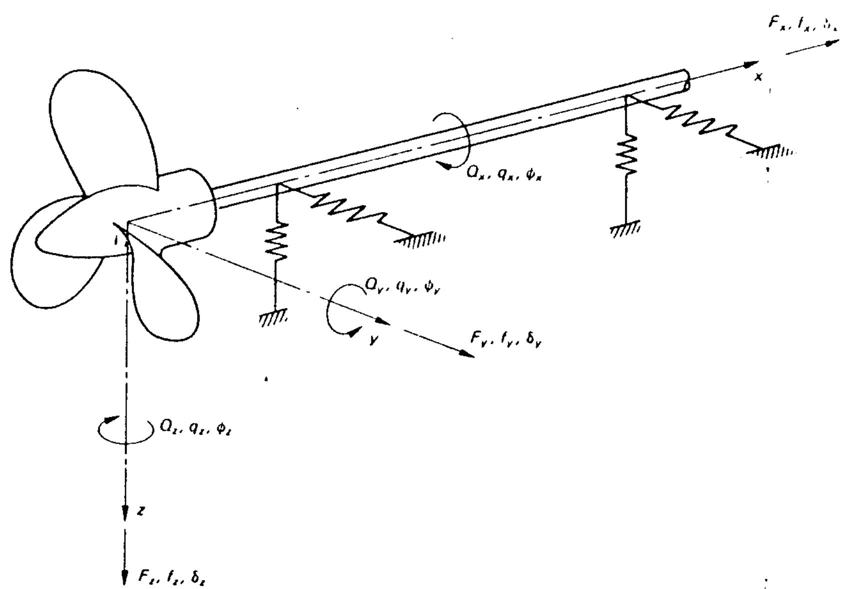

Figure 11.2 Propulsion shafting vibration parameters

not be the case, for example, with a surface piercing propeller. As a consequence, equation (11.11) can be simplified to

$$\mathbf{f}_H = -M_a\ddot{\mathbf{x}} - C_p\dot{\mathbf{x}} \quad (11.11(a))$$

Now by combining equations (11.11(a)) and (11.10) the resulting equation of motion for the propeller is derived:

$$[M + M_a]\ddot{\mathbf{x}} + C_p\dot{\mathbf{x}} - \mathbf{f}_s = \mathbf{f}_e \quad (11.12)$$

The forms of the matrices M_a and C_p are identical, each having a full leading diagonal of linear and rotational terms with a set of non-diagonal coupling terms. The added mass matrix has the form

$$M_a = \begin{bmatrix} m_{11} & 0 & 0 & m_{41} & 0 & 0 \\ 0 & m_{22} & -m_{32} & 0 & m_{52} & -m_{62} \\ 0 & m_{32} & m_{22} & 0 & m_{62} & m_{52} \\ m_{41} & 0 & 0 & m_{44} & 0 & 0 \\ 0 & m_{52} & -m_{62} & 0 & m_{55} & -m_{65} \\ 0 & m_{62} & m_{52} & 0 & m_{65} & m_{55} \end{bmatrix} \quad (11.13)$$

From this matrix it can be seen that several of the terms, for example m_{22} and m_{33}, have identical values, and hence this represents the simplest form of interactions between orthogonal motions. The matrix, as can be seen, is symmetrical, with the exception of four sign changes which result from the 'handedness' of the propeller. An alternative form of the matrix in equation (11.13) which demonstrates the physical meaning of the terms in relation to Figure 11.2 can be seen in equation (11.13(a)). In addition the physical correspondence of the terms is also revealed by this comparison:

$$M_a = \begin{bmatrix} F_x/\ddot{\delta}_x & 0 & 0 & F_x/\ddot{\phi}_x & 0 & 0 \\ 0 & F_y/\ddot{\delta}_y & -F_y/\ddot{\delta}_z & 0 & F_y/\ddot{\phi}_y & F_y/\ddot{\phi}_z \\ 0 & F_z/\ddot{\delta}_y & F_z/\ddot{\delta}_z & 0 & F_z/\ddot{\phi}_y & F_z/\ddot{\phi}_z \\ M_x/\ddot{\delta}_x & 0 & 0 & M_x/\ddot{\phi}_x & 0 & 0 \\ 0 & M_y/\ddot{\delta}_y & -M_y/\ddot{\delta}_z & 0 & M_y/\ddot{\phi}_y & -M_y/\ddot{\phi}_z \\ 0 & M_z/\ddot{\delta}_y & M_z/\ddot{\delta}_z & 0 & M_z/\ddot{\phi}_y & M_z/\ddot{\phi}_z \end{bmatrix} \quad (11.13(a))$$

Similarly for the damping matrix C_p the same comparison can be made as follows:

$$C_p = \begin{bmatrix} c_{11} & 0 & 0 & c_{41} & 0 & 0 \\ 0 & c_{22} & -c_{32} & 0 & c_{52} & -c_{62} \\ 0 & c_{32} & c_{22} & 0 & c_{62} & c_{52} \\ c_{41} & 0 & 0 & c_{44} & 0 & 0 \\ 0 & c_{52} & -c_{62} & 0 & c_{55} & -c_{65} \\ 0 & c_{62} & c_{52} & 0 & c_{65} & c_{55} \end{bmatrix}$$

$$= \begin{bmatrix} F_x/\dot{\delta}_x & 0 & 0 & F_x/\dot{\phi}_x & 0 & 0 \\ 0 & F_y/\dot{\delta}_y & -F_y/\dot{\delta}_z & 0 & F_y/\dot{\phi}_y & -F_y/\dot{\phi}_z \\ 0 & F_z/\dot{\delta}_y & F_z/\dot{\delta}_z & 0 & F_z/\dot{\phi}_y & F_z/\dot{\phi}_z \\ M_x/\dot{\delta}_x & 0 & 0 & M_x/\dot{\phi}_x & 0 & 0 \\ 0 & M_y/\dot{\delta}_y & M_y/\dot{\delta}_z & 0 & M_y/\dot{\phi}_y & M_y/\dot{\phi}_z \\ 0 & M_z/\dot{\delta}_y & M_z/\dot{\delta}_z & 0 & M_z/\dot{\phi}_y & M_z/\dot{\phi}_z \end{bmatrix} \quad (11.14)$$

When considering the vibratory characteristics of the propulsion shafting the coefficients in equations (11.13) and (11.14) need careful evaluation and it is insufficient to use arbitrary values, for example 0.25 times the polar dry inertia for m_{44} in equation (11.13), as many of these parameters vary considerably with differences in propeller design. Six added mass and damping terms are needed for coupled torsional axial motion, and these are

$$\{m_{11}, m_{44}, m_{41}, c_{11}, c_{44} \text{ and } c_{41}\}$$

Alternatively

$$\left\{\frac{F_x}{\ddot{\delta}_x}, \frac{M_x}{\ddot{\phi}_x}, \left(\frac{F_x}{\ddot{\phi}_x} = \frac{M_x}{\ddot{\delta}_x}\right), \frac{F_x}{\dot{\delta}_x}, \frac{M_x}{\dot{\phi}_x}, \left(\frac{F_x}{\dot{\phi}_x} = \frac{M_x}{\dot{\delta}_x}\right)\right\}$$

For lateral motion of the shafting system twelve terms are needed, which can be separated into two groups. The first group is where the forces and moments in the lateral directions are in the same direction as the motion:

$$\{m_{22}, m_{55}, m_{52}, c_{22}, c_{55} \text{ and } c_{52}\}$$

that is,

$$\left\{\left(\frac{F_y}{\ddot{\delta}_y} = \frac{F_z}{\ddot{\delta}_z}\right), \left(\frac{M_y}{\ddot{\phi}_y} = \frac{M_z}{\ddot{\phi}_z}\right), \left(\frac{F_y}{\ddot{\phi}_y} = \frac{F_z}{\ddot{\phi}_z} = \frac{M_y}{\ddot{\delta}_y} = \frac{M_z}{\ddot{\delta}_z}\right),\right.$$
$$\left(\frac{F_y}{\dot{\delta}_y} = \frac{F_z}{\dot{\delta}_z}\right), \left(\frac{M_y}{\dot{\phi}_y} = \frac{M_z}{\dot{\phi}_z}\right) \text{ and}$$
$$\left.\left(\frac{F_y}{\dot{\phi}_y} = \frac{F_z}{\dot{\phi}_z} = \frac{M_y}{\dot{\delta}_y} = \frac{M_z}{\dot{\delta}_z}\right)\right\}$$

and the second group has forces and moments in the lateral directions which are normal to the direction of motion:

$$\{m_{32}, m_{65}, m_{62}, c_{32}, c_{65} \text{ and } c_{62}\}$$

that is,

$$\left\{\left(\frac{F_y}{\ddot{\delta}_z} = \frac{F_z}{\ddot{\delta}_y}\right), \left(\frac{M_y}{\ddot{\phi}_z} = \frac{M_z}{\ddot{\phi}_y}\right), \left(\frac{F_y}{\ddot{\phi}_z} = \frac{F_z}{\ddot{\phi}_y} = \frac{M_y}{\ddot{\delta}_z} = \frac{M_z}{\ddot{\delta}_y}\right),\right.$$
$$\left(\frac{F_y}{\dot{\delta}_z} = \frac{F_z}{\dot{\delta}_y}\right), \left(\frac{M_y}{\dot{\phi}_z} = \frac{M_z}{\dot{\phi}_y}\right) \text{ and}$$
$$\left.\left(\frac{F_y}{\dot{\phi}_z} = \frac{F_z}{\dot{\phi}_y} = \frac{M_y}{\dot{\delta}_z} = \frac{M_z}{\dot{\delta}_y}\right)\right\}$$

In the past considerable research efforts have been devoted to determining some or all of these coefficients. In the early years, the added axial mass, polar entrained inertia and the corresponding damping coefficients were the prime candidates for study (i.e. m_{11}, m_{44}, c_{11} and c_{44}). However, in recent years all of the coefficients have been studied more easily due to the advent of modern analytical and computational capabilities. Whilst a knowledge of these components is a prerequisite for shafting system analysis, it must be emphasized that they should be applied in conjunction with the corresponding coefficients for the lubrication films in the bearings, particularly the stern tube bearing, as these are known to have a significant effect on the shaft vibration characteristics in certain circumstances.

Archer (Reference 2) in attempting to solve marine shafting vibration problems considered the question of torsional vibration damping coefficient, c_{44}. Archer derived an approximation based on the open water characteristics of the Wageningen B screw series as they were presented at that time. He argued that when torsional vibration is present the changes in rotational speed of the shaft are so rapid and the inertia of the ship so great that they can be regarded as taking place at constant advance speed. This implies that the propeller follows a law in which the torque Q and rotational speed n are connected by a law of the form $Q \propto n^r$, where $r > 2$. If such a relation is assumed to hold over the range of speed variation resulting from the torsional vibration of the propeller, then by differentiating at a constant speed of advance V_a

$$\left.\frac{\partial Q}{\partial \omega}\right|_{V_a = \text{const.}} = \frac{1}{2\pi} \left.\frac{\partial Q}{\partial n}\right|_{V_a = \text{const.}} = K$$

where K, the propeller damping coefficient, is a constant. Hence

$$K = \frac{1}{2\pi} \frac{\partial}{\partial n}(bn^r)$$

where b is a constant, and

$$K = a\frac{Q}{N}$$

where a is constant and equal to $9.55r$.

Now by taking $K_Q = f(J)$, Archer derived an expression for the index r as:

$$r = \left[2 - \frac{J(dK_Q/dJ)}{K_Q}\right]$$

Table 11.4 Derivation of Burrill blade form parameters for entrained inertia and mass

$x = r/R$	p	$\theta = \tan^{-1}(p/2\pi r)$	$(cx \sin\theta)^2$	SM	$(SM \times (cx \sin\theta)^2)$	$(c \cos\theta)^2$	SM	$(SM \times (c \cos\theta)^2)$
0.250	p_1	θ_1		1/2			1/2	
0.375	p_2	θ_2		2			2	
0.500	p_3	θ_3		1			1	
0.625	p_4	θ_4		2			2	
0.750	p_5	θ_5		1			1	
0.875	p_6	θ_6		2			2	
1.000	p_7	θ_7		1/2			1/2	
				$\sum_I =$			$= \sum_A =$	

which can be solved by appeal to the appropriate open water torque characteristic of the propeller under consideration. To this end, Archer gives a series of some nine diagrams to aid solution.

Lewis and Auslander (Reference 3) considered the longitudinal and torsional motions of a propeller, and as a result of conducting a series of experiments, supported by theory, derived a set of empirically based formulae for the entrained polar moment of inertia, the entrained axial mass both with and without rotational constraint, and a coupling inertia factor.

Burrill and Robson some two years later (Reference 4) again considered this problem and produced a method of analysis – again based on empirical relations, albeit supported by a background theory – which has found favour for many years in some areas of the propeller manufacturing and consultancy industry. The basis of the Burrill and Robson approach was the derivation of experimental coefficients for a series of some forty-nine 16-inch propellers which were subject to torsional and axial excitation. To apply this approach to an arbitrary propeller design Burrill generalized the procedure as shown in Table 11.4.

From which the entrained inertial I_e about the shaft axis, equivalent to the m_{44} term in equation (11.13), can be estimated as

$$I_e = \frac{\pi \varrho}{48} Z K_I R^3 \sum_I \quad (11.15)$$

Similarly, for the axial entrained mass m_a, equivalent to m_{11} in equation (11.13),

$$m_a = \frac{\pi \varrho}{48} Z K_A R \sum_A \quad (11.16)$$

From Table 11.4 it can be seen that the blade form parameters Σ_I and Σ_A are the result of two integrations radially along the blade. The empirical factors K_A and K_I are given in Table 11.5.

An analysis of the hydrodynamic coefficients based on unsteady propeller theory was undertaken by Schwanecke (Reference 5). This work resulted in the production of a set of calculation factors based on principal propeller dimensions such as blade area ratio, pitch ratio and blade number. The equations derived by Schwanecke are as follows:

Table 11.5 The Burrill and Robson K_A and K_I factors

$\frac{BAR}{Z}$	K_I	K_A
0.11	0.893	0.969
0.12	0.845	0.920
0.13	0.805	0.877
0.14	0.772	0.841
0.15	0.741	0.808
0.16	0.714	0.773
0.17	0.691	0.750
0.18	0.670	0.725
0.19	0.650	0.702
0.20	0.631	0.691
0.21	0.611	0.660
0.22	0.592	0.639
0.23	0.573	0.619
0.24	0.555	0.600
0.25	0.538	0.582
0.26	0.522	0.564
0.27	0.506	0.546
0.28	0.490	0.529
0.29	0.476	0.512
0.30	0.462	0.498
0.31	0.448	0.484
0.32	0.435	0.470
0.33	0.423	0.457
0.34	0.412	0.444
0.35	0.400	0.432
0.36	0.398	0.420

(A) *Added mass coefficients*

$$m_{11} = 0.2812 \frac{\pi \varrho D^3}{Z} \left(\frac{A_e}{A_o}\right)^2 \text{kg s}^2/\text{m}$$

$$m_{22} = m_{33} = 0.6363 \frac{\varrho D^3}{\pi Z} \left(\frac{P}{D}\right)^2 \left(\frac{A_e}{A_o}\right)^2 \text{kg s}^2/\text{m}$$

$$m_{44} = 0.0703 \frac{\varrho D^5}{\pi Z} \left(\frac{P}{D}\right)^2 \left(\frac{A_e}{A_o}\right)^2 \text{kp s}^2\,\text{m}$$

$$m_{55} = m_{66} = 0.0123 \frac{\pi \varrho D^5}{Z} \left(\frac{A_e}{A_o}\right)^2 \text{kp s}^2\,\text{m}$$

$$m_{41} = -0.1406\frac{\varrho D^4}{Z}\left(\frac{P}{D}\right)\left(\frac{A_e}{A_o}\right)^2 \text{kps}^2$$

$$m_{52} = 0.0703\frac{\varrho D^4}{Z}\left(\frac{P}{D}\right)\left(\frac{A_e}{A_o}\right)^2 \text{kps}^2$$

$$m_{62} = 0.0408\frac{\varrho D^4}{Z^2}\left(\frac{P}{D}\right)\left(\frac{A_e}{A_o}\right)^3 \text{kps}^2$$

$$m_{65} = 0.0030\frac{\pi\varrho D^5}{Z^2}\left(\frac{A_e}{A_o}\right)^3 \text{kps}^2\text{m}$$

(B) *Damping coefficients*

$$c_{11} = 0.0925\pi\varrho\omega D^3\left(\frac{A_e}{A_o}\right)\text{kps m}$$

$$c_{22} = c_{33} = 0.1536\frac{\varrho\omega D^2}{\pi}\left(\frac{P}{D}\right)^2\left(\frac{A_e}{A_o}\right)\text{kps m}$$

$$c_{44} = 0.0231\frac{\varrho\omega D^5}{\pi}\left(\frac{P}{D}\right)^2\left(\frac{A_e}{A_o}\right)\text{kps m}$$

$$c_{55} = c_{66} = 0.0053\pi\varrho\omega D^5\left(\frac{A_e}{A_o}\right)\text{kps m}$$

$$c_{41} = -0.0463\varrho\omega D^4\left(\frac{P}{D}\right)\left(\frac{A_e}{A_o}\right)\text{kps}$$

$$c_{52} = 0.0231\varrho\omega D^4\left(\frac{P}{D}\right)\left(\frac{A_e}{A_o}\right)\text{kps}$$

$$c_{62} = 0.0981\frac{\varrho\omega D^4}{Z}\left(\frac{P}{D}\right)\left(\frac{A_e}{A_o}\right)^2\text{kps}$$

$$c_{65} = 0.0183\frac{\pi\varrho\omega D^5}{Z}\left(\frac{A_e}{A_o}\right)^2\text{kps m}$$

$$c_{35} = 0.1128\frac{\varrho\omega D^4}{Z}\left(\frac{P}{D}\right)\left(\frac{A_e}{A_o}\right)^2\text{kps}$$

With regard to the damping coefficients, Schwanecke draws a distinction between the elements c_{26} and c_{35} which is in contrast to some other contemporary works.

The foregoing discussion relates specifically to fixed pitch propellers and the dependency on pitch is clearly evident in all of the formulations. Clearly, therefore, a controllable pitch propeller working at a reduced off-design pitch setting has a lower entrained inertia than when at design pitch. Van Gunsteren and Pronk (Reference 6) suggested a reduction, of the order of that shown in Table 11.6, based on results from a series of controllable pitch propellers.

Table 11.6 Typical reduction in entrained inertia at off-design pitch settings

Percentage of design pitch setting	0	20	40	60	80	100
Percentage of entrained polar moment (m_{44}) at design pitch	4	5	15	36	66	100

The provision of a reliable data base of either theoretical or experimental results has always been a problem in attempting to correlate the calculations of the elements of the matrices defined in equations (11.13) and (11.14) with experimental data. Experimental data, either at full or model scale, is difficult to obtain, and only limited data is available – notably the work of Burrill and Robson (Reference 4). Hylarides and van Gent (Reference 7), however, attempted to rectify this problem to some extent from the theoretical viewpoint by considering calculations based on a number of propellers from the Wageningen B Screw series. The calculations were based on unsteady lifting surface theory for four-bladed propellers of the series in order to derive the coefficients shown in Table 11.7. Examination of this table clearly shows the fallacy, noted earlier, of using fixed percentages in vibration calculations for rigorous shafting behaviour analysis purposes.

Parsons and Vorus (Reference 8) using the work of Hylarides and van Gent as basis, investigated the correlation that could be achieved by calculating the added mass and damping estimates from lifting surface and lifting line procedures. In addition they also examined the implications of changing the blade skew from the standard B Screw Series design, as well as that of changing the vibration frequency. Their work resulted in a series of regression based formula based on the Wageningen B Screw series geometry and suitable for initial design purposes. These regression equations, which are based on a lifting line formulation, have the form

$$\begin{Bmatrix} m_{ij} \\ c_{ij} \end{Bmatrix} = C_1 + C_2(A_E/A_O) + C_3(P/D) + C_4(A_E/A_O)^2 + C_5(P/D)^2 + C_6(A_E/A_O)(P/D) \quad (11.17)$$

The coefficients C_1 to C_6 are given in Tables 11.8 to 11.11 for the 4-, 5-, 6- and 7-bladed Wageningen B Series propellers respectively. The range of application of equation (11.17) is for expanded area ratios in the range 0.5 to 1.0 and pitch ratios in the range 0.6 to 1.2. Parsons and Vorus also developed a set of lifting surface corrections which can be applied to equation (11.17) to improve the accuracy of the estimate, and these are given by Table 11.12. In Table 11.12 the blade aspect ratio AR is given by

$$\text{AR} = \frac{0.22087Z}{A_E/A_O}$$

where Z is the blade number. The corrections given by Table 11.12 are introduced into equation (11.17) as follows:

$$\begin{Bmatrix} m_{ij} \\ c_{ij} \end{Bmatrix}_{\substack{\text{Lifting}\\\text{surface}}} = \begin{Bmatrix} m_{ij} \\ c_{ij} \end{Bmatrix}_{\text{eqn (11.7)}} \times LSC \quad (11.18)$$

Table 11.7 Dimensionless values of the propeller coefficients

Propeller type	B4-40-50	B4-40-80	B4-40-120	B4-70-50	B4-70-80	B4-70-120	B4-100-50	B4-100-80	B4-100-120
A_E/A_O	0.40	0.40	0.40	0.70	0.70	0.70	1.00	1.00	1.00
P/D	0.50	0.80	1.20	0.50	0.80	1.20	0.50	0.80	1.20
Axial vibrations									
F_x/δ_x	$-6.24\ 10^{-1}$	$-5.95\ 10^{-1}$	$-5.42\ 10^{-1}$	$-8.37\ 10^{-1}$	$-7.27\ 10^{-1}$	$-6.30\ 10^{-1}$	$-8.53\ 10^{-1}$	$-6.71\ 10^{-1}$	$6.12\ 10^{-1}$
$F_x/\ddot{\delta}_x$	$-2.91\ 10^{-2}$	$-2.74\ 10^{-2}$	$-2.31\ 10^{-2}$	$-8.37\ 10^{-2}$	$-7.34\ 10^{-2}$	$-6.01\ 10^{-2}$	$-1.34\ 10^{-1}$	$-1.18\ 10^{-1}$	$9.68\ 10^{-2}$
$F_x/\dot{\phi}_x$	$4.96\ 10^{-2}$	$7.58\ 10^{-2}$	$1.04\ 10^{-1}$	$6.66\ 10^{-2}$	$9.26\ 10^{-2}$	$1.20\ 10^{-1}$	$5.82\ 10^{-2}$	$8.54\ 10^{-2}$	$1.17\ 10^{-1}$
$F_x/\ddot{\phi}_x$	$2.31\ 10^{-3}$	$3.48\ 10^{-3}$	$4.42\ 10^{-3}$	$6.66\ 10^{-3}$	$9.34\ 10^{-3}$	$1.15\ 10^{-2}$	$1.07\ 10^{-2}$	$1.50\ 10^{-2}$	$1.85\ 10^{-2}$
$M_x/\dot{\delta}_x$	$4.96\ 10^{-2}$	$7.58\ 10^{-2}$	$1.04\ 10^{-1}$	$6.66\ 10^{-2}$	$9.26\ 10^{-2}$	$1.20\ 10^{-1}$	$5.82\ 10^{-2}$	$8.54\ 10^{-2}$	$1.17\ 10^{-1}$
$M_x/\ddot{\delta}_x$	$2.31\ 10^{-3}$	$3.48\ 10^{-3}$	$4.42\ 10^{-3}$	$6.66\ 10^{-3}$	$9.34\ 10^{-3}$	$1.15\ 10^{-2}$	$1.07\ 10^{-2}$	$1.50\ 10^{-2}$	$1.85\ 10^{-2}$
$M_x/\dot{\phi}_x$	$-3.95\ 10^{-3}$	$-9.65\ 10^{-3}$	$-1.98\ 10^{-2}$	$-5.30\ 10^{-3}$	$-1.18\ 10^{-2}$	$-2.30\ 10^{-2}$	$-4.63\ 10^{-3}$	$-1.09\ 10^{-2}$	$-2.23\ 10^{-2}$
$M_x/\ddot{\phi}_x$	$-1.84\ 10^{-4}$	$-4.43\ 10^{-4}$	$-8.44\ 10^{-4}$	$-5.30\ 10^{-4}$	$-1.19\ 10^{-3}$	$-2.19\ 10^{-3}$	$-8.48\ 10^{-4}$	$-1.91\ 10^{-3}$	$3.53\ 10^{-3}$
Transverse vibrations, loads and motions parallel									
$F_y/\dot{\delta}_y$	$-2.69\ 10^{-2}$	$-5.56\ 10^{-2}$	$-1.12\ 10^{-1}$	$-3.67\ 10^{-2}$	$-7.01\ 10^{-2}$	$-1.42\ 10^{-1}$	$-5.11\ 10^{-2}$	$-8.15\ 10^{-2}$	$-1.62\ 10^{-1}$
$F_y/\ddot{\delta}_y$	$-1.72\ 10^{-3}$	$-3.56\ 10^{-3}$	$-5.97\ 10^{-3}$	$-3.94\ 10^{-3}$	$-8.66\ 10^{-3}$	$-1.51\ 10^{-2}$	$-4.02\ 10^{-3}$	$-1.46\ 10^{-2}$	$2.57\ 10^{-2}$
$F_y/\dot{\phi}_y$	$-2.38\ 10^{-2}$	$-3.55\ 10^{-2}$	$-5.02\ 10^{-2}$	$-2.92\ 10^{-2}$	$-4.41\ 10^{-2}$	$-6.33\ 10^{-2}$	$-3.90\ 10^{-2}$	$-5.28\ 10^{-2}$	$7.31\ 10^{-2}$
$F_y/\ddot{\phi}_y$	$-1.35\ 10^{-3}$	$-1.93\ 10^{-3}$	$-2.33\ 10^{-3}$	$-3.04\ 10^{-3}$	$-4.67\ 10^{-3}$	$-5.89\ 10^{-3}$	$-4.95\ 10^{-3}$	$-7.89\ 10^{-3}$	$1.01\ 10^{-2}$
$M_y/\dot{\delta}_y$	$-2.60\ 10^{-2}$	$-3.64\ 10^{-2}$	$-5.06\ 10^{-2}$	$-3.18\ 10^{-2}$	$-4.40\ 10^{-2}$	$-6.28\ 10^{-2}$	$-4.36\ 10^{-2}$	$-5.23\ 10^{-2}$	$7.17\ 10^{-2}$
$M_y/\ddot{\delta}_y$	$1.31\ 10^{-3}$	$1.88\ 10^{-3}$	$2.28\ 10^{-3}$	$3.12\ 10^{-3}$	$4.64\ 10^{-3}$	$5.82\ 10^{-3}$	$5.06\ 10^{-3}$	$7.86\ 10^{-3}$	$9.97\ 10^{-3}$
$M_y/\dot{\phi}_y$	$3.51\ 10^{-2}$	$-3.26\ 10^{-2}$	$3.09\ 10^{-2}$	$3.88\ 10^{-2}$	$3.79\ 10^{-2}$	$3.71\ 10^{-2}$	$4.90\ 10^{-2}$	$4.44\ 10^{-2}$	$4.20\ 10^{-2}$
$M_y/\ddot{\phi}_y$	$-1.66\ 10^{-3}$	$-1.51\ 10^{-3}$	$-1.27\ 10^{-3}$	$-3.74\ 10^{-3}$	$-3.58\ 10^{-3}$	$-3.12\ 10^{-3}$	$-5.96\ 10^{-3}$	$-5.90\ 10^{-3}$	$5.21\ 10^{-3}$
Transverse vibrations, loads and motions mutually perpendicular									
$F_z/\dot{\delta}_y$	$2.65\ 10^{-3}$	$2.23\ 10^{-3}$	$2.97\ 10^{-3}$	$4.77\ 10^{-3}$	$9.99\ 10^{-4}$	$9.27\ 10^{-4}$	$1.77\ 10^{-2}$	$5.26\ 10^{-3}$	$2.30\ 10^{-3}$
$F_z/\ddot{\delta}_y$	$6.18\ 10^{-5}$	$-6.45\ 10^{-5}$	$-8.26\ 10^{-5}$	$2.96\ 10^{-4}$	$1.42\ 10^{-5}$	$1.81\ 10^{-6}$	$5.74\ 10^{-4}$	$5.50\ 10^{-5}$	$2.14\ 10^{-5}$
$F_z/\dot{\phi}_y$	$1.23\ 10^{-2}$	$1.24\ 10^{-2}$	$1.63\ 10^{-2}$	$1.62\ 10^{-2}$	$1.70\ 10^{-2}$	$2.76\ 10^{-2}$	$2.70\ 10^{-2}$	$2.52\ 10^{-2}$	$4.20\ 10^{-2}$
$F_z/\ddot{\phi}_y$	$4.19\ 10^{-4}$	$2.75\ 10^{-4}$	$7.45\ 10^{-5}$	$1.13\ 10^{-3}$	$8.79\ 10^{-4}$	$5.56\ 10^{-4}$	$1.80\ 10^{-3}$	$1.49\ 10^{-3}$	$1.05\ 10^{-3}$
$M_z/\dot{\delta}_y$	$-6.22\ 10^{-3}$	$-6.07\ 10^{-3}$	$-4.21\ 10^{-3}$	$-5.33\ 10^{-3}$	$-6.10\ 10^{-3}$	$-1.27\ 10^{-3}$	$-1.40\ 10^{-3}$	$-4.88\ 10^{-3}$	$3.71\ 10^{-3}$
$M_z/\ddot{\delta}_y$	$-4.79\ 10^{-4}$	$-5.27\ 10^{-4}$	$-4.91\ 10^{-4}$	$-9.11\ 10^{-4}$	$-1.06\ 10^{-3}$	$-1.01\ 10^{-3}$	$-1.41\ 10^{-3}$	$-1.67\ 10^{-3}$	$1.57\ 10^{-3}$
$M_z/\dot{\phi}_y$	$3.51\ 10^{-3}$	$2.64\ 10^{-3}$	$3.83\ 10^{-3}$	$6.09\ 10^{-3}$	$5.18\ 10^{-3}$	$9.44\ 10^{-3}$	$1.13\ 10^{-2}$	$8.91\ 10^{-3}$	$1.64\ 10^{-2}$
$M_z/\ddot{\phi}_y$	$-1.01\ 10^{-4}$	$-1.53\ 10^{-4}$	$-1.89\ 10^{-4}$	$6.19\ 10^{-6}$	$-1.53\ 10^{-4}$	$-2.52\ 10^{-4}$	$-1.74\ 10^{-5}$	$-1.99\ 10^{-4}$	$-3.37\ 10^{-4}$

11.1.4 Propeller forces and moments

The mean and fluctuating forces and moments produced by a propeller working in the ship's wake field have to be reacted at the bearings, and therefore form a substantial contribution to the bearing forces. In the early stages of design the main components of the force F_x and moment M_x (Figure 11.3) are calculated from open water propeller data assuming a mean wake fraction for the vessel. However, as the design progresses and more of the detailed propeller geometry and structure of the wake field emerges then more refined estimates must be made.

The effective thrust force of a propeller is seldom, if ever, directed along the shaft axis. This is due to the effects of the wake field and/or the shaft inclination relative to the flow; see Chapter 6. In general the line of action of the effective thrust force will be raised above the shaft axis as a direct result of the slower water velocities in the upper part of the propeller disc. Furthermore, due to the effects of the tangential velocity components, the effective thrust force is unlikely to lie on the plane of symmetry of the axial wake field. The thrust eccentricity $e_T(t)$ is the distance from the shaft centre-line to the point through which the effective thrust force acts. Thus it has two components, one in the thwart ship direction $e_{Ty}(t)$ and the other in the vertical direction $e_{Tz}(t)$ such that,

$$e_T^2(t) = e_{Ty}^2(t) + e_{Tz}^2(t) \quad (11.19)$$

Table 11.8 Regression equation coefficients for B4 propellers ($E \pm N = \times 10^{\pm N}$) (taken from Reference 8)

Parameter / Component	C_1	C_2	C_3	C_4	C_5	C_6
Torsional/axial						
m_{44}	0.30315E−2	−0.80782E−2	−0.40731E−2	0.34170E−2	0.43437E−3	0.99715E−2
m_{41}	0.12195E−2	0.17664E−1	−0.85938E−2	−0.23615E−1	0.94301E−2	−0.26146E−1
m_{11}	−0.62948E−1	0.17980	0.58719E−1	0.17684	−0.21439E−2	−0.15395
c_{44}	−0.35124E−1	0.81977E−1	0.32644E−1	−0.41863E−1	0.60813E−2	−0.37170E−1
c_{41}	0.13925	−0.48179	−0.14175	0.27711	−0.94311E−2	0.17407
c_{11}	0.32017	0.29375E+1	−0.90814	−0.19719E+1	0.53868	−0.65404
Lateral: parallel						
m_{55}	−0.26636E−2	0.61911E−2	0.26565E−2	0.77133E−2	−0.66326E−3	−0.40324E−2
m_{52}	−0.19644E−2	−0.47339E−2	0.45533E−2	0.89144E−2	−0.44606E−2	0.11823E−1
m_{22}	0.17699E−1	−0.59698E−1	−0.18823E−1	0.29066E−1	−0.33316E−2	0.73554E−1
c_{55}	−0.63518E−2	0.22851	−0.31365E−1	−0.14332	0.25084E−1	−0.49546E−1
c_{52}	−0.11690	0.36582	0.10076	−0.21326	0.18676E−3	−0.12515
c_{22}	−0.35968	0.87537	0.29734	−0.47961	0.14001E−1	−0.33732
Lateral: perpendicular						
m_{65}	0.12333E−3	0.35676E−2	−0.35561E−3	−0.36381E−2	0.65794E−3	−0.17943E−2
m_{62}	−0.17250E−2	0.64561E−2	0.19195E−2	−0.40546E−2	0.40439E−3	−0.47506E−2
m_{32}	−0.99403E−2	0.23315E−1	0.10895E−1	−0.11360E−1	−0.71528E−3	−0.15718E−1
c_{65}	0.59756E−1	−0.18982	−0.17653E−1	0.82400E−1	0.61804E−2	−0.80790E−2
c_{62}	0.78572E−1	−0.18627	−0.37105E−1	0.11053	0.17847E−1	−0.55900E−1
c_{32}	0.14397	−0.32322	−0.15348E−1	0.24992	0.14289E−1	−0.21254

Table 11.9 Regression equation coefficients for B5 propellers ($E \pm N = \times 10^{\pm N}$) (taken from Reference 8)

Parameter / Component	C_1	C_2	C_3	C_4	C_5	C_6
Torsional/axial						
m_{44}	0.27835E−2	−0.71650E−2	−0.37301E−2	0.30526E−2	0.46275E−3	0.85327E−2
m_{41}	−0.26829E−3	0.17208E−1	−0.55064E−2	−0.21012E−1	0.72960E−2	−0.22840E−1
m_{11}	−0.47372E−1	0.13499	0.43428E−1	0.15666	0.41444E−1	−0.12404
c_{44}	−0.30935E−1	0.69382E−1	0.27392E−1	−0.37293E−1	0.63542E−2	−0.21635E−1
c_{41}	0.14558	−0.44319	−0.17025	0.24558	0.14798E−1	0.12226
c_{11}	0.16202	0.30392E+1	−0.59068	−0.17372E+1	0.37998	−0.71363
Lateral: parallel						
m_{55}	−0.18541E−2	0.40694E−2	0.20342E−2	0.72761E−2	−0.47031E−3	−0.33269E−2
m_{52}	−0.20455E−3	−0.73445E−2	0.26857E−2	0.95299E−2	−0.34485E−2	0.10863E−1
m_{22}	0.17180E−1	−0.54519E−1	−0.17894E−1	0.27151E−1	−0.19451E−2	0.62180E−1
c_{55}	−0.25532E−2	0.20018	−0.22067E−1	−0.10971	0.18255E−1	−0.43517E−1
c_{52}	−0.98481E−1	0.28632	0.10154	−0.15975	−0.10484E−1	−0.79238E−1
c_{22}	−0.27180	0.61549	0.24132	−0.33370	0.10475E−1	−0.19101
Lateral: perpendicular						
m_{65}	−0.51073E−3	0.36044E−2	0.12804E−3	−0.30064E−2	0.25624E−3	−0.11174E−2
m_{62}	−0.18142E−2	0.56442E−2	0.15906E−2	−0.35420E−2	0.72381E−4	−0.27848E−2
m_{32}	−0.68895E−2	0.16524E−1	0.62244E−2	−0.87754E−2	−0.38255E−3	−0.82429E−2
c_{65}	0.33407E−1	−0.99682E−1	−0.68219E−2	0.22669E−1	0.56635E−2	−0.22639E−1
c_{62}	0.33507E−1	−0.66800E−1	−0.73992E−2	0.33112E−1	0.13061E−1	−0.80862E−1
c_{32}	0.15158E−1	−0.10109E−1	0.63232E−1	0.50161E−1	0.35720E−2	−0.27201

Table 11.10 Regression equation coefficients for B6 propellers ($E \pm N = \times 10^{\pm N}$) (taken from Reference 8)

Parameter / Component	C_1	C_2	C_3	C_4	C_5	C_6
Torsional/axial						
m_{44}	0.23732E−2	−0.62877E−2	−0.30606E−2	0.27478E−2	0.29060E−3	0.73650E−2
m_{41}	−0.17748E−2	0.14993E−1	−0.51316E−2	−0.18451E−1	0.64733E−2	−0.19096E−1
m_{11}	−0.39132E−1	0.10862	0.37308E−1	0.13359	−0.33222E−3	−0.10387
c_{44}	−0.27873E−1	0.61760E−1	0.23242E−1	−0.35004E−1	0.70046E−2	−0.11641E−1
c_{41}	0.14228	−0.41189	−0.1770	0.22644	0.26626E−1	0.83269E−1
c_{11}	0.11113	0.29831E+1	−0.44133	−0.15696E+1	0.28560	−0.66976
Lateral: parallel						
m_{55}	−0.16341E−2	0.33153E−2	0.19742E−2	0.64129E−2	−0.52004E−3	−0.29555E−2
m_{52}	−0.40692E−4	−0.68309E−2	0.24412E−2	0.86298E−2	−0.30852E−2	0.92581E−2
m_{22}	0.13668E−1	−0.46198E−1	−0.12970E−1	0.24376E−1	−0.29068E−2	0.52775E−1
c_{55}	0.63116E−3	0.18370	−0.17663E−1	−0.92593E−1	0.13964E−1	−0.37740E−1
c_{52}	−0.85805E−1	0.24006	0.10020	−0.13176	−0.16091E−1	−0.52217E−1
c_{22}	−0.24147	0.52269	0.23271	−0.28526	0.68691E−2	0.13848
Lateral: perpendicular						
m_{65}	−0.46261E−3	0.27610E−2	0.11516E−3	−0.21853E−2	0.13978E−3	−0.66927E−3
m_{62}	−0.13553E−2	0.40432E−2	0.11434E−2	−0.25422E−2	−0.10052E−4	−0.17182E−2
m_{32}	−0.45682E−2	0.10797E−1	0.41254E−2	−0.57931E−2	−0.33138E−3	−0.50724E−2
c_{65}	0.21438E−1	−0.54389E−1	−0.73262E−2	−0.54776E−2	0.76065E−2	−0.24165E−1
c_{62}	0.14903E−1	−0.10434E−1	−0.40106E−2	−0.31096E−2	0.14738E−1	−0.83101E−1
c_{32}	−0.15579E−1	0.83912E−1	0.52866E−1	−0.24903E−1	0.93828E−2	−0.24420

Table 11.11 Regression equation coefficients for B7 propellers ($E \pm N = \times 10^{\pm N}$) (taken from Reference 8)

Parameter / Component	C_1	C_2	C_3	C_4	C_5	C_6
Torsional/axial						
m_{44}	0.21372E−2	−0.56155E−2	−0.27388E−2	0.24553E−2	0.26675E−3	0.64805E−2
m_{41}	−0.50233E−3	0.13927E−1	−0.41583E−2	−0.16454E−1	0.56027E−2	−0.17030E−1
m_{11}	−0.32908E−1	0.88748E−1	0.32596E−1	0.11886	−0.96860E−3	−0.87831E−1
c_{44}	−0.24043E−1	0.51680E−1	0.18585E−1	−0.31175E−1	0.75424E−2	−0.10541E−2
c_{41}	0.14003	−0.37358	−0.18904	0.20133	0.40056E−1	0.45135E−1
c_{11}	0.34070E−1	0.29353E+1	−0.24280	−0.13929E+1	0.17571	−0.65123
Lateral: parallel						
m_{55}	−0.14132E−2	0.26715E−2	0.18052E−2	0.56906E−2	−0.52314E−3	−0.24846E−2
m_{52}	0.17646E−3	−0.65252E−2	0.19867E−2	0.78350E−2	−0.26907E−2	0.82990E−2
m_{22}	0.12144E−1	−0.40599E−1	−0.11616E−1	0.21395E−1	−0.24429E−2	0.46140E−1
c_{55}	−0.26383E−2	0.17179	−0.29958E−2	−0.79085E−1	0.50612E−2	−0.33233E−1
c_{52}	−0.78069E−1	0.20492	0.10121	−0.10980	−0.21608E−1	−0.28950E−1
c_{22}	−0.20348	0.42553	0.19690	−0.23664	0.11822E−1	−0.69910E−1
Lateral: perpendicular						
m_{65}	−0.38383E−3	0.19693E−2	0.17327E−3	−0.15326E−2	0.26748E−4	−0.36439E−3
m_{62}	−0.96395E−3	0.28059E−2	0.80259E−3	−0.17783E−2	−0.37139E−4	−0.10340E−2
m_{32}	−0.29000E−2	0.69281E−2	0.24977E−2	−0.37440E−2	−0.12487E−3	−0.30407E−2
c_{65}	0.10617E−1	−0.24040E−1	−0.19931E−2	−0.20636E−1	0.60272E−2	−0.26183E−1
c_{62}	0.15152E−2	−0.20965E−1	−0.36583E−2	−0.22580E−1	0.11790E−1	−0.80079E−1
c_{32}	−0.36770E−1	0.13433	0.56417E−1	−0.62648E−1	0.74649E−2	−0.22397

Table 11.12 Lifting surface corrections for Parsons and Vorus added mass and damping equations (Reference 8)

$$LSC(m_{44}) = 0.61046 + 0.34674(P/D) + 0.60294(AR)^{-1} - 0.56159(AR)^{-2} - 0.80696(P/D)(AR)^{-1} + 0.45806(P/D)(AR)^{-2}$$

$$LSC(m_{41}) = 0.65348 + 0.28788(P/D) + 0.39805(AR)^{-1} - 0.42582(AR)^{-2} - 0.61189(P/D)(AR)^{-1} + 0.33373(P/D)(AR)^{-2}$$

$$LSC(m_{11}) = 0.61791 + 0.23741(PD) + 0.42253(AR)^{-1} - 0.43911(AR)^{-2} - 0.46697(P/D)(AR)^{-1} + 0.25124(P/D)(AR)^{-2}$$

$$LSC(c_{44}) = 0.82761 - 0.41165(AR)^{-1} + 1.2196(P/D)(AR)^{-1} + 6.3993(AR)^{-3} - 13.804(P/D)(AR)^{-3} - 6.9091(AR)^{-4} + 15.594(P/D)(AR)^{-4}$$

$$LSC(c_{41}) = 0.80988 - 0.63077(AR)^{-2} + 1.3909(P/D)(AR)^{-1} + 7.5424(AR)^{-3} - 15.689(P/D)(AR)^{-3} - 8.0097(AR)^{-4} + 17.665(P/D)(AR)^{-4}$$

$$LSC(c_{11}) = 0.82004 - 0.67190(AR)^{-2} + 1.3913(P/D)(AR)^{-1} + 7.7476(AR)^{-1} - 16.807(P/D)(AR)^{-3} - 8.2798(AR)^{-4} + 19.121(P/D)(AR)^{-4}$$

$$LSC(m_{55}) = -0.1394 + 0.89760(AR) + 0.34086(P/D) - 0.15307(AR)^2 - 0.36619(P/D)(AR) + 0.70192(P/D)(AR)^2$$

$$LSC(m_{52}) = 0.0010398 + 0.66020(AR) + 0.39850(P/D) - 0.10261(AR)^2 - 0.34101(P/D)(AR) + 0.060368(P/D)(AR)^2$$

$$LSC(m_{22}) = 0.78170 + 0.36153(AR - 2) - 0.19256(P/D)(AR - 2) + 0.17908(P/D)(AR - 2)^2 - 0.16110(AR - 2)^2 - 0.061038(P/D)^2(AR - 2)$$

$$LSC(c_{55}) = 0.78255 + 0.061046(AR) - 2.5056(AR)^{-3} + 1.6426(AR)^{-4} + 1.8440(P/D)(AR)^{-4}$$

$$LSC(c_{52}) = 1.0121 + 0.73647(AR)^{-2} - 3.8691(AR)^{-3} - 1.5129(P/D)(AR)^{-3} + 3.0614(AR)^{-4} + 3.0984(P/D)(AR)^{-4}$$

$$LSC(c_{22}) = 0.84266 + 6.7849(AR)^{-2} + 0.12809(P/D)(AR)^{-1} - 21.030(AR)^{-3} - 3.3471(P/D)(AR)^{-3} + 15.842(AR)^{-4} + 5.1905(P/D)(AR)^{-4}$$

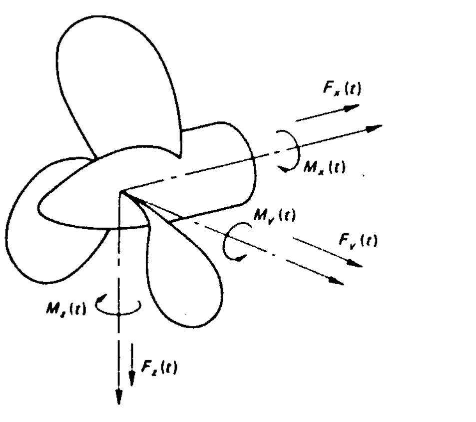

Figure 11.3 Hydrodynamic forces and moment activity on a propeller

Equation (11.19) also underlines the functionality of the thrust eccentricity with time (t) since as each blade rotates around the propeller disc it is continuously encountering a different inflow field and hence the moments and forces are undergoing a cyclic change in their magnitude. In Chapter 5, it was seen that the wake field could be expressed as the sum of a set of Fourier components. Since the blade sections operate wholly within this wake field the cyclic lift force generated by the sections and the components of this force resolved in either the thrust or torsional directions can also be expressed as the sum of Fourier series expansions:

$$\left.\begin{aligned} F(t) &= F_{(0)} + \sum_{k=1}^{n} F_{(k)}\cos(\omega t + \phi_k) \\ &\text{and} \\ M(t) &= M_{(0)} + \sum_{k=1}^{n} M_{(k)}\cos(\omega t + \phi_k) \end{aligned}\right\} \quad (11.20)$$

Hence the resulting forces and moments can all be expressed as a mean component plus the sum of a set of harmonic components. In the case of high shaft inclinations the movement of the effective thrust force can be considerable in the athwart direction (see Chapter 6). In such cases the term thrust eccentricity can also apply to that direction. Whilst the discussion, for illustration purposes, so far has centred on the thrust force, a similar set of arguments also applies to

Table 11.13 Typical first and second order dynamic forces for preliminary estimation purposes

				Blade number		
				4	5	6
Blade rate frequency component	Thrust	$F_{x(1)}$	Mean	$0.084T_0$	$0.020T_0$	$0.036T_0$
			Range	$\pm 0.031T_0$	$\pm 0.006T_0$	$\pm 0.024T_0$
	Vertical force	$F_{z(1)}$	Mean	$0.008T_0$	$0.011T_0$	$0.003T_0$
			Range	$\pm 0.004T_0$	$\pm 0.009T_0$	$\pm 0.002T_0$
	Horizontal force	$F_{y(1)}$	Mean	$0.012T_0$	$0.021T_0$	$0.008T_0$
			Range	$\pm 0.011T_0$	$\pm 0.016T_0$	$\pm 0.004T_0$
	Torque	$M_{x(1)}$	Mean	$0.062Q_0$	$0.001Q_0$	$0.030Q_0$
			Range	$\pm 0.025Q_0$	$\pm 0.0008Q_0$	$\pm 0.020Q_0$
	Vertical moment	$M_{z(1)}$	Mean	$0.075Q_0$	$0.039Q_0$	$0.040Q_0$
			Range	$\pm 0.050Q_0$	$\pm 0.026Q_0$	$\pm 0.015Q_0$
	Horizontal moment	$M_{y(1)}$	Mean	$0.138Q_0$	$0.125Q_0$	$0.073Q_0$
			Range	$\pm 0.090Q_0$	$\pm 0.085Q_0$	$\pm 0.062Q_0$
Twice blade rate frequency component	Thrust	$F_{x(2)}$	Mean	$0.022T_0$	$0.017T_0$	$0.018T_0$
			Range	$\pm 0.004R_0$	$\pm 0.003T_0$	$\pm 0.002T_0$
	Vertical force	$F_{z(2)}$	Mean	$0.008T_0$	$0.002T_0$	$0.001T_0$
			Range	$\pm 0.004T_0$	$\pm 0.002T_0$	$\pm 0.001T_0$
	Horizontal force	$F_{y(2)}$	Mean	$0.001T_0$	$0.006T_0$	$0.003T_0$
			Range	$\pm 0.001T_0$	$\pm 0.003T_0$	$\pm 0.001T_0$
	Torque	$M_{x(2)}$	Mean	$0.016Q_0$	$0.014Q_0$	$0.010Q_0$
			Range	$\pm 0.010Q_0$	$\pm 0.008Q_0$	$\pm 0.002Q_0$
	Vertical moment	$M_{z(2)}$	Mean	$0.019Q_0$	$0.012Q_0$	$0.007Q_0$
			Range	$\pm 0.013Q_0$	$\pm 0.011Q_0$	$\pm 0.002Q_0$
	Horizontal moment	$M_{y(2)}$	Mean	$0.040Q_0$	$0.080Q_0$	$0.015Q_0$
			Range	$\pm 0.036Q_0$	$\pm 0.040Q_0$	$\pm 0.002Q_0$

the shaft torque and its eccentricity which, together with the thrust action, give rise to loading components in the mutually orthogonal direction, as shown in Figure 6.24.

In the absence of high shaft inclination the magnitude of the bearing forces depend on the characteristics of the wake field, the geometric form of the propeller (in particular the skew and blade number), the ship speed and the rotational speed of the propeller. Indeed, for a given application, the forces and moments generated by the fixed pitch propeller are, in general, proportional to the square of the revolutions, since for a considerable part of the upper operational speed range the vessel will work at a nominally constant advance coefficient. Some years ago an investigation by theoretical means of the dynamic forces at blade and twice blade frequency was carried out on some 20 ships (Reference 9). The results of these calculations are useful for making preliminary estimates of the dynamic forces at the early stages of design and Table 11.13 shows the results of these calculations in terms of the mean values and their ranges. From the table it will be seen that each of the six loading components are expressed in terms of the mean thrust T_0 or the mean torque Q_0.

The majority of the theoretical methods discussed in Chapter 8 can be applied to calculate the bearing forces. In essence, the calculation is essentially a classical propeller analysis procedure conducted at incremental steps around the propeller disc. However, probably the greatest bar to absolute accuracy is the imprecision with which the wake field is known due to the scale effects between model scale, at which the measurement is carried out, and full scale. Sasajima (Reference 10) specifically developed a simplified quasi-steady method of establishing the propeller forces and moments which relied on both the definition of the propeller open water characteristics and a weighted average wake distribution. A wake field prediction is clearly required for this level of analysis, and radial weighting function is then applied to the wake field at each angular position, the weighting being applied in proportion to the anticipated thrust loading distribution. Improved results in this analysis procedure are also found to exist by averaging the wake over the chord using a weight function similar to the vortex distribution over a flat plate. The expressions derived by Sasajima for the fluctuating forces around the propeller disc are given below:

$$\tilde{K}_T(\theta) = \frac{1}{z}\sum_{i=1}^{z} K_T(J(\theta + \theta_i))$$

$$\tilde{K}_Q(\theta) = \frac{1}{z}\sum_{i=1}^{z} K_Q(J(\theta + \theta_i))$$

$$\bar{F}_y(\theta) = -\frac{2}{z\xi_f}\sum_{i=1}^{z} K_Q(J(\theta+\theta_i))\cdot\cos(\theta+\theta_i)$$

$$\bar{F}_z(\theta) = \frac{2}{z\xi_f}\sum_{i=1}^{z} K_Q(J(\theta+\theta_i))\cdot\sin(\theta+\theta_i)$$

$$\bar{M}_y(\theta) = -\frac{\xi_f}{2z}\sum_{i=1}^{z} K_T(J(\theta+\theta_i))\cdot\cos(\theta+\theta_i)$$

$$\bar{M}_z(\theta) = \frac{\xi_f}{2z}\sum_{i=1}^{z} K_T(J(\theta+\theta_i))\cdot\sin(\theta+\theta_i)$$

where

$\{\bar{F}_y, \bar{F}_z\}$ $= \dfrac{\{F_y, F_z\}}{\rho n^2 D^4}, \{\bar{M}_y, \bar{M}_z\} = \dfrac{\{M_y, M_z\}}{\rho n^2 D^5}$

ξ_f $= \dfrac{r_f}{R}$; non-dimensional radius of the loading point.

θ_i $= \dfrac{2\pi(i-1)}{z}$

z = number of blades

$J(\theta + \theta_i)$ = advance coefficient at each angular position of each blade.

$K_T(J), K_Q(J)$ = open-water characteristics of the propeller.

Figure 11.4 shows a typical thrust fluctuation for a propeller blade of a single-screw ship; the asymmetry noted is due to the tangential components of the wake field acting in conjunction with axial components. Furthermore, Figure 11.5 illustrates a typical locus of the thrust eccentricity $e_T(t)$; the period of travel around this locus is of course dependent upon the blade number, because of symmetry, and is therefore $1/nz$. The computation of this locus generally requires the computation of the effective centres of thrust of each blade followed by a combination of these centres together with their thrusts to form an equivalent moment arm for the total propeller thrust.

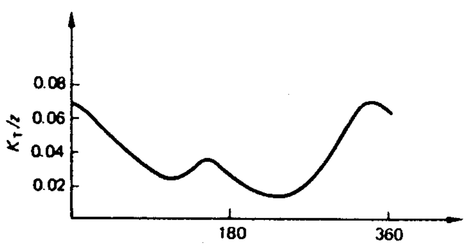

Figure 11.4 Typical propeller thrust fluctuation

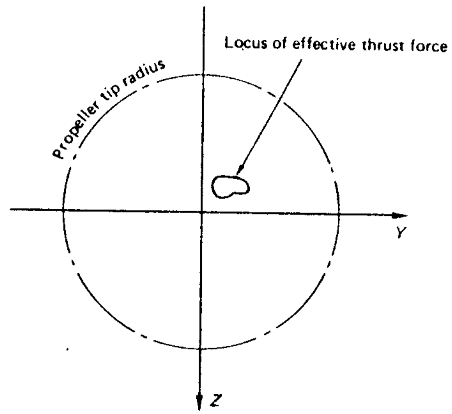

Figure 11.6 Typical locus of thrust eccentricity for a single screw vessel

11.1.5 Out of balance forces and moments

A marine shafting system will experience a set of significant out of balance forces and couples if either the propeller becomes damaged so as to alter the distribution of mass or the propeller has not been balanced prior to installation.

For large propellers ISO 484/1 (Reference 11) defines a requirement for static balancing to be conducted such that the maximum permissible balancing mass m_b at the tip of the propeller is governed by the equation

$$m_b \leq C\frac{M}{RN^2}\,\text{kg or } KM\,\text{kg, whichever is the smaller}$$

where M is the mass of the propeller (kg)
R is the tip radius (m)
and N is the designed shaft speed (RPM).

The coefficients C and K are defined in Table 11.14 according to the manufacturing class.

Table 11.14 ISO balance constants

ISO class	*S*	*I*	*II*	*III*
C	15	25	40	75
K	0.0005	0.001	0.001	0.001

For the larger-diameter propellers a static balance procedure is normally quite sufficient and will lead to a satisfactory level of out-of-balance force which can both be accommodated by the bearing and also will not cause undue vibration to be transmitted to the vessel.

In the case of smaller propellers, ISO 484/2 (Reference 12) applies for diameters between 0.80 and 2.50 m; the ISO standard also calls for static balance without further definition. For many of these smaller propellers this is a perfectly satisfactory procedure; however, there exists a small subset of high rotational speed, high blade area ratio propellers where dynamic balance is advisable. With these propellers, because of their relatively long axial length, considerable out-of-balance couples can be exerted on the shafting if this precaution is not taken.

When a propeller suffers the loss of a significant part or the whole of blade through either blade mechanical impact or material fatigue and a spare propeller or repair capability is not available, then in order to minimize the vibration that will result from the out-of-balance forces the opposite blade of an even number bladed propeller should be similarly reduced. In the case of an odd bladed propeller a corresponding portion should be removed from the two opposite blades so as to conserve balance. The amount to be removed can conveniently be calculated from the tables of Figure 11.1 used in association with a vectorial combination of the resulting centrifugal forces. The vibration resulting from the out-of-balance forces of a propeller will be first shaft order in frequency.

Additional out-of-balance forces can also be generated by variations in blade-to-blade tolerances. These are generally first order and of small magnitude; however, they can on occasions have noticeable effects. Chapter 24 disusses these matters further.

11.2 Hydrodynamic interaction

The hydrodynamic interaction between the propeller and the hull originates from the passage of the blades beneath or in the vicinity of the hull and also from the cavitation dynamics on the surfaces of the blades. The pressure differences caused by these two types of action are then transmitted through the water to produce a fluctuating pressure over the hull surface which, due to its acting over a finite area, produces an excitation force to the vessel. As a consequence the analysis of the hydrodynamic interaction can most conveniently be considered in three parts; each part, however, eventually combines with the others to form the total pressure signal on the hull surface. These component parts are detailed in Table 11.15.

Table 11.15 Hydrodynamic interaction components

Pressure from the passage of the non-cavitating blade $p_0(t)$
Pressure from the cavity volume variations on each blade $p_c(t)$
The effect of the hull surface on the free space pressure signal – termed the solid boundary factor (SBF)

For the purposes of this discussion we will, in the main, consider only the pressures produced by the rotating propeller rather than the resultant force on the hull, which is simply the integration of the pressure field over the hull surface, taking into account the curvature and form of the hull in the region of the propeller.

11.2.1 Non-cavitating blade, contribution

The contribution to the total pressure signal on the hull from the passage of the non-cavitating blade is in the form of a continuous time series $p_0(t)$ and is generally considerably smaller than the cavitating component. Thus the non-cavitating component will be overwhelmed by the cavitating component for most ships once the cavitation inception point is passed; this is generally well below the design point for the vessel. The exception to this is where the propeller has been designed to be non-cavitating, such as may be found in some naval and research ship applications

In the case of the non-cavitating propeller the pressure fluctuation derives from the thickness of the propeller blades and the hydrodynamic loading over the surfaces of the blades. Huse (Reference 13) proposes a method in which the thickness effect is accounted for by an equivalent symmetrical profile, which is defined by a distribution of sources and sinks located along the chord line of the equivalent profile. The pressure signal derived in this way varies linearly with the equivalent profile thickness and the method is shown to give a good agreement with experiment.

The contribution from the blade loading can be considered in two portions; a contribution from the mean hydrodynamic loading and one from the fluctuating load component. In the case of the mean loading a continuous layer of dipoles distributed along the section mean line to simulate shockless entry can be used whilst the fluctuating loading can be simulated by dipoles clustered at the theoretical thin aerofoil aerodynamic centre of the section; that is, at 0.25c from the leading edge.

The most important of the propeller parameters in determining the non-cavitating pressure signal are considered to be the blade number and the blade thickness, and the pressure $p_0(t)$ can be expressed as

$$p_0(t) = -\varrho\frac{\partial\phi(t)}{\partial t}$$

in which ϱ is the density of the water
$\phi(t)$ is the velocity potential
t is time.

Several theoretical solutions have appeared in the literature in addition to the work of Huse (Reference 13). The alternative approach by Breslin and Tsakonas (Reference 14) provides a good example of these other aproaches.

11.2.2 Cavitating blade contribution

In Chapter 9 it was shown that a propeller may be subjected to many forms of cavitation that depend on the propeller operating point, the wake field and the detailed propeller geometry. Typically the propeller may experience the following: suction side sheet cavitation; tip vortex cavitation which may collapse off the blade, as indeed can suction side sheet cavitation; pressure face cavitation or propeller–hull vortex cavitation. Clearly it is difficult to develop a unifying analytical treatment which will embrace all of these cavitation types, although the underlying physics of the pressure transmission processes are largely similar.

The need for such an all embracing treatment can to some extent be reduced by consideration of the cavitation types and their known effects on vibration. For example, face cavitation does not normally contribute significantly to the overall hull excitation, although it contributes to high-frequency noise emissions from the propeller. Similarly, the hub vortex, unless it is particularly strong, does not contribute to the hull pressure fluctuations, although it may cause excitation of the rudder which in turn leads to hull excitation. The tip vortex contributes to excitation at multiples of the blade rate frequency and this is of particular concern for vessels with hull form which extends well aft of the propeller station. In addition English (Reference 15) has drawn attention to certain cases in which instabilities can arise in the tip vortex that cause the tip vortex to burst – a phenomenon well known in the aircraft industry. In these cases excitation and noise frequencies above blade rate are experienced. The problem in calculating the contribution of tip vortex cavitation effects stems largely from the work necessary to define reliable tip vortex inception behaviour: indeed much research is currently progressing in this field.

The cavitating blade contribution to the hull pressure field is therefore generally considered to derive from the pulsation of the suction side sheet and tip vortex cavities. Hence these types of cavitation may collapse either on or off the blade; in the former case they are generally responsible for blade rate and the first three or four harmonic frequencies of its excitation, whereas in the latter case the collapse occurs at the higher harmonics of blade rate frequency. In order to calculate the effects of the cavity volume variations on the cavitating pressures it is necessary to model the volume of the cavity on the blade. This is done by constructing a system of sources, the strengths of which vary with blade angular position, in order to model the changing cavitation volume as the propeller rotates in the wake field. From a model of this type it is possible to derive an expression for the velocity potential of the sources with time from which an expression for the blade rate harmonics of the pressures can be developed. The expression developed by Breslin (Reference 16) in this way is

$$p_{c_{qz}} = -\frac{\varrho Z^3}{2\pi}\cdot\frac{(q\omega)^2}{R_p}\mathrm{Re}[V_{qz}e^{iqz\phi}] \qquad (11.21)$$

in which
- q is the harmonic order (blade rate, $q = 1$)
- ϱ fluid mass density
- Z is the blade number
- ω is the angular velocity
- R_p is the distance of the field point $\sqrt{(r^2 + x^2)}$
- V_{qz} is the qzth harmonic component of the complex amplitude of the cavity volume

and ϕ is the blade position angle

Consequently by expressing V_{qz} in its complex form as

$$V_{qz} = a_{qz} + ib_{qz}$$

and then extracting the real part it can be shown that

$$p_{c_{qz}} = -\frac{\varrho Z^3}{2\pi}\frac{(q\omega)^2}{R_p}\sqrt{(a_{qz}^2 + b_{qz}^2)}\cos(qz\phi + \varepsilon) \qquad (11.21(a))$$

where $\varepsilon = \tan^{-1}(b_{qz}/a_{qz})$.

From this expression it can be seen that the asymptotic pressure due to the cavity volume variation at a particular blade rate harmonic frequency depends upon the blade rate harmonic of the cavity volume. Furthermore, the dependence of the field point pressure on the inverse of the distance R_p:

$$p_{c_{qz}} \propto \frac{1}{R_p}$$

becomes apparent and clearly demonstrates how the field point pressure from a cavitating propeller decays with increasing distance from the propeller – hence the advantage of providing adequate clearances around the propeller. This proportionality for the cavitating propeller of $p_c \propto R_p^{-1}$ is in contrast to that for a non-cavitating propeller, which is more closely expressed by $p_0 \propto R_p^{-1.5}$ and as a consequence decays more rapidly with distance

Expressions of the type shown in equation (11.21) or (11.21(a)) are a simplification of the actual conditions and as such are only valid at distances that are large compared to the propeller radius. This can lead to some difficulty when calculating the field point pressures in cases where the tip clearances are small.

Skaar and Raested (Reference 17) developed an expression based on similar assumptions to that of equation (11.21) which provides further insight into the behaviour of the cavitating pressure signature. Their relationship is

$$p_c \simeq \frac{\varrho}{4\pi}\frac{1}{R_p}\frac{\partial^2 V}{\partial t^2} \qquad (11.22)$$

in which V is the total cavity volume variation.

From this expression it can further be seen that the cavitating pressure signature is proportional to the second derivative of the total cavitation volume variation with time. This demonstrates why the pressures encountered upon collapse of the cavity, which is usually more violent, are greater than those experienced when the cavity is growing: typically, in a single-screw vessel with a right-handed propeller the pressures measured above the propeller plane are greater on the starboard side than on the port side. Skaar and Raestad show the equivalence of equation (11.22) to that of (11.21) in the discussion to Reference 17.

The dependence of the pressure on the $\partial^2 V/\partial t^2$ term shows the implied dependence of the pressure on the quality of the wake field and hence any steps taken to improve the wake field are very likely to have a beneficial effect on the pressure signature. The alternative is to approach the problem from the blade design viewpoint. In this case, then, attention to the radial and chordal distribution of loading, the skew distribution and the blade area are all known parameters that have a significant influence on the cavitating pressure impulses. Blade number, unlike the non-cavitating pressure impulses, in general has a very limited influence on the cavitating pressure characteristics.

11.2.3 Influence of the hull surface

The discussion so far has concerned itself with the free field pressures from cavitating and non-cavitating propellers. When a solid boundary is introduced into the vicinity of the propeller then the pressures acting on that boundary are altered significantly. If, for example, a flat plate is introduced at a distance above the propeller, then the pressure acting on the plate surface is twice the free field pressure which leads to the concept of a solid boundary factor. The solid boundary factor is defined as follows:

$$\mathrm{SBF} = \frac{\text{pressure acting on the boundary surface}}{\text{free field pressure in the absence of the solid boundary}} \qquad (11.23)$$

In the case of the flat plate cited above, which is of infinite stiffness, the SBF = 2. However, in the case of a ship form a lesser value would normally be expected due to the real hull form being different from the flat plate and also the influence of pressure release at the sea surface. Garguet and Lepeix (Reference 18) discussed the problems associated with the use of a value of 2 for the SBF in giving misleading results to calculations. Subsequently Ye and van Gent (Reference 19) using a potential flow calculation with panel methods suggested a value of 1.8 as being more appropriate for ship calculations.

In practice the solid boundary factor SBF can be considered as a composite factor having one component S_b which takes into account the hull form and another S_f which accounts for the proximity of the free surface. Hence equation (11.23) can be written as

$$\mathrm{SBF} = S_b S_f \qquad (11.24)$$

Wang (Reference 20) and Huse (Reference 21) have both shown that the dominant factor is S_f. In their work the variability of the solid boundary factor is discussed, and it falls from a value of just under 2.0 at the shaft centre line to a value of zero at the free surface–hull interface. Huse gives relationships for S_b and S_f for an equivalent clearance ratio of 0.439 which are as follows:

$$\left.\begin{aligned} S_b &= 2.0 + 0.0019\alpha - 0.00024\alpha^2 \\ S_f &= 9.341\delta - 30.143\delta^2 + 33.19\delta^3, \quad 0 < \delta \leq 0.35 \\ S_f &= 1.0 \qquad \text{for } \delta > 0.35 \end{aligned}\right\} \qquad (11.25)$$

in which α is the inclination of the section with respect to the horizontal measured in the thwart direction.

and δ is the ratio of the field point immersion depth to the shaft immersion depth.

11.2.3 Methods for predicting hull surface pressures

In essence there are three methods for predicting hull surface pressures; these are by means of empirical methods, by calculations using advanced theoretical methods and by experimental measurements.

With regard to the empirical class of methods the most well known and adaptable is that due to Holden *et al.* (Reference 22). This method is based on the analysis of some 72 ships for which full-scale measurements were made. The method is intended for a first estimate of the likely hull surface pressures using a conventional propeller form. Holden proposes the following regression based formula for the estimation of the non-cavitating and cavitating pressures respectively:

$$\left.\begin{aligned} p_0 &= \frac{(ND)^2}{70}\frac{1}{Z^{1.5}}\cdot\left(\frac{K_0}{d/R}\right) \quad \mathrm{N/m^2} \\ &\text{and} \\ p_c &= \frac{(ND)^2}{160}\frac{V_s(w_{T_{max}} - w_e)}{\sqrt{(h_a + 10.4)}}\cdot\left(\frac{K_c}{d/R}\right) \quad \mathrm{N/m^2} \end{aligned}\right\} \qquad (11.26)$$

in which
- N is the propeller RPM
- D is the diameter (m)
- V_s is the ship speed (m/s)
- Z is the blade number
- d is the distance from $r/R = 0.9$ to a position on the submerged hull when the blade is at the T.D.C. position (m)
- R is the propeller radius (m)
- $w_{T_{max}}$ is the maximum value of the Taylor wake fraction in the propeller disc
- w_e is the mean effective full scale Taylor wake fraction

h_s is the depth to the shaft centre line

and K_0 and K_c are given respectively by the relationships

$K_0 = 1.8 + 0.4\,(d/R)$ for $d/R \leq 2$

and $K_c = 1.7 + 0.7\,(d/R)$ for $d/R < 1$

$K_c = 1.0$ for $d/R > 1$

The total pressure impulse which combines both the cavitating and non-cavitating components of equation (11.26) acting on a local part of the submerged hull is then found from

$$p_z = \sqrt{(p_0^2 + p_c^2)} \qquad (11.27)$$

Empirical methods of this type are particularly useful as a guide to the expected pressures. They should not, however, be regarded as a definitive solution, because differences, sometimes quite substantial, will occur when corellated with full-scale measurements. For example, equation (11.26) gives results having a standard deviation of the order of 30% when compared to the base measurements from which it was derived.

In the case of a more rigorous calculation, more detail can be taken into account which is conducive to a higher level of accuracy. Theoretical models which would be used in association with this form of analysis are those which can be broadly grouped into the lifting surface or vortex lattice categories, Chapter 8. In particular unsteady lifting surface theory is a basis for many advanced theoretical approaches in this field. Notwithstanding the ability of analytical methods to provide an answer, care must be exercised in the interpretation of the results, since these are particularly influenced by factors such as wake scaling procedures, the description of the propeller model and the hull surface, the distribution of solid boundary factors and the harmonic order of the pressure considered in the analysis. Furthermore, propeller calculation procedures assume a rigid body condition for the hull, and as a consequence do not account for the self-induced pressures resulting from hull vibration: these have to be taken into account by other means, typically finite element models of the hull structure. As a consequence of all of these factors considerable care must be exercised in interpreting the results and the method used should clearly be subjected to a validation process.

Model measurement methods of predicting hull surface pressures can be conducted in either cavitation tunnels or specialized facilities such as depressurized towing tanks. Originally the arrangement in a cavitation tunnel comprised a simple modelling of the hull surface by a flat or angled plate above a scale model of the propeller. Although this technique is still used in some establishments a more enlightened practice is to use a dummy model with a shortened centre body, as shown in Figure 11.6; however, in some large facilities the towing tank model is used. The advantage of using a model of the actual hull form is twofold: firstly it assists in modelling the flow of water around the hull surface and requires wake screens, which are essentially arrangements of wire mesh, for fine tuning purposes of the wake field, and secondly it makes the interpretation of the measured hull surface pressures easier since the real hull form is simulated.

In order to interpret model test results appeal can be made to dimensional analysis, from which it can be shown that the pressure at a point on the hull surfaces above a propeller has a dependence on the following set of dimensional parameters:

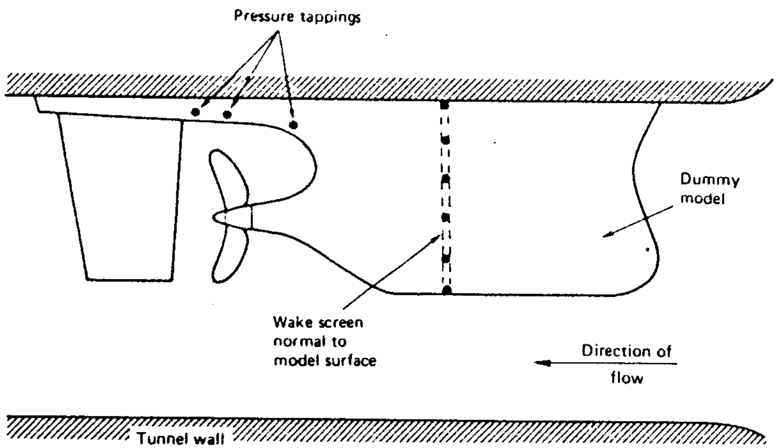

Figure 11.6 Dummy model and propeller in a cavitation tunnel

$$p = \varrho n^2 D^2 \Phi\{J, K_T, \sigma, R_n, F_n, (z/D)\} \qquad (11.28)$$

in which J is the advance coefficient
K_T is the propeller thrust coefficient
σ is the cavitation number
R_n is the Reynolds number
F_n is the Froude number
and z is the distance from the propeller to the point on the hull surface.

In equation (11.28), the quantities ϱ, n and D have their normal meaning.

As a consequence of this relationship a pressure coefficient K_p can be defined as

$$K_p = \frac{p}{\varrho n^2 D^2} \qquad (11.29)$$

which has the functional dependence defined in equation (11.28).

Equation (11.28) defines the hull surface pressure as a function of propeller loading, cavitation number, geometric scaling and Reynolds and Froude identity. By assuming, therefore, that the geometric scaling, cavitation and thrust identity have all been satisfied, the hull surface pressure at ship scale can be derived from equation (11.29) as follows, using the suffixes m and s for model and ship respectively. By assuming the identity of K_p between model and full scale we may write

$$\frac{p_s}{p_m} = \frac{\varrho_s}{\varrho_m}\left(\frac{n_s}{n_m}\right)^2\left(\frac{D_s}{D_m}\right)^2$$

and for Froude identity $(F_{n_s} = F_{n_m})$

$$\frac{p_s}{p_m} = \frac{\varrho_s}{\varrho_m}\left(\frac{D_m}{D_s}\right)\cdot\frac{\varrho_s}{\varrho_m}\lambda \qquad (11.30)$$

where λ is the model scale of the propeller.

Equation (11.30) implies that the Reynolds condition over the blades has also been satisfied, which is clearly not the case when the Froude identity is satisfied. Hence it is important to ensure that the correct flow conditions exist over the blade in order to ensure a representative cavitation pattern over the blades and hence pressure coefficient on the model as discussed in Chapter 9.

References and further reading

1. Jakeman, R.W. Analysis of Dynamically Loaded Hydrodynamic Journal Bearings with Particular Reference to the Mis-aligned Marine Stern Tube Bearing. Ph.D. Thesis, 1988.
2. Archer, S. Torsional vibration damping coefficients for marine propellers. *Engineering*, May, 1955.
3. Lewis, F.M., Auslaender, J. Virtual inertia of propellers, *J. Ship Res.*, March, 1960.
4. Burrill, L.C., Robson, W. Virtual mass and moment of inertia of propellers. *Trans. NECIES*, **78**, 1962.
5. Schwanecke, H. Gedanken wur Frage de Hydrodynamischen Erregungen des Propellers und der Wellenleitung. *STG*, **57**, 1963.
6. Gunsteren, L.A. van, Pronk, C. Determining propeller speed and moment of inertia. *Diesel and Gas Turbine Progress*, November December, 1973.
7. Hylarides, S., Gent, W. van. Propeller hydrodynamics and shaft dynamics. *Symp. on High Powered Propulsion of Large Ships*, NSMB, 1974.
8. Parsons, M.G., Vorus, W.S. Added mass and damping estimate for vibrating propellers. *Propellers' 81 Symp. Trans. SNAME*, 1981.
9. *Vibration Control in Ships*, Veritec, 1985.
10. Sasajima, T. Usefulness of quasi-steady approach for estimation of propeller bearing forces. *Propellers' 78 Symp., Trans. SNAME*, 1978.
11. ISO 484/1. *Shipbuilding Ship Screw Propellers Manufacturing Tolerances – Part 1: Propellers of Diameter Greater than 2.50 m*, 1981.
12. ISO 484/2. *Shipbuilding Ship Screw Propellers Manufacturing Tolerances – Part 2: Propellers of Diameter Between 0.80 and 2.50 m Inclusive*, 1981.
13. Huse, E. The Magnitude and Distribution of Propeller Induced Surface Forces on a Single Screw Ship Model, Publ. 100, Ship model tank, Trondheim, 1968.
14. Breslin, J.P., Tsakonas, S. Marine propeller pressure field due to loading and thickness effects. *Trans. SNAME*, **67**, 1959.
15. English, J. Cavitation induced hull surface pressures measurements in water tunnels, *Symp. on Propeller Induced Ship Vibration, Trans. RINA*, 1979.
16. Breslin, J.P. Discussion on Reference 17.
17. Skaar, K.T., Raestad, A.E. The relative importance of ship vibration excitation forces. *Symp. on Propeller Induced Ship Vibration, Trans. RINA*, 1979.
18. Garguet, M., Lepeix, R. The problem of influence of solid boundaries on propeller-induced hydrodynamic forces. *Symp. on High Powered Propulsion of Large Ships*, Wageningen, 1974.
19. Ye, Y., Gent, W. van. The Solid Boundary Factor in Propeller Induced Hull Excitation – Characteristics and Calculations. MARIN Report No. 50812-2-RF, May, 1988.
20. Wang, G. The influence of solid boundaries and free surface on propeller-induced pressure fluctuations. *Norwegian Mar. Res.*, **9**, 1981.
21. Huse, E. Cavitation induced excitation forces on the hull. *Trans. SNAME*, **90**, 1982.
22. Holden, K.O., Fagerjord, O., Frostad, R. Early design-stage approach to reducing hull surface forces due to propeller cavitation. *Trans. SNAME*, November, 1980.

12 Ship resistance and propulsion

Contents

Prior to the mid-19th Century comparatively little was known about the laws governing the resistance of ships and the power that was required to give a particular speed. Brown (Reference 1) gives an account of the problems of that time and depicts the role of William Froude, who can be justly considered as the father of ship resistance studies. An extract from Brown's account reads as follows:

'... In the late 1860s Froude was a member of a committee of the British Association set up to study the problems of estimating the power required for steamships. They concluded that model tests were unreliable and often misleading and that a long series of trials would be needed in which actual ships were towed and the drag force measured. Froude wrote a minority report pointing out the cost of such a series of trials and the fact that there could never be enough carried out to study all possible forms. He believed that he could make sense from the results of model tests and carried out a series of experiments in the River Dart to prove his point. By testing models of two different shapes and three different sizes he was able to show that there were two components of resistance, one due to friction and the other to wavemaking and that these components obeyed different scaling laws. Froude was now sufficiently confident to write to Sir Edward Reed (Chief Constructor of the Navy) on 24 April 1868, proposing that an experiment tank be built and a two year programme of work be carried out. After due deliberation, in February 1870, Their Lordships approved the expenditure of £2000 to build the world's first ship model experiment tank at Torquay and to run it for two years. The first experiment was run in March 1872 with a model of HMS Greyhound. Everything was new. The carriage was pulled along the tank at constant speed by a steam engine controlled by a governor of Froude design. For this first tank he had to design his own resistance dynamometer and followed this in 1873 by his masterpiece, a propeller dynamometer to measure thrust, torque and rotational speed of model propellers. This dynamometer was made of wood, with brass wheels and driving bands made of leather boot laces. It continued to give invaluable service until 1939 when its active life came to an end with tests of propellers for the fast minelayers ...

... William Froude died in 1879, having established and developed a sound approach to hull form design, made a major contribution to the practical design of ships, developed new experiment techniques and trained men who were to spread the Froude tradition throughout the world. William was succeeded as Superintendent AEW by Edmund Froude, his son, whose first main task was to plan a new establishment since the Torquay site was too small and the temporary building was nearing the end of its life. Various sites were considered but the choice fell on Haslar, Gosport, next to the Gunboat Yard, where AEW, now known as the Admiralty Marine Technology Establishment (Haslar) or AMTE(H),* remains to this day. A new ship tank, 400 ft long, was opened in 1887 ...

... Edmund was worried about the consistency of results being affected by the change to Haslar. He was a great believer in consistency, as witness a remark to Stanley Goodall, many years later, 'In engineering, uniformity of error may be more desirable than absolute accuracy'. As Goodall said 'That sounds a heresy, but think it over'. Froude took two measures to ensure consistent results; the first, a sentimental one, was to christen the Haslar tank with water from Torquay, a practice repeated in many other tanks throughout the world. The flask of Torquay water is not yet empty — though when Hoyt analysed it in 1978 it was full of minute animal life! The more practical precaution was to run a full series of tests on a model of HMS Iris at Torquay just before the closure and repeat them at Haslar. This led to the wise and periodical routine of testing a standard model, and the current model, built of brass in 1895, is still known as Iris, though very different in form from the ship of that name. Departures of the Iris model resistance from the standard value are applied to other models in the form of the Iris Correction. With modern water treatment the correction is very small but in the past departures of up to 14.5 per cent have been recorded, probably due to the formation of long chain molecules in the water reducing turbulence in the boundary layer. Another Froude tradition, followed until 1960, was to maintain water purity by keeping eels in the tanks. This was a satisfactory procedure, shown by the certification of the tank water as emergency drinking water in both World Wars, and was recognised by an official meat ration, six pence worth per week, for the eels in the Second World War! ...

So much then for the birth of the subject as we know it today and the start of the tradition of 'christening' a new towing tank from the water of the first tank, sited at Froude's home, Chelston Close, at Torquay; alas, all that remains today of that first tank is a bronze plaque in the wall of the Chelston Manor Hotel in Torquay commemorating its presence.

12.1 Froude's analysis procedure

William Froude (Reference 2) recognized that ship models of geosymmetric form would create similar wave systems, albeit at different speeds. Furthermore, he showed that the smaller models had to be run at

* As from April 1991 AMTE(H) became part of the Defence Research Establishment Agency (DREA).

Prior to the mid-19th Century comparatively little was known about the laws governing the resistance of ships and the power that was required to give a particular speed. Brown (Reference 1) gives an account of the problems of that time and depicts the role of William Froude, who can be justly considered as the father of ship resistance studies. An extract from Brown's account reads as follows:

'... In the late 1860s Froude was a member of a committee of the British Association set up to study the problems of estimating the power required for steamships. They concluded that model tests were unreliable and often misleading and that a long series of trials would be needed in which actual ships were towed and the drag force measured. Froude wrote a minority report pointing out the cost of such a series of trials and the fact that there could never be enough carried out to study all possible forms. He believed that he could make sense from the results of model tests and carried out a series of experiments in the River Dart to prove his point. By testing models of two different shapes and three different sizes he was able to show that there were two components of resistance, one due to friction and the other to wavemaking and that these components obeyed different scaling laws. Froude was now sufficiently confident to write to Sir Edward Reed (Chief Constructor of the Navy) on 24 April 1868, proposing that an experiment tank be built and a two year programme of work be carried out. After due deliberation, in February 1870, Their Lordships approved the expenditure of £2000 to build the world's first ship model experiment tank at Torquay and to run it for two years. The first experiment was run in March 1872 with a model of HMS Greyhound. Everything was new. The carriage was pulled along the tank at constant speed by a steam engine controlled by a governor of Froude design. For this first tank he had to design his own resistance dynamometer and followed this in 1873 by his masterpiece, a propeller dynamometer to measure thrust, torque and rotational speed of model propellers. This dynamometer was made of wood, with brass wheels and driving bands made of leather boot laces. It continued to give invaluable service until 1939 when its active life came to an end with tests of propellers for the fast minelayers ...

... William Froude died in 1879, having established and developed a sound approach to hull form design, made a major contribution to the practical design of ships, developed new experiment techniques and trained men who were to spread the Froude tradition throughout the world. William was succeeded as Superintendent AEW by Edmund Froude, his son, whose first main task was to plan a new establishment since the Torquay site was too small and the temporary building was nearing the end of its life. Various sites were considered but the choice fell on Haslar, Gosport, next to the Gunboat Yard, where AEW, now known as the Admiralty Marine Technology Establishment (Haslar) or AMTE(H),* remains to this day. A new ship tank, 400 ft long, was opened in 1887 ...

... Edmund was worried about the consistency of results being affected by the change to Haslar. He was a great believer in consistency, as witness a remark to Stanley Goodall, many years later, 'In engineering, uniformity of error may be more desirable than absolute accuracy'. As Goodall said 'That sounds a heresy, but think it over'. Froude took two measures to ensure consistent results; the first, a sentimental one, was to christen the Haslar tank with water from Torquay, a practice repeated in many other tanks throughout the world. The flask of Torquay water is not yet empty though when Hoyt analysed it in 1978 it was full of minute animal life! The more practical precaution was to run a full series of tests on a model of HMS Iris at Torquay just before the closure and repeat them at Haslar. This led to the wise and periodical routine of testing a standard model, and the current model, built of brass in 1895, is still known as Iris, though very different in form from the ship of that name. Departures of the Iris model resistance from the standard value are applied to other models in the form of the Iris Correction. With modern water treatment the correction is very small but in the past departures of up to 14.5 per cent have been recorded, probably due to the formation of long chain molecules in the water reducing turbulence in the boundary layer. Another Froude tradition, followed until 1960, was to maintain water purity by keeping eels in the tanks. This was a satisfactory procedure, shown by the certification of the tank water as emergency drinking water in both World Wars, and was recognised by an official meat ration, six pence worth per week, for the eels in the Second World War! ...

So much then for the birth of the subject as we know it today and the start of the tradition of 'christening' a new towing tank from the water of the first tank, sited at Froude's home, Chelston Close, at Torquay; alas, all that remains today of that first tank is a bronze plaque in the wall of the Chelston Manor Hotel in Torquay commemorating its presence.

12.1 Froude's analysis procedure

William Froude (Reference 2) recognized that ship models of geosymmetric form would create similar wave systems, albeit at different speeds. Furthermore, he showed that the smaller models had to be run at

* As from April 1991 AMTE(H) became part of the Defence Research Establishment Agency (DREA).

slower speeds than the larger models in order to obtain the same wave pattern. His work showed that for a similarity of wave pattern between two geosymmetric models of different size the ratio of the speeds of the models was governed by the relationship

$$\frac{V_1}{V_2} = \sqrt{\frac{L_1}{L_2}} \qquad (12.1)$$

By studying the comparison of the specific resistance curves of models and ships Froude noted that they exhibited a similarity of form although the model curve was always greater than that for the ship (Figure 12.1). This led Froude to the conclusion that two components of resistance were influencing the performance of the vessel and that one of these, the wave making component R_w, scaled with $V/\sqrt{L}$ and the other did not. This second component, which is due to viscous effects, derives principally from the flow of the water around the hull but also is influenced by the air flow and weather acting on the above-water surfaces. This second component was termed the frictional resistance R_F.

Froude's major contribution to the ship resistance problem, which has remained useful to the present day, was his conclusion that the two sources of resistance might be separated and treated independently. In this approach, Froude suggested that the viscous resistance could be calculated from frictional data whilst the wave-making resistance R_w could be deduced from the measured total resistance R_T and the calculated frictional resistance R_F as follows:

$$R_w = R_T - R_F \qquad (12.2)$$

In order to provide the data for calculating the value of the frictional component Froude performed his famous experiments at the Admiralty owned model tank at Torquay. These experiments entailed towing a series of planks ranging from 10 to 50 feet in length, having a series of surface finishes of shellac varnish, paraffin wax, tin foil, graduation of sand roughness and other textures. Each of the planks was 19 inches deep and $\frac{3}{16}$ inch thick and was ballasted to float on its edge. Although the results of these experiments suffered from errors due to temperature differences, slight bending of the longer planks and laminar flow on some of the shorter planks, Froude was able to derive an empirical formula which would act as a basis for the calculation of the frictional resistance component R_F in equation (12.2). The relationship Froude derived took the form

$$R_F = fSV^n \qquad (12.3)$$

in which the index n had the constant value of 1.825 for normal ship surfaces of the time and the coefficient f varied with both length and roughness, decreasing with length but increasing with roughness. In equation (12.3), S is the wetted surface area.

As a consequence of this work Froude's basic procedure for calculating the resistance of a ship is as follows:

(1) Measure the total resistance of the geosymmetrically similar model R_{TM} in the towing tank at a series of speeds embracing the design $V/\sqrt{L}$ of the full-size vessel.
(2) From this measured total resistance subtract the calculated frictional resistance values for the model R_{FM} in order to derive the model wave making resistance R_{WM}.
(3) Calculate the full size frictional resistance R_{FS} and add these to the full size wave making resistance R_{WS}, scaled from the model value, to obtain the total full size resistance R_{TS}.

$$R_{TS} = R_{WM}\left(\frac{\Delta_S}{\Delta_M}\right) + R_{FS} \qquad (12.4)$$

In equation (12.4) the suffixes M and S denote model and full scale respectively and Δ is the displacement.

The scaling law of the ratio of displacements derives from Froude's observations that when models of various sizes, or a ship and its model, were run at corresponding speeds dictated by equation (12.1), their resistances would be proportional to the cubes of their linear dimensions or, alternatively, their displacements. This was, however, an extension of a law of comparison which was known at that time.

Froude's law, equation (12.1), states that the wave making resistance coefficients of two geometrically similar hulls of different lengths are the same when moving at the same $V/\sqrt{L}$ value, V being the ship or model speed and L being the waterline length. The ratio $V/\sqrt{L}$ is termed the speed length ratio and is of course dimensional; however, the dimensionless Froude number can be derived from it to give

$$F_n = \frac{V}{\sqrt{(gL)}} \qquad (12.5)$$

in which g is the acceleration due to gravity (9.81 m/s²). Care needs to be exercised in converting between the speed length ratio and the Froude number:

$$F_n = 0.3193\frac{V}{\sqrt{L}} \quad \text{where } V \text{ is in m/s; } L \text{ is in metres}$$

$$F_n = 0.1643\frac{V}{\sqrt{L}} \quad \text{where } V \text{ is in knots; } L \text{ is in metres}$$

Froude's work with his plank experiments was carried out prior to the formulation of the Reynolds number criteria and this undoubtedly led to errors in his results: for example, the laminar flow on the shorter planks. Using dimensional analysis, after the manner shown in Chapter 6, it can readily be shown today that the resistance of a body moving on the surface, or at an interface of a medium, can be given by

$$\frac{R}{\varrho V^2 L^2} = \phi\left\{\frac{VL\varrho}{\mu}, \frac{V}{\sqrt{gL}}, \frac{V}{a}, \frac{\sigma}{g\varrho L^2}, \frac{p_0 - p_v}{\varrho V^2}\right\} \qquad (12.6)$$

In this equation the left-hand side term is the resistance coefficient C_R whilst on the right-hand side of the equation,

the 1st term is the Reynolds number R_n
the 2nd term is the Froude number F_n (equation (12.5))
the 3rd term is the Mach number M_n
the 4th term is the Weber number W_e
the 5th term is the Cavitation number σ_0

For the purposes of ship propulsion the 3rd and 4th terms are not generally significant and can, therefore, be neglected. Hence equation (12.6) reduces to the following for all practical ship purposes:

$$C_R = \phi\{R_n, F_n, \sigma_0\} \qquad (12.7)$$

in which

ϱ is the density of the water
μ is the dynamic viscosity of the water
p_0 is the free stream undisturbed pressure
and p_v is the water vapour pressure.

12.2 Components of calm water resistance

In the case of a vessel which is undergoing steady motion at slow speeds, that is where the ship's weight balances the displacement upthrust without the significant contribution of hydrodynamic lift forces, the components of calm water resistance can be broken down into the contributions shown in Figure 12.2. From this figure it is seen that the total resistance can be decomposed into two primary components, pressure and skin friction resistance, and these can then be broken down further into more discrete components. In addition to these components there is of course the air resistance and added resistance due to rough weather: these are, however, dealt with separately in Sections 12.8 and 12.5 respectively.

Each of the components shown in Figure 12.2 can be studied separately provided that it is remembered that each will have an interaction on the others and, therefore, as far as the ship is concerned, need to be considered in an integrated way.

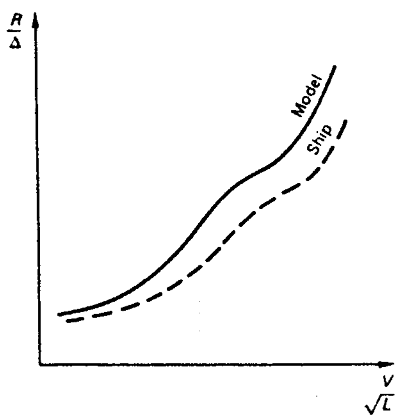

Figure 12.1 Comparison of a ship and its model's specific resistance curves

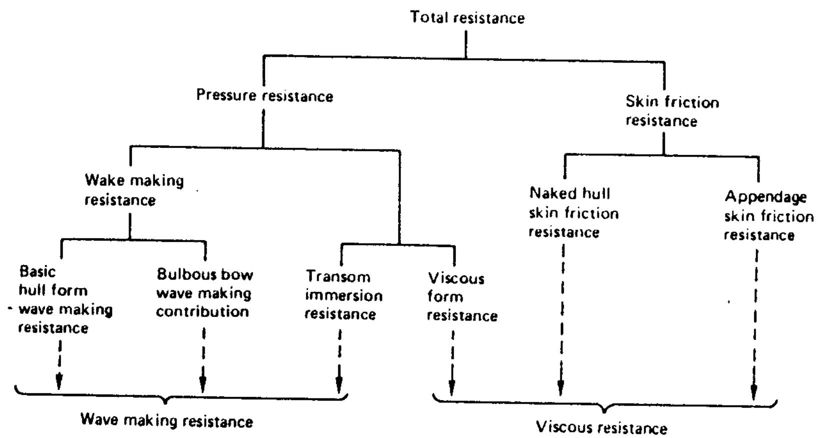

Figure 12.2 Components of ship resistance

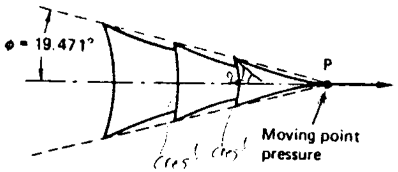

Figure 12.3 Wave pattern induced by a moving-point pressure in calm water

12.2.1 Wave making resistance R_W

Lord Kelvin (References 3–5) in 1904 studied the problem of the wave pattern caused by a moving pressure point. He showed that the resulting system of waves comprises a divergent set of waves together with a transverse system which are approximately normal to the direction of motion of the moving point. Figure 12.3 shows the system of waves so formed. The pattern of waves is bounded by two straight lines which in deep water are at an angle ϕ to the direction of motion of the point, where ϕ is given by

$$\phi = \sin^{-1}(\tfrac{1}{3}) = 19.471°$$

The interference between the divergent and transverse systems give the observed wave their characteristic shape, and since both systems move at the same speed, the speed of the vessel, the wavelength λ between successive crests is

$$\lambda = \frac{2\pi}{g}V^2 \qquad (12.8)$$

The height of the wave systems formed decreases fairly rapidly as they spread out laterally because the energy contained in the wave is constant and it has to be spread out over an increasingly greater length. More energy is absorbed by the transverse system than by the divergent system, and this disparity increases with increasing speed.

A real ship form, however, cannot be represented adequately by a single moving pressure point as analysed by Kelvin. The simplest representation of a ship, Figure 12.4, is to place a moving pressure field near the bow in order to simulate the bow wave system, together with a moving suction field near the stern to represent the stern wave system. In this model the bow pressure field will create a crest near the bow, observation showing that this occurs at about $\lambda/4$ from the bow, whilst the suction field will introduce a wave trough at the stern; both of these wave systems have a wavelength $\lambda = 2\pi V^2/g$.

The divergent component of the wave system derived from the bow and the stern generally do not exhibit any strong interference characteristics. This is not the case, however, with the transverse wave systems created by the vessel, since these can show a strong interference behaviour. Consequently, if the bow and stern wave systems interact such that they are in phase a reinforcement of the transverse wave patterns occurs at the stern and large waves are formed in that region. For such a reinforcement to take place, Figure 12.5(a), the distance between the first crest at the bow and the stern must be an odd number of half-wavelengths as follows:

$$L - \frac{\lambda}{4} = k\frac{\lambda}{2} \qquad \text{where } k = 1,3,5,\ldots,(2j+1) \text{ with } j = 0,1,2,3,\ldots$$

From which

$$\frac{4}{2k+1} = \frac{\lambda}{L} = \frac{2\pi V^2}{gL} = 2\pi(F_n)^2$$

that is,

$$F_n = \sqrt{\frac{2}{\pi(2k+1)}} \qquad (12.9)$$

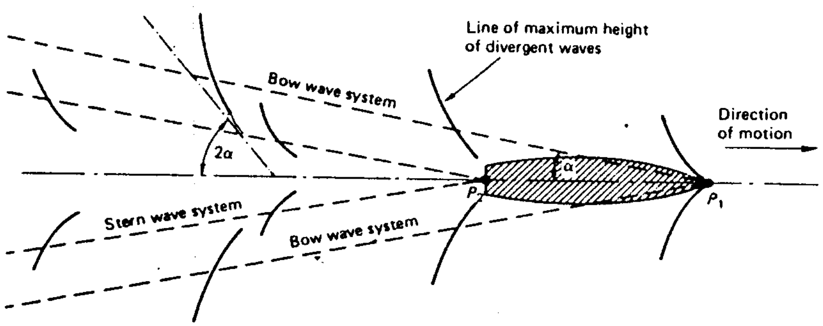

Figure 12.4 Simple ship wave pattern representation by two pressure points

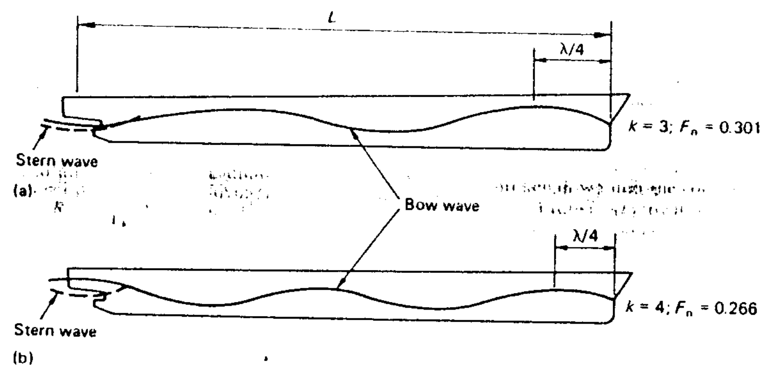

Figure 12.5 Wave reinforcement and cancellation at stern: (a) wave reinforcement at stern; (b) wave cancellation at stern

For the converse case when the bow and stern wave systems cancel each other, and hence produce a minimum wave making resistance condition, the distance $L - \lambda/4$ must be an even number of half wave lengths (Figure 12.5(b)):

$$L - \frac{\lambda}{4} = k\frac{\lambda}{2} \qquad \text{where } k = 2,4,6,\ldots,2j \text{ with } j = 1,2,3,\ldots$$

Hence

$$F_n = \sqrt{\frac{2}{\pi(2k+1)}}$$ as before, but with k even in this case

Consequently from equation (12.9) Table 12.1 can be derived, which for this particular model of wave action identifies the Froude numbers at which reinforcement (humps) and cancellation (hollows) occur in the wave making resistance.

Table 12.1 Froude numbers corresponding to maxima and minima in the wave making resistance component

k	F_n	*Description*
1	0.461	1st hump in R_w curve
2	0.357	1st hollow in R_w curve
3	0.301	2nd hump in R_w curve
4	0.266	2nd hollow in R_w curve
5	0.241	3rd hump in R_w curve
⋮	⋮	⋮

Each of the conditions shown in Table 12.1 relates sequentially to maximum and minimum conditions in the wave making resistance curves. The 'humps' occurring because the wave profiles and hence the wave making resistance are at their greatest in these conditions whilst the converse is true in the case of the 'hollows'. Figure 12.6 shows the general form of the wave making resistance curve together with the

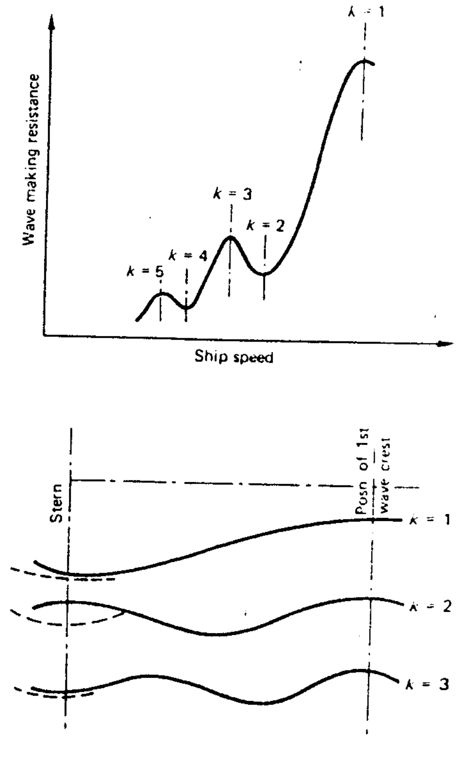

Figure 12.6 Form of wave-making resistance curve

schematic wave profiles associated with the various values of k.

The hump associated with $k = 1$ is normally termed the 'main hump' since this is the most pronounced hump and occurs at the highest speed. The second hump, $k = 3$, is called the 'prismatic hump' since it is influenced considerably by the prismatic coefficient of the particular hull form.

The derivation of Figure 12.6 and Table 12.1 relies on the assumptions made in its formulation; for example, a single pressure and suction field, bow wave crest at $\lambda/4$; stern trough exactly at the stern, etc. Clearly, there is some lattitude in all of these assumptions, and therefore the values of F_n at which the humps and hollows occur vary. In the case of warships the distance between the first crest of the bow wave and the trough of the stern wave has been shown to approximate well to $0.9L$, and therefore this could be used to rederive equation (12.9), and thereby derive slightly differing values of Froude numbers corresponding to the 'humps' and 'hollows'. Table 12.2 shows these differences, and it is clear that the greatest effect is formed at low values of k. Figure 12.6 for this and the other reasons cited is not unique but is shown here to provide awareness and guidance on wave making resistance variations.

A better approximation to the wave form of a vessel can be made by considering the ship as a solid body

Table 12.2 Effect of difference in calculation basis on prediction of hump and hollow Froude numbers

k	1	2	3	4	5
$L - \lambda/4$ basis	0.46	0.36	0.30	0.27	0.24
$0.9\ L$ basis	0.54	0.38	0.31	0.27	0.24

rather than two point sources. Wigley initially used a simple parallel body with two pointed ends and showed that the resulting wave pattern along the body could be approximated by the sum of five separate disturbances of the surface (Figure 12.7). From this figure it is seen that a symmetrical disturbance corresponds to the application of Bernoulli's theorem with peaks at the bow and stern and a hollow, albeit with cusps at the start and finish of the parallel middle body, between them. Two wave forms starting with a crest are formed by the action of the bow and stern whilst a further two wave forms commencing with a trough originates from the shoulders of the parallel middle body. The sum of these five wave profiles is shown in the bottom of Figure 12.7 and compared with a measured profile which shows good general agreement. Since the wave length λ varies with speed and the points at which the waves originate are fixed, it is easy to understand that the whole profile of the resultant wave form will change with speed length ratio.

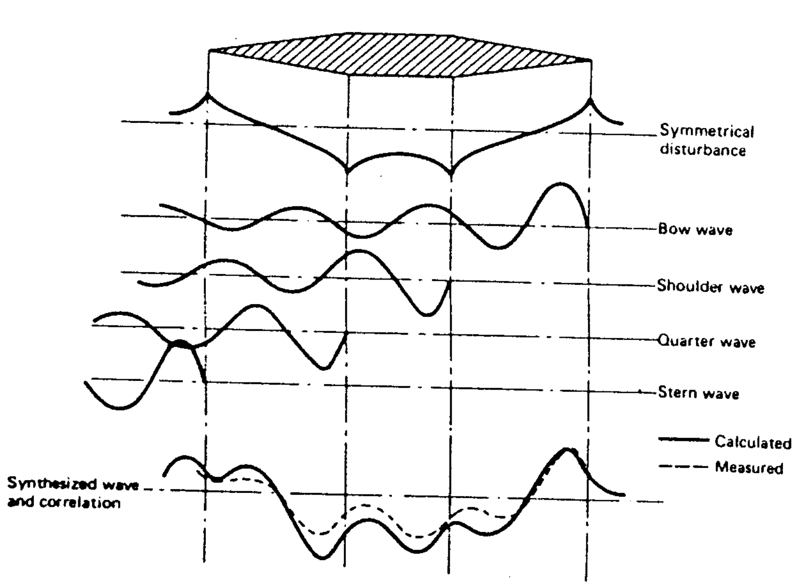

Figure 12.7 Components of wave systems for a simple body

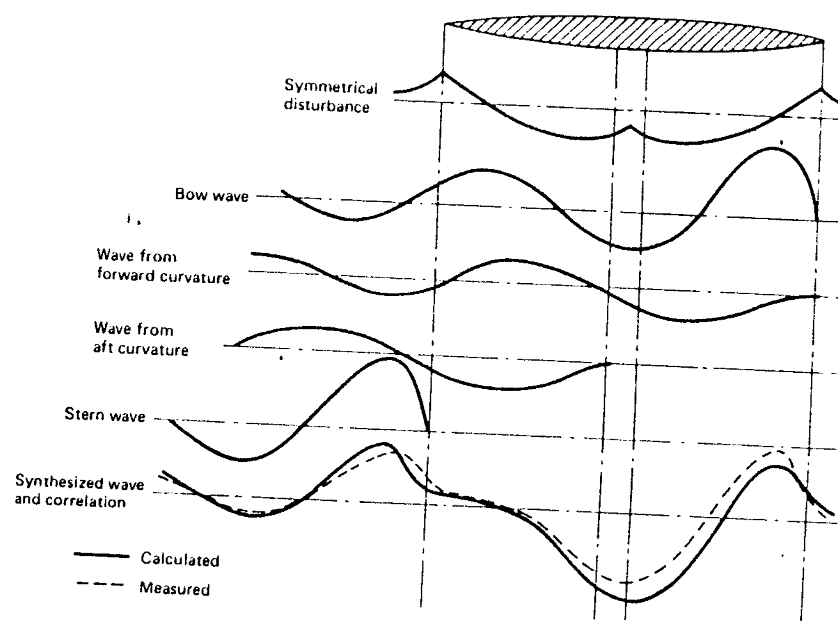

Figure 12.8 Wave components for a body with convex ends and a parallel middle body

This analysis procedure was extended by Wigley for a more realistic hull form comprising a parallel middle body and two convex extremities. Figure 12.8 shows the results in terms of the same five components and the agreement with the observed wave form.

Considerations of this type lead to endeavouring to design a hull form to produce a minimum wave making resistance using theoretical methods. The basis of these theories are developed from Kelvin's work on a travelling pressure source; however, the mathematical boundary conditions are difficult to satisfy with any degree of precision. Results of work based on these theories has been mixed in terms of their ability to represent the observed wave forms, and consequently there is still considerable work to undertake in this field.

12.2.2 The contribution of the bulbous bow

Bulbous bows are today commonplace in the design of ships. Their origin is to be found before the turn of the century, but the first application appears to have been in 1912 by the US Navy. The general use in merchant applications appears to have waited until the late 1950s and early 1960s.

The basic theoretical work on their effectiveness was carried out by Wigley (Reference 6) in which he showed that if the bulb was nearly spherical in form, then the acceleration of the flow over the surface induces a low-pressure region which can extend toward the water surface. This low-pressure region then reacts with the bow pressure wave to cancel or reduce the effect of the bow wave. The effect of the bulbous bow, therefore, is to cause a reduction, in the majority of cases, of the effective power required to propel the vessel, the effective power P_E being defined as the product of the ship resistance and the ship speed at a particular condition. Figure 12.9 shows a typical example of the effect of a bulbous bow from which it can be seen that a bulb is, in general, beneficial above a certain speed and gives a penalty at low speeds. This is because of the balance between the bow pressure wave reduction effect and increase in frictional resistance caused by the presence of the bulb on the hull.

The effects of the bulbous bow in changing the resistance and delivered power characteristics can be attributed to several causes. The principal of these are as follows:

1. the reduction of bow pressure wave due to the pressure field created by the bulb and the consequent reduction in wave making resistance;

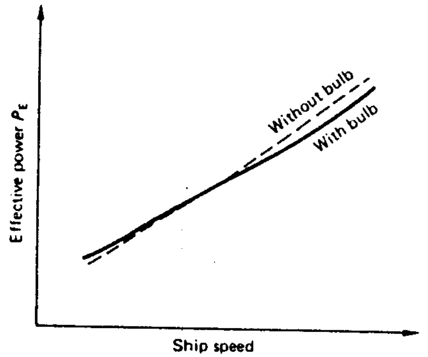

Figure 12.9 Influence of a bulbous bow of the effective power requirement

2. the influence of the upper part of the bulb and its intersection with the hull to introduce a downward flow component in the vicinity of the bow;
3. an increase in the frictional resistance caused by the surface area of the bulb;
4. a change in the propulsion efficiency induced by the effect of the bulb on the global hull flow field;
5. the change induced in the wave breaking resistance.

The shape of the bulb is particularly important in determining its beneficial effect. The optimum shape for a particular hull depends on the Froude number associated with its operating regime, and bulbous bows tend to give good performance over a narrow range of ship speeds. Consequently, they are most commonly found on vessels which operate at clearly defined speeds for much of their time. The actual bulb form, Figure 12.10, is defined in relation to a series of form characteristics as follows:

(1) length of projection beyond the forward perpendicular;
(2) cross-sectional area at the forward perpendicular (A_{BT});
(3) height of the centroid of cross section A_{BT} from the base line (h_B);
(4) bulb section form and profile;
(5) transition of the bulb into the hull.

With regard to section form many bulbs today are designed with non-circular forms so as to minimize the effects of slamming in poor weather. There is, however, still considerable work to be done in relating bulb form to power saving and much contemporary work is proceeding. For current design purposes reference can be made to the work of Inui (Reference 7), Todd (Reference 8), Yim (Reference 9) and Schneekluth (Reference 10).

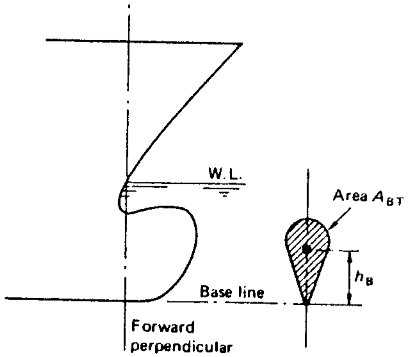

Figure 12.10 Bulbous bow definition

In addition to its hydrodynamic behaviour the bulb also introduces a further complication into resistance calculations. Traditionally the length along the waterline has formed the basis of many resistance calculation procedures because it is basically the fundamental hydrodynamic dimension of the vessel. The bulbous bow, however, normally projects forward of the forward point of the definition of the water line length, and since the bulb has a fundamental influence on some of the resistance components, there is a case for redefining the basic hydrodynamic length parameter for resistance calculations.

12.2.3 Transom immersion resistance

In modern ships a transom stern is now normal practice. If at the design powering condition a portion of the transom is immersed, this leads to separation taking place as the flow from under the transom passes out beyond the hull (Figure 12.11). The resulting vorticity that takes place in the separated flow behind the transom leads to a pressure loss behind the hull which is taken into account in some analysis procedures.

The magnitude of this resistance is generally small and, of course, vanishes when the lower part of the transom is dry. Transom immersion resistance is largely a pressure resistance that is scale independent.

12.2.4 Viscous form resistance

The total drag on a body immersed in a fluid and travelling at a particular speed is the sum of the skin friction components, which is equal to the integral of the shearing stresses taken over the surface of the body, and the form drag, which is in the integral of the normal forces acting on the body.

In an inviscid fluid the flow along any streamline is governed by Bernoulli's equation and the flow around an arbitrary body is predictable in terms of the changes between pressure and velocity over the surface. In the case of Figure 12.12(a) this leads to the net axial force in the direction of motion being equal to zero since in the two-dimensional case shown in Figure 12.12(a),

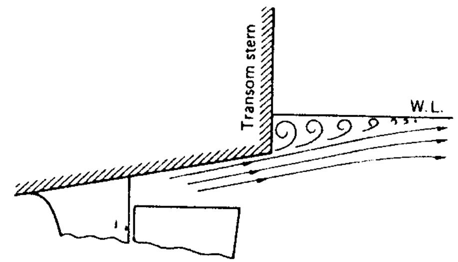

Figure 12.11 Flow around an immersed transom stern

$$\oint p \cos \theta \, ds = 0 \tag{12.10}$$

When moving in a real fluid, a boundary layer is created over the surface of the body which, in the case of a ship, will be turbulent and is also likely to separate at some point in the after body. The presence of the boundary layer and its growth along the surface of the hull modifies the pressure distribution acting on the body from that of the potential or inviscid case. As a consequence, the left-hand side of equation (12.10) can no longer equal zero and the viscous form drag R_{VF} is defined for the three-dimensional case of a ship hull as

$$R_{VF} = \sum_{k=1}^{n} p_k \cos \theta_k \delta S_k \tag{12.11}$$

in which the hull has been split into n elemental areas δS_k and the contribution of each normal pressure p_k acting on the area is summed in the direction of motion; Figure 12.12(b).

Equation (12.11) is an extremely complex equation to solve since it relies on the solution of the boundary layer over the vessel and this is a solution which at the present time can only be approached using considerable computational resources for comparatively simple hull forms. As a consequence, the viscous form resistance is normally accounted for using empirical or pseudo-empirical methods at this time.

12.2.5 Naked hull skin friction resistance

The original data upon which to calculate the skin friction component of resistance was that provided by Froude in his plank experiments at Torquay. This data, as discussed in the previous section, was subject to error and in 1932 Schoenherr re-evaluated Froude's original data in association with other work in the light of the Prandtl–von Karman theory. This analysis resulted in an expression of the friction coefficient C_F as a function of Reynolds number R_n and the formulation of a skin friction line, applicable to smooth surfaces, of the following form:

$$\frac{0.242}{\sqrt{C_F}} = \log(R_n \cdot C_F) \tag{12.12}$$

This equation, known as the Schoenherr line, was adopted by the American Towing Tank Conference (ATTC) in 1947 and in order to make the relationship applicable to the hull surfaces of new ships an additional allowance of 0.0004 was added to the smooth surface values of C_F given by equation (12.12). By 1950 there was a variety of friction lines for smooth turbulent flows in existence and all, with the exception of Froude's work, were based on Reynolds number. Phillips-Birt (Reference 11) provides an interesting comparison of these friction formulations for a Reynolds number of 3.87×10^9 which is applicable to ships of the length of the former trans-Atlantic liner *Queen Mary* and is rather less than that for the large supertankers: in either case lying way beyond the range of direct experimental results. The comparison is shown in Table 12.3 from which it is seen that close agreement is seen to exist between most of the results except for the Froude and Schoenherr modified line. These last two, whilst giving comparable results,

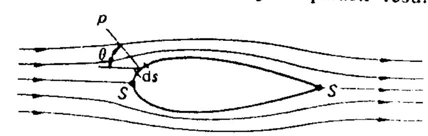

(a)

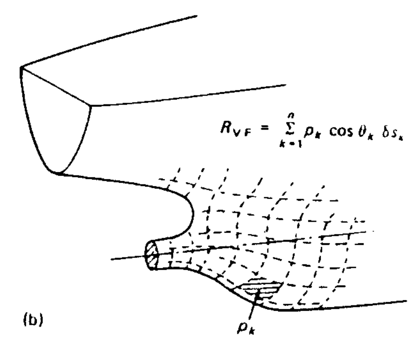

(b)

Figure 12.12 Viscous form resistance calculation: (a) inviscid flow case on an arbitrary body; (b) pressures acting on shell plate of a ship

Table 12.3 Comparison of C_F values for different friction lines for a Reynolds number $R_n = 3.87 \times 10^9$ (taken from Reference 11)

Friction line	C_F
Gerbers	0.00134
Prandtl - Schlichting	0.00137
Kemph - Karham	0.00103
Telfer	0.00143
Lackenby	0.00140
Froude	0.00168
Schoenherr	0.00133
Schoenherr + 0.0004	0.00173

include a correlation allowance in their formulation. Indeed the magnitude of the correlation allowance is striking between the two Schoenherr formulations: the allowance is some 30% of the basic value.

In the general application of the Schoenherr line some difficulty was experienced in the correlation of large and small model test data and wide disparities in the correlation factor C_A were found to exist upon the introduction of all welded hulls. These shortcomings were recognized by the 1957 International Towing Tank Conference (ITTC) and a modified line was accepted. The 1957 ITTC line is expressed as

$$C_F = \frac{0.075}{(\log_{10} R_n - 2.0)^2} \qquad (12.13)$$

and this formulation, which is in use with most ship model basins, is shown together with the Schoenherr line in Figure 12.13. It can be seen that the present ITTC line gives slightly higher values of C_F at the lower Reynolds numbers than the Schoenherr line whilst both lines merge toward the higher values of R_n.

The frictional resistance R_F derived from the use of either the ITTC or ATTC lines should be viewed as an instrument of the calculation process rather than producing a definitive magnitude of the skin friction associated with a particular ship. As a consequence

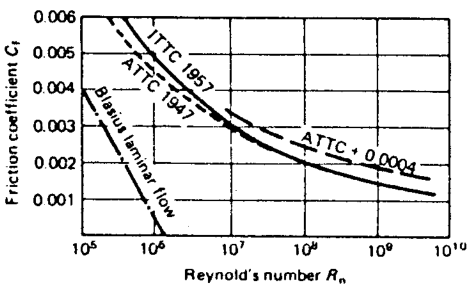

Figure 12.13 Comparison of ITTC(1957) and ATTC(1947) friction lines

when using a Froude analysis based on these, or indeed any friction line data, it is necessary to introduce a correlation allowance into the calculation procedure. This allowance is denoted by C_A and is defined as

$$C_A = C_{T(\text{measured})} - C_{T(\text{estimated})} \qquad (12.14)$$

In this equation, as in the previous equation, the resistance coefficients C_T, C_F, C_W and C_A are non-dimensional forms of the total, frictional, wave making and correlation resistances, and are derived from the basic resistance summation

$$R_T = R_W + R_V$$

by dividing this equation throughout by $\frac{1}{2}\rho V_s^2 S$, $\frac{1}{2}\rho V_s^2 L^2$ or $\frac{1}{2}\rho V_s^2 \nabla^{2/3}$ according to convenience.

12.2.6 Appendage skin friction

The appendages of a ship such as the rudder, bilge keels, stabilizers, transverse thruster openings and so on introduce a skin friction resistance above that of the naked hull resistance.

At the ship scale the flow over the appendages is turbulent, whereas at model scale it would normally be laminar unless artificially stimulated, which in itself may introduce a flow modelling problem. In addition, many of the hull appendages are working wholly within the boundary layer of the hull, and since the model is run at Froude identity and not Reynolds identity this again is a source of problem. As a consequence the prediction of appendage resistance needs care if significant errors are to be avoided. The calculation of this aspect is further discussed in Section 12.3.

In addition to the skin friction component of appendage resistance, if the appendages are located on the vessel close to the surface then they will also contribute to the wave making component since a lifting body close to a free surface, due to the pressure distribution around the body, will create a disturbance on the free surface. As a consequence, the total appendage resistance can be expressed as the sum of the skin friction and surface disturbance effects as follows:

$$R_{APP} = R_{APP(F)} + R_{APP(W)} \qquad (12.15)$$

where $R_{APP(F)}$ and $R_{APP(W)}$ are the frictional and wave making components respectively of the appendages. In most cases of practical interest to the merchant marine $R_{APP(W)} \simeq 0$ and can be neglected: this is not the case, however, for some naval applications.

12.2.7 Viscous resistance

Figure 12.2 defines the viscous resistance as being principally the sum of the form resistance, the naked hull skin friction and the appendage resistance. In the discussion on the viscous form resistance it was said that its calculation by analytical means was an extremely complex matter and for many hulls of a complex shape was not possible with any degree of accuracy at the present time.

Hughes (Reference 12) attempted to provide a better empirical foundation for the viscous resistance calculation by devising an approach which incorporated the viscous form resistance and the naked hull skin friction. To form a basis for this approach Hughes undertook a series of resistance tests using planks and pontoons for a range of Reynolds numbers up to a value of 3×10^8. From the results of this experimental study Hughes established that the frictional resistance coefficient C_F could be expressed as a unique inverse function of aspect ratio AR and, furthermore, that this function was independent of Reynolds number. The function derived from this work had the form:

$$C_F = C_F\Big|_{AR=\infty} \cdot f\left(\frac{1}{AR}\right)$$

in which the term $C_F|_{AR=\infty}$ is the frictional coefficient relating to a two-dimensional surface; that is, one having an infinite aspect ratio.

This function permitted Hughes to construct a two-dimensional friction line defining the frictional resistance of turbulent flow over a plane smooth surface. This took the form

$$C_F\Big|_{AR=\infty} = \frac{0.066}{[\log_{10} R_n - 2.03]^2} \qquad (12.16)$$

Equation (12.16) quite naturally bears a close similarity to the ITTC 1957 line expressed by equation (12.13). The difference, however, is that the ITTC and ATTC lines contain some three-dimensional effects, whereas equation (12.16) is defined as a two-dimensional line. If it is plotted on the same curve as the ITTC line, it will be found that it lies just below the ITTC line for the full range of R_n and in the case of the ATTC line it also lies below it except for the very low Reynolds numbers.

Hughes proposed the calculation of the total resistance of a ship using the basic relationship

$$C_T = C_V + C_W$$

in which $C_V = C_F|_{AR=\infty} + C_{FORM}$, thereby giving the total resistance as

$$C_T = C_F|_{AR=\infty} + C_{FORM} + C_W \qquad (12.17)$$

in which C_{FORM} is a 'form' resistance coefficient which takes into account the viscous pressure resistance of the ship. In this approach the basic skin friction resistance coefficient can be determined from equation (12.16). To determine the form resistance the ship model can be run at a very slow speed when the wave making component is very small and can be neglected; when this occurs, that is to the left of point A in Figure 12.14, then the resistance curve defines the sum of the skin friction and form resistance components. At the point A, when the wave making resistance is negligible, the ratio

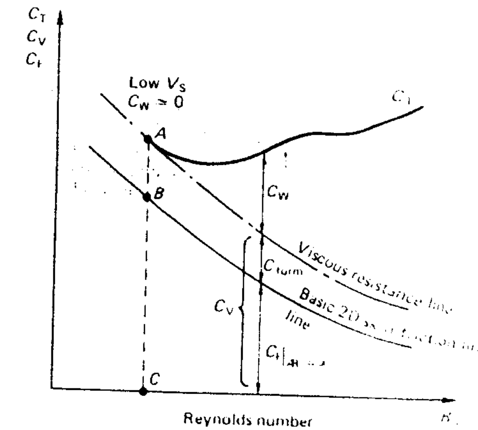

Figure 12.14 Hughes model of ship resistance

$$\frac{AC}{BC} = \frac{\text{viscous resistance}}{\text{skin friction resistance}}$$

$$= \frac{\text{skin friction resistance} + \text{viscous form resistance}}{\text{skin friction resistance}}$$

$$= 1 + \frac{\text{viscous form resistance}}{\text{skin friction resistance}}$$

$$\text{and if } k = \frac{\text{viscous form resistance}}{\text{skin friction resistance}}$$

$$\text{then } \frac{AC}{BC} = (1 + k) \qquad (12.18)$$

In equation (12.8), $(1 + k)$ is termed the form factor and is assumed constant for both the ship and its model. Indeed the form factor is generally supposed to be independent of speed and scale in the resistance extrapolation method. In practical cases the determination of $(1 + k)$ is normally carried out using a variant of the Prohashka method by a plot of C_T against F_n^4 and extrapolating the curve to $F_n = 0$ (Figure 12.15). From this figure the form factor $(1 + k)$ is deduced from the relationship

$$1 + k = \lim_{F_n \to 0} \left(\frac{R}{R_F}\right)$$

This derivation of the form factor can be used in the resistance extrapolation only if scale-independent pressure resistance is absent; for example, there must be no immersion of the transom and slender appendages which are oriented to the direction of flow.

Although traditionally the form factor $(1 + k)$ is treated as a constant with varying Froude number the fundamental question remains as to whether it is valid to assume that the $(1 + k)$ value, determined at

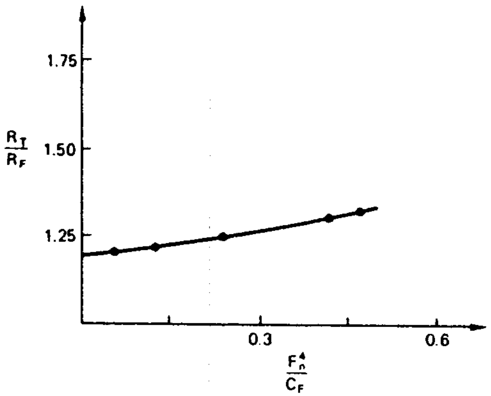

Figure 12.15 Determination of $(1 + k)$ using Prohaska method

vanishing Froude number, is valid at high speed. This is of particular concern at speeds beyond the main resistance hump where the flow configuration around the hull is likely to be very different from that when $F_n = 0$, and therefore a Froude number dependency can be expected for $(1 + k)$. In addition a Reynolds dependency may also be expected since viscous effects are the basis of the $(1 + k)$ formulation. The Froude and Reynolds effects are, however, likely to effect most the high-speed performance and have a lesser influence on general craft.

The extrapolation from model to full scale using Hughes' method is shown in Figure 12.16(a), from which it is seen that the two-dimensional skin friction line, equation (12.16), is used as a basis and the viscous resistance is estimated by scaling the basic friction line by the form factor $(1 + k)$. This then acts as a basis for calculating the wave making resistance from the measured total resistance on the model which is then equated to the ship condition along with the recalculated viscous resistance for the ship Reynolds number. The Froude approach (Figure 12.15(b)), is essentially the same, except that the frictional resistance is based on one of the Froude, ATTC (equation (12.12)) or ITTC (equation (12.13)) friction lines without a $(1 + k)$ factor. Clearly the magnitude of the calculated wave making resistance, since it is measured total resistance minus calculated frictional resistance, will vary according to the friction formulation used. This is also true of the correlation allowances as defined in equation (12.15), and therefore the magnitudes of these parameters should always be considered in the context of the approach and experimental facility used.

In practice both the Froude and Hughes approaches are used in model testing; the latter, however, is most frequently used in association with the ITTC 1957 friction formulation rather than equation (12.16).

12.3 Methods of resistance evaluation

To evaluate the resistance of a ship the designer has several options available. These range, as shown in Figure 12.17, from what may be termed the traditional methods through to advanced computational fluid dynamics methods. The choice of method depends not only on the capability available but also on the accuracy desired, the funds available and the degree to which the approach has been developed. Figure 12.17 identifies four basic classes of approach to the problem; the traditional and standard series; the regression based procedures; the direct model test; and the computational fluid dynamics approach. Clearly these are somewhat artificial distinctions, and consequently break down on close scrutiny; they are, however, convenient classes for discussion purposes.

Unlike the computational fluid dynamics and direct model test approaches, the other methods are based on the traditional naval architectural parameters of hull form; for example, block coefficient, longitudinal centre of buoyancy, prismatic coefficient, etc. These form parameters have served the industry well in the past for resistance calculation purposes; however, as requirements become more exacting and hull forms become more complex these traditional parameters are less able to reflect the growth of the boundary layer and wave making components. As a consequence much current research is being expended in the development of form parameters which will reflect the hull surface contours in a more equable way.

12.3.1 Traditional and standard series analysis methods

A comprehensive treatment of these methods would require a book in itself and would also lie to one side of the main theme of this text. As a consequence an outline of four of the traditional methods starting with that of Taylor and proceeding through Ayer's analysis to the later methods of Auf'm Keller and Harvald are presented in order to illustrate the development of these methods.

Taylor's method (1910–1943)

Taylor in 1910 published the results of model tests on a series of hull forms. This work has since been extended (Reference 13) to embrace a range of $V/\sqrt{L}$ from 0.3 to 2.0. The series comprised some 80 models in which results are published for beam draught ratios of 2.25, 3.0 and 3.75 with five displacement length ratios. Eight prismatic coefficients were used spanning the range 0.48 to 0.80, which tends to make the series useful for the faster and less full vessels.

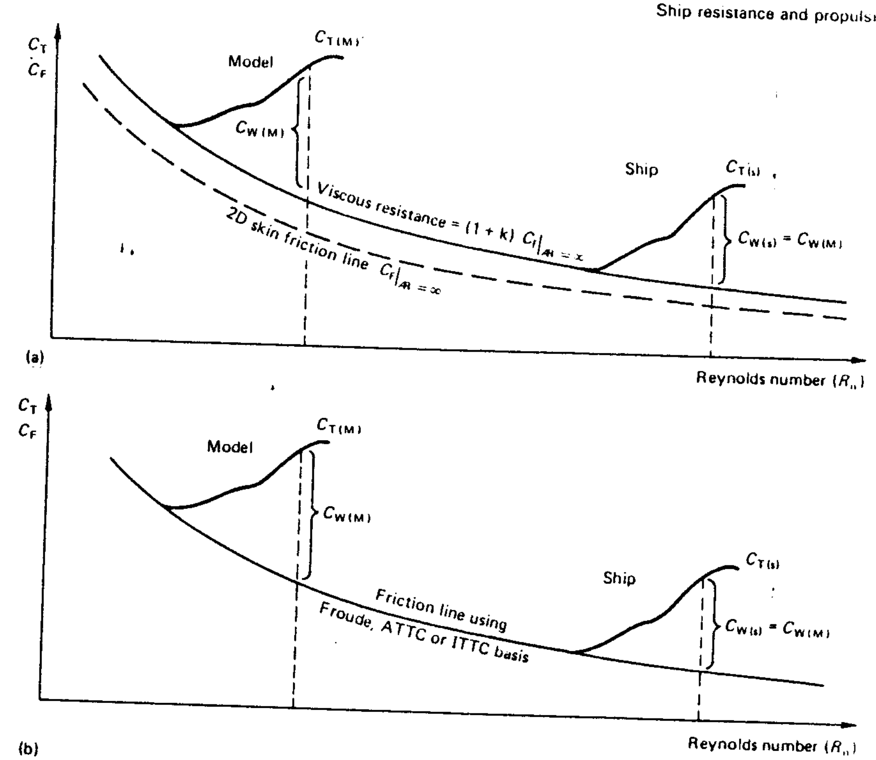

Figure 12.16 Comparison of extrapolation approaches: (a) extrapolation using Hughes approach; (b) extrapolation using Froude approach

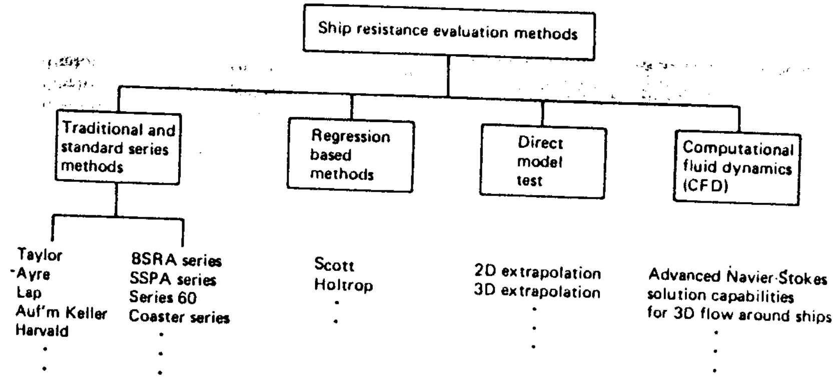

Figure 12.17 Ship resistance evalution methods and examples

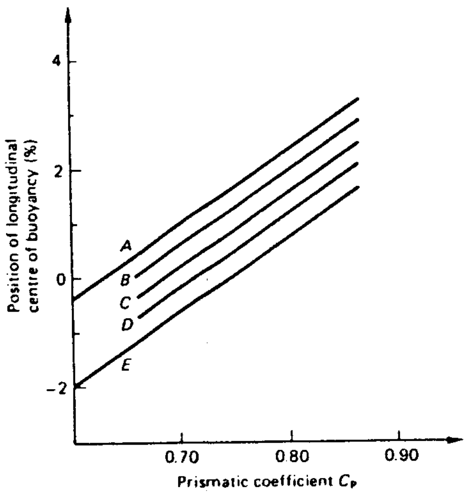

Figure 12.18 Definition of ship class

The procedure is centred on the calculation of the residual resistance coefficients based on the data for each B/T value corresponding to the prismatic and $V/\sqrt{L}$ values of interest. The residual resistance component C_R is found by interpolation from the three B/T values corresponding to the point of interest. The frictional resistance component is calculated on a basis of Reynolds number and wetted surface area together with a hull roughness allowance. The result of this calculation is added to the interpolated residuary resistance coefficient to form the total resistance coefficient C_T from which the naked effective horsepower is derived for each of the chosen $V/\sqrt{L}$ values from the relation

$$\mathrm{EHP}_n = AC_T V_S^3 \qquad (12.19)$$

where A is the wetted surface area.

Ayre's method (1942)

Ayre (Reference 14) developed a method in 1927, again based on model test data, using a series of hull forms relating to colliers. In his approach, which in former years achieved widespread use, the method centres on the calculation of a constant coefficient C_2 which is defined as

$$\mathrm{EHP} = \frac{\Delta^{0.64} V_S^3}{C_2} \qquad (12.20)$$

This relationship implies that in the case of full-sized vessels of identical forms and proportions, the EHP at corresponding speeds varies as $(\Delta^{0.64} V_S^3)$ and that C_2 is a constant at given values of $V/\sqrt{L}$. In this case the use of $\Delta^{0.64}$ avoids the necessity to treat the frictional and residual resistances separately for vessels of around 30 m.

The value of C_2 is estimated for a standard block coefficient. Corrections are then made to adjust the standard block coefficient to the actual value and corrections applied to cater for variations in the beam–draught ratio, position of the l.c.b. and variations in length from the standard value used in the method's derivation.

Auf'm Keller method

Auf'm Keller (Reference 15) extended the earlier work of Lap (Reference 16) in order to allow the derivation of resistance characteristics of large block coefficient, single-screw vessels. The method is based on the collated results from some 107 model test results for large single-screw vessels and the measurements were converted into five sets of residuary resistance values. Each of the sets is defined by a linear relationship between the longitudinal centre of buoyancy and the prismatic coefficient. Figure 12.18 defines these sets, denoted by the letters A to E, and Figure 12.19 shows the residuary resistance coefficient for set A. As a consequence it is possible to interpolate between the sets for a particular l.c.b. versus C_P relationship.

The procedure adopted is shown in outline form by Figure 12.20 in which the correction for ζ_r and the ship model correlation C_A are given by equation (12.21) and Table 12.4 respectively:

$$\%\ \text{change in}\ \zeta_r = 10.357[e^{1.1296(6.5 - L/B)} - 1] \qquad (12.21)$$

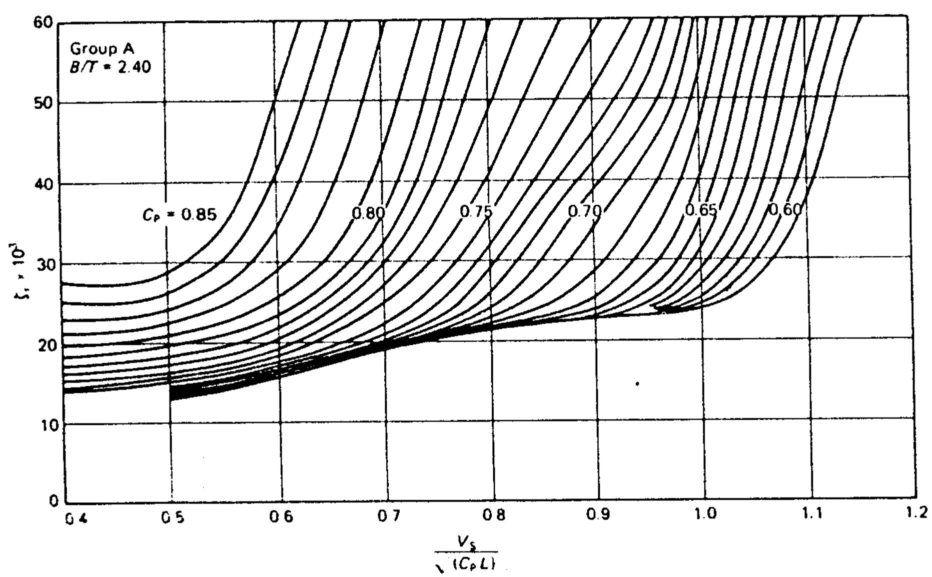

Figure 12.19 Diagram for determining the specific residuary resistance as a function of $V_s/\sqrt{(C_p L)}$ and C_p (Reproduced from Reference 15, with permission)

Table 12.4 Values of C_A used in Auf'm Keller method (taken from Reference 15)

Length of vessel (m)	*Ship model correlation allowance*
50–150	0.0004 → 0.00035
150–210	0.0002
210–260	0.0001
260–300	0
300–350	−0.0001
350–450	−0.00025

As in the case of the previous two methods the influence of the bulbous bow is not taken into account but good experience can be achieved with the method within its area of application.

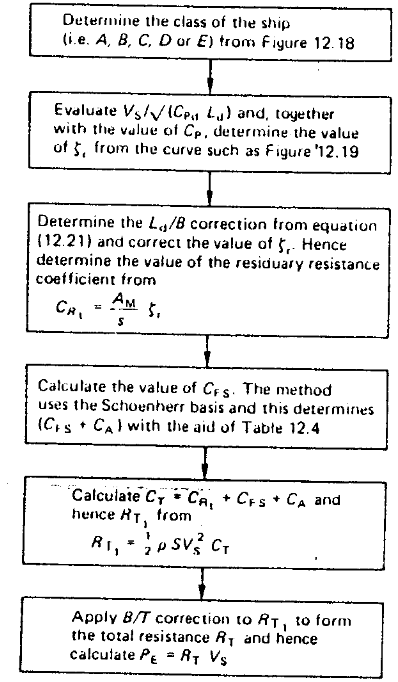

Figure 12.20 Auf'm Keller resistance calculation

Harvald method

The method proposed by Harvald (Reference 17) is essentially a preliminary power prediction method designed to obtain an estimate of the power required to drive a vessel. The approach used is to define four principal parameters upon which to base the estimate; the four selected are

(1) the ship displacement (Δ);
(2) the ship speed (V_S);
(3) the block coefficient (C_b);
(4) the length displacement ratio ($L/\nabla^{1/3}$).

By making such a choice all the other parameters that may influence the resistance characteristics need to be standardized, such as hull form, B/T ratio, l.c.b., propeller diameter, etc. The method used by Harvald is to calculate the resistance of a standard form for a range of the four parameters cited above and then evaluate the shaft power using a QPC based on the wake and thrust deduction method discussed in Chapter 5 and a propeller open water efficiency taken from the Wageningen B Series propellers. The result of this analysis led to the production of seven diagrams

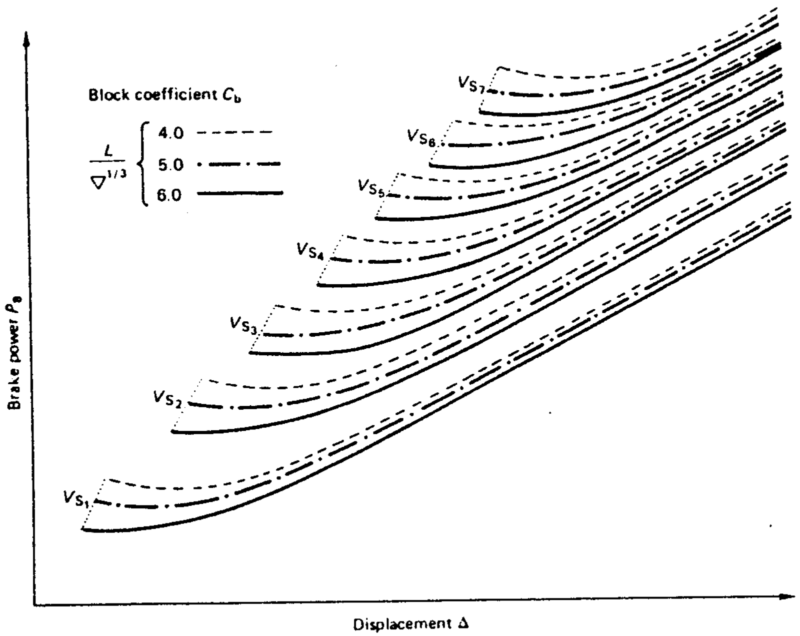

Figure 12.21 Harvald estimation diagram for ship power

for a range of block coefficient from 0.55 to 0.85 in 0.05 intervals of the form shown in Figure 12.21. From these diagrams an estimate of the required power under trial conditions can be derived readily with the minimum of effort. However, with such a method it is important to make allowance for deviations of the actual form from those upon which the diagrams are based.

Standard series data

In addition to the more formalized methods of analysis there is a great wealth of data available to the designer and analyst in the form of model data and more particularly in model data relating to standard series hull forms. That is, those in which the geometric hull form variables have been varied in a systematic way. Much data has been collected over the years and Bowden (Reference 18) gives a very useful guide to the extent of the data available for single-screw ocean-going ships between the years 1900 and 1969. Some of the more recent and important series and data are given in References 19–31. Unfortunately, there is little uniformity of presentation in the work as the results have been derived over a long period of time in many countries of the world. The designer therefore has to accept this state of affairs and account for this in his calculations. In addition hull form design has progressed considerably in recent years and little of these changes is reflected in the data cited in these references. Therefore, unless extreme care is exercised in the application of such data, significant errors can be introduced into the resistance estimation procedure.

In more recent times the Propulsion Committee of the ITTC have been conducting a cooperative experimental programme between tanks around the world (Reference 32). The data so far reported relates to the Wigley parabolic hull and the Series 60, $C_b = 0.60$ hull forms.

12.3.2 Regression based methods

Ship resistance prediction based on statistical regression methods has been a subject of some interest for a number of years. Early work by Scott in the 1970s (References 33, 34) resulted in methods for predicting the trial performance of single- and twin-screw merchant ships.

The theme of statistical prediction was then taken up by Holtrop in a series of papers (References 35–39). These papers trace the development of a power prediction method based on the regression analysis of random model and full-scale test data together with, in the latest version of the method, the published results of the Series 64 high-speed displacement hull terms. In this latest version the regression analysis is now based on the results of some 334 model tests. The results are analysed on the basis of the ship resistance equation.

$$R_T = R_F(1 + k_1) + R_{APP} + R_W + R_B + R_{TR} + R_A \qquad (12.22)$$

In this equation the frictional resistance R_F is calculated according to the 1957 ITTC friction formulation, equation (12.13), and the hull form factor $(1 + K_1)$ is based on a regression equation and is expressed as a function of afterbody form, breadth, draught, length along the waterline, length of run, displacement, prismatic coefficient:

$$\begin{aligned}(1 + k_1) = 0.93 + 0.487118(1 + 0.011C_{stern}) \\ \times (B/L)^{1.06806}(T/L)^{0.46106} \\ \times (L_{WL}/L_R)^{0.121563}(L_{WL}^3/\nabla)^{0.36486} \\ \times (1 - C_P)^{-0.604247}\end{aligned} \qquad (12.23)$$

in which the length of run L_R is defined by a separate relationship, if unknown, as follows:

$$L_R = L_{WL}\left(1 - C_P + \frac{0.06C_P \text{l.c.b.}}{(4C_P - 1)}\right)$$

The sternshape parameter C_{stern} in equation (12.23) is defined in relatively discrete and coarse steps for different hull forms, as shown in Table 12.5.

Table 12.5 C_{stern} parameters according to Holtrop

Afterbody form	C_{stern}
Pram with gondola	−25
V-shaped sections	−10
Normal section ship	0
U-shaped sections with Hogner stern	10

The appendage resistance according to the Holtrop approach is evaluated from the equation

$$R_{APP} = \tfrac{1}{2}\varrho V_S^2 C_F(1 + k_2)_{equv}\sum S_{APP} + R_{BT} \qquad (12.24)$$

in which the frictional coefficient C_F of the ship is again determined by the ITTC 1957 line and S_{APP} is the wetted area of the particular appendages of the vessel. To determine the equivalent $(1 + k_2)$ value for the appendages, denoted by $(1 + k_2)_{equv}$, appeal is made to the relationship

$$(1 + k_2)_{equv} = \frac{\sum(1 + k_2)S_{APP}}{\sum S_{APP}} \qquad (12.25)$$

The values of the appendage form factors are tentatively defined by Holtrop as shown in Table 12.6.

Table 12.6 Tentative appendage form factors $(1 + k_2)$

Appendage type	$(1 + k_2)$
Rudder behind skeg	1.5–2.0
Rudder behind stern	1.3–1.5
Twin-screw balanced rudders	2.8
Shaft brackets	3.0
Skeg	1.5–2.0
Strut bossings	3.0
Hull bossings	2.0
Shafts	2.0–4.0
Stabilizer fins	2.8
Dome	2.7
Bilge keels	1.4

If bow thrusters are fitted to the vessel their influence can be taken into account by the term R_{BT} in equation (12.24) as follows:

$$R_{BT} = \pi\varrho V_S^2 d_T C_{BTO}$$

in which d_T is the diameter of the bow thruster and the coefficient C_{BTO} lies in the range 0.003 to 0.012. When the thruster lies in the cylindrical part of the bulbous bow, $C_{BTO} \to 0.003$.

The prediction of the wave making component of resistance has proved difficult and in the last version of Holtrop's method (Reference 39) a three-banded approach is proposed to overcome the difficulty of finding a general regression formula. The ranges proposed are based on the Froude number F_n and are as follows:

Range 1: $F_n > 0.55$
Range 2: $F_n < 0.4$
Range 3: $0.4 < F_n < 0.55$

within which the general form of the regression equations for wave making resistance in ranges 1 and 2 is

$$R_W = K_1K_2K_3\nabla\varrho g \exp[K_4F^{K_6} + K_5\cos(K_7F_n^{-2})] \qquad (12.26)$$

The coefficients K_1, K_2, K_3, K_4, K_5, K_6 and K_7 are defined by Holtrop in Reference 39 and it is of interest to note that the coefficient K_2 determines the influence of the bulbous bow on the wave resistance. Furthermore, the difference in the coefficients of equation (12.26) between ranges 1 and 2 above lie in the coefficients K_1 and K_4. To accommodate the intermediate range, Range 3, a more or less arbitrary interpolation formula is used of the form

$$R_W = R_W|_{F_n=0.4} + \frac{(10F_n - 4)}{1.5} \times [R_W|_{F_n=0.55} - R_W|_{F_n=0.4}] \qquad (12.27)$$

The remaining terms in equation (12.22) relate to the additional pressure resistances of the bulbous bow near the surface R_B and the immersed part of the transom R_{TR} and are defined by relatively simple regression formulae. With regard to the model-ship correlation resistance the most recent analysis has shown the formulation in Reference 38 to predict a value some 9–10% high; however, for practical purposes that formulation is still recommended by Holtrop:

$$R_A = \tfrac{1}{2}\varrho V_S^2 S C_A$$

where

$$C_A = 0.006(L_{WL} + 100)^{-0.16} - 0.00205 + 0.003\sqrt{(L_{WL}/7.5)}C_B^4 K_2(0.04 - c_4) \quad (12.28)$$

in which $c_4 = T_F/L_{WL}$ when $T_F/L_{WL} \leqslant 0.04$
and $c_4 = 0.04$ when $T_F/L_{WL} > 0.04$

where T_F is the forward draught of the vessel and S is the wetted surface area of the vessel.

K_2, which also appears in equation (12.26) and determines the influence of the bulbous bow on the wave resistance is given by

$$K_2 = \exp[-1.89\sqrt{c_3}]$$

where

$$c_3 = \frac{0.56(A_{BT})^{1.5}}{BT(0.31\sqrt{A_{BT}} + T_F - h_B)}$$

in which A_{BT} is the transverse area of the bulbous bow and h_B is the position of the centre of the transverse area A_{BT} above the keel line with an upper limit of $0.6T_F$; see Figure 12.10.

Equation (12.28) is based on a mean apparent amplitude hull roughness $k_S = 150\,\mu$m. In cases where the roughness may be larger than this use can be made of the ITTC-1978 formulation, which gives the increase in roughness as

$$\Delta C_A = (0.105k_S^{1/3} - 0.005579)/L^{1/3} \quad (12.29)$$

The Holtrop method provides a most useful estimation tool for the designer. However, like many analysis procedures it relies to a very large extent on traditional naval architectural parameters. As these parameters cannot fully act as a basis for representing the hull curvature and its effect on the flow around the vessel there is a natural limitation on the accuracy of the approach without using more complex hull definition parameters. At the present time considerable research is proceeding in this direction to extend the viability of the resistance prediction method.

12.3.3 Direct model test

Model testing of a ship in the design stage is an important part of the design process and one that, in a great many instances, is either not explored fully or is not undertaken. In the author's view this is a false economy, bearing in mind the relatively small cost of model testing as compared to the cost of the ship and the potential costs that can be incurred in design modification to rectify a problem or the through life costs of a poor performance optimization.

General procedure for model tests

Whilst the detailed procedures for model testing differ from one establishment to another the underlying general procedure is similar. Here the general concepts are discussed, but for a more detailed account reference can be made to Philips-Birt (Reference 11). With regard to resistance and propulsion testing there are fewer kinds of experiment that are of interest: the resistance test, the open water propeller test, the propulsion test and the flow visualization test. The measurement of the wake field was discussed in Chapter 5.

Resistance tests

In the resistance test the ship model is towed by the carriage and the total longitudinal force acting on the model is measured for various speeds (Figure 12.22). The breadth and depth of the towing tank essentially governs the size of the model that can be used. Todd's original criteria that the immersed cross-section of the vessel should not exceed one per cent of the tank's cross-sectional area was placed in doubt after the famous *Lucy Ashton* experiment. These showed that to avoid boundary interference from the tank walls and bottom this proportion should be reduced to the order of 0.4%.

The model, constructed from paraffin wax, wood or glass-reinforced plastic, requires to be manufactured to a high degree of finish and turbulence simulators placed at the bow of the model in order to stimulate the transition from a laminar into a turbulent boundary layer over the hull. The model is positioned under the carriage and towed in such a way that it is free to heave and pitch, and ballasted to the required draught and trim.

In general there are two kinds of resistance tests: the naked hull and the appended resistance test. If appendages are present local turbulence tripping is applied in order to prevent the occurrence of uncontrolled laminar flow over the appendages. Also the propeller should be replaced by a streamlined cone to prevent flow separation in this area.

The resistance extrapolation process follows Froude's hypothesis and the similarity law is followed. As such the scaling of the residual, or wave making component, follows the similarity law

$$R_{W_{ship}} = R_{W_{model}}\lambda^3(\varrho_S/\rho_M)$$

provided that $V_S = V_M\sqrt{\lambda}$, where $\lambda = L_S/L_M$.

In general, the resistance is scaled according to the relationship

$$R_S = [R_M - R_{F_M}(1 + k)]\lambda^3\left(\frac{\varrho_S}{\varrho_M}\right) + R_{F_S}(1 + k) + R_A$$

$$= [R_M - F_D]\lambda^3\left(\frac{\varrho_S}{\varrho_M}\right) \quad (12.30)$$

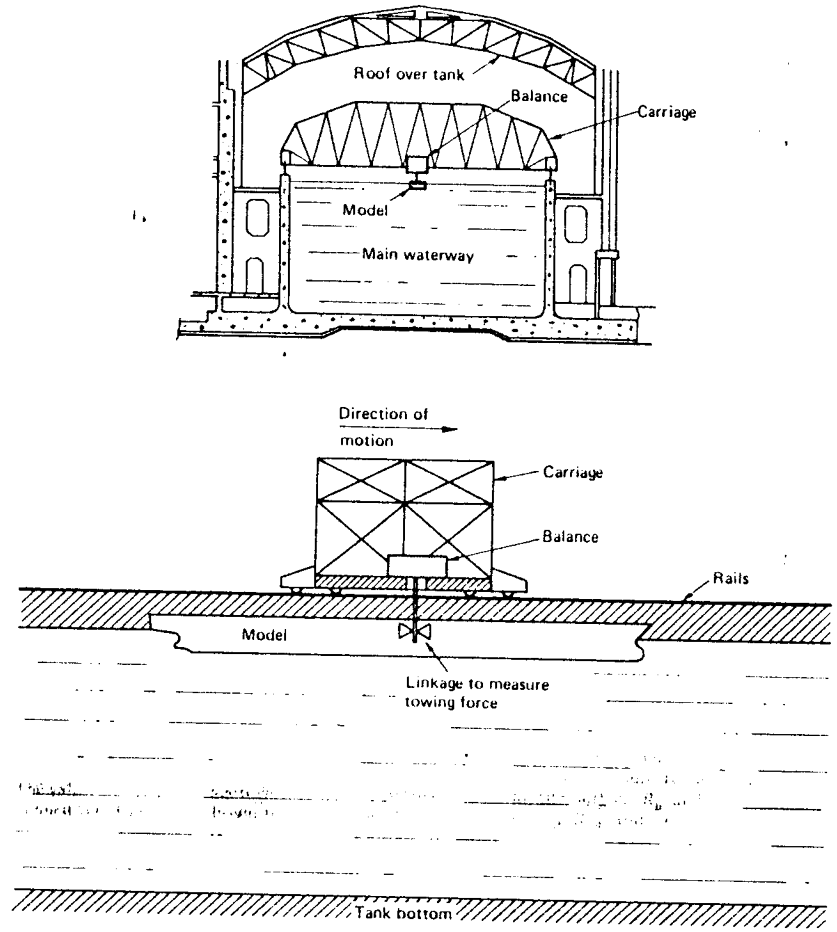

Figure 12.22 Ship model test facility

in which

$$F_D = \tfrac{1}{2}\varrho_M V_M^2 S_M(1 + k)(C_{F_M} - C_{F_S}) - \frac{\varrho_M}{\varrho_S}R_A/\lambda^3$$

that is,

$$F_D = \tfrac{1}{2}\varrho_M V_M^2 S_M[(1 + k)(C_{F_M} - C_{F_S}) - C_A] \quad (12.31)$$

The term F_D is known as both the scale effect correction on resistance and the friction correction force. The term R_A in equation (12.30) is the resistance component, which is supposed to allow for the following factors: hull roughness; appendages on the ship but not present during the model experiment; still air drag of the ship and any other additional resistance component acting on the ship but not on the model. As such its non-dimensional form C_A is the incremental resistance coefficient for ship–model correlation.

When $(1 + k)$ in equation (12.30) is put to unity, the extrapolation process is referred to as a two-dimensional approach since the frictional resistance is then taken as that given by the appropriate line, Froude flat plate data, ATTC or ITTC 1957 etc.

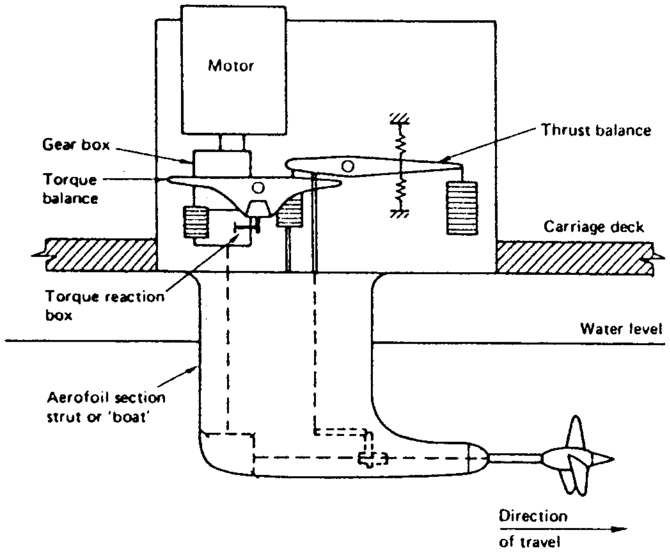

Figure 12.23 Propeller open water test using towing tank carriage

The effective power (P_E) is derived from the resistance test by the relationship

$$P_E = R_s V_s \tag{12.32}$$

Open water tests

The open water test is carried out on either a stock or actual model of the propeller to derive its open water characteristics in order to derive the propulsion coefficients. The propeller model is fitted on a horizontal driveway shaft and is moved through the water at an immersion of the shaft axis frequently equal to the diameter of the propeller (Figure 12.23).

The loading of the propeller is normally carried out by adjusting the speed of advance and keeping the model revolutions constant. However, when limitations in the measuring range, such as a J-value close to zero or a high carriage speed needed for a high J-value, are reached the rate of revolutions is also varied. The measured thrust values are corrected for the resistance of the hub and streamlined cap, this correction being determined experimentally in a test using a hub only without the propeller.

The measured torque and corrected thrust are expressed as non-dimensional coefficients K_{TO} and K_{QO} in the normal way, see Chapter 6; the suffix O being used in this case to denote the open rather than the behind condition. The open water efficiency and the advance coefficient are then expressed as

$$\eta_0 = \frac{J}{2\pi} \frac{K_{TO}}{K_{QO}}$$

and

$$J = \frac{V_c}{nD}$$

where V_c is the carriage speed.

Unless explicitly stated it should not be assumed that the propeller open water characteristics have been corrected for scale effects. The data from these tests are normally plotted on a conventional open water diagram together with a tabulation of the data.

Propulsion tests

In the propulsion test the model is prepared in much the same way as for the resistance test and turbulence stimulation on the hull and appendages is again applied. For this test, however, the model is fitted with the propeller used in the open water test together with an appropriate drive motor and dynamometer. During the test the model is free to heave and pitch as in the case of the resistance test.

In the propulsion test the propeller thrust T_M, the propeller torque Q_M and the longitudinal towing force F acting on the model are recorded for each tested combination of model speed V_M and propeller revolutions n_M.

Propulsion tests are carried out in two parts. The first comprises a load variation test at one or sometimes more than one constant speed whilst the other comprises a speed variation test at constant apparent advance coefficient or at the self-propulsion point of the ship. The ship self-propulsion point being defined when the towing force (F) on the carriage is equal to the scale effect correction on viscous resistance (F_D), equation (12.31).

The required thrust T_S and self-propulsion point of the ship is determined from the model test using the equation:

$$T_S = \left[T_M + (F_D - F)\frac{\partial T_M}{\partial F} \right] \lambda^3 \frac{\varrho_S}{\varrho_M} \tag{12.33}$$

In equation (12.33) the derivative $\partial T_M/\partial F$ is determined from the load variation tests which form the first part of the propulsion test. In a similar way the local variation test can be interpolated to establish the required torque and propeller rotational speed at self-propulsion for the ship.

In the extrapolation of the propulsion test to full scale the scale effects on resistance (F_D), on the wake field and on the propeller characteristics need to be taken into account. At some very high speeds the effects of cavitation also need to be taken into account. This can be done by analysis or through the use of specialized facilities.

Flow visualization tests

Various methods exist to study the flow around the hull of a ship. One such method is to apply stripes of an especially formulated paint to the model surface, the stripes being applied vertical to the base line. The model is then towed at Froude identity and the paint will smear into streaks along the hull surface in the direction of the flow lines.

In cases where the wall shear stresses are insufficient tufts are used to visualize the flow over the hull. In general, wooden threads of about 5 cm in length will be fitted on to small needles driven into the hull surface. The tufts will be at a distance of between 1 and 2 cm from the hull surface and the observation made using an underwater television camera. The interaction phenomenon between the propeller and ship's hull can also be studied in this way by observing the behaviour of the tufts with and without the running propeller.

Model test facilities

Many model test facilities exist around the world almost all of which possess a ship model towing tank. Some of the model facilities available are listed in Table 12.7; this, however, is by no means an exhaustive list of facilities but is included here to give an idea of the range of facilities available.

Table 12.7 Examples of towing tank facilities around the world (Reproduced from Reference 55, with permission)

Facilities	*Length* (m)	*Width* (m)	*Depth* (m)	*Max. carriage speed* (m/s)
European facilities				
AMTE Haslar (UK)	164	6.1	2.4	7.5
	270	12.0	5.5	12.0
Experimental and	76	3.7	1.7	9.1
Electronic Lab.	188	2.4	1.3	13.1
B.H.C. Cowes (UK)	197	4.6	1.7	15.2
MARIN, Wageningen (NL)	100	24.5	2.5	4.5
	216	15.7	1.25	5
	220	4.0	4.0	15 30
	252	10.5	5.5	9
MARIN Depressurized Facility, Ede (NL)	240	18.0	8.0	4
Danish Ship Research Laboratories	240	12.0	6.0	14
Ship Research	27	2.5	1.0	2.6
Institute of Norway (NSFI)	175	10.5	5.5	8.0
SSPA, Göteborg, Sweden	260	10.0	5.0	14.0
Bassin d'Essais de	155	8.0	2.0	5
Carènes, Paris	220	13.0	4.0	10
VWS West	120	8.0	1.1	4.2
Germany	250	8.0	4.8	20
H.S.V. Hamburg	30	6.0	1.2	0.0023 1.9
West Germany	80	4.0	0.7	3.6
	80	5.0	3.0	3.6
	300	18.0	6.0	8.0
B.I.Z. Yugoslavia	37.5	3.0	2.5	3
	23	12.5	6.2	8
	293	5.0	3.5	12
N. American Facilities				
NSRDC Bethesda	845	15.6	6.7	10
USA	905	6.4	3.0–4.8	30
NRC, Marine Dynamics and Ship Laboratory, Canada	137	7.6	3.0	8
Far East Facilities				
Meguro Model	98	3.5	2.25	7
Basin, Japan	235	12.5	7.25	10
	340	6.0	3.0	20
Ship Research	20	8.0	0–1.5	2
Institute, Mitaka	50	8.0	4.5	2.5
Japan	140	7.5	0–3.5	6
	375	18.0	8.5	15
KIMM – Korea	223	16.0	7.0	
Hyundia Korea	232	14.0	6.0	

Two-dimensional extrapolation method

This as discussed previously is based on Froude's original method without the use of a form factor. Hence the full-scale resistance is determined from

$$R_s = (R_M - F_D)\lambda^3\left(\frac{\varrho_S}{\varrho_M}\right)$$

where

$$F_D = \tfrac{1}{2}\varrho_M V_M^2 S_M(C_{F_M} - C_{F_S} - C_A)$$

and when Froude's friction data is used C_A is set to zero, but this is not the case if the ATTC-1947 or ITTC-1957 line is used.

When the results of the propulsion test are either interpolated for the condition when the towing force (F) is equal to F_D or when F_D is actually applied in the self-propulsion test the corresponding model condition is termed the 'self-propulation point of the ship'. The direct scaling of the model data at this condition gives the condition generally termed the 'tank condition'. This is as follows:

$$\left.\begin{aligned} P_{DS} &= P_{DM}\lambda^{3.5}\left(\frac{\varrho_S}{\varrho_M}\right) \\ T_S &= T_M\lambda^3\left(\frac{\varrho_S}{\varrho_M}\right) \\ n_S &= n_M\sqrt{\lambda} \\ V_S &= V_M\sqrt{\lambda} \\ R_S &= (R_M - F_D)\lambda^3\left(\frac{\varrho_S}{\varrho_M}\right) \end{aligned}\right\} \qquad (12.34)$$

The power and propeller revolution determined from the tank condition as given by equation (12.34) require to be converted into trial prediction figures for the vessel. In the case of the power trial prediction this needs to be based on an allowance factor for the results of trials of comparable ships of the same size or alternatively on the results of statistical surveys. The power trial allowance factor is normally defined as the ratio of the shaft power measured on trial to the power delivered to the propeller in the tank condition.

The full-scale propeller revolution prediction is based on the relationship between the delivered power and the propeller revolutions derived from the tank condition. The power predicted for the trial condition is then used in this relationship to devise the corresponding propeller revolutions. This propeller speed is corrected for the over- or underloading effect and often corresponds to around $\tfrac{1}{2}$% decrease of r.p.m. for a 10% increase of power. The final stage in the propeller revolution prediction is to account for the scale effects in the wake and propeller blade friction. For the trial condition these scale effects are of the order of

$\tfrac{1}{2}\sqrt{\lambda}$% for single-screw vessels

1–2% for twin-screw vessels

The allowance for the service condition on rotational speed is of the order 1%.

Three-dimensional extrapolation method

The three-dimensional extrapolation method is based on the form factor concept. Accordingly the resistance is scaled under the assumption that the viscous resistance of the ship and its model is proportional to the frictional resistance of a flat plate of the same length and wetted surface area when towed at the same speed, the proportionality factor being $(1 + k)$ as discussed in Section 12.2. In addition it is assumed that the pressure resistance due to wave generation, stable separation and induced drag from non-streamlined or misaligned appendages follow the Froude similarity law.

The form factor $(1 + k)$ is determined for each hull from low-speed resistance or propulsion measurements when the wave resistance components are negligible. In the case of the resistance measurement of form factor then this is based on the relationship:

$$(1 + k) = \lim_{F_n \to 0}\left(\frac{R}{R_F}\right)$$

In the case of the propulsion test acting as a basis for the $(1 + k)$ determination then this relationship takes the form

$$(1 + k) = \lim_{F_n \to 0}\left[\frac{F - T/(\partial T/\partial F)}{(F|_{T=0}/R)R_F}\right]$$

The low-speed measurement of the $(1 + k)$ factor can only be validly accomplished if scale-independent pressure resistance is absent, which means, for example, that there is no immersed transom. In this way the form factor is maintained independent of speed and scale in the extrapolation method.

In the three-dimensional method the scale effect on the resistance is taken as

$$F_D = \tfrac{1}{2}\varrho_M V_M^2 S_M[(1 + k)(C_{F_M} - C_{F_S}) - C_A]$$

in which the form factor is normally taken relative to the ITTC-1957 line and C_A is the ship–model correlation coeffficient. The value of C_A is generally based on an empirically based relationship and additional allowances are applied to this factor to account for extreme hull forms at partial draughts, appendages not present on the model, 'contract' conditions, hull roughness different from the standard of 150 µm, extreme superstructures or specific experience with previous ships.

In the three-dimensional procedure the measured relationship between the thrust coefficient K_T and the apparent advance coefficient is corrected for wake scale effects and for the scale effects on propeller blade friction. At model scale the model thrust coefficient is defined as

$$K_{TM} = f(F_n, J)_M,$$

whereas at ship scale this is

$$K_{TS} = f\left(F_n, \ldots\left(\frac{1 - w_{TS}}{1 - w_{TM}}\right) + \Delta K_T\right)$$

According to the ITTC 1987 version of the manual for the use of the 1978 performance reduction method, the relationship between the ship and model Taylor wake fractions can be defined as

$$w_{TS} = (t + 0.04) + (w_{TM} - t - 0.04) \times \frac{(1 + k)C_{FS} + \Delta C_F}{(1 + k)C_{FM}}$$

where 0.04 is included to take account of the rudder effect and ΔC_F is the roughness allowance given by

$$\Delta C_F = \left[105\left(\frac{k_S}{L_{WL}}\right)^{1/3} - 0.64\right] \times 10^{-3}$$

The measured relationship between the thrust and torque coefficient is corrected for the effects of friction over the blades such that

$$K_{TS} = K_{TM} + \Delta K_T \qquad \text{and} \qquad K_{QS} = K_{QM} + \Delta K_Q$$

where the factors ΔK_T and ΔK_Q are determined from the ITTC procedure as discussed in Chapter 6.

The load of the full-scale propeller is obtained from the relationship

$$\frac{K_T}{J^2} = \frac{S}{2D^2}\cdot\frac{C_{TS}}{(1 - t)(1 - w_{TS})^2}$$

and with K_T/J^2 as the input value the full-scale advance coefficient J_{TS} and torque coefficient K_{QTS} are read off from the full-scale propeller characteristics and the following parameters calculated:

$$\left.\begin{aligned} n_S &= \frac{(1 - w_{TS})V_S}{J_{TS}D} \\ P_{DS} &= 2\pi\varrho D^5 n_S^3\frac{K_{QTS}}{\eta_R} \times 10^{-3} \\ T_S &= \frac{K_T}{J^2}J_{TS}^2\varrho D^4 n_S^2 \\ Q_S &= \frac{K_{QTS}}{\eta_R}\varrho D^5 n_S^2 \end{aligned}\right. \qquad (12.35)$$

The required shaft power P_S is found from the delivered power P_{DS} using the shafting mechanical efficiency η_S as

$$P_S = P_{DS}/\eta_S$$

12.3.4 Computational fluid dynamics

The analysis of ship forms to predict total resistance using the computational fluid dynamics (CFD) approach is generally still in its infancy, although considerable research effort is being devoted to the topic.

With regard to the wave making part of the total resistance, provided that the viscous effects are neglected, then the potential flow can be defined by the imposition of boundary conditions at the hull and free surface. The hull conditions are taken into account by placing a distribution of source panels over its surface. The problem comes in satisfying the free surface boundary conditions which ought to be applied at the actual free surface, which of course is unknown at the start of the calculation. A solution to this problem was developed by Dawson (Reference 40) and is one method in the class of 'slow-ship' theories. With this method the exact free surface condition is replaced by an approximate one that can be applied at a fixed location such as the undisturbed water surface. In such a case a suitable part of the undisturbed free surface is covered with source panels and the source strengths determined so as to satisfy the boundary conditions. Figure 12.24 shows the wave pattern calculated (Reference 41) using a variation of the Dawson approach for a Wigley hull at a Froude number of 0.40.

In the case of the viscous resistance, again panel methods are used to represent the hull form and the flow field is often evaluated in three separate stages: the potential flow zone, the boundary layer zone and the stern flow and wake zone. Figure 12.25 shows the various zones used in some calculation procedures. In the third zone, that of the stern flow and wake, it is necessary to compute the Reynolds averaged Navier–Stokes equation of viscous flow to define the flow over the after part of the hull. Such models can in general make a reasonably good approximation to the boundary layer growth over simple hull forms; however, the more complex hull forms that introduce high curvature just ahead of the propeller disc are not so well represented at the present time. Models for these types of calculation can typically involve some 2000 panels and their solution can require significant amounts of time on large computers.

Clearly CFD methods represent a significant predictive capability for the future when further development has taken place. In the meantime the traditional, statistical and model test methods of analysis have to satisfy the requirements of design analysis.

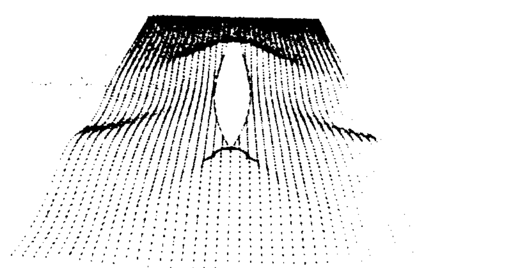

Figure 12.24 Calculated wave profile for Wigley hull at F_n = 0.4 (Courtesy MARIN)

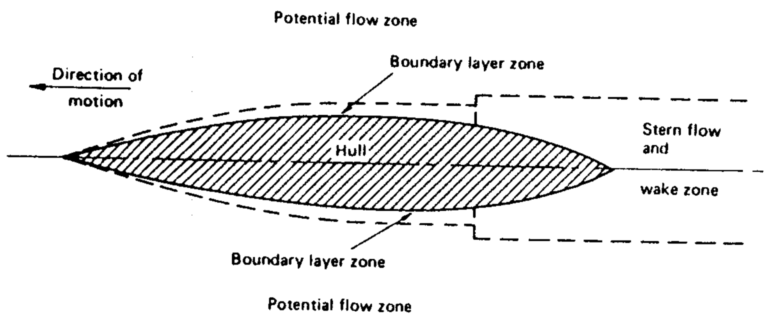

Figure 12.25 Zones for CFD analysis

12.4 Propulsive coefficients

The propulsive coefficients of the ship performance form the essential link between the effective power required to drive the vessel, obtained from the product of resistance and ship speed, and the power delivered from the engine to the propeller.

The power absorbed by and delivered to the propeller P_D in order to drive the ship at a given speed V_S is

$$P_D = 2\pi nQ \qquad (12.36)$$

where n and Q are the rotational speed and torque at the propeller. Now the torque required to drive the propeller Q can be expressed for a propeller working behind the vessel as

$$Q = K_{Qb}\varrho n^2 D^5 \qquad (12.37)$$

where K_{Qb} is the torque coefficient of the propeller when working in the wake field behind the vessel at a mean advance coefficient J. By combining equations (12.36) and (12.37) the delivered power can be expressed as

$$P_D = 2\pi K_{Qb}\varrho n^3 D^5 \qquad (12.38)$$

If the propeller were operating in open water at the same mean advance coefficient J the open water torque coefficient K_{Qo} would be found to vary slightly from that measured behind the ship model. As such the ratio K_{Qo}/K_{Qb} is known as the relative rotative efficiency η_r

$$\eta_r = \frac{K_{Qo}}{K_{Qb}} \qquad (12.39)$$

this being the definition stated in Chapter 6.

Hence, equation (12.38) can then be expressed in terms of the relative rotative efficiency as

$$P_D = 2\pi \frac{K_{Qo}}{\eta_r}\varrho n^3 D^5 \qquad (12.40)$$

Now the effective power P_E is defined as

$$P_E = RV_s$$
$$= P_D \text{QPC}$$

where the QPC is termed the quasi-propulsive coefficient.

Hence, from the above, in association with equation (12.40),

$$RV_s = P_D \text{QPC}$$
$$= 2\pi \frac{K_{Qo}}{\eta_r}\varrho n^3 D^5 \text{QPC}$$

which implies that

$$\text{QPC} = \frac{RV_s\eta_r}{2\pi K_{Qo}\varrho n^3 D^5}$$

Now the resistance of the vessel R can be expressed in terms of the propeller thrust T as $R = T(1 - t)$, where t is the thrust deduction factor as explained later. Also from Chapter 5 the ship speed V_s can be defined in terms of the mean speed of advance V_a as $V_a = V_s(1 - w_t)$, where w_t is the mean Taylor wake fraction. Furthermore, since the open water thrust coefficient K_{To} is expressed as $T_o = K_{To}\varrho n^2 D^4$, with T_o being the open water propeller thrust at the mean advance coefficient J,

$$\frac{T_o}{K_{To}} = \varrho n^2 D^4$$

and the QPC can be expressed from the above as

$$\text{QPC} = \frac{T_o(1 - t) \cdot V_a \cdot K_{To} \cdot \eta_r}{(1 - w_t)2\pi K_{Qo} nDT_o}$$

which reduces to

$$\text{QPC} = \left(\frac{1 - t}{1 - w_t}\right)\eta_0\eta_r$$

since, from equation (6.8),

$$\eta_0 = \frac{J}{2\pi}\frac{K_{To}}{K_{Qo}}$$

The quantity $(1 - t)/(1 - w_t)$ is termed the hull efficiency η_h and hence the QPC is defined as

$$\text{QPC} = \eta_h\eta_0\eta_r \qquad (12.41)$$

or, in terms of the effective and delivered powers,

$$P_E = P_D \text{QPC}$$

that is,

$$P_E = P_D\eta_h\eta_0\eta_r \qquad (12.42)$$

12.4.1 Relative rotative efficiency

The relative rotative efficiency (η_r), as defined by equation (12.39), accounts for the differences in torque absorption characteristics of a propeller when operating in mixed wake and open water flows. In many cases the value of η_r lies close to unity and is generally within the range

$$0.95 \leq \eta_r \leq 1.05$$

In a relatively few cases it lies outside this range. Holtrop (Reference 39) gives the following statistical relationships for its estimation:

For conventional stern single-screw ships:

$$\eta_r = 0.9922 - 0.05908(A_E/A_0) + 0.07424(C_P - 0.0225\,\text{l.c.b.})$$

For twin-screw ships

$$\eta_r = 0.9737 + 0.111(C_P - 0.0225\,\text{l.c.b.}) - 0.06325\,P/D \qquad (12.43)$$

If resistance and propulsion model tests are performed, then the relative rotative efficiency is determined at model scale from the measurements of thrust T_m and torque Q_m with the propeller operating behind the model. Using the non-dimensional thrust coefficient K_{Tm} as input data the values J and K_{Qo} are read off from the open water curve of the model propeller used in the propulsion test. The torque coefficient of the propeller working behind the model is derived from

$$K_{Qb} = \frac{Q_M}{\varrho n^2 D^5}$$

Hence the relative rotative efficiency is calculated as

$$\eta_r = \frac{K_{Qo}}{K_{Qb}}$$

The relative rotative efficiency is assumed to be scale independent.

12.4.2 Thrust deduction factor

When water flows around the hull of a ship which is being towed and does not have a propeller fitted a certain pressure field is set up which is dependent on the hull form. If the same ship is now fitted with a propeller and is propelled at the same speed the pressure field around the hull changes due to the action of the propeller. The propeller increases the velocities of the flow over the hull surface and hence reduces the local pressure field over the after part of the hull surface. This has the effect of increasing, or augmenting, the resistance of the vessel from that which was measured in the towed resistance case and this change can be expressed as

$$T = R(1 + a_r) \qquad (12.44)$$

where T is the required propeller thrust and a_r is the resistance augmentation factor. An alternative way of expressing equation (12.44) is to consider the deduction in propeller effective thrust which is caused by the change in pressure field around the hull. In this case the relationship

$$R = T(1 - t) \qquad (12.45)$$

applies, in which t is the thrust deduction factor. The correspondence between the thrust deduction factor and the resistance augmentation factor can be derived from equations (12.44) and (12.45) as being

$$a_r = \left(\frac{t}{1 - t}\right)$$

If a resistance and propulsion model test has been performed, then the thrust deduction factor can be readily calculated from the relationship defined in the 1987 ITTC proceedings.

$$t = \frac{T_M + F_D - R_c}{T_M}$$

in which T_M and F_D are defined previously and R_c is the resistance corrected for differences in temperature between the resistance and propulsion tests:

$$R_c = \frac{(1 + k)C_{FMC} + C_R}{(1 + k)C_{FM} + C_R} R_{TM}$$

where C_{FMC} is the frictional resistance coefficient at the temperature of the self-propulsion test.

In the absence of model tests an estimate of the thrust deduction factor can be obtained from the work of Holtrop (Reference 39) and Harvald (Reference 17). In the Holtrop approach the following regression-based formulas are given:

For single-screw ships:

$$t = \frac{0.25014(B/L)^{0.28956}(\sqrt{(BT)}/D)^{0.2624}}{(1 - C_P + 0.0225\,\text{l.c.b.})^{0.01762}} + 0.0015C_{stern}$$

For twin-screw ships:

$$t = 0.325C_B - 0.1885D/\sqrt{(BT)} \qquad (12.46)$$

In equation (12.46) the value of the parameter C_{stern} is found from Table 12.5.

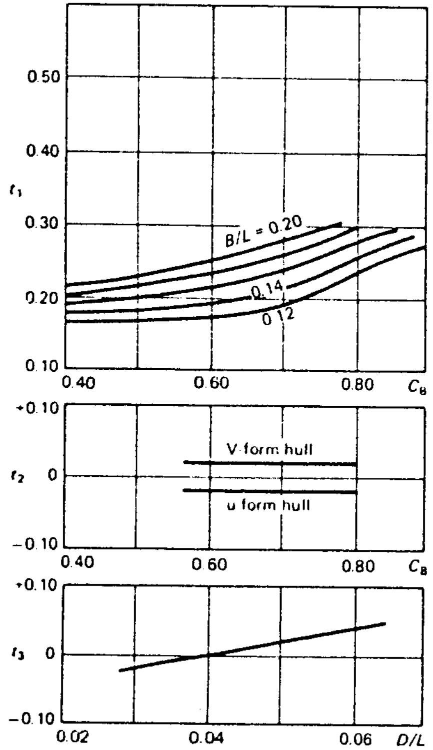

Figure 12.26 Thrust deduction estimation of Harvald for single-screw ships (Reproduced from Reference 17, with permission)

The alternative approach of Harvald to the calculation of the thrust deduction factor is to assume that it comprises three separate components as follows:

$$t = t_1 + t_2 + t_3 \qquad (12.47)$$

in which t_1, t_2 and t_3 are basic values derived from hull form parameters, a hull form correction and a propeller diameter correction respectively. The values of these parameters for single-screw ships are reproduced in Figure 12.26.

12.4.3 Hull efficiency

The hull efficiency can readily be determined once the thrust deduction and mean wake fraction are known. However, because of the pronounced scale effect of the wake fraction there is a difference between the full-scale ship and model values. In general, because the ship wake fraction is smaller than the corresponding model value, due to Reynolds effects, the full-scale efficiency will also be smaller.

12.4.4 Quasi-propulsive coefficient (QPC)

It can be deduced from equation (12.41) that the value of the quasi-propulsive coefficient is dependent upon the ship speed, pressure field around the hull, the wake field presented to the propeller and the intimate details of the propeller design such as diameter, rate of rotation, radial load distribution, amount of cavitation on the blade surfaces, etc. As a consequence, the QPC should be calculated from the three component efficiencies given in equation (12.41) and not globally estimated.

Of particular interest when considering general trends is the effect that propeller diameter can have on the QPC; as the diameter increases, assuming the rotational speed is permitted to fall to its optimum value, the propeller efficiency will increase and hence for a given hull form the QPC will tend to rise. In this instance the effect of propeller efficiency dominates over the hull and relative rotative efficiency effects.

12.5 The influence of rough water

The discussion so far has centred on the resistance and propulsion of vessels in calm water or ideal conditions. Clearly the effect of bad weather is either to slow the vessel down for a given power absorption or, conversely, an additional input of power to the propeller in order to maintain the same ship speed.

In order to gain some general idea of the effect of weather on ship performance appeal can be made to the NSMB Trial Allowances 1976 (Reference 42). These allowances were based on the trial results of 378 vessels and formed an extension to the 1965 and 1969 diagrams. Figure 12.27 shows the allowances for ships with a trial displacement between 1000 and 320 000 tonnes based on the Froude extrapolation method and coefficients. Analysis of the data upon which this diagram was based showed that the most significant variables were the displacement, Beaufort wind force, model scale and the length between perpendiculars. As a consequence a regression formula was suggested as follows:

$$\text{trial allowance} = 5.75 - 0.793\Delta^{1/3} + 12.3B_n + (0.0129L_{PP} - 1.864B_n)\lambda^{1/3} \qquad (12.48)$$

where B_n and λ are the Beaufort number and the model scale respectively.

Apart from global indicators and correction factors such as Figure 12.27 or equation (12.48) considerable work has been undertaken in recent years to establish methods by which the added resistance due to weather can be calculated for a particular hull form. Latterly

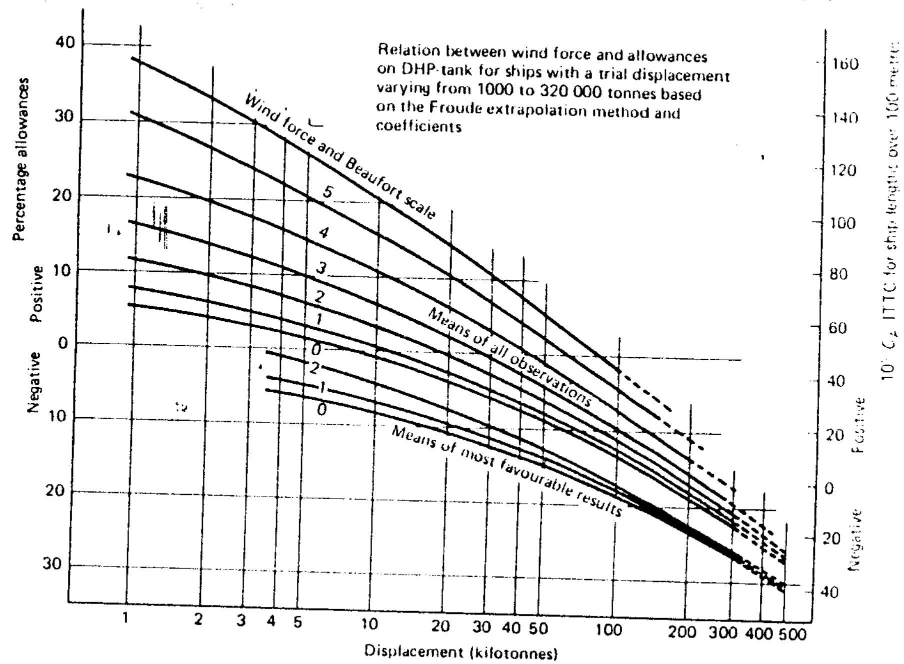

Figure 12.27 NSMB 1976 trial allowances (Reproduced from Reference 42, with permission)

particular attention has been paid to the effects of diffraction in short waves which is a particularly difficult area.

In general estimation methods range from those which work on data bases for standard series hull forms whose main parameter have been systematically varied to those where the calculation is approached from fundamental considerations. In its most simplified form the added resistance calculation is of the form

$$R_{TW} = R_{TC}(1 + \Delta_R) \qquad (12.49)$$

where R_{TW} and R_{TC} are the resistances of the vessel in waves and calm water respectively and Δ_R is the added resistance coefficient based on the ship form parameters, speed and irregular sea state. Typical of results of calculation procedures of this type are the results shown in Figure 12.28 for a container ship operating in different significant wave heights H_S and a range of heading angles from directly ahead ($\theta = 0°$) to directly astern ($\theta = 180°$).

Shintani and Inoue (Reference 43) have established charts for estimating the added resistance in waves of ships based on a study of the Series 60 models. This data takes into account various values of C_B, B/T,

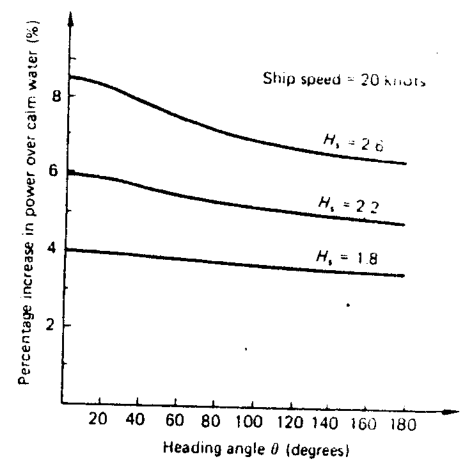

Figure 12.28 Estimated power increase to maintain ship speed in different sea states for a container ship

L/B and l.c.b. position and allows interpolation to the required value for a particular design. In this work the compiled results have been empirically corrected by comparison with model test data in order to enhance the prediction process.

In general the majority of the practical estimation methods are based in some way on model test data: either for deriving regression equations or empirical correction factors. As regards theoretical methods a wholly reliable and practical method for predicting the added resistance in waves is not yet available, although significant progress has been made towards this aim in recent years.

12.6 Restricted water effects

Restricted water effects derive essentially from two sources. These are first a limited amount of water under the keel and secondly, a limitation in the width of water each side of the vessel which may or may not be in association with a depth restriction.

In order to assess the effects of restricted water operation, these being particularly complex to define mathematically, the ITTC (Reference 32) have expressed typical influencing parameters. These are as follows:

1. An influence exists on the wave resistance for values of the Froude depth number F_{nh} in excess of 0.7. The Froude depth number is given by

$$F_{nh} = \frac{V}{\sqrt{(gh)}}$$

where h is the water depth of the channel.
2. The flow around the hull is influenced by the channel boundaries if the water depth to draught ratio (h/T) is less than 4. This effect is independent of the Froude depth number effect.
3. There is an influence of the bow wave reflection from the lateral boundary on the stern flow if either the water width to beam ratio (W/B) is less than 4 or the water width to length ratio (W/L) is less than unity.
4. If the ratio of the area of the channel cross-section to that of the mid-ship section (A_c/A_M) is less than 15, then a general restriction of the waterway will start to occur.

In the case of the last ratio it is necessary to specify at least two of the following parameters; width of water, water depth or the shape of the canal section because a single parameter cannot identify unconditionally a restriction on the water flow.

The most obvious sign of a ship entering into shallow water is an increase in the height of the wave system in addition to a change in the ship's vibration characteristics. As a consequence of the increase in the height of the wave system the assumption of small wave height, and consequently small wave slopes, cannot be used for restricted water analysis. This,

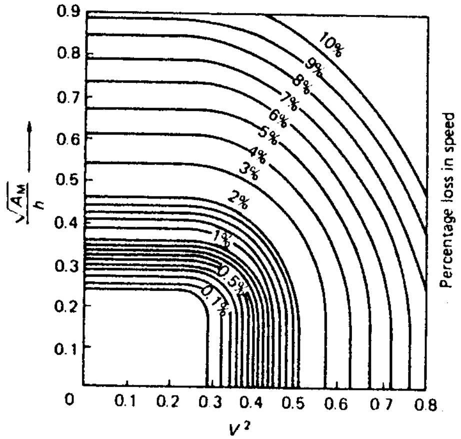

Figure 12.29 Loss of speed in transfer from deep to shallow water (Reproduced from Reference 45)

therefore, implies a limitation to the use of linearized wave theory for this purpose; as a consequence higher-order theoretical methods need to be sought. Currently several researchers are working in this field and endeavouring to enhance the correlation between theory and experiment.

Barrass (Reference 44) suggests the depth/draught ratio at which shallow water just begins to have an effect is given by the equation

$$h/T = 4.96 + 52.68(1 - C_W)^2$$

in which the C_W is the water-plane coefficient. Alternatively, Schneekluth (Reference 45) provides a set of curves based on Lackenby's work (Figure 12.29) to enable the estimation of the speed loss of a vessel from deep to shallow water. The curves are plotted on a basis of the square of Froude depth number to the ratio $\sqrt{A_M}/h$. Beyond data of this type there is little else currently available with which to readily estimate the added resistance in shallow water.

One further effect of shallow water is the phenomenon of ship squat. This is caused by a venturi effect between the bottom of the vessel and the bottom of the seaway which causes a reduction of pressure to occur. This reduction of pressure then induces the ship to increase its draught in order to maintain equilibrium.

12.7 High-speed hull form resistance

In the case of a conventional displacement ship the coefficient of wave making resistance increases with the Froude number based on water line length until a value of $F_n \simeq 0.5$ is reached. After this point it tends to reduce in value such that at high Froude numbers, in excess of 1.5, the wave making resistance becomes a small component of the total resistance. The viscous resistance, however, increases due to its dependence on the square of the ship speed; this is despite the value of C_F reducing with Froude number. As a consequence of this rise in the viscous resistance a conventional displacement hull requires excessive power at high speed and other hull forms and modes of support require to be introduced. Such forms are the planning hull form, the hydrofoil and the hovercraft.

The underlying principle of high speed planning craft resistance and propulsion have been treated by several authors: for example, DuCane (Reference 46) and Clayton and Bishop (Reference 47). These authors not only examine high-speed displacement and planning craft but also hydrofoils and hovercraft. As a consequence for the detailed principles of their motion reference can be made to these works.

The forces acting on a planning hull are shown by Figure 12.30 in which the forces shown as W, F_p, F_h, F_s and T are defined as follows:

W is the weight of the craft;
F_p is the net force resulting from the variation of pressure over the wetted surface of the hull;
F_h is the hydrostatic force acting at the centre of pressure on the hull;
F_s is the net skin friction force acting on the hull;
T is the thrust of the propulsor.

By the suitable resolution of these forces and noting that for efficient planning, the planning angle should be small it can be shown that the total resistance comprises three components:

$$R_T = R_I + R_{WV} + R_{FS} \tag{12.50}$$

where R_I is the induced resistance or drag derived from the inclination of F_p from the vertical due to the trim angle of the craft;
R_{WV} derives from the wave making and viscous pressure resistance;
R_{FS} is the skin friction resistance.

At high speed the wave making resistance becomes small but the vessel encounters an induced drag component which is in contrast to the case for conventional displacement hulls operating at normal speeds.

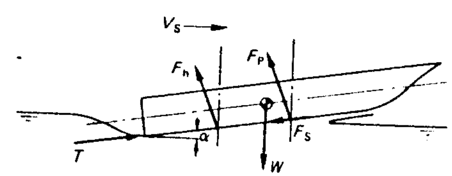

Figure 12.30 Forces experienced by a planing craft

To estimate the resistance properties of high speed displacement and planning craft use can be made of either standard series data or specific model test results.

12.7.1 Standard series data

A considerable amount of data is available by which an estimate of the resistance and propulsion characteristics can be made. Table 12.8 identifies some of the data published in the open literature for this purpose.

In addition to basic test data of this type various

Table 12.8 Published data for displacement and planning craft

Standard series data	
Displacement data	*Planning data*
Norstrom Series (1936)	Series 50 (1949)
de Groot Series (1955)	
Marwood and Silverleaf (1960)	Series 62 (1963)
Series 63 (1963)	Series 65 (1974)
Series 64 (1965)	
SSPA Series (1968)	
NPL Series (1984)	
NSMB Series (1984)	
Robson Naval Combatants (1988)	

regression based analyses are available to help the designer in predicting the resistance characteristics of these craft; for example, van Oortmerssen (Reference 48) and Mercier and Savitsky (Reference 49). In addition Savitsky and Ward Brown (Reference 50) offer procedures for the rough water evaluation of planning hulls.

12.7.2 Model test data

In specific cases model test data is derived for a particular hull form. In these cases the principles for model testing outlined in Reference 51 and the various ITTC proceedings should be adhered to in order to achieve valid test results.

12.8 Air resistance

The prediction of the air resistance of a ship can be evaluated in a variety of ways ranging from the extremely simple to undertaking a complex series of model tests in a wind tunnel.

At its simplest the still air resistance can be estimated as proposed by Holtrop (Reference 52) who followed the simple approach incorporated in the ITTC-1978 method as follows:

$$R_{AIR} = \tfrac{1}{2}\varrho_a V_S^2 A_T C_{air} \tag{12.51}$$

in which V_S is the ship speed, A_T is the transverse area of the ship and C_{air} is the air resistance coefficient.

taken as 0.8 for normal ships and superstructures. The density of air ϱ_a is normally taken as $1.23\,kg/m^3$.

For more advanced analytical studies appeal can be made to the works of van Berlekom (Reference 53) and Gould (Reference 54). The approach favoured by Gould is to determine the natural wind profile on a power law basis and select a reference height for the wind speed. The yawing moment centre is then defined relative to the bow and the lateral and frontal elevations of the hull and superstructure are subdivided into so-called 'universal elements'. In addition the effective wind speed and directions are determined from which the Cartesian forces together with the yawing moment can be evaluated.

The determination of the air resistance from wind tunnel measurement would only be undertaken in exceptional cases and would most probably be associated with flow visualization studies to, for example, design suitable locations for helicopter landing and take-off platforms. For more commercial applications the cost of undertaking wind tunnel tests cannot be justified since air resistance is by far the smallest of the resistance components.

References and further reading

1. Brown, D.K. *A Century of Naval Construction*. Conway, 1983.
2. Froude, W. The papers of William Froude, *Trans. R.I.N.A.*, 1955.
3. Kelvin, Lord. On deep water two-dimensional waves produced by any given initiating disturbance. *Proc. Roy. Soc.* (Edin.) **25**, 185–196, 1904.
4. Kelvin, Lord. On the front and rear of a free procession of waves in deep water. *Proc. Roy. Soc.* (Edin.) **25**, 311–327, 1904.
5. Kelvin, Lord. Deep water ship waves. *Proc. Roy. Soc.* (Edin.) **25**, 562–587, 1904.
6. Wigley, W.C.S. The theory of the bulbous bow and its practical application. *Trans. NECIES*, **52**, 1936.
7. Inui, T. *Wavemaking Resistance of Ships. Trans SNAME*, **70**, 1962.
8. Todd, F.H. *Resistance and Propulsion*, Chapter 7, Principles of Naval Architecture, *SNAME*.
9. Yim, B. A simple design theory and method for bulbous bows of ships, *J. Ship Research*, **18**, 1974.
10. Schneekluth, H. *Ship Design for Efficiency and Economy*. Butterworths, London, 1987.
11. Phillips-Birt, D. *Ship Model Testing*, Leonard-Hill, 1970.
12. Hughes, G. Friction and form resistance in turbulent flow and a proposed formulation for use in model and ship correlation. *Trans. RINA*, **96**, 1954.
13. Taylor, D.W. *The Speed and Power of Ships*, US Govt. Printing Office, Washington, 1943.
14. Ayre, Sir Amos L. Approximating EHP – revision of data given in papers of 1927 and 1948. *Trans. NECIES*.
15. Auf'm Keller, W.H. Extended diagrams for determining the resistance and required power for single-screw ships. *ISP*, **20**, 1973.
16. Lap, A.J.W. Diagrams for determining the resistance of single screw ships. *ISP* **1**(4), 1954.
17. Harvald, Sv. Aa. Estimation of power of ships, *ISP*.
18. Bowden, B.S. A Survey of Published Data for Single-Screw Ocean Going Ships. NPL Ship Report 139, May, 1970.
19. Dawson, J. Resistance and propulsion of single-screw coasters – Parts I, II, III and IV. *Trans. IESS*, Paper Nos. 1168, 1187, 1207 and 1247 in 1953, 1954, 1956, 1959 respectively.
20. Moor, D.I. The © of some $0.80C_b$ forms. *Trans. RINA*, 1960.
21. The DTMB Series 60 – Presented in a set of papers by various authors 1951, 1953, 1954, 1956, 1957 and 1960. *Trans. SNAME*.
22. Moor, D.I. The effective horse power of single screw ships – average modern attainment with particular reference to variations of C_b and LCB. *Trans. RINA*, 1960.
23. Manen, J.D. Van and others. Scale effect experiments on the victory ships and models - Parts I, II, III and IV in three papers. *Trans. RINA*, 1955, 1958 and 1961.
24. Moor, D.I., Parker, M.N., Pattullo, R.N. The BSRA methodical series – an overall presentation – geometry of forms and variations of resistance with block coefficient and longitudinal centre of buoyancy. *Trans. RINA*, **103**, 1961.
25. Moor, D.I. Resistance, propulsion and motions of high speed single screw cargo liners. *Trans. NECIES*, **82**, 1965/1966.
26. Lackenby, H., Parker, M.N. The BSRA methodical series – an overall presentation – variation of resistance with breadth-draught ratio and length-displacement ratio. *Trans. RINA*, **108**, 1966.
27. Moor, D.I., Pattullo, R.N.M. The Effective Horsepower of Twin-Screw Ships – Best Modern Attainment for Ferries and Passenger Liners with Particular Reference to Variations of Block Coefficient. BSRA Report No. 192, 1968.
28. The SSPA Standard Series published in a set of papers from SSPA 1948–1959 and summarized in 1969.
29. Moor, D.I. Standards of ship performance. *Trans. IESS*, **117**, 1973.
30. Moor, D.I. Resistance and propulsion qualities of some modern single screw trawler and bulk carrier forms. *Trans. RINA*, 1974.
31. Pattullo, R.N.M. The resistance and propulsion qualities of a series of stern trawlers – variations of longitudinal position of centre of buoyancy, breadth, draught and block coefficient. *Trans. RINA*, 1974.
32. *18th ITTC Conference*, Japan, 1987.

33. Scott, J.R. A method of predicting trial performance of single screw merchant ships. *Trans. RINA*, 1972.
34. Scott, J.R. A method of predicting trial performance of twin screw merchant ships. *Trans. RINA*, 1973.
35. Holtrop, J. A statistical analysis of performance test results. *ISP*, **24**, February, 1977.
36. Holtrop, J. Statistical data for the extrapolation of model performance tests. *ISP*.
37. Holtrop, J., Mennen, G.G.J. A statistical power prediction method. *ISP*, **25**, October, 1978.
38. Holtrop, J., Mennen, G.G.J. An approximate power prediction method. *ISP*, **29**, July, 1982.
39. Holtrop, J. A statistical re-analysis of resistance and propulsion data. *ISP*, **31**, November, 1988.
40. Dawson, C.W. A practical computer method for solving ship–wave problems. *2nd Int. Conf. on Numerical Ship Hydrodynamics*, Berkeley, 1977.
41. MARIN Report No. 26, September, 1986.
42. Jong, H.J. de, Fransen, H.P. N.S.M.B. trial allowances 1976. *ISP*, 1976.
43. Shintani, A., Inoue, R. Influence of hull form characteristics on propulsive performance in waves. *SMWP*. December, 1984.
44. Barrass, C.B. Ship-handling problems in shallow water. *MER*, November, 1979.
45. Schneekluth, H. *Ship Design for Efficiency and Economy*, Butterworths, London, 1987.
46. Cane, P.du. *High Speed Craft*.
47. Clayton, B.R., Bishop, R.E.D. *Mechanics of Marine Vehicles*. Spon, London, 1982.
48. Oortmerssen, G. van. A power prediction method and its application to small ships. *ISP*, **18**(207), 1971.
49. Mercier, J.A., Savitsky, D. Resistance of Transom-Stern Craft in the Pre-Planing Regime. Davidson Laboratory, Stevens Institute of Tech., Rep. No. 1667, 1973.
50. Savitsky, D., Ward Brown, P. Procedures for hydrodynamic evaluation of planing hulls in smooth and rough waters. *Maritime Technology*, 13(4), October, 1976.
51. Status of Hydrodynamic Technology as Related to Model Tests of High Speed Marine Vehicles. DTNSRDC Rep. No. 81/026, 1981.
52. Holtrop, J. A statistical resistance prediction method with a speed dependent form factor. *SMSSH '88*, Varna, October, 1988.
53. Berlekom, W.B. van. Wind forces on modern ship forms - effects on performance. *Trans. NECIES*, 1981.
54. Gould, R.W.F. The Estimation of Wind Loads on Ship Superstructures, Mar. Tech. Monograph No. 8, *Trans. RINA*, 1982.
55. Clayton, B.R., Bishop, R.E.D. Mechanics of Marine Vehicles, E. & F.N. Spon, London, 1982.

13 Thrust augmentation devices

Contents

The last decade or so has seen a proliferation of hydrodynamically based energy-saving devices enter the marine market.

For discussion purposes these energy-saving devices can be considered as operating in three basic zones of the hull. Some are located before the propeller, some at the propeller station and some after the propeller. Figure 13.1 defines these three stages as Zones I, II and III respectively for devices which act before, at or astern of the propeller location. Clearly some devices transcend these boundaries but these three zones are useful to broadly group the various devices.

In Zone I the thrust augmentation device is reacting with the final stages of the growth of the boundary layer around the stern of the ship, in order to gain some direct benefit or present the propeller with a more advantageous flow regime – in some cases perhaps both, whilst in Zones II and III they are working within both the hull wake field and the slipstream of the propeller and attempting to recover energy which would otherwise be lost. Table 13.1 identifies some of the principal thrust augmentation devices and attempts to categorize them into their zones of operation.

To consider the effect of an energy saving device its effect on the various components of the quasi-propulsive coefficient (QPC) needs to be considered. From Chapter 12 it will be recalled that the QPC is defined by

$$\text{QPC} = \eta_O \eta_H \eta_R \quad (13.1)$$

where $P_E = P_D \cdot \text{QPC}$. As a consequence, each of the devices listed in Table 13.1 will be considered briefly and, in doing so, an outline explanation will be given of their modes of operation together with some idea of the changes that may occur in the components of equation (13.1).

Table 13.1 Zones of operation of energy-saving devices

Energy-saving device	*Zone(s) of operation*
Wake equalizing duct	I
Asymmetric stern	I
Grothues spoilers	I
Stern tunnels, semi or partial ducts	I
Reaction fins	I/II
Mitsui integrated ducted propellers	I II
Hitachi Zosen nozzle	I II
Increased diameter/low RPM propellers	II
Grim vane wheels	II
Propellers with end-plates	II
Propeller boss fins	II III
Additional thrusting fins	III
Rudder bulb fins	III

QPC = η_D (Hydrodynamic efficiency)

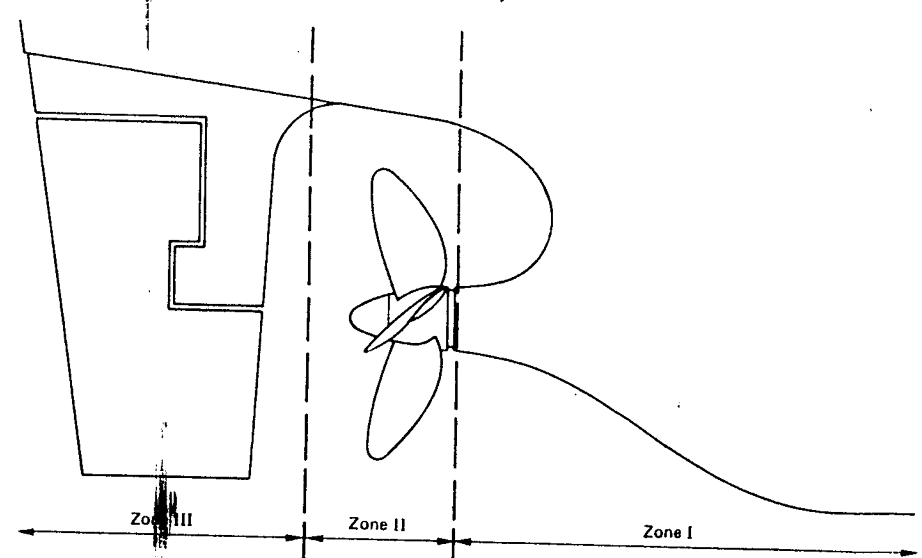

Figure 13.1 Zones for classification of energy-saving devices

13.1 Devices before the propeller

Within Zone I it is seen from Table 13.1 that the wake equalizing duct, asymmetric stern, Gruthues spoilers and stern tunnels of various forms operate on the flow in this region. Furthermore, reaction fins, the Mitsui integrated ducted propellers and the Hitachi Zozen nozzle operate at the boundary of Zones I and II: as a consequence these devices will be considered within this section. Figure 13.2 illustrates all of these devices in outline form.

13.1.1 Wake equalizing duct

The wake equalizing duct (References 1, 2) was proposed by Schneekluth and aims to improve the overall propulsive efficiency by reducing the amount of separation over the afterbody of the vessel; by helping to establish a more uniform inflow into the propeller by accelerating the flow in the upper part of the propeller disc and by attempting to minimize the tangential velocity components in the wake field. In addition, it is claimed that a larger diameter propeller may be applied better in some cases since the wake field is made more uniform and hence is likely to give rise to smaller pressure impulses transmitted to the hull. As a consequence it may be expected that the mean wake fraction and thrust deduction may be reduced, the latter probably more so, thereby giving rise to moderate increase in hull and open water efficiency components of the quasi-propulsive coefficient. There is little reason to expect that the relative rotative efficiency component will change significantly in this or any of the other devices listed in Table 13.1. In general it can be expected that the power savings with a wake improvement duct will depend on the extent of the flow separation and non-uniformity of the wake field.

This device was first introduced in 1984 and since that time many ducts have been built. This device lends itself to retrofitting on vessels; however, the designs need to be effected by experienced personnel and preferably with the aid of model tests, although scale effects are uncertain. Calculations of the effects by numerical flow computation are not generally possible at the present time, since the device is primarily operating within Zone I.

13.1.2 Asymmetric stern

The asymmetric stern (References 3, 4) was patented in Germany by Nonnecke and is aimed at reducing separation in the afterbody of a vessel when the flow is influenced by the action of the propeller. However, efficiency gains have occurred where separation has not been noticed at model scale, and accordingly the disparity in Reynolds number between model and full scale must not be overlooked when considering this type of device in the model tank. Model tests show that this concept can be chiefly expected to influence the hull efficiency by causing a significant reduction in the thrust deduction factor coupled with a slight reduction in the mean wake fraction. In this way the increase in hull efficiency is translated into an increase in the QPC for the vessel. Clearly, the asymmetry in the hull also has an effect on the swirl of the flow into the propeller.

Whilst such a concept could be fitted to an existing ship this would entail major hull modification, and therefore is probably most suitable for a new building. The design of an assymetric stern requires to be done in connection with model tests in order to gain an idea of the extent of any separation present, subject to the reservations expressed previously and the flow configuration at the stern.

In the period 1982 to 1987 some 30 vessels were built or were in the process of construction utilizing the concept of the asymmetric stern.

13.1.3 Grothues spoilers

The Grothues spoilers (Reference 5) are a hydrodynamic fin system fitted to the stern of a vessel immediately ahead of the propeller; as a consequence it is only applicable to single-screw vessels. The mode of action of these fins is to prevent cross-flow in the vicinity of the hull from reinforcing the bilge vortex and its consequent energy loss. Each fin is curved with the intention that the leading edge of the fin aligns with the local flow directions within the boundary layer flow over the stern of the vessel whilst the trailing edge is parallel to the shaft line over the whole span. Consequently, the fin system comprises a plurality of spoilers that are capable of diverting the downward cross-flow over the hull surface to a horizontal flow through the propeller.

The spoilers in general can be expected to cause a reduction in hull resistance together with an increase of propeller efficiency caused by the homogenizing effect of the fins on the wake field. In addition to suppressing the effects of the bilge vortices, thereby giving less hull resistance, it is also possible that the fins, by changing the direction for the flow, contribute a component of thrust in the forward direction to overcome resistance. As a consequence an effect of the spoiler system will be a reduction in hull effective power (P_E) together with an increase in hull and open water efficiency of the propeller.

Since the spoiler system endeavours to inhibit the bilge vortex formation it can be expected to perform best on moderately to significantly U-shaped hull forms. The spoiler needs careful design both in terms of hydrodynamic design, preferably with the aid of model tests, and also in the mechanical design to ensure the correct strength margin to prevent failure of the fin or hull structure.

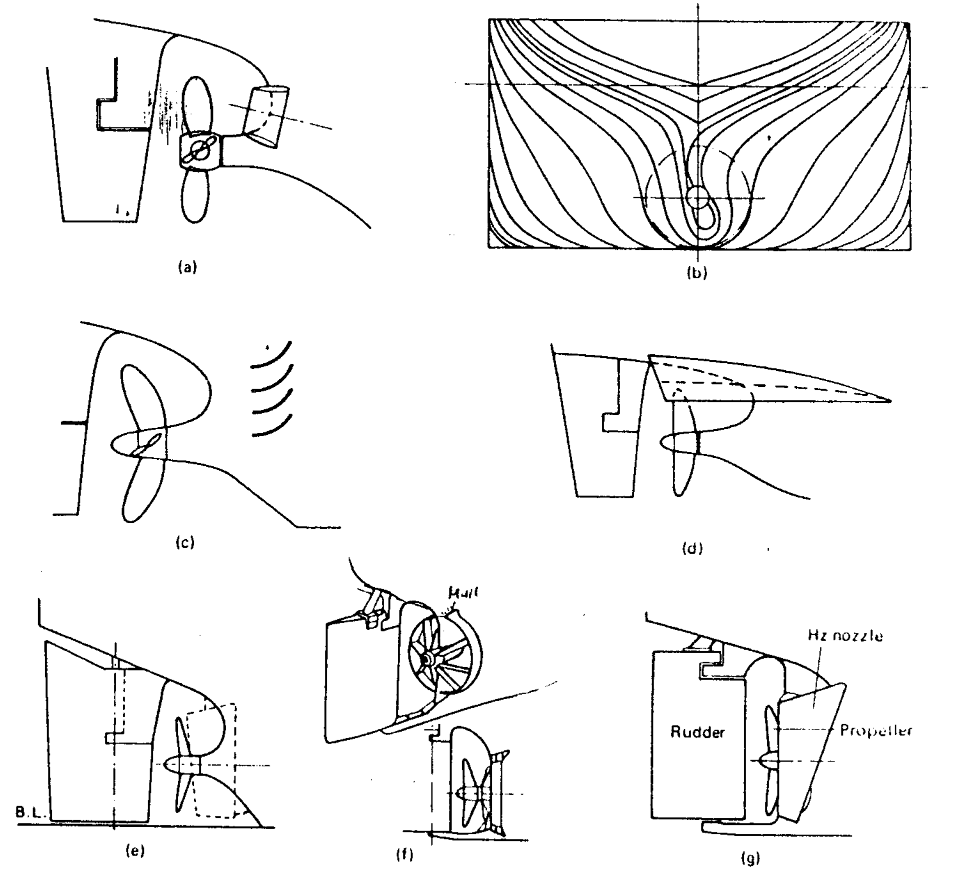

Figure 13.2 Zone 1 and Zone 1/2 devices: (a) wake equalizing duct; (b) asymmetic stern-body plan; (c) Gruthues spoilers (d) stern tunnel; (e) Mitsui integrated ducted propeller; (f) reaction fins; (g) Hitachi-Zosen nozzle

13.1.4 Stern tunnels, semi or partial ducts

These appendages exist in many forms and have been applied over a considerable number of years for one reason or another. Their use has not always been aimed at propulsive efficiency improvement and originally they were more frequently used to help with propeller induced vibration problems by attempting to reduce the wake peak effect of pronounced V-form hulls (Reference 6). Indeed, today this is still perhaps their chief role.

When used with the purpose of improving efficiency, their aim is frequenty to help accommodate large-diameter, slow RPM propellers and to ensure that the propeller is kept sufficiently immersed in the ballast draught. Their design should be based on model flow visualization studies, otherwise detrimental influences on the ship speed have been known to result: a loss of up to one knot due to poor design of the tunnel has not been unknown. Since their primary role is in the reduction of separation, then the chief influences will be a reduction in ship effective power, thrust deduction and wake fraction. As a consequence the hull efficiency and propeller open water efficiency can be expected to reflect these changes.

Bilge vortex fins, Figure 22.5(a), are fitted to the surface of the hull upstream of the propeller. In contrast to the stern tunnel concept discussed above the role of the bilge vortex fin is to inhibit the cross-flows on the hull surface which stimulate the formation of bilge vortices and hence give rise to energy losses, sources of vibration, etc.

13.1.5 Reaction fins

The reaction fin (References 7, 8) normally comprises some six radially located fins which are reinforced by a slim ring nozzle circumscribing them. The device is placed immediately in front of the propeller as shown in Figure 13.2. The diameter of the nozzle ring, which has an aerofoil profiled section, is of the order of 10% greater than the propeller diameter. The radial fins have a uniform aerofoil section profile along their length; however, the inflow angles are different for each radial station.

The design of the reaction fin is based on the nominal wake field measurement at model scale and aims chiefly at creating a pre-swirl of the flow into the propeller. The pre-swirl created by the reaction fin needs to be sufficiently strong so that rotational flow aft of the propeller is prevented from occurring. If the reaction fin is fitted to an exiting vessel then, due to this pre-swirl initiation, a decrease in propeller RPM will be found to occur: this is normally of the order of 2–3 RPM. As a consequence it is necessary to adjust the propeller design to prevent it becoming too 'stiff' in the vessel's later life. The fitting of a reaction fin does not appear from either model or full-scale tests to cause a deterioration in the cavitation or induced vibration behaviour of the propeller; see Reference 8.

A further effect which can accrue from the application of the reaction fin in the mixed wake behind a hull is the production of a thrust on the fins. This tends to have greatest effect when the fins are placed in regions of the wake field having transverse velocity components.

As a consequence the introduction of the reaction fin can be expected to increase the magnitude of the mean wake field in which the propeller operates, which will both increase hull efficiency but also to some extent reduce propeller open water efficiency. At the same time it can also be expected that the reaction fin will decrease the rotational losses and gain some benefit, in certain applications, from a positive thrust on the fins. In view of this and the proximity of the fin to the propeller care needs to be exercised in the strength aspect of the reaction fin design.

13.1.6 Mitsui integrated ducted propulsion unit (MIDP)

In principal the MIDP system (Reference 9) comprises a slightly non-axisymmetric duct which is located immediately ahead of the propeller. With systems of this type the interactions between the hull, duct and propeller are extremely complex and, as a consequence, they cannot be considered in isolation.

Mitsui, in their development of the concept, have carried out extensive model tests. In these tests the effects of varying the axial location of the duct, duct entrance configuration and duct chord profiles have all been considered. From these tests the propulsive efficiency of the system is shown to be intimately related to the longitudinal location of the duct. Furthermore, the non-axisymmetric units, having larger chords at the top, appear to perform better than their axisymmetric counterparts.

To date a considerable number of these units have been manufactured and installed on relatively full form vessels ranging in size from 43 000 DWT to 450 000 DWT.

13.1.7 Hitachi Zosen nozzle

Although developed separately, the Hitachi Zosen system (Reference 10) closely resembles the MIDP system except that the degree of asymmetry in the nozzle appears far greater.

Kitazawa *et al.* (Reference 11) made an extensive study of propeller–hull interaction effects and essentially concluded the following:

(1) The resistance of an axi-symmetric body increases after fitting a duct due to the pressure at the afterbody. However, the required propeller thrust decreased because the duct thrust is larger than the change in resistance.
(2) For a given propeller thrust and RPM, the duct thrust increased significantly when placed behind a body.
(3) The total propulsive efficiency of the vessel increases and of the components which comprise this total efficiency the relative rotative efficiency remains constant, the open water efficiency increases and the hull efficiency decreases.

As in the previous case, several ships have been fitted with this system, some new buildings and some retro-fits, and the vessels so fitted tend toward having high block coefficients.

13.2 Devices at the propeller

Zone II devices are those which essentially operate at the propeller station. As such they include increased diameter – low RPM propellers, Grim vane wheels, tip vortex free propellers and propeller cone fins.

13.2.1 Increased diameter – low RPM propellers

It is well known, and can be simply demonstrated with the aid of a B_p–δ chart that, for a given propulsion problem, the propeller open water efficiency can be increased by reducing RPM and allowing the diameter of the propeller to increase freely. As a consequence propeller design should always take account of this within the constraints of the design problem.

The constraints which limit the design option are the available space within the propeller aperture, insufficient immersion and the weight of the resulting propeller. Whilst the latter can normally be accommodated by suitable stern bearing design the former two constraints generally act as the limiting criteria for this concept.

The principal effects of these propellers are to be found in increased open water efficiency; because of the increased diameter, however, the mean wake fraction decreases slightly which has a reducing effect on the hull efficiency. The net effect, nevertheless, is generally an overall increase in QPC.

13.2.2 Grim vane wheel

The Grim vane wheel (References 12–14), deriving its name from its inventor Professor Grim, is a freely rotating device which is installed behind the propeller. In the greater majority of cases it is sited on a stub shaft bolted to the tail shaft; however, there have been proposals to locate the stub shaft on the rudder horn.

The diameter of the vane wheel is larger than that of the propeller and its function is to extract energy from the propeller slipstream, which would otherwise be lost, and convert this energy into an additional propulsive thrust. As such the inner part of the vane wheel blades act as a turbine whilst the outer part acts as propeller, Figure 13.3. The design basis of the vane wheel is, therefore, centred on satisfying the following two relationships:

$$\int_{r_t}^{R} \frac{dQ}{dr} dr + \int_{r_0}^{r_t} \frac{dQ}{dr} dr = 0 \quad \text{(ignoring bearing friction)}$$

$$\int_{r_t}^{R} \frac{dT}{dr} dr + \int_{r_0}^{r_t} \frac{dT}{dr} dr > 0$$

where dT and dQ are the thrust and torques acting on the blade section and R, r_t and r_0 are the vane wheel tip radius, transition (between propeller and turbine parts) radius and the boss radius respectively.

In less formal terms the 'propeller' and turbine torques must balance, ignoring the small frictional component and the net effect of the 'propeller' and turbine axial forces must be greater than zero.

Vane wheels in general have rather more blades than the propeller, typically greater than six, and rotate at a somewhat lower speed which is of the order of 30–50% of the propeller RPM. Consequently, the blade passing frequencies in addition to the blade natural frequencies need careful consideration: blade failure may result if this is not taken into account.

Figure 13.4 shows the velocity diagrams relating to the inner and outer portions of the vanes. The in-flow velocities into the vane wheel are defined from the induced velocities in the slipstream created by the

propeller and, therefore, the in-flow conditions to the vane wheel are derived from the propeller calculations. In view of the axial separation of the propeller and vane wheel these velocities need to be corrected for this effect in design: the extent of the correction will, however, depend on the type of mathematical model used in the propeller design process. The blade design of the vane wheel, together with an RPM and blade number optimization, is then effected either on a blade element or lifting line basis. From these analyses the resulting blade loadings and radial stress distribution in the vane wheel blade can be readily determined. The vane wheel diameter is determined primarily from the geometric constraints of the ship.

In the design process, if model tests are undertaken, care needs to be taken to interpret the results since differential scale effects between the propeller and vane wheel can manifest themselves; calculation of the performance of the Grim vane wheel is, therefore, an essential feature of the design process.

When considering applying a Grim vane wheel to a vessel the greatest advantage can be gained in cases where the rotational energy losses are high, hence giving a greater potential for conversion of this component of slipstream energy. As a consequence it is to be expected that single screw vessels will provide a greater potential for energy saving than a high-speed twin screw form. In real terms the increase in propulsive efficiency is governed by the value of C_T for the parent propeller. In the author's experience, the improvement in propulsive efficiency can be as low as 2 or 3% for high-speed, low-wake fraction vessels to something of the order of 13% for a full-form, single-screw vessel.

13.2.3 Propellers with end-plates

The reason for the introduction of blade end-plate technology is to give the designer a greater level of freedom in the choice of the distribution of circulation over the propeller blades. Although the basic concept has been known for many years it was Perez Gomez who developed the concept into a practical proposition in the mid 1970s in the form of the Tip Vortex Free (TVF) propeller. The early TVF propellers were designed to work in association with a duct such that the propeller was located at the aft end of the duct. This allowed the flow into the propeller to be controlled so as to create shock free entry of the incident flow on to the tip plates.

Subsequent to the introduction of the TVF propeller considerable development work was undertaken which gave rise to the present generation of CLT propellers. The difference between these two propeller types being that with the CLT propeller the tip plates are intended to be aligned to the direction of the flow through the propeller disc which will then minimize the viscous resistance of the tip plates and allow the desired pressure distribution over the blades to be maintained. This is in contrast to the TVF propellers whose tip

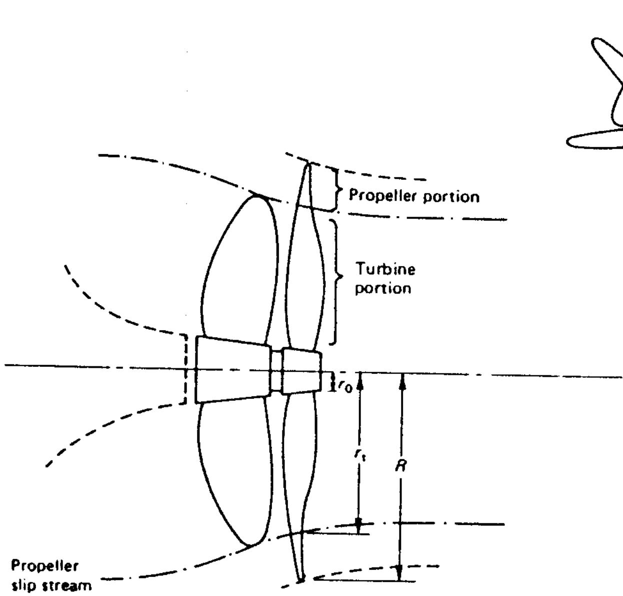

Figure 13.3 Grim vane wheel general arrangement

plates were effectively tangential to the cylindrical sections.

To date, a number of TVF and CLT propellers have been fitted to ships and an extensive literature has been published by the designers of the system. References 15 and 16 are examples of this information; the latter reference provides a much fuller reference list. Theoretical development of the concept has also been provided by Klaren and Sparenberg (Reference 17) and de Jong (Reference 18).

13.2.4 Propeller cone fins

The idea of fitting fins to the cone of a propeller, located behind the blades, was proposed by Ouchi *et al.* (Reference 19) with the aim of enhancing the efficiency of the screw propeller by reducing the energy loss associated with the propeller hub vortex. In principle a number of small fins of a flat plate form and having a span of the order of 10% of the propeller blade span are fitted at a given pitch angle to the cone of the propeller. The number of fins corresponds to the propeller blade number.

The role of the fins is to weaken the strength of the hub vortex and in so doing recover the kinetic energy from the rotating flow around the propeller cone. In this way the fins contribute to an increase in propeller efficiency.

Much model testing of this concept has been undertaken and flow measurements in the propeller wake have been made using laser Doppler methods. From such tests it is clear that the fins have a considerable influence on the hub vortex and that at model scale there is a beneficial influence on the open water efficiency of the parent MAU standard series propeller. Clearly scale effects between model and full-scale manifest themselves, but the inventors claim that the analysis of full-scale trial results from several ships show a beneficial improvement in propulsion efficiency by using these fins.

13.3 Devices behind the propeller

Zone III devices, as implied by Figure 13.1, operate behind the propeller and, therefore, operate within the slipstream of the propeller. Rudder-bulb fins and additional thrusting fins fall into this category.

13.3.1 Rudder-bulb fins systems

This is a system developed by Kawasaki Heavy Industries and comprises a large bulb, having a

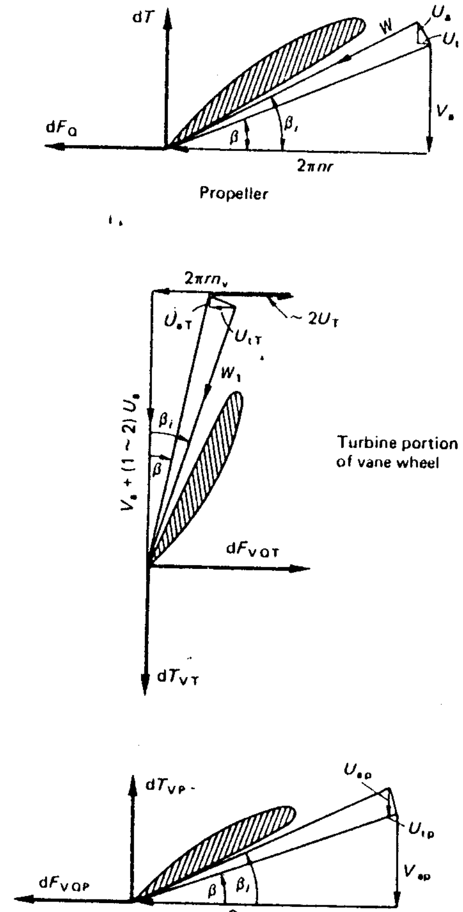

Figure 13.4 Velocity diagram of propeller-vane wheel combination

diameter of some 30–40% of the propeller diameter, which is placed on the rudder close behind the propeller boss. The system appears in two versions, one with just a bulb and the other comprising a set of four fins in an X-shape protruding normally from the hub and extending to about 0.9R as indicated in Figure 13.6.

When applied without the fins, it is not dissimilar to the Costa Bulb which was applied in the 1950s to some vessels (Reference 20). This system aimed to prevent flow separation and excessive vorticity behind

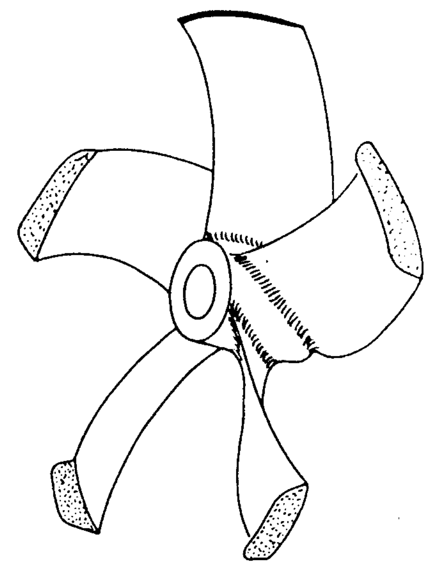

Figure 13.5 Propeller fitted with end plates

the hub by effectively extending the propeller boss. When the fins are fitted to the system these clearly produce a lift force since they are operating in the helical slipstream of the propeller, and therefore receive flow at incidence. A component of this lift force then acts in the forward direction to produce a thrust augmentation. The design of the fins need to be based on fatigue considerations since the fins are working within the flow variations caused by the vortex sheets emanating from the propeller.

13.3.2 Additional thrusting fins

The additional thrusting fins (References 21, 22) were developed and patented by Ishikawajima-Harima

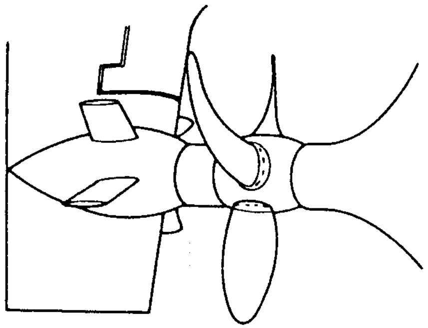

Figure 13.6 Rudder-bulb fins

Heavy Industries. The system essentially comprises two fins, placed horizontally in the athwart ships directions on the rudder and in line with or slightly above the propeller axis. Figure 13.7 shows this system in schematic form. The chord length of the fins is of the order of about half that of the rudder and the span is about 40% of the propeller diameter.

The design of the fins is aimed at optimizing their lift-drag ratio whilst operating in the slipstream of the propeller and hence use is made of cambered aerofoil sections of variable incidence. The principle of operation can be seen from Figure 13.7 by examining the four positions in the propeller disc; top and bottom dead centre and port and starboard athwart ships. At the top dead centre position it can be seen that the flow, which comprises an axial component V_x and tangential component V_θ, is incident on the rudder and, therefore, produces a horizontal force on the rudder, a component of which is directed in the forward direction. Similarly with the conditions at the bottom dead centre position. In the case of fins that are set normally to the rudder and at an incidence relative to the propeller shaft centre line, again a similar situation occurs. Now, provided that the magnitude of the lift force can be made sufficiently great, by adjusting the incidence of the fin with respect to the hydrodynamic pitch angle of the propeller slipstream to overcome the drag of the fins, a positive contribution to the thrust of the vessel can be produced (Figure 13.7).

This system has been applied to full-scale practice and in doing so attention has to be paid to the system of steady and non-steady forces acting on the fins; for example, added mass, slamming forces, lift, drag, weight and so on. These factors have important consequences for the rudder strength.

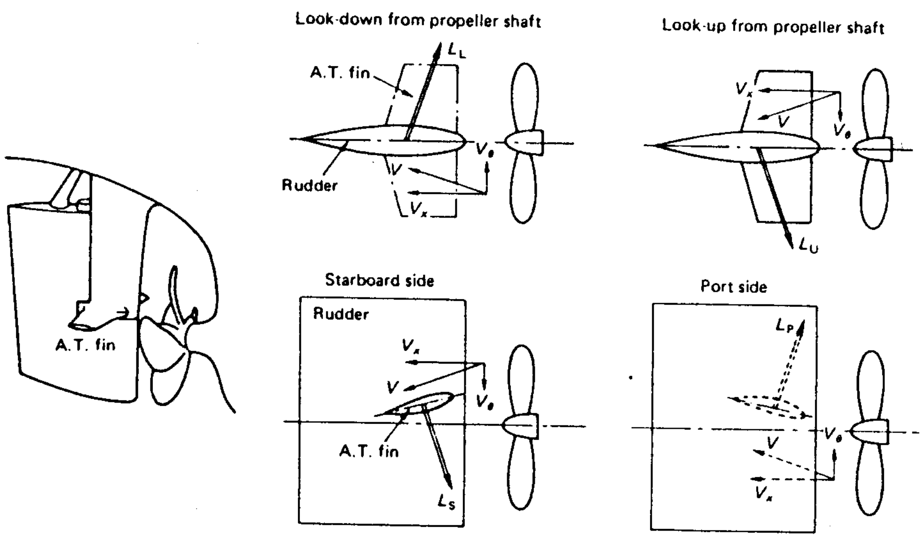

Principle of the A.T. fin for a clockwise propeller. Thrust is produced as propeller axial components of lift L_L, L_U act on the rudder with additional thrust produced as propeller axial components of lift L_S, L_P act on the fin.

Figure 13.7 Additional thrusting fins (Reproduced from Reference 23, with permission)

Table 13.2 Guide to device compatibility

	Wake equ. duct	Asymmetric stern	Grothues spoilers	Semi partial ducts	Reaction fins	MIDP system	HZ nozzle	Inc. dia. low RPM prop.	Grim vane wheel	Propellers with end-plates	Prop. boss fins	Rudder bulb fins	Addit. thrusting fins	
Wake equ. duct		C						C	C	C	C	C	C	Zone I
Asymetric stern			C		C			C	C	C	C	C	C	
Grotheus spoilers								C	C	C	C	C	C	
Semi-partial ducts					C	PC		C	C	C	C	C	C	
Reaction fins								C		C	C			Zone I II
MIDP system								C	C	C	C	C	C	
HZ nozzle								C	C	C	C	C	C	
Inc. dia/low RPM									C¹	C²	C	C	C	Zone II
Grim vane wheel										C				
Propellers with end-plates											C	C	C	
Prop boss fins												PC	PC	
Rudder bulb fins														Zone III
Addit. thrust fins														

Notes: C Compatible in principle
PC Partially compatible
1 Depending on clearance
2 Would be incorporated in design

13.4 Combinations of systems

In many cases it is asked whether the various energy saving devices are compatible with each other so as to enable a cumulative benefit to be gained from fitting several devices to a ship. The general answer to this question is no, because some devices remove the flow regimes upon which others work; however, several of the devices can be used in combination in order to gain a greater benefit. Table 13.2 outlines in general terms this compatibility relationship between the various devices discussed in Table 13.1.

References and further reading

1. Schneekluth, H, Schneekluth wake equalising duct. *The Naval Architect*.
2. Beek, T. van., Verbeek, R., Schneiders, C.C. Saving Fuel Cost – Improving Propulsive Efficiency with Special Devices and Designs. Lips BV Paper, August, 1986.
3. Collatz, G., The asymmetric afterbody, model tests and full scale experiences. *Int. Symp. on Ship Hydrodynamics and Energy Saving*, El Pardo, September, 1983.

4. Collatz, G. Non-symmetrical Afterbodies. MARIN Workshop on Developments in Hull Form Designs, Wageningen, October, 1985.
5. Grothues-Spork, K. Bilge vortex control devices and their benefits for propulsion. *Int. Shipbuilding Prog.*, **35**(402), 1988.
6. Carlton, J.S., Bantham, I. Full scale experience relating to the propeller and its environment. *Propellers 78 Symposium. Trans. SNAME*, 1978.
7. Takekuma, K. *et al.* Development of reaction fin as a device for improvement of propulsion performance of high block coefficient ships. *Soc. Nav. Arch. of Japan*, **150**, December, 1981.
8. Talekuma, K. Evaluations of various types of nozzle propeller and reaction fin as the devices for the improvement of propulsive performance of high block coefficient ships. *Shipboard Energy Conservation Symposium*, SNAME, New York, September, 1980.
9. Narita, H. *et al.* Development and full scale experiences of a novel integrated duct propeller. *SNAME Annual Meeting*, New York, November, 1981.
10. Kitazawa, T., Hikino, M., Fujimoto, T., Ueda, K. Increase in the Propulsive Efficiency of a Ship with the Installation of a Nozzle Immediately Forward of the Propeller. Hitachi Zosen Annual Research Report, 1983.
11. Kitazawa, T. *et al.* Increase of the propulsive efficiency of a ship by a nozzle installed just in front of a propeller. *Kansai Soc. Nav. Arch.*, Japan, November, 1981.
12. Grim, O. Propeller and vane wheel, Second George Weinblum Memorial Lecture, *J. Ship. Res.*, 24(4), December, 1980.
13. Grim, O. Propeller and vane wheel, contrarotating propeller. *WEGEMT*, 8th School, Gothenburg, August, 1983.
14. Kubo, H., Nagase, M., Itadani, Y., Omori, J. and Yoshioka, M. Free rotating propeller installed on ship. *Bull. MESJ*, **16**(1), March, 1988.
15. Ruiz-Fornells, R. *et al.* Full scale results of first TVF propellers. *Int. Symp. on Ship Hydrodynamics and Energy Saving*, Madrid, 1983.
16. Sistemar. Fairplay Advertising Supplement. *Fairplay*, 6 February, 1992.
17. Klaren, L. and Sparenberg, J.A. On optimum screw propellers with end plates, inhomogeneous inflow. *J. Ship. Res.*, **25**(4), December, 1981.
18. Jong, K. de. On the design of optimum ship screw propellers, including propellers with end plates. Int. Symp. on Propulsors and Cavitation, Hamburg, June, 1992.
19. Ouchi, K.B., Kono, Y., Shiotsu, T., Koizuka, H. PBCF (propeller boss cap fins). *J. Soc. Nav. Arch. of Japan*, **163**, 1988.
20. Gregor, O. Etudes récentes du Bulbe de Propulsion Costa. Assoc. Technique Maritime et Aéronautiques, Paris, 1983.
21. Ishida, S. Study on recovery of rotational energy in propeller slipstream. *IHI Eng. Review*, **16**, July, 1983.
22. Mori, M. IHI A.T. Fin - 1st Report, Its Principle and Development. *IHI Eng. Review*, **17**, January, 1984.
23. *The Naval Architect*, May, E172, 1984.

14 Transverse and azimuthing thrusters

Contents

Many vessels in service today depend to a very large extent for their effectiveness on possessing a good capability to manoeuvre in confined waters. Figure 14.1 shows just such a case of ferries manoeuvring in confined waters and berthing stern first into a set of link spans in some cases, in order to maintain schedules, under poor weather conditions. In addition to the ferry many other vessels also require a considerable manoeuvring capability; typical of these are research vessels, drill ships, various types of offshore platforms and of course minesweepers. To satisfy these requirements several methods of providing a directional thrusting capability are available to the naval architect; one of these is the provision of transverse propulsion units or azimuthing thrusters. The various options available and their comparative merits have to be carefully considered at the vessel's design stage and the primary purpose of this chapter is to outline the various characteristics of these thrusting devices.

Transverse propulsion units and azimuthing thrusters fall principally into three categories, although of course some propriety designs transcend these boundaries. For convenience of discussion, however, these units can be described as follows:

1. transverse, fixed tunnel systems;
2. azimuthing thrusters;
3. steerable, internal duct systems.

These three types of units are shown schematically in Figure 14.2.

14.1 Transverse thrusters

These systems essentially comprise an impeller mounted inside a tunnel which is aligned athwart the vessel. The essential features of the system are illustrated in Figure 14.3 and it is important to emphasize that the system must be considered as 'a whole'; that is impeller, tunnel, position in the hull, drive unit fairings, tunnel openings and the protective grid all

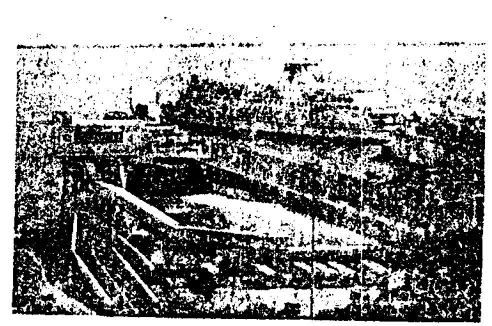

Figure 14.1 Ro-Ro ships manoeuvring in ferry terminal

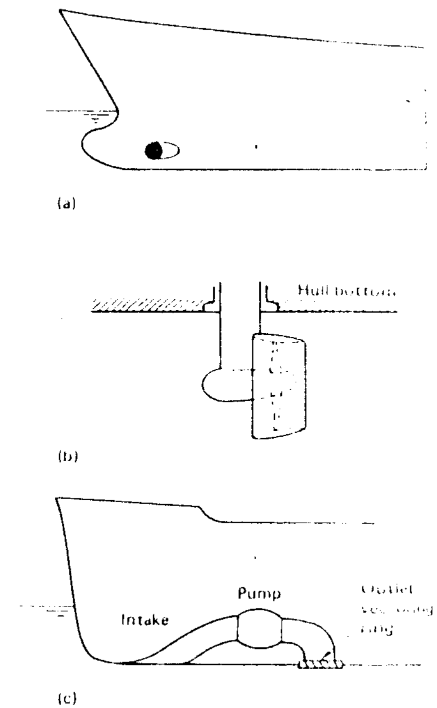

Figure 14.2 Types of thruster units (a) transverse propulsion unit; (b) azimuthing thruster; (c) steerable internal duct thruster

need to be evaluated as a complete concept if the unit is to satisfy any form of optimization criteria. Incorrect or at best misleading results, will be derived if the individual components are considered in isolation or, alternatively, some are neglected in the analysis. Although Figures 14.2 and 14.3 generally show a transverse propulsion unit located in the bow of the vessel, and in this position the unit is termed a bow thruster, such units can and are located at the stern of the ship. The bow location is, however, the more common and for large vessels and where enhanced manoeuvrability, such as in the case of a ferry, is required they are often fitted in pairs. The decision as to whether to fit one or two units to a vessel is normally governed by the power or thrust requirement and the available draught.

The design process for a transverse propulsion unit for a given vessel has two principal components: firstly, to establish the thrust, or alternatively the power, required for the unit to provide an effective manoeuvring capability, and secondly, how best to design the unit to give the required thrust in terms of

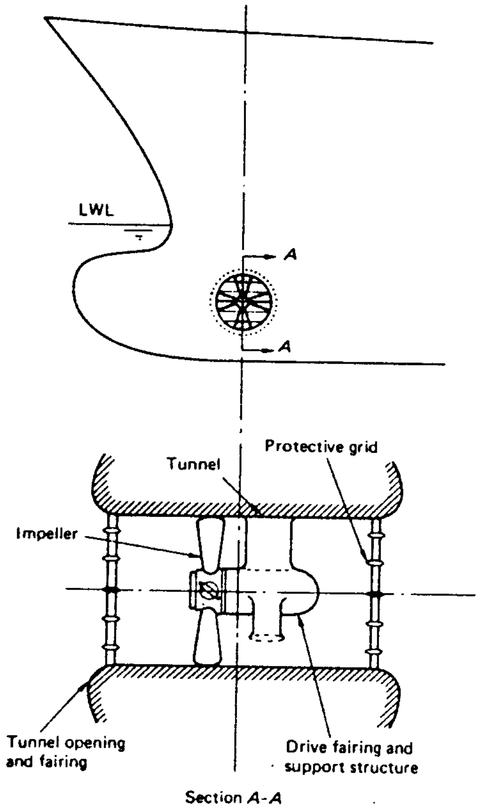

Figure 14.3 Transverse propulsion unit—general arrangement in hull

unit geometry. In the case of thrusters of this type many manufacturers have elected to provide standard ranges of units covering, for example, a power range of 150 to around 4000 horsepower and then selecting the most appropriate unit from the range for the particular duty. Other manufacturers, who perhaps tend to be in the minority, design a particular unit for a given application.

In order to determine the size of a transverse propulsion unit for a given application two basic philosophical approaches can be adopted. In both cases the vessel is considered to be stationary with regard to forward ahead speed. The first approach is to perform a fairly rigorous calculation, or undertake model tests, or perhaps a combination of both to determine the resistance of the hull in lateral and rotational motion. Such an exercise would also probably be undertaken for a range of expected currents. Additionally the wind resistance of the vessel would also be evaluated either by calculation, typically using a method such as Reference 1, or by model tests in a wind tunnel. The various wind and hydrodynamic forces on the vessel could then be resolved to determine the required thrust at a particular point on the ship to provide the required motion. A method of this type, whilst attempting to establish the loading from first principles suffers particularly from correlation problems, scale effects and not least the cost of undertaking the exercise. As a consequence, although this method is adopted sometimes, more particularly with the aximuthing thruster design problem, it is more usual to use the second design approach for the majority of vessels. This alternative approach uses a pseudo-empirical formulation of the ship manoeuvring problem coupled with experience of existing vessels of similar type. In essence this type of approach attempts to establish a global approximation to the relationship between turning time, required thrust and wind speed on a particular class of vessel. An approximation to the turning motion of a ship then can be represented by equation (14.1) assuming the vessel rotates about a point (as seen in Figure 14.4):

$$J_P \frac{(\mathrm{d}^2\theta)}{\mathrm{d}t^2} = M_H + M_W + M_P \qquad (14.1)$$

where M_H and M_W are the hydrodynamic and wind moments respectively and M_P is the moment produced by the thruster about some convenient turning axis. J_P is the polar moment of inertia of the ship and $\mathrm{d}^2\theta/\mathrm{d}t^2$ the angular acceleration. However, by assuming a constant turning rate the left-hand side of equation (14.1) can be put to zero, thereby removing any difficulties with the polar inertia term:

$$M_H + M_W + M_P = 0 \qquad (14.2)$$

In pursuing this pseudo-empirical approach it can be argued that the hydrodynamic moment is largely a function $(\dot{\theta})^2$ and the wind moment is a function of the maximum wind moment times sin 2θ. The thruster moment is simply the thrust times the distance from the point of rotation and, assuming a constant power input to the unit, is a constant k_3. Hence, equation (14.2) can be rewritten as

$$k_1\left(\frac{\mathrm{d}\theta}{\mathrm{d}t}\right)^2 + k_2 \sin 2\theta + k_3 = 0 \qquad (14.3)$$

where the coefficients k_1 and k_2 depend on the water and air densities (ϱ_W and ϱ_A), the underwater and above water areas (A_U and A_A), the vessel's length (L), wind speed (V), etc., as follows:

$$\left.\begin{aligned} k_1 &= 0.5\varrho_W A_U L^3 C_{MW} \\ \text{and}& \\ k_2 &= 0.5\varrho_A A_A L V^2 C_{MAI} \end{aligned}\right\} \qquad (14.3(a))$$

in which C_{MW} and C_{MAI} are the water and maximum air moment coefficients respectively.

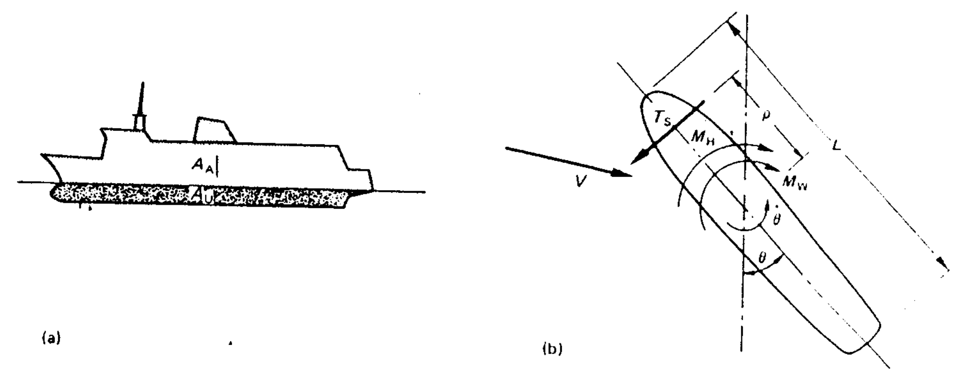

Figure 14.4 Transverse propulsion unit nomenclature: (a) surface area definition; (b) force, moment and velocity definitions

Consequently equation (14.3) can be rewritten as

$$\left(\frac{\mathrm{d}\theta}{\mathrm{d}t}\right) = -\frac{[(k_2 \sin 2\theta + k_3)]^{0.5}}{k_1}$$

from which the time to turn through 90° can be estimated as follows:

$$t_{90} = \int_0^{\pi/2} \left(\frac{\mathrm{d}t}{\mathrm{d}\theta}\right) \mathrm{d}\theta \qquad (14.4)$$

Several authors have considered this type of relation for transverse propulsion unit sizing. One such approach (Reference 2) uses a form of equation (14.4) to derive a set of approximate turning times for three classes of vessel in terms of the turning time for a quarter of a turn as a function of thruster power and with wind speed as a parameter. The relationship used in this case is

$$t_{90} = \left[\frac{0.308 C_{MW} \varrho_W A_U L_{pp}^2}{k T_S - 0.5 C_{MA} \varrho_A A_A V^2}\right]^{0.5}$$

in which k is distance of the thruster from the point of rotation non-dimensionalized by ship length between perpendiculars, T_S is the propulsion unit thrust, and C_{MA} is a mean wind resistive moment coefficient. The vessels considered by Reference 2 are ferries, cargo liners and tankers or bulk carriers, and Figure 14.5 reproduces the results of the prediction. Implicit in this type of prediction is, of course, the coefficient of performance of the unit which relates the unit thrust T to the brake horsepower of the motor; however, such values should not introduce large variations between units of similar types; that is controllable pitch, constant speed units. Whilst curves such as those shown in Figure 14.5 can only give a rough estimate of turning capability they are useful for estimation purposes. With ships having such widely differing forms, one with another, due account has to be taken in the sizing procedure of the relative

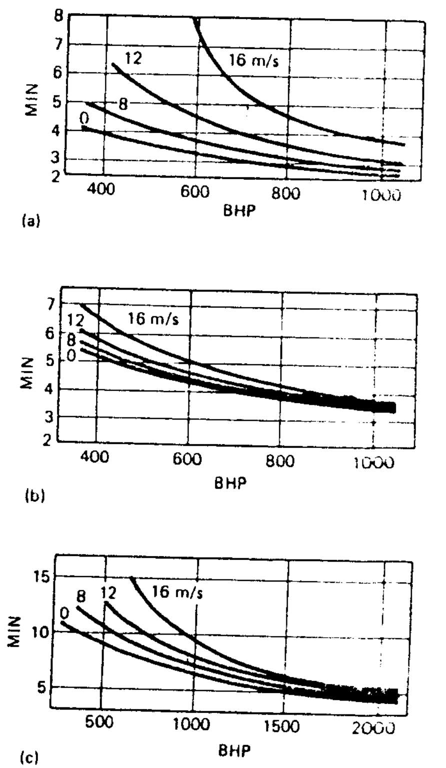

Figure 14.5 Average relationship between turning time and power of unit (Reference 2): (a) Ro/Ro and ferries, (b) cargo ships; (c) tankers and bulk carriers (Reproduced from Reference 2, with permission)

Table 14.1 Guide to thrust per unit area requirements

Ship type	T/A_U (kp/m²)	T/A_A (kp/m²)
Ro/Ro and ferries	10–14	4–7
Cargo, ships, tugs	6–10	4–8
Tankers/bulk carriers	4–7	14–16
Special craft (i.e. dredgers, pilot vessels, etc.)	10–12	5–8

amounts of the vessel exposed to the wind and to the water. An alternative approach is to consider the thrust per unit area of underwater or above water surface of the vessel. Table 14.1 shows typical ranges of these parameters, compiled from References 3, 4.

Clearly in interpreting Table 14.1 one should be guided by the larger resulting thrust derived from the coefficients. This is particularly true of the latest generation of Ro/Ro ferry in which considerable wind exposure is an inherent design feature; furthermore, in the case of tankers and bulk carriers the assessment of thruster size by the above water area is not a good basis for the calculation.

The question of an acceptable turning rate is clearly always a subjective issue and as such depends on the purpose to which the vessel is put and the conditions under which it is expected to operate. Consequently, there is no single answer to this problem; Hawkins *et al.* (Reference 5) made an extensive study of several types of manoeuvring propulsion devices for the US Maritime Administration and Figure 14.6 presents curves based on his work showing measured turning rates as a function of displacement. The band shown in the figure represents turning rates which have been considered satisfactory in past installations.

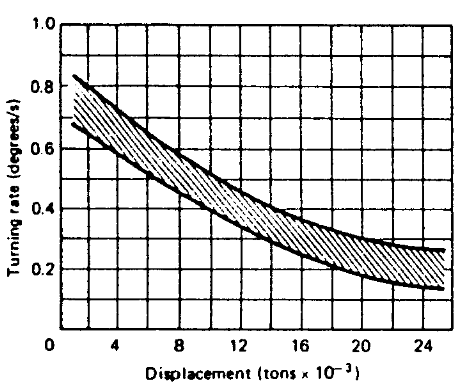

Figure 14.6 Band of rotation rates versus displacement at zero ship speed (Reproduced from Reference 13, with permission)

14.1.1 Performance characterization

The usual measure of propeller performance defined by the open water efficiency (η_0) and given by equation (6.2) decrease to zero as the advance coefficient J tends to zero. However, at this condition thrust is still produced and as a consequence another measure of performance is needed in order to compare the thrust produced with the power supplied.

Several such parameters have been widely used in both marine and aeronautical applications, in the latter case to characterize the performance of helicopter rotors and VTOL aircraft. The most widely used are the static merit coefficient (C) and the Bendemann static thrust factor (ζ), these coefficients are defined by the following relationships:

$$\left.\begin{aligned} C &= \frac{0.001827T^{3/2}}{\mathrm{SHP}\sqrt{(\varrho\pi D^2/4)}} = \frac{K_T^{3/2}}{\pi^{3/2}K_Q} \\ \zeta &= \frac{T}{P_S^{2/3}D^{2/3}(\varrho\pi/2)^{1/3}} = \frac{K_T}{K_Q^{2/3}}\frac{1}{[\pi(2)^{1/3}]} \end{aligned}\right\} \qquad (14.5)$$

In the above equations the following nomenclature applies.

- T = total lateral thrust taken as being equal to the vessel's reactive force (i.e. the impeller plus the induced force on the vessel)
- SHP = shaft horsepower
- P_s = shaft power in consistent units
- D = tunnel diameter
- ϱ = mass density of the fluid

and K_T and K_Q are the usual thrust and torque coefficient definitions.

Both of these expressions given in equation (14.5) are derived from momentum theory and can be shown to attain ideal, non-viscous maximum values for $C = \sqrt{2}$ and $\zeta = 1.0$ for normal, non-ducted propellers. In the case of a ducted propeller with no duct diffusion these coefficients become $C = 2$ and $\zeta = \sqrt[3]{2}$.

Clearly it is possible to express the coefficient of merit (C) in terms of the Bendemann factor (ζ); from equation (14.5) it can easily be shown that

$$C = \zeta^{3/2}\sqrt{2} \qquad (14.6)$$

14.1.2 Unit design

Having determined the required size of the unit it is necessary to then configure the geometry of the unit to provide the maximum possible thrust. The fundamental decision at this stage is to determine whether the unit will be a controllable pitch, constant speed machine or a fixed pitch, variable speed unit; the former units being perhaps the most common amongst larger vessels. In the case of the controllable pitch unit the blades are designed as constant pitch angle blades to enable a nominal equality of thrust to be achieved in either direction for a given pitch angle. The term 'nominal equality of thrust' is used to signify that this

is not exactly the case in practice due to the pod arrangement and its position in the tunnel. The blades of the controllable pitch unit are frequently termed 'flat-plate blades' on account of their shape. In the alternative case of the fixed pitch unit the radial distribution of pitch angle over the blade can be allowed to vary in order to develop a suitable hydrodynamic flow regime over the blades, reversal of thrust in this case being achieved by a reversal of rotation of the impeller.

In both the controllable and fixed pitch cases the blade sections are symmetrical about their nose–tail lines; that is the blades do not possess camber. Furthermore, the fixed pitch blade sections need to be bisymmetrical since both edges of the blade have to act as the leading edge for approximately equal times, whereas for the controllable pitch unit a standard NACA or other non-cambered aerofoil section is appropriate.

Transverse propulsion units are a source of noise and vibration, these largely resulting from the onset of cavitation and the flow of water through a tunnel within the vessel. The question of noise emission is considered in Chapter 10; however, in order to design a unit which would both be able to perform reliably and not cause undue nuisance, this being particularly important in passenger vessels, the blade tip speed should be kept within the band of 30–34 m/s.

Blade design can be achieved by use of either model test data or by theoretical methods. Taniguchi *et al.* (Reference 6) understood a series of model tests on a set of six transverse thrusters. These models had an impeller diameter of 200 mm; two had elliptic form blades whilst the remaining four were of the Kaplan type, and it is this latter type that is of most interest in controllable pitch transverse propulsion unit design. Taniguchi considers Kaplan blade designs having expanded area ratios of 0.300, 0.450 and 0.600 in

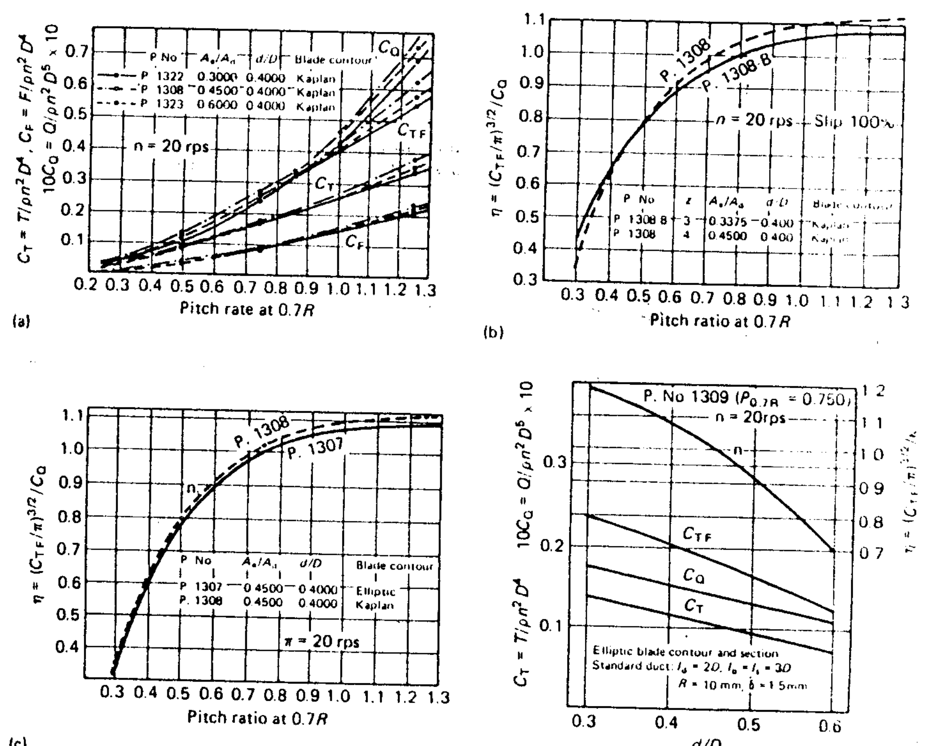

Figure 14.7 Examples of test data from CP transverse propulsion unit tests: (a) effect of A_E/A_O; (b) effect of blade number (c) effect of blade form; (d) effect of hub diameter (Reproduced from Reference 6, with permission)

association with a blade number of 4 and a 0.3375 expanded area ratio version having three blades. Each of the blades for these units was designed with NACA 16-section thickness forms in association with a non-dimensional hub diameter of 0.400 and a capability to vary the pitch ratio between 0 and 1.3. Using these models Taniguchi evaluated the effects of changes in various design parameters on performance; Figure 14.7 shows a selection of these results highlighting the effects of variations in expanded area ratio and pitch ratio, the effects of blade number and boss ratio. This latter test was carried out with an elliptic blade form; the results show, however, that there is little difference between the efficiency (η) of the elliptic and Kaplan blade forms with the exception that the Kaplan form performs marginally better at all pitch settings. In Figure 14.7 K_T and K_Q are the conventional thrust and torque coefficients respectively and C_F represents the force measured on the simple block body containing the tunnel (Figure 14.8). The efficiency of the unit is defined by

$$\eta = \frac{1}{K_Q}\left(\frac{K_T + C_F}{\pi}\right)^{3/2} \qquad (14.7)$$

The effects of cavitation on these blades forms can be seen in results from a different series of flat plate blades shown in Figure 14.9. This set of curves, which relates to a blade area ratio of 0.5 and a blade number of four, shows how the breakdown of the thrust and torque characteristics occurs with reducing cavitation number for a series of pitch ratios. In comparing the results, it should be noted that the test configurations between Figures 14.7 and 14.9 are somewhat different.

With regard to theoretical methods for impeller design several methods exist. These range from empirically based types of approaches such as that by van Manen *et al.* (Reference 7) to advanced computational procedures of the type discussed in Chapter 8.

As mentioned earlier in the chapter the impeller design process is only one aspect of the system design. The position of the impeller in the hull presents an equally important design consideration. Taniguchi *et al.* (Reference 6) in their model test study examined this problem using simple block models of the hull in which the vertical position of the tunnel relative to the base line, the tunnel length, and the effects of the frame slope in way of the tunnel opening could be investigated. Figure 14.10 shows the effects of these changes at model scale, from which it can be seen that they exert an important influence on the overall thrust performance of the unit. As a consequence it is seen that care needs to be exercised in determining the location of the unit in the hull, both to avoid any unnecessary losses and also to maximize the turning moment of the unit. It will be seen from Figure 14.10 that these two constraints are partially conflicting, and therefore an element of compromise must be achieved within the design process.

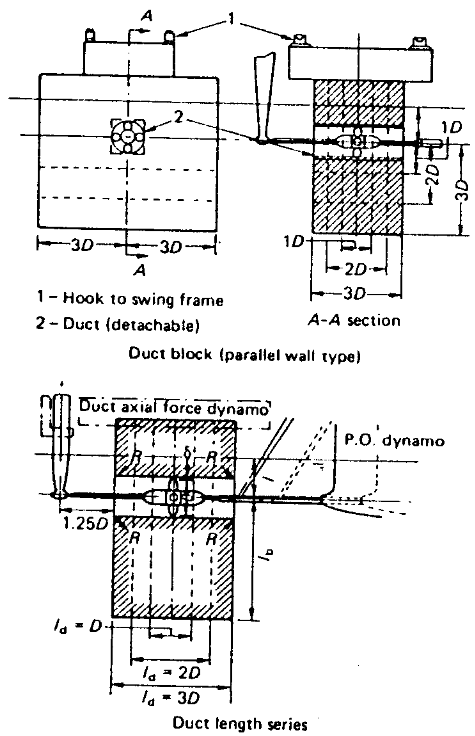

Figure 14.8 Taniguchi's simplified hull form arrangement (Reproduced from Reference 6, with permission)

The tunnel openings need to be faired to some degree in order to prevent any undue thrust losses from the unit and also to minimize any hull resistance penalty resulting from the discontinuity in the hull surface. Again the type of fairing required to enhance the thrust performance is not that required to minimize hull resistance during normal ahead operation and consequently, some measure of compromise is again required.

Transverse propulsion units are at their most effective when the vessel is stationary in the water with respect to normal ahead speed. These propulsion units tend to lose effectiveness as the vessel increases its ahead, or alternatively astern, speed. English (Reference 8) demonstrated this effect by means of model tests, from which it can be seen that the side thruster loses a significant amount of its effect with ship speeds, or conversely current speeds, of the order of 2–3 knots. The cause of this fall-off in net thrusting performance is due to the interaction between the fluid forming the jet issuing from the thruster tunnel and the flow over

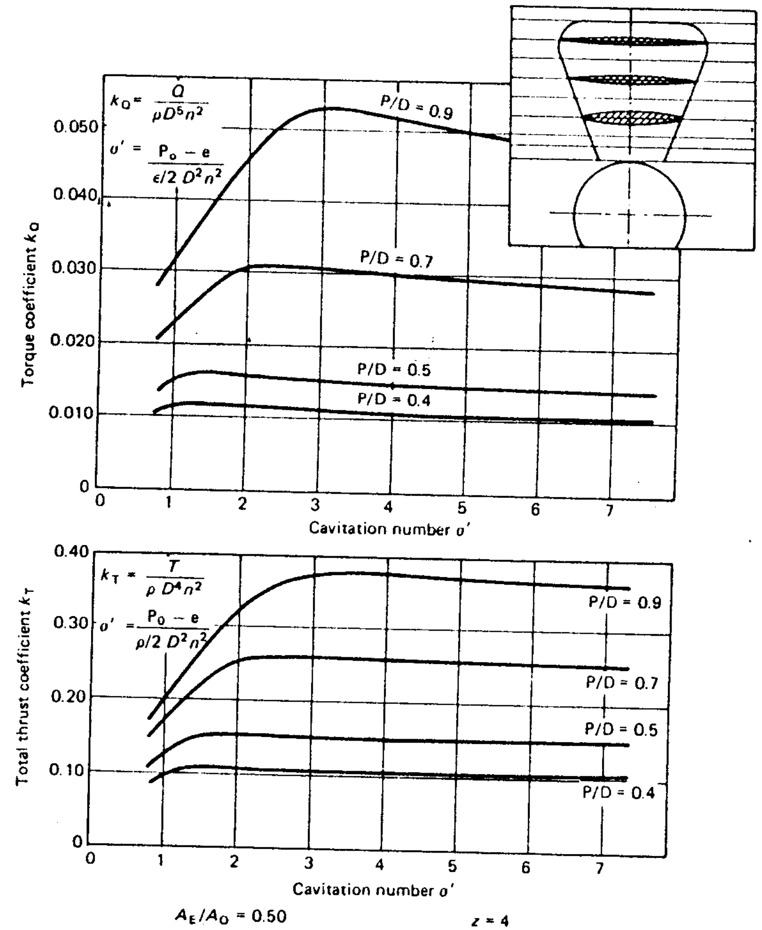

Figure 14.9 Effect of cavitation on K_t and K_Q for a Kaplan blade form

the hull surface, due principally to the translational motion of the hull but also in part to the rotational motion. Figure 14.11 shows the effect in diagrammatic form. This interaction causes a reduced pressure region to occur downstream of the tunnel on the jet efflux side, which can extend for a considerable way downstream. This induces a suction force on that side, which reduces the effect of the impeller thrust and alters the effective centre of action of the force system acting on the vessel (Reference 9). Considerations of this type had led some designers (Reference 10) to introduce a venting tube, parallel to the axis of the tunnel, in order to induce a flow from one side of the hull to the other, as seen in Figure 14.12. From this figure the effects of fitting such a device to two types of vessel can be seen as shown by Reference 10.

Wall effects are also important when considering the performance of a transverse propulsion unit. A low-pressure region can be created between the hull surface and the jetty wall in the presence of a jet from a bow thruster unit. This causes a suction between the wall and the hull which, in the case of an idealized

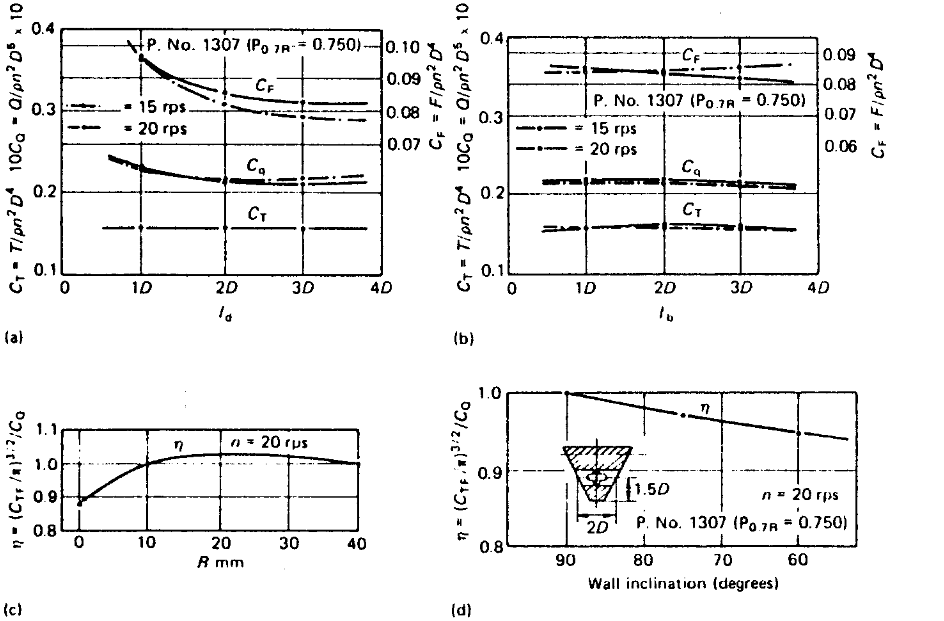

Figure 14.10 Effects of tunnel location, frame shape an entrance radius on model scale: (a) tunnel length series; (b) bottom immersion series; (c) tunnel entrance shape series; (d) hull frame inclination (Reproduced from Reference 6, with permission)

flat plate at about three jet diameters from the wall, experiences a suction of the order of the jet thrust. Such a magnitude, however, decays rapidly with increasing separation distance, so that at about six jet diameters the suction is only about 10% of the jet thrust.

14.2 Azimuthing thrusters

Azimuthing thrusters have, as a class of propulsion units, gained considerable importance over the last few years due to the increasing demand for dynamic positioning capabilities and directional thrust requirements. These units fall into two distinct classes; the first is that where a propeller is mounted on a rotatable pod beneath the ship and the second is the Voith Schneider or Kirsten–Boeing propulsion concept; this latter concept was considered in Chapter 2. With regard to the former concept, that where a propeller is mounted on a pod beneath the ship, Figure 14.13 shows the basic features of the system. It can be seen that there are two basic types of unit: the pusher unit shown in Figure 14.13(a) and the tractor unit shown in Figure 14.13(b). In general these types of azimuthing units are fitted with ducted propellers having ducts of the Wageningen 19A form since, for many dynamically positioning applications, it is required to maintain station against only tide or wind forces and at low advance speeds this type of ducted propeller has a greater thrusting capability. For other applications, such as canal barge propulsion, the non-ducted propeller may have the advantage and is commonly used.

The resulting thrust from an azimuthing thruster is the sum of three components:

$$T = T_P + T_D + T_G \qquad (14.8)$$

where T_P, T_D and T_G are the component thrusts from the propeller, duct and the pod respectively and T is net unit thrust. Clearly, as with any other propulsion device, the effective thrust is the net thrust adjusted by the augment of resistance (thrust deduction factor) induced by the unit on the vessel.

These types of unit experience a complex system of forces and moments which are strongly dependent on the relative alignment of the unit to the incident flow as seen in Figure 14.14. The forces and moments which

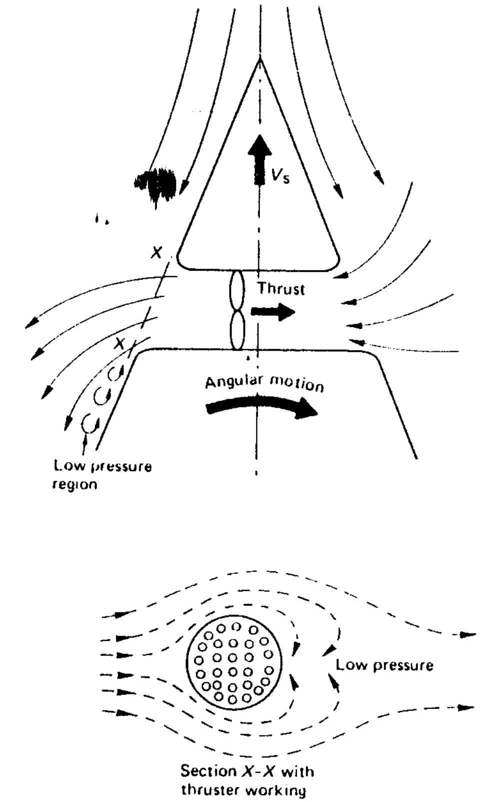

Figure 14.11 Transverse propulsion unit jet interactions with forward ship speed

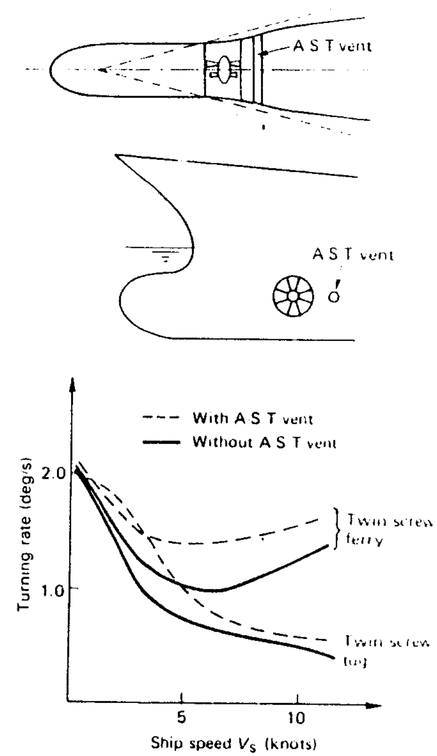

Figure 14.12 Effect of AST vent (Reference 10)

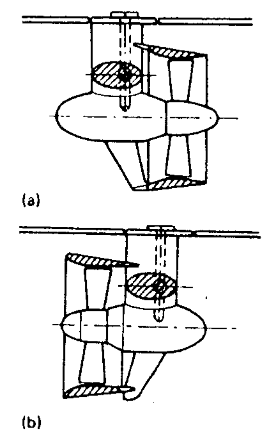

Figure 14.13 Azimuthing thruster unit types. (a) pusher unit; (b) tractor unit

occur are

- F_x longitudinal force in the propeller shaft direction;
- F_y transverse force perpendicular to the propeller shaft;
- Q the propeller torque;
- M_z the steering or turning moment of the unit.

All of these forces and moments are dependent upon the in flow incidence angle δ and of course the magnitude of the in flow velocity. For a uniform in flow these are the only forces and moments produced; however, if a mixed wake field is offered to the unit then the six components of loading $\{F_x, F_y, F_z, M_x, M_y \text{ and } M_z\}$ will be present.

For design purposes two sets of model test data are commonly used. The first, and most comprehensive (Reference 11) reports a set of test data conducted in

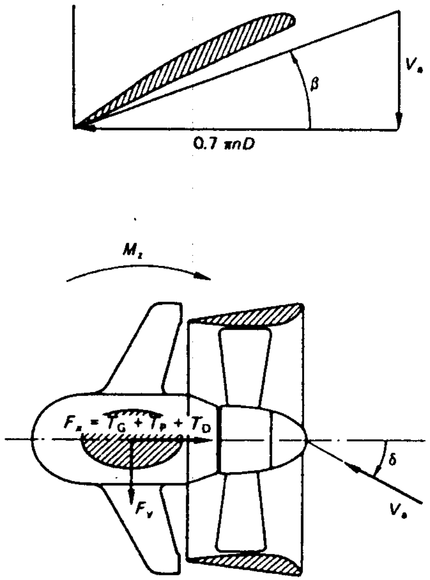

Figure 14.14 Forces and moments acting on an azimuthing thruster in uniform flow

both the cavitation tunnel and also a towing tank. This test data considers three blade forms, two with 'flat plate blades' and the other with an elliptical outline and cambered aerofoil sections, mounted inside a duct of the Wageningen 19A form in each of the tractor and pusher configurations. The model propeller diameters are 250 mm and the only difference between the two planar blade forms is the radial thickness distribution; all of the blade forms have the same blade area ratio of 0.55.

The analysis of the model test results shows, as might be expected, that the open water efficiency of the propeller with the cambered sections was considerably better than for the propeller with 'flat plate' blades. This latter blade form, however, whilst losing on efficiency, has the advantage of a nominal equality of thrust in each direction, as in the case of the transverse propulsion units discussed previously, and also prevents the otherwise cambered sections from working at negative angles of incidence.

The pusher unit was shown to have a slightly better efficiency than the tractor version; however, due to the uniform in-flow conditions experienced by the tractor unit less cyclic variation in cavitation pattern was observed as compared to the pusher unit, where the propeller is operating in the wake of the gear house. With regard to turning moment (M_z) the tractor unit showed a much higher moment than the pusher unit under equivalent conditions.

Noise levels on the pusher unit was found to be some 10–20 dB higher than on the tractor unit and the propeller with cambered sections gave the lowest noise levels of the propellers tested. Figure 14.15 shows a typical set of characteristic curves for a propeller unit of this type. The conventional open water curves are shown in Figure 14.15(a) from which the behaviour of the components of Equation 14.8 can be seen; most notable here is the negative behaviour of the pod thrust components, indicating that this is a drag. In the corresponding diagram of Figure 14.15(b) we see the way in which the various force and moment coefficient change with the angle β. This angle and the force and moment coefficients are consistent with the definitions given in Chapter 6. In this diagram the component relating to the lateral force F_y is plotted to half scale and, consequently, for large angles of β this force can be dominant.

The second source of data is due to Oosteveldt (Reference 12). This data is considerably more limited than the Minsaas data just discussed and relates to open water data using the K_a4-55 propeller in a 19A Duct form. Data of the type shown in Figure 14.15(b) is given for this single propeller duct combination; however, the force components are not broken down so as to differentiate the pod drag.

The model testing of azimuthing units can present particular scale problems if it is intended to model experimentally the performance of, for example, an offshore structure. In these cases the model propeller size becomes very small and introduces hydrodynamic scale effect problems, and in addition, if more than one unit is fitted, interaction problems between the units. Consequently, considerable care needs to be exercised in the design of such experiments, the use to which they are put and a proper identification of the various thruster interactions made.

In an attempt to increase the propulsion efficiency of azimuthing units, contra-rotating propeller versions have been placed on the market by certain manufacturers.

References and further reading

1. Gould, R.W.F. The Estimation of Wind Loads on Ship Superstructures. Maritime Technology Monograph No 8, *RINA*.
2. *Steering Propellers with Controllable Pitch*, Ka-Me-Wa, 1968.
3. *Steering Propellers*, Ka-Me-Wa, 1976.
4. *Lips Transverse Tunnel Thrusters*, Lips Publ.
5. Hawkins, Seth *et al.* The Use of Maneuvering Propulsion Devices on Merchant Ships. Robert Taggart, Inc. Report RT-8518, Contract MA-3293, January, 1965.

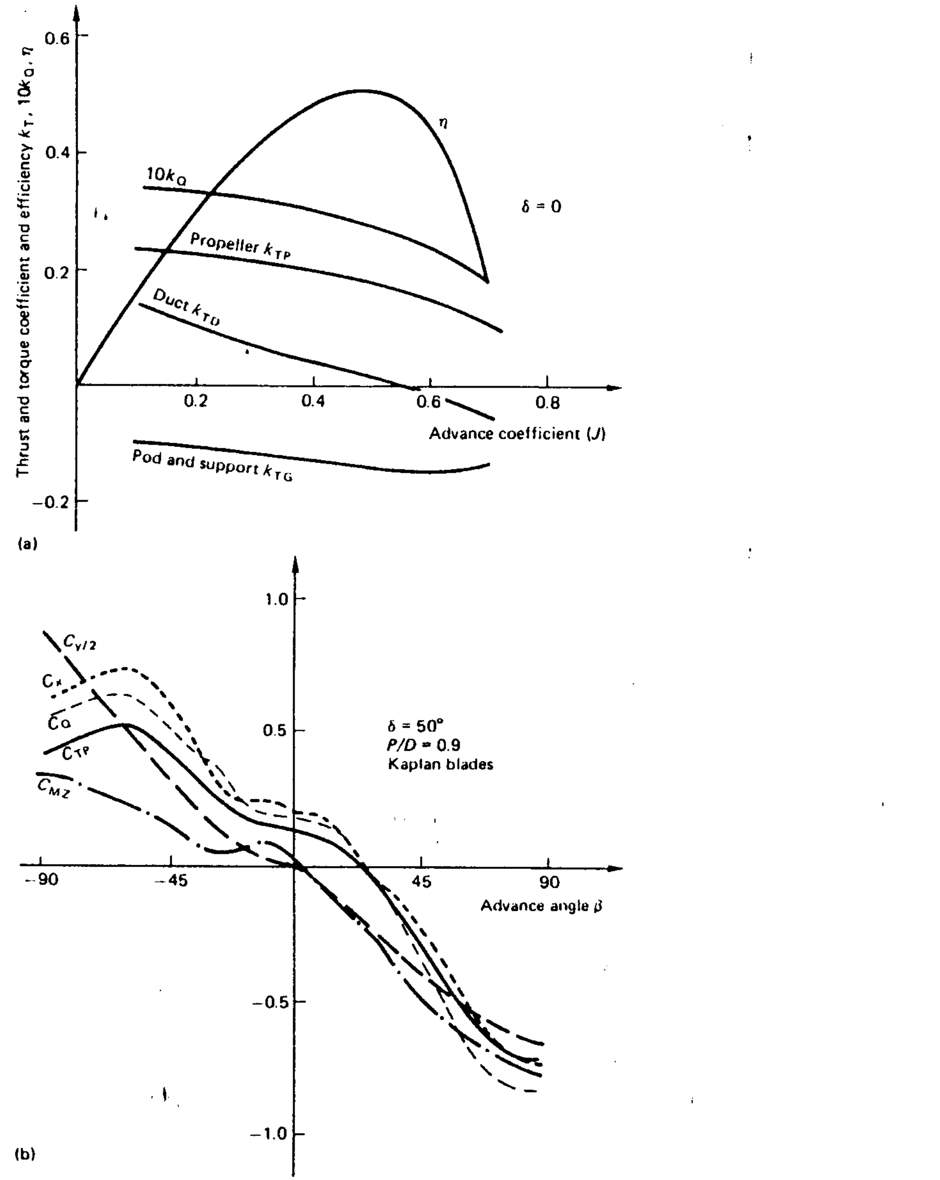

Figure 14.15 Azimuthing thruster characteristic curves: (a) open water curves with ahead advance; (b) open water curves for ahead and astern advance with $\delta = 50°$

6. Taniguchi, K., Watanabe, K., Kasai, H. Investigations into Fundamental Characteristics and Operating Performances of Side Thrusters. Mitsubishi Tech Bulletin, 1966.
7. Manen, van. J.D., Superine, A. Design of screw propellers in nozzles. *ISP*, 6(55), March, 1959.
8. English, J.W. The design and performance of lateral thrust units for ships – hydrodynamic considerations! *Trans. RINA*, 103(3), 1963.
9. Chislett, M.S., Bjorheden, O. Influence of Ship Speed on the Effectiveness of a Lateral Thrust Unit. Hydro-og Aerodynamisk Laboratorium, Rep. No. Hy-8 Lyngby, 1966.
10. Modern Lateral Thrusters With Increased Performance – The Anti-Suction – Tunnel A-S-7. Schottel Nederland b.v., 1985.
11. Minsaas, K.J., Lehn, E. Hydrodynamical Characteristics of Rotable Thrusters. NSFI Report R-69.78, 1978.
12. Oosteveld, M.W.C. Ducted propeller characteristics. *Ducted Propeller Symposium*, Paper No. 5, Trans. RINA, 1973.
13. Beveridge, J.L. Design and performance of bow thrusters, *Marine Technology*, October, 1972.

15 Waterjet propulsion

Contents

The concept of waterjet propulsion dates back to 1661 when Toogood and Hays first proposed this form of propulsion. Its use in the intervening years has been confined principally to small high-speed pleasure craft and work boat situations where high manoeuvrability is required with perhaps a draught limitation. It is only in recent years that the waterjet has been considered for large high-speed craft and as a consequence the sizes of the units increased considerably during the last few years.

The reason for the comparatively infrequent use of the waterjet in comparison to the screw propeller was that the propeller was generally considered to be a simpler, lighter and more efficient propulsor. However, the introduction of more efficient pumps and the commercial demand for higher-speed craft are the principal reasons for their rapid growth.

As shown in Figure 2.8 the waterjet has three main components; an inlet ducting, a pump and an outlet or nozzle. This rather simplified diagram can be enhanced as shown in Figure 15.1 which shows, albeit in schematic form, a typical waterjet in rather more detail. From the figure it is seen that the basic system comprises an inlet duct which is faired into the hull system in the most convenient way for the vessel concerned. From this inlet duct the water then passes through the impeller, which may take a variety of forms. Most usually this is a mixed or axial flow device comprising a number of blades ranging from four to eight. The next phase in the passage of the water through the unit is normally to pass through a stator ring which has the dual function of straightening the flow and also acting as a support for the hub body. The stator ring is likely to comprise some 7 to 13 blades but it should be noted that not all designs exhibit this feature. In some designs the nozzle is steerable and in others deflector plates are used to control the direction of the flow and hence impart steering forces to the vessel through the change in direction of the momentum of the waterjet. The last feature is the reversing bucket.

The 'bucket' is a mechanically or hydraulically actuated device which can be lowered over the waterjet exit so as to produce a retarding force on the vessel, again through a change in momentum. In some designs the bucket is designed so that it can, as well as providing a total braking capability, 'spill' part of the jet so that a fine control can be exerted over the propulsion force generated by the unit.

15.1 Basic principle of waterjet propulsion

As a basis for considering the underlying principles of waterjet propulsion reference should be made to Figure 15.2, which shows an idealized waterjet system. Based on this diagram, suppose that the water enters the system with the velocity V_1 and leaves with a different velocity V_2 by means of a nozzle of area A_2. The mass flow of the water through the waterjet is then given by

$$\dot{m} = \varrho A_2 V_2$$

where ϱ is the density of the water.

Hence, the increase in the rate of change of momentum of the water passing through the waterjet is given by $\varrho A_2 V_2(V_2 - V_1)$. Since force is equal to the rate of change of momentum, the thrust produced by the system is

$$T = \varrho A_2 V_2(V_2 - V_1)$$

and the useful propulsion power P_T is given by

$$P_T = TV_S = \dot{m}V_S(V_2 - V_1) \qquad (15.1)$$

where V_S is the speed of the vessel.

Now in order to derive a useful expression for the power required to drive the waterjet system it is necessary to appeal to the general energy equation of fluid mechanics and to apply this between the inlet and outlet of the unit. Hence we can write for the system,

$$\frac{p_1}{\varrho g} + \frac{V_1^2}{2g} + H_p = \frac{p_2}{\varrho g} + \frac{V_2^2}{2g} + \Delta h + h_{loss} \qquad (15.2)$$

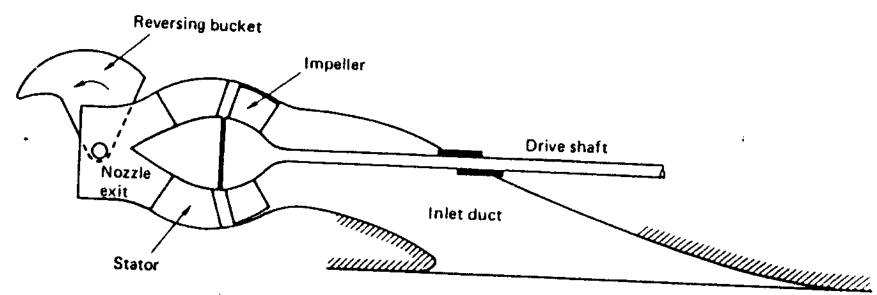

Figure 15.1 Typical waterjet general arrangement

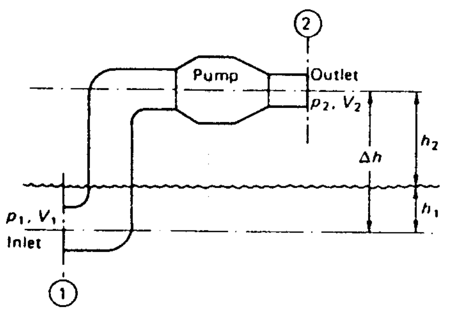

Figure 15.2 Idealized waterjet arrangement

where H_p = the head associated with the energy supplied to the system (i.e. the pump head);
Δh = the difference in static head between the inlet and outlet of the waterjet (i.e. $\Delta h = h_1 + h_2$);
and h_{loss} = the losses associated with the flow through the system and also the pump losses.

In the case of the difference in static head between the inlet and outlet of the waterjet system it should be noted that this will be a variable between start-up and sailing conditions. This is particularly true for hydrofoils which are propelled by waterjets, and of which Figure 15.2 is particularly representative in the cruising condition. With regard to the loss term, h_{loss}, this is associated with frictional and eddy shedding losses which occur around bends in the ducting, in way of inlet grillages and the various obstructions through the system which may impede the flow during its passage through the unit.

Returning now to equation (15.2) and for practical purposes assuming that p_2 is constant above the water line since the altitudes involved and their effect on ambient pressure are small, equation (15.2) can be rewritten as

$$H_p = \frac{V_2^2 - V_1^2}{2g} + h_2 + h_{loss} \qquad (15.3)$$

since $p_1 = p_2 + h_1 \rho g$.

Now the power transferred to the water by the pump can be expressed in terms of energy per unit time as $\dot{m}gH_p$, which from equation (15.3) leads to the expression

$$P_{pump} = \dot{m}[\tfrac{1}{2}(V_2^2 - V_1^2) + g(h_2 + h_{loss})] \qquad (15.4)$$

Hence the equivalent open water efficiency of a waterjet unit can be defined from equation (15.1) and (15.4) as being the ratio of the thrust horsepower to the delivered horsepower as follows:

$$\eta_o = \frac{V_S(V_2 - V_1)}{[\tfrac{1}{2}(V_2^2 - V_1^2) + g(h_2 + h_{loss})]} = \frac{P_T}{P_D} \qquad (15.5)$$

The loss term h_{loss} in equation (15.5) is the sum of two independent losses; those defined as internal losses h_D and those relating to the pump head loss h_p. Hence h_{loss} can be written as

$$h_{loss} = h_D + h_p \qquad (15.6)$$

Now the internal losses are of course primarily dependent on the waterjet configuration and comprise the intake losses h_{DI}, the diffuser head losses h_{DD} and the skin friction losses h_{DSF}. Therefore,

$$h_D = h_{DI} + h_{DD} + h_{DSF} \qquad (15.7)$$

The intake losses are in themselves the sum of the losses arising from the intake guard, the guide vanes and the various bends. All of these losses are principally a function of the intake velocity V_1 and can consequently be expressed in the form

$$h_{DI} = k\frac{V_1^2}{2g}$$

The coefficient k, according to Reference 1, is the sum of two other factors k_1 and k_2 which represent the losses due to the guard and guide vanes and the losses due to the bends respectively. Typically values for k_1 and k_2 are 0.10 and 0.015 respectively.

The diffuser head loss can be estimated from normal hydraulic methods, from which an expression for h_{DD} can be obtained as

$$h_{DD} = (1 - \eta_D)(1 - \varepsilon^2)\frac{V_1^2}{2g}$$

in which η_D is the diffuser efficiency of the order of 90% in normal circumstances and ε is ratio of the entrance and exit areas of the diffuser.

The final term in equation (15.7), h_{DSF}, which defines the skin friction losses can be estimated from calculating the wetted surface areas of the intake, ducting, diffusers, supporting struts and vanes and the nozzle in association with their respective frictional coefficients.

If then the sum of the internal losses h_D, as defined in equation (15.7), are then represented in terms of a single loss coefficient as follows:

$$h_D = k_D\frac{(V_S + \Delta V)^2}{2g}$$

where $\Delta V = (V_2 - V_1)$, then van Walree (Reference 1) suggests that the value of k_D would normally lie in the range $0.04 < k_D < 0.10$.

The pump head loss term h_p of equation (15.6) is related solely to the pump configuration and its associated losses. This head loss can be expressed in terms of the pump head H and the efficiency of the pump η_p as

$$h_p = H\left(\frac{1 - \eta_p}{\eta_p}\right)$$

and for a modern well-designed axial or mixed flow pump the value of η_p should be of the order of 0.90.

By analogy with propellers the pump efficiency can be expressed as

$$\eta_p = \frac{\phi}{2\pi}\frac{\psi}{K_Q} \qquad (15.8)$$

where ϕ and ψ are the flow, energy transfer coefficients defined by

$$\phi = \frac{Q}{ND^3}, \quad \psi = \frac{gH}{N^2D^2}$$

and K_Q is the normal torque coefficient of propeller technology.

Whilst the value of η_p is clearly higher for a waterjet than a propeller, this is not the basis upon which the comparison should be made. A proper comparison can only be made in terms of the corresponding quasi propulsive coefficients which for the propeller include the hull and relative rotative efficiency and for the waterjet equation (15.5) together with the appropriate hull coefficient embracing the effect of the waterjet.

15.2 Impeller types

When designing a waterjet to perform a given duty, one of the first problems encountered is to establish the most appropriate type of pump for the intended duty. The choice of pumps will lie between a centrifugal, mixed flow, axial flow or an inducer. Figure 15.3 categorizes the first three types of turbomachine whilst Figure 15.4 shows an inducer that has been laid out for inspection.

For a given hydraulic turbomachine there is a unique relationship between the unit's efficiency and the flow coefficient assuming that both Reynolds and cavitation effects are negligible: this is analogous to the propeller efficiency curves. For a pump unit the efficiency versus flow coefficient curve will take the form shown in Figure 15.5.

In addition, other performance coefficients can be determined from dimensional analysis, and in this context the energy transfer coefficient ψ is particularly important. From Figure 15.5, it will be seen that as the flow coefficient is increased, the efficiency tends to rise and then reach a maximum value after which it will fall off rapidly. The optimum efficiency point can be used to identify a unique value of the flow coefficient.

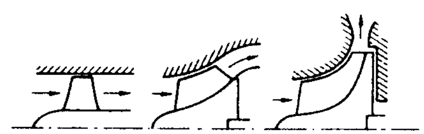

Figure 15.3 Pump impeller types

Figure 15.4 Typical inducer design

Additionally a corresponding value of ψ can be uniquely determined. In pump technology, it is customary to define the specific speed N_s of a machine from the values of ϕ and ψ which correspond to the maximum efficiency point as being

$$N_S = \left.\frac{\phi^{1/2}}{\psi^{3/4}}\right|_{\eta_{max}}$$

which reduces to

$$N_S = \frac{NQ^{1/2}}{(gH)^{3/4}}$$

or more typically in its dimensional form

$$N_S = \frac{NQ^{1/2}}{H^{3/4}} \qquad (15.9)$$

Because of the dependence of the specific speed on the maximum efficiency point on the pump characteristic curve, this parameter is of considerable importance in selecting the type of turbomachine required for the given duty. To change the maximum efficiency point with respect to the flow coefficient, as shown in Figure

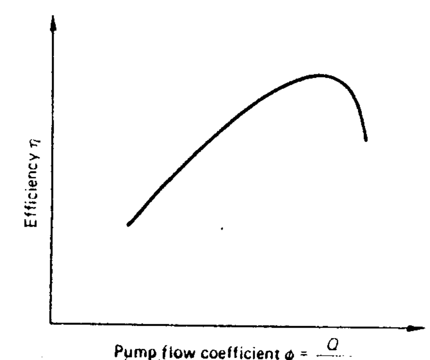

Figure 15.5 Typical pump efficiency characteristic

15.5, requires that the pump geometry must change; as a consequence the maximum efficiency condition replaces the geometric similarity condition. Furthermore, each of the different classes of machine shown in Figures 15.3 and 15.4 have their optimum efficiencies defined within a fairly narrow band of specific speed. In general, the physical size of the impeller, for a given duty defined by the flow and head required, varies with specific speed. Hence the higher the specific speed the more likely it is that an axial flow machine will be specified which is smaller physically than its centrifugal counterpart.

As a consequence, since high specific speed implies a smaller machine it is desirable to select the highest specific speed, consistent with good efficiency, for a particular application.

The centrifugal pump exhibits low-flow–high-pressure characteristics while the converse is generally true for the axial flow machine. Table 15.1 indicates the general ranges that the various pump classes suitable for waterjet design would be expected to operate in:

Table 15.1 Typical specific speed ranges of various pump types

Pump type	*Approximate N_s (rad)*
Centrifugal pump	below 1.2
Mixed flow pump	1.2–3.0
Axial flow pump	3.0–7.0
Inducers	above 7.0

Whilst the centrifugal and axial flow pumps were the original types of machine used for waterjets the mixed flow type, which is a derivative of the centrifugal machine, rapidly established itself. This was because it provided a smaller diameter unit than the centrifugal pump and offered an easier conversion of pump head to kinetic energy.

The machines shown in Figure 15.3 are well known and their theoretical background is well defined in many textbooks – for example References 2, 3.

The inducer, Figure 15.4, was developed originally in response to the need for large liquid fuel pumps for rocket propulsion. From the Figure it is seen that the waterjet inducer in this case comprises four full blades in the initial stage with a further four partial blades which allow the suction stage to be shortened to some extent. These large blades are then followed by a row of short blades which produce about 60% of the head rise through the machine.

15.3 Manoeuvring aspects of waterjets

The waterjet principle lends itself particularly well to a propulsion system with integral steering capabilities. The majority of waterjet units are fitted with either a steerable nozzle or deflectors of one form or another in order to provide a directional control of the jet. The steering capability in each of these cases is produced by the reaction to the change in momentum of the jet (Figure 15.6(a)). The angle through which the jet can be directed is of course a variable depending on the manufacturer's particular design; however, it would generally be expected to be of the order of ±30°.

With regard to the stopping or retarding force capabilities of waterjets, these are normally achieved with the aid of a reversing bucket with the stopping force being produced by change of momentum principles. The reversing bucket design can be of the simple form shown in Figure 15.1 or alternatively of a more sophisticated form which allows a 'spilling' of the jet flow in order to give a fine control to the braking forces (Figure 15.6(b)). With this latter type of system the resultant thrust can also be continuously varied from zero to maximum at any power setting for the prime mover.

15.4 Waterjet component design

The literature on the design and analysis of waterjet propulsion system is extensive. The references at the end of this chapter give several examples from which further works can be traced. This section, however, is not so much concerned with the underlying mathematical and theoretical engineering principles which were dealt with in Section 15.1 but with the practical design aspects of the various components.

In terms of a general design approach to the problem, the fundamental parameter is the inlet velocity ratio IVR. This parameter is defined as

$$\mathrm{IVR} = \frac{V_1}{V_s} \tag{15.10}$$

where V_1 is the water inlet velocity and V_s is the craft velocity.

This parameter in effect controls the flow rate through the waterjet together with the velocity ratio, the pump head, the overall efficiency and in addition the inception of cavitation at the intake lips.

The basic design procedure is to consider a range of IVR values at the craft design speed from which a pump design, delivered power and efficiency can be calculated. Then for each of these pump designs the off-design performance can be considered and again a set of delivered powers, efficiencies and cavitation conditions can be considered. From the resulting matrix of values, Table 15.2, the designer can then select the most suitable combination of results to suit the craft conditions; typically the cruise and hump speeds. With this choice the designer can then move on to another iteration of the above procedure if necessary or continue on to the detailed design of the unit. In this case the question then arises as to whether the waterjet should have a variable area water intake in order to allow some variation in the IVR. Depending on the answer to this question, a further iteration of Table 15.2 may be necessary. With regard to the details of the calculation for a given IVR value, then this would take the form shown in Figure 15.7. In practical terms this outline design procedure can be used to design a unique waterjet unit or, alternatively, to select the closest model from a predefined range for a particular duty.

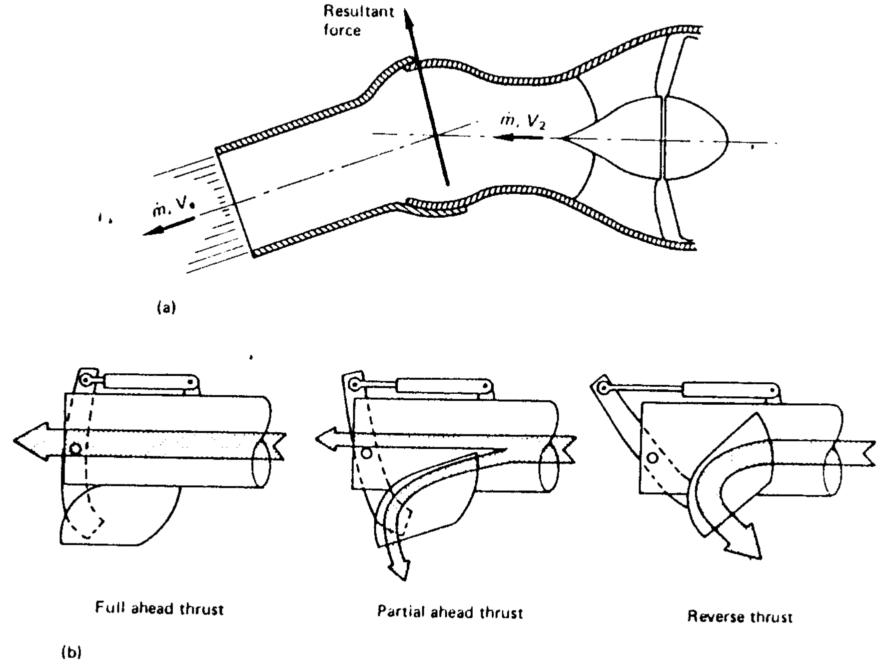

Figure 15.6 (a) Principle of waterjet steering capability; (b) waterjet thrust control mechanism

Table 15.2 Waterjet design matrix

IVR design/condition	1	2	3	4	5
Off-design condition 1	•	•	•	•	•
Off-design condition 2	•	•	•	•	•
⋮	⋮	⋮	⋮	⋮	⋮
Off-design condition *N*	•	•	•	•	•

With respect to the design of the various components of the waterjet unit, several aspects, in addition to strength, need to be taken into consideration. To detail the most important of these, it is necessary to consider each component separately.

15.4.1 Tunnel, inlet and supporting structures

The inlet to the tunnel, in order to protect the various internal waterjet components, is frequently fitted with an inlet guard to prevent the ingress of large objects. Clearly the smaller the mesh of the guard the better it is at its job of protection; however, the design of the guard must strike a balance between undue efficiency loss due to flow restriction and viscous losses, the size of the object allowed to pass and the guard's susceptibility to clog with weed and other flow restricting matter. Clearly for small tunnels a guard may be unnecessary or indeed undesirable since a compromise between the above constraints may prove unviable; for the large tunnels, this is not the case. In this latter event the strength of guard needs careful attention since the flow velocities can be high.

The profile of the tunnel needs to be designed so that it will provide a smooth uptake of water over the range of vessel operating trims, and therefore avoid

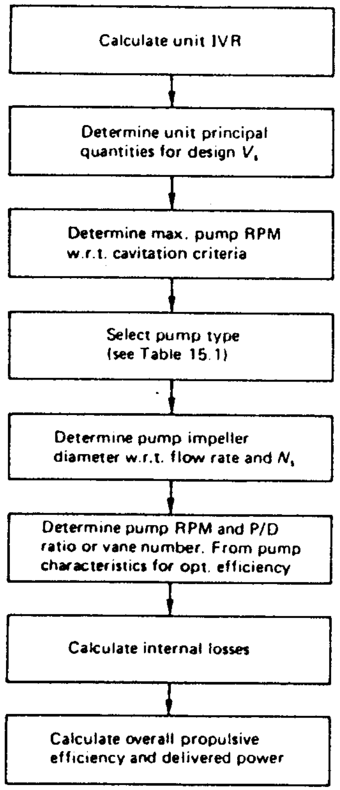

Figure 15.7 Outline waterjet calculation procedure

any significant separation of the flow or cavitation at the tunnel intake.

In some waterjet applications, typically hydrofoil applications where the water flow has to pass up the foil legs, it is necessary to introduce guide vanes into the tunnel in order to assist the water flow around bends in the tunnel. The strength of these guide vanes needs careful attention, both from steady and fluctuating sources, and if they form an integral part of the bend by being, for example, a cast component, then adequate root fillets should be provided. The guide vanes need to be carefully aligned to the flow and the leading and trailing edges of the vanes should be faired so as not to cause undue separation or cavitation. Guide vanes where fitted also need to be inspected for fracture or impending failure during service. Therefore, some suitable means of inspection needs to be provided; this can be either directly by visual inspection or indirectly through the use of a boroscope.

Within the tunnel the dimensions are sometimes such that the drive shaft for the pump needs support from the tunnel walls. In such cases the supports, which should normally number three arranged at 120° spacing if there is danger of shaft lateral vibration, need to be aligned to the flow and have an aerofoil section to minimize flow disturbance of the incident flow into the pump and also the probability of cavitation erosion on the strut. The form and character of the wake field immediately ahead of the impeller is generally unknown. Some model tests have been undertaken in the past, References 3 and 4, and an example is shown in Figure 15.8. However, the aim should be to provide the pump with as small a variation in the flow field as possible in order to minimize the fluctuating blade loading. This can be done only by scrupulous attention to detail in the upstream tunnel design.

Integrity of the tunnel wall in intact and failure modes of operation is essential. If the wall fails this can lead to extensive flooding of the compartment in which the waterjet is contained and hence have ship safety implications. Hence there is a need for considerable attention to detail, for example in adequately radiusing any penetrations or flanged connections, and in terms of producing an adequate stress analysis of the tunnel both in the global and detailed senses. In addition to considering the waterjet as an integral component, the tunnel must be adequately supported, framed and fully integrated into the hull structure, taking due account of the different nature, response and interactions of the various materials used; for example, GRP, steel, aluminium, etc.

15.4.2 Impeller

The hydrodynamic design of the pump impeller follows the general line of Figure 15.7 and Table 15.2; the detailed features and form of the impeller are defined in this way. The detailed calculation of impeller components in terms of their strength and integrity has to be based on the maximum rated power of the machinery. Hence the mean loads on the blading need to be predicted on this basis, and from there the stress analysis of the various components can be undertaken. One method of undertaking this prediction is to use an adaptation of the cantilever beam technique described in Chapter 18. However, it must be remembered that the impeller blades, certainly for mixed flow pumps, axial pumps and inducers, have in general a low aspect ratio, and therefore cantilever beam analysis has an inherent difficulty in coping with this situation. Due allowance has therefore to be made for this in the eventual fatigue analysis of the blades and in determining the appropriate factor of safety. Some guidance can be obtained, however, by undertaking finite element calculations on certain classes of blade and from these

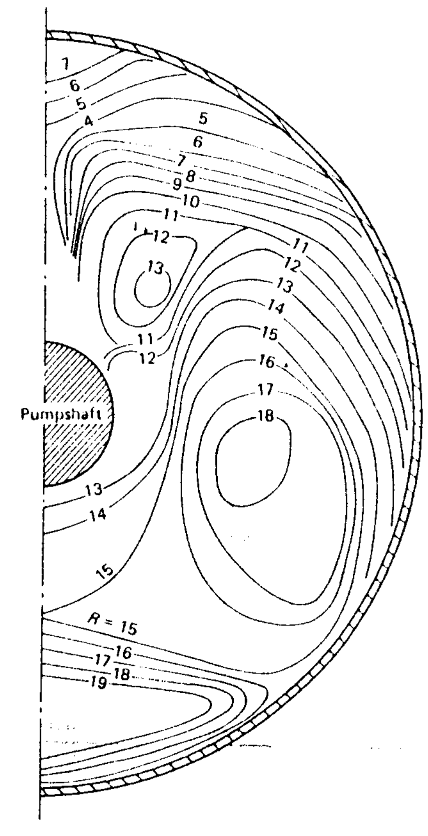

Figure 15.8 Typical wake survey of a waterjet inlet just upstream of the pump impeller (Reproduced from Reference 5, with permission)

determining the likely level of inaccuracy in the cantilever beam result.

In the absence of wake field data a true estimate of the fluctuating stresses is difficult to achieve in practice. A realistic estimate is nevertheless required and this has to be based on a consideration of the upstream obstructions and their effect on flow into the impeller. Once this estimate has been completed it can be used in association with the mean stress and an estimate for the residual stress (see Chapter 18) to undertake a fatigue evaluation of the design using the Soderberg or modified Goodman approaches.

The blades of the impeller must be provided with adequate fillets at the root. Such fillets need to be designed with care in order to provide the required degree of stress relief; in this context the elliptical or compound fillet design is to be preferred, although a single radius will suffice, provided its radius is greater than the blade thickness, but will not be so effective as the compound design. In addition if, as in some designs, the blades are bolted on to the pump hub, then extreme attention to detail of the bolting arrangements and the resulting stresses in the palms and hub body is required, as this is a potential source of failure.

The blade section design of the impeller demands considerable attention. Pump impellers work at high rotational speeds, in comparison to the majority of propellers; consequently, whilst their overall design is based on acceptable cavitation and the control of its harmful effects, lack of attention to detailed design can completely destroy this overall concept. As a consequence in all but centrifugal pumps, the blades require aerofoil forms to assist in controlling the cavitation properties of the pump. The blading can be either of the cambered or non-cambered type according to the head required to be developed by the pump. Furthermore, adequate control must be exercised over the manufacture of the blading in order to ensure that the manufacturing accuracy of the blade profiles are adequate for their proper cavitation performance.

The blade tip clearances need to be kept to a minimum for hydrodynamic purposes to prevent undue losses. However, this need must be balanced by the conflicting need to provide adequate clearance to cater for any transient vibrational behaviour of the rotating mechanism, axial shaft movement or differential thermal expansion of different parts of the transmission system.

In order to guard against blade failure by vibration, the natural frequency of the blading should be calculated by a suitable means (see Chapter 20). The results of this calculation then require to be shown to lie outside of the primary operating ranges of the pump unit. In making this calculation the appropriate allowance needs to be made for the effects of the water on the blades rather than simply undertaking a calculation of the blades in air.

Since the pump impellers work at high speed there is clearly a need for them to be balanced. In many cases, where the resulting couple is likely to be small, it is sufficient to limit the balancing operation to a statical procedure to an appropriate standard; typically the ISO standard. However, if it is considered that the 'out-of-balance' couple is likely to be significant in terms of the shafting system, then dynamic balancing must be considered.

Because of the nature of the pump impeller and its inherent susceptibility to damage, provision needs to be made for this component to be inspected during service, preferably without dismantling the whole unit. In the case of the impeller, it is clearly preferable that the inspection is visual; however, if this is not practical for whatever reason, then boroscope inspection will suffice, but this will never be as satisfactory as provision for a direct visual capability.

A fundamental starting requirement for a pump impeller is that it should be self-priming. That is, it should, when the vessel is at rest in the water, have sufficient water to be able to start and effectively develop the required head. If the self-priming condition cannot be satisfied, then this is likely to involve a very expensive priming capability which may have important safety implications.

15.4.3 Stator blading

Not all waterjet units are designed with a stator blade stage; however, where they are then the design has to consider both the maximum continuous power free running condition and also stopping manoeuvres, since these will introduce a back pressure on to the unit. The effects of steering manoeuvres generally produce less severe conditions than stopping manoeuvres.

As with the impeller blading then much the same principles apply to the blade design with regard to their section form, loading and strength. However, in the case of the stator blades a root fillet should be introduced at both ends of the blade and the effects on the tunnel strength of the reactive forces at the blade–tunnel interaction need to be considered. Furthermore, the natural frequency of the stator blades needs to be shown to lie outside of the range of anticipated rotor blade passing frequencies.

15.4.4 Nozzles, steering nozzles and reversing buckets

The nozzle design and its fixing or actuating arrangements, whether it be a steering nozzle or otherwise, needs to be designed in the full knowledge of the forces acting on it during the various modes of operation of the waterjet unit. In particular these relate to the pressure distribution along the nozzle internal surface and also the reactive forces produced by the rate of change of momentum of the fluid in the case of a steering nozzle.

The design of the bucket and its supporting and actuating mechanism has critical implications for the vessel's safety, as it is the only means of stopping the craft. As a consequence it regularly experiences significant amounts of transient loading, and therefore requires a careful assessment of its mechanical integrity. This, however, is far from easy from direct calculation, and therefore a measure of design experience based on previous installations is required for a proposed new unit. Model tests can also assist; however, questions of scaling and representation need careful attention.

Since the bucket and also the nozzle is normally exposed at the stern of the vessel the influence on these components of external loadings must be considered. These loadings would normally comprise those from the impact of the sea in various weather conditions, the collision from harbour walls and other vessels, and fouling with buoys etc. Consequently, care needs to be taken either to ensure that the unit can withstand these interferences or, alternatively, that a suitable level of protection is provided.

References and further reading

1. Walree, F. van. The powering characteristics of hydrofoil craft. 6th Int. High Speed Surface Craft Conf., January, 1988.
2. Dixon, S.L. *Fluid Mechanics and Thermodynamics of Turbomachinery*. Pergamon Press, Oxford.
3. Sayers, A.T. *Hydraulic and Compressible Flow Turbomachines*. McGraw-Hill.
4. Holden, K. *et al.* On development and experience of waterjet propulsion systems. *2nd Int. Cong. of Int. L. Maritime Ass. of the East Mediterranean*, Trieste, 1981.
5. Haglund, K. *et al.* Design and testing of a high performance waterjet propulsion unit. *Proc. 2nd Symp. on Small Fast Warships and Security Vessels.*
6. Johnson, Jr., V.E. Waterjet propulsion for high speed hydrofoil craft. *J. Aircraft.*, 3(3), March/April, 1966.
7. Barham, H.L. Application of Waterjet Propulsion to High Performance Boats. June, 1976.
8. Brandau, J.H. Performance of waterjet propulsion systems – a review of the state of the art. *J. Hydronautics*, 2(2), April, 1968.
9. Alder, R.S., Denny, S.B. Full Scale Evaluation of Waterjet Pump Impellers. Rep. No. SPD-718-02, DTNSRDC, Bethesda, September, 1977.
10. Svensson, R. Experience with waterjet propulsion in the power range up to 10000 kW. *SNAME Power Boat Symposium*, February, 1985.
11. Venturini, G. Waterjet propulsion in high speed surface craft. *High Speed Surface Craft.*

16 Full-scale trials

Contents

Model tests and full-scale measurements are two equally important sources of data for the study of ship model correlation. Full-scale data, however, derive a further particular importance in providing both a basis for the demonstration of a ship's contractual requirements and also in defining an experimental data base from which the solution of in-service problems can be developed. As a consequence the accuracy of the trials data, in both of these cases, is of the utmost importance and calls for precision in measurement, as far as is realistic under sea trial conditions, and a consistency of approach.

Full-scale trials on ships which relate specifically to the propeller fall broadly into two classes. The first relates to power absorption and the second to the measurement of propeller induced vibration and noise on the vessel. In addition, there are several other specific measurements and trials that can be conducted, but these normally are dealt with on an *ad hoc* basis.

16.1 Power absorption measurements

Measurements to define the power absorption characteristics of a vessel fall broadly into two categories. These are a full ship speed trial as would normally be conducted for the demonstration of contractual conditions and the less comprehensive power absorbed versus shaft speed characteristic: this latter trial is, however, merely a subset of the former. Whilst accepting the second type of trial is a useful diagnostic tool its limitation in preparing propeller design remedial action must be recognized, since it ignores the ship speed component of the design triumvirate of power, revolutions and ship speed. As such, the discussion will centre of the former type of trial.

A full-speed trial can be conducted either on a measured distance as specified on a maritime chart or by the use of electronic navigational position of fixing systems. With the exception of ship speed measurement, many of the measurement requirements are common to both types of trial in order to obtain a valid result. The basic requirements of these trials are as follows:

1. *Measured distance trial area.* The area selected for the trial should not be one where the effects of tide are large since this will introduce large corrections into the trial analysis procedure. Furthermore, if the direction of flow is oblique to the trial course, this may lead to difficulty in course keeping in strong tides leading to further errors in the measured speeds.

   In addition to the requirement for reasonable tidal activity, it is also necessary to ensure that there is both sufficient water depth at the intended time of the trial and adequate space to conduct approach runs both from geographical and marine traffic density considerations. With regard to water depth a value of $3\sqrt{BT}$ or $2.75\,V^2/g$, whichever is greater, is recommended by the ITTC (Reference 1). Similarly, the length of the approach run to the start of the measured distance must be adequate to allow the vessel to reach a uniform state of motion after the various course changes that will occur between one run on the measured distance and another. It is difficult to specify these distances precisely, but for guidance purposes a distance of 25 and 40 ship lengths have been suggested (Reference 1) for a high-speed cargo liner and a 65 000–100 000 dwt tanker respectively.
2. *Measured distance course.* The measured distance course should be of the standard form shown in Figure 16.1. Where the measured distance is parallel to a coast line the direction of the turn after completing the measured course should normally be away from the coast in order to take advantage of any deep water and also enhance navigational safety. Upon completion of the measured distance, the angle of turn in preparation for the return run should comprise gradual rudder movements which should be limited to around 15° in bringing the vessel back on to a reciprocal course.
3. *Vessel condition.* The condition of the ship should be checked prior to the trials to ensure that both the hull and propeller are in a clean state. The inspection should in all cases be done in a dry dock and only exceptionally by an in-water survey. The cleanliness of the underwater surfaces should be checked in this way as close to the trial date as possible but not at a greater time interval than two weeks. This is because considerable biological growth can occur in a very short period of time given the correct conditions of light, temperature and so on (see Chapter 23). Where possible at the time of cleaning an observation and measurement of the topography of the hull and propeller surfaces should take place.
4. *Weather conditions.* In order to avoid undue corrections to the trial results the trials should be run in sea states of preferably less than force 2–3 on the Beaufort Scale and low swell. This condition clearly cannot always be met in view of the constraints on time and location.
5. *Number of runs on the measured distance.* The number of runs should comprise at least four double runs; that is, consecutive traverses of the measured distance in each direction. The nominal power of each of the double runs and their total span is largely dependent on the purpose for which the trial is being conducted. However, it is suggested that at least two double runs at full power should be considered.
6. *Trial procedure.* The trials should be under the overall control of a 'trials master' on whom the responsibility of the trial should rest. It is he who should make certain that all those responsible for the safe navigation and control of the vessel

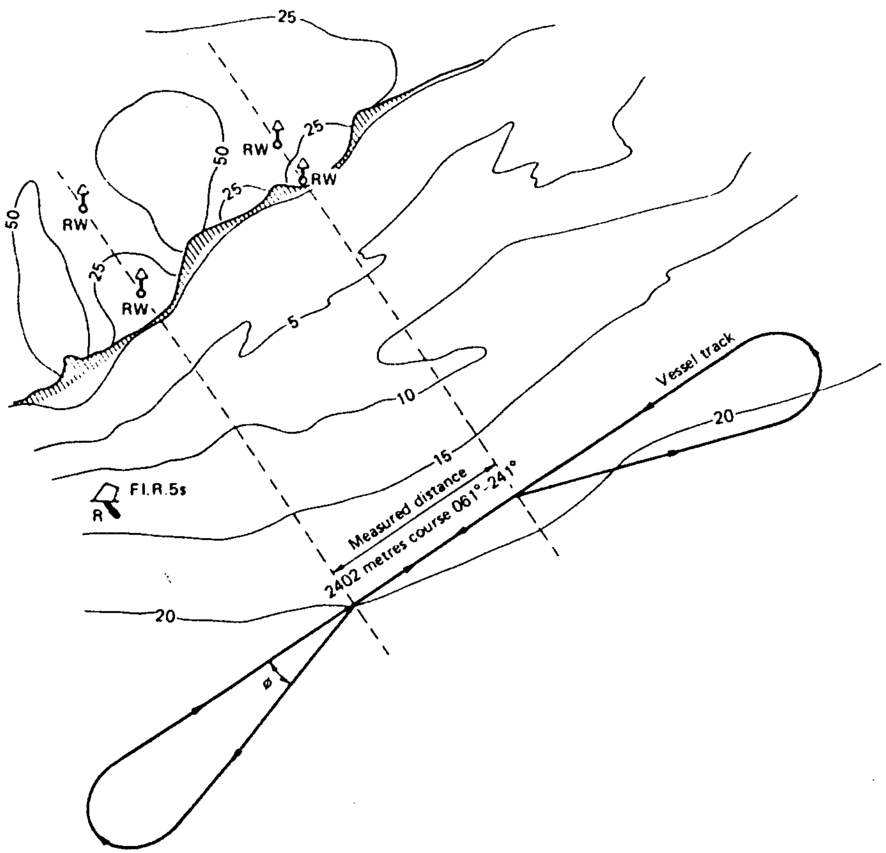

Figure 16.1 Measured distance course

understand clearly what is required at all times within the trial period.

When a new power setting is required this should be set immediately upon leaving the measured distance at the previous measurement condition. All adjustments should then be completed prior to the vessel turning in order to make a new approach to the measured distance. Under no circumstances must the engine or propeller pitch, in the case of a controllable pitch propeller, then be altered until the full set of double runs at that condition has been completed. When the vessel is turning the propeller revolutions will tend to decrease; this is perfectly normal and these will recover themselves when the vessel straightens course on the approach to the measured distance. If the engine or propeller controls are altered during a double run, for whatever reason, then the results should be discarded and that part of the trial recommenced.

The use of rudder adjustments to maintain course on the measured distance should be kept to the absolute minimum consistent with the prevailing conditions. If this is not done it will introduce additional resistance components to the vessel.

Prior to the trial commencing it is essential that all instrumentation to be used is properly calibrated and 'zero values' taken. A repeat set of 'zeros' should also be undertaken upon completion of the trial and for some instrumentation it is desirable to take intermediate 'zero' readings. If time is not allowed for collecting this reference data then the value of the measurement will be degraded; in some cases to the extent of calling the accuracy of the whole trial into question.

7. *Measurements required.* In order to demonstrate that the vessel has achieved a certain hydrodynamic performance, or to provide data from which a solution to some propulsion problem can be generated, it is necessary to measure an adequate set of data. This data should comprise the following:

(a) draught and trim;
(b) ambient conditions;
(c) ship motions;
(d) machinery measurements;
(e) ship speed and course.

(a) *Draught and static trim.* This should ideally be measured both before and after the trials for all vessels: in the case of small high-speed craft, however, a 'before' and 'after' measurement is an essential requirement. This measurement for small vessels should be taken immediately prior to and after finishing the measured distance runs, since the fuel weight and, indeed, personnel weight can often form a significant component of the total craft weight. In addition, for small craft not subject to survey during building, or in cases of doubt, the draught marks should be checked by a competent person; in a significant number of cases, in the author's experience, these marks are found to be in error. In some cases there is need to put temporary draught marks on to the hull where none exist; this can easily be done in most cases with some form of waterproof tape.

(b) *Ambient conditions.* These include measurements of the prevailing weather and sea conditions at the time of and during the trial. For the atmospheric conditions these should include: air temperature, wind speed and direction, atmospheric pressure and both relative humidity and visibility in order that the analyst of the trial results might have a true picture of the trial conditions. In the case of sea conditions, the measurements need to include: sea temperature, sea state, an estimate of the swell height and direction. It is important to distinguish between sea state and swell since the sea state largely defines the local surface conditions whereas the swell defines the underlying perturbation which may originate from a remote sea area. In most cases, these observations are made by reference to experienced personnel on board the vessel: for example, the senior navigational officers. When more detailed analysis is required, typically for research purposes or difficult contractual situations, then wave buoys may be used for these measurements.

It is the author's practice, under normal circumstances, to require that ambient conditions are recorded on either a half-hourly or hourly basis, since for protracted trials the weather in many areas can change significantly in a comparatively short space of time.

(c) *Ship motions.* Some record should be kept of the ship motions in terms of pitch and roll magnitude and period during the trials; this record should be kept on a 'run by run' basis. Normal ship's equipment is usually sufficient for this purpose. In addition, for craft which change their trim considerably during high speed runs, the dynamic running trim should be recorded by means of a suitable inclinometer placed in the fore and aft direction on the vessel. The instrument used for this purpose needs to have a measure of damping inherent in it, otherwise it will be difficult to read during the trials due to sea induced transients occurring during the trial runs.

(d) *Machinery measurements.* From the viewpoint of the ship resistance and propulsion the principal measurements required are shaft horsepower, propeller revolutions and propeller pitch in the case of a controllable pitch propeller. Shaft axial thrust, measured between the thrust block and the propeller, is also an extremely useful, and in some cases essential although notoriously difficult, measurement to record for trial analysis purposes.

Naturally during a contractor's or acceptance trial many other engine measurements will be taken that are of value in quantifying the machinery performance. However, as a means of support to the resistance and propulsion analysis additional data such as engine exhaust temperatures, turbo-charger speeds, temperatures and pressures, fuel rack setting etc. should always be obtained where possible.

(e) *Ship speed and course.* Clearly in any propulsion trial this is an essential ingredient in the measurement programme; without this measurement the trilogy of parameters necessary to define propeller performance cannot be established. It can be measured using a variety of methods such as by the conventional measured distance or by means of a position fixing navigation system. Coincident with the speed measurement the course steered, together with any deviations, should be noted by both magnetic and gyrocompass instruments; the dates when these instruments were last 'swung' or calibrated also need to be ascertained.

16.1.1 Techniques of measurement

There are many techniques available for the measurement of the various propulsion parameters; some of the more common methods are outlined here for guidance purposes.

(a) *Propeller pitch angle.* In the case of a controllable pitch propeller the pitch should be read from the oil distribution (OD) box scale, or its equivalent, and this value interpreted via a valid calibratioin into blade pitch angle at the propeller. On no account should a bridge or engine room consul indicator be taken as any more than an approximate guide, unless this has a proven calibration attached to it. This is because zero and other adjustments are often made to electrical dials during the life of the vessel and blade pitch angle changes of the order of 1° make significant alterations to the power absorbed.

(b) *Propeller shaft power.* Shaft power measurements can be principally measured in one of two ways, these being classified as being either permanent or temporary for the purposes of the trial. Permanent methods principally involve the use of a torsion meter fitted to the vessel in which a value of the torque being transmitted is read either directly or in terms of a coefficient which needs scaling by a calibration factor. Whilst such instruments, in whatever state of calibration, are frequently sufficient for measurements between one power setting and the next, if they are intended for a quantitative scientific measurement then their calibration should be validated immediately prior to the trial.

Temporary methods of measurement normally involve strain gauge methods. The most fundamental of these measurements is to place a four strain gauge bridge as shown in Figure 16.2(a) onto the shaft. This bridge is activated by a battery pack and the strain signals sent via a radio telemetry transmitter, both strapped to the shaft, to a stationary receiver. Variants of this strain gauge bridge system are in use; for example where the two halves of the Wheatstone bridge are placed diametrically on opposite sides of the shaft. This can be very helpful in cases where space is limited or the effects of shear in the shaft are significant. The size of the strain gauges does not need to be particularly small as beneficial effects can accrue from the averaging of the strain signal that takes place over the strain gauge length; typically the gauge length can be of the order of 5 mm or so. Calibration of the system can be effected by means of high-quality standard resistances shunted across the arms of the bridge to simulate the torsional strain in the shaft when under load. The reader is referred to Reference 4 for a detailed account of strain measurement techniques.

(c) *Propeller revolutions.* Most vessels are fitted with shaft speed instruments and in general these are reasonably accurate. Notwithstanding this generalization, the calibration should always be checked prior to a trial. When more specialized trials requiring greater accuracy or where independence is needed then inductive proximity or optical techniques may be used. In ship vibration studies, Section 16.3, a separate shaft speed measurement technique of this type is considered essential for vibration order reference purposes.

(d) *Propeller thrust measurements.* The measurement of propeller thrust on a long-term basis is notoriously difficult to undertake from a measurement reliability and stability point of view. Several techniques exist for permanent installation; however, for trial purposes the experimenter is well advised to check the calibration of these measurements.

If a short-term installation is required, then a strain gauge technique is probably the most reliable at the present time and also the easiest to use. In applying strain gauge techniques to marine propeller thrust measurement, the problem is that the axial strain on the vessel's intermediate shaft is generally of an order of magnitude less than the torsional shear strain and this leads to cross-interference problems if the measurement installation is not carefully and accurately completed. A useful experimental technique for axial strain measurement, and hence thrust determination, is the Hylarides bridge, Figure 16.2(b). This bridge system has the benefit, through its eight strain gauges, four of which have a compensating function, of alleviating the worst effects of the strain cross sensitivity. The strain signal is transmitted from the rotating shaft in much the same way as for the torsional strain signals. An alternative procedure to strain gauge methods is to measure the thrust in terms of the axial deflection of the intermediate shaft using a ring gauge coupled with rods fitted parallel to the shaft (Reference 5).

Thrust measurements on trials are relatively infrequently recorded; however, the information that these measurements provide completes the necessary propulsion information required to undertake a complete and rigorous propulsion factor analysis of the vessel.

(e) *Ship speed measurement.* The traditional measurement of ship speed requires the use of at least three independent observers timing the vessel over the measured distance with the aid of stop watches. These stop watches need to be of high quality with a measurement resolution of the order of one hundredth of a second. On trials the observers should be left to measure the time that the ship takes to travel along the measured distance independently and without any prompting from one of their number or, alternatively, from an independent observer as to when the vessel is 'on' or 'off' the mile. Indeed, the author has found it advisable for observers to be sufficiently far apart so that they do not hear, and therefore become subject to influence by, the activating clicks of each other's stop watches.

The alternative form of speed measurement is to use an electronic navigational position fixing system in which a specified distance can be traversed

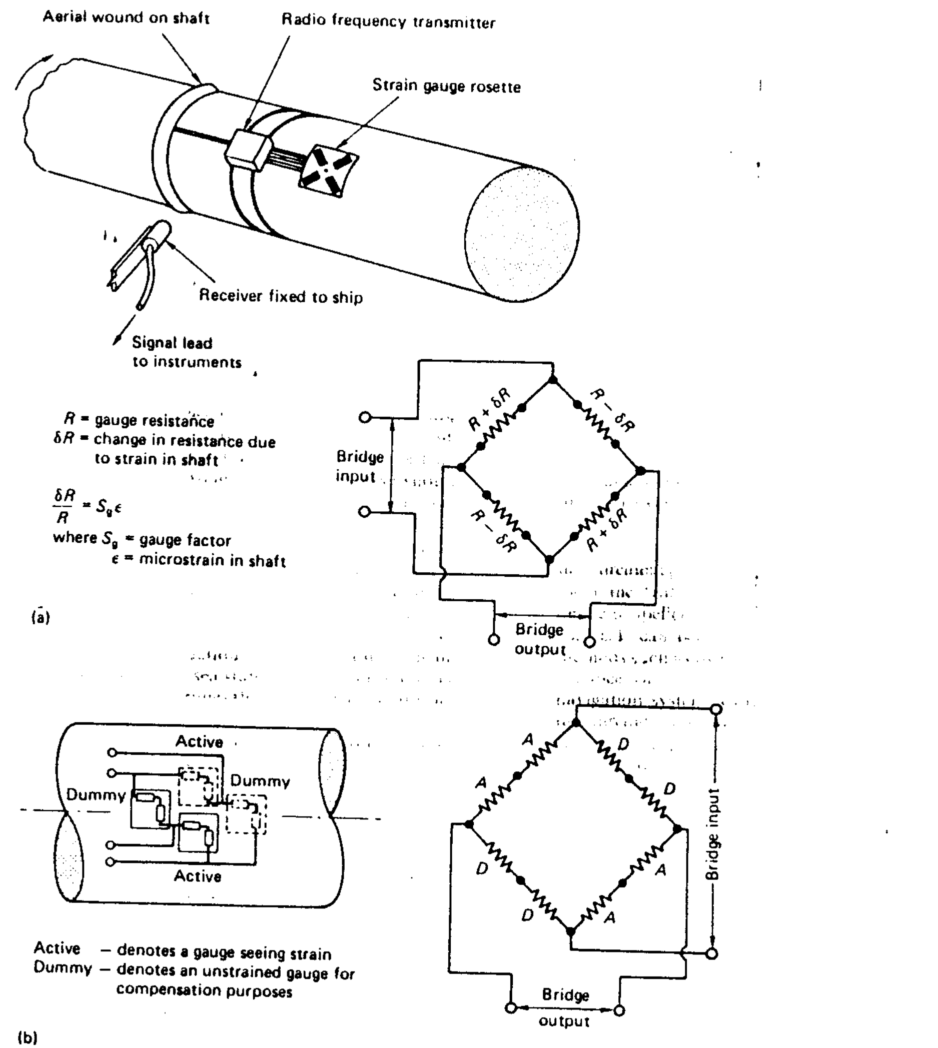

Figure 16.2 Measurement of thrust and torque by strain gauge methods: (a) measurement of shaft torque. (b) Hylarides bridge for thrust measurement

and the time recorded. When using this type of equipment, however, it must be first ascertained that the system is working correctly and is free of any interference or astronomical aberration at the time of the trial.

16.1.2 Methods of analysis

The machinery measurements are relatively easy to analyse and the quantities derived from the measurement are normally readily deduced; for example, K_T and K_Q. In the case of the torque coefficient K_Q it should be remembered that it is normal to measure shaft power and not delivered power. Hence an allowance for the transmission efficiency needs to be made: typically this will lie between 0.98 and unity for most vessels assuming the measurement is made aft of any shaft-driven auxiliaries. If this is not the case, then the appropriate allowances will need to be made.

Ship speed presents perhaps the greatest problem. If the mean speed is taken between a consecutive pair of runs on the measured distance this implicitly assumes the tidal variation is linear. In many instances this is reasonable provided the time between runs is short compared to the prevailing tidal change. If more than a single double run is made, then a mean of means can be taken, as shown in the example illustrated in Table 16.1, where each run was made at a regular time interval.

Table 16.1 Example of a mean of means analysis

Time	*Measured speed (knots)*	*Mean 1*	*Mean 2*	*Mean 3*
14:00	25.18			
		24.70		
			24.71	
14:45	24.22			
		24.72		24.72
15:30	25.22		24.73	
		24.74		
16:15	24.27			
		Mean Ship Speed = 24.72 kts		

Table 16.1 shows what may be termed the standard textbook way of performing the analysis. In practice, however, regular time intervals between runs seldom, if ever, occur. Notwithstanding this, it is still valid to use a mean-value analysis between any two runs forming a consecutive pair on a measured distance provided that all parties to the trial analysis are happy with the use of a linear approximation for the tide over the time interval concerned. However, the trials analyst, whatever method is used, is well advised to check the tidal assumptions with the predictions for the sea area in which the trial was carried out, both in terms of magnitudes and tidal flows.

If a higher-order tidal model is felt desirable, then several methods are available. It is most common, however, to use either a polynomial or sinusoidal approximation depending on the circumstances prevailing and, of course, the analyst's own preferences. In the polynomial expression, the standard textbook technique is to adopt a quadratic approximation:

$$\text{speed of tide } v_t = a_0 + a_1 t + a_2 t^2 \tag{16.1}$$

where t is the time measured from the initial run on the measured distances. This tidal speed is then used in the analysis procedure by assuming the measured ship speed V_m represents the ship speed V_s in the absence of the tide plus the speed of the tide v_t:

$$V_m = V_s + v_t \tag{16.2}$$

Hence by taking any set of four consecutive runs on the measured distance, either at regular or irregular time intervals, a set of four linear equations is formed from equations (16.1) and (16.2):

$$\begin{bmatrix} V_{m1} \\ V_{m2} \\ V_{m3} \\ V_{m4} \end{bmatrix} = \begin{bmatrix} 1 & 1 & t_1 & t_1^2 \\ 1 & -1 & -t_2 & -t_2^2 \\ 1 & 1 & t_3 & t_3^2 \\ 1 & -1 & -t_4 & -t_4^2 \end{bmatrix} \begin{bmatrix} V_s \\ a_0 \\ a_1 \\ a_2 \end{bmatrix} \tag{16.3}$$

The difference in signs in equation (16.3) merely indicates that the tide is either with or against the ship. If equation (16.3) is applied to the example of Table 16.1, then the resulting mean ship speed is given by the vector

$$\begin{bmatrix} 25.18 \\ 24.22 \\ 25.22 \\ 24.27 \end{bmatrix} = \begin{bmatrix} 1 & 1 & 0 & 0 \\ 1 & -1 & -0.75 & -0.5625 \\ 1 & 1 & 1.5 & 2.25 \\ 1 & -1 & -2.25 & -5.0625 \end{bmatrix} \begin{bmatrix} V_s \\ a_0 \\ a_1 \\ a_2 \end{bmatrix}$$

from which

$V_s = 24.721$ knots, $a_0 = 0.4587$, $a_1 = 0.08667$, $a_2 = -0.03999$

giving the equation of the tide as

$$V_t = 0.4587 + 0.08667t - 0.03999t^2 \text{ knots}$$

where t is measured in hours.

Such a tidal model is sufficient provided the measurement is not conducted over a protracted period of time. A quadratic function, being a second-order polynomial, only has one turning point, and therefore cannot adequately represent the periodic nature of the tide. Figure 16.3 illustrates this point, from which it can be seen that the above tidal model cannot predict accurately the tidal effect after about two hours from the start of the trial described in Table 16.1. However, it would not be the first time the author has seen such a model, based on four such points as those in Table 16.1, used to predict the tidal effect at a much later time and then use this prediction to

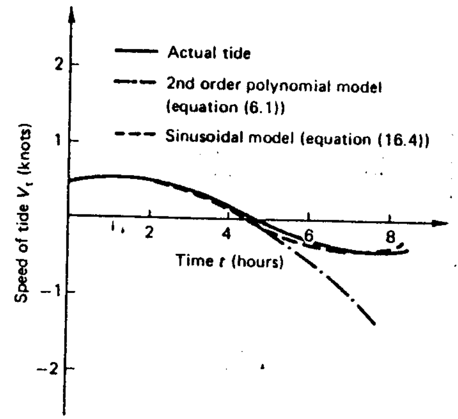

Figure 16.3 Comparison of tidal models

justify a trial speed! Alternatively, such a second-order representation will prove inadequate if the trial is conducted over a period greater than about four or five hours, even in the absence of extrapolation, due to the form of the polynomial and the tide characteristics.

As a consequence of these problems one can either use a higher-order polynomial, requiring rather more double runs to be conducted on the measured distance, or use a sinusoidal model of the general form

$$v_t = a\sin(\omega t + \phi) \tag{16.4}$$

An equation of the form of equation (16.4) can, by judicious construction of the coefficients, be made to approximate the true physics of the tidal motion. Figure 16.3, however, shows its use in its simplest form of constant coefficients.

16.2 Bollard pull trials

In general the bollard pull trial is conducted to satisfy a contractual requirement and, as such, would normally make use of the vessel's own instrumentation with the exception of a calibrated load cell which is introduced into the vessel's tethering line system. For those cases where either the vessel's instrumentation fit is insufficient or where an independent certification is required, temporary instrumentation would be fitted and the relevant parts of the discussion of the previous section would normally apply. Some authorities identify three different definitions of bollard pull for certification purposes. These are as follows:

1. *Maximum bollard pull*, which is the maximum average of the recorded tension in the towing wire over a period of one minute at a suitable trial location. As such this would normally correspond to the maximum engine output.
2. *Steady bollard pull*, which is the continuously maintained tension in the towing wire which is achievable over a period of 5 minutes at a suitable trial location.
3. *Effective bollard pull*, which is the bollard pull that the vessel can achieve in an open seaway. Since this is not ascertainable in a normal trial location it is normally characterized as a certain percentage of the steady bollard pull. This fraction is frequently taken as 78% after making due allowance for the weather conditions.

The general bollard pull characteristic of a vessel is outlined in Figure 16.4. From the Figure it is seen

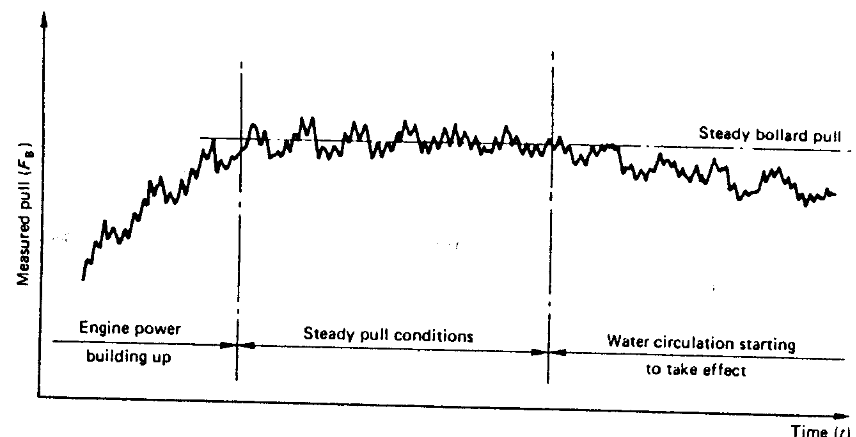

Figure 16.4 Measured bollard pull time history

that there is a general rise in bollard pull in the initial stages of the trial as the engine speed is increased. The pull then remains sensibly constant for a period of time, after which a decay is then frequently observed as water recirculation through the propeller starts to build up. A vibratory component of thrust superimposed on the mean trend of the bollard pull normally occurs, having cyclic variation which appears to relate to the rudder movements required to keep the vessel on station. In addition, higher-frequency thrust components, having a period of around an order of magnitude less than those rudder induced variations, will also be observed which correspond to the natural period of oscillation of the vessel on the end of the cable.

16.2.1 Trial location and conditions

Bollard pull trials should be conducted at a location which provides a sufficient extent of deep and unobstructed water together with a suitable anchorage point on the shore. The extent of water required is largely governed by the recirculation effects into the propeller and the attempt to try and minimize these as far as practicable. The reason for this concern is that at the bollard pull condition the advance coefficient $J = 0$; however, if water circulation, in either the vertical or horizontal planes, becomes significant, then the effective value of J increases and an inspection of any open water characteristic curve will show that under these conditions the value of the propeller thrust coefficient will fall off. Each trial location should clearly be treated on its merits with due regard to the vessel and its installed power. The trial location should preferably be that shown in Figure 16.5(a), which has clear water all around the vessel: the alternative location indicated in Figure 16.5(b) cannot be considered satisfactory since it encourages recirculation. When undergoing bollard pull trials it is normal for the vessel to 'range around' to a limited extent: this requires consideration when determining the trial location as does accommodating the emergency situation of the vessel breaking free and the consequent need for clear water ahead. For general guidance purposes the following conditions should be sought in attempting to achieve the best possible bollard pull trial location:

1. The stern of the vessel should not be closer than two ship lengths from the shore and in general the greater this distance becomes the better.
2. The vessel should have at least one ship length of water clear of the shore on each beam.
3. The water depth under the keel of the ship should not be less than twice the draught at the stern with a minimum depth of 10 m.
4. Current and tidal effects should ideally be zero, and consequently a dock location is preferable from this view point. If these effects are unavoidable, then the trial should be conducted at the 'top of the tide' with an ambient water speed not exceeding 0.5 m/s.
5. The wind conditions should not exceed Force 3 or 4 and the sea or river should be calm with no swell or waves.

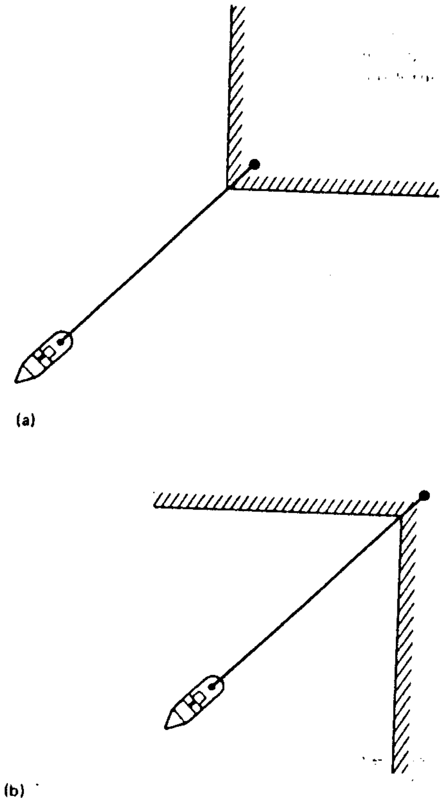

Figure 16.5 Bollard pull trial location: (a) good location for trial; (b) poor location for trial

16.2.2 Measurements required

The required measurements, in addition to the ambient weather and sea conditions, are the bollard pull, the engine power, propeller speed and the propeller pitch if the ship is fitted with a controllable pitch propeller. In addition a record of the rudder movements and vessel position with time should be kept as should the angle of yaw of the vessel so that these measurements can be synchronized with the recorded bollard pull signature.

In general the comments of Section 16.1 apply as far as the measurement methods are concerned. The load cell which could be either mechanically or electrically based must be calibrated and should form part of the tow line at the shore end of the tethering system. The reason for locating the gauge at the shore end is that it is generally easier to protect the gauge in this location and it is not influenced by external effects such as friction on the towing horse of a tug. Ideally, the trial results from all of the various measurements should be continuously and simultaneously measured against time which will then enable them to be fully considered for analysis purposes.

16.3 Propeller induced hull surface pressure measurements

The propeller induced hull surface pressures are of interest from the vibration that they induce on the vessel. It is normal for these measurements to use pressure transducers inserted flush into the hull surface at appropriate locations above the propeller. The signal from these transducers is then recorded together with other measured ship parameters, as desired, but in all cases in association with propeller shaft speed and a reference mark on the shaft; in some instances these are combined. The pressure recorded by the transducer is the apparent propeller induced pressure $p'(t)$, which is given by

$$p'(t) = p_H(t) + p_V(t) \quad (16.5)$$

where $p_H(t)$ is the true propeller induced pressure and $p_V(t)$ is the hull induced pressure caused by its own vibration.

In order, therefore, to correct the measured result for the pressure induced by the vibration of the hull, it is necessary to measure the vibration of hull surface in the vicinity of the pressure transducer. From the recorded vibration signals, the local motion of the hull can be determined from which a first-order correction, $p_V(t)$, can be determined on the basis of a vibrating plate in an infinite medium. As such, the propeller induced pressures on the hull surface can be derived from equation (16.5) by rewriting it as

$$p_H(t) = p'(t) - p_V(t) \quad (16.5(a))$$

References and further reading

1. ITTC Guide for Measured Mile Trials. Rep. of Perf. Comm., Proc. 12th ITTC, Rome, 1969.
2. BSRA Code of Procedure for Measured-Mile Trials. BSRA, 1977.
3. Norwegian Standard Association, 1985.
4. Dally, J.W., Riley, W.F. *Experimental Stress Analysis*. McGraw-Hill, 1978.
5. Hylarides, S. Thrust measurement by strain gauges without the influence of torque, *Shipping World and Shipbuilder*, December, 1974.

Part Two

Materials and mechanical considerations

17 Propeller materials

Contents

The materials from which propellers are made today can broadly be classed as members of the bronzes or stainless steels. The once popular material of cast iron has now virtually disappeared, even for the production of spare propellers, in favour of the materials with better mechanical and cavitation-resistant properties. Figure 17.1 introduces the better-known materials that have been in use for the manufacture of all types of propellers ranging from the large commercial vessels and warships through to pleasure run-abouts and model test propellers.

Even with the two major materials groupings in use today their relative popularity has changed, as can be seen from Figure 17.2, which shows the relative numbers of propellers constructed and classed with Lloyd's Register from different materials during the period 1960–88 (Reference 1). In the early 1960s, the use of high-tensile brass accounted for some 64% of all of the propellers produced with manganese–aluminium bronze and nickel–aluminium bronze accounting for comparatively small proportions: 12% and 19% respectively. However, it can be seen that by the last time interval, 1985 to 1988, nickel–aluminium bronze has gained an almost complete dominance over the other materials by accounting for some 82% of the propellers classed during that period. Furthermore, from Figure 17.2 it is apparent that this has been a steady trend developing over the last quarter of a century. High-tensile brass, which in the early 1960s was the major material, now only accounts for some 7% of the propellers used, and manganese–aluminium bronze around 8%. Whilst the swing from high-tensile brass to nickel–aluminium bronze is evident from the figure, we also see that the manganese aluminium bronze propellers have generally fluctuated in popularity between some 5 and 15% of the total propellers classed over the period. The title 'other materials', shown in Figure 17.2, includes principally the stainless steels but also embraces cast iron and the relatively few applications of high damping alloys and polymers. From the Figure we see that these other materials, principally in the form of stainless steels, gained a comparatively popular usage in the period from the mid-1960s through to the mid-1970s, but have then progressively lost favour to the copper-based materials to a point where today they appear to account for some 3% of the materials used for propeller manufacture.

17.1 General properties of propeller materials

Pure copper, which has a face-centred-cubic structure as illustrated in Figure 17.3, has a good corrosion resistance and is a particularly ductile material having an elongation of around 60% in its soft condition together with a tensile strength of the order of 215 N/mm^2. Thus, when considered in terms of its tensile strength properties it is a relatively weak material in its pure form and since plastic deformation of metallic crystals normally result from the slipping of close-packed planes over each other in the close-

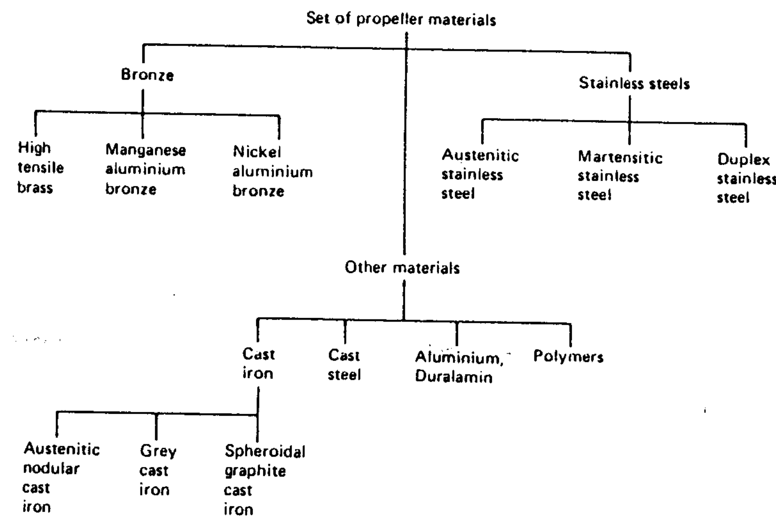

Figure 17.1 Set of propeller materials

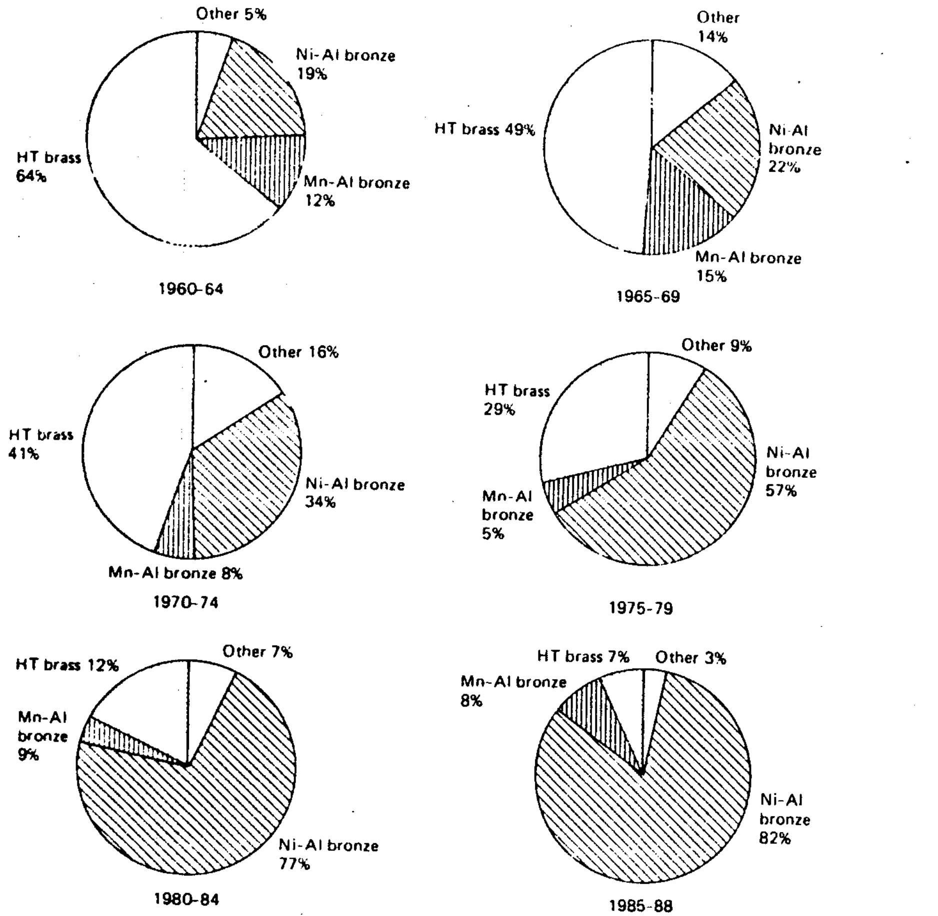

Figure 17.2 Relative popularity of propeller materials for propellers classed with Lloyd's Register

packed directions, the high ductility of copper is explained on the basis of its face-centred-cubic structure.

By combining copper with quantities of other materials to form a copper-base alloy the properties of the resulting material can be designed to give an appropriate blend of high ductility, good corrosion resistance coupled with reasonable strength and stiffness characteristics. One such alloy is the copper–zinc alloy which contains up to about 45% zinc, frequently in association with small amounts of other elements. Such copper–zinc alloys, where zinc has the closed-packed hexagonal structure, are collectively known as the brasses and the phase diagram for these materials is shown in Figure 17.4(a). In their α phase, containing up to about 37% zinc, the brasses are noted principally for their high ductility which reaches a maximum for a 30% zinc composition. If higher levels of zinc are used, in the region of 40% to 45%, then the resulting structure is seen from Figure 17.4(a) to be of a duplex form. In the β' phase, which exhibits an ordered structure, the material is found to be hard and brittle which is in contrast to the β phase which has a disordered solid solution and which has a particularly malleable characteristic. From the figure it is readily

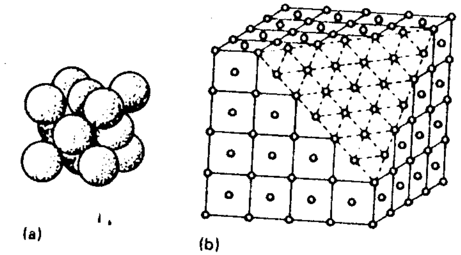

Figure 17.3 Face-centred-cubic structure of copper: (a) cell unit; (b) arrangement of atoms on the (111) close packed plane

seen that when a brass having a 40% zinc composition is heated to around 700°C, the alloy becomes completely β in structure. A second important alloy composition is the copper–nickel system whose phase diagram is shown in Figure 17.4(b). Nickel, like copper, is a face-centred-cubic structured element and has similar atomic dimensions and chemical properties to copper, and so these two elements form a substitutional solid solution when combined in all proportions. The resulting material is tough, ductile, reasonably strong and has good corrosion resistance.

The properties required in a propeller material will depend to a very large extent on the duty and service conditions of the vessel to which the propeller is being fitted. However, the most desirable set of properties which it should possess are as follows:

1. high corrosion fatigue resistance in sea water.
2. high resistance to cavitation erosion;
3. good resistance to general corrosion;
4. high resistance to impingement attack and crevice corrosion;
5. high strength to weight ratio;
6. good repair characteristics including weldability and freedom from subsequent cracking;
7. good casting characteristics.

The majority of propellers are made by casting, however, cast metal is not homogeneous from one part of a casting to another and the larger the casting the more these differences are accentuated. The differences in properties are due to differences in the rate of cooling in various parts of the casting; presuming that the liquid metal is initially of uniform temperature and composition. Clearly the rate of cooling of the metal at a blade tip, which may be of the order of 15 mm in thickness, will be very much faster than that

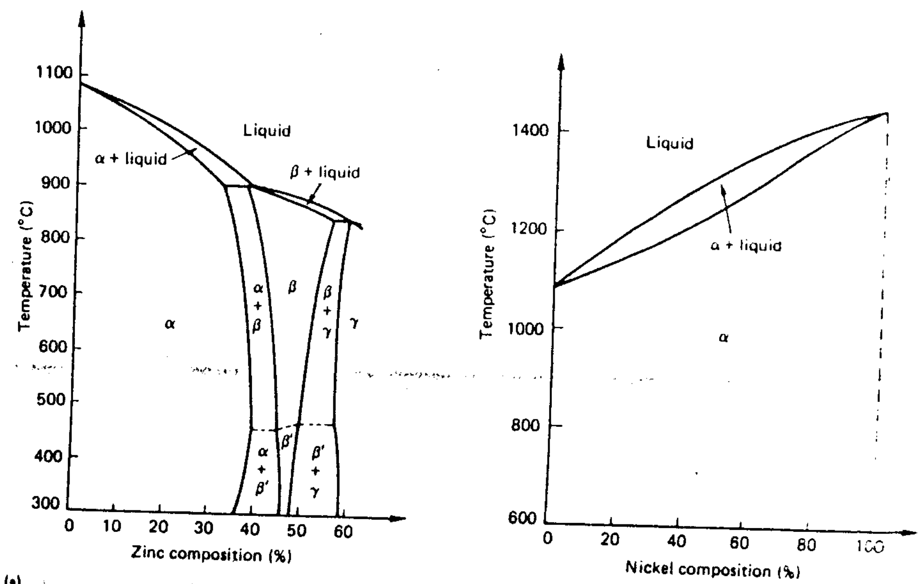

Figure 17.4 Phase diagram for: (a) copper–zinc; (b) copper–nickel alloy

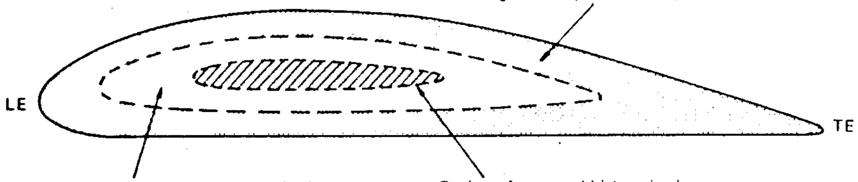

Figure 17.5 General macrostructure characteristics of a thick propeller section

at the boss which may be 1000 mm thick for the same propeller.

In general, the faster the cooling rate the smaller the crystal or grain size of the material will be. The slower the cooling rate, the more nearly equilibrium conditions will be reached; consequently, at the centre of the boss of a large propeller the structure of the alloy tends to approach the conditions defined by the phase diagram. The difference in the microstructure, therefore, between the metal in the blade tip and in the boss region can be considerable depending upon the level of control exercised and the type of alloy being cast. This difference assumes a considerable importance in propeller technology because, for conventional propellers, the maximum stress in service is normally incurred in thick sections of the casting at the blade root.

Apart from differences from thin to thick parts of the same casting, there are also differences through the section thickness. The difference in through-section properties arises because the metal at the skin of the casting is the first to freeze, since the metal here is chilled by contact with the mould. Consequently, the cooling rate is fast and hence the grain size of the material is the smallest here. However, towards the centre of the section there is a slower cooling rate and the metal at the location is last to freeze. Therefore, because alloys solidify over a range of temperatures, the actual composition can be expected to vary in the metal between that which is the first to freeze and that which is last to freeze. Additionally, any material that is not in solution in the liquid state, such as slag or other impurities, is pushed, while still liquid, towards the centre as the dendrites of the solidifying metal grow from the sides. Furthermore, in a casting which is not adequately fed by liquid metal, there may not be sufficient metal to fill the space in the centre of the casting and unsoundness due to shrinkage will result. Consequently, the poorest properties can be expected near the centre of a thick casting. Figure 17.5 shows the expected variation in grain size through a propeller root section.

As a consequence of the differences in the through-thickness and across-blade properties that can take place in a propeller casting, it is reasonable to expect that the through-thickness mechanical properties of the material will also show a considerable variation. This is indeed the case and considerable care needs to be taken in selecting the location, size and test requirements of material specimens in order to gain representative mechanical properties for use in design: these aspects are discussed more fully in Section 17.4. In more general terms, however, the stress–strain relationship for the bronze materials takes the form of Figure 17.6(a). Since these materials, like the stainless steels, do not possess a clearly defined yield point as in the case of steel and, consequently, the stress–strain curve is characterized in terms of 0.1% and 0.2% proof stresses. The more important mechanical characteristic, the fatigue resistance curve, is shown in Figure 17.6(b). In the case of propeller design it is important to consider data at least to 10^8 cycles, preferable more, if realistic mechanical properties are to be derived. For example, a ship having a propeller rotating at 120 RPM and operating for 250 days per year will accumulate on each blade 8.6×10^8 first-order stress cycles over a twenty-year life. It is, however, instructive to consider the way in which cyclic fatigue life builds up on a propeller blade: Table 17.1 demonstrates this accumulation for the example cited above.

A moment's consideration of Table 17.1 in relation to Figure 17.6(b) gives a measure of support to the fatigue failure 'rule of thumb' for propellers which implies that 'If a propeller lasts more than two or three years, then it is probably unlikely to suffer a fatigue action failure from normal loadings causing the loss of a blade.'

When considering the fatigue characteristics of a material it is important to consider the relationship shown in Figure 17.6 in relation to the amount of tensile stress acting on the material in question. The effect of tensile stress on the fatigue resistance of the bronzes has been quite extensively investigated; for example Webb *et al.* (Reference 2). From these studies it has been shown that the effect of the tensile stress is considerable, as shown in Figure 17.7.

The chemical composition of the metal is of extreme importance in determining the mechanical properties of the material. Langham and Webb (Reference 3) show, for example, how the effects of changes to the manganese and aluminium contents of Cu–Mn–Al alloys influence the mechanical strength of the material (Figure 17.8).

Table 17.1 Build-up of first-order fatigue cycles on a blade of propeller

Time	*1st hour*	*1st day*	*1st month*	*1st year*	*2nd year*	*10th year*	*20th year*
No. of first-order fatigue cycles	7.2×10^3	1.7×10^5	3.6×10^6	4.3×10^7	8.6×10^7	4.3×10^8	8.6×10^8

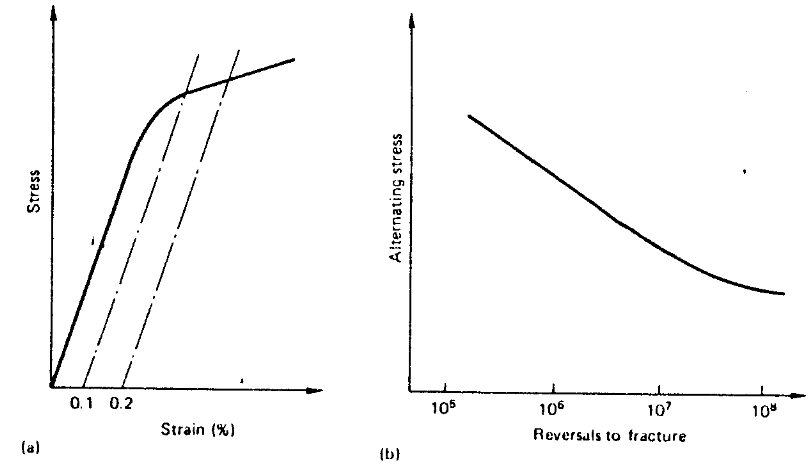

Figure 17.6 Mechanical characteristics of propeller materials: (a) stress–strain relationship; (b) fatigue resistance

17.2 Specific properties of propeller materials

The preceding discussion has considered in general terms both the properties and influences on copper-based materials starting from the nature of pure copper and finishing with the basic characteristics of realistic propeller alloys. From this basis, the discussion now turns to an outline consideration of the specific properties of the more common propeller materials shown in Figure 17.1. For a more detailed review of propeller materials, particularly from the metallurgical viewpoint, the reader is referred to References 4 and 5 which have acted as a basis of the summary given in the remainder of Section 17.2.

17.2.1 High-tensile brass

These alloys are frequently referred to as 'manganese bronze'; however, this is a misnomer, as they are essentially alloys of copper and zinc, and as such are brasses rather than bronzes. Furthermore, although a small amount of manganese is usually present, this is not an essential constituent of these alloys.

High-tensile brasses have the advantage of being able to be melted very easily and cast without too much difficulty. Care, however, has to be exercised in melting the alloy for the manufacture of very large propellers, since any contamination with hydrogen gas leads to an unsoundness in the propeller casting. The composition of these alloys varies considerably, but they are essentially based on 60% copper, 40% zinc brass together with additions of aluminium, tin, iron, manganese and sometimes nickel. Aluminium is a strengthening addition which also helps to improve the corrosion resistance, and is generally present in proportions of between 0.5% and 2%; this component, however, is sometimes increased to around 3% in order to produce a stronger alloy. If tin is omitted from the material, then the alloys corrode rapidly by the process of dezincification so that the surface appearance of the material remains unchanged except for some degree of coppering.

The high-tensile brasses basically comprise two separate phases; however, when dezincification occurs, the beta phase in the structure is initially

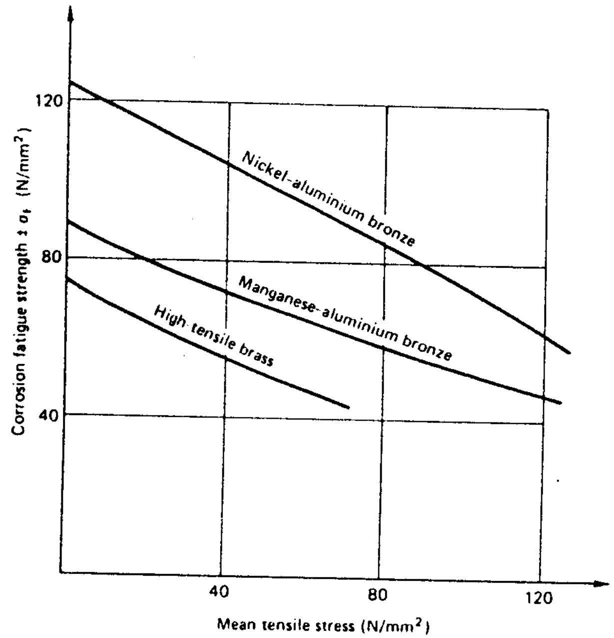

Figure 17.7 Effect of mean tensile stress on corrosion fatigue properties

replaced by copper. Whilst dezincification can occur when in fast flowing sea water, it most readily occurs under stagnant conditions, particularly where there are crevices in the material. To give reasonable resistance against this form of attack a tin content of at least 0.2% has to be incorporated in the alloy and the higher the tin content the greater the resistance against this type of corrosion. High tin contents, however, lead to difficulties in propeller casting and the alloys become more sensitive to stress corrosion cracking. Tin contents, therefore, seldom exceed 0.8% and never exceed 1.5%.

The properties obtained in castings are very dependent upon the grain size, the maximum strength being obtained with fine-grained material. Iron is an essential constituent to produce grain refinement in the alloy and is present, in the absence of high aluminium or nickel contents, at levels of the order of 0.7–1.2%. In cases where the aluminium or nickel contents are high, higher iron contents are necessary in order to achieve the requisite degree of grain refinement; however, little benefit is gained by increasing the iron content above 1.2%. Manganese appears to have a generally beneficial but non-critical influence on the alloy properties, and about 1% is usually present in the material. Nickel is not harmful, but at the same time does not appear to introduce any worthwhile benefits which could not be obtained more economically by an increase in the aluminium content.

The copper and zinc contents are adjusted to give the best balance of properties: these are obtained when the microstructure of the alloy contains about 40% of the softer more ductile alpha phase, and 60% of the harder, less ductile, beta phase. The relative proportions of these two phases have a controlling influence on the tensile properties and fatigue strength of the alloy, as outlined in the previous section. If the zinc content is raised to too high a level, the alloy will contain none of the alpha phase (Figure 17.4(a)) and in that condition it will be very susceptible to stress corrosion in sea water. Therefore, if a high-tensile stress is continuously experienced in the material while it is immersed in sea water, then spontaneous cracking can occur. This susceptibility to stress corrosion exists even when some of the alpha phase is present in the alloy; however, sensitivity to stress corrosion cracking is believed to decrease as the alpha content is increased: an alpha content of 25% is generally regarded as a minimum in a material used for propeller manufacture. As in the case of the simple Cu–Zn alloy discussed in Section 17.1 when the two-phase alloy is heated, the alpha particles gradually dissolve into the beta phase

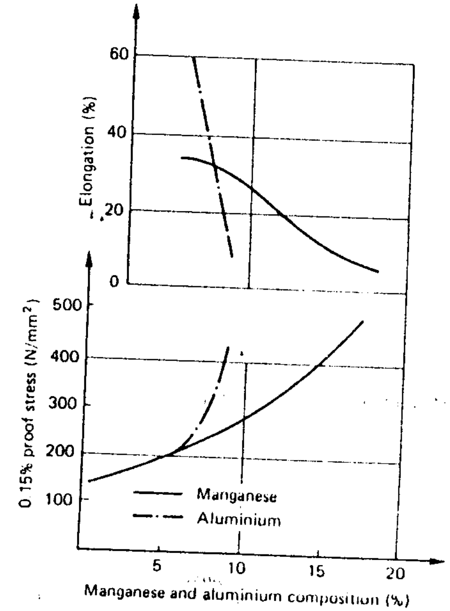

Figure 17.8 Typical effect of chemical composition on mechanical properties of a copper–manganese–aluminium alloy

until, at temperatures of the order of 550 °C, the alloy consists entirely of the beta phase. If the metal is allowed to cool slowly to room temperature, the alpha particles precipitate out once more, and a structure similar to the original one is recovered. Alternatively, if the cooling is rapid the alpha phase does not precipitate fully, and with very fast cooling, a completely beta structure can be retained down to room temperature. Similar structures are frequently produced in areas adjacent to welds where residual internal stresses can be of a very high order, and this combination of high residual stress and undesirable microstructure, in terms of low alpha phase, has frequently led to stress corrosion cracking in high-tensile brass propellers. It is of the utmost importance, therefore, that welds in these materials be stress relieved by heat treatment.

Stress relief can be effected by heating the material at temperatures in the range of 350–550 °C as referenced in Chapter 25, the higher temperatures allowing full precipitation of the alpha phase. Residual stresses can be reduced by localized heating of the surface of a high-tensile brass propeller, and this should be effected wherever possible.

High-tensile brass is an easy material to machine, and can be bent or worked at any temperature. When it is heated above 600 °C it consists entirely of the beta phase and is quite soft and ductile, facilitating any straightening repairs which may be necessary.

17.2.2 Aluminium bronzes

For discussion purposes it is possible to classify aluminium bronzes into three types:

1. those containing more than 4% of nickel and very little manganese;
2. those containing in excess of 8% of manganese;
3. those containing very little nickel or manganese.

The majority of large aluminium bronze propellers are manufactured using either the first or second types of alloy, which are normally known by the names of nickel–aluminium bronze and manganese–aluminium bronze respectively. The latter of the three alloys has low impact strength and poor corrosion resistance.

The first of the manganese–aluminium bronzes was patented around 1950 and had a composition of some 12% manganese, 8% aluminium, 3% iron and 2% nickel. These manganese and aluminium contents were selected at that time to give a phase structure comprising about a 60–70% alpha content. Whilst some alloys containing 6–9% of manganese have been used for propeller manufacture it is found that an increase in manganese content above 10% results in a general improvement in mechanical properties. The presence of the manganese at around 8 to 10% concentration inhibits a decomposition of the beta phase into a brittle eutectoid mixture containing a hard gamma phase which would otherwise occur in heavy cast sections. Indeed some alloys contain up to about 15% manganese.

All manganese–aluminium alloys have similar microstructures and, therefore, somewhat similar characteristics. Their structures are similar to those of the high-tensile brasses; however, the structure tends to be finer and the proportion of the alpha phase is higher with the manganese–aluminium bronzes. In keeping with the high-tensile brasses they have no critical temperature range in which they lose ductility, and are susceptible, but less sensitive, to stress corrosion in sea water in the presence of high internal stresses. This lower sensitivity is probably due to their lower beta content. The same precautions as recommended for the high-tensile brasses regarding stress relief after welding should be applied, although the risk of cracking is less in manganese–aluminium alloys if these precautions are are not taken.

The nickel–aluminium bronze alloys usually contain some 9–9.5% aluminium with nickel and iron contents each in excess of 4%: this level of nickel is required to obtain the best corrosion resistance. In BS 1400-AB2, lead is normally permitted up to a level of 0.05%, except where welding is to be carried out, when it should be limited to a maximum of 0.01%. Manufacturers, however, can experience difficulty in maintaining the lead as low as 0.01%, owing to its tramp persistence in secondary metal. Although published work dealing with the effect of lead on the weldability of nickel–aluminium bronze is sparse, it is generally considered that its presence should not be detrimental to weldability if maintained below 0.03%.

The microstructure of nickel–aluminium bronze is quite different from that of high-tensile brass. It comprises a matrix of the alpha phase in which are distributed small globules and plates of a hard constituent which is frequently designated a kappa phase. At ambient temperature the alloy is tough and ductile but as the temperature is raised it becomes less ductile and tough with elongation values at about 400 C that are only about a quarter of those at room temperature. The ductility is recovered, however, at higher temperatures and bent propeller blades can be straightened at temperatures in excess of 700 C. At temperatures above 800 C nickel-aluminium bronze becomes quite malleable and ductile, allowing repairs to be made with relative ease.

The nickel-aluminium bronzes have considerably higher proof stress than the high-tensile brasses, together with a somewhat higher impact strength. The corrosion fatigue resistance in sea water is approximately double that of high-tensile brasses and this allows the use of higher design stresses and hence reduced section thicknesses of the propeller blades. Nickel–aluminium bronze is also found to be more resistant to cavitation erosion than high-tensile brass by a factor of two or three, and it is also much more resistant to the impingement type of corrosion, often referred to as wastage, which removes metal from the leading edges and the tips of propeller blades.

17.2.3 Stainless steels

There are two principal types of stainless steel that have been used for propeller manufacture. These are the 13% chromium martensitic and the 18% chromium, 8% nickel, 3% molybdenum austenitic stainless steel. The former is perhaps the more widely used; however, its use has generally been confined to small propellers and the component parts of controllable pitch propellers. The austenitic type of stainless steel has been mainly used in service on vessels on inland waterways. The main advantages of austenitic stainless steel lie both in its toughness, which enables it to withstand impact damage, and its good repairability.

Both types of stainless steel have a good resistance to impingement corrosion, but tend to suffer under crevice corrosion conditions. Their resistance to corrosion fatigue in sea water, and also to cavitation erosion, is generally lower than those of the aluminium bronzes. In recent years, stainless steels with more than 20% chromium and about 5% nickel with microstructures containing roughly equal proportions of austenitic and ferrite phases have been designed for propeller manufacture. These materials have better resistance to corrosion fatigue in sea water than either the martensitic or austenitic types.

Much work has been undertaken, particularly in Japan, on the development of stainless steels for marine propellers. In essence the main thrust of this development work has been to make stainless steel more competitive to nickel-aluminium bronze in terms of their relative corrosion fatigue strength. Currently, many stainless steels have a reduced allowable corrosion fatigue strength when compared to nickel-aluminium bronze of around 27% (Reference 6); such a reduction translates to an increased blade section, thickness requirement of the order of 17% for a zero-raked propeller. Kawazoe *et al.* (Reference 7) discuss the development of a stainless steel and the results of laboratory and full-scale trials on a number of vessels of differing types. The chemical composition for this stainless steel is nominally an 18% chromium, 5–6% nickel, 1–2% molybdenum with manganese less than 3% and cobalt and silicon less than 1.5%. Indications are that this material, based on Wöhler rotating beam tests, can develop a fatigue strength of the order of 255 N/mm² at 10^8 reversals.

17.2.4 Cast iron

Ordinary flake graphite cast iron has in the past been used mainly for spare propellers that are carried on board a ship for emergency purposes. This material has a very poor resistance to corrosion, particularly of the impingement type, and the life of a cast iron propeller must be regarded as potentially very short. Because the resistance to corrosion is adversely affected by removal of the cast skin, it is not normal to grind the blades to close dimensional control and this, together with the fact that much heavier section thicknesses are required for strength purposes, makes the propeller far less efficient. Cast iron is of course brittle, and this renders it susceptible to breakage on impact with an underwater object; only very minor repairs can be affected.

The enhanced ductility of spheroidal graphite cast iron compared with grey iron makes it a more attractive material for propeller usage. It is, however, subject to rapid corrosion and erosion and the use of heavy section thicknesses is still necessary.

Austenitic nodular cast iron has been used for the manufacture of small propellers. It contains 20–22% nickel and 2.5% chromium and the microstructure has an austenitic matrix with graphite in spheroidal form. Its resistance to impingement attack and corrosion approaches that of high-tensile brass, but its impact strength and resistance to cavitation erosion are somewhat lower.

17.2.5 Cast steel

Low alloy and plain carbon cast steels are occasionally used for the manufacture of spare propellers. The tensile properties are reasonable; however, the resistance to corrosion and erosion in sea water is much inferior to that of the copper-based alloys. Cathodic protection is essential when using this material for propellers.

Table 17.2 Typical comparative material properties

	Material	Modulus of elasticity (kgf/cm²)	0.15% proof stress (kgf/mm²)	Tensile strength (kgf/mm²)	Brinell hardness number	Specific gravity	Elongation (%)
Copper-based alloys	High-tensile brass	1.05×10^6	19	45–60	120–165	8.25	28
	High-manganese alloys	1.20×10^6	30	66–72	160–210	7.45	27
	Nickel–aluminium alloys	1.25×10^6	27.5	66–71	160–190	7.6	28
Stainless steels	13% chromium	2.0×10^6	45.5	69.5	220	7.7	20
	Austenitic	1.9×10^6	17	50.5	130	7.9	50
	Ferritic austenitic	1.8×10^6	55	80	260	7.9	18
Cast iron	Grey cast iron	1.1×10^6		23.5	200	7.2	
	Austenitic S G	1.1×10^6		44	150	7.3	25
Polymers	Nylon	0.008×10^6	1.1	4.7			35
	Fibreglass	0.14×10^6		20	—	—	1.5

17.3 Mechanical properties

The form of the general stress-strain curve for the copper based alloys and the stainless steels was shown in Figure 17.6(a). Table 17.2 shows typical comparative properties of the more common materials used for propeller manufacture as determined by separately cast test pieces.

These properties are important from the general stress analysis viewpoint and especially in the cases where numerical analysis capabilities are used to determine the stresses in a blade. In determining the allowable stress, however, it is the fatigue properties that are of most importance. In Table 17.1 it was shown that 10^9 cycles can be attained in a matter of 20 years or so for, say, a large bulk carrier, and correspondingly sooner for many smaller vessels. However, if fatigue tests on these materials were carried out to this number of cycles and over a sufficiently large number of specimens for the results to become meaningful, the necessary design data would take an inordinately long time to collect. Consequently, it is more usual to conduct tests up to 10^8 reversals, and although it can be argued that this data tends to be suspect when extrapolated to 10^9 cycles, the criteria of assessment are normally based on the lower figure for marine propellers.

Throughout the development of propeller materials many tests using the Wöhler fatigue testing procedure have been made for the various materials. However, these tests have several limitations in this context since they do not readily permit the superimposition of mean loads on the specimen and the stress gradients across the test specimen tend to be large. For these reasons, and furthermore, since the exposed areas of the test piece tend to be small, the results from these tests are used primarily for qualitative analysis purposes. In order to overcome these difficulties and thereby provide quantitative fatigue data for use in propeller design, fatigue testing machines such as the one shown by Figure 17.9 have been designed. Machines of this type are usually able to test material specimens of the order of 75 mm in diameter and in addition to applying a fluctuating component of stress, a mean stress can also be superimposed by using hollow specimens, thereby permitting pre-stressing by means of a suitable linkage. In order to simulate the corrosive environment a 3% sodium chloride solution is normally sprayed on to the specimen in the majority of cases. The use of this solution to simulate sea water is generally considered preferable for testing purposes, since the properties of sea water are found to vary considerably with time, and unless the sea water is continuously replaced, it decays to such an extent that it becomes unrepresentative.

Testing machines of the type shown in Figure 17.9 have been used extensively in order to examine the behaviour of various propeller materials. Figure 17.7, by way of demonstration of these researches, shows the comparative behaviour of three copper alloys based on a fatigue life of 10^8 cycles as determined by the authors of Reference 2. From these test results the superior corrosion fatigue properties of the nickel aluminium bronzes become evident. However, in establishing these results extreme care is necessary in controlling the solidification and cooling rates of the test specimens after pouring in order that they can correctly simulate castings of a significantly greater

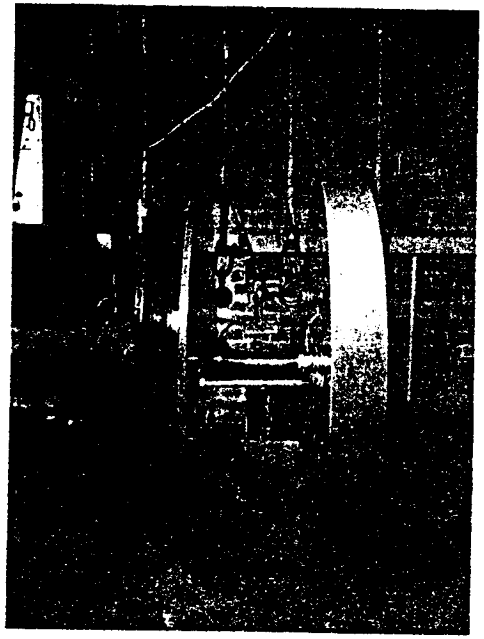

Figure 17.9 Corrosion fatigue testing machine for propeller materials

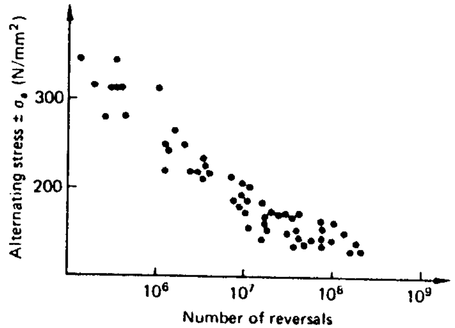

Figure 17.10 Typical scatter of corrosion fatigue tests on a nickel–aluminium bronze alloy

weight. In the case of Figure 17.7 a simulation of a casting weight of around 4 tonnes was attempted.

Casting size has long been known to affect the material properties as witnessed by the sometimes significant differences between test bar results and the mechanical properties of the blade when destructively tested. For these reasons controllable pitch propeller blades are generally believed to have superior mechanical properties to monoblock propellers of an equivalent size. Many attempts have been made to correlate this effect by using a variety of parameters. Webb *et al.* (Reference 2) from their researches some years ago suggested a relationship based on blade weight referred to a base casting weight of 10 tonf. The relationship proposed is as follows:

$$\sigma_w = \sigma_{10}\left(0.70 + \frac{30}{w + 90}\right) \qquad (17.1)$$

where σ_w is the estimated fatigue strength at zero mean stress of a propeller weighing w tons in relation to that for a 10-ton propeller σ_{10}. Values of f_{10} for high-tensile brass, manganese–aluminium bronze and nickel–aluminium bronze were proposed as being 6.8, 9.2 and 11.8 kgf/mm² respectively.

The approach by Meyne and Rauch (Reference 8), in which tensile strength and proof stress are plotted to a base of propeller weight divided by the product of blade number and the area of one blade, gives encouraging results. This approach, which is effectively defining a pseudo blade thickness correlation parameter, takes the analysis procedure a stage further than simpler methods using blade weight alone. The correlation of elongation with casting size is, however, still far from resolved.

Later work by Wenschot (Reference 9) in examining some hundred or so nickel aluminium bronze propellers undertook mechanical and corrosion fatigue studies on material taken from the thickest parts of propeller castings. From the various castings included in this study, section thicknesses varied from 25 mm to 450 mm and the analysis resulted in a relationship between cast section thickness and fluctuating stress amplitude for zero mean stress of the form

$$\sigma_a = 160.5 - 24.4\log(t) \qquad (17.2)$$

where the cast section thickness (t) is measured in mm and the corrosion fatigue strength in sea water (σ_a) is based on 10^8 reversals.

17.4 Test procedures

Because of the variations of properties within one casting it is practically impossible to cast a test bar, or test bars, which will represent the properties of the material in all parts of a casting. The best that can be done is to cast a number of test bars in separate moulds using the same molten metal as for the casting. The mould for the test bar should be correctly designed so that the part from which test pieces are to be cut is properly fed to obtain sound metal. In other words, the test bar represents the properties of the metal which is being cast and not the properties of the test bar casting itself. Test bars or coupons which are cast in an integral way with the casting may give an indication of the properties in the casting near to the position of the test bar provided the section thickness is the same. However, there is always the danger with cast-on bars that they are not properly fed and their properties may be inferior to those of the adjacent metal. Alternatively, there may be overriding requirements, such as the assurance that a test bar is cast from the same metal it is supposed to represent, that insist that it should be integral with the casting.

The usual form of test bar for propeller alloys is the keel bar casting having a circular cross-section of diameter 25 mm and a feeder head along its full length. From such a bar it is not possible to machine a tensile test piece with a parallel portion much more than 15 mm in diameter, and clearly a test piece of this type will not represent the properties of the thick sections of a large propeller. It is nevertheless quite satisfactory for sorting out a poor cast of metal from a number of casts. When examining the microstructure of high-tensile brass, the test specimen should be cut from the test bar to ensure that it has been cooled at a standard rate for comparison of the amount of alpha and beta phases present.

Most fatigue testing is carried out on rotating beam Wöhler machines, using a round specimen held in a chuck with a load applied in bending as a cantilever. In this way a complete reversal of the stress is applied to the specimen with each revolution of the test piece. Other types of fatigue tests employ rectangular specimens with the load applied in the plane of bending and others apply the fluctuating stress axially in tension and compression by a pulsating load. For testing in air using rotating beam machines, the specimen is usually about 10–15 mm in diameter and good reproducibility of results is obtained for most wrought materials with this method. When cast materials are to be tested the results show more scatter, but still give an indication of the fatigue limit which can be expected on a comparative basis. Clearly, the larger the test piece of a cast material is, the more useful the results will be in representing the fatigue properties of large castings.

The evaluation of the resistance of a material to a fluctuating stress in a corrosive environment is a much more difficult proposition: since the conditions involve corrosion, short-time tests are of little value. Because there is no stress, however low, which will not induce failure if the corrosive conditions are maintained for long enough, the longer the time of the test the better. Clearly some time limit must be resolved before testing starts and for this purpose a year is a good criterion; however, from the practical consideration of getting results for design purposes shorter periods must be permitted.

As the corrosion fatigue test relies on the stress and corrosion acting together, account must be taken of the fact that the stress acts through the material whereas corrosion acts on the surface area. The ratio of the area of the cross-section of the test piece to its diameter is therefore important, and the smaller the diameter of the specimen, the greater will be the effect of the corrosion parameter while maintaining a constant stress on the specimen.

Since rotating beam fatigue tests in air use a specimen of about 10 mm in diameter, this size has frequently been pursued for corrosion fatigue testing. Work in Japan has, however, shown a 30% reduction in corrosion fatigue resistance when the specimen size was increased from 25 mm to 250 mm dia. This work was carried out over a short time frame, and is therefore not a realistic appraisal of corrosion fatigue resistance, but does show the effect of specimen size on the fatigue resistance of cast copper alloys.

When large specimens are used, the contact with the environment becomes difficult to arrange with a rotating specimen and machines have been devised (Figure 17.9); to apply reversed bending on a static specimen by a rotating out-of-balance load through counterweights attached to the specimen. Such machines can test specimens of 76 mm in diameter exposing about 225 cm² to the corrosive medium. It is also recognized that a copper alloy propeller as cast contains significant internal stresses. In corrosion fatigue testing, therefore, it is useful to be able to apply a mean stress to the test piece so that a fluctuating stress can be superimposed on it. The large 76 mm specimens referred to above are made hollow and a screwed insert within enables a tensile stress of known magnitude to be applied during the cyclic fatigue test. Failures in these tests have fractures very similar to those on propellers in service which have failed.

It will be appreciated that with all the variables contingent on corrosion fatigue testing, the test results on a particular material can have a great deal of scatter, as shown in Figure 17.10. Each spot on the figure is the result of the failure of an aluminium bronze test bar, all cast to the same specification, and the scatter is not unusual for such tests on cast material. Apart from the difficulty of choosing the best curve through the values plotted, any attempt to extrapolate the curve beyond 2×10^8 reversals in such a case is very unwise.

References and further reading

1. Carlton, J.S. Propeller service experience. *7th Lips Symposium*, 1989.
2. Webb, A.W.O., Eames, C.F.W., Tuffrey, A. Factors affecting design stresses in marine propellers. *Propellers '75 Symposium, Trans. SNAME*, 1975.
3. Langham, M.A., Webb, A.W.O. The new high strength copper–manganese–aluminium alloys their development, properties and applications. *Proc. Int. Foundry Congress*, Detroit, 1962.

4. Webb, A.W.O. High Strength Propeller Alloys. SMM Technical Paper No. 5, May, 1965.
5. Webb, A.W.O., Capper, H. Propellers.
6. *Rules and Regulations for the Classification of Ships*. Part 5, Chapter 7. Lloyd's Register, January, 1991.
7. Kawazoe, T., Matsuo, S., Sasajima, T., Daikoku, T., Nishikido, S. Development of Mitsubishi corrosion resistance steel (MCRS) for marine propeller. *4th Int. Symp. on Mar. Eng., Trans. MESJ*, 1990.
8. Meyne, K.J., Rauch, O. Some results of propeller material investigations. *Propellers '78 Symposium, Trans. SNAME*, 1978.
9. Wenschot, P. The properties of Ni–Al bronze sand cast ship propellers in relation to section thickness. *JSP*, 34, June, 1987.

18 Propeller blade strength

Contents

Ch. 18: استحکام پره پروانه

The techniques of propeller stressing have remained in essence unchanged throughout the development of screw propulsion until the early 1970s. Traditionally the cantilever beam method has been the instrument of stress calculation and today forms the cornerstone of commercial propeller stressing practice. This method was originally proposed by Admiral Taylor in the early years of this century and since that time a steady development of the method can be traced (References 1–7). Currently several expositions of this method have been made in the technical literature, all of which, although developing the same basic theme, have differing degrees of superficial emphasis. The version published by Sinclair (Reference 8) and based on the earlier work of Burrill (Reference 5) is typical of the methods in current use today.

18.1 Cantilever beam method

The cantilever beam method relies on being able to represent the radial distribution of thrust and torque force loading, as shown in Figure 18.1, by equivalent loads, F_T and F_Q, at the centre of action of these distributions. Having accepted this transformation, the method proceeds to evaluate the stress at the point of maximum thickness on a reference blade section by means of estimating each of the components in the equation

$$\sigma = \sigma_T + \sigma_Q + \sigma_{CBM} + \sigma_{CF} + \sigma_\perp \qquad (18.1)$$

where σ_T = stress component due to thrust action
σ_Q = stress component due to torque action
σ_{CBM} = stress component due to centrifugal bending
σ_{CF} = stress component due to direct centrifugal force
$\sigma_\perp$ = stress component due to out of plane stress components.

Using the definitions of Figure 18.1 the bending moment due to hydrodynamic action (M_H) on a helical section of radius (r_0) is given by

$$M_H = F_T a \cos\theta + F_Q b \sin\theta$$

in which F_T and F_Q are the integrated means of the thrust and torque force distributions and a and b define their respective centres of action.

The mechanical loadings on a particular section of a propeller blade are a function of the mass of the blade outboard of the section considered and the relative position of its centre of gravity with respect to the neutral axis of the section being stressed. Hence, a system of forces and moments is produced, which can be approximated, for all practical purposes in conventional non-skewed propeller forms, to a direct centrifugal loading together with a centrifugal bending moment acting about the plane of minimum section inertia. In the case of conventional propeller designs the centrifugal loadings can be readily calculated as indicated by Figure 18.2, and in general it will be found that they give rise to much smaller stresses than do their hydrodynamic counterparts; the exception to this is in the case of small high-speed propellers.

The total bending moment (M) acting on the blade section due to the combined effects of hydrodynamic and centrifugal action is therefore given by

$$M = M_H + M_C \qquad (18.2)$$

the centrifugal component (M_C), being the product of the centrifugal force by that part of the blade beyond the stress radius at which the stress is being calculated and the distance perpendicular to the neutral axis of the line of this force vector.

Hence from equations (18.1) and (18.2) the maximum tensile stress exerted by the blade on the section under consideration is given by

$$\sigma = \frac{M}{Z} + \frac{F_C}{A} \qquad (18.3)$$

where F_C is the centrifugal force exerted by the blade on the section. The term M/Z embraces the first three terms of equation (18.1), the term F_C/A is the fourth term of equation (18.1), whilst the final term $\sigma_\perp$ is considered negligible for most practical purposes. The calculation of the section area and modulus are readily undertaken from the information contained on the propeller drawing. The procedure, in its most fundamental form, being basically to plot the helical section profile according to the information on the propeller drawing, and then, if undertaking the calculation by hand, to divide the section chord into ten equally spaced intervals, see Chapter 11. The appropriate values of the local section thickness (t) and the pressure face ordinate (y_p) can then be interpolated and integrated numerically according to the following formulae:

$$A = \int_0^c t \, dc \qquad (18.4)$$

and for the section tensile modulus

$$Z_m = \frac{2\int_0^c [3y_p(y_p + t) + t^2] t \, dc \cdot \int_0^c t \, dc}{3\int_0^c (2y_p + t) t \, dc} - \frac{1}{2}\int_0^c (2y_p + t) t \, dc \qquad (18.5)$$

It will be noted that the final form of the blade stress equation (18.3) ignores the components of stress resulting from bending in planes other than about the plane of minimum inertia. This simplification has been shown to be valid for all practical non-highly skewed propeller blade forms, and therefore is almost universally used by the propeller industry for conventional propeller blade stressing purposes.

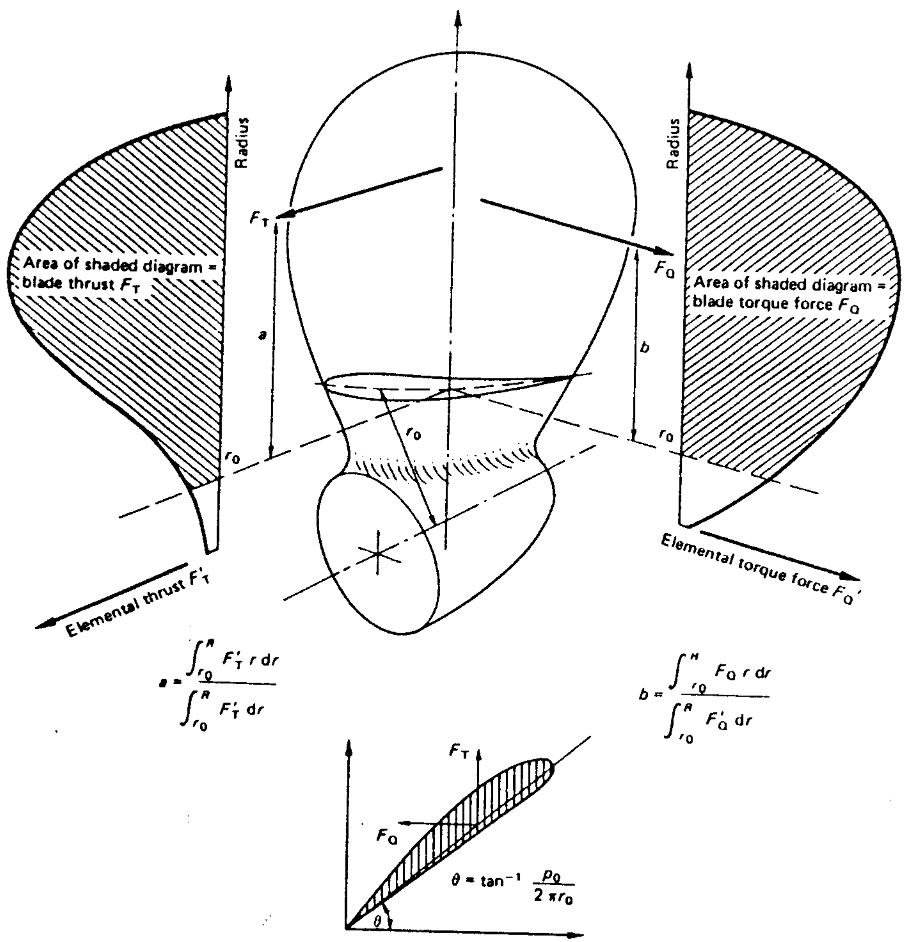

Figure 18.1 Basis of the cantilever beam method of blade stressing

Clearly the cantilever beam method provides a simple and readily applicable method of estimating the maximum tensile, or alternatively maximum compressive stress on any given blade section. In order to illustrate the details of this method, a worked example appears in Table 18.1. This example considers the evaluation of the mean value of the maximum tensile stress at the 0.25*R* section of a propeller blade and it can be seen that the calculation is conveniently divided into six steps. The first two steps are devoted principally to the collection of the necessary data required prior to performing the calculations. Propeller section data is given at a variety of chordal stations, depending upon the manufacturer's preference; consequently, it is usually necessary to obtain values by interpolation at intermediate stations in order to satisfy the requirements of the numerical integration method. It has been found by experience that for hand calculations a conventional Simpson's rule integration procedure over 11 ordinates is perfectly adequate for calculating section areas and moduli and the appropriate stages for this calculation are outlined by steps 3 and 4. Having evaluated the section properties the calculation proceeds as shown in the remainder of the Table 18.1.

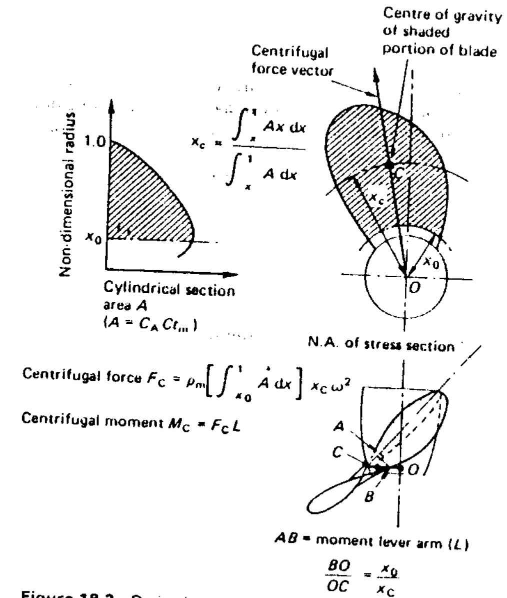

Figure 18.2 Derivation of mechanical blade loading components

A method of this type depends for its ease and generality of application upon being able to substitute values for the moment arm lengths *a* and *b* without recourse to a detailed analysis of the blade radial loading distribution. Again, experience has shown that this can be satisfactorily done providing that the propeller type is adequately taken into account. Typically, for a conventional, optimally loaded fixed pitch propeller, the moment arms *a* and *b* would be of the order of 0.70*R* and 0.66*R* respectively, whereas, for the corresponding controllable pitch propeller, these values would be marginally higher. Similar considerations also apply to the position of the blade centroid.

Cantilever beam analysis provides a very useful means of examining the relative importance of the various blade stress components delineated in equation (18.1). Table 18.2 shows typical magnitudes of these components expressed as percentages of the total stress for a variety of ship types, and although variations will naturally occur within a given ship group, several important trends can be noted from such a comparison. It becomes apparent from the table that the thrust component accounts for the greatest part of the total stress for each class of vessel, and that the direct centrifugal components, although comparatively small for the larger propellers, assume a greater significance for the smaller and higher-speed propellers. However, probably most striking is the

Table 18.1 Blade stress computation using the cantilever beam method

Calculation of the maximum tensile stress acting on a helical section of a propeller blade by the cantilever beam method

(1) Stress basis

P_s	10 820 kW
RPM	140
V_s	18.7 knots
w_T	0.26
D	4900 mm
x_0	0.25
x_c	0.51
P_0	5000 mm
A_E/A_O	0.73
ρ_m	7600 kg/m³
L	80 mm
Z	4
η_m	0.98
η_o	0.55
a	0.7*R*
b	0.66*R*

(2) **Stress section data**

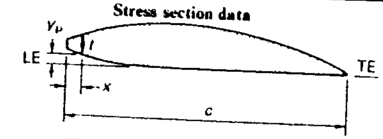

$C = 1000$ mm $\quad t_0 = N_0 R = 0.25 \times (4900/2) = 612.5$ mm

$r_0 = x_0 R = 0.25 \times (4900/2) = 612.5$ mm

x	0	55	110	220	330	497	665	832	1000	mm
y_p	55.0	39.0	25.0	6.5	0	0	0	0	0	mm
t	30.0	92.5	143.5	211.0	238.5	226.5	187.5	114.0	15.0	mm

(3) **Interpolated section data**

x	0	100	200	300	400	500	600	700	800	900	1000	mm
y_p	55.0	26.0	10	1	0	0	0	0	0	0	0	mm
t	30	136	195	232	236	226	205	173	128	73	15	mm

Chordal increment $\Delta C = \frac{C}{10} = 100$ mm

(4) **Evaluation of section properties**

Column	1	2	3	4	5	6	7	8	9
Ordinate	x	y_p	t	*Simpson's mult.*	$t \times S.M.$	$(2y_p + t)t$	$(2y_p + t)t \times S.M.$	$[3y_p(y_p + t) + t^2]t$	$[3y_p(y_p + t) + t^2]t \times S.M.$
1	0	55	30	$\frac{1}{2}$	15	4 200	2 100	447 750	223 875
2	100	26	136	2	272	25 568	51 136	4 233 952	8 467 904
3	200	10	195	1	195	41 925	41 925	8 614 125	8 614 125
4	300	1	232	2	464	54 288	108 576	12 649 336	25 298 672
5	400	0	236	1	236	55 696	55 696	13 144 256	13 144 256
6	500	0	226	2	452	51 076	102 152	11 543 176	23 086 352
7	600	0	205	1	205	42 025	42 025	8 615 125	8 615 125
8	700	0	173	2	346	29 929	59 858	5 177 717	10 355 434
9	800	0	128	1	128	16 384	16 384	2 097 152	2 097 152
10	900	0	73	2	146	5 329	10 638	389 017	778 034
11	1000	0	15	$\frac{1}{2}$	7	225	112	3 375	1 687
Total	—	—	—	—	2466	—	490 622	—	1 006 826 616

$$A = \int_0^c t\,dc = \frac{2 \times \sum \text{Col. 5} \times \Delta C}{3} = \frac{2 \times 2466 \times 100}{3} = \underline{164\,400\ \text{mm}^2}$$

$$\int_0^c (2y_p + t)t\,dc = \frac{2 \times \sum \text{Col. 7} \times \Delta C}{3} = \frac{2 \times 490\,622 \times 100}{3} = 32\,708\,133\ \text{mm}^3$$

$$\int_0^c [3y_p(y_p + t) + t^2]t\,dc = \frac{2 \times \sum \text{Col. 9} \times \Delta C}{3} = \frac{2 \times 1\,006\,826\,616 \times 100}{3} = 6\,712\,177\,733\ \text{mm}^4$$

From equation (18.5)

$$Z_m = \frac{2 \times 6\,712\,177\,733 \times 164\,400}{3 \times 32\,708\,133} - \frac{1}{2} \times 32\,708\,133 = \underline{6\,137\,424\ \text{mm}^3}$$

(5) **Blade centrifugal force**

(a) Calculate blade mass by

either

Evaluating Cols. (1)–(5) of the previous step for each defined helical section, thereby obtaining the radial distribution of section area (A). The blade mass (m) is then calculated from

$$m = \rho_m \int_{r_0}^{R} A\,dr$$

N.B. (The position of the blade centroid (x_c) can also be calculated in an analogous way as shown in Figure 11.1)

or

by use of approximation

$$m = 0.75 \times \text{mean radial thickness above stress section} \times \left(\frac{\text{total surface area}}{\text{No. of blades}}\right) \times \text{density}$$

viz. $$m = 0.75 \times 0.110 \times \left(\frac{0.73 \times \pi(4.90)^2}{4 \times 4}\right) \times 7600\ \text{kg}$$

$$m = 2158\ \text{kg}$$

(b) Centrifugal force is given by

$$F_c = 2\pi^2 m x_c D n^2$$

$$F_c = 2\pi^2 \times 2158 \times 0.51 \times 4.90 \times \left(\frac{140}{60}\right)^2\ \text{N}$$

i.e. $F_c = 580\ \text{kN}$

(6) **Calculation of section maximum tensile stress**

Section pitch angle $$\theta = \tan^{-1}\left(\frac{p_0}{\pi x_0 D}\right) = \tan^{-1}\left(\frac{5000}{\pi \times 0.25 \times 4900}\right) = 52.41^\circ$$

Propeller speed of advance $$V_a = V_s(1 - w_T) = 18.7 \times (1 - 0.26) = 13.8\ \text{knots} = 13.8 \times 0.515 = 7.10\ \text{m/s}$$

(a) Component due to propeller thrust:

$$\sigma_T = \frac{P_s \times \eta_m \times \eta_o \times (a - r_0) \times \cos\theta}{V_a \times Z \times Z_m} = \frac{(10\,820 \times 10^3) \times 0.98 \times 0.55 \times (0.7 - 0.25) \times 2450 \times \cos(52.41) \times 10^6}{7.10 \times 4 \times 6\,137\,424} = 22.50\ \text{MPa}$$

$P_E = T V_A \Rightarrow T = \frac{P_E}{V_A} = \frac{P_S\,\eta_m\,\eta_o}{V_A}$

(b) Component due to propeller torque:

$$\sigma_Q = \frac{P_s \times \eta_m \times (b - r_0) \times \sin\theta}{2\pi \times n \times b \times Z \times Z_m} = \frac{(10\,820 \times 10^3) \times 0.98 \times (0.66 - 0.25) \times \sin(52.14) \times 10^9}{2\pi \times \left(\frac{140}{60}\right) \times 0.66 \times 4 \times 6\,137\,424} = 14.50\ \text{MPa}$$

$P_D = 2\pi Q n \Rightarrow Q = \frac{P_D}{2\pi n} = \frac{P_S \cdot \eta_m}{2\pi n}$

(c) Component due to centrifugal bending moment:

$$\sigma_{CBM} = \frac{F_c \times L}{Z_m} = \frac{580\,000 \times 80 \times 10^6}{6\,137\,424} = 7.56\ \text{MPa}$$

(d) Component due to centrifugal force:

$$\sigma_{CF} = \frac{F_c}{A} = \frac{580\,000}{164\,400} = \underline{3.53\ \text{MPa}}$$

TOTAL $\underline{48.09\ \text{MPa}}$

Maximum tensile stress acting on section (σ) = 48.09 MPa

Table 18.2 Breakdown of the total maximum root tensile stress for a set of four different vessels

Component of stress	*Ship type*				
	Bulk carrier	*Fast cargo vessel*		*Twin-screw ferry*	*High-speed craft*
		5° astern rake	*15° forward rake*		
Thrust	72%	58%	71%	54%	51%
Torque	23%	33%	41%	36%	35%
Centrifugal bending	1%	5%	−17%	2%	3%
Centrifugal force	4%	4%	5%	8%	11%
Total	100%	100%	100%	100%	100%

effect of propeller rake as shown by the two propellers designed for the same fast cargo vessel. These propellers, although designed for the same powering conditions, clearly demonstrate a potential advantage of employing a reasonable degree of forward rake, since this effect leads to a compressive stress on the blade face. Consequently, this effect can allow the use of slightly thinner blade sections, which is advantageous from blade hydrodynamic considerations although, if carried too far, may lead to casting problems. Nevertheless, although the use of forward rake is desirable and indeed relatively commonly used, its magnitude is normally limited by propeller-hull interaction considerations; typically classification society clearance limitations or more reently propeller induced hull surface pressure calculations and studies.

In addition to providing a procedure for calculating the maximum stress at a given reference section, the cantilever beam method is frequently used to determine radial maximum stress distributions by successively applying the procedure described by Table 18.1 at discrete radii over the blade span. If such a procedure is adopted, then the resulting blade stress distributions have the form shown by Figure 18.3, where the typical bands of radial stress distribution for both linear and

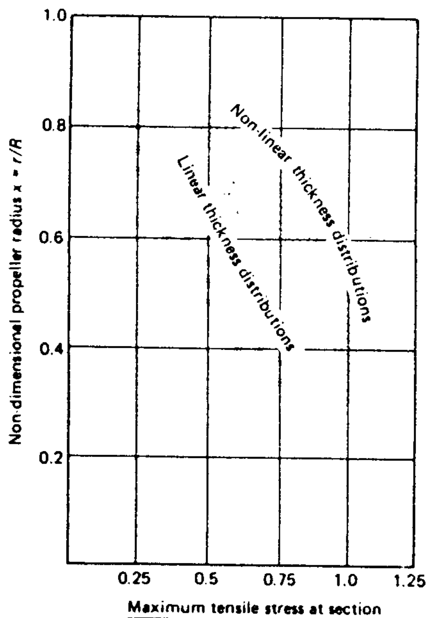

Figure 18.3 Comparative relationship between thickness and radial stress distribution

non-linear thickness distributions can be seen. The non-linear distribution is the most commonly employed, since although it encourages higher blade stresses, it permits a lower blade weight and also the use of thinner blade sections, which is advantageous from both the hydrodynamic efficiency and cavitation inception viewpoints. Linear thickness distributions are frequently adopted in the case of many smaller propellers for the sake of simplicity in manufacture. This design philosophy can, however, sometimes be mistakenly employed, since many small high-speed patrol craft have presented considerably more difficult hydrodynamic design problems than the largest bulk carrier. The linear distribution is also frequently employed in towing and trawling situations in order to give an added margin against failure.

Although the cantilever beam method provides the basis for commercial propeller stressing, it does have certain disadvantages. These become apparent when the calculation of the chordal stress distribution is attempted, since it has been found that the method tends to give erroneous results away from the maximum thickness location. This is partly due to assumptions made about the profile of the neutral axis in the helical sections since the method, as practically applied, assumes a neutral axis approximately parallel to the nose-tail line of the section. However, the behaviour of propeller blades tends to indicate that a curved line through the blade section would perhaps be more representative of the neutral axis when used in conjunction with this theory. Complementary reservations are also expressed since the analysis method is based on helical sections, whereas observations of blade failures tend to show that propellers break along 'straight' sections as typified by the failure shown in Figure 18.4.

18.2 Numerical blade stress computational methods

In order to overcome these fairly fundamental problems, which manifest themselves when more advanced studies are attempted, intensive research efforts led in the first instance to the development of methods based upon shell theory (References 9, 10). However, as computers became capable of handling more extensive computations and data, work concentrated on the finite element approach using plate elements initially and then more recently isoparametric and superparametric solid elements. Typical of these latter methods are the approaches developed by Ma and Atkinson (References 11-13). The principal advantage of these methods over cantilever beam methods is that they evaluate the stresses and strains over a much greater region of the blade than can the simpler methods, assuming of course, that it is possible to define the hydrodynamic blade loadings accurately. Furthermore, unlike cantilever beam methods, which essentially produce a

Figure 18.4 Propeller blade failure

criterion of stress, finite element techniques develop blade stress distributions which can be correlated more readily with model and full-scale measurement.

In order to evaluate blade stress distributions by finite element methods of the type referenced, the propeller blade geometry is discretized into some 60 or 70 thick-shell finite elements; in some approaches more elements can be required, depending upon the element type and their formulation. In each of the approaches the finite elements naturally require the normal considerations of aspect ratio and of near-orthogonality at the element corners that are normally associated with these types of element. Figure 18.5 shows some discretizations for a range of biased skew propellers: clearly in the extreme tip regions the conditions of near orthogonality are sometimes difficult to satisfy completely and compromises have to be made.

The finite element method is of particular importance for the stressing of highly skewed propellers, since the presence of large amounts of skew influence the distribution of stress over the blades considerably. Figure 18.6, taken from Carlton (Reference 14) shows the distributions of blade stress for a range of balanced and biased skew designs of the same blade in comparison to a non-skewed version. In each case the blade thickness distribution remains unchanged. For ease

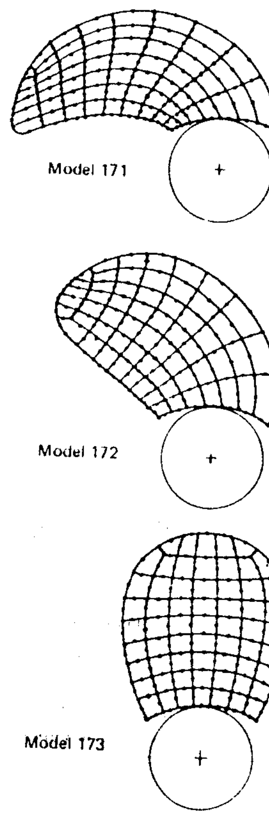

Figure 18.5 Finite element discretizations

of comparison, the isostress contour lines in this Figure are drawn at 20 MPa intervals on each of the expanded blade outlines. It is immediately obvious from this comparison that the effect of skew, whether of the balanced or biased type, is to redistribute the stress field on each blade so as to increase the stresses near the trailing edge. In particular, both propellers *C* and *E* give trailing edge stresses of similar magnitudes and also relatively high stresses, of the order of the root stress for a symmetrical design, on the leading edge. This is not the case for the symmetrical or low-skew designs. The highly stressed region on propeller *E* is also seen to be rather more concentrated than that on propeller *C*. Furthermore, the tendency for the tip stresses on the blade face, which are of a low tensile or compressive nature in the symmetrical and biased skew designs, does not so clearly manifest itself in the balanced design. The accuracy of the tip

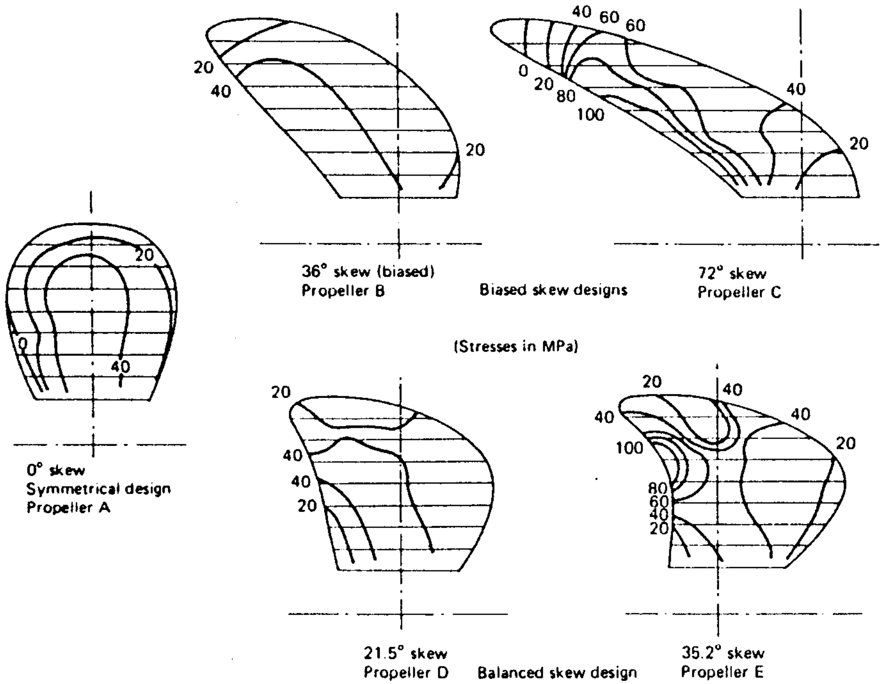

Figure 18.6 Distribution of maximum principal stress about a series of blades having different skew designs

stress prediction is, however, limited by both the finite element representation and the accuracy of the hydrodynamic load prediction.

An important feature also noted, although not directly shown in Figure 18.6, is that small changes in the trailing edge curvature can cause a marked change in the trailing edge stress distribution. For example, if the blade surface area were reduced by, say, 5–10% but the leading edge profile were kept constant, thus effectively increasing the skew or blade curvature, this would significantly increase the trailing edge stresses.

The orientation and nature of the stress field which exists on the propeller blade is an important consideration from many aspects. For the traditional low skewed designs of propeller, the orientation of the maximum principal stresses is generally considered to be approximately in the radial direction for the greater part of the blade away from the tips and also the leading and trailing edges at the root. Furthermore, the chordal stress components are generally considered to be less than about 25% of the maximum radial stress. Analysis of the results obtained from propeller studies shows that these ideas, although requiring modification can to a very large extent be generalized to highly skewed designs. It is seen that the orientation of the maximum principal stresses normally lies within a band 30° either side of the radial direction. With regard to the magnitudes of the chordal stresses, it is also generally found that these rise to between 30% and 40% of the maximum radial stress in the case of the highly skewed designs. As might be expected in the case of biased skew designs the magnitude of the chordal component of stress tends to achieve a maximum nearer to the trailing edge than for the other propellers at the root section.

Blade deflection, although not of primary importance for the strength integrity of the blade, is important for hydrodynamic considerations of the section angle of attack and camber distribution. For conventional and balanced skew propellers the deflection characteristics seem to be predominantly influenced by a linear displacement of the section together with a slight rotation. In the case of a biased skew propeller, however, the rotational and translational components of the blade deflection are considerably magnified. These changes effectively reduce the section angle of attack, and owing to the non-linear values of the deflection curve, the section camber is reduced as a result of the 'lifting' of leading and trailing edges. In the case shown for propeller *C* in Figure 18.6, the rotational component approximated to a reduction in pitch of the section of the order of 0.5° relative to its unloaded condition. The problem of the hydro-elastic response of propeller blades is an important one, and this has been addressed by Atkinson and Glover (Reference 15).

When undertaking finite element studies the choice of element is critical if valid results are to be obtained from the analysis. It is insufficient to simply use arbitrary formulations for the blades; use needs to be made of elements which can readily accept all of the loadings conventionally met in blade analysis problems. This point can be readily illustrated by considering comparative studies; for example, those undertaken by the ITCC (Reference 16) in which the results derived from finite element computations from six organizations, using some seven different finite element formulations of the problem, were compared to experimental results at model scale. The propeller chosen for the study was a 254 mm diameter, 72° biased skew design – Propeller *C* of Figure 18.6 taken from Reference 14. The model had been subjected, experimentally, to point loading at the 0.7*R* and 50% chordal location, and was instrumented with four sets of strain gauge rosettes located in the root section of the blade on the pressure side at 0.3*R*. Figure 18.7 shows the results obtained from the subsequent ITTC exercise and the correlation that was derived with the experimental results from the various finite element studies undertaken by the contributing organizations. Also shown in the Figure is the result of a cantilever beam calculation for the same loading condition. It can be seen that although the general trend of the measured result tends to be followed by the various finite element computations, there is a considerable scatter in terms of the magnitudes achieved between the various methods employed. As a consequence, Figure 18.7 underlines the need for a proper validation of the finite element methods used for the analysis of highly skewed propellers. Such validation can only be undertaken by a correlation between a theoretical method with either a model or full-scale test, since whilst the trends may be predicted by a non-validated procedure as seen by the Figure, it is the actual stress magnitudes which are important for fatigue assessment purposes. Furthermore, Figure 18.7 amply demonstrates that the cantilever beam method does not realistically predict the magnitudes of the loadings experienced in the root section of highly skewed blade.

18.3 Detailed strength design considerations

The detailed design of propeller thickness distributions tends to be a matter of individual choice between the propeller manufacturers, based largely on a compromise between strength, hydrodynamic and manufacturing considerations. Additionally, in the case of the majority of vessels, there is also a requirement for the propeller blade thickness to meet the requirements of one of the classification societies. In the case of Lloyd's Register of Shipping, as indeed with most of the other classification societies, these rules are based upon the cantilever beam method of analysis and essentially derived from equation (18.3).

The techniques of propeller blade stressing discussed in Sections 18.1 and 18.2 are applied to all types of propeller and it is, therefore, relevant to consider briefly the special characteristics of particular types of propeller in relation to the conventional fixed pitch propeller upon which the discussion has so far centred.

1. *Ducted propellers.* As ducted propellers, in common with transverse propulsion unit propellers, tend to have rather more heavily loaded blade outer sections than conventional propellers, the effective centres of action of the hydrodynamic loading tend to act at slightly larger radii. However, it must also be remembered that since a proportion of the total thrust is taken by the duct, the appropriate adjustment must be made for this in the stress calculation. Additionally, the duct can also have an attenuating influence over the wake field, which to some extent improves the fluctuating load acting on the blades.
2. *Tip-unloaded propellers.* Noise reduced or tip-unloaded propellers, which have largely evolved from naval practice and modern thinking on reducing hull pressures in merchant vessels, tend to concentrate the blade loading nearer the root sections as shown by Figure 18.8. This feature, which tends to reduce the effective centres of action of the hydrodynamic loading, coupled with the slightly lower propulsive efficiency of these propellers, tends to provide less onerous mean root stresses than would be the case with conventional propellers.
3. *Controllable pitch propellers.* Controllable pitch propellers, by way of contrast, tend to present a more difficult situation in contrast to fixed pitch propellers due to the problems of locating the blade onto the palm. The designers of hub mechanisms prefer to use the smallest diameter blade palms in order to maximize the hub strength, and, conversely, the hydrodynamicist prefers to use the largest possible palm in order to give the greatest flexibility to the blade root design. These conflicting requirements inevitably lead to a compromise, which frequently results in the root sections of the blade

Symbol	Element type	No. of elements
■	3-dimensional hexahedra	70
▲	Superparametric thick shell	97
◇	3-dimensional hexahedra	160
△	Isoparametric shell	161
○	2-dimensional triangular plane	161
□	2-dimensional triangular plane	161
●	3-dimensional hexahedra	300

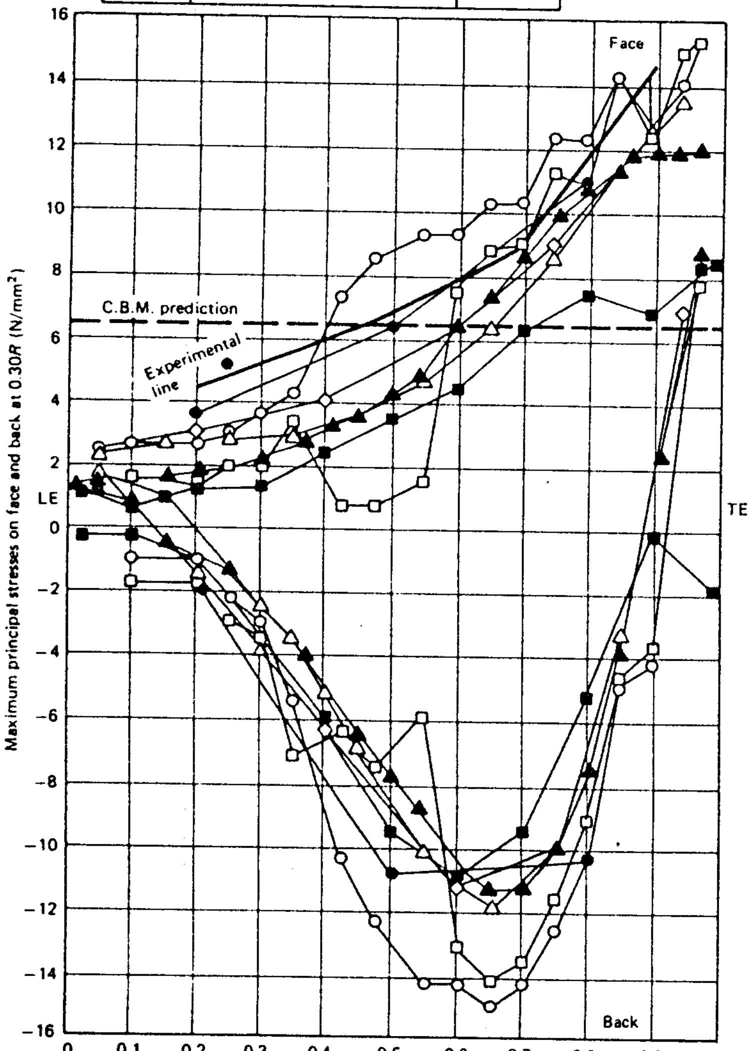

Figure 18.7 Correlation of different finite element calculation methods with experiment (Reproduced from Reference 16, with permission)

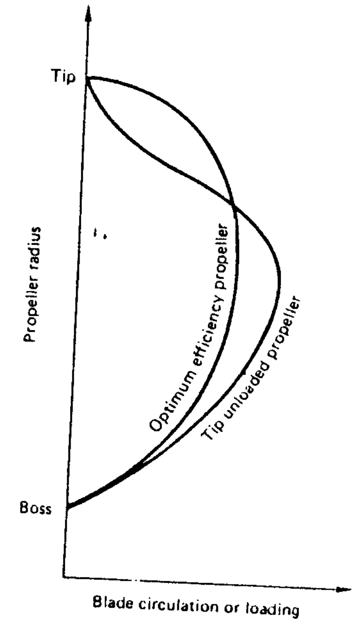

Figure 18.8 Comparison between tip unloaded and optimum efficiency radial loadings

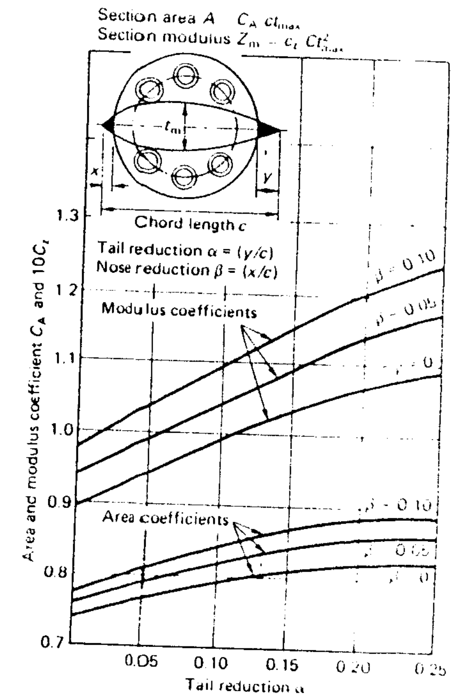

Figure 18.9 Typical variations in root section properties for controllable pitch propeller

being allowed to 'overhang' the palm. This feature, although introducing certain discontinuities into the design, is not altogether undesirable, since it allows both the root section modulus and area to be increased, as shown for a typical controllable pitch propeller root section profile by Figure 18.9. Additionally, in many designs of controllable pitch propeller the blade bolting arrangements are such as to place a further limitation on the maximum section thickness. It therefore becomes necessary on occasions, although undesirable, for the blade bolt holes to significantly penetrate the root fillets in order to fit the blade onto the palm.

The modes of operation of a controllable pitch propeller are very varied, as discussed in Reference 17. Generally, however, from the stressing point of view these off-design operating conditions remain unconsidered unless prolonged working in any given mode is indicated.

Ice class requirements can also present additional problems for controllable pitch propellers. Since the blades have restricted root chord lengths, the additional ice class thickness requirements in some instances result in root section thickness to chord ratios in excess of 0.35, which from the hydrodynamic viewpoint gives both poor efficiency and greater susceptibility to cavitation erosion.

4. *High-speed propellers.* High-speed propellers generally have better in-flow conditions than their larger and slower-running counterparts, although poorly designed shafting support brackets are sometimes troublesome. Consequently, high wake induced cyclic loads are not usually a problem unless the shafting is highly inclined. Centrifugal stresses, as shown by Table 18.2, tend to take on a greater significance due to the higher rotational speeds, and therefore greater attention needs to be paid to the calculation of the mechanical loading components.

Naturally these propellers, if in either a ducted or controllable pitch form, can take on some of the characteristics of the previously discussed classes. One feature, however, which may be introduced occasionally in attempts to control root cavitation erosion, is a system of holes bored through the blade along the root section as sketched in Figure

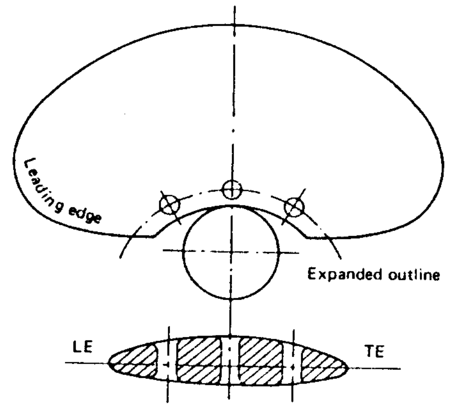

Figure 18.10 A method of root cavitation relief

18.10. Whilst the purpose of these holes is to relieve the pressure differential across the blade section and to modify the flow behind the fixed cavitation at the point of its break-up, their presence necessitates a careful review of the root section thicknesses. In addition, large blending radii need to be specified so as to merge the holes into the blade surface in as fair a way as possible.

18.4 Propeller backing stresses

When a propeller undergoes a transient manoeuvre considerable changes occur in blade stress levels and their distribution. Figure 18.11 shows typical changes in the stress measured on the blades of a single screw coaster undergoing a stopping manoeuvre. This vessel was fitted with a conventional non-highly skewed fixed pitch propeller.

Experience with highly skewed propellers when undertaking emergency stopping manoeuvres has led to the bending of the blade tips in certain cases (Reference 18). This bending which frequently occurs in the vicinity of a line drawn between about 0.8*R* on the leading edge to a point at about 0.60*R* on the trailing edge is thought to be due to two principal cases, see Figure 22.10. The first is due to simple mechanical overload of the blade tips from the quasi-steady hydrodynamic loads causing stresses leading to plastic deformation of the material; the second is from the transient vibratory stresses, of the type shown in Figure 18.11, which occur during the manoeuvre. These latter stresses are not wholly predictable within the current state of theoretical technology but need to be estimated.

As part of the design process a fixed pitch, highly skewed propeller should always be checked for overload from the quasi-steady mean hydrodynamic stresses using a suitable hydrodynamic criterion. Most commonly this criterion is the bollard pull astern condition since at present this is thought to be most representative of the worst condition a propeller is likely to see in a transient manoeuvre. Clearly these backing stress predictions need to be based on a lifting surface hydrodynamic model together with a finite element analysis. However, it must be recognized that hydrodynamic codes, when used for backing stress calculations, are operating far from their originally intended purpose: as a consequence, the analysis must be viewed in this context.

18.5 Blade root fillet design

In this chapter consideration has centred only upon the blade stresses, without any account being made for the root fillets where the blade meets either the propeller boss or blade palm. The root fillet geometry is complex, since it is required to change, for conventional propellers, in a continuous manner from a maximum cross-sectional area in the mid-chord regions of the blade to comparatively small values at the leading and trailing edges. Notwithstanding the complexities of the geometry, the choice of root fillet radius is of extreme importance. For conventional propeller types, if a single radius configuration is to be deployed, it is considered that the fillet radius should not be less than the thickness of 0.25*R*.

The use of a single radius at the root of the blade always introduces a stress concentration; however, the introduction of a compound radiused fillet reduces these concentrations considerably. Therefore the use of fillet profiles of the type described by Baud and Tum and Bautz is desirable which, for most marine propeller applications, can be approximated to two single radii having common tangents. Typically, such a representation may be achieved by using radii of magnitudes 3*t* and *t*/3, having common tangents with each other and with the blade and boss respectively.

The results of the blade surface stress distribution for symmetrical and balanced skew designs imply that the full size of the fillet should be maintained at least over the middle 50% of the root chord. In the case of extreme biased skew designs, there is a sound case for continuing the full fillet configuration to the trailing edge of the blade in order to minimize the influence of the stress concentration factor in the highly stressed trailing edge regions.

18.6 Residual blade stresses

The steady and fluctuating design stresses as produced by the propeller absorbing power in a variable wake

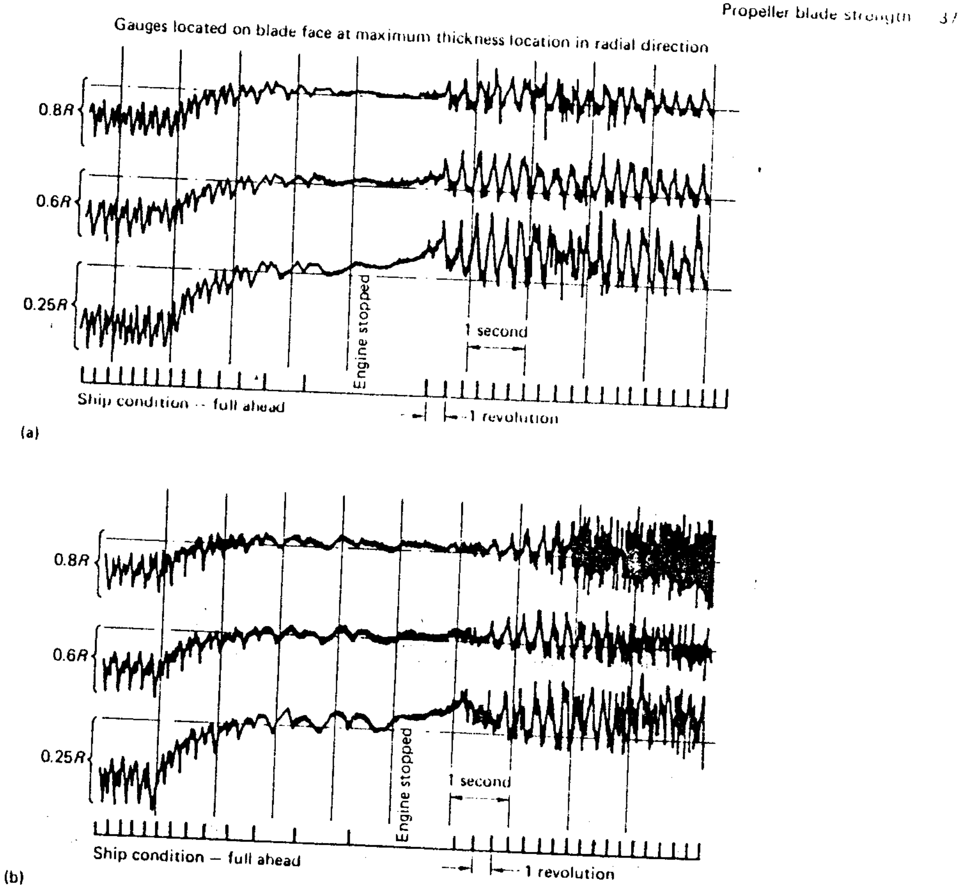

Figure 18.11 Crash stop manoeuvres measured on a single-screw coaster

field represent only one aspect of the total blade stress distribution. Residual stresses, which are introduced during manufacture or during repair, represent the complementary considerations.

Full-scale experience relating to residual stresses is limited to a comparatively few studies. Work by Webb *et al.* (Reference 19) is typical of these studies in which measurements have been made for propellers subjected to local heating. These measurements relate to high-tensile brass and manganese–aluminium bronze propellers which have been subjected to heating subsequent to manufacture. In these cases, residual stresses of the order of 155 MPa and 185 MPa were measured by the trepanning technique for residual stress measurement. Little published information exists, however, for the level or nature of residual stress in new or unrepaired castings. Clearly this must, in some measure, be due to the semi-destructive nature of the measurement procedure involved in determining the residual stress field.

Investigations by Lloyd's Register of Shipping (Reference 14) into propeller failures, from causes other than by poor repair or local heating of the boss, have shown that residual surface stresses measured in blades adjacent to the failed blade can attain significant magnitudes. The technique used for these latter measurements is that of bonding purpose-designed strain gauge rosettes to the surface of the blade and then incrementally milling a carefully aligned hole through the centre of the three rosette configuration.

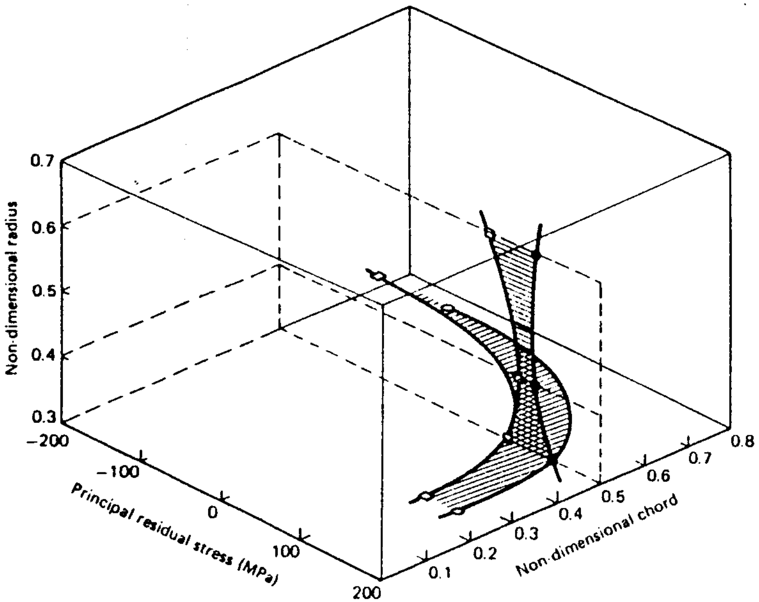

Figure 18.12 Measured residual stresses on a propeller blade

At each increment of hole depth, a measurement of the relaxed strain recorded by each guage of the rosette is made. This method, used in association with a correctly designed milling guide, is relatively easy to apply and also has been proved to give reliable results in the laboratory on specially designed calibration test specimens. An example of the results gained using this procedure is given in Figure 18.12 for a five-blade, nickel–aluminium bronze, forward-raked propeller having an approximate finished weight of 14 tonnes. From the figure it is seen that the measured residual stresses in this case are of a significant magnitude and also tensile in nature over much of the blade. Indeed, the magnitudes in this case reach tensile values of between two and three times the normally accepted design stress levels. Furthermore, it can also be seen that the principal stresses at a given measurement point are of similar magnitudes. This, therefore, implies the introduction of a strong biaxiality into the stress field on the blade surface, which from pure design considerations would be expected to be of a predominantly radial nature. Analysis of the through-thickness characteristics of the relieved strain for the same propeller blade suggest that the residual stresses possess a strong through-thickness variation with high stresses on the blade surface, which then decay fairly rapidly within the first 1–2 mm below the surface.

To extrapolate the results of a particular residual stress measurement to other propellers would clearly be unwise. Nevertheless, since these stresses play a part in the fatigue assessment of the propeller, the designer should be aware that they can obtain high magnitudes, although full-scale experience in terms of the number of propeller failures would suggest that residual stresses are not normally this high. The magnitudes of residual stress, although unclear in their precise origins, are strongly influenced by the thermal history of the casting, material of manufacture and the type or nature of the finishing operation. Furthermore, it is also known from measurements that large variations can exist between measurements made at equivalent positions on consecutive blades of the same propeller.

18.7 Allowable design stresses

The strength design of a propeller must be based on a fatigue analysis, it is insufficient and inaccurate to base designs on simple tensile strength or yield stress criteria. In order to relate the blade stresses, both steady state and fluctuating, to a design criteria some form of fatigue analysis is essential. Clearly, the most obvious choices are the modified Goodman and

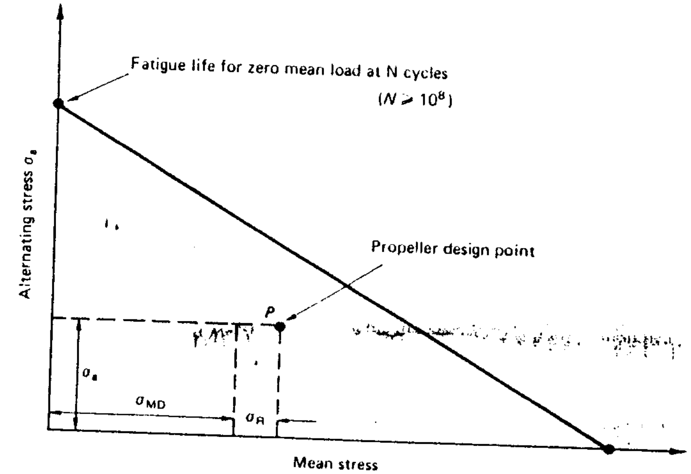

Figure 18.13 Propeller fatigue analysis

Soderberg approaches of classical fatigue analysis. In these approaches the mean stress is plotted on the abscissa and the fluctuating stress on the ordinate (Figure 18.13). To evaluate the acceptability of the particular design a linear relationship is plotted between the fatigue life at zero mean load and some point on the abscissa. The fatigue life should always relate to 10^8 cycles or greater as discussed in Chapter 17; however, the point on the abscissa at which the linear relationship should be drawn is less certain. In general engineering practice the ultimate tensile strength is the basis of the modified Goodman approach, which is generally considered a satisfactory basis for analysis; however, there is a body of experimental material data (Reference 19) which suggests the point of intersection may well be in the region of the 0.15% proof stress. If this is the case then the more conservative Soderberg approach is probably the more correct for marine propellers.

As is seen in Figure 18.13, the magnitude of the alternating stress σ_a is a single component dependent on the fluctuations in the wake field in which the propeller blade is working. The steady-state component is the sum of two components σ_{MD} and σ_R, where these relate respectively to the mean design component, as determined from either cantilever beam or finite element studies, and the level of residual stress considered appropriate.

The comparison of the design stresses with fatigue characteristics of the propeller material is a complex procedure. Figure 18.14 demonstrates this procedure in outline form as part of the overall propeller design process, which is discussed more fully in Chapter 21. From Figure 18.14 it is apparent that the design mean σ_{MD} and alternating σ_a stresses derive directly from the hydrodynamic analyses of the blade working in the wake field. Hence these parameters are directly related to the blade design and the environment in which the propeller is operating. The residual stress allowance σ_R is a function of the casting size, propeller material and manufacturing technique. The magnitude of this stress allowance is therefore very largely indeterminate in the general sense; however, in the absence of any other information or indications to the contrary, it would be prudent to allow a value of between 15 and 25% of the 0.15% proof stress for σ_R. The propeller fatigue characteristics are clearly dependent on the choice of material (see Figure 17.7), however, these basic characteristics need to be modified to account for casting size and other environmental factors, as discussed in Chapter 17. Having, therefore, defined the various parameters in Figure 18.13, a judgement based on normal engineering principles can be made as to whether the apparent factor of safety is appropriate. In propeller technology it is unikely that a factor of safety of less than 1.5 would be considered acceptable.

Casting quality has a profound influence on the life of a propeller in service. The defects found in copper alloy propellers are generally attributable to porosity in the form of small holes resulting from either the releasing of excess gases or shrinkage due to solidification. Alternatively, the defects can be oxide inclusions in the form of films of alumina, formed during the pouring stage of propeller manufacture, which have a tendency to collect near the skin of the casting. The location of a defect is obviously critical. For conventional, low skew propellers, defects in the centre of

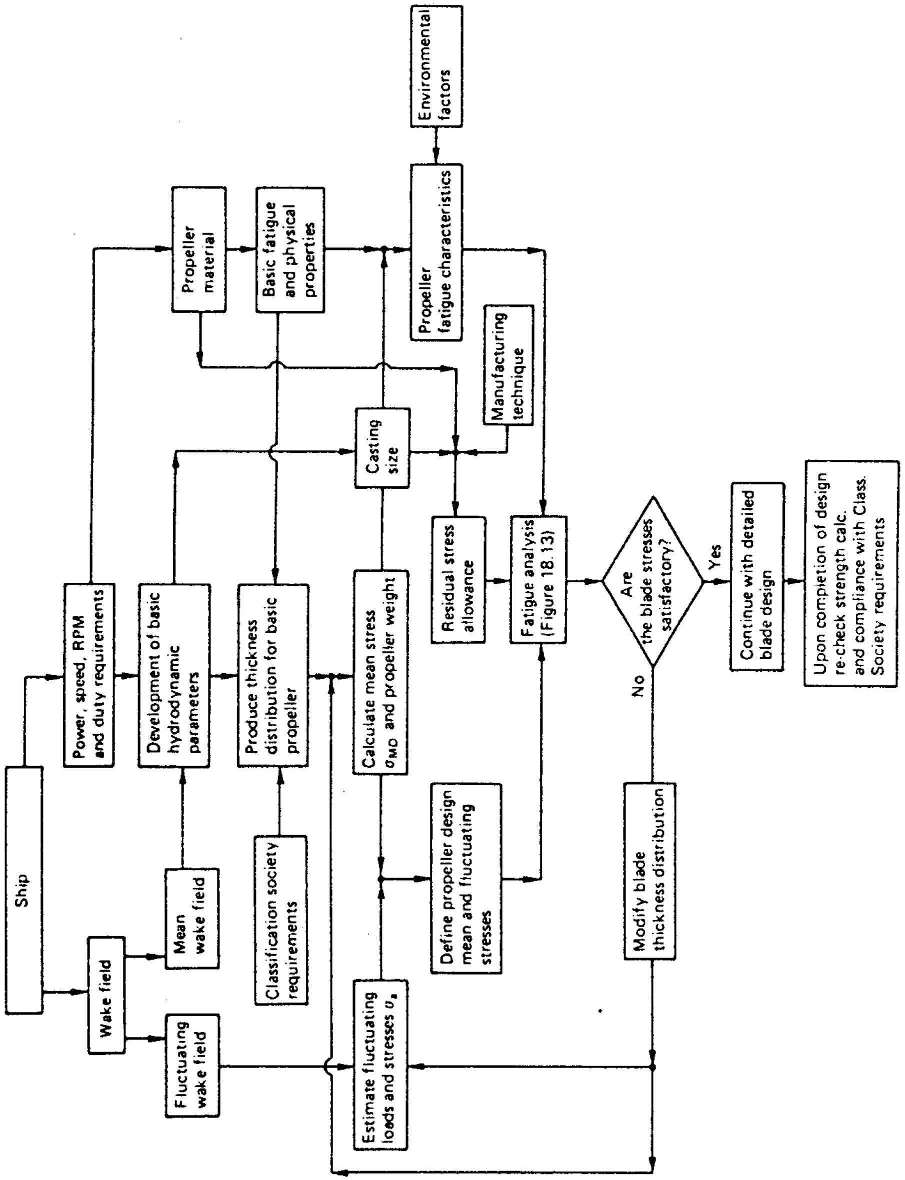

Figure 18.14 Propeller strength analysis design procedure

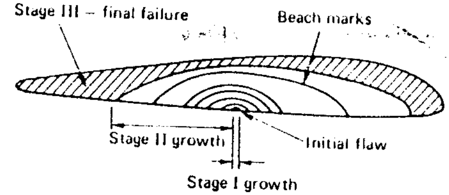

Figure 18.15 Visual characteristics of fatigue failure

the blade section and on the suction face are of less concern than those located on or near the pressure face in the mid-chord region just above the run-out of the fillet radii. Alternatively, in the case of highly skewed propellers casting defects in the trailing edge region of the blade are of critical importance in view of the location of the stress concentrations within the blade. Considerations of this type lead to the concept of acceptable defect criteria for marine propellers, which in turn introduces the subject of fracture mechanics.

The visual characteristics, as shown by Figures 18.15 and 22.9, of a propeller blade which has failed by fatigue action, are generally similar for all propellers, although in some cases the beach marks are more clearly visible than in others. Attempts at correlating the relative geometric form of these markings during the crack growth have been made from observations of failed propellers. The advantages of obtaining such a relationship are that the aspect ratio of the crack can be directly related to the stress intensity factor, which may then be used in conjunction with fracture toughness information to assess acceptable defects and crack propagation rates. Work by Roren (Reference 20) and Tokuda (Reference 21) has given coefficients for the Stage II crack propagation equation:

$$\frac{da_c}{dN} = c(\Delta k)^m \qquad (18.6)$$

as delineated in Table 18.3, these results being derived from samples cut from failed propeller blades. The tests for the manganese–aluminium alloy used the centre slotted type specimen, whilst those for the nickel–aluminium alloy were defined as being of the wedge opening load type.

Notwithstanding the encouraging work that has been done in the field of acceptable defects and on Stage II crack propagation, for example References 22 and 23, in which the crack moves from its initiation phase, Stage I, through to eventual rapid failure in Stage III, much work remains to be done in understanding fully the mechanisms of the Stage I crack growth for propeller materials.

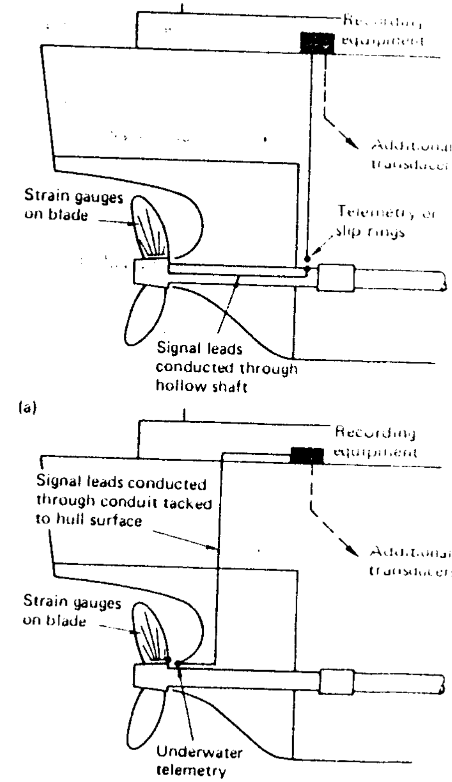

Figure 18.16 Full-scale blade strain measurement techniques (a) hollow bored shaft method; (b) underwater telemetry method

18.8 Full-scale blade strain measurement

By comparison with the amount of theoretical work undertaken on the subject of propeller stresses, there have been few full-scale measurement exercises. The reason for this comparative dearth of full-scale data has undoubtedly been due to the difficulties hitherto encountered in instrumenting the chosen ship. Traditionally if propeller strain measurements were contemplated it has always been necessary to hollow bore the tail shaft of the vessel in order to conduct the signal wires from the strain gauges located on the propeller blades through to a system of slip rings inside the vessel. Figure 18.16(a) shows in schematic form

Table 18.3 Material constants for crack propagation equation

Material	*c*	*m*	*Mean stress* (kgf/mm²)	*Condition*
Mn–Al bronze	6.6×10^{-11}	3.7	7.0	Sea water at 4 Hz
Ni–Al bronze	4.97×10^{-13}	4.7	0	Simulated sea water at 2.5 Hz
	3.37×10^{-14}	5.2	0	Simulated sea water at 5 Hz
				(Threshold value = 25 kgf/mm$^{3/2}$)

this arrangement. Despite the obvious disadvantages of this method some notable full-scale studies have been conducted (References 24–31) and these, together with others, have formed the nucleus of full-scale data in the publicly available literature.

In recent years the use of underwater telemetry techniques have been explored as an alternative form of measurement (Reference 14). The use of telemetry methods has obvious advantages in that the signal can be transmitted at radio frequencies across a suitable water gap and thus avoid the need to bore the tail shaft. The most usual procedure is to fix the transmitter to the forward face of the propeller boss, under the rope guard, and transmit the signals to a receiver located on the stern seal carrier, as seen in Figure 18.16(b). Having bridged the rotating to static interface in this way the signal leads can be conducted over the hull surface, protected by conduit tacked to the hull skin, to a convenient location for the recording instruments.

With regard to the conduct of blade strain measurement trials, the general principles of ship speed trials discussed in Chapter 16 should be adhered to, including the requirements for the measurement of ship speed.

References and further reading

1. Hecking, J. Strength of propellers. *Mar. Eng. & Shipping Age*, October, 1921.
2. Rosingh, W.H.C.E. Design and strength calculations for heavily loaded propellers. *Schip en Werf*, 1937.
3. Romson, J.A. Propeller strength calculation. *Mar. Eng. & Nav. Arch.*, **75**, 1952.
4. Morgan, W.B. An Approximate Method of Obtaining Stress in a Propeller Blade. DTMB Rep. 919, 1954.
5. Burrill, L.C. A short note on the stressing of propellers. *The Shipbuilder and Mar. Eng. Builder*, August, 1959.
6. Weber, R. Festigkeitsberechnung für Schiffspropeller. *Schiffbautechnik*, II, 8/1961.
7. Schoenherr, K.E. Formulation of propeller blade strength. *Trans. SNAME*, April, 1963.
8. Sinclair, L. Propeller blade strength. *Trans. IESS*, **119**, 1975/76.
9. Cohen, J.W. On Stress Calculations in Helicoidal Shells and Propeller Blades. TNO Rep. No. 215.
10. Conolly, J.E. Strength of Propellers. *Trans. RINA*, **103**, 1961.
11. Atkinson, P. The prediction of marine propeller distortion and stresses using a superparametric thick shell finite element model. *Trans. RINA*, **115**, 1973.
12. Ma, J.H. Stresses in marine propellers. *J. Ship Res.*, **18**(4), 1974.
13. Atkinson, P. A practical stress analysis procedure for marine propellers using curved finite elements. *Propellers '75 Symp., Trans. SNAME*, 1975.
14. Carlton, J.S. Marine propeller blade stresses, *Trans. I.Mar.E.*, 1984.
15. Atkinson, P., Glover, E.J. Propeller hydroelastic effects. *Propellers '88 Symp., Trans. SNAME*, 1988.
16. 18th Proc – Report of Propulsor Committee, Kobe, 1987.
17. Hawdon, L., Carlton, J.S., Leathard, F.I. The analysis of controllable pitch propellers at off-design conditions. *Trans. I.Mar.E.*, **88**, 1976.
18. Blake, W.K., Meyne, K., Kerwin, J.E., Weithedorf, E., Frisch, J. Design of APL C-10 propeller with full scale measurements and observations under service conditions. *Trans. SNAME*, 1990.
19. Webb, A.W.O., Eames, C.F.W., Tuffrey, A. Factors affecting design stresses in marine propellers. *Propellers '75 Symp., Trans. SNAME*, 1975.
20. Roren, E., Solumsmoen, O, Tenge, P., Sontvedt, T. Marine propeller blades – allowable stresses, cumulative damage and significance of sharp surface defects. *2nd Lips Propeller Symp.*, 1973.
21. Tokuda, S., Okuyamu, Y., Inoue, H., Denoh, S. Fatigue failure in marine propeller blades. *Propellers '78 Symp., Trans. SNAME*, 1978.
22. Denoh, S., Morimoto, K., Nakano, I., Moriya, K. Fatigue strength in marine propeller blades, Part I. Fatigue strength of propeller materials. *J. MESJ*, **15**(4), 1979.
23. Nakano, I., Oka, M., Gotoh, N., Moriya, K., Denoh, S, Sasaki, Y. Fatigue strengh in marine propeller blades, Part II. Allowable flaw size in propeller blades. *J. MESJ.*, **15**(5), 1979.
24. Wereldsma, R. Stress measurements on a propeller blade of a 42 000 ton tanker on full scale. *ISP*, 1964.

25. Chirila, J.V. Dynamische Beanspruchung von Propellerflugeln auf dem Motorschiff 'Pekari'. *Schiff und Hafen*, 3, 1970.
26. Dashnaw, F.J., Everett Reed, F. Propeller strain measurements and vibration measurements on the SS Michigan. *Marine Technology*, October, 1971.
27. Keil, H.G., Blaurock, J.J., Weitendorf, E.A. Stresses in the blades of a cargo ship propeller. *J. Hydronautics*, 1, January, 1972.
28. Chirila, J.V. Investigation of stresses at the propeller blade of a container ship. *Shipping World and Shipbuilder*, November, 1971.
29. Watanabe, K., Hieda, N., Sasajima, T., Matsuo, T. Propeller Stress Measurements on the Container Ship 'Hakone Maru'.
30. Ueta, Y., Maebashi, M., Shiode, K., Jakesawa, S., Takai, M. Stress measurements on a propeller blade. *Bulletin MESJ*, 2, March, 1974.
31. Sontvedt, T., Johansson, P., Murgass, B., Vaage, B. Loads and response of large ducted propeller systems. *Symp. on Ducted Propellers, Trans. RIN* 1, 1973.

19 Propeller manufacture

Contents

Propeller manufacture is an extensive subject, embracing not only many engineering machine shop skills but also foundry techniques related to the casting of quantities of metal, sometimes of the order of 200 tonnes, into a precise geometric form. Furthermore, the importance of propeller manufacture lies both in interpreting the hydrodynamic design into physical reality and in ensuring that the manufacturing process does not give rise to defects which could bring about the premature failure of the propeller.

Propeller manufacture relies on two basic techniques; the use of full wooden patterns for multiple use, or the construction of a unique mould which after casting will be broken up. Which technique is used is a techno-economic question depending on the type of propeller, the number to be produced, the finishing technique and the size of the propeller. However, in order to gain an understanding of the manufacturing process in generalized terms, the traditional method of manufacture will be described before outlining the range of variants to this process.

19.1 Traditional manufacturing method

Originally propellers were of simple shape and made in either cast iron or steel. These early propellers were usually cast in the engine builder's own foundry and were fitted to the vessel in a largely 'as-cast' condition, except for some necessary fettling and machining of the bore. Today the materials, as discussed in Chapter 17, have largely changed to the bronzes and propellers are manufactured to a high standard of surface finish and dimensional accuracy in foundries and workshops devoted solely to the manufacture of propellers.

Each propeller is nominally of a different design, and as a consequence it is quite rare for a propeller manufacturer to receive a significant run of propellers to the same design. The traditional method of manufacture, therefore, reflects this situation and is based on the production of a mould for each propeller which is to be manufactured.

In some propeller foundries the propeller will be cast in large pits sunk into the floor, whilst in others the mould will be built onto the actual floor of the foundry. There is no general procedure for this and each manufacturer works out an individual technique which takes into account safety, versatility, space available and costs of production. Hence the whole manufacturing process will be found to vary from one manufacturer to another in matters of detail, but the general theme of manufacture follows the same pattern and it is the underlying theme which will be outlined here.

The mould for each propeller is constructed in two halves: the bed, the upper surface of which defines the pressure side or pitch face of the blade, and the top, the lower surface of which defines the suction surface or back of the propeller blades. As a consequence, propellers are generally cast 'face downwards' in the mould.

The traditional mould material is a pure washed silica sand, having an average grading of between 20 and 50 mesh, and is mixed with controlled amounts of ordinary Portland cement and water using the Randupson process (Reference 1).

A typical Randupson sand mixing and reclamation plant is shown in Figure 19.1. From this figure it can be seen that previous moulds, once they have been broken into manageable proportions and the reinforcing rods have been broken out, are passed through a crusher and then mechanically transported to a series of vibrating sieving screens, the first of which is sufficient to reject lumps and foreign matter such as nails and so on, whilst the latter stages pass only grains and dust. From the vibrating screens the reconditioned sand passes into a hopper which is adjacent to two other hoppers, one containing new sand and the other cement. The mixing mill is then fed in the required amounts from each of these hoppers and after dry mixing for a period of time, of the order of 2–5 minutes, water is then added in carefully controlled amounts which depends upon the moisture content of the new sand and also the shop humidity. The wet mixing is then continued for a period of time, whereupon the contents are discharged into a portable skip for transport to the moulding site elsewhere in the foundry. In many cases, for economy reasons, previous mould material is used to construct those parts of the mould which are not directly in contact with the molten metal of the new propeller; however, a new sand mixture should be used for those parts which are in contact with the molten metal.

Prior to the Randupson process being introduced, loam was almost universally used; however, extensive artifical drying is necessary with this mould material, and therefore this represents a disadvantage in addition to its lower strength properties.

The first stage in the manufacture is to construct the bed of the mould around the shaft centre line, which is defined to be vertical relative to the shop floor. Using this line as the basic reference datum, the angular spacing of the directrices of each of the blades is carefully marked out on the floor and the approximate shape of each blade defined about the blade directrices. Based on this approximate shape, a wooden shuttering is then erected to form a box into which the mould material is rammed together with suitable reinforcing rods. Having formed the body of the bed of the mould in this way the pitch face of the propeller is formed by a technique known as 'strickling'. This process uses a striking board fixed to a long arm at one end and has a roller at the other. The arm is free to rotate about and slide vertically up and down a spindle which has been erected vertically on the shaft centre line of the propeller: the roller, at the other end of the striking board, runs on a pitch rail. Figure 19.2 shows this

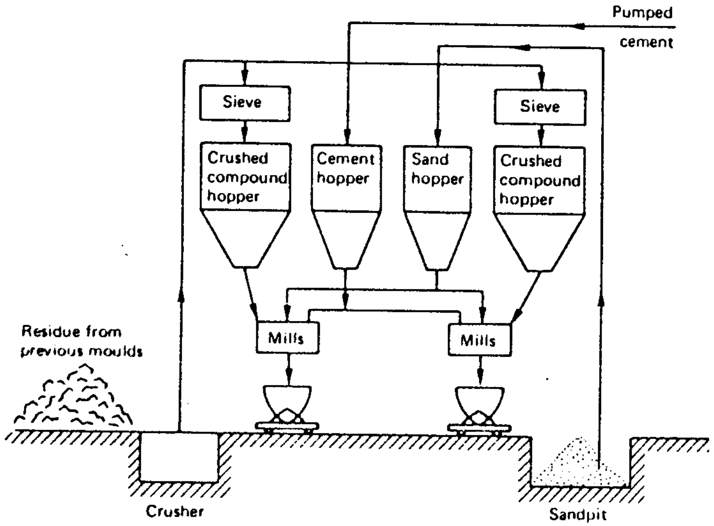

Figure 19.1 Randupson sand plant

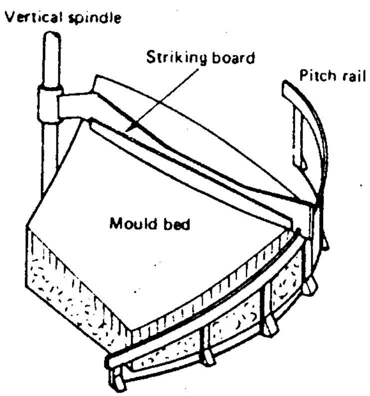

Figure 19.2 Sweeping the mould bed

arrangement in schematic form. The pitch rail defines a portion of a helix which is constructed on a suitable radius, centred on the shaft centre line, which is greater in magnitude than the propeller tip radius. The slope or pitch angle of the helical rail is appropriate to the required pitch and radius of the propeller under construction. The striking board is then pushed up the rail to generate a true helicoidal surface. To cater for a non-uniform pitch distribution the maximum pitch is either first swept and the surface corrected for other radii by rubbing down to templates, or in some cases it is possible to use articulated striking boards and multiple pitch rails. Whichever method is used, the resulting surface is then sleeked by hand. To cater for propeller rake the striking board is set to the appropriate angle relative to the rotating arm.

To form the outside profile of the propeller boss, assuming it is a fixed pitch propeller, another striking board, seen schematically in Figure 19.3, is rotated about the shaft centre line.

The next stage in the construction is to construct the blade form on the mould bed by means of patterns. These patterns are accurately cut from either thin wooden sheet or metal, most usually the former material, and represent the designed cylindrical section profiles together with appropriate contraction and machining allowances. When the bed of the mould has dried and is hard these patterns, defining the helical sections of the blade, are carefully positioned at the appropriate radii and fixed vertically such that they lie along circumferential paths, Figure 19.4. The space between these patterns is then packed with a sand and cement mixture, whereupon the resulting surface is again carefully sleeked to form an upper surface and edge contour of the blade.

When this second sand–cement mixture forming the blade has dried a reinforcing iron grillage is placed over the blade at a height of some 50–70 mm above it and wooden shuttering is positioned to form a box for the construction of the top half of the mould. The

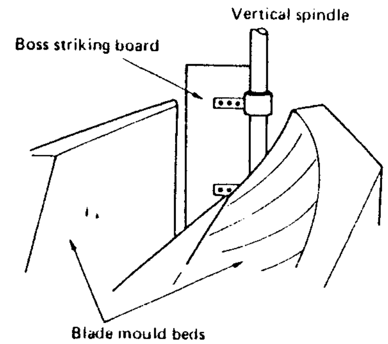

Figure 19.3 Sweeping the propeller boss

sand–cement mixture is then rammed into the box against the blade pattern to form the top of the mould in a similar way to the procedure that was adopted for the bed. At a convenient height above the blade pattern the top of the mould is levelled off and allowed to dry. When thoroughly dry the top of the mould is parted and the top is lifted off by means of lifting hooks which are attached to the reinforcing frame. In this open state of the mould the sand and wood patterns are completely removed and the formation of the root fillets generally takes place next by rubbing down the sharp edges of both the bed and top of the mould to the designed fillet form with the aid of templates.

This method of construction is then applied to each blade in turn and when complete the mould surfaces are then cleaned and dressed to a high state of finish. The mould tops are then fitted back onto their beds and secured by means of mechanical ties and braces

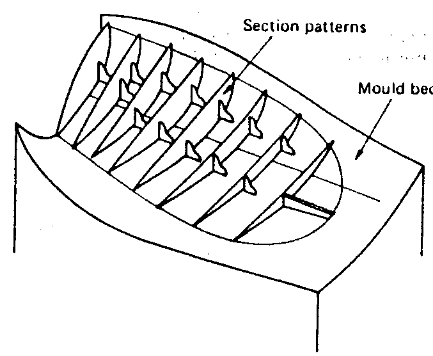

Figure 19.4 Location of section patterns

to prevent relative slippage or bursting during the pouring process.

Prior to pouring the metal, the mould is heated for several hours by blowing hot air through the boss aperture and out through vents near the blade tips. When a predetermined temperature is reached, typically of around 110–120°C, at the outlet vents it is then fairly certain that the surfaces of the mould are free from moisture and sufficient pre-heat of the mould has been achieved. A uniformity of pre-heat throughout the mould is essential and this is achieved by means of suitable ducts.

The final stage in the propeller mould construction, as distinct from the casting feeder system, is the securing of the head ring on top of the mould such that it is concentric with the shaft axis. At this time the core is also inserted, and will form the shaft hole and lightning chamber if one is needed. This core is of course fitted to be concentric with the shaft centre line and has been frequently constructed of alternate layers of foam and straw rope on a former which may be, for example, a perforated iron cylinder. This construction gives a measure of flexibility to the core so that it does not offer serious resistance when the casting cools and contracts around it.

During the construction of the mould a runner system is also built into it to enable the molten metal to be fed into the mould in a controlled and proper way. Figure 19.5 shows a typical runner system. From this figure it can be seen that the molten metal is poured into a runner box, which is fitted with a simple control valve to govern the flow of metal into the mould. For large castings there may well be two or more of these runner systems fed from different ladles simultaneously and providing metal to different points at the base of the casting. From the runner box the metal passes down a vertical down-gate which was built into the mould at the time of construction. These runners are made of pre-cast sand pipe sections and it is found that the exact shape and dimensions of the runners are very important in order to get an efficient flow into the casting which minimizes turbulence and oxide formation. From the down-gate an in-gate is constructed so as to have either a cylindrical or rectangular section. The in-gate is built to run up an inclined line from just above the dirt trap at the bottom of the down-gate to the bottom of the boss. The entry into the bottom boss is normally flared and made tangentially to avoid a direct impact of the metal flow onto the core. It has been found that the construction of a chamber below the box enhances the pouring of the casting by eliminating much of the initial turbulence and allows the molten metal to rise gently into the casting.

The metal is transported from the furnaces in one or more ladles, depending on the size of the cast. The metal is poured into the ladles at a slightly higher temperature than is required for casting in order to allow for cooling during the transportation process.

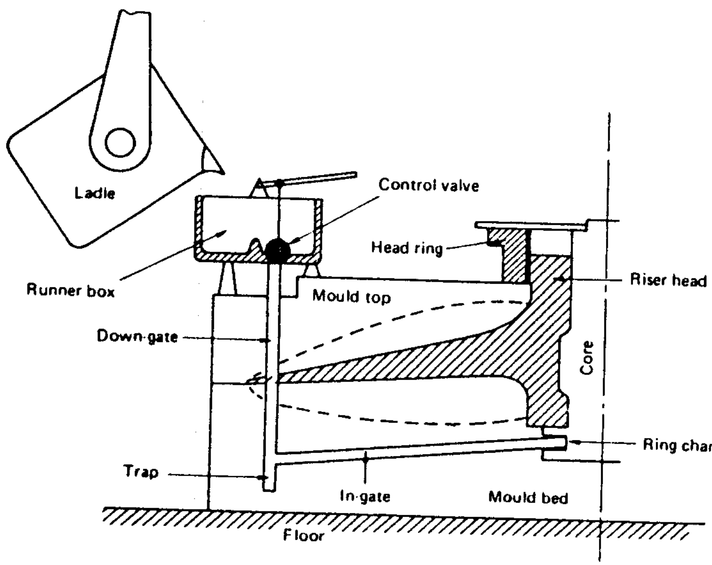

Figure 19.5 Runner system for a typical mould

Accordingly, upon arrival at the mould the temperature of the molten metal is checked using optical pyrometers and the casting operation is delayed until the correct temperature is reached.

Notwithstanding the primary need to minimize turbulence during casting operations, the propeller mould needs to be filled through the runner system as quickly as possible. Langham (Reference 2) quotes rates of up to 8 tons/min although this is a variable depending on the size of the propeller. Throughout the pouring operation the rising surface of the metal that is accessible within the mould is skimmed in order to prevent oxide being trapped in the blades or in the core. In general a large feeding head in the form of an extension to the boss at the forward end is needed for two reasons: the first is to allow for the contraction of the metal during cooling and the second is to provide a reservoir of heat to help provide uniform cooling and directional solidification. Hence the mould is filled to a predetermined head during the initial casting and after casting the surface is skimmed and covered with an insulating compound. During the cooling process the casting is 'topped up' with small additions of molten metal at certain intervals. Exothermic materials are regularly used to assist in the feeding process. These applications are usually in the form of direct applications of powder to the surface: the amount of powder and the interval between applications is dependent upon the size of the cast.

The cooling of the mould takes place over a number of days, depending on the size of the casting. When ready, the mould is dismantled and the cast propeller lifted. The first process after lifting the casting is fettling, which involves the removal of all extraneous riser and venting appendages. The general dimensions are checked next and various datum lines are established by means of measurement, whereupon the propeller is bolted with its shaft axis horizontal to a large horizontal boring machine. Subsequent to this, the first process is to remove the riser head. The taper bore of the propeller is then machined to suit the appropriate plug gauge or template by means of an concentric boring bar through the cored hole of the casting. After this the forward and aft faces of the boss are machined by means of facing arms attached to the boring bar; during this process the various features found on these faces are also finished.

The next stage in production is the lining out of the blades in order to determine the amount of material to be removed. In former times this amount was considerable and required considerable amounts of pneumatic chiselling to be undertaken, and this process made parts of propeller foundries extremely noisy and unpleasant places in which to work. Today, with the greater use of precision casting techniques, less metal needs to be removed. In the case of the traditional manufacturing method datum grooves or spot drillings are cut into the blade and pneumatic chisels are used to remove excess metal. In certain areas templates are deployed. Eventually the whole propeller is ground and polished using high-speed portable grinders, after which the blade edges, leading and trailing, are contoured to the designed shape. The whole propeller is then statically balanced as the final stage of manufacture.

The traditional manufacturing method described is based on the use of a sand–cement pattern constructed around thin wooden or metal section patterns and both Langham (Reference 2) and Tector (Reference 3) describe this process more fully. A good photographic record of the traditional manufacturing technique is seen in Reference 4. The alternative to the traditional procedure is to use solid patterns. In the case of fixed pitched propellers this technique is rarely used on account of costs; however, for controllable pitch propellers, or the once popular built-up propeller, their use is more common, since the extra cost of building a solid pattern are justified when an increased number of blades to the same design is required. In these cases the manufacturing process is analogous to that described, but making use of the solid pattern often in conjunction with separate casting boxes.

19.2 Changes to the traditional technique of manufacture

Modern foundry techniques permit the use of finer casting allowances through the use of precision casting methods. This gives the benefit of requiring considerably less material to be removed during the manufacturing process and hence enables production costs to be potentially reduced. Such techniques, however, need to be used in controlled environments, so that an increased incidence of surface imperfections is not encountered.

The machining or mechanical working process of propeller blades subsequent to casting has undergone major changes in many manufacturers' works since the advent of numerically controlled machine tools. Early usage of automated machinery required the use of a solid pattern which acted as a master blade from which the machine could work a new casting. However, the advances in geometry handling using computer techniques, together with interfaces to multi-axis machines, enable such computer-assisted manufacture machines to be used for propeller manufacture. Several of the major manufacturers have introduced these methods and since about 1970 machines ranging from

three axis numerically controlled gantry units to nine-axis and fully automated flexible manufacturing propeller blade machining cells have been supplied to many manufacturers.

Some manufacturers are today working towards an integrated design, manufacturing and inspection concept (Reference 5). Such methods start with the preliminary design of the blade based on polynomial representations of methodical propeller series data and cavitation criteria to which pitch and thickness distributions are added in order to define the overall power absorption characteritics. Once these are approved the design proceeds by means of lifting surface and finite element methods to produce a fully detailed propeller design tailored to the particular ship. When the design is completed, the blade geometry is filed within a computer and carried forward into the NC blade milling process and final geometric inspection.

Whilst NC machines coupled to CAD/CAM facilities clearly provide a means of enhancing the manufacturing process from both a machining and inspection viewpoint, many propellers are manufactured using approximations to the traditional methods. In either case a highly satisfactory propeller is likely to result provided the appropriate tolerance specification procedures are deployed. The decision as to which manufacturing process to use in a particular case to satisfy the required design tolerance requirements is largely one of production economics.

References and further reading

1. Rowe, F.W. *The Randupson Sand-Mixing Process* Institute of British Foundrymen, 1938.
2. Langham, J.M. The manufacture of marine propellers with particular reference to the foundry *Proc. 21st Inst. Foundry Congress*, Florence, September, 1954; also SMM Technical Paper No. 1, February, 1964.
3. Tector, F.J. The manufacture of ships propellers. *The Marine Engineer and Naval Architect*, April/May, 1951.
4. *Lips Drunen*. Anniversary Publication, Lips, Drunen, 1974.
5. Navarra, P., Rivara, G., Rollando, G., Grossi, L. Propeller Blade Manufacturing – Fincantieri Advanced Technology of Production by CAM-Procedure. Nav '88–WEMT '88 Symp., Trieste, October, 1988.

20 Propeller blade vibration

Contents

The modes of vibration of a propeller blade, beyond the fundamental and first torsional and flexural modes, are extremely complex. This complexity arises from the non-symmetrical outline of the blade, the variable thickness distribution both chordally and radially and the twist of the blade caused by changes in the radial distribution of pitch angle. In addition, the effect of the water in which the propeller is immersed introduces an added degree of complexity in so far as it causes a reduction in modal frequency and a modified mode shape compared with the corresponding characteristics in air. To introduce the problem of blade vibration, it is easiest to consider the vibration of a symmetrical flat blade form in air; in this way many of the practical complexities are eliminated for a first consideration of the problem.

20.1 Flat plate blade vibration in air

Some experiments with a flat plate propeller form by Grinstead are cited by Burrill (Reference 1) as a basis for understanding the basic composition of the modal form of vibrating blades. These tests were conducted on a symmetrical blade having an elliptical form and a constant thickness in the chordal and radial direction. The blade was cantilevered at one end of its major axis and the various modes of vibration in air were excited by bowing with the aid of a rotating disc. In these experiments the nodes in the various modes of vibration were traced by means of sand patterns. The blade used for this work was small in propeller terms since it had a span of 131.32 mm and at maximum chord length the minor axis of the ellipse was 86.11 mm; the thickness of the plate was 13.59 mm. As a consequence, the frequencies of the various modal forms are considerably higher than would be expected from a full-size propeller blade. The modal forms established by Grinstead are shown in Figure 20.1 for the first ten modes beyond the fundamental, which is a simple flexural cantilevered mode with its node coincident with the blade root. The various modal forms are identified in Table 20.1 together with the measured frequencies.

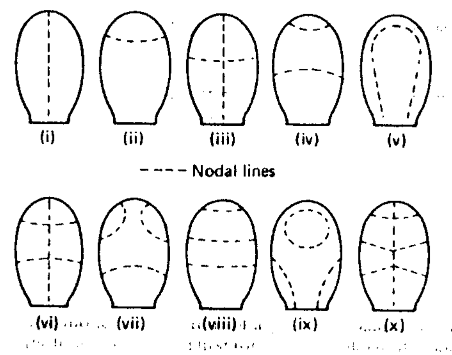

Figure 20.1 Mode shapes for an elliptical, flat plate blade

Table 20.1 Modes of vibration of blade shown in Figure 20.1 (compiled from Reference 1)

Mode no.	*Mode form*	*Frequency (Hz)*
0	Fundamental mode	73
i	One-node torsional mode	249
ii	One-node flexural mode	415
iii	One-node torsional and one-node flexural mode	889
iv	Two-node flexural mode	1135
v	Two-node torsional or 'hoop' mode	1365
vi	Two-node flexural and one-node torsional mode	1819
vii	First cross-coupled mode	2155
viii	Three-node flexural mode	2202
ix	Second cross-coupled	2418
x	Cross-coupled, three-node flexural and one-node torsional	3009

The results of the frequencies can be plotted as shown in Figure 20.2, from which it can be seen that the pure flexural frequencies have the lowest frequencies with the one-node and two-node torsional based frequencies having progressively higher frequencies. In the case of the two-node torsional, one-node flexural, the experiment could not distinguish the pure mode owing to its proximity to the three-node flexural. The results of these model tests show that in addition to the pure modes, cross and diaphram modes arise if the frequencies for the secondary lateral modes are close to the natural flexural modes.

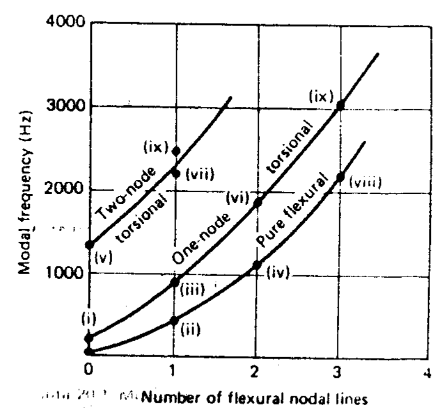

Figure 20.2 Modal frequencies of flat plate blade

20.2 Vibration of propeller blades in air

Having identified the major vibration characteristics associated with a flat plate approximation to a propeller blade, the actual vibratory characteristics of a propeller blade can now be considered more easily. Burrill (References 1 and 2) conducted a series of model and full-scale experiments on propellers and Figure 20.3 shows the results of one set of vibratory tests on a propeller in air. The propeller chosen was a four-bladed, 1320 mm diameter propeller having a mean pitch ratio of 0.65 and a blade area ratio of 0.524. The propeller was of a conventional design for the period. The tests were performed in a 6.4 m square tank and the blades vibrated by means of a vibrator, acting through a universal ball-joint clip, capable of a range from around 20 Hz to 2000 Hz. The similarities

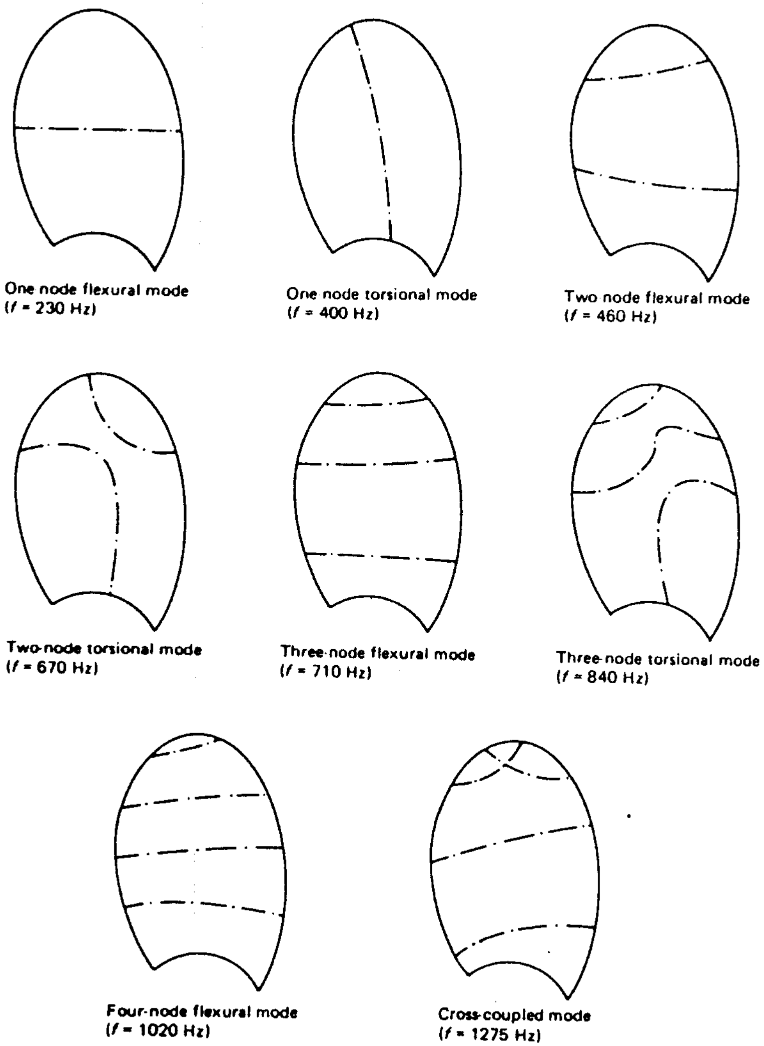

Figure 20.3 Modal form of propeller blade vibration in air

in modal forms between Figures 20.1 and 20.3 are immediately apparent, although the torsional modes are noticed to undergo some changes. The fundamental frequency of the propeller shown in Figure 20.3 was 160 Hz.

The effect of blade area can to some extent be seen by comparing the results shown by Figure 20.3 with the work of Hughes (Reference 3). Hughes examined the response of a series of blades but for these purposes a four-bladed propeller having a blade area ratio of 0.85 is of interest. Figure 20.4 shows the comparison from which a far more complex pattern of modal forms is observed. In particular, the importance of the blade 'edge nodes' is apparent for this type of propeller. This particular propeller had circular back sections, and therefore possessed symmetry about the directrix.

Blade form clearly has an important influence on the modal form of the vibrating blade. Some years ago Carlton and Filcek, in hitherto unpublished work, examined the effects of blade form on the vibration characteristics of controllable pitch propellers. Figure 20.5 shows the differences in vibration patterns derived from two different blade forms, one highly skewed and the other of conventional form, both propellers having diameters in the region 3.0–3.5 m. The symmetrical blade outline clearly shows analogous modes to those derived by Hughes with the smaller and simpler design (see Figure 20.4). In the case of the highly skewed blade the pattern is somewhat more complex, although the presence of distinct flexural modes is clearly apparent. In both cases the presence of edge modes is apparent – more so with the symmetrical design. Both propellers shown in Figure 20.5 have aerofoil sections.

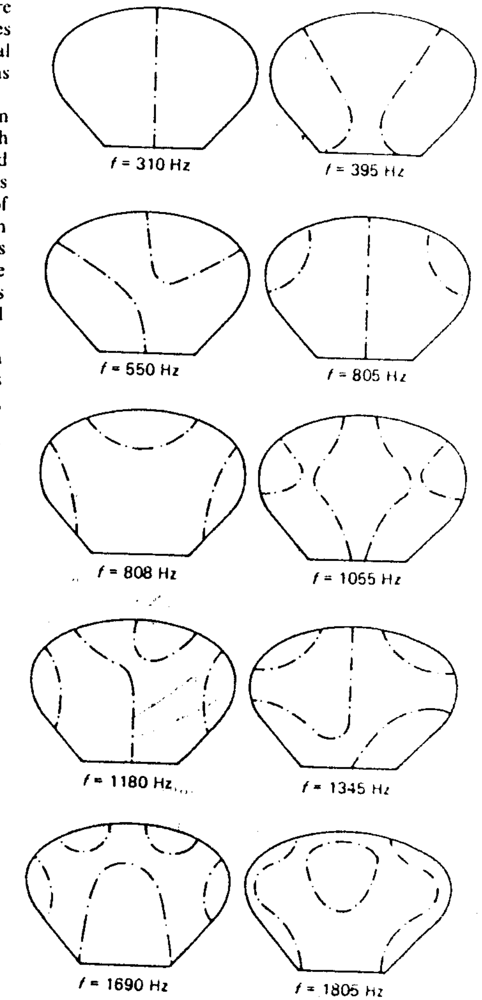

Figure 20.4 Vibratory characteristics of a wide-bladed propeller in air

20.3 The effect of immersion in water

The principal effect of immersing the propeller in water is to cause a reduction in the frequency at which a particular mode of vibration occurs. This reduction is not a constant value for all modes of vibration and appears to be larger for the lower modes than for the higher modes. In order to investigate this effect in global terms one can define a frequency reduction ratio Λ as

$$\Lambda = \frac{\text{frequency of mode in water}}{\text{frequency of mode in air}} \qquad (20.1)$$

Burrill (Reference 1) investigated this relationship for the propeller whose vibratory characteristics in air are shown by Figure 20.3. The results of his investigation are shown in Table 20.2 for both the flexural and torsional modes of vibration. From the Table it is seen that for this particular propeller the value of Λ increases with the number of modes in each of the flexural and torsional modes. With regard to the higher blade area ratio propeller results of Hughes shown in Figure 20.4, Table 20.3 shows the corresponding trends. Again from this Table the general trend of increasing values of Λ with increasing complexity of the modal form is clearly seen. Hughes, in his study, also investigated the effect of pitch on frequency by comparing the characteristics of pitched and flat-plate blades, and found that for most modes, with the exception of the first torsional mode, the

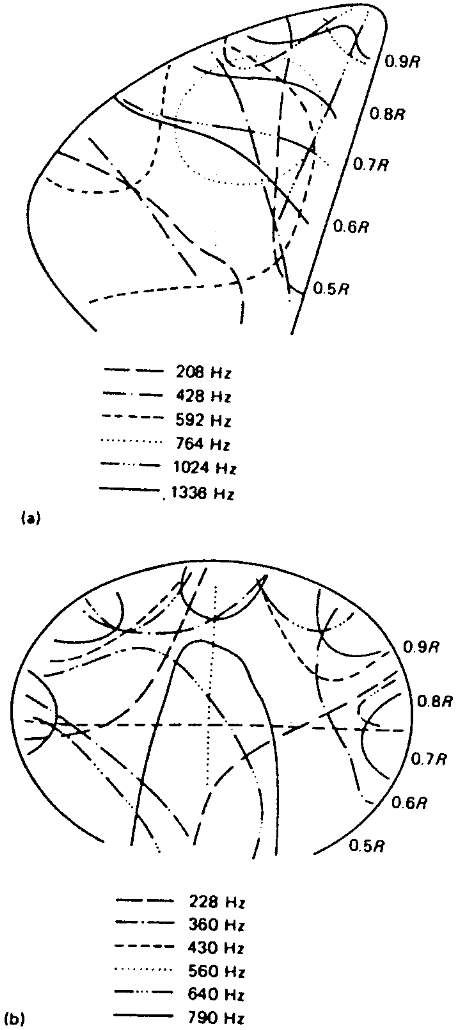

Figure 20.5 Vibration characteristics of two controllable pitch propeller blades

pitched blade had a frequency of around 10% higher than the flat-plate blade; in the case of the first torsional mode the increase in frequency was of the order of 60%. The influence of water immersion on these variations was negligible. In this study it was also shown that for a set of other blade forms, having broadly similar dimensions except for blade area and

Table 20.2 The effect on modal frequency of immersion in water for a four-bladed propeller with a BAR of 0.524 and $P/D = 0.65$ (compiled from Reference 1)

Flexural vibration modes	*Frequency (Hz)*		Λ
	in air	*in water*	
Fundamental	160	100	0.625
One-node mode	230	161	0.700
Two-node mode	460	375	0.815
Three-node mode	710	625	0.880
Four-node mode	1020	1000	0.980
Torsional vibration modes			
One-node mode	400	265	0.662
Two-node mode	670	490	0.731
Three-node mode	840	—	—

Table 20.3 The effect of modal frequency of immersion for a four-bladed propeller with a BAR of 0.85 and a $P/D = 1.0$ (compiled from Reference 1)

Mode shape	*Frequency (Hz)*		Λ
	in air	*in water*	
i	310	200	0.645
ii	395	280	0.709
iii	550	395	0.718
iv	805	605	0.751
v	808	650	0.804
vi	1055	810	0.768
vii	1180	910	0.771
viii	1345	1055	0.784
ix	1690	1330	0.786
x	1805	1435	0.795

outline, a reasonable correlation existed between the value of Λ and the frequency of vibration in air. It is likely, however, that such a correlation would not be generally applicable.

The influence of immersing a blade in water is chiefly to introduce an added mass term due to the inertia of the water which is set in motion by the blade. If the blade is considered as a single degree of freedom system at each of the critical frequencies, then the following relation holds from simple mathematical analysis for undamped motion:

$$f = \frac{1}{2\pi}\sqrt{\frac{k}{m}} \qquad (20.2)$$

Now by assuming that the stiffness remains unchanged, then by combining equations (20.1) and (20.2) we have

$$\Lambda = \frac{\text{equivalent mass of the blade}}{\text{equivalent mass of the blade + added mass due to water}}$$

The effect of the modal frequency on the value of Λ can be explained by considering the decrease in

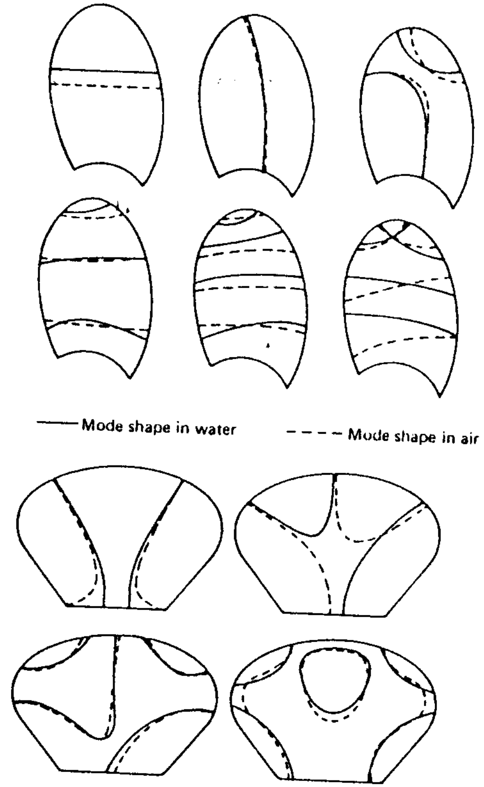

Figure 20.6 Mode shapes in air and water for the two different propeller forms

virtual inertia due to the increased cross-flow induced by the motion of adjacent blade areas which are vibrating out of phase with each other: the greater the number of modal lines, the greater is this effect.

With respect to the effect of immersing the propeller blades on the mode shapes, Figure 20.6 shows that this is generally small in the examples taken from Burrill's and Hughes' work, in so far as whilst the basic mode shape is preserved there is sometimes a shift in position of the modal line on the blade.

20.4 Simple estimation methods

The estimation of the modal forms and their associated frequencies is clearly a complex matter and one that lies outside the scope of simple estimation methods. As a consequence, estimation techniques are normally confined to the determination of the fundamental

flexural mode of vibration in air and a correction Λ, as identified in equation (20.1), applied to account for the immersion of the blade in water.

In the case of the associated problem of turbine and compresor blading, several solution procedures have been produced over the years. These methods, which rely in varying degrees on the mathematical formulation of the elasticity problem, are designed generally for comparatively high aspect ratio blades, and so are not always suitable for direct application to the propeller problem. In the case of the propeller blade, the method proposed by Baker (Reference 4) still finds fairly widespread use as an estimation technique for non-highly skewed propellers. The method, whilst giving a reasonable approximation to the fundamental frequency, also has the advantage of being simple to use and does not require the application of advanced computational facilities. According to Baker the fundamental frequency of a propeller blade in air approximates to

$$f_{air} = \frac{0.305}{(R - r_h)^2}\left[\left(\frac{gE}{\varrho_m}\right)\left(\frac{t}{\bar{c}}\right)c_h t_h\right]^{1/2} \qquad (20.3)$$

where $\bar{c}$ is the blade mean chord length
c_h is the blade chord at the root section
t is the blade mean thickness
t_h is the blade thickness at the root section
R is the tip radius
r_h is the root radius
E is Young's modulus of elasticity
ϱ_m is the material density
and g is the acceleration due to gravity.

Equation (20.3) is based on classical analysis procedures used in association with the results of experimental work conducted on flat-plate blades. This series of propellers, numbering seven in total, had a diameter of 305 mm and two blades; each propeller had differences in section form and blade outline ranging from circular back to aerofoil sections and from symmetrical to moderate skew forms of the day.

In order to estimate the fundamental frequency in water, equations (20.1) and (20.3) are combined as follows:

$$f_{water} = \frac{0.305\Lambda}{(R - r_h)^2}\left[\frac{gE}{\varrho_m}\left(\frac{t}{\bar{c}}\right)c_h t_h\right]^{1/2} \qquad (20.4)$$

where the value of Λ would normally take a value in the range 0.62 to 0.64.

Baker also attempted an estimation formula for the primary torsional frequency of vibration which he estimated to have an accuracy of ±5% based on the tests and model forms used. His formula is

$$f_{t\,air} = \frac{0.92}{(R - r_h)}\left(\frac{t_{0.5}}{c_{0.5}}\right)\left(\frac{c_n}{\bar{c}}\right)\sqrt{\frac{gG}{\varrho_m}} \qquad (20.5)$$

in which $c_{0.5}$ and $t_{0.5}$ are the chord length and thickness at 0.5R respectively and G is the modulus of rigidity of the material. To estimate the torsional frequency f_t in water, it is necessary to introduce the appropriate value of Λ into equation (20.5) as was the case in equation (20.4).

In general terms, equations of the type (20.4) and (20.5) are very useful for estimating purposes at the design stage or in trouble-shooting exercises. They provide an approximation to the basic vibration characteristics of the propeller blade; for more detailed examinations, it is necessary to employ finite element based studies which enable the further exploration of the blade vibration problem.

20.5 Finite element analysis

The finite element technique offers a solution technique which can define the blade natural frequencies and mode shapes with a potentially greater accuracy than by the use of the estimation formulae discussed in the previous section. The finite element method, however, when applied to propeller calculations of this type, relies on both the satisfactory modelling the blade in terms of the type and geometric form of the elements and also the adequate representation of the effect of the water in which the propeller is immersed.

In the first instance, the choice of element type is governed by the nature of the problem and reasonable correlation has been derived from the use of quadrilateral plate or isoparametric elements. The latter is particularly useful when blade rotation is included. With regard to the geometric form of the elements, the requirements of the particular elements with regard to aspect ratio and included angle at the element corners must clearly be adhered to if erroneous results are to be avoided.

Figure 20.7 shows an example of a blade descretization taken from Holden (Reference 5). The conditions at the blade root require some consideration in order to achieve realistic conditions, since some authorities suggest that a fully built-in condition at the root is unrepresentative and that some relaxation of that condition should be made. Clearly the amount that can be done to meet this criticism depends upon the flexibility of the finite element capability being used.

With regard to the fluid effect on the blade, appeal can first be made to the two-dimensional analysis for laminae, since the effect of blade thickness is likely to be small. For the case of a lamina, three motions can be identified which are of interest: translation motion of the lamina, rotational motion about the lamina axis and transverse or chordwise flexure. In the case of translational motion, if this is normal to the plane of the lamina, then the added mass of water per unit length is $\pi \varrho b^2$ for a chord length $c = 2b$. Hence in the case of oblique motion at an angle θ to the plane of the lamina, then the added mass per unit length is given by

$$m_{ai} = \pi \varrho b^2 \sin^2 \theta \qquad (20.6)$$

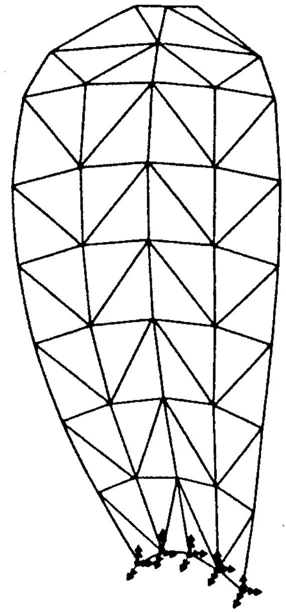

Figure 20.7 Finite element mesh for blade vibration analysis (Reproduced from Reference 5, with permission)

For rotational motion about the blade axis the effective added moment of inertia of the blade section per unit length of the section is

$$I_{ar} = \frac{\pi}{8} \varrho b^4 \qquad (20.7)$$

In the case of a segmental section Lockwood Taylor (Reference 6) suggests that for transverse or chordwise flexure the ratio of fluid to blade inertia can be approximated by

$$\frac{I_{af}}{I_f} = 1.2 \left(\frac{\varrho}{\varrho_m}\right)\left(\frac{b}{t}\right) \qquad (20.8)$$

where ϱ_m and t are the blade material density and thickness.

Lockwood Taylor suggests that equations (20.6) and (20.8) can be used directly for a propeller blade provided the blade is of sufficiently large aspect ratio. For wider blades of more common interest to propeller designers, three-dimensional corrections must be applied, for example as outlined by Lindholm *et al.* (Reference 7).

In the various pseudo-empirical approaches to the prediction of blade vibratory characteristics the blade

Table 20.4 Damping factors for three propeller blades measured experimentally (compiled from Reference 1)

Propeller dimensions	*Material*	*Natural frequency in air (Hz)*	*Damping factor ζ*	
			In air	*In water*
Model propeller: Dia = 1770 mm; $Z = 6$; $A_E/A_O = 0.595$	Al	118.5	0.0044	0.0405
Full-scale propeller: Dia. = 8850 mm; $Z = 6$; $A_E/A_O = 0.595$	Cu–Al–Ni	20.8	—	0.0073
Full-scale propeller: Dia. = 2050 mm; $Z = 3$; $A_E/A_O = 0.40$	Cu–Al–Ni	95.0	0.0044	0.0060

is assumed to be stationary, and so the effect of centrifugal stiffening is not considered. This situation is, however, partially redressed in numerical approaches to the problem. For conventional propeller designs the centrifugal stiffening effect is not thought to be significant; however, this may not necessarily be the case for very high rotational speed applications.

20.6 Propeller blade damping

As with all mechanical structures the propeller blade material exerts a degree of damping to the vibration characteristics exhibited on the blades. Holden (Reference 5) investigated this relationship for a series of three propellers, one model and two full scale. The results obtained are shown in Table 20.4 for free oscillations at natural frequency.

In Table 20.4 the damping factor is defined by

$$\zeta = \frac{1}{2\pi n} \ln\left(\frac{a_1}{a_n}\right) \qquad (20.9)$$

and was calculated from the variation in amplitude a of strain gauge measurements at 0.6R over twenty oscillations; that is, $n = 20$ in equation (20.9).

Under forced oscillations the damping factors were found to increase slightly to 0.0100 and 0.0328 for air and water, respectively.

Whilst propeller materials in general exhibit low damping for most commercial applications, it is possible to use material with a very high damping if the blade design demands a high level of suppression of the vibration characteristics. Such materials, an example of which is given in Reference 8, have a damping characteristic as shown in Figure 20.8(b) and can be compared to that for the three-bladed propeller of Table 20.4 shown in Figure 20.8(a).

20.7 Propeller singing

Singing is a troublesome phenomenon that affects some propellers, and its incidence on a particular design is unpredictable within the bounds of present analysis capabilities. It is quite likely that, and indeed known, that two propellers can be manufactured to the same design and one propeller will sing whilst the other will not.

Singing can take many forms ranging from a deep sounding grunting noise through to a high-pitched warbling noise such as might be expected from an incorrectly set operation on a lathe. The deeper 'grunting' noise is most commonly associated with the larger vessels such as bulk carriers, and in general the faster and smaller the propeller the higher the frequency will be. The noise may be intermittent or may have

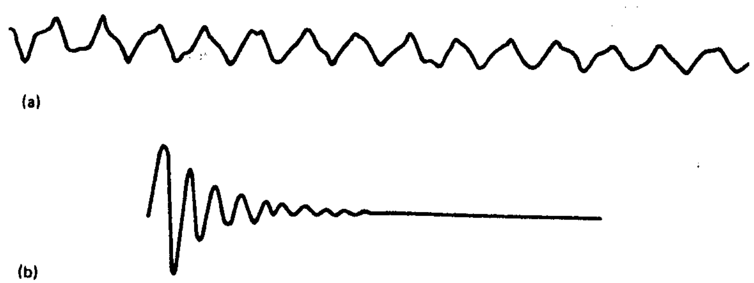

Figure 20.8 Comparison of propeller alloy damping properties: (a) free vibration signature of three-bladed propeller in Table 20.4; (b) example of a high damping alloy for propeller manufacture

an apparent period of about once per revolution, most frequently the latter. Furthermore, it is unlikely that singing will occur throughout the whole range of propeller loading but will occur only within certain specific revolution ranges. There is the classic example in this respect of some controllable pitch propellers which, when working at slightly reduced pitch settings, will sing for a short period of time.

The phenomenon of propeller singing has inspired many researchers to investigate the problem, much of this work being done in the 1930s and 1940s; for example, References 9–15. Today singing is generally believed to be caused by a vortex shedding mechanism in the turbulent and separated part of the boundary layer on the blade surface exciting the higher-mode frequencies of the blade and particularly those associated with blade edge modes. As a consequence, it is not possible at this time to predict the conditions for the onset of singing in a propeller design procedure or indeed whether a particular design will be susceptible to the singing phenomenon. In addition to the theoretical complexity of the problem, the practical evidence from propellers manufactured to the same design and specification, one of which sings whilst the others do not, leads to the conclusion that small changes in dimensional tolerances are sufficient, given the appropriate circumstances, to induce singing.

Although prediction of singing inception is not possible, the cure of the phenomenon is normally not difficult; indeed some manufacturers incorporate the cure as a standard feature of their design whilst others prefer not to take this measure so as not to weaken the edges of the blade. The cure is to introduce a chamfer to the trailing edge of the blade and to ensure that the knuckle of the chamfer and trailing edge wedge, points *a*, *b* and *c* in Figure 20.9, are sharp. The purpose of this edge form is to deliberately disrupt the boundary layer growth in the trailing edge region and hence alleviate the effects of the vortex shedding mechanism. Van Lammeren, in the discussion to Reference 1, suggests that the dimensions of an anti-singing edge can be calculated from

$$x = [20 + 5(D - 2)]|_{max = 30} \text{ mm} \qquad (20.10)$$
$$y = 0.1x \text{ mm}$$

where D is the propeller diameter in metres and where the parameters are defined in Figure 20.9. The anti-singing edge is normally defined between the geometric tip of the propeller and a radial location of around $0.4R$ on the trailing edge, where it is then faired into the normal edge detail. The anti-singing edge is applied to the suction surface of the blade; there are, however, some anti-singing edge forms which are applied to both sides of the blade at the trailing edge. These latter forms are used less frequently used since the flow on the suction face of the blade, because it separates earlier, is the most likely cause of the singing problem. Edge forms of the type shown

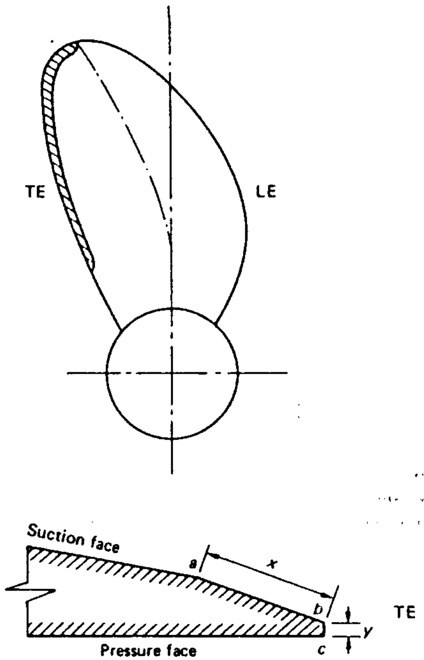

Figure 20.9 Anti-singing edge design

in Figure 20.9 do not cause any particular power absorption problems since, although modifying the trailing edge after the manner shown in Chapter 22, the anti-singing edge operates wholly within the separated flow in the wake of the blade section.

It has been found that on occasions with highly skewed propellers it is necessary to extend the anti-singing edge forward by a small amount from the geometric tip onto the leading edge of the blade in order to cure a singing problem. This extension, however, should be done with caution so as not to introduce unwanted cavitation problems due to the sharpened leading edge which results. When this extension of the anti-singing edge has been found necessary the cure of the singing problem has been completely satisfactory.

References and further reading

1. Burrill, L.C. Underwater propeller vibration tests. *Trans. NECIES*, 1949.

2. Burrill, L.C. Marine propeller blade vibrations: full scale tests. *Trans. NECIES*, 1946.
3. Hughes, W.L. Propeller blade vibrations. *Trans. NECIES*, 1949.
4. Baker, G.S. Vibration patterns of propeller blades. *Trans. NECIES*, 57, 1040–41, 19??.
5. Holden, K. Vibrations of marine propeller blades. *Norwegian Mar. Res.* No. 3, 1974.
6. Lockwood Taylor, J. Propeller blade vibrations. *Trans. RINA*, 1945.
7. Lindholm, Kana, Chu, Abramson. Elastic vibration characteristics of cantilever plates in water. *J. Ship. Research*, June, 1965.
8. Sonoston High Damping Capacity Alloy. SMM Tech. Brief No. 7.
9. Report of the 'singing' propeller committee. *Trans. RINA*, 1936.
10. Conn, J.F.C. Marine propeller blade vibration. *Trans. IESS*, 1939.
11. Shannon, J.F., Arnold, R.N. Statistical and experimental investigations on the singing propeller problem. *Trans. IESS*, 1939.
12. Davis, A.W. Characteristics of silent propellers. *Trans. IESS*, 1939.
13. Kerr, W., Shanon, J.F., Arnold, R.N. The problem of the singing propeller. *Trans. I.Mech.E.*, 143, 1940.
14. Hughes, G. Influence of the shape of blade section on singing of propellers. *Trans. IESS*, 1941.
15. Hughes, G. On singing propellers. *Trans. RINA*.

Part Three

Design, operation and performance

21 Propeller design

Contents

Each of the chapters in this book has considered different aspects of the propeller in detail. This chapter attempts to provide a basis for drawing together the various threads of the subject, so that the propeller and its design process can be considered as an integrated entity. The completed propeller depends for its success on the satisfactory integration of several scientific disciplines. These disciplines are principally hydrodynamics, stress analysis, metallurgy and manufacturing technology with supportive inputs from mathematics, dynamics and thermodynamics. It is not uncommon to find that several of the requirements of the principal disciplines for a particular design are in partial conflict, to a greater or lesser extent, in their aim to satisfy a particular set of requirements and constraints. The test of the designer is in how satisfactorily he resolves these conflicts to produce an optimal design: optimal in the sense of satisfying the various constraints. It may therefore be inferred that in propeller technology, as in all other forms of engineering design, there is no single correct solution to a particular propulsion problem.

21.1 The design and analysis loop

The phases of the design process, given that there is a requirement for a particular ship to be propelled, can be summarized in the somewhat abstract terms of design textbooks as shown in Figure 21.1. From the figure, it is seen that the creation of the artefact commences with the definition of the problem, which requires the complete specification for the design. This specification must include a complete definition of the inputs and the required outputs together with the limitations on these quantities and the constraints on the design. Following the design definition phase, the process passes on to the synthesis phase, in which the basic design is formulated from the various 'building blocks' that the designer has at his disposal. In order to provide the optimal solution, the synthesis phase cannot exist in isolation and has to be conducted with the analysis and optimization phase in an interactive loop in order to refine the design to that required that is, a design that complies with the original specification and also has the optimal property. The design loop must be flexible enough, should an unresolvable conflict arise with the original definition of the problem, to allow an appeal for change to the definition of the design problem from either of the synthesis or analysis and optimization phases. Indeed it is also likely that either of these phases of design will lead to the identification of areas for long-term research to aid future design problems. As was noted, design is an interactive process in which one passes through several steps, evaluates the results, and then returns to an earlier phase of the procedure. Consequently, we may synthesize many components of the design, analyse and optimize them, and return to the synthesis to see what effect this has on the remaining parts of the system. When the design loop of synthesis, analysis and optimization is complete, the process then passes on to the evaluation phase. This phase is the final proof of the design, from which its success is determined, since it usually involves the testing of a prototype. In propeller design, the luxury of a prototype is rare, since the propeller is a unit volume item under normal circumstances. Hence, the evaluation stage is normally the sea trial phase of the ship-building programme. Nevertheless, when the design does not perform as expected, then it is normal, as in the generalized design process, to return to an earlier phase to explore the reasons for failure and propose modification.

These general design ideas, although abstract, are nevertheless useful and directly applicable to the propeller design process. How then are they applied? In the first instance it must be remembered that in general a propeller can only be designed for a single design point which involves a unique specification of

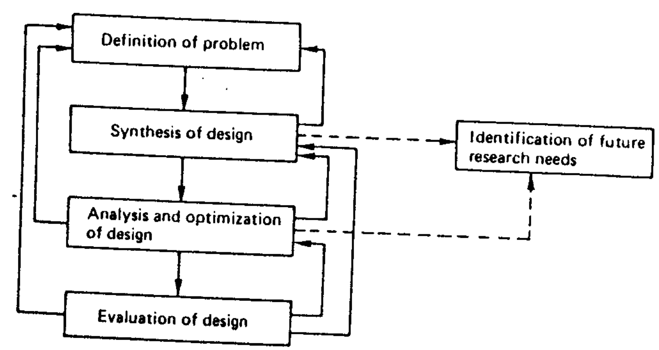

Figure 21.1 Phases of engineering design

a power, rotational speed, ship speed and a mean radial wake field. The controllable pitch propeller is the exception to this rule when it would be normal to consider two or more design points. Although there is a unique design point in general the propeller operates in a variable circumferential wake field and may be required to work at off-design points: in some instances the sea trial condition is an off-design point. Therefore, there is in addition to the synthesis phase of Figure 21.1 also an analysis and optimization phase, as also shown in the figure.

In the case of propeller design, the conceptual design approach shown in Figure 21.1 can be translated in the following way. The definition of the problem is principally the specification of the design point, or points in the case of controllable pitch propellers, for the propeller together with the constraints which are applicable to that particular design or the vessel to which it is to be fitted. In both of these activities the resulting specification should be a jointly agreed document into which the owner, shipbuilder, engine builder and propeller designer have contributed: to do otherwise can lead to a grossly inadequate or unreasonable specification being developed. Following the production of the design specification the synthesis of the design can commence. This design will be for the propeller type agreed during the specification stage, because it is very likely that some preliminary propeller design studies will have been conducted during the design specification phase. At that time propeller type, blade number and so on are most likely to have been chosen. As a consequence, during the synthesis phase the basic design concept will be worked up into a detailed design proposal typically using, for advanced designs, a wake adapted lifting line with lifting surface correction capability. The choice of method, however, will depend on the designer's own capability and the data available, and may, for small vessels, be an adaptation of a standard series propeller which may work in a perfectly satisfactory manner from the cost-effective point of view.

The design that results from the synthesis phase, assuming the former of the two synthesis approaches have been adopted, will then pass into the analysis and optimization phase. This phase may contain elements of both theoretical analysis and model testing. The theoretical analysis will vary, depending upon the designer's capabilities and the perceived cost benefit of this stage, from adaptations of Burrill's vortex analysis procedure through to unsteady lifting surface and vortex lattice capabilities (Chapter 8). With regard to model testing in this phase, this can embrace a range of towing tank studies for resistance and propulsion purposes through to cavitational tunnel studies for determination of cavitation characteristics and noise prediction. The important lesson in propeller technology is to appreciate that each of the analysis techniques, theoretical and model testing, gives a partial answer, since although today our understanding of the various phenomena has progressed considerably from that of say 20 or 30 years ago, there are still many areas where our understanding is far from complete. As a consequence, the secret of undertaking a good analysis and optimization phase is not simply to take the results of the various analysis at face value, but to examine them in the light of previous experience and a knowledge of their various strengths and weaknesses to form a balanced view of the likely performance of the proposed propellers; this is only the essence of good engineering practice.

Figure 21.2 translates the more abstract concept of the phases of engineering design, shown in the previous figure, into a propeller related design concept in the light of the foregoing discussion.

21.2 Design constraints

The constraints on propeller design may take many forms: each places a restriction on the designer and in most cases if more than one constraint is placed then this places a restriction on the upper bound of performance that can be achieved in any one area. For example, if a single constraint is imposed, requiring the most efficient propeller for a given rotational speed, then the designer will most likely choose the propeller with the smallest blade area ratio, consistent with any blade cavitation erosion criteria, in order to maximize efficiency. If then a second constraint is imposed, requiring the radiated pressures on the hull surface not to exceed a certain value, then the designer will start to increase the blade chord lengths and adjust other design parameters in order to control the cavitation. Therefore, since the blade area is no longer minimized, this will cause a reduction in efficiency but enhance the hull pressure situation.

Although this is a somewhat simplified example, it adequately illustrates the point and as a consequence, it is important that all concerned with the ship design consider the various constraints in the full knowledge of their implications and the realization that the setting of unnecessary or over-strict constraints will most likely lead to a degradation in the propeller's overall performance.

21.3 The choice of propeller type

The choice of propeller type for a particular propulsion application can be a result of the consideration of any number of factors. These factors may, for example, be the pursuit of maximum efficiency, noise reduction, ease of manoeuvrability, cost of installation and so on. Each vessel and its application has to be considered on its own merits taking into account the items listed in Table 21.1.

In terms of optimum open water efficiency van Manen (Reference 1) developed a comparison for a variety of propeller forms based on the results of

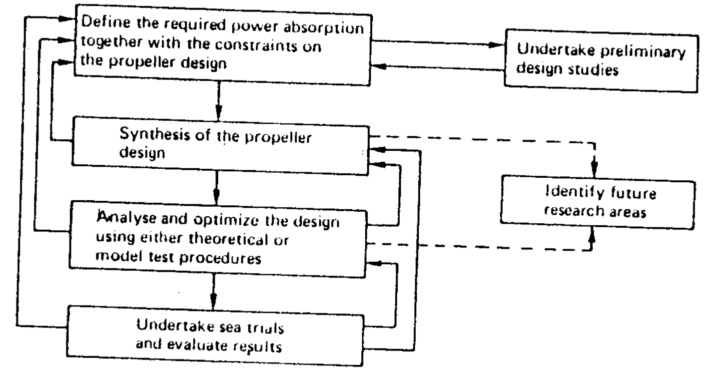

Figure 21.2 The phases of propeller design

Table 21.1 Factors affecting choice of propulsor

Role of vessel
Special requirements
Initial installation costs
Running costs
Maintenance requirements
Service availability
Legislative requirements

systematic series data. In addition to the propeller data from experiments at MARIN he also included data relating to fully cavitating and vertical axis propellers (References 2, 3) and the resulting comparison is shown in Figure 21.3. The figure shows the highest obtainable open water efficiency for the different types of propeller as a function of the power coefficient B_p. As can be seen from the legend at the top of the figure the lightly loaded propellers of fast ships lie to the left-hand side whilst the more heavily loaded propellers of the large tankers and bulk carriers and also the towing vessels lie to the right-hand side of the figure. Such a diagram is able to give a quick indication of the type of propeller that will give the best efficiency for a given type of ship. As is seen from the diagram the accelerating duct becomes a more attractive proposition at high values of B_p whereas the contra-rotating and conventional propellers are most efficient at the lower values of B_p.

In cases where cavitation is a dominant factor in the propeller design such as in high-speed craft, Tachmindji *et al.* (Reference 4) developed a useful basic design diagram to determine the applicability of different propeller types with respect to cavitating conditions of these type of craft. This diagram is reproduced in Figure 21.4. From the figure it is seen that it comprises a series of regions which define the applicability of different types of propeller. In the top right-hand region are to be found the conventional propellers fitted to most merchant vessels, whilst in the bottom right-hand region are the conditions where supercavitating propellers will give the best efficiences. Propellers that fall toward the left-hand side of the diagram are seen to give low efficiency for any type of propeller and since low advance coefficient equates with high B_p the correspondence between these Figures 21.4 and 21.3 can be seen by comparison.

The choice between fixed pitch propellers and controllable pitch propellers has been a long contested debate between the proponents of the various systems. In Chapter 2 is was shown that the controllable pitch propellers has gained almost complete dominance in the Ro/Ro, ferry, fishing, offshore and tug markets with vessels of over 2000 BHP. This is clearly because there is a demand for either high levels of manoeuvrability or a duality of operation that can best be satisfied with a controllable pitch propeller rather than a two-speed reduction gearbox for these types of vessel. For the classes of vessel which do not have these specialized requirements, then the simpler fixed pitch propeller appears to provide a satisfactory propulsion solution. With regard to reliability of operation, as might be expected the controllable pitch propeller has a higher failure rate due to its increased mechanical complexity. Table 21.2 details the failure rates for both fixed pitch propellers and controllable pitch propellers over a period of about a quarter of a century (Reference 5). In either case, however, it is seen that the propeller has achieved the status of being a very reliabile marine component.

The controllable pitch propeller does have the advantage of permitting constant operation of the propeller. Although this generally establishes a more onerous set of cavitation conditions, it does readily allow the use of shaft-driven generators should the economics of the ship operation dictate that this is

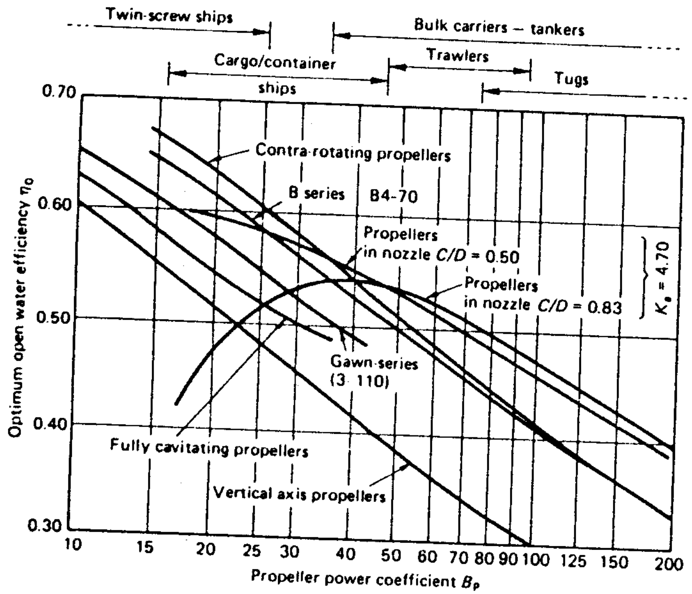

Figure 21.3 Typical optimum open water efficiencies for different propeller types (Reproduced from Reference 1, with permission)

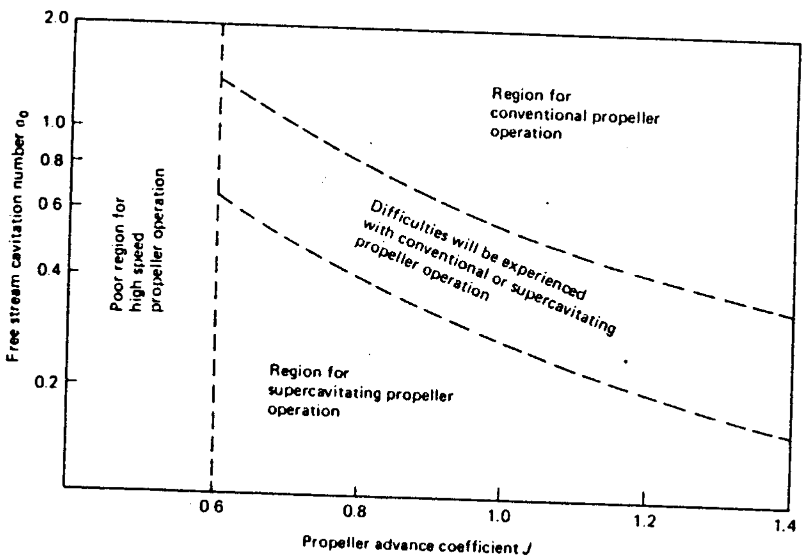

Figure 21.4 The effect of cavitation number on propeller type for high-speed propellers

Table 21.2 Change in the propeller defect incidence with time for propellers in the range 5000 < BHP < 10 000. Defects recorded in defect incidence per year per unit.

	1960 –64	*1965 –69*	*1970 –74*	*1975 –79*	*1980 –84*	*1985 –89*
Fixed pitch propeller	0.018	0.044	0.067	0.066	0.065	0.044
Controllable pitch propellers	0.080	0.161	0.128	0.157	0.106	0.079

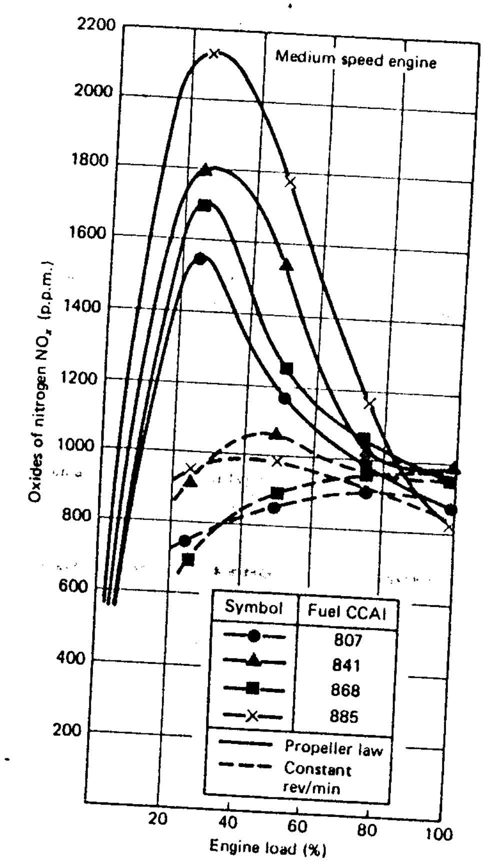

Figure 21.5 Influence of engine operating conditions and fuel CCAI number

advantageous. In addition, in this present age of environmental concern, there is some evidence to suggest (Reference 6) that the NO_x exhaust emissions can be reduced on a volumetric basis at intermediate engine powers when working at constant shaft speed. Figure 21.5 shows this trend from which a reduction in the NO emissions, these forming about 90% of the total NO_x component, can be seen at constant speed operation for a range of fuel qualities. Such data, however, needs to be interpreted in the context of mass emission for particular ship applications.

Table 21.3 Some important characteristics of propeller types

Propeller type	*Characteristics*
Fixed pitch propellers	Ease of manufacture Design for a single condition (i.e. design point) Blade root dictates boss length No restriction on blade area or shape Rotational speed varies with power absorbed Relatively small hub size
Controllable pitch propellers	Can accommodate multiple operating conditions Constant or variable speed operation Restriction on blade area to maintain blade reversibility Blade root is restricted by palm dimensions Increased mechanical complexity Larger hub size governed by spindle torque requirements
Ducted propellers	Can accommodate fixed and controllable pitch propellers Duct form should be simple to facilitate manufacture Enhanced thrust at low ship speed Duct form can be either accelerating or decelerating Accelerating ducts tend to distribute thrust equally between duct and propeller at bollard pull Ducts can be made steerable
Azimuthing units	Good directional control of thrust Increased mechanical complexity Can employ either ducted or non-ducted propellers of either fixed or controllable pitch type
Cycloidal propellers	Good directional control of thrust Avoids need for rudder on vessel Increased mechanical complexity
Contra-rotating propellers	Provides ability to cancel torque reaction Enhanced propulsive efficiency in appropriate conditions Increased mechanical complexity Can be used with fixed shaft lines or azimuthing units

In cases where manoeuvrability or directional control are important, the controllable pitch propeller, steerable duct, azimuthing propeller and the cycloidal propeller can offer various solutions to the problem, depending on the specific requirements.

By way of summary, Table 21.3 lists some of the important features of the principal propeller types.

21.4 The propeller design basis

The term 'propeller design basis' refers to the power, rotational speed and ship speed that are chosen to act as the basis for the design of the principal propeller geometric features. This is an extremely important matter even for the controllable pitch propellers, since in this latter case the design helical sections will only be absolutely correct for one pitch setting. This discussion, however, will largely concentrate on the fixed pitch propeller since for this type of propeller the correct choice of the design basis is absolutely critical to the performance of ship.

The selection of the design basis starts with a consideration of the mission profile for the vessel. Each vessel has a characteristic mission profile which is determined by the owner to meet the commercial needs of the particular service under the economic conditions prevailing. It must be recognized that the mission profile of a particular ship may change throughout its life, depending on a variety of circumstances. When this occurs it may then be necessary to change the propeller design, as witnessed by the slow steaming of the large tankers after the oil crisis of the early 1970s and the consequent change of propellers by many owners in order to enhance the ship's efficiency at the new operating conditions. The mission profile is determined by several factors, but is governed chiefly by the vessel type and its intended trade pattern; Figure 21.6 shows three examples relating to a container ship, a Ro/Ro ferry and a warship. The wide divergence in the form of these curves amply illustrates that the design basis for a particular vessel must be chosen with care such that the propeller will give the best overall performance in the areas of operation required. This may well require several preliminary design studies in order to establish the best combination of diameter, pitch ratio and blade area to satisfy the operational constraints of the ship.

In addition to satisfying the mission profile requirements it is also necessary that the propeller and engine characteristics match, not only when the vessel is new but also after the vessel has been in service for some years. Since the diesel engine at the present time is used for the greater majority of propulsion plants, we will use this is as the primary basis for the discussion. The diesel engine has a general characteristic of the type shown in Figure 21.7 with a propeller demand curve superimposed on it which is shown in this

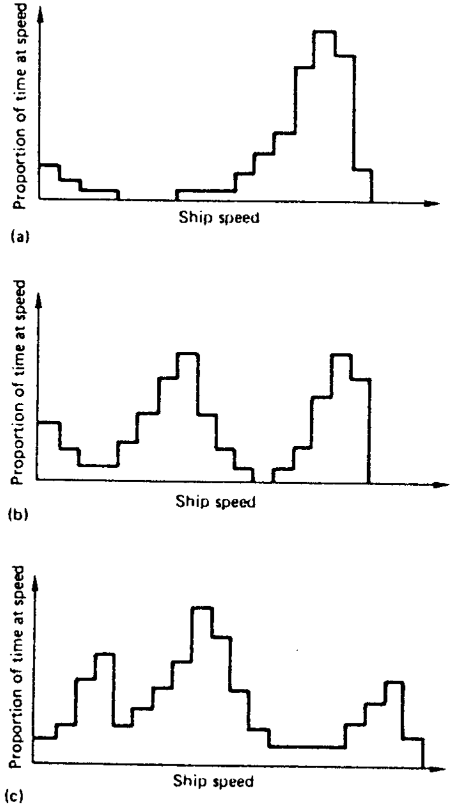

Figure 21.6 Examples of ship mission profiles: (a) container ship; (b) Ro/Ro passenger ferry; (c) warship

instance to pass through the maximum continuous rating (MCR) of the engine. The propeller demand curve is frequently represented by the so-called 'propeller law', which is a cubic curve. This, however, is an approximation, since the propeller demand is dependent on all of the various hull resistance and propulsion components, and therefore has a more complex functional relationship. In practice, however, the cubic approximation is generally valid over limited power ranges. If the pitch of the propeller has been selected incorrectly, then the propeller will be either over-pitched (stiff), curve A, or underpitched (easy), curve B. In either case, the maximum power of the engine will not be realized, since in the case of over-pitching the maximum power attainable will be X at a reduced RPM, this being governed by the engine torque limit. In the alternative under-pitching case, the maximum

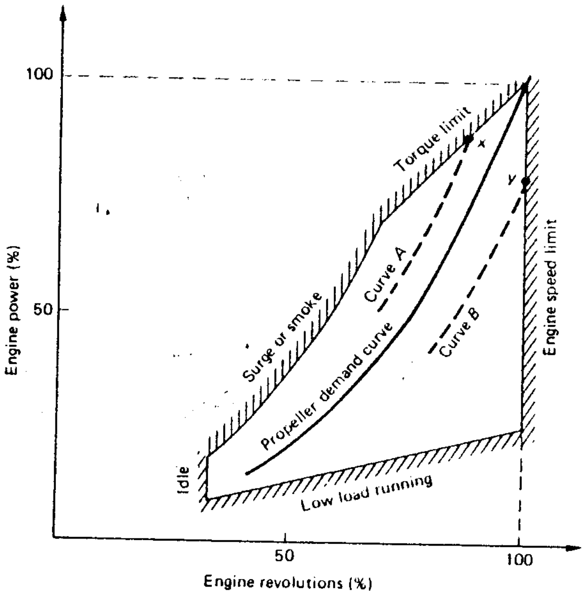

Figure 21.7 Engine characteristic curve

power attainable will be Y at 100% RPM, since the engine speed limit will be the governing factor.

In addition to purely geometric propeller features, a number of other factors influence the power absorption characteristics. Typical of these factors are sea conditions, wind strength, hull condition in terms of roughness and fouling, and, of course, displacement. It is generally true that increased severity of any of these conditions requires an increase in power to drive the ship at the same speed. This has the effect of moving the power demand curve of the propeller (Figure 21.7) to the left in the direction of curve A. As a consequence, if the propeller is designed to operate at the MCR condition when the ship is clean and in a light displacement with favourable weather, such as might be found on a trial condition, then the ship will not be able to develop full power in subsequent service when the draughts are deeper and the hull fouls or when the weather deteriorates. Under these conditions the engine torque limit will restrict the brake horse power developed by the engine.

Clearly this is not a desirable situation and a method of overcoming this needs to be sought. This is most commonly achieved by designing the propeller to operate at a few revolutions fast when the vessel is new, so that by mid-docking cycle the revolutions will have fallen to the desired value. In addition, when significant changes of draught occur between the trial condition and the operating conditions, appropriate allowances need to be made for this effect. Figure 21.8 illustrates one such scenario, in which the propeller has been selected so that in the most favourable circumstances, such as the trial condition, the engine is effectively working at a derated condition and hence the ship will not attain its maximum speed; this is because the engine will reach its maximum speed before reaching its maximum power. As a consequence in poorer weather or when the vessel fouls or works at a deeper draught, the propeller characteristic moves to the left so that the maximum power becomes available. Should it be required on trials to demonstrate the vessel's full-speed capability, then engine manufacturers often allow an overspeed margin with a restriction on the time the engine can operate at this condition. This concept of the difference in performance of the vessel on trial and in service introduces the term of a 'sea margin', which is imposed by the prudent owner in order to ensure the vessel has sufficient power available in service and throughout the docking cycle.

In practice the propeller designer will use a derated engine power as the basis for the propeller design. This is to prevent excessive maintenance costs in keeping the engine at peak performance throughout its life. Hence the propeller is normally based on a normal continuous rating (NCR) of between 85 and 90% of the MCR condition; Figure 21.9 shows a

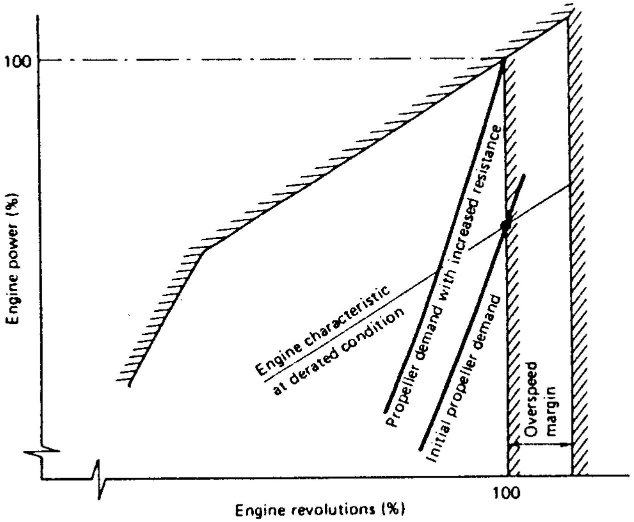

Figure 21.8 Change in propeller demand due to weather, draught changes and fouling

typical propeller design point for a vessel working with a shaft generator. For this ship an NCR of 85% of the MCR was chosen and the power of the shaft generator P_G deducted from the NCR. This formed the propeller design power. The rotational speed for the propeller design was then fixed such that the power absorbed by the propeller in service, together with the generator power when in operation, could absorb the MCR of the engine at 100% RPM. This was done by deducting the power required by the generator from the combined service propeller and generator demand curve to arrive at the service propulsion only curve and then applying the sea margin which enables the propeller to run fast on trial. In this way the design power and revolutions basis became fixed.

In the particular case of a propeller intended for a towing duty, the superimposition of the propeller and engine characteristics presents an extreme example of the relationship between curve *A* and the propeller demand curve shown in Figure 21.7. In this case, however, curve *A* is moved far to the left because of the added resistance to the vessel caused by the tow. Such situations normally require correction by the use of a two-speed gearbox in the case of the fixed pitch propeller, or by the use of a controllable pitch propeller.

The controllable pitch propeller presents an interesting extension to the fixed pitch performance maps shown in Figures 21.7–21.9. A typical example is shown in Figure 21.10, in which the controllable pitch propeller characteristic is superimposed on an engine characteristic. The propeller demand curve through the design point clearly does not pass through the minimum specific fuel consumption region of the engine maps: this is much the same as for the fixed pitch propeller. However, with the controllable pitch propeller it is possible to adjust the pitch at partial load condition to move towards this region. In doing so it can be seen that the propeller mapping may come very close to the engine surge limit, and this is not a desirable feature. Nevertheless, the controllable pitch propeller pitch–RPM relationship, frequently termed the 'combinator diagram' can be programmed to give an optimal overall efficiency for the vessel.

In general, in any shaft line three power definitions are assumed to exist, these being the brake horse power, the shaft horse power and the delivered horse power. The following definitions generally apply:

Brake power (P_B) — The power delivered at the engine coupling or flywheel.

Shaft power (P_S) — The power available at the output coupling of the gearbox, if fitted. If no gearbox is fitted then $P_S = P_B$. Also, if a shaft-driven generator is fitted on the line shaft, then two shaft powers exist; one before the generator P_{SI} and the one aft of the generator $P_{SA} = P_{SI} - P_G$. In this latter case some bearing losses may also be taken into account.

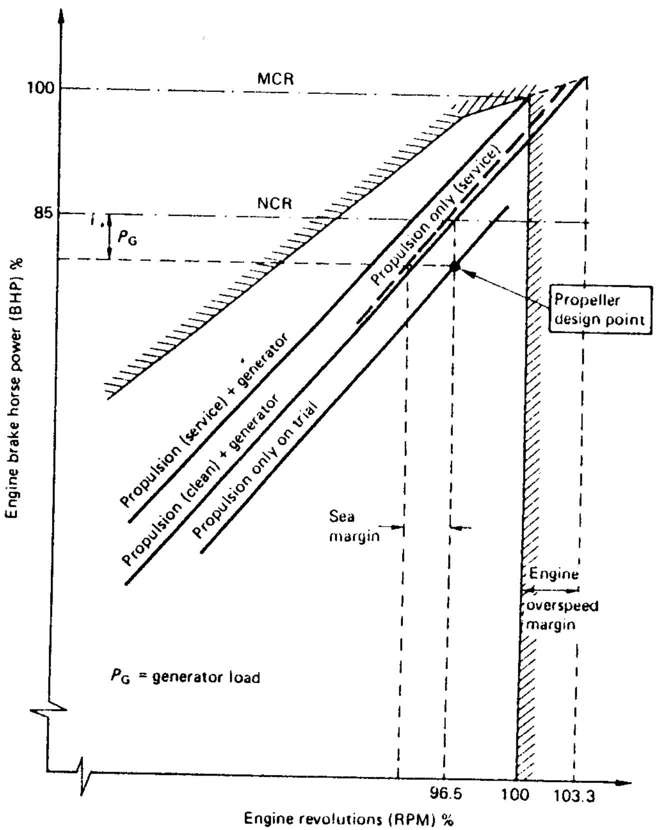

Figure 21.9 Typical propeller design point

Delivered power (P_D) — The power available at the propeller after the bearing losses have been deducted.

In design terms, where no shaft generators exist to absorb power it is normally assumed that P_D is between 98 and 99% of the value of P_S depending on the length of the line shafting and the number of bearings. When a gearbox is installed, then P_S is between 96 and 98% of the value of P_B, depending on the gearbox type.

21.5 The use of standard series data in design

Standard series data is one of the most valuable tools the designer has at his disposal for preliminary design and feasibility study purposes. Design charts, or in many cases today regression formulae, based on standard series data can be used to explore the principal dimensions of a propeller and their effect on performance and cavitation prior to the employment of more detailed design or analysis techniques. In many cases, however, propellers are designed solely on the basis of standard series data, the only modification being to the section thickness distribution for strength purposes. This practice not only commonly occurs for small propellers but is also seen to a limited extent on the larger merchant propellers.

When using design charts, however, the user should be careful of the unfairness that exists between some of the early charts, and therefore should always, where possible, use a cross-plotting technique with these earlier charts between the charts for different blade area ratios. These unfairnesses arose in earlier times

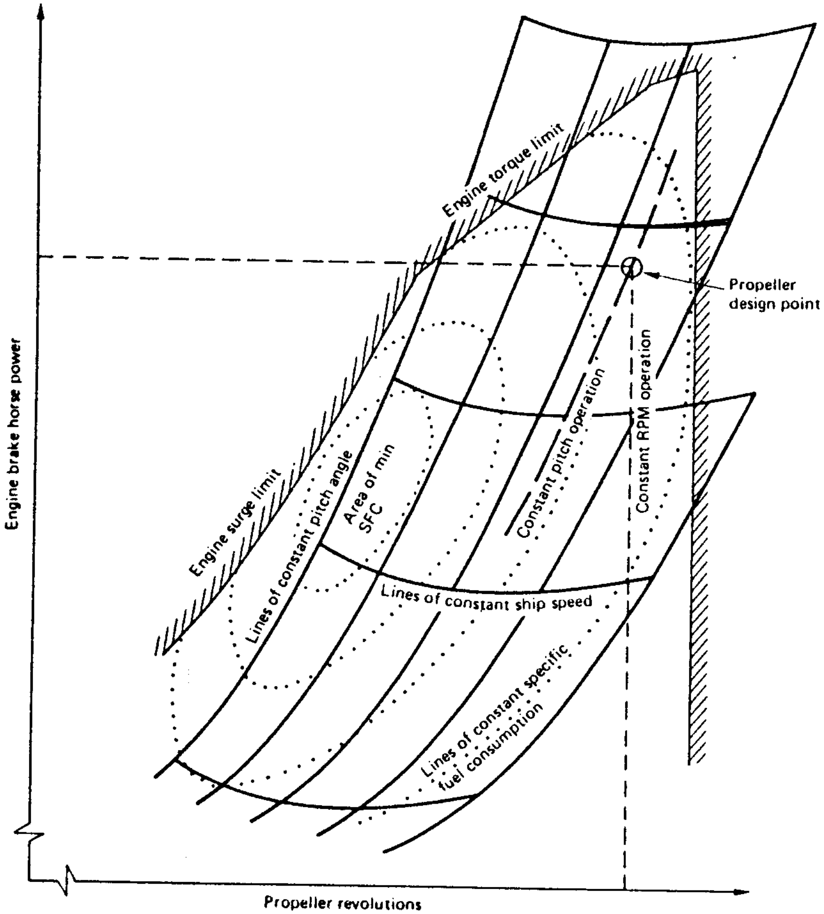

Figure 21.10 Controllable pitch propeller characteristic curve superimposed on a typical engine mapping

when scale effects were less well understood than they are today, and in several of the series this has now been eradicated by recalculating the measured results to a common Reynolds number base.

Some examples of the use of standard series data are given below. In each of these cases, which are aimed to illustrate the use of the various design charts, the hand calculation procedure has been adopted. This is quite deliberate, since if the basis of the procedure is understood, then the computer-based calculations will be more readily accepted and be able to be critically reviewed. The examples shown are clearly not exhaustive, but serve to demonstrate the underlying use of standard series data.

21.5.1 The determination of diameter

To determine the propeller diameter D for a propeller when absorbing a certain delivered power P_D and a rotational speed N and in association with a ship speed V_s, it is first necessary to determine a mean design Taylor wake fraction (w_T) from either experience, published data or model test results. From this the mean speed of advance V_a can be determined as

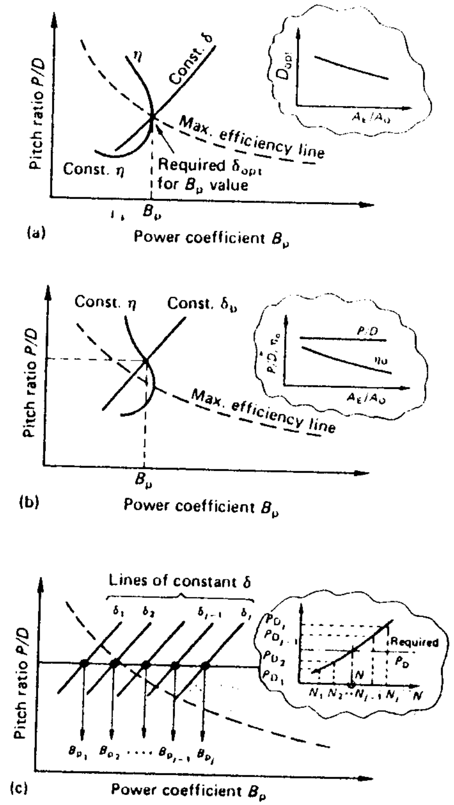

Figure 21.11 Examples of use of standard series data in the $B_p \sim \delta$ form: (a) diameter determination; (b) pitch ratio and open water efficiency determination; (c) power absorption analysis of a propeller

$V_a = (1 - w_T)V_s$. This then enables the power coefficient B_p to be determined as follows:

$$B_p = \frac{P_D^{1/2} N}{V_a^{2.5}}$$

which is then entered into the appropriate design chart as seen in Figure 21.11(a). The value of δ_{opt} is then read off from the appropriate 'constant δ line' at the point of intersection of this line and the maximum efficiency line for the required B_p value. From this the optimum diameter D_{opt} can be calculated from the equation

$$D_{opt} = \frac{\delta_{opt} V_a}{N} \tag{21.1}$$

If undertaking this process manually this should be repeated for a range of blade area ratios in order to interpolate for the required blade area ratio: in general optimum diameter will decrease for increasing blade area ratio, see insert to Figure 21.11(a).

Several designers have produced regression equations for calculating the optimum diameter. One such example produced by van Gunsteren (Reference 7) and, based on the Wageningen B-series, is particularly useful and is given here as

$$\delta_{opt} = 100\left[\frac{B_p^3}{(155.3 + 75.11B_p^{0.5} + 30.76B_p)}\right]^{0.2} \times \left[0.9365 + \frac{1.49}{Z} - \left(\frac{2.101}{Z} - 0.1478\right)^2 \times \frac{A_E}{A_O}\right] \tag{21.2}$$

where B_p is calculated in British units of British horse power, RPM and knots; Z is the number of blades and A_E/A_O is the expanded area ratio.

Having calculated the optimum diameter in either of these ways, it then needs to be translated to a behind hull diameter D_b in order to establish the diameter for the propeller when working under the influence of the ship rather than in open water. Section 21.6 discusses this aspect of design.

21.5.2 Determination of mean pitch ratio

Assuming that the propeller B_p value is known and the behind hull diameter D_b is known, then to evaluate the mean pitch ratio of the standard series equivalent propeller is an easy matter. First the behind hull δ value is calculated as

$$\delta_b = \frac{ND_b}{V_a} \tag{21.3}$$

from which this value together with the power coefficient B_p is entered onto the B_p–δ chart, as shown in Figure 21.11(b). From this chart the equivalent pitch ratio (P/D) can be read off directly. As in the case of propeller diameter this process should be repeated for a range of blade area ratios in order to interpolate for the required blade area ratio. It will be found, however, that P/D is relatively insensitive to blade area ratio under normal circumstances.

In the case of the Wageningen B series all of the propellers have constant pitch with the exception of the four-blade series, where there is a reduction of pitch toward the root, see Chapter 6. In this latter case, the P/D value derived from the chart needs to be reduced by 1.5% in order to arrive at the mean pitch.

21.5.3 Determination of open water efficiency

This is derived at the time of the mean pitch determination when the appropriate value of η_o can be read off from the appropriate constant efficiency curve corresponding to the value of B_p and δ_b derived from equation (21.3).

21.5.4 To find the RPM of a propeller to give the required P_D or P_E

In this case, which is valuable in power absorption studies, a propeller would be defined in terms of its diameter, pitch ratio and blade area ratio and the problem is to define the RPM to give a particular delivered power P_D or, by implication, P_E. In addition it is necessary to specify the speed of advance V_a either as a known value or as an initial value to converge in an iterative loop.

The procedure is to form a series of RPM values, N_j (where $j = 1, \ldots, k$) from which a corresponding set of δ_j can be produced. Then by using the B_p–δ chart in association with the P/D values, a set of B_{p_j} values can be produced, as seen in Figure 21.11(c). From these values the delivered powers P_{D_j} can be calculated, corresponding to the initial set of N_j, and the required RPM can be deduced by interpolation to correspond to the particular value of P_D required. The value of P_D is, however, associated with the blade area ratio of the chart, and consequently this procedure needs to be repeated for a range of A_E/A_O values to allow the unique value of P_D to be determined for the actual A_E/A_O of the propeller.

By implication this can be extended to the production of the effective power to correlate with the initial value of V_a chosen. To accomplish this the open water efficiency needs to be read off at the same time as the range of B_{p_j} values to form a set of η_{o_j} values. Then the efficiency η_o can be calculated to correspond with the required value of P_D in order to calculate the effective power P_E as

$$P_E = \eta_o \eta_H \eta_r P_D$$

Figure 21.12 demonstrates the algorithm for this calculation, which is typical of many similar procedures that can be based on standard series analysis to solve erparticular problems.

21.5.5 Determination of propeller thrust at given conditions

The estimation of propeller thrust for a general free running condition is a trivial matter once the open water efficiency η_o has been determined from a B_p–δ diagram and the delivered power and speed of advance are known. In this case the thrust becomes

$$T = \frac{P_D \eta_o}{V_a} \tag{21.4}$$

However, at many operating conditions such as towing or the extreme example of zero ship speed, the determination of η_o is difficult or impossible since, when V_a is small, then $B_p \to \infty$ and, therefore, the B_p–δ chart cannot be used. In the case when $V_a = 0$ the open water efficiency η_o looses significance because it is the ratio of thrust power to the delivered power and the thrust power is zero because $V_a = 0$; in addition, equation (21.4) is meaningless since V_a is zero. As a consequence, a new method has to be sought.

Use can be made either of the standard K_T–J propeller characteristics or alternatively of the μ–σ diagram. In the case of the K_T–J curve, if the pitch ratio and the RPM and V_a are known, then the advance coefficient J can be determined and the appropriate value of K_T read off directly, and from this the thrust can be determined. Alternatively, the μ–σ approach can be adopted as shown in Figure 21.13.

21.5.6 Exploration of the effects of cavitation

In all propellers the effects of cavitation are important. In the case of general merchant propellers some standard series give guidance on cavitation in the global sense; see for example, the KCD series of propellers where generalized face and back cavitation limits are given. The problem of cavitation for merchant ship propellers, whilst addressed early in the design process, is nevertheless generally given more detail assessment, in terms of pressure distribution etc., in later stages of the design. In the case of high-speed propellers, however, the effects of cavitation need particular consideration at the earliest stage in the design process.

Many of the high-speed propeller series include the effects of cavitation by effectively repeating the model tests at a range of free stream cavitation numbers based on advance velocity. Typical in this respect is the KCA series. From propeller series of this kind the influence of cavitation on the propeller design can be explored, for example, by taking a series of charts for different blade area ratios and plotting for a given advance coefficient K_Q against the values of σ tested to show the effect of blade area against thrust or torque breakdown for a given value of cavitation number. Figure 21.14 demonstrates this approach. In the design process for high-speed propellers several analogous design studies need to be undertaken to explore the effects of different diameters, pitch ratios and blade areas on the cavitation properties of the propeller.

21.6 Basic design considerations

The design process of a propeller should not simply be a mechanical process of going through a series of steps such as those defined in the previous section. Like any design it is a creative process of resolving the various constraints to produce an optimal solution. An eminent propeller designer once said 'It is very difficult to produce a bad propeller design but it is equally difficult to produce a first class design.' These

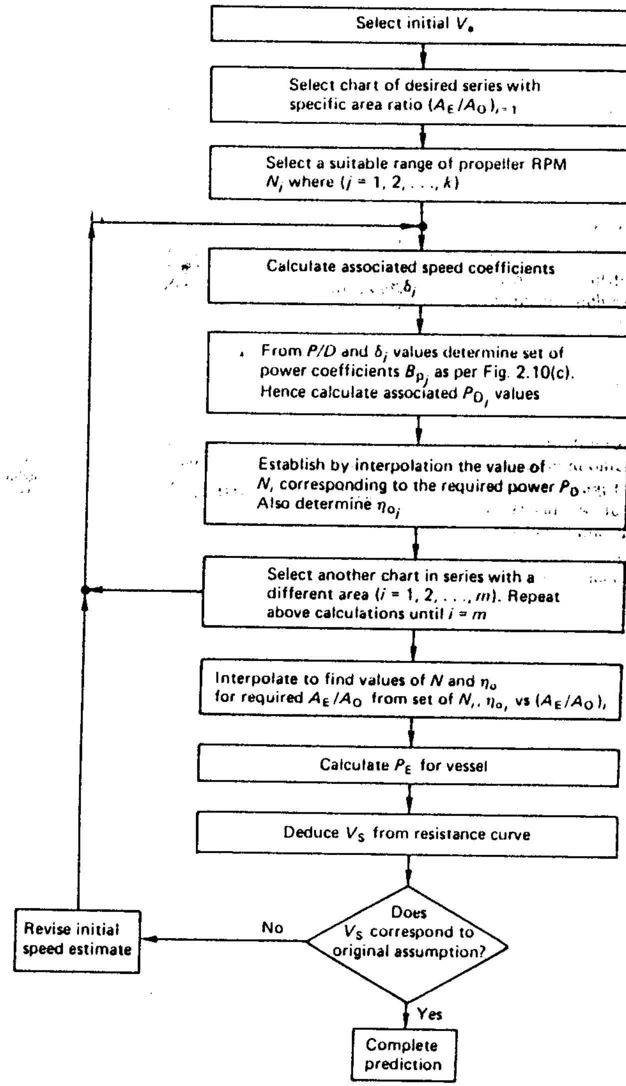

Figure 21.12 Calculation algorithm for power absorption calculations by hand calculation

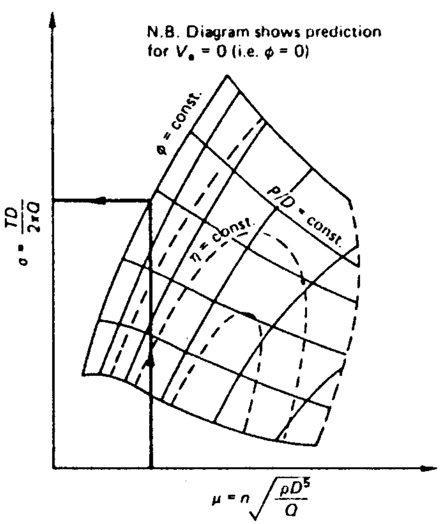

Figure 21.13 The use of the μ-σ chart in thrust prediction

words are very true and should be engraved on any designer's heart.

21.6.1 Direction of rotation

The direction of rotation of the propeller has important consequences for manoeuvring and also for cavitation and efficiency considerations with twin-screw vessels. In terms of manoeuvring, for a single-screw vessel the influence on manoeuvring is entirely determined by the 'paddle wheel effect'. When the vessel is stationary and the propeller started, the propeller will move the afterbody of the ship in the direction of rotation: that is in the sense of a paddle or road wheel moving relative to the ground. Thus with a fixed pitch propeller, this direction of initial movement will change with the direction of rotation, that is ahead or astern thrust, whilst in the case of a controllable pitch propeller the movement will tend to be unidirectional. In the case of twin-screw vessels, certain differences become apparent. In addition to the paddle wheel effect other forces due to the pressure differential on the hull and shaft eccentricity come into effect. The pressure differential, due to reverse thrusts of the propellers, on either side of the hull gives a lateral force and turning moment, Figure 21.15, which remains largely unchanged for fixed and controllable pitch propellers and direction of rotation. The magnitude of this thrust is of course a variable depending on the

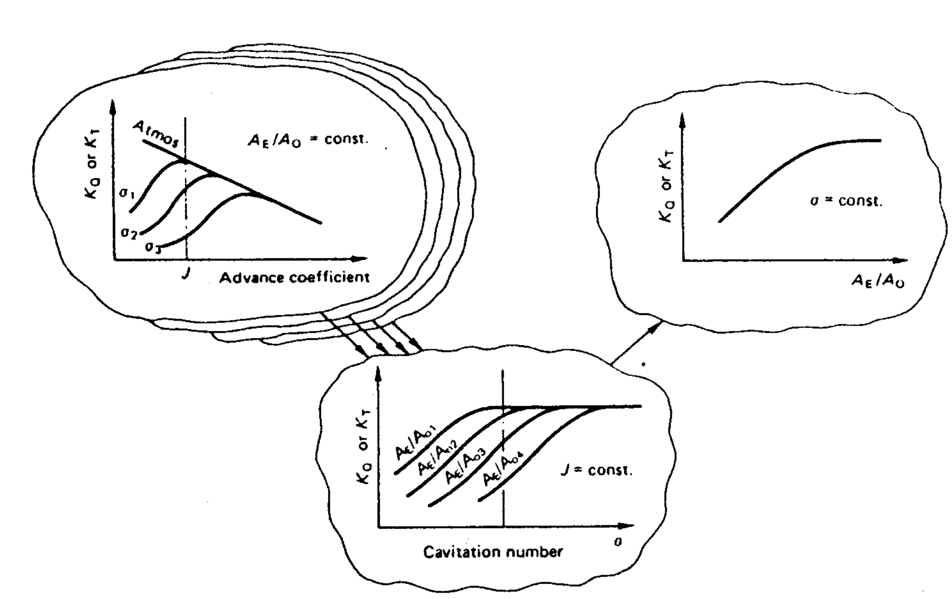

Figure 21.14 The use of high-speed standard series data to explore the effects of cavitation

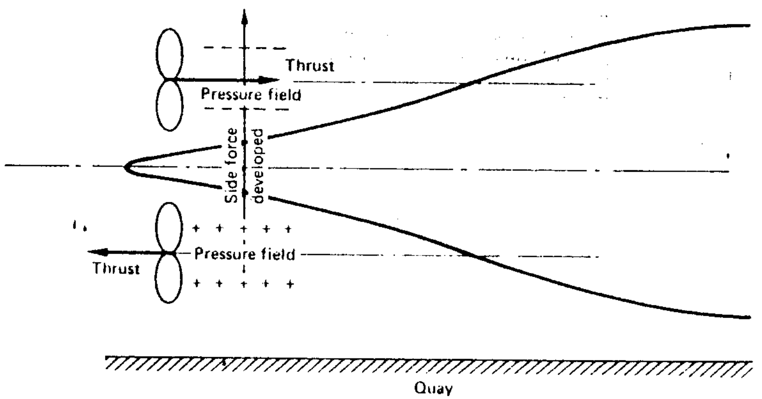

Figure 21.15 Side force developed by reversing thrusts of propellers on a twin-screw vessel due to pressure field in hull

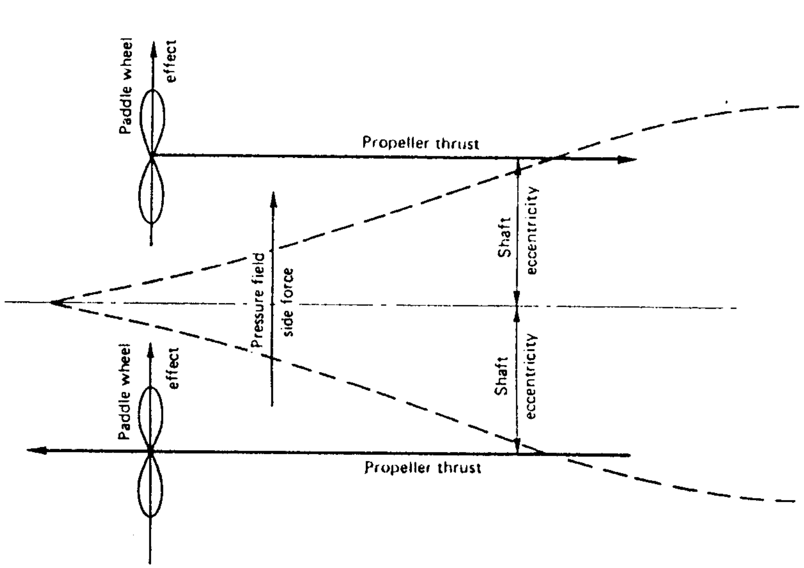

Induced turning moment = propeller thrust eccentricity + paddle wheel effect + pressure field side force

Figure 21.16 Induced turning moment components

underwater hull form: in the case of some gondola hull forms, it is practically non-existent. However, in the general case of manoeuvring van Gunsteren (Reference 7) undertook an analysis between rotation direction and fixed and controllable pitch propellers to produce a ranking of the magnitude of the turning moment produced. This analysis took into account shaft eccentricity, the axial pressure field and the paddle wheel effect (Figure 21.16) based on full-scale measurements (Reference 8) for frigates. The results of his analysis are shown in Table 21.4 for manoeuvring with two propellers giving equal thrusts and in Table

Table 21.4 Turning moment ranking of two propellers producing equal thrusts (compiled from Reference 7)

Twin-screw installation (reverse thrusts)	*Turning moment ranking*
F.p.p.; inward turning	−2.1
F.p.p.; outward turning	10.1
C.p.p.; inward turning	3.3
C.p.p.; outward turning	4.6

C.p.p. = controllable pitch propeller.
F.p.p. = fixed pitch propeller.

Table 21.5 Turning moment ranking of one propeller operating on a twin-screw installation (compiled from Reference 7)

Twin-screw installation (single propeller operation)	*Direction of thrust*	*Turning moment ranking*
F.p.p.; inward turning	Forward	−1.2
F.p.p.; inward turning	Astern	−1.1
F.p.p.; outward turning	Forward	5.6
F.p.p.; outward turning	Astern	4.5
C.p.p.; inward turning	Forward	−1.2
C.p.p.; inward turning	Astern	4.5
C.p.p.; outward turning	Forward	5.6
C.p.p.; outward turning	Astern	−1.1

21.5 for manoeuvring on a single propeller.

Whilst the magnitudes in Tables 21.4 and 21.5 relate to particular trials, they do give guidance on the effect of propeller rotation on manoeuvrability. The negative signs were introduced to indicate a turning moment contrary to nautical intuition. From the manoeuvrability point of view it can be deduced that fixed pitch propellers are best when outward turning; however, no such clear-cut conclusion exists for the controllable pitch propeller.

From the propeller efficiency point of view, it has been found that the rotation present in the wake field, due to the flow around the ship, at the propeller disc can lead to a gain in propeller efficiency when the direction of rotation of the propeller is opposite to the direction of rotation in the wake field. However, if concern over cavitation extent is present, then this can to some extent be helped by considering the propeller rotation in relation to the wake rotation. If the problem exists for a twin screw ship at the tip, then the blades should turn in the opposite sense to the rotation in the wake, whilst if the concern is at root then the propellers should rotate in the same sense as the wake rotation. As a consequence the dangers of blade tip and tip vortex cavitation need to be carefully considered against the possibility of root cavitation.

21.6.2 Blade number

The number of blades is primarily determined by the need to avoid harmful resonant frequencies of the ship structure and the machinery. However, as blade number increases for a given design the extent of the suction side sheet cavity generally tends to decrease. At the root, the cavitation problems can be enhanced by choosing a high blade number, since the blade clearances become less in this case.

In addition to resonant excitation and cavitation considerations, it is also found that both propeller efficiency and optimum propeller diameter increase as blade number reduces. As a consequence of this latter effect, it will be found, in cases where a limiting propeller diameter is selected, that propeller rotational speed will be dependent on blade number to some extent.

The cyclical variations in thrust and torque forces generated by the propeller are also dependent on blade number and this dependence was discussed in Chapter 11 – in particular, in Table 11.13.

21.6.3 Diameter, pitch–diameter ratio and rotational speed

The choice of these parameters is generally made on the basis of optimum efficiency. However, efficiency is only moderately influenced by small deviations in the diameter, P/D and revolutions when the delivered horse power is held constant. The effect of these parameters on the cavitation behaviour of the propeller is extremely important, and so needs careful exploration at the preliminary design stage. For example, it is likely the propellers of high-powered or fast ships should have an effective pitch diameter ratio larger than the optimum value determined on the basis of optimum efficiency. Furthermore, it is generally true that a low rotational speed of the propeller is a particularly effective means of retarding the development of cavitation over the suction faces of the blades.

In Section 21.5.1 the optimum diameter calculation was discussed. For an actual propeller working behind a ship the diameter needs to be reduced from the optimum value predicted from the standard series data, and traditionally this was done by reducing the optimum diameter by 5% and 3%, for single and twin screw vessels respectively. This correction is necessary because the resultant propulsion efficiency of the vessel is a function of both the open water propeller efficiency, to which the chart optimum diameter refers, and the propeller–hull interaction effects. Hawdon *et al.* (Reference 9) conducted a study into the effects of the character of the wake field on the optimum diameter. From this study they derived a relationship of the form shown in Figure 21.17; however, the authors note that, in addition to the mean effective wake, it is necessary to take into account the radial wake distribution as implied by the distinction between different hull forms.

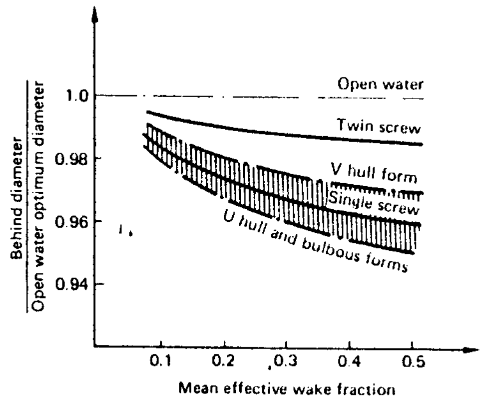

Figure 21.17 Correction to optimum open water diameter (Reference 9)

21.6.4 Blade area ratio

In general, the required expanded area ratio when the propeller is operating in a wake field is larger than that required to simply avoid cavitation at shock-free angles of attack. Furthermore, a larger variation in the section angle of attack can to some extent be supported by increasing the expanded area ratio of the propeller. Nevertheless, in the case of a controllable pitch propeller there is a limit to the extent of the blade area due to the requirement of blade–blade passing in order to obtain reversibility of the blades. Notwithstanding the advantages of increasing blade area, it must be remembered that this leads to an increase section drag and hence a loss in efficiency of the propeller (see Figure 21.11(b)).

21.6.5 Section form

In terms of section form, the most desirable thickness distribution from the cavitation viewpoint is an elliptic form. This, however, is not very practical in section drag terms and in practice the NACA 16, 65 and 66 (modified) forms are the most utilized. With regard to mean lines, the NACA $a = 1.0$ is not generally considered a good form since the effect of viscosity on lift for this camber line is large and there is doubt as to whether the load distribution can be achieved in practice. The most favoured form would seem to be the NACA $a = 0.8$ or 0.8 (modified).

21.6.6 Cavitation

Sheet cavitation is generally caused by the suction peaks in the way of the leading edge being too high whilst bubble cavitation tends to be induced by too high cambers being used in the mid-chord region of the blade.

The choice of section pitch and the associated camber line should aim to minimize or eradicate the possibility of face cavitation. Hence the section form and its associated angle of attack requires to be designed so that it can accommodate the full range of negative incidence.

There are few propellers in service today which do not cavitate at some point around the propeller disc. The secret of design is to accept that cavitation will occur but to minimize its effects, both in terms of the erosive and pressure impulse effects.

The initial blade design can be undertaken using one of the basic estimation procedures, notably the Burrill cavitation chart or the Keller formula, see Chapter 9. These methods give a reasonable first approximation to the blade area ratio required for a particular application. The full propeller design process needs to incorporate within it procedures to design the radial distribution of chord length and camber in association with cavitation criteria rather than through the use of standard outlines.

If the blade area, or more specifically the section chord length, is unduly restricted, then in order to generate the same lift from section, this being a function of the product cc_l, the lift coefficient must increase. This generally implies a larger angle of attack or camber, which in turn leads to higher suction pressures, and hence greater susceptibility to cavitation. Hence, in order to minimize the extent of cavitation, the variations in the angle of attack around the propeller disc should only give rise to lift coefficients in the region of shock-free flow entry for the section if this is possible.

In general terms the extent of sheet cavitation, particularly with high-powered fast ships, tends to be minimized when the blade section thickness is chosen to be sufficiently high to fall just below the inception of bubble cavitation on the blades. With respect to the other section parameters, the selection of the blade camber and pitch should normally be such that the attitude of the resultant section can accommodate the negative incidence range that the section has to meet in practice whilst the radial distribution of chord length needs to be selected in association with the variations in in-flow angle.

Tip vortex cavitation is best controlled by adjustment of the radial distribution of blade loading near the tip. The radial distribution of bound circulation at the blade tip lies within the range:

$$0 \leqslant \frac{d\Gamma}{dr} < \infty \tag{21.5}$$

Hence, the closer $d\Gamma/dr$ is to zero, the greater will be the control of the tip vortex strength. In addition to the control exerted by equation (21.5) further control can be exerted by choosing the highest number of

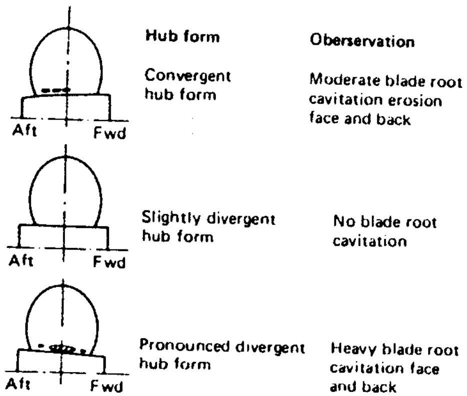

Figure 21.18 Observed blade root cavitation erosion on a fast patrol craft propeller

Figure 21.19 Truncated fairwater cone fitted to a high-speed patrol vessel

propeller blades, since this means that the total load is distributed over a greater number of blades.

21.6.7 Skew

The use of skew has been shown to be effective in reducing both shaft vibratory forces and hull pressure induced vibration (see Figure 22.6). The effectiveness of a blade skew distribution for retarding cavitation development depends to a very large extent on the matching of the propeller skew with the skew of the maximum or minimum in-flow angle in the radial sense.

21.6.8 Hub form

It is clearly advantangeous for the propeller hub to be as small as possible consistent with its strength and the flexibility it gives to the blade root section design.

In addition to the hub diameter consideration, the form of the hub is of considerable importance. A convergent hub form is normally quite satisfactory for slow merchant vessels; however, for higher-speed ships and fast patrol vessels or warships experience indicates that a slightly divergent hub form is best from the point of view of avoiding root erosion problems. In the case of a fast patrol craft van Gunsteren and Pronk (Reference 10) experimented with different hub profiles, and the results are shown in Figure 21.18. The convergent hub enlarges the flow disc area between the hub and the edge of the slipstream, which has only minimal contraction, from forward to aft, and therefore decelerates the flow which results in positive pressure gradient. This may introduce flow separation that promotes cavitation. The strongly divergent hub accelerates the flow, and therefore reduces the pressure, which again promotes cavitation.

In addition to the use of a slightly divergent hub form, where appropriate, the use of a parallel or divergent cone (Figure 21.19) can assist greatly in reducing the strength of the root vortices and their erosive effects on the rudder.

21.6.9 Shaft inclination

If the propeller shafts are inclined in any significant way, this gives rise to a cyclic variation in the advance angle of the flow entering the propeller. The amplitude of this variation is given by

$$\Delta\beta = \frac{\sin\phi}{1 + \left(\frac{\pi x}{J}\right)} \qquad (21.6)$$

where ϕ is the inclination of the shaft relative to the flow and β is the advance angle at the particular radius. It should be noted that ϕ varies between a static and dynamic trim condition, and this can in some cases be quite significant. In addition to the consequences for cavitation at the root sections, since equation (21.6) gives a larger value for $\Delta\beta$ at the root than at the tip, shaft inclination can give rise to significant lateral and shaft eccentricity forces and moments as discussed in Chapter 6.

21.6.10 Duct form

When a ducted propeller is selected a choice of duct form is required. In choosing a duct form for normal commercial purposes it is necessary to ensure that the form is both hydrodynamically reasonable and also practical and easy to manufacture. For many commercial purposes a duct form of the Wageningen 19a type will suffice when a predominately unidirectional accelerating duct form is required. When an improved astern performance is required, then a duct based on the Wageningen No. 36 form usually provides an acceptable compromise between ahead and astern operation.

The use of decelerating duct forms are comparatively rare outside of naval practice and generally operate at rather higher B_p values than the conventional accelerating duct form.

21.7 Detailed design considerations

The level of detail to which a propeller design process is taken is almost as variable as the number of propeller designers in existence. The principal manufacturers all have detailed design capabilities, albeit based on different methods. Whilst computational capability of the designer plays a large part in the detail of the design process, the information available upon which to base the design is also an important factor: there is little value in using advanced and high-level computational techniques requiring detailed input when gross assumptions have to be made concerning the basis of the design. Figures 21.20 and 21.21 show two extreme examples of the design processes used in propeller technology.

Leaving to one side the design of propellers which are standard 'off the shelf' designs such as may be found on outboard motor boats, the design process shown in Figure 21.20 represents the most basic form of propeller design that could be considered acceptable by any competent designer. Such a design process might be expected to be applied to, say, a small fishing boat or large workboat, where little is known of the in-flow into the propeller. It is not unknown, however, to see standard series propellers applied to much larger vessels of a 100 000 tonnes deadweight and above; such occurrences are, however, comparatively rare and more advanced design processes normally need to be used for these vessels. The design of high speed propellers can also present a complex design problem. In the calculation of such propellers the second box, which identifies the calculation of the blade dimensions, may involve a considerable amount of chart work with standard series data: this is particularly true if unfavourable cavitation conditions are encountered.

Blade stresses should always, in the author's view, be calculated as a separate entity by the designer, using as a minimum the cantilever beam technique followed by a fatigue estimate based on the material's properties. The use of classification society minimum thicknesses should always be used as a check to see that the design satisfies these conditions, since they are generalized minimum standards of strength.

Since many standard series propellers are of the flat face type an increase in thickness gives an implied increase in camber which will increase the propeller blade effective pitch. After the propeller has been adjusted for strength the design needs to be analysed for power absorption using the methods of Chapters 3 and 6 in order to derive the appropriate blade pitch distribution. During the design process the question of design tolerances need to be addressed whatever level of design is used, otherwise significant departures between design and practice will occur. Chapter 24 discusses the issue further.

Whilst Figure 21.20 shows the simplest form of design method and such processes are used to design perfectly satisfactory propellers for many vessels, more complex design procedures become necessary when increasing constraints are placed on the design and increasing amounts of basic information are available upon which to base the design. Variants of the design process shown in Figure 21.20 normally increase in complexity when a mean circumferential wake distribution is substituted for the mean wake fraction. This then enables the propeller to become wake adapted through the use of lifting line or higher-order design methods and the analysis phase may then embody a blade element, lifting line or lifting surface based analysis procedure for different angular positions in the propeller disc: this presupposes that model wake data is available rather than the mean radial wake distribution being estimated from the procedures discussed in Chapter 5. As the complexity of the design procedure increases, the process outlined in Figure 21.21 is approached, which embodies most of the advanced design and analysis techniques available today. Each designer, however, will use different theoretical methods and his correlation with full-scale experience will be dependent on the methods used. This underlines the reason why it may be dangerous and unjust to criticize a designer for not using the most up-to-date theoretical methods, since the extent of his theoretical to full-scale correlation data base may outweigh the advantages given by use of more up-to-date methods.

Theoretical design methods, and analysis methods too for that matter, will only take the designer so far. Current knowledge is lacking in many detailed aspects of propeller design; nowhere is this more true than in defining the flow at the blade–boss interface of all propellers. In such cases careful assumptions regarding the assumed blade loading at the root have to be made in the context of the anticipated severity of the in-flow conditions – this may dictate that a zero circulation or some other condition, determined from experience,

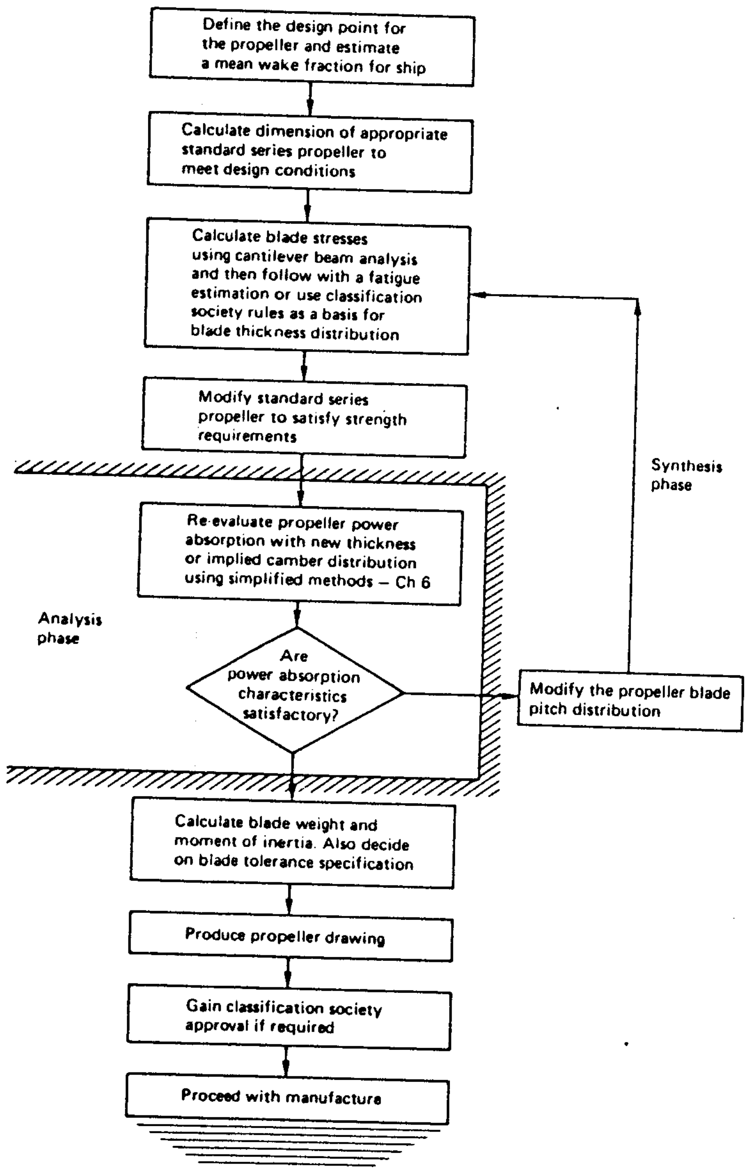

Figure 21.20 Example of a simplified design procedure

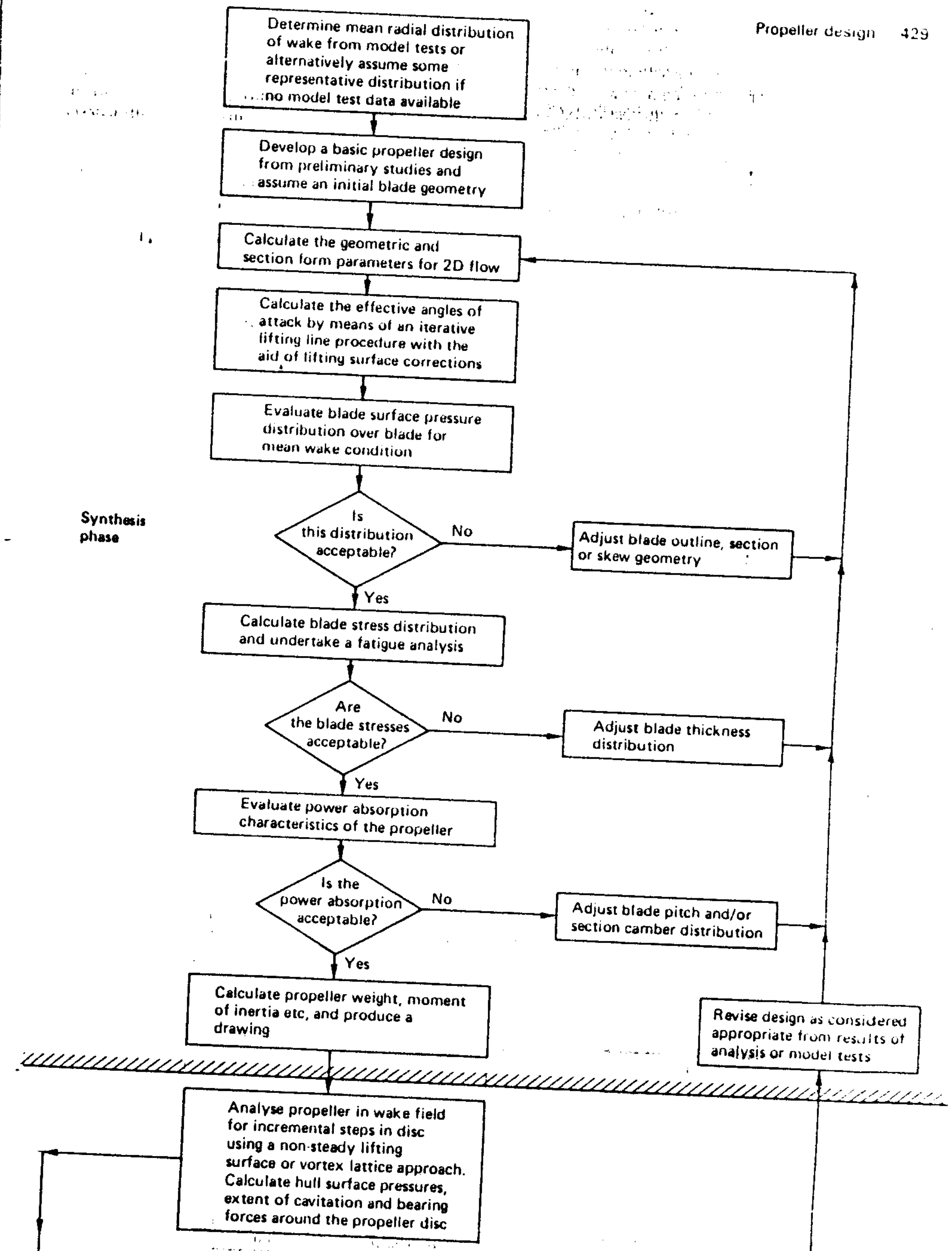

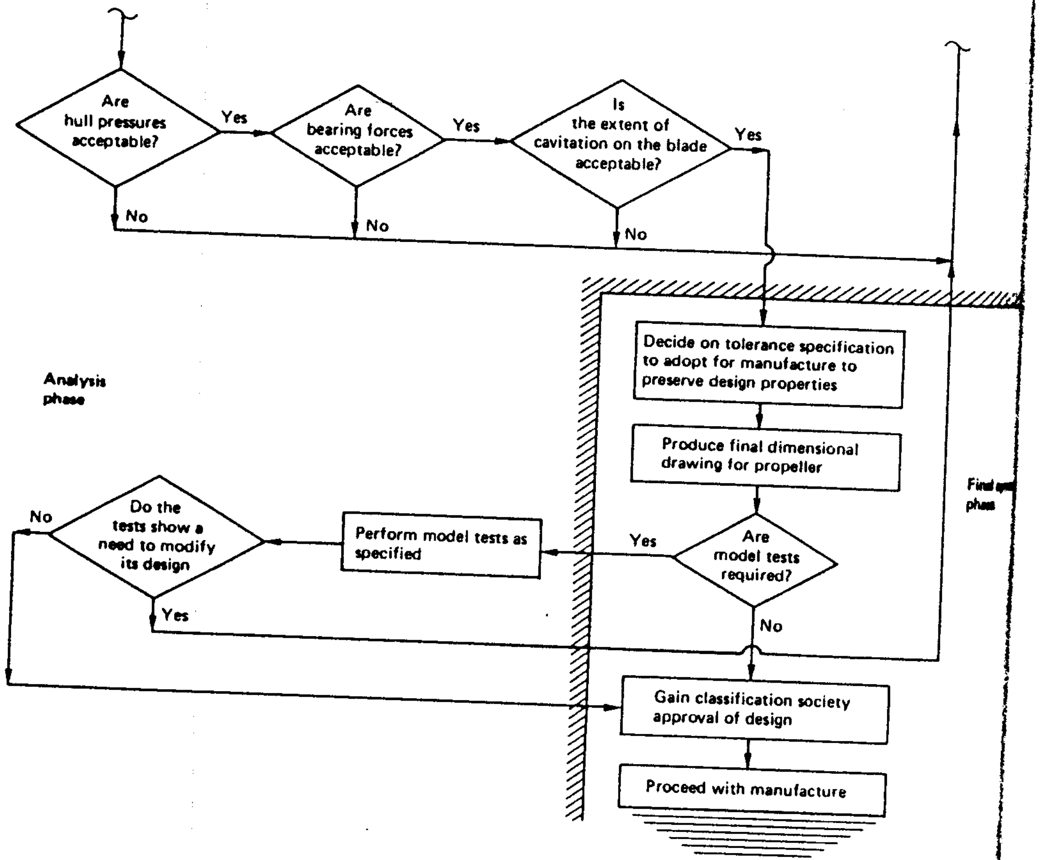

Figure 21.21 *(Continued from previous page)* Example of a fully integrated synthesis and analysis procedure

is an appropriate assumption. In either case the actual circulation which occurs on the blade will not be known due to the nature of the complex three-dimensional flow regime in this region of the blade. Another classic example is the definition of the geometric and flow conditions that cause singing, although in this case the remedy is well known for normal propeller types.

It will, however, be noted that each of the design processes shown in Figures 21.20 and 21.21 contain the elements of synthesis and analysis phase shown in Figure 21.2. Much has been written on the subject of propeller design and analysis by many practitioners of the subject. The references in this book contain a considerable amount of this information, however, References 11 through to 26 in this chapter contain work specifically related to design and analysis which is not referred to elsewhere in this book.

References and further reading

1. Manen, J.D. van. The choice of the propeller, *Marine Technology*, April, 1966.
2. Tachmindji, A.J., Morgan, W.B. The design and estimated performance of a series of supercavitating propellers. *2nd Symp. on Naval Hydrodynamics*, Washington, 1958.
3. Manen, J.D. van. Ergebnisse systematischer versuche mit propellern mit annahernd senkrecht slehender achse. *Jahrbuch* STG, 1963.
4. Tachmindji, A.J., Morgan, W.B., Miller, M.L., Hecher, R. The Design and Performance of Supercavitating Propellers. DTMB Rep. C-807, February, 1957.
5. Carlton, J.S. Propeller service experience. *7th Lips Symposium*, 1989.
6. Carlton, J.S. Marine diesel engine exhaust emissions when operating with variable quality fuel and under service conditions. *Trans. I.Mar.E., IMAS 90 Conf.*, May, 1990.
7. Gunsteren, L.A. van. Design and performance of controllable pitch propellers. *Trans. SNAME*, New York Sect.
8. Voorde, C.B. van de. Effect of Inward and Outward Turning Propellers on Manoeuvring Alongside for Ships of the Frigate Class. NSMB Report No. 68-015-BT, 1968.
9. Hawdon, L., Patience, G., Clayton, J.A. The effect of the wake distribution on the optimum diameter of marine propellers. *Trans. NECIES, NEC100 Conf.*, 1984.
10. Gunsteren, L.A. van, Pronk, C. Propeller design concepts. *ISP*, **20**(227), July, 1973.
11. Burrill, L.C. *Considérations sur le Diamètre Optimum des Hélices*, Assoc. Tech. Maritime et Aéronautique, Paris, 1955.
12. Burrill, L.C. Progress in marine theory, design and research in Great Britain. *Appl. Mech. Convention, Trans. I.Mech.E.*, 1964.
13. Hannan, T.E. *Strategy for Propeller Design*. Thos. Reed Publ., 1971.
14. Hannan, T.E. Principles and Design of the Marine Screw Propeller.
15. Cummings, R.A. *et al.* Highly skewed propellers. *Trans. SNAME*, November, 1972.
16. Sinclair, L., Emerson, A. Calculation, experiment and experience in merchant ship propeller design. *IMAS 73 Conf. Trans. I.Mar.E.*, 1973.
17. Boswell, R.J., Cox, G.G. Design and model evaluation of a highly skewed propeller for a cargo ship. *Mar. Tech.*, January, 1974.
18. Parsons, C.G. Tuning the screw. *Marine Week*, September 12, 1975.
19. Oossanen, P. van. Trade Offs in the Design of Sub-Cavitating Propellers. NSMB Publ. No. 491, 1976.
20. Dyne, G. A note on the design of wake-adapted propellers. *J. Ship. Res.*, **24**(4), December, 1980.
21. Hawdon, L., Patience, G. Propeller design for economy. *3rd Int. Marine Propulsion Conf.*, London, 1981.
22. Hadler, K.B. *et al.* Large diameter propellers of reduced weight. *Trans. SNAME*, **90**, 1982.
23. Holden, K., Kvinge, T. On application of skew propellers to increase propulsion efficiency. *5th Lips Propeller Symposium*, 1983.
24. Beek, T. van, Verbeek, R. Design aspects of efficient marine propellers. *Jahrbuck der Schiffbautechnischen Gesellschaft*, 1983.
25. Norton, J.A., Elliot, K.W. Current practices and future trends in marine propeller design and manufacture. *Mar. Tech.*, **25**(2), April, 1988.
26. Klintorp, H. Integrated design for efficient operation. *Motor Ship*, January, 1989.

22 Operational problems

Contents

When a propeller enters service, despite the best endeavours of the designers and manufacturers, problems in performance can, from time to time, arise. Equally, during the service life of the ship a wide range of problems may also be encountered. Figure 22.1 outlines some of the more common problems that can be encountered during the lifetime of the propeller.

Figure 22.1 essentially draws the distinction between accidental damage, due to impact or grounding of the blades, and the other class of problem which relate to the performance and integrity of the propeller in the 'as designed' condition. Each of these classes of problem needs a different treatment, and as a consequence, requires separate consideration.

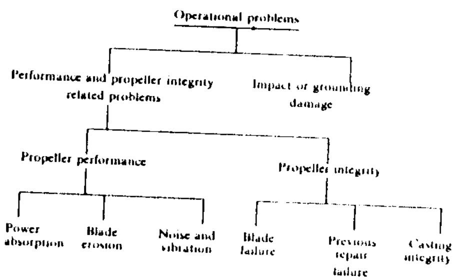

Figure 22.1 Common operational problems

22.1 Performance related problems

Problems related to propeller performance can in a great many cases be traced to a lack of knowledge during the design process of the wake field in which the propeller is operating. When a ship has had the benefit of model testing prior to construction, a model nominal wake field is very likely to have been measured. This then allows the designer to understand in a qualitative sense the characteristics of the wake field in which the propeller is to operate. As discussed in Chapters 5 and 21, the designer needs to transform the model nominal wake field into a ship effective velocity distribution before it can be used for quantitative design purposes. This transformation is far from clearly defined within the current state of knowledge, and so errors may develop in the definition of the effective wake field. In the case where the ship has not been model tested, the designer has less information to work with, and in these cases must rely on his knowledge of other similar ships and the way they performed as well as making empirically based estimates of the type discussed in Chapter 5.

Clearly not all performance problems are traceable to lack of knowledge about the wake field. Other causes, such as poor tolerance specification, poor specification of design criteria, incorrect design and manufacture and so on are also causes of poor performance of the propeller. Figure 22.1 identified three principal headings under performance related problems, and these are now considered individually.

22.1.1 Power absorption problems

Such problems are normally identified by observing that the engine will not produce the required power at either the NCR or MCR conditions. In such conditions the engine attains the required power at either too low or too high an engine speed, and this condition is reflected in the engine exhaust temperatures. Indeed, if engine speed rises too much the engine may not be able to develop the necessary rated power. Alternatively, in vessels where a torsion meter is fitted and assuming it has been calibrated properly and also that it has maintained its calibration, the condition becomes obvious. Another class of power absorption problem is seen in twin-screw vessels, where a power imbalance can sometimes be noted between the port and starboard shaft systems.

Consider these two cases separately. In the first case, and assuming the vessel is new and in a clean state, it is quite likely that the cause will be found in the choice of pitch for the propeller. Notwithstanding this, before attempting to change the effective pitch of the propeller, the blade manufacturing tolerances should be checked against specification and also a check should be made to ensure that the level tolerances specified for the vessel were adequate (see Chapter 24). The effective pitch of the propeller can be changed in one of two ways: either by reducing the diameter of the propeller, frequently termed 'cropping' the blades, or by modifying the blade section form to change the pitch of the blades. If the change required is small, then one or either of these methods will be found to be satisfactory; however, for situations requiring larger changes a combination of the two methods should be undertaken in order to preserve the efficiency of the propeller to its highest level. References 1–3 discuss these effects and show the type of modification that can be achieved. Figure 22.2, taken from Reference 2, shows the effects of modifying the blades by 'cropping' and pitch reduction.

In the case where the vessel is not new and a 'stiffening' of the propeller is seen to take place, assuming the original propeller is still in place and is clean and undamaged, then the most likely cause of the problem is the roughening or fouling of the hull. Clearly in such cases the hull should be cleaned, but if the problem still persists and the engine cannot, over a docking cycle, work within the original design RPM band, then an 'easing' of the propeller pitch may prove desirable since, despite shot blasting and repainting of the hull, an old ship tends to roughen and increase in resistance.

When an imbalance between shaft powers in a twin-screw installation occurs this may be due either

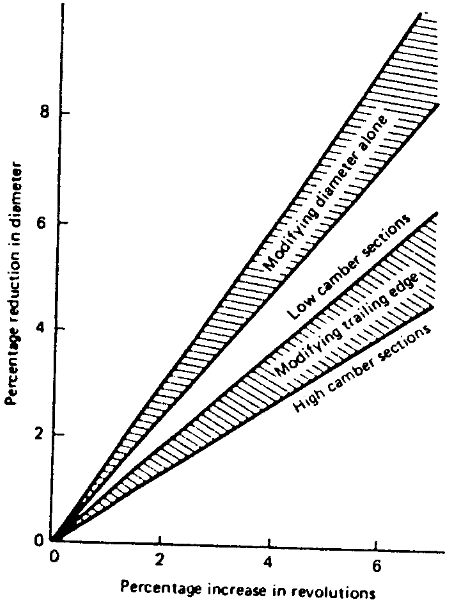

Figure 22.2 The effect of changes in propeller diameter and pitch on performance (Reproduced from Reference 2, with permission)

to one or both propellers being out of specification or to the chosen manufacturing tolerance being too wide and allowing a significant change of effective pitch to occur between the propellers. Although in general there is always difference between the propellers of twin-screw ships this is normally too small to cause concern; however, there are cases where one propeller tends to be at one end of the tolerance band whilst the other is at the opposite end. If this difference in power absorption is too large, then the tolerance specification needs to be tightened and the appropriate geometric changes made.

Two further examples of power absorption problems are to be found in deficiencies in the bollard pull characteristics of tugs, etc., and in thrust breakdown on propellers. In the first case, that of a lack of bollard pull, and assuming that the propeller design is satisfactory, the most common cause of a deficiency is that insufficient clear water has been allowed around the propeller at the trial location. If the water around the propeller is restricted in both width and depth, water circulation tends to take place, which effectively increases the propeller advance coefficient, sometimes quite considerably, and causes a reduction in thrust generated by the propeller. Chapter 16 discusses the conditions desirable for conducting bollard pull trials to ensure a realistic propulsor performance. Furthermore, when considering bollard pull conditions, it is important not to confuse the terms 'propeller thrust' and 'bollard pull'.

Thrust breakdown of propellers due to cavitation is a condition rarely seen today, since it is caused by a grossly inadequate blade area being specified for the propeller. Figure 6.4 shows this effect in terms of K_T vs J diagram in which at low J the K_T characteristic can be seen to fall off rapidly due to the effects of extensive cavitation. For conventional propeller types, that is not supercavitating or surface piercing designs, this occurs only when significant back sheet cavitation occurs; of the order of 30–40% and above of the total area of the backs of the blades. In machinery terms this condition manifests itself as the shaft revolutions building up very quickly at the higher RPM of the spectrum without a corresponding increase in vessel speed. The cure normally involves a re-design of the propeller; however, it is important to ensure that the cause is thrust breakdown due to cavitation and not air-drawing due to high thrusts, and hence high suction pressures, at the propeller in association with low immersions relative to the free surface: the symptoms described above apply to both conditions. Air can be drawn into propellers by a variety of routes; for example, down an 'A' or 'P' bracket. To differentiate between the two causes can sometimes be difficult and requires consideration of the propeller design in terms of whether it is likely to cavitate sufficiently to cause thrust breakdown, together with observing the noise emanating from the propeller. In addition, air-drawing often leads to a snatching characteristic in small boats and vessels.

22.1.2 Blade erosion

The avoidance of the harmful effects of cavitation on the marine propeller blade again hinges on being able to predict accurately the effective wake field of the vessel, since it is this wake field that forms the basis of the incident flow into the propeller and, hence, affects the distribution of loading over the propeller blade surfaces.

The gross effects of cavitation caused by the lack of provision of sufficient blade surface area are now comparatively infrequently seen, since designers can effectively predict, in global terms, the amount of blade surface required for a given propulsion application. More common, however, are the localized effects of cavitation due either to variations in the local angles of attack encountered by the propeller at some point during its passage around the propeller disc or to the use of too high cambers for a particular application. Localized cavitation caused by deviations in incidence angles from those anticipated in design can frequently be alleviated by the traditional method of either 'lifting' or 'dropping' the leading edge (Figure 22.3) or by reprofiling the leading edge in terms of its radius

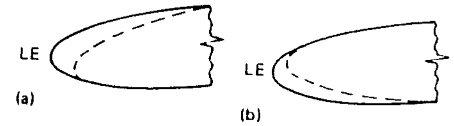

Figure 22.3 Traditional LE modifications to alleviate local cavitation problems

and blending this change into the rest of the section to make the blade section more tolerant to the changes in angle of attack that it experiences. The effects of the use of too high a camber in a particular situation are more difficult to deal with, since this frequently involves attempting to both generate a new section profile from the existing section form and preserve the strength integrity of that particular blade section. In such a process this inevitably leads to the loss of some blade chord length and the consequent effect on blade strength.

The incidence of root cavitation and its associated erosive effect is due largely to the difficulty of calculating the flow regime in this area and such problems when encountered can be difficult to solve. Whilst a certain amount can be done to alleviate a root cavitation erosion problem by section modification, the interference with the mechanical strength of the propeller blade in this region is always of concern, and is therefore uppermost in determining the extent of the modification that can be conducted. Notwithstanding this, the intractability of certain root cavitation problems has led designers, on occasions, to the somewhat desperate measure of drilling comparatively large holes in the blade root, from the pressure surface through to the suction face of the blade, in an attempt to alleviate the problem (Figure 18.10). Such measures, however, are not to be recommended except as a very last resort.

Much can be done at the design stage to alleviate potential cavitation problems in the blade root area by making the correct choice of hub profile since comparatively small changes from mildly convergent hub forms to a divergent hub form will have a significant effect on the resulting root cavitation inception properties of the blade in this region. Van Gunsteren and Pronk (Reference 4) outlined this effect some twenty years ago, but it is one that is often, in the author's experience, found to be ignored today and is the source of many root cavitation problems. Figure 21.17 shows the changes caused by the use of convergent, divergent and parallel forms. In cases where a strongly convergent hull form is used, this can on occasions lead to a very strong root vortex being formed which collapses on the rudder. This often leads to erosion on the rudder and this effect has been noted on vessels as diverse in size and duty as container ships and pilot cutters. The cure for this is to change the form of the cone on the propeller to either a divergent or parallel form as shown in Figure 21.18.

An effective treatment of root cavitation problems can often be achieved by means of injecting air into the root sections of the propeller blade at a station just immediately ahead of the propeller. Figure 22.4 illustrates, in generalized terms, how the effect of air content in the water influences the cavitation erosion rate. The form of the curve can be explained on the basis that when no dissolved air is present in the water or boundary crevices the tensile strength of the fluid is very great and therefore inhibits the inception of cavitation. However, as air is introduced, this provides a basis for nuclei to form which in turn will lead to greater levels of cavitation being experienced until an air content is reached in which further nuclei seeding does not materially increase the cavitation development. Beyond this point, which lies somewhere in the range $0.1 < \alpha_k < 0.8$, if the amount of air introduced into the system is increased, then the presence of this excess air will essentially have a cushioning effect on the isentropic collapse of the cavitation bubbles which would otherwise lead to the erosion mechanism, both with respect to the formation of pressure waves during the rapid bubble collapse and microjets from the collapsing bubbles directed at the blade surface. If the air content is increased significantly beyond saturation, as shown in Figure 22.4, then the erosion rate has been observed by various experimenters to reduce significantly. In the context of cavitation erosion in the propeller blade root, the author has used this technique with considerable effect on a number of high-speed vessels. However, care needs to be exercised, particularly with the smaller propellers, in choosing the amount of air for the particular application in order to prevent a fall-off in thrust performance of the propeller by effectively reducing the density of the fluid. Notwithstanding this, by the correct choice of air mass flow a significant erosion problem, for example of the order of 4–5 mm incurred over a period of some twelve hours, has been reduced to zero over a similar trial period by deploying the air injection technique.

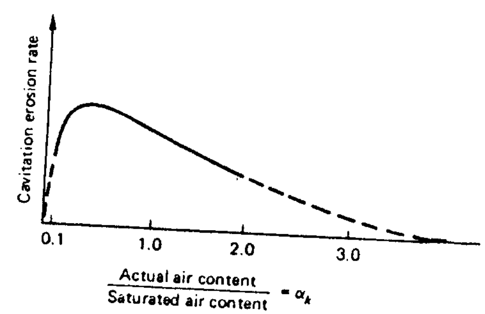

Figure 22.4 Effect of air content on cavitation erosion rate

Another technique which is frequently debated as a means to protect a blade from erosion is the use of protective epoxy type coatings. Opinion is divided as to the usefulness of this approach; however, several new and improved materials are coming on to the market. In order that a coating has a fair chance of survival in the hostile environment on the propeller surface it should be applied to the propeller under strict conditions of cleanliness and environmental control: this implies at the very least enclosing it within an 'environmentally controlled' tent in a dock bottom, but most preferably in a workshop.

22.1.3 Noise and vibration

The vibratory behaviour of a ship can in general take two forms; it may be either resonant or forced in character. In the case of a resonant behaviour of some part of the ship structure this can manifest itself as either a single component, such as the vibration of a bridge wing or a small appendage, or a major structure such as the entire deckhouse or the superstructure. As a consequence, for resonant vibration problems one is left with two alternatives. Either the resonant frequency of the offending component can be changed by structural modification and this is generally easier and less costly in the case of smaller components or, alternatively, the propeller blade number can be changed to alter the blade rate frequency or some multiple of it. This latter approach is usually the most convenient option where resonances at frequencies of nZ (n = 1, 2, 3, ...) of large structural components are encountered, or in certain classes of torsional vibration problems. Nevertheless, when changing blade number in an attempt to solve resonant vibration problems, whilst the effects of blade rate excitation are predictable by calculation for the natural frequency characteristics of the particular structural member, and are normally of over-riding concern, it must not be forgotten that the magnitude of the propeller-induced excitation at blade rate harmonics will change also–not always downwards. Care, therefore, needs to be taken to ensure that these will not cause further problems of either a forced or a resonant nature.

In the case of forced vibration, this is almost invariably caused by the harmonic pressures generated by the variations in the cavitation dynamics on the propeller blades as the blades rotate through the propeller disc. In Chapter 11 (Equation (11.22)), it was shown that the pressure (p) induced at some distance from a fluctuating cavity volume is related by the following function:

$$p \propto \left(\frac{\partial^2 V}{\partial t^2}\right)$$

where V is the cavity volume and t is time.

As a consequence, if a forced vibration problem is to be attacked at source, then a method must be found to reduce the cavity volume and the rate of its structural variation. In practical terms this means a change either to the blade geometry, which in turn frequently implies a change to the skew and radial load distributions along the blade, or to the in-flow conditions into the propeller.

In the latter case this implies the fitting of some appendages to the hull, which can take a variety of forms, in order to control a known or anticipated undesirable feature of the wake field. Examples of these appendages were shown in Figure 13.2. The particular device used depends on the type of wake feature which needs attention: for example in Figure 22.5, device (a) is normally used to control bilge vortex formation whilst that of (b) attempts to modify wake peak of a highly 'V' formed hull. The fitting of such devices as these needs great care and skill and should not be attempted on a *ad hoc* basis unless one is prepared to accept a high risk of failure. The reason for caution in this area is because within the current 'state of the art' it is not possible to calculate the effects of these devices with any degree of accuracy, since they are located within the thick and frequently separated part of the ship's boundary layer: Chapter 12 provides a related discussion. As a consequence, their choice and fitting needs a considerable reliance on past experience coupled with the results of model tests if at all possible. The model test results are, however, only another guide to the designer because the model is run at Froude identity and hence considerable Reynolds dissimilarity exists in this region where the particular device is being located. Whilst recognizing these problems, there are many cases where devices of the types shown in Figure 22.5 have been used with considerable success without incurring significant speed penalties, device fractures and so on.

The alternative approach to the forced vibration problem is to modify the propeller blade in such a way as to relieve the particular condition which is being experienced by the vessel. The designer's choices in this case are many; for example, he can vary the radial load distribution along the blade, change the skew of the blades, increase the blade chord lengths or adjust the relationship governing the proportion of the section lift generated from angle of attack and section camber. Generally, the use of increasing amounts of skew alleviates a hull pressure problem, but in the case of bearing forces, the skew distribution should be matched to the harmonic content of the wake field if undesirable results are to be avoided. The particular technique, or more frequently combination of techniques used depends on which of the many types of cavitation related vibration or noise problem requires solution.

The radial distribution of loading near the blade tip has an important influence on the strength of the tip vortex, as discussed in Chapter 9. Consequently, it is frequently desirable to limit the rate of change of load in the tip region of the propeller as shown in Figure 18.18; the penalty for doing this, however, can

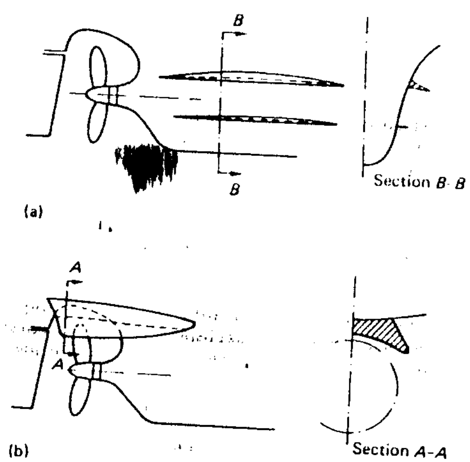

Figure 22.5 Fin arrangements commonly used in flow correction problems: (a) type of fin normally associated with 'U' form hulls; (b) type of fin normally associated with 'V' form hulls

be a loss in propulsive efficiency, because the design has then deviated from the optimum radial loading. The strength of the tip vortex needs to be carefully controlled since the collapse of this vortex can, if the correct circumstances prevail, give rise to excessive noise and, in some circumstances, high levels of vibration in the aftbody of the ship due to the pressure waves of the cavitation collapse mechanism being transmitted through the water and onto the hull surface. The control of the strength of this vortex can most realistically be achieved by attention to the radial distribution of blade loading near the tip. However, should the phenomenon of vortex bursting occur, as potentially identified by English (Reference 5) and has been known in aerodynamic problems for some considerable time, then this mechanism can be the source of significant higher order excitation on the hull. Furthermore, the presence of a strong tip vortex which impinges on the rudder has been known in many cases to cause significant cavitation erosion on either the rudder or the rudder horn. Much yet needs to be learnt about the adequate prediction and behaviour of the tip vortex both in terms of its prediction from theoretical methods to that of its scaling from model tests. As a consequence, this is again an area where the current research efforts being undertaken in various countries need to be continued.

The highly skewed propeller has shown an increase in popularity, as demonstrated by Table 22.1, which was taken from the records of Lloyds' Register.

The highly skewed propeller has been particularly successful in overcoming certain classes of vibration

Table 22.1 Corporative numbers of highly skewed propellers classed by LR during period 1980–89

	1980–84	*1985–89*
Number of highly skewed propellers compared to the total number of propellers classed by LR	1%	15%

and noise problem in both its 'biased' and 'balanced' forms, although the balanced blade form has become pre-eminent in recent years. Bjorheden (Reference 6) discusses their use, particularly with reference to controllable pitch propeller applications, and Figure 22.6(a) shows one example of the reduction in first and second-order hull pressure induced vibration on a Ro/Ro vessel resulting from the change to a highly skewed form from a conventional design. Also from this figure it can be seen that in this particular case the third and fourth harmonics increased slightly and this underlines the importance of acknowledging, whilst not being able to predict theoretically, that changes to the higher harmonics will inevitably occur by changing the propeller form. The alternative figure, Figure 22.6(b), taken from Carlton and Bantham (Reference 7) shows the use of a highly skewed propeller in reducing the axial vibratory characteristics on a fishing trawler. In the context it must be recalled, from Chapter 11, that propeller–ship interactions manifest themselves in terms of both hull surface pressures and mechanical excitations of the line shafting and its supports. The highly skewed propeller form is particularly useful in solving problems where the cavitation growth and collapse rate and cavity structure are considered to be the cause of the problem. Set against these advantages are a tendency toward increased manufacturing costs and the advisability of undertaking wake field tests if the design is to be properly optimized: this latter aspect is of course a general point, but is particularly true of the highly skewed propeller.

Detailed blade geometry changes, other than the skew or radial load distribution, are normally used where cavity structural changes or extent are required to be made. These can be particularly effective in many cases and they can frequently be carried out on an existing propeller or, alternatively, be incorporated into a new propeller of similar generic form. The use of analysis procedures based on unsteady lifting surface methods is of considerable assistance in determining the effect of changes in blade geometry and in-flow on first and second blade order excitation frequencies. At higher orders reliance has to be made on the results of experimental cavitation studies, although here questions of the adequacy of the flow field simulation, cavitation scaling and model geometry need to be carefully considered.

A particular form of cavitation which can, on occasions, be troublesome in ship vibration terms is

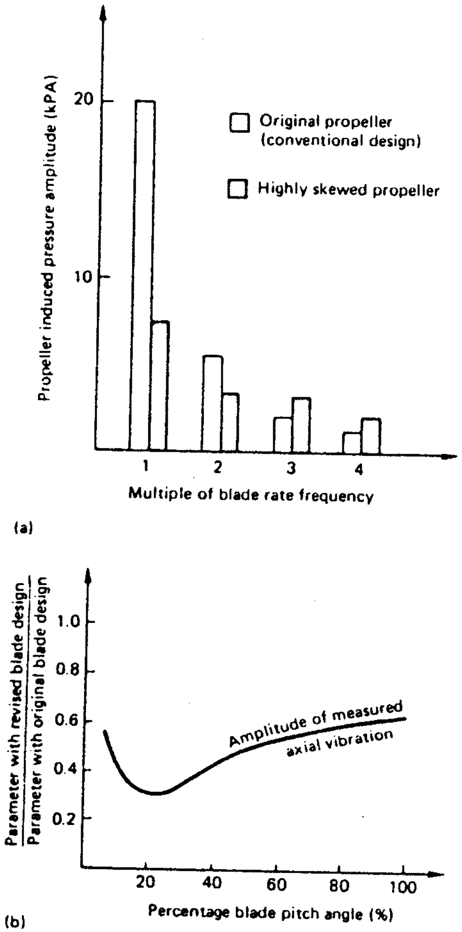

Figure 22.6 Some effects of changing from conventional to highly skewed propeller designs: (a) propeller-induced hull pressures recorded on a Ro/Ro vessel; (b) influence of highly skewed propeller on axial shaft vibration

propeller–hull vortex (PHV) cavitation. The formation of this type of cavitation was discussed in Chapter 9, as were the conditions favourable to its formation. In those cases where PHV cavitation occurs a small amount of erosion can often, but not always, be observed on the hull plating in the region above the propeller and the vibration signature will be intermittent in character, as seen in Figure 22.7. The noise generated, again of an intermittent nature, sounds much like a series of single sharp blows with a scaling

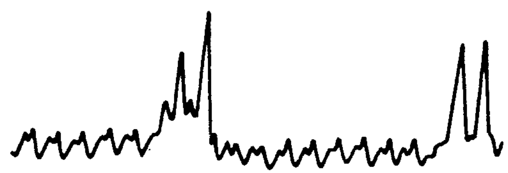

Figure 22.7 Typical hull pressure fluctuation indicating possible presence of PHV cavitation

hammer on the hull surface above the propeller. The cure for this type of cavitation is simple and effective for a non-ducted propeller: it comprises the fitting of a single vertical fin above the propeller as shown in Figure 22.8(a). This fin prevents the formation of the vortex motion necessary to the formation of the cavity discussed in Chapter 9. By way of example, the effects of fitting such a fin on a coaster are shown in Figure 22.8(b) from which it can be seen that a marked reduction in vibration level can be observed.

In the case of a ducted propulsion system it is suggested (Reference 8) that the formation of PHV cavitation can be prevented by fitting an appendage between the hull and the duct which is aimed at accelerating the flow into the upper part of the duct.

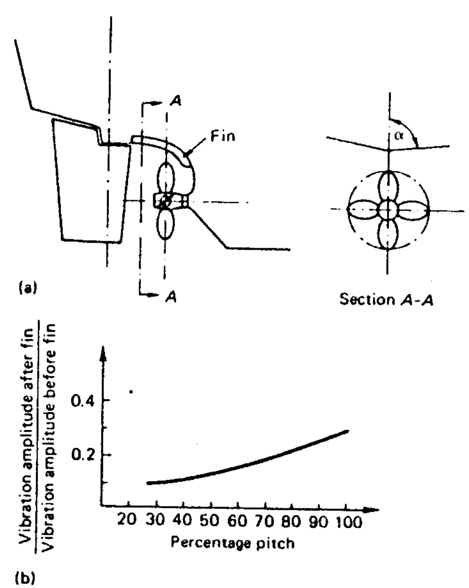

Figure 22.8 Propeller–hull vortex cavitation problems and their solution

Noise for the greater majority of merchant forms is intimately connected with the cavitation behaviour of the propellers and as such the noise control problem, to some extent, reduces to a cavitation control problem. In dealing with these problems it is important, however, to differentiate between the sympathetic 'chattering' of loose fittings to vibration and the true level of noise originating from the propeller or other machinery components. In the case of research vessels, for example, or in many naval applications where noise emissions interfere with the operation of the ship then it is necessary to consider in great detail the structure of the flow around the propeller blade sections, see Chapter 10, notwithstanding the unknowns concerning the nature of the inflow to the propeller at full scale.

Propeller singing and its cure was discussed in Chapter 20. In practical terms it manifests itself as a periodic noise which ranges from a low frequency 'grunt' to a high pitch 'worble'. The low frequency 'grunt' tends to be associated with larger vessels whilst the high notes arise from smaller high-speed propellers.

22.2 Propeller integrity related problems

In Figure 22.1 three areas of propeller integrity problems were identified, although in reality these often interact. Nevertheless, within this section we will consider each individually for the convenience of discussion.

22.2.1 Blade failure

The over-stressing of blades in relation to the generally expected properties of materials at the design stage is an extremely rare occurrence in merchant vessels which have been designed under classification society requirements. These rules govern the strength requirements of marine propellers in relation to the absorption of the full machinery power and any special operational regimes that the vessel is required to undertake.

Depending upon the integrity of the casting and the size and distribution of defects within the casting, the material properties vary continuously over the surface and throughout the blade. The factors of safety incorporated in the design procedure attempt to take this into account; however, the defect geometry, location and proximity to other defects cause stress raisers which can induce a propagating fatigue crack in the blade. In the very great majority of cases a propeller blade fails by fatigue action, as shown in Figure 22.9. In the great majority of these cases the 'beach marks' seen in Figure 22.9 are clearly visible and represent points of crack arrest during the fatigue crack growth. When looking at a failure the Stage I area around the defect is normally visible with the Stage II area containing the beach marks forming the major part of the failure surface. The final rupture area, Stage III, caused by mechanical overload of the material forms a band around the edge of the failure. By undertaking simple fracture mechanics calculations in relation to a failed propeller's lifetime, it can be easily deduced that the crack spends about 90% of its life in Stage I growing to a size where Stage II propagation according to the Paris law (equation (18.6)) can take place. Hence, it is unlikely that a crack will be observed by inspection other than when it is in its Stage I phase and is very small. Stage III is effectively an instantaneous failure. When a blade fails in this way, since the failure is normally between 0.6R and the root then the propeller, or blade in the case of a controllable pitch propeller, is unsuitable for repair. In these cases the spare propeller should be fitted as soon as possible, and in the meantime the vessel should be run at reduced speed. The reduction in speed can be determined practically on the vessel at the time of failure but should be checked by calculation of the out-of balance forces in relation to the hydrodynamic loading of the stern bearing. If, as is sometimes the case, the spare propeller is in another part of the world, then it may be necessary to run for some time in this failed condition. When this situation occurs and a significant portion of the blade is lost, then the opposite blade, in the case of an even-bladed propeller, should be suitably cropped, and for odd-bladed propeller the opposite pair of blades partially cropped. This action, although altering the power–RPM relationship of the propeller and increasing the thrust loading per blade and hence the tendency toward cavitation, helps protect the stern tube bearing from damage from the out-of-balance force generated by the failure. If a spare propeller does not exist, then the propeller should be approximately balanced in the manner described above until a new propeller can be produced. For lesser damage, in which smaller parts of the blade are lost, drastic cropping action is normally unnecessary since the propeller may be able to be repaired; nevertheless, the effect of the damage should always be considered in relation to its effect on the lubrication film in the stern tube bearing.

If a propeller fails in fatigue, the underlying cause should always be sought, since this will have an influence on whether redesign is necessary or whether a repeat propeller can be ordered to the same design.

In Chapter 18, the effect of backing on highly skewed propellers was discussed. In a limited number of cases this leads to bending, which is normally in the region shown by Figure 22.10. Whilst in many cases this could be straightened, the plastic behaviour would recur the next time the offending astern manoeuvre was undertaken. As a consequence blade redesign is necessary to either thicken the blade or adjust the blade shape, perhaps a combination of both.

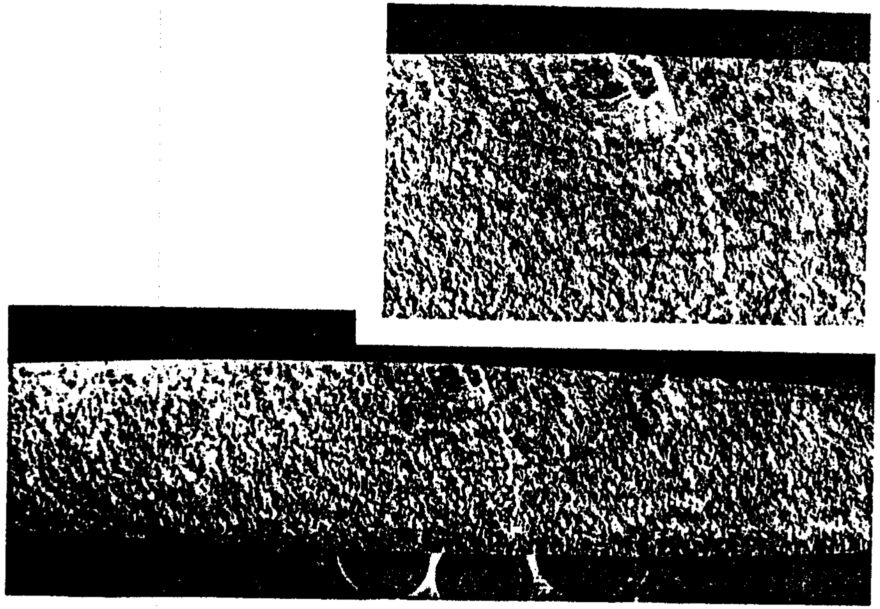

Figure 22.9 Typical fatigue failure of a propeller blade

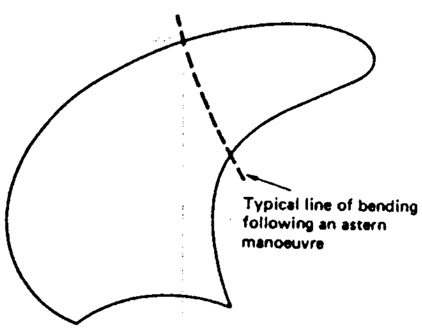

Figure 22.10 Typical location of bending following an astern manoeuvre with a highly skewed propeller

22.2.2 Previous repair failures

As discussed in Chapter 25 propeller repairs need to be conducted strictly in accordance with the manufacturer's recommendations and classification society requirements. Otherwise failure of the repair will very likely result and other undesirable features such as stress corrosion cracking may occur. In these circumstances the failure of a local repair can act as the origin of a blade fatigue failure and actually cause failure in a very short space of time.

22.2.3 Casting integrity

It is practically impossible to produce a propeller casting without defects and as a consequence potential sites for fatigue cracking initiation. In the majority of cases the defects are of no consequence to the long term integrity of the propeller. The question of defining an acceptable defect size has occupied several research workers in recent years, but as yet no generally accepted criteria has evolved.

In several cases it is possible and perfectly valid to repair a casting by welding; however, as in the case of service repairs the manufacturer's recommendations and the rules of the various classification societies must be rigidly adhered to when undertaking this type of repair.

With castings it is unlikely that their inherent defect state will deteriorate in service, except in the case of the joining up of defect sites under the action of a tensile stress field. Hence the casting integrity is defined at the time of manufacture.

22.3 Impact or grounding

Propellers by virtue of their position and mode of operation are likely to suffer impact or grounding damage during their life. This sometimes results in a complete or partial blade failure due to overload or, more likely, in blade bending or the tearing of small pieces from the blade edges. In by far the majority of cases these damages can be rectified by repair—again with the caveat of the use of repair specialists and under the jurisdictions of the appropriate classification society.

References and further reading

1. Modifying the propeller for optimum efficiency. *Shipping World and Shipbuilder*, April, 1972.
2. Patience G., Modifying propeller characteristics for better efficiency in ageing ships. *The Motor Ship*, January 1973.
3. *Edge Modification of Propeller*. Kobe Steel Ltd, 1979
4. Gunsteren L.A. van, Pronk C., Propeller design concepts. *2nd Lips Symp.*, 1973.
5. English J.W. Cavitation induced hull surface pressures–measurements in a water tunnel. *Symp on Propeller Induced Ship Vibration. Trans RINA*, 1979.
6. Bjorheden O. Vibration performance of highly skewed CP propellers. *Symp. on Propeller Induced Vibration, Trans. RINA*, 1979.
7. Carlton J.S., Bantham I., Full scale experience relating to the propeller and its environment. *Propellers '78 Symp., Trans. SNAME*, 1978.
8. Kooij J. van der, Berg W. van den. Influence of hull inclination and hull–duct clearance on performance, cavitation and hull excitation of a ducted propeller: Part II. NSMB.

23 Service performance and analysis

Contents

In general the performance of a ship in service is different from that obtained on trial. Apart from any differences due to loading conditions such as might be found in a bulk carrier, and for which due correction should be made, these differences arise principally from the weather, fouling and surface deterioration of the hull and propeller.

The subject of service performance quite naturally, therefore, can be divided into four component parts for discussion purposes as follows:

1. effects of weather both sea and wind;
2. hull roughness and fouling;
3. propeller roughness and fouling;
4. the monitoring of ship performance.

As such the discussion in this chapter will essentially fall into these four categories.

23.1 Effects of weather

The influence of the weather, both in terms of wind and sea conditions, is an extremely important factor in ship performance analysis. The analytical aspects of the prediction of the effects of wind and sea state was discussed in Chapter 12, and therefore need not be reiterated here. In the case of the service data returned from the ship for analysis purposes it is insufficient to simply record wind speed and sea state according to the Beaufort scale. In the case of wind, it is important to record both its speed and direction, since both of these parameters clearly influence the drag forces experienced by the vessel. With regard to sea conditions, this is somewhat more complex since in many instances the actual sea state will contain both a swell component and a local surface disturbance which are not related. For example, if a sea is not fully developed, then the apparent Beaufort number may not be representative of the conditions actually prevailing at the time. Consequently, both the swell and surface disturbance effects and their direction relative to the ship's heading need to be taken into account if a realistic evaluation is to be made of the weather effects in the analysis procedures. In making these comments it is fully recognized, in the absence of instrumented data as opposed to subjective judgement, that the resulting data will be subject to an observational error bound on the part of the deck officer. Nevertheless, an experienced estimate of the conditions is essential to good analysis practice.

23.2 Hull roughness and fouling

The surface texture or hull roughness of a vessel is a continuously changing parameter which has a comparatively significant effect on the ship performance. This effect derives from the way in which the roughness of the hull surface influences the boundary layer and its growth over the hull. Hence, the effect of hull roughness can be considered as an addition to the frictional component of resistance of the hull. Table 23.1 shows typical comparative proportions of frictional resistance (C_F) to total resistance (C_T) at design speed for a series of ship types.

Table 23.1 Typical proportions of frictional to total resistance for a range of ship types

Ship type		C_F/C_T
ULCC - 516893 DWT	(loaded)	0.85
Crude carrier - 140803 DWT	(loaded)	0.75
	(ballast)	0.63
Product tanker - 50801 DWT	(loaded)	0.62
Refrigerated cargo ship 8500 DWT		0.53
Container ship - 37000 DWT		0.62
Ro/Ro ferry		0.55
Cruise liner		0.66
Offshore tug supply vessel		0.38

From this table it is clearly seen that the frictional components play a large role for almost all types of vessel. Naturally the larger full form vessels have the largest frictional components.

The roughness of a hull can be considered to be the sum of two separate components as follows:

hull surface roughness = permanent roughness + temporary roughness

in which the permanent roughness refers to the amount of unevenness in the steel plates and the temporary roughness is that caused by the amount and composition of marine fouling.

Permanent roughness derives from the initial condition of the hull plates and the condition of the painted surface directly due to either the application or the drying of the paint on the hull. The condition of the hull plates embraces the bowing of the ships plates, weld seams and the condition of the steel surface. The bowing of the plates or 'hungry horse' appearance has a comparatively small effect on resistance, generally not greater than about 1%. Similarly, the welded seams also have a small contribution: for example, a VLCC or container ships might incur a penalty of the order of $\frac{3}{4}$% and so it may be cost effective to remove these by grinding the surface of the weld. By far the greatest influence on resistance is to be found in the local surface topography of the steel plates. This topography is governed by a wide range of variables: corrosion, mechanical damage, deterioration of the paint film, a build-up of old coatings, rough coating caused by poor application, cold flow resulting from too short a drying time prior to immersion, scoring of the paint film resulting from scrubbing to remove fouling, poor cleaning prior to repainting, etc. Consequently, it can be seen that the permanent roughness, which is permanent in the sense of providing the base surface after building or drydocking during service, cannot be eliminated by subsequent coating, and therefore, to improve it in terms of local surface topography, complete removal of the old coatings is necessary to restore the hull surface.

In contrast temporary roughness can be removed or reduced by the removal of the fouling organisms or subsequent coating treatment. It is caused in a variety of different ways: for example, the porosity of leached-out anti-fouling, the flaking of the current coating caused by internal stresses, and corrosion caused by the complete breakdown of the coating system and by marine fouling. Whilst permanent roughness can be responsible for an annual increment of, say, 30–60 μm in roughness perhaps, the effects of marine fouling can be considerably more dramatic and can be responsible, given the right circumstances, for 30–40% increases in fuel consumption in a relatively short time.

The sequence of marine fouling commences with slime, comprising bacteria and diatoms, which then progresses to algae and in turn on to animal foulers such as barnacles, culminating in the climax community. Within this cycle Christie (Reference 1) describes the colonization by marine bacteria of a non-toxic surface as being immediate, their numbers reaching several hundreds in a few minutes, several thousands within a few hours and several millions within two to three days. Diatoms tend to appear within the first two or three days and grow rapidly, reaching peak numbers within the first fortnight. Depending on local conditions this early diatom growth may be overtaken by fouling algae.

The mixture of bacteria, diatoms and algae in this early stage of surface colonization is recognized as the primary slime film. The particular fouling community which will eventually establish itself on the surface is known as the climax community and is particularly dependent on the localized environment. In conditions of good illumination this community may be dominated by green algae, or by barnacles or mussels, as is often observed on static structures such as pier piles or drilling rigs.

The vast numbers and diversity of organism comprising the primary slime film results in the inevitable formation of 'slime' on every submerged marine surface, whether it is 'toxic' or 'non-toxic'. The adaptability of the bacteria is such that these organisms are found in nature colonizing habitats varying in temperature from below zero to 75° C. The adaptability of diatoms is similarly impressive; they can be found in all aquatic environments from fresh water to hyper-saline conditions and are even found growing on the undersides of ice floes. These life cycles and the adaptability of the various organisms combine to produce a particularly difficult control problem.

Severe difficulty of fouling control is not, however, restricted to microfouling; recent years have seen the emergence of oceanic, stalked barnacles as a serious problem fouling VLCC's working between the Persian Gulf and Northern Europe. This group of barnacles is distinguished from the more familiar 'acorn' barnacles in both habitat and structure.

Whereas acorn barnacles are found in coastal waters, characteristically attached directly to fixed objects such as rocks, buoys, ships, pilings and sometimes to other organisms, such as crabs, lobsters and shellfish, stalked barnacles are usually found far from land attached to flotsam or to larger animals such as whales, turtles and sea snakes by means of a long, fleshy stalk. The species, the most important of which is the Conchoderma, is recognized as a problem for large slow-moving vessels, and much research dealing with their life cycle and habits has been undertaken. The conclusions of this work indicate that VLCCs become fouled with Conchoderma while under way in open ocean. The results of the shipboard studies suggest that vessels travelling between the Gulf and Northern Europe are most likely to become fouled in the Atlantic Ocean between the Canary Islands and South Africa and particularly in an area between 17 S and 34 S. Adult Conchoderma, however, have been reported to be in every ocean in the world, and so there are no areas of warm ocean where vessels can be considered immune from attack.

The fouling of underwater surfaces is clearly dependent on a variety of parameters such as ship type, speed, trading pattern, fouling pattern, drydock interval, basic roughness and so on. To assist in quantifying some of these characteristics Evans and Svensen (Reference 2) produced a general classification of ports with respect to their fouling or cleaning characteristics; Table 23.2 reproduces this classification.

In recent years paint systems have developed from traditional anti-fouling coatings to self-polishing anti-fouling (SPA) and reactivatable anti-foulings (RA) in order to provide greater protection against fouling problems. SPAs are based on components which dissolve slowly in sea water and due to the friction of the sea water passing over the hull, toxins are continuously released. Thus, this overcomes the weakness of traditional anti-fouling where only part of the anti-fouling is water soluble, and where an inactive layer slowly develops through which the toxins have to migrate. Reactivatable coatings depend on a mechanical polishing with special brushes in order to remove the inactive layer formed at the surface of the anti-fouling. Both SPA and RA systems depend upon high-quality anti-corrosive systems to act as a basis, and the service life is proportional to the thickness of the film at application. Figure 23.1 shows in schematic form the action of a an SPA type of coating.

The life of an SPA coating, which if correctly applied can extend hull protection considerably beyond that afforded by traditional anti-foulings. Typically in the order of five years, dependent on the ship speed, hull permanent roughness, distance travelled and the thickness and polishing rate of the coats applied. The

Table 23.2 Port classification according to Reference 2

Clean ports	*Fouling ports*		*Cleaning ports*	
	Light	*Heavy*	*Non-scouring*	*Scouring*
Most UK ports	Alexandria	Freetown	Bremen	Calcutta
Auckland	Bombay	Macassar	Bribane	Shanghai
Cape Town	Colombo	Mauritius	Buenos Aires	Yangtze Ports
Chittagong	Madras	Rio de Janeiro	E. London	
Halifax	Mombasa	Seurabaya	Hamburg	
Melbourne	Negapatam	Lagos	Hudson Ports	
Valparaiso	Karadu		La Plata	
Wellington	Pernambuco		St Lawrence Ports	
Sydney*	Santos		Manchester	
	Singapore			
	Suez			
	Tuticorin			
	Yokohama			

* Variable conditions.

wear-off rate or polishing rate of anti-foulings is not always completely uniform, since it depends on both the turbulence structure of the flow and the local friction coefficient. The flow structure and turbulence intensities and distribution within the boundary layer change with increasing ship speed, which gives a thinner lamina sublayer, and consequently a hydrodynamically rougher surface, since more of the roughness peaks penetrate the sublayer at higher ship speeds. A further consequence of the reduced lamina sublayer at high speed is that the diffusion length for the chemically active ingredients is shorter, which leads to a faster chemical reaction, and therefore faster renewal, at the surface. In addition to the ship speed considerations, the hull permanent roughness is also of considerable importance. Whilst this will not in general affect the polishing rate of the coating, one will find that in the region of the peaks the antifouling will polish through more quickly since the coating surface will be worked harder by the increased shear stresses and turbulent vortices. Figure 23.2 shows this effect in schematic form. Whilst the average polishing rate for the coating will be the same for a rough or smooth hull, the standard deviation on the distribution curve for polishing rate will give a much bigger spread for rough hulls. Figure 23.3 demonstrates this effect by showing the results of model experiments (Reference 3) for both a smooth and rough surface, 50 μm and 500 μm respectively; similar effects are noted on vessels at sea. Consequently, it will be seen that the paint coating needs to be matched carefully to the operating and general conditions of the vessel.

The standard measure of hull roughness that has been adopted within the marine industry is $R_{t(50)}$. This is a measure of the maximum peak to valley height over 50 mm lengths of the hull surface, as shown in

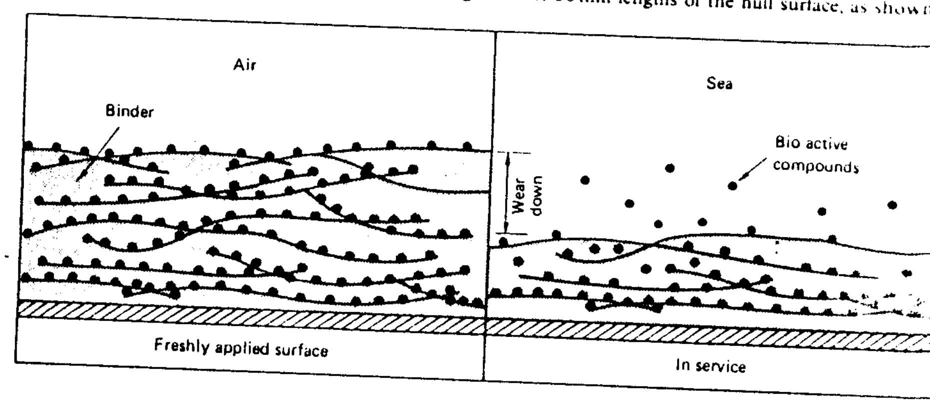

Figure 23.1 Principle of self-polishing process

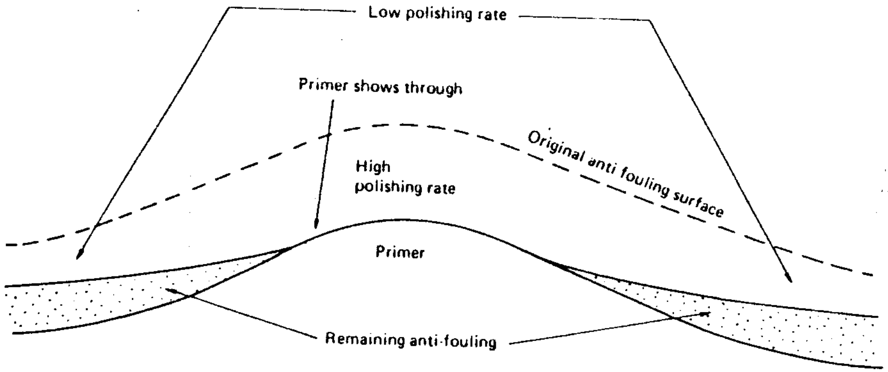

Figure 23.2 Influence of surface roughness on polishing anti-fouling paints

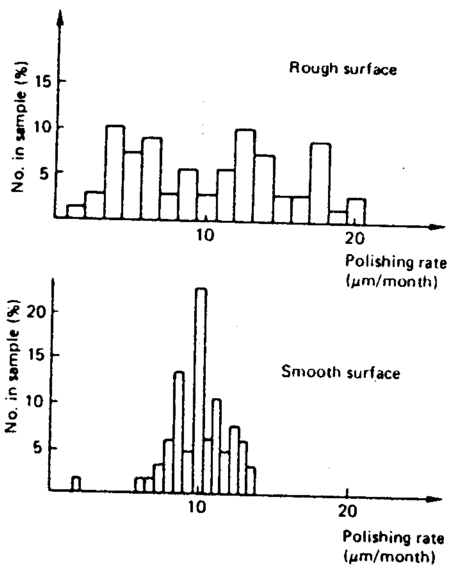

Figure 23.3 Influence of roughness on polishing rate (Reference 3)

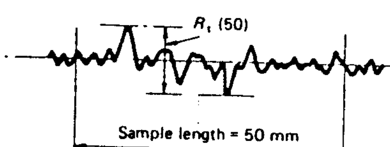

Figure 23.4 Definition of R_t(50) roughness measure

Figure 23.4. When undertaking a survey of a hull, several values of $R_{t(50)}$ will be determined at a particular station and these are combined to give a mean hull roughness at that location defined by

$$\text{mean hull roughness (MHR)} = \frac{1}{n}\sum_{i=1}^{n} h_i \qquad (23.1)$$

where h_i are the individual $R_{t(50)}$ values measured at that location.

The average hull roughness (AHR) is an attempt to combine the individual MHR values into a single parameter defining the hull conditions at a particular time. Typically the vessel may have been divided up into a number of equal areas, perhaps 100, and a value of MHR determined. These MHR values are then combined in the same way as equation (23.1) to give the AHR for the vessel:

$$\text{average hull roughness for vessel (AHR)} = \frac{\sum_{j=1}^{m} w_j(\text{MHR})_j}{\sum_{j=1}^{m} w_j} \qquad (23.2)$$

where w_j is a weight function depending on the location of the patch on the hull surface. For many purposes w_j is put equal to unity for all j values; however, by defining the relation in this way some flexibility is given to providing a means for giving greater weight to important areas of the hull with respect to hull roughness. Most notable here are the regions in the fore part of the vessel.

Townsin *et al.* (Reference 4) suggests that if a full hull roughness survey is made, the AHR will be statistically correct using $w_j = 1$ in equation (23.2). However, should some stations be left out for reasons of access etc., then the AHR can be obtained in the following way:

$$\begin{aligned}\text{AHR for vessel} = {} & (\text{MHR of sides}) \\ & \times \text{fraction of the sides covered} \\ & + (\text{MHR of flats}) \\ & \times \text{fraction of the flats covered} \\ & + (\text{MHR of boot topping}) \\ & \times \text{fraction of the boot topping covered} \qquad (23.3)\end{aligned}$$

Much debate has centred on the use of a simple parameter, such as $R_{t(50)}$ in representing non-homogenous surfaces. The arguments against this parameter suggest that the lack of data defining the surface in terms of its texture is serious and has led to the development of replica-based criteria for predicting power loss resulting from hull roughness (Reference 5). With this method, the surface of the actual ship is compared to those reproduced on replica cards, which themselves have been cast from other ships in service and the surfaces tested in a water tunnel to determine their drag. When a particular card has been chosen as being representative of a particular hull surface, a calculation of power penalty is made by use of diagrams relating the principal ship particulars; these diagrams having been constructed from a theoretical analysis procedure.

There is unfortunately limited data to be found that gives a statistical analysis and correlation with measured roughness functions for typical hull surfaces. Amongst the tests carried out, Musker (Reference 12), Johannson (Reference 13) and Walderhaug (Reference 14), feature as well-known examples. In the case of Musker, for example, he found that the measured roughness function for a set of five surfaces did not show a good correlation with $R_{t(50)}$ and used a combination of statistical parameters to improve the correlation.

The parameters used in his study were:

1. the standard deviation (σ_r);
2. the average slope (S_p);
3. the skewness of the height distribution (S_k);
4. the Kurtosis of the distribution (K_u);

and he combined them into an 'equivalent height' (h') which correlated with the measured roughness function using a filtered profile with a 2 mm long wavelength cut off. The relationship used was

$$h' = \sigma_r(1 + aS_p)(1 + bS_kK_u) \qquad (23.4)$$

With regard to $R_{t(50)}$ as a parameter, Townsin (Reference 6) concludes that for rough surfaces, including surface-damaged and deteriorated antifouling coatings – in excess of around 250 μm AHR, it is an unreliable parameter to correlate with added drag. However, for new and relatively smooth hulls it appears to correlate well with other available measures of roughness function, and so can form a basis to assess power penalties for ships.

It is found that the majority of new vessels have average hull roughness of the order of 90–130 μm provided that they have been finished in a careful and proper manner. McKelvie (Reference 7) notes, however, that values for new vessels of 200–250 μm have not been uncommon in the period preceding 1981. The way in which this value increases with time is a variable depending on the type of coating used. To illustrate this Figure 23.5 shows a typical scenario (Reference 8) for a vessel in the first eight years of its life. In the figure it will be seen that the initial roughness AHR increased after four years to a value of around 250 μm using traditional antifouling coatings (Point A on the diagram). If the vessel is shot-blasted, it can be assumed that the initial hull roughness could be reinstated since an insignificant amount of corrosion should have taken place. If, after cleaning, the vessel is treated with a reactivateable or self-polishing antifouling, after a further period of four years in service the increase in roughness would be small. Alternatively, if the vessel had been treated with traditional antifouling, as in the previous four-year period, then a similar increase in roughness would be noted. As illustrated in the diagram, the rate of increasing roughness depends on the coating system employed and the figures shown in Table 23.3 will give some general indication of the probable increases.

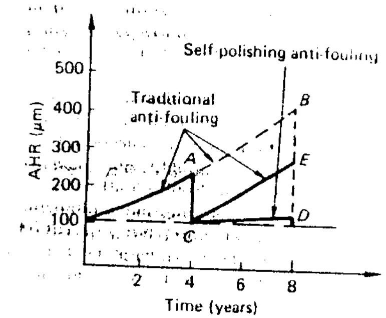

Figure 23.5 Effect of different coatings on hull roughness (Reproduced from Reference 8)

Table 23.3 Typical annual hull roughness increments

Coating type	*Annual increase in roughness* (μm/y)
Self-polishing paints	10–30
Traditional coating	40–60

Clearly, significant deviations can occur in these roughening rates in individual circumstances for a wide variety of reasons. Figure 23.6, which is taken from Townsin (Reference 9) shows the scatter that can be obtained over a sample of some 80 surveys conducted over the two-year period 1984–5.

Table 23.4 Values of coefficient $f_{i,p}$ (taken from Reference 15)

p	$f_{0,p} \times 10^3$	$f_{1,p} \times 10^3$	$f_{2,p} \times 10^3$	$f_{3,p} \times 10^3$
1	−0.05695	−0.08235	−0.48093	0.43460
2	−0.25473	−0.73105	1.01946	−1.37640
3	−0.18337	−2.01563	1.31724	−0.11176
4	0.38401	0.79786	2.02432	−2.30461
5	−0.27985	0.27460	−2.56908	2.26801
6	0.12397	0.47117	1.30053	−1.43575
7	1.95506	−10.87320	35.18020	−24.04790
8	−4.89111	17.57430	−63.66010	49.25690
9	1.70315	−5.44915	19.77400	−15.92990
10	0.72533	−2.50564	9.33041	−7.31122
11	−0.07676	−0.74104	0.62533	−0.06440
12	−2.93232	9.38549	−36.49980	29.61980
13	1.88597	−0.39504	6.04098	−11.67790
14	6.04607	−23.66800	88.78930	−64.38880
15	−5.02286	17.10700	−64.93670	49.93150
16	0.07829	0.00438	0.56607	−0.56425
17	0.04596	0.25232	−0.09525	−0.39173
18	3.04651	−10.75950	42.36420	−31.51610
19	−7.47250	23.29540	−93.06020	72.79150
20	4.26166	−13.00580	51.38600	−40.80970

Table 23.5 Coefficients b_j (taken from Reference 15)

j	$b_j \times 10^3$
1	−0.09440
2	0.01126
3	0.13756

23.8. The range of values predicted for $(\bar{k}_B/\bar{k}_1)$ in the range 4 to 8, typical values for painted surfaces, embrace the result from Bowden's formula. Nevertheless, Bowden's formula does not consider the effects of R_n and C_B, and consequently in other examples differences may occur. With regard to Townsin and Johansson's formula, close agreement is also seen in the region where $\bar{K}_1$ is of the order of 30 µm.

Walderhaug (Reference 14) suggests an approximation to the procedure outlined above, which has the form

$$\Delta C_F \times 10^3 \simeq 0.5\left(\frac{k_E \times 10^6}{L}\right)^{0.2} \cdot \left[1 + \left(\frac{C_B - 0.75}{0.7}\right)^2\right] \cdot \left[\ln\left(1 + \frac{u_t k_E}{\nu}\right)\right]^{0.7} \qquad (23.9)$$

where the effective roughness k_E is given by

$$k_E = \left(\frac{\bar{k}}{\lambda}\right)_1 (R_{t50} - K_A)$$

with the roughness to wavelength ratio $(\bar{k}/\lambda)_1$ at = 1 mm and the admissible roughness k_A given by

$$k_A = \frac{f\nu}{V}(\ln R_n)^{1.2}$$

with $f = 2.5$ for painted surfaces and the friction velocity

$$u_t = \frac{V}{(\ln R_n)^{1.2}}$$

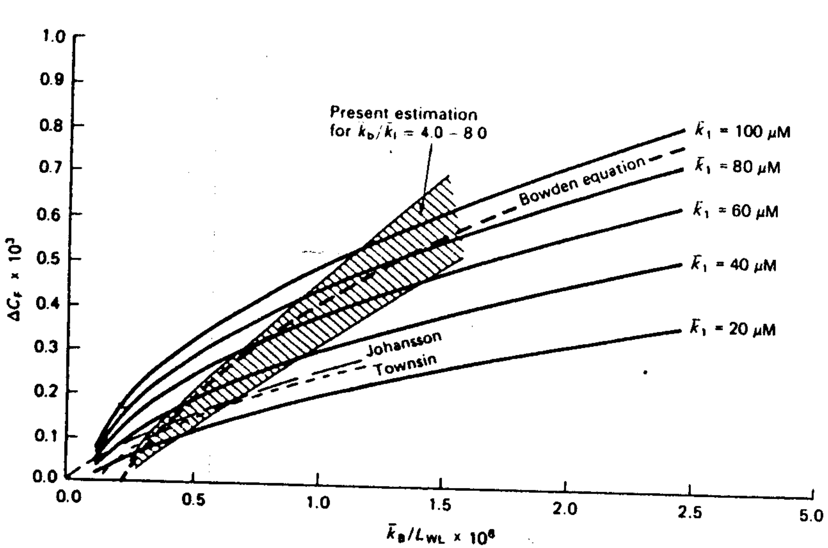

$\Delta C_F \times 10^3$ vs. $\bar{k}_B/L_{WL} \times 10^6$ at constant R_n and C_B

Figure 23.8 Comparison of roughness ΔC_F values (Reproduced from Reference 15, with permission)

23.3 Propeller roughness and fouling

Propeller roughness is a complementary problem to that of hull roughness and one which is no less important. As in the hull roughness case, propeller roughness arises from a variety of causes, chief of which are marine growth, impingement attack, corrosion, cavitation erosion, poor maintenance and contact damage.

Marine growth found on propellers is similar to that observed on hulls except that the longer weed strands tend to get worn off. Notwithstanding this, weed having a length of the order of 10–20 mm is not uncommon on the minor regions of the blade, as indeed are stalked barnacles which are frequently found alive on the blades after a vessel has docked subsequent to a considerable journey. Marine fouling of these types increase the power absorption of the propeller considerably, which for a fixed pitch propeller will result in a reduction of service rotational speed.

Impingement attack resulting from the passage of the water and the abrasive particles held in suspension over the blade surfaces normally affects the blades in the leading edge region and particularly in the outer radii of the blade where the velocities are highest. This results in a comparatively widespread area of fairly shallow depth surfaces roughness. Similarly with corrosion of either the chemical or electrochemical kind. Furthermore, with both corrosive and impingement roughness the severity of the attack tends to be increased with the turbulence levels in the boundary layer of the section. Consequently, subsequent to an initial attack, increased rates of surface degradation could be expected with time.

Cavitation erosion is normally, but not always, confined to localized areas of the blade. It can vary from a comparatively slight and relatively stable surface deterioration of a few millimetres in depth to a very rapid deterioration of the surface reaching depths of the order of the section thickness in a few days. Fortunately, the latter scenario is comparatively rare. Cavitation damage, however, presents a highly irregular surface, as seen in Figures 23.9 and 25.1, which will have an influence on the drag characteristics of the blade sections. Blade-to-blade differences are likely to occur in the erosion patterns caused by cavitation, and also to some extent with the forms of roughness. This will of course influence the individual drag characteristics of the sections.

Finally, poor maintenance and contact damage influence the surface roughness; in the former case perhaps by the use of too coarse grinding discs and incorrect attention to the edge forms of the blade, and in the latter case, by gross deformation leading both to a propeller drag increase and also to other secondary problems; for example, cavitation damage. With regard to the frequency of propeller polishing there is a consensus of opinion between many authorities that it should be undertaken in accordance with the saying 'little and often' by experienced and specialized personnel. Furthermore, the pursuit of super-fine

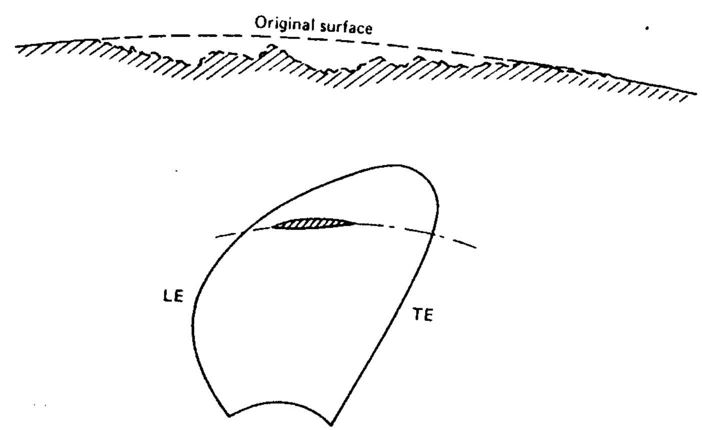

Figure 23.9 Typical cavitation damage profile

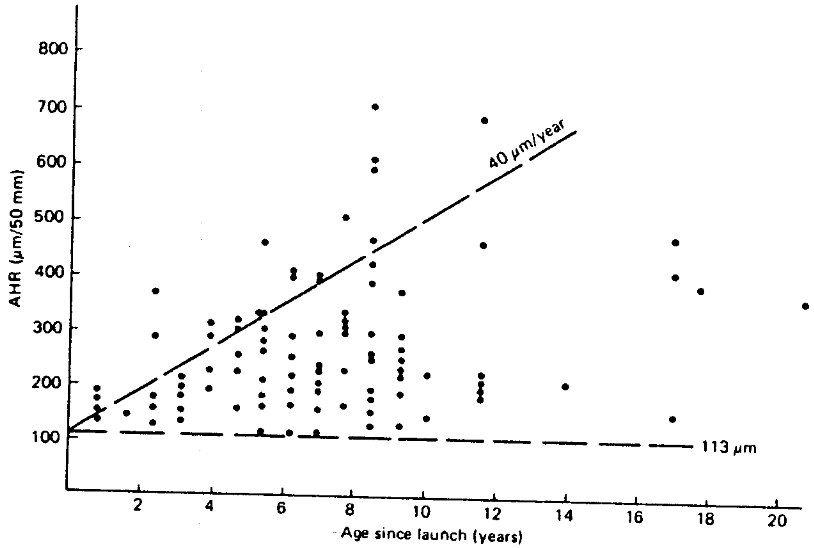

Figure 23.6 Survey of hull roughness conducted during period 1984-85. (Reproduced from Reference 9, with permission)

Assuming that the average hull roughness can be evaluated, this value then has to be converted into a power penalty if it is to be of any practical significance beyond being purely an arbitrary measure of paint quality. Lackenby (Reference 10) proposed an early approximation that for every 25 μm increase in roughness an increase in fuel consumption of around 2.5% could be anticipated.

More recently Bowden and Davison (Reference 11) proposed the relationship

$$\frac{\Delta P_1 - \Delta P_2}{P} \times 100\% = 5.8[(k_1)^{1/3} - (k_2)^{1/3}] \qquad (23.5)$$

where k_1 and k_2 are the average hull roughness for the rough and smooth ship respectively and ΔP_1 and ΔP_2 are the power increments associated with these conditions, P is the maximum continuous power rating of the vessel.

This relationship was adopted by the 1978 ITTC as the basis for the formulation of power penalties and appeared in those proceedings in the form:

$$\Delta C_F \times 10^3 = 105\left(\frac{k_s}{L}\right)^{1/3} - 0.64 \qquad (23.6)$$

in which k_s is the mean apparent amplitude of the surface roughness over a 50 mm wavelength and L is the ship length. With equation (23.6) a restriction in length of 400 m was applied, and it is suitable for resistance extrapolation using a form factor method and the 1957 ITTC friction line. It assumes a standard roughness of 150 μm.

Towsin (Reference 6) has recently produced a modified expression for the calculation of ΔC_F based on the AHR parameter and applicable to new and relatively smooth vessels:

$$\Delta C_F \times 10^3 = 44\left[\left(\frac{\text{AHR}}{L}\right)^{1/3} - 10(R_n)^{-1/3}\right] + 0.125 \qquad (23.7)$$

The effects of the distribution of roughness on the skin friction of ships has been explored by Kauczynski and Walderhaug (Reference 15). They showed the most important part of the hull with respect to the increase in resistance due to roughness is the bow region. However, the length of the significant part of this portion of the hull decreases as the block coefficient increases. In the case of vessels with higher block coefficients, of the order of 0.7–0.8, the afterbody also plays a significant role. Figure 23.7, based on Reference 15, illustrates this point by considering two smoothing regimes for a vessel. In case A, a smooth strip equal to 25% of L_{WL} was fixed to the bow, whereas in case B the smooth area was divided into two equal portions, both with a length equal to 12.5% L_{WL}. In both cases the smoothed areas were equal. Calculations

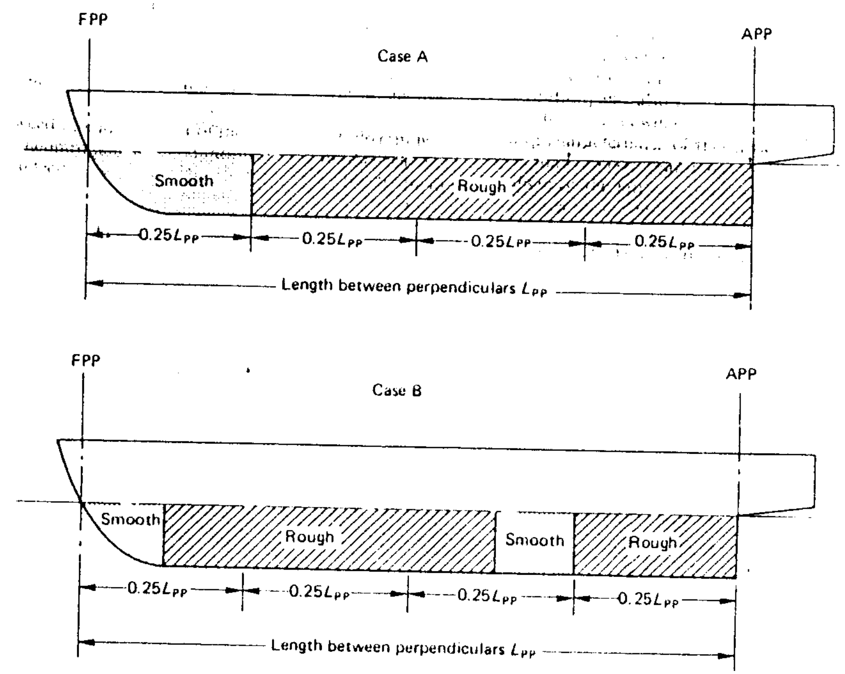

Figure 23.7 Hull smoothing regimes considered by Kauczynski and Walderhaug (Reproduced from Reference 15)

showed that the reduction in C_F compared to the whole rough surface were 0.105×10^{-3} and 0.119×10^{-3} for cases A and B respectively, thus showing an advantage for the smoothing regimes of case B. In order to compute the value of C_F corresponding to paint roughness, Kaucynski and Walderhaug based their calculations on a conformal mapping technique for describing the hull form and used a momentum integral method for the calculation of the three-dimensional turbulent boundary layer characteristics. The results of these calculations for five hull forms of the Series 60 models with block coefficients between 0.60 and 0.80 have shown that the increase of frictional resistance due to roughness ΔC_F is a function of block coefficient, Reynolds number, $R_{n(50)}$ and $R_{n(1)}$. A regression procedure was applied by the authors to these results in order to give a readily applicable approximation of the form

$$\Delta C_F = a_0 + a_i \bar{k}_B^{*i} + b_j \Delta C_B^{*j} \frac{\bar{k}_B^*}{L_{WL}} \bar{k}_1^* R_n^* \qquad (23.8)$$

where $i, j = 1, 2, 3$ and

$$\bar{k}_B^* = \frac{\bar{k}_B/L_{WL}}{3.32 \times 10^9}; \qquad R_n^* \frac{R_n}{2.7 \times 10^6}; \qquad \bar{k}_1^* = \frac{k_1}{105}$$

with

$$\Delta C_B^* = \frac{C_B - 0.6}{0.2}$$

In order to derive the coefficients a_0 and a_i in equation (23.8) a further polynomial expression has been derived as follows:

$$a_i = \sum_{n=1}^{4} \sum_{m=1}^{5} f_{i,p} (\bar{k}_1^*)^{n-1} (R_n^*)^{m-1}$$

where $i = 0, 1, 2, 3$

$p = m + 5(n - 1)$

The coefficients $f_{i,p}$ are given by Table 23.4 for all values of $p = 1, 2, 3, \ldots, 20$. The coefficients b_j are given by Table 23.5.

The calculation procedure is subject to the constraints imposed by the model series and the conditions examined. Thus $\bar{k}_{1_{max}}$, $(\bar{k}_B/L_{WL})_{max}$, $R_{n_{max}}$ and $C_{B_{min}}$ are defined as 105 μm, 3.32×10^9, 2.7×10^6 and 0.6 respectively. The method described has been examined in comparison with others, notably those by Hohansson, Townsin and Bowden, for a 16 knot, 350 m tanker, and the results are shown in Figure

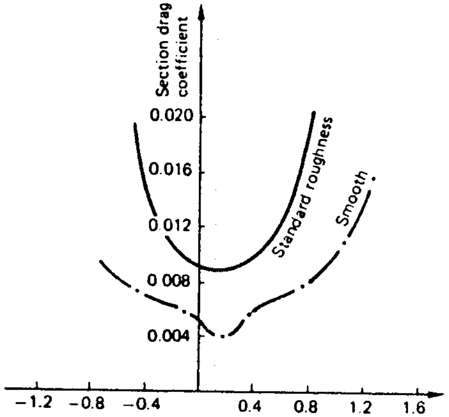

Figure 23.10 Effect of roughness on NACA 65-209 profile

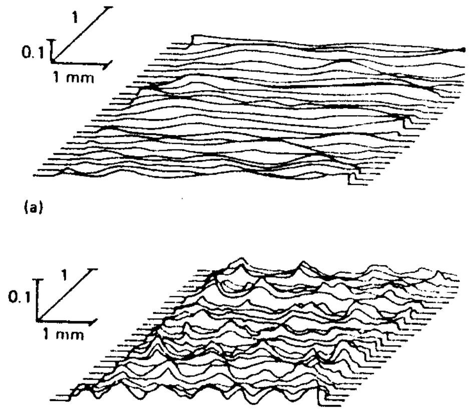

Figure 23.11 Example of two different textures having approximately the same roughness amplitude (Reproduced from Reference 17, with permission)

finishes to blades is generally not worth the expenditure, since these high polishes are often degraded significantly during transport or in contact with ambient conditions.

The effects of surface roughness on aerofoil characteristics have been known for a considerable period of time. These effects are principally confined to the drag coefficient and a typical example taken from Reference 16 is seen in Figure 23.10 for a NACA 65-209 profile.

The effect on section lift is small since the lift coefficient is some 20–30 times greater than the drag coefficient and studies conducted by the ITTC showed that the influence of roughness on the lift coefficient can be characterized by the relationship

$$\Delta C_L = -1.1\Delta C_D \qquad (23.10)$$

Results such as those shown in Figure 23.10 are based on a uniform distribution of sand grain roughness over the section surface. In practice, however, this is far from the case, and this implies that a multi-parameter statistical representation of the propeller surface embracing both profile and texture might be more appropriate than a single parameter such as the maximum peak-to-valley height. Grigson (Reference 17) shows two surfaces to illustrate this point (Figure 23.11) which have approximately the same roughness amplitudes but quite different textures. In general propeller surface roughness is of the Colebrook–White type and can be characterized in terms of the mean apparent amplitude and a surface texture parameter.

The topography of a surface can be reduced into three component terms: roughness, waviness and form errors as shown in Figure 23.12. Clearly, the definition of which category any particular characteristic lies is related to the wavelength of the characteristic. The International Standards Organisation (ISO) has used two standards in the past; these are the peak-to-valley average (PVA) and the centre-line average (CLA or R_a) and, the definition of these terms are as follows:

Peak-to-valley average (PVA): This is the sum of the average height of the peaks and the average depth of the valleys. It does not equate to the R_t parameter, since this latter term implies the maximum rather than the average value.

Centre-line average (CLA or Ra): This is the average deviation of the profile about the mean line and is given by the relation

$$R_a = \frac{1}{l}\int_{x=0}^{l} |y(x)|\,dx \qquad (23.11)$$

where l is the length of the line over which the roughness distribution $y(x)$ is measured.

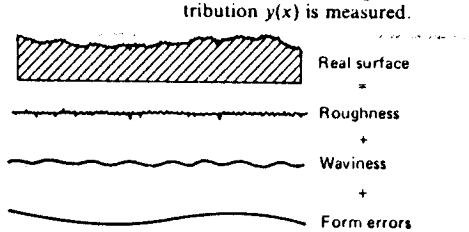

Figure 23.12 Reduction of surface profile into components

Type	Shape	PVA (μm)	PVA/CLA
Sinusoidal		8	π = 3.142
Triangular		10	4
Occasional triangular protrusions	x 4x x	15.5	6.2
Occasional triangular indentations	x 4x x	15.5	6.2
Occasional triangular protrusions and indentations	4x x 4x x x	50	20
Parabolic indentations (mathematical scratches)		9.7	3.9
Occasional parabolic indentations (scratches)	x 4x x	22.5	9
Parabolic cusps		9.7	3.9
Occasional parabolic cusps	4x x x	22.5	9

CLA = centre line average (the average deviation from the mean line)
PVA = peak-to-valley average (the average height of the peaks plus the average depth of the valleys)

Figure 23.13 Comparison between CLA and PVA measurements of roughness for constant CLA value of 2.5 μm R_a (Reproduced from Reference 18, with permission)

There is unfortunately very little correspondence between the values derived from a PVA or CLA analysis. Some idea of the range of correspondence can be deduced from Figure 23.13, taken from Reference 18, for mathematically defined forms. The authors of Reference 18 suggest a value of the order of 3.5 when converting from CLA to PVA for propeller surfaces. The difference between these two measurement parameters is important when comparing the 1966 and 1981 ISO surface finish requirements for propellers, since the former was expressed in terms of PVA whilst the latter was in CLA. Sherrington and Smith (Reference 19) discuss the wider aspects of characterizing the surface topography of engineering surfaces.

Table 23.6 itemizes these requirements for Class 'S' and Class 'I' propellers.

Several methods of surface roughness assessment exist and these range from stylus based instruments through to the 'Rubert' comparator gauge. For the stylus based instruments it has been generally found that a wavelength cut-off value of the order of 2.5 mm gives satisfactory values for the whole range of propellers. The stylus based instrument will give a direct measure of the surface profile, which is in contrast to the

Table 23.6 ISO surface finish requirements

Specification		*Class 'S'*	*Class 'I'*	*Units*
ISO R484	1966	3	9	μm (PVA)
ISO R484/1 } ISO R484/2 }	1981	3	6	μm (Ra)

comparator gauge method in which the surface of the blades at particular points are 'matched' to the nearest surface on the reference gauge. The 'Rubert' gauge which is perhaps the most commonly used comprises six individual surfaces tabulated A through to F as seen in Figure 23.14. These surfaces have been the subject of extensive measurement exercises by a number of authorities. Townsin *et al.* (Reference 20) undertook a series of studies to determine the value of Muskers' apparent height h' from both his original definition and a series of approximations. The values derived for the apparent roughness together with the maximum peak to valley amplitude $R_t(2.5)$ quoted by the manufacturers of the Rubert gauge is given in Table 23.7. Also in this table is shown the approximation

Figure 23.14 The Rubert gauge

to h' derived from the relation

$$h' \simeq 0.0147 R_a^2 (2.5) P_c \qquad (23.12)$$

where P_c is the peak count per unit length and is used as a texture parameter.

Table 23.7 Rubert gauge surface parameters

Rubert surface	*h' equ.* (23.4) (μm)	*h' (approx.) equ.* (23.12) (μm)	R_t (2.5) (μm)	R_a (2.5) (μm)
A	1.32	1.1	6.7	0.65
B	3.4	5.4	14.2	1.92
C	14.8	17.3	31.7	4.70
D	49.2	61	50.8	8.24
E	160	133	97.2	16.6
F	252	311	153.6	29.9

Note: *a* and *b* in equation (23.4) taken as 0.5 and 0.2 respectively.

When measuring the roughness of a propeller surface it is not sufficient to take a single measurement or observation on a blade. This is because the roughness will vary over a blade and different parts of the blade will be more significant than others, chiefly the outer sections since the flow velocities are higher. Furthermore, differences will exist from blade to blade. To overcome this problem a matrix of elements should be superimposed on the suction and pressure surfaces, as shown in Figure 23.15. In each of the twelve regions defined by the matrix on each surface of the blade several roughness measurements should be taken in the direction of the flow and widely spaced apart. A minimum of three measurements is recommended in each patch from which a mean value can be taken (Reference 20).

23.4 Generalized equations for the roughness induced power penalties in ship operation

Townsin *et al.* (Reference 20) established a valuable and practical basis upon which to analyse the effects of roughness on the hull and propeller of a ship. In this analysis they established a set of generalized equations, the derivations of which form the basis of this section. The starting point for their analysis is to consider the power delivered to the propeller in order to propel a ship at a given speed V_s through the water:

$$P_D = \frac{R V_s}{\text{QPC}}$$

where R is the resistance of the ship at the speed V_s and the QPC is the quasi-propulsive coefficient given by

$$\text{QPC} = \eta_H \eta_r \eta_0$$

$$= \eta_H \eta_r \frac{K_T}{K_Q} \frac{J}{2\pi}$$

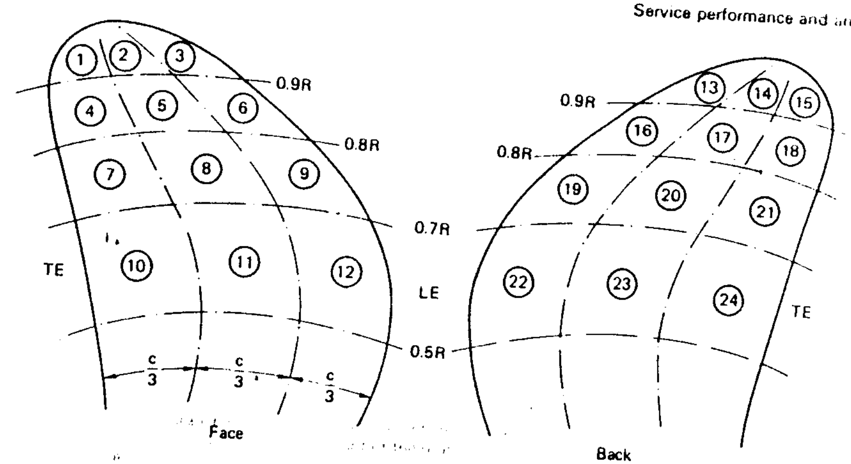

Figure 23.15 Definition of patches for recording propeller roughness

Consequently, the basic relationship for the delivered power P_D can be re-expressed as follows:

$$P_D = \frac{\pi \varrho S V_s^3 C_T K_Q}{K_T J \eta_H \eta_r} \qquad (23.13)$$

by writing the ship resistance R as $\frac{1}{2} S V_s^2 C_T$. Equation (23.13) can be linearized by taking logarithms and differentiating the resulting equation to give

$$\frac{dP_D}{P_D} = \frac{d\varrho}{\varrho} + \frac{dS}{S} + \frac{3dV_s}{V_s} + \frac{dC_T}{C_T} + \frac{dK_Q}{K_Q} - \frac{dK_T}{K_T} - \frac{dJ}{J} - \frac{d\eta_H}{\eta_H} - \frac{d\eta_r}{\eta_r}$$

In this equation it can be assumed for all practical purposes that the density (ϱ), the wetted surface area (S) and the relative rotative efficiency (η_r) are unaffected by increases in roughness of the order normally expected in ships in service. As a consequence these terms can be neglected in the above equation to give

$$\frac{dP_D}{P_D} = \frac{3dV_s}{V_s} + \frac{dC_T}{C_T} + \frac{dK_Q}{K_Q} - \frac{dK_T}{K_T} - \frac{dJ}{J} - \frac{d\eta_H}{\eta_H}$$

In addition, since roughness, as distinct from biological fouling, will cause only relatively small changes in the power curve, these can then be approximated to linear functions. Consequently, the differentials can be considered in terms of finite differences:

$$\frac{\Delta P_D}{P_D} = \frac{3\Delta V_s}{V_s} + \frac{\Delta C_T}{C_T} + \frac{\Delta K_Q}{K_Q} - \frac{\Delta K_T}{K_T} - \frac{\Delta J}{J} - \frac{\Delta \eta_H}{\eta_H} \qquad (23.14)$$

This equation clearly has elements relating to both the propeller and the hull, and can be used to determine the power penalty for propulsion at constant ship speed V_s:

$$\frac{\Delta P_D}{P_D} = \frac{\Delta C_T}{C_T} + \frac{\Delta K_Q}{K_Q} - \frac{\Delta J}{J} - \frac{\Delta K_T}{K_T} - \frac{\Delta \eta_H}{\eta_H} \qquad (23.15)$$

Clearly, it will simplify matters considerably if equation (23.15) can be decoupled into hull and propeller components, and therefore treated separately. This can be done subject to certain simplifications in the following way.

The terms $\Delta K_T / K_T$ and $\Delta K_Q / K_Q$ can be divided into two components; one due to propeller roughness and one due to the change in operating point assuming the propeller remained smooth:

$$\left.\begin{aligned} \frac{\Delta K_Q}{K_Q} &= \left(\frac{\Delta K_Q}{K_Q}\right)_R + \left(\frac{\Delta K_Q}{K_Q}\right)_J \\ \frac{\Delta K_T}{K_T} &= \left(\frac{\Delta K_T}{K_T}\right)_R + \left(\frac{\Delta K_T}{K_T}\right)_J \end{aligned}\right\} \qquad (23.16)$$

where the suffixes R and J denote propeller roughness and operating point respectively. This distinction is shown in Figure 23.16 for the torque coefficient characteristics. The relative changes to the propeller characteristic due to roughness alone can be estimated from Lerb's theory of equivalent profiles.

Considering the second term in each of equations (23.16), since for a smooth propeller

$$\Delta K_Q = \frac{dK_Q}{dJ} \Delta J$$

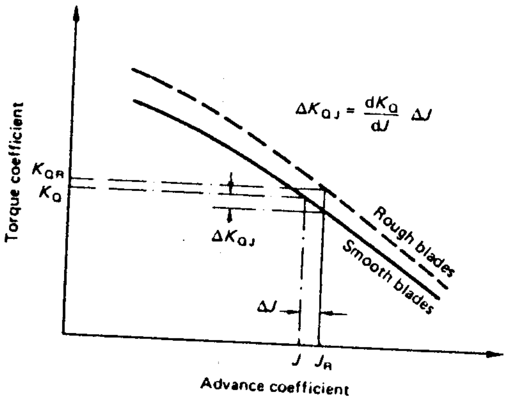

Figure 23.16 Effect of change of operating advance on propeller torque characteristics with rough and smooth blades

and similarly for ΔK_T, we write for the change in operating point terms in equations (23.16):

$$\left.\begin{aligned}\left(\frac{\Delta K_Q}{K_Q}\right)_J &= \frac{J}{K_Q}\left(\frac{dK_Q}{dJ}\right)\left(\frac{\Delta J}{J}\right)\\ \left(\frac{\Delta K_T}{K_T}\right)_J &= \frac{J}{K_T}\left(\frac{dK_T}{dJ}\right)\left(\frac{\Delta J}{J}\right)\end{aligned}\right\} \qquad (23.17)$$

Now the term ΔJ is the difference between the rough and smooth or original operating points, as seen in Figure 23.16:

$$\Delta J = J_R - J$$

that is,

$$\Delta J = \frac{V_a}{D}\left[\frac{(1 - w_{TR})}{N_R} - \frac{(1 - w_T)}{N}\right]$$

since V_a is assumed constant from equation (23.15). Hence by referring to the original operating point

$$\frac{\Delta J}{J} = \left(\frac{1 - w_{TR}}{1 - w_T}\right)\frac{N}{N_R} - 1 \qquad (23.18)$$

Furthermore, since $\Delta K_T = (K_{TR} - K_T)$,

$$\frac{\Delta K_T}{K_T} = \left(\frac{K_{TR}}{K_T} - 1\right)$$

that is,

$$\frac{\Delta K_T}{K_T} = \frac{T_R}{T}\left(\frac{N}{N_R}\right)^2 - 1 \qquad (23.19)$$

and by assuming an identity of thrust deduction between the rough and original smooth condition for a given ship speed, this implies

$$\frac{T_R}{T} = \frac{R_R}{R} = \frac{C_{TR}}{C_T}$$

$$= \frac{C_T + \Delta C_T}{C_T} = \left[1 + \frac{\Delta C_T}{C_T}\right]$$

Hence, substituting this relationship into equation (23.19), eliminating propeller revolutions between equations (23.18) and (23.19) and noting that C_T is wholly viscous so that $\Delta C_T = \Delta C_V$, we obtain

$$\frac{\Delta J}{J} = \left(\frac{1 - w_{TR}}{1 - w_T}\right)\left[\frac{1 + (\Delta K_T/K_T)}{1 + (\Delta C_V/C_T)}\right]^{1/2} - 1 \qquad (23.20)$$

By applying the binomial theorem to equation (23.20) and since $\Delta K_T/K_T$ and $\Delta C_V/C_T$ are small,

$$\frac{\Delta J}{J} = \left(\frac{1 - w_{TR}}{1 - w_T}\right)\left[1 + \frac{1}{2}\left(\frac{\Delta K_T}{K_T}\right) - \left(\frac{\Delta C_V}{C_T}\right)\right]$$

Hence from equations (23.16) and (23.17) and substituting these into the above an explicit relationship can be found for the term $\Delta J/J$ as follows:

$$\frac{\Delta J}{J} = \frac{\left(\frac{1 - w_{TR}}{1 - w_T}\right)\left[1 + \frac{1}{2}\left(\frac{\Delta K_T}{K_T}\right)_R - \frac{\Delta C_V}{C_T}\right] - 1}{1 - \frac{1}{2}\left(\frac{1 - w_{TR}}{1 - w_T}\right)\frac{J}{K_T}\left(\frac{dK_T}{dJ}\right)}$$

In this equation the terms C_V and w_T relate to the hull roughness, excluding any propeller induced wake considerations, and the term $(\Delta K_T/K_T)_R$ relates to the propeller roughness. Separating these terms out, we have

$$\frac{\Delta J}{J} = \frac{\left(\frac{1 - w_{TR}}{1 - w_T}\right)\left[1 - \frac{\Delta C_V}{C_T}\right] - 1}{1 - \frac{1}{2}\left(\frac{1 - w_{TR}}{1 - w_T}\right)\frac{J}{K_T}\frac{dK_T}{dJ}} + \frac{\frac{1}{2}\left(\frac{\Delta K_T}{K_T}\right)_R}{\left(\frac{1 - w_T}{1 - w_{TR}}\right) - \frac{1}{2}\frac{J}{K_T}\frac{dK_T}{dJ}} \qquad (23.21)$$

The first term in equation (23.21) is a function of hull roughness only and is the relative change in advance coefficient due to hull roughness only, $(\Delta J/J)_H$. The second term is a function of both propeller and hull roughness; this can, however, be reduced to a propeller roughness function by assuming that

$$\left(\frac{1 - w_T}{1 - w_{TR}}\right) \simeq 1$$

when the change in propeller roughness can be approximated by the function

$$\left(\frac{\Delta J}{J}\right)_R \simeq \frac{\frac{1}{2}\left(\frac{\Delta K_T}{K_T}\right)_R}{1 - \frac{1}{2}\left(\frac{J}{K_T}\right)\left(\frac{dK_T}{dJ}\right)}$$

Consequently, the total change in advance coefficient, equation (23.21), can be decoupled into the sum of independent changes in hull and propeller roughness:

$$\frac{\Delta J}{J} \simeq \left(\frac{\Delta J}{J}\right)_{\text{Hull rough}} + \left(\frac{\Delta J}{J}\right)_{\text{Prop. rough}}$$

This immediately allows the power penalty $\Delta P_D/P_D$, expressed by equation (23.15), to be decoupled into the following:

$$\left(\frac{\Delta P_D}{P_D}\right)_{\text{Prop. rough}} = \left(\frac{\Delta K_Q}{K_Q}\right)_{\text{Prop. rough}} - \left(\frac{\Delta J}{J}\right)_{\text{Prop. rough}} - \left(\frac{\Delta K_T}{K_T}\right)_{\text{Prop. rough}} \qquad (23.22)$$

and

$$\left(\frac{\Delta P_D}{P_D}\right)_{\text{Hull rough}} = \frac{\Delta C_V}{C_T} - \frac{\Delta \eta_H}{\eta_H} + \left(\frac{\Delta K_Q}{K_Q}\right)_{\text{Hull rough}} - \left(\frac{\Delta J}{J}\right)_{\text{Hull rough}}$$

but since propellers generally work in a region of the propeller curve, where the ratio, over small changes, of K_T/K_Q is relatively constant, this latter equation reduces to

$$\left(\frac{\Delta P_D}{P_D}\right)_{\text{Hull rough}} = \frac{\Delta C_V}{C_T} - \frac{\Delta \eta_H}{\eta_H} - \left(\frac{\Delta J}{J}\right)_{\text{Hull rough}} \qquad (23.23)$$

Equations (23.15), (23.22) and (23.23) form the generalized equations of roughness induced power penalties in ship operation. These latter two equations can, however, be expanded to give more explicit relationship for the hull and propeller penalties.

In the case of equation (23.22) for the propeller penalty, the propeller roughness effects $(\Delta K_Q/K_Q)$ and $(\Delta K_T/K_T)$ can be estimated from Lerb's equivalent profile method, from which the following relationship can be derived in association with Burrill's analysis:

$$\left(\frac{\Delta P_D}{P_D}\right)_{\text{Prop. rough}} = \left[\frac{2.2}{(P/D)} - 1.1 + \left\{\frac{3.3(P/D) - 2J}{2.2(P/D) - J}\right\} \times (0.45(P/D) + 1.1)\right]\left(\frac{\Delta c_D}{c_L}\right)_{0.7} \qquad (23.24)$$

For the hull roughness contribution, Townsin *et al.* (Reference 20) shows that by assuming a constant thrust deduction factor and employing the ITTC 1978 formula for wake scaling such that

$$w_{TR} = t + (w_t - t)\left[\frac{\Delta C_{FS} - \Delta C_{FT}}{(1 + k)C_{FS} + \Delta C_{FT}} + 1\right]$$

Then the full roughness power penalty becomes

$$\left(\frac{\Delta P_D}{P_D}\right)_{\text{Hull rough}} = \left[1 - \left(\frac{w_T - t}{1 - w_{TR}}\right)\frac{C_T}{(1 + k)C_{FS} + \Delta C_{FT}}\right] \times \left(\frac{\Delta C_F}{C_T}\right) - \left(\frac{\Delta J}{J}\right)_{\text{Hull rough}} \qquad (23.25)$$

where P_D = delivered power at the propeller;
C_T = ship thrust coefficient;
C_F = ship frictional coefficient;
C_{FS} = smooth ship frictional coefficient;
J = advance coefficient;
P = propeller pitch;
D = propeller diameter;
Δc_{d_t} = change in reference section drag coefficient;
c_l = reference section lift coefficient;
ΔC_{FT} = increment in ship skin friction coefficient in trial condition.

23.5 Monitoring of ship performance

The role of the ship service analysis is summarized in Figure 23.17. Without for the moment considering the means of transmitting the data from the vessel, this information should have two primary roles for the ship operator. The first is to develop a data bank of information from which standards of performance under varying operational and environmental conditions can be derived. The resulting standards of performance, derived from this data, then become the basis of operational and chartering decision by providing a reference for a vessel's performance in various weather conditions and a reliable comparator against which the performance of sister or similar vessels can be measured. The role for the data records is to enable the analysis of trends of either the hull or machinery to be undertaken, from which the identification of potential failure scenarios and maintenance decisions can be derived.

Table 23.8 identifies the most common set of parameters that are traditionally recorded to a greater or lesser extent by seagoing personnel in the ship's engine and bridge log books. It is this information which currently forms the data base from which analysis can proceed. In the table the measurement of shaft power has been noted with an asterisk; this is to draw attention to the fact that this extremely important parameter is only recorded in relatively few cases, due to the lack of a torsion meter having been fitted, and, as such, this cannot be considered to be a commonly available parameter at the present time.

Traditionally, Admiralty coefficient (A_c) based methods have formed the basis of many practical service performance analysis procedures used by shipowners and managers. Current practice with some ship operators today is to simply plot a curve of Admiralty coefficient against time. Figure 23.18(a) shows a typical example of such a plot for a 140 000 tonne DWT bulk carrier, from which it can be seen that it is difficult to interpret in any meaningful way due to the inherent scatter in this type of plot. One can, nevertheless, move a stage further with this type of study by analysing the relationship between the

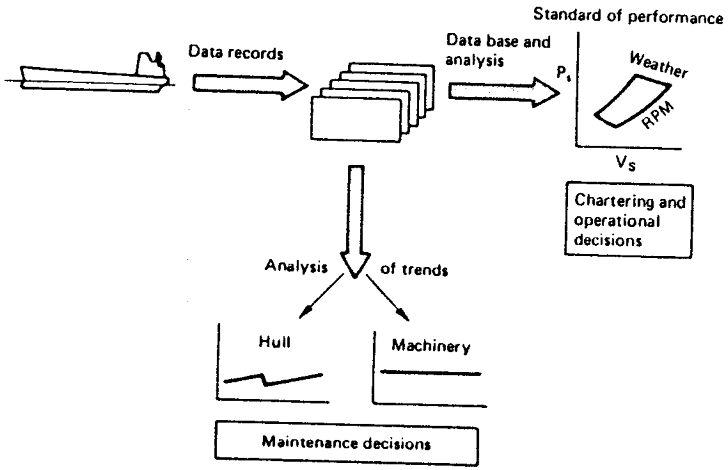

Figure 23.17 Role of ship service analysis

Admiralty coefficient and the apparent slip (S_a) as seen in Figure 23.18(b) which shows a convergence in the data and invites the drawing of a trend line through the data. The form of these coefficients is given by the well-known relationships

$$A_c = \frac{\Delta^{2/3} V_s^3}{P_s}$$

and

$$S_a = 1 - 30.86\left(\frac{V_s}{PN}\right) \text{ metric}$$

The data for this type of analysis has been extracted from the ship's deck and engine room log abstracts and the resulting curves of A_c plotted against S_a would normally be approximated by a linear relationship over the range of interest. Furthermore, apparent slip can be correlated to the weather encountered by the vessel by converting the description of the sea state, as recorded by the ship's navigating officers, to wave height according to some approved scale for that purpose. The wave heights derived in this way can be modified to take account of their direction relative to the ship and, having established the wave height versus apparent slip lines for the propeller, the Admiralty coefficient or other similar variable can be plotted against the appropriate line using the recorded apparent slip from the log book. Methods such as these, whilst providing a basis for analysis, can lead in some circumstances to misinterpretation. Furthermore, the Admiralty coefficient, although a useful criterion, is a somewhat 'blunt instrument' when used as a performance criterion since it fails to effectively distinguish between the engine and hull related parameters. The same is also true for the alternative version of this equation, termed the fuel coefficient, in which the shaft horsepower (P_s) is replaced with the fuel consumption. This latter derivative of the Admiralty coefficient serves where the vessel is not fitted with a torsion meter.

In recent years, several coefficients of performance have been proposed based on various combinations of the parameters listed in Table 23.8. Whipps (Reference 21), for example, attempts to split the overall performance of the vessel into two components – the responsibility of the engine room and the responsibility of the bridge watchkeepers. Accordingly, three coefficients of performance are proposed:

(1) K_1 – nautical miles/tonne of fuel (overall performance).
(2) K_2 – meters travelled/shp/h (navigational performance).
(3) K_3 – grammes of fuel/shp/h (engine performance).

Clearly, these coefficients require the continuous or frequent monitoring of the parameters concerned and the presentation of the coefficients of performance to the ship's staff on a continuous or regular basis. Experience with these and other similar monitoring techniques suggests that they do aid the ship's staff to enhance the performance of the vessel by making them aware of the economic consequences of their decisions at the time of their actions in terms that are readily understandable, this latter aspect being particularly important.

Table 23.8 Traditionally recorded parameters in ship log books

Deck log
Ship draughts (fore and aft)
Time and distance travelled (over the ground)
Subjective description of the weather (wind, see state etc.)
Ambient air and sea water temperature
Ambient air pressure
General passage information
Engine log
Cooling sea water temperature at inlet and outlet
Circulating fresh water cooling temperature and pressures for all engine components
Lubricating oil temperature and pressures
Fuel lever, load indicator and fuel pump settings
Engine/shaft revolution count
Turbocharger speed
Scavenge and injection pressures
Exhaust gas temperatures (before and after turbocharger)
Main engine fuel and lubricating oil temperatures
Bunker data
Generator and boiler performance data
Evaporator and boiler performance data
Torsion meter reading*

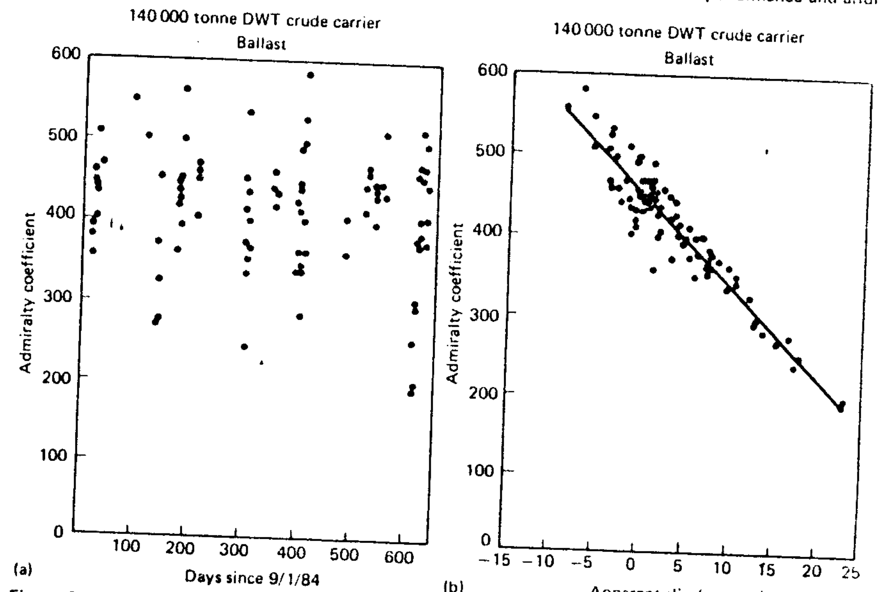

Figure 23.18 Common ship service procedures in use by the shipping community: (a) Admiralty coefficient versus time. (b) Admiralty coefficient versus apparent slip

In order to progress beyond the basic stages of performance monitoring it is necessary to attempt to address the steady-state ship powering equations:

$$P_s = \frac{RV_s}{\eta_0 \eta_r \eta_m}\left[\frac{1 - w_T}{1 - t}\right]$$

$$R = (1 - t)T$$

These equations clearly require a knowledge of the measured shaft power and thrust together with the ship and shaft speeds in association with the appropriate weather data. All of these parameters are potentially available, with the possible exception of shaft axial thrust. Thrust measurement has, in the past, proved notoriously difficult. In many instances this is due to the relative order of the magnitudes of the axial and torsional strain in the shaft, and has generally only been attempted for specific measurement exercises under carefully controlled circumstances, using techniques such as the eight gauge Hylarides bridge (Chapter 16). When this measurement has been attempted on a continuous service basis the long-term stability of the measurement has frequently been a problem.

Consequently, at the present time, it is generally possible to attempt only a partial solution to the steady-state powering equations defined above. In order to undertake this partial solution, the first essential is to construct a propeller analysis model so as to determine the thrust, torque, and hence efficiency characteristics with advanced coefficient. The method of constructing these characteristics can vary depending on the circumstances and the data available and, as such, can range from standard series open water curves to more detailed lifting line or vortex lattice techniques. The resulting model of propeller action should, however, have the capability to accommodate allowances for propeller roughness and fouling, since this can, and does, influence the power absorption and efficiency charactertistics to a marked extent. For analysis purposes it is clearly desirable to have as accurate a representation of the propeller characteristics as possible, especially if quantitative cost penalties are the required outcome of the exercise. However, if it is only performance trends that are required, then the absolute accuracy requirements can be relaxed somewhat since the rates of change of thrust and torque coefficients, dK_q/dJ and dK_t/dJ, are generally similar for similar types of propeller.

Figure 23.19 demonstrates an analysis algorithm. It can be seen that the initial objective, prior to developing standards of actual performance, is to develop two time series – one expressing the variation of effective wake fraction and the other expressing the specific fuel consumption with time. In the case of the effective wake fraction analysis this is a measure, over a period of time, of the change in the condition of the underwater surfaces of the vessel, since if either the hull or propeller surfaces deteriorate, the effective analysis wake fraction can be expected to reflect this change in particular ways. The second series, relating the specific fuel consumption to time, provides a global measure of engine performance. Should this latter parameter tend to deteriorate, and it is shown by analysis that it is not a false trend, for example an instrument failure, then the search for the cause of the fault can be carried on using the other parameters listed in Table 23.8. Typically, these other parameters might be exhaust temperatures, turbocharger performance, bearing temperatures and so on.

The capabilities of this type of analysis can be seen in Figure 23.20, which relates to the voyage performance of a bulk carrier some 20 years ago. The upper time

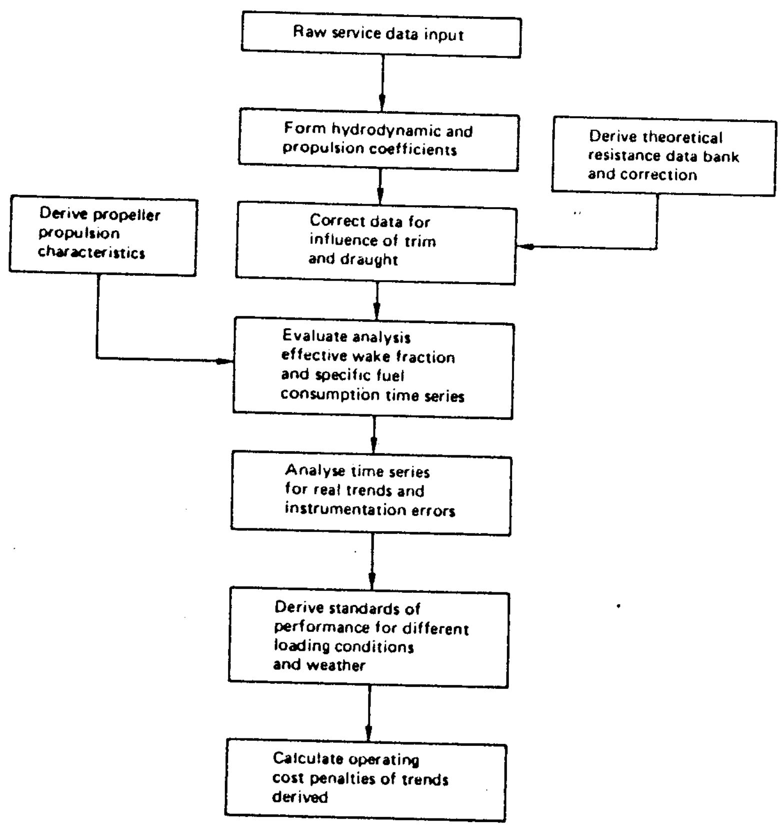

Figure 23.19 Service analysis algorithm

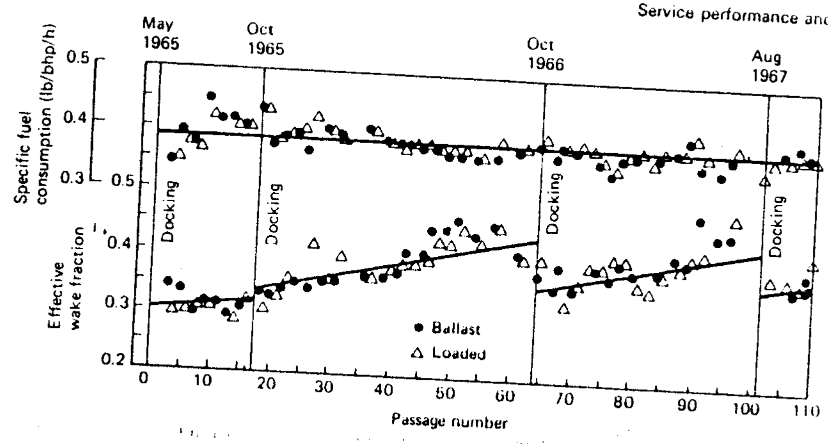

Figure 23.20 Service analysis for a bulk carrier (mid-1960s)

series relates to the specific fuel consumption, from which it is apparent that, apart from the usual scatter, little deterioration takes place in this global engine characteristic over the time interval shown. The second series is that of the analysis effective wake fraction, from which it can be seen that a marked increase in the wake fraction occurs during each docking cycle and coincident with the dry docking periods, when cleaning and repainting takes place, the wake fraction falls to a lower level. It is of interest to note that after each dry docking the wake fraction never actually regains its former value, and consequently underlines the fact that hull deterioration has at least two principal components. The first is an irreversible increase with age of the vessel and the consequent general deterioration of the hull condition with time, and the second is on a shorter time cycle and related to repairable hull deterioration and biological fouling; see Section 23.2.

Comparison of this analysis with that of a recent 140 000 dwt crude oil carrier (Figure 23.21) shows how the deterioration between docking cycles has been reduced despite the docking cycle having increased from the order of a year in Figure 23.20 to around three and a half years in this latter example. As might be expected, in Figure 23.20 there is still an upward trend in the wake fraction with time, but nothing so dramatic as in the earlier case. The improvement in this case is almost entirely due to the use of modern paints and good propeller maintenance. Indeed, modern paint technology has advanced to such an extent that providing good application practice is adhered to then it can be expected that the hull condition will deteriorate relatively slowly.

Instrumentation errors are always a potential source of concern in performance analysis methods. Such errors are generally either in the form of instrument drift, leading to a progressive distortion of the reading and, these can generally be detected by the use of trend analysis techniques or alternatively they are in the form of a gross distortion of the reading in which case the principles of deductive logic can be applied.

On many ships today a complete record in the ship's logs of all of the engine measured parameters and ship's operational entries are made relatively few times a day. Typically, one entry per day for the comprehensive set of data on many deep sea vessels assuming an automatic data logging system is not installed. Provided that the vessel is working on deep sea passages lasting a number of days, then this single entry practice, although not ideal from the analysis viewpoint, will probably be satisfactory for the building up of a profile of the vessel's operating characteristics over a period of time. Data logging by automatic or semi-automatic means clearly enhances this situation and leads to a much more accurate profile of the ship operation in a much shorter time frame. This is to some extent only an extension of the present procedures for alarm monitoring. In the alternative case, of a short sea route ferry for example, this once or twice per day level of recording is not appropriate since the vessel may make many passages in a day lasting of the order of one or two hours.

Over a suitable period of time a data bank of information can be accumulated for a particular ship or group of vessels. This data bank enables the average criterion of performance for the ship to be derived. A typical example of such a criterion is shown in Figure 23.22 for a medium-sized container ship. This diagram, which is based on the actual ship measurements and corrected for trim, draught and fouling, relates the

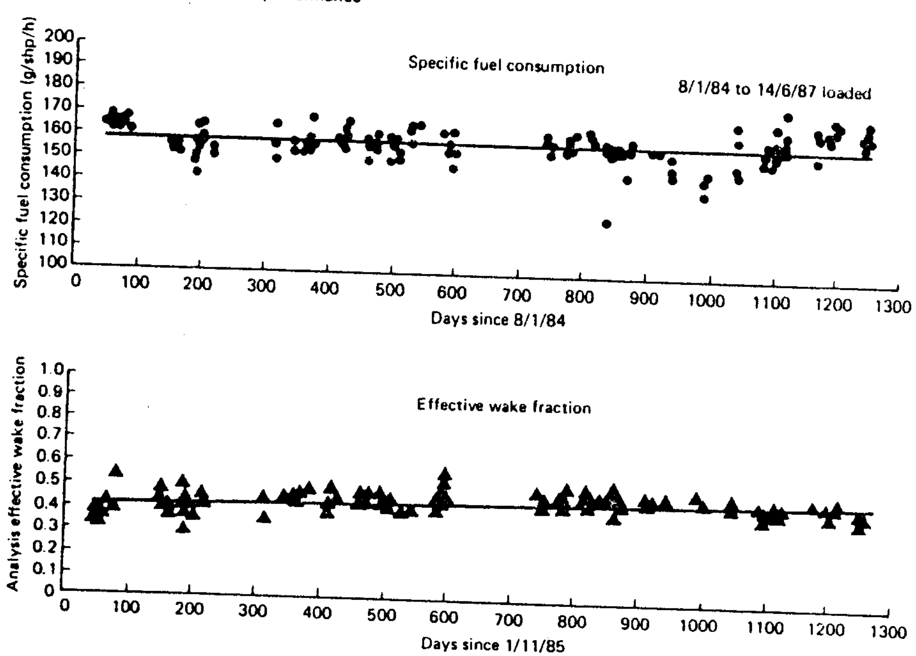

Figure 23.21 Service analysis for a 140 000 tonne DWT crude carrier

principal operational parameters of power, ship and shaft speed, and weather. Consequently, such data, when compiled for different trim draught and hull conditions can provide a reliable guide to performance for chartering purposes on any particular class of trade route.

Trim and draught have important influences on the performance of the vessel. Draught is clearly a variable determined by the cargo that is being carried. Trim, however, is a variable over which, for a great many vessels, some control can be exercised by the ship's crew. If this is done effectively and with due regard to weather conditions, then this can result in considerable savings in the transport efficiency of the vessel.

The traditional method of data collection is via the deck and engine room log, and this is the most commonly used method today. In terms of current data processing, capabilities, which involve both significant statistical trend analysis and detailed hydrodynamic analysis components, this method of data collection is far from ideal since, of necessity, it involves the translation of the data from one medium to another.

The immediate solution to this problem is to be found in the use of the desktop or personal computers working in either the on-line or off-line mode. Such computers are ideal for many shipboard applications since, in addition to having large amounts of memory, they are small and user friendly, can readily be provided with custom-built software and spare parts and are easily obtainable in most parts of the world. When used in the off-line mode, they are to some extent an extension of the traditional method of log entries, where instead of being written by hand in the book the data is typed directly into the computer for both storage on disk media and also for the production of the normal log sheet. This permits both easy transfer of the data to shore-based establishments for analysis and the undertaking of simple trend analysis studies on board. Such 'on board' analyses methods produce tangible benefits if conducted advisedly.

When the small computer is used in the 'on-line' mode the measured parameters are input directly from the transducers via a data acquisition system to the computer and its disk storage. In this way, a continuous or periodic scanning of the transducers can take place and the data, or representative samples of it, can be stored on disk as well as providing data for a continuous statistical analysis. Such methods readily raise alarms when a data parameter moves outside a predetermined bound in a similar way to conventional alarm handling.

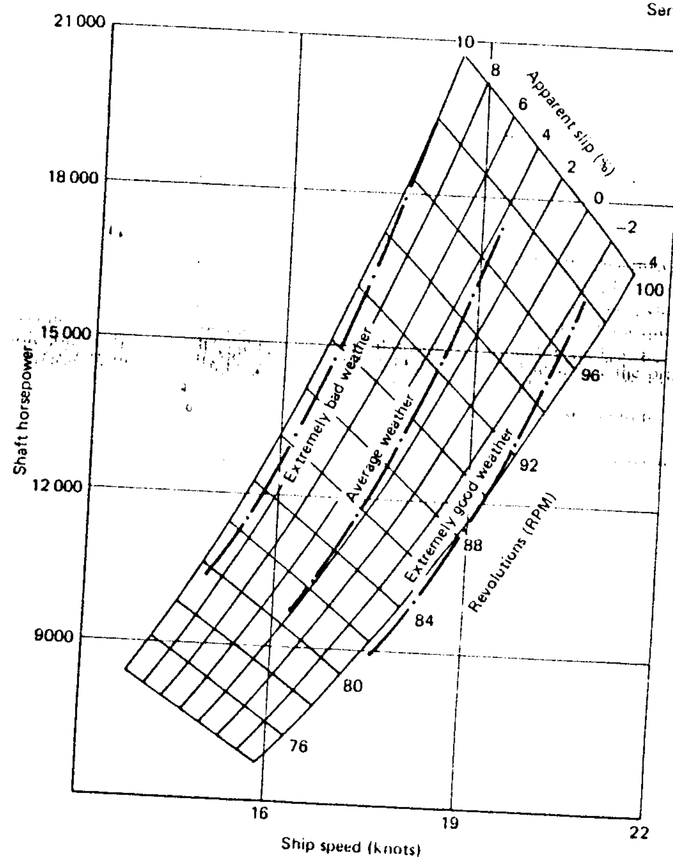

Figure 23.22 Typical power diagram for a container ship

This clearly has advantages in terms of man-hours but does tend to add to the degree of remoteness between operator and machine unless considerable attention has been paid to the 'user-friendliness' of the system. This ergonomic aspect of data presentation is particularly important if the system is to be accepted and used to its full potential by the ship's operating personnel. All too often poorly designed computer based monitoring equipment is seen lying largely discarded in the engine control room or on the bridge either because it has been insufficiently ruggedly designed for marine use and is, thus, prone to failure and regular breakdown or, more frequently, because the engineering design has been adequately undertaken, but the data and information it presents is not in an easily assimilative form for the crew and the manuals describing its operation contain too much specialized jargon which is unfamiliar to the operator. This underlines the importance of choosing a monitoring system which satisfies the company's commercial objectives as well as being compatible with the operator's actual and perceived requirements.

These small on-line systems are the first step towards an integrated ship management system embracing the activities of the deck, engine room and catering departments. Such systems are beginning to make their appearance. With these systems, the vessel's operating staff and shore based managers are still required to assimilate this data, albeit presented in a much more generally comprehensible form than has previously been the case, and use it in the context of the commercial constraints, classification society requirements and statutory regulations. The next generation of computer based systems is likely to involve the use of expert systems and neural network technologies. By introducing this type of technology, the ship operator will be provided with an interpretive back-up of accumulated knowledge and expertise which has been introduced into the computer based system and will be available in the form of supplementary information and suggested courses of action at the time the particular problem occurs. Such techniques will, if carefully constructed, introduce a level of consistency of decision making, hitherto unprecedented, and also prevent knowledge and experience being lost when staff members leave or retire from a company. In the specific case of diagnostic information, such as might occur from the data transmitted from a diesel engine, the artificial intelligence aspects and neural network will encompass pattern recognition techniques or determine the probability of a particular fault or failure scenario. Reference 22 details some of the machinery and ship management based research currently being conducted in this area.

Figure 23.23 schematically illustrates a system where a shipboard based monitoring system provides a level of intelligent support to the ship operators for local operational and maintenance decision making. The data collected by the various sensory systems can then be transmitted as data streams via narrow band satellite communication links to a shore based station at some convenient location which undertakes more detailed and long term analysis of the data and also supports a data base for the vessel. Such a shore based analysis facility is then in a position to provide data for the various interested communities, since the analysis will contain not only commercial data but also technical data on both ambient conditions and any impending short- and long-term failures.

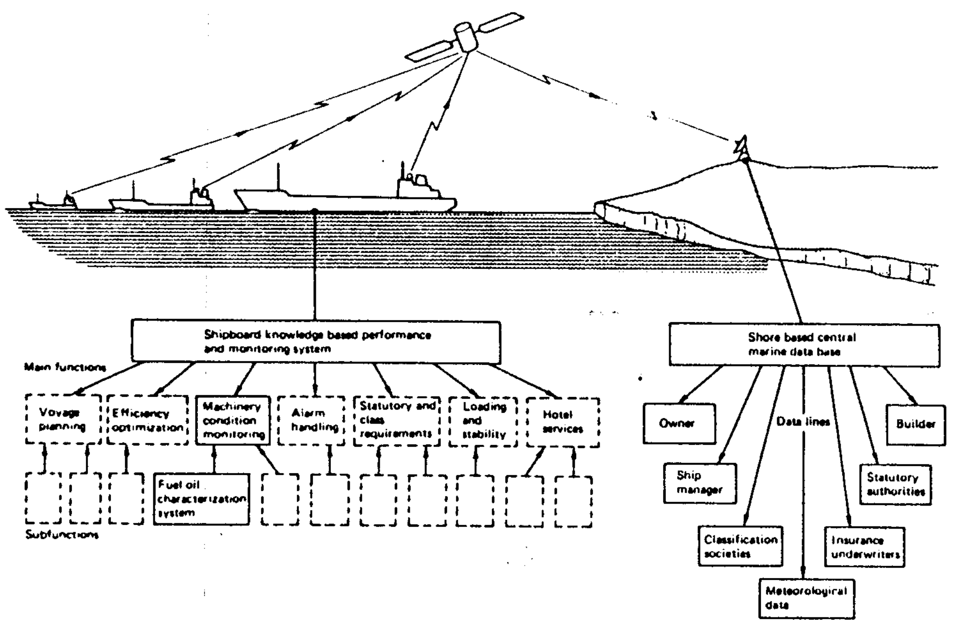

Figure 23.23 Computer based integrated ship management structure

References and further reading

1. Christie, A.O. Hull roughness and its control. *Marintech Conference*, Shanghai, China, 1981.
2. Evans, J.P., Svensen, T.E. Voyage simulation model and its application to the design and operation of ships. *Trans. RINA*, November, 1987.
3. Bidstrup, K. *et al.* Self activating module systems, a new approach to polishing antifouling paints. *21st Annual Marine and Offshore Coatings Conference*, California, 1981.
4. Townson, R.L., Byrne, D., Svensen, T.E., Milne, A. Estimating the technical and economic penalties of hull and propeller roughness. *Trans. SNAME*, 1981.
5. A hull roughness evaluation project. *Marine Propulsion*, February, 1987.
6. Townsin, R.L. Developments in the circulation of rough underwater surface power penalties. *Celena 25th Anniversity Symp.*, Genoa, 1987.
7. KcKelvie, A.N. Hull preparation and paint application: their effect on smoothness. *Marine Engineers Review*, July, 1981.
8. Naess, E. Reduction of drag resistance by surface roughness and marine fouling. *Norwegian Maritime Research*, No. 4, 1980.
9. Townsin, R.L., Byrne, D., Svensen, T.E., Milne, A. Fuel economy due to improvements in ship hull surface conditions 1976 -1986. *ISP*, July, 1986.
10. Lackenby, H. The resistance of ships with special reference to skin friction and hull surface conditions. 34th Thomas Lowe Grey Lecture. *Trans. I.Mech.E.*, 1962.
11. Bowden, B.S., Davison, N.J. Resistance increments due to hull roughness associated with form facter extrapolation methods. *NMI* Ship TM 3800, January, 1974.
12. Musker, A.J. Turbulent Shear-flow Near Irregularly Rough Surfaces with Particular Reference to Ship's Hulls. Ph.D. Thesis, University of Liverpool, December, 1977.
13. Johansson, L.E. The local effect of hull roughness on skin friction. Calculations based on floating

element data and three dimensional boundary layer theory. *Trans. RINA*, 127, 1985.
14. Waldenhaug, H. Paint roughness effects on skin friction. *ISP*, 33(382), June, 1986.
15. Kauczynski, W., Walderhaug, H. Effects of distributed roughness on the skin friction of ships. *ISP*, 34(389), January, 1987.
16. Abbott, Ira H. and Doenhoff, A.F. von. *Theory of Wing Sections*. Dover, New York.
17. Grigson, C.W.B. Propeller roughness, its nature and its effect upon the drag coefficients of blades and ship power. *Trans. RINA*, 1981.
18. Propeller Surface Roughness and Fuel Economy. SMM Technical Brief No. 18.
19. Sherrington, I., Smith, E.H. Parameters for characterising the surface topography of engineering components. *Trans. I.Mech.E.*, 1987.
20. Towsin, R.L., Spencer, D.S., Mosaad, M., Patience, G. Rough propeller penalties. *Trans. SNAME*, 1985.
21. Whipps, S.L. On-line ship performance monitoring system: operational experience and design requirements. *Trans. I.Mar.E.* (TM), 98, Paper 8, 1985.
22. Katsoulakos, P.S., Hornsby, C.P.W. and Rowe, R. Advanced ship performance information systems. *Trans. I.Mar.E.* (C), 101, Conf. 3, 1989.

24

Propeller tolerances and inspection

Contents

Although part of the manufacturing process, the related subject of propeller tolerances and inspection deserve particular attention. This is because it is only by the correct specification of the tolerances and by checking that these have been adhered to that the intentions of the designer can be properly realized. Without this proper attention to blade manufacturing tolerances many serious problems can be encountered in the service life of the propeller: for example, cavitation, power absorption, noise, fatigue failure and so on.

Table 24.1 Normal propeller tolerances specification parameters

Diameter
Mean pitch
Local section pitch
Section thickness
General section form (camber)
Section chord length
Blade form and relative location
Leading edge form
Rake and axial position
Surface finish
Static balance

24.1 Propeller tolerances

For general propeller design,work the ISO specifications (References 1 and 2), for propellers greater than 2.5 m and between 0.80 and 2.5 m respectively, usually serve as the criteria for assessment. In certain particular cases, such as naval applications, the purchasers of the propeller may impose their own particular tolerance specifications and methods: for example, the US Navy standard drawing method.

In general tolerances are normally specified on the set of dimensions shown in Table 24.1, since they affect the performance of the propeller or adjacent components in some particular way.

Table 24.1 deals only with geometric parameters, but a propeller should also be shown to meet both the required chemical composition tolerances for the material and the minimum mechanical properties. The latter requirements are of course classification society requirements for those vessels built under survey. For all vessels, however, attention needs to be given to the actual characteristic of the material for strength and repair purposes.

Of the geometric properties quoted in Table 24.1, each has some bearing on performance, and it is essential to understand the ways in which they influence the various operational characteristics if the correct tolerance is to be specified. Unfortunately, the precise importance of each characteristic requires particular consideration for each case; notwithstanding this, certain general conclusions can be drawn and these are shown in Table 24.2. In this table an attempt is made to distinguish between the primary and secondary effects of the various parameters specified earlier, but not necessarily in relation to the ISO requirements which reduce some of the effects defined in Table 24.2 to negligible proportions.

As a consequence of the various effects detailed in Table 24.2, the designer and purchaser of the propeller need to determine what level of tolerance is required such that the propeller will be fit for the purpose for which it is intended. Indeed, one could specify the most stringent tolerance for every propeller; this, however, would be extremely wasteful in terms of additional costs of manufacture. The ISO specification defines four levels of tolerance; Class S, I, II and III, these being in descending order of stringency. Again there is some latitude in deciding the correct tolerance level for a particular ship, but as a rough guide Table 24.3 has been prepared.

Table 24.2 Principal effects of the various propeller geometric variations

Parameter	*Primary effect*	*Secondary effect*
Diameter	Power absorption	—
Mean pitch	Power absorption	Cavitation extent
Local section pitch	Cavitation inception and extent	Power absorption
Section thickness	Cavitation inception, blade strength	Power absorption
General section form (camber)	Power absorption, cavitation inception	Blade strength
Section chord length	Cavitation inception	Blade strength power absorption
Blade form and relative location (excluding leading edge)	Generally small effects on cavitation inception and shaft vibratory forces at frequencies dependent on wake harmonics and blade irregularities	—
Leading edge form	Critical to cavitation inception	
Rake and axial position	Minor mechanical vibratory forms	—
Surface finish	Blade section drag and hence power absorption	—
Static balance	Shaft vibratory loads	

Table 24.3 Typical tolerances for certain ship types

ISO tolerance	*Typical ships where tolerance might apply*
S	Naval vessels* (e.g. frigates, destroyers, submarines, etc.). High-speed craft with a speed greater than 25 knots; research vessels; certain special purpose merchant vessels where noise or vibration is of paramount importance (e.g. cruise vessels, high-grade ferries).
I	General merchant vessels; deep sea trawlers; tugs, ferries, naval auxiliaries.
2	Low-power, low-speed craft, typically inshore fishing vessels, work boats, etc.
3	As for class 2.

* Naval vessels are often specified on an 'ISO S Class Plus' basis

Table 24.3 is generally self-explanatory and other ship types and the appropriate tolerance classes can be deduced from those given in the table. Of particular concern, however, are the small high-speed vessels such as patrol or chase boats. All too often, in the author's experience, the subject of blade tolerances is completely neglected with these vessels leading to a host of cavitation problems. Such vessels, by virtue of their speed, both in terms of ship and shaft rotational speeds, in association with a low static pressure head, should generally qualify the propeller for a class S or I tolerance notation.

24.2 Propeller inspection

The inspection of propellers requires to be undertaken both during the manufacture of the propeller and also during its service life. In general the former is undertaken in the relatively controlled conditions of the manufacturer's works whilst the latter frequently but not always takes place in a dock bottom. Both types of inspection are important; the former to ensure design compliance and the latter to examine the propeller condition in service.

24.2.1 Inspection during manufacture and initial fitting

In the case of the fixed pitch propeller the inspection procedure is carried out with the aid of purpose-built machines. Such machines, whether they be manually operated or part of a CAM system, are in general a variant of the drop height measurement system. With this system the measurements are either made on the cylindrical sections or, alternatively, at various points defining a matrix over the blade surface. In the former case direct comparison with the cylindrical design sections can be made, whereas the latter, as this frequently requires an interpolation procedure to be invoked, raises questions of the validity of the mathematical model of the blade surface.

In its most fundamental form the classical cylindrical measurement requires that the propeller be mounted in a gravitational or other known plane with a vertical pole, relative to the plane of mounting, erected on the shaft centre line. To this pole is fixed a rotating arm which is free to rotate in a plane parallel to the plane on which the propeller is mounted (Figure 24.1). From this arm the various radii can be marked on the blade surface and drop heights to the blade surface measured at known intervals along the chord length. By undertaking this exercise on both surfaces of the propeller the blade section shape can be compared to the original design section. Whilst this is the basis of the measurement system, many refinements aimed at improving accuracy have been incorporated by manufacturers, each having their own version of the system.

The area which causes most concern is the detail of the leading edge. In a great many cases this is checked with the aid of a template (References 1 and 2). However, there is also a considerable use of optical methods for leading and trailing edge inspection: this is particularly true in the case of model propeller manufacture for model testing purposes.

The current trend in manufacturing tolerance checking is to progress toward the introduction of electronic techniques. These developments embrace electronic pitchometers, numerically controlled geometric inspection through to fully integrated design, manufacturing and inspection capabilities outlined in Chapter 19. In all cases, however, it is of fundamental importance to define a sufficient set of inspection points in order to define the actual blade surface adequately to act as a basis of comparison.

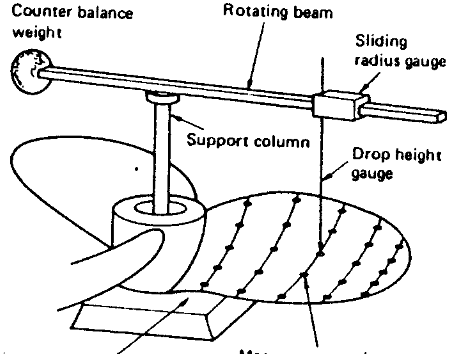

Figure 24.1 Principle of mechanical pitch measurement

In addition to the blade profile tolerances, in the case of fixed pitch propellers, rigorous inspection needs to be given to the bore of the boss. The fitting of the propeller to the shaft requires considerable attention, and is a concern governed by classification society requirements. For keyed propellers a satisfactory fit between the propeller and the shaft should show a light, overall marking of the cone surface of the shaft taper with a tendency towards heavier marking in way of the larger diameter of the cone face. When conducting these inspections the final fit to the cone should be made with the key in place. In some cases the propeller is offered up to a shaft mandril in the manufacturer's works so that the proper degree of face contact can be developed as required by the classification society rules. In cases where hand fitting is required this must be done by scraping the bore of the propeller; it should never be done by filing of the shaft cone.

With regard to the axial push-up required, Table 24.4 gives some guidance values for a shaft having a cone taper of 1 in 12.

Table 24.4 Typical axial push-up values for copper alloy propellers

Propeller material	*Axial push-up*
Aluminium bronage	$0.006D_s$
High-tensile brass	$0.005D_s$

In Table 24.4, D_s in the diameter of the shaft at the top of the cone and the axial push-up is measured from a reliable and stable zero mark obtained from the initial bedding of the propeller to the shaft. In cases where hydraulic nuts are used, great care needs to be exercised to ensure that the hub is not overstressed in way of the key way and that the appropriate classification rule requirements are adhered to.

In the case of the keyed propeller it is of the utmost importance to prevent the ingress of sea water to the cone; as a consequence inspection needs to be particularly rigorous in this area. When the sealing arrangement comprises a rubber ring completely enclosed in a recess in the propeller boss, ample provision must be made for the rubber to displace itself properly to form a good seal. Alternatively, if an oil gland is fitted the following points should be carefully considered:

1. To ensure that rubber rings for forming the seal between the flange of the oil gland sleeve and the propeller boss are of the correct size and properly supported in way of the propeller keyway.
2. The fair water cones protecting propeller nuts and the flanges of sleeves of oil glands should be machined smooth and fitted with efficient joints at their connection to propellers.
3. Drilling holes through the propeller boss should be discouraged but, when these are essential to the design, special attention needs to be paid to the efficient plugging of the holes.
4. The arrangement for locking all screwed components should be verified.
5. The propeller boss should be provided with adequate radius at the large end of the bore.
6. When the design of the oil gland attachment to the propeller is similar to that shown in Figure 24.2, it is good practice to subject the propeller boss to a low-pressure air test, checking all possible sources of leakage with a soapy water solution in order to prove tightness.

When a keyless propeller is fitted to the shaft the inspector should pay particular attention to ensuring that the design and approved interference fit is attained. As a prerequisite for this procedure the inspector needs to know the start point load to be applied and the axial 'push-up' required. These should normally be supplied at two temperatures, typically 0 °C and 35 °C, to allow interpolation between the two values to take place to cater for the actual fitting conditions. The inspector should carefully examine the final marking of the screw shaft cone fit, which should show a generally mottled pattern over the entire surface with harder marking at the larger end of the cone.

Two basic techniques are employed to fit keyless propellers: the dry press-fit or the oil injection method. With both methods the propeller is pushed up the shaft cone by means of a hydraulic nut, but the fitting procedure differs somewhat between the two methods, however, the manufacturer's fitting procedure must be rigidly adhered to in all cases. As a final stage in the inspection it is essential that the propeller, both working and spare, be hard-stamped with information

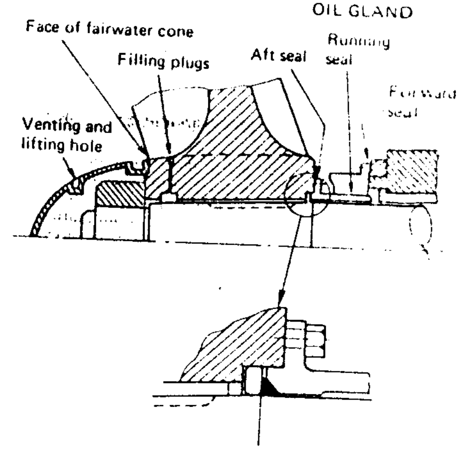

Figure 24.2 Propeller shaft assembly

of the form detailed below on the outside of the boss away from any stress raisers or fillets:

1. *Oil injection type of fitting*
   Start point load (tonnes)
   Axial push-up at 0°C (mm)
   Axial push-up at 35°C (mm)
   Identification mark on associated screw shaft
2. *Press fit type of fitting (dry)*
   Start point load (tonnes)
   Push-up load 0°C (tonnes)
   Push-up load 35°C (tonnes)
   Axial push load 0°C (mm)
   Axial push load 35°C (mm)
   Identification mark on associated screw shaft

With regard to the process of fitting the propeller to the shaft a good review of methods is given by Eames and Sinclair (Reference 3).

24.2.2 Inspection during service

In-service inspections are normally carried out for one of two reasons: to examine the propeller after suspected damage or to check for fouling, or to form part of a survey of the vessel. In the former case this may be carried out in the water by a diver if a superficial check is required, or in a dry dock for a more detailed survey. As a general comment on in-water and out-of-water inspections it should be remembered that a commercial diver is usually a very highly trained person but not normally a propeller technologist, and so can give only generalized engineering reports. Furthermore, in many instances, typically in the North Sea area, whilst looking at one part of the propeller the diver cannot see the rest of the propeller due to the clarity of the water. Irrespective of water clarity, the in-water survey is greatly enhanced if the diver can talk, preferably with the aid of video techniques, to a propeller specialist while undertaking the survey so that important details will not be missed and other less important features given undue weight.

When a propeller is operating any small cracks or defects tend to collect salt deposits. As a consequence, before conducting a blade surface inspection in a dry dock aimed at identifying cracks the surface should be lightly cleaned to remove marine growth and then washed with a 10% concentration of a sulphuric acid in water to dissolve the salts. If the propeller is removed from the shaft for this examination, then this is extremely helpful to the inspector and increases considerably his chance of finding small defects. Furthermore, if the propeller is removed from the shaft and placed on the forward face of the boss, then it is also useful to place weights on the blade tips in order to help open up any cracks present. It is completely pointless to attempt an examination designed to look for small cracks in water.

To undertake a general propeller inspection it is a prerequisite to have an outline of the propeller which, although not needing to be absolutely correct in every geometric detail, must represent the main propeller features adequately. Without this diagram, of both the face and back of the blades, with suitable cylindrical lines marked on it at say 0.9*R*, 0.8*R*, 0.6*R*, 0.4*R*, serious misrepresentations of information can occur. In the author's experience the best blade outline to use for damage recording is the developed blade outline, since this tends to represent the blade most closely to the way an inspector studies it. In addition to a blade outline there should also be a consistent way of recording information to signify, for example, cavitation damage, bending, missing portions, marine growth and so on. Figure 24.3 shows a typical diagram for inspection purposes and in addition to showing the location of the damages on the blade typical dimensions of length, width and depth need to be recorded. Such records need to be taken individually for each blade, on both the back and face of the propeller, so as to answer questions of the similarities of blade damage since a propeller may exhibit damage from different sources simultaneously.

In the case of a classification society inspection the propeller is normally required to be removed from the tail shaft at each screw shaft survey. On these occasions particular attention should be paid to the roots of the blades for signs of cracking.

If a new propeller is to be installed, the accuracy of fit on the shaft cone should be tested with and without the key in place. Identification marks stamped on the propeller should be reported for record purposes, and if the new propeller is substantially different from the old one, it should be recalled that the existing approval of torsional vibration characteristics may be affected.

It is particularly important to ensure that rubber rings between propeller bosses and aft ends of liners are the correct size and so fitted that the shaft is protected from sea water. Failure in this respect is often found at the ends of keyways due to the fact that the top part of the key itself is not extended to provide a local bedding for the ring in way of the recess in the boss. In such cases it may be found practicable to weld an extension to the forward end of the key. It should also be recollected that water may enter the propeller boss at the aft end and attention should therefore be paid to this part of the assembly. Filling the recess between the aft end of the liner and the forward part of the propeller boss with grease, red lead or similar substance is not in itself a satisfactory method of obtaining water-tightness. Sealing rings in connection with approved type oil glands should be similarly checked.

If an oil gland is fitted, the various parts should be examined at each inspection and particular attention should be paid to the arrangement for preventing ingress of water to the shaft cone. All oil glands, on

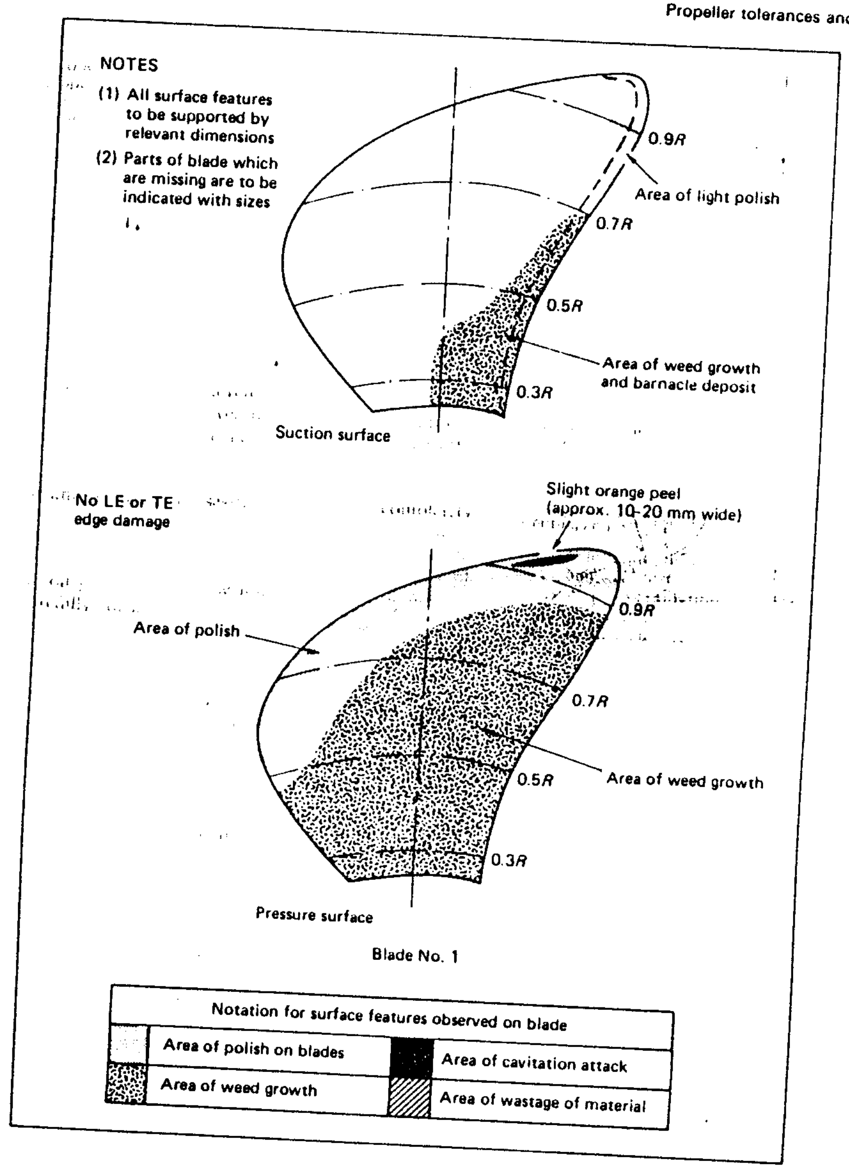

Figure 24.3 Typical blade inspection diagram

reassembling, should be examined under pressure and shown to be tight.

If the ship has a controllable pitch propeller, the working parts and control gear should be opened up sufficiently to enable the inspector to satisfy himself of their condition. In the case of directional propellers at each docking the propeller and fastenings should be examined as far as practicable and the manoeuvring of the propeller blades should be tested.

References and further reading

1. ISO 484/ 1. Shipbuilding – Ship Screw Propellers – Manufacturing tolerances – Part 1: Propellers of Diameter Greater than 2.50 m, 1981.
2. ISO 484/ 2. Shipbuilding – Ship Screw Propellers – Manufacturing Tolerances – Part 2: Propellers of Diameter between 0.80 and 2.50 m Inclusive, 1981.
3. Eames, C.F.W., Sinclair, L. Methods of attaching a marine propeller to the tailshaft. *Trans. I.Mar.E.*, **92**, 1980.

25 Propeller maintenance and repair

Contents

The repair and maintenance of a propeller is of the utmost importance if a propeller is to give a reliable and high-performance service throughout its life. Damage can arise from a number of causes and the propeller should be regularly examined for signs of this.

25.1 Causes of propeller damage

In general terms, propeller damage can be classified into four distinct types: cavitation erosion damage, maltreatment, mechanical service damage and wastage.

25.1.1 Cavitation erosion damage

Cavitation damage will occur in situations where the propeller is either working in a particularly onerous environment in terms of immersion or in-flow conditions that cannot be accommodated by good design, or when a propeller is poorly designed. In either of these cases the cavitation is a primary source of damage. Conversely, cavitation damage can result in the wake of some mechanical damage such as a leading edge tear or bend, in which case the cavitation erosion is a secondary damage source. Figure 25.1 shows a typical example of cavitation erosion on a propeller blade and the mechanism by which this damage occurs is discussed in Chapter 9. A further example of cavitation damage is the phenomenon of trailing edge curl, which is also discussed in Chapter 9 and shown in Figure 9.25.

Cavitation erosion damage may either stabilize or continue to progress. If it progresses this can be at either a relatively slow or an extremely fast rate. As a consequence when cavitation damage is first noticed a check should be made to determine the rate at which the erosion attack is progressing, so that effective repair and remedial action can be planned and implemented.

25.1.2 Maltreatment damage

Maltreatment damage can result from many causes; for example, incorrect handling, surface deterioration or severe heating of the boss or blades of a propeller.

Incorrect handling most commonly leads to edge or tip damage on the blades during transport. This damage should be avoided by the proper use of soft metal edge protectors, typically copper or lead, to prevent the propeller coming into direct contact with craneage slings. Additionally these edges should be combined with the use of timbers or heavy tyres in the appropriate fulcrum positions. If lifting eyebolts are fitted these should always be used.

Surface deterioration is most commonly the result of a loss of protective coating, paint splashes or other markings. Although the protective coating, which is normally a colourless varnish or a self-hardening dewatering oil, should be completely removed before the vessel enters service after fitting out, its purpose is to prevent fouling and other light damage such as paint splashing and light impact damage. During painting operations the propeller should be covered at all stages in its life to prevent splashes adhering to the surface, as these can lead to cavitation erosion and severe local pitting.

If heating is applied in an arbitrary manner to a propeller, this can create internal stresses in the material. These internal stresses occur when a local region of metal is heated and tries to expand, but is prevented from doing so by the surrounding cooler metal. As a consequence compressive stresses build up until they are relieved eventually by the onset of plasticity, which occurs until red heat is reached when internal stresses in the heated member can no longer exist. On cooling the heated area contracts and the incipient tensile stresses are relieved by plastic flow but as the cooling progresses the plastic flow becomes slow, and at about 250°C ceases, and this allows a tensile stress field to build up in the cooling metal. Typical causes of this local heating abuse are incorrect heating of the boss to aid removal and the repair of the blade by inappropriate methods. In the first instance stress corrosion cracks are frequently initiated

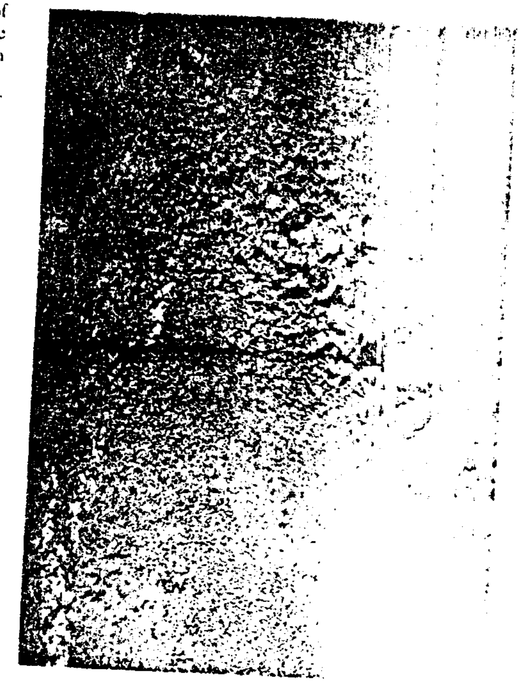

Figure 25.1 Typical cavitation erosion damage

Figure 25.2 Boss cracking due to local heating abuse

by concentrated heat sources such as oxy-acetylene and oxy-propane being applied to the boss, producing high tensile residual stresses in the manner described above, and although giving the appearance of a satisfactory removal and replacement operation, will lead to cracking some weeks or months after re-immersion in the sea water. Figure 25.2 shows a typical cracking pattern caused by local heating abuse. When heat is applied to the boss this should be done with great care using either steam or low temperature electric blankets all over the boss surface. Alternatively, the use of a soft flame can be acceptable provided it is applied to each section of the boss and kept moving to prevent hot spots from occurring.

25.1.3 Mechanical service damage

This is perhaps the most common form of damage to a propeller blade and is normally caused through contact with floating debris, cables or chains. Figure 25.3 shows a propeller after having fouled the chains of a mooring buoy.

In most cases impact damage involves only minor damage to the blade, typically in the edge region. Whilst such damage does not normally impair the strength integrity of the blade, advice should be sought as to whether there is the likelihood of secondary

Figure 25.3 Propeller damage due to impact damage with mooring chains

cavitation damage occurring, and if so a temporary grinding repair may prove advantageous and save further damage if the full repair cannot be effected immediately.

When a large piece of the propeller is damaged and perhaps missing, or if the blade suffers a fatigue failure, then immediate attention is required. It may be, however, that a dry dock or the replacement propeller is some considerable distance away; in such cases a calculation of the out-of-balance forces should be made to establish the rotational speed at which the lubricant film can just be maintained in the stern bearing and a suitably de-rated shaft speed determined.

25.1.4 Wastage damage

All propellers will exhibit damage throughout their life, due to wastage, when compared to their new state: this is a quite normal process of corrosion.

For example, in the case of a high-tensile brass propeller it would be reasonable to expect a loss of the order of 0.05 mm per annum, assuming that the composition of the material was such that dezincification did not occur and that the propeller was lying at rest in still or slowly moving water. If, however, the propeller were operating normally with tip speeds in the region of 30 m/s, then this wastage may well rise to around 0.15 or 0.20 mm per annum and perhaps more in the case of suction dredgers or trawlers. This effect leads to a general roughening of the propeller when compared to its new state.

Wastage is principally a process of corrosion, and it is well known that when small anodic areas are adjacent to large cathodic surfaces a severe electrochemical attack can take place; this attack is accelerated when the surfaces are exposed to high-velocity turbulent flows. When abnormal wastage occurs on a propeller it is generally due to a corrosion process taking place. A typical example of such corrosion taking place is often found during the fitting out stage of the vessel. At this time the propeller becomes a cathode in the propeller hull electrolytic

cell, and a hard and strongly adherent coating of magnesium and calcium carbonate appears on the surfaces. When the vessel enters service this coating of cathodic chalk film becomes worn away in a patchy manner in the outer region of the blade. These areas and others where the establishment of the film has been delayed allow corrosion to proceed at an abnormally high rate, leading to localized depressions and pitting of the surface; this also increases the turbulence level and hence promotes the conditions to enhance the corrosion rates.

25.2 Propeller repair

Propeller repair is an extremely complex and extensive subject and the details of repair methods should be left to specialists in this field.

The owner who, for whatever reason, allows non-experienced personnel or companies to repair a damaged propeller may well find that the action will eventually result in the premature loss of the propeller. The propeller is an extremely complex engineering artefact, manufactured from complex and advanced materials and operating in a hostile and corrosive environment. Its maintenance and repair therefore deserve considerable care and respect.

As a consequence of these remarks, this section will set out some of the underlying principles of repair but leave the detail which relates to each material specification to the specialist repairer.

25.2.1 Blade cracks

Experience has shown that all cracks in propeller blades are potentially dangerous and this is particularly true of cracks close to the leading edge. Cracks normally grow by fatigue action, but in cases where the propeller fouls some substantial object they can act as a notch and initiate rapid failure.

In cases where the crack is found on the leading edge the crack should be ground out after any straightening has been carried out. In the grinding process great care must be taken to ensure that the crack tip has been eradicated, otherwise this can introduce a further initiation point for another crack. If the crack is very small, then it is generally best to just fair the ground-out portion into the existing blade form; however, if this is not possible, then recourse has to be made to a weld repair. In the case of highly skewed propellers, if cracks are found in the vicinity of the trailing edges of the blades, then this is a potentially very serious situation. As discussed in Chapter 18 and shown in Figure 18.6, the highly skewed propeller can exhibit high stress concentrations along the trailing edge. Therefore, if cracks occur in these regions, this is akin to finding cracks in the root region of a conventionally skewed propeller. Hence, immediate advice should be sought on how to tackle the problem should cracks be observed in the trailing edge regions of highly skewed blades. Simply grinding the cracks out may not solve the problem, since if significant sub-surface defects are found in this region these may only accentuate the additional stress field induced by the re-profiling operation of grinding and may act as further crack initiation sites. When cracks are noticed in this region of the blades of a controllable pitch propeller, the affected blades should be replaced with spares.

If the crack is in the body of the blade then it should first be ground out to a significant depth into the section, typically rather more than half the thickness of the section at that point, to give a 'V' form with an included angle of the order of 90°. The repair must then be effected with a suitable welding technique. After completion of the weld repair the surface of the weld must be ground down to conform with the designed blade surface profile, and the repair examined for lack of penetration and other similar defects prior to initiating the stress-relieving operation.

If cracks are found close to the boss, inboard of about 0.45R, then welding processes leave high residual stress fields which in general can only be removed by annealing the whole propeller. If the crack is small in this inner region, then consideration should be given to just grinding the crack out and fairing the resulting depression into the blade form; the determinant in this situation is the strength of the blade.

25.2.2 Boss cracks

Cracks in the propeller boss, or hub of a controllable pitch propeller are always serious. They are, however, not normally found until they are too deep to repair. If they are sufficiently shallow to permit their complete removal by grinding, then this should be done, and before returning the propeller to service a strength evaluation should be made. When the boss is capable of repair in this way it would clearly be beneficial to apply some low-temperature stress relief.

25.2.3 Repair of defective castings

The propeller casting which is free from defect has yet to be made; however, most propellers are cast with an acceptable level of defects present. When a defect needs repair, caution needs to be exercised to ensure that this is done properly.

In general small surface defects such as pores of the order of 1 mm in diameter do not need rectification except where they occur in close packed groups in highly stressed regions of the blade. However, when an unacceptable defect is found in a blade the defect should be ground out and faired into the surrounding blade and a check made on the effect of this action on the blade strength. The integrity of the blade should then be demonstrated by a dye penetrant examination.

The repair of defects by welding should not be the first response after noticing a defect, since welding can potentially introduce a greater problem than the original defect if it is not properly carried out. Classification societies in general impose limits on the extent of weld repairs to propeller castings, as discussed in Section 25.3. In addition welds having an area of less than 5 cm² are not to be encouraged.

25.2.4 Edge damage to blade

Edge damage generally takes the form of local bending or tearing of the metal; sometimes cracking also occurs, in which case the previous comments apply.

If the tearing is of a minor nature, then the affected edges should be dressed back to shape, which may result in some slight loss of blade area. If this loss is confined to around 10 mm, then there should be no undue effect on the propeller's performance, provided that proper attention has been paid to reprofiling the blade edge. Should the tearing be greater than that identified above, then consideration should be given to replacement of that section of the blade by cutting the blade back and inserting a new piece. As discussed in Section 25.3, care needs to be exercised in the case of the trailing edge of highly skewed propellers.

Small distortions of the blade along the edge can normally be corrected by cold working with the use of clamps; for greater distortions, hot straightening techniques need to be deployed.

After repair of edge damage the edges need to be examined closely for signs of any remaining cracks that may give trouble in the future. The extent of these cracks may be very small and difficult to see with the unaided eye, and therefore a dye pennant inspection should be made.

25.2.5 Erosion damage

Erosion damage is generally repaired by welding, and therefore the propeller normally needs to be transferred to a protected area, where good environmental control can be exercised. The area subjected to attack needs to be cut out cleanly and then filled by welding. After welding the repaired surface must be ground to the blade profile and the repair examined for its integrity. Stress relieving should then be carried out to the manufacturer's recommendations.

In all cases where cavitation erosion damage is seen, the modifications necessary to the blade form to prevent recurrence, assuming the erosion is not secondary to some other damage, should be determined and if feasible implemented. If this is not done, then erosion repair will become a regular feature of the docking cycle.

25.2.6 Maintenance of the blade in service

During the life of a propeller it should be regularly checked to see that it remains in a clean and unfouled state. The implications of fouling on the propeller were discussed in Chapter 23.

If when inspected the blade surfaces are smooth, showing no roughness, chalking, fouling or wastage, then they should not be touched, but left to the next inspection. If, however, any of these attributes are seen, then the blade should be lightly ground and polished by a competent organization: to allow this work to be done by others can lead to the abuse of the propeller and a consequent set of other in-service problems. To allow a propeller to continue in operation with local pits or more widespread roughness can in time give rise to the need for repair rather than simple and straightforward polishing.

Even when a propeller has been neglected, provided the local pits and depressions are not more than 1 mm or so deep, this can generally be rectified by light grinding and polishing. If the neglect has resulted in a worse state than this, then more serious attention is necessary and this is best left to a manufacturer, since heavy grinding of the surface can lead to surface changes sufficient to affect efficiency and cavitation performance.

25.2.7 Replacement of missing blade sections

If a large section of a blade is partially torn off, or lost by impact damage, or cut away to remove a severely bent or damaged area, then this can often be replaced. The affected area is trimmed and dressed and a new blade piece, which has been especially cast for the purpose, is either welded or burnt on.

Before considering this action the extent of the repair has to be carefully considered. Such action is possible for a blade tip or parts of the edge, but it is not suitable for a complete blade replacement. The replacement of part of a blade is a major undertaking, and therefore requires expert craftmanship and advice.

25.2.8 Straightening of distorted blades

Apart from cold straightening methods for small areas of damage, as mentioned earlier when discussing edge damage, the method for straightening large bending damage is through the use of hot working techniques.

With these techniques, after having carefully assessed the extent of the damage, the back of the blade should be heated slowly in the area of damage and for a significant area around it. The ideal method for this is to use a coke brazier which can be blown up to the appropriate temperature by forced draught fans; an alternative to the coke brazier would be a soft flame such as paraffin, coal gas or propane air burners. On no account should a hard flame be used, for example oxy-gas burners, because of the risk of local melting of the blade. During the heating process the top surface of the blade should be lagged to prevent heat loss.

When the blade has been heated to a suitable temperature for working, about 150–250° C below the material melting point, depending on the material, the straightening process is best carried out using weights and levers. This process should not be hurried, but carried out very slowly avoiding the use of hammers as far as practicable. When the straightening process has been completed the propeller should be allowed to cool very slowly with the blade lagging in place. With this process stress relief should not normally be necessary, but if doubt exists, then a full heat treatment should be applied.

Clearly after such a process has been carried out the blade geometry must be checked, and this normally requires that the propeller is removed from the shaft. As a consequence this type of blade straightening exercise would normally be carried out off the shaft; this is especially true if major straightening is required and needs the use of a hydraulic press.

In addition to the repair of damage, these methods have been deployed to adjust the pitch of a propeller which has not given the correct power absorption characteristics. In this case the blade needs to be carefully instrumented with thermocouples and the process is preferably done with a number of flexible electrical heating mats which are easily controlled to give the correct temperature distribution: in these applications the leading and trailing edges heat up more quickly than the central body of the blade. When the blade has been heated to the hot forming temperature, it is twisted using a hydraulic ram placed near the tip of the blade. The forces involved are generally small and the twisting process takes only a short time.

25.3 Welding and the extent of weld repairs

As a general rule all welding on a propeller should be done with metal arc processes using approved electrodes or wire filler. In certain circumstances gas welding can be done on high tensile brass but not on the other materials, and most classification societies do not approve of this latter technique.

The area to be welded needs to be both clean and dry, and so it is preferable to conduct these operations under cover and in places relatively free from dust, moisture or draughts. If flux-coated electrodes are used they should be preheated for about one hour at a temperature of about 120°C, and where required by the material specification the area to be repaired should be preheated to the desired temperature and the preheat maintained until the welding is complete: welding should always be conducted in the downhand position and all slag must be chipped away from any undercuts or pockets between consecutive weld runs. Upon completion of the weld repair the area should be stress relieved, with the exception in some cases of nickel–aluminium bronzes. With these materials classification societies (see, for example, Reference 1) require that stress relief be implemented where the weld has been carried out to the blade edge between 0.7*R* and the hub. Stress relief for the nickel–aluminium bronzes is also required where welding has been carried out between the bolt holes on controllable pitch propeller blades.

When the weld repair is complete then the weld should be ground smooth for visual examination and dye penetrant testing. If stress relief is to be employed, then a visual examination should be carried out prior to the stress relief and both a visual and a dye penetration examination carried out afterwards.

The extent of welding is governed by the requirements of the various classification societies. These requirements are based on the likely stress fields and the consequences of welding in the various parts of the propeller. For example, the permitted area is given in Table 25.1 and the zones A, B and C are defined for conventional, highly skewed and vane wheel blade forms. The zones *A*, *B*, *C* are defined for illustration purposes in Figure 25.4 taken from Reference 1: in practice the current

Table 25.1 Permissible areas of welding as defined by LR rules 1994

Severity zone or region	*Maximum individual area of repair*	*Maximum total area of repairs*
Zone A	Weld repair not generally permitted	
Zones B, C	60 cm² or 0.6% × S, whichever is the greater	200 cm² or 2% × S, whichever is the greater in combined zones B and C, but not more than 100 cm² or 0.8% × S, whichever is the greater, in Zone B on the pressure side
Other regions	17 cm² or 1.5% × area of the region, whichever is the greater	50 cm² or 5% × area of the region, whichever is the greater

S = area of one side of a blade = $0.79D^2A_D/Z$
D = finished diameter of propeller
A_D = developed area ratio
Z = number of blades

Note: When separately cast blades have integral journals, weld repairs are not generally permitted in the fillet radii or within 12 mm of the ends of the radii. When repairs are proposed in these locations, full particulars are to be submitted for special consideration.

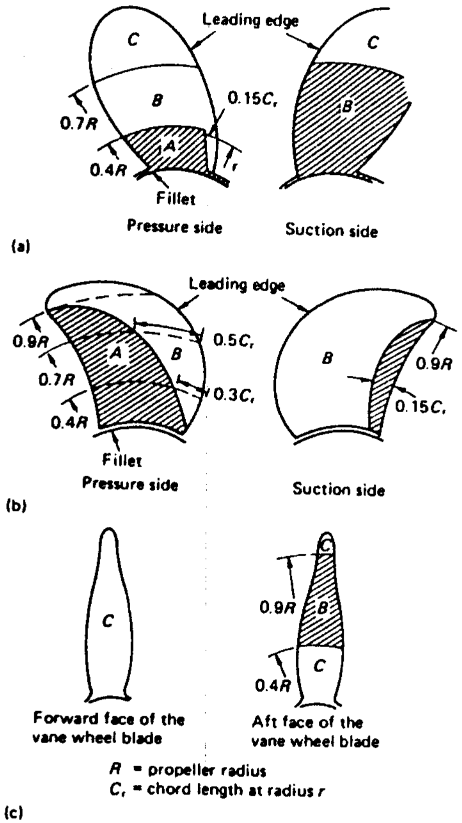

Figure 25.4 Blade welding severity zones

rules of the appropriate classification society must be used. In addition to the blade requirements the boss of the fixed pitch propellers is divided into three individual regions whilst the palms of controllable pitch propeller blades are similarly divided into two other regions. These regions are given in Table 25.2 for the current edition of these regulations (Reference 1) and relate to the other regions defined in Table 25.1.

25.4 Stress relief

The stress relief of a propeller blade after a repair involving heat, particularly welding, is a most important matter. The residual stresses induced by these heating operations are sufficient to lead to stress corrosion cracking in high-tensile brass and the manganese–aluminium bronzes. The operations of chief concern

Table 25.2 Other regions of the propeller as defined by LR rules

Fixed pitch propeller bosses	*Controllable pitch propeller and built-up propeller blades*
The bore	The surfaces of the flange to the start of the fillet radius
The outer surfaces of the boss to the start of the fillet radius	The integrally cast journals
The forward and aft faces of the boss	

in this respect are welding, straightening and burning on the sections of blade. In the case of hot straightening of the blade it is normally sufficient to lag the heated area with asbestos blankets so that it cools slowly: if the method of heating has been via a coke brazier, then it is helpful to let the fire die down naturally under the blade.

In the case of the high-tensile brasses and manganese–aluminium bronzes a large area of the blade which embodies the repair should be heated to a predetermined temperature, around 550 °C in the case of high-tensile brass and 650 °C in the case of manganese–aluminium bronze. The heat should be applied slowly and uniformly such that the isothermals are generally straight across the blade. The blade should then be allowed to cool as slowly as possible by lagging the blade and protecting the area from draughts. During the stress relief process control of the temperature needs to be carefully monitored. When the stress relief process is complete it is desirable to grind a portion of the blade surface and polish and etch it in order to demonstrate that a satisfactory microstructure has been produced.

For the nickel–aluminium bronzes the production of residual stresses can be minimized by ensuring that a large enough area of the blade is heated during the repair process, and to allow this to cool as slowly as possible so as to allow a slow plastic flow and relief of stress at the lower temperatures. During this process and particularly in the region of 300–400°C, the isothermals should be maintained as straight as possible across the blade.

Classification societies have strict procedures for stress relief and require that for all materials, except in certain cases for the nickel–aluminium bronzes, stress relief be carried out for weld repairs. Reference 1 gives the exception for nickel–aluminium bronze, as where the weld repair has not been carried out to the blade edge in board of the 0.7R and where repairs have not been made between the bolt holes or flange of a separately cast blade. Table 25.3 illustrates soaking times for the various propeller materials, again taken from Reference 1.

Table 25.3 Stress relief soaking times taken from LR rules 1989

Stress relief temperature (°C)	*Manganese bronze and nickel–manganese bronze*		*Nickel–aluminium bronze*		*Manganese–aluminium bronze*	
	Hours per 25 mm of thickness	*Maximum recommended total time (hours)*	*Time per 25 mm of thickness (hours)*	*Maximum recommended times (hours)*	*Time per 25 mm of thickness (hours)*	*Maximum recommended time (hours)*
350	5.0	15.0	—	—	—	—
400	1.0	5.0	—	—	—	—
450	0.5	2.0	—	—	5.0	15.0
500	0.25	1.0	1.0	5.0	1.0	5.0
550	0.25	0.5	0.5	2.0	0.5	2.0
600	—	—	0.25	1.0	0.25	1.0
650	—	—	0.25	0.5	0.25	0.5

References and further reading

1. Rules for the manufacture, testing and certification of materials. *Lloyd's Register of Shipping*, January, 1994.
2. Sinclair, L. The economics and advisability of ships propellers care and maintenance. *Ships Gear Int. Symp.*, July, 1968.
3. Meyne, K.J. Propeller repairs. *Ship Repair*, May, 1977.

Bibliography

Bahgat, F. *Marine Propellers*, Al Maaref. Est., Alexandria, 1966.
Bavin, Zavadovski, Levkovski, Mishevich. *Propellers: Modern Methods of Analysis*, Idatelstvc Sudoostroyeniye, Leningrad.
Biles, Sir J.H. *The Design and Construction of Ships*, Vol. 2, Griffin, London, 1923.
Cane, P. du. *High Speed Small Craft*, Temple Press Books, 1951.
Geer, D. *Propeller Handbook*, Nautical, 1989.
Hannan, T.E. *Strategy for Propeller Design*, Reed, 1971.
Isay, W.H. *Kavitation*, Schiffahrts-Verlag, Hansa C. Schroedter, 1981.
Lammeren, W.P.A. van. *Resistance, Propulsion and Steering of Ships*, The Technical Publishing Company H. Stam, Haarlem, Holland, 1948.
Milne-Thompson, L.M. *Theoretical Hydrodynamics* (5th edn), Macmillan, 1968.
Newman, J.N. *Marine Hydrodynamics*, MIT Press, 1977.
O'Brien, T.P. *The Design of Marine Screw Propellers*, Hutchinson, 1962.
Phillips-Birt, D. *Ship Model Testing*, Leonard Hill, 1970.
Rusetskii, A.A. *Hydrodynamics of Controllable Pitch Propellers*, Sudoostroyeniye, 1968.
Taggart, R. *Marine Propulsion: Principles and Evolution*, Gulf, 1969.
Young, F.R. *Cavitation*, McGraw-Hill, 1989.